DAPNIA/STCM 99-05 September 1999

ARGONNE LECTURES ON PARTICLE ACCELERATOR MAGNETS

VOLUME A

Arnaud Devred

(Prepared for the US Particle Accelerator School at Argonne National Laboratory, sponsored by the University of Chicago, June 14-25, 1999)

ARGONNE LECTURES ON PARTICLE ACCELERATOR MAGNETS

VOLUME A

Arnaud Devred

Service des Techniques de Cryogénie et de Magnétisme
Commissariat à l'Energie Atomique/Saclay
F–91191 GIF-SUR-YVETTE CEDEX
FRANCE

(Prepared for the US Particle Accelerator School
at Argonne National Laboratory,
sponsored by the University of Chicago,
June 14–25, 1999)

SYLLABUS

The quest for elementary particles has promoted the development of particle accelerators producing beams of increasingly higher energies. In a synchrotron, the particle energy is directly proportional to the product of the machine's radius times the bending magnets' field strength. Present proton experiments at the TeV scale require facilities with circumferences ranging from a few to tens of kilometers and relying on a large number (several hundred to several thousand) high field dipole magnets and high field gradient quadrupole magnets. These electro-magnets use high-current-density, low-critical-temperature superconducting cables and are cooled down at liquid helium temperature. They are among the most costly and the most challenging components of the machine.

After explaining what are the various types of accelerator magnets and why they are needed (lecture 1), we briefly recall the origins of superconductivity and we review the parameters of existing superconducting particle accelerators (lecture 2). Then, we review the superconducting materials that are available at industrial scale (chiefly, NbTi and Nb_3Sn) and we explain in details the manufacturing of NbTi wires and cables (lecture 3). We also present the difficulties of processing and insulating Nb_3Sn conductors, which so far have limited the use of this material in spite of its superior performances. We continue by discussing the two-dimensional current distributions which are the most appropriate for generating pure dipole and quadrupole fields and we explain how these ideal distributions can be approximated by so-called $\cos\theta$ and $\cos2\theta$ coil designs (lecture 4). We also present a few alternative designs which are being investigated and we describe the difficulties of realizing coil ends. Next, we present the mechanical design concepts that are used in existing accelerator magnets (lecture 5) and we describe how the magnets are assembled (lecture 6). Some of the toughest requirements on the performance of accelerator magnets are related to field quality. Lecture 7 summarizes the different sources of field errors (lecture 7). We follow by a brief overview of the cooling schemes which have been implemented in the various accelerator rings and we discuss the issues related to quench performance (lecture 8). Finally, we detail the quench protection schemes which are needed to ensure safe operations of the magnets (lecture 9).

A Why. S. pour tout

ACKNOWLEDGMENTS

This edition of the Argonne Lectures on Magnets would not have been possible without valuable contributions from

G. Ambrosio (FNAL)
P. Bauer (FNAL)
L. Bottura (CERN)
A. den Ouden (Twente Univ.)
C. Gourdin (CEA/Saclay)
S. Gourlay (LBNL)
E. Gregory (IGC)
R. Gupta (LBNL)
D. Hagedorn (CERN)
J. Jackson (FNAL)
P.J. Lee (Univ. of Wisconsin)
A. McInturff (LBNL)
P. McIntyre (TAMU)
F. Rodriguez-Mateos (CERN)
A. Siemko (CERN)
C. Verwaerde (Alstom)
A. Verweij (CERN)
M.N. Wislon (Oxford Instruments)
P. Wanderer (BNL)
R. Wolf (CERN)
S. Zlobin (FNAL)

Many thanks to M. Poinsot for helping me out with the preparation of the transparencies and of the paper copies.

SOURCES

The material used in these lectures is based upon and updated from previous lectures given on related topics, including:

– *Superconducting Magnets*, a 1-week course co-taught with T. Ogitsu at the US Particle Accelerator School sponsored by the University of Texas at Austin, January 6–17, 1992.

– *Waxahachie Lectures on Magnets*, a series of seminars given at SSC Laboratory in the Fall of 1992.

– *Magnetic Measurements of Accelerator Magnets*, a 1-week course co-taught with R.I. Schermer at the US Particle Accelerator School sponsored by the University of California at Los Angeles, January 17–28, 1994.

– *High Field Superconducting Magnets*, a short course taught at the Joint US–CERN–Japan School on Accelerator Physics & Technology, Maui, Hawaii, November 3–9, 1994.

– *Hawaiian Lectures on Magnets, Revisited*, a 2-day course taught at CEA/Saclay in early 1995.

– *Impact of Persistent and Eddy Currents on Accelerator Performances*, a seminar given at the CERN Accelerator School on Superconductivity in Particle Accelerators, jointly organized by DESY at Hauss Rissen, Hamburg , 17–24 May 1995.

The lectures also rely intensively on:

– A. Devred, Review of Superconducting Dipole and Quadrupole Magnets for Particle Accelerators, prepared for J.G. Webstor (ed.), *Encyclopedia of Electrical and Electronics Engineering*, New York: J. Wiley & Sons, 1999; revised for the Proceedings of the CERN Accelerator School on Measurement and Alignment of Accelerator and Detector Magnets, CERN/ 98–05, Geneva: CERN, pp. 43–78, 1998; revised for internal publication at CEA/Saclay, DAPNIA/STCM 98–07, Gif-sur -Yvette DAPNIA, August 1998.

SUGGESTED READINGS

– C. Quigg, *The Third Bernard Gregory Lectures*, CERN/89–11, Geneva: CERN, December 1989 (background articles on the goals of high energy physics).

– M.N. Wilson, *Superconducting Magnets*, Oxford: Clarendon Press, 1983 (*the* reference on superconducting magnets).

– S.W. Van Sciver, *Helium Cryogenics*, New York: Plenum Press, 1986 (*the* reference on helium).

– K.-H. Mess, P. Schmüser and S. Wolf, *Superconducting Accelerator Magnets*, Singapore: World Scientific, 1996.

– *Proceedings of the CERN Accelerator School on Superconductivity in Particle Accelerators*, CERN/ 96–03, Geneva: CERN, pp. 47–69, 1996 (collection of articles on superconductivity applied to accelerators, inlcuding: P. Schmüser, Superconductivity, pp. 1–45, and: M.N. Wilson, Superconducting materials for magnets, pp. 47–69.)

– P.J. Lee, Abridged metallurgy of ductile alloy superconductors, prepared for J.G. Webstor (ed.), *Encyclopedia of Electrical and Electronics Engineering*, New York: J. Wiley & Sons, 1999.

TABLE OF CONTENTS

VOLUME A

Lecture 1: Magnet Systems for Large Circular Accelerators 1–1

1.1 On the Need of High Energy Accelerators 1–3
1.2 Accelerator Types 1–9
1.3 Synchrotron-Type Accelerators 1–25
1.4 Layout of Large Circular Accelerators 1–37
1.5 Dipole and Quadrupole Magnets for Large Circular Accelerators 1–37
1.6 How to Produce Ideal Dipole and Quadrupole Magnetic Flux Densities? 1–55 1–71

Lecture 2: Superconductivity Applied to Particle Accelerator Magnets 2–1

2.1 Why Superconductivity? 2–3
2.2 Origin of Superconductivity and Critical Temperature 2–9
2.3 Magnetic States of Superconductors and Critical Fields 2–27
2.4 Transport Properties of Superconductors and Critical Current Density 2–51
2.5 Critical State Model 2–63
2.6 Review of Superconducting Particle Accelerators 2–85
2.7 Prominent Features of Superconducting Accelerator Magnets 2–107
2.8 Superconducting Accelerator Magnet R&D 2–119

Lecture 3: Conductor and Conductor Insulation for Particle Accelerator Magnets 3–1

3.1 Review of Superconducting Materials 3–3
3.1.1 NbTi Alloys 3–3
3.1.2 Nb_3Sn Compounds 3–15
3.1.3 HTS 3–27
3.2 Superconducting Multifilamentary Composites 3-31
3.3 Transition of Multifilamentary Wires 3–47
3.4 Manufacturing of NbTi Wires 3–69

3.5 Manufacturing of Nb3Sn Wires 3–91
3.6 Critical Surface Parametrizations 3–119
3.7 Rutherford-Type Cables 3–131
3.8 Interstrand Resistances in Rutherford-Type Cables 3–157
3.9 Critical Current Measurements on Rutherford-Type Cables 3–171
3.10 Cable Insulation 3–183
Appendix: Material Properties at Low Temperatures 3–203

VOLUME B

Lecture 4: Magnetic Design of Particle Accelerator Magnets 4–1

4.1 Complex Formalism for Two-Dimensional Fields 4–3
4.2 Multipole Field Expansion for Two-Dimensional Fields 4–15
4.3 Field Computations for Simple Current Distributions 4–33
4.4 Two-Dimensional Cosθ and Cos2θ Coil Designs 4–59
4.5 Iron Yoke Contribution 4–81
4.6 Operating Current Margin 4–87
4.7 Saddle-Shaped Coil End Designs 4–99
4.8 Other Designs 4–121
4.9 Sagitta of Arc Dipole Magnets 4–135
4.10 High Order Multipole Field Corrector Magnets 4–139

Lecture 5: Mechanical Design of Particle Accelerator Magnets 5–1

5.1 Components of the Lorentz Force in Cosθ and Cos2θ Magnetic Designs 5–3
5.2 Azimuthal Pre-Compression 5–15
5.3 Coil Mechanical Properties 5–31
5.4 Collar Designs 5–47
5.5 Radial Support 5–75
5.5.1 Designs with Self-Supported Collared-Coil Assemblies 5–75
5.5.2 Designs with Fully-Mated Yoke 5–79
5.5.3 Design with Yoke Midplane Gap 5–119
5.5.4 RHIC Magnets 5–143
5.5.5 Azimuthal Pre-Compression Versus Radial Support 5–149
5.6 End Support 5–161
5.7 Other Designs 5–185

Lecture 6: Asssembly of Particle Accelerator Magnets 6–1

6.1 Coil Winding 6–3
6.2 Coil Curing 6–17
6.3 Azimuthal Coil Size Measurements 6–31
6.4 Coil Assembly and Internal Splicing 6–45

6.5	Collaring	6–55
6.6	Collar Deflection Measurements	6–77
6.7	External Splicing	6–87
6.8	Yoke Stacking and Shell Welding	6–93
6.9	Yoke Midplane Gap Measurements	6–107
6.10	Cryostating	6–121
6.11	Instrumentation	6–135

VOLUME C

Lecture 7: Field Quality of Particle Accelerator Magnets **7–1**

7.1 Field Quality Requirements 7–3
7.2 Field Quality Measurements 7–13
7.3 Geometric Errors 7–29
7.4 Iron Saturation 7–63
7.5 Superconductor Magnetization 7–91
7.6 Time Drift of Superconductor Magnetization at Injection 7–109
7.7 Interstrand Coupling Currents 7–149
7.8 Periodic Pattern 7–197

Lecture 8: Quench Performance of Particle Accelerator Magnets **8–1**

8.1 Temperature and Enthalpy Margins 8–3
8.2 Magnet Cooling 8–17
8.3 What is a quench? 8–41
8.4 Magnet Training and Quench Plateau 8–47
8.5 Quench Origins 8–61
8.6 Phenomenological Model of Mechanical Training 8–73
8.7 Improving Quench Performance 8–77
8.8 Quench Performance as a Function of Ramp Rate 8–97
8.9 Specifications on Quench Performance 8–119

Lecture 9: Quench Protection of Particle Accelerator Magnets **9–1**

9.1 Quench Development 9–3
9.1.1 Simple Theoretical Model 9–3
9.1.2 Measuring Quench Propagation Using Voltage Taps 9–15
9.1.3 Measuring Quench Propagation Using Quench Antenna 9–27
9.1.4 Review of Propagation Velocity Measurements 9–39
9.2 The Effects of a Quench 9–51
9.3 Hot Spot Temperature 9–59
9.4 Quench Detection 9–79
9.5 Quench Protection Heaters 9–87
9.6 Protection of a Single Magnet 9–101
9.7 Protection of a Magnet String 9–113

LECTURE 1: MAGNET SYSTEMS FOR LARGE CIRCULAR ACCELERATORS

1.1 On the need of high energy accelerators 1–3

1.2 Accelerator types 1–9

1.3 Synchrotron-type accelerators 1–25

1.4 Layout of large circular accelerators 1–37

1.5 Dipole and quadrupole magnets for large circular accelerators 1–55

1.6 How to produce ideal dipole and quadrupole magnetic flux densities? 1–71

LECTURE 1: INTRODUCTION TO HIGH ENERGY CIRCULAR ACCELERATORS

1.1 On the need of high energy accelerators

1.2 Accelerator types

1.3 Synchrotron-type accelerators

1.4 Layout of high energy circular accelerators

1.5 Dipole and quadrupole magnets for high energy circular accelerators

1.6 How to produce ideal dipole and quadrupole magnetic flux densities

ON THE NEED OF HIGH ENERGY ACCELERATORS

– The main activity in nuclear and high energy physics is the study of the internal structures of charged particles.

– The research is carried out by smashing particles into pieces and by analyzing the nature and characteristics of the pieces.

– The particles are broken by accelerating them to high momenta and either by blasting them against a fixed target or by colliding them among themselves.

– To achieve high event rates, the particles are bunched together and the bunches are formatted into high intensity beams.

– The more elementary the particles, the higher the energy needed to smash them: experiments at the proton scale require beam energies of the order of 1 TeV or more (1 TeV $\approx$ $1.6\ 10^{-7}$ J).

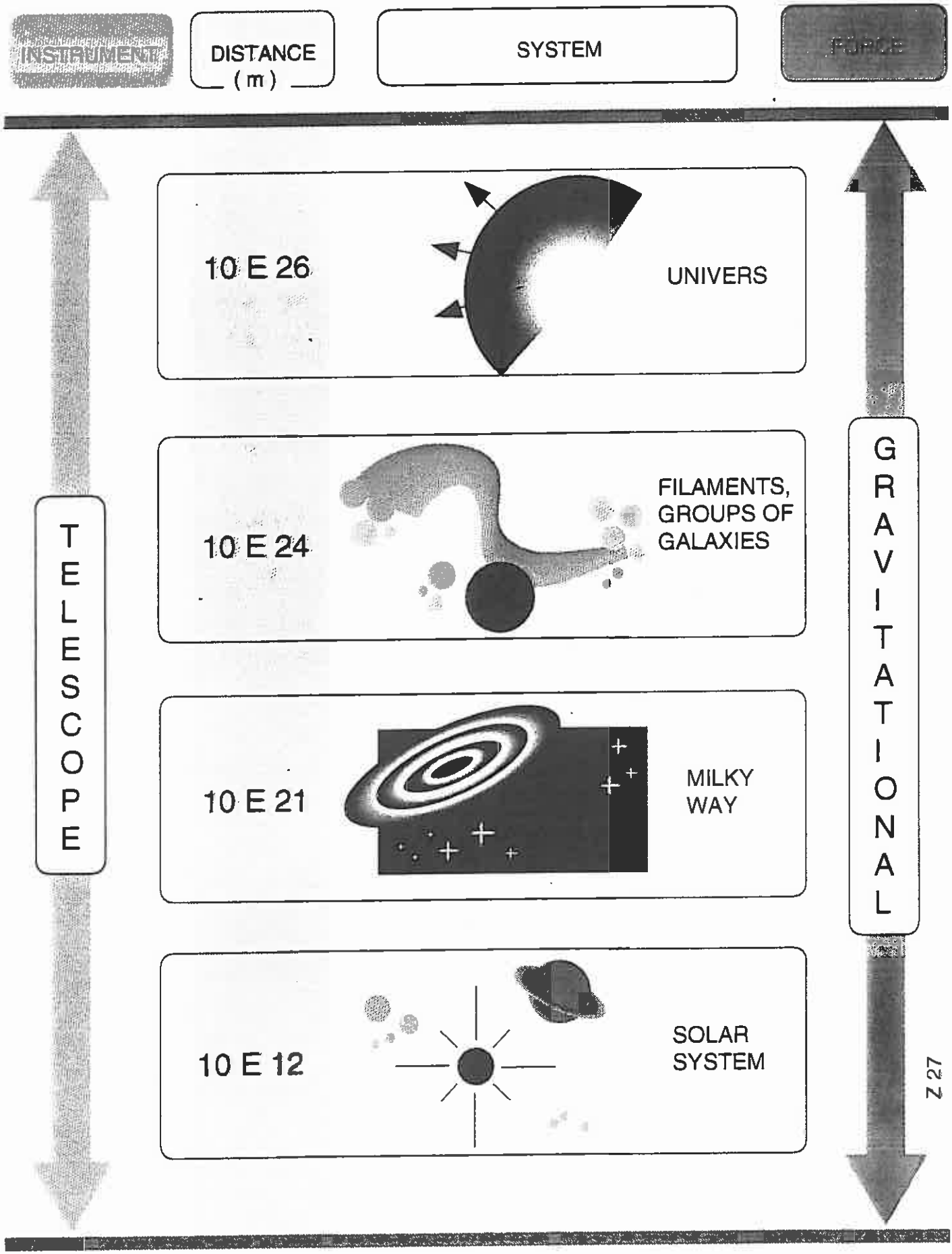
INSTRUMENT
DISTANCE
(m)
SYSTEM
FORCE
TELESCOPE
10 E 26
UNIVERS
10 E 24
FILAMENTS,
GROUPS OF
GALAXIES
10 E 21
MILKY
WAY
10 E 12
SOLAR
SYSTEM
GRAVITATIONAL
Z 27

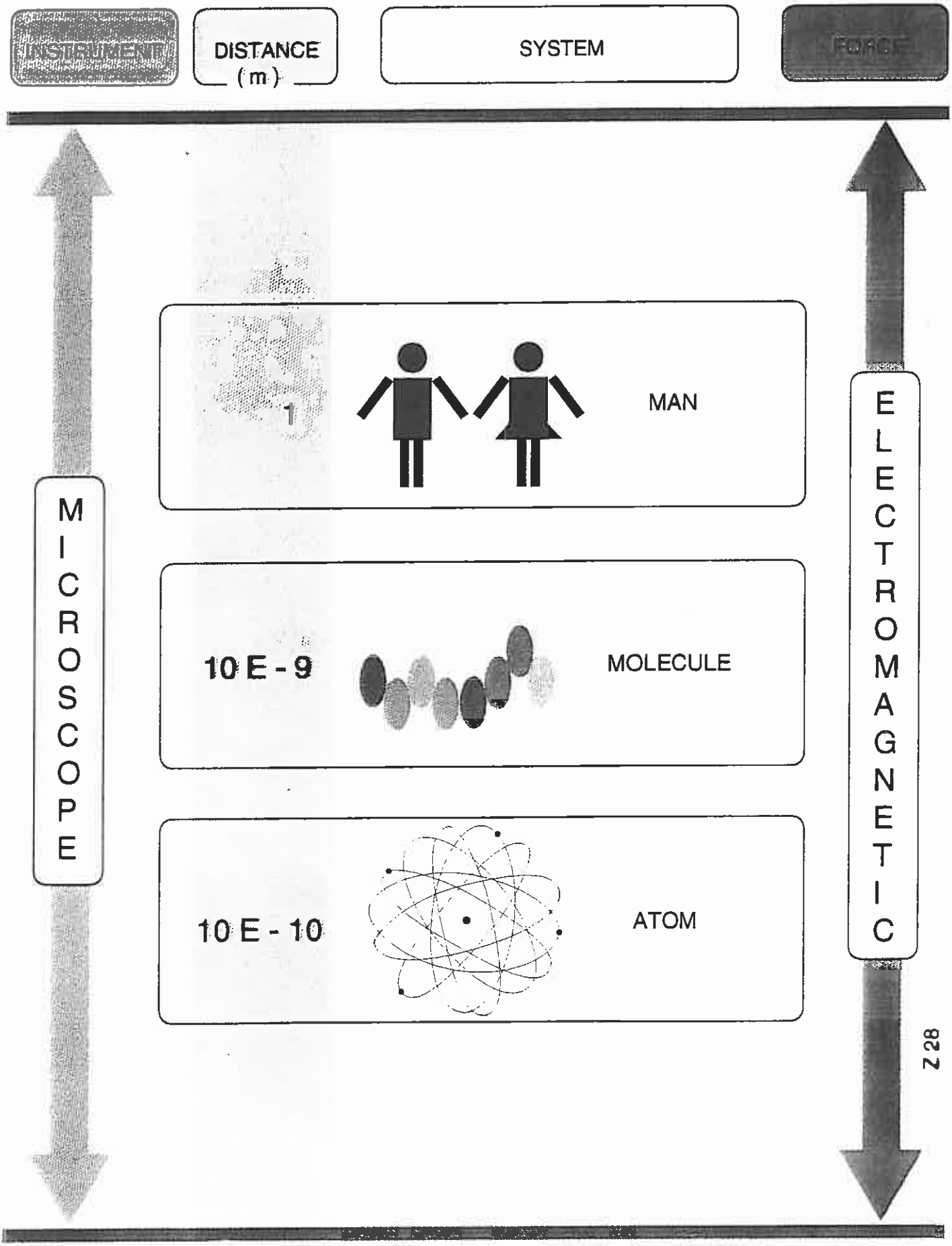
INSTRUMENT
DISTANCE
(m)
SYSTEM
FORCE
MICROSCOPE
ELECTROMAGNETIC
1
MAN
10 E - 9
MOLECULE
10 E - 10
ATOM
Z 28

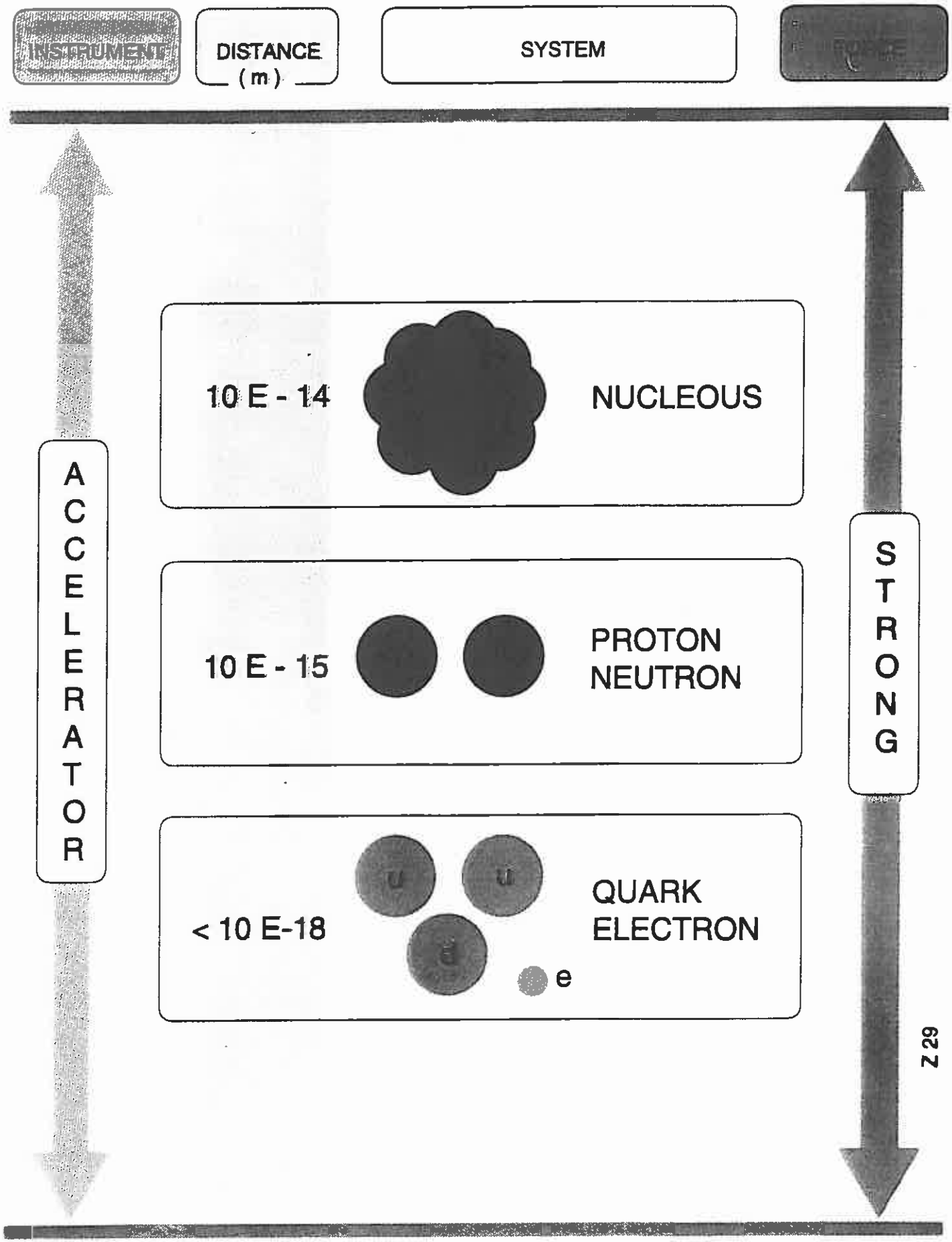
INSTRUMENT
DISTANCE
(m)
SYSTEM
FORCE
ACCELERATOR
10 E - 14
NUCLEOUS
10 E - 15
PROTON
NEUTRON
< 10 E-18
u
u
d
e
QUARK
ELECTRON
STRONG
Z 29

LECTURE 1: MAGNET SYSTEMS FOR LARGE CIRCULAR ACCELERATORS

1.1 On the need of high energy accelerators

1.2 Accelerator types

1.3 Synchrotron-type accelerators

1.4 Layout of large circular accelerators

1.5 Dipole and quadrupole magnets for large circular accelerators

1.6 How to produce ideal dipole and quadrupole magnetic flux densities?

ACCELERATOR TYPES

There are two main types of accelerators:

- **Linear Accelerators (linacs)**

In a linac, the charged particles travel along a mostly straight trajectory and go successively through a large number of accelerating stations.

Example: The 2-mile-long linac at Stanford Linear Accelerator Center (SLAC), capable of producing electron or positron beams with energies up to 50 GeV.

- **Circular Accelerators**

In a circular accelerator, the beam is circulated many times around a closed orbit.

A circular accelerator only relies on a few accelerating stations, through wich the charged particles go at every turn, but it requires a large number of guiding elements which are distributed over the accelerator arcs.

Example: The Large Electron Positron (LEP) Collider at the European Laboratory for Particle Physics (CERN). It has a 27 km circumference and is operated as an electron/positron collider with an energy of about 100 GeV per beam.

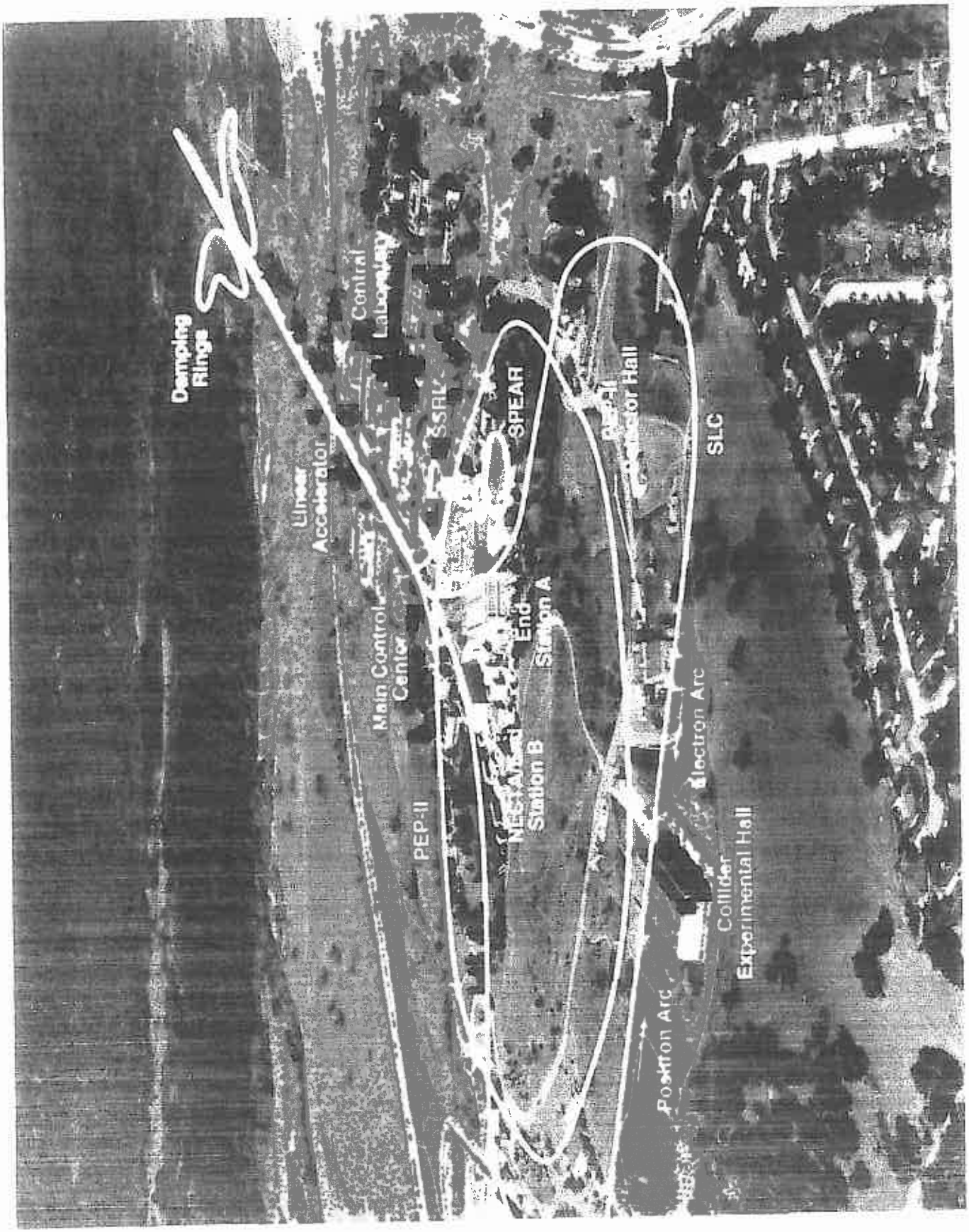
Damping Rings
Central Laboratory
Linear Accelerator
SSRL
SPEAR
Main Control Center
End Station A
Station B
PEP-II
SLC
Electron Arc
Collider Experimental Hall
Positron Arc

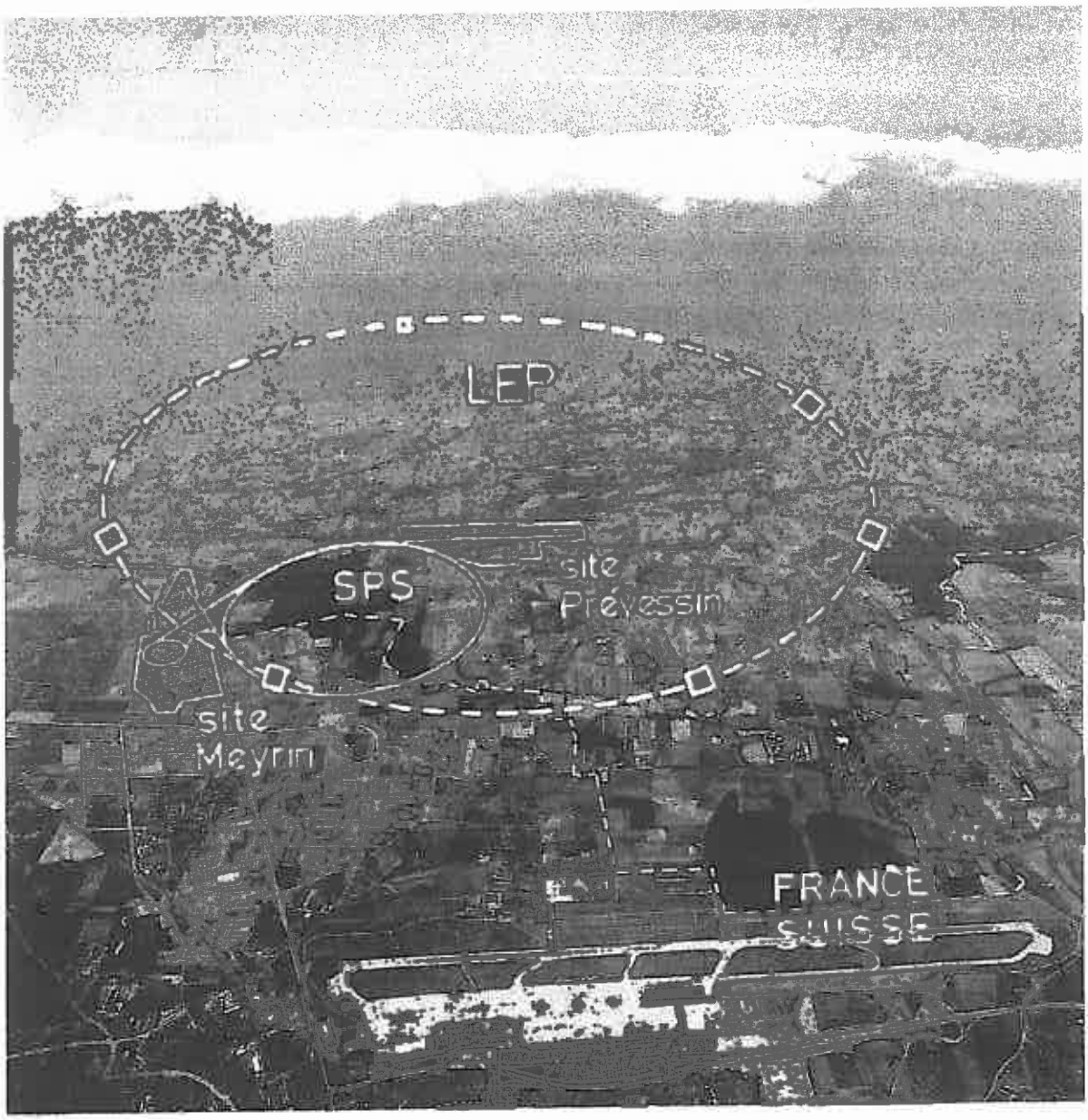
LEP
SPS
site
Préyessin
site
Meyrin
FRANCE
SUISSE

ACCELERATOR CHAINS

– The most powerful machines are made up of several stages, which progressively raise the beam energy.

– Each stage is a fully fledged accelerator which can be of either type.

Example: The CERN Accelerator Complex.

CERN Accelerators

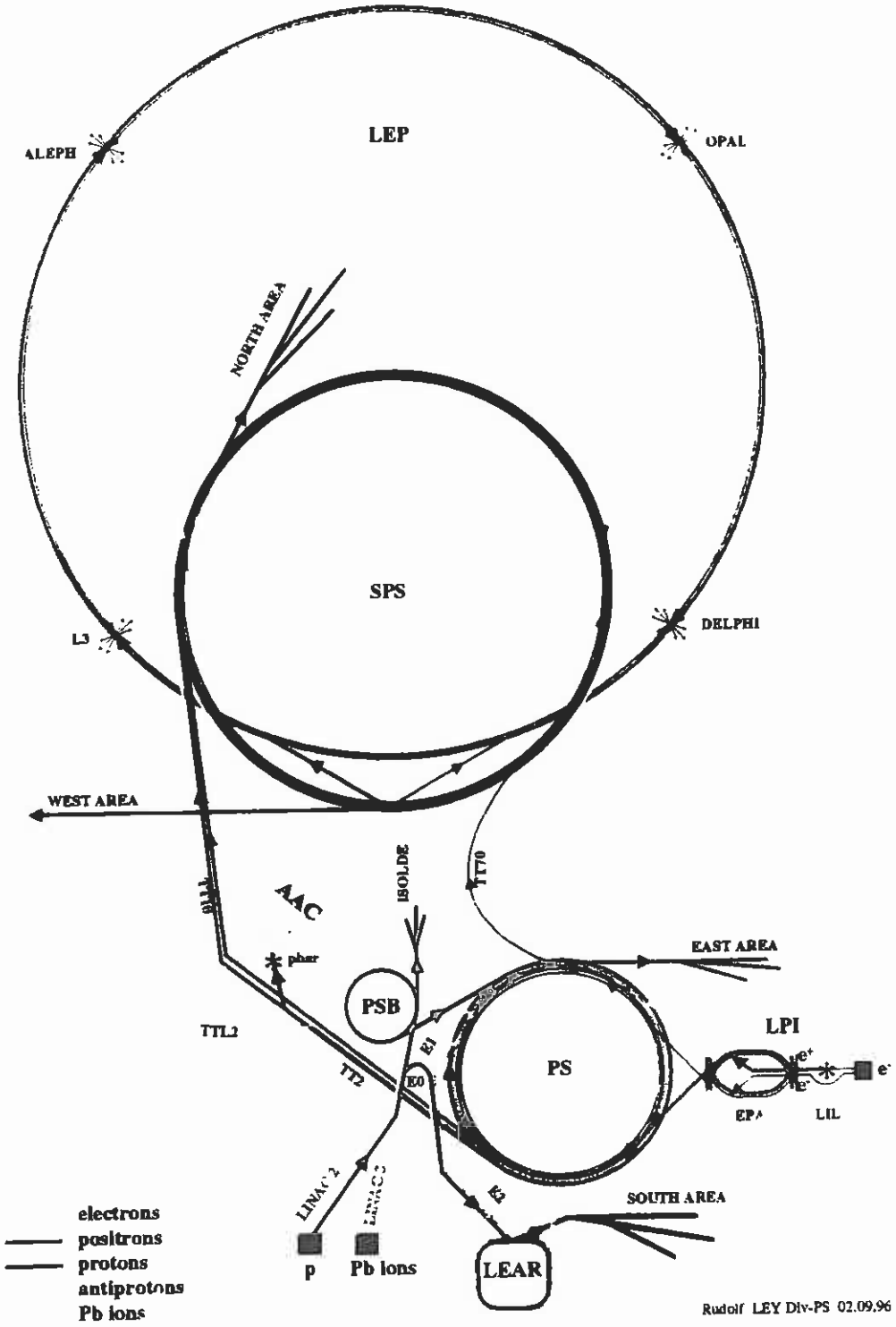

LEP: Large Electron Positron Collider
SPS: Super Proton Synchrotron
AAC: Antiproton Accumulator Complex
ISOLDE: Isotope Separator Online Device
PSB: Proton Synchrotron Booster
PS: Proton Synchrotron

LPI: Lep Pre-Injector
EPA: Electron Positron Accumulator
LIL: Lep Injector Linac
LINAC: Linear Accelerator
LEAR: Low Energy Antiproton Ring

CERN ACCELERATOR RINGS

- **Protron Synchrotron Booster (PSB)**

  – Diameter: 50 m
  – Maximum Proton Energy: 1 GeV

- **Protron Synchrotron (PS)**

  – Diameter: 200 m
  – Maximum Proton Energy: 26 GeV
  – Commissioning: 1959

- **Super Proton Synchrotron (SPS)**

  – Circumference: 6.9 km
  – Tunnel Depth: 25 to 65 m
  – Maximum Proton Energy: 450 GeV
  – Commissioning: 1976

- **Large Electron Positron (LEP) Collider**

  – Circumference: 27 km
  – Tunnel Depth: 50 to 150 m
  – Maximum Energy (per beam): 100 GeV
  – Commissioning: 1989

LHC AT CERN

– In December 1994, CERN has approved the construction in the LEP tunnel of the Large Hadron Collider (LHC).

– LHC will be a proton/proton collider with a maximum energy of 7 TeV per beam that will use the PSB, PS and SPS as injector chain.

– Commissioning is planned for 2005.

LEP EXPERIMENTS AT CERN

– The electron and positron beams of LEP are designed to collide at four interaction points.

– Each of the four interaction points are surrounded by experiments, made up of a large magnet system embedded in numerous arrays of detectors.

Example: The ALEH experiment includes a 7-m-long, 5-m-inner-bore superconducting solenoid, producing a 1.5 T central field with a stored energy of 140 MJ.

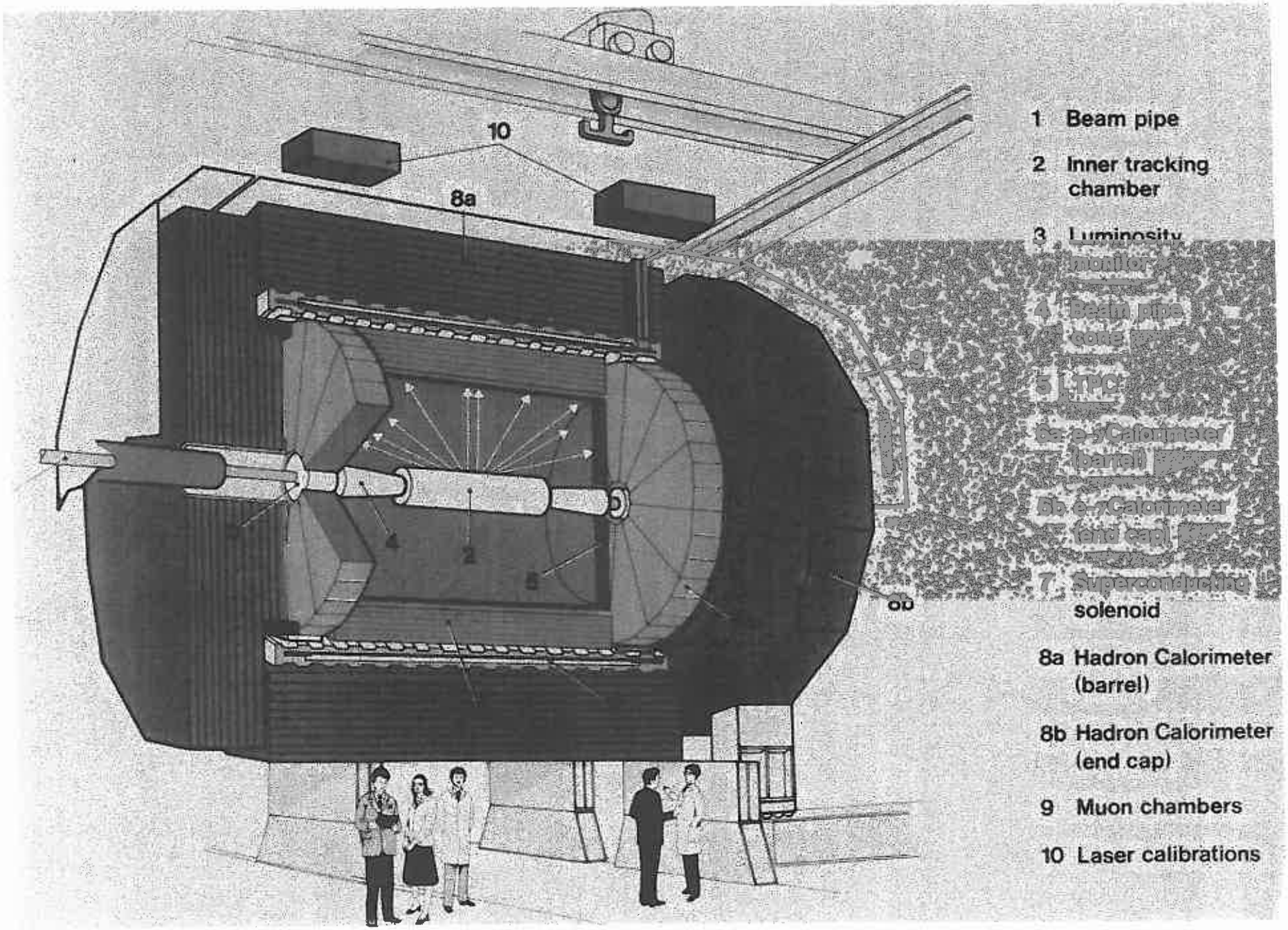
10
8a
1 Beam pipe
2 Inner tracking chamber
3 Luminosity monitor
4 Beam pipe coil
5 TPC
6a e.m. Calorimeter (barrel)
6b e.m. Calorimeter (end cap)
7 Superconducting solenoid
8a Hadron Calorimeter (barrel)
8b Hadron Calorimeter (end cap)
9 Muon chambers
10 Laser calibrations

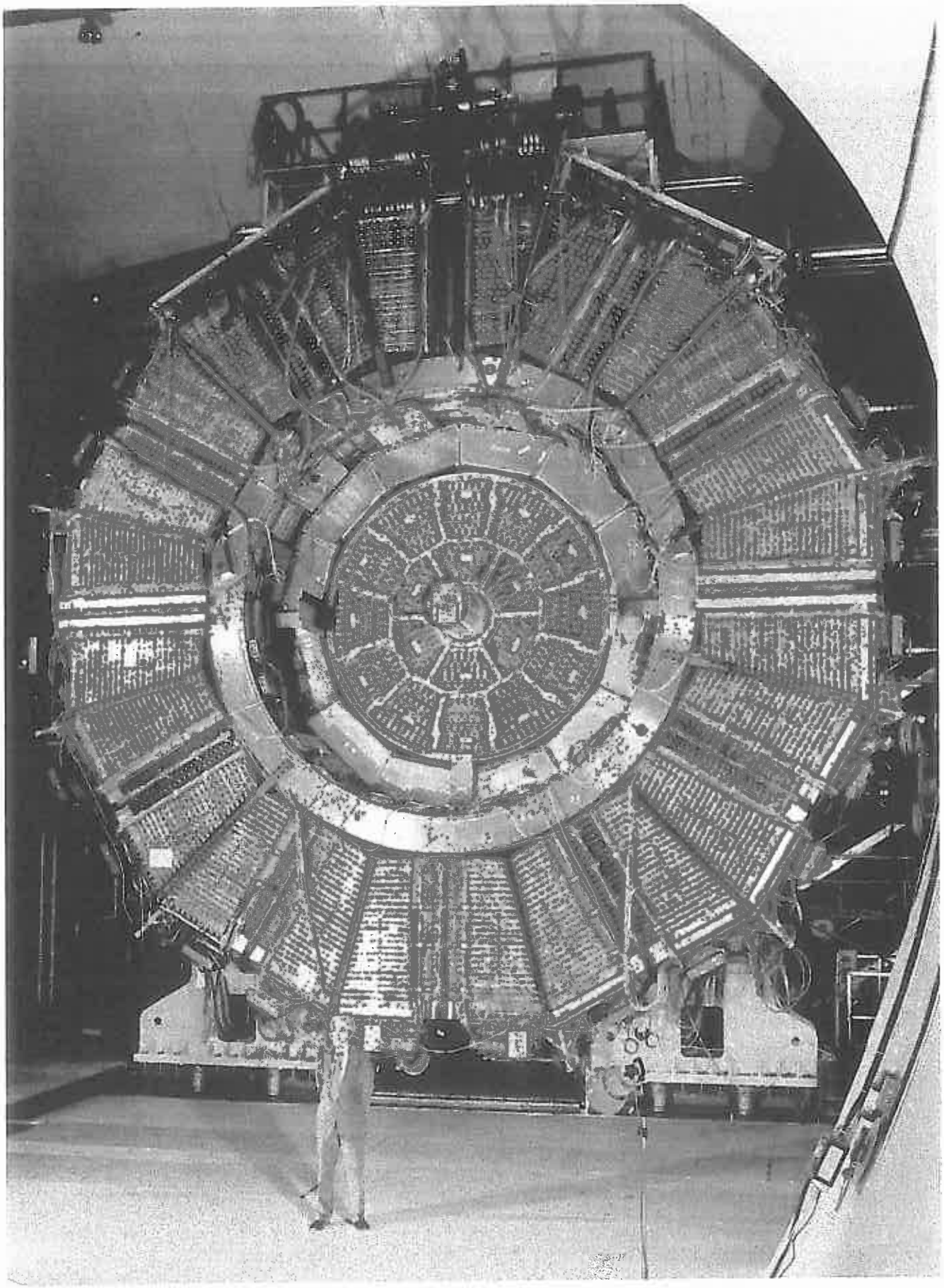

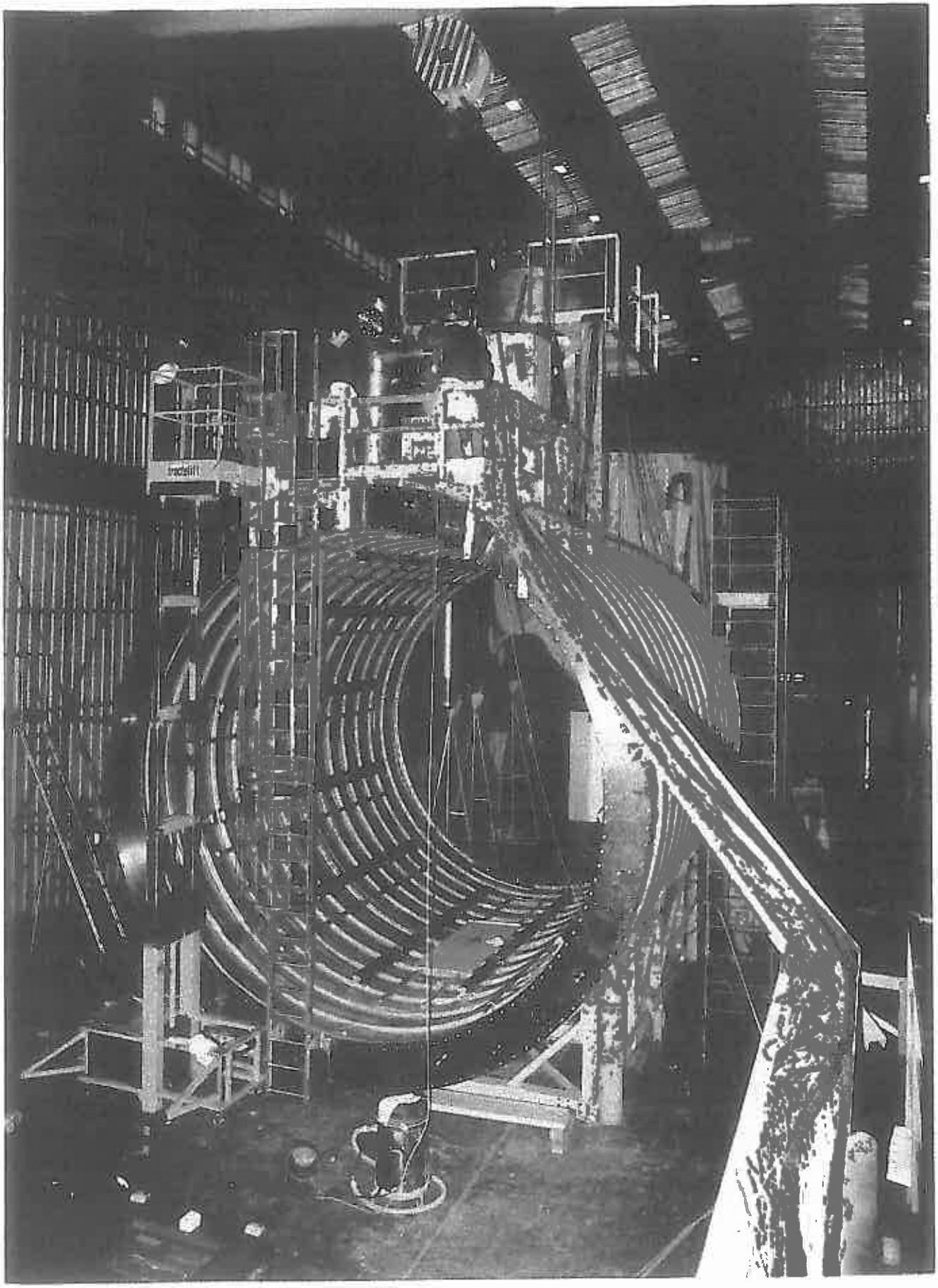

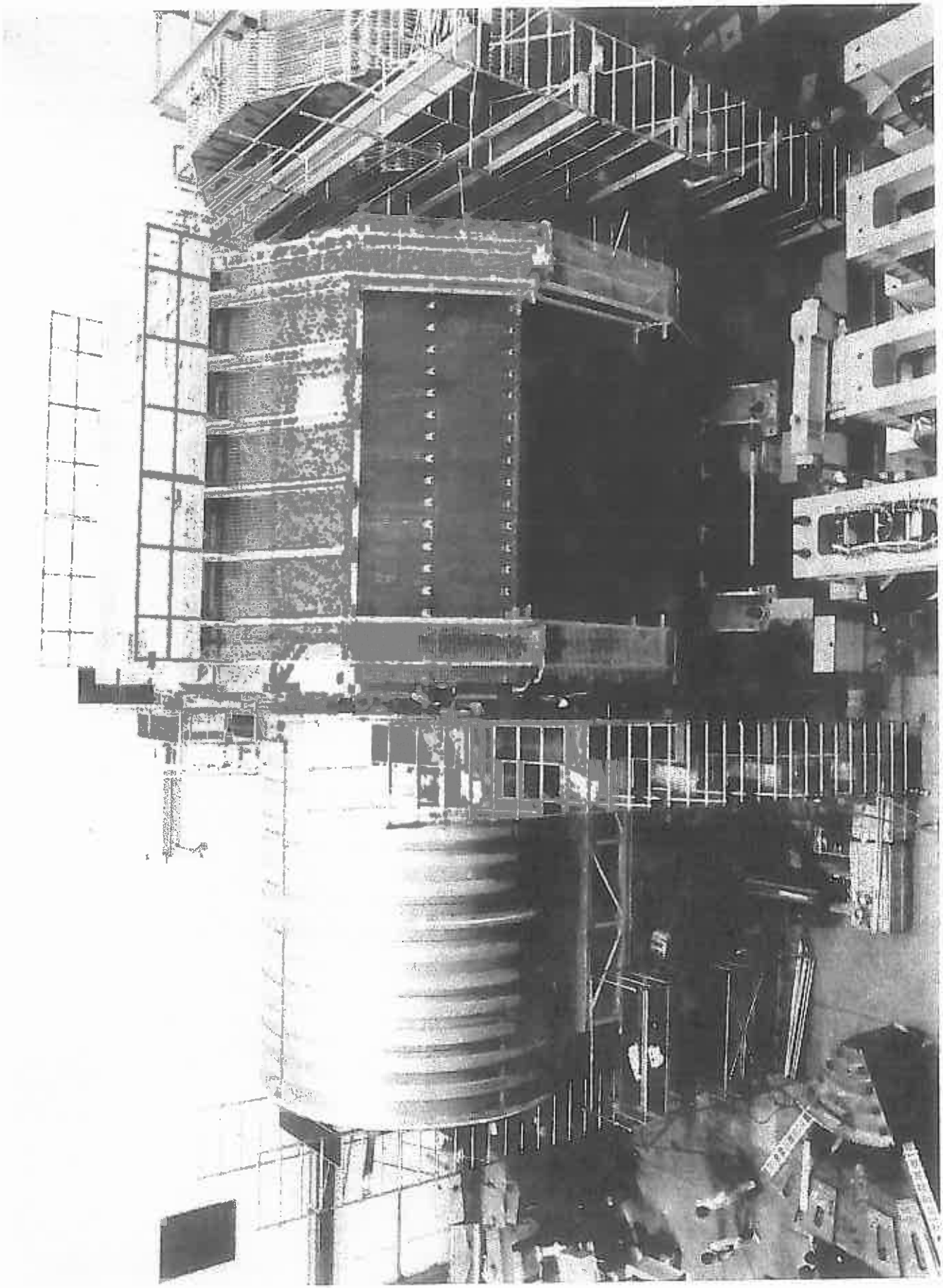

LECTURE 1: MAGNET SYSTEMS FOR LARGE CIRCULAR ACCELERATORS

1.1 On the need of high energy accelerators

1.2 Accelerator types

1.3 Synchrotron-type accelerators

1.4 Layout of large circular accelerators

1.5 Dipole and quadrupole magnets for large circular accelerators

1.6 How to produce ideal dipole and quadrupole magnetic flux densities?

ACCELERATOR MAIN RING

– In this series of lectures, we only consider accelerator systems whose last stage is a closed-orbit ring and we limit ourselves to the study of the guiding elements distributed over the ring arcs.

– Such a ring is operated in three phases:

• ***Injection,*** during which the beam, which has been prepared in various pre-accelerators, is injected at low energy,

• ***Acceleration,*** during which the beam is accelerated to nominal energy,

• ***Storage,*** during which the beam is circulated at nominal energy for as long as possible and is made available for physics experiments.

– Such a ring can be used for two types of experiments:

• ***Fixed-target*** experiments, for which a single beam is extracted from the main ring to be blasted against a fixed target,

• ***Colliding-beam*** experiments, for which two counter-rotating beams are blasted at each other.

SYNCHROTRON-TYPE ACCELERATORS

– The main ring of an accelerator chain is designed as a synchrotron-type accelerator where the beam is circulated on a closed orbit which remains the same throughout injection, acceleration and storage.

– It includes a small series of accelerating elements, which are located in one ring section, and through which the charged particles go at every turn.

– It also includes a large number of guiding elements, which are distributed over the ring arcs, and which are used to circulate and control the beam around its design orbit.

ACCELERATION

– The charged particles are accelerated by means of electric fields.

– The force, $\vec{F}_C$, exerted by an electric field, $\vec{E}$, on a charge, q, is given by Coulomb's law

$$\vec{F}_C = q\,\vec{E}$$

and results in an acceleration parallel to $\vec{E}$.

– In most particle accelerators, the accelerating stations are made up of Radio Frequencies (RF) cavities which can be superconducting.

Example: 12-m-long superconducting RF cavity modules for LEP2 at CERN. The modules are made up of 4 sections of 4 quasi-spherical cells, with an operating electric field of 6 MV/m.

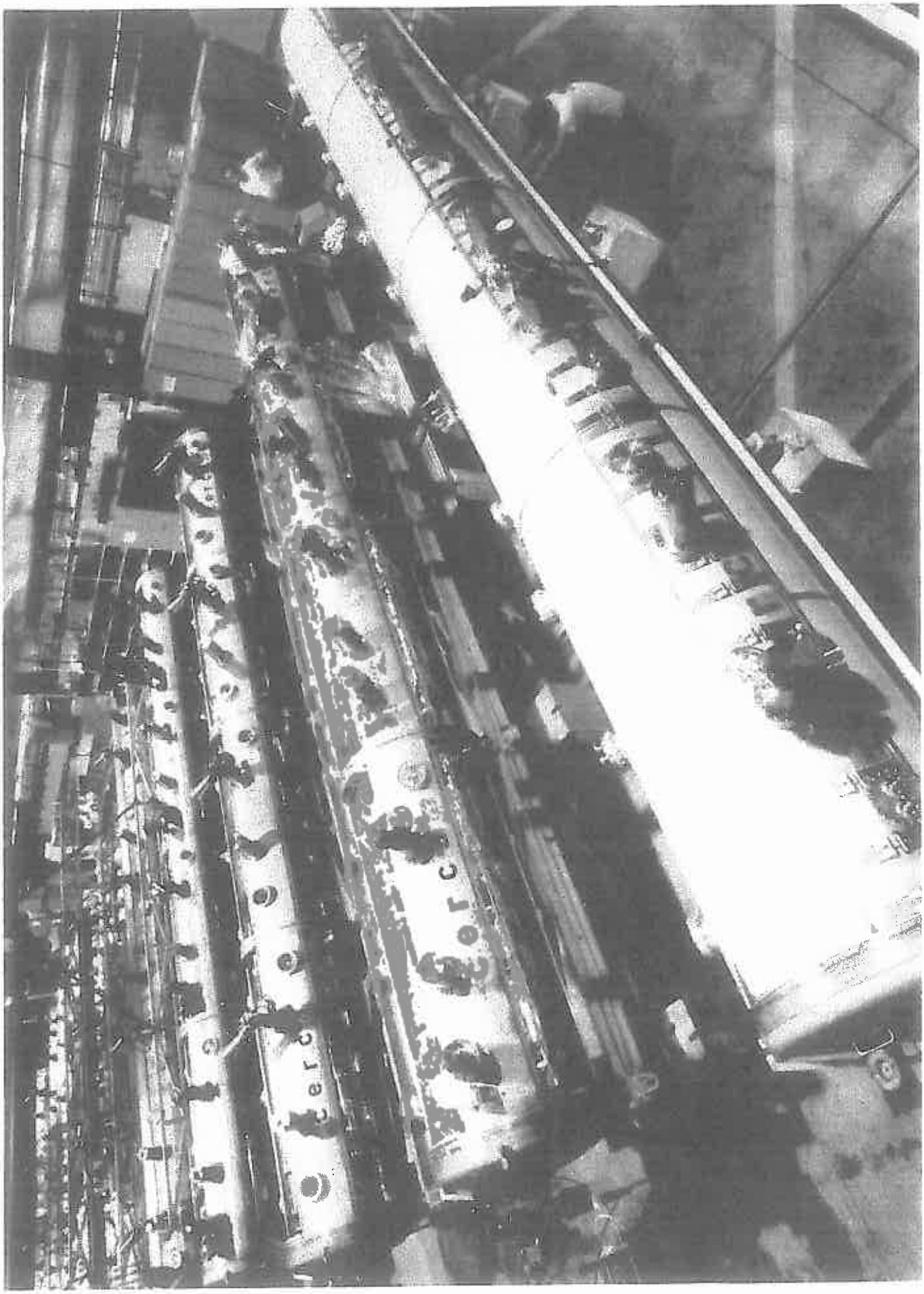

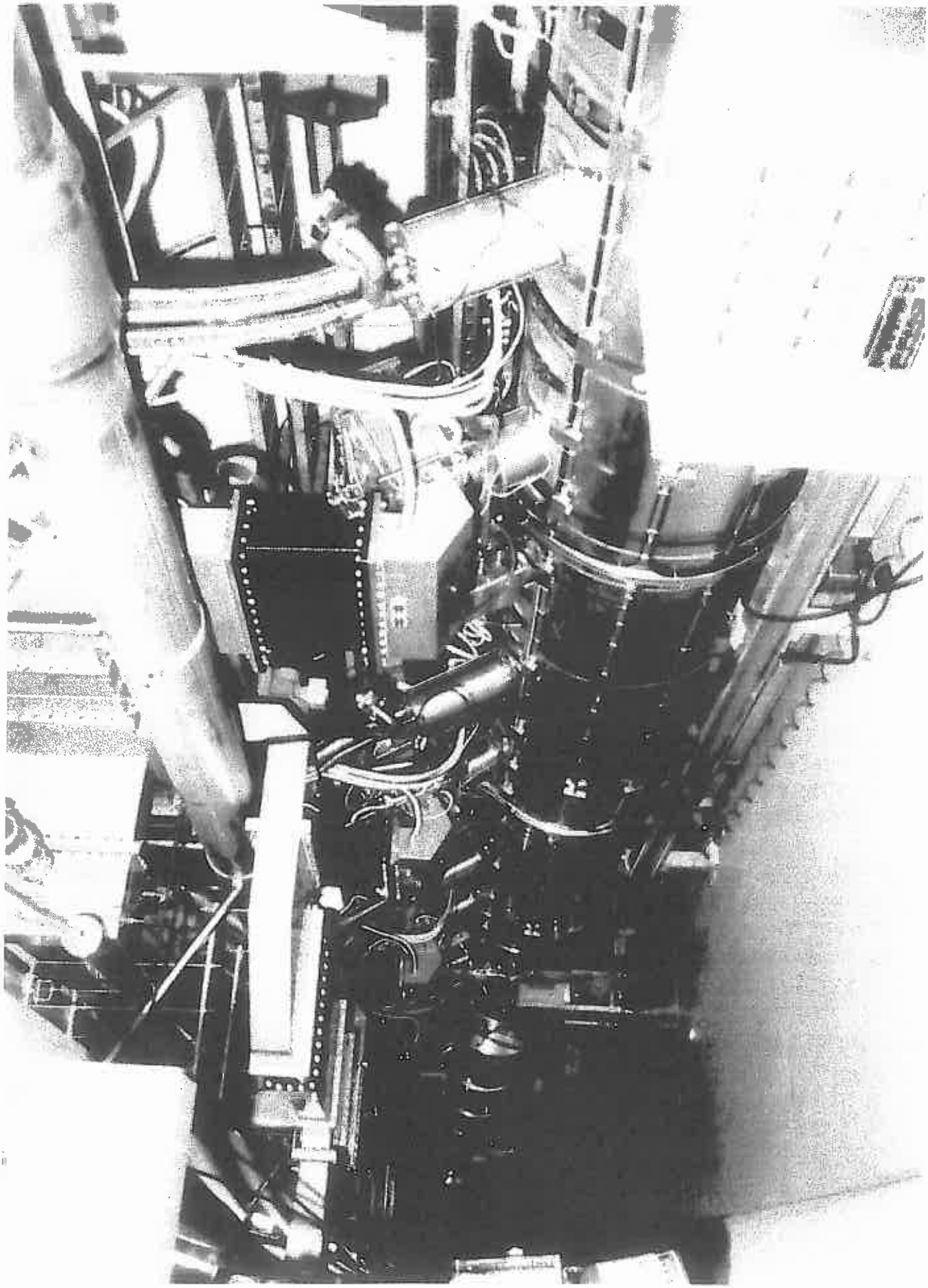

BENDING

– The particle beam is guided and focused by means of magnetic flux densities.

– The force, $\vec{F}_L$, exerted by a magnetic flux density, $\vec{B}$, on a charge, q, traveling at a velocity, $\vec{v}$, is given by Lorentz' law

$$\vec{F}_L = q\ \vec{v} \times \vec{B}$$

It is perpendicular to the direction of $\vec{v}$ and $\vec{B}$ and its only action is to bend the particle trajectory.

– In synchrotron-type accelerators, the magnetic flux densities are provided by electromagnets distributed around the ring.

Example: 6-m-long superconducting magnets for the Tevatron at Fermi National Accelerator Laboratory (FNAL).

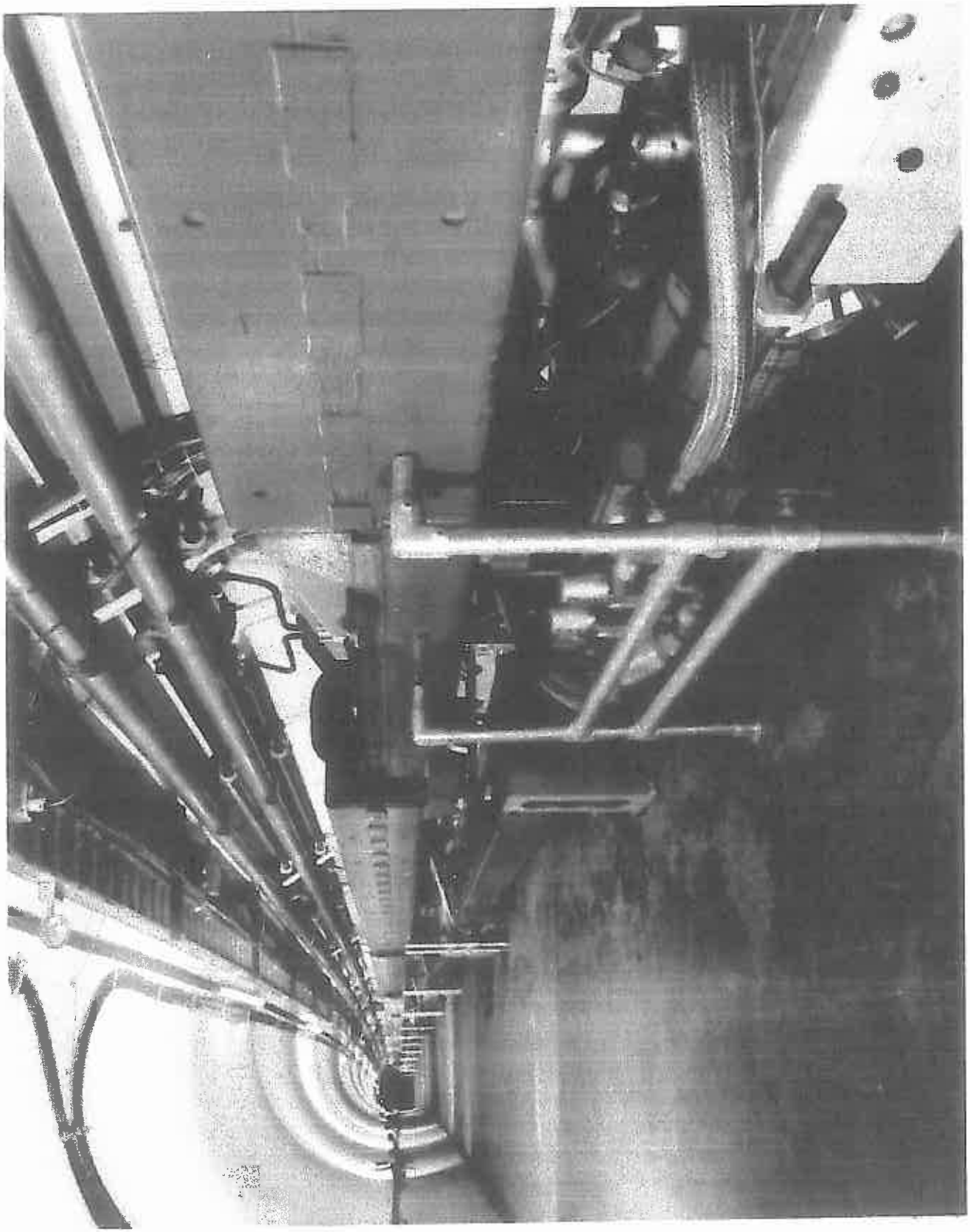

CIRCULAR ORBIT

– If $\vec{v}$ and $\vec{B}$ are perpendicular, the particle is deviated on an arc of a circle tangent to $\vec{v}$ and of radius, χ, which can be estimated as

$$\chi \approx \frac{\mathcal{E}_{\mathrm{GeV}}}{0.3\, q_e\, B}$$

Here, χ is in meters, B is the amplitude of $\vec{B}$ in teslas, q_e is the particle charge in units of electron charge, and $\mathcal{E}_{\mathrm{GeV}}$ is the particle energy in giga electron volts (GeV).

– The above equation shows that, to maintain a constant radius of curvature as the particle is accelerated, B must be ramped linearly with $\mathcal{E}_{\mathrm{GeV}}$.

BEAM ENERGY VERSUS BENDING RADIUS

– Let us use the equation for χ to dimension a 10 TeV proton accelerator:

	B (T)	χ (km)	Circumf. (km)
Low Field	2	16.7	105
Med. Field	6	5.6	35
High Field	10	3.3	21

– This simple computation shows that when designing a large synchrotron-type accelerator a trade-off must be found between the availability of land and the tunnelling costs, on one hand, and the faisability and the costs of the electromagnets, on the other hand.

BEAM ENERGY VERSUS BENDING RADIUS (CONT.)

– For the LHC at CERN, the χ-value is limited by the radius of curvature of the existing LEP tunnel.

– In the present (1999) design, χ is worth 2784.32 m and the magnetic flux density of the bending magnets in the storage/collision phase is set to 8.386 T.

– It follows from that the maximum proton energy is 7000 GeV.

LECTURE 1: MAGNET SYSTEMS FOR LARGE CIRCULAR ACCELERATORS

1.1 On the need of high energy accelerators

1.2 Accelerator types

1.3 Synchrotron-type accelerators

1.4 Layout of large circular accelerators

1.5 Dipole and quadrupole magnets for large circular accelerators

1.6 How to produce ideal dipole and quadrupole magnetic flux densities?

MAGNET LATTICE

– The main ring of an accelerator system includes a large number of electromagnets which are distributed over its arcs. These magnets have two main functions:

• *Bending* of the beam on a closed and constant orbit,

• *Focusing* of the beam to achieve a proper size and intensity.

– In large machines, the bending and focusing functions are separated: the former is provided by *dipole magnets* whereas the latter is provided by pairs of *focusing/defocusing quadrupole magnets.*

– The magnets are arranged around the ring arcs in a regular lattice of cells, each made up of a focusing quadrupole, a string of bending dipoles, a defocusing quadrupole and another string of bending dipoles.

– Several correction magnets are also implemented within each cell to allow better control of the beam optics.

Example: Present (1999) magnet lattice for the LHC arcs.

LHC LAYOUT

– The LHC ring is divided into 8 *bending arcs* separated by 8 quasi-straight *insertion regions.*

– The ring circumference is 26658.883 m and the length of the insertion regions is about 528 m.

– The two counter-rotating proton beams are circulated around the eight arcs and cross at the middle of four of the insertion regions.

– The accelerating RF cavities are located in one of the insertion regions where the beams do not cross.

– The points where the two beams cross are referred to as *interaction points* and the space around them is available for physics experiments.

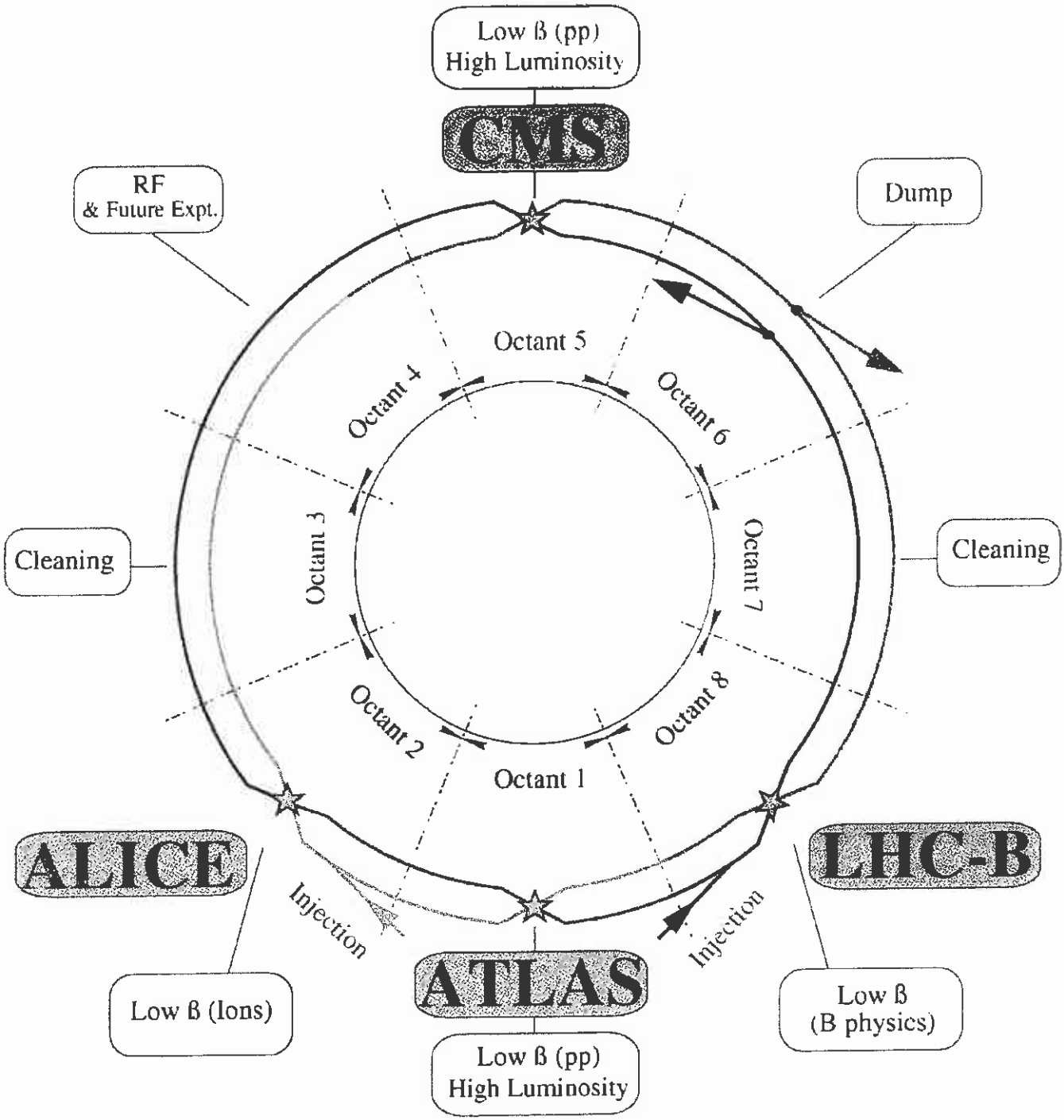

LHC layout

239 EXP

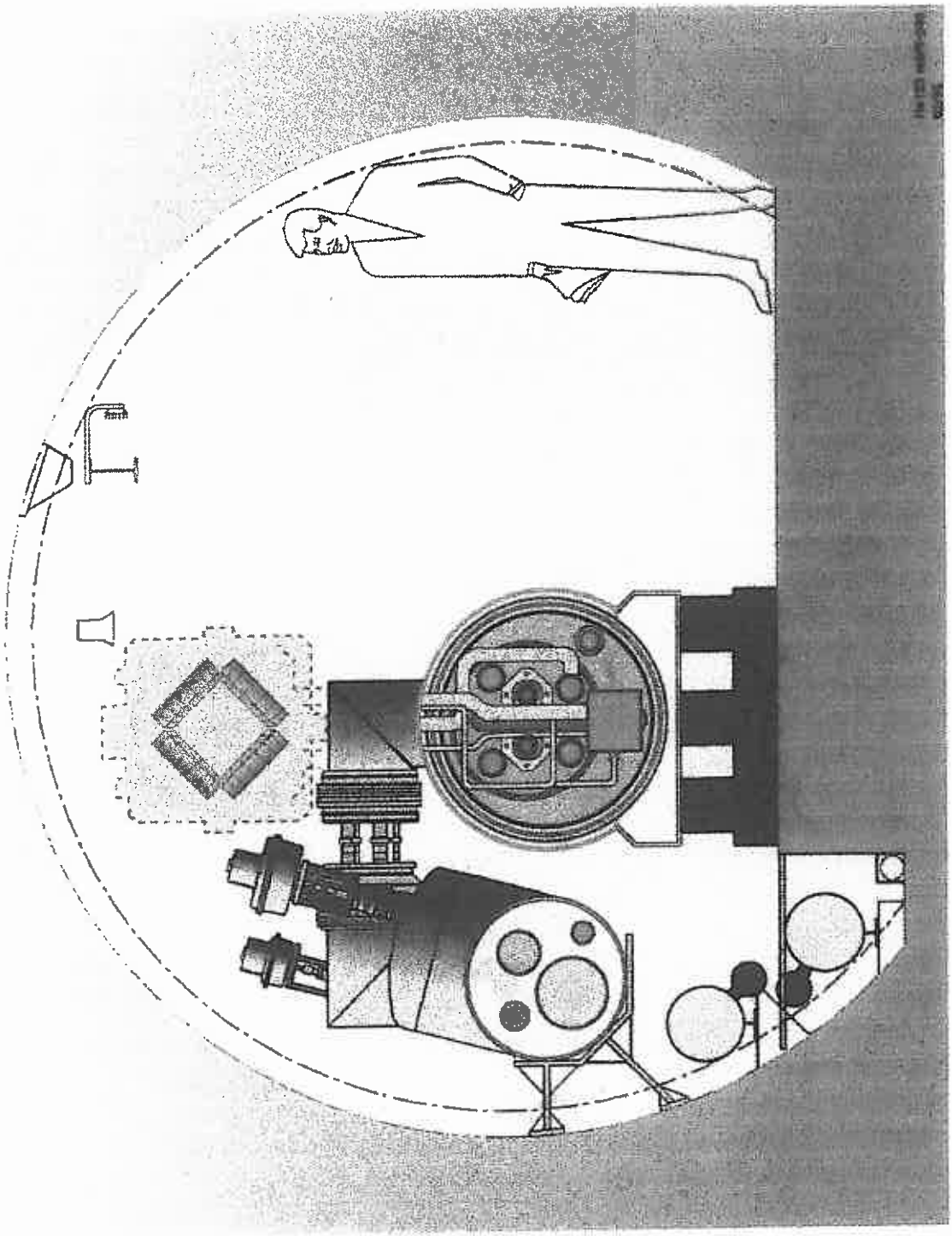

LHC ARCS

– Each of the 8 bending arcs includes 23 magnet cells, and each cell is made up of 6 dipole magnets, 2 quadrupole magnets and several corrector magnets.

– The arc dipole and quadrupole magnets have two apertures, one for each beam, and are referred to as *twin-aperture* magnets.

– The arc dipole magnets are 14.2 m long and the arc quadrupole magnets are 3.1 m long. The cell length is of the order of 106.9 m.

Schematic layout of LHC half-cell with 23 periods per octant

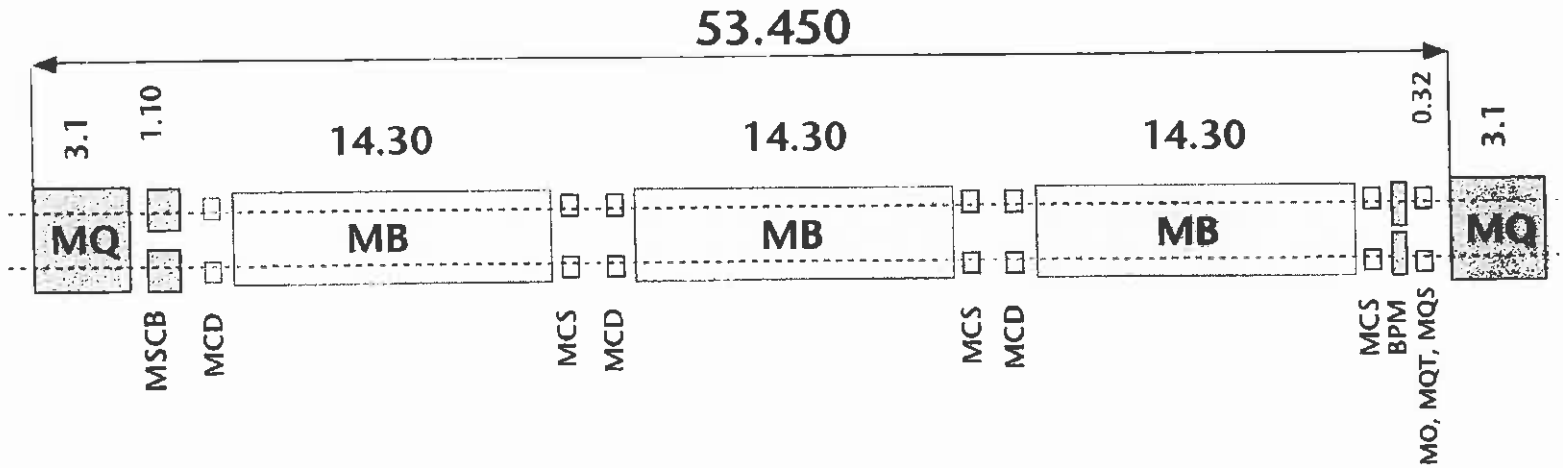

MQ : Lattice Quadrupoles
MB : Dipole magnet
MSCB : Combined Sextupole and Dipole correcteur

MO : Landau Octupole
MQT : Tuning Quadrupole
MQS : Skew Quadrupole

MCS : Local Sextupole corrector
MCD : Local Decapole corrector
BPM : Beam position monitor

LHC INSERTION REGIONS

– In addition to the arc dipole and quadrupole magnets and to the arc corrector magnets, an accelerator such as the LHC includes a number of other electromagnets, which are used to handle the beams in the insertion regions.

– In particular, there are sets of strongly focusing quadrupole magnets located near the interaction points.

– The design and fabrication of the insertion dipole and quadrupole magnets are similar to those of the arc dipole and quadrupole magnets.

ATLAS
INNER TRIPLET
Q1
Q2a
Q2b
Q3
D1
D2

LHC EXPERIMENTS

– At present (1999), two high energy physics experiments are being developed for the LHC:

• **ATLAS**, which stands for Air core Toroid for Large Acceptance Spectrometer, and includes a large toroid, made up of 8 racetrack-type coils, which are 25 m long and produce a useful field of 1 T for a total (8 coils) stored energy of 1.1 GJ. (The peakfield on the conductors is of the order of 4 T.)

• **CMS**, which stands for Compact Muon Solenoid, includes a 12.5-m-long solenoid with an inner bore of 6 m, which produces a useful field of 4 T for a stored energy of 2.7 GJ. (The peakfield on the conductors is of the order of 4.6 T.)

– The technology of detector magnets is very different from the technology of accelerator magnets and will not be discussed in the present lectures.

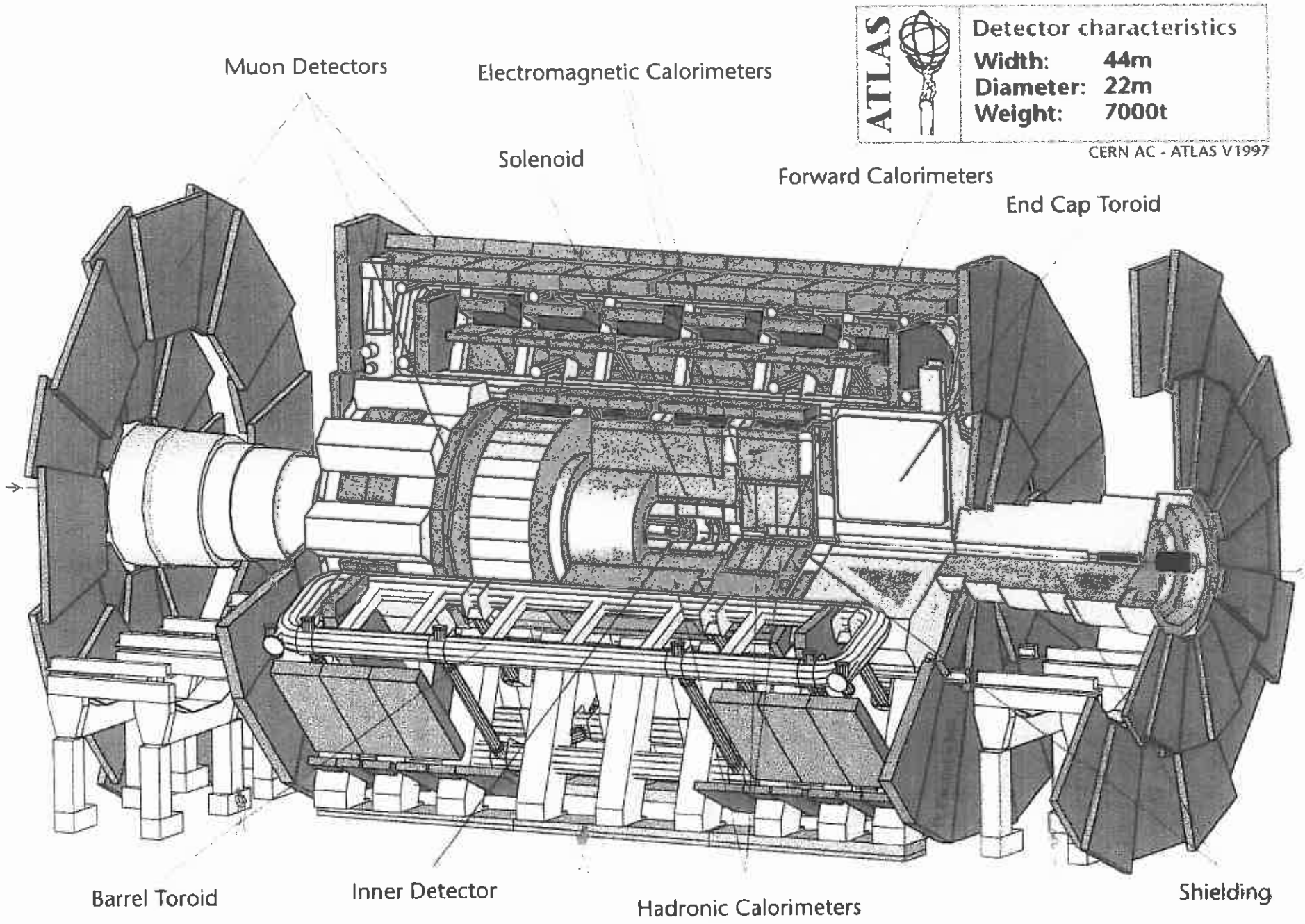
ATLAS
Detector characteristics
Width: 44m
Diameter: 22m
Weight: 7000t
CERN AC - ATLAS V1997
Muon Detectors
Electromagnetic Calorimeters
Solenoid
Forward Calorimeters
End Cap Toroid
Barrel Toroid
Inner Detector
Hadronic Calorimeters
Shielding

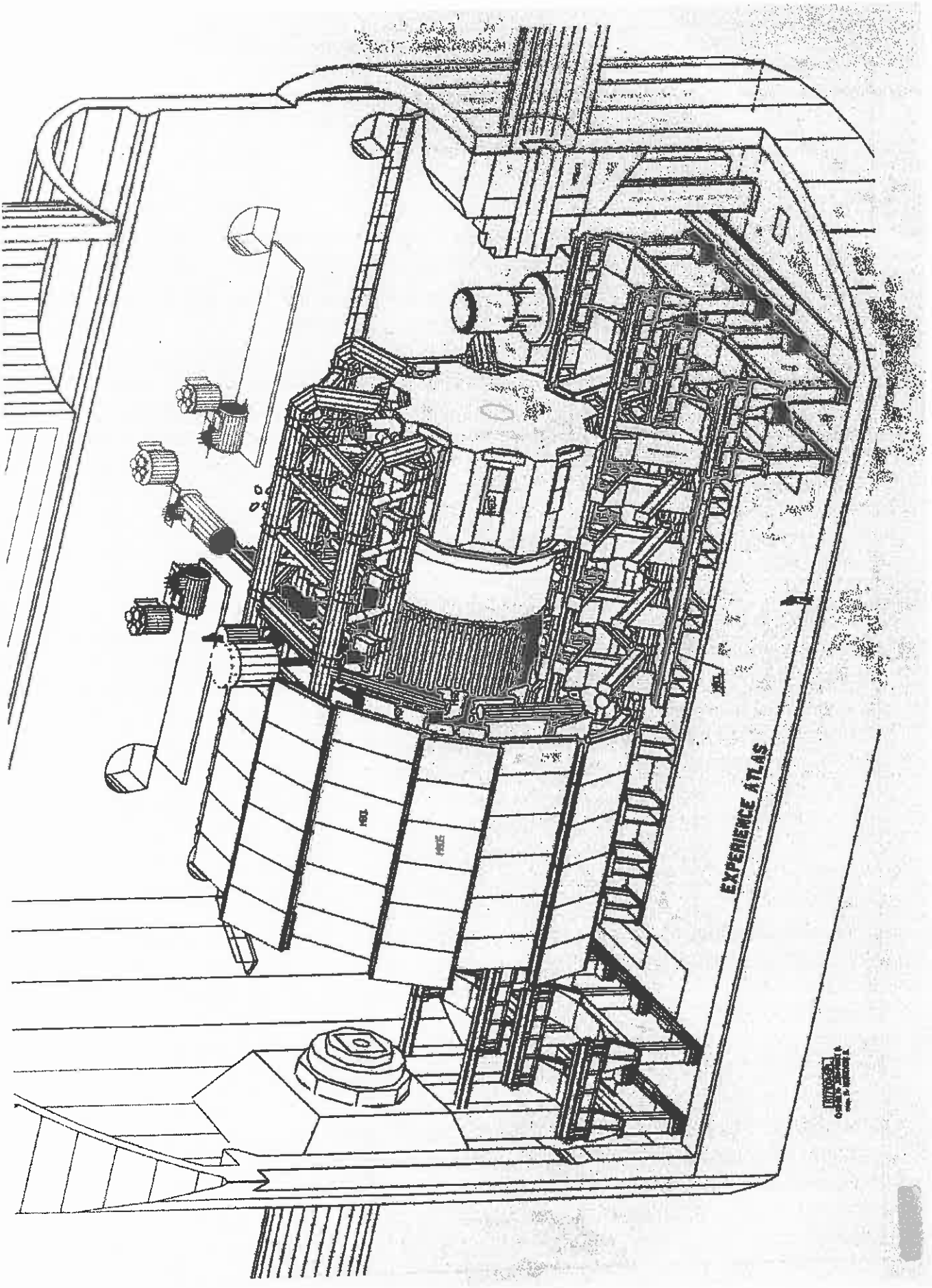
EXPERIENCE ATLAS

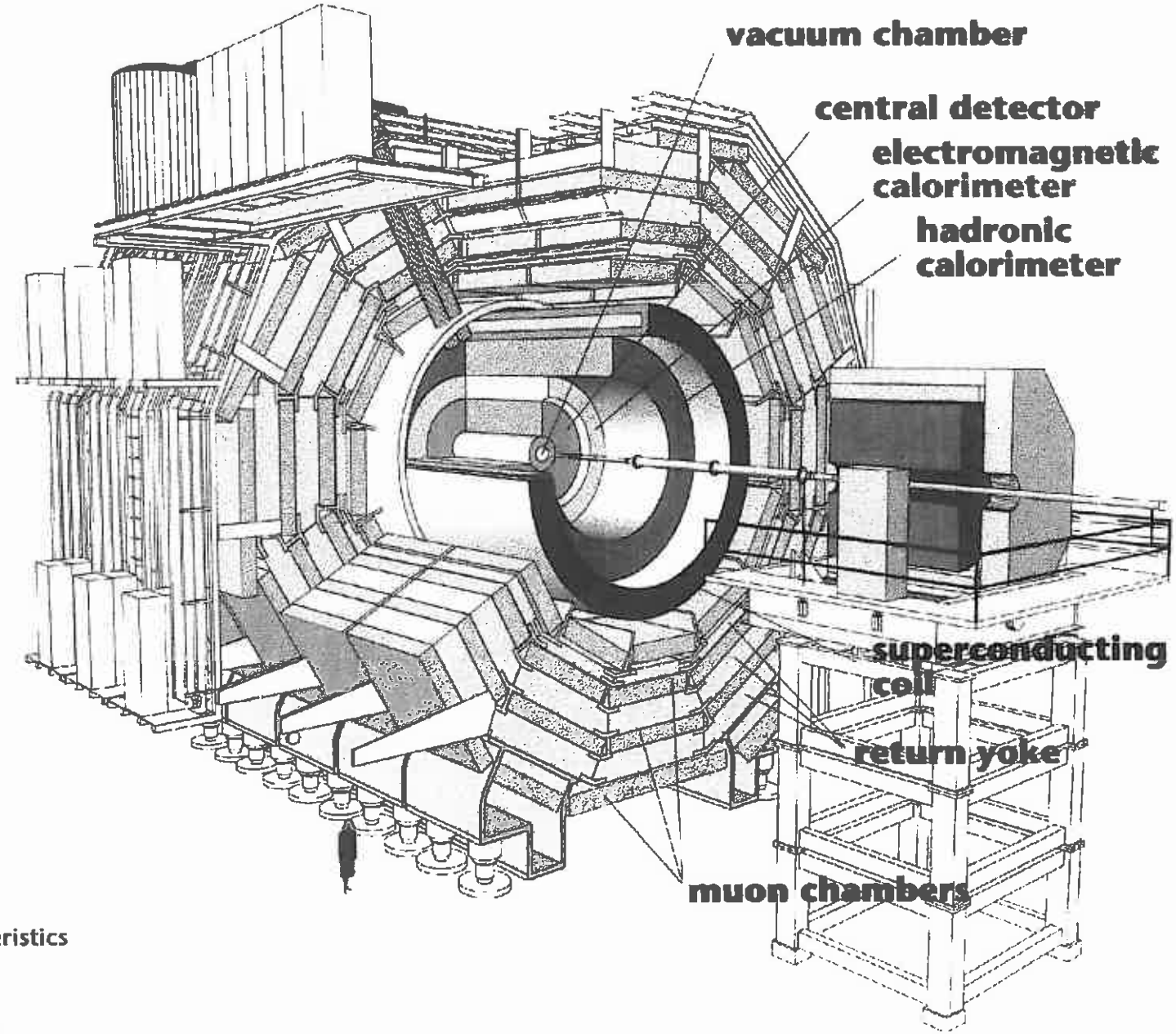

Detector characteristics

Width: 22m
Diameter: 15m
Weight: 14'500t

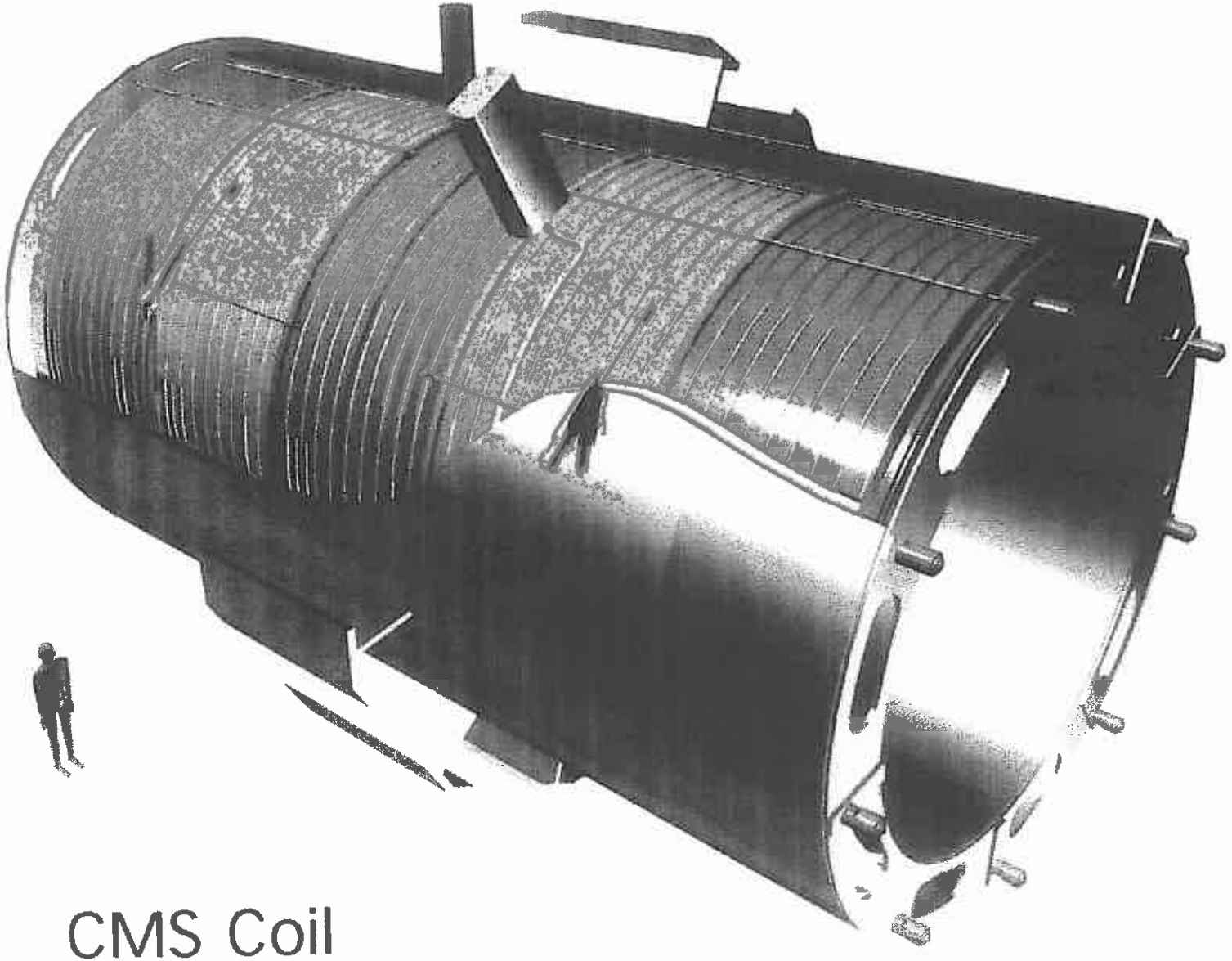

CMS Coil

MAGNET SUMMARY

– A machine such as the LHC requires a large number of superconducting magnets of various kinds.

– These magnets are by far the most challenging and the most costly items of the accelerator.

– They must be as reliable and as cost-effective as possible.

Table 1: Total number of magnets

Name	Equipment description	Total Number
MB	Arc dipole	1232
MBS	Separation dipole	8
MBT	Separation dipole	8
MBRS	Separation dipole	8
MBRT	Separation dipole	4
MBW	Warm separation dipole	16
MQ	Arc quadrupole	386
MQR	RF quadrupole	24
MQL	DS quadrupole	112
MQLT	DS trim quadrupole	68
MQX	Inner triplet quadrupole	32
MQXT	Inner triplet trim quadrupole	16
MQY	Wide aperture quadrupole	6
MQW	Cleaning warm quadrupole	48
MQS	Skew quadrupole	96
MSCBH	Arc sextupole/dipole corrector (horizontal)	360
MSCBV	Arc sextupole/dipole corrector (vertical)	360
MO	Arc octupole	360
MCB	Dipole corrector	228
MCBM	Mid-arc dipole corrector	16
MCBX	Inner triplet (h/v) dipole corrector	16
MCBY	Wide aperture dipole corrector	8
MCBW	Warm dipole corrector	24
MCQS	Inner triplet (a2) corrector	8
MCS	Sextupole corrector	2464
MCD	Decapole corrector	2464
MCDD	Inner triplet (b6) corrector	16
MCDDS	Inner triplet (a6) corrector	8

Yellow Book Design

LECTURE 1: MAGNET SYSTEMS FOR LARGE CIRCULAR ACCELERATORS

1.1 On the need of high energy accelerators

1.2 Accelerator types

1.3 Synchrotron-type accelerators

1.4 Layout of large circular accelerators

1.5 Dipole and quadrupole magnets for large circular accelerators

1.6 How to produce ideal dipole and quadrupole magnetic flux densities?

COORDINATE SYSTEM DEFINITIONS

– Let $(\Omega, \vec{X}, \vec{Y}, \vec{Z})$ designate a rectangular coordinate system, and let us consider an accelerator ring whose design orbit is planar and is located in the $(\Omega, \vec{X}, \vec{Z})$ plane.

– Let O be a given point of the design orbit, and let $(O, \vec{x}, \vec{y}, \vec{z})$ designate a rectangular coordinate system associated with O, such that $\vec{y}$ and $\vec{Y}$ are one and the same and $\vec{z}$ is tangent to the design orbit at O.

– In the following:

- The ***x*-axis** defines the **horizontal** direction,
- The ***y*-axis** defines the **vertical** direction,
- The ***z*-axis** corresponds to the main direction of particle motion.

COORDINATE SYSTEM DEFINITIONS (CONT.)

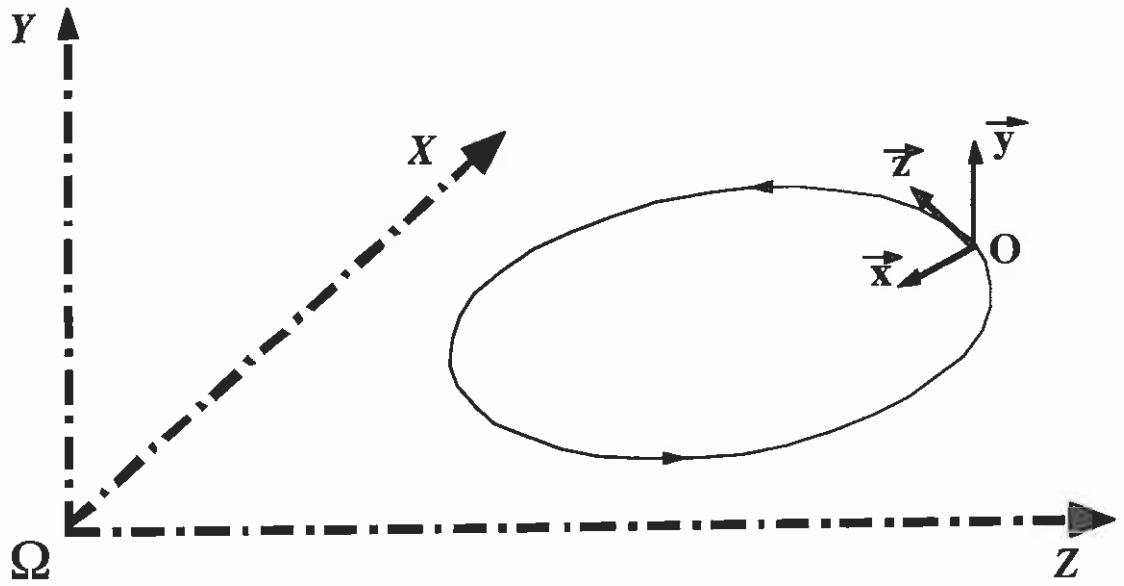

NORMAL DIPOLE MAGNET

– An ideal normal dipole magnet whose center is positioned at O is a magnet, which, within its aperture, produces a two-dimensional magnetic flux density parallel to the $(\vec{x}, \vec{y})$ plane and such that

$$B_x = 0 \qquad \text{and} \qquad B_y = B_1$$

where B_x and B_y are the x- and y-components of the magnetic flux density and B_1 is a constant referred to as the *dipole field strength* (in teslas).

FIELD LINES OF AN IDEAL NORMAL DIPOLE MAGNET

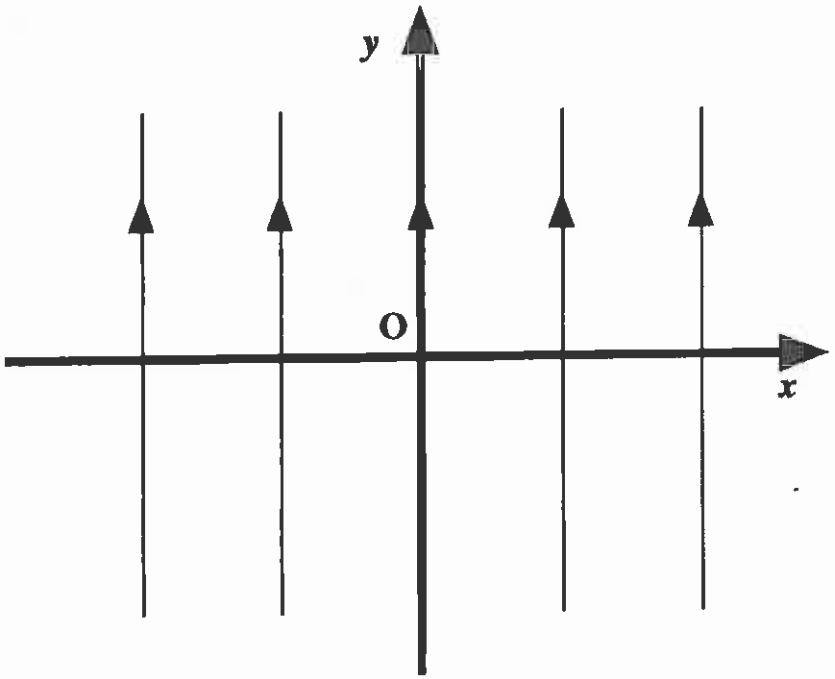

– **The field lines of an ideal normal dipole magnet are straight lines parallel to the *y*-axis.**

EFFECT OF A NORMAL DIPOLE MAGNET ON A BEAM OF CHARGED PARTICLES

– A charged particle traveling along the direction of the z-axis through the aperture of a normal dipole magnet of length, l_d, describes an arc of circle parallel to the horizontal $(\vec{x}, \vec{z})$ plane.

– This effect can be compared to that of a prism on a light ray.

BENDING ANGLE OF A NORMAL DIPOLE MAGNET

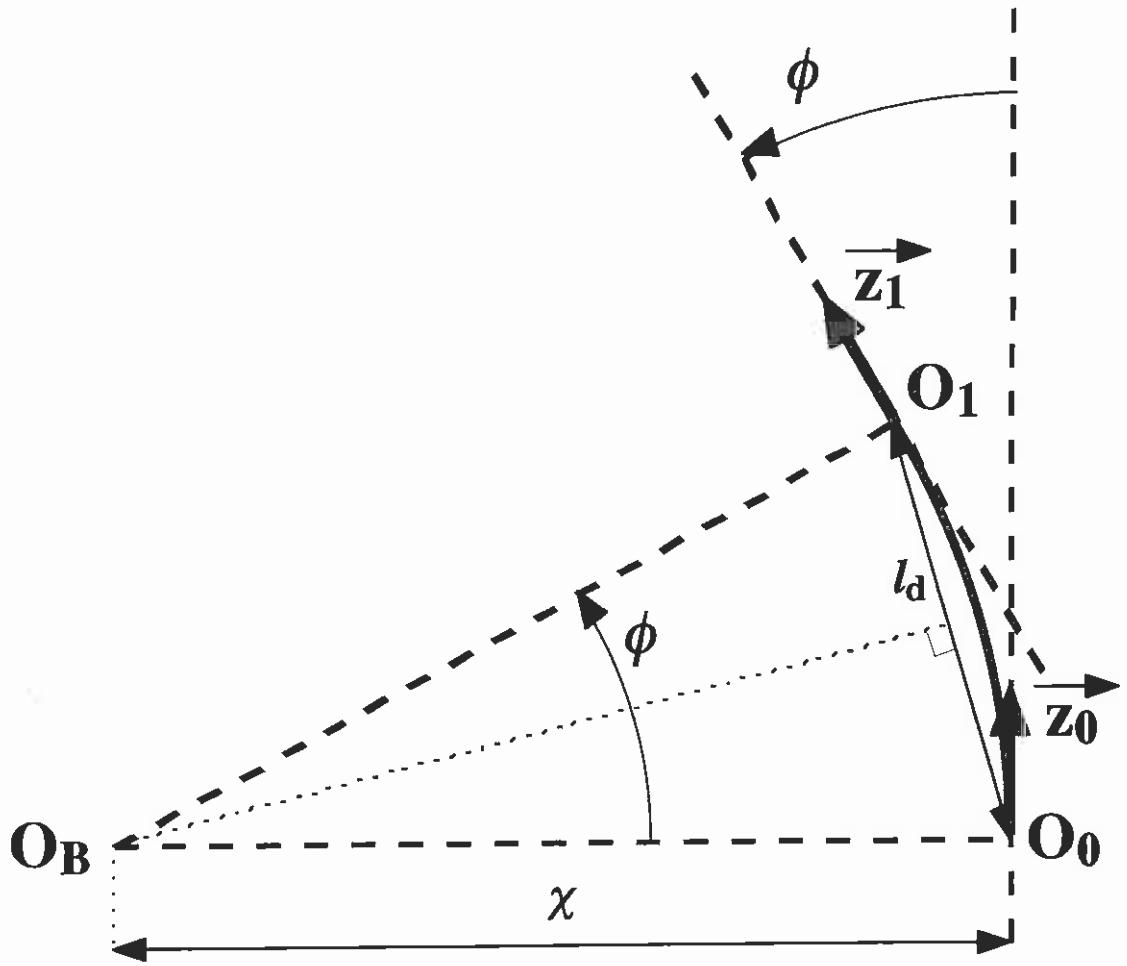

– The angular deflection, ϕ, of the particle trajectory can be estimated as:

$$\phi \approx \frac{0.3\, q_e\, B_1\, l_d}{\varepsilon_{GeV}} = \frac{l_d}{\chi}$$

where ϕ is in radians, l_d and χ are in meters, q_e is in units of electron charge, B_1 is in teslas, and ε_{GeV} is in GeV.

BENDING ANGLE OF LHC ARC DIPOLE MAGNETS

– For the storage/collision phase of the LHC at CERN, we have:

$$B_1 = 8.386 \text{ T}, \; l_d = 14.2 \text{ m}, \text{ and } \varepsilon_{GeV} \approx 7000$$

– It follows that a single arc dipole magnet bends the proton trajectory by an angle:

$$\phi \approx \frac{0.3 \, q_e \, B_1 \, l_d}{\varepsilon_{GeV}} = 5.2 \text{ mrad}$$

– A full (2π) rotation requires a number, N_d, of dipole magnets, where:

$$N_d = \frac{2\pi}{\phi} \approx 1232$$

NORMAL QUADRUPOLE MAGNET

– An ideal normal quadrupole magnet whose center is positioned at O is a magnet, which, within its aperture, produces a two-dimensional magnetic flux density parallel to the $(\vec{x}, \vec{y})$ plane and such that

$$B_x = g\,y \qquad \text{and} \qquad B_y = g\,x$$

where g is a constant referred to as the *quadrupole field gradient* (in teslas per meter).

FIELD LINES OF AN IDEAL NORMAL QUADRUPOLE MAGNET

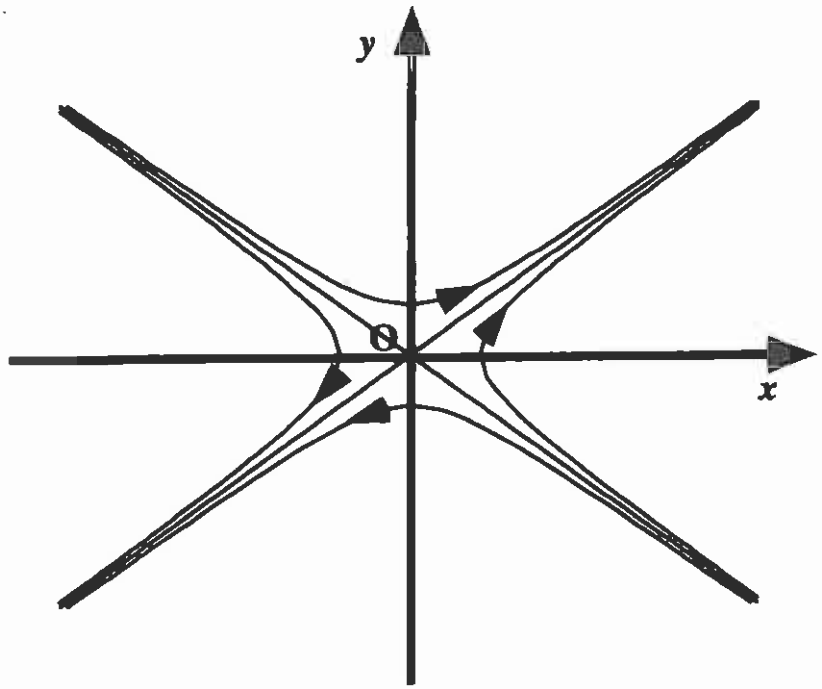

– The field lines of an ideal normal quadrupole magnet are hyperbolae of center O whose asymptotes are the first and second bisectors.

EFFECT OF A NORMAL QUADRUPOLE MAGNET ON A BEAM OF CHARGED PARTICLES

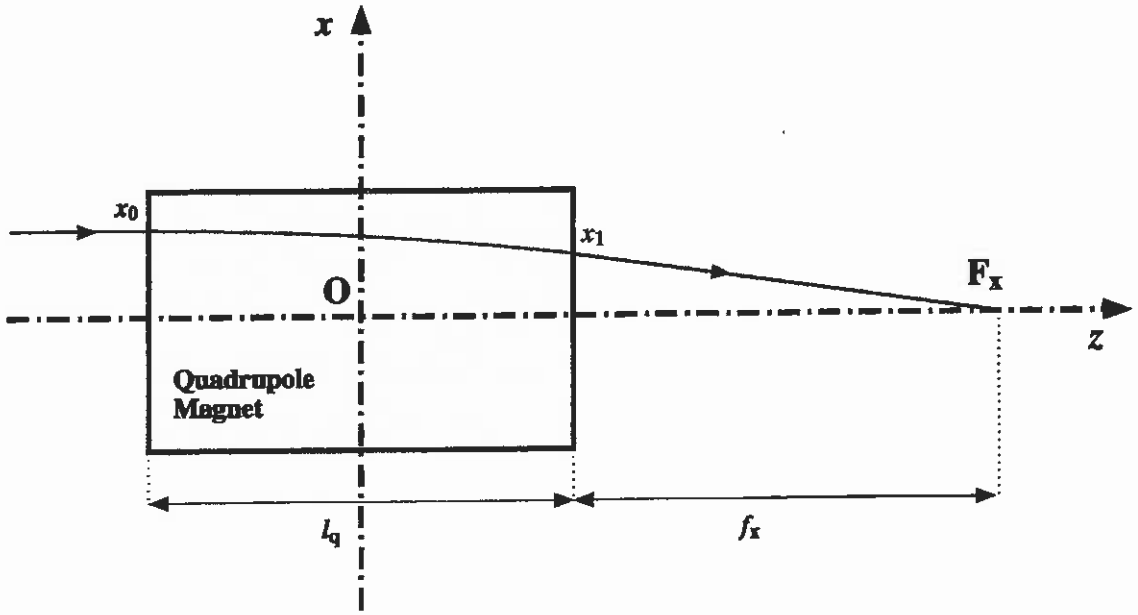

– A beam of positively charged particles traveling along the direction of the *z*-axis through the aperture of an ideal normal quadrupole magnet with a positive gradient is horizontally focused.

– This effect is similar to that of a focusing lens on a light ray.

EFFECT OF A NORMAL QUADRUPOLE MAGNET ON A BEAM OF CHARGED PARTICLES (CONT.)

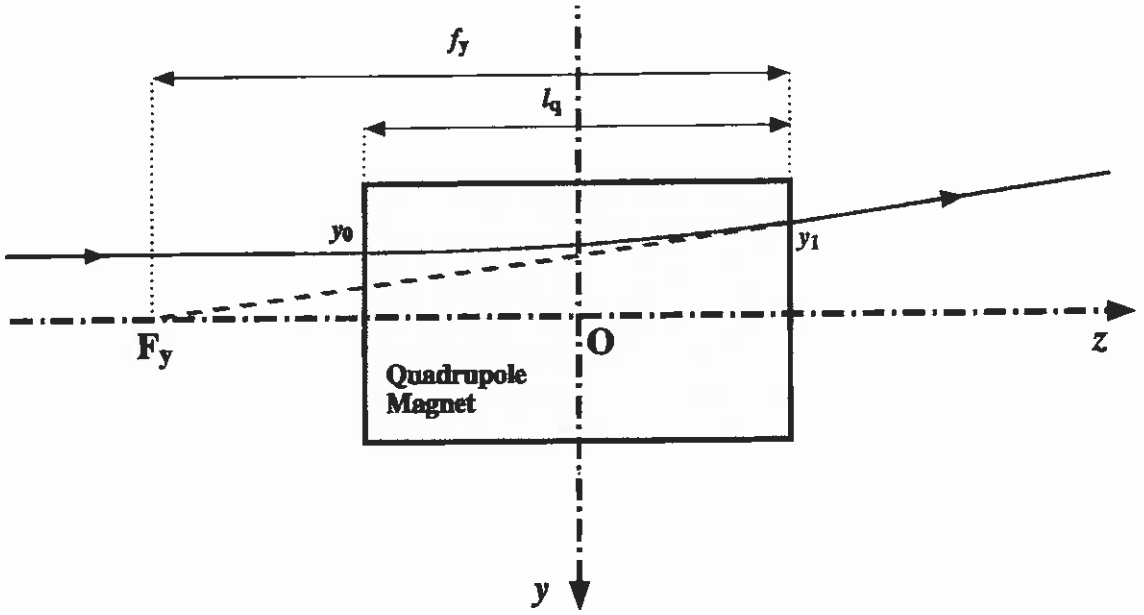

– A beam of positively charged particles traveling along the direction of the *z*-axis through the aperture of an ideal normal quadrupole magnet with a positive gradient is vertically defocused.

– This effect is similar to that of a defocusing lens on a light ray.

FOCUSING/DEFOCUSING QUADRUPOLE MAGNETS

– In summary, a beam of positively charged particles traveling along the direction of the z-axis through the aperture of an ideal normal quadrupole magnet is horizontally focused and vertically defocused when g is positive.

– Conversely, the beam is vertically focused and horizontally defocused when g is negative.

– In reference to its action along the x-axis (on a beam of positively charged particles traveling in the positive z-direction), a magnet with a positive gradient is called a *focusing* quadrupole magnet, while a magnet with a negative gradient is called a *defocusing* quadrupole magnet.

– To obtain a net focusing effect along both x- and y-axes, focusing and defocusing quadrupole magnets must be alternated in the magnet lattice.

FOCAL LENGTHS OF NORMAL QUADRUPOLE MAGNETS

– By analogy with optical lenses, the focusing effect of a normal quadrupole magnet of length, l_q, can be characterized by the *focal length*, f, given by

$$f \approx \frac{1}{\sqrt{\kappa_g}} \cot(\sqrt{\kappa_g} l_q)$$

– Similarly, the defocusing effect of a normal quadrupole magnet can be characterized by the *focal length*, f', given by

$$f' \approx \frac{-1}{\sqrt{\kappa_g}} \coth(\sqrt{\kappa_g} l_q)$$

Here f and f' are taken from the magnet end where the beam exits and κ_g is the normalized gradient defined as

$$\kappa_g \approx \frac{0.3\, q_e\, g}{\varepsilon_{GeV}}$$

where κ_g is in $(\text{rad/m})^2$, q_e is in units of electron charge, g is in teslas per meter, and ε_{GeV} is in GeV.

FOCAL LENGTHS OF LHC ARC QUADRUPOLE MAGNETS

– For the storage/collision phase of the LHC at CERN, we have:

$$g = 223 \text{ T/m}, \; l_q = 3.1 \text{ m}, \text{ and } \varepsilon_{\text{GeV}} \approx 7000$$

– It follows that

$$\kappa_g \approx 0.01 \text{ (rad/m)}^2$$

$$f_x \approx 32.7 \text{ m}$$

$$f_y \approx -34.8 \text{ m}$$

– The LHC arcs count a total number of 386 quadrupole magnets.

LECTURE 1: MAGNET SYSTEMS FOR LARGE CIRCULAR ACCELERATORS

1.1 On the need of high energy accelerators

1.2 Accelerator types

1.3 Synchrotron-type accelerators

1.4 Layout of large circular accelerators

1.5 Dipole and quadrupole magnets for large circular accelerators

1.6 How to produce ideal dipole and quadrupole magnetic flux densities?

Ampère Theorem

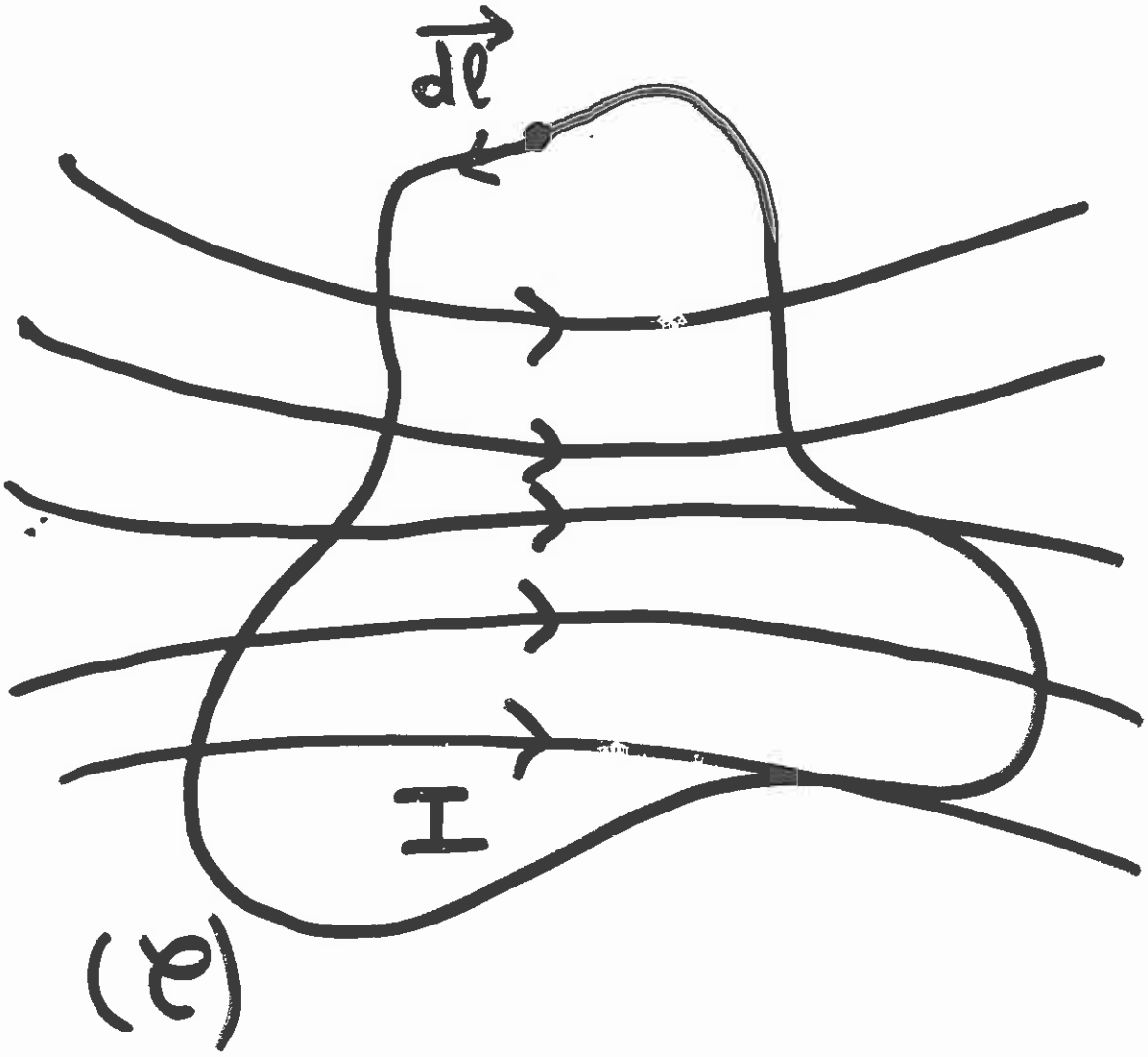

$$\int \vec{H} . d\vec{\ell} = \sum I$$

(In a vacuum : $\vec{B} = \mu_0 \vec{H}$)

Generating a Pure Dipole Field

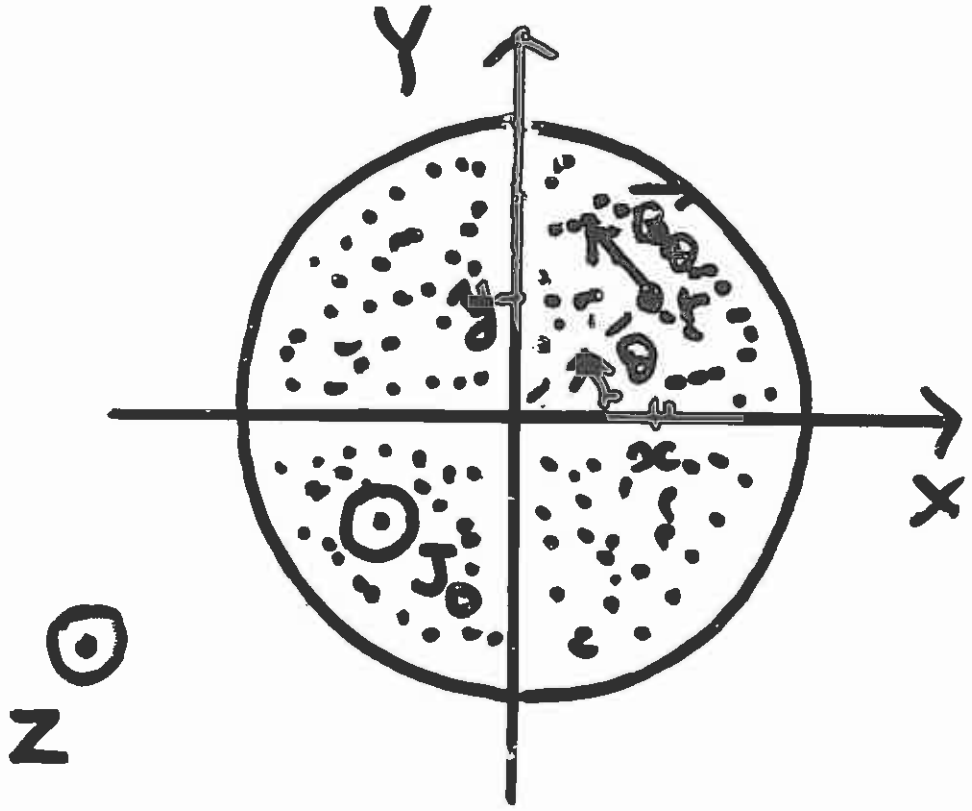

$\vec{J}(r,\theta) = J_0 \vec{z}$ $\quad \vec{B}(r,\theta) = B_\theta(r)\vec{v}$

- From Ampère Theorem

$$2\pi r B_\theta = \mu_0 \pi r^2 J_0$$

$$\begin{cases} B_x = -B_\theta \sin\theta = -\dfrac{\mu_0 J_0}{2} y \\ B_y = B_\theta \cos\theta = \dfrac{\mu_0 J_0}{2} x \end{cases}$$

Generating a Pure Dipole Field (Cont.)

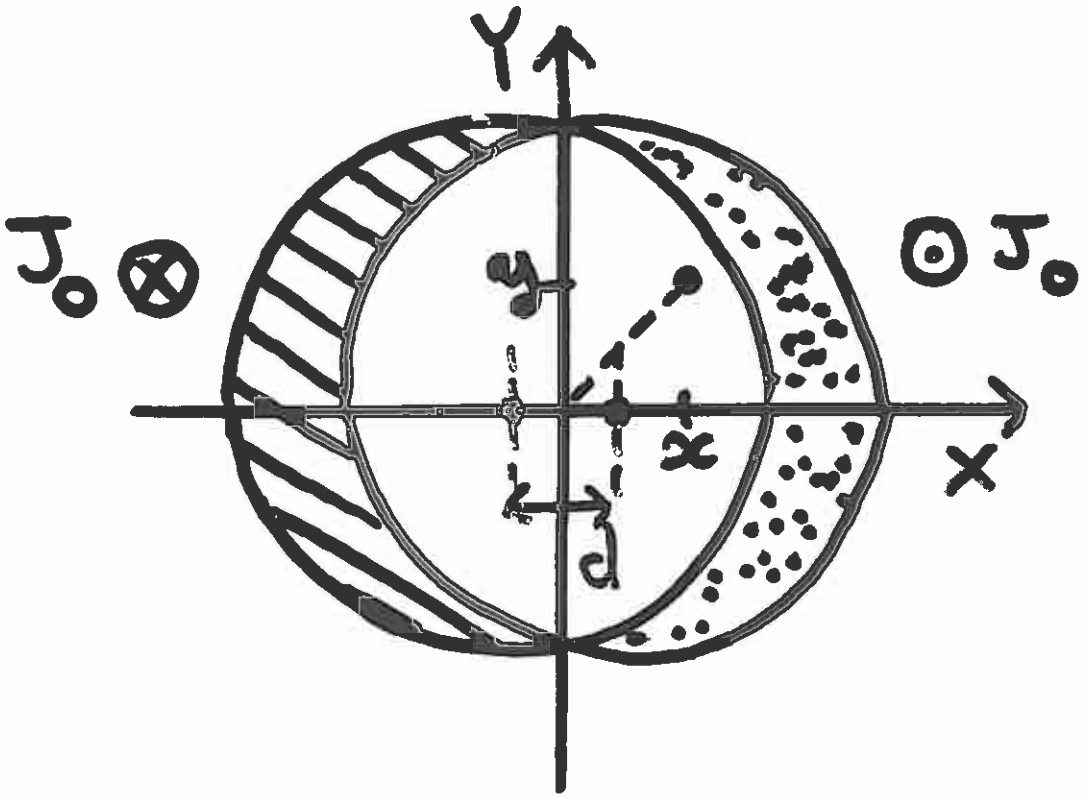

$$\begin{cases} B_x = -\frac{\mu_0 J_0}{2}(y - y) = 0 \\ B_y = \frac{\mu_0 J_0}{2}\left[\left(x - \frac{d}{2}\right) - \left(x + \frac{d}{2}\right)\right] = -\frac{\mu_0 J_0 d}{2} \end{cases}$$

$\Rightarrow$ Uniform Vertical Field of Amplitude $\frac{\mu_0 J_0 d}{2}$

Generating a Pure Dipole Field (Cont.)

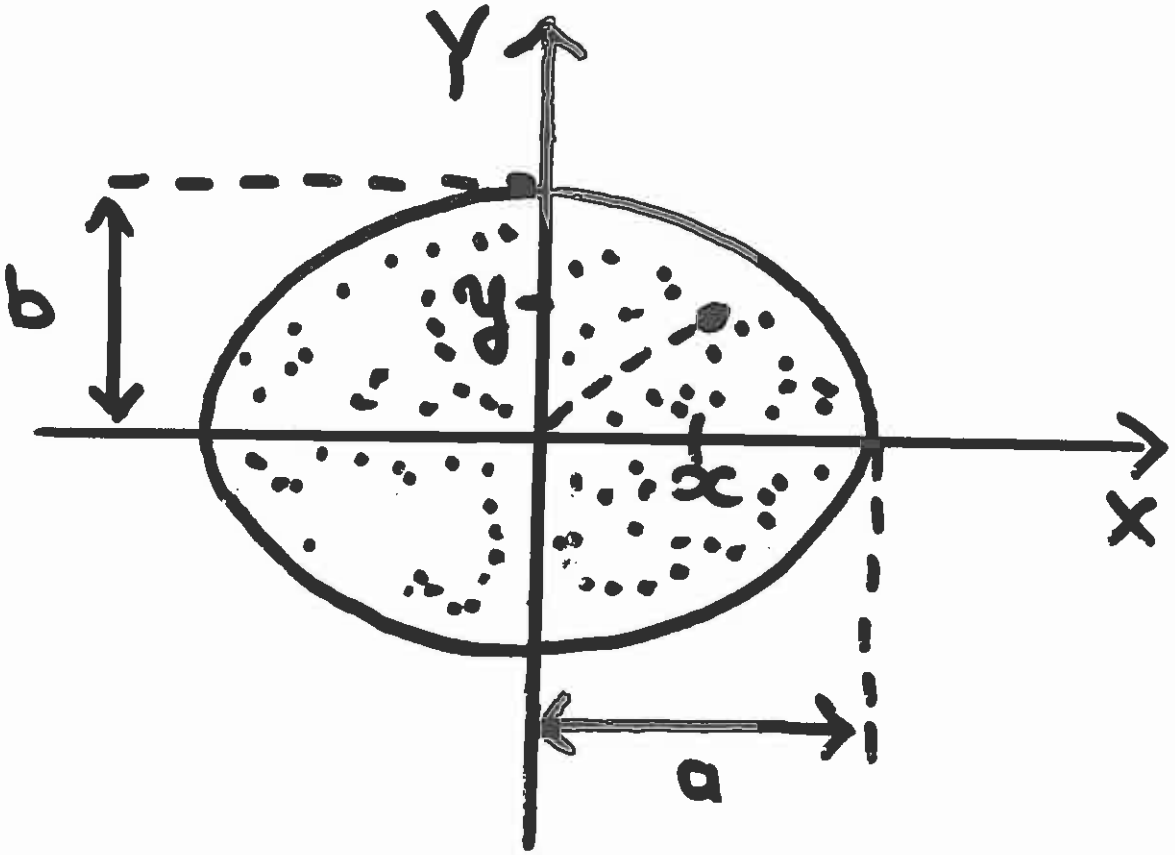

$$\begin{cases} B_x = -\dfrac{\mu_0 J_0 a}{a+b}\, y \\ B_y = \dfrac{\mu_0 J_0 b}{a+b}\, x \end{cases}$$

Generating a Pure Dipole Field (Cont.)

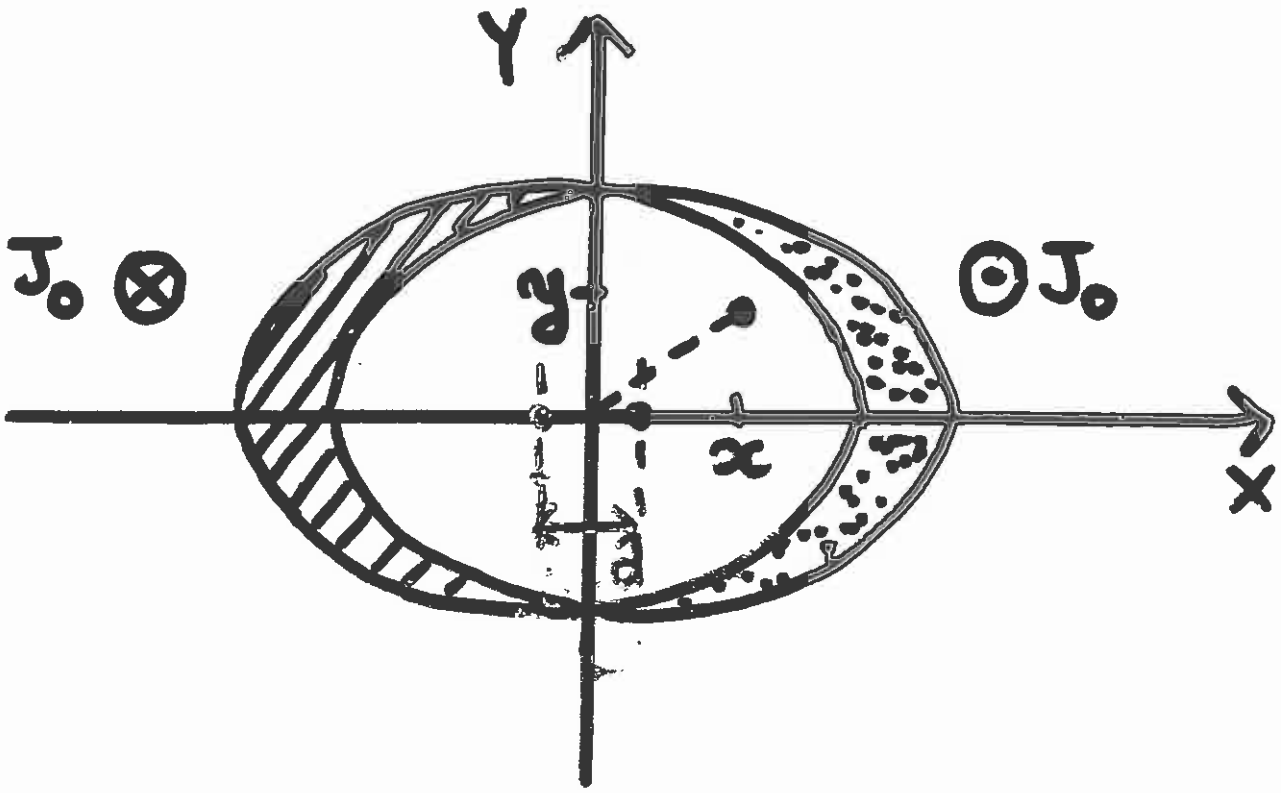

$$B_x = -\frac{\mu_0 J_0 a}{a+b}(y-y) = 0$$

$$B_y = \frac{\mu_0 J_0 b}{a+b}\left[\left(x-\frac{d}{2}\right)-\left(x+\frac{d}{2}\right)\right] = -\frac{\mu_0 J_0 b d}{(a+b)}$$

$\Rightarrow$ Uniform Vertical Field of Amplitude $\frac{\mu_0 J_0 b d}{(a+b)}$

Approximating a Dipole Field

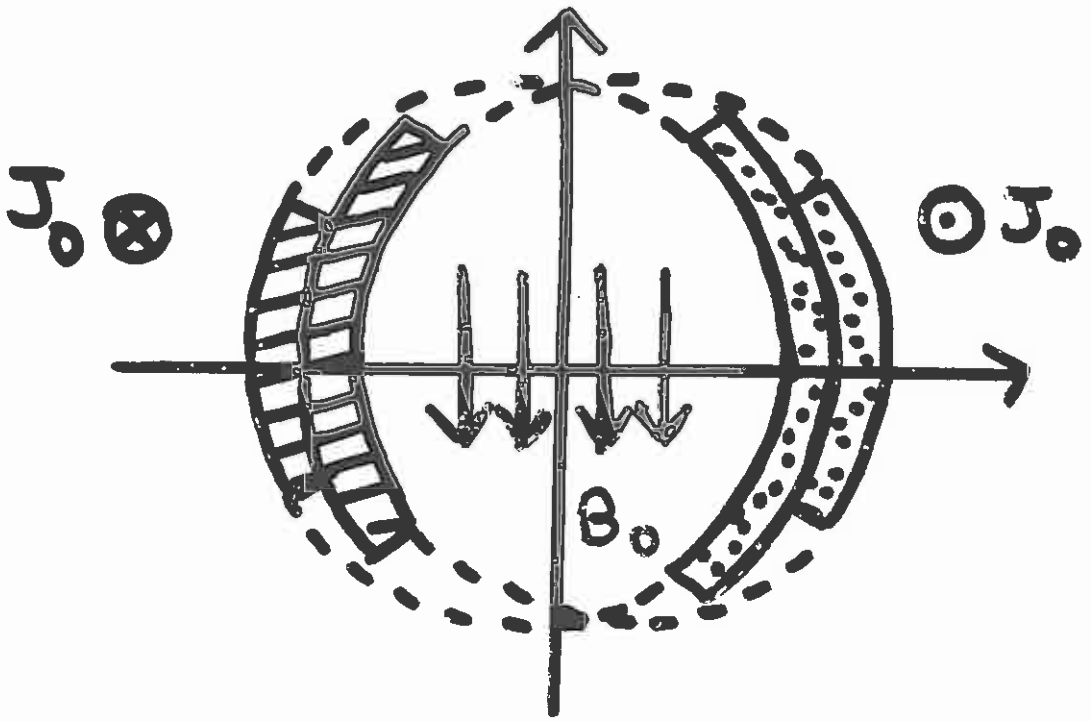

A dipole field can be approximated by mean of one (or more)

"Current shell(s)"

Most Commonly Used Dipole Magnet Configuration

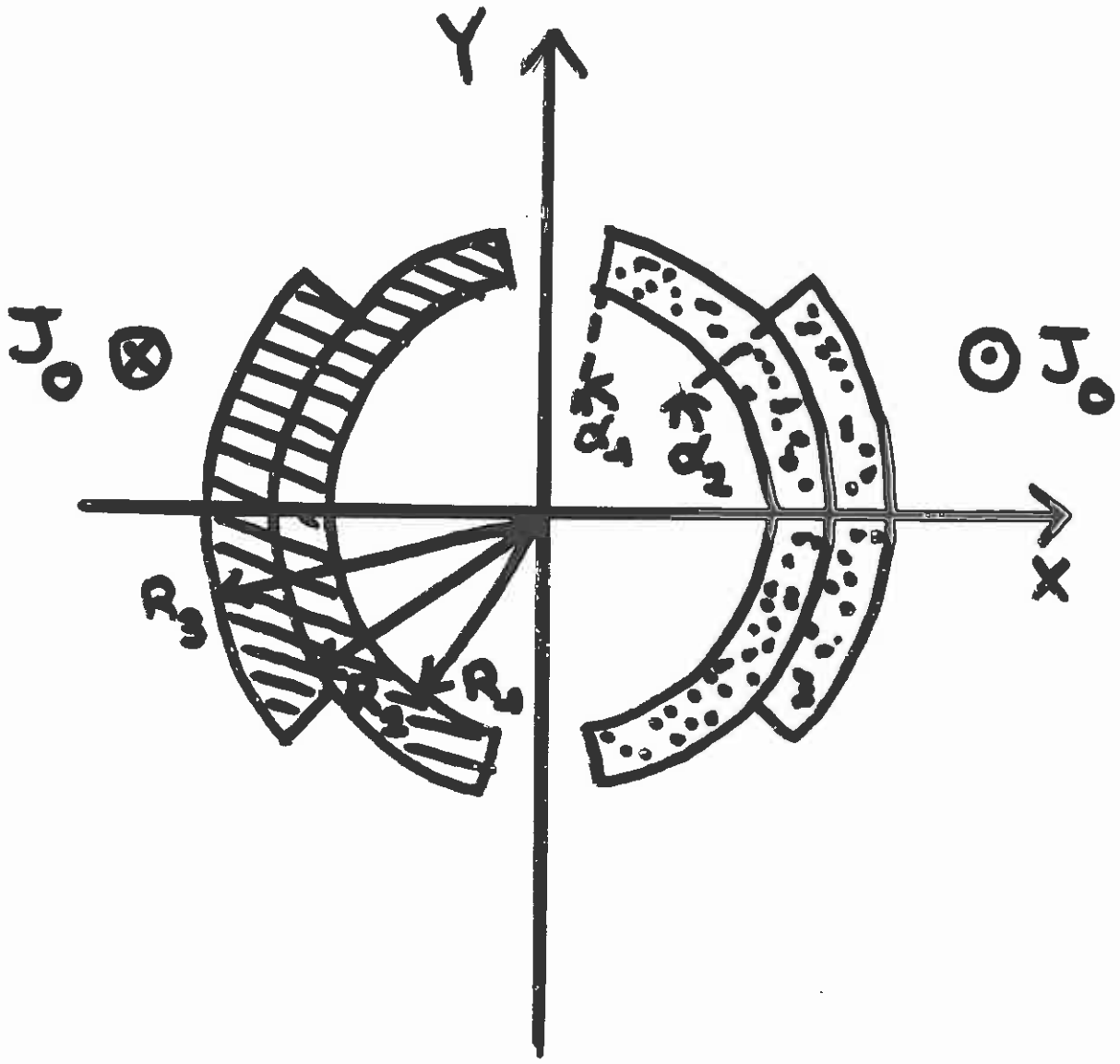

Generating a Pure Quadrupole Field

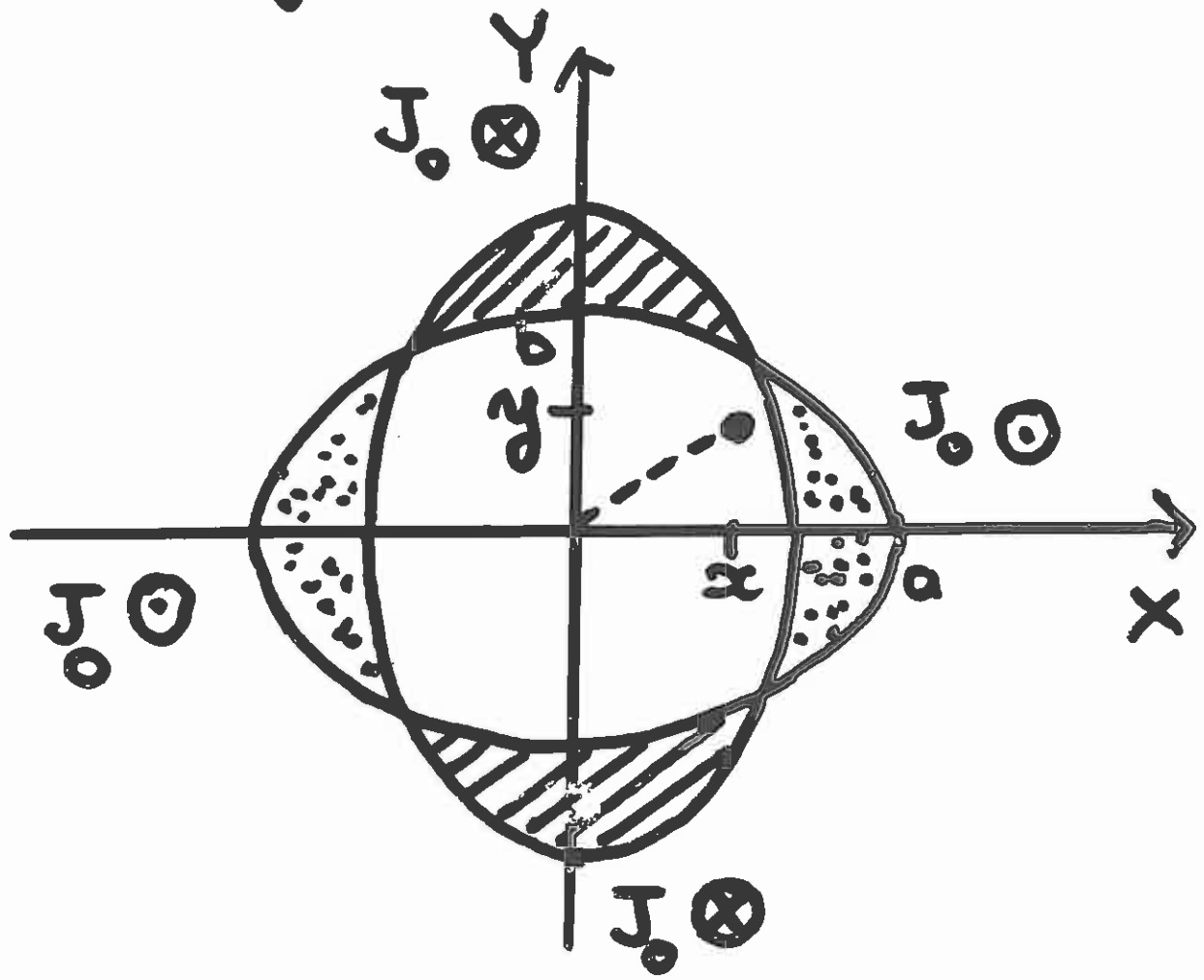

$$\begin{cases} B_x = -\dfrac{\mu_0 J_0 a}{a+b} y + \dfrac{\mu_0 J_0 b}{a+b} y = -\dfrac{\mu_0 J_0 (a-b)}{a+b} y \\ B_y = \dfrac{\mu_0 J_0 b}{a+b} x - \dfrac{\mu_0 J_0 a}{a+b} x = -\dfrac{\mu_0 J_0 (a-b)}{a+b} x \end{cases}$$

$\Rightarrow$ Pure Quadrupole Field of Gradient $-\dfrac{\mu_0 J_0 (a-b)}{a+b}$

Most Commonly Used Quadrupole Magnet Configuration

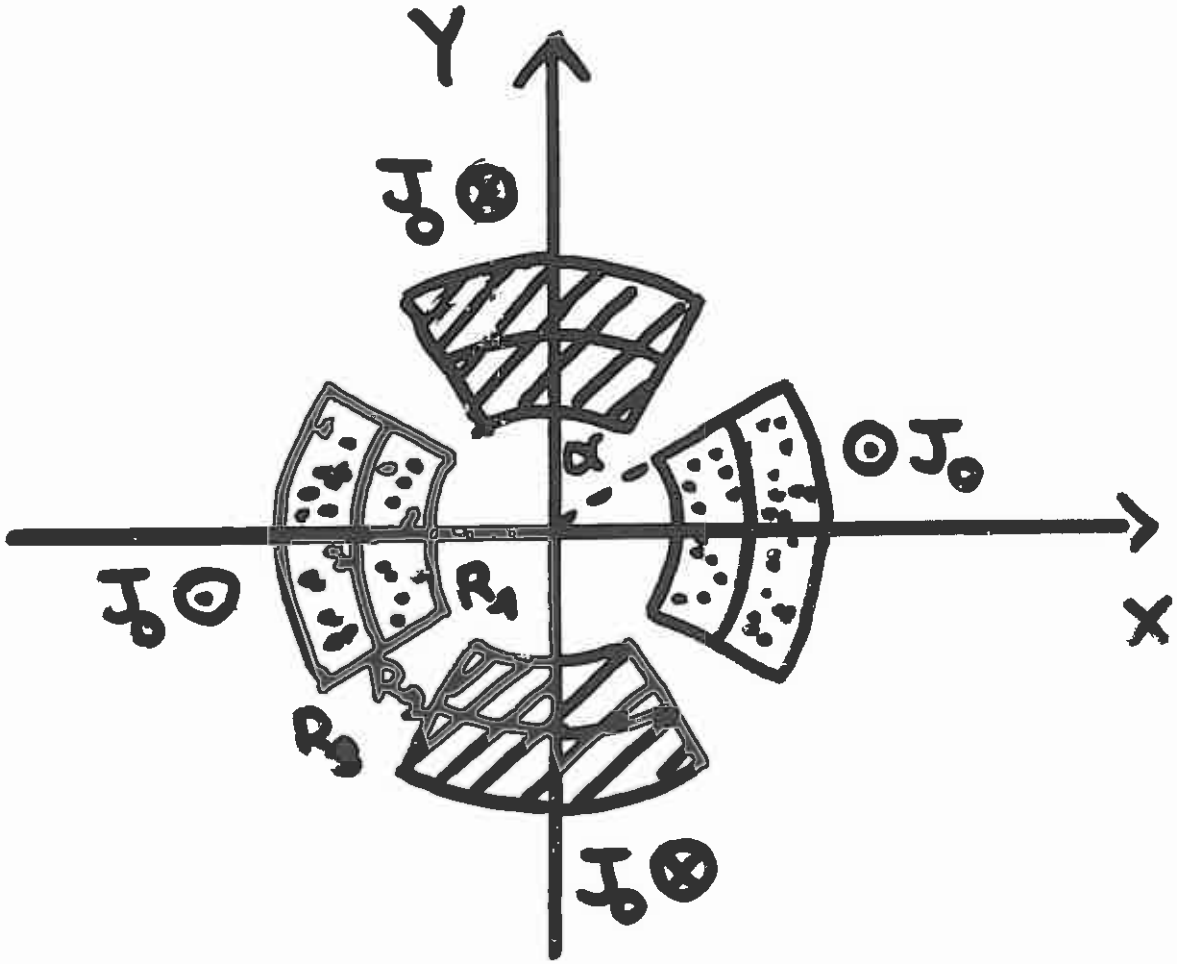

LECTURE 2: SUPERCONDUCTIVITY APPLIED TO PARTICLE ACCELERATOR MAGNETS

2.1 Why superconductivity? 2–3

2.2 Origin of Superconductivity and critical temperature 2–9

2.3 Magnetic states of superconductors and critical fields 2–27

2.4 Transport properties of superconductors and critical current density 2–51

2.5 Critical State Model 2–63

2.6 Review of superconducting particle accelerators 2–85

2.7 Prominent features of superconducting accelerator magnets 2–107

2.8 Superconducting accelerator magnet R&D 2–119

LECTURE 2: SUPERCONDUCTIVITY APPLIED TO PARTICLE ACCELERATOR MAGNETS

2.1 Why superconductivity?

2.2 Origin of Superconductivity and critical temperature

2.3 Magnetic states of superconductors and critical fields

2.4 Transport properties of superconductors and critical current density

2.5 Critical State Model

2.6 Review of superconducting particle accelerators

2.7 Prominent features of superconducting accelerator magnets

2.8 Superconducting accelerator magnet R&D

WHY SUPERCONDUCTIVITY?

– For a synchrotron-type accelerator, the particle energy is directly related to the product (χB), where χ is the bending radius and B is the bending magnetic flux density.

– To achieve higher energies, one must increase either the accelerator radius or the strength of the arc dipole magnets (or both).

– Increasing the bending radius means a longer tunnel, while increasing the bending magnetic flux density above 2 T implies the use of superconducting magnets.

– The trade-off between tunneling costs, magnet development costs and accelerator operating costs is, since the late 1970's, in favor of using superconducting magnets generating the highest possible fields and field gradients.

WHAT IS SUPERCONDUCTIVITY?

– **Superconductivity is a unique property exhibited by some materials at low temperatures where the resistivity drops to zero.**

– **As a result, materials in the superconducting state can transport current without power dissipation by the Joule effect.**

ADVANTAGES OF SUPERCONDUCTIVITY

– Superconductivity offers at least two advantages for large magnet systems such as those needed in high energy accelerator rings:

• A significant reduction in electrical power consumption,

• The possibility of relying on much higher overall current densities in the magnets coils.

DRAWBACKS OF SUPERCONDUCTIVITY

– There are at least three drawbacks in using superconducting magnets:

• Superconductors generate magnetization effects which result in field distortions that have to be corrected (see lecture on field quality),

• To reach the superconducting state, the magnets must be cooled down and maintained at low temperatures, which requires large cryogenic systems (see section on magnet cooling).

• It can happen that an energized magnet, initially in the superconducting state, abruptly and irreversibly switches back to the normal resistive state in a phenomenon referred to as a *quench* (see lecture on quench performance).

The occurrence of a quench causes an instantaneous beam loss and requires that all or part of the magnet ring be rapidly ramped down to limit conductor heating and possible damage (see section on quench protection).

Once the quenching magnet is discharged, it can be cooled down again and restored into the superconducting state, and the machine operations can resume.

A quench is seldom fatal but is always a serious disturbance. All must be done to prevent it from happening and all cautions must be taken to ensure the safety of the installation when it does happen.

LECTURE 2: SUPERCONDUCTIVITY APPLIED TO PARTICLE ACCELERATOR MAGNETS

2.1 Why superconductivity?

2.2 Origin of Superconductivity and critical temperature

2.3 Magnetic states of superconductors and critical fields

2.4 Transport properties of superconductors and critical current density

2.5 Critical State Model

2.6 Review of superconducting particle accelerators

2.7 Prominent features of superconducting accelerator magnets

2.8 Superconducting accelerator magnet R&D

NORMAL CONDUCTORS

– Metals and alloys of metals are conductors of electrical current.

– In a simple model, a normal metal can be represented by a lattice of positively charged ions, connected with each other by springs, through which free electrons flow.

– The free electrons move at velocities of the order of the *Fermi velocity*, v_F.

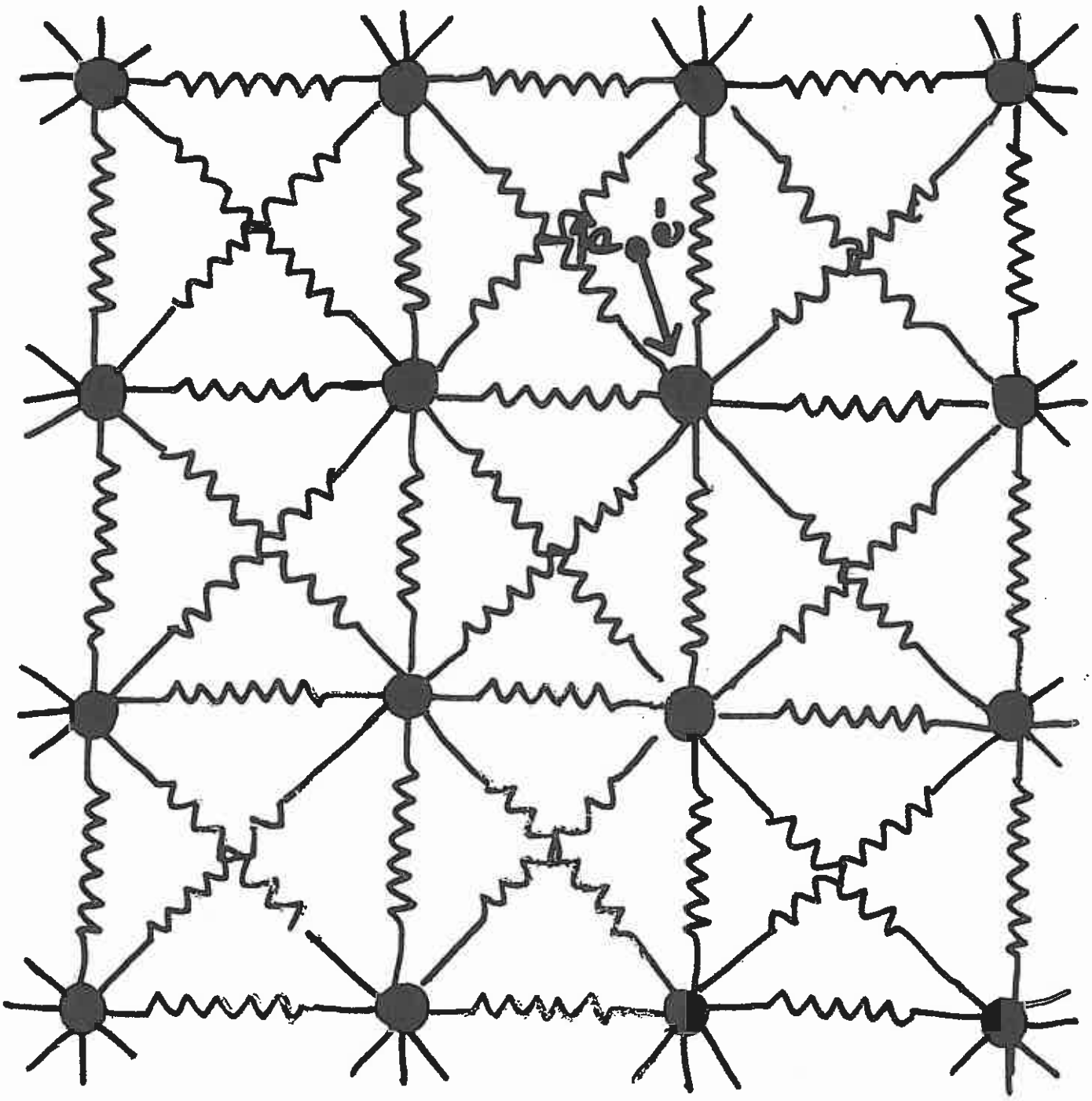

RESISTANCE OF NORMAL METALS AT ROOM TEMPERATURE

– At room temperature, the ions of the lattice are oscillating around their positions (thermal motion) and, from time to time, the free electrons flowing through the lattice hit the ions.

– These repeated shocks reduce the electrons' momenta and increase the ions' vibrations.

– For an external observer, the lattice's ions oppose a resistance to the flow of current and the metal heats up.

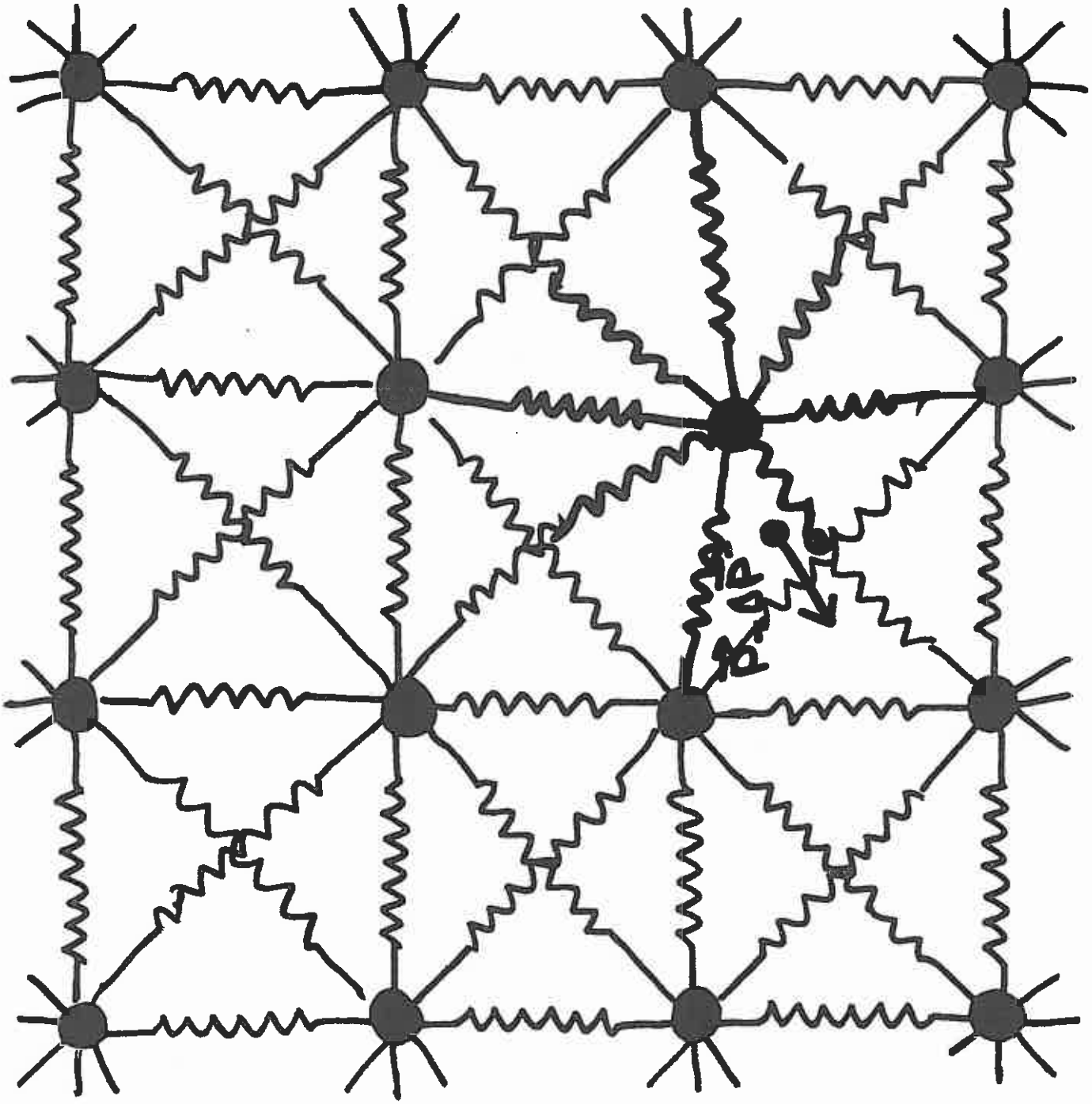
ADP

RESISTANCE OF NORMAL METALS AT LOW TEMPERATURES (CONT.)

– As the temperature of a normal metal is decreased, the thermal motion and thus, the vibrations of the lattice's ions, reduce. As a result, the free electrons experience less and less shocks and the resistivity decreases with decreasing temperatures.

– If the ions' lattice was ideal (*i.e.*, had no irregularities and no impurities), the resistivity would drop to zero when the temperature approaches the absolute zero.

– In practice, the ions' lattice exhibit dislocations due to cold work and not all of the impurities can be removed from the original ores. As a result, it appears that at low temperatures, the resistivity levels off and reaches a plateau. This plateau is called the *residual resistivity*.

– The residual resistivity is representative of the amount of impurities and of cold work in the metal: the purer the metal, and the less cold work, the lower the residual resistivity.

Resistivity of Normal Metal at low Temperatures e.g., Copper

Fracture and Deformation Div., NBS, Boulder, CO
9-13-67 S.J.S., R.P.R

CRYOGENIC PROPERTIES OF COPPER AND COPPER ALLOYS

MATERIAL	C10100 – C10700 COPPER (ANNEALED, COLD-WORKED)	PROPERTY	ELECTRICAL RESISTIVITY vs. TEMPERATURE, RRR

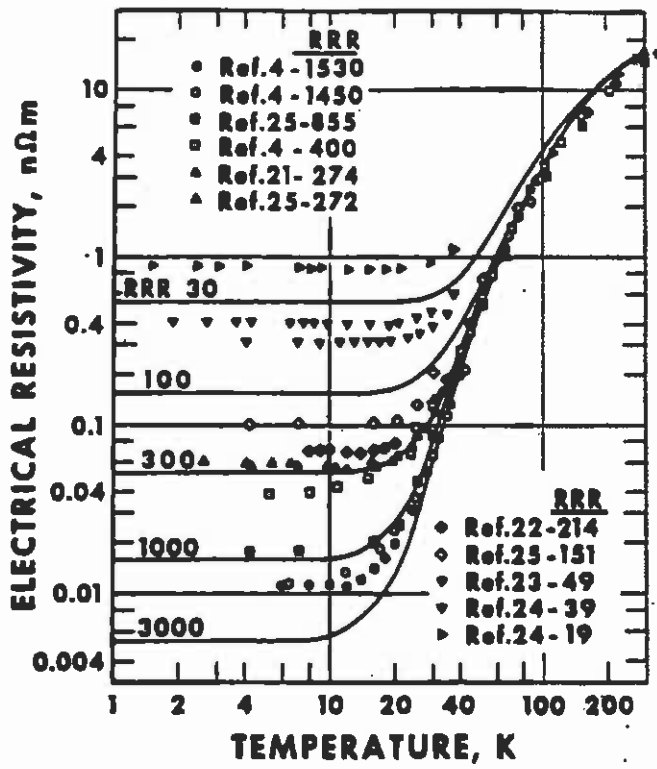

$1.6\ 10^{-8}\ \Omega m$

$$RRR = \frac{\rho(\text{Room Temp.})}{\rho(\text{Low Temp.})}$$

Figure 1. The data shown were used in the analysis described in Reference 27 to compute the constants for Equation (1). The curves represent Equation (1) for the series of RRR values indicated.

RESIDUAL RESISTIVITY RATIO

– The behavior of a normal metal at low temperatures can be characterized by the Residual Resistivity Ratio, RRR, defined as

$$\text{RRR} = \frac{\rho(273\ \text{K})}{\rho(\text{low temp.})}$$

where $\rho(273\ \text{K})$ is the resistivity at 273 K and ρ(low temp.) is the residual resistivity at low temperatures.

– The higher the RRR, the purer the metals.

– For applications in superconducting magnets, one uses OFHC copper, with RRR of the order of 100.

SUPERCONDUCTORS

– **Some materials are such that, when they are cooled down, their resistivity abruptly drops to zero below some temperature, referred to as the** *critical temperature.*

– **These materials are called** *superconductors.*

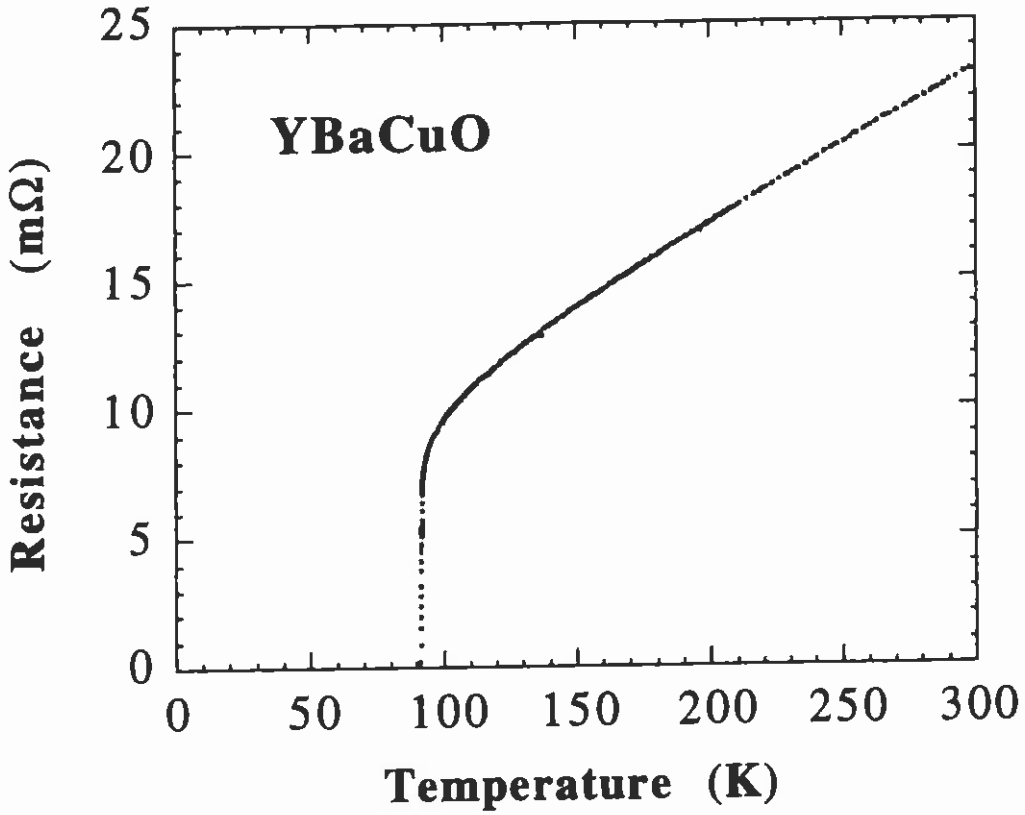

(O. Laborde, CNRS - CRTBT)

Resistance of Superconductors

Small B 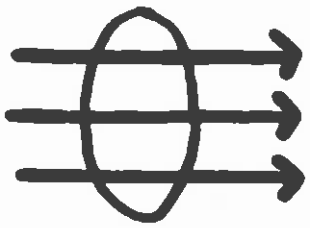 $T > T_c$

Small B 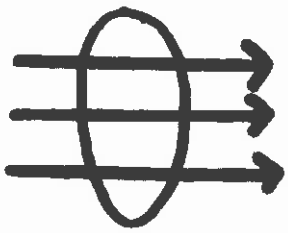 $T < T_c$

$B \searrow 0$ $T < T_c$

$I(t) = I(t=0) \exp(-t/\tau)$

where $\tau = L/R$

$\Rightarrow \rho < 10^{-25}\ \Omega m$ (over 2 years)

COOPER PAIRS

– In the superconducting state, the electrons are bound into so-called *Cooper pairs.*

– The origin of the binding force between the two electrons of a Copper pair is as follows: the first electron moves through the lattice and attracts the positive ions. As a result, the lattice is deformed, creating an accumulation of positive charges, which, in turn, attracts the second electron.

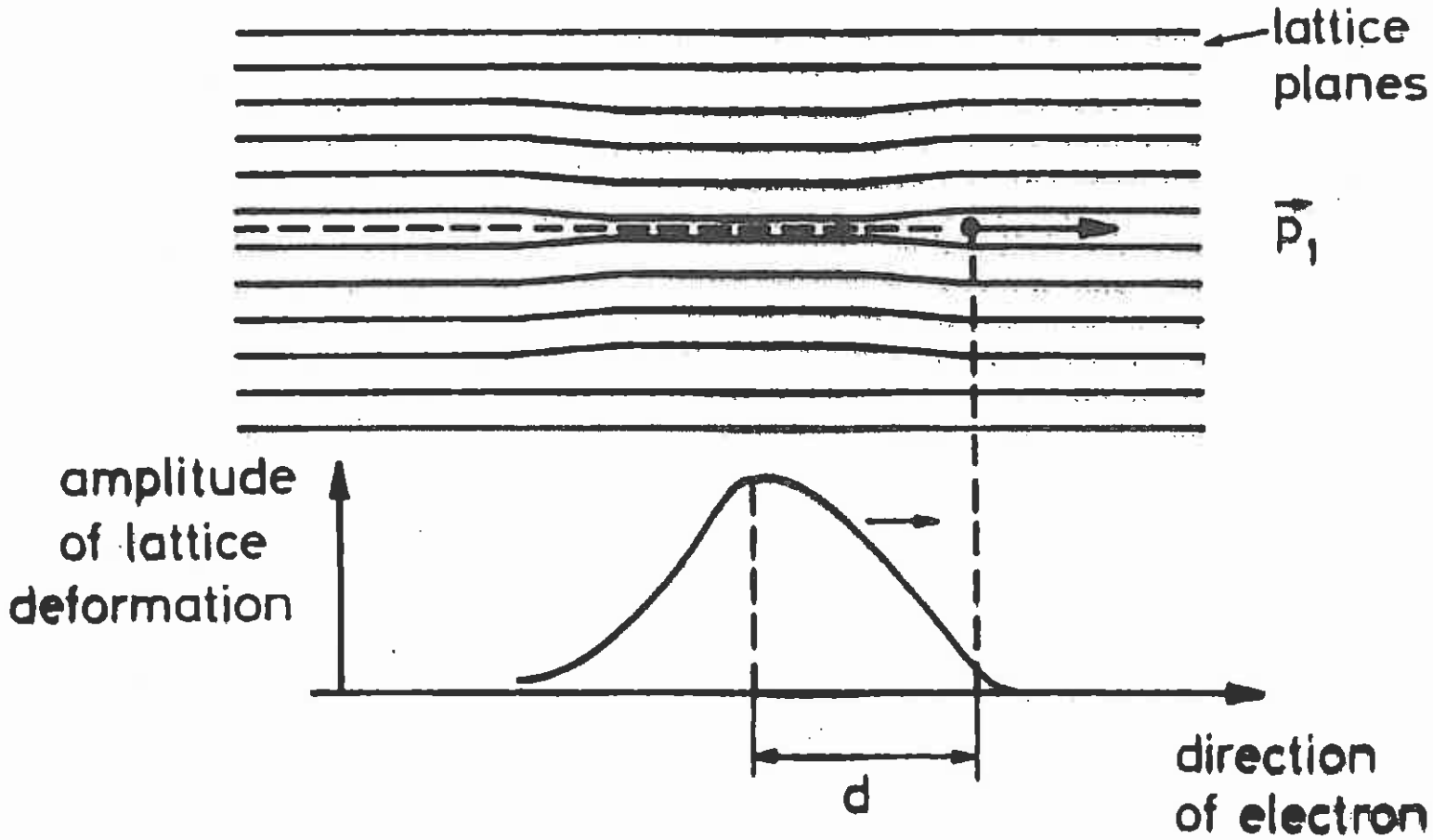

Courtesy P. Schmüser

COOPER PAIRS (CONT.)

– Due to the inertia of the lattice's ions, the deformation is not instantaneous but lags behind the passage of the first electron. This time lag can be estimated as

$$\tau_D \approx \frac{2\pi}{\omega_D}$$

where ω_D is the Debye frequency of the lattice.

– If the first electron moves at the Fermi velocity, v_F, the maximum lattice deformation follows at a distance, d, behind the first electron, where

$$d \approx v_F \tau_D \approx v_F \frac{2\pi}{\omega_D}$$

– As a result, Cooper pairs are very extended objects, which may be several 100 or 1000 lattice constants apart, and which overlapp each other.

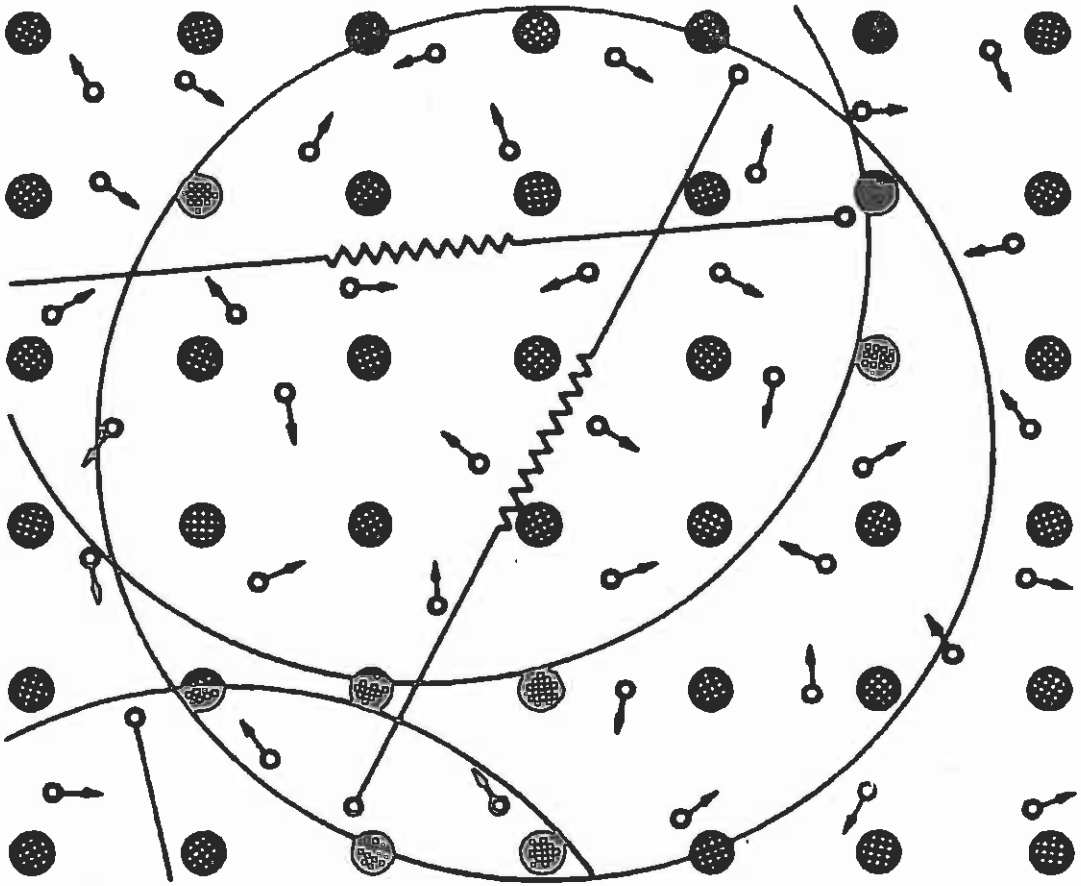

metal ion

Cooper pair

single electron

Courtesy P. Schmüser

ENERGY GAP AND CRITICAL TEMPERATURE

– The binding energy of Cooper pairs is very small, and the pairs can only exist at temperatures where this energy is not overcome by thermal agitation.

– The critical temperature, T_C (at zero field and zero current), is related to the so-called *gap energy*, $\Delta(0)$ (at zero temperature), by

$$\Delta(0) \approx 1.76\, k_B T_C$$

where K_B is Boltzmann's constant ($1.38\ 10^{-23}$ J/K).

– $\Delta(0)$ and T_C are mainly determined by the chemistry of the material.

VANISHING RESISTANCE OF SUPERCONDUCTORS

– As long as cooper pairs exist, the bound electrons no longer scatter on impurities, lattice dislocations or thermal lattice vibrations, and the material can transport current without dissipation.

LECTURE 2: SUPERCONDUCTIVITY APPLIED TO PARTICLE ACCELERATOR MAGNETS

2.1 Why superconductivity?

2.2 Origin of Superconductivity and critical temperature

2.3 Magnetic states of superconductors and critical fields

2.4 Transport properties of superconductors and critical current density

2.5 Critical State Model

2.6 Review of superconducting particle accelerators

2.7 Prominent features of superconducting accelerator magnets

2.8 Superconducting accelerator magnet R&D

STATES OF A SUPERCONDUCTOR

– Superconductors are characterized by a critical temperature above which they are no longer superconducting. Their behavior is also strongly affected by magnetic field.

– Depending on temperature and magnetic field conditions, and on material type, superconductors can be found in three different states:

- ***Meissner state***
- ***Mixed state***
- ***Surface current state***

– There are two main types of superconductors:

- ***Type I superconductors*** include many pure metals and some compounds. They only exist in the Meissner state or the surface current state and are not suitable for use in high field accelerator magnets.

- ***Type II superconductors*** include most superconducting alloys and compounds. They exhibit all three states and are used for magnet applications.

MEISSNER STATE

– Let us consider a slab made of type-I or type-II material, initially in the superconducting state, and let us assume that this slab is placed in an uniform background field which is raised progressively from zero to a low value.

– When the external magnetic field is varied, the superconductor reacts in order to shield its inner core from these variations. Screening currents are generated at the slab periphery which create their own field, equal in strength but opposite in direction to the external field. As a result, the magnetic flux density in the material bulk is nil.

– In this state, called the *Meissner state*, the superconductor totally excludes or expells the magnetic flux lines from its interior, and acts as an ideal *diamagnetic* material.

Meissner State

$H < H_{c1}(T)$

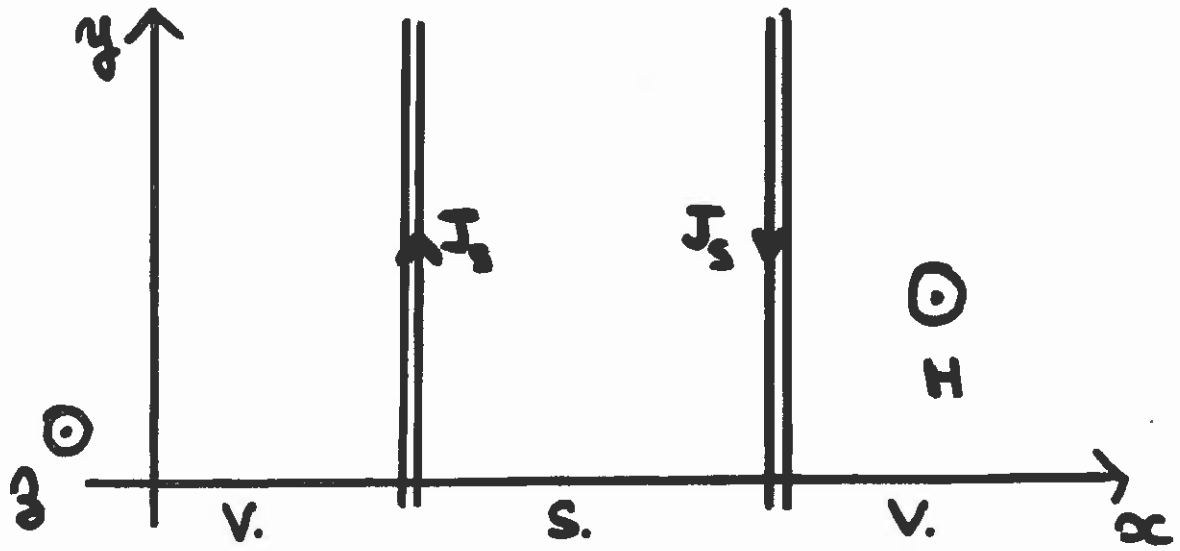

Perfect Diamagnetism, except in a depth λ, called the London penetration depth

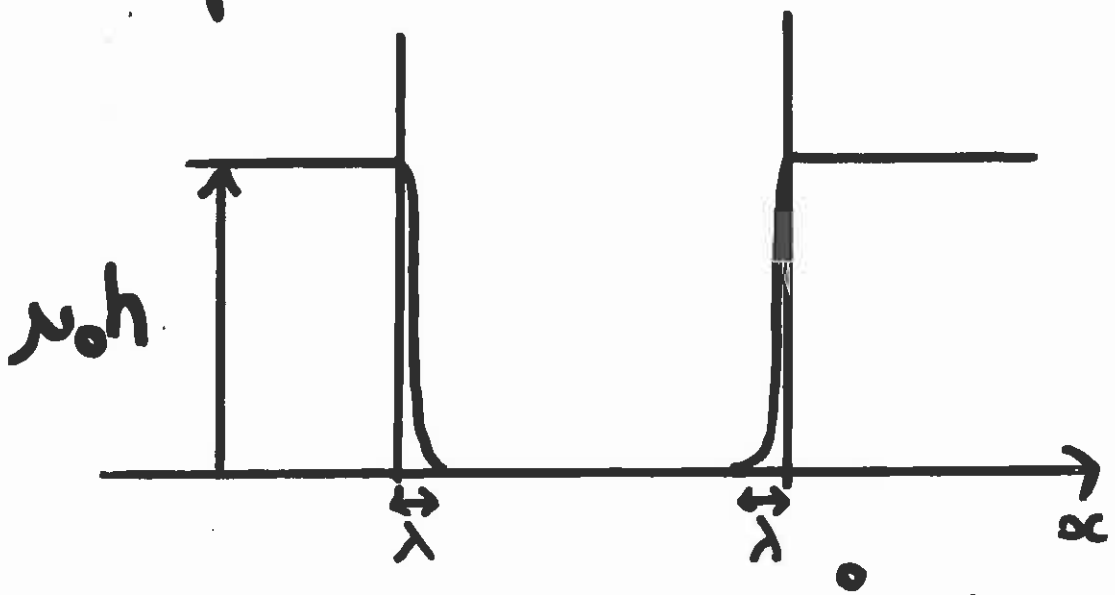

For NbTi : $\lambda \sim 3000$ Å (at T=0K)

LONDON PENETRATION DEPTH

– In the Meissner state, the field only penetrates at the periphery of the superconductor, and decreases exponentially with depth. The characteristic length of the exponential decay is referred to as the *London penetration depth*, λ_L.

– For a type-I superconductor like lead (Pb), λ_L is about 30 nano-meters, while for a type-II superconductor like NbTi, λ_L is about 10 times longer (300 nano-meters).

– In the Meissner state, both types of superconductors can transport current without losses, but the current flow is limited to the London penetration depth at the material periphery.

MEISSNER STATE LIMITATIONS

– Let us again consider a slab of type-I or type-II material, initially in the Meissner state, and let us keep raising the external field. Upon exceeding a certain field value, the superconductor leaves the Meissner state. For a type–I material, this field value is called the critical field and is noted H_C, while for a type–II material, it is called the lower critical field and is noted H_{C1}. The values of H_C or H_{C1} depend on temperature.

– When the field applied to a type-I material exceeds H_C (at a given temperature), the shielding breaks down and the material reverts abruptly to the normal, or non-superconducting state. In the case of a type-II superconductor, the material enters the so-called *mixed-state* where it remains superconducting and can still carry current without losses.

– It follows that type-I materials are only superconducting for fields below the critical field. Given the low values of ($\mu_0 H_C$) (no more than a few hundredths of tesla at 4.2 K), these materials are not useful for magnet applications.

MIXED STATE OF A TYPE-II SUPERCONDUCTOR

– Let us now consider a slab of ideal type–II superconductor, and let us assume that the external field has been risen above H_{C1} (at a given temperature).

– Then, the field starts penetrating the interior of the superconductor in the form of tubes of magnetic flux known as *fluxoids.*

– Each fluxoid carries a quantum of flux, ϕ_0, where:

$$\phi_0 = \frac{h}{2e} = 2.07\ 10^{-15}\ \text{Wb}$$

Here, h is Planck's constant (6.63 10^{-34} J.s) and e is the electron charge (1.6 10^{-19} C).

Mixed State of Ideal Type-II Superconductor

$$H_{c_1}(T) < H < H_{c_2}(T)$$

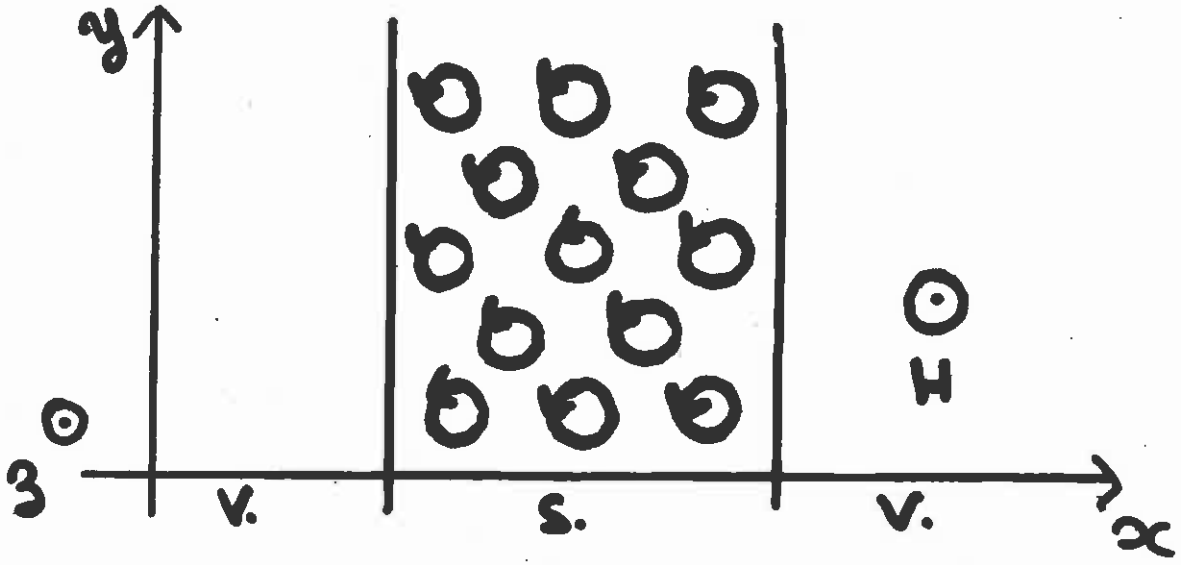

Triangular Lattice of Vortices :

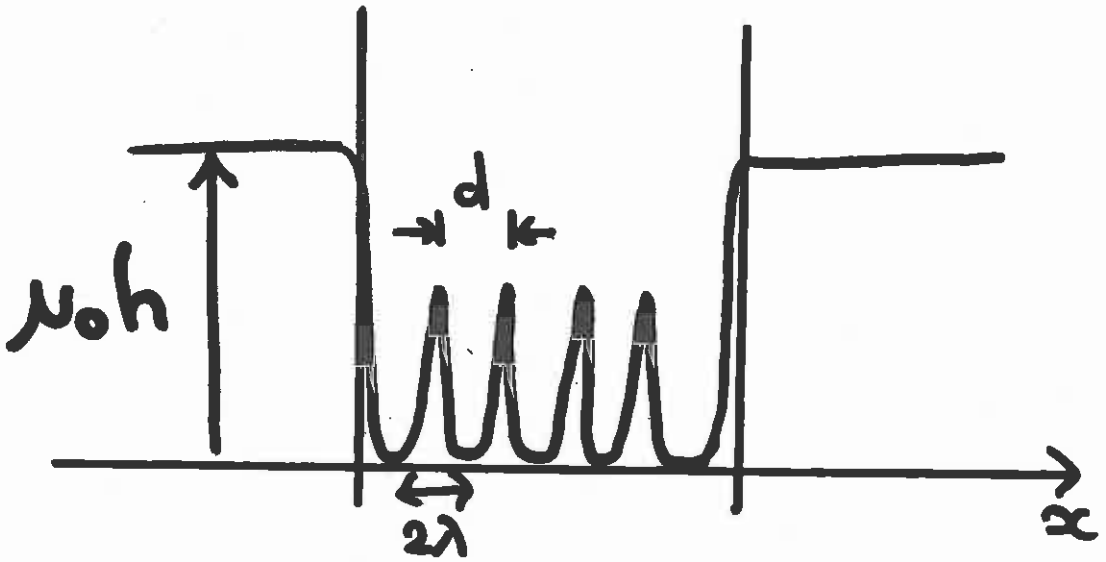

FLUXOIDS IN A TYPE-II SUPERCONDUCTOR

– A fluxoid can be represented as a tube carrying a quantum of magnetic flux, ϕ_0, surrounded by annular currents. These currents shield the outside of the fluxoid from the magnetic flux it carries.

– The field profile associated with a fluxoid is of a bell-type. It is centered on the fluxoid axis and goes to zero on the fluxoid outside. As for the Meissner state, the field variations occur over a distance of the order of the London penetration depth, λ_L. Hence, the field perturbation associated with a fluxoid extends over $(2\lambda_L)$.

– In addition, the core of the fluxoid is in the normal state. Hence, when approaching the fluxoid axis, the density of Cooper pairs, n_s, decreases and goes to zero. This decrease takes place over a length, ξ, known as the coherence length.

Single Vortex in Infinite Type-II Superconductor

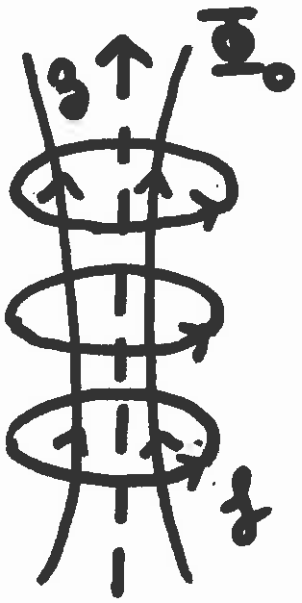

Each vortex carries a quantum of flux ϕ_0

$$\phi_0 = \frac{h}{2e} = 2.07 \times 10^{-15} \text{ Wb}$$

Annular currents circulate around the flux line to screen out the field for $r \gtrsim \lambda$

Single Vortex in Infinite Type-II Superconductor (Cont.)

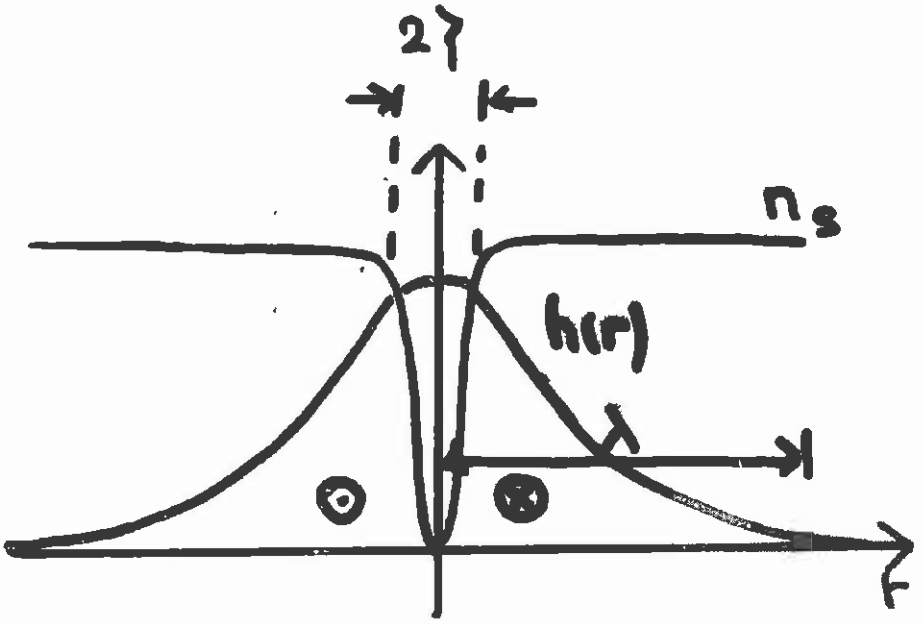

The density of superconducting electrons, n_s, is only reduced in a small core region of radius ξ, where ξ is the coherence length

For NbTi

$\lambda \sim 3000$ Å

$\xi \sim 50$ Å

Maximum Field is

$$h(r=0) = \frac{\phi_0}{2\pi\mu_0\lambda^2} \ln\frac{\lambda}{\xi}$$

COHERENCE LENGTH

– Let us consider a piece of superconducting material which is half in the normal resistive state and half in the superconducting state. At the inferface between the two, the density of Cooper pairs does not rise abruptly from zero, but increases progressively over a length referred to as ξ and called the *coherence length.*

– The coherence length, as the London penetration depth, is an intrinsinc property of the material.

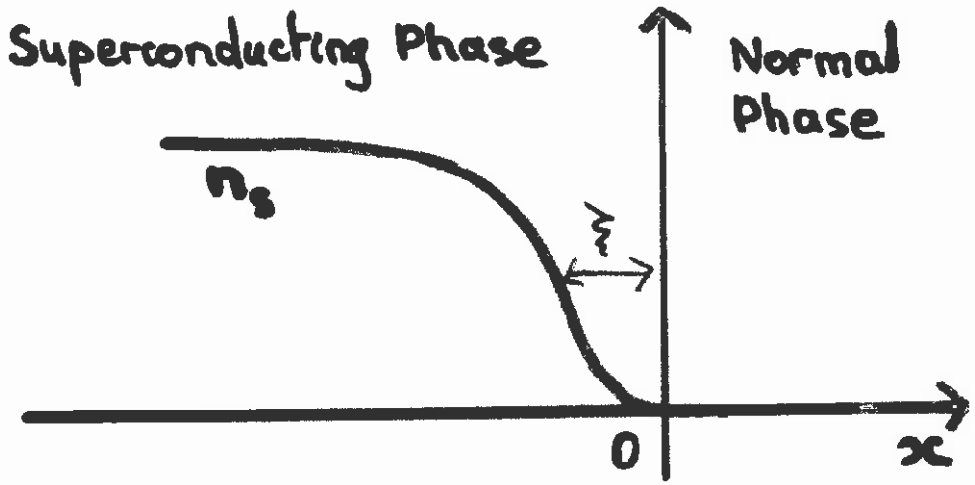
Superconducting Phase
Normal Phase
n_s
ξ
0
x

GINZBURG AND LANDAU PARAMETER

– V.L. Ginzburg and L.D. Landau introduce the parameter, κ, defined as:

$$\kappa = \frac{\lambda_L}{\xi}$$

and they show that, type-I superconductors are characterized by:

$$\kappa < \frac{\sqrt{2}}{2}$$

while type II-superconductors are characterized by:

$$\kappa > \frac{\sqrt{2}}{2}$$

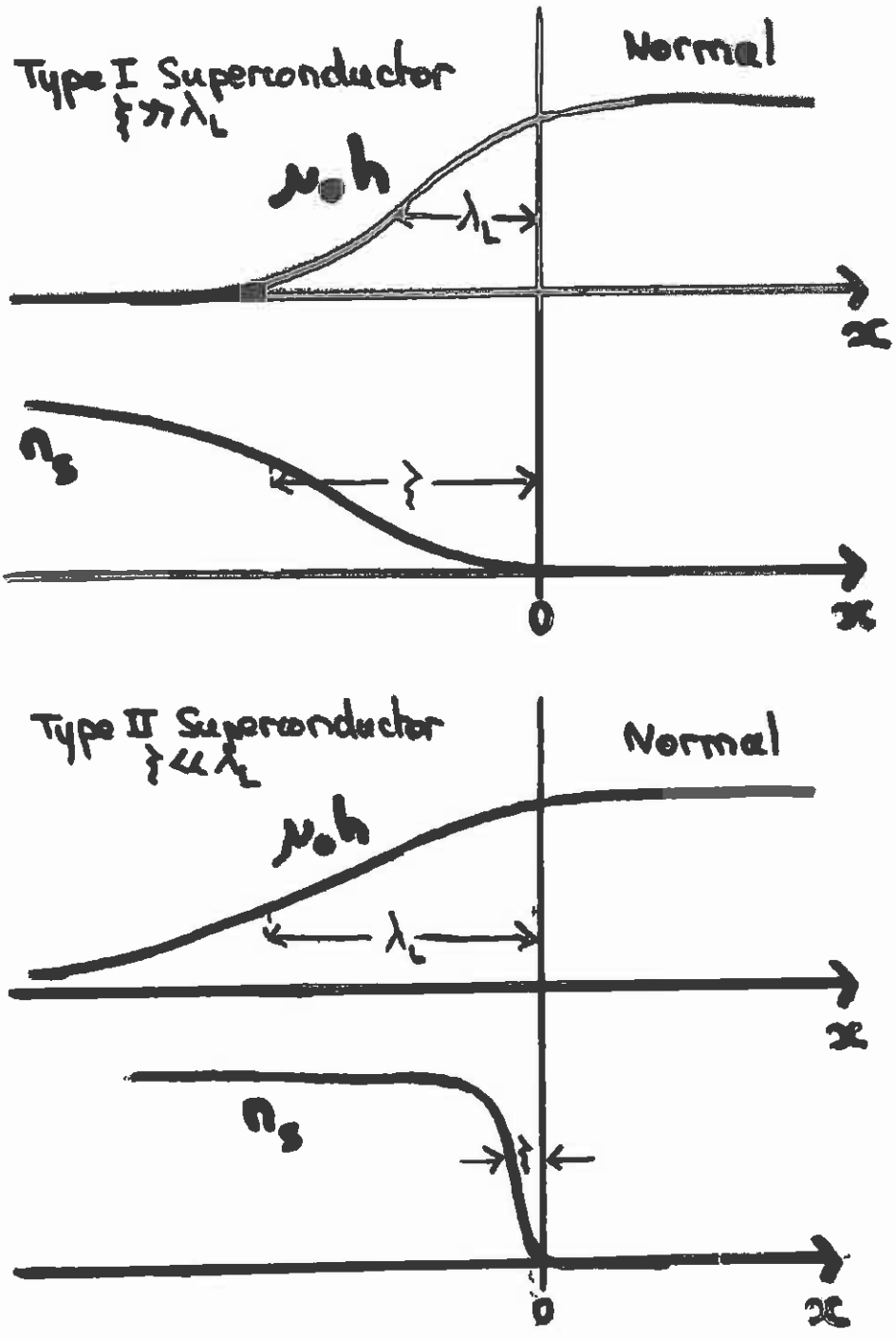
Type I Superconductor
$\xi \gg \lambda_L$
Normal
$\mu_0 h$
λ_L
x
n_s
ξ
0
x
Type II Superconductor
$\xi \ll \lambda_L$
Normal
$\mu_0 h$
λ_L
x
n_s
0
x

TYPICAL VALUES OF PENETRATION AND COHERENCE LENGTHS

– The table lists values of penetration depths, λ_L, and of coherence lengths, ξ, for typical type-I and type-II superconductors.

Material	Type	Penetration Depth (10^{-9} m)	Coherence Length (10^{-9} m)
Indium (In)	I	24	360
Lead (Pb)	I	32	510
Tin (Sn)	I	≈ 30	≈ 170
Niobium (Nb)	II	32	39
NbTi	II	300	5
Nb_3Sn	II	65	3

IDEAL TYPE-II SUPERCONDUCTORS

– In an ideal type II superconductor, the fluxoids occupy a triangular lattice.

– For fluxoids arranged in a triangular lattice and producing an average magnetic fux density, $<B>$, we have:

$$<B> \sim n_f \phi_0 = \frac{2}{\sqrt{3}} \frac{\phi_0}{d_f^2}$$

where n_f is the density of fluxoids and d_f is the fluxoid spacing.

– As the external field is raised, the density of fluxoids in the material increases and the spacing between the fluxoids decreases.

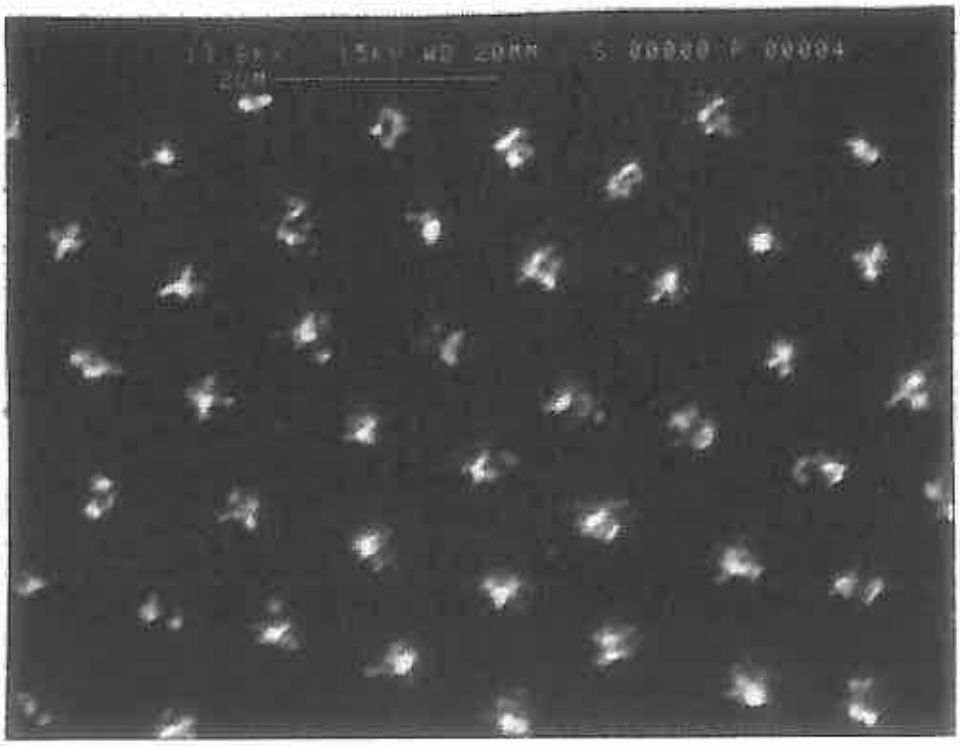

Fluxoid lattice observed by means of small ferromagnetic particles

(K. Runge, CNRS - CRTBT)

UPPER CRITICAL FIELD OF TYPE-II SUPERCONDUCTORS

– Let us keep raising the external field applied to a type-II superconductor in the mixed state.

– The density of fluxoids in the materials keeps increasing and the spacing between the fluxoids keeps decreasing, until the fluxoids start to overlapp.

– The fluxoids have a normal core which extends over a distance of the order of ξ. When the spacing, d_f, between the fluxoids becomes of the order of ξ, the bulk superconductivity disappears and the material ends up in the normal resistive state.

– The field for which the bulk superconductivity disappears is called the *upper critical field*, H_{C2}.

SURFACE SUPERCONDUCTIVITY

– It was shown in the early sixties that superconductivity can persist close to the surface of a superconductor in contact with an insulator (including vaccuum), even in a magnetic field whose strengh is sufficient to drive the bulk material normal.

– The surface superconducting layer persists in applied magnetic fields up to a certain field strength, referred to as H_{C3}. The value of B_{C3} depends on the angle the applied magnetic field makes with the surface. For a type-II superconductor, it varies between H_{C2} and $(1.69\,H_{C2})$ (the maximum is obtained when the applied field is parallel to the surface).

– Surface superconductivity is not a special property of type II superconductors, but also appears in a number of type I superconductors.

– In the surface superconductivity state, the material is still able to carry a very small, resistanceless current, but this current is rapidly decreasing with H.

– As surface superconductivity only occurs at the interface between a superconductor and a dielectric, it does not appear in practical wines and cables used in superconducting magnets where the superconductor is embedded in a matrix of normal metal.

SUMMARY OF TYPE-II BEHAVIOR

– The behavior of a type-II superconductor in a magnetic field can be summarized as follows:

• **For fields below** H_{C1}, the superconductor is in the Meissner State, and it expels the magnetic flux lines from its interior.

• **For fields between** H_{C1} **and** B_{C2}, the superconductor is in the mixed state, and it is penetrated by the magnetic flux in the form of fluxoids.

• **For fields above** H_{C2}, the bulk superconductivity disappears. If the superconductor is in contact with an insulator (including vaccuum), there remains a surface superconductivity state at the interface for fields up to H_{C3}.

– The values of H_{C1}, H_{C2} **and** H_{C3} **all depend on temperature.**

Behavior of a Type-II Superconductor in a Magnetic Field

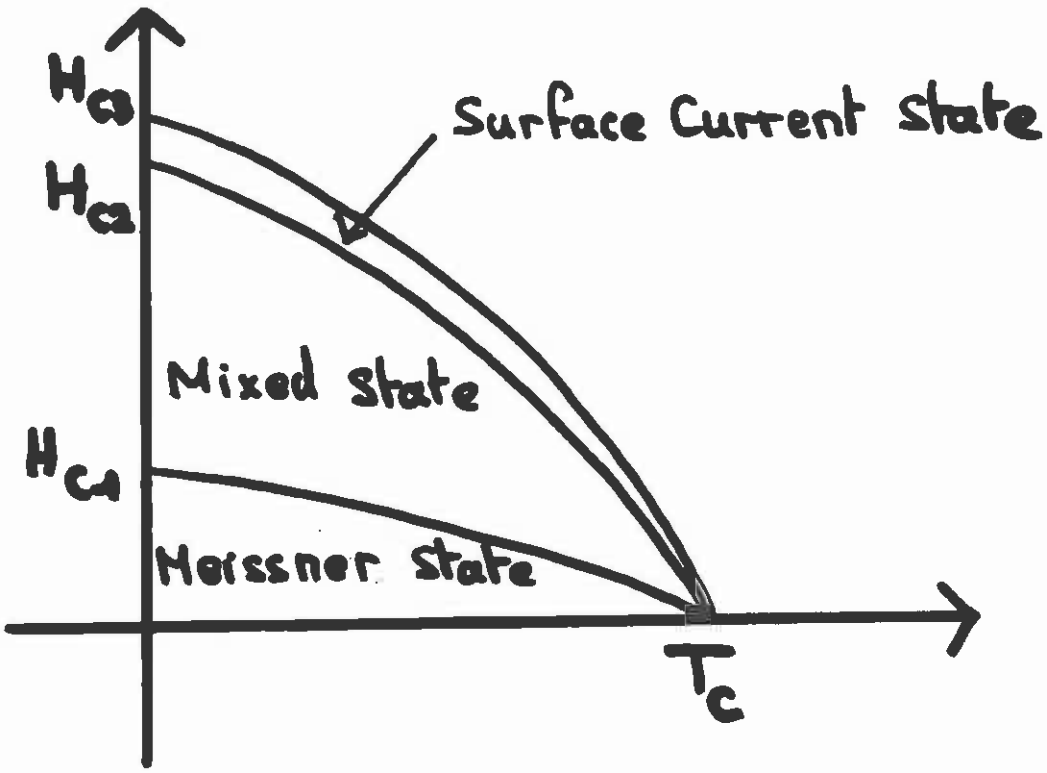

TYPICAL VALUES OF CRITICAL FIELDS AND TEMPERATURES

– The following table lists the values of the critical temperature at zero field (T_C) and of the lower and upper critical magnetic flux densities at 4.2 K [$B_{C1} = (\mu_0 H_{C1})$ and $B_{C2} = (\mu_0 H_{C2})$] for some type-II superconducting materials:

Material	T_C (K)	B_{C1} (T)	B_{C2} (T)
Nb	9.2	0.125	0.26
NbTi	9.5	0.01	11
Nb_3Sn	18	0.017	23
Nb_3Al	19		30
Nb_3Ge	23		35

LECTURE 2: SUPERCONDUCTIVITY APPLIED TO PARTICLE ACCELERATOR MAGNETS

2.1 Why superconductivity?

2.2 Origin of Superconductivity and critical temperature

2.3 Magnetic states of superconductors and critical fields

2.4 Transport properties of superconductors and critical current density

2.5 Critical State Model

2.6 Review of superconducting particle accelerators

2.7 Prominent features of superconducting accelerator magnets

2.8 Superconducting accelerator magnet R&D

TYPE-II SUPERCONDUCTORS CARRYING TRANSPORT CURRENT

– Let us now consider a type-II superconductor in the mixed state, and let us assume that it carries a transport current of density, J.

– The combination of transport current and magnetic flux density generates a Lorentz-like force, F_L:

$$F_L \sim (n_f \phi_0) J$$

where n_f is the density of fluxoids (which depends on the external field strength).

– The lorentz-like force acts on the fluxoids and tends to move them.

FLUX FLOW IN TYPE-II SUPERCONDUCTORS

– In an ideal type-II superconductor, nothing prevents the fluxoids from moving. The fluxoids' motion engenders dissipation and the material heats up. Then, the material behaves as if it had on ohmic resistance and soon reverts to the normal, non-superconducting state.

– This dissipative phenomenon, referred to as *flux flow*, limits the amount of transport current that can be carried by an ideal type-II superconductor.

PINNING IN TYPE-II SUPERCONDUCTORS

– In practice, the motion of the fluxoids can be prevented by pinning them at certain sites in the lattice.

– The pinning mechanisms are not fully understood. They usually take place at sites where there is a defect in the lattice or where there is a local area of lower (or zero) superconducting properties.

– These sites exert a pinning force, F_P, on the fluxoids, which hold them in position as long as

$$F_L \leq F_P$$

– The pinning force depends on temperature : the lower the temperature, the stronger the pinning.

Mixed State of Non-Ideal Type-II Superconductor

$H_{c_1}(T) < H < H_{c_2}(T)$

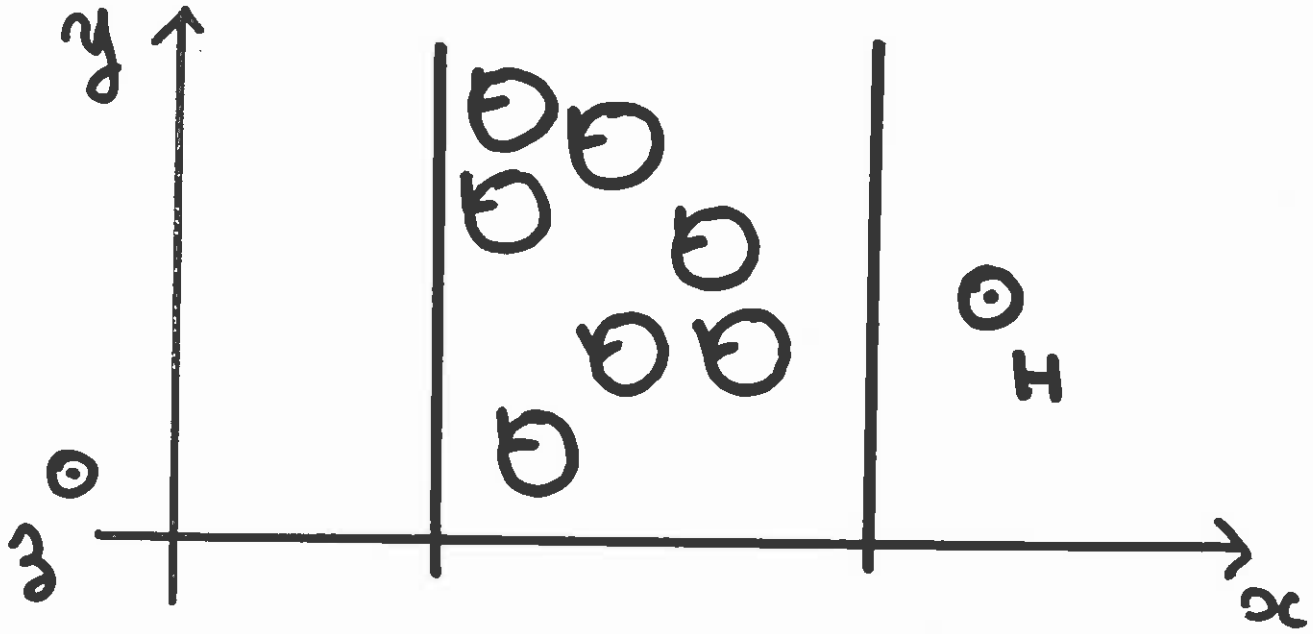

Vortices are <u>pinned</u> by irregularities of material

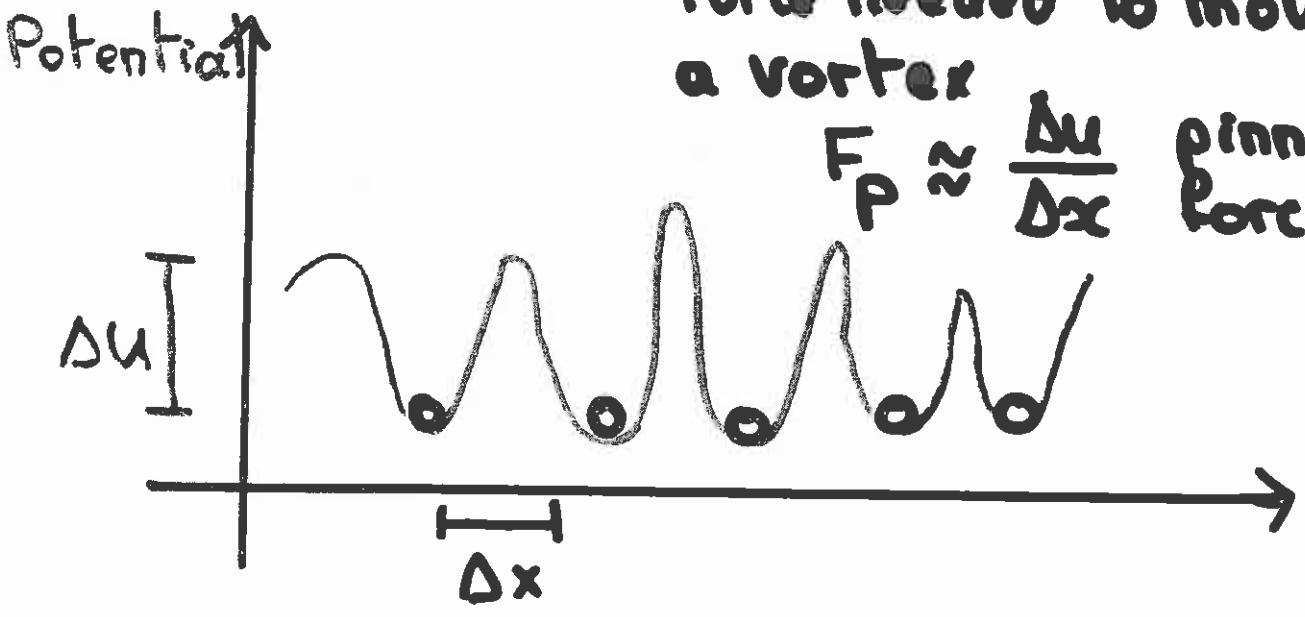

Force needed to move a vortex

$F_p \approx \frac{\Delta u}{\Delta x}$ pinning force

CRITICAL CURRENT DENSITY OF PRACTICAL SUPERCONDUCTORS

– Let us consider a practical type-II superconductor at a temperature, T, subjected to an external magnetic flux density, B, and carrying a transport current with a density, J.

– The presence of the external magnetic flux density results in the creation of fluxoids, with a density $n_F(B)$, which are pinned with a force $F_P(T)$.

– The circulation of the transport current results in a Lorentz-like force, F_L, acting on the fluxoids and such that

$$F_L \sim J\, n_F(B)\, \phi_0$$

CRITICAL CURRENT DENSITY OF PRACTICAL SUPERCONDUCTORS (CONT.)

– As long as F_L is lower than F_P, the material can transport current without dissipation, but when F_L becomes larger than F_P, the fluxoids are liberated from the pinning sites and start to move. The material then progressively reverts to the normal resistive state.

– The density of transport current for which F_L is equal to F_P is called the *critical current density*, J_C.

– From the above equations, we have:

$$J_C \sim \frac{F_P(T)}{n_F(B)\ \phi_0}$$

– J_C is a function of T (the higher the temperature, the lower the pinning force, and the lower J_C), and of B (the higher B, the larger the density of fluxoids, and the lower J_C).

Critical Current Density of a Non-Ideal Type-II Superconductor

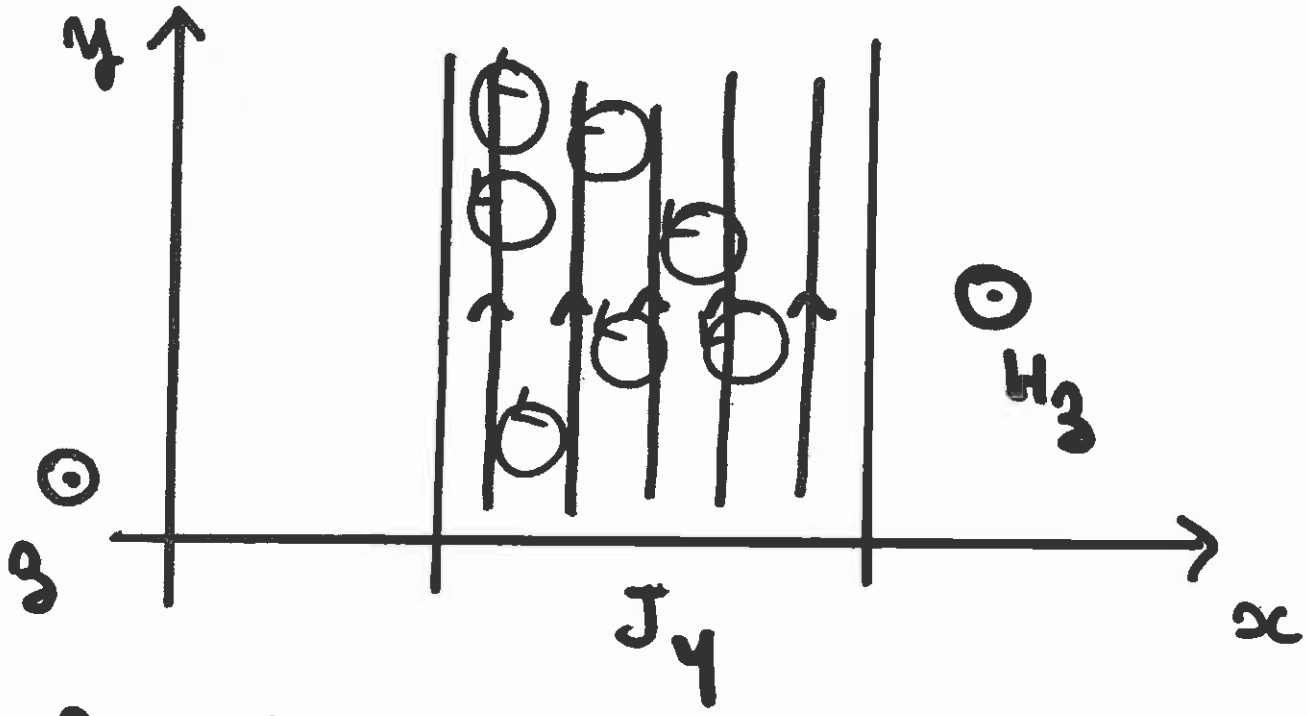

The vortices will be subjected to a Lorentz-like force

$$F_L = J_y \times n \phi_0 \leq F_p$$

the critical current density $J_c(T,B)$ is the value of J for which

$$F_L = F_p$$

CRITICAL SURFACE OF PRACTICAL SUPERCONDUCTORS

– In practice, the boundary between the superconducting state and the normal resistive state of a practical superconductor can be represented by a three-dimensional surface which depends on operating temperature, applied magnetic flux density and transport current density. This surface is called the *critical surface.*

Critical Surface For NbTi

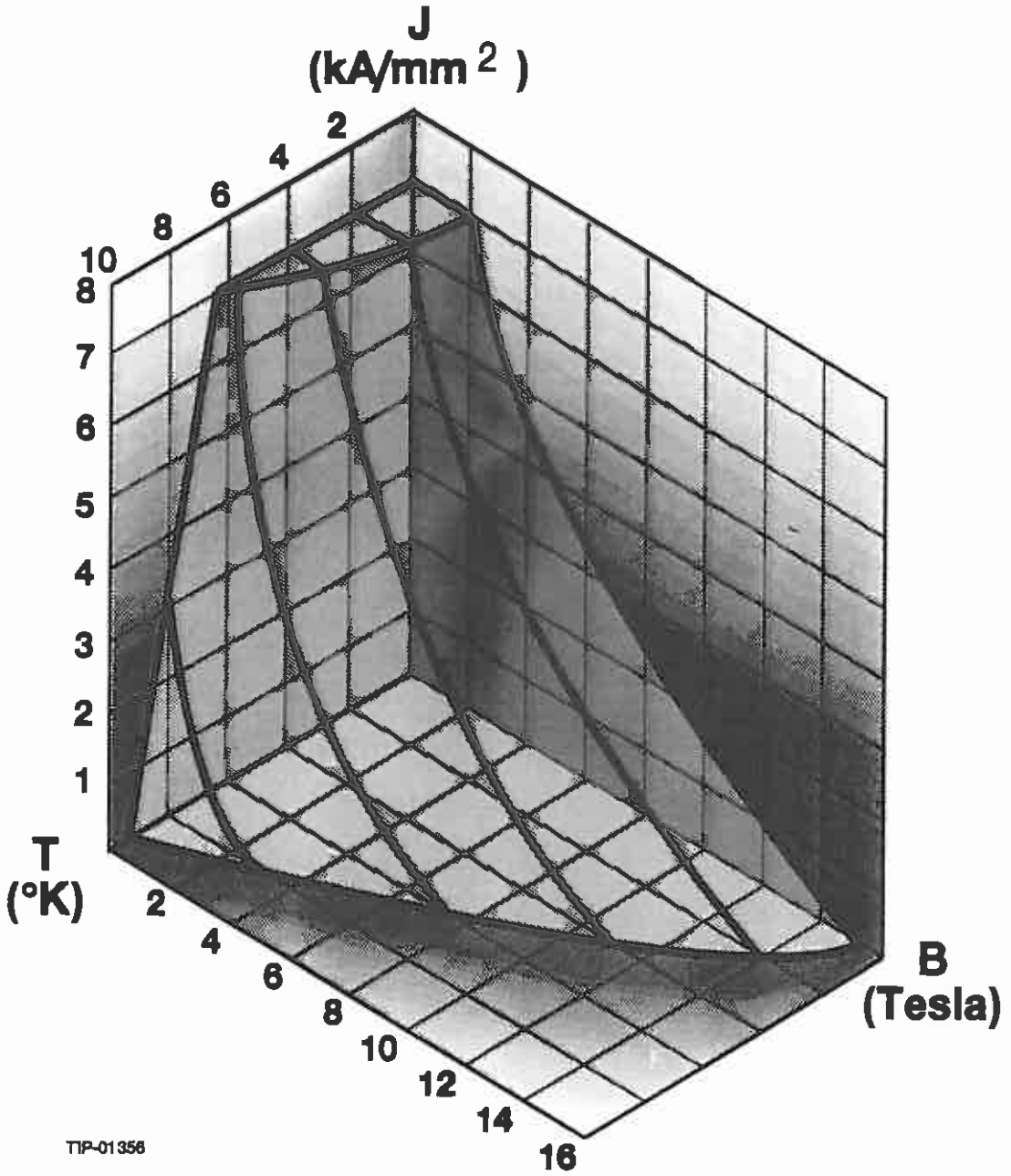

LECTURE 2: SUPERCONDUCTIVITY APPLIED TO PARTICLE ACCELERATOR MAGNETS

2.1 Why superconductivity?

2.2 Origin of Superconductivity and critical temperature

2.3 Magnetic states of superconductors and critical fields

2.4 Transport properties of superconductors and critical current density

2.5 Critical State Model

2.6 Review of superconducting particle accelerators

2.7 Prominent features of superconducting accelerator magnets

2.8 Superconducting accelerator magnet R&D

SUPERCONDUCTOR MAGNETIZATION

– We have seen that, in the mixed state, the magnetic flux penetrates within the bulk of type-II superconductors in the form of fluxoids.

– We have seen also that, in practical type-II superconductors, defects are introduced in the lattice to pin down the fluxoids and prevent them from moving.

– Let us now describe how the pinning sites are populated when rising the applied magnetic field above the lower critical magnetic field, H_{C1}, and how a type-II superconductor gets magnetized.

SEMI-INFINITE SLAB MODEL

– Let $(O,\vec{x},\vec{y},\vec{z})$ designate a rectangular coordinate system, and let us assume that the half-space $x \leq 0$ is occupied by a semi-infinite slab of type-II superconductor, while the half-space $x \geq 0$ is in a vacuum.

– Let us also assume that the superconductor includes pinning sites, and let $n_p(x)$ designate the pinning site density at abscissa x.

– Initially, the superconductor is at an uniform temperature, T_0, below the critical temperature, and no magnetic field is applied. Hence, the superconductor is in the superconducting state and the pinning sites are all empty. The superconductor is said to be in a *virgin state*.

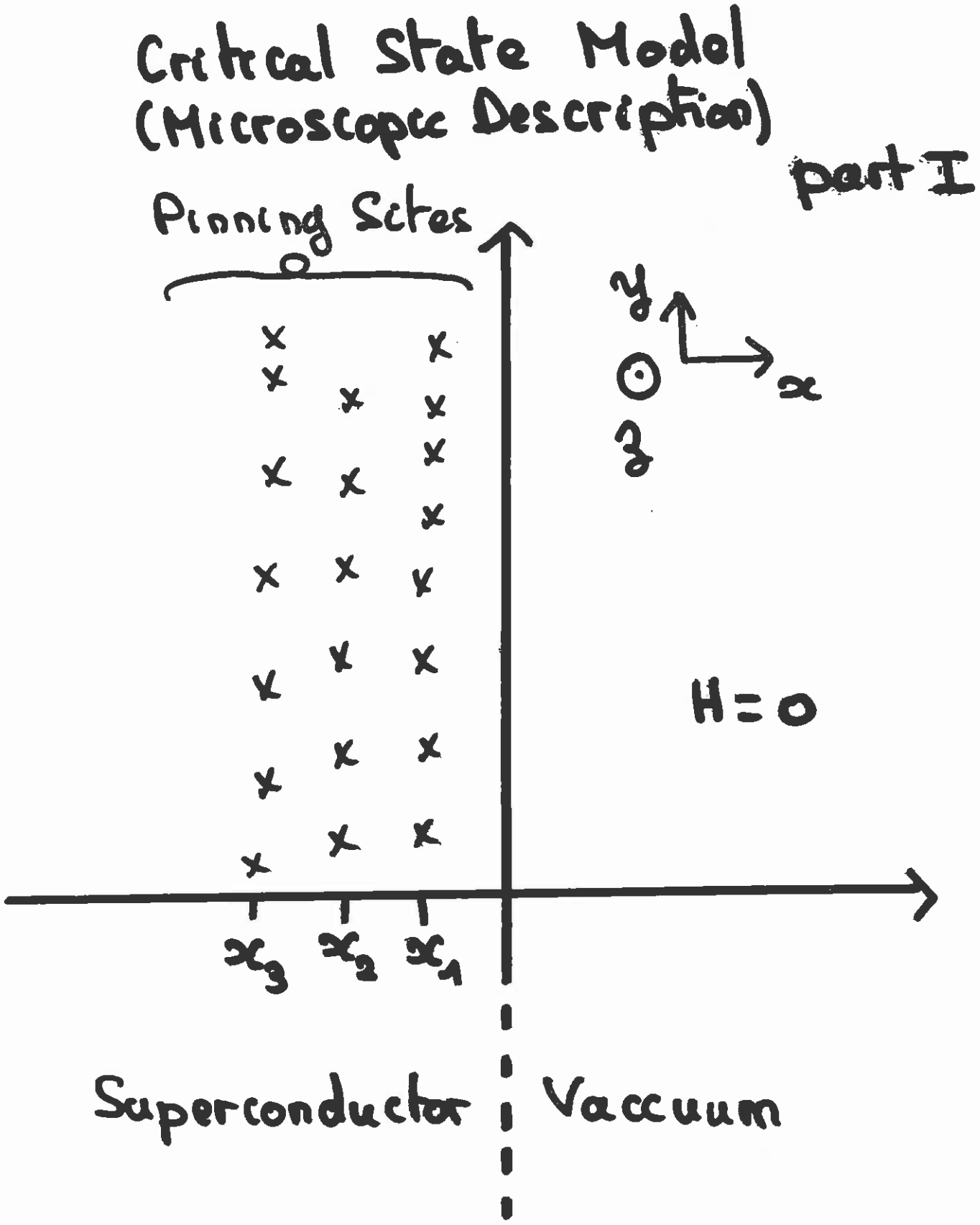
Critical State Model
(Microscopic Description)
part I
Pinning Sites
y
x
z
H = 0
x_3
x_2
x_1
Superconductor
Vaccuum

PINNING SITES POPULATION

– Let us now assume that an uniform magnetic field is risen in the whole space from 0 to H_0. Let us assume that the direction of H_0 is parallel to the z-axis and that its amplitude is between $H_{C1}(T_0)$ and $H_{C2}(T_0)$.

– As the superconductor enters the mixed state, fluxoids are created near its surface, which drift towards the negative x and start to occupy the pinning sites.

– Let $N_p(x)$ designates the density of pinning sites which are occupied at abscissa x. The function N_p increases with H_0 and decreases with negative x: the further away from the interface, the less pinning sites are likely to be occupied.

Critical State Model (Microscopic Description)

part II

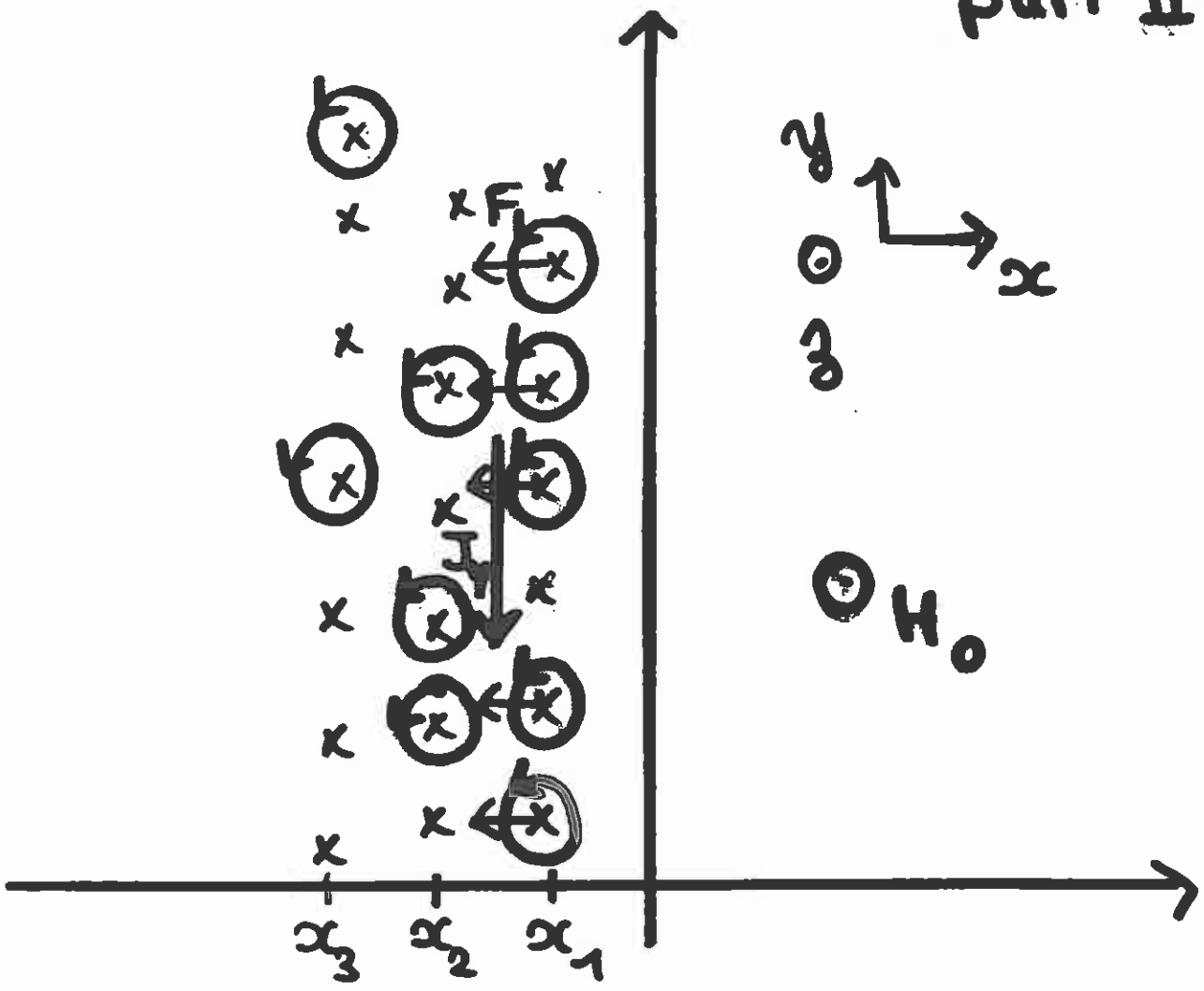

$J_y \propto N_\beta(x_1) - N_\beta(x_2)$

where $N(x)$ is the density of occupied pinning sites at abscissa x

SUPERCURRENT DENSITY

– Let x_1 and x_2 designate the abscissas of two (hypothetically) adjacent rows of pinning sites, and let A be an observer located at an abscissa x, between x_1 and x_2, and looking in the direction of the y-axis.

Observer A sees, on his right-handside, the row x_1 of pinning sites which are occupied by a density $N_p(x_1)$ of fluxoids. These fluxoids are surrounded by annular supercurrents, which, for the observer, seem to flow along the y-direction and coming towards him.

Similarly, Observer A sees, on his left-handside, the row x_2 of pinning sites, which are occupied by a density $N_p(x_2)$ of fluxoids. These fluxoids are surrounded by annular suppercurrents, which, for the observer, seem to flow along the y-direction and going away from him.

SUPERCURRENT DENSITY (CONT.)

– In summary, Observer A sees a net density of supercurrents, flowing along the y-axis, which is proportional to the difference $[N_p(x_2) - N_p(x_1)]$.

– In more physical terms, the distribution of fluxoids results in a macroscopic current density, $J_y(x,B_0)$, parallel to the y-axis, and such that:

$$J_y(x,B_0) \sim \frac{\partial N_p(x,B_0)}{\partial x}$$

EQUILIBRIUM OF FLUXOID DISTRIBUTION

– As we have seen, an uneven fluxoid distribution results in a macroscopic current density, $J_y(x,B_0)$, parallel to the y-axis.

– The combination of this current density with the magnetic flux carried by the fluxoids, results in a lorentz-like force which tends to move the fluxoids along the x-axis. This Lorentz-like force is responsible for the fluxoids' drift towards the interior of the material.

– As we described earlier, an equilibrium is reached when the Lorentz-like force becomes equal to the pinning force. By definition, we have then:

$$J_y(x,B_0) = J_C(T,B_0)$$

where $J_C(T,B_0)$ is the superconductor critical current density at the given temperature and field.

– Hence the fluxoids redistribute themselves and drift towards the interior of the superconductor until the macroscopic current density seen by Observer A reaches $J_C(T,B_0)$.

CURRENT AND FIELD PROFILE IN A SEMI-INFINITE SLAB

– According to Maxwell-Ampère's equation, the macroscopic field B is related to the macroscopic current density, J_C, by:

$$\nabla \times \vec{B} = \mu_0 \vec{J_C}$$

– In our case, the above equation reduces to:

$$\frac{\partial B_z}{\partial x} = -\mu_0 J_C$$

where B_z is parallel to the z-axis.

This yields:

$$B_z(x) = B_0 + \mu_0 J_C x$$

Critical State Model
(Macroscopic Description)

From Maxwell's Equations

$\overrightarrow{\text{curl}}\ \vec{H} = \vec{J}$

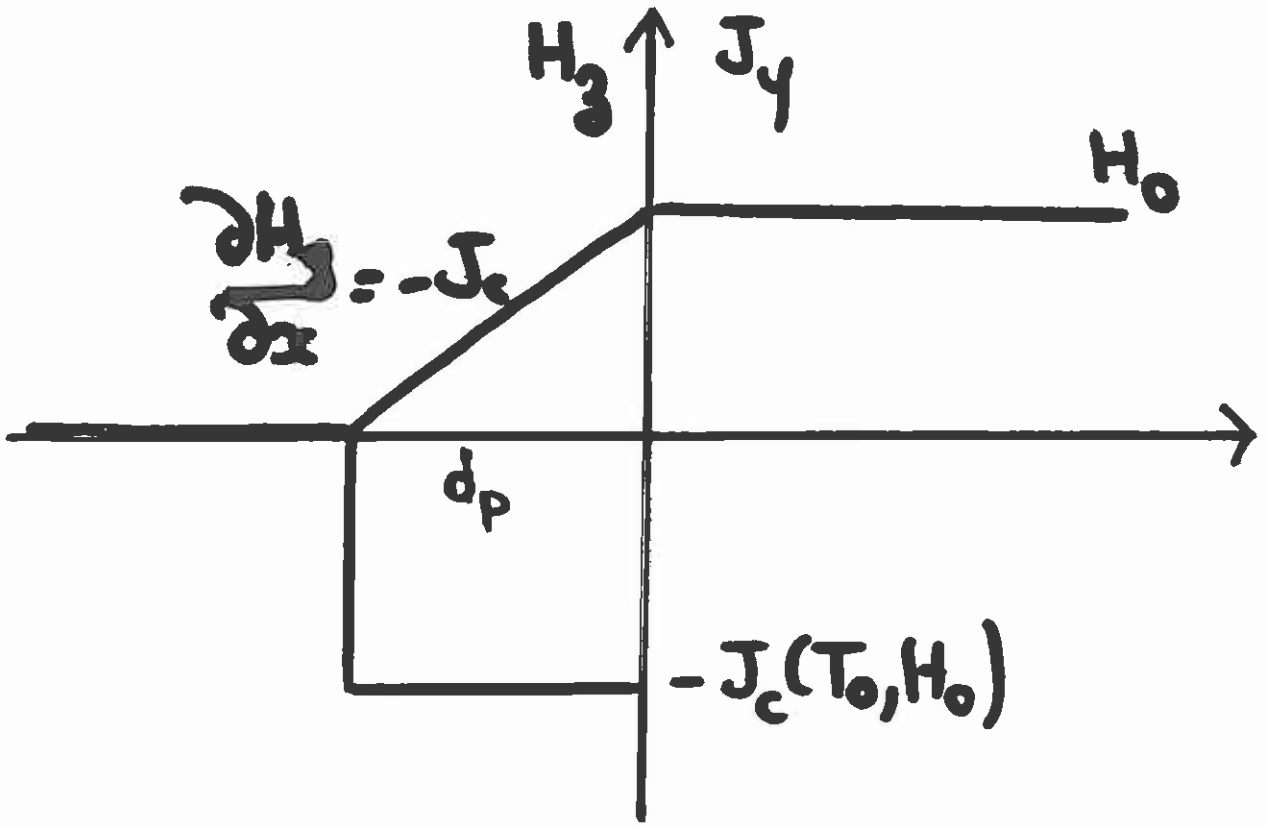

The macroscopic current is established to shield the inside of the superconducting slab from the change in external field. The shielding current is called persistent magnetization current.

CURRENT AND FIELD PROFILE IN A SEMI-INFINITE SLAB (CONT.)

– When starting from a superconductor in a virgin state, there is no reason why, for $x \leq 0$, B_z should drop below zero. It follows that field variations are limited to a depth, d_p, called the *penetration depth*, given by:

$$d_p = \frac{B_0}{\mu_0 J_C}$$

– It follows also that the magnetic flux density is nil for x, $x \leq -d_p$, and that no pinning sites are occupied beyond the depth d_p.

CRITICAL STATE MODEL

– When describing the macroscopic behavior of a type-II superconductor subjected to an external magentic flux density change, there is no need to go back to the fluxoids and on how they distribute themselves among the pinning sites.

– The results described in the previous slides can be summerized as follows: when the magnetic flux density applied to a type-II superconductor is varied, the superconductor reacts by generating currents at its periphery which shield its core from the external field variation.

– The density of the shielding currents is the superconductor critical current density at the given temperature and magnetic flux density. Their distribution is such that they produce within the superconductor, a magnetic flux density, $\vec{B}_i$, exactly opposite to the applied field variations, $\Delta\vec{B}_0$:

$$\vec{B}_i + \Delta\vec{B}_0 = 0$$

CRITICAL STATE MODEL (CONT.)

– In the case of a semi-infinite slab, the application of this simple model leads directly to the current and field profiles derived in the previous slides.

– This simple model is called the *critical state model* and was first proposed by C.P. Bean in 1964.

– Note that the shielding currents which are produced are proportional to the amplitude of applied field change but do not depend on the rate of field variations. Also, once they are produced, they do not decay with time. These shielding currents are very different in nature from the conventional eddy currents. They are called *persistent magnetization currents.*

Field Distribution in a Slab of Type II Superconductor

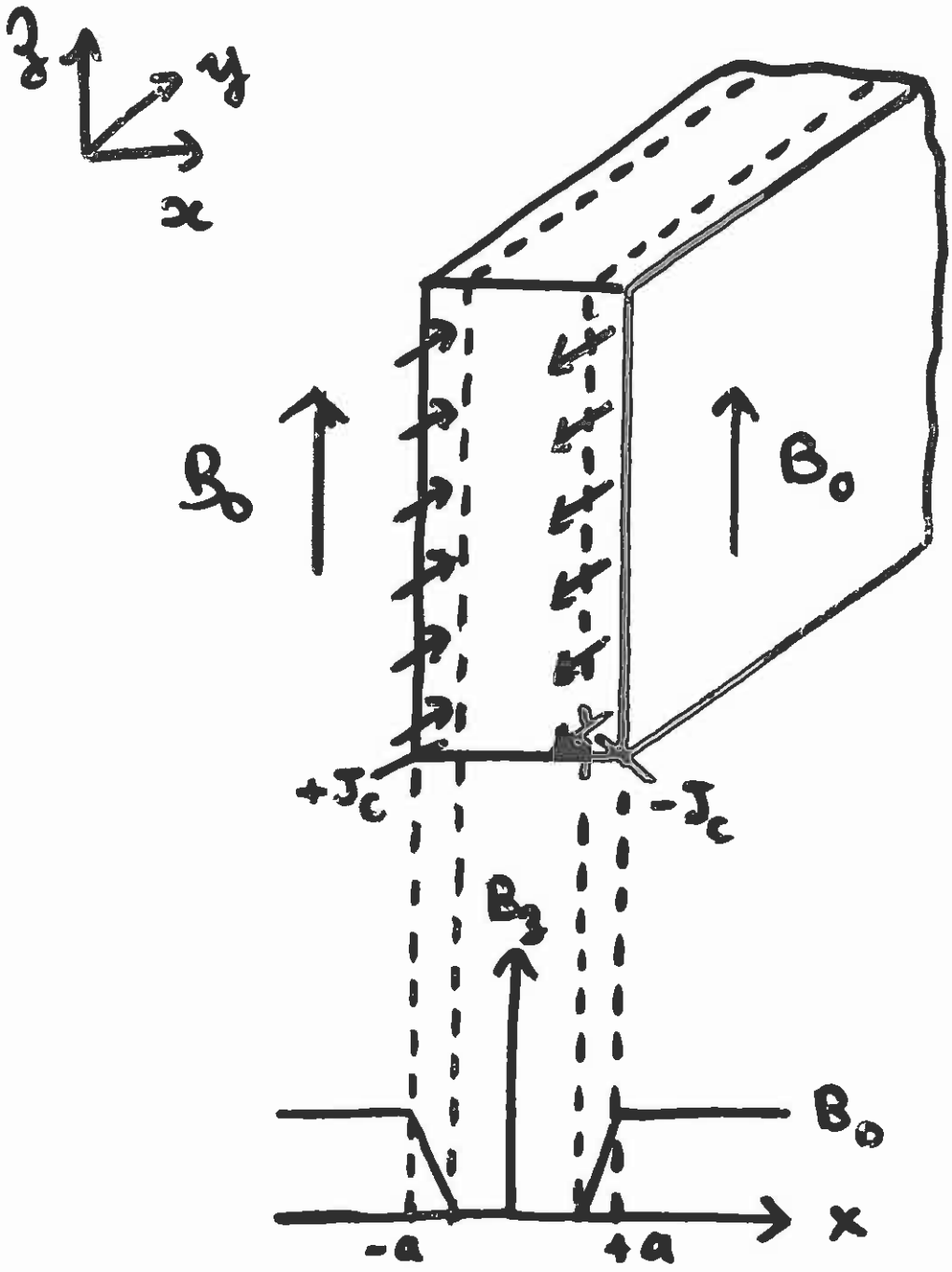

MAGNETIZATION OF A SUPERCONDUCTING FILAMENT

– Let us now consider a rectilinear and infinite superconducting filament, initially in a virgin state, and let us vary the aplied field from O to B_0 where B_0 is perpendicular to the filament axis.

– Several models have been developed to determine the persistant magnetization current distribution generated in the filament. In the simplest ones, the magnetization currents flow in a shell at the filament periphery with an elleptical inner boundary. The ellipse excentricity decreases as a function of the applied field, until the filament is fully penetrated.

Filament Magnetization

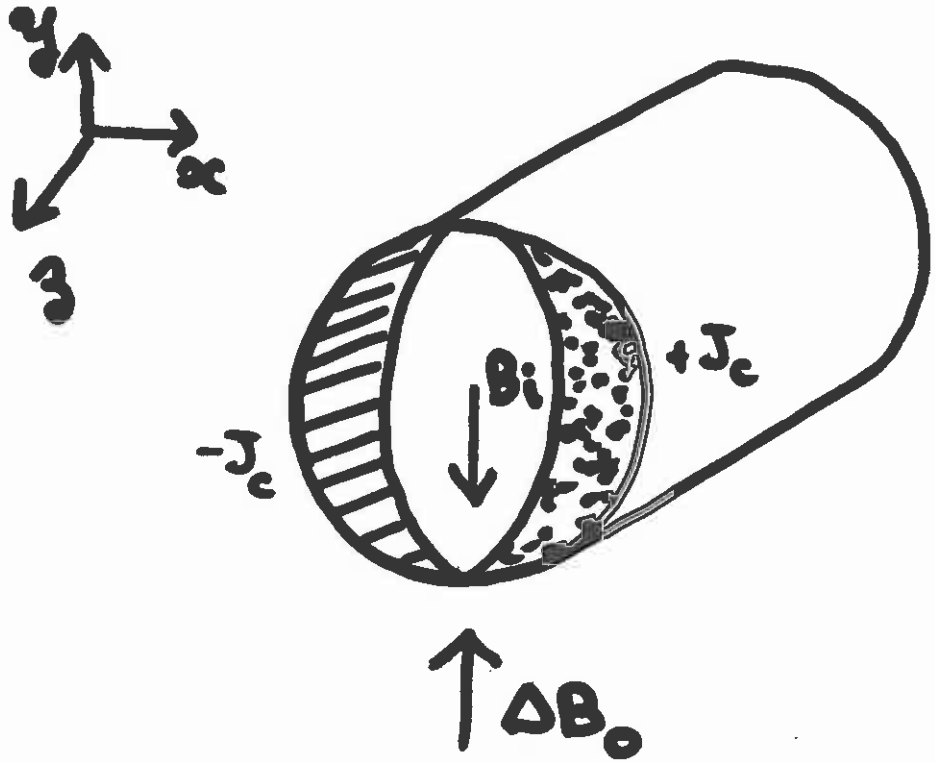

A shell of persistent magnetization currents is created at the filament periphery in order to shield the filament core from the change in external field. The distribution of persistent magnetization currents is such that

$$B_i = -\Delta B_0$$

Filament Magnetization*

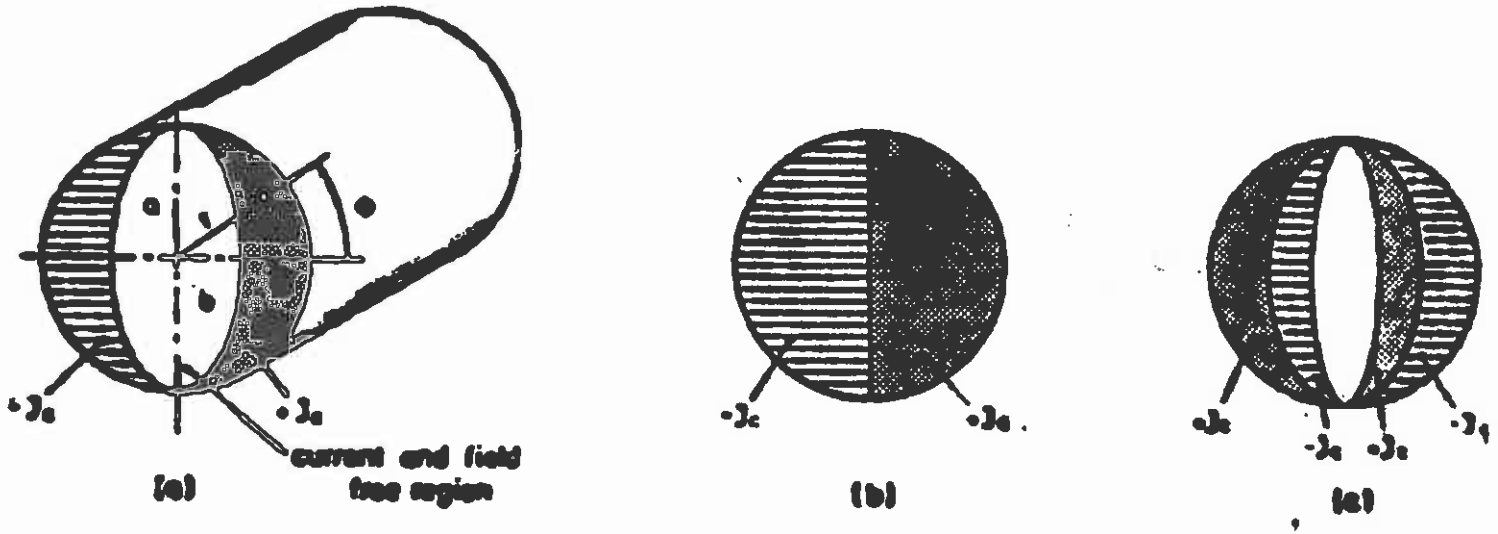

Fig. 4.4 a) A NbTi filament in an external field in vertical direction

b) "Fully magnetized" filament, i.e. $B_a = B_p$

c) Current distribution resulting from a sign reversal in $\frac{dB}{dx}$

* Courtesy P. Schmüser

PENETRATION FIELD

– The field at which the magnetization currents fill up the whole filament is called the *penetration field.* For a field ramp from the virgin state, the penetration field is determined by the implicit equation.

$$B_p = \frac{2\,\mu_0\, J_C(T_0,B_p)\, r_f}{\pi}$$

where μ_0 is the permeability of vacuum, $J_C(T_0,B_p)$ is the superconductor critical current density at the given temperature, T_0 and B_p, and r_f is the filament radius.

– If the applied field is increased beyond, B_p, the distribution of magnetization currents remains the same.

– In practice, B_p is rather small. For a filament with a radius of 5 μm and a critical current density of 2500 A/mm², we get:

$$B_p \approx 0.01 \text{ T}.$$

Hence, for most applications, the filaments can always be considered as fully penetrated.

Filament Magnetigation (Cont.)*

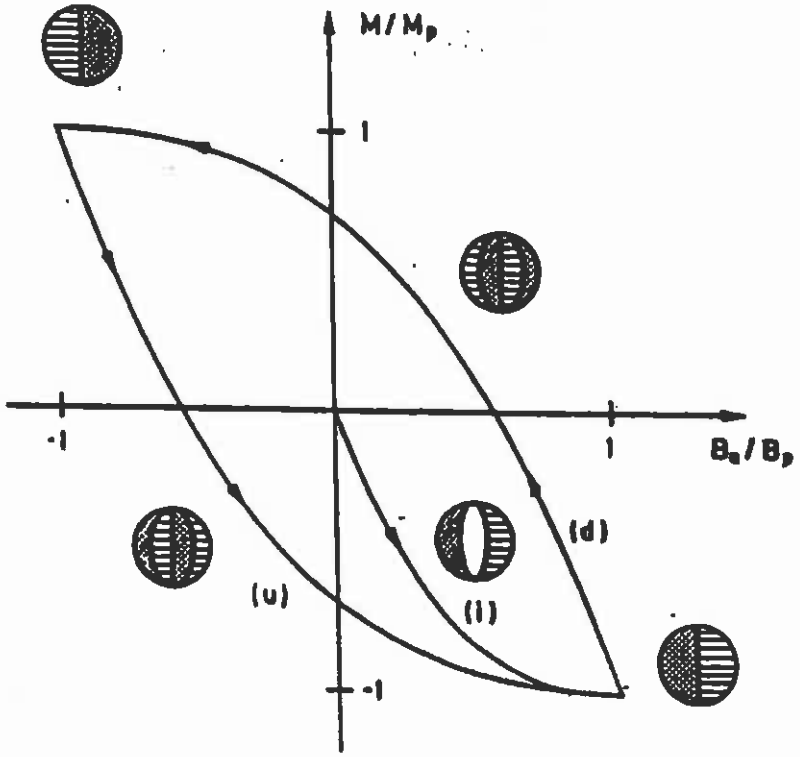

Fig. 4.5 Normalized magnetization of a NbTi filament as a function of the applied field. (i): initial curve, (d): down-ramp branch; (u): up-ramp branch. Also shown are the current distributions in the filament.

* Courtesy P. Schmüser

LECTURE 2: SUPERCONDUCTIVITY APPLIED TO PARTICLE ACCELERATOR MAGNETS

2.1 Why superconductivity?

2.2 Origin of Superconductivity and critical temperature

2.3 Magnetic states of superconductors and critical fields

2.4 Transport properties of superconductors and critical current density

2.5 Critical State Model

2.6 Review of superconducting particle accelerators

2.7 Prominent features of superconducting accelerator magnets

2.8 Superconducting accelerator magnet R&D

TEVATRON

– The first large scale application of superconductivity was the Tevatron. It includes one large ring made up of about 1000 superconducting dipole and quadrupole magnets.

Site:	FNAL, near Chicago, IL
Type:	Proton/antiproton collider
Circumference:	6.3 km
Energy:	900 GeV per beam
Commissioning:	1983

– The Tevatron arc dipole and quadrupole magnets were developed at FNAL.

Aperture:	3" (76.2 mm)
Dipole Field:	4 T
Dipole Length:	6.1 m
Quadrupole gradient:	76 T/m
Quadrupole Length:	1.7 m

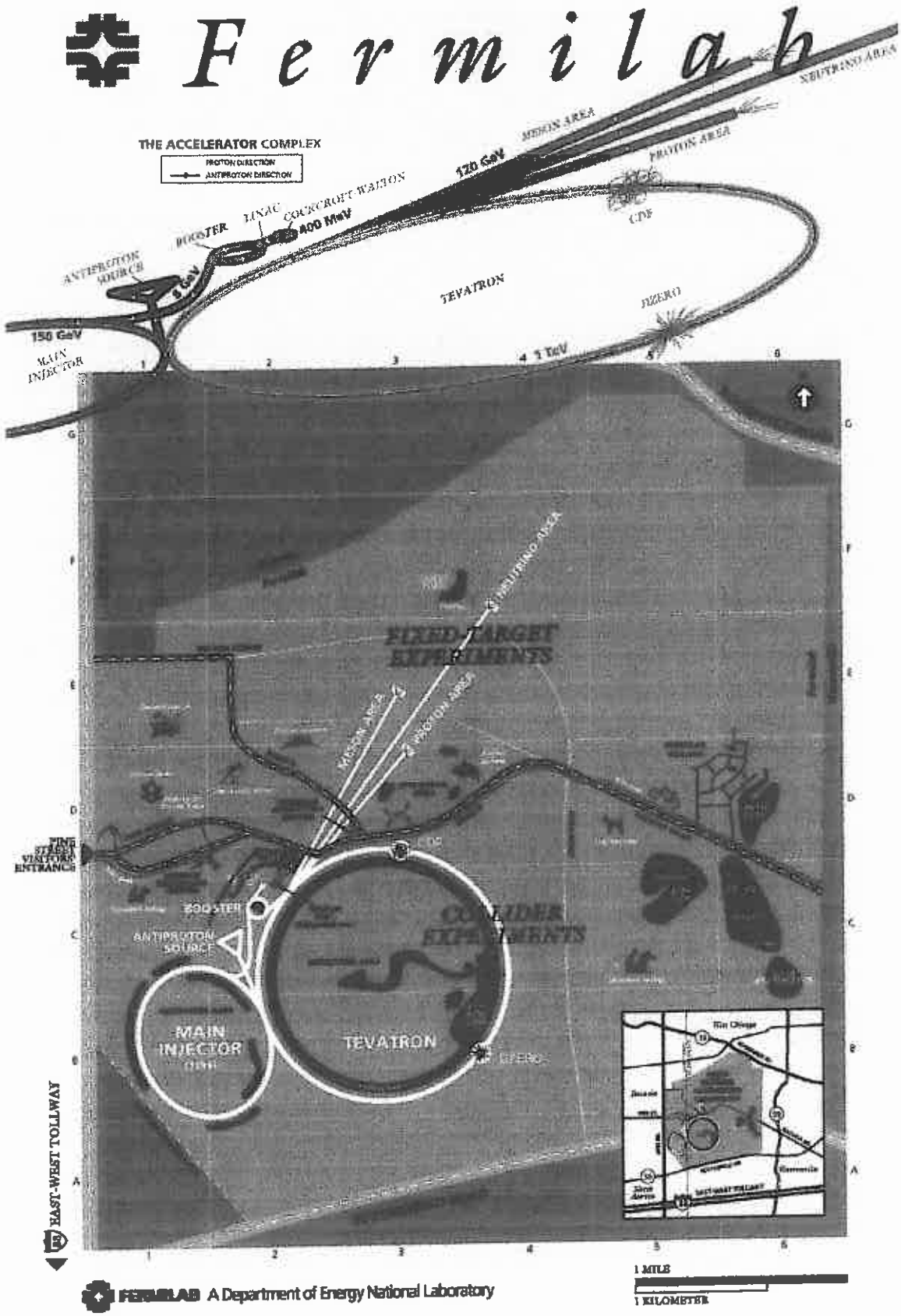
Fermilab
THE ACCELERATOR COMPLEX
PROTON DIRECTION
ANTIPROTON DIRECTION
120 GeV
MUON AREA
NEUTRINO AREA
PROTON AREA
BOOSTER
LINAC
COCKCROFT-WALTON
400 MeV
ANTIPROTON SOURCE
8 GeV
CDF
TEVATRON
DZERO
150 GeV
MAIN INJECTOR
1 TeV
FIXED-TARGET EXPERIMENTS
COLLIDER EXPERIMENTS
MAIN INJECTOR
TEVATRON
EAST-WEST TOLLWAY
1 MILE
1 KILOMETER
FERMILAB A Department of Energy National Laboratory

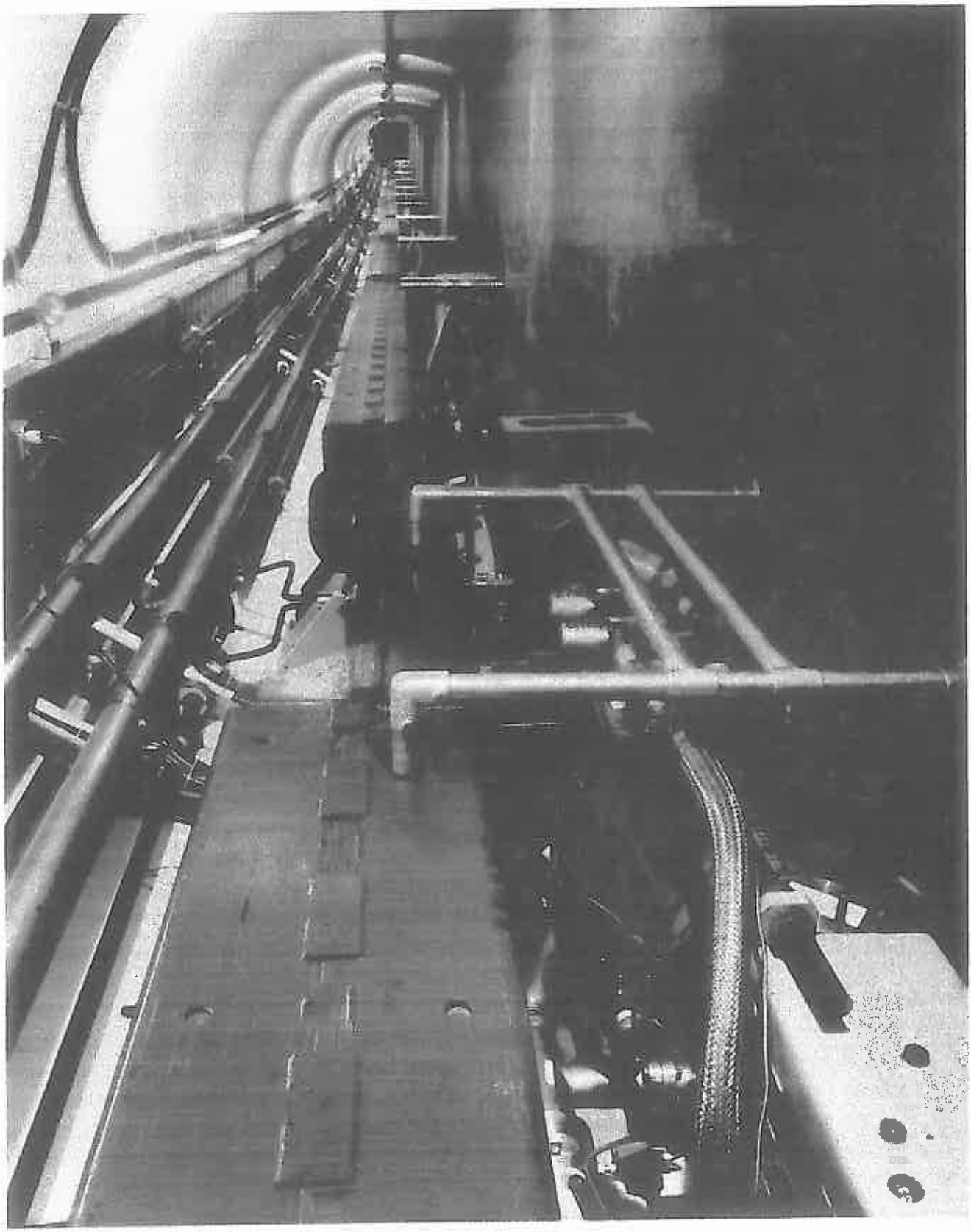

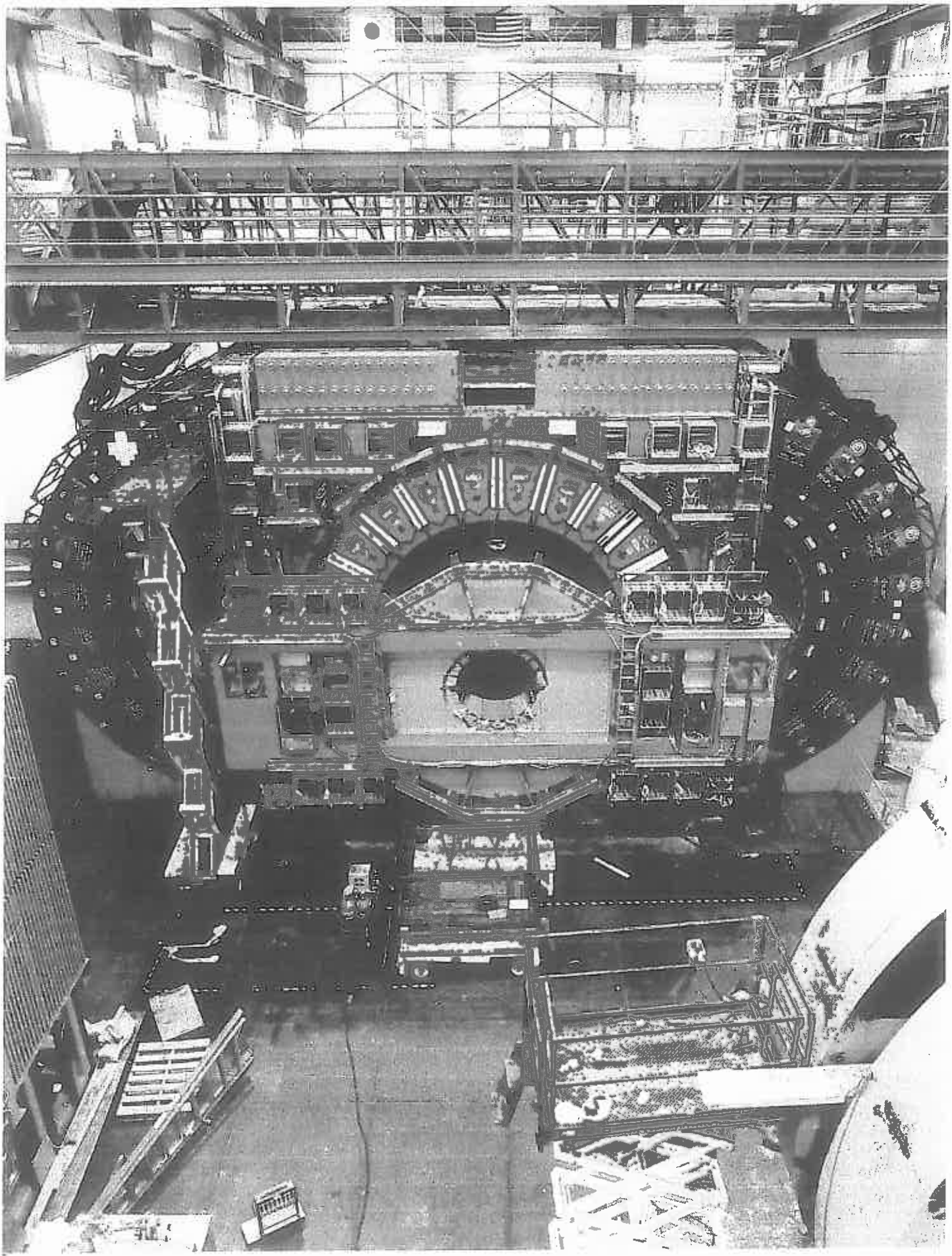

HERA

– The next large particle accelerator to rely massively on superconducting magnet technology was HERA (Hadron Elektron Ring Anlage). It includes two large rings: (1) an electron ring, relying on conventional magnets and (2) a proton ring, relying on superconducting magnets.

Site:	DESY, near Hamburg, Germany
Type:	Electron/proton collider
Circumference:	6.4 km
Energy:	30 GeV for the electron beam and 820 GeV for the proton beam
Commissioning:	1990

– The arc dipole magnets of the proton ring were developed at DESY, while the arc quadrupole magnets were developed at CEA/Saclay.

Aperture:	75 mm
Dipole Field:	4.68 T
Dipole Length:	8.8 m
Quadrupole gradient:	91.2 T/m
Quadrupole Length:	1.9 m

PETRA

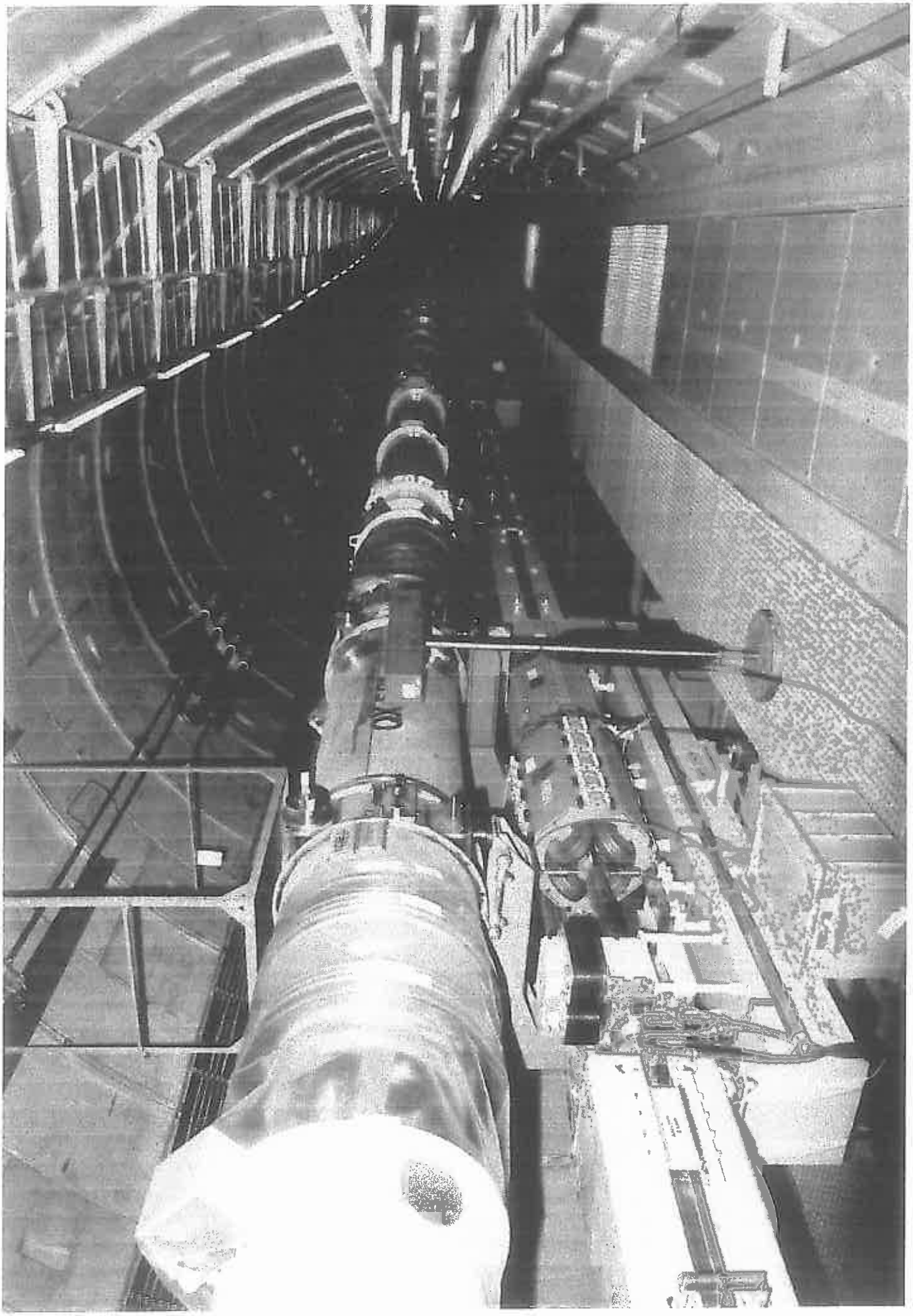

UNK

– Since the early 1980's, the Institute for High Energy Physics (IHEP) located in Protvino, near Moscow, Russia is working on a project of proton accelerator named UNK (Uskoritelno-Nakopitelniy Komplex). UNK includes a single ring of superconducting magnets.

Site:	IHEP, near Moscow, Russia
Type:	Proton synchrotron
Circumference:	21 km
Energy:	3 TeV in fixed target mode
Commissioning:	*undecided*

– The arc dipole and quadrupole magnets are developed at IHEP.

Aperture:	70 mm
Dipole Field:	5.0 T
Dipole Length:	5.8 m
Quadrupole gradient:	70 T/m
Quadrupole Length:	3.0 m

SSC

– In the mid 1980's, the USA started the Superconducting Super Collider (SSC) project. The last stage of the SSC complex would have been made up of two identical rings of superconducting magnets installed on top of each other. The project was eventually cancelled in October 1993 by decision of the United States Congress.

Site:	SSCL, near Dallas, TX
Type:	Proton/proton collider
Circumference:	87 km
Energy:	20 Tev per beam
Commissioning:	*Cancelled*

– The SSC arc dipole magnets were developed by a collaboration between SSCL, BNL and FNAL, while the arc quadrupole magnets were developed by a collaboration between SSCL and LBNL.

Aperture:	50 mm
Dipole Field:	6.79 T
Dipole Length:	15 m
Quadrupole gradient:	194 T/m
Quadrupole Length:	5.7 m

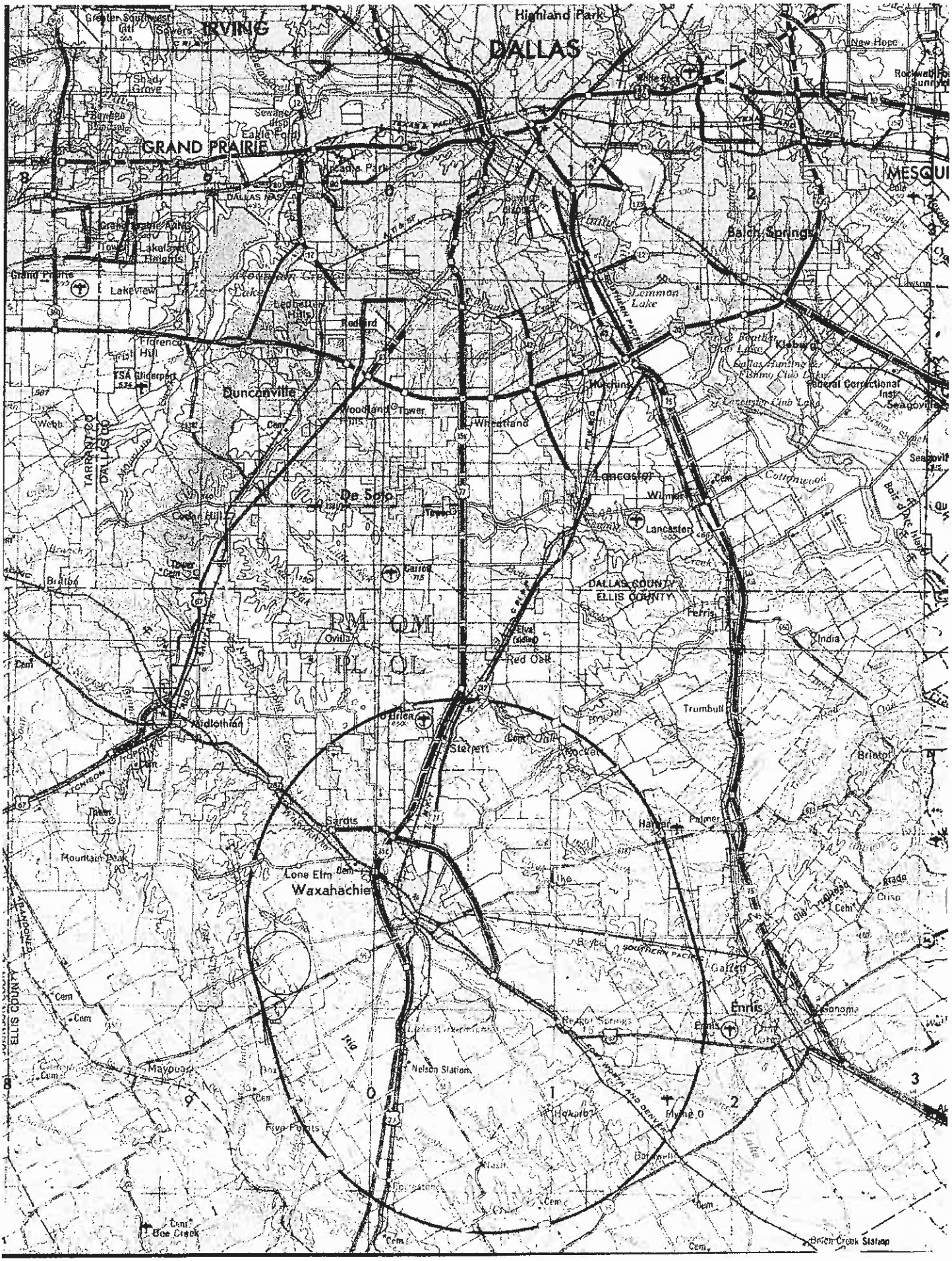
IRVING
DALLAS
Highland Park
GRAND PRAIRIE
Balch Springs
Lemmon Lake
Dunconville
Lancaster
De Soto
DALLAS COUNTY
ELLIS COUNTY
Red Oak
Midlothian
Waxahachie
Lone Elm
Sardis
Sterrett
Trumbull
Ferris
Ennis
Maypearl
Nelson Station
Five Points
Bee Creek
Union Creek Station
Lakeview
Florence Hill
Wheatland
Hutchins
Kleberg
Seagoville
Bristol
Palmer
Ike
Garrett
Rocket
Ovilla
Carrol
Cedar Hill
Woodland Hills
Redbird
Ledbetter Hills
Lakeland Heights
Grand Prairie
Shady Grove
Eagle Ford
Arcadia Park
Sewage disp
Lancaster Club Lake
Federal Correctional Inst
Cottonwood
Mountain Peak
Hokaro
Flying O
Crisp
Grade
Cem
Tower
Webb
Britton
TARRANT CO
DALLAS CO
ELLIS COUNTY
ATCHISON
SOUTHERN PACIFIC
TEXAS & PACIFIC
RM
QM
PL
QL

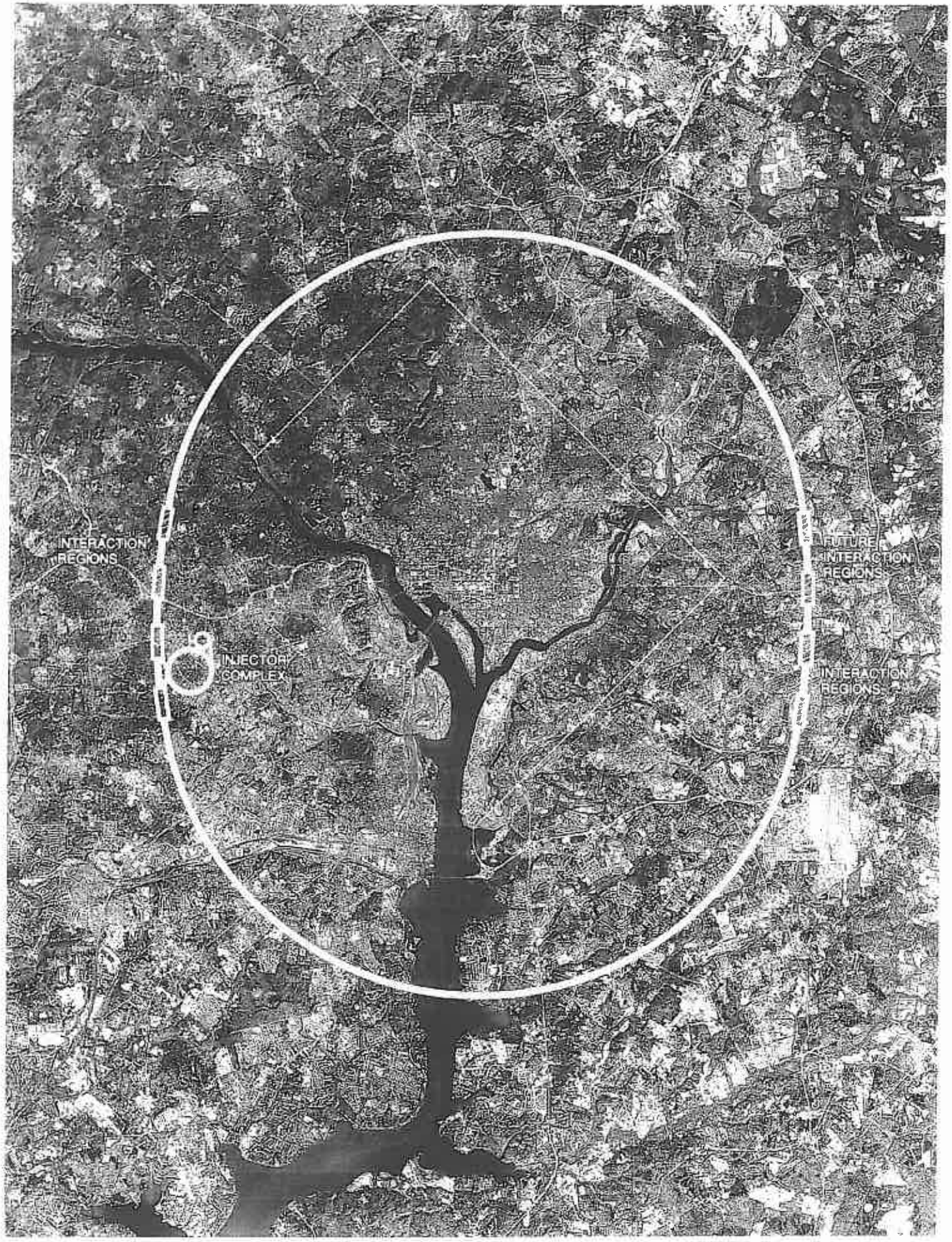
INTERACTION REGIONS
INJECTOR COMPLEX
FUTURE INTERACTION REGIONS
INTERACTION REGIONS

(Billy Haynes Photo)

SSC dancer — *Young Stephanie Moore of Midlothian was among the tiny tutu-clad dancers helping to celebrate the grand opening of the SSC Lab office in DeSoto this week.*

Superconducting Super Collider Project
N-15 Construction Site

1. ASST Compressor Building
2. ASST String Enclosure
3. ASST Cryogenic Refrigeration Service Building
4. Magnet Power Supply Control Room
5. Magnet Delivery Shaft
6. Magnet Development Laboratory
7. Magnet Test Laboratory
8. Personnel Shaft
9. Utility Shaft

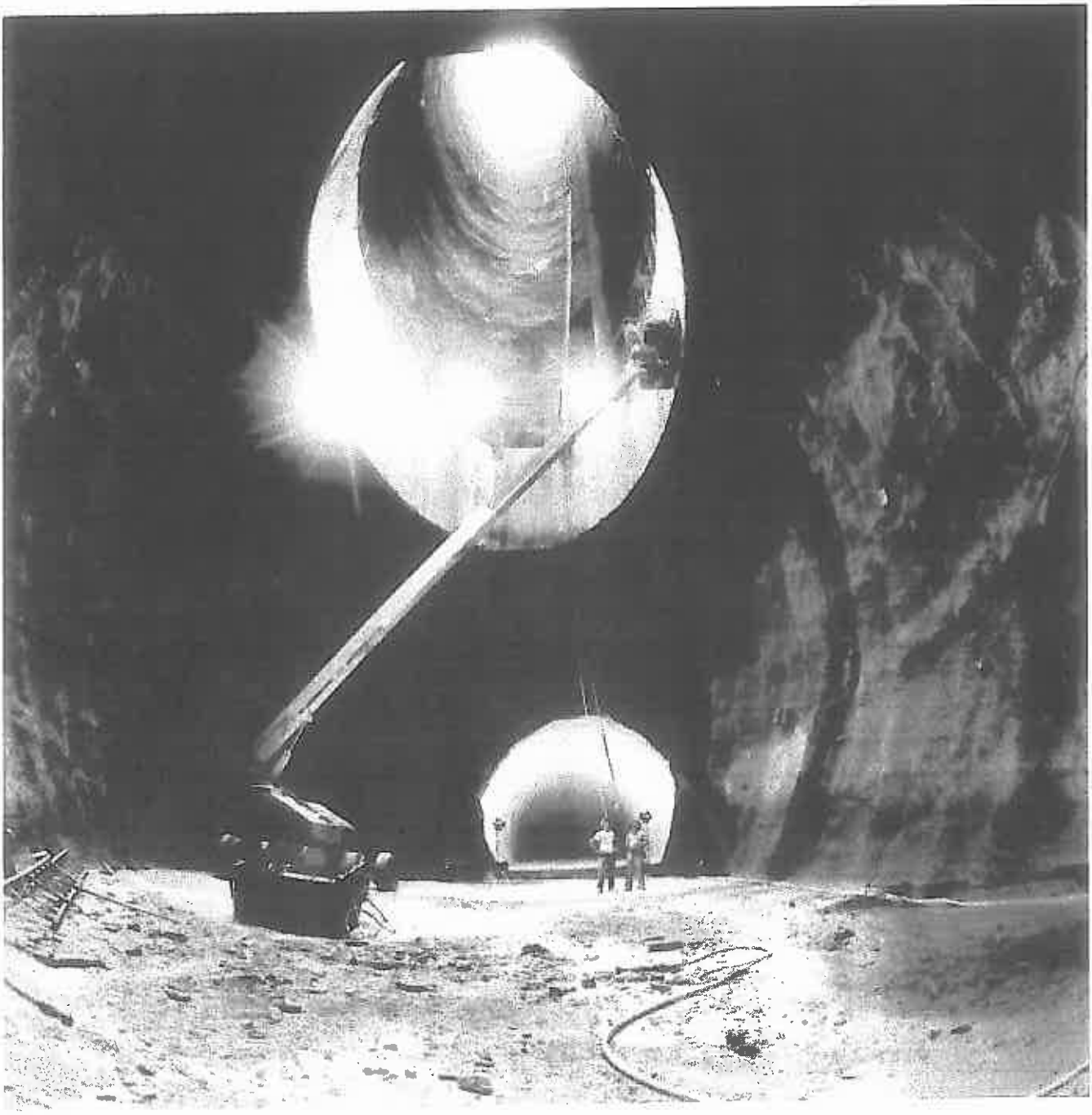

Completion of
Accelerator System String Test Milestone
SSC Laboratory
August 14, 1992

RHIC

– BNL is completing the construction on its site of the Relativistic Heavy Ion Collider (RHIC), which includes two identical rings of superconducting magnets.

Site:	BNL, on Long Island, NY
Type:	Heavy ions collider
Circumference:	3.8 km
Energy:	Up to 100 GeV per beam and per unit of atomic mass
Commissioning:	1999

– The RHIC arc dipole and quadrupole magnets were developed at BNL.

Aperture:	80 mm
Dipole Field:	3.4 T
Dipole Length:	9.7 m
Quadrupole gradient:	71 T/m
Quadrupole Length:	1.1 m

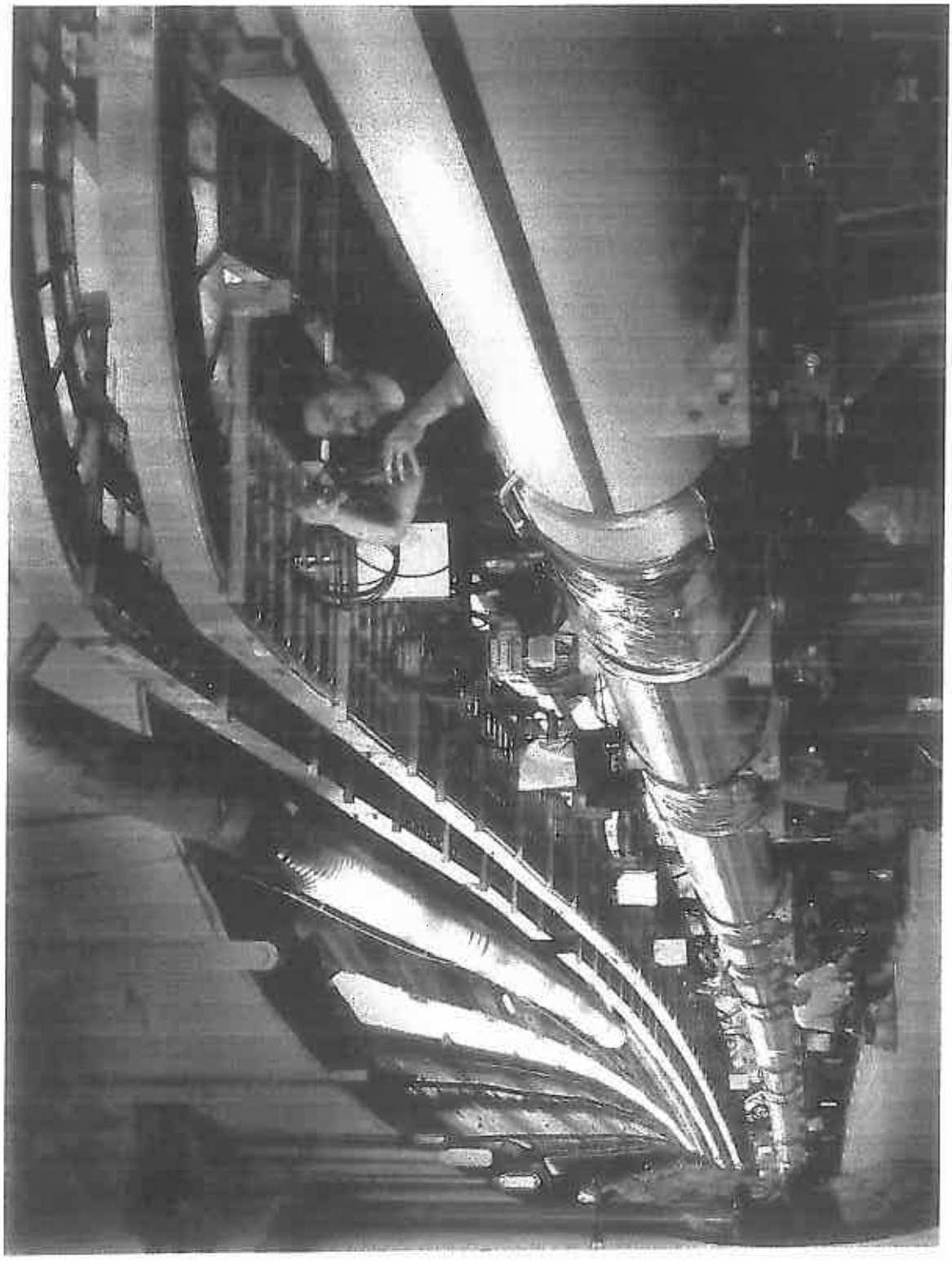

LHC

– In December 1994, CERN has approved the construction of the Large Hadron Collider (LHC). LHC will have a single ring of twin-aperture superconducting magnets, housing within the same mechanical structure, the pipes for two counter-rotating proton beams.

Site:	CERN, at the Swiss/French border near Geneva
Type:	Proton/proton collider
Circumference:	27 km
Energy:	7 TeV per beam
Commissioning:	2005

– The LHC arc dipole magnets are developed at CERN, while the arc quadrupole magnets are developed at CEA/Saclay.

Aperture:	56 mm
Dipole Field:	8.36 T
Dipole Length:	14.2 m
Quadrupole gradient:	223 T/m
Quadrupole Length:	3.1 m

LECTURE 2: SUPERCONDUCTIVITY APPLIED TO PARTICLE ACCELERATOR MAGNETS

2.1 Why superconductivity?

2.2 Origin of Superconductivity and critical temperature

2.3 Magnetic states of superconductors and critical fields

2.4 Transport properties of superconductors and critical current density

2.5 Critical State Model

2.6 Review of superconducting particle accelerators

2.7 Prominent features of superconducting accelerator magnets

2.8 Superconducting accelerator magnet R&D

PROMINENT FEATURES OF SUPERCONDUCTING ACCELERATOR MAGNETS

– The magnets used in superconducting accelerators around the world rely on similar design principles.

– The field is produced by saddle shape coils which, in their long straight sections, approximate $\cos\theta$ conductor distributions for dipole magnets and $\cos 2\theta$ conductor distributions for quadrupole magnets.

–The coils are wound from Rutherford-type cables made of NbTi multifilamentary strands and are mechanically restrained by means of laminated collars.

– The collared-coil assembly is placed within an iron yoke providing a return path for the magnetic flux.

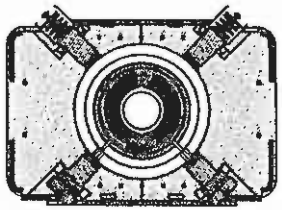

Tevatron

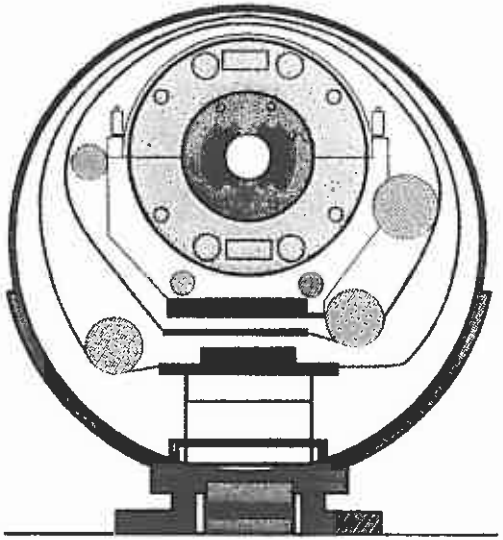

SSC

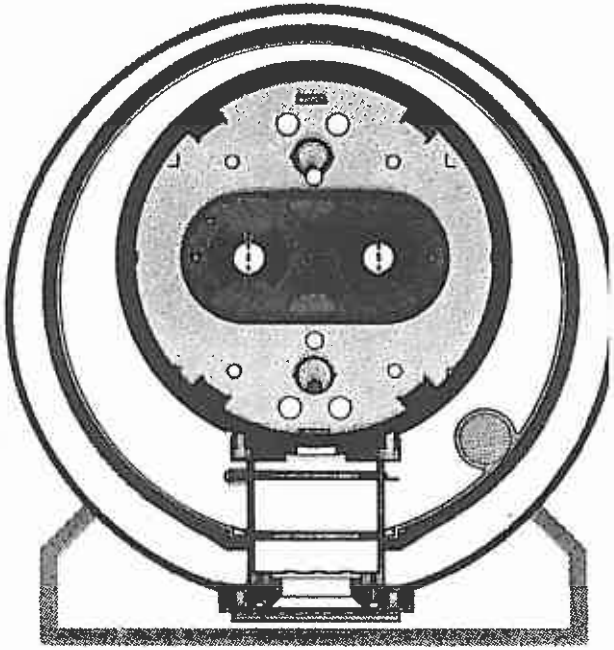

LHC

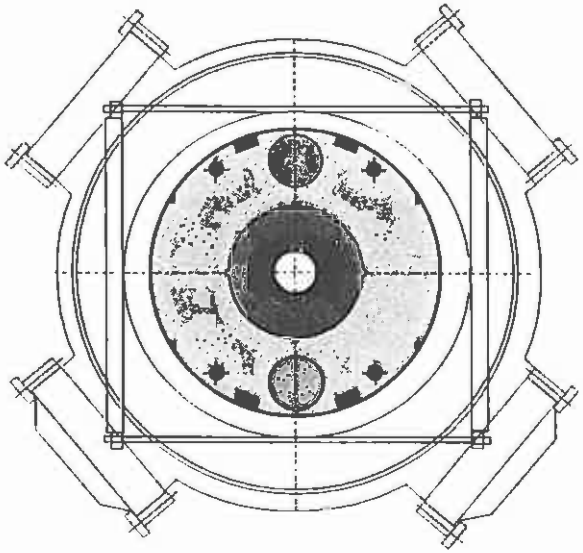

HERA

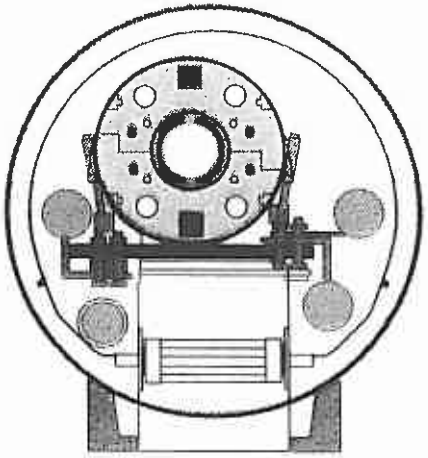

RHIC

PROMINENT FEATURES OF SUPERCONDUCTING ACCELERATOR MAGNETS (CONT.)

– In the case of the Tevatron, the collared-coil assembly is cold while the iron yoke is warm.

– Starting with HERA, the iron yoke is included in the magnet cryostat and the cold mass is completed by an outer shell delimiting the region of helium circulation.

– In the case of LHC, the cold mass includes two collared-coil assemblies within a common iron yoke.

– Tevatron, HERA, UNK, SSC and RHIC magnets are cooled by boiling helium at 1 atmosphere (4.2 K) or supercritical helium at 3 to 5 atmosphere (between 4.5 and 5 K).

– LHC magnets are cooled by superfluid helium at 1.9 K.

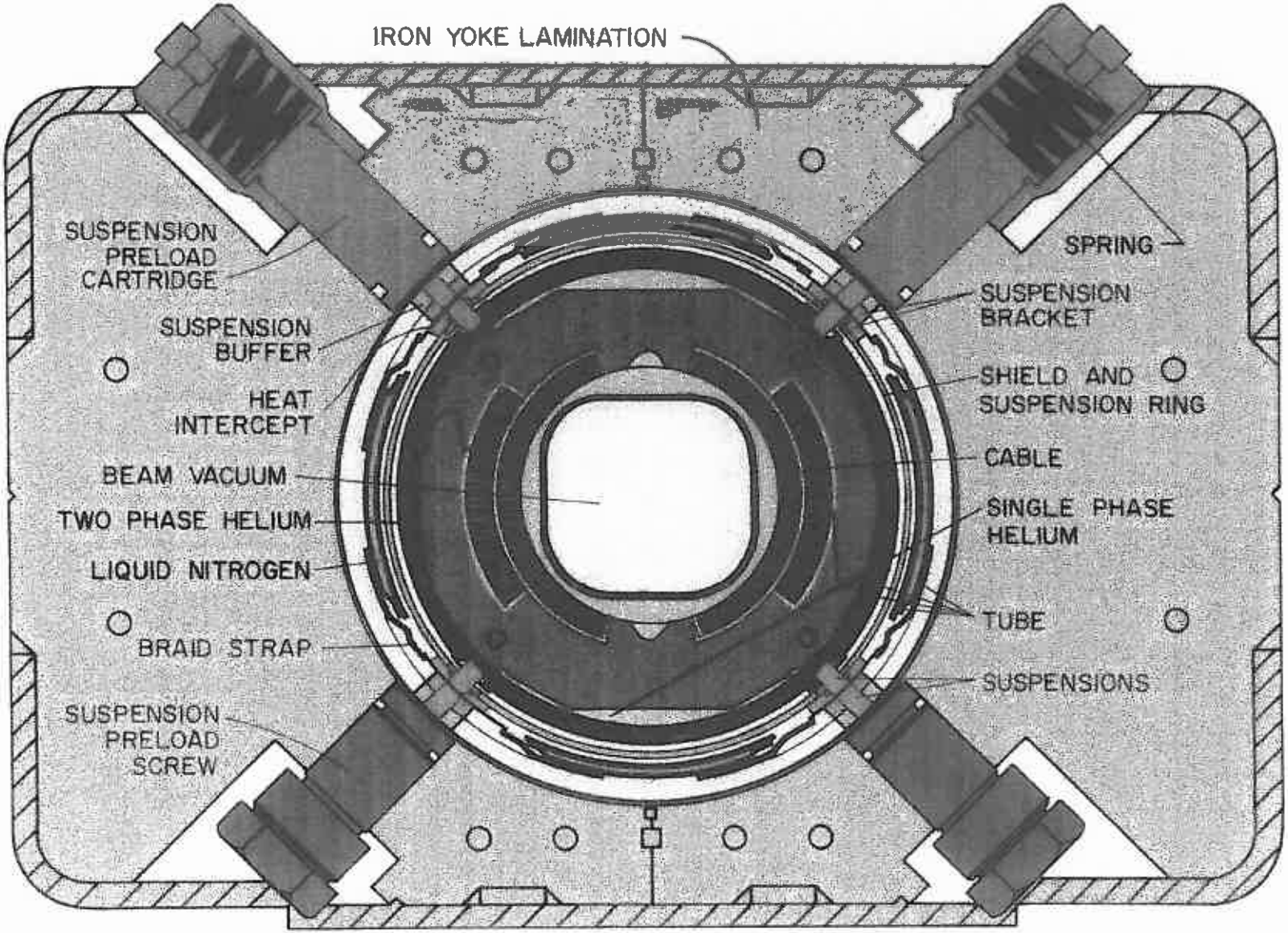

Tevatron Dipole Magnet

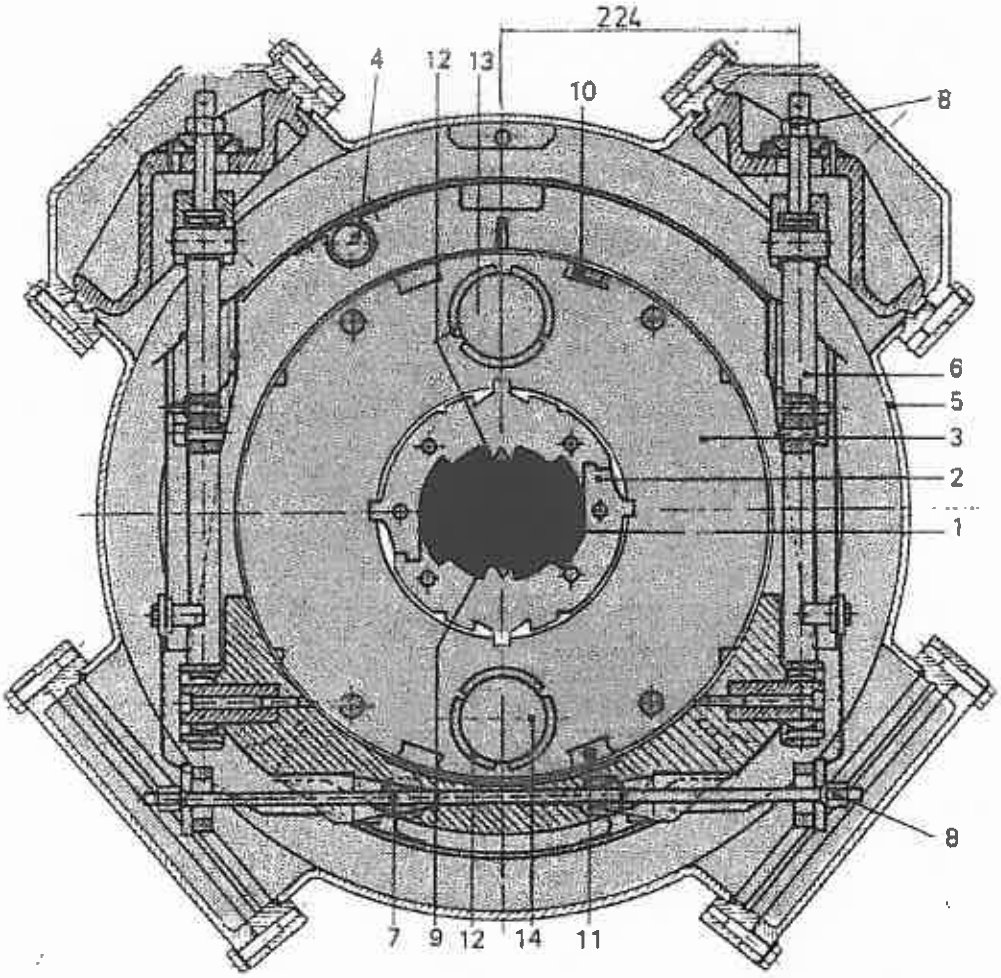

HERA Dipole Magnet

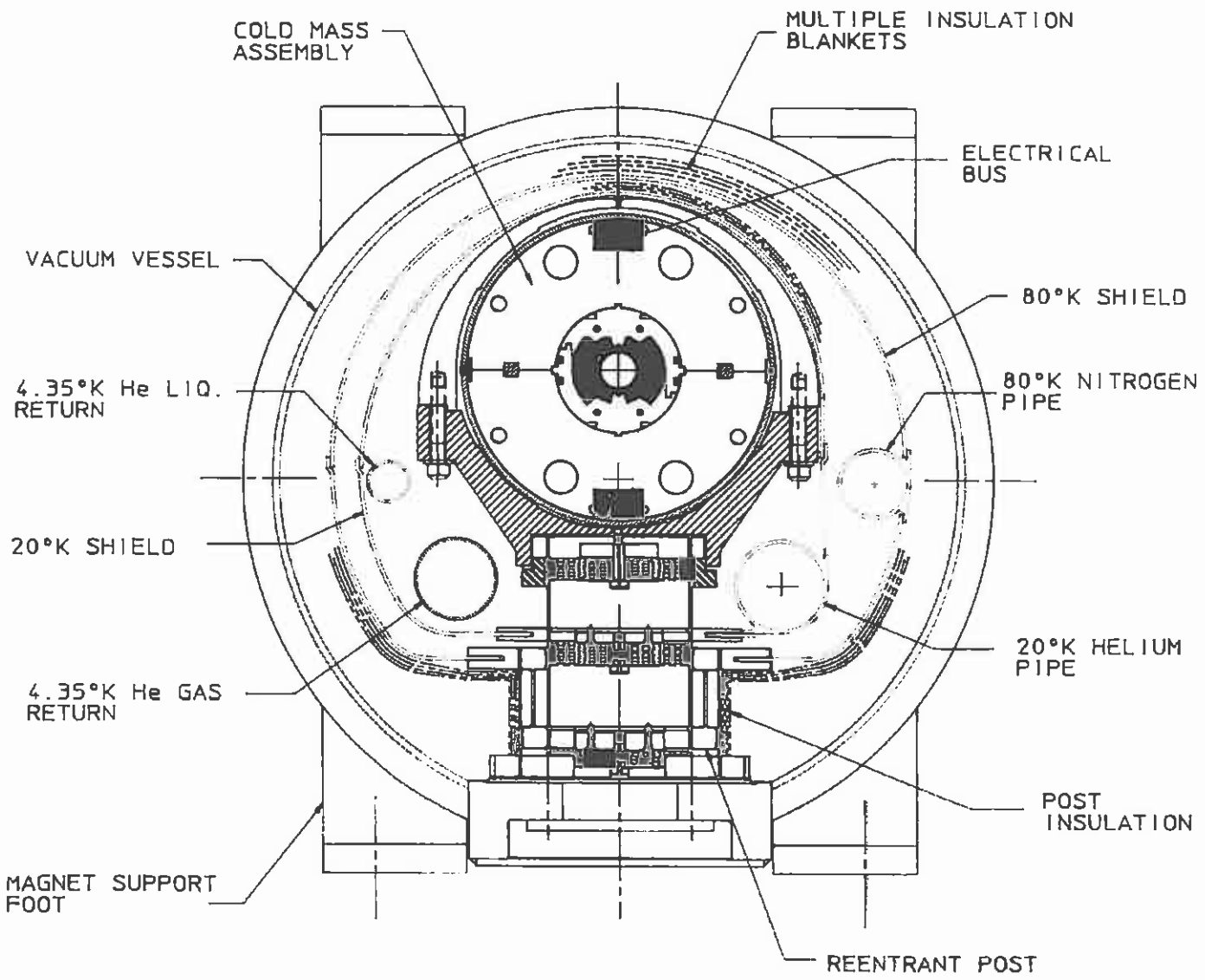

SSC 4-cm-Aperture Dipde Magnet

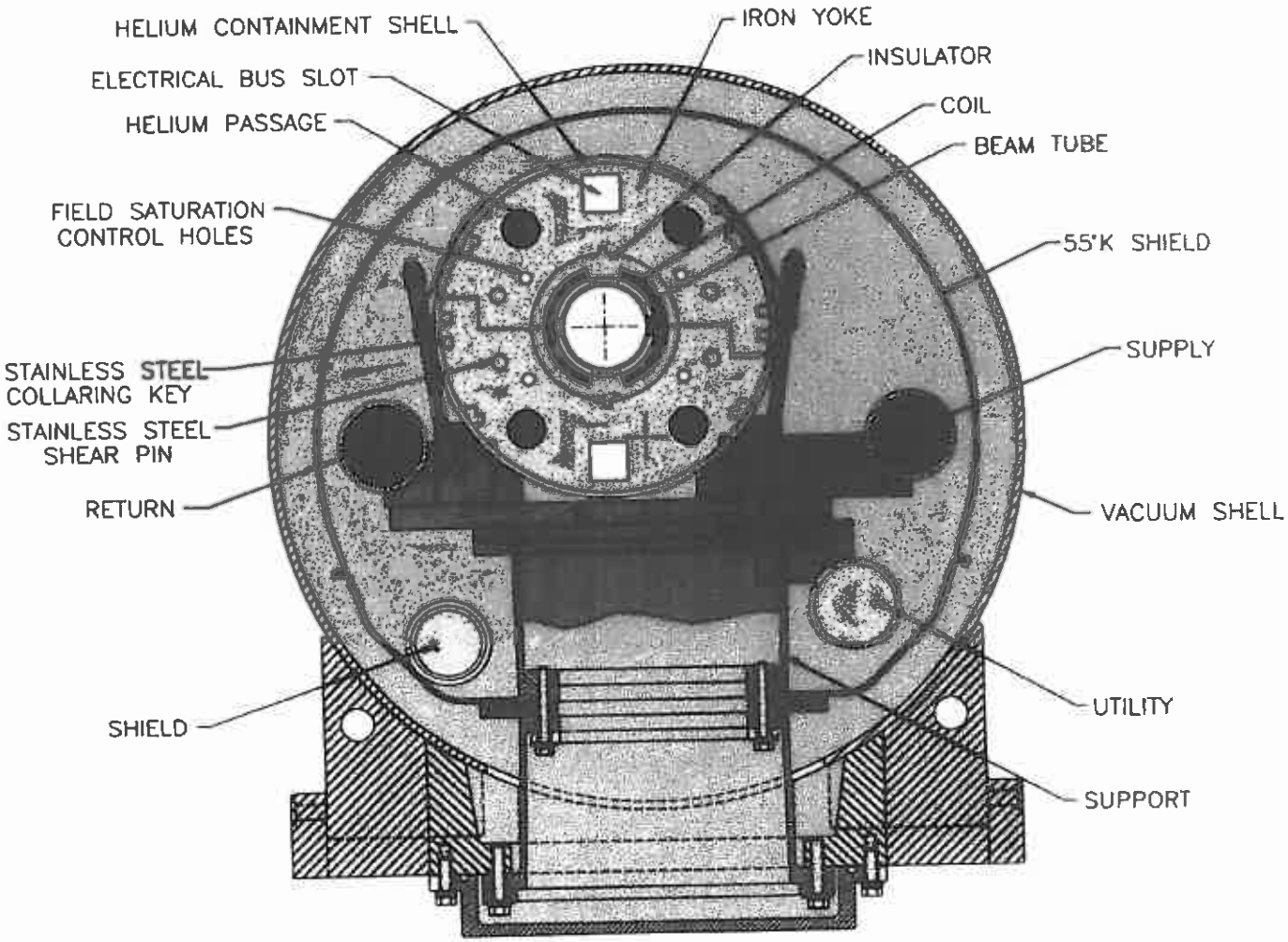

RHIC Dipole Magnet

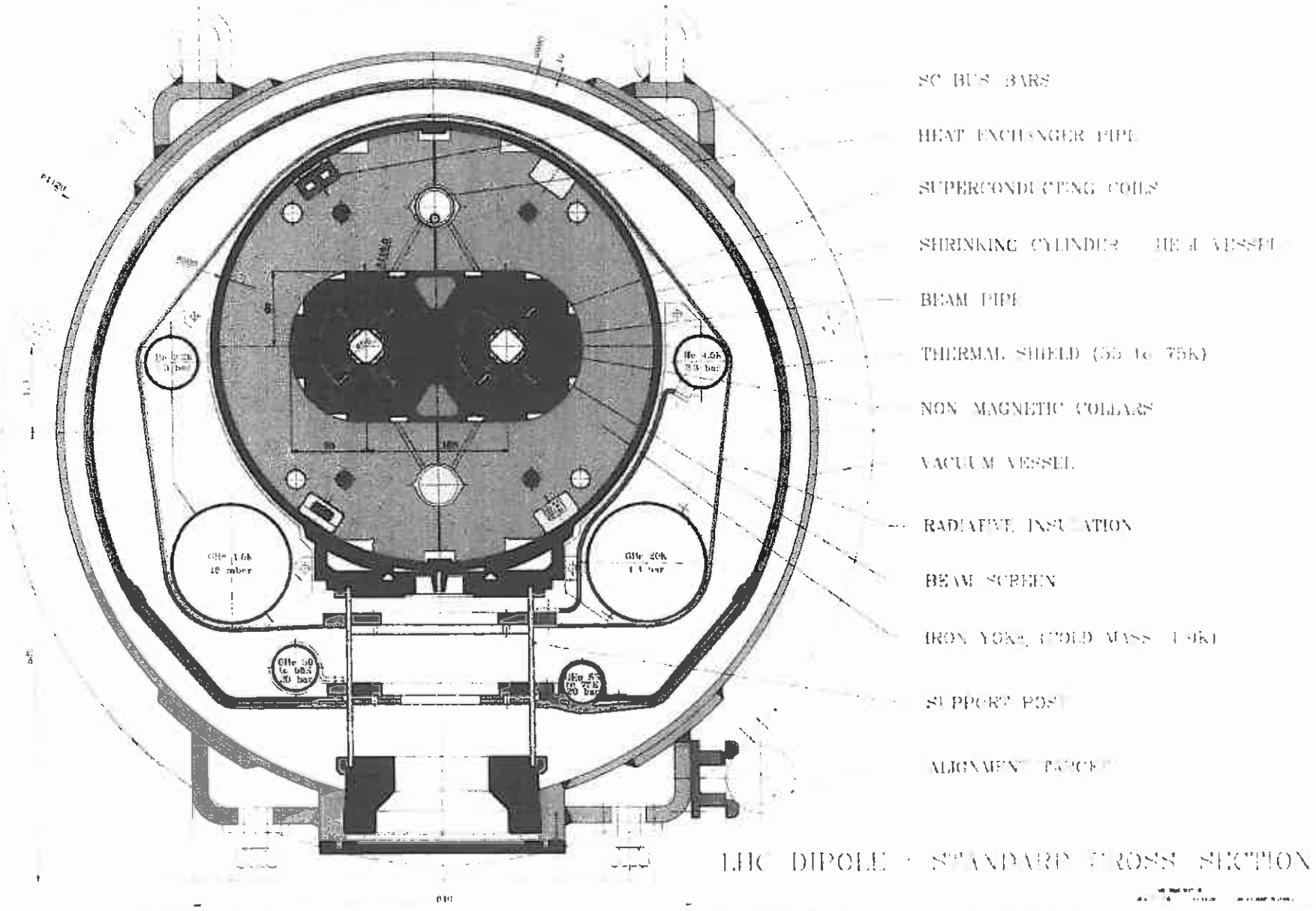

LHC 2nd Generation Dipole Magnet

COMPARISON OF PARAMETERS OF SUPERCONDUCTING ACCELERATOR MAGNETS

Laboratory	FNAL	DESY	IHEP	SSCL	BNL	CERN
Name	Tevatron	HERA	UNK	SSC	RHIC	LHC
Circumference (km)	6.3	6.3	21	87	3.8	27
Particle type	$p\bar{p}$	ep	pp	pp	heavy ions	pp
Energy/beam (TeV)	0.9	0.82	3	20	up to 0.1[a)]	7
Number of dipoles	774	416	2168	7944	264	1232[b)]
Aperture (mm)	76.2	75	70	50	80	56
Magnetic length (m)	6.1	8.8	5.8	15	9.7	14.2
Field (T)	4	4.68	5.0	6.79	3.4	8.36
Number of quadrupoles	216	256	322	1696	276	386[b)]
Aperture (mm)	88.9	75	70	50	80	56
Magnetic length[c)] (m)	1.7	1.9	3.0	5.7	1.1	3.1
GradientT/m)	76	91.2	97	194	71	223
Commissioning	1983	1990	undecided	cancelled	1999	2005

a) per unit of atomic mass
b) two-in-one magnets
c) quadrupoles come in several lengths

– Major Trends (with the exception of RHIC):

• Decrease in magnet aperture (to limit conductor volume and minimize cost of superconductor),

• Increase in dipole field strength and quadrupole field gradient,

• Increase in magnet length (to limit number of magnet interconnects).

LECTURE 2: SUPERCONDUCTIVITY APPLIED TO PARTICLE ACCELERATOR MAGNETS

2.1 Why superconductivity?

2.2 Origin of Superconductivity and critical temperature

2.3 Magnetic states of superconductors and critical fields

2.4 Transport properties of superconductors and critical current density

2.5 Critical State Model

2.6 Review of superconducting particle accelerators

2.7 Prominent features of superconducting accelerator magnets

2.8 Superconducting accelerator magnet R&D

HIGH FIELD ACCELERATOR MAGNET R&D

– In recent years, several dipole magnet magnet models have crossed the 10 T threshold:

• **MFISC,** a short, 56-mm-twin-aperture dipole magnet model built and cold-tested at CERN in 1995 (using NbTi cables), which reached 10.53 T at 1.77 K in a limited number of quenches,

• **MSUT,** a short, 50-mm-single-aperture dipole magnet model built at Twente University and cold-tested at CERN in 1995 (using Nb_3Sn cables), which reached 11 T on its first quench at 4.4 K,

• **D20,** a short, 50-mm-single aperture dipole magnet model built and cold-tested at LBNL (also using Nb_3Sn cables), which, after a number of training quenches, reached a record dipole field of 13.5 T at 1.8 K.

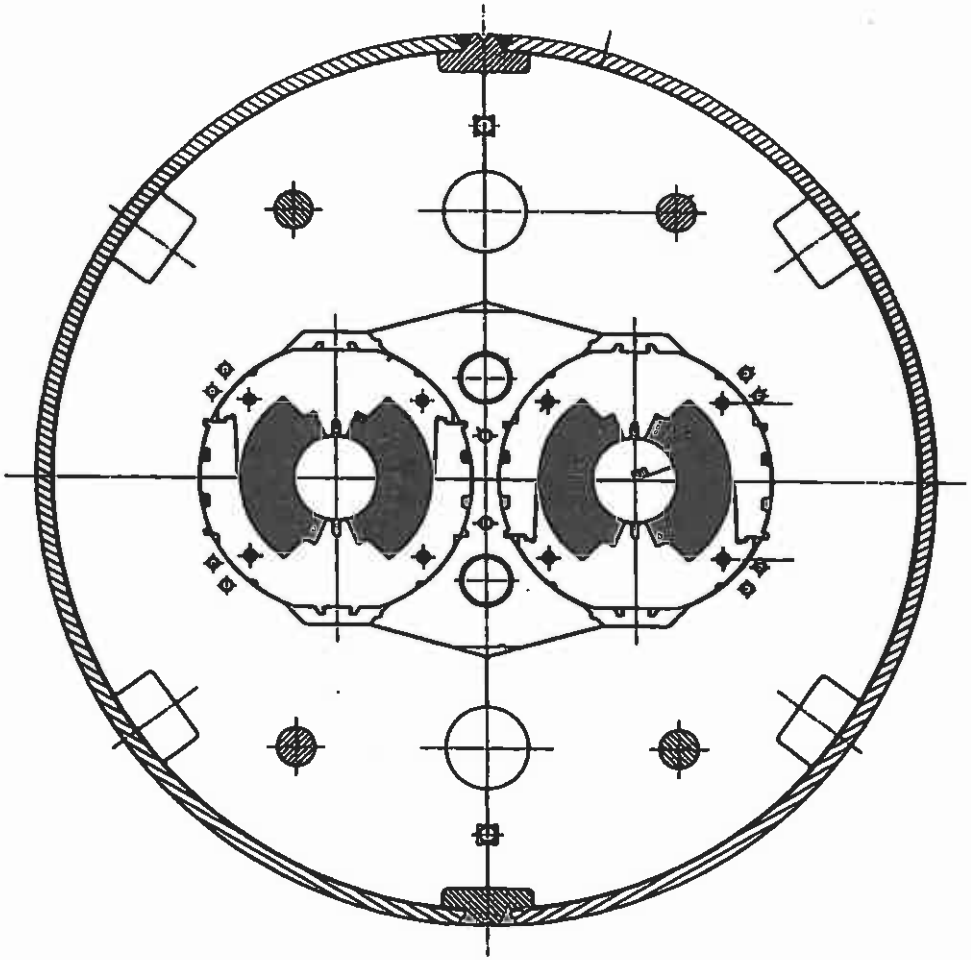

Short 56-mm_Twin_Aperture Dipole Magnet Model
MFISC (Courtesy D. Leroy)

Quench Performance of MFISC (Courtesy A. Siemko)

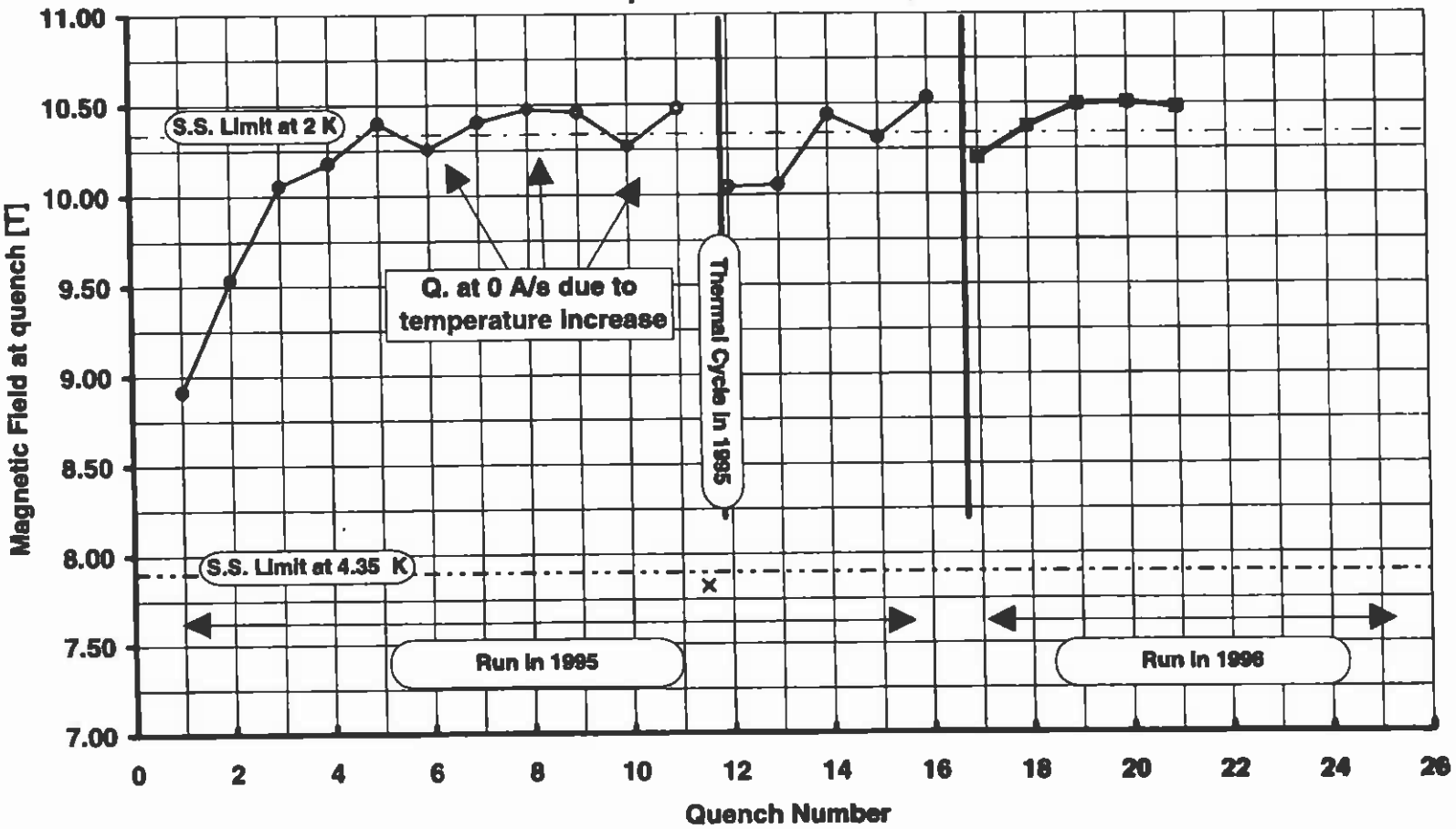

Fisc2as - trcurve - 10/2/97

Single aperture supporting system

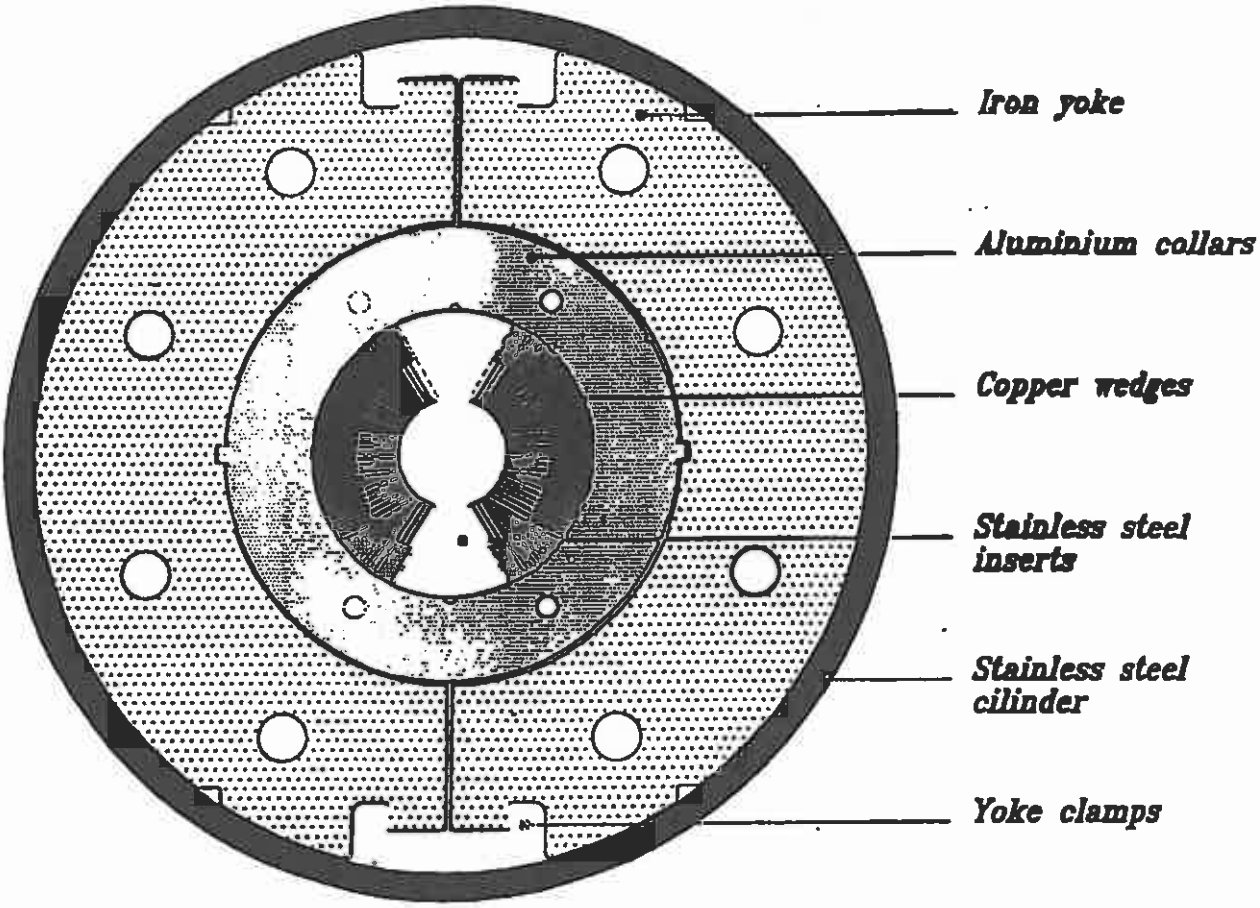

University of Twente 50-mm-Apert. 1-m-long Dipole Model

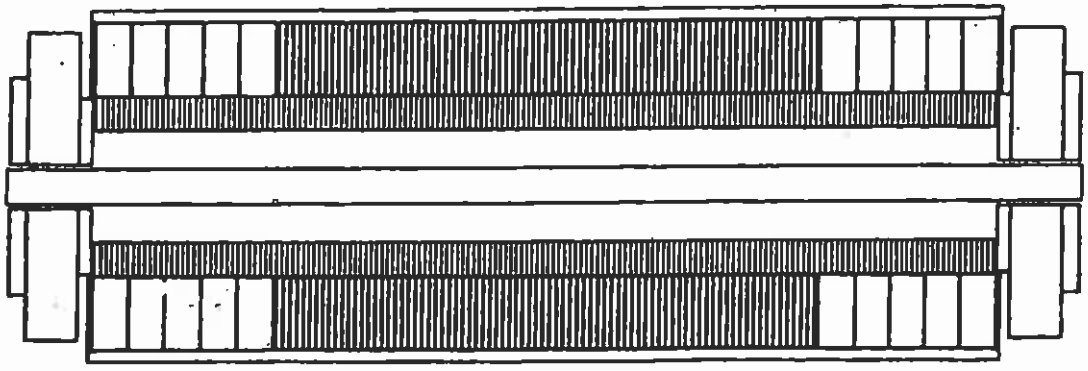

H.H.J. ten Kate, 1995

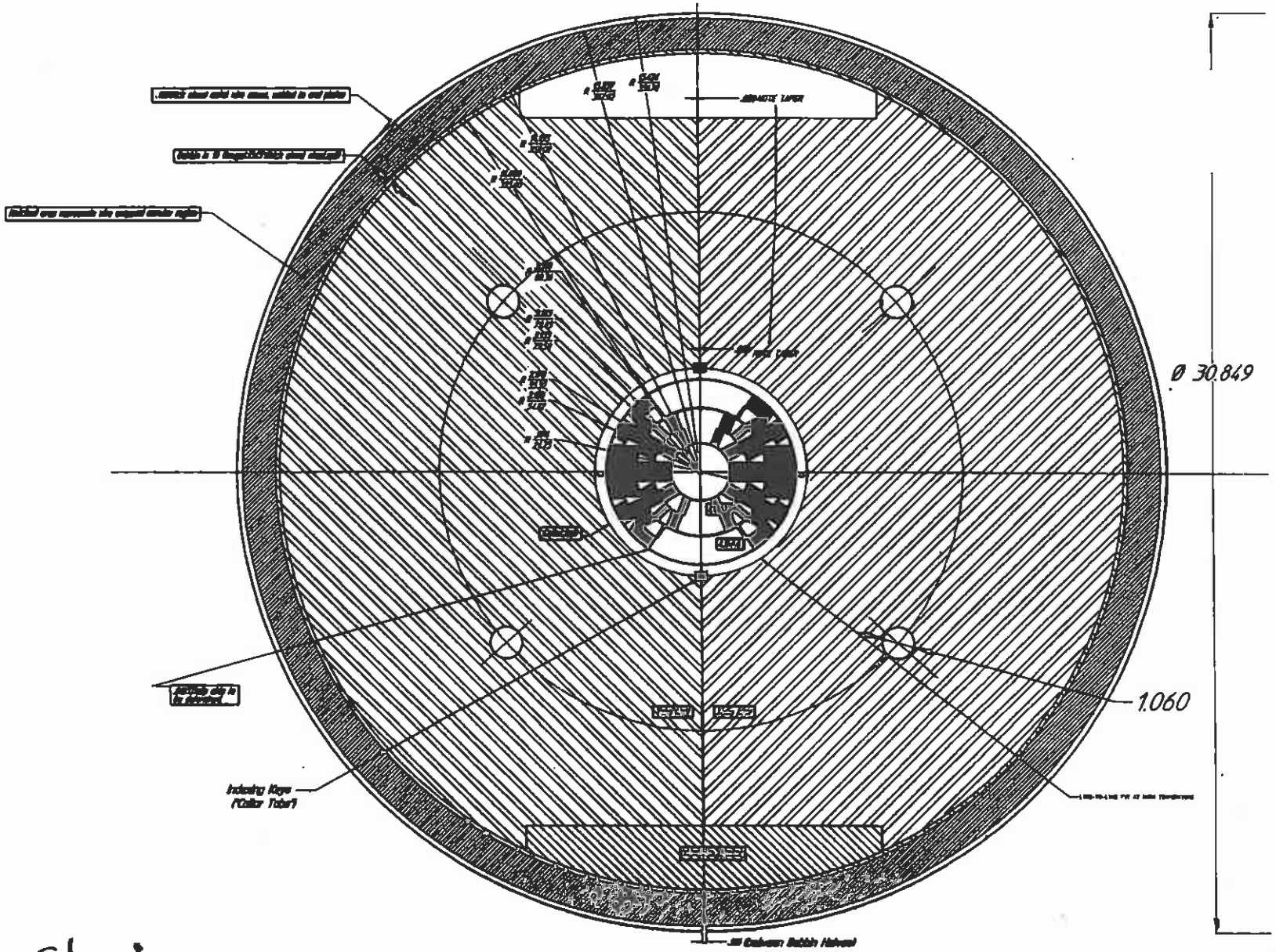

Short LBL 50-mm-Aperture Dipole Magnet Model D20
(Courtesy R. Scanlan)

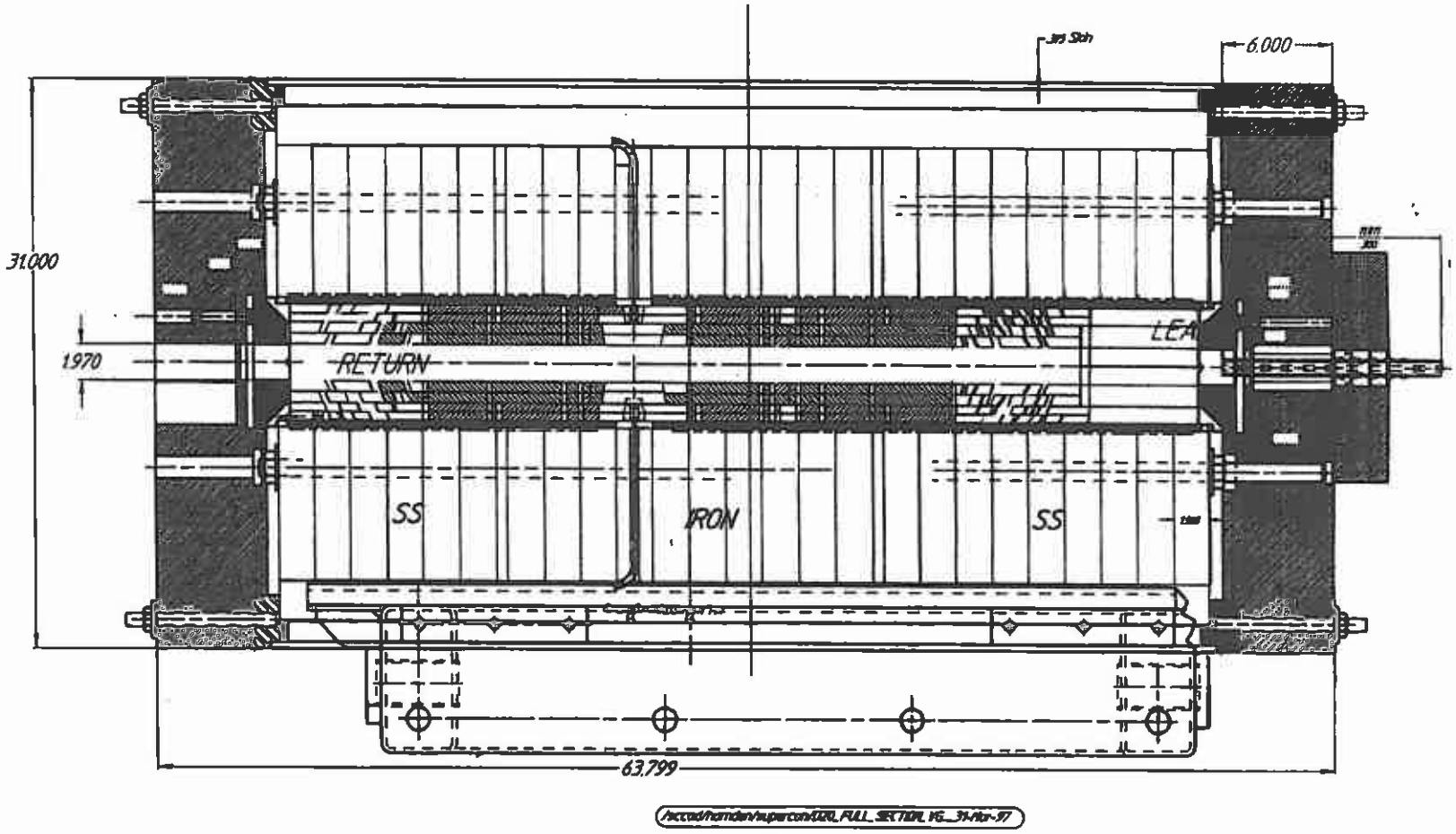

Short LBL 50-mm-Aperture Dipole Magnet Model D20
(Courtesy R. Scanlan)

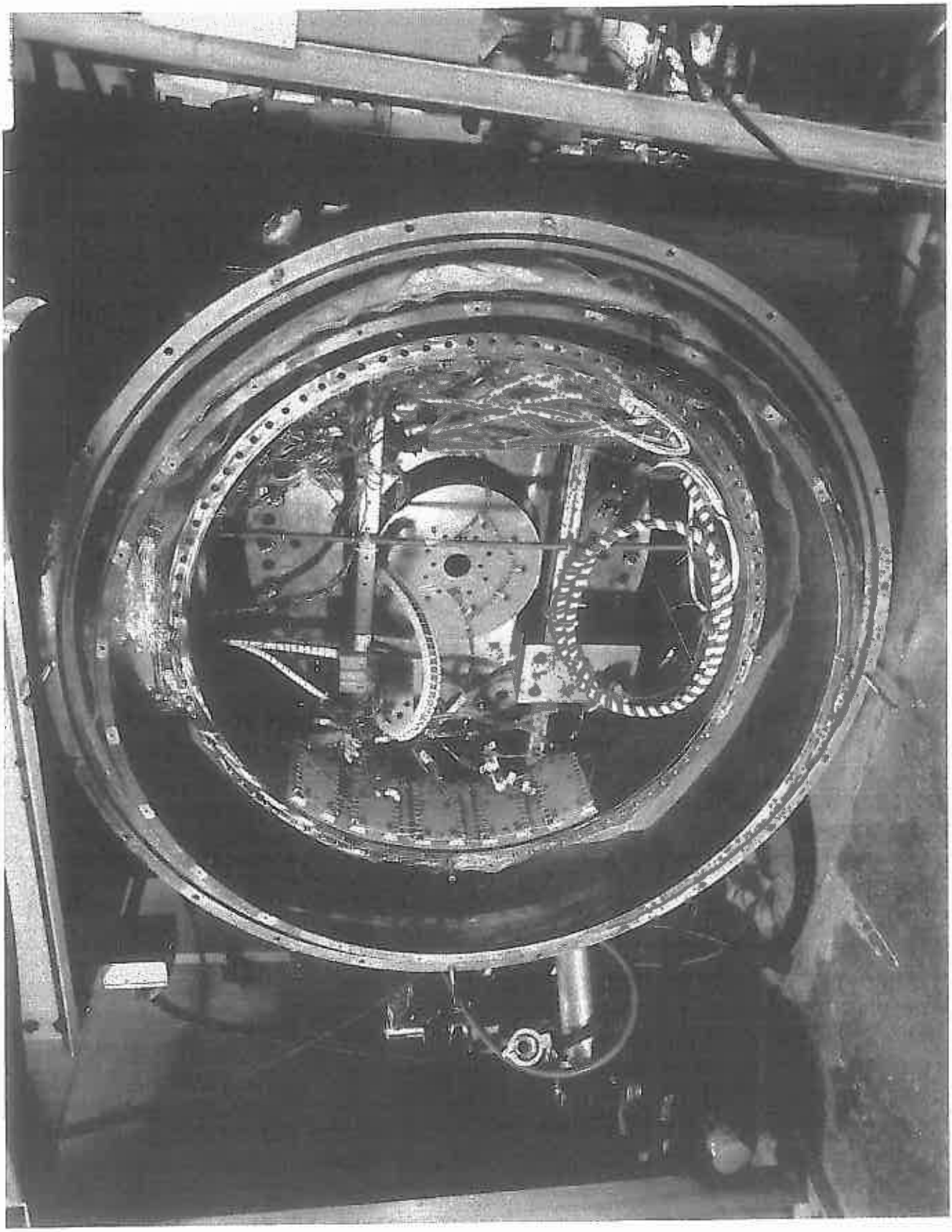

D20 at LBL (Courtesy A. McInturff)

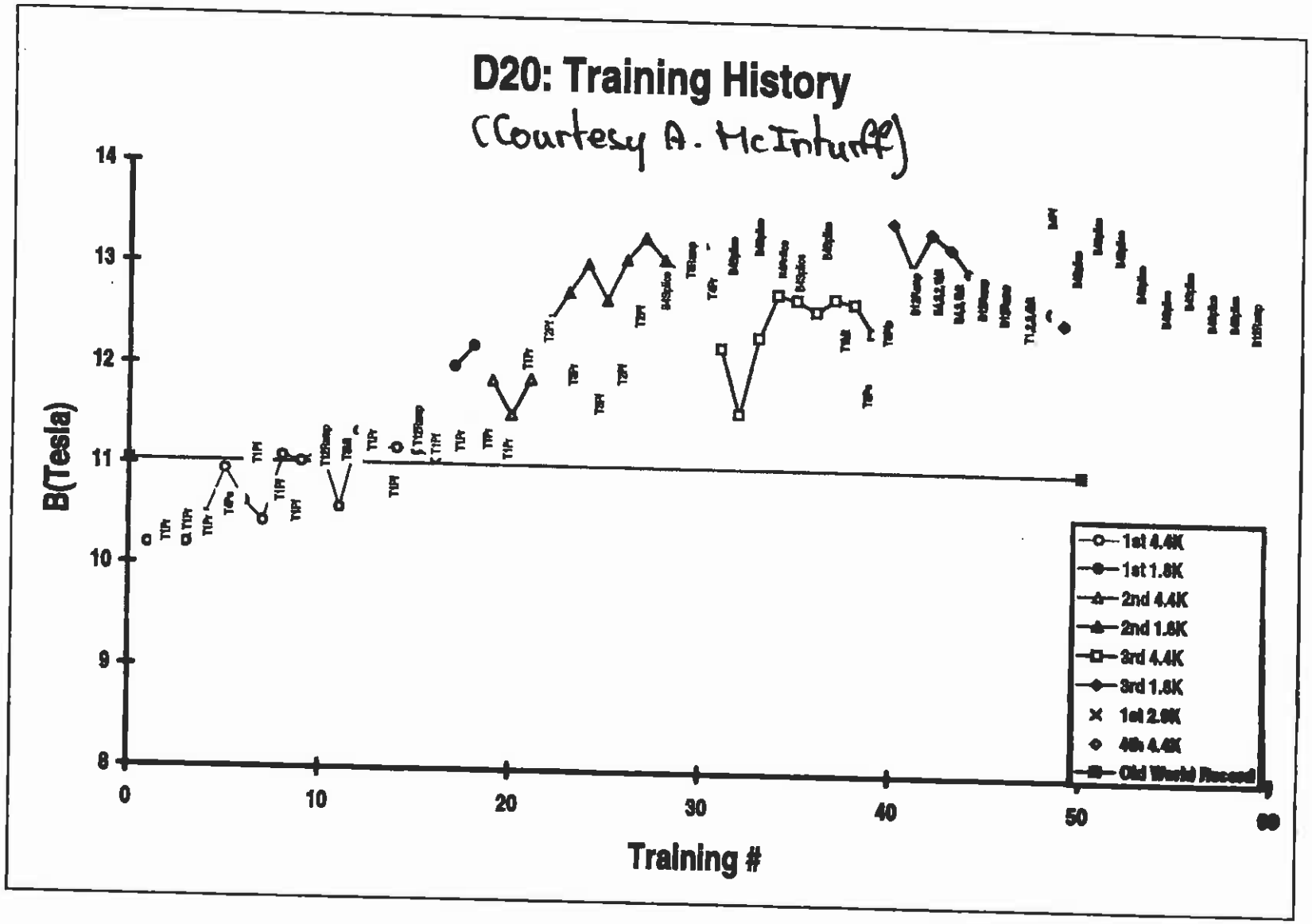
D20: Training History
(Courtesy A. McInturff)
B(Tesla)
Training #
14
13
12
11
10
9
8
0
10
20
30
40
50
60
1st 4.4K
1st 1.8K
2nd 4.4K
2nd 1.8K
3rd 4.4K
3rd 1.8K
1st 2.8K
4th 4.4K
Old World Record

HIGH FIELD ACCELERATOR MAGNET R&D (CONT.)

– A number of laboratories are presently involved in R&D work on high field or high field gradient accelerator magnets. Among them are:

- **CEA/Saclay:** demonstration Nb_3Sn quadrupole magnet model,
- **FNAL**: 12-T dipole magnet for VLHC,
- **INFN/LASA:** conceptual design of IR quadrupole magnet for LHC upgrade,
- **LBNL**: dual-bore, ractrack dipole magnets,
- **Texas A&M University**: 16 T, block-coil dual dipole magnet,
- **Twente University**: 10–T, beam-separator dipole magnet model for LHC upgrade.

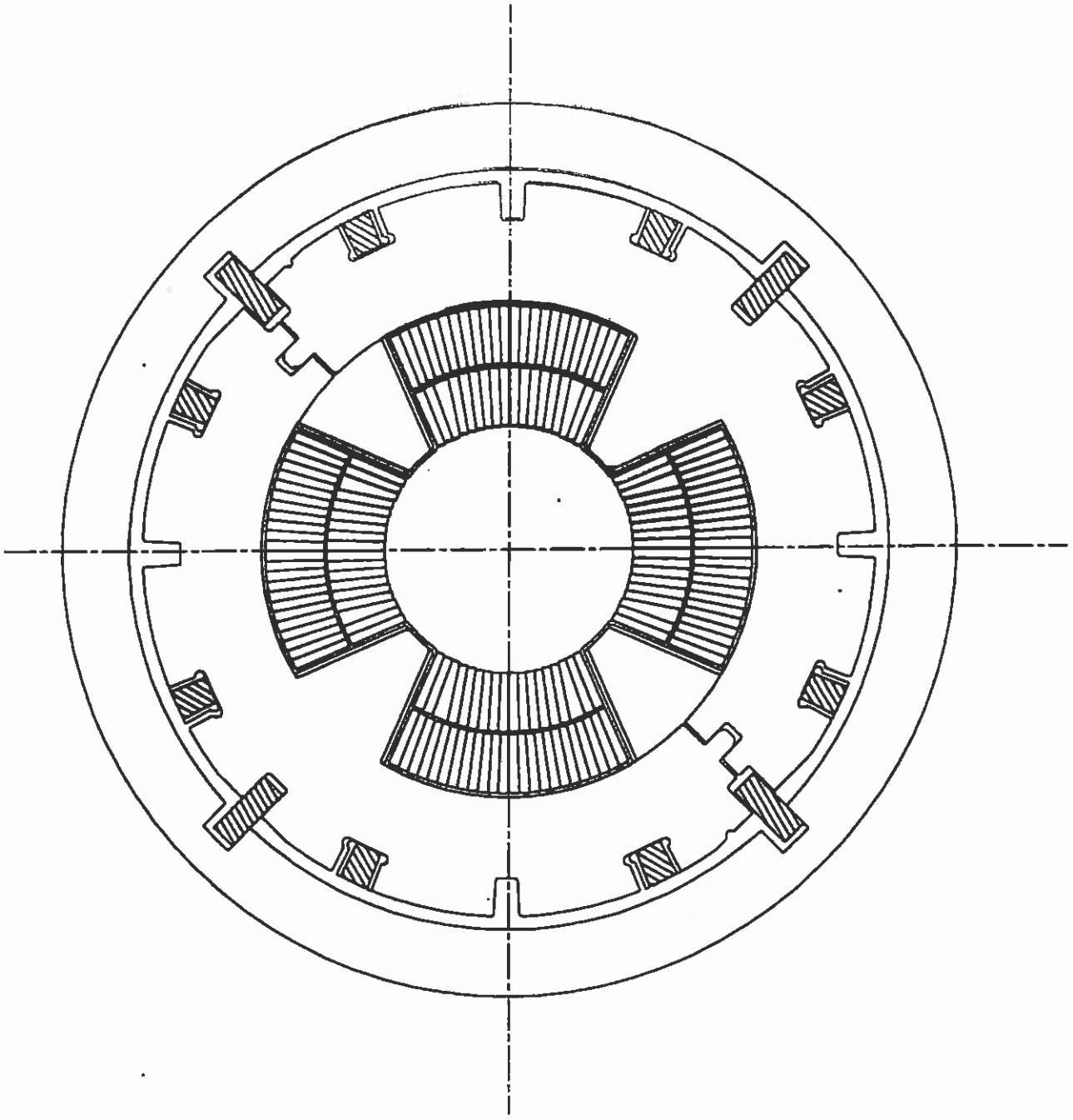

Proposed design for a 56-mm-Aperl.,
1-m-long Prototype in Nb_3Sn
(CEA / Saclay)

FNAL - Nb3Sn Dipole Model

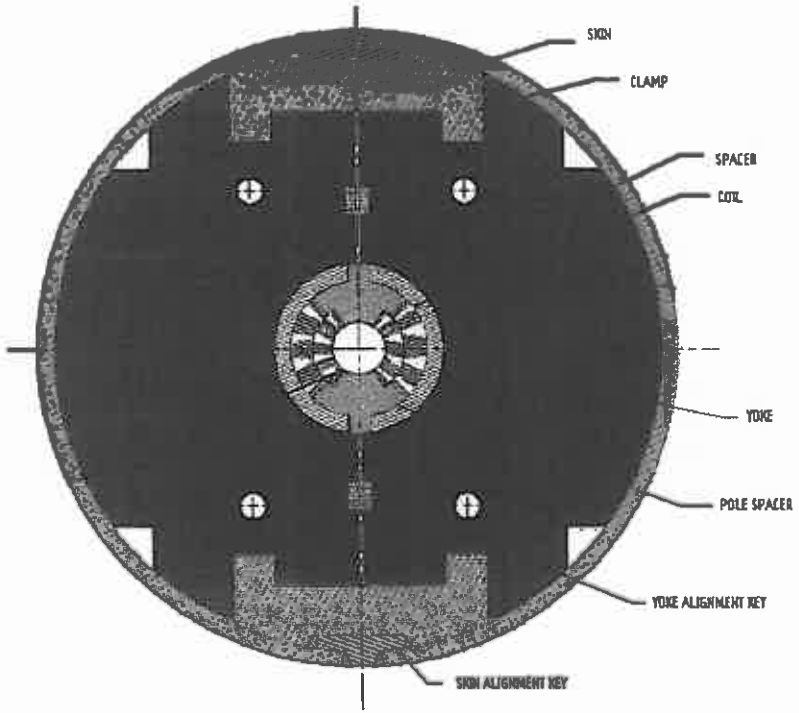

-Field: 12.3 T at 18.1 kA

-Good field region: $\Delta B/B<10^{-4}$ @ $\phi<3$cm

-Design: two-layer cosθ type

-Coil diameter: 45 mm

-Minimized coil cross-section

-Magnet length: 1 m

-Strand: Nb_3Sn (IGC, IT), ϕ1.00 mm,
Jc(12T;4.2K)=1886 A/mm^2

-Cable: N=28, 1.800mm*14.24 mm

-Insulation: high temperature ceramics

-New magnet assembling technology

-Fermilab/KEK/LBNL collaboration

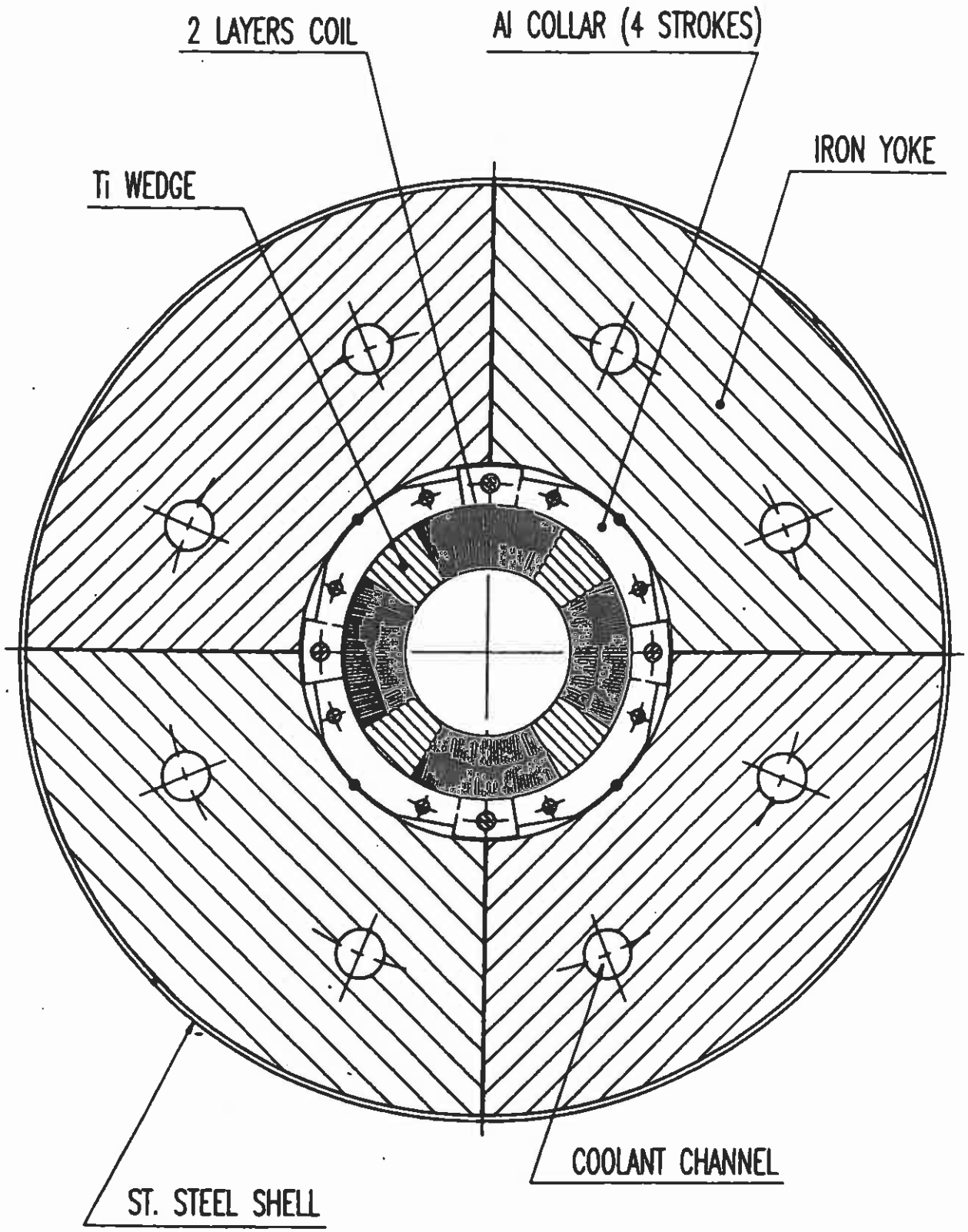

INFN/LASA Conceptual Design

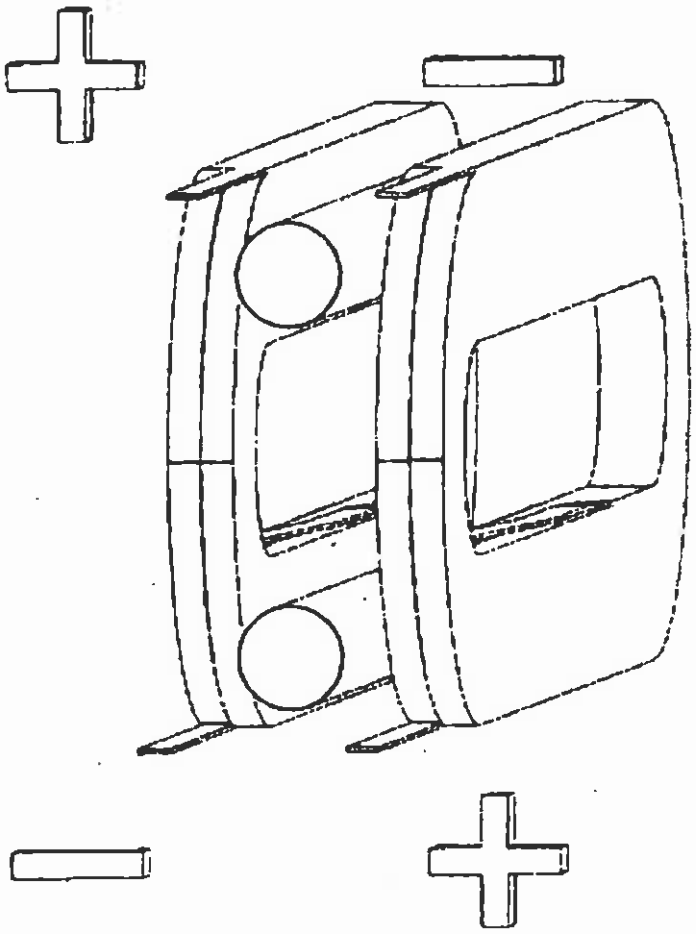

Figure. 1: Schematic of "Common-Coil" Magnet

LBNL Dual-Racetrack Dipole Magnet
(Courtesy S. Gourlay)

LBNL

HIGH FIELD (10T-15T) TWIN APERTURE SUPERCONDUCTING DIPOLE

COMMON COIL DESIGN

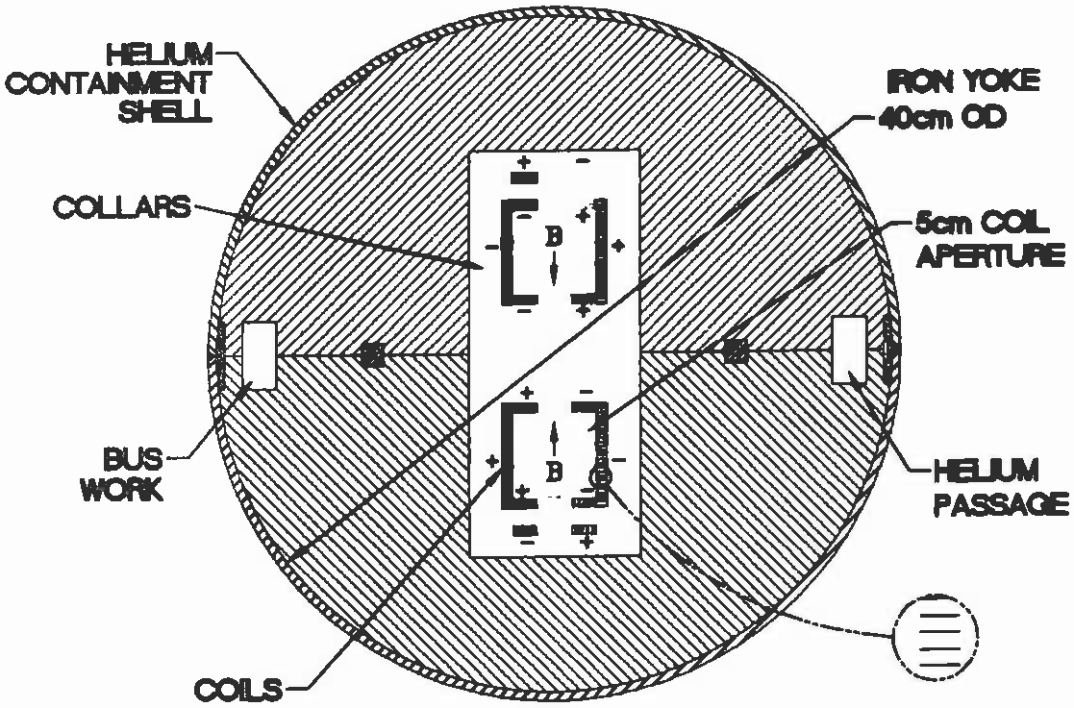

COLD MASS CROSS-SECTION

SCALE 1/4

(Courtesy R. Gupta)

Texas A and M University

16 Tesla Block-Coil Dual Dipole

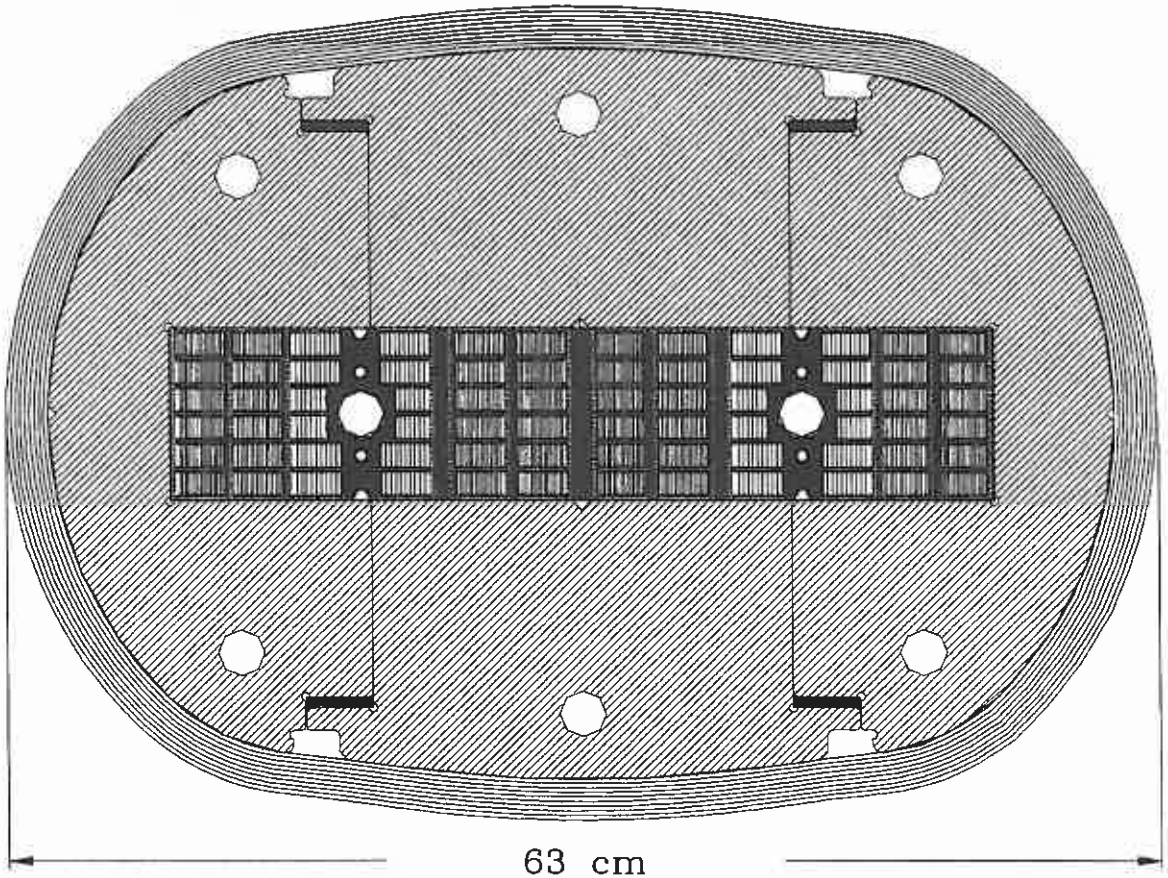

(Courtesy P. McIntyre)

Texas A and M Dipole Magnet

Coil Ends

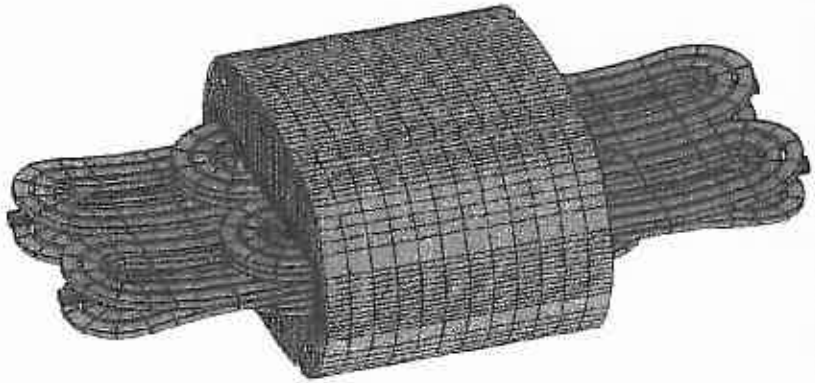

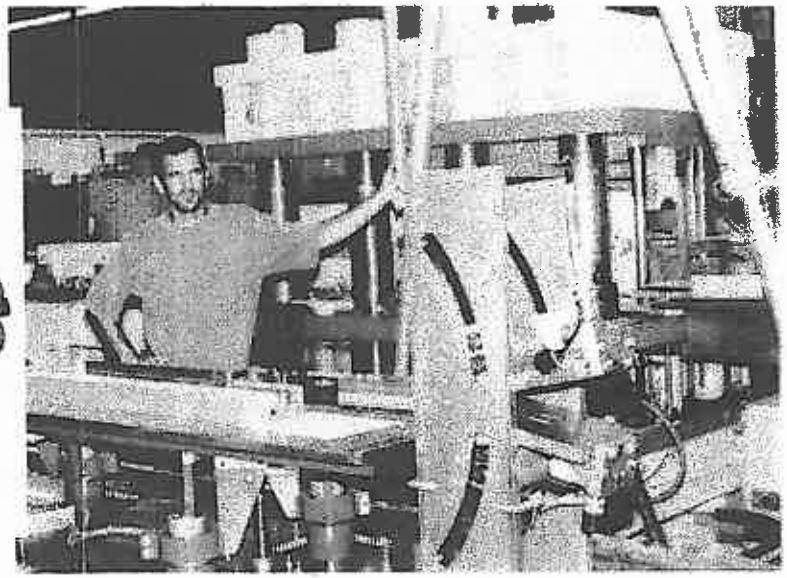

(Courtesy P. McIntyre)

Nb_3Sn-D1 system characteristics

operating field @ 4.4 K		10.0	T
max. field on conductor		10.8	T
operating current		13	kA
inner bore diameter		88	mm
outer diameter		650	mm
self induction		3.1	mH/m
resulting forces per quadrant	Fx	3.32	MN/m
	Fy	-1.62	MN/m
	Fz	0.55	MN

Nb_3Sn-D1 coil characteristics

conductor	PIT Nb_3Sn	
strand diameter	0.90	mm
twist pitch	118	mm
Cu percentage	50	%
number of filaments	504	
filament diameter	22	μm
filament twist pitch	20	mm
cable dimensions (bare)	1.47/1.79 x 16.4	mm
st. steel core dimensions	12.7 x 0.025	mm
number of strands	35	
cable insulation	glass/mica + S2 glass wrap	
insulation thickness	0.14	mm
fully epoxy resin impregnated coils		
effective Young's modulus	30	GPa
max. eq. stress in cable	140	MPa

Twente University Dipole Magnet Model
(Courtesy A. den Ouden)

Nb_3Sn-D1 mechanical support structure and conductor lay-out

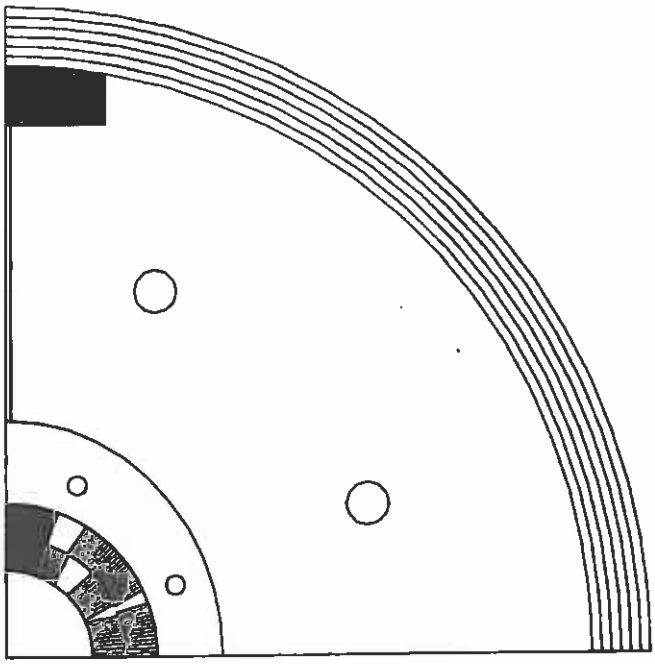

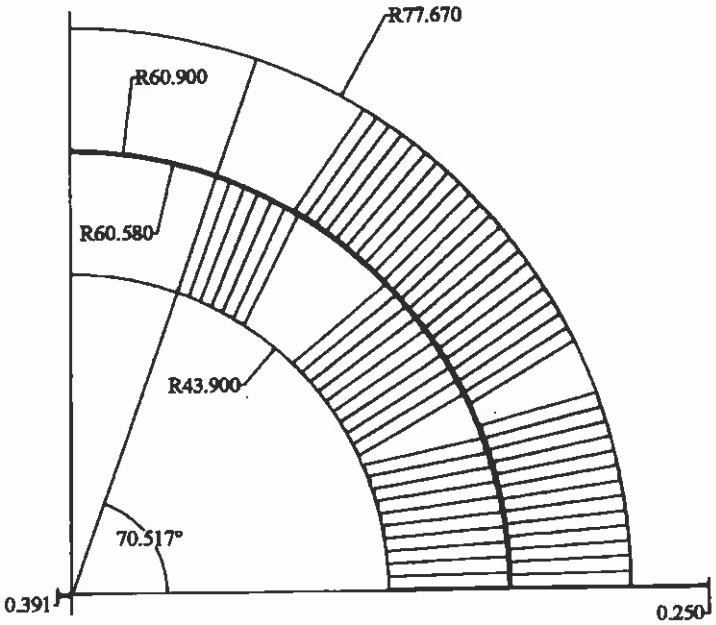

Twente University Dipole Magnet Model
(Courtesy A. den Ouden)

LECTURE 3: CONDUCTOR AND CONDUCTOR INSULATION FOR PARTICLE ACCELERATOR MAGNETS

3.1 Review of Superconducting Materials
- 3.1.1 NbTi Alloys 3–3
- 3.1.2 Nb_3Sn Compounds 3–15
- 3.1.3 HTS 3–27

3.2 Superconducting Multifilamentary Composites 3–31

3.3 Transition of Multifilamentary Wires 3–47

3.4 Manufacturing of NbTi Wires 3–69

3.5 Manufacturing of Nb_3Sn Wires 3–91

3.6 Critical Surface Parametrizations 3–119

3.7 Rutherford-Type Cables 3–131

3.8 Interstrand Resistances in Rutherford-Type Cables 3–157

3.9 Critical Current Measurements on Rutherford-Type Cables 3–171

3.10 Cable Insulation 3–183

Appendix: Material Properties at Low Temperatures 3–203

LECTURE 3: CONDUCTOR AND CONDUCTOR INSULATION FOR PARTICLE ACCELERATOR MAGNETS

3.1 Review of Superconducting Materials
3.1.1 NbTi Alloys
3.1.2 Nb_3Sn Compounds
3.1.3 HTS

3.2 Superconducting Multifilamentary Composites

3.3 Transition of Multifilamentary Wires

3.4 Manufacturing of NbTi Wires

3.5 Manufacturing of Nb_3Sn Wires

3.6 Critical Surface Parametrizations

3.7 Rutherford-Type Cables

3.8 Interstrand Resistances in Rutherford-Type Cables

3.9 Critical Current Measurements on Rutherford-Type Cables

3.10 Cable Insulation

Appendix: Material Properties at Low Temperatures

NBTI ALLOYS

– The most widely used superconductor is a ductile alloy of niobium and titanium (NbTi).

– Niobium and titanium have very similar atomic sizes and are mutually soluble over a wide composition range.

– At high temperatures, they combine into a body-centered cubic phase, referred to as *β–phase.* When cooled down to temperatures below about 10 K, the β–phase becomes a type-II superconductor.

PINNING IN NBTI ALLOYS

– When the NbTi alloy is severely cold-worked and presents a large number of lattice dislocations, heat treatments at moderate temperatures lead to precipitations of other phases at grain boundaries.

– Among them is an hexagonal close packed phase, rich in titanium (of the order of 95% in weight), referred to as α–*phase*.

– The α–phase remains normal resistive at low temperatures and has been shown to be a significant source of fluxoid pinning sites.

– The α–Ti precipitates can be engineered to achieve high critical current densities in the desired ranges of operating field and temperature.

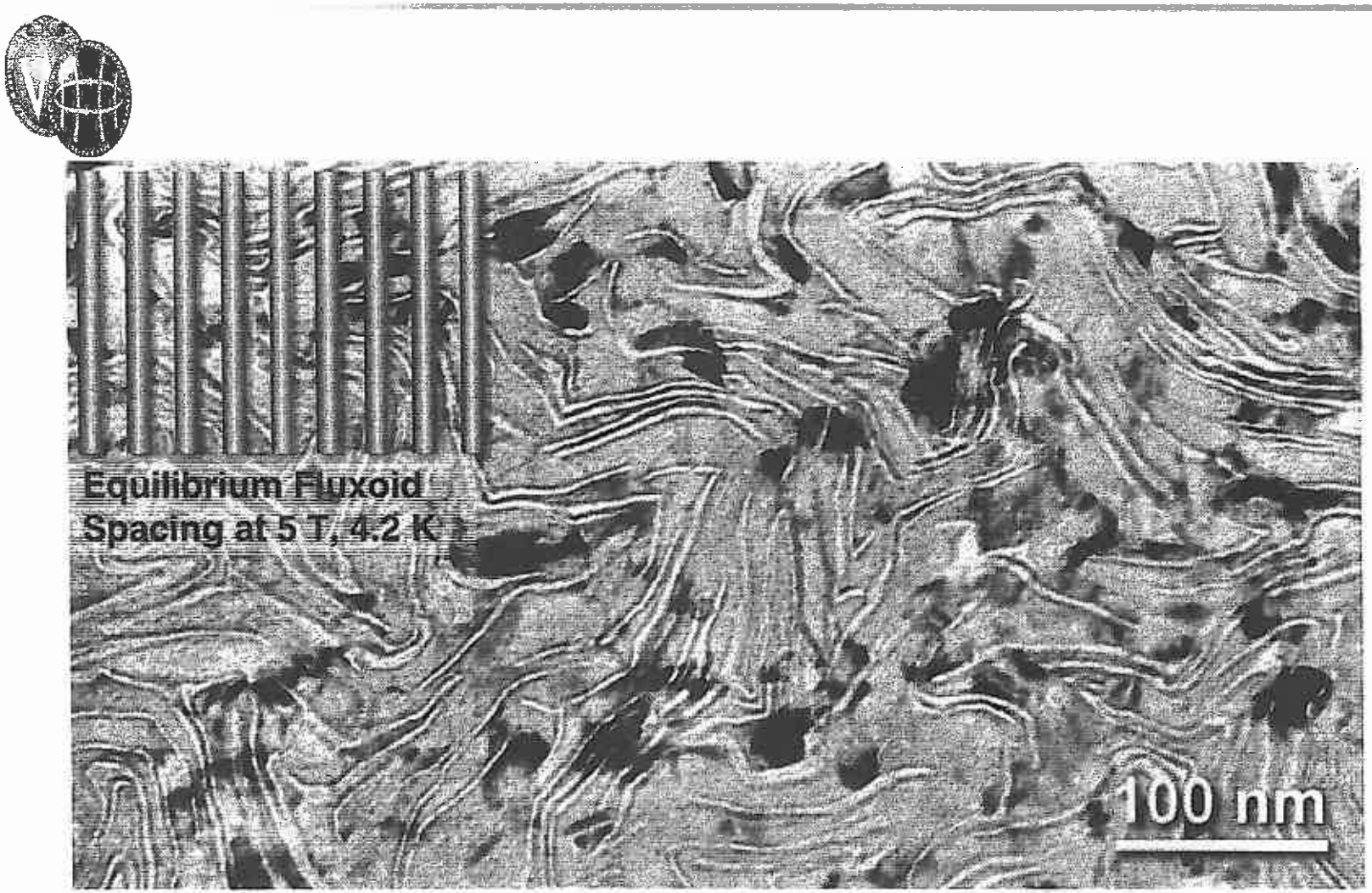

Conventionally Processed High J_c Nb-Ti

Courtesy P.J. Lee

The relationship between peak critical current and volume of precipitate in conventionally processed Nb-Ti

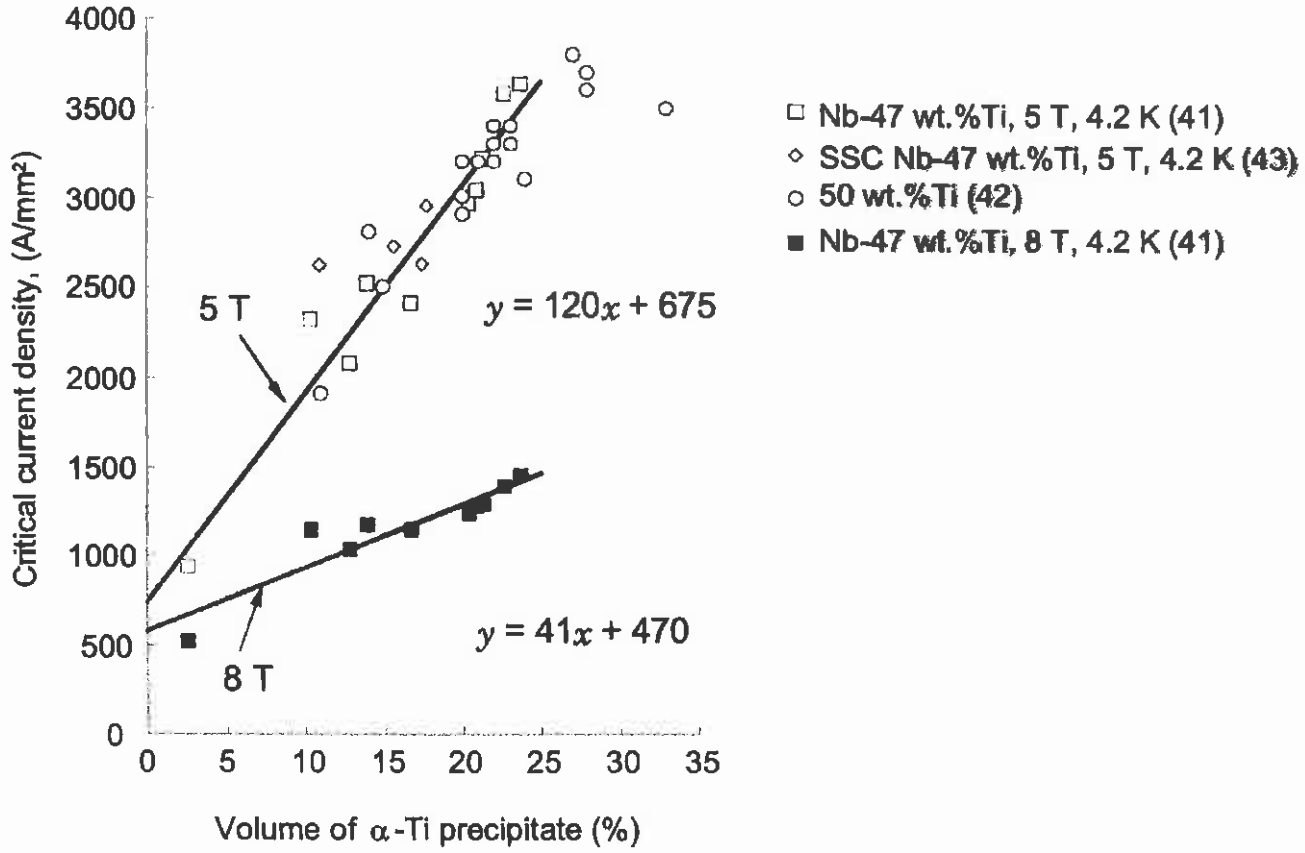

Courtesy P.J. Lee

CRITICAL TEMPERATURE AND FIELD OF NBTI ALLOYS

– The critical temperature, T_C, and the upper critical magnetic flux density, B_{C2}, of niobium-titanium are mainly determined by the alloy composition and are little affected by subsequent processing.

– The Ti content of practical conductors is in the range 45 to 50% in weight and corresponds to an optimum in B_{C2}.

– For such alloy compositions, the critical temperature at zero magnetic flux density, T_{C0}, is between 9 and 9.2 K and the upper critical magnetic flux density at zero temperature, B_{C20}, is about 14.5 T.

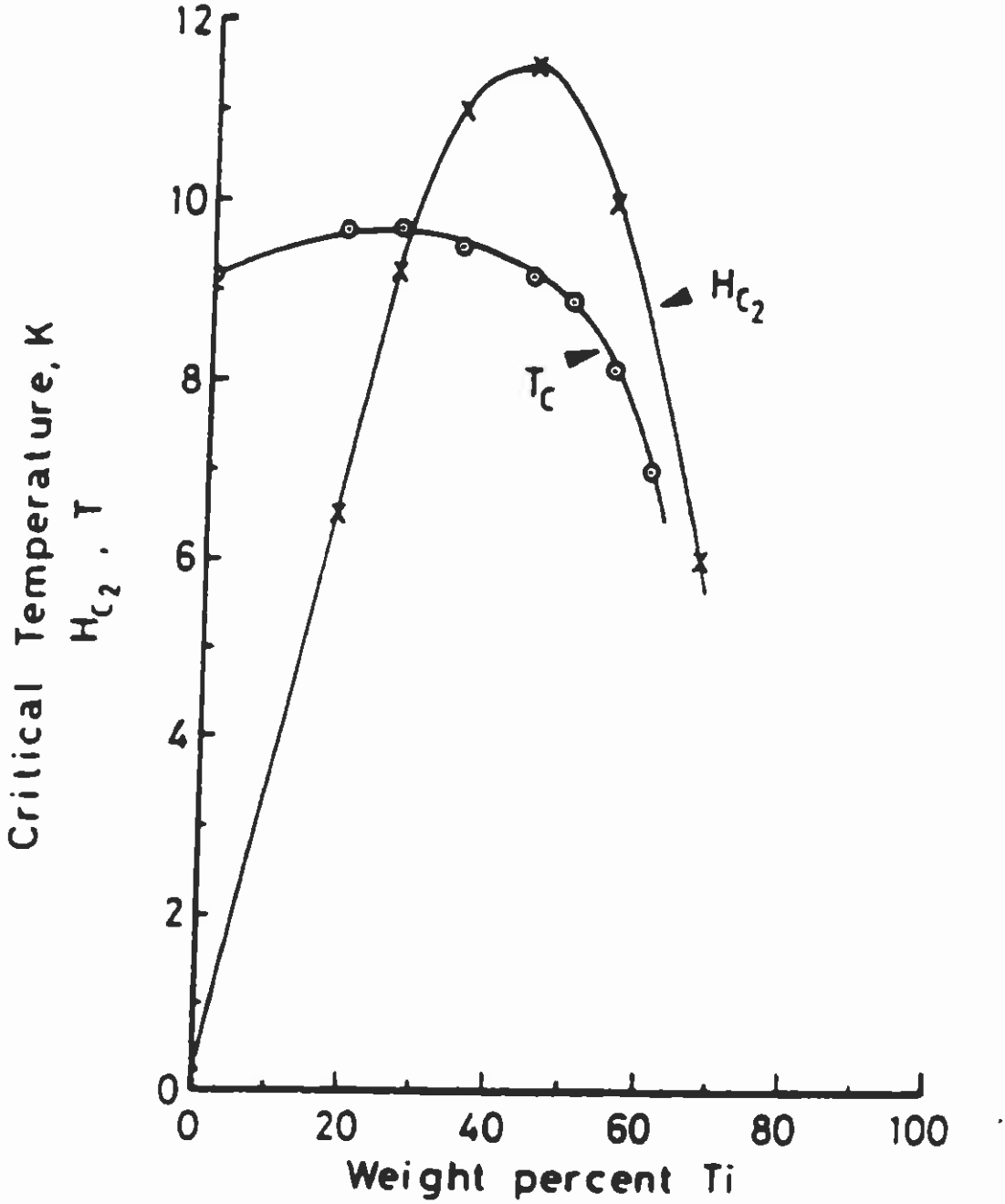

Fig. 4 The critical temperature and upper critical field of NbTi at 4.2 K as a function of alloy composition [4]

Courtesy P.J. Lee

TERNARY NBTI ALLOYS

– The upper critical magnetic flux density of NbTi alloys can be raised slightly by addition of a high-atomic-number ternary component such as tantalum.

– The increase in B_{C2} is small at 4.2 K (0.1 to 0.2 T) but can reach 1 T at 2 K.

– Little work has been carried out on optimizing the critical current density of ternary NbTi alloys and, at present (1999), their J_C are lower than those of binary NbTi alloys.

Nb-Ti-Ta - 4.2K and 2K H_{c2}

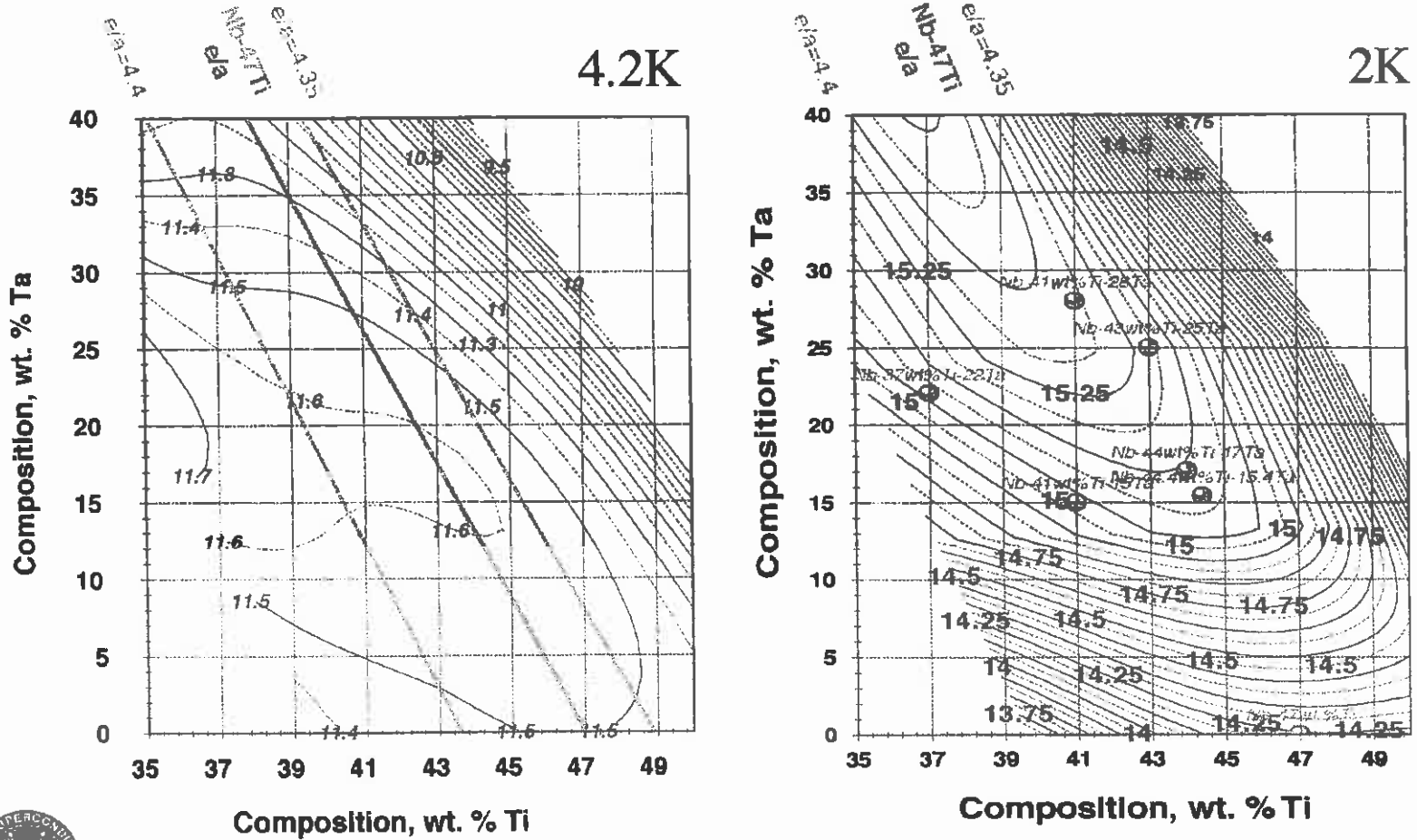

Courtesy P.J. Lee

Critical Current Density at 4.2K

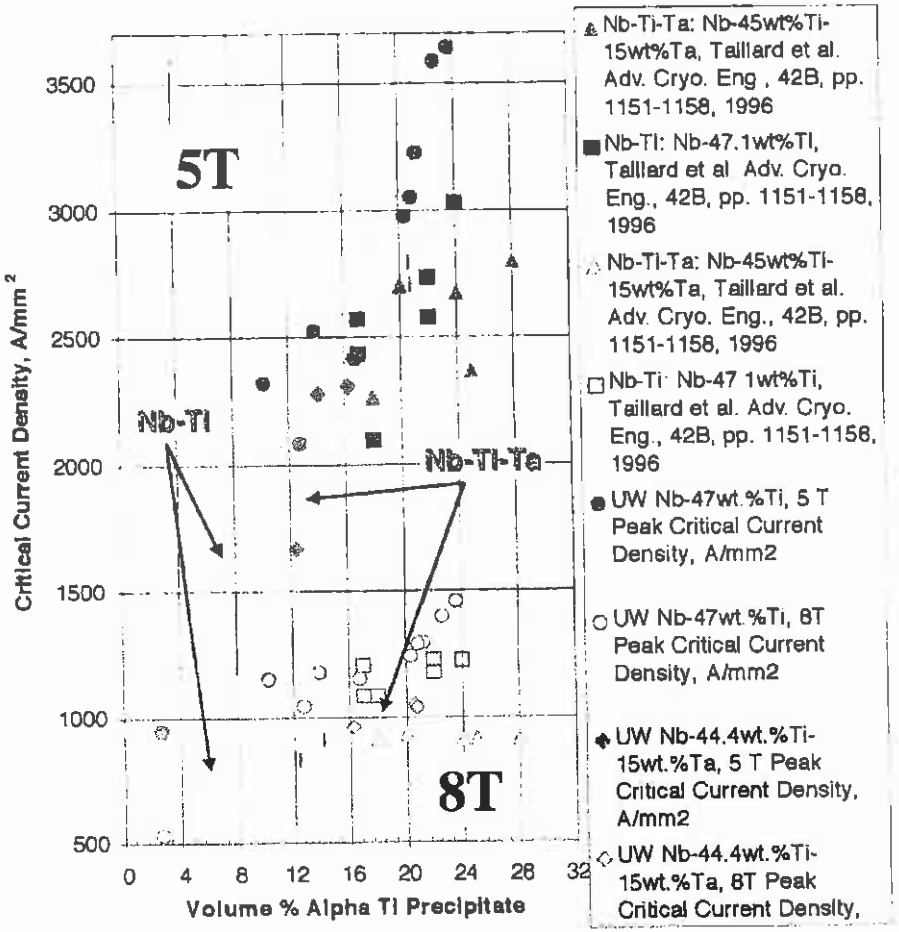

Increased critical current density with volume % alpha-Ti at 5T (closed symbols) and 8T (open symbols) for the high prestrain monofilaments in this study (red diamonds).

Slopes similar to Nb-Ti in earlier studies (purple circles) but shifted to lower critical current density.

Courtesy P.J. Lee

LECTURE 3: CONDUCTOR AND CONDUCTOR INSULATION FOR PARTICLE ACCELERATOR MAGNETS

3.1 Review of Superconducting Materials
- 3.1.1 NbTi Alloys
- **3.1.2 Nb_3Sn Compounds**
- 3.1.3 HTS

3.2 Superconducting Multifilamentary Composites

3.3 Transition of Multifilamentary Wires

3.4 Manufacturing of NbTi Wires

3.5 Manufacturing of Nb_3Sn Wires

3.6 Critical Surface Parametrizations

3.7 Rutherford-Type Cables

3.8 Interstrand Resistances in Rutherford-Type Cables

3.9 Critical Current Measurements on Rutherford-Type Cables

3.10 Cable Insulation

Appendix: Material Properties at Low Temperatures

NB3SN COMPOUNDS

– The only other superconducting material that is readily available at (small) industrial scale is an intermetallic compound of niobium and tin, having a well defined stoichiometry (Nb_3Sn), and belonging to the A15 crystallographic family.

– The A15 compounds, A_3B, have a simple cubic structure, with 2 B atoms in the unit cell at the body center and at the apical positions and six A atoms paired on each face of the cells.

– All A15 compounds (including Nb_3Sn) are very brittle and must be handled with care.

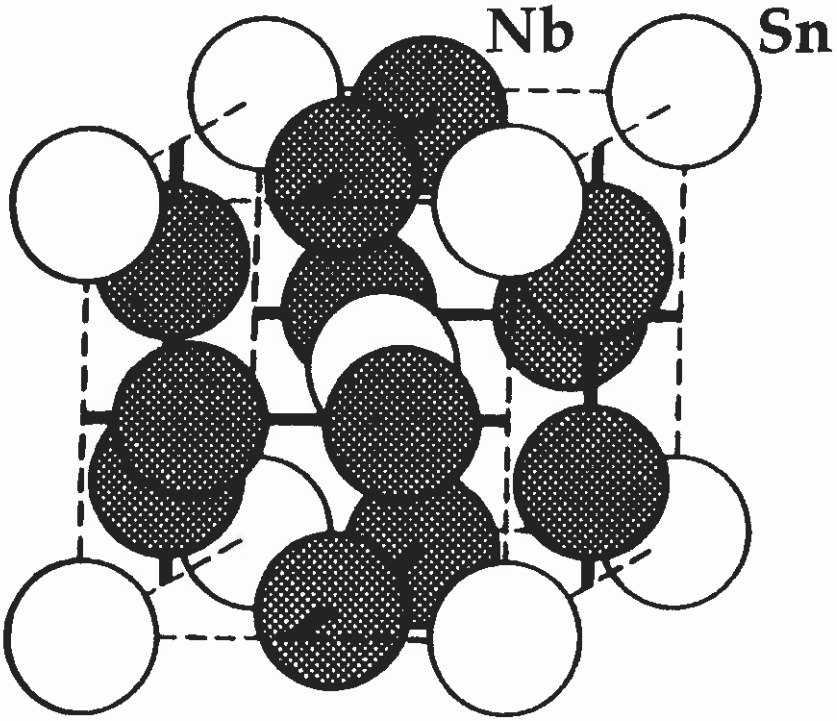

Figure 3.19 The unit cell of the $A15$ compound A_3B showing B atoms at the apical and body center positions and A atoms in pairs on the faces of the cube (Vonsovsky *et al.*, 1982, p. 260; see also Wyckoff, 1964, p. 119).

TERNARY NB3SN COMPOUNDS

– The critical temperature at zero magnetic flux density and zero strain, T_{Com}, of binary Nb_3Sn is of the order of 16 K, while its upper critical magnetic flux density at zero temperature and zero strain, B_{C20m}, is of the order of 24 T.

– An addition of a few percents in weight of titanium or tantalum in the niobium boosts T_{Com} to about 18 K and B_{C20m} to about 28 T.

– The most commonly used Nb_3Sn compounds are ternary compounds.

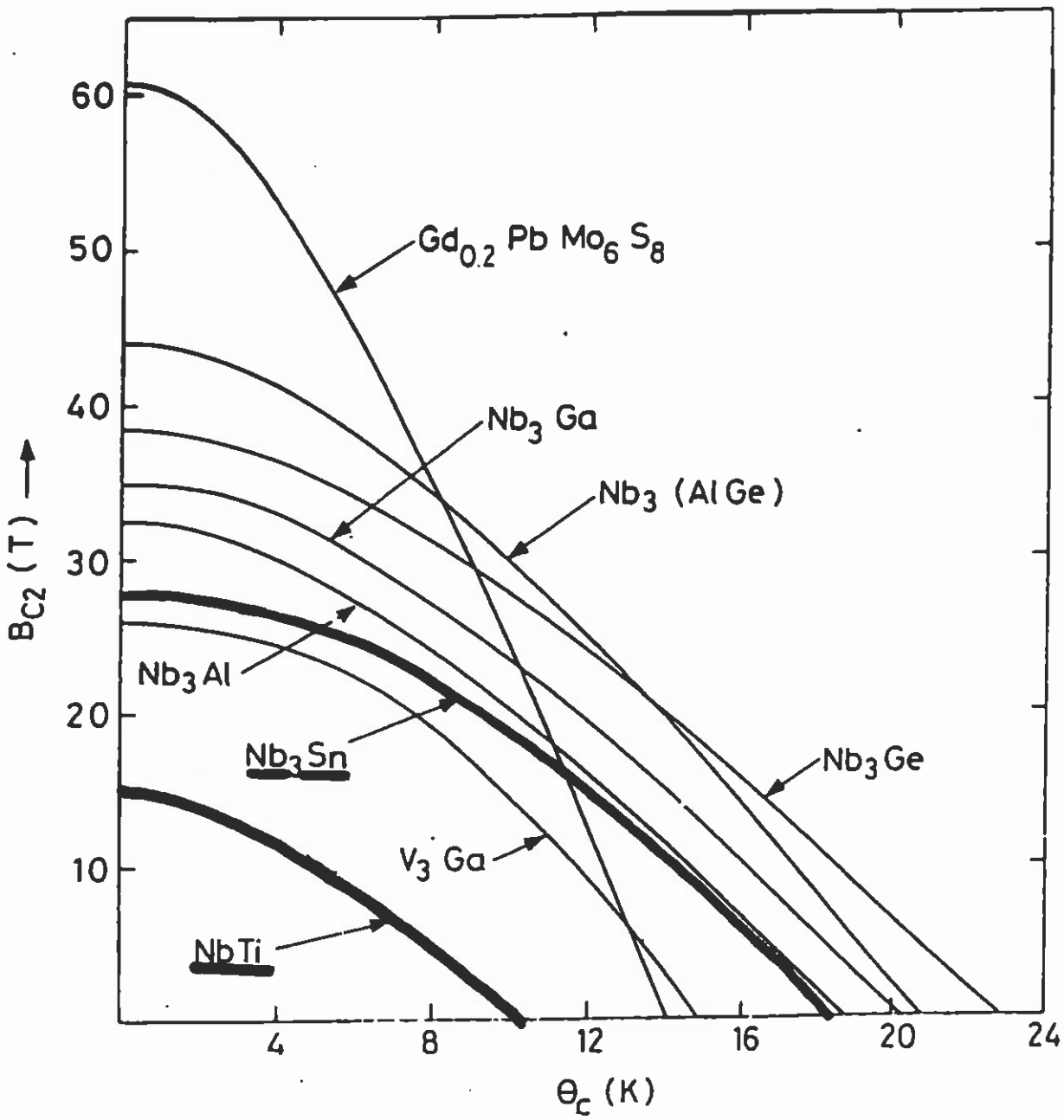

Courtesy M.N. Wilson

PINNING IN NB3SN COMPOUNDS

– The dominant source of flux pinning in NbSn compounds is believed to be grain boundaries.

– To achieve high J_C, it is therefore necessary to produce fine grain structures.

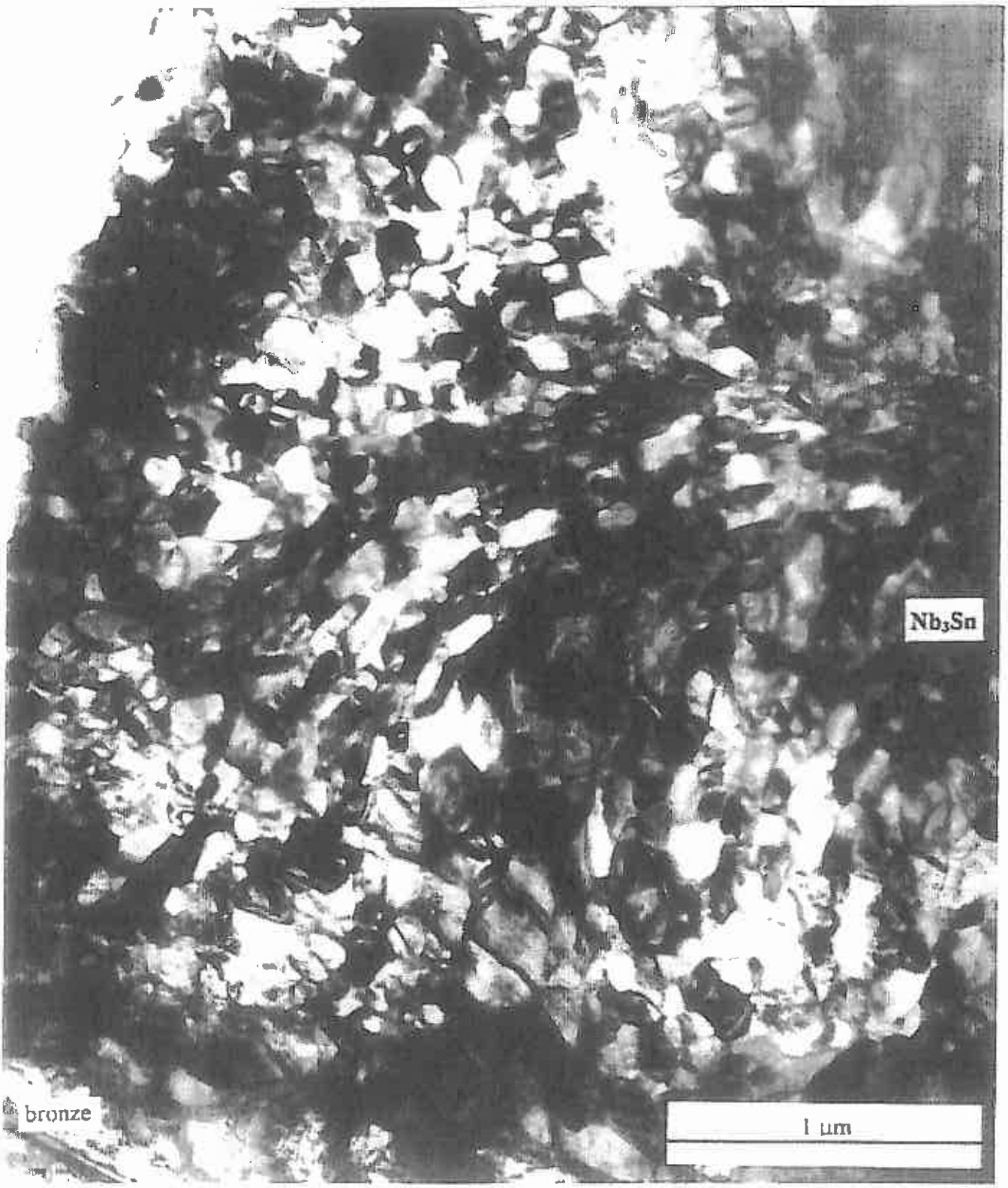

(Courtesy C. Verwaerde)

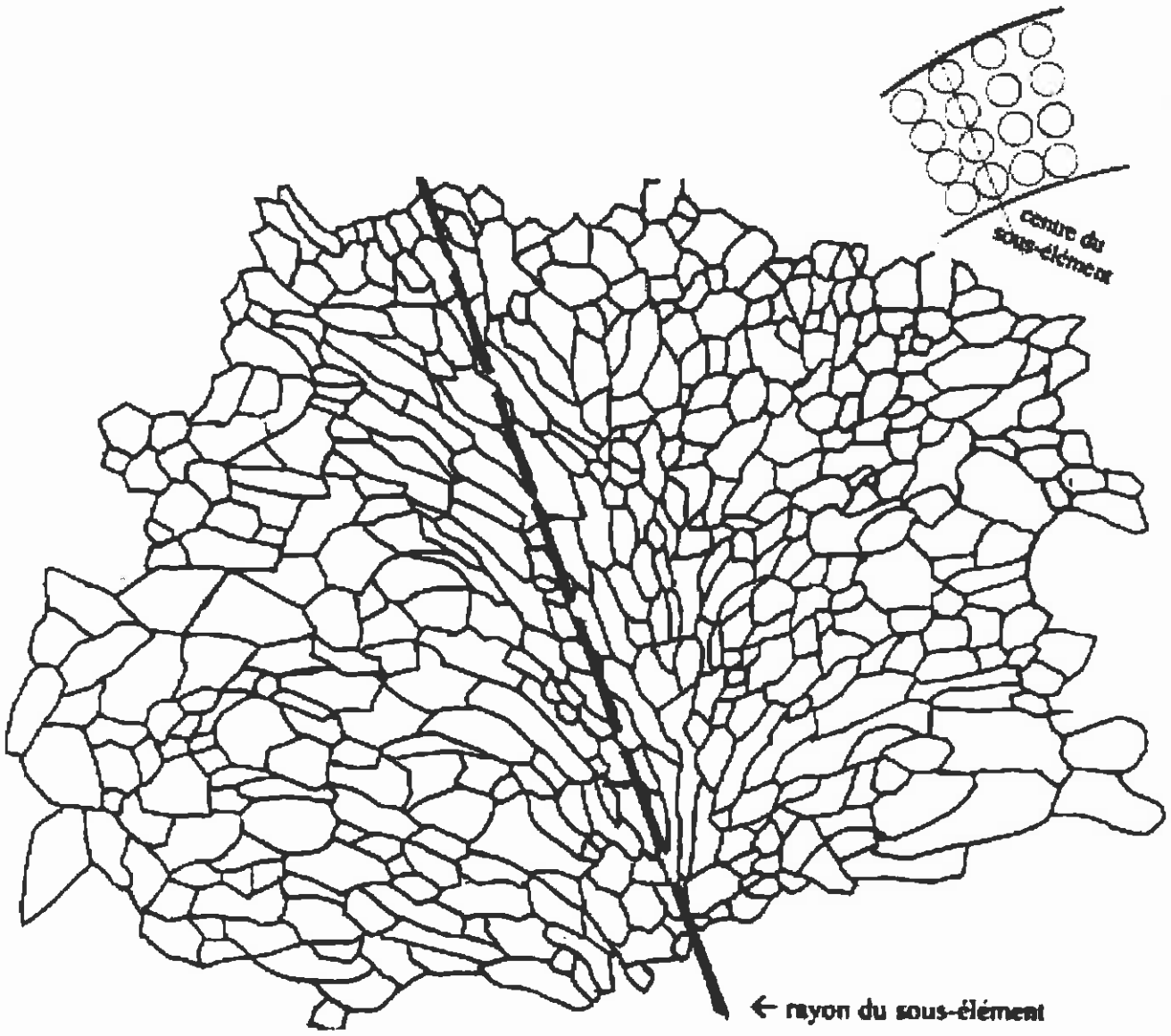

(Courtesy C. Verwaerde)

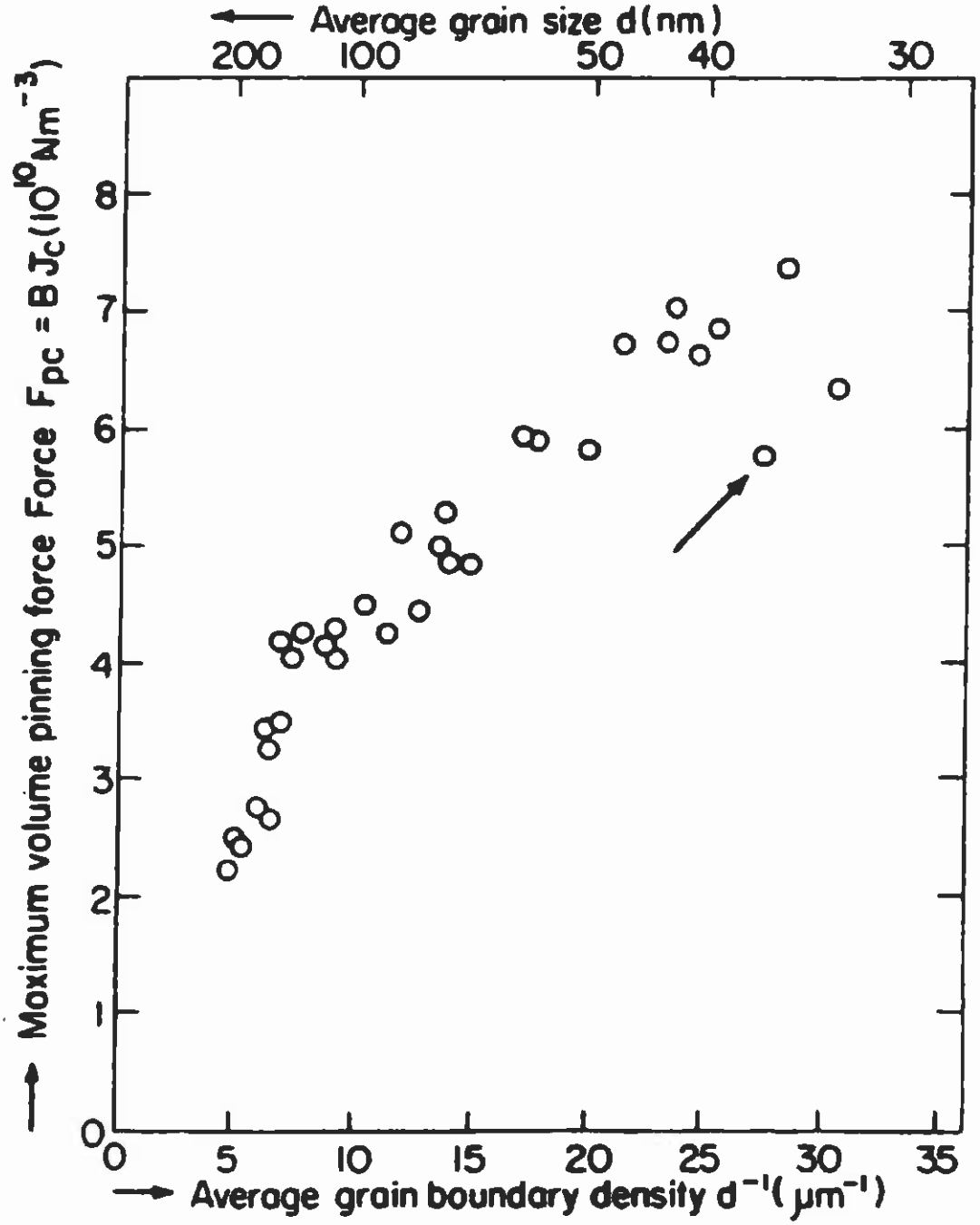

Fig. 8 The maximum pinning force per unit volume $F = B^* J_c$ versus effective grain size for a Nb_3Sn conductor produced via the bronze process

Courtesy M.N. Wilson

STRAIN SENSITIVITY OF NB3SN COMPOUNDS

– In addition to being brittle, Nb_3Sn exhibits a strong strain sensitivity.

– The critical temperature, the upper critical magnetic flux density, and the critical current density of Nb_3Sn depends on strain, ε.

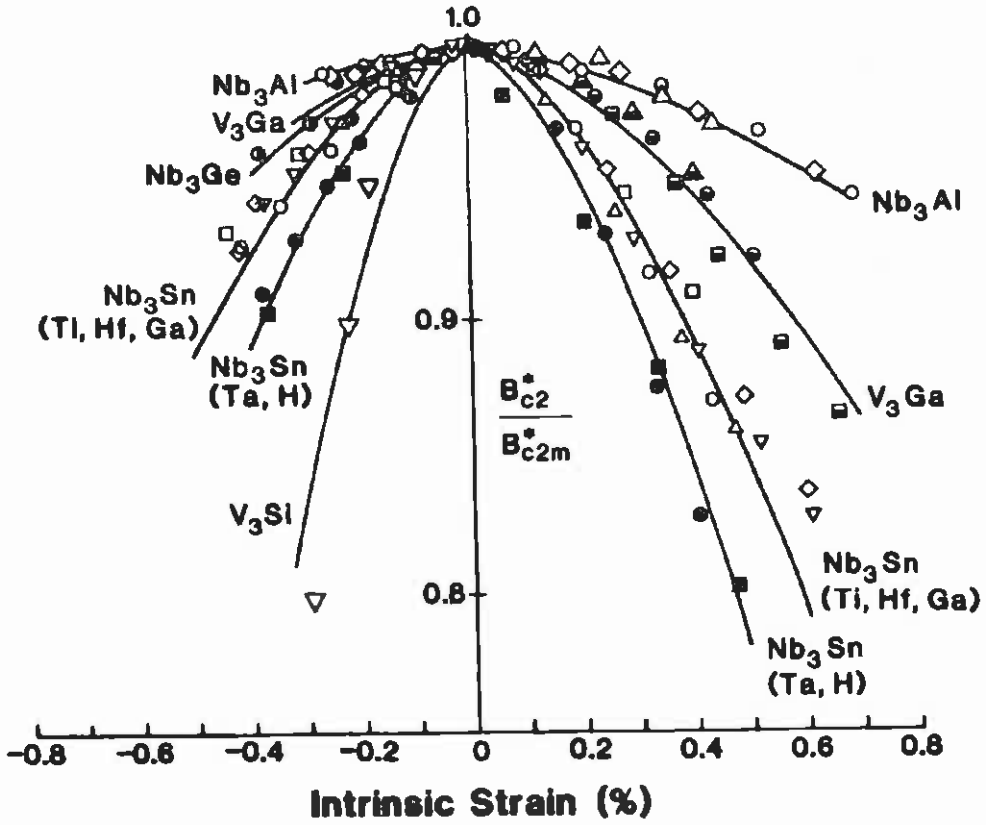

Fig. 4. Effect of uniaxial strain on the upper-critical field of practical A15 superconductors; B^*_{c2} has been normalized by it's maximum (nearly strain-free) value B^*_{c2m}. Binary Nb_3Sn is represented by the same curve as for Nb_3Sn (Ti, Hf, Ga).

J.W. Ekin, 1984-1987

LECTURE 3: CONDUCTOR AND CONDUCTOR INSULATION FOR PARTICLE ACCELERATOR MAGNETS

3.1 Review of Superconducting Materials
- 3.1.1 NbTi Alloys
- 3.1.2 Nb_3Sn Compounds
- **3.1.3 HTS**

3.2 Superconducting Multifilamentary Composites

3.3 Transition of Multifilamentary Wires

3.4 Manufacturing of NbTi Wires

3.5 Manufacturing of Nb_3Sn Wires

3.6 Critical Surface Parametrizations

3.7 Rutherford-Type Cables

3.8 Interstrand Resistances in Rutherford-Type Cables

3.9 Critical Current Measurements on Rutherford-Type Cables

3.10 Cable Insulation

Appendix: Material Properties at Low Temperatures

HIGH TEMPERATURE SUPERCONDUCTORS

– Although great progresses have been made in the development of the so-called *High Temperature Superconductors* (HTS), such as bismuth copper oxydes, $Bi_2Sr_2CaCu_2O_x$ and $(Bi,Pb)_2Sr_2Ca_2Cu_3O_x$, and yttrium copper oxides, $YBa_2Cu_3O_7$, these materials are not ready yet for applications requiring low costs, mass-production and high critical current densities.

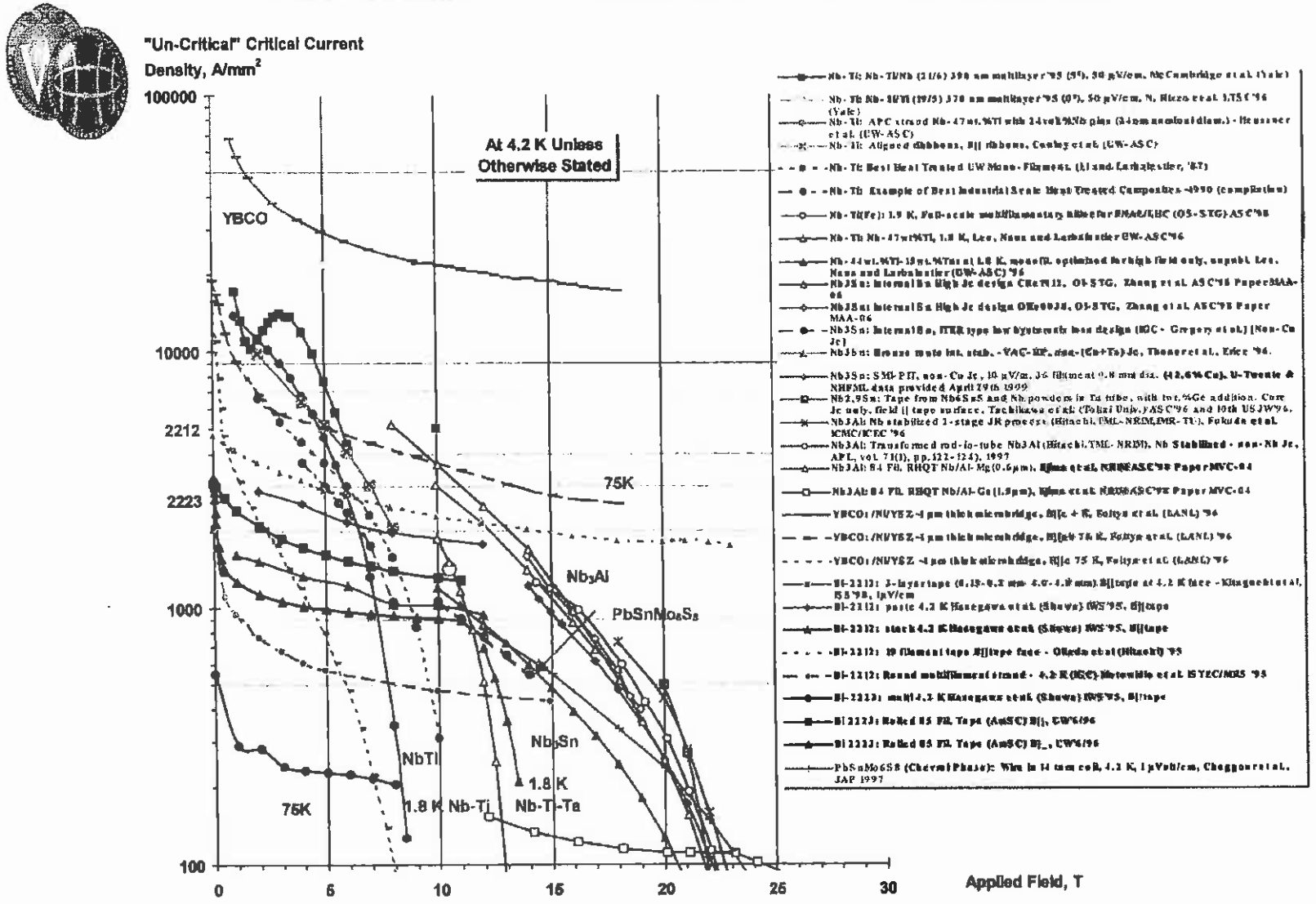

Courtesy P.J. Lee

LECTURE 3: CONDUCTOR AND CONDUCTOR INSULATION FOR PARTICLE ACCELERATOR MAGNETS

3.1 Review of Superconducting Materials
- 3.1.1 NbTi Alloys
- 3.1.2 Nb_3Sn Compounds
- 3.1.3 HTS

3.2 Superconducting Multifilamentary Composites

3.3 Transition of Multifilamentary Wires

3.4 Manufacturing of NbTi Wires

3.5 Manufacturing of Nb_3Sn Wires

3.6 Critical Surface Parametrizations

3.7 Rutherford-Type Cables

3.8 Interstrand Resistances in Rutherford-Type Cables

3.9 Critical Current Measurements on Rutherford-Type Cables

3.10 Cable Insulation

Appendix: Material Properties at Low Temperatures

SUPERCONDUCTING MULTIFILAMENTARY COMPOSITES

– For practical applications, the superconductor is subdivided into fine filaments, which are twisted together and embedded in a low resistivity matrix of normal metal.

– The subdivision into fine filaments is required to eliminate instabilities in the superconductor known as *flux jumping*.

– The filament twisting is introduced to reduce inter-filament coupling under time-varying fields.

– The low resistivity matrix is used as current shunt in the case of transition of the filaments to the normal resistive state, thereby limiting power dissipation and conductor heating.

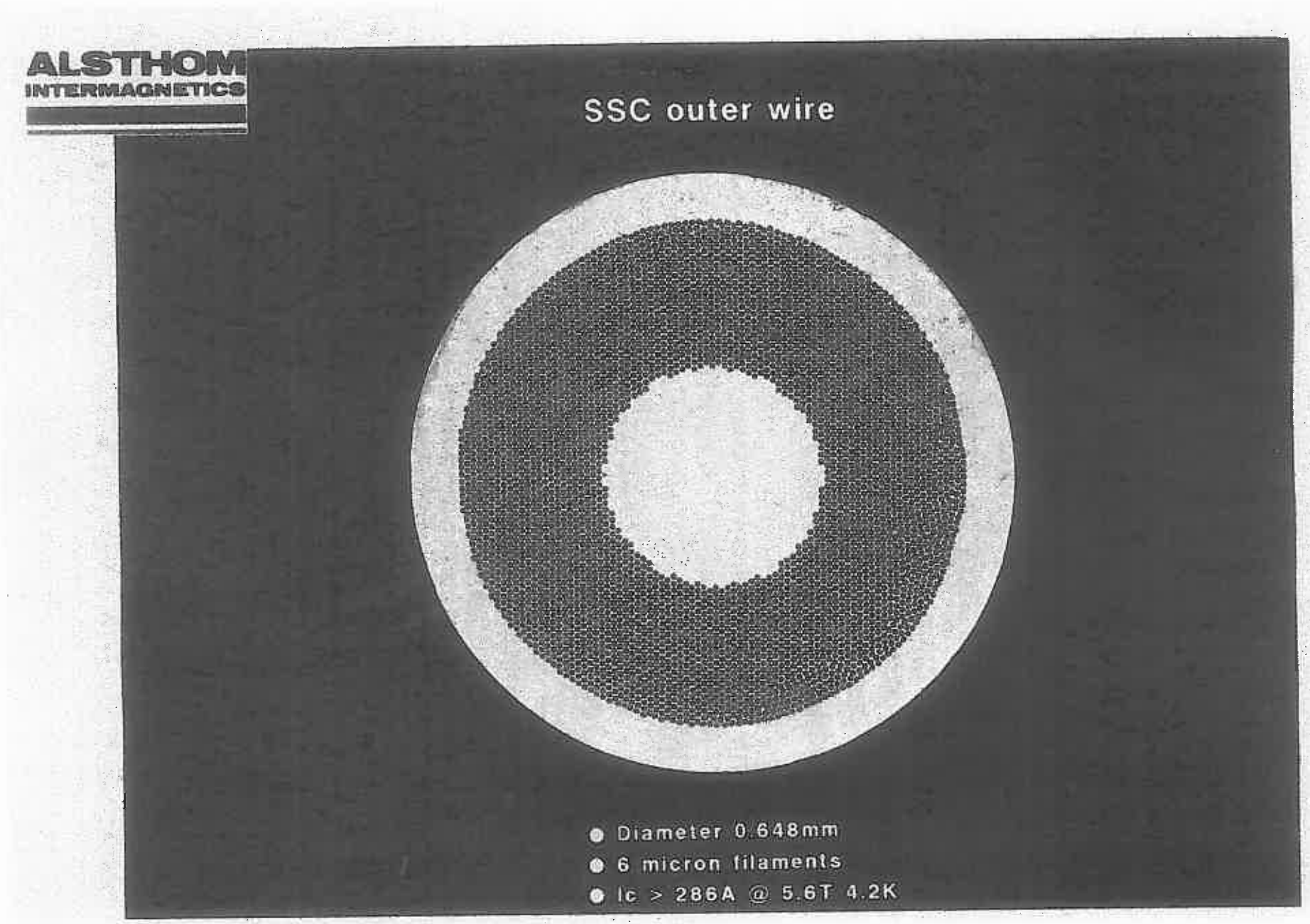
ALSTHOM
INTERMAGNETICS
SSC outer wire
Diameter 0.648mm
6 micron filaments
Ic > 286A @ 5.6T 4.2K

FLUX JUMPING

– Flux jumping is an instability that occurs in the mixed state of type-II superconductors. This instability arises as follows:

Small thermal perturbation,
⇒ Temperature rise in superconductor bulk,
⇒ Decrease of pinning force and J_C,
⇒ Fluxoid redistribution to accomodate this decrease,
⇒ Energy dissipation by moving fuxoids,
⇒ Further temperature rise,
And so on.

– It can be shown that the energy per unit volume dissipated by moving fluxoids during a flux jump is proportionnal to the square of superconductor size.

PREVENTING FLUX JUMPING

– Flux jumping can be prevented by subdividing the superconductor into fine filaments (to reduce superconductor size) and by embedding the filaments into a matrix of normal metal (to improve handling and heat removal capabilities by conduction through the normal matrix).

– In practical superconducting multifilamentary composite, filament diameter is less than 50 μm.

INTRASTRAND COUPLING CURRENTS

– Let us consider a superconducting multifilamentary composite. In the steady state, the transport current flows in the superconducting filaments whose resistance is nil.

– When subjected to a time-varying magnetic flux density, the presence of a low resistivity matrix between the filaments can allow the formation of current loops which are superimposed to the transport current.

– The current of such a loop circulates along a first filament, crosses the low resistivity matrix to reach a second filament, comes back along the second filament and crosses again the low resistivity matrix to get back to the first filament.

– These current loops are referred to as *intrastand* coupling currents.

Inter-filament Coupling
(case of untwisted filaments)

Interfilament Coupling
(case of untwisted filaments)

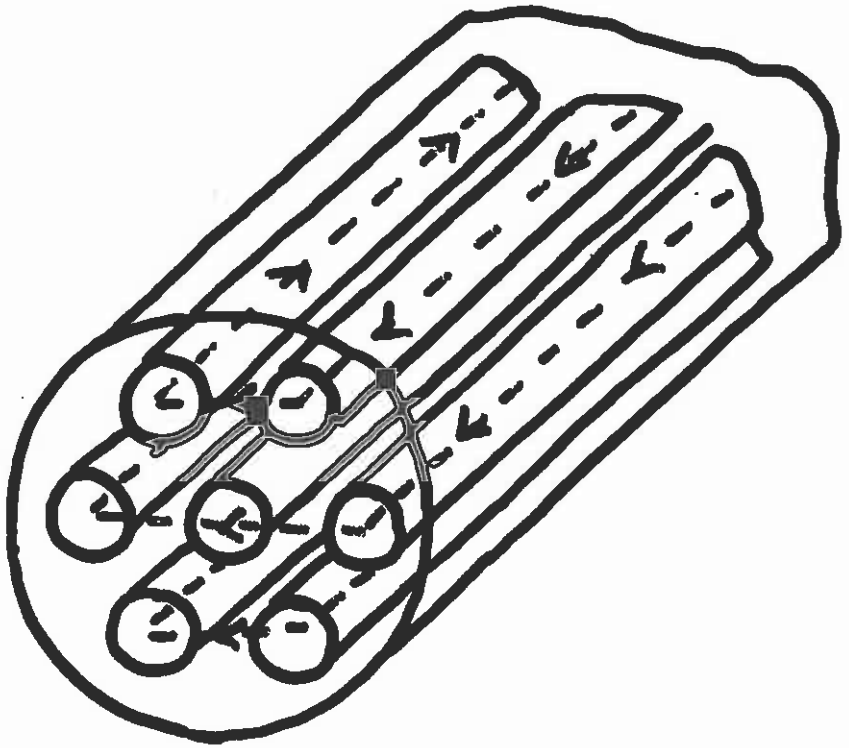

$\dot{B}$ ↑

REDUCING INTRASTRAND COUPLING CURRENTS

– Intrastrand coupling currents can be greatly reduced by twisting the filaments together.

Strand Eddy Current Model (Case of twisted filaments) *

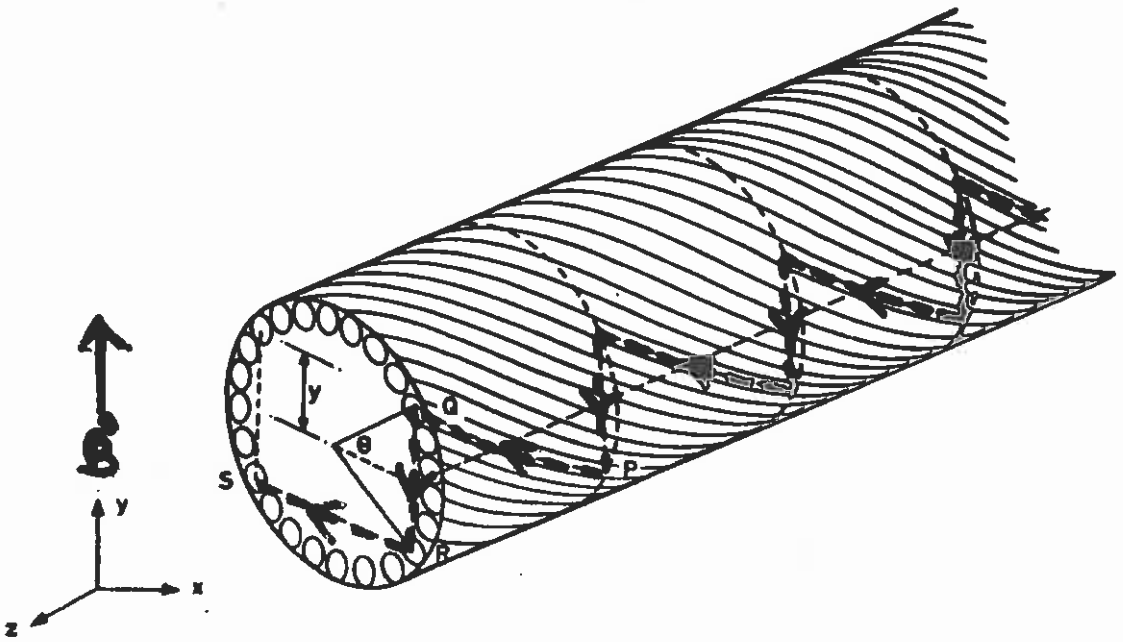

Fig. 8.15. Twisted filamentary composite in changing transverse field showing zig-zag path used to calculate flux linkages.

* Courtesy M. Wilson

Conductor Heating During a Quench

- If NbTi alone:

  ρ_{NbTi} normal state $\sim 5\text{-}6\ 10^{-7}\ \Omega m$

  Conductor can burn ($T > 1000K$) in less than a ms

  $\Rightarrow$ Danger!

- Stabilized conductors:

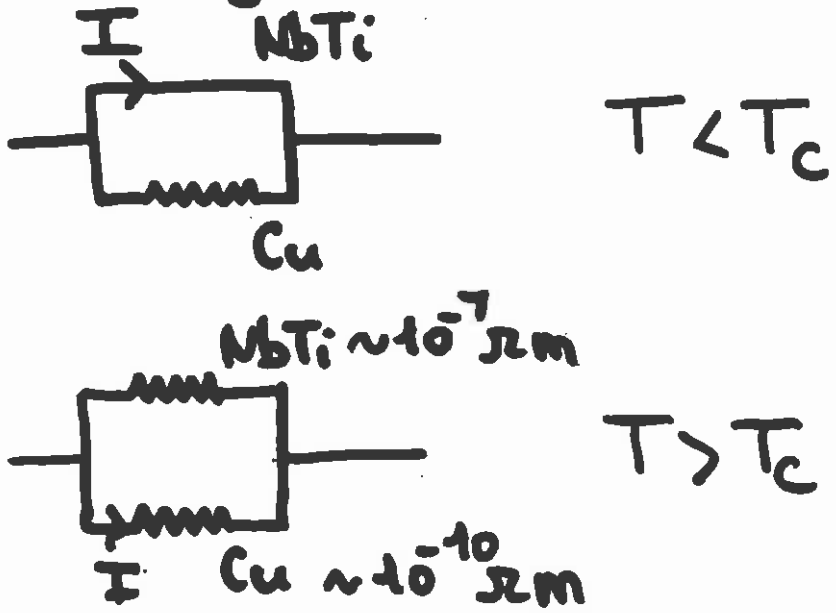

  It takes several 100 ms to burn conductor

  $\Rightarrow$ Safer!

SUPERCONDUCTING WIRES FOR PARTICLE ACCELERATOR MAGNETS

– Accelerator magnets rely on cables made from round wires of superconducting multifilamentary composites.

– Wire diameter ranges from 0.5 to 1.3 mm.

– Except for a few R&D magnet models, the filaments are made of binary niobium-titanium alloy and the matrix is high purity copper.

– The filament diameter of HERA wires is of the order of 15 μm while that of SSC, RHIC and LHC wires is of the order of 5 μm. The use of fine filaments is required to limit field distortions resulting from superconductor magnetization (see lecture on field quality).

– There are several thousand filaments per wire.

– The copper-to-superconductor ratio, r_{Cus}, (defined as the ratio of the area of copper to the area of niobium-titanium in the wire cross-section), varies from 1.3 to 1.8, except for RHIC wire where it is 2.25.

Annex I

GEC ALSTHOM
POWER GENERATION

Wire : IT# 1 B2/1890

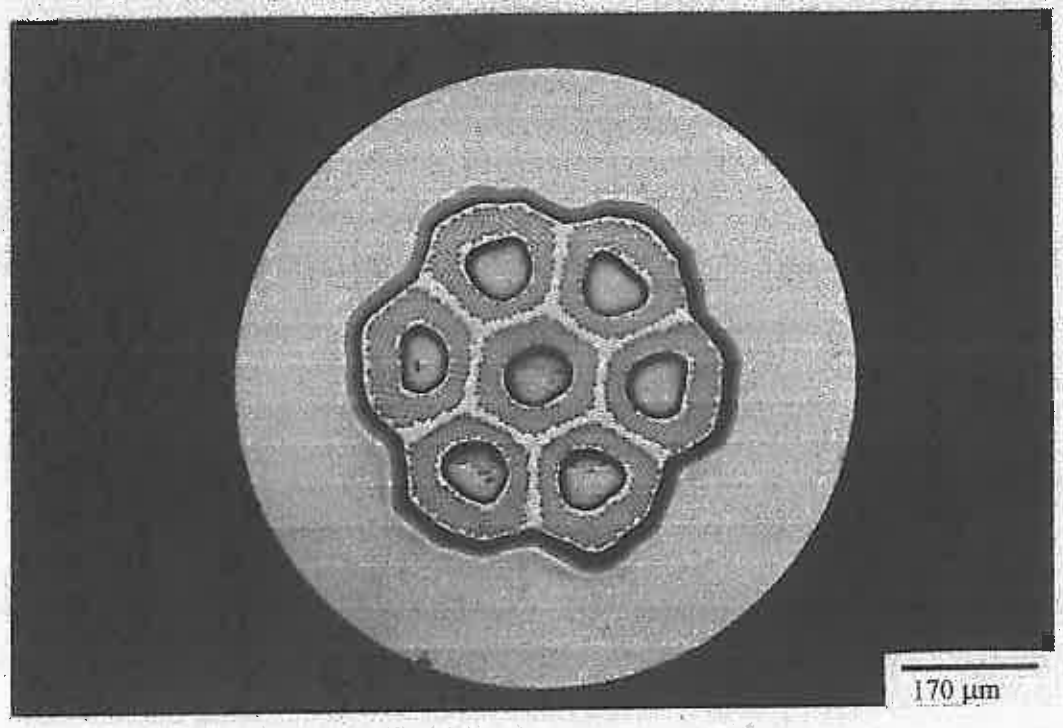

AI -1 Cross section of the wire before reaction

Diameter	0.78 mm
Number of filaments	1 890
Filament diameter	5 µm
Twist pitch	10 mm
Cu/Non Cu (micrographies)	1,7 ± 0,02
Cu/Non Cu (etching)	1,69 ± 0,02

Round Wire Option: BSCCO-2212

Wire Performance:

- **1 meter helical samples**
- **Highest Ic(4.2K, 0T) = 141 A**

Jc(4.2K, 0T) = 93 kA/cm^2

- **Highest Ic(4.2K, 15T) = 43 A**

Jc(4.2K, 15T) = 28 kA/cm^2

- **250 m piece lengths**

Cable Performance:

- **19 Strand Ic(4.2K, 6T) = 950 A**

Jc(4.2K, 6T) = 32.6 kA/cm 2

- **18 Strand Ic(4.2K, 6T) = 920 A**

Jc(4.2K, 6T) = 33.3 kA/cm 2

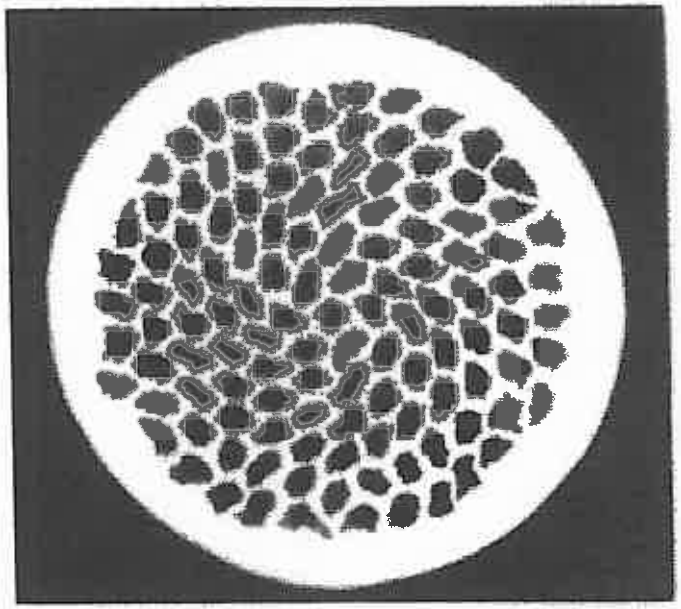

OXFORD
Superconducting Technology

Marken Napa Workshop 1998

Courtesy P.J. Lee

LECTURE 3: CONDUCTOR AND CONDUCTOR INSULATION FOR PARTICLE ACCELERATOR MAGNETS

3.1 Review of Superconducting Materials
- 3.1.1 NbTi Alloys
- 3.1.2 Nb_3Sn Compounds
- 3.1.3 HTS

3.2 Superconducting Multifilamentary Composites

3.3 Transition of Multifilamentary Wires

3.4 Manufacturing of NbTi Wires

3.5 Manufacturing of Nb_3Sn Wires

3.6 Critical Surface Parametrizations

3.7 Rutherford-Type Cables

3.8 Interstrand Resistances in Rutherford-Type Cables

3.9 Critical Current Measurements on Rutherford-Type Cables

3.10 Cable Insulation

Appendix: Material Properties at Low Temperatures

TRANSITION OF SUPERCONDUCTING WIRES

– The maximum current-carrying capacity of a superconducting multifilamentary composite wire at a given temperature and field can be determined by measuring the voltage-current curve of a wire short sample.

– To do so, the wire short sample is mounted on a test fixture providing a mechanical support. It is equipped with potential taps and is connected to current leads. Sample and holder are then inserted into the bore of a magnet providing the background field and are cooled down (using liquid helium) to the desired temperature.

– In the case of Nb_3Sn wires, great care must be taken in the sample preparation to ensure that the Nb_3Sn filaments of the wire are at a known and reproducible strain (VAMAS standard).

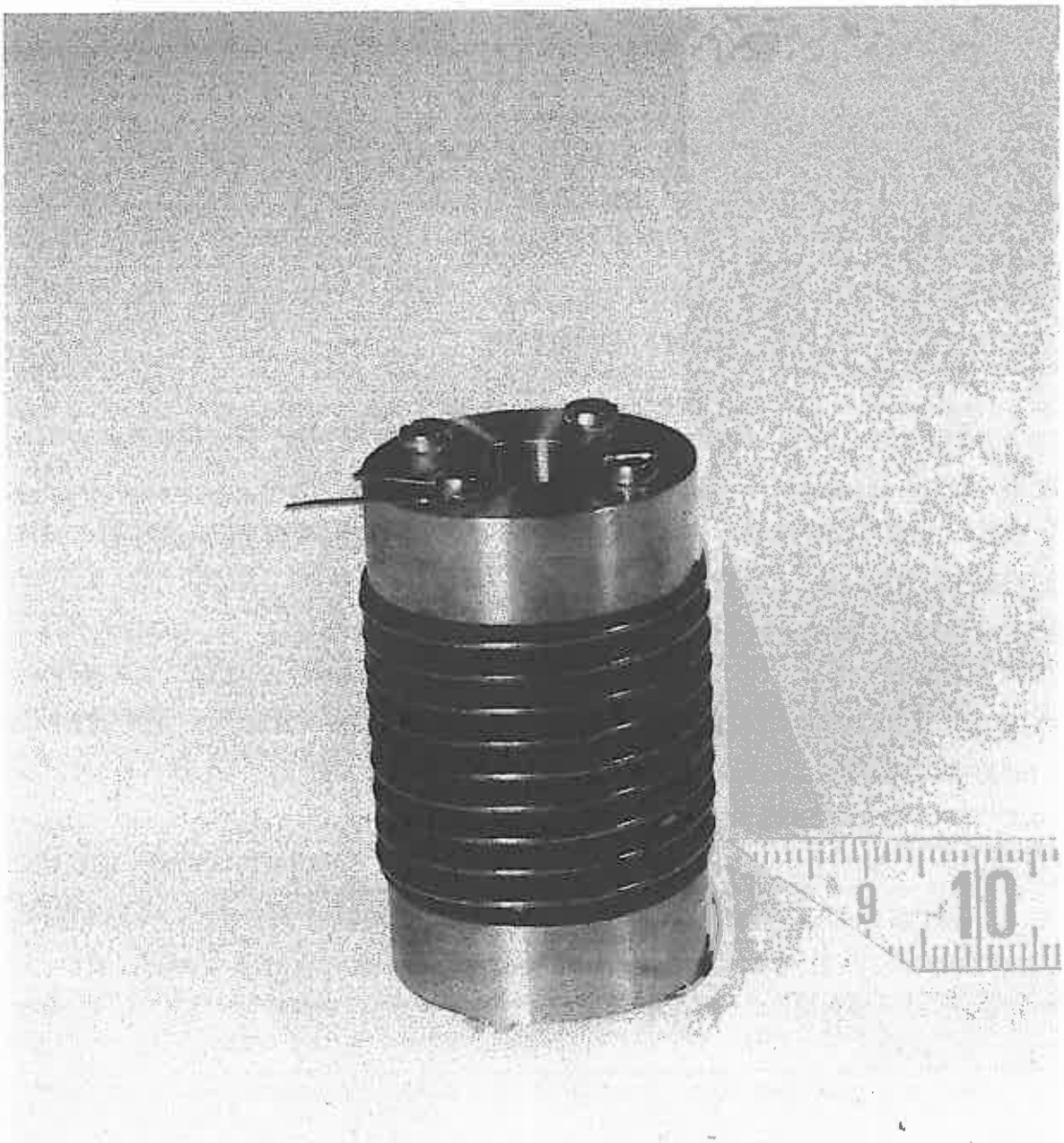

VAMAS Sample
for Critical Current Measurements

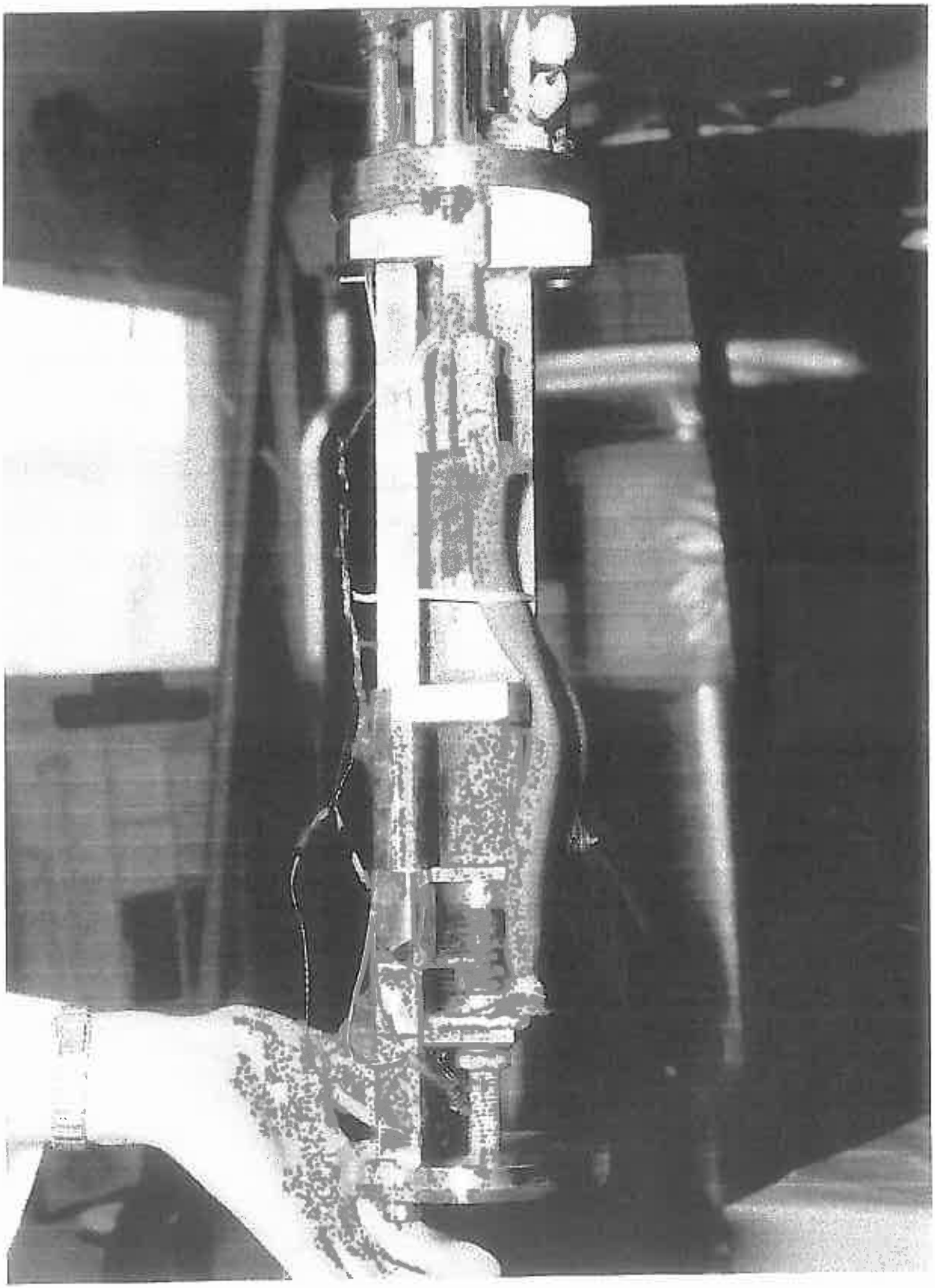

VOLTAGE-CURRENT CURVE

– The transition from the superconducting state to the normal resistive state is not abrupt but takes place over a certain current range:

• At low transport currents, the voltage, V, across the wire short sample is nil,

• Then, as the current, I, is increased, there appears a domain where V becomes non-zero and starts to rise.

At the beginning, the voltage rise is reversible, *i.e.*, if the current is lowered, the voltage decreases following the same curve as during the up-ramp.

However, above a certain current, the phenomenon becomes irreversible, and the voltage takes off rapidly and uncontrollably. Such irreversible voltage run-away is the signature of a quench.

– The current at which the run-away occurs is referred to as the wire short sample *quench current*, I_{qss}.

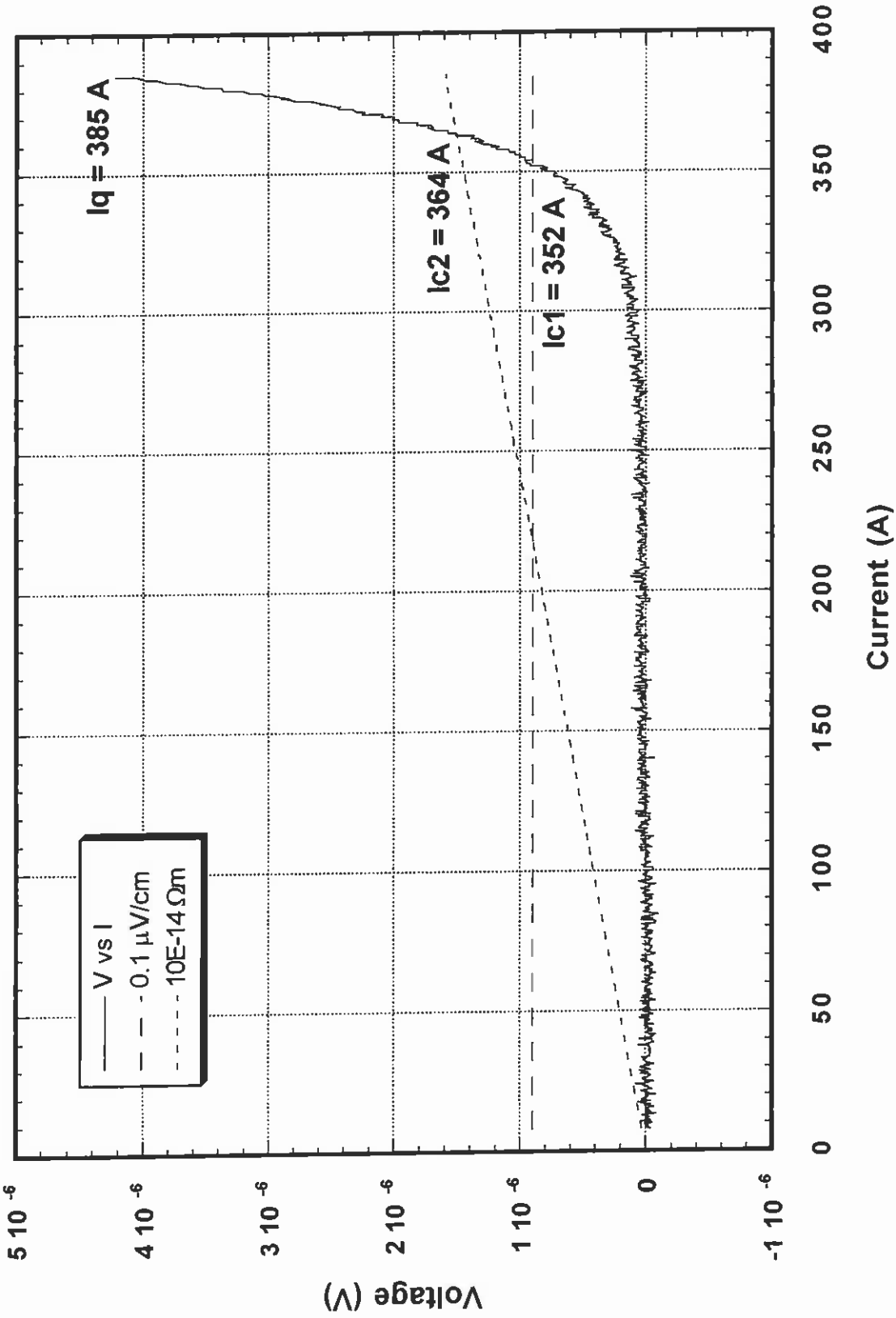
Iq = 385 A
Ic2 = 364 A
Ic1 = 352 A
V vs I
0.1 μV/cm
10E-14 Ωm
Voltage (V)
5 10 -6
4 10 -6
3 10 -6
2 10 -6
1 10 -6
0
-1 10 -6
0
50
100
150
200
250
300
350
400
Current (A)

INTERPRETATION OF *V–I* CURVE

– The bottom (reversible) part of the *V–I* curve of a superconducting multifilamentary composite wire corresponds to the progressive release of the fluxoids from the pinning sites under the effect of the Lorentz-like forces. The released fluxoids start to move and their motion is accompanied by energy dissipation.

– As more and more fluxoids are released and move, more and more energy is dissipated, which, in turn, heats up the filaments, decreases the pinning forces (while the Lorentz-like force keep increasing) and causes the release of even more fluxoids.

– At some point, the conductor heating resulting from fluxoid motion becomes too large and the sample quenches.

– From this simple description, it appears that the bottom part of the *V–I* curve is mainly determined by the pinning characteristics at the given temperature and field, while the top part of the curve is strongly affected by the cooling condition of the wire sample, which depends on the experimental setup.

– The question then arises of what engineering value to use to characterize the maximum current capability of a wire.

CRITICAL CURRENT DENSITY

– The critical current determined by either of the aforementioned criterions can be translated into an average critical current density in the superconductor, J_C, by writing

$$I_C = J_C \frac{S}{1+r}$$

– I_C and J_C both depend on T and B.

CRITICAL CURRENT

– The engineering value used to characterize the maximum current capability of a superconducting wire is referred to as *critical current*, I_C, and is defined by relying on empirical criterions.

– Let us consider a wire sample of length, L, cross-sectional area, S, and non-superconductor to superconductor ratio, r, and let V designate the voltage across the sample. An apparent electrical field, E_s, and an apparent resistivity of the superconductor, ρ_s, can be defined as

$$E_s = \frac{V}{L} \qquad \text{and} \qquad \rho_s = \frac{S}{(1+r)L}\,\frac{V}{I}$$

– For NbTi and Nb_3Sn wires, the two criterions the most commonly used to define the critical current are:

- The current value corresponding to an apparent electrical field, E_C, of 0.1 μV/cm,
- The current value corresponding to an apparent resistivity of the superconductor, ρ_C, of 10^{-14} Ωm.

– For measurements on a wire short sample, I_c is usually lower than I_{qss}.

RESISTIVE TRANSITION INDEX

– To fully characterize the wire, it is also interesting to quantify the sharpness of the transition from the superconducting to the normal resistive state. This can be done by plotting $\ln(V)$ [or $\ln(\rho_s)$], as a function of $\ln(I)$.

– It appears that $\ln(V)$ [and similarly, $\ln(\rho_s)$] increases quasi-linearly as a function $\ln(I)$ over a broad range (typically from E_C to $10E_C$ or ρ_C to $10\rho_C$).

– Hence, the onset of the resistive transition can be fitted by simple power laws of the form:

$$\frac{V}{V_C} = \left(\frac{I}{I_C}\right)^N \qquad \text{or} \qquad \frac{\rho_s}{\rho_C} = \left(\frac{I}{I_C}\right)^{(N-1)}$$

where V_C is the voltage across the wire sample corresponding to E_C:

$$V_C = E_C L$$

– The index N is referred to as *resistivity transition index*, or more simply, *N-value*.

– The N-value is representative of the curvature of the voltage-current curve: the larger N, the sharper the transition.

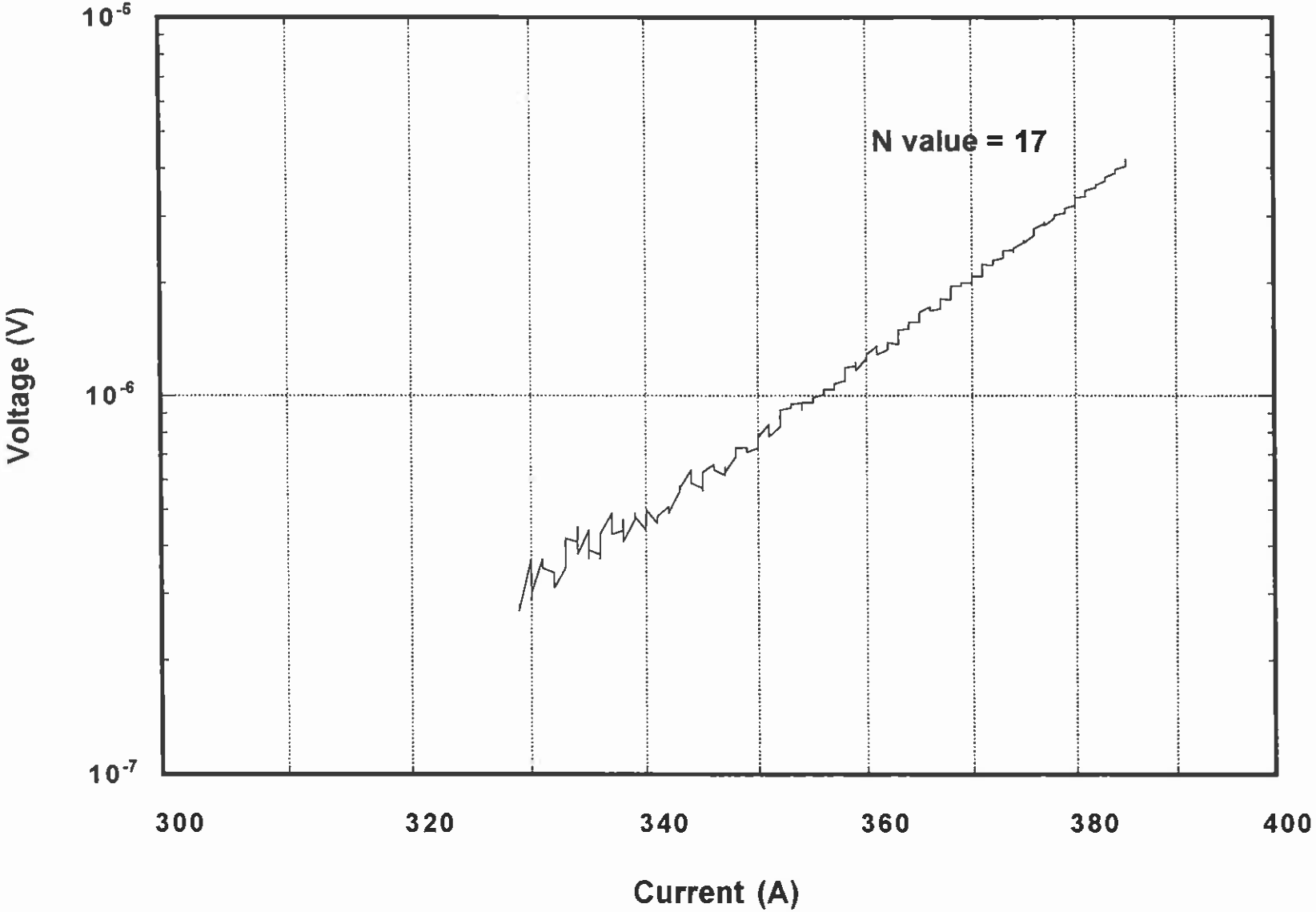
N value = 17
Voltage (V)
10-5
10-6
10-7
300
320
340
360
380
400
Current (A)

FACTORS INFLUENCING THE N-VALUE

– The N-value, like I_C, depends on temperature and field.

– In the case of NbTi wires, there is a clear correlation between filament distortions, often referred to as *sausaging*, and N-value: the wider the distribution of filament diameters in the wire cross-section, the lower the N-value.

Transition Index as a function of Temperature and field for HIP Nb_3Sn *

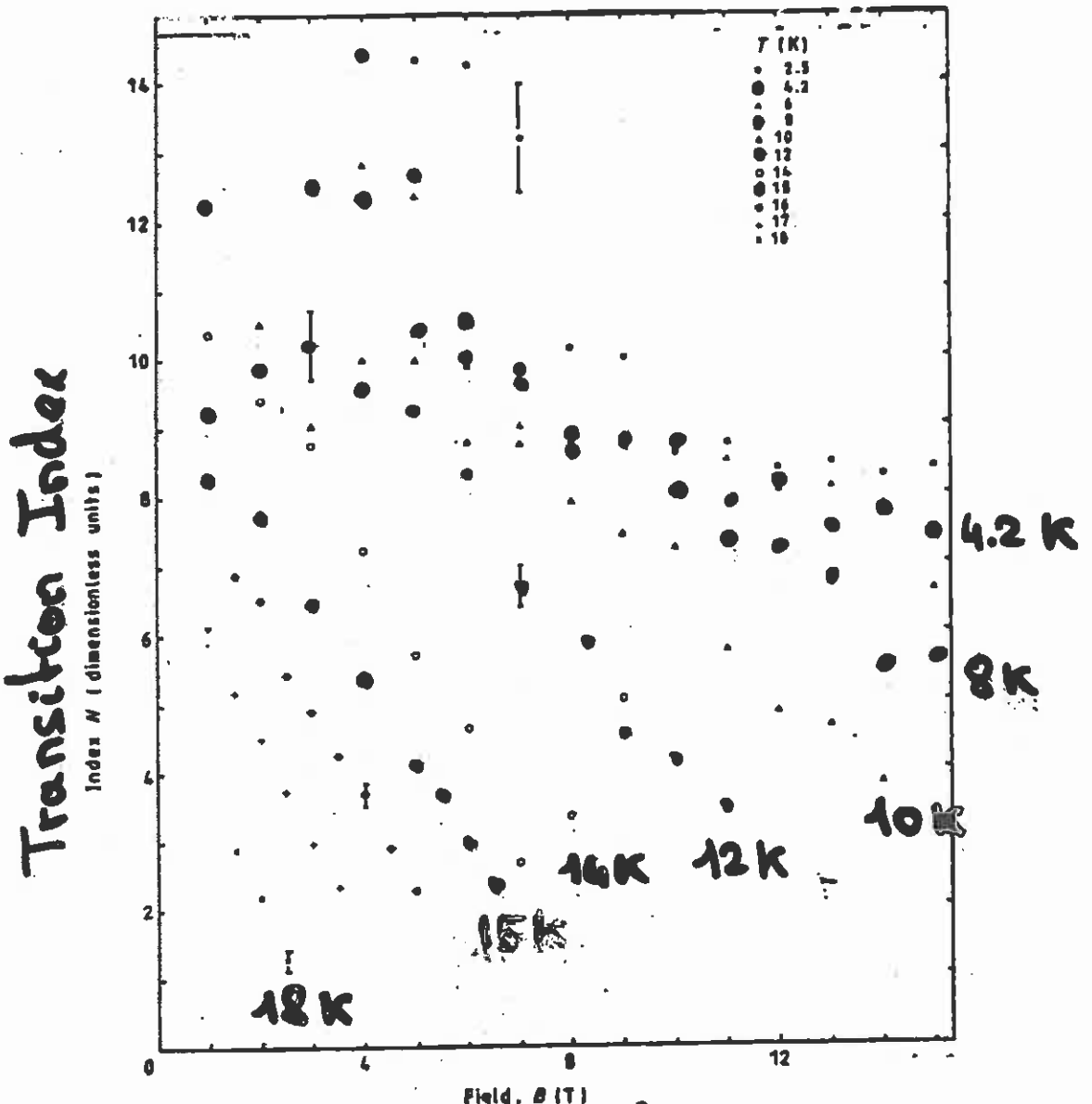

* Hampshire and Jones, 1987

Origin of N-Value*

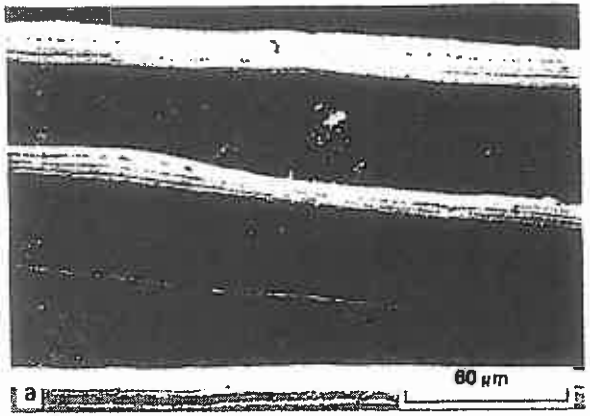

Figure 3 Longitudinal (a) and cross-sectional (b) views of the filaments in sample A

Sample A
N ~ 18

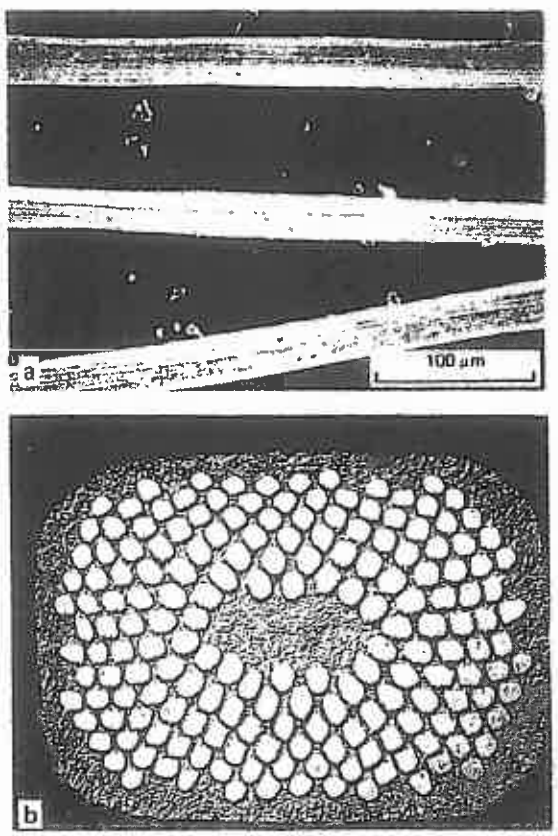

Figure 4 Longitudinal (a) and cross-sectional (b) views of the filaments in sample B

Sample B
N ~ 35

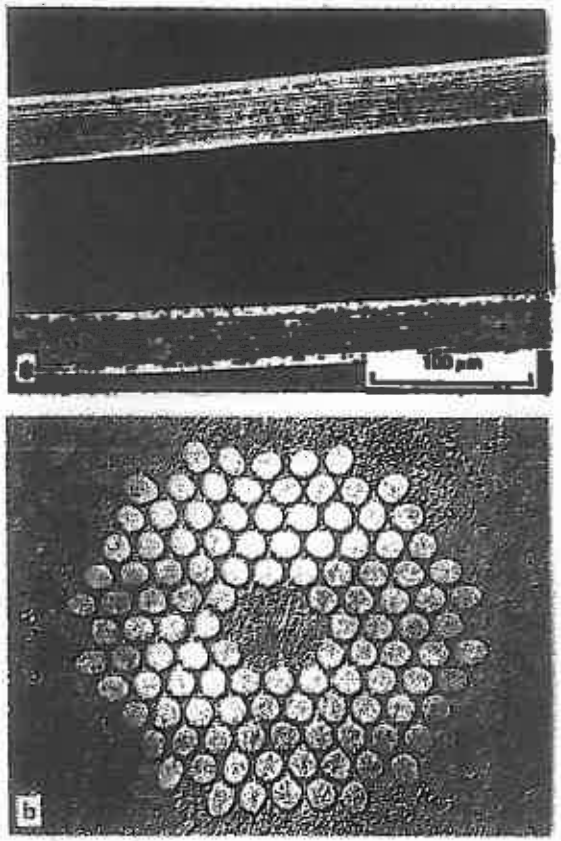

Figure 5 Longitudinal (a) and cross-sectional (b) views of the filaments in sample C

Sample C
N ~ 53

* J. W. Ekin, 1987

Origin of N-Value (Cont.)*

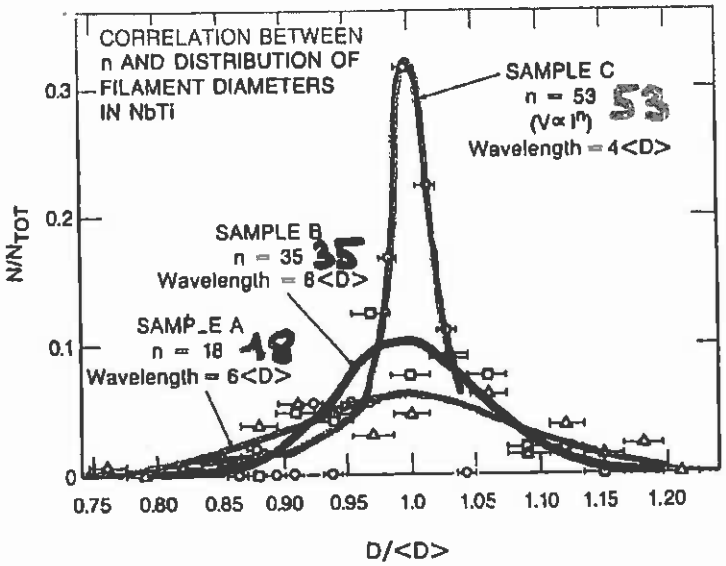

Figure 6 Distribution of filament diameters in samples A, B and C. Horizontal bars indicate the sampling interval for each histogram. Irregularities in the cross-sectional area of each filament mainly determine *n*, rather than variations in the *average* filament diameter from filament to filament. In these samples, the average filament diameter varied with radial position in the composite. The radial effect was eliminated from the plotted distribution by determining the variation in diameter of each filament relative to the average diameter of other filaments at the same radial position

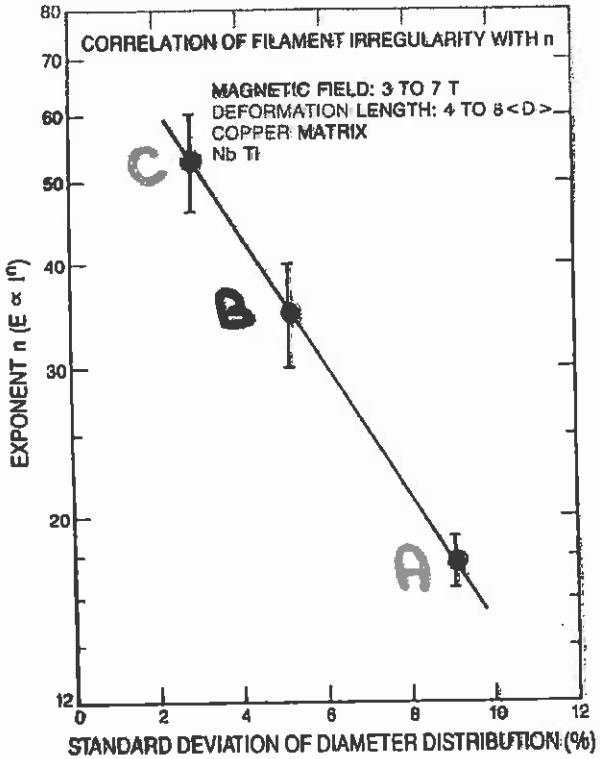

Figure 7 Approximate relationship between *n* and the standard deviation of the filament diameter distribution for several multifilamentary Nb-Ti superconductors (from *Figure 6*)

* J. W. Ekin, 1987

FIELD DEPENDENCE OF *N*-VALUE

– The field dependence of the *N*-value can be used as a criterion to determine if the critical current is limited by:

- ***intrinsic factors,*** **related to fluxon-microstructure interactions within the superconducting material,**

- ***extrinsic parameters,*** **related to macroscopic irregularities, such as local reductions in filament cross-sectional areas.**

N vs. B Dependence (Cont.)*

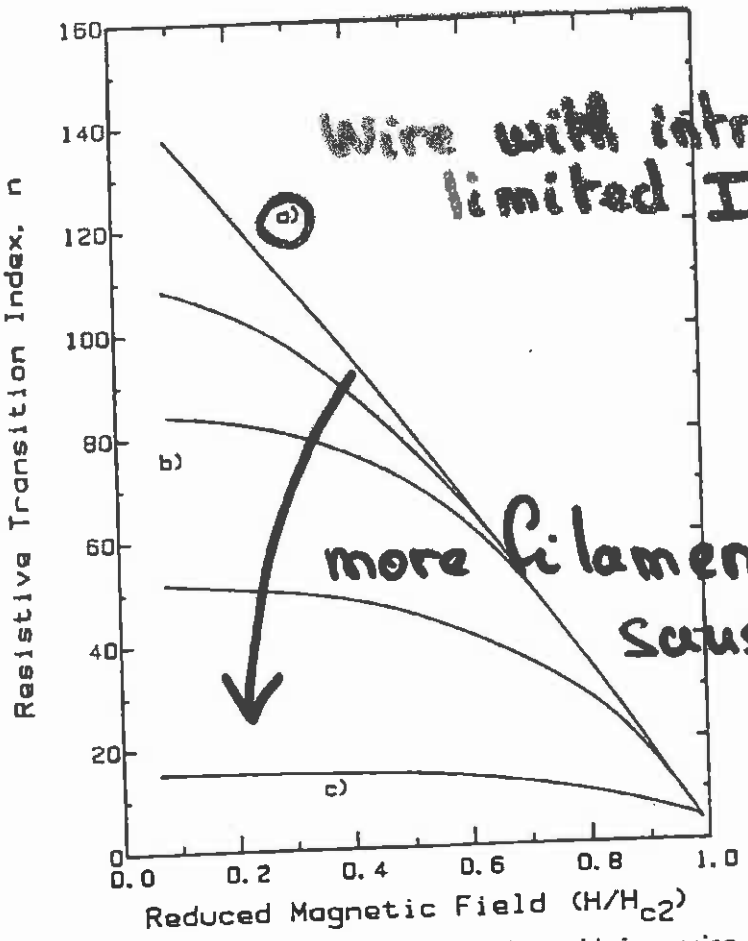

Figure 1 The *n–H* plot for a series of wires with increasing extrinsic limitations to the I_c. The composites shown are (a) intrinsically limited; (b) mildly sausaged; (c) badly sausaged

N vs. B curve can be used to characterize wire quality

Good Number for SSC cable

N ~ 30

*3. H. Warnes, D. Larbalestier, 1986

N vs. B Dependence*

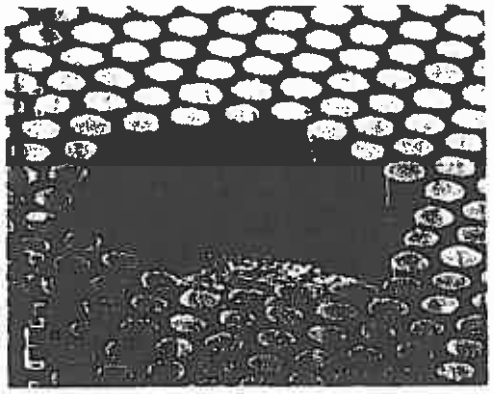

High Quality Wire

Fig. 4B SEM micrograph of high quality CBA wire. n = 40, J_c = 2000 A/mm^2.

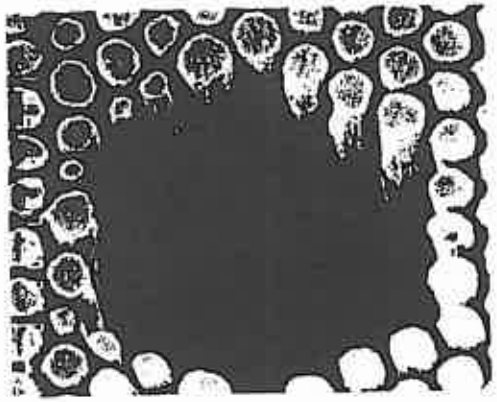

Badly Sausaged Filaments

Fig. 4A SEM micrograph of filaments of low quality wire. n = 14, J_c = 1400 A/mm^2.

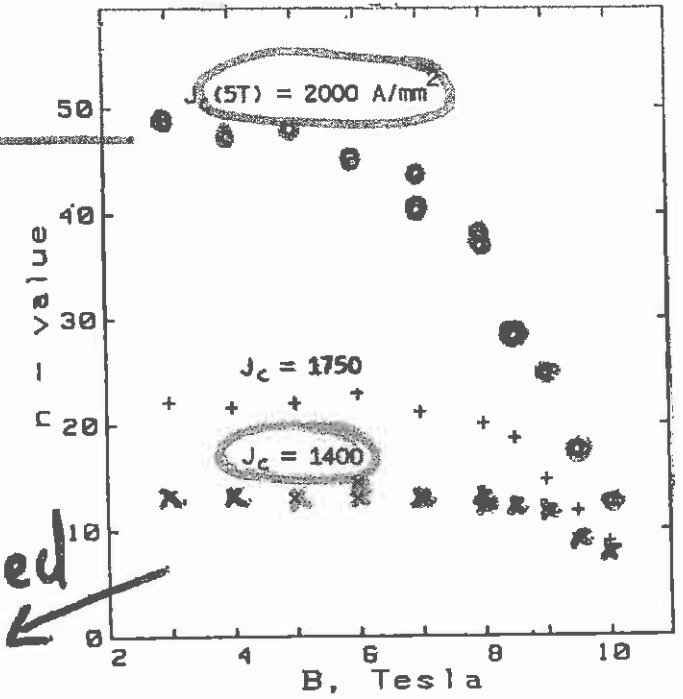

Fig. 5 n vs B for CBA wires of varying filament uniformity.

* Garber, Suenaga, et al., 1986

Theory of Critical Current Distribution*

Part I: Case of an Ideal Superconductor

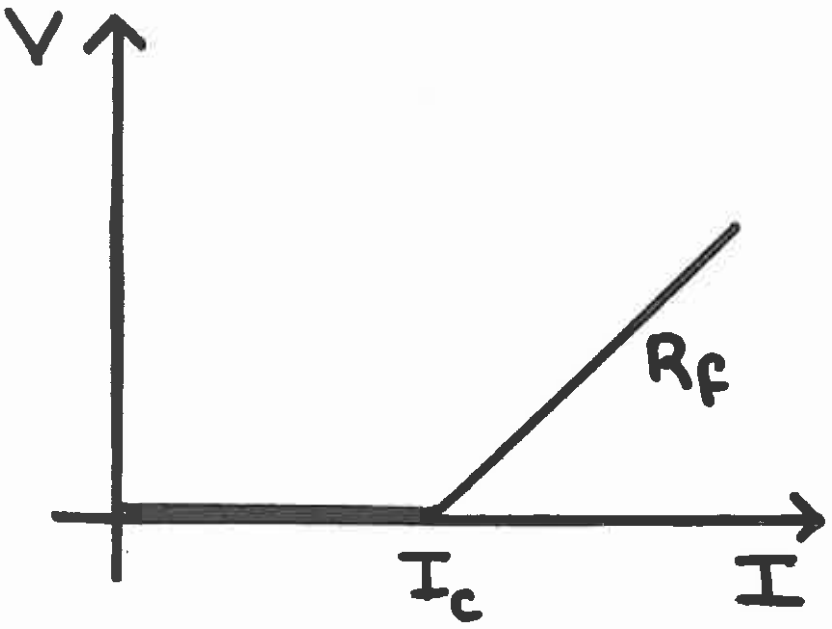

$$\begin{cases} V = 0 & \text{for } I < I_c \\ V = R_f(I - I_c) & \text{for } I > I_c \end{cases}$$

*W. H. Warnes and D.C Larbalestier, 1986

Theory of Critical Current Distribution *

Part II: Case of a Conductor with a Statistical Distribution of I_c

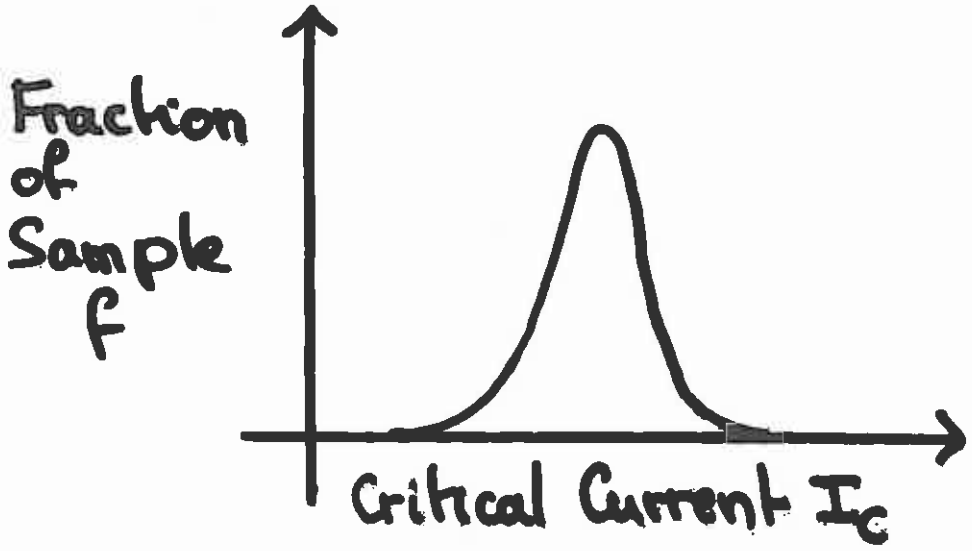

$$V(I) = R_f \int_0^I dI_c \, f(I_c)(I - I_c)$$

Taking two derivatives with respect to I yields

$$f(I) = \frac{1}{R_f} \frac{d^2V}{dI^2}$$

Can be computed numerically from measured V-I curve

* W. H. Warnes and D.C. Larbalestier, 1986

Measurements of Critical Current Distribution (NbTi wire)*

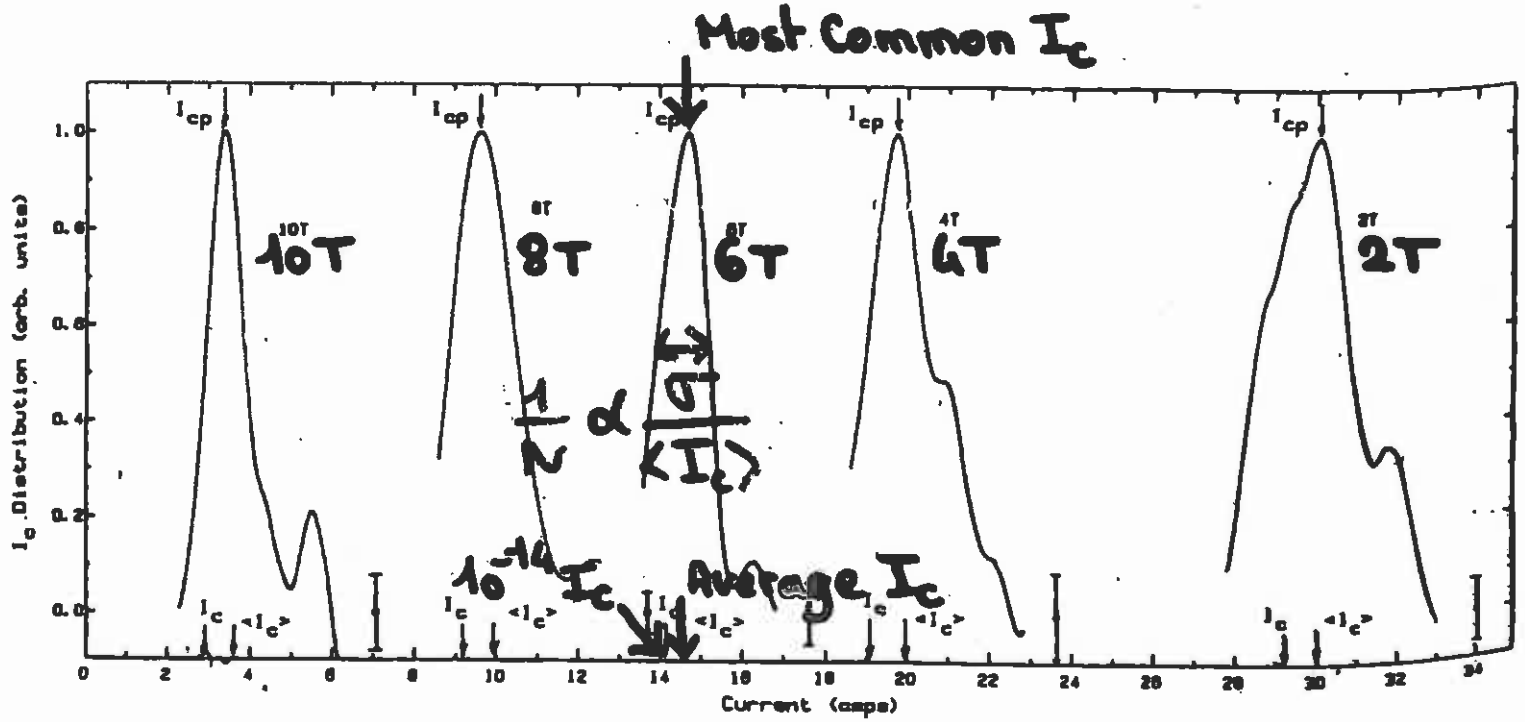

Figure 9 The I_c distributions for SC4164 1 HT for magnetic fields from 2 to 10 T. At each field, the value for the high sensitivity (10^{-14} Ωm) measurement of the critical current, I_c, is shown, as well as the average critical current, $\langle I_c \rangle$, and the most common critical current, I_{cp}, as derived from the differential analysis

*W. H. Warnes and D.C. Larbalestier, 1986

LECTURE 3: CONDUCTOR AND CONDUCTOR INSULATION FOR PARTICLE ACCELERATOR MAGNETS

3.1 Review of Superconducting Materials
- 3.1.1 NbTi Alloys
- 3.1.2 Nb_3Sn Compounds
- 3.1.3 HTS

3.2 Superconducting Multifilamentary Composites

3.3 Transition of Multifilamentary Wires

3.4 Manufacturing of NbTi Wires

3.5 Manufacturing of Nb_3Sn Wires

3.6 Critical Surface Parametrizations

3.7 Rutherford-Type Cables

3.8 Interstrand Resistances in Rutherford-Type Cables

3.9 Critical Current Measurements on Rutherford-Type Cables

3.10 Cable Insulation

Appendix: Material Properties at Low Temperatures

MANUFACTURING OF NBTI WIRES

– NbTi alloys are very ductile and have very low work-hardening coefficients making them easy to co-process with copper.

– A multifilamentary wire is fabricated in three main steps:

• Production of **high homogeneity NbTi alloy** by consummable arc vacuum melting.

• Extrusion and drawing of a ***mono-filament billet*** made up of a cylindrical ingot of NbTi alloy inserted into a copper can.

At the last dawing pass, the mono-filament rods are given an hexagonal shape.

• Extrusion and drawing of a ***multi-filament billet,*** made up of hexagonal, mono-filament rods stacked into a thick-walled copper can.

The wire twist is applied prior to the final drawing pass, with a typical twist pitch of 25 mm.

Production of Multifilamentary Superconducting Wire for the SSC

- A monofilament billet consists of a single niobium-titanium bar of about 15-cm diameter and 50 to 75-cm long, wrapped with niobium foil and inserted into a 20-cm diameter thick-walled copper can. Top and bottom end caps are attached by electron-beam welding. The sealed can is evacuated and compressed.

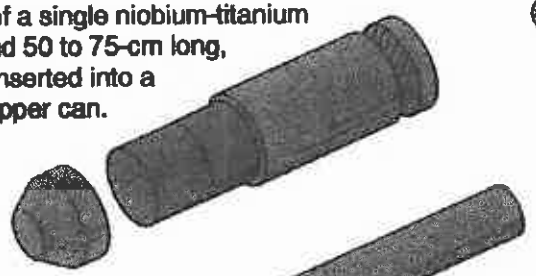

- The monofilament billet is hot-extruded at 600-700 °C to a composite rod approximately 3-5 cm in diameter.

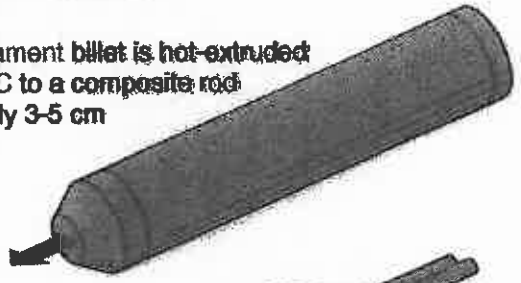

- The extruded rod is drawn down in multiple passes to a smaller size.

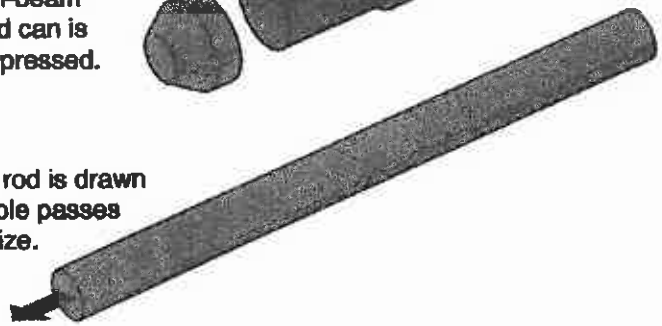

- Resulting bar is compacted to a hexagonal-shaped cross section about 3.5 mm across, cut into 50 to 75-cm lengths, and cleaned.

- A multifilament billet is now formed from approximately 7,200 hexagonal monofilament rods (for inner SSC cable) or 4,200 rods (for outer SSC cable). The rods are tightly packed into another 30-cm diameter thick-walled copper can, with a center copper island and filler copper added at the edges to reduce the voids. The billet goes through the same process of compaction, extrusion and drawing as described earlier, except that now the wire is drawn to the final wire size needed for cable production. During the drawing, the wire is heat treated several times to optimize its current-carrying capacity. The wire is twisted just before the last drawing step.

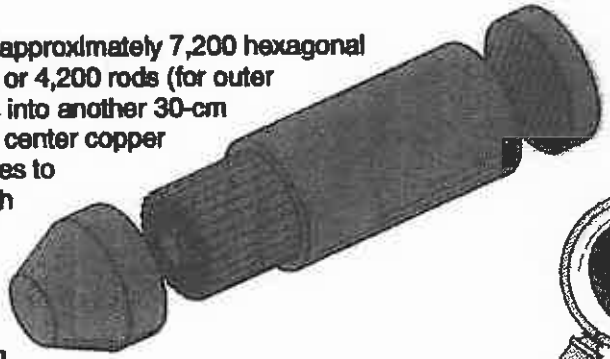

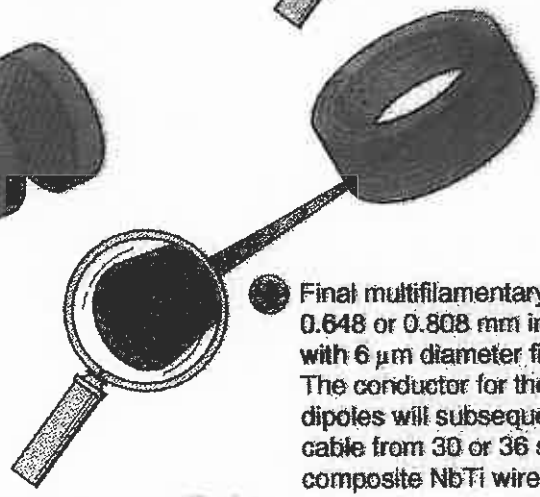

- Final multifilamentary wire, 0.648 or 0.808 mm in diameter with 6 μm diameter filaments. The conductor for the SSC dipoles will subsequently be cable from 30 or 36 such composite NbTi wires.

Thus, one multifilament billet for inner wire yields approximately 80,000 meters of wire, sufficient for about 2 SSC dipole magnets. One billet for outer wire yields ~ 130,000 meters of wire, again sufficient for 2 dipoles.

TIP-01405

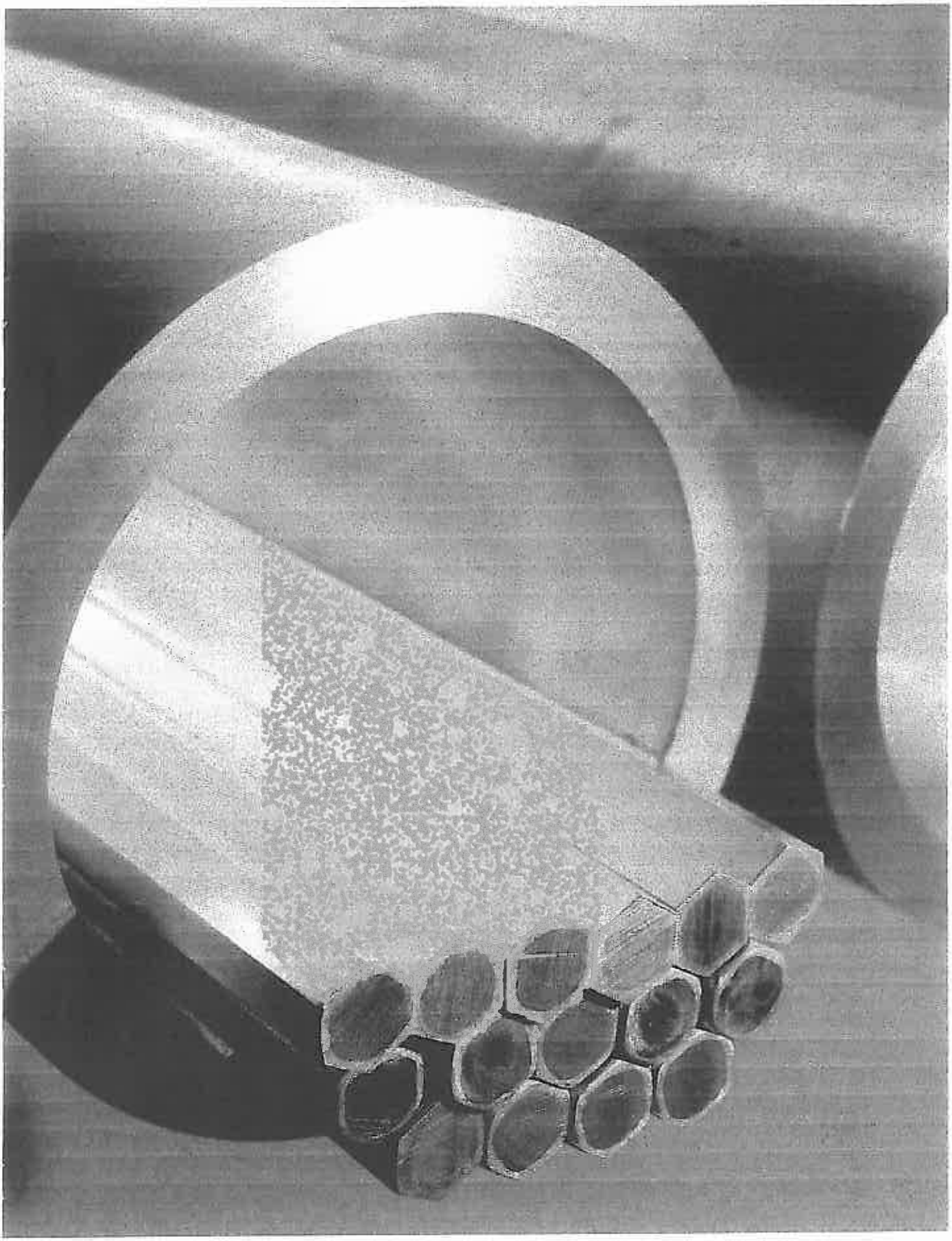

PROCESS SCHEDULE FOR NBTI WIRES

– The drawing-down of the billets is realized in multiple passes and heat treatments are applied at well defined strain intervals (corresponding to integer numbers of standard die passes).

– The cold-work and heat treatment schedule is established so as to produce the desired lattice of α–Ti precipitates in order to match the parameters (size and spacing) of the fluxoid lattice.

As the characterisitcs of the fluxoid lattice depends on temperature and field, the process schedule may be different for different applications with different operating conditions.

– At the end of drawing, the wire copper is severely cold-worked and it is preferable to include in the process schedule an annealing step on the wire at final size.

This annealing step should not be too aggressive to prevent alterations of the NbTi microstructure and degradations of the critical current density (heating of the NbTi microstructure results in a growth of the β–phase grains which affects the distribution of α–Ti precipitates).

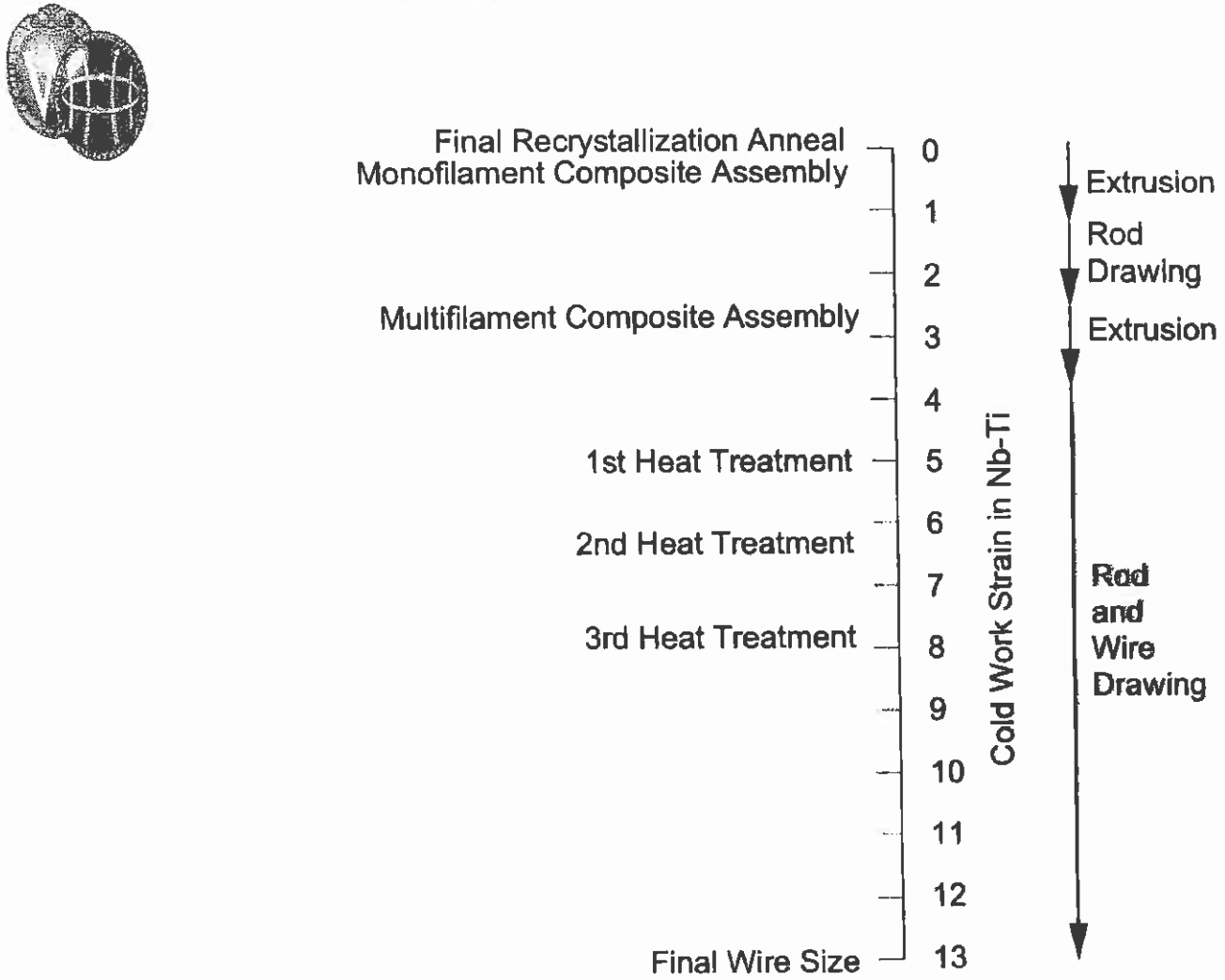
Final Recrystallization Anneal
Monofilament Composite Assembly
Multifilament Composite Assembly
1st Heat Treatment
2nd Heat Treatment
3rd Heat Treatment
Final Wire Size
0
1
2
3
4
5
6
7
8
9
10
11
12
13
Cold Work Strain in Nb-Ti
Extrusion
Rod
Drawing
Extrusion
Rod
and
Wire
Drawing

Development of Nano-scale Microstructures in Conventionally Processed Nb-Ti

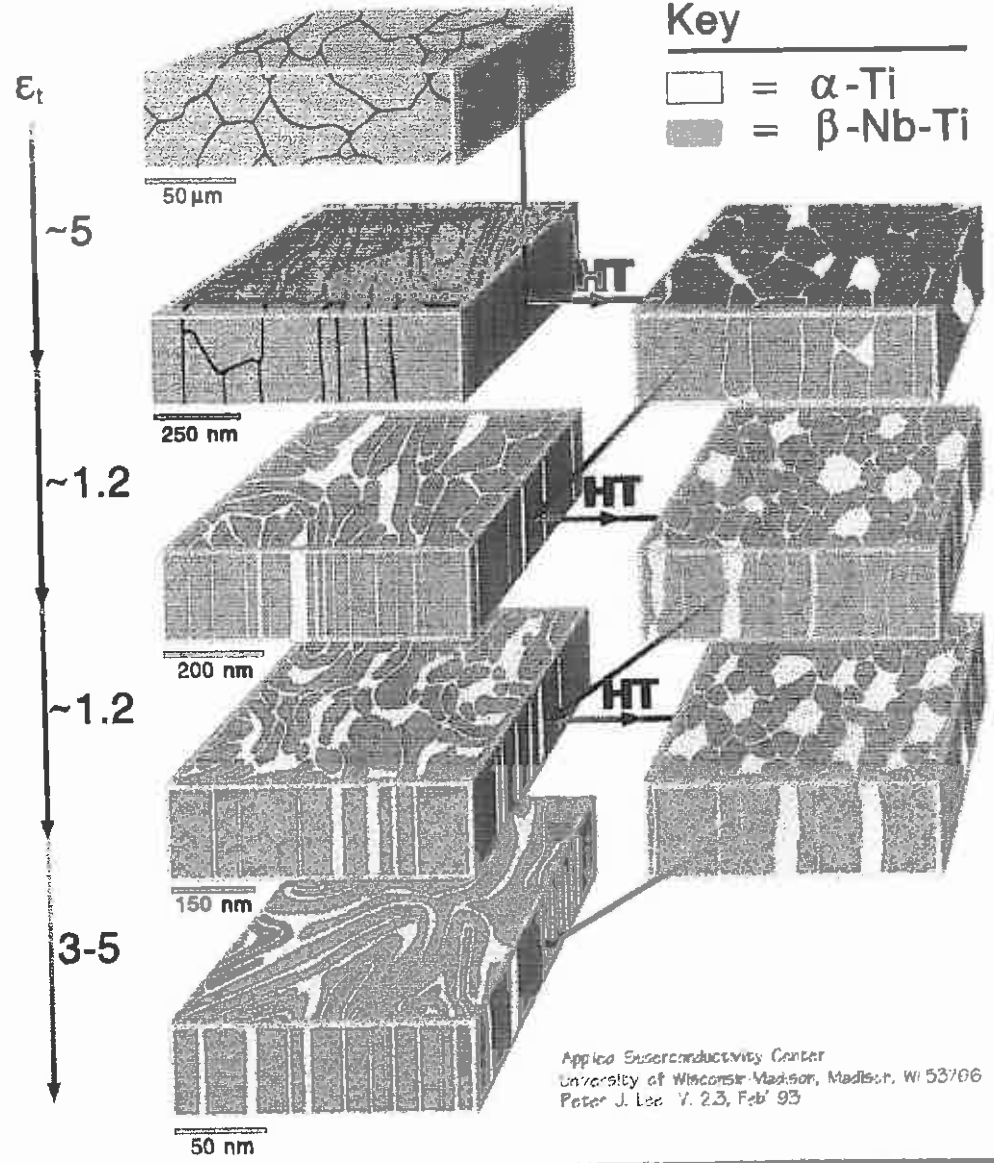

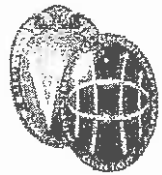

Microstructure of Conventionally Processed Nb-Ti after final Heat Treatment but before wire drawing.

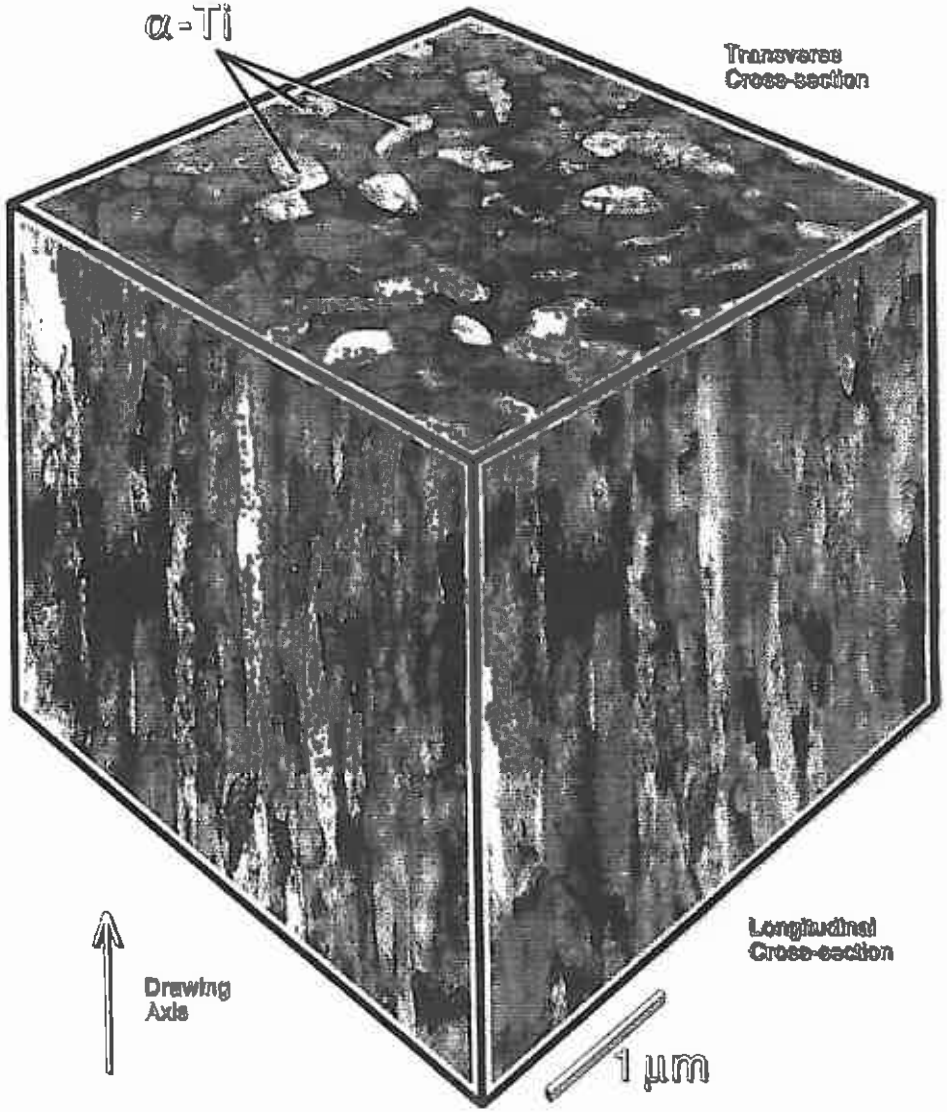

NB BARRIER

– For the production of fine filament wires, such as those used for SSC, RHIC and LHC, the niobium-titanium ingot of the mono-filament billet is wrapped with a niobium foil.

– The niobium barrier prevents the formation, during the multiple heat treatments, of hard and brittle intermetallic compounds such as $TiCu_4$.

– The $TiCu_4$ compounds do not deform well, resulting in filament sausaging and, ultimately, wire breakages upon subsequent drawing operations.

DOUBLE STACKING VERSUS SINGLE STACKING

– When the number of filaments is very large, rods made from a drawn-down multi-filament billet can be re-stacked into a new multi-filament billet, which, in turn is extruded and drawn. Such process is referred-to as *double-stacking* as opposed to *single-stacking*.

MAIN ISSUES FOR NBTI WIRE DESIGN

– The main issues for NbTi wire design are:

• ***Copper-to-superconductor ratio,*** which should not be too small to limit conductor heating in case of a quench and should not be too large to achieve a high overall critical current,

• ***Filament size,*** which should be optimized to limit field distortions resulting from superconductor magnetization while keeping wire processing cost down,

• ***Inter-filament spacing,*** which should not be too large to allow mutual support of the filaments during wire processing and should not be too small to avoid *proximity effect coupling*.

– In addition, it is desirable to leave a copper core at the wire center and a copper sheath at the wire periphery to protect the multifilamentary area from cabling degradation.

SSC AND LHC WIRE DESIGN

– For SSC and LHC wires, the filament diameter is 6 μm, the interfilament spacing is of the order of 1 μm, the cross-sectional area of the copper core is less than 10% of the total wire cross-sectional area, and the thickness of the copper outer sheath is in the range 50 to 100 μm.

SSC Strand

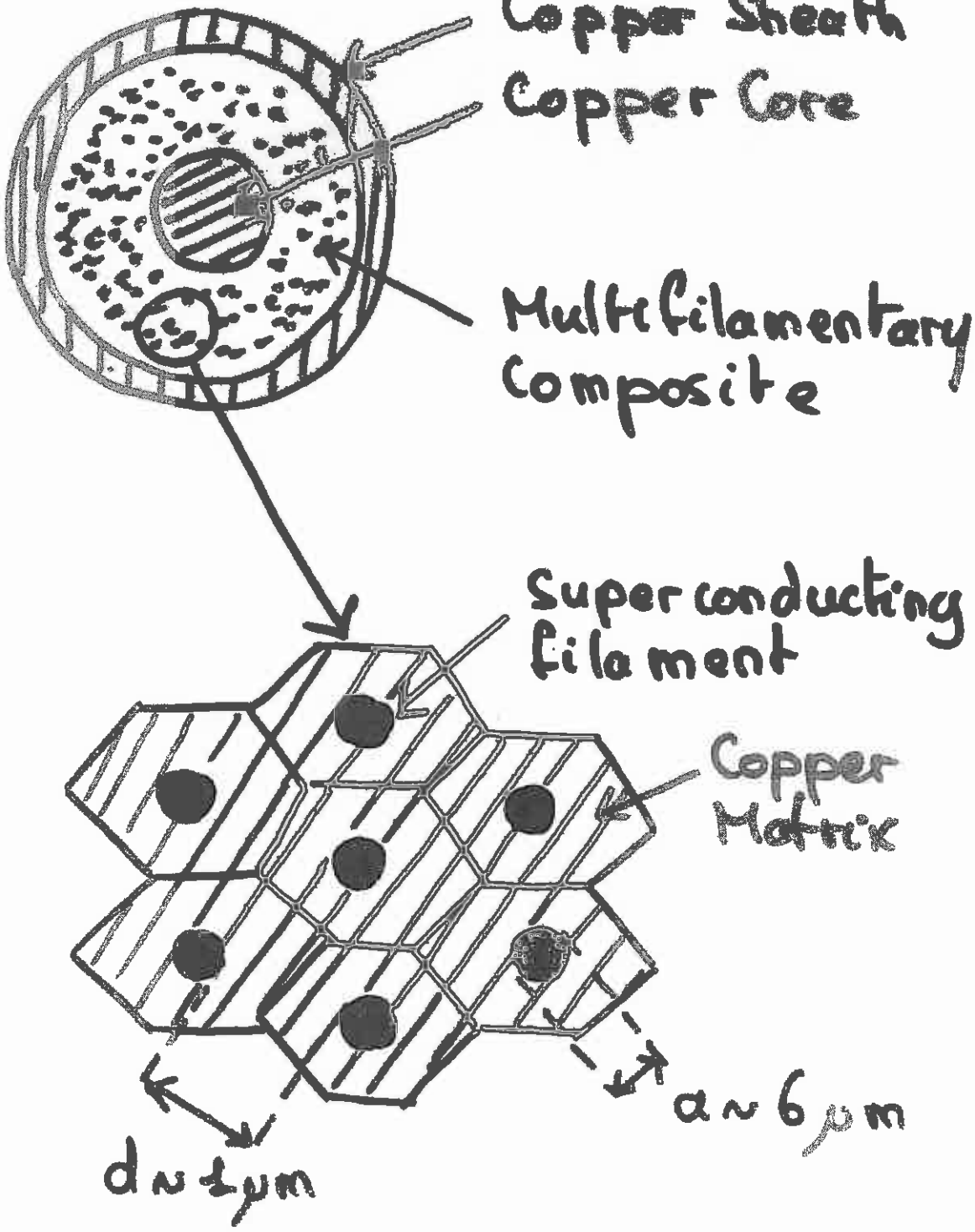
Copper Sheath
Copper Core
Multifilamentary Composite
Superconducting filament
Copper Matrix
d ~ 1 μm
a ~ 6 μm

Local Area Ratio

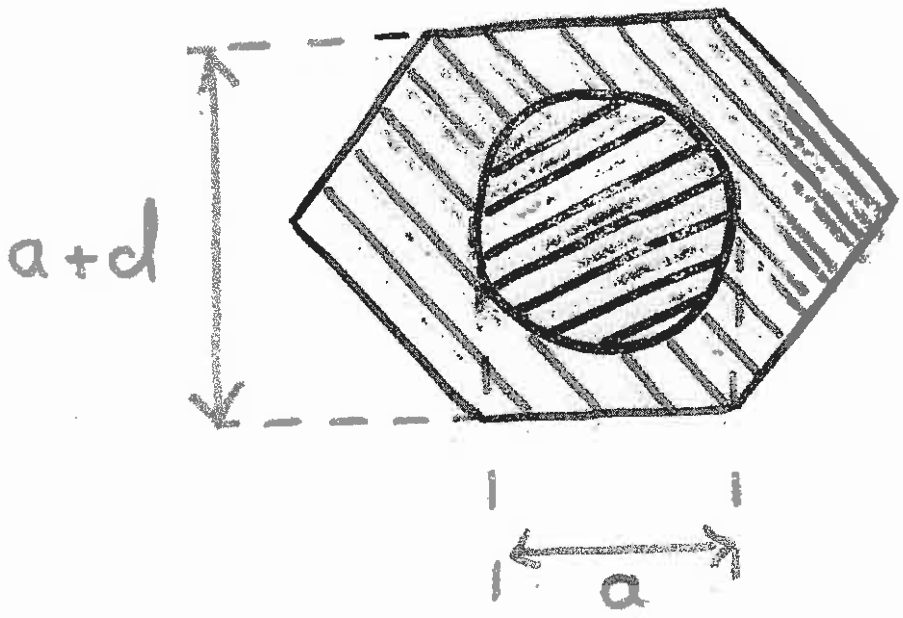

$$A_{NbTi} = \frac{\pi a^2}{4}$$

$$A_{Cu} = \frac{\sqrt{3}}{2}(a+d)^2 - A_{NbTi}$$

$$X_L = \frac{A_{Cu}}{A_{NbTi}} = \frac{2\sqrt{3}}{\pi}\left(1+\frac{d}{a}\right)^2 - 1$$

$X_L \approx 0.5$

MAIN ISSUES FOR NBTI WIRE MANUFACTURING

– The main issues regarding wire manufacturing are:

- *Piece length,*
- *Critical current optimization.*

PIECE LENGTH REQUIREMENTS

– Breakages during wire drawing are unavoidable, resulting in multiple piece lengths.

– Most magnet builders prefer to wind coils with weld-free cables made from single-piece wires. Hence, the average wire piece length must be at least equal to the cable length needed for a coil.

– In addition, a low breakage rate in wire production is an assurance of quality and uniformity.

Example: For LHC, wires are accepted on a billet basis, and it is required that, for each billet, at least 90% of the final-size pieces be longer than 1 km.

FACTORS INFLUENCING PIECE LENGTH

– The factors influencing piece length are:

• ***Cleanliness of billet assembly,*** to avoid inclusions of foreign particles,

• ***Precipitation of unwanted, hard-to-draw phases in NbTi alloy,*** which must be prevented,

• ***Formation of $TiCu_4$ compounds at the matrix/filament interface,*** which must also be restricted.

FACTORS INFLUENCING CRITICAL CURRENT DENSITY

– The factors influencing critical current density can be classified into two categories:

• *Intrinsic factors,* related to NbTi alloy microstructure and affecting fluxon pinning,

• *Extrinsic factors,* related to macroscopic irregularities and causing local reductions in filament cross-sectional areas.

– A way of determining if the critical current of a wire is limited by intrinsic or extrinsic parameters, is to study the evolution of its *N*-value as a function of field (see section on transition of multifilamentary wires).

INTRINSINC FACTORS

– Among the intrinsinc factors influencing the critical current density are:

• Homogeneity of the NbTi ingots used for the mono-filament billets, which must be tightly controlled (typically +/- 1% in weight of Ti),

• Parameters and schedule of cold-work and heat treatment cycles during wire production.

EXTRINSINC FACTORS

– The extrinsic factors influencing the critical current densityare basically the same as the factors influencing piece length.

– In addition, it is preferable to maintain a small inter-filament spacing, so that the NbTi filaments, which are much harder than the high purity copper matrix, can support each other during the multiple drawing operations.

LECTURE 3: CONDUCTOR AND CONDUCTOR INSULATION FOR PARTICLE ACCELERATOR MAGNETS

3.1 Review of Superconducting Materials
- 3.1.1 NbTi Alloys
- 3.1.2 Nb_3Sn Compounds
- 3.1.3 HTS

3.2 Superconducting Multifilamentary Composites

3.3 Transition of Multifilamentary Wires

3.4 Manufacturing of NbTi Wires

3.5 Manufacturing of Nb_3Sn Wires

3.6 Critical Surface Parametrizations

3.7 Rutherford-Type Cables

3.8 Interstrand Resistances in Rutherford-Type Cables

3.9 Critical Current Measurements on Rutherford-Type Cables

3.10 Cable Insulation

Appendix: Material Properties at Low Temperatures

MANUFACTURING OF NB_3SN WIRES

– Because of its brittleness, Nb_3Sn cannot be fabricated by a wire-drawing process, but must be formed in situ in the wire at final size.

– There four main methods of producing multifilamentary Nb_3Sn wires:

- *Bronze*
- *Internal Tin*
- *Modified Jelly Roll (MJR)*
- *Powder in Tube (PIT)*

BRONZE METHOD

– The most traditionnal method of producing Nb_3Sn wires is the so-called *bronze method.*

– It is done in two steps:

• Production (by extrusion and drawing) of a multifilamentary composite wire made up of Nb filaments (doped with Ti or Ta) embedded in a bronze (CuSn) matrix,

• Heat treatment on the wire at final size (or even preferably on the cable wound in its final coil shape) during which the tin diffuses through the bronze matrix and reacts with the niobium filaments to produce Nb_3Sn.

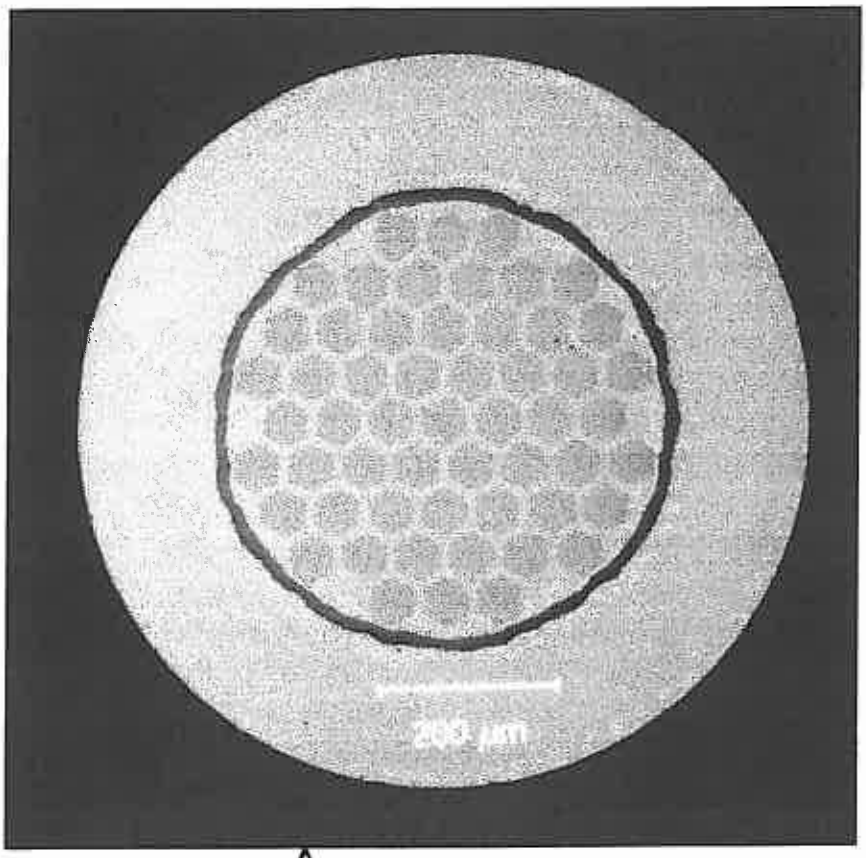

Vacuumschmelze, GmbH
(Courtesy T. Schild)

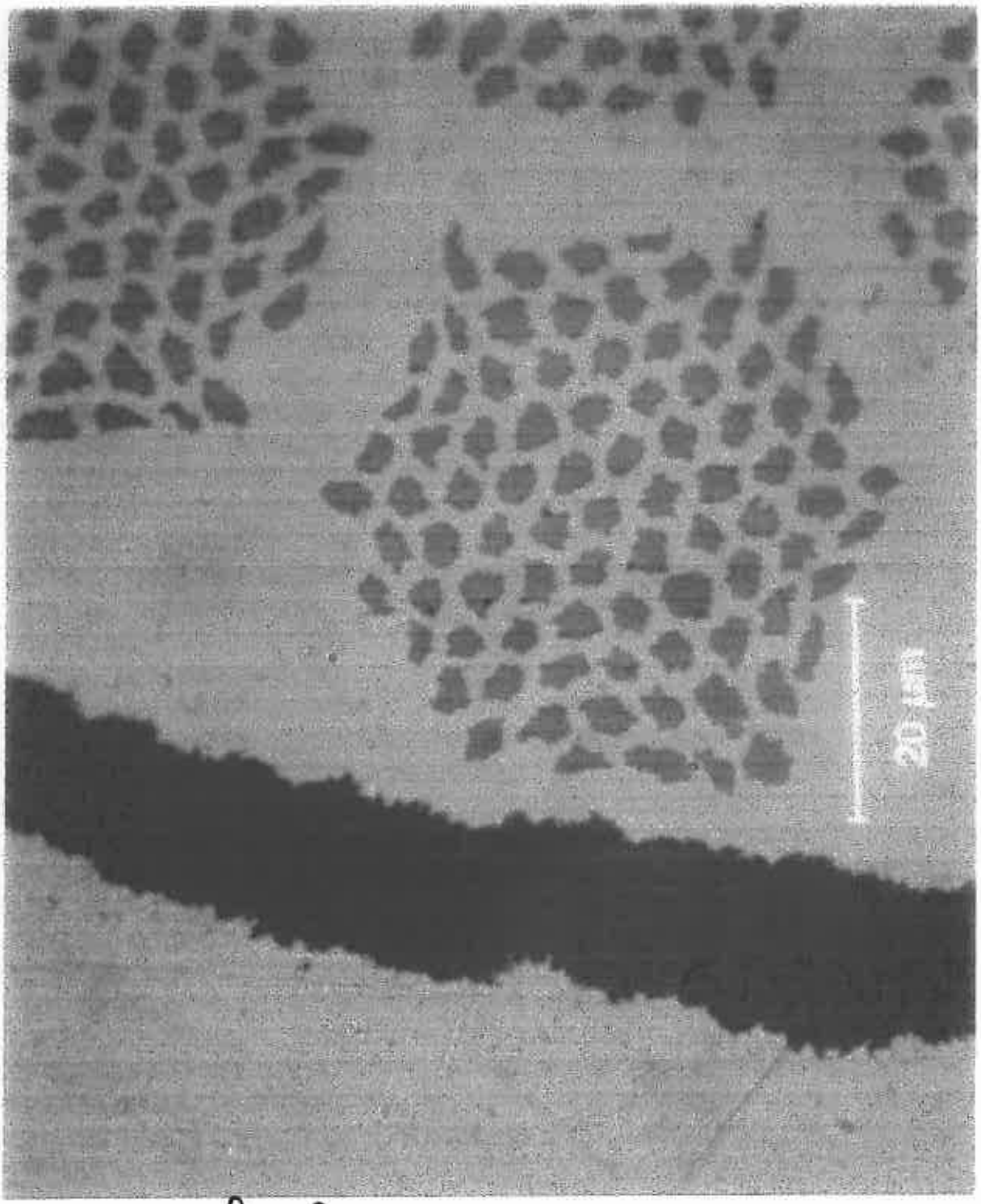

Vacuumschmelze, GmbH
(Courtesy T. Schild)

HEAT TREATMENT FOR NB_3SN WIRES PRODUCED BY THE BRONZE PROCESS

– The heat treatment parameters for Nb_3Sn wires produced by the bronze process must be optimized in order to achieve:

• good stoichiometry and full reaction of Nb_3Sn filaments for high T_C and B_{C2} (which requires long heat treatment at high temperature),

• fine grain structures for high J_C (which imposes upper limits on the duration and temperature of the heat treatment to limit grain growth).

– A typical heat treatment for a wire produced by the bronze method is: 570 °C for 144 hours followed by 650 °C for 200 hours.

LIMITATIONS OF BRONZE METHOD

– To remain ductile enough for wire drawing, the bronze of the billet must contain no more than 15% of tin.

– Given this tin concentration, a full reaction of a volume, V, of Nb requires the equivalent of tin contained in a volume of the order of $(4V)$ of bronze.

– Furthermore, after heat treatment, the depleted bronze around the filaments has very poor electrical and thermal conductivities, and is not sufficient to stabilize the wire. Hence, a copper sheath must be added at the wire periphery.

– The unfavorable local CuSn/Nb_3Sn ratio in the multifilamentary area and the addition of the copper sheath results in a reduction of the overall critical current density of the wire.

INTERNAL TIN METHOD

– One expedient to limit the reduction of the overall critical current density of the wire is to incorporate pools of pure tin within the wire cross-section, as is done in the so-called *internal-tin* method.

– In this case, the wire is made up of sub-elements surrounded by metallic barriers and a copper sheath. The sub-elements themselves are made up of a large number of Nb filaments (doped with Ti or Ta) positionned within a copper matrix around a tin pool.

– As in the bronze method, the Nb_3Sn is formed by subjecting the wire at final size (or the wound coil) to a lengthy heat treatment, during which the tin migrates through the matrix copper, which turns into bronze, and reacts with the Nb filaments. (The role of the barriers is to prevent tin pollution in the copper outer sheath.)

– A typical heat treatment for a wire produced by the internal-tin method is: ramp at 6 °C up to 660 °C, followed by a plateau at 660 °C for 240 hours.

IGC ADVANCED SUPERCONDUCTORS
A DIVISION OF INTERMAGNETICS GENERAL CORPORATION

IGC ITER Strand

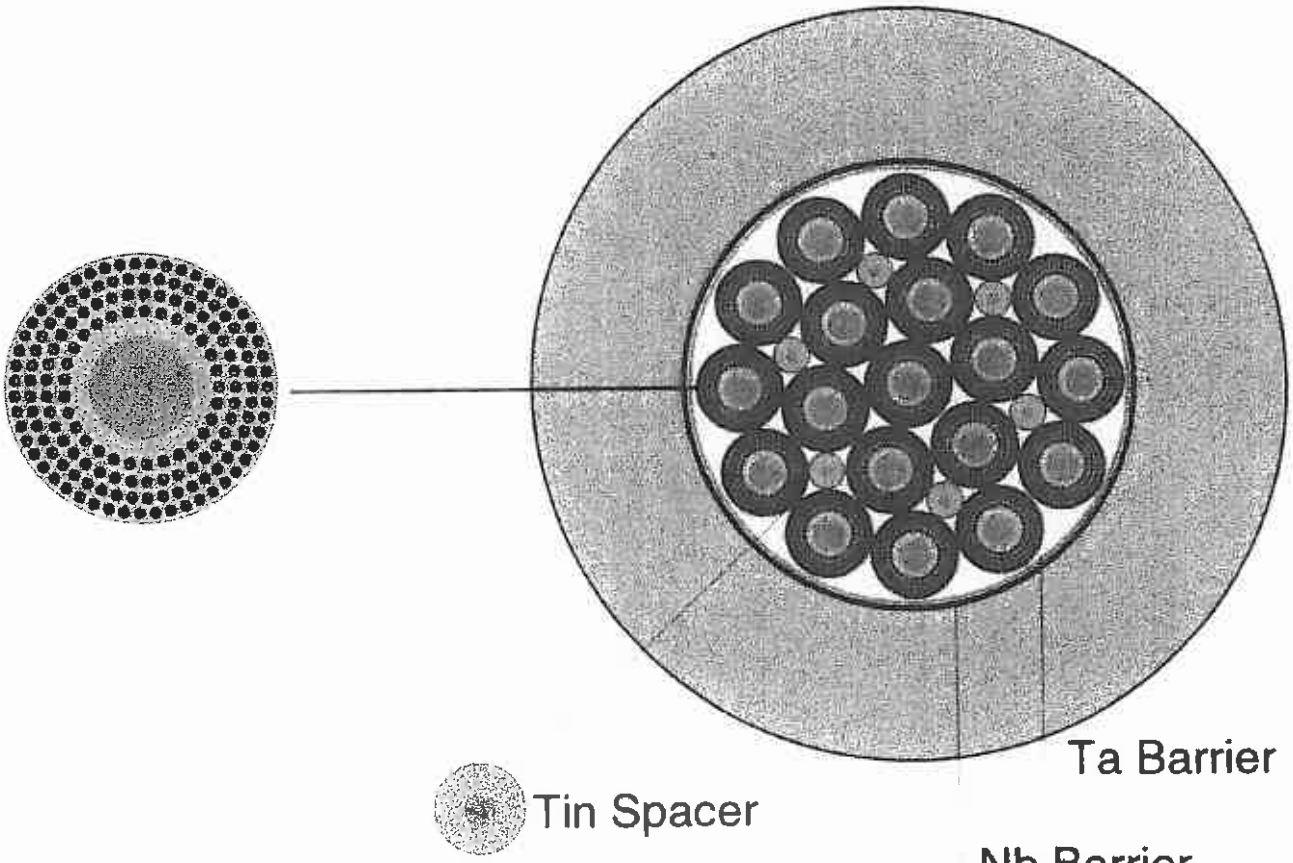

Erice, Italy, May 12-17 ,1995

IGC ADVANCED SUPERCONDUCTORS
A DIVISION OF INTERMAGNETICS GENERAL CORPORATION

IGC ITER Strand

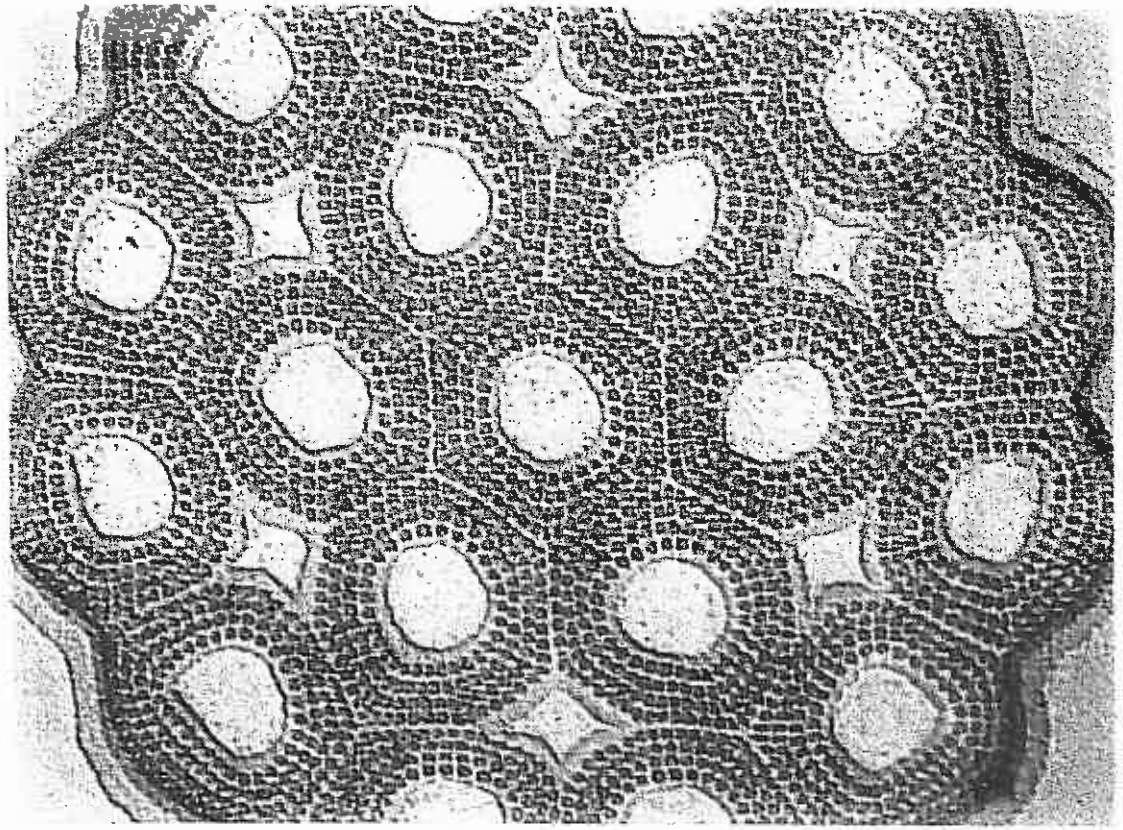

INTERNAL TIN VERSUS BRONZE

– The pools are dimensioned to supply all the tin needed to fully react the filaments and the local $CuSn/Nb_3Sn$ ratios in the multifilamentary areas are much smaller than for bronze-processed wires.

As a result, the overall critical current density of internal-tin-processed wires can be much larger than for bronze-processed wires.

– However, the tin diffusion through a closely spaced array of filaments, somewhat deformed by the extrusion and drawing processes, results in filament bridging.

The filament bridging causes, in turn, the filaments to react more or less collectively when solicited by an external magnetic flux density.

This collective behavior engenders magnetization effects that can be significantly larger than what is expected from the physical size of individual filaments.

As a result, the effective filament diameter to be taken into account when computing the persistent magnetization currents can be much larger, and is much more difficult to control, than for bronze-processed wires.

ESTIMATING THE EFFECTIVE FILAMENT SIZE OF NB_3SN WIRES

– An estimate of the effective filament dimater, d_{eff}, of Nb_3Sn wires can be obtained by measuring the wire losses under a slowly-varying, tansverse magnetic flux density (the field ramp must be slow enough to limit instrastrand coupling currents).

– Let w designate the losses per unit length and per unit of cross-sectional area measured during a magnetic flux density cycle between $(-B_0)$ and $(+B_0)$. It can be shown that, if B_0 is large enough

$$d_{eff} \approx \frac{3\,\pi\,w}{8\,J_C(B_0)\,B_0}$$

where J_C is the critical current density of the wire (normalized to the same unit of cross-sectional area as w).

– In practice, w and J_C are normalized per unit of non-copper area in the wire cross-section.

R&D DEVELOPMENT FOR ITER

– In recent years, a significant R&D work has been carried out to improve the performance of Nb_3Sn multifilamentary wires, thanks to the International Thermonuclear Experimental Reactor (ITER) program

– Following ITER specifications, it is customary to show plots of $w(\pm 3\ T)$ versus $J_C(12\ T)$ at 4.2 K.

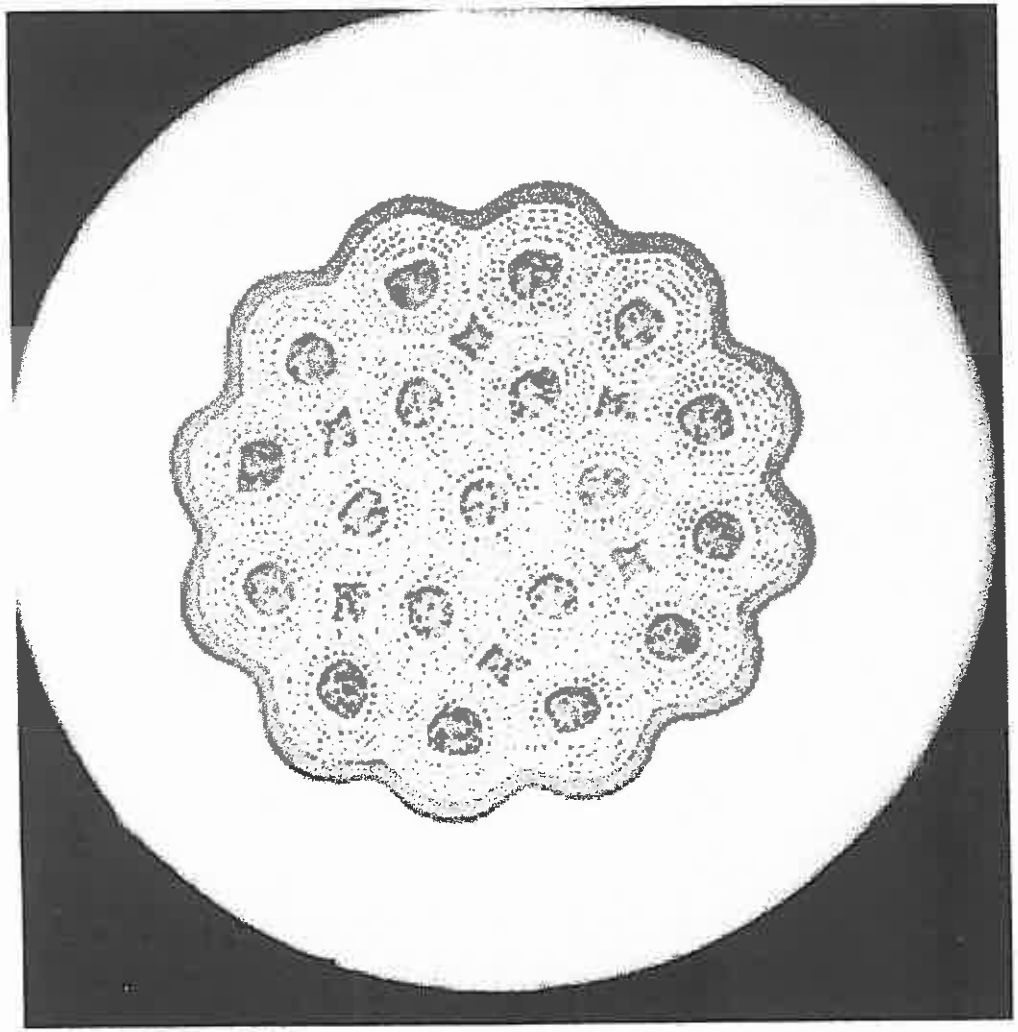

ADVANCED SUPERCONDUCTORS
A DIVISION OF INTERMAGNETICS GENERAL CORPORATION

ITER Design

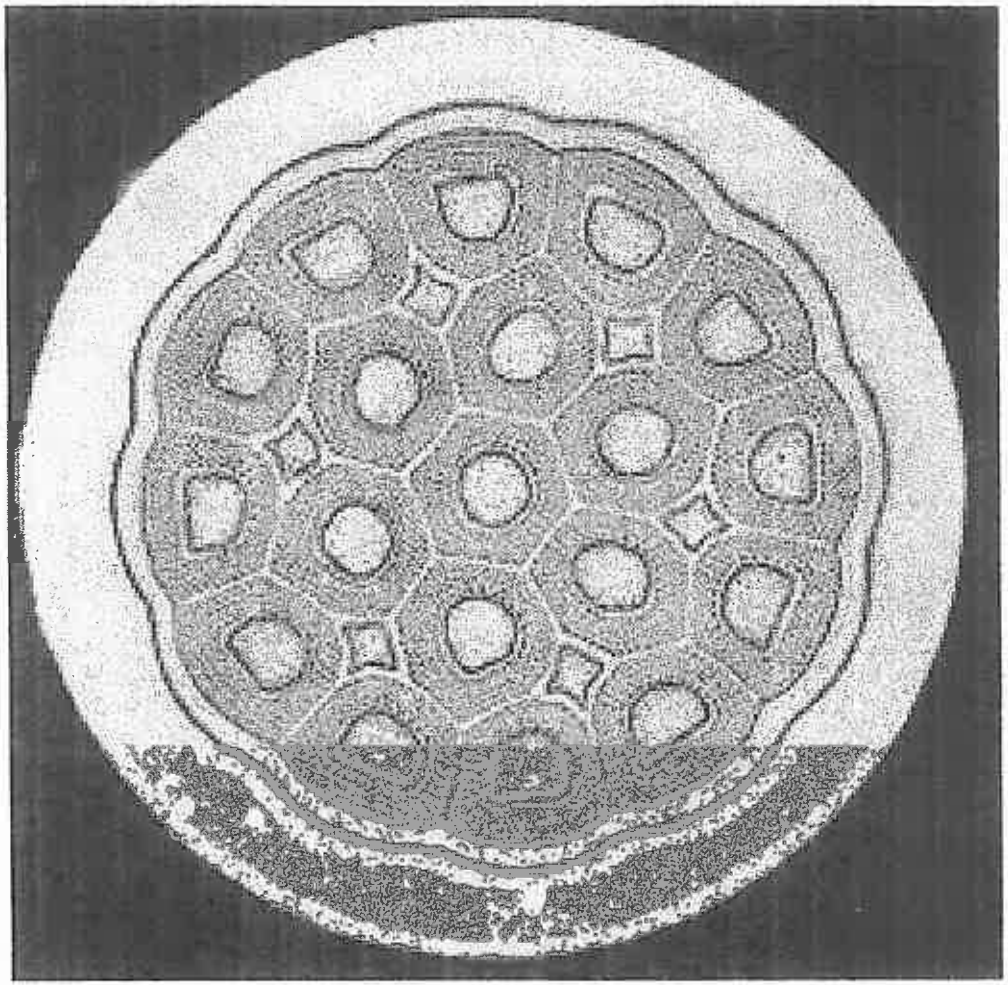

IGC ADVANCED SUPERCONDUCTORS
A DIVISION OF INTERMAGNETICS GENERAL CORPORATION

D 20

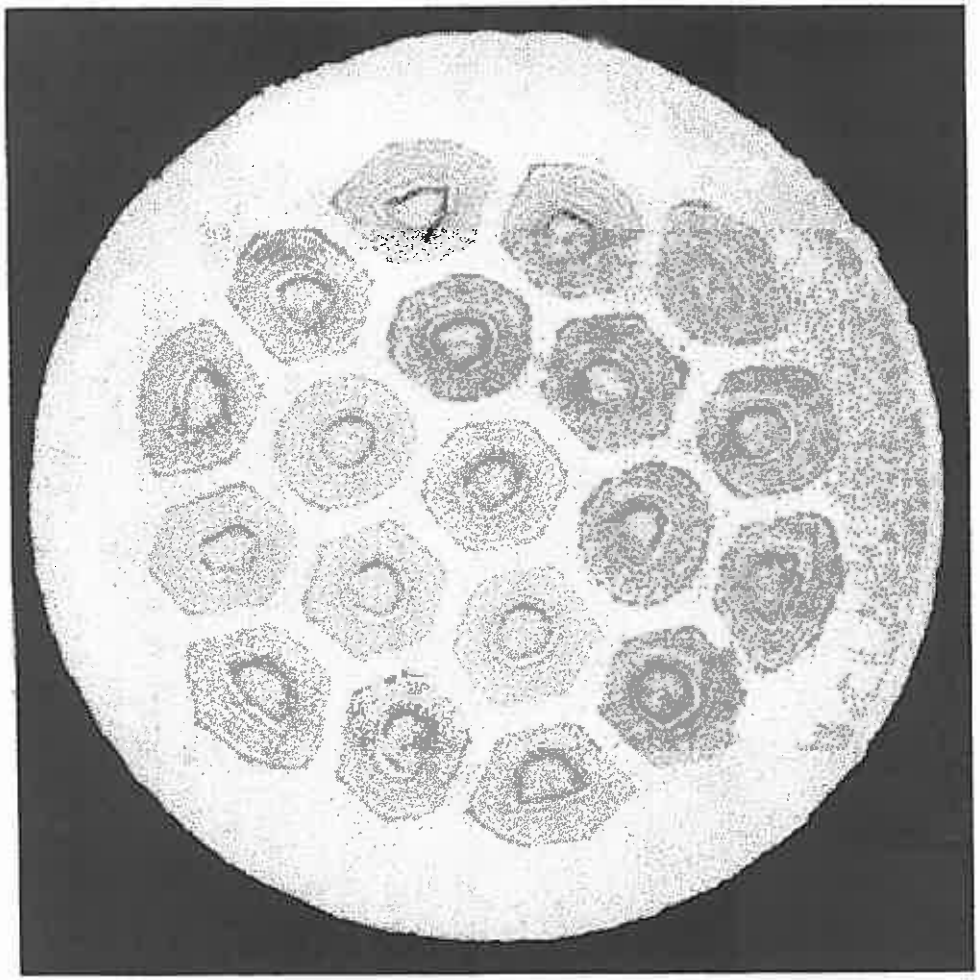

19 subelement individual barriers

IGC ADVANCED SUPERCONDUCTORS
A DIVISION OF INTERMAGNETICS GENERAL CORPORATION

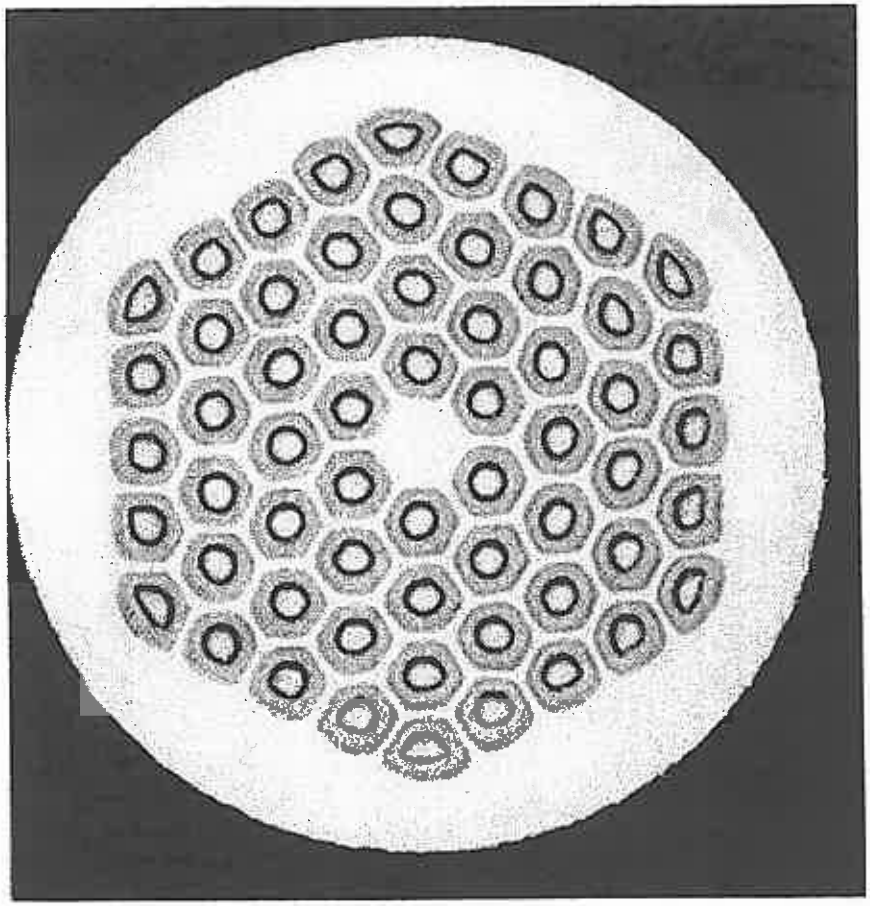

Cross Section 60 subelement restack

IGC ADVANCED SUPERCONDUCTORS
A DIVISION OF INTERMAGNETICS GENERAL CORPORATION

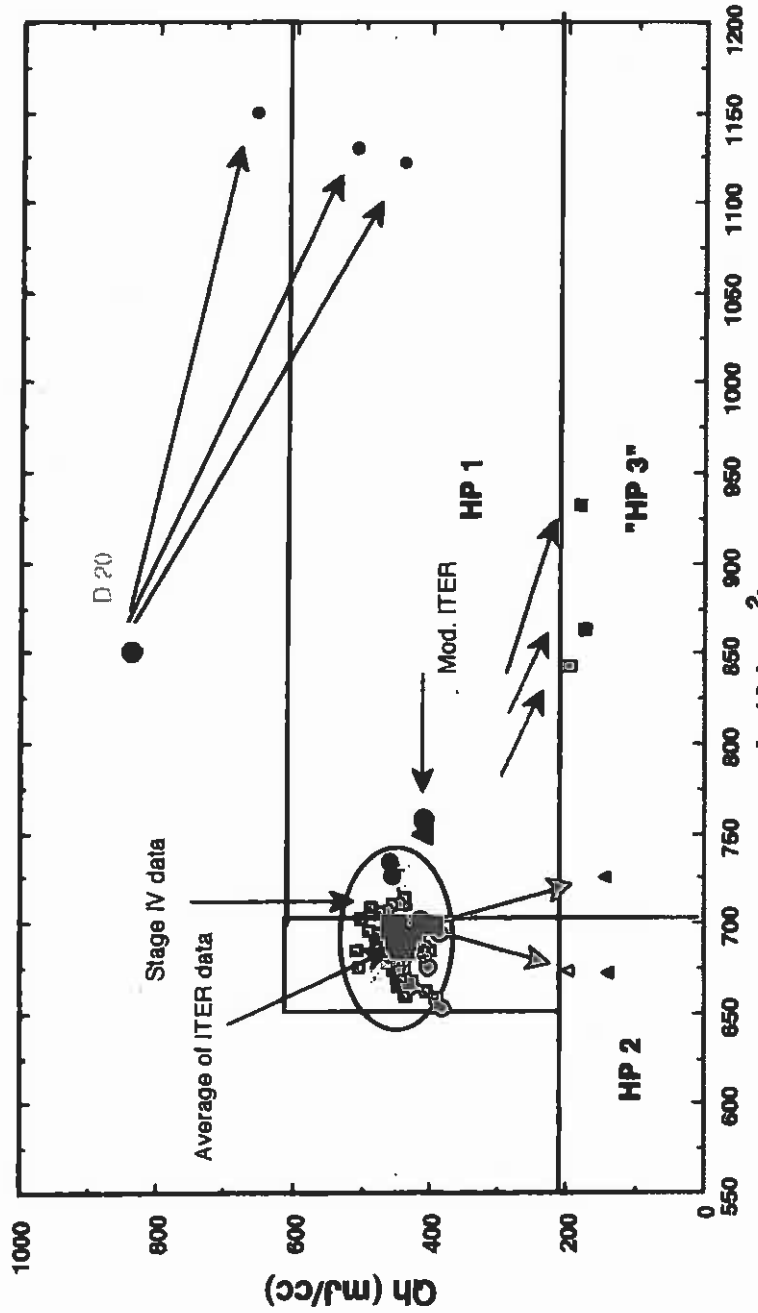

Courtesy E. Gregory (IGC)

MJR METHOD

– The MJR method differs from the two previous methods by the billet assembly process.

– Instead of starting from niobium tubes which are inserted into holes drilled in a bronze or copper matrix, the niobium is made in the form of a sheet of expanded metal which is rolled up with a sheet of bronze, like a jelly roll.

The jelly roll is then packed and sealed in a copper can to be extruded and drawned down the usual way.

During extrusion and subsequent drawing, the junctures in the niobium sheet are elongated and the material develops a multifilamentary structure.

– The tin provided by the bronze sheet can be supplemented by the addition of a tin core at the center of the jelly roll.

– In practical wires, many tin core MJR units are rebundled to reduce the tin diffusion distance from the core of each jelly roll.

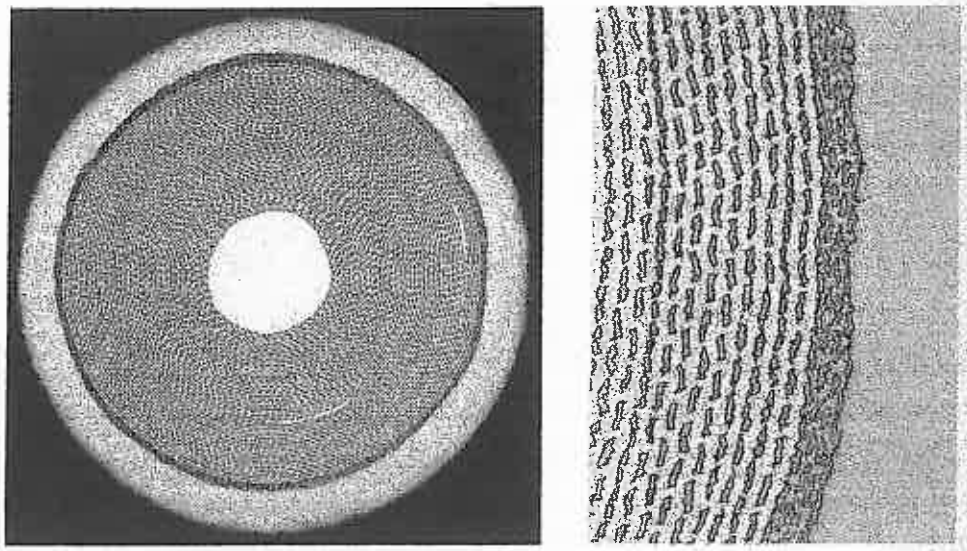

Figure 3. Bronze route MJR wire from Billet M112, overall cross section and close up of the V+Nb1Ti expanded metal diffusion barrier. The bronze to Nb1Ti ratio in this unreacted .036" dia. wire is 3.02:1. Of the non-Cu volume, 23.2% is Nb1Ti, 70.3% is Cu13.5Sn, and 6.5% is the diffusion barrier. The diffusion barrier thickness is 11 microns.

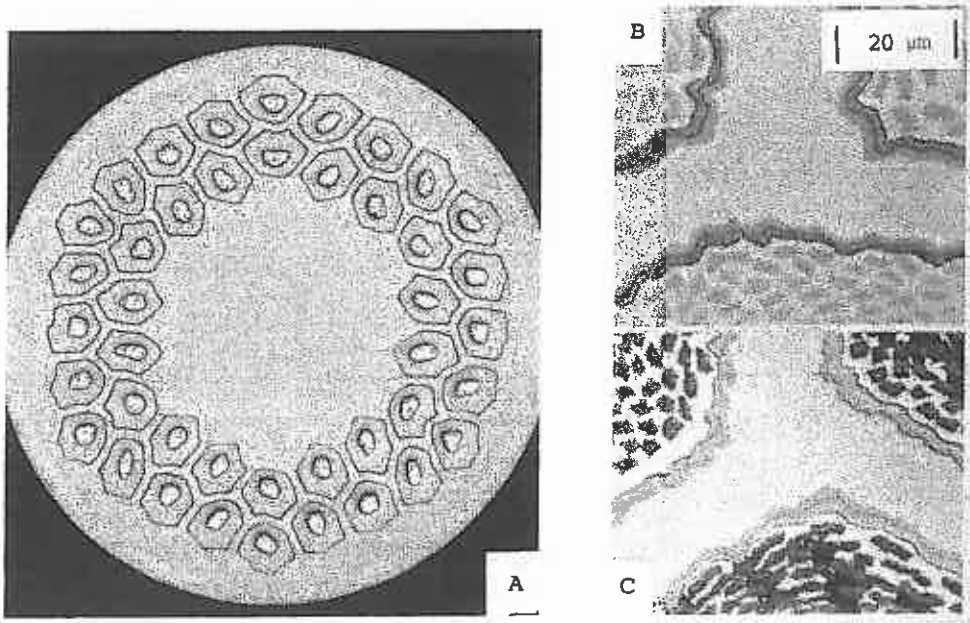

Figure 4. Overall and close up micrographs of tin core MJR billet Crel062 at 0.033" dia. (A) overall, (B) close up, unreacted, showing concentric V/Nb diffusion barrier, and (C) close up, reacted 650°C/160 hrs.

D. Smathers, et al., 1988.

MJR VERSUS INTERNAL TIN

– The MJR method is potentially more cost effective than the internal-tin method, but the efffective filament diameter is even more difficult to control.

PIT METHOD

– An alernative method to produce Nb_3Sn multifilamentary wire is the so-colled *Powder In Tube Method,* developed by the Netherland Energy Research Foundation (ECN).

– In this process, Nb_2Sn powder of particle size less than 3 μm is mixed with tin powder and packed into a thick-walled copper tube.

The filled tube is reduced in diameter to densify the powder and is put into a niobium tube surrounded by a copper tube.

The assembly is extruded and drawn down to a rod of hexagonal cross-section.

The rod is cut into lengths and the lengths are re-stacked in a copper can, which is again extruded and drawn down to produce the final-size wire.

– As for other methods, the Nb_3Sn compound is formed by subjected the wire at final size (or the wound coil) to a heat treatment.

During heat treatment, the tin contained in the powder cores migrates through the copper tubes, turning them into bronze, and reacts with the inner surfaces of the niobium tubes to create a growing Nb_3Sn layer.

Note that the copper-turning-into-bronze liners positioned within the niobium tubes are necessary to ensure the formation of Nb_3Sn at a suitable temperature.

Powder-In-Tube Nb_3Sn wire manufactured by ShapeMetal Innovation B.V.

d_{wire}=0.9 mm, %Cu = 52, d_{if}=12 μm, d_{ol}=22 μm

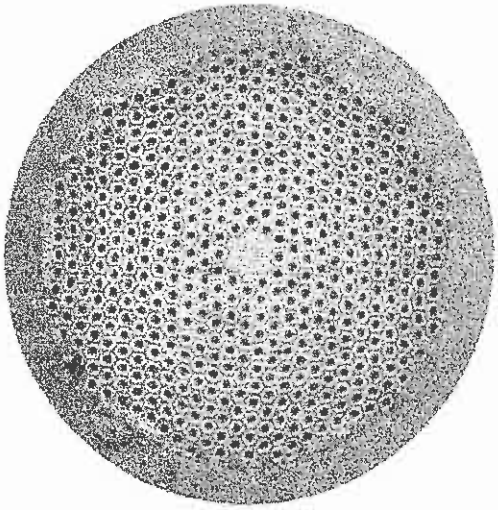

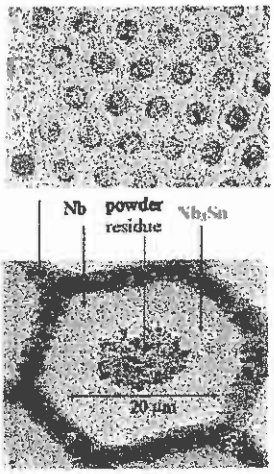

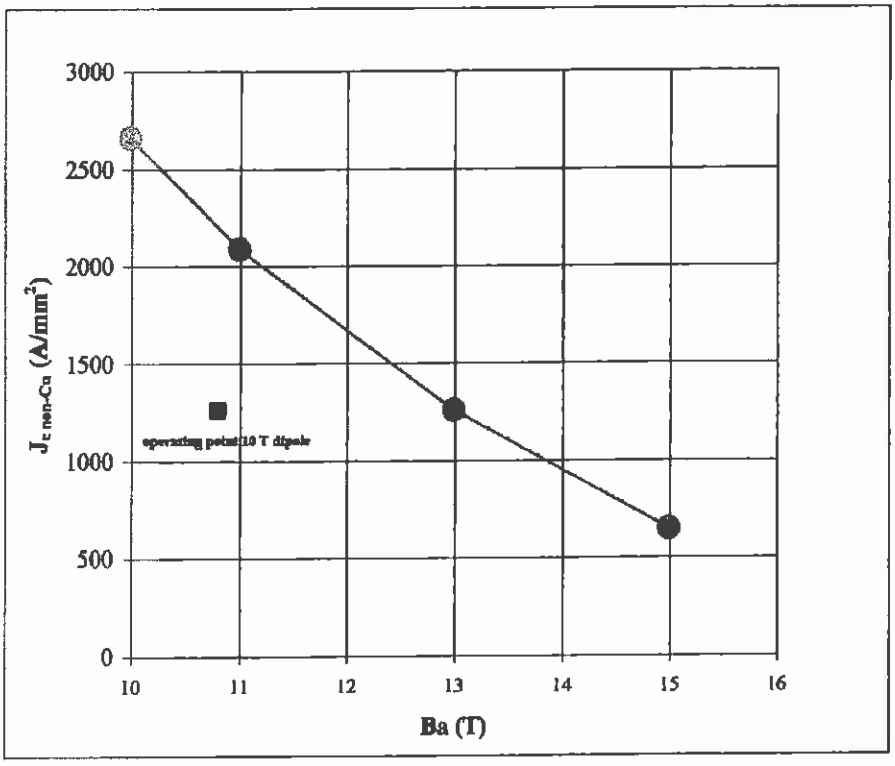

Courtesy A. den Ouden

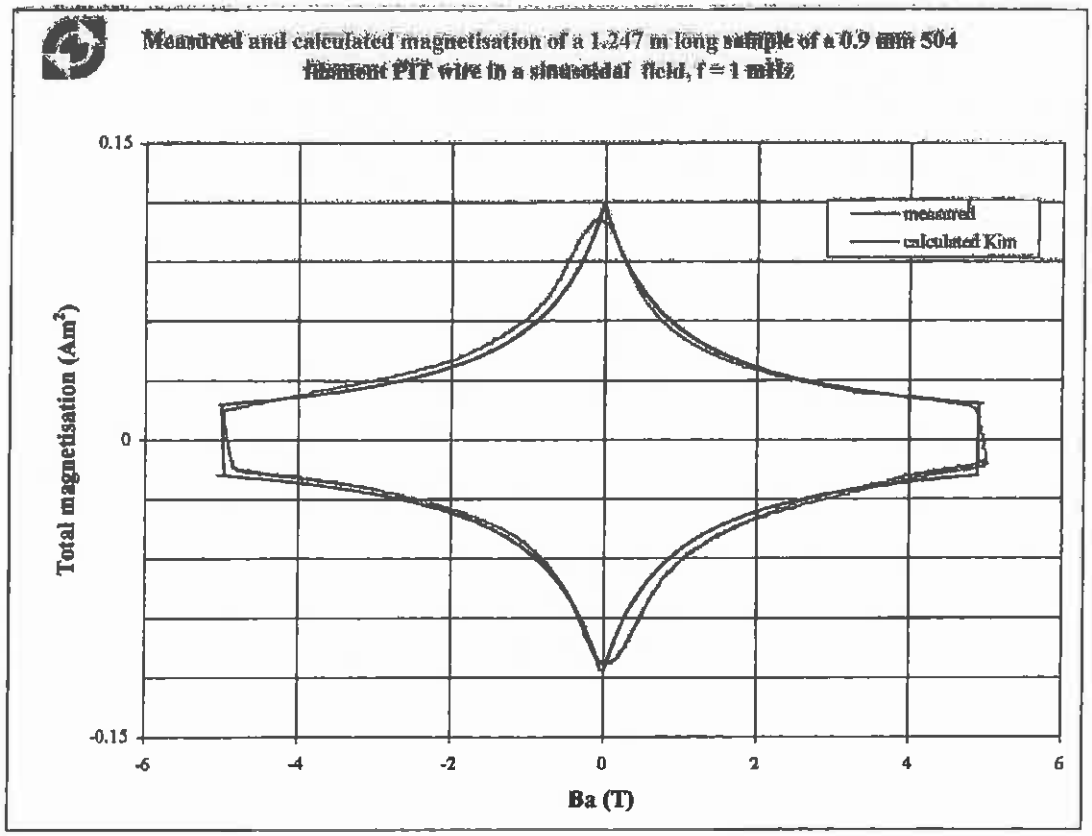

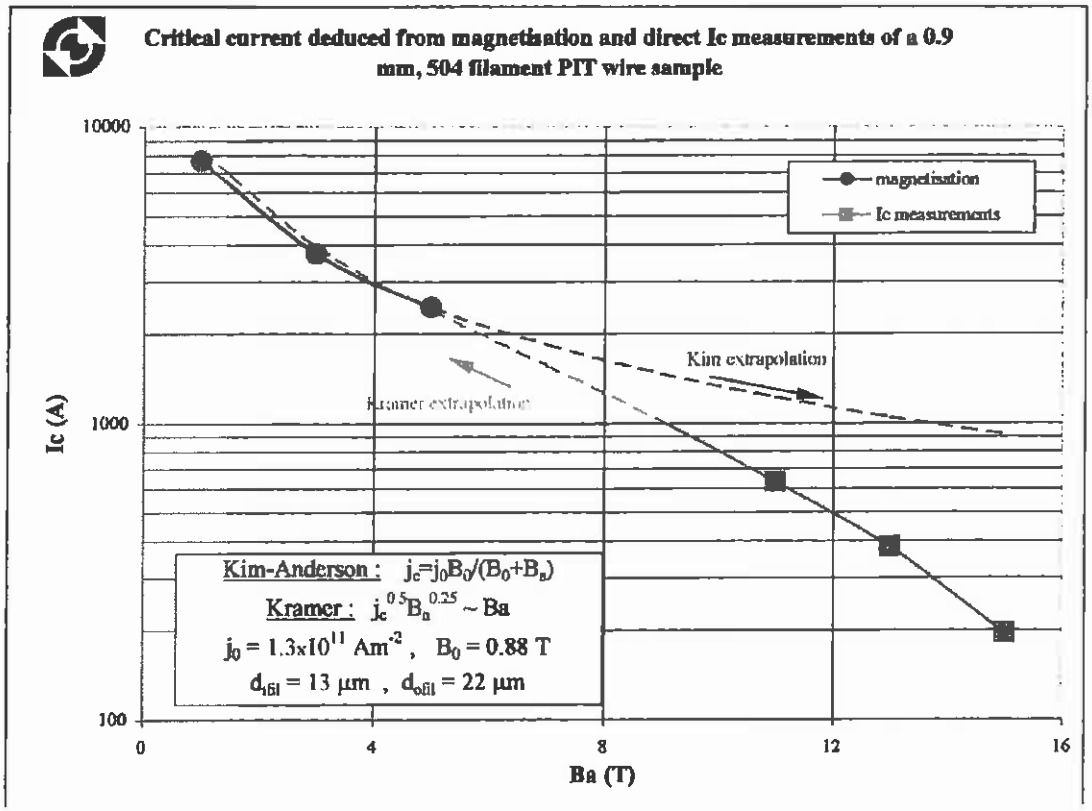

Courtesy A. den Ouden

ADVANTAGES OF PIT METHOD

– Given the proximity of the tin sources to the niobium, the required heat treatment is short: typically, 680 °C for 47 hours.

– Another advantage of the PIT method is that the niobium tubes can be made thick enough to ensure that the tin does not react right through the tube wall and does not pollute the outside copper.

Then, the outside copper remains pure enough to ensure wire stabilization and no other copper addition is required.

– As a result, the achieved critical current densities per unit of non-copper area can be very large, with more than 2000 A/mm^2 (non-copper) at 4.23 K and 11 T.

DISADVANTAGES OF PIT METHOD

– **Limited number of filaments (~ 500) with large physical diameter (10 to 20 μm).**

– **Costly.**

– **At present (1999) only a small Dutch company is able to produce PIT Nb_3Sn wires.**

LECTURE 3: CONDUCTOR AND CONDUCTOR INSULATION FOR PARTICLE ACCELERATOR MAGNETS

3.1 Review of Superconducting Materials
- 3.1.1 NbTi Alloys
- 3.1.2 Nb_3Sn Compounds
- 3.1.3 HTS

3.2 Superconducting Multifilamentary Composites

3.3 Transition of Multifilamentary Wires

3.4 Manufacturing of NbTi Wires

3.5 Manufacturing of Nb_3Sn Wires

3.6 Critical Surface Parametrizations

3.7 Rutherford-Type Cables

3.8 Interstrand Resistances in Rutherford-Type Cables

3.9 Critical Current Measurements on Rutherford-Type Cables

3.10 Cable Insulation

Appendix: Material Properties at Low Temperatures

PARAMETRIZATION OF CRITICAL TEMPERATURE AND FIELD OF NBTI ALLOYS

– For NbTi, B_{C2} is related to T and T_C is related to B by *

$$B_{C2}(T) = B_{C20}\left[1 - \left(\frac{T}{T_{C0}}\right)^{1.7}\right]$$

$$T_C(B) = T_{C0}\left(1 - \frac{B}{B_{C20}}\right)^{1/1.7}$$

Example:

T	0 K	1.9 K	4.2 K
B_{C2}	14.5 T	13.5 T	10.7 T

B	0 T	5 T	9 T
T_C	9.2 K	7.2 K	5.2 K

* M.S. Lubell, 1983.

CRITICAL CURRENT DENSITY PARAMETRIZATION FOR NBTI WIRES

– The critical current density per unit area of superconductor, J_C, can be parametrized as a function of temperature, T, magnetic flux density, B, and critical current density at 4.2 K and 5 T, J_{Cref}, using *

$$\frac{J_C(B,T)}{J_{Cref}} = \frac{C_0}{B}\left[\frac{B}{B_{C2}(T)}\right]^{\alpha}\left[1-\frac{B}{B_{C2}(T)}\right]^{\beta}\left[1-\left(\frac{T}{T_{C0}}\right)^{1.7}\right]^{\gamma}$$

where C_0, α, β and γ are fitting parameters.

– Since the time of Tevatron, a factor of about 2 has been gained on the critical current density at 4.2 K and 5 T, thanks to the understanding of the role played by α–Ti precipitates in pinning mechanisms. Values of J_{Cref} in excess of 3000 A/mm² are now obtained in industrial production.

*L. Bottura, 1997

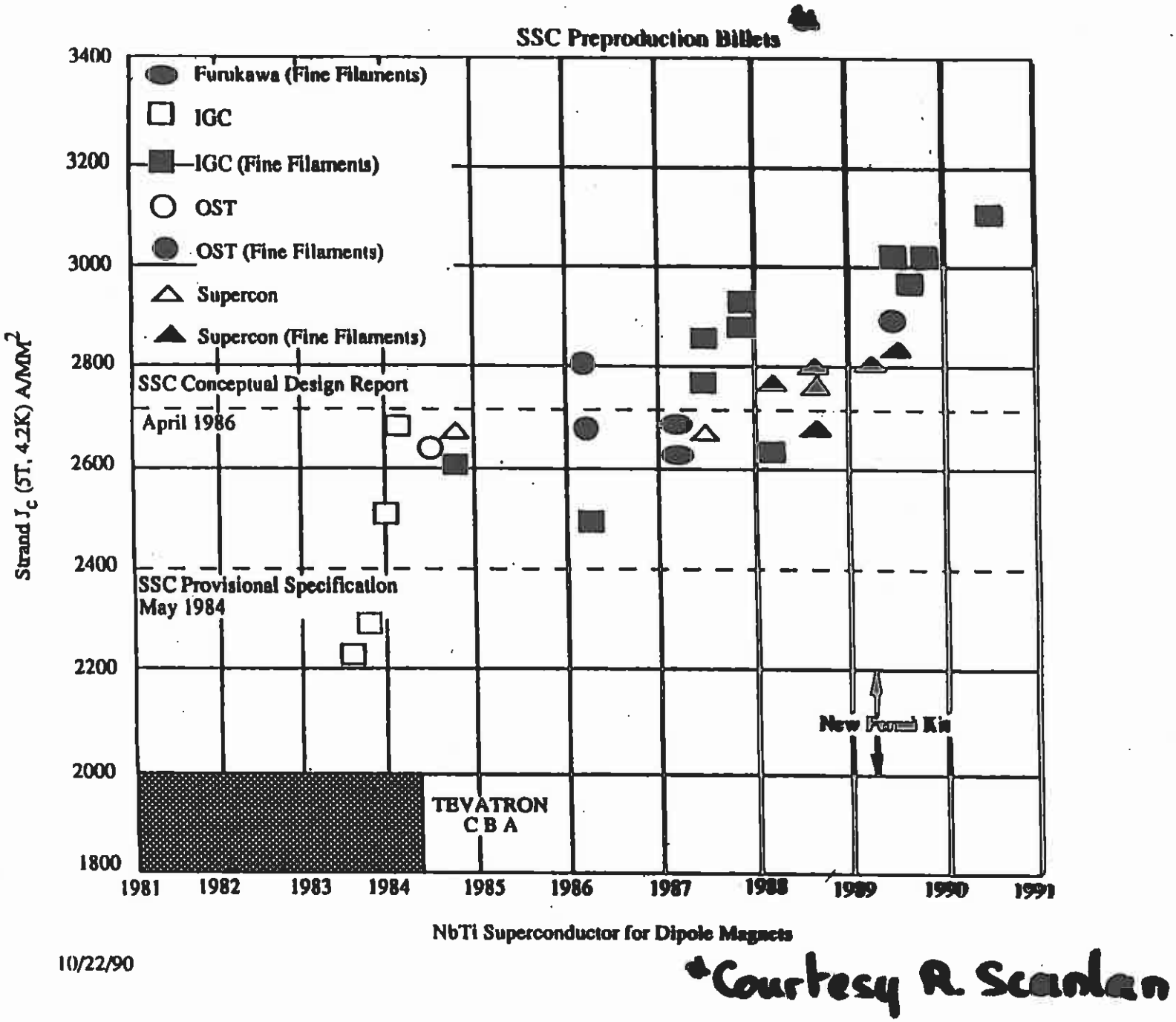

*Courtesy R. Scanlan

CRITICAL CURRENT DENSITY PARAMETRIZATION FOR NBTI WIRES (CONT.)

– **Typical fitting parameters values for LHC strands are:**

$$C_0 = 31.4\ \text{T},\ \alpha = 0.63,\ \beta = 1.0 \text{ and } \gamma = 2.3$$

This yields for J_C (in A/mm²):

	5	6	7	8	9	10	11	12	13
4.2 K	2800	2200	1600	1100	670	260	0	0	0
1.9 K	4900	4100	3300	2700	2100	1600	1100	630	210

– **The "J_C versus B" curve is shifted by about +3 T when lowering the temperature from 4.2 K to 1.9 K.**

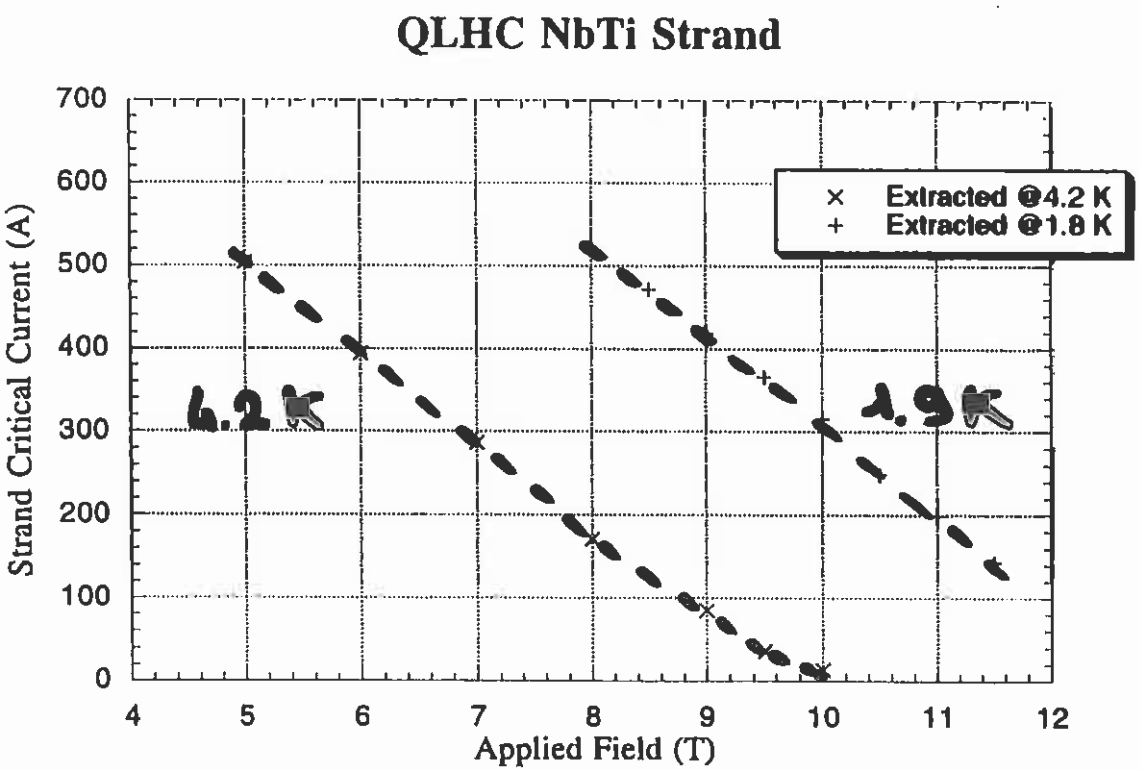
QLHC NbTi Strand
Strand Critical Current (A)
Applied Field (T)
Extracted @4.2 K
Extracted @1.8 K
4.2 K
1.9 K
0
100
200
300
400
500
600
700
4
5
6
7
8
9
10
11
12

CRITICAL FIELD OF Nb_3Sn COMPOUNDS

– The upper critical magnetic flux density, B_{C2}, of binary or ternary Nb_3Sn can be parametrized as a function of temperature, T, and strain, ε, using*

$$\frac{B_{C2}(T,\varepsilon)}{B_{C20}(\varepsilon)} = \left[1 - \left(\frac{T}{T_{C0}(\varepsilon)}\right)^2\right]\left\{1 - 0.31\left(\frac{T}{T_{C0}(\varepsilon)}\right)^2\left[1 - 1.77\ln\left(\frac{T}{T_{C0}(\varepsilon)}\right)\right]\right\}$$

where B_{C20} is the upper critical magnetic flux density at zero temperature:

$$B_{C20}(\varepsilon) = B_{C20m}\,(1 - a\,|\,\varepsilon\,|^{1.7})$$

and T_{C0} is the critical temperature at zero magnetic flux density:

$$T_{C0}(\varepsilon) = T_{C0m}\,(1 - a\,|\,\varepsilon\,|^{1.7})^{1/3}$$

Here, $a = 900$ for $\varepsilon \leq 0$ (compressive strain) and $a = 1250$ for $0 \leq \varepsilon$ (tensile strain), B_{C20m} is the upper critical magnetic flux density at zero temperature and zero strain and T_{C0m} is the critical temperature at zero magnetic flux density and zero strain.

* L.T. Summers, 1991

CRITICAL CURRENT DENSITY OF NB_3SN WIRES

– The critical current density per unit area of non-copper, J_C, can be parametrized as a function of temperature, magnetic flux density, B, and strain, ε, using *

$$J_C(B,T,\varepsilon) = \frac{C(\varepsilon)}{\sqrt{B}} \left[1 - \frac{B}{B_{C2}(T,\varepsilon)}\right]^2 \left[1 - \left(\frac{T}{T_{C0}(\varepsilon)}\right)^2\right]^2$$

where

$$C(\varepsilon) = C_0 (1 - a\,|\varepsilon|^{1.7})^{1/2}$$

Here C_0 is a fitting parameter ($AT^{1/2}m^{-2}$).

* L.T. Summers, 1991

CRITICAL CURRENT DENSITY OF Nb_3Sn WIRES (CONT.)

– For binary compounds, T_{C0m} and B_{C20m} are of the order of 16 K and 24 T, while for ternary compounds, they are of the order of 18 K and 28 T.

– The strain in a freestanding, reacted Nb_3Sn wire is estimated at about –0.25%.

– Following the ITER program, critical current density values of 700 to 750 A/mm² at 4.2 K and 12 T with effective filament diameters of 15 to 20 μm are now reached in industrial production (such values correspond to a C_0 of the order 12000 $AT^{1/2}m\,m^{-2}$).

– Higher critical current densities can be achieved when relaxing the specification on effective filament diameter.

– The "J_C versus B" curve shifts by only 1 to 1.5 T when lowering the temperature from 4.2 K to 1.9 K.

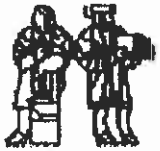

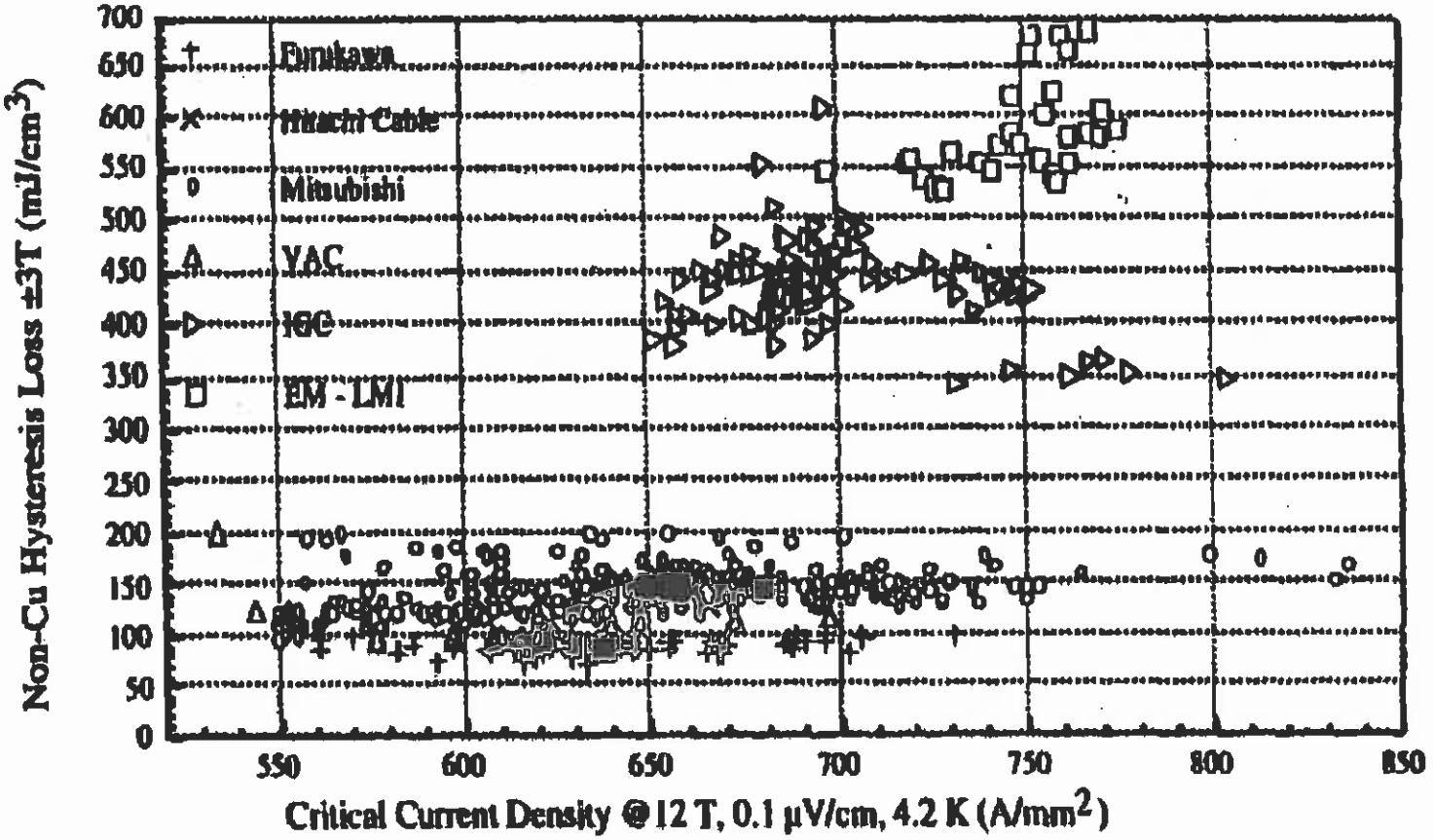

Figure 5: Strand J_c and hysteresis performance

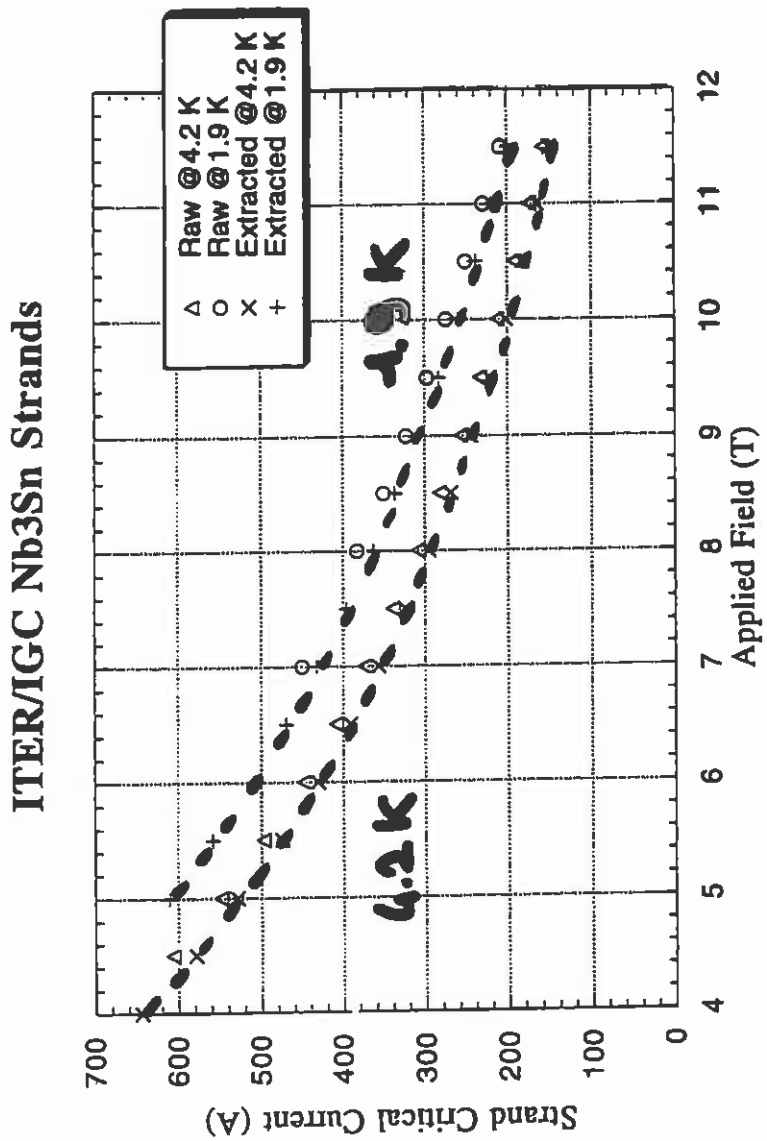
ITER/IGC Nb3Sn Strands
Raw @4.2 K
Raw @1.9 K
Extracted @4.2 K
Extracted @1.9 K
4.2K
1.9K
Strand Critical Current (A)
Applied Field (T)
0
100
200
300
400
500
600
700
4
5
6
7
8
9
10
11
12

LECTURE 3: CONDUCTOR AND CONDUCTOR INSULATION FOR PARTICLE ACCELERATOR MAGNETS

3.1 Review of Superconducting Materials
- 3.1.1 NbTi Alloys
- 3.1.2 Nb_3Sn Compounds
- 3.1.3 HTS

3.2 Superconducting Multifilamentary Composites

3.3 Transition of Multifilamentary Wires

3.4 Manufacturing of NbTi Wires

3.5 Manufacturing of Nb_3Sn Wires

3.6 Critical Surface Parametrizations

3.7 Rutherford-Type Cables

3.8 Interstrand Resistances in Rutherford-Type Cables

3.9 Critical Current Measurements on Rutherford-Type Cables

3.10 Cable Insulation

Appendix: Material Properties at Low Temperatures

RUTHERFORD-TYPE CABLES

– Superconducting particle accelerator magnet coils are wound from so-called *Rutherford-type* cables.

– A Rutherford-type cable consists of a few tens of strands, twisted together, and shaped into a flat, two-layer, slightly keystoned cable.

– As explained in the lecture on magnetic design, the slight keystone is introduced to allow stacking of the conductors into an arch and forming coils of the desired shape.

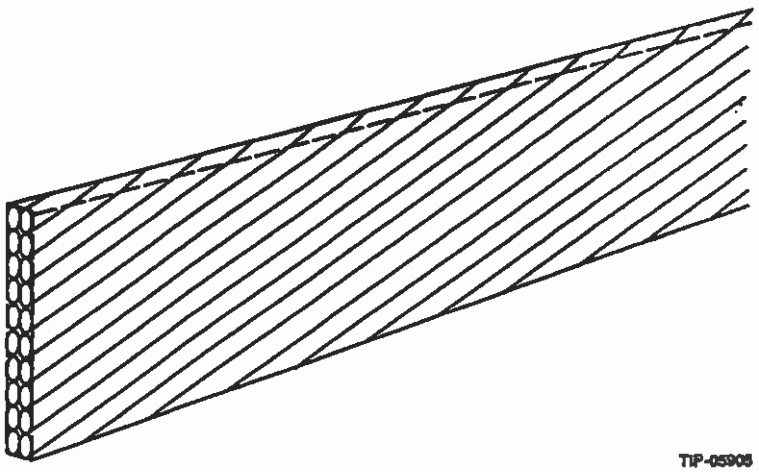

Courtesy T. Ogitsu

GEC ALSTHOM
BELFORT

ALSTHOM
INTERMAGNETICS

Câble supraconducteur pour dipôles LHC - Couche externe
NbTi Superconducting cable for LHC dipoles - Outer layer

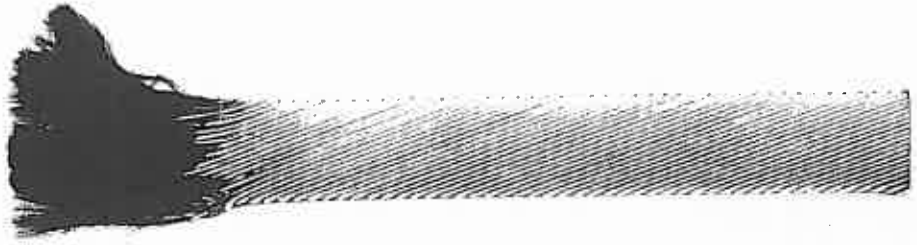

CARACTERISTIQUES

Câble trapézoidale.

40 brins de diamètre 0,84 mm.

Supraconducteur étamé 1/2.

Grande épaisseur : 1,67 mm.

Petite épaisseur : 1,30 mm.

Largeur : 17 mm.

Non émaillé.

CHARACTERISTICS

Keystone type cable.

40 strands 0.84 in diameter

Half-tinned SC wires.

Thick edge thickness : 1.67 mm.

Thin edge thickness : 1.30 mm.

Width : 17 mm.

Not enamelled.

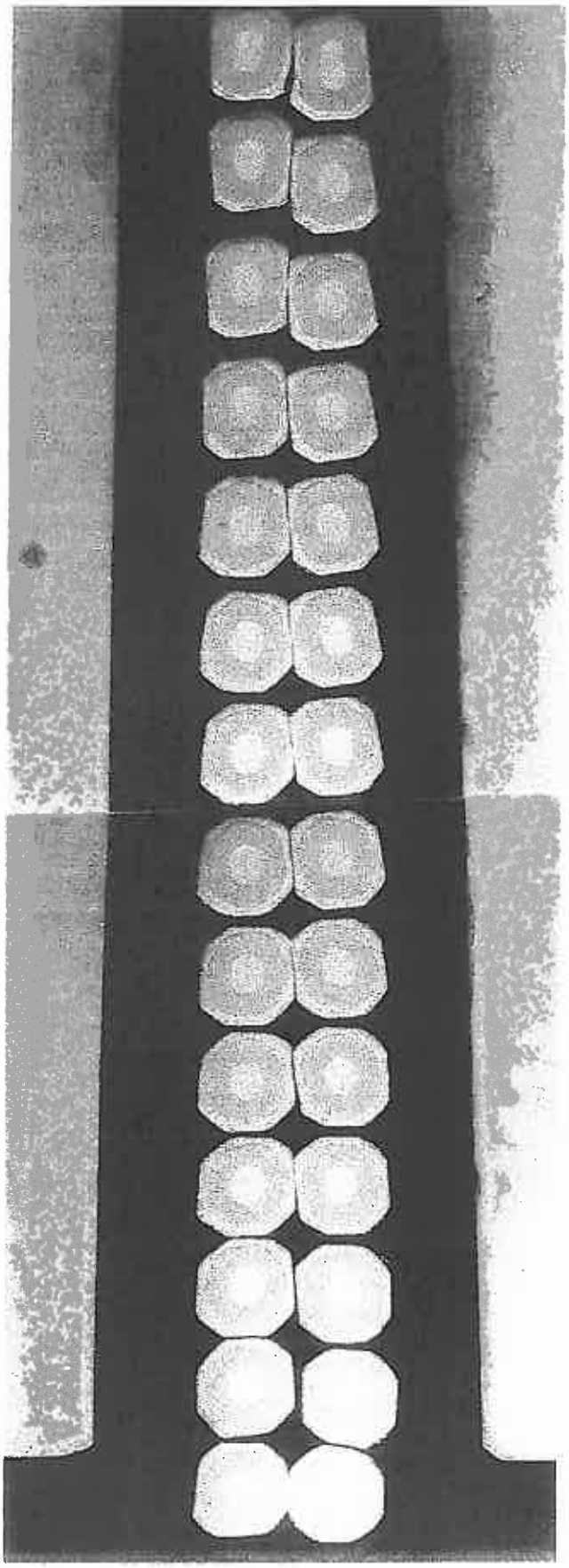

WHY USING A CABLE?

– The small radii of curvature of the coil ends preclude the use of a monolithic conductor because it would be too hard to bend.

– A multi-strand cable is preferred to a single wire for at least four reasons:

• *It limits piece length requirement for wire manufacturing* (a coil wound with a N-strand cable requires piece lengths which are $1/N$ shorter than for a similar coil wound with a single wire),

• *It allows strand-to-strand current redistribution* in the case of a localized defect or when a quench originates in one strand,

• *It limits the number of turns* and facilitates coil winding,

• *It limits coil inductance* [the inductance of a coil wound with a N-strand cable is $(1/N)^2$ smaller than that of a similar coil wound with a single wire].

A smaller inductance reduces the voltage requirement on the power supply to ramp-up the magnets to their operating current in a given time and it limits the maximum voltage to ground in the case of a quench (see lecture on quench protection).

– The main disadvantage of using a cable is the high operating current (over a few thousand ampères) which requires large current supplies and large current leads.

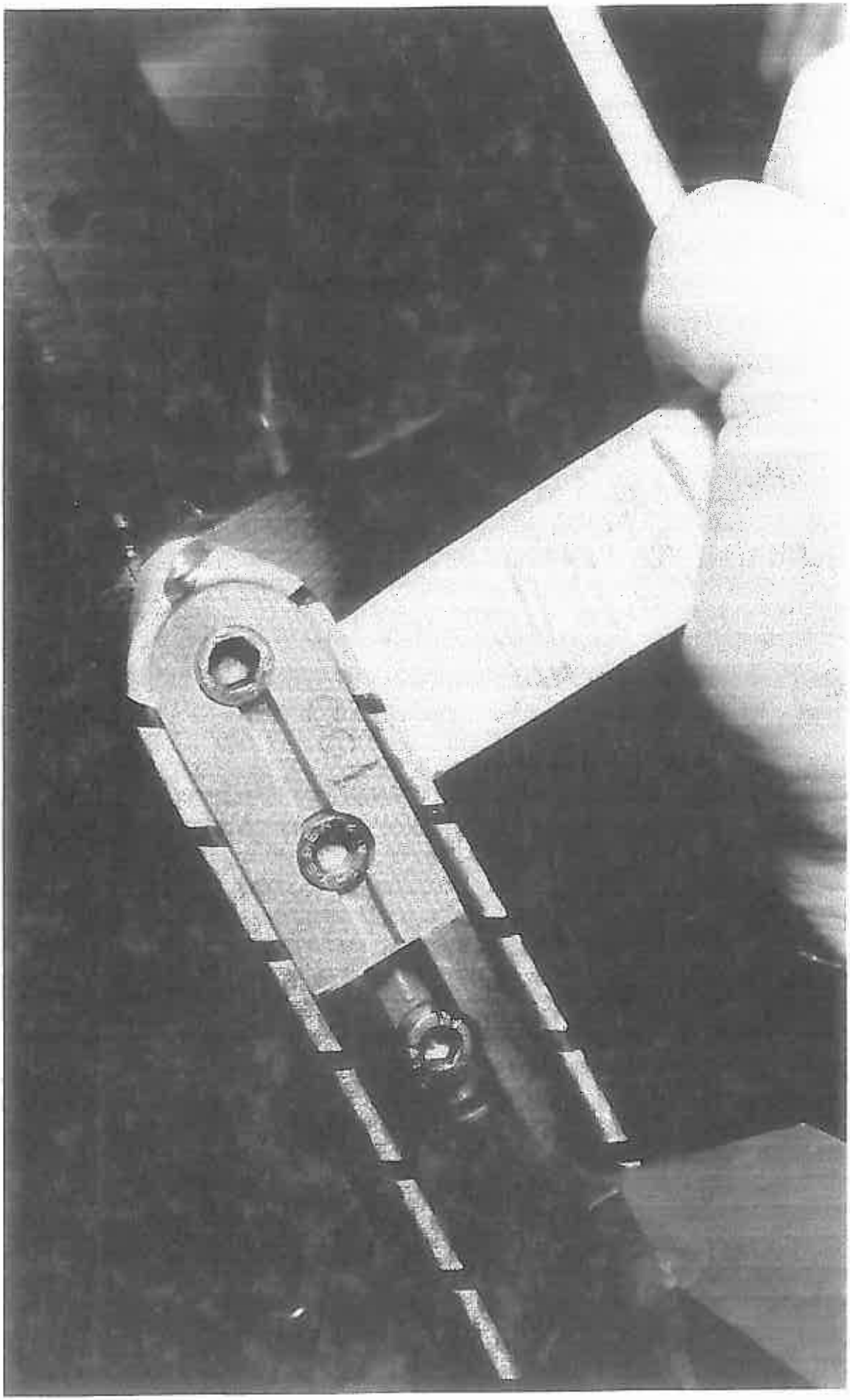

CABLING MACHINE

– Spools of strands are distributed on a rotating drum.

– The strands are twisted together around a cabling mandrel shaped like a screwdriver.

– As the cable leaves the blade of the screw driver, it enters a Turk's-head roller die, which consists of four rollers arranged at given angles to form a trapezoidal orifice.

– The Turk's-head die squeezes the cable into its final configuration.

– The cable is driven by a caterpillar-type pulling device that is perfectly synchronized with the drum rotation.

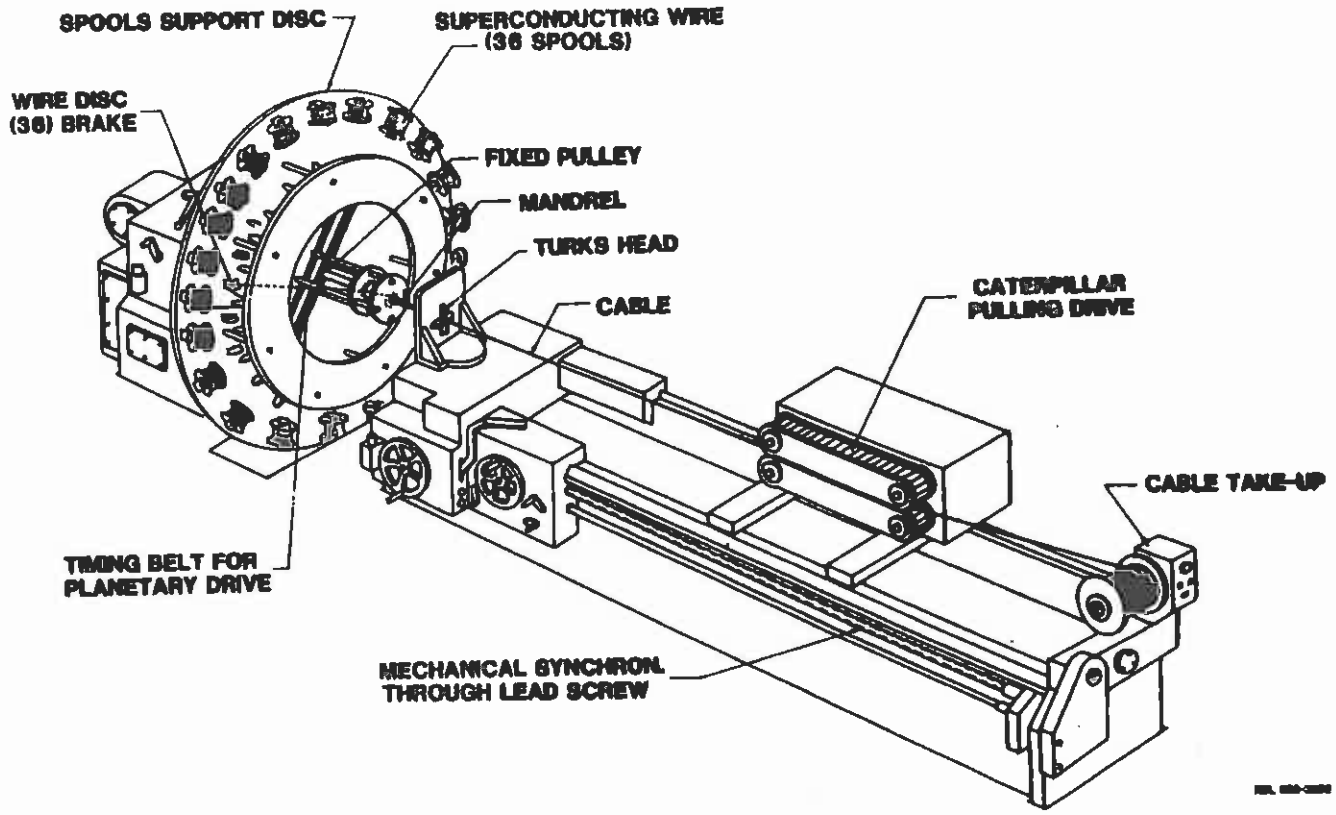

FIG. 4. Experimental Cabling Machine

Courtesy J. Royet

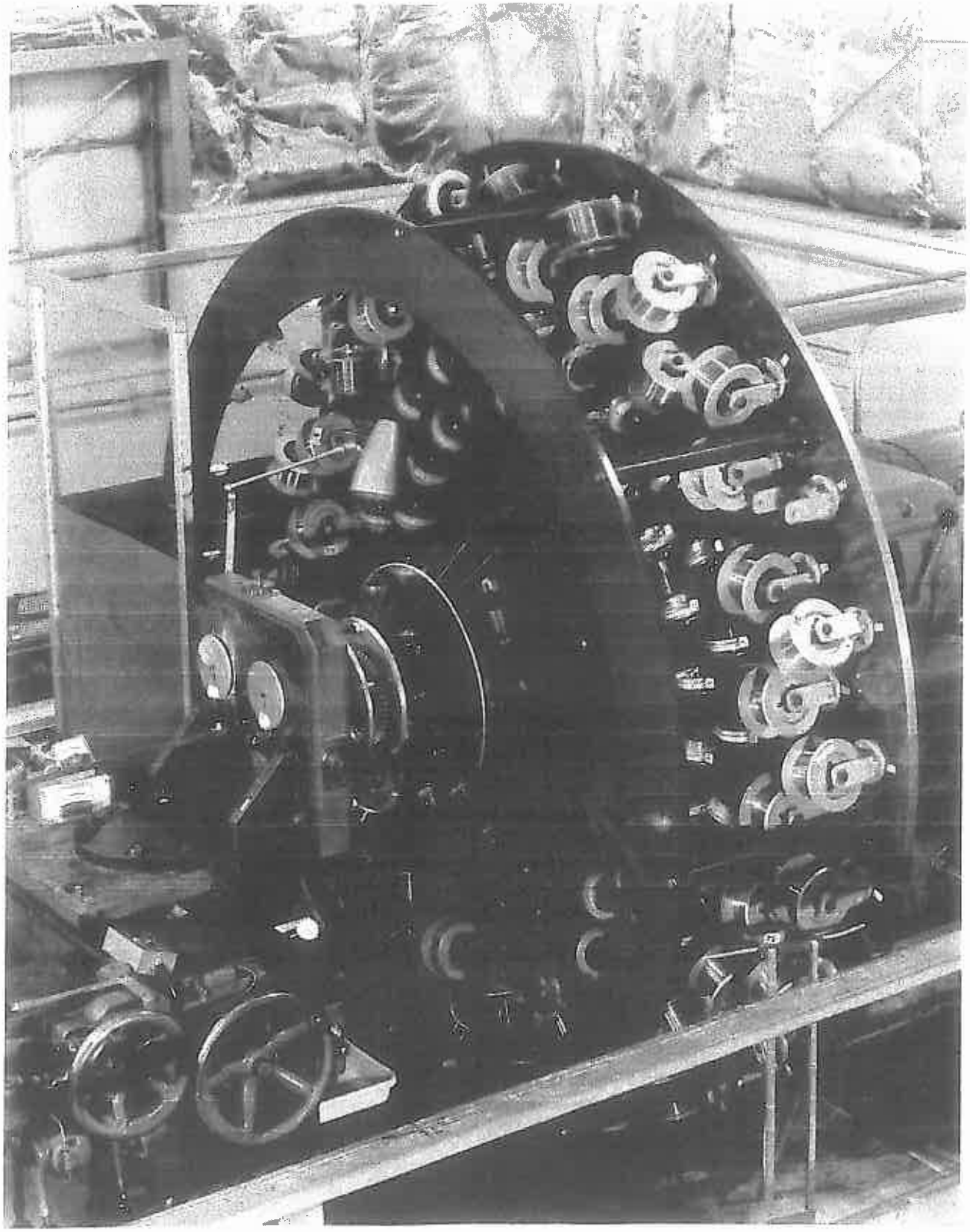

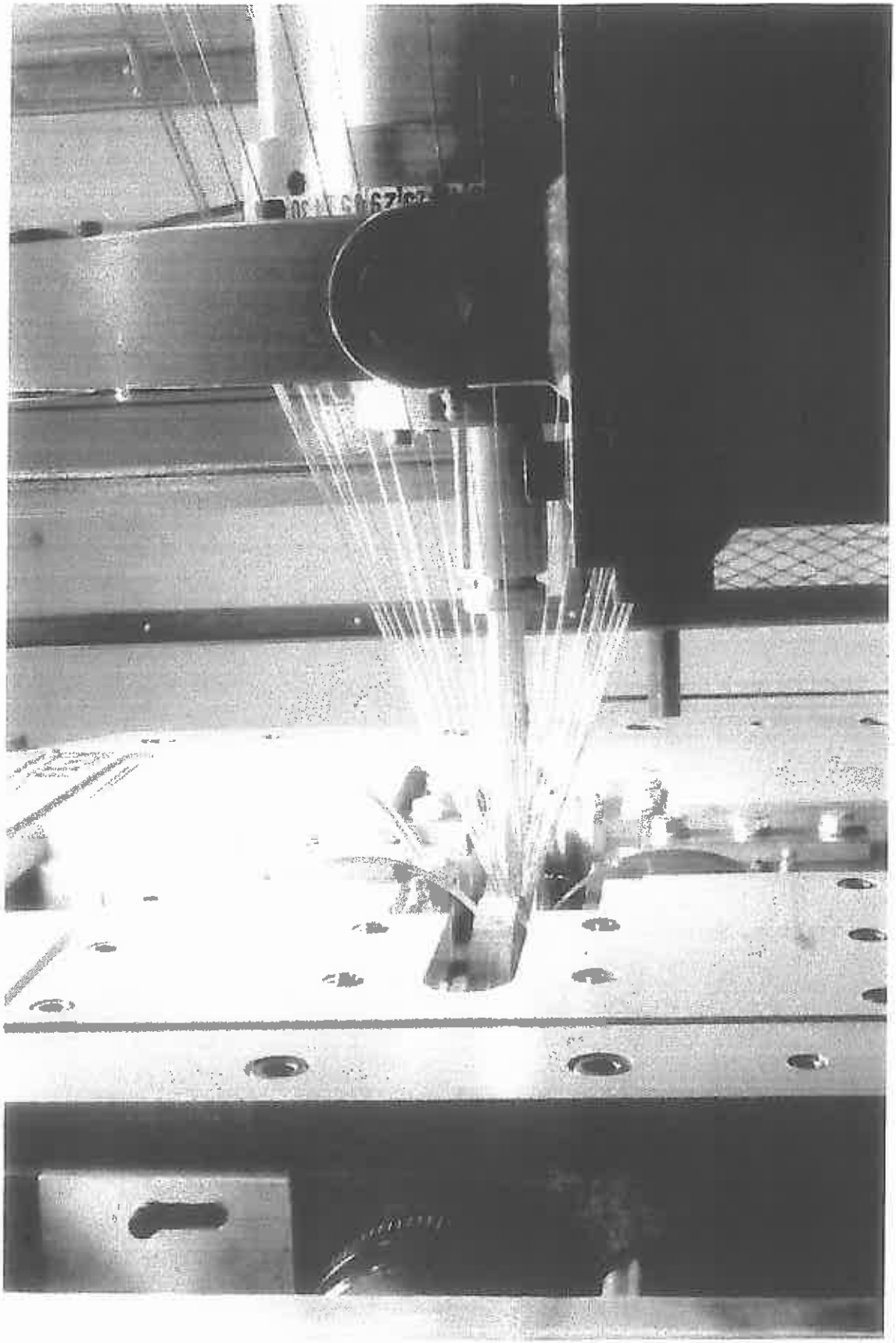

MAIN ISSUES FOR CABLE DESIGN AND MANUFACTURING

– The main issues for cable design and fabrication are:

• ***Compaction,*** which should be large enough to ensure good mechanical stability and high overall current density while leaving enough void (typically of the order of 10% in volume) for liquid helium cooling,

• ***Control of outer dimensions*** to achieve suitable coil geometry and mechanical properties,

• ***Limitation of critical current degradation*** due to strand and filament degradations at the cable edges,

• ***Control of interstrand resistance,*** which should not be too small to limit field distortions induced by interstrand coupling currents while ramping (see lecture on field quality) and should not be too large to allow current redistribution among cable strands.

CABLE COMPACTION

– Cable compaction is not uniform for a keystoned cable.

– It is customary to define an *overall compaction, P,* as the ratio of the sum of the areas of undeformed strand cross sections to the area of the enclosing trapezoid.

As the strands are twisted together, their cross-sectionnal area is computed in a plane perpendicular to the cable axis and we have:

$$P = \frac{N\pi d^2}{4wt_m \cos\psi}$$

where N is the number of cable strands, d is the strand diameter, w is the cable width, t_m is the cable midthickness, and ψ is the cable pitch angle, given by:

$$\tan\psi = \frac{2w}{L}$$

Here, L is the cable pitch length.

EXAMPLE OF CABLE COMPACTION

– For the cable used in the outer layer of the LHC dipole magnet coils we have:

$$w = 15.1 \text{ mm and } L = 100 \text{ mm}$$

which yields:

$$\psi = 16.8^{\circ}$$

– Furthermore, we have:

$$N = 36,\ d = 0.825 \text{ mm, and } t_m = 1.48 \text{ mm,}$$

and we get:

$$P \approx 90\%$$

– The manufacturing of the LHC coils requires about 4600 km (736 metric tons) of this cable. The specification on the minimum overall current capacity is 12960 A at 9 T and 1.9 K and the minimum unit length is 750 m.

CABLE DIMENSIONS

– Cable dimensions must be tightly controled during production.

– Measurements are performed on-line and can be cross-checked using stacks of 10 conductor samples (which are alternated to compensate keystone angle).

CABLING DEGRADATION

– Cabling of the strands result in strand deformations at the cable edges, where the strands are bent in a hairpin-like manner.

– The deformations are accentuated at the thin edge of keystoned-cables.

– These deformations can result in local reductions of the filament areas, therebye lowering the critical current of the cabled wires with respect to that of un-cabled wires.

– The introduction of a copper core and of a copper sheath in the wire design has been shown to reduce cabling degradation.

– The cabling degradation is a strong function of keystone angle.

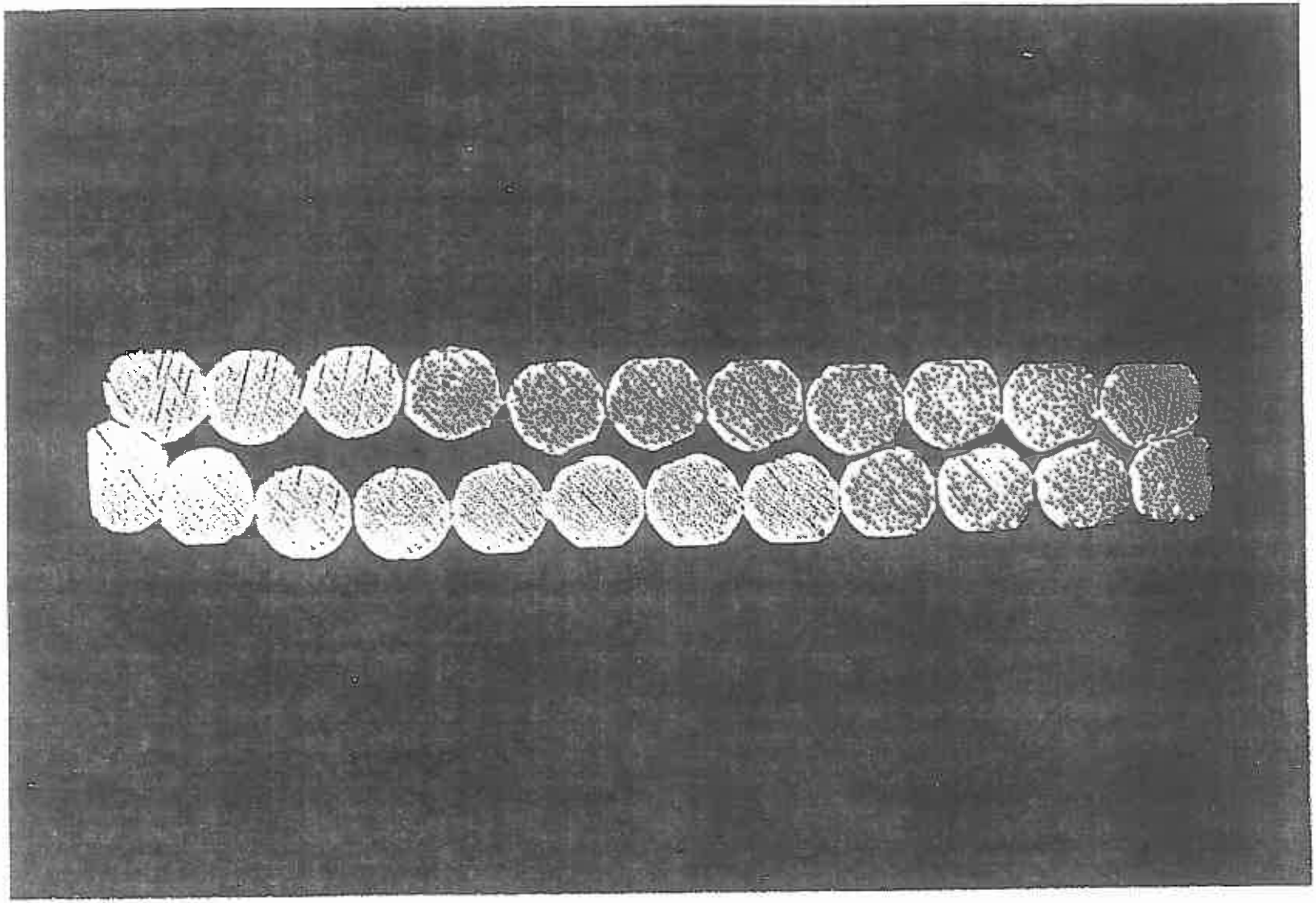

KEYSTONE ANGLE 1.6°

Courtesy T. Shintomi

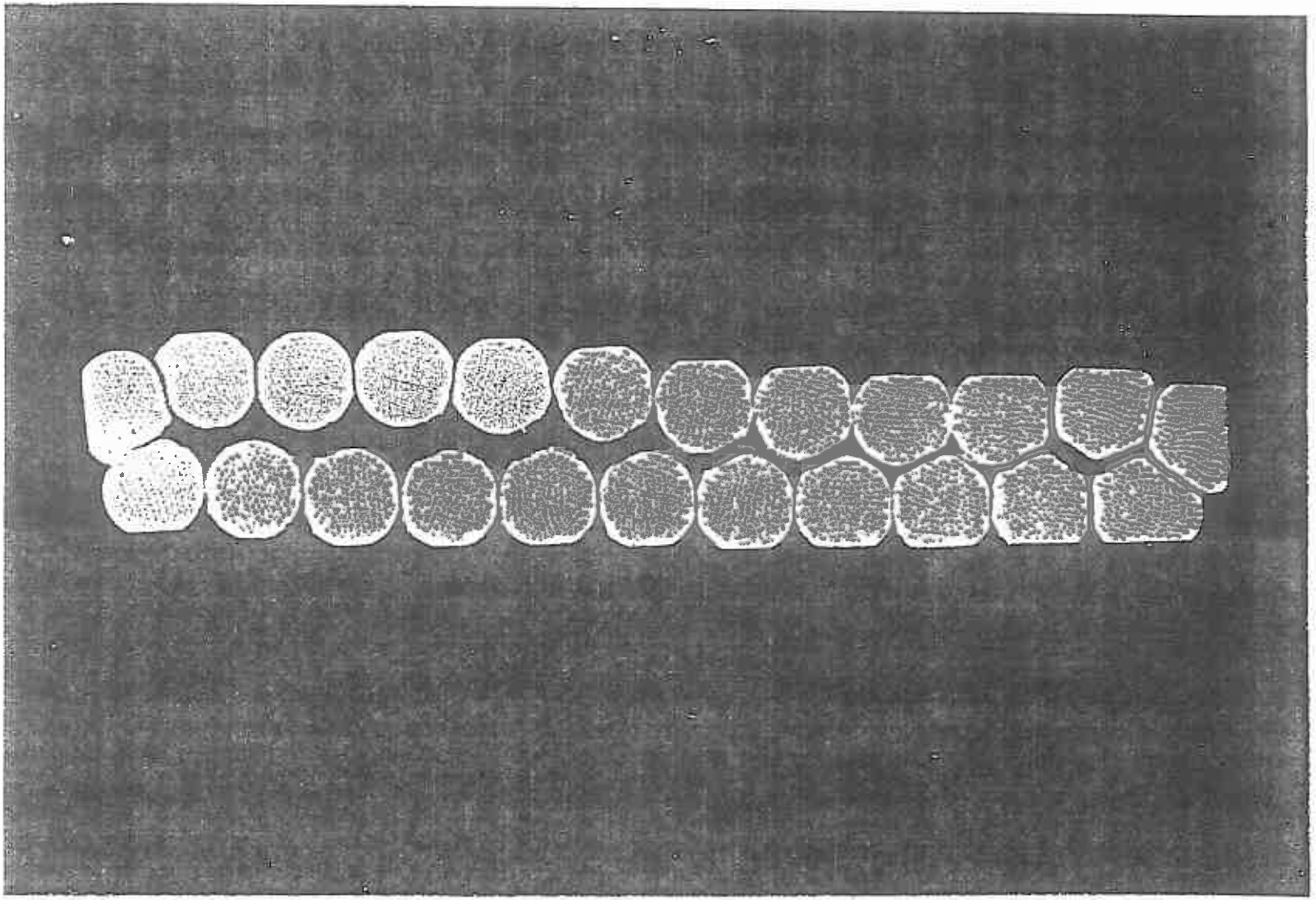

KEYSTONE ANGLE 2.0°

Courtesy T. Shintomi

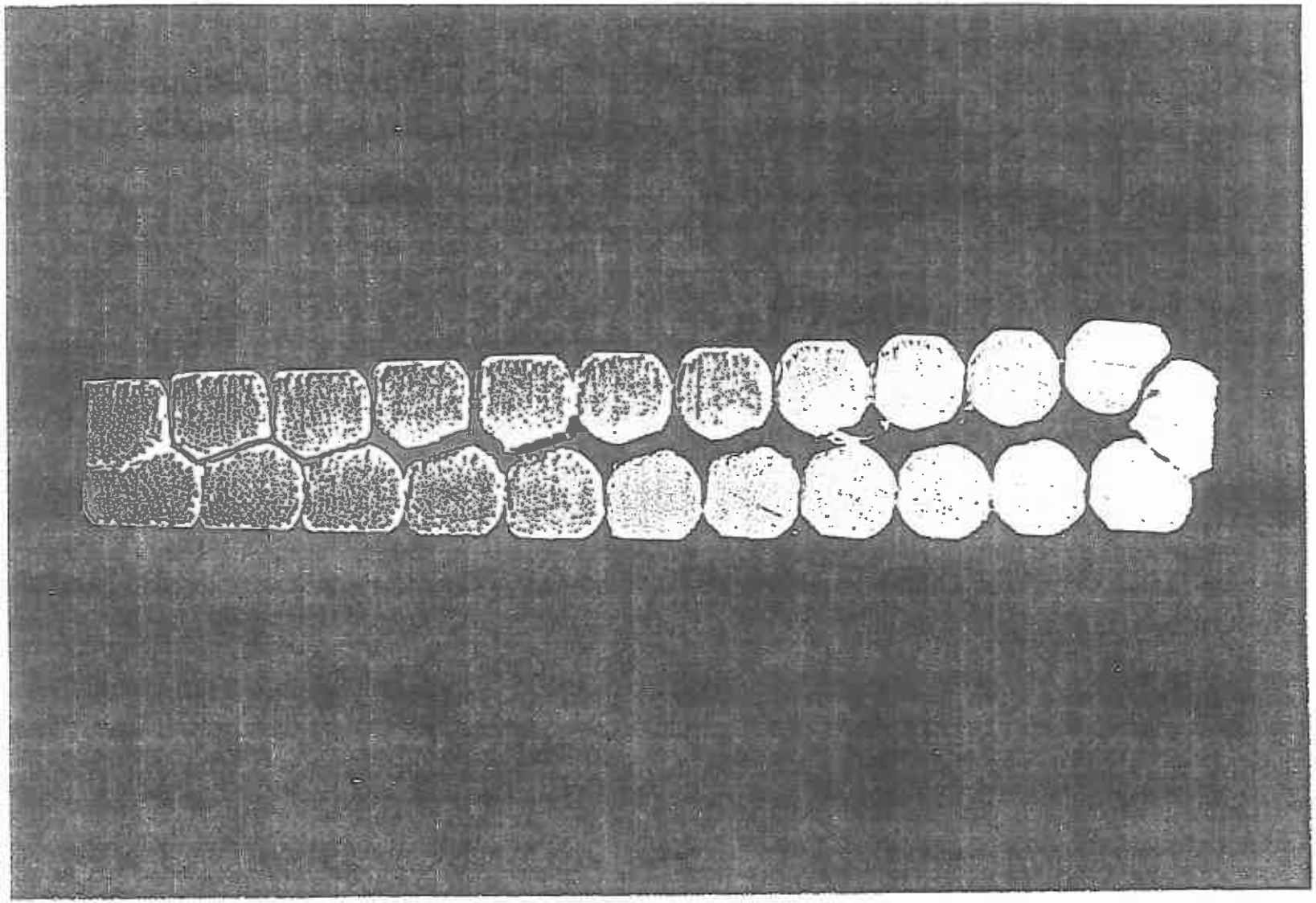

KEYSTONE ANGLE 2.4°

Courtesy T. Shintomi

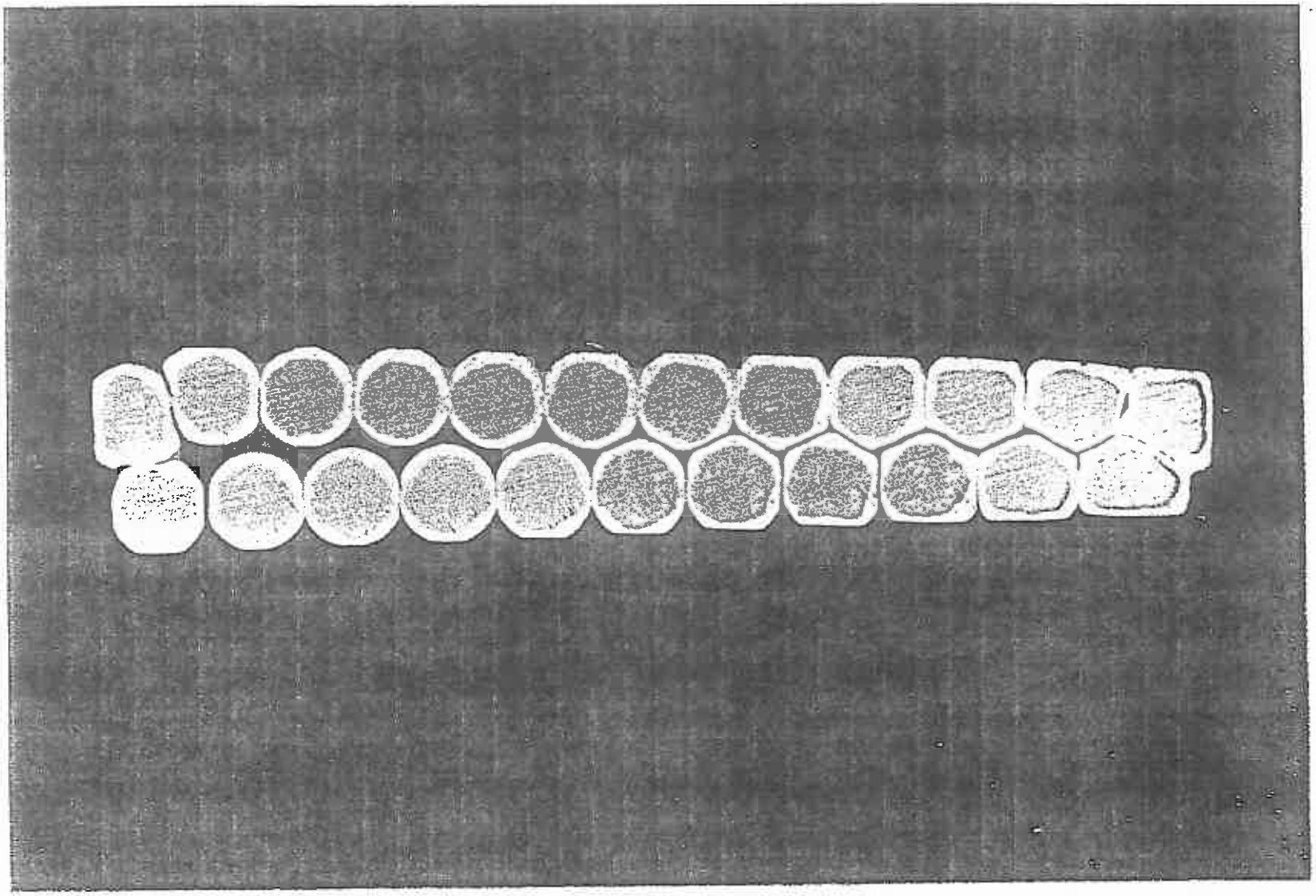

KEYSTONE ANGLE 3.1°

Courtesy T. Shintomi

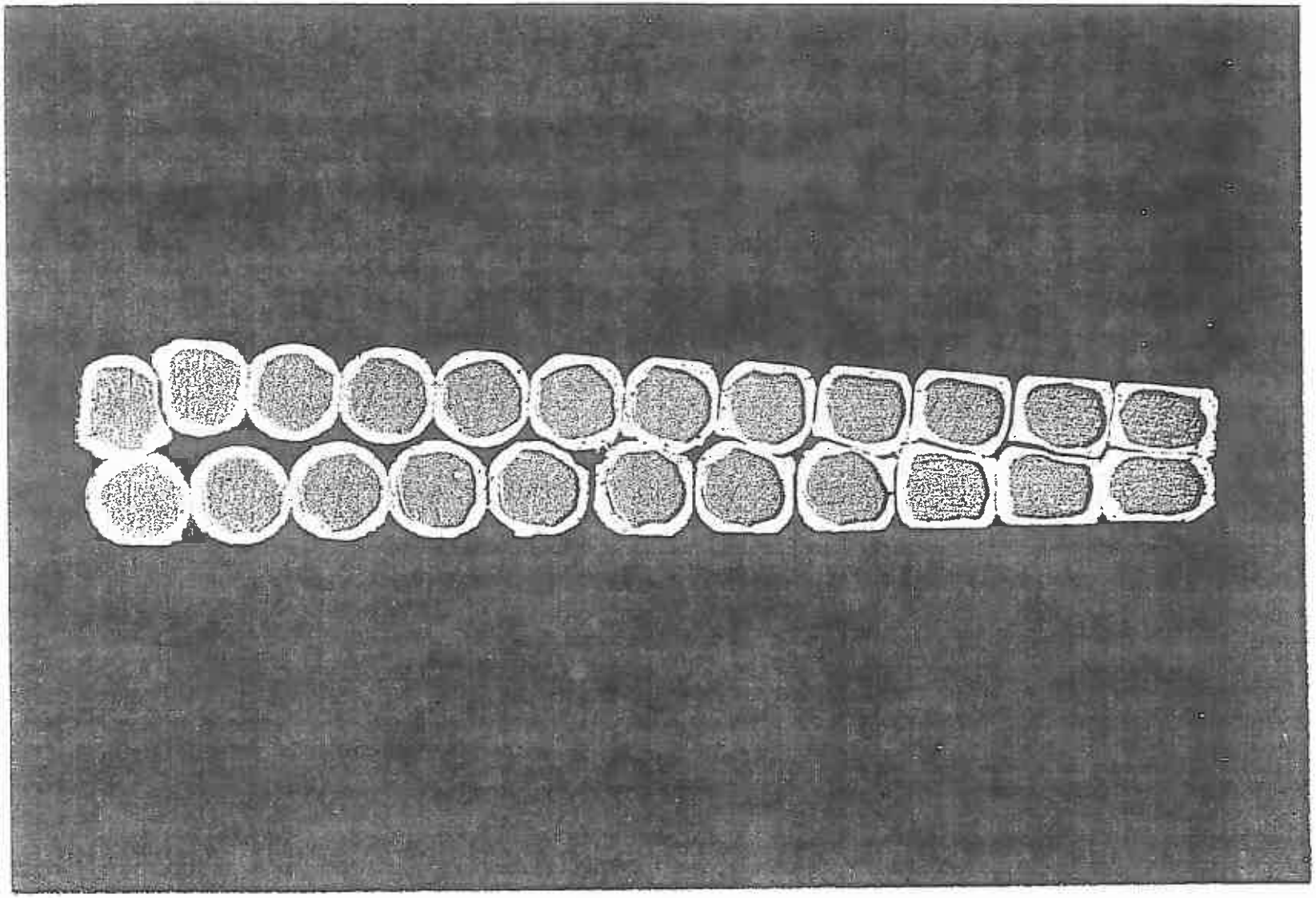

KEYSTONE ANGLE 3.6°

Courtesy T. Shintomi

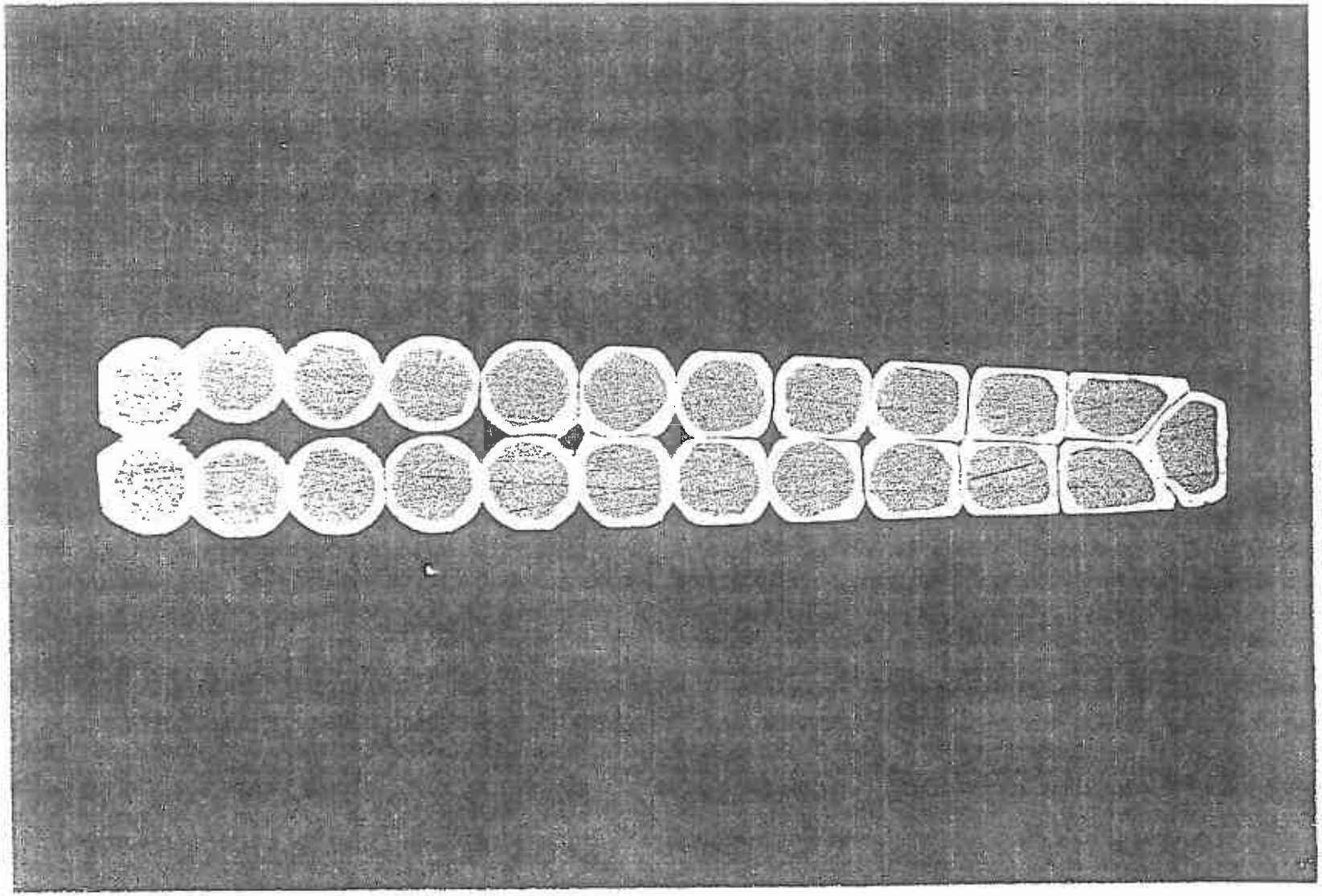

KEYSTONE ANGLE 4.2°

Courtesy T. Shintomi

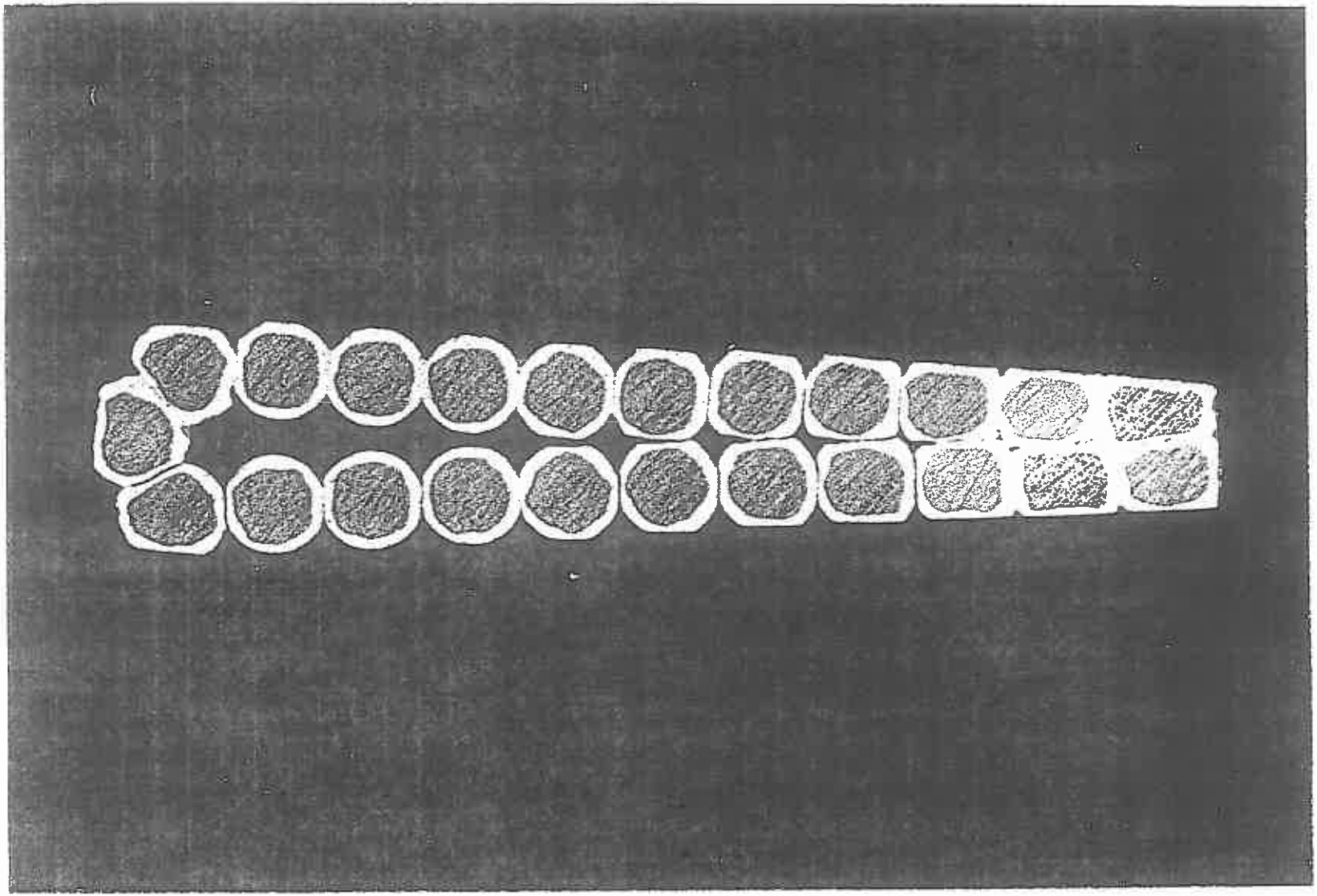

KEYSTONE ANGLE 4.8°

Courtesy T. Shintomi

Cable Degradation*

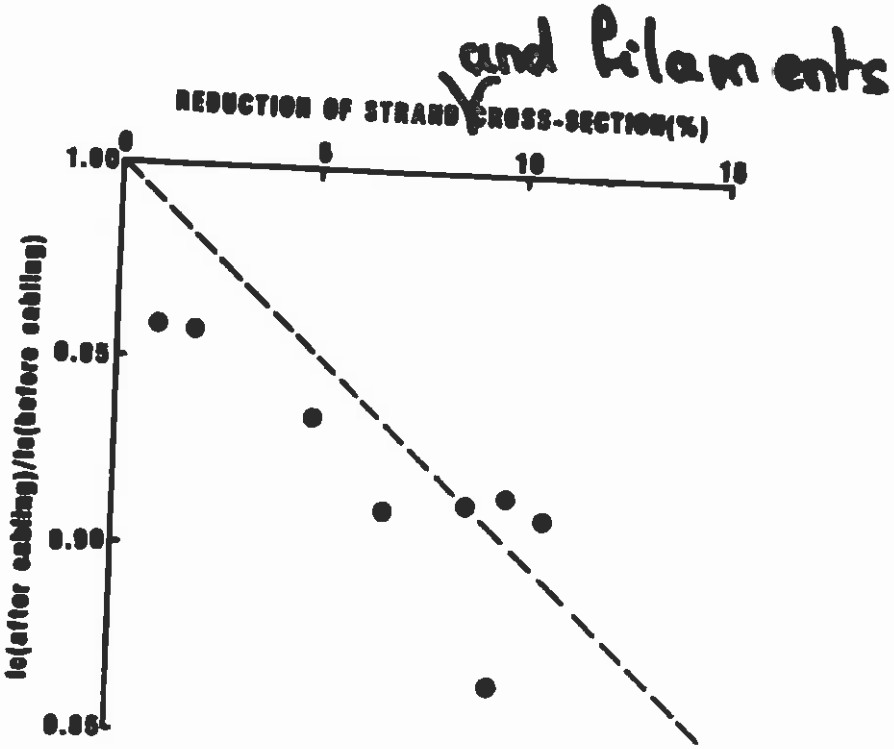

Fig. 4. Relationship between critical current degradation due to cabling and strand cross-sectional area reduction. On the dashed line, the critical current degradation equals to the strand cross-sectional area reduction.

M. Ikeda, H. Li, 1990

LECTURE 3: CONDUCTOR AND CONDUCTOR INSULATION FOR PARTICLE ACCELERATOR MAGNETS

3.1 Review of Superconducting Materials
- 3.1.1 NbTi Alloys
- 3.1.2 Nb_3Sn Compounds
- 3.1.3 HTS

3.2 Superconducting Multifilamentary Composites

3.3 Transition of Multifilamentary Wires

3.4 Manufacturing of NbTi Wires

3.5 Manufacturing of Nb_3Sn Wires

3.6 Critical Surface Parametrizations

3.7 Rutherford-Type Cables

3.8 Interstrand Resistances in Rutherford-Type Cables

3.9 Critical Current Measurements on Rutherford-Type Cables

3.10 Cable Insulation

Appendix: Material Properties at Low Temperatures

INTERSTRAND RESISTANCES

– A rutherford type-cable presents two types of interstrand contacts:

• Discrete contacts at the crossovers between strands of the two layers,

• Continuous contacts between adjacent strands of a same layer.

– The strand deformations due to cabling and the high pressures applied to the coil during magnet assembly can result in low contact resistances.

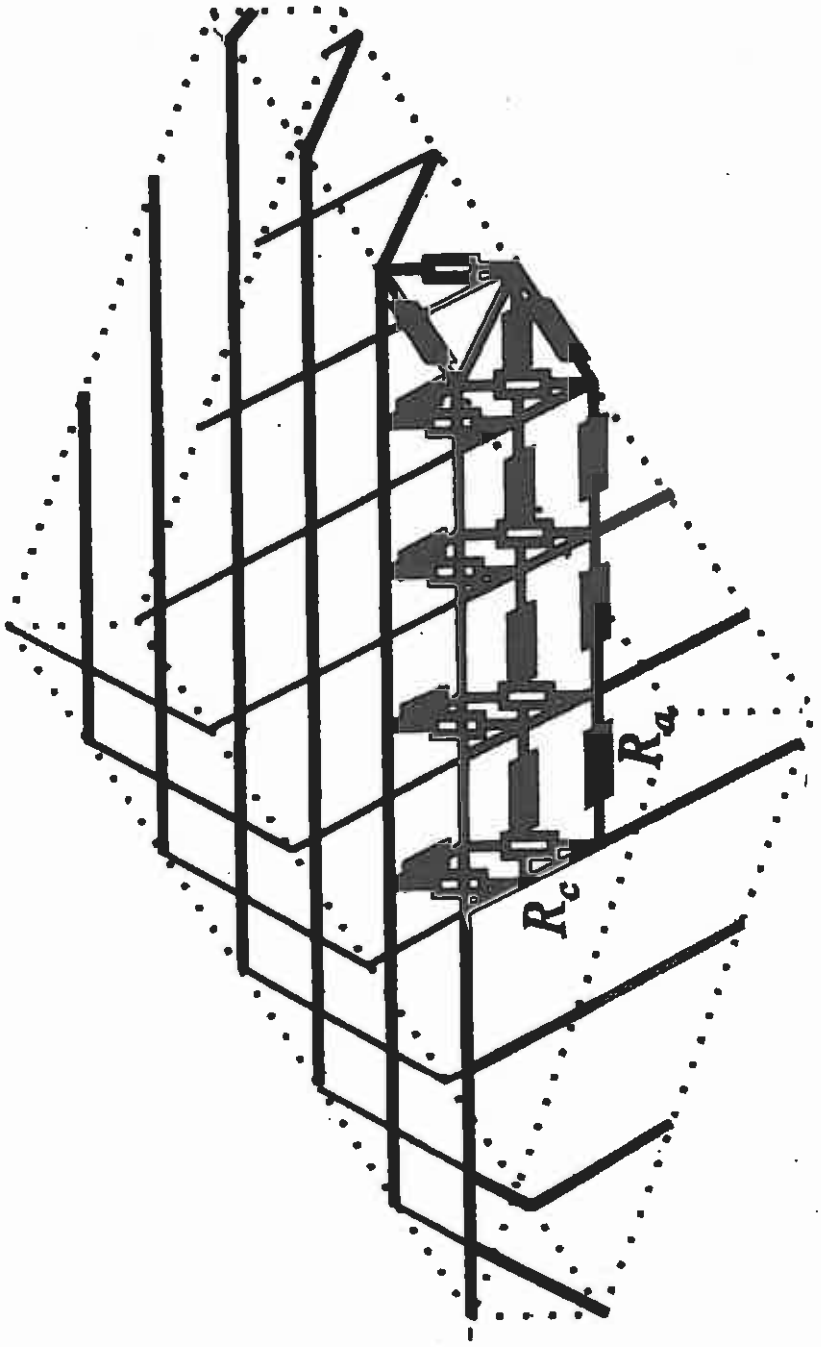

Courtesy A. Verweij

INTERSTRAND COUPLING CURRENTS

– When a Rutherford-type cable is subjected to a transverse, time-varying field, the network of interstrand resistances is the seat of current loops, referred to as *interstrand coupling currents.*

– The interstrand coupling currents produce field distorsions in the magnet bore and dissipate power in the interstrand resistances.

– The field distortions are very damageable for accelerator operation, even for a slow-ramping machine, such as the Large Hadron Collider (LHC). (The LHC current ramp rate is 10 A/s, which, for dipole magnets, corresponds to a field ramp rate of about 7.5 mT/s.)

– At high ramp rates, the power dissipated by interstrand coupling currents can degrade quench performance.

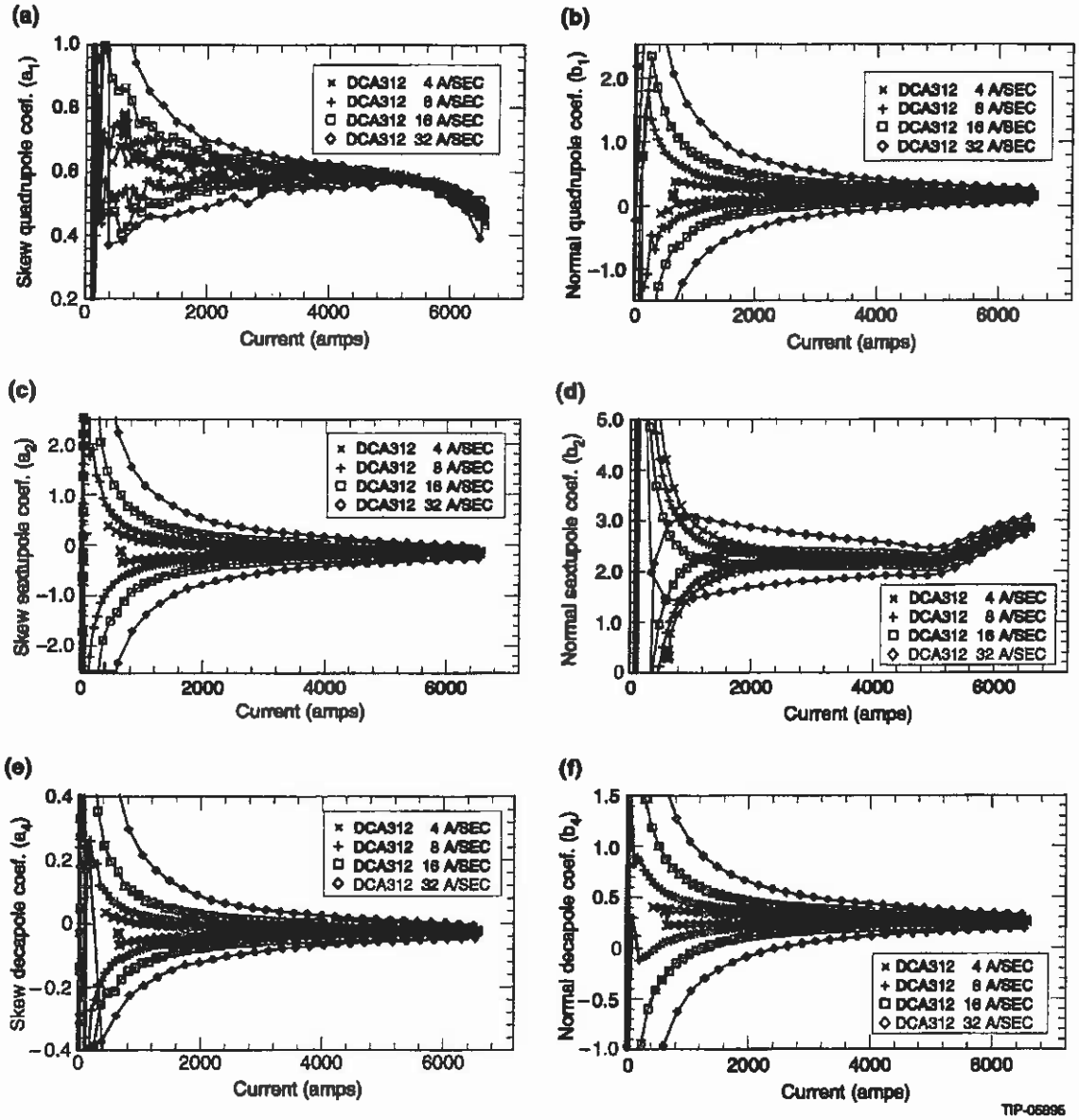
(a)
Skew quadrupole coef. (a_1)
1.0
0.8
0.6
0.4
0.2
0
2000
4000
6000
Current (amps)
× DCA312 4 A/SEC
+ DCA312 8 A/SEC
□ DCA312 16 A/SEC
◇ DCA312 32 A/SEC
(b)
Normal quadrupole coef. (b_1)
2.0
1.0
0
−1.0
0
2000
4000
6000
Current (amps)
× DCA312 4 A/SEC
+ DCA312 8 A/SEC
□ DCA312 16 A/SEC
◇ DCA312 32 A/SEC
(c)
Skew sextupole coef. (a_2)
2.0
1.0
0
−1.0
−2.0
0
2000
4000
6000
Current (amps)
× DCA312 4 A/SEC
+ DCA312 8 A/SEC
□ DCA312 16 A/SEC
◇ DCA312 32 A/SEC
(d)
Normal sextupole coef. (b_2)
5.0
4.0
3.0
2.0
1.0
0
0
2000
4000
6000
Current (amps)
× DCA312 4 A/SEC
+ DCA312 8 A/SEC
□ DCA312 16 A/SEC
◇ DCA312 32 A/SEC
(e)
Skew decapole coef. (a_4)
0.4
0.2
0
−0.2
−0.4
0
2000
4000
6000
Current (amps)
× DCA312 4 A/SEC
+ DCA312 8 A/SEC
□ DCA312 16 A/SEC
◇ DCA312 32 A/SEC
(f)
Normal decapole coef. (b_4)
1.5
1.0
0.5
0
−0.5
−1.0
0
2000
4000
6000
Current (amps)
× DCA312 4 A/SEC
+ DCA312 8 A/SEC
□ DCA312 16 A/SEC
◇ DCA312 32 A/SEC
TIP-05895

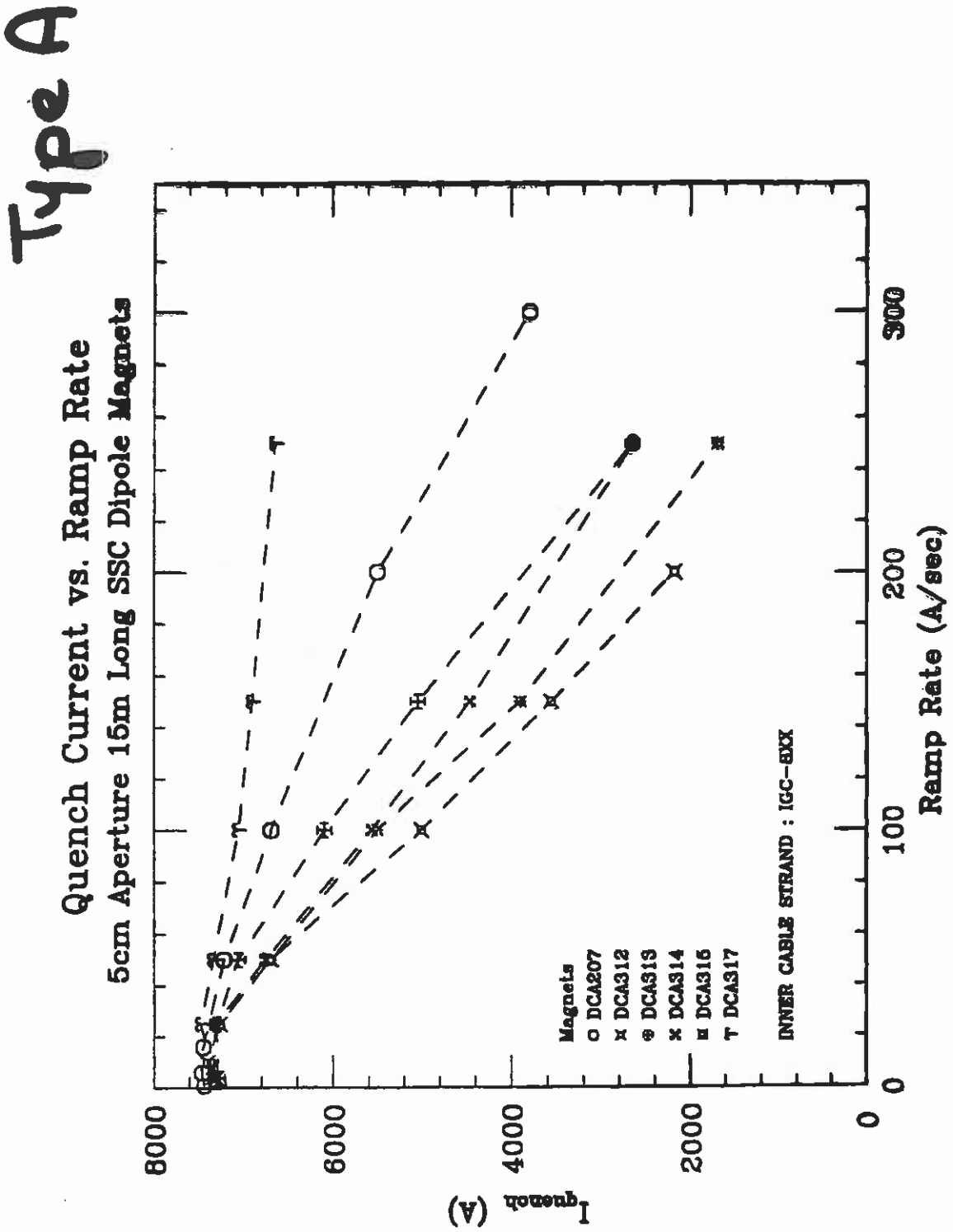
Type A
Quench Current vs. Ramp Rate
5cm Aperture 15m Long SSC Dipole Magnets
I_{quench} (A)
8000
6000
4000
2000
0
0
100
200
300
Ramp Rate (A/sec)
Magnets
o DCA207
x DCA312
⊕ DCA313
x DCA314
▪ DCA316
T DCA317
INNER CABLE STRAND : IGC-6XX

RUTHERFORD-TYPE CABLE MODEL

– An N-strand Rutherford-type cable in the steady state or subjected to a magnetic field varying at a constant rate can be represented by a simple equivalent electrical circuit.

– In this model, the strands are represented by equipotential lines.

Over a twist pitch, each strand crosses two times every other strands. The crossings are represented by elementary resistances, referred to as *crossover resistances*, R_c.

The points where the crossover resistances are connected to the lines define the network nodes.

Furthermore, the continuous contacts between adjacent strands are represented by discrete elementary resistances, referred to as *adjacent resistances*, R_a, connected to the network nodes.

– Over a pitch length, each strand encounters $(2N-2)$ crossover resistances and is connected to each of its neighbors by $(2N)$ adjacent resistances.

R_A VERSUS R_C

– When subjecting an N-strand Rutherford-type cable to an uniform, transverse field, B_t, varying at a constant rate, the power, P_c, dissipated in the crossover resistances can be estimated as

$$P_c \approx \frac{N^2 w L}{120 t_m R_c} \left(\frac{dB_t}{dt}\right)^2$$

where w is the cable width, t_m is the cable midthickness and L is the cable pitch length.

– Similarly, the power, P_a, dissipated by the coupling currents in the adjacent resistances can be estimated as

$$P_a \approx \frac{w L}{6 t_m R_a} \left(\frac{dB_t}{dt}\right)^2$$

– The above equations show that, to obtain similar levels of power dissipation, R_a and R_c should be in the ratio $(20/N^2)$.

For $N = 36$, this implies that R_a must be about 65 times smaller than R_c.

– The interstrand coupling currents of regular cables (without internal cores) are usually dominated by crossover resistances.

INTERSTRAND RESISTANCE REQUIREMENTS

– The effects of interstrand coupling currents can be limited by preventing interstrand resistances from being too low.

– However, it is also desirable to keep the strands from being electrically insulated from each other, to preserve the possibility of interstrand current redistribution.

– A compromise must be found between these conflicting demands, and the cables must be designed and manufactured so as to ensure a suitable, reproducible and uniform level of interstrand resistances in the magnet coil assemblies.

– For LHC cables, the target value of crossover resistance is: 20 $\mu\Omega \pm 10\ \mu\Omega$.

CONTROLING INTERSTRAND RESISTANCES

– The interstrand resistance can be modified by oxidizing or by coating strand surface.

– Also, a thin, insulating foil (such as stainless steel) can be inserted between the two layers of cable strands in order to increase the resistances at the strand crossovers.

– The interstrand coupling currents of cored cables are dominated by adjacent resistances.

CONTROLING INTERSTRAND RESISTANCES OF NBTI CABLES

– Half of the strands of the Tevatron cable are coated with a silver-tin solder, called *stabrite*, while the other half are coated with *ebanol*, a chemical that favors the development of black copper oxide.

The stabrite- and ebanol-coated strands are alternated, yielding a pattern of black and silver stripes. Such cable is referred to as *zebra* cable.

– The strands of the UNK, SSC and RHIC cables are bare.

– The strands of the HERA and LHC cables are stabrite-coated.

– In addition, the LHC cables are subjected, at the end of cabling, to a heat treatment at 200 °C for 8 to 12 hours on special reels allowing air circulation.

This heat treatment is optimized to prevent alterations of the niobium-titanium alloy microstructure, while favoring oxidation of the staybrite coating to achieve the desired level of crossover resistance (20±10 μΩ).

Also, it contributes to a last annealing of the high purity copper of the strand matrix (to recover from the cold-work produced by the cabling operation).

CONTROLING INTERSTRAND RESISTANCES OF NB_3SN CABLES

– Control of interstrand resistances is even more difficult for Nb_3Sn cables, because of the required heat treatment that is usually performed in situ, on wound coils.

– If nothing is done, the heat treatment can result in a sintering of the strands, engendering undesirably low interstrand resistances (less than 1 $\mu\Omega$ for R_c).

– To prevent sintering, the ITER program has considered chromium-plating of the strands. However, for accelerator magnets, the chromium plating may yield too high interstrand resistances (more than 100 $\mu\Omega$ for R_c).

– An alternative is to use a cable made from bare strands but with a stainless steel core.

Such a cable should yield a low R_a (of the oder of 1 $\mu\Omega$) and a high R_c (of the order of 100 $\mu\Omega$), therebye reducing the most damaging crossover coupling currents, while still allowing the possibiliy of current redistribution through the adjacent resistances.

CEA/Saclay and University of Twente are considering such a cable for their Nb_3Sn model magnets.

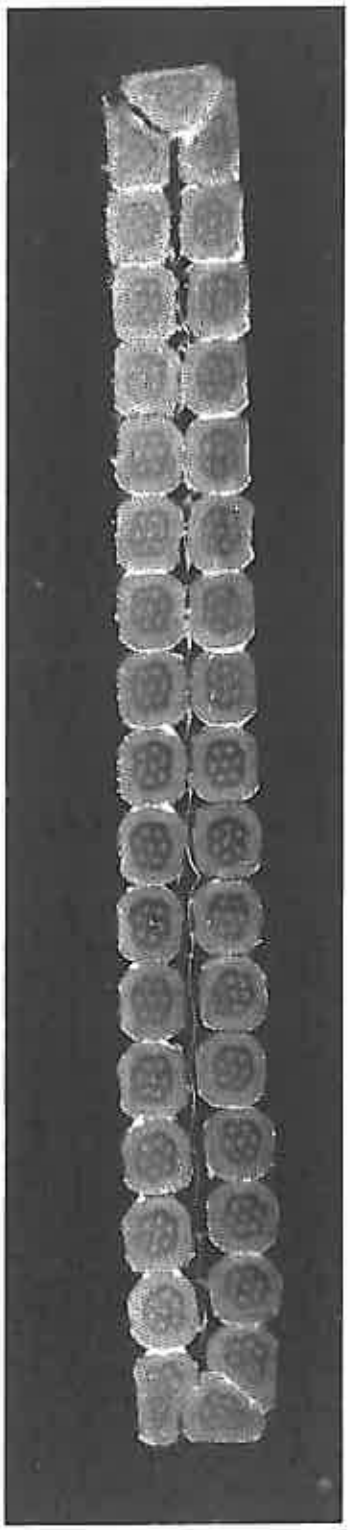

Nb_3Sn Cable With Stainless Steel Core

LECTURE 3: CONDUCTOR AND CONDUCTOR INSULATION FOR PARTICLE ACCELERATOR MAGNETS

3.1 Review of Superconducting Materials
- 3.1.1 NbTi Alloys
- 3.1.2 Nb_3Sn Compounds
- 3.1.3 HTS

3.2 Superconducting Multifilamentary Composites

3.3 Transition of Multifilamentary Wires

3.4 Manufacturing of NbTi Wires

3.5 Manufacturing of Nb_3Sn Wires

3.6 Critical Surface Parametrizations

3.7 Rutherford-Type Cables

3.8 Interstrand Resistances in Rutherford-Type Cables

3.9 Critical Current Measurements on Rutherford-Type Cables

3.10 Cable Insulation

Appendix: Material Properties at Low Temperatures

CRITICAL CURRENT MEASUREMENTS ON CABLES

– Similarly to wires, the maximum current-carrying capacity of cables can be determined from measurements on short samples.

– The voltage-current curves of cable short samples are similar to that of wire short samples and the cable performances can be characterized using the same definitions of critical current and N-value.

CRITICAL CURRENT MEASUREMENTS ON NBTI CABLES

– BNL has developed a cable short sample test facility that is widely used as a bench mark for NbTi Rutherford-type cables.

– The critical current values measured at BNL provides accurate estimations of the maximum quench currents of accelerator magnets.

Short Sample Test (Courtesy A. Ghosh)

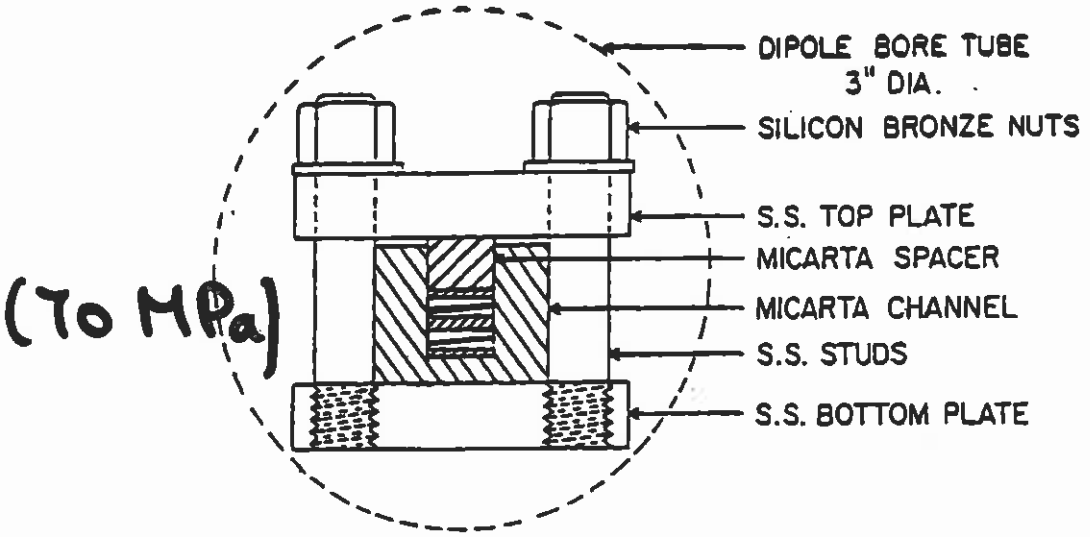

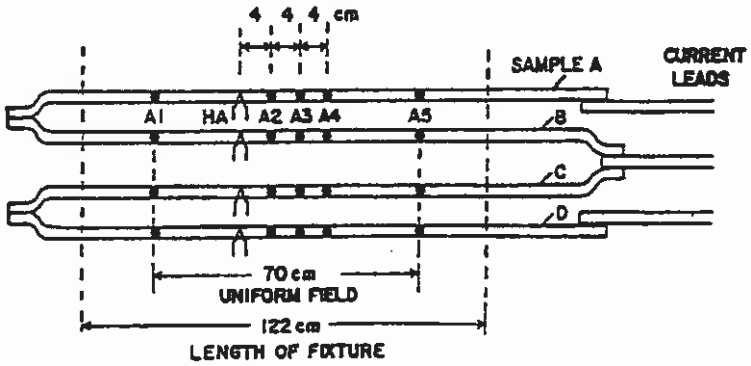

Fig. 4. Setup for short-sample measurement. Four cable samples are clamped together in a micarta channel with compression applied by the bolts which run along each side of the channel. The voltage across each sample can be measured independently. The whole fixture is placed in the bore of a dipole which provides the magnetic field.

V-I Characteristic of Cables
part I: Critical Current

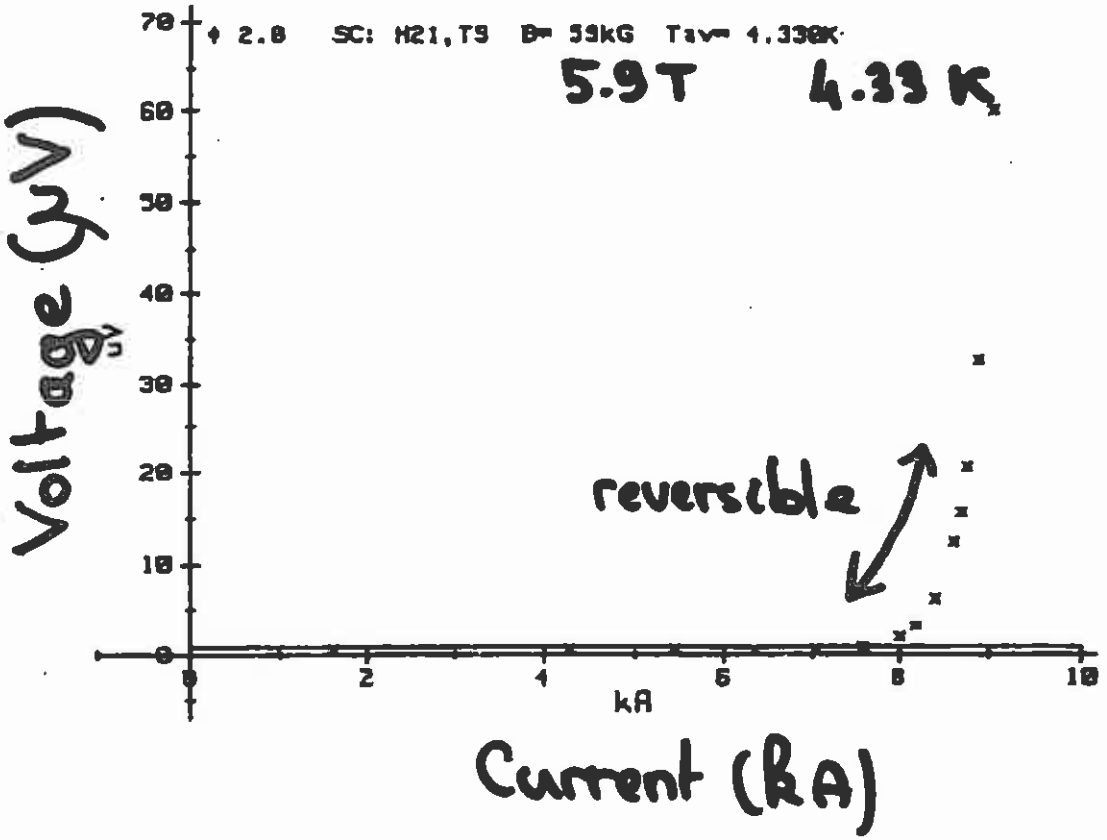

I_c is commonly defined as the current for which

$\left(\frac{V}{I}\right) \sim 10^{-14}\,\Omega m$

$I_c \sim 8375\,A$

$I_q \sim 9100\,A$

V-I Characteristic of Cables
part II: Transition Index

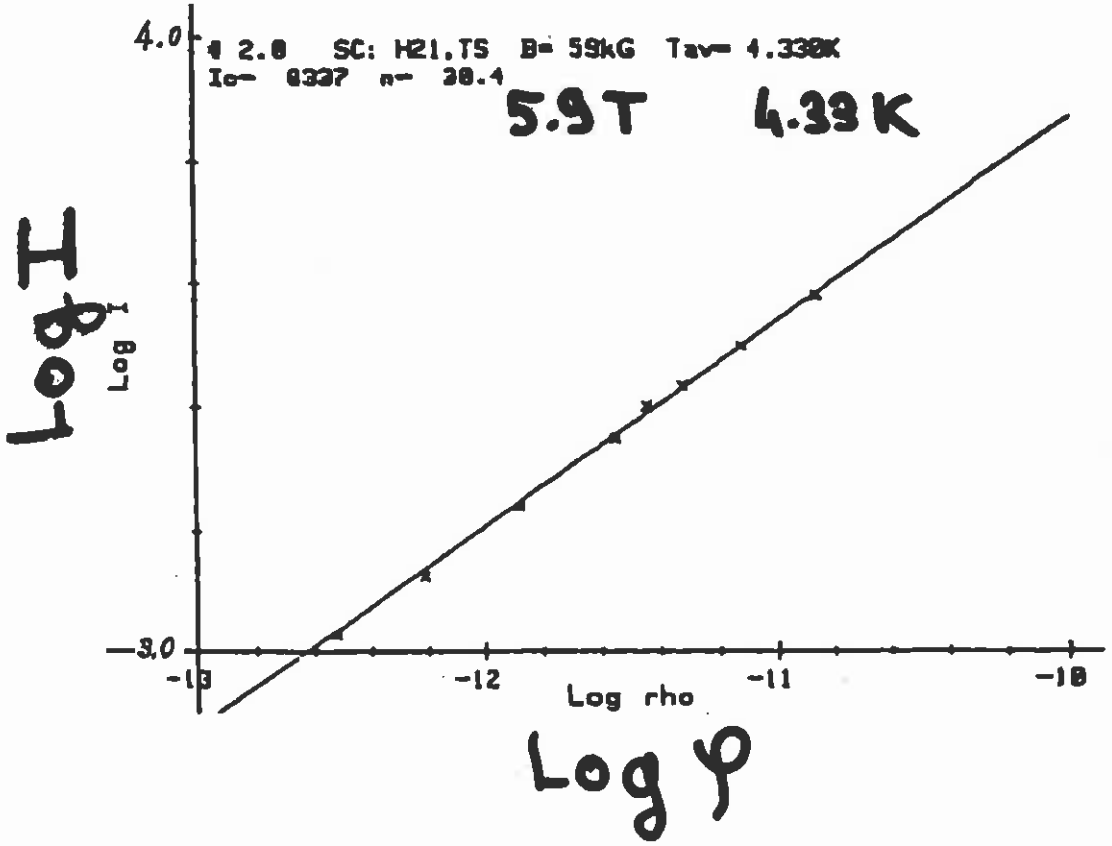

$$\rho = 10^{-N}\left(\frac{H}{H_c}\right)^N$$

where N characterises the transition width

N ≈ 30

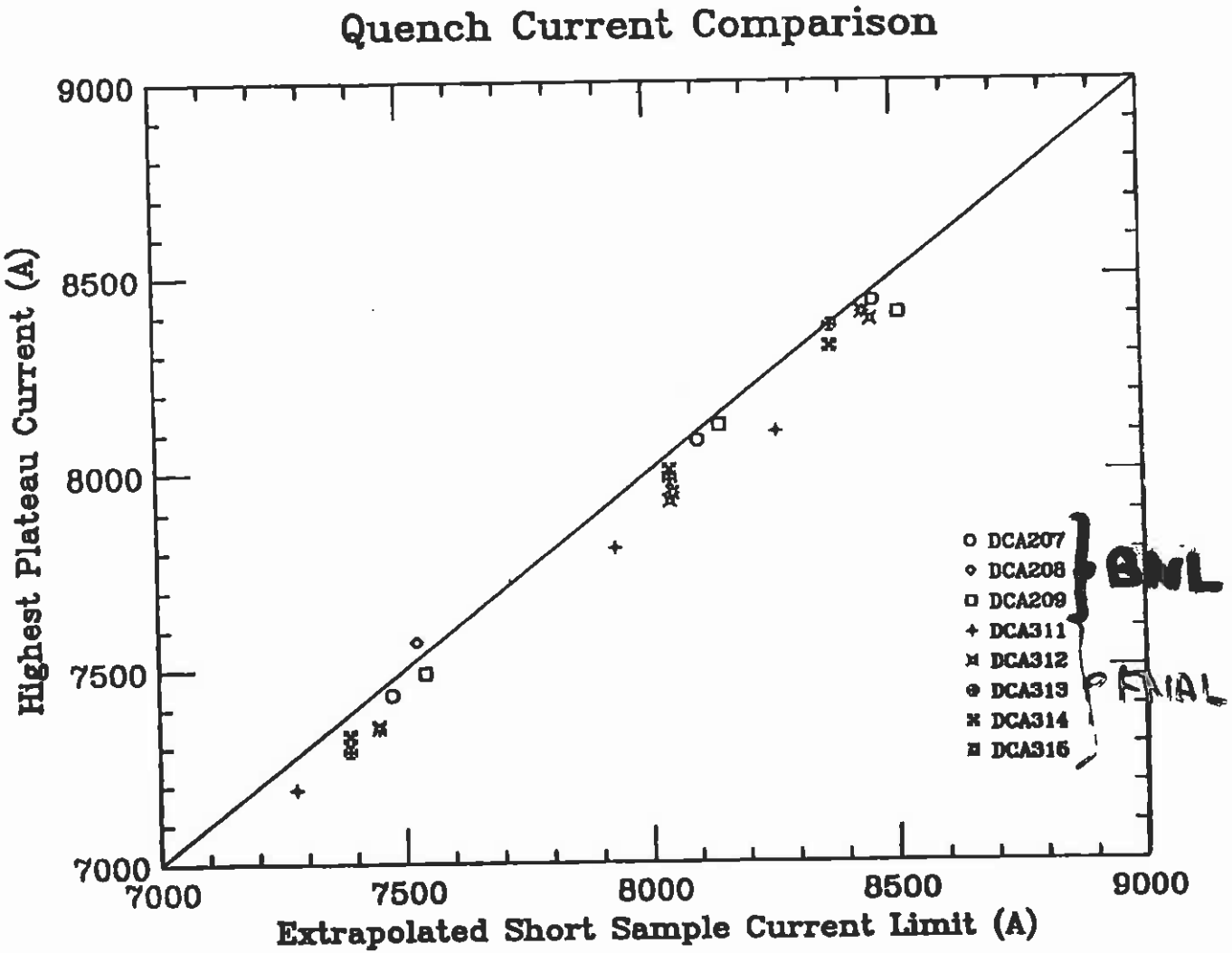
Quench Current Comparison
Highest Plateau Current (A)
Extrapolated Short Sample Current Limit (A)
9000
8500
8000
7500
7000
7000
7500
8000
8500
9000
DCA207
DCA208
DCA209
DCA311
DCA312
DCA313
DCA314
DCA315
BNL
FNAL

CRITICAL CURRENT MEASUREMENTS ON NB3SN CABLES

– The critical current of Nb_3Sn Rutherford-type cables has been shown to be sensitive to transverse pressure and requires elaborate test setups to be measured in conditions relevant to accelerator magnet operations.

I_c vs. σ experimental setup at University of Twente

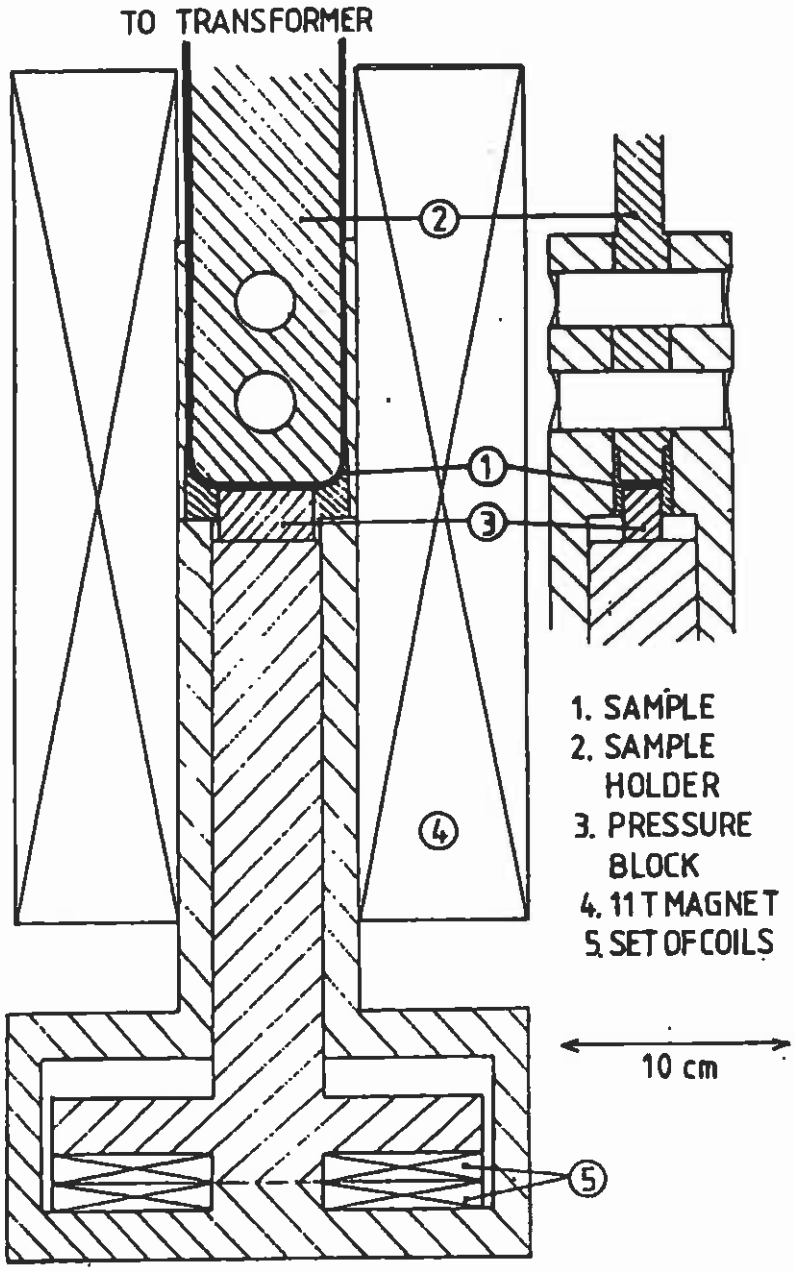

Fig. 1. Schematic view of press-arrangement.

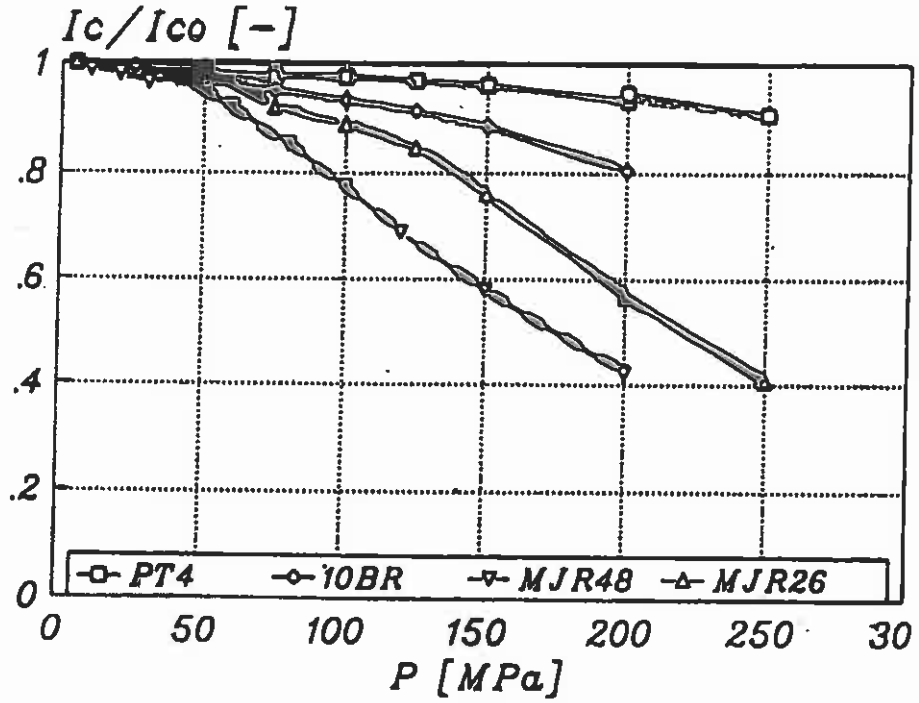

Fig. Scaled critical current versus the applied transverse stress for several cable samples.

H.H.J. ten Kate, 1993

Table Characteristics of the Nb_3Sn Rutherford type of cabled conductors.

Type:	(1) ecn lhc-b	(2) ecn sultan	twca/lbl (3)	twca/lbl (4)	vac-lhc-a (5)
Production:	powder in tube	powder in tube	MJR 26	MJR 48	bronze route
Model:	keystoned	rectangular	keystoned	keystoned	keystoned
Dimensions [mm]:	(1.53/1.85)16.6	(1.82/1.82)18.2	(2.21/2.51)17.0	(1.07/1.29)15.8	(2.19/2.69)16.8
Number of strands:	36	36	26	48	24
Number of filaments:	192	192	6 subelements	36 subelements	50000
Diameter strand [mm]:	0.90	1.00	1.29	0.65	1.38
Matrix:	Cu	Cu	Cu/CuSn/barr.	Cu/CuSn/barr.	Cu/CuSn/barr.
% Cu [%]	57	55	48	56	29
Pitch cable [mm]	120	160	119	109	150
Measured Ic@11T [kA]:	16.5	19.6	9.2	3.3	15.1
Samples:	1PT	2,3,4,5 PT	7,8,9 MJR26	6 MJR48	10,11 BR

LECTURE 3: CONDUCTOR AND CONDUCTOR INSULATION FOR PARTICLE ACCELERATOR MAGNETS

3.1 Review of Superconducting Materials
- 3.1.1 NbTi Alloys
- 3.1.2 Nb_3Sn Compounds
- 3.1.3 HTS

3.2 Superconducting Multifilamentary Composites

3.3 Transition of Multifilamentary Wires

3.4 Manufacturing of NbTi Wires

3.5 Manufacturing of Nb_3Sn Wires

3.6 Critical Surface Parametrizations

3.7 Rutherford-Type Cables

3.8 Interstrand Resistances in Rutherford-Type Cables

3.9 Critical Current Measurements on Rutherford-Type Cables

3.10 Cable Insulation

Appendix: Material Properties at Low Temperatures

CABLE INSULATION REQUIREMENTS

– The main requirements for cable insulation are:

• ***good dielectric strength*** in helium environment and under high transverse pressure (up to 100 Mpa),

(Note that, although the dielectric strength of liquid helium at 4.2 K is fairly good, that of helium gas is significantly worse and keeps degrading with increasing temperature.)

• ***Small thickness*** (to maximize overall current density in the magnet coil) ***and good physical uniformity*** (to ensure proper conductor positioning for field quality),

• ***Retention of mechanical properties*** over a wide temperature range,

• ***Ability to withstand radiations*** in an accelerator environment.

– In addition, the insulation system is required to provide a mean of bonding the coil turns together so as to give the coil a semi rigid shape and facilitate its manipulation during the subsequent steps of magnet assembly.

– It is also desirable that the insulation be somewhat porous to helium and/or offers good heat transfer for conductor cooling.

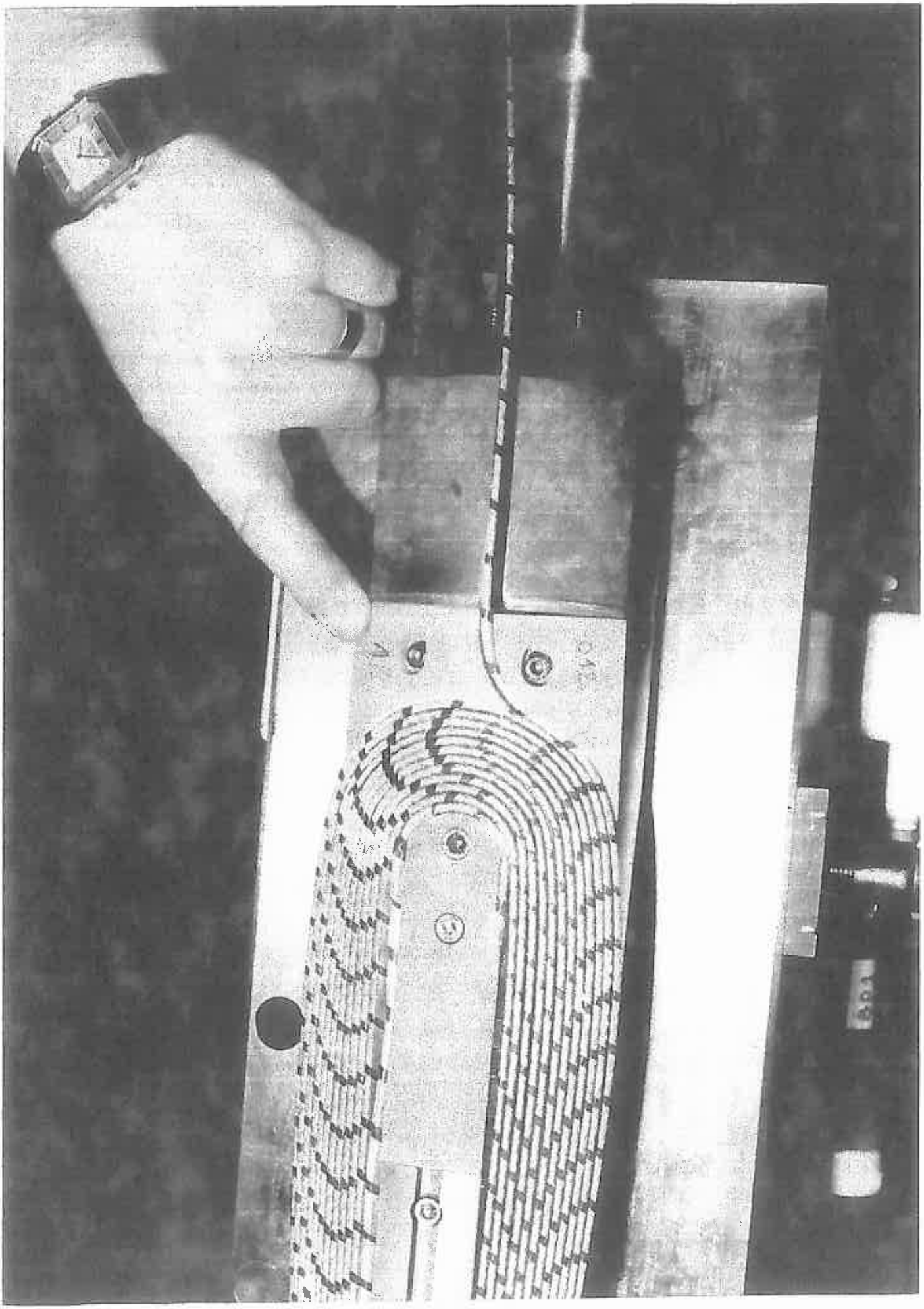

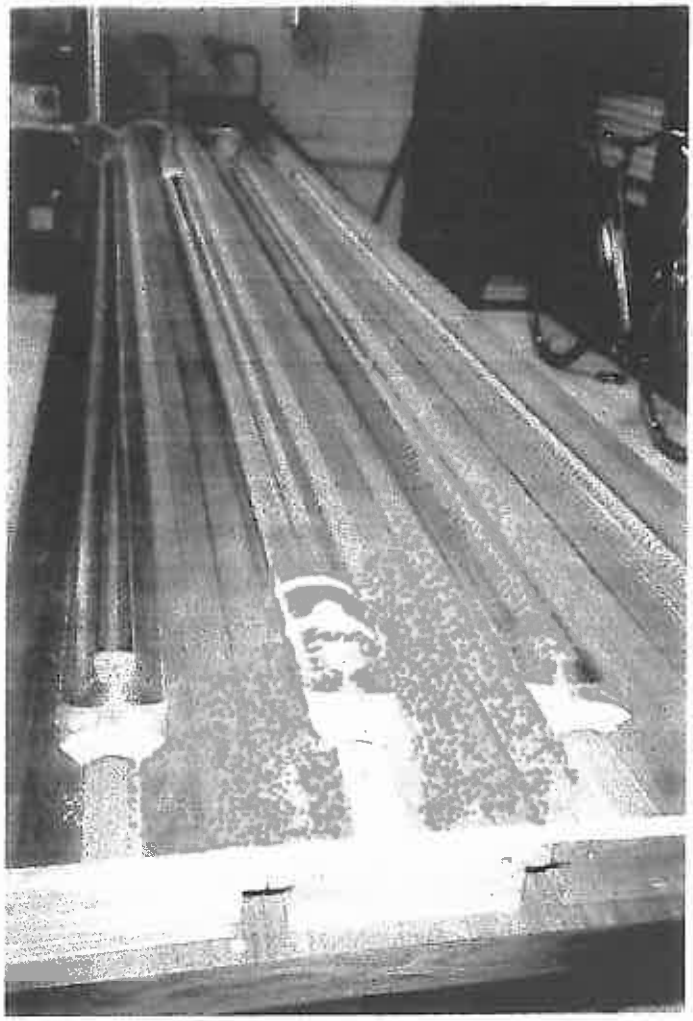

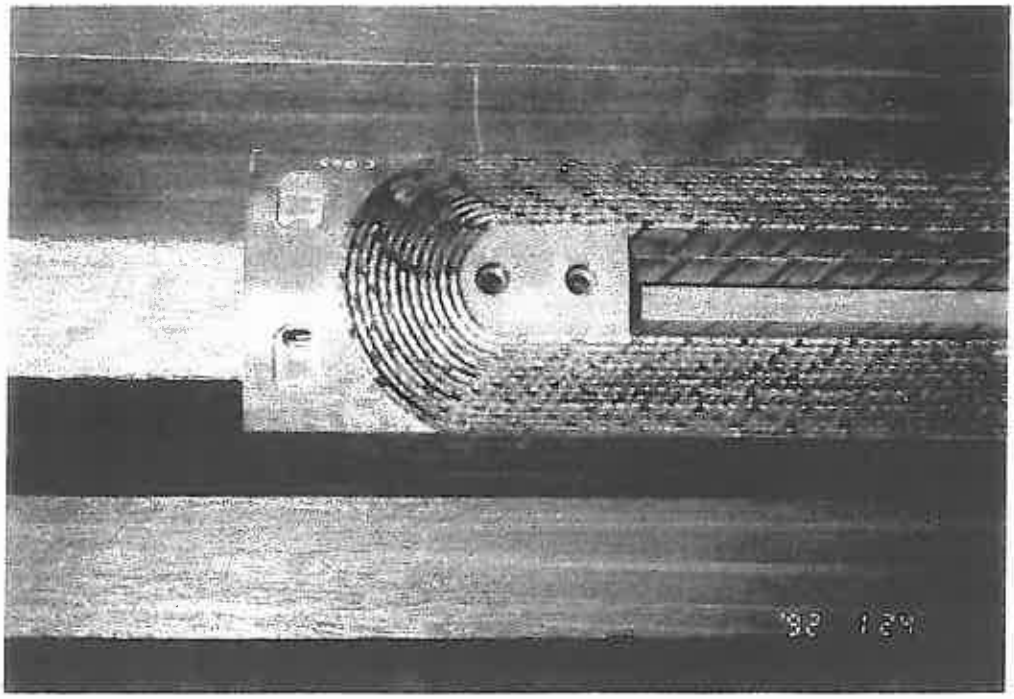

INSULATION OF NBTI CABLES

– The insulation of Tevatron, HERA and UNK magnets, of most SSC magnets and of the early LHC magnet models is made up of one or two inner layers of polyimide film, wrapped helically with a 50-to-60% overlap, completed by an outer layer of resin-impregnated glass fiber tape, wrapped helically with a small gap.

– The inner layer is wrapped with an overlap for at least two reasons:

- *The polyimide film may contain pin holes* which have to be covered (the probability of having two superimposed pin holes in the overlapping layer is very low),

- *The Tevatron experience has shown that it was preferable to prevent the resin impregnating the glass wrap from entering in contact with the NbTi cable* (the energy released by cracks in the resin is believed to be sufficient to initiate a quench).

– The outer layer is wrapped with a gap to set up helium cooling channels between coil turns.

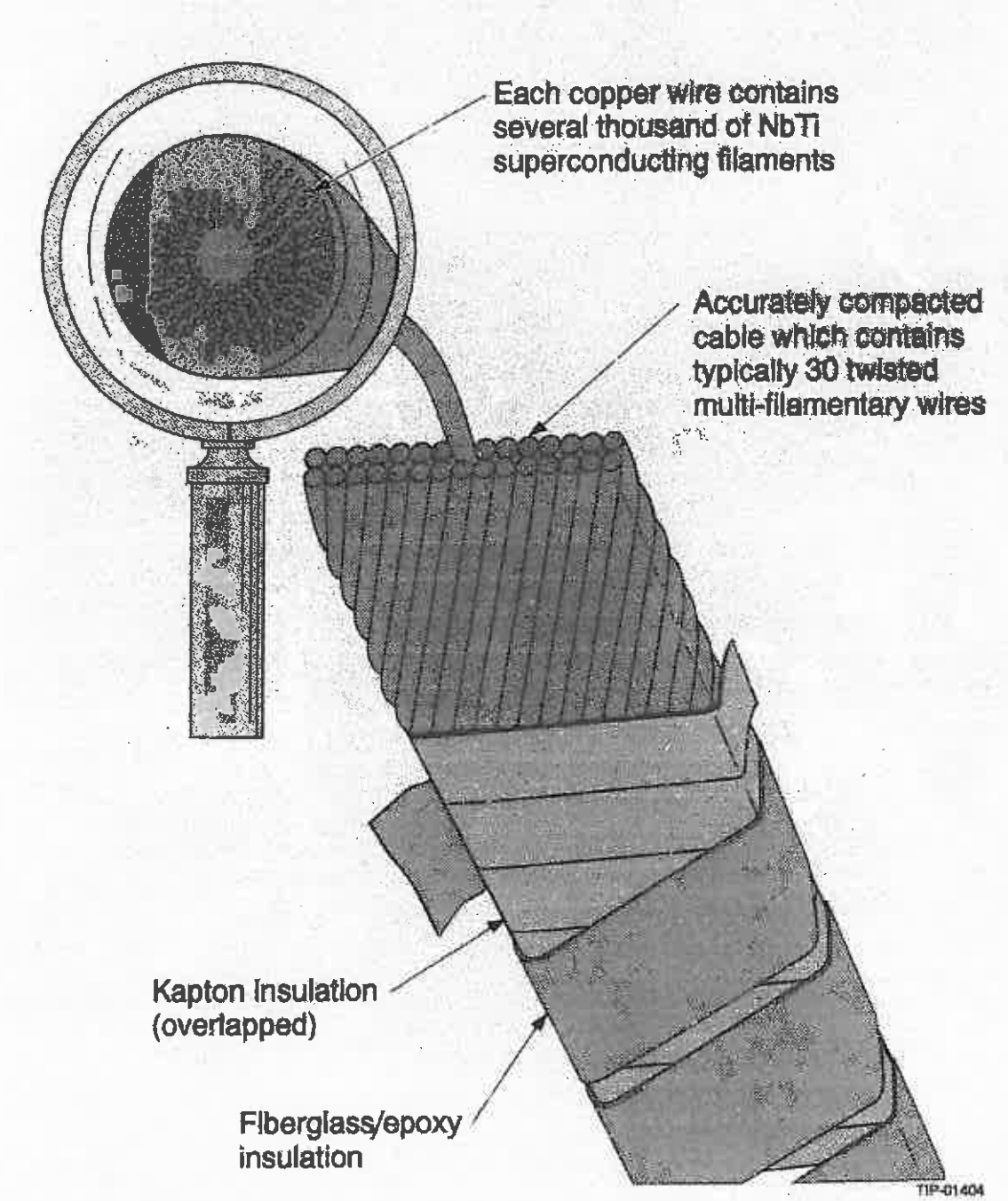
Each copper wire contains several thousand of NbTi superconducting filaments
Accurately compacted cable which contains typically 30 twisted multi-filamentary wires
Kapton insulation (overlapped)
Fiberglass/epoxy insulation
TIP-01404

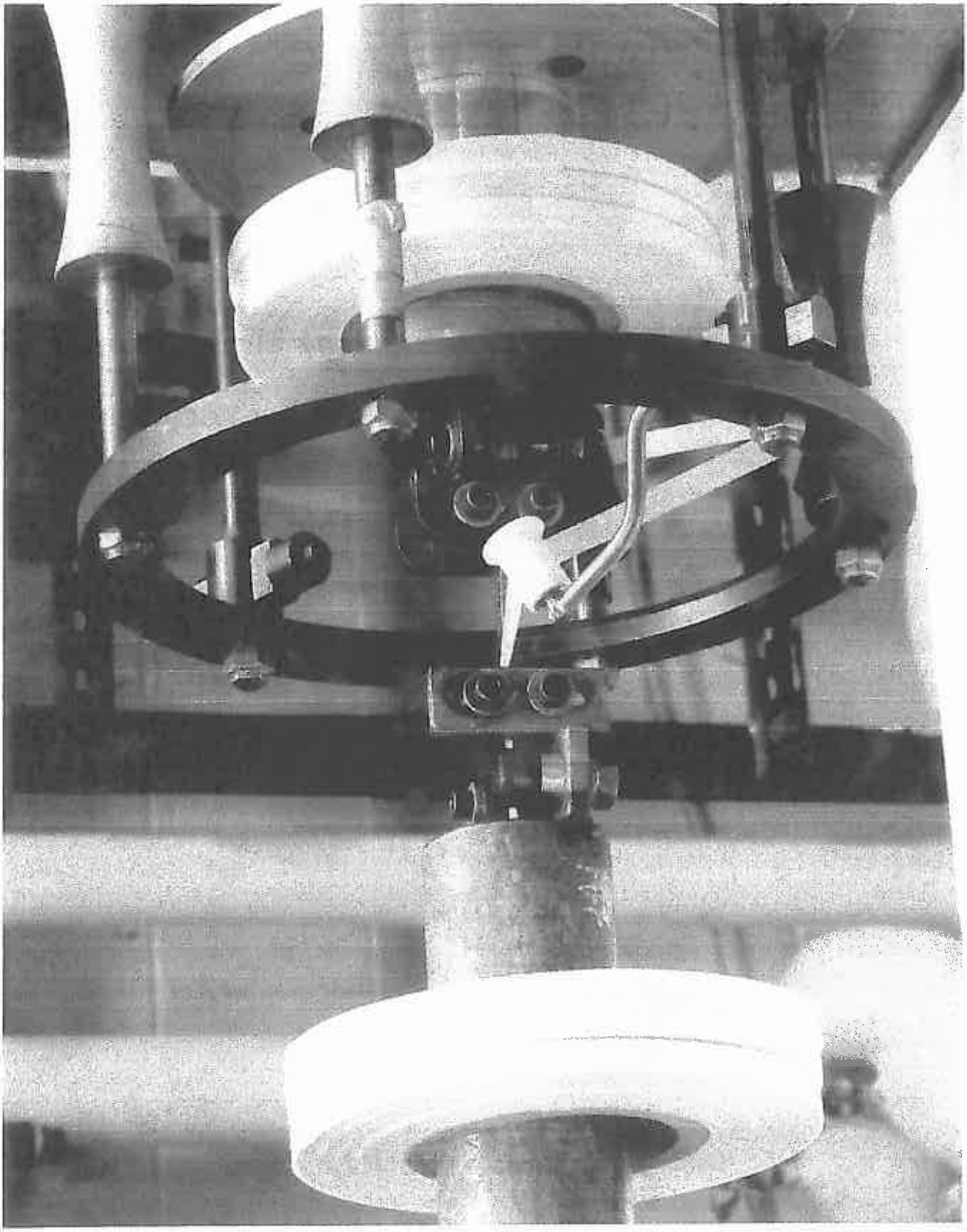

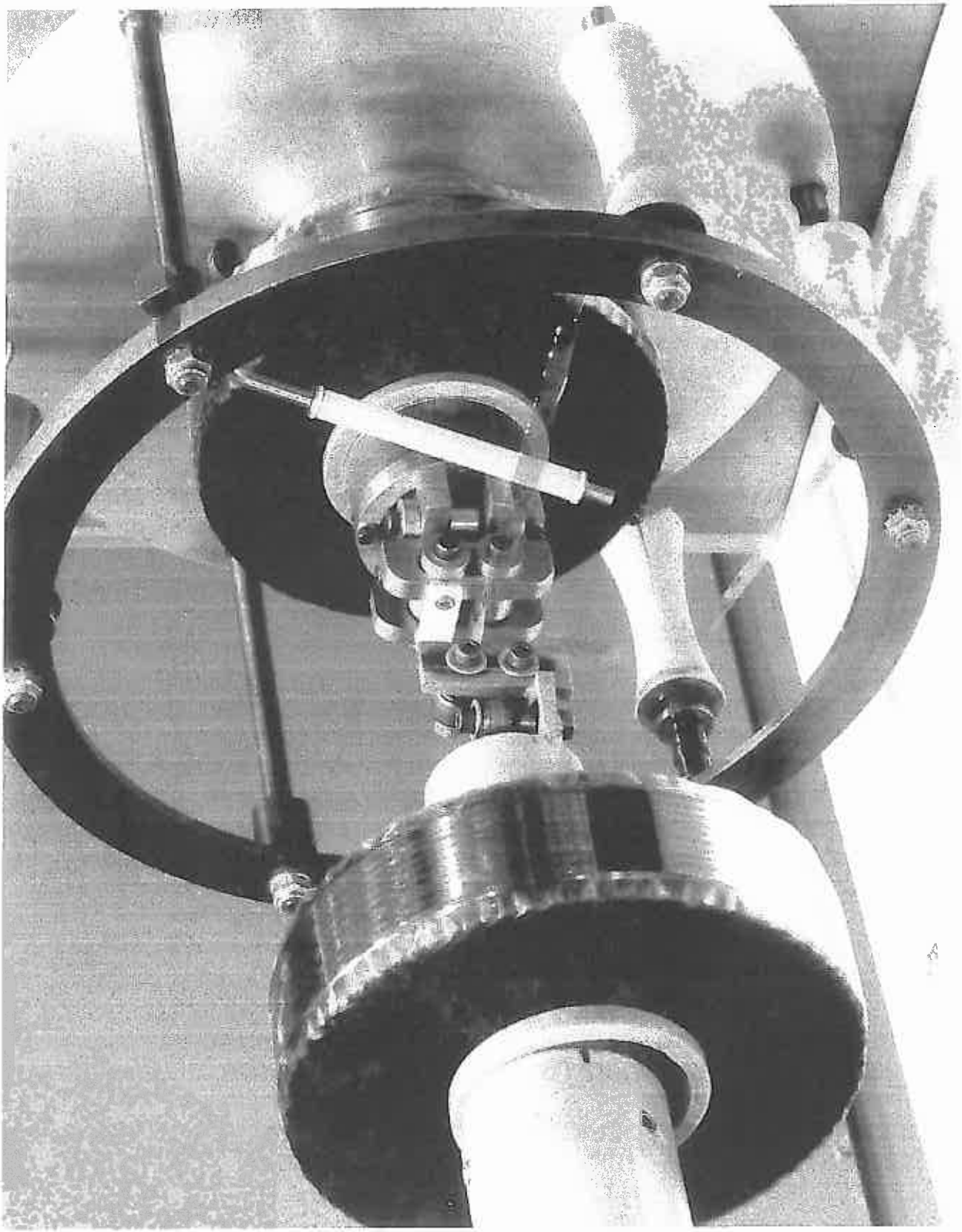

INSULATION OF NBTI CABLES (CONT.)

– The resin is of thermosetting-type and requires heat to increase cross link density and cure into a rigid bonding agent.

– The curing is realized after winding completion in a mold of very accurate dimensions to control coil geometry and Young's modulus.

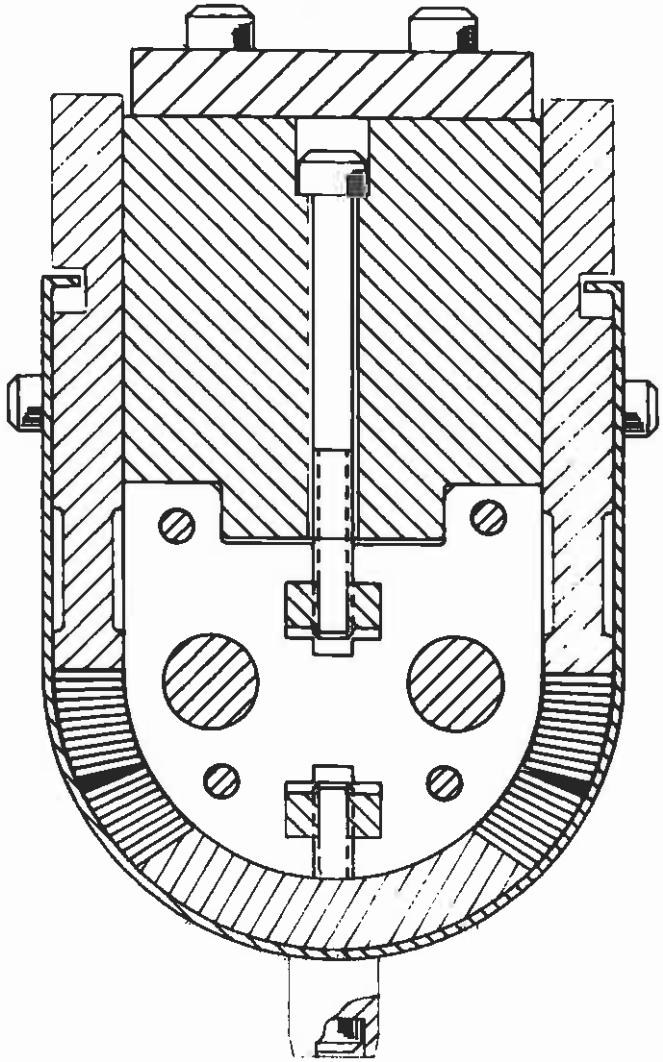

MANDREL, COIL, PUSHER BAR & RETAINER

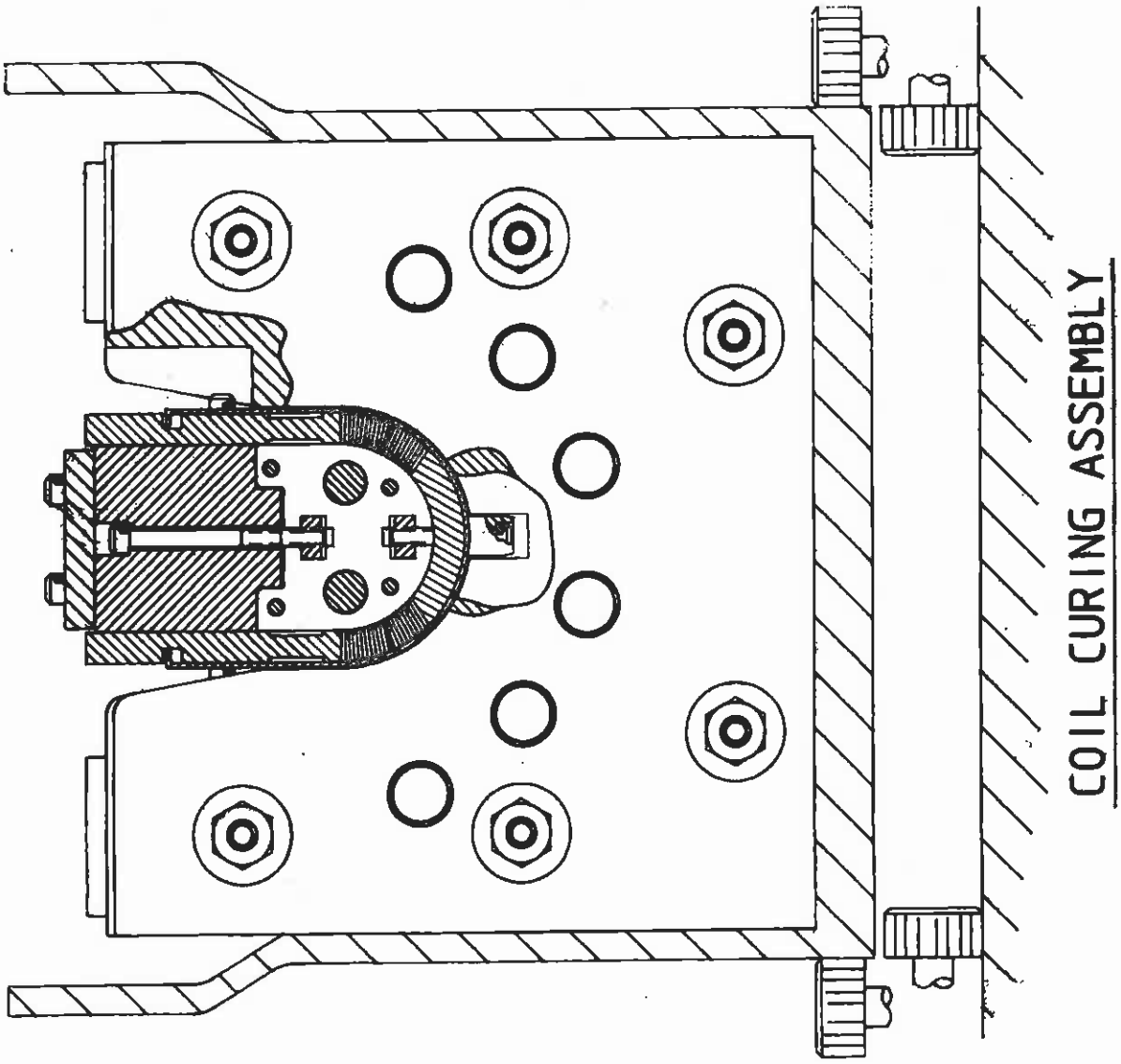
COIL CURING ASSEMBLY

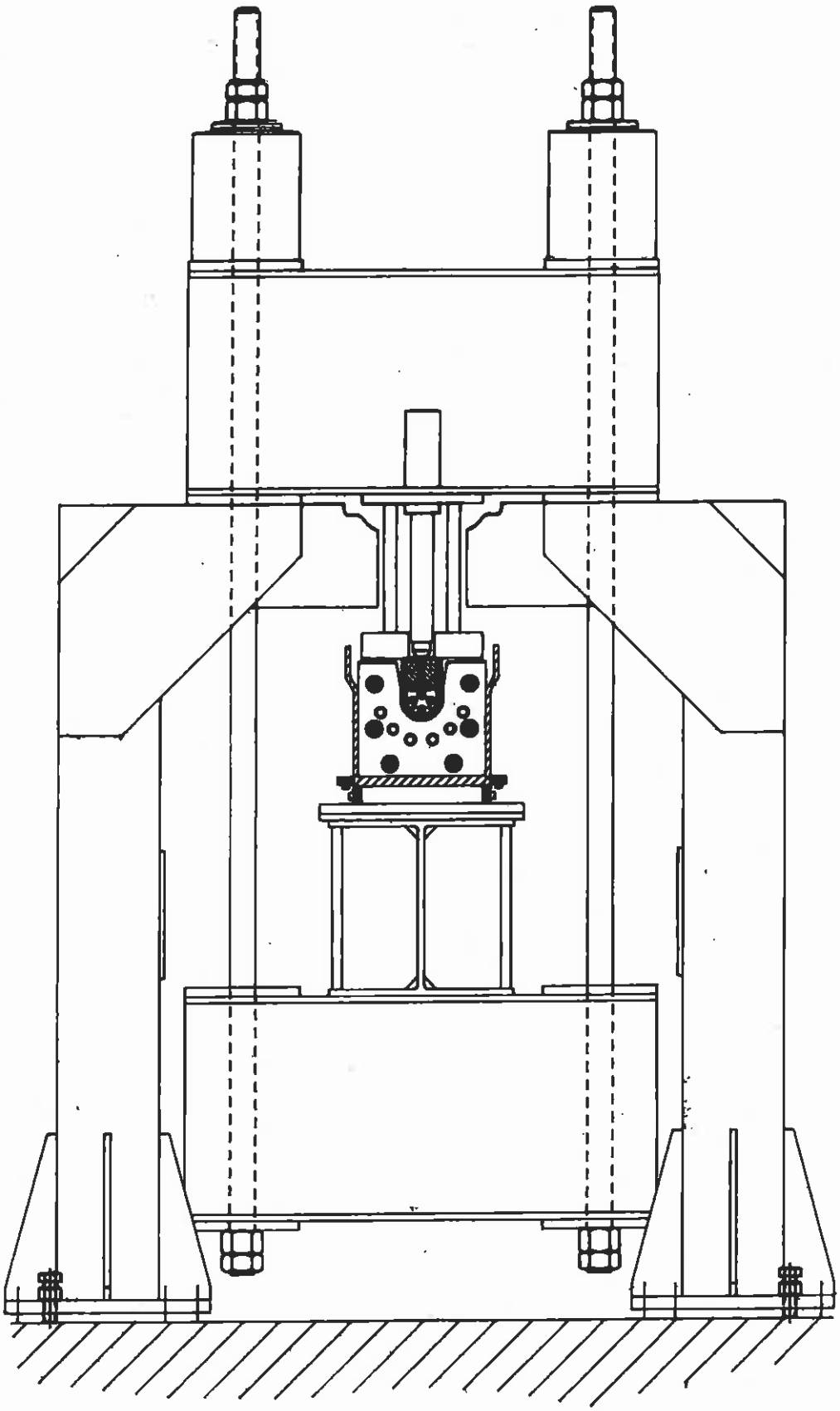

COIL CURING FIXTURE & PRESS

ALL-POLYIMIDE INSULATION OF NBTI CABLES

– RHIC magnets and the most recent LHC magnet models use a so-called *all-polyimide* insulation where the outer glass fiber wrap is replaced by another layer of polyimide film with a polyimide adhesive on its surface.

– The all-polyimide insulation has a better resistance to puncture but the softening temperature of the adhesive can be higher than the temperature needed to cure a conventional resin (225 °C for RHIC-type all-polyimide insulation compared to 135 °C for SSC-type polyimide/glass insulation).

HEAT TRANSFER THROUGH CABLE INSULATION

– For NbTi cables operated in superfluid helium, it has been shown that the heat transfer through the insulation (upon static heat deposition on the cables simulating the effects of synchrotron radiation) was strongly influenced by:

- The number of layer wrap,
- The percentage of overlap of each wrap.

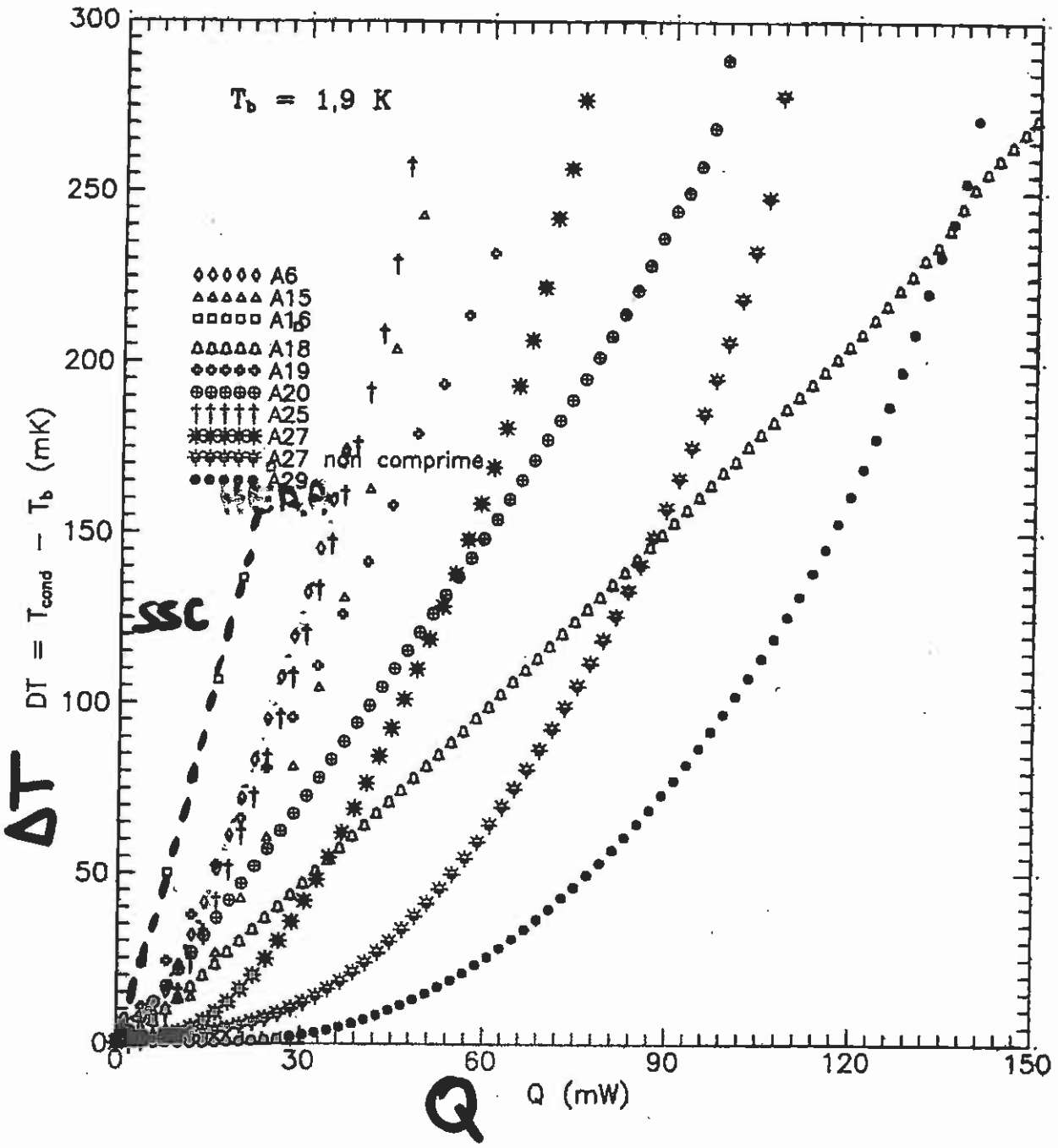

Echauffement du conducteur central J_8 lorsque trois conducteurs sont chauffés Comparaison de différents échantillons

(Courtesy C. Meuris)

INSULATION OF NB_3SN CABLES

– The insulation of Nb_3Sn cables is usually based on a glass fiber tape or a glass fiber sleeve put on the un-reacted conductor prior to winding. Upon winding completion, the coil is heat-treated to form Nb_3Sn. It is then transferred to a precision molding fixture to be vacuum impregnated with resin.

– The glass fibers used for the tape or the sleeve must be able to sustain the heat treatment without degradation.

– Also, all organic materials, such as sizing or finish, must be removed from the fibers to prevent the formation of carbon compounds that may lower the dielectric strength. The sizing removal is performed by carbonization in air prior to conductor insulation.

INSULATION OF NB_3SN CABLES (CONT.)

– The implementation of such an insulation system adds to the difficulty of manufacturing Nb_3Sn coils for at least two reasons:

• De-sized glass fiber tapes or sleeves are fragile and easy to tear off by friction,

• Vacuum impregnation is a delicate operation.

– Furthermore, a full impregnation prevents any helium penetration in the coil, thereby reducing greatly cooling capabilities.

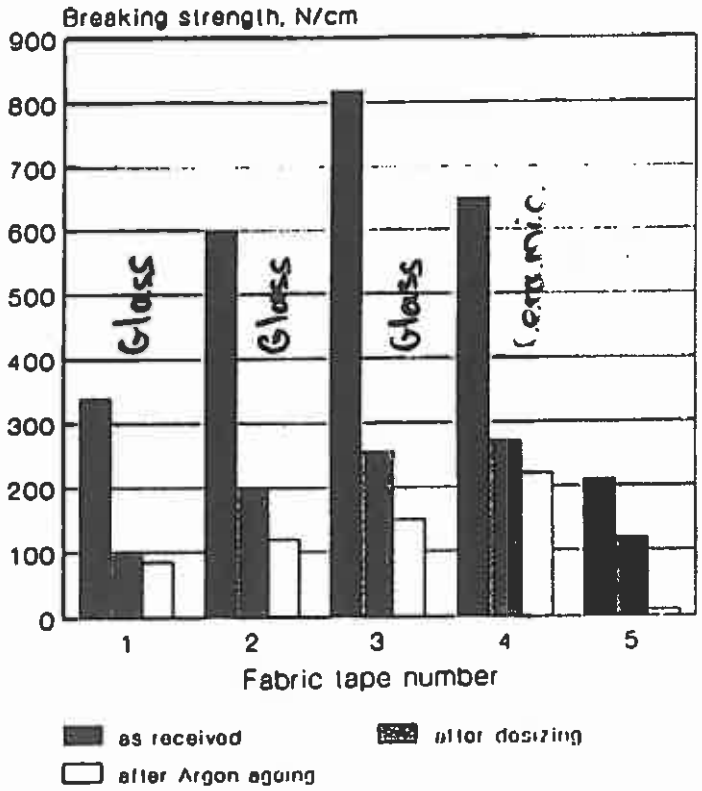

Fig. The breaking strength of the selected fabric tapes before and after desizing

P. Bruggone, 1990

Table : Technical data of the fabric tapes selected for the tests

Tape number	*Type of fiber*	*Fiber size [μm]*	*Fiber number warp*	*woof*	*Tape thickness [mm]*	*Specific weight [g/m²]*
1	R-glass	1	15	11x2	0.16	189
2	R-glass	5	14	6x2	0.23	244
3	R-glass	9	20	6x2	0.33	333
4	ceramic	5	12	5	0.33	362
5	quartz	4	23	10	0.30	232

LECTURE 3: CONDUCTOR AND CONDUCTOR INSULATION FOR PARTICLE ACCELERATOR MAGNETS

3.1 Review of Superconducting Materials
- 3.1.1 NbTi Alloys
- 3.1.2 Nb_3Sn Compounds
- 3.1.3 HTS

3.2 Superconducting Multifilamentary Composites

3.3 Transition of Multifilamentary Wires

3.4 Manufacturing of NbTi Wires

3.5 Manufacturing of Nb_3Sn Wires

3.6 Critical Surface Parametrizations

3.7 Rutherford-Type Cables

3.8 Interstrand Resistances in Rutherford-Type Cables

3.9 Critical Current Measurements on Rutherford-Type Cables

3.10 Cable Insulation

Appendix: Material Properties at Low Temperatures

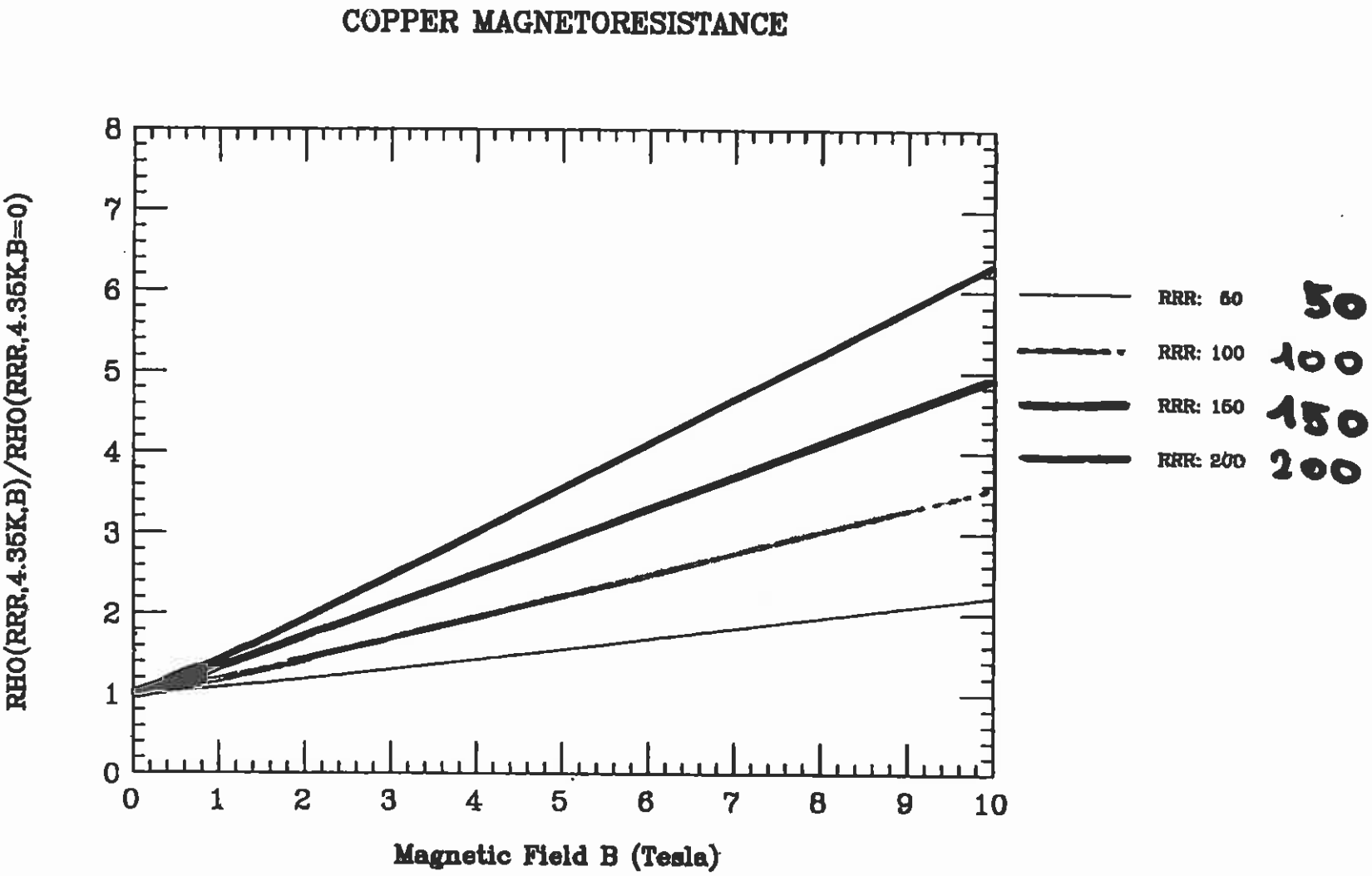
COPPER MAGNETORESISTANCE
RHO(RRR,4.35K,B)/RHO(RRR,4.35K,B=0)
Magnetic Field B (Tesla)
0
1
2
3
4
5
6
7
8
9
10
RRR: 50
RRR: 100
RRR: 150
RRR: 200
50
100
150
200

Resistivity Comparison

Copper :

at Room Temp. : $1.6\ 10^{-8}\ \Omega m$

at 10 K, 0 T : $1.6\ 10^{-10}\ \Omega m$
(RRR = 100)

at 10 K, 7 T : $4.3\ 10^{-10}\ \Omega m$
(RRR = 100)

NbTi :

in Normal State : $5\text{-}6\ 10^{-7}\ \Omega m$

Resistivity of Interfilament Copper (part I)

For Copper:

$$\rho_{Cu} \times l = \frac{m v_F^*}{n e^2} \sim 6.56\ 10^{-16}\ \Omega m^2$$

where l is the electron mean free path

- At Room Temperature

  $\rho_{Cu} = 1.6\ 10^{-8}\ \Omega m$

  $l \sim 0.04\ \mu m \ll d$

- At 4.2 K

  RRR ~ 100

  $\rho_{Cu} = 1.6\ 10^{-10}\ \Omega m$

  $l \sim 4.1\ \mu m > d$

where d is the interfilament spacing

* Kittel, pp 216-217

Resistivity of Interfilament Copper (part II)

$\Rightarrow$ At cryogenic temperatures, surfaces of NbTi filaments act as boundary scatterers, resulting in a resistivity enhancement

$$\rho_{interfil} \sim \rho_{Cu} \times \left(1 + \frac{l}{d}\right)$$

$$RRR_{interfil} \sim RRR \times \left(1 + \frac{l}{d}\right)^{-1}$$

e.g., for SSC wire

$RRR \sim 100$

$RRR_{interfil.} \sim 20$

Equivalent Resistivity of Wire in the normal state (T ~ 10K)

$$\frac{1}{\rho_e} = \underbrace{\frac{X - X_L}{1+X}\,\frac{1}{\rho_{Cu}}}_{\text{Copper Core and Sheath}} + \underbrace{\frac{X_L}{1+X}\,\frac{1}{\rho_{Cu}\left(1+\frac{l}{d}\right)}}_{\text{Interfilament Copper}}$$

where:

- ρ_{Cu} is resistivity of copper bulk
- X copper-to-superconductor ratio
- X_L local area ratio of composite
- l electron mean free path
- d interfilament spacing

Thermal Conductivity at Low Temperatures

- Normal Metals

  $k\rho = LT$ $\quad T < 10\text{–}20\ K$

  Wiedeman–Franz Law

  $L = 2.44\ 10^{-8}\ V^2/K^2$

  (Lorentz Constant)

  Remain true under field

- Niobium–Titanium

  $k = 7.5\ 10^{-3}\ T^{1.85}$ * $\quad T < 10\ K$

* C. Schmidt, 1979

Thermal Conductivity of Kapton vs. Temperature

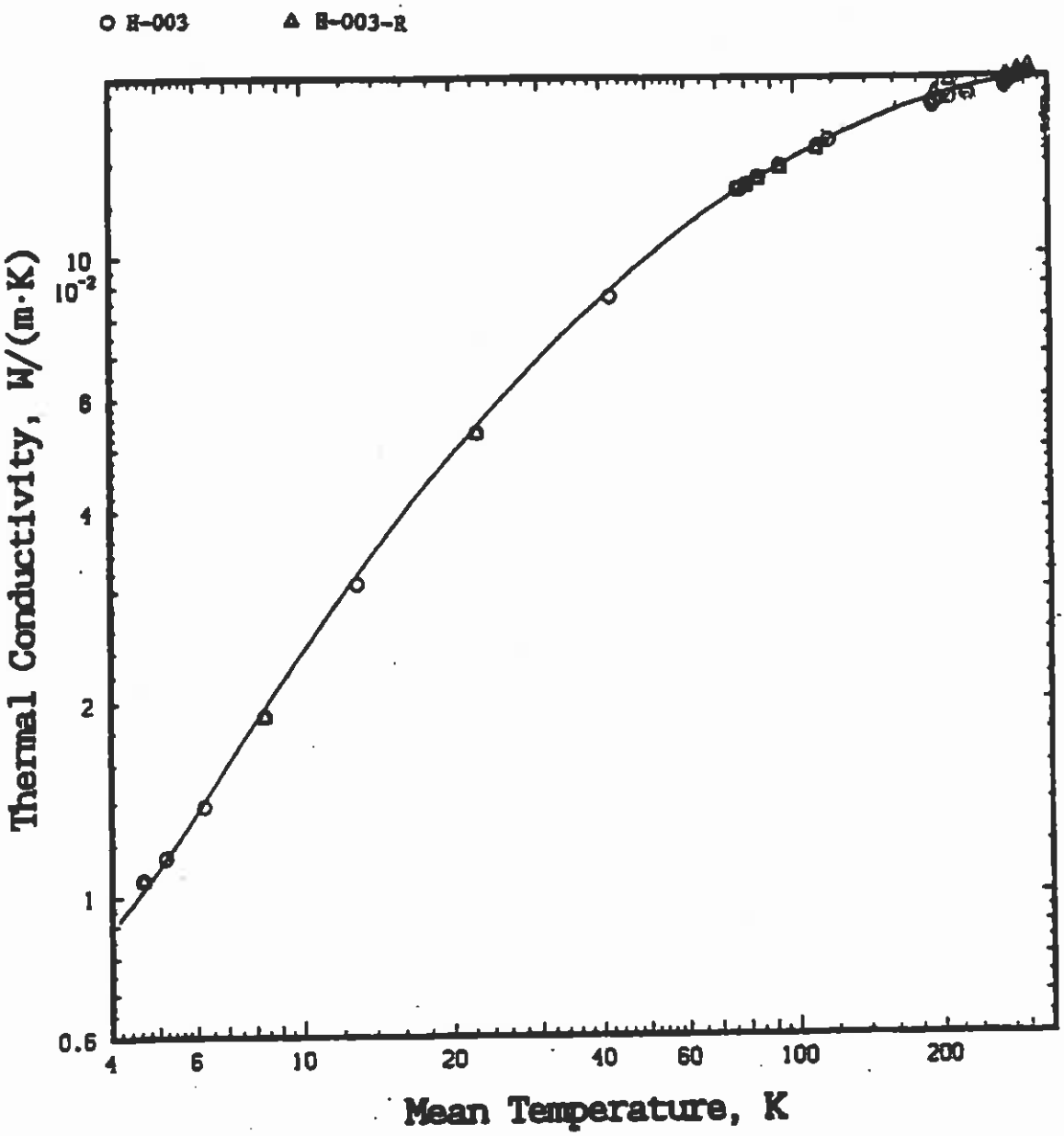

Figure 7. Thermal conductivity of PPMI film specimen H-003. Experimental data are presented as discrete points. Two specimens were tested to determine reproducibility. Note that both scales are logarithmic, which clarifies the behavior at low temperatures.

Thermal Conductivity Comparison (in $W m^{-1} K^{-1}$)

	4.35 K	10 K
Copper (RRR: 100) at 0 T	680	1540
Copper (RRR: 100) at 7 T	250	570
NbTi	0.11	0.53
Kapton H	0.012	0.031

Specific Heat of Normal Metals at Low Temperatures

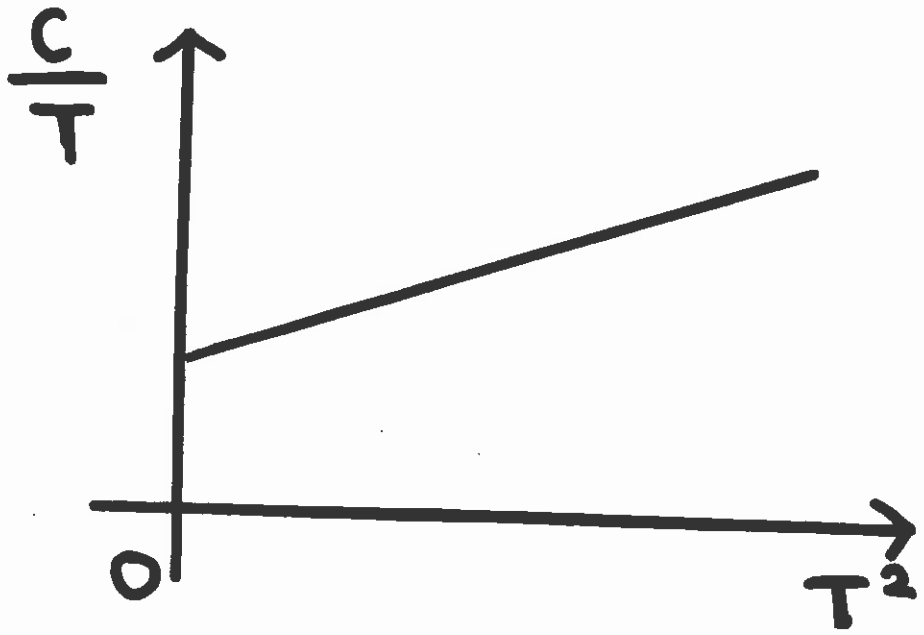

$$C = \underbrace{\beta T^3}_{\text{Phonons (Debye)}} + \underbrace{\gamma T}_{\text{Electrons (Sommerfeld)}}$$

Specific Heat of Superconductors at low Temperatures

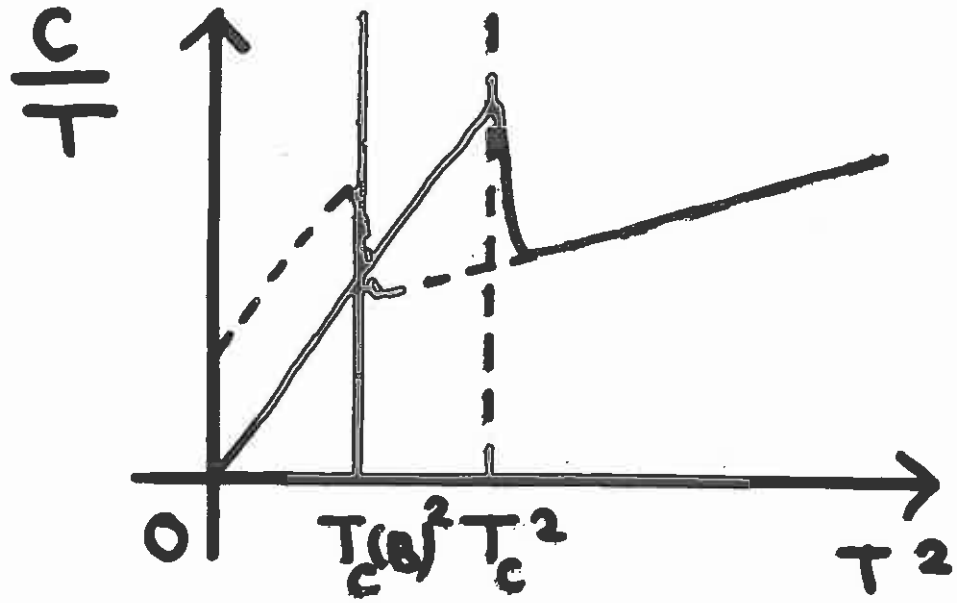

- For $T > T_c(B)$

$$C = \beta T^3 + \gamma T$$

- For $T < T_c(B)$

$$C = \left(\beta + \frac{3\gamma}{T_{c(B)}^2}\right) T^3 + \underbrace{\frac{\gamma}{H_c} B.T}_{\text{If in Magnetic Field}}$$

Specific Heat Data*

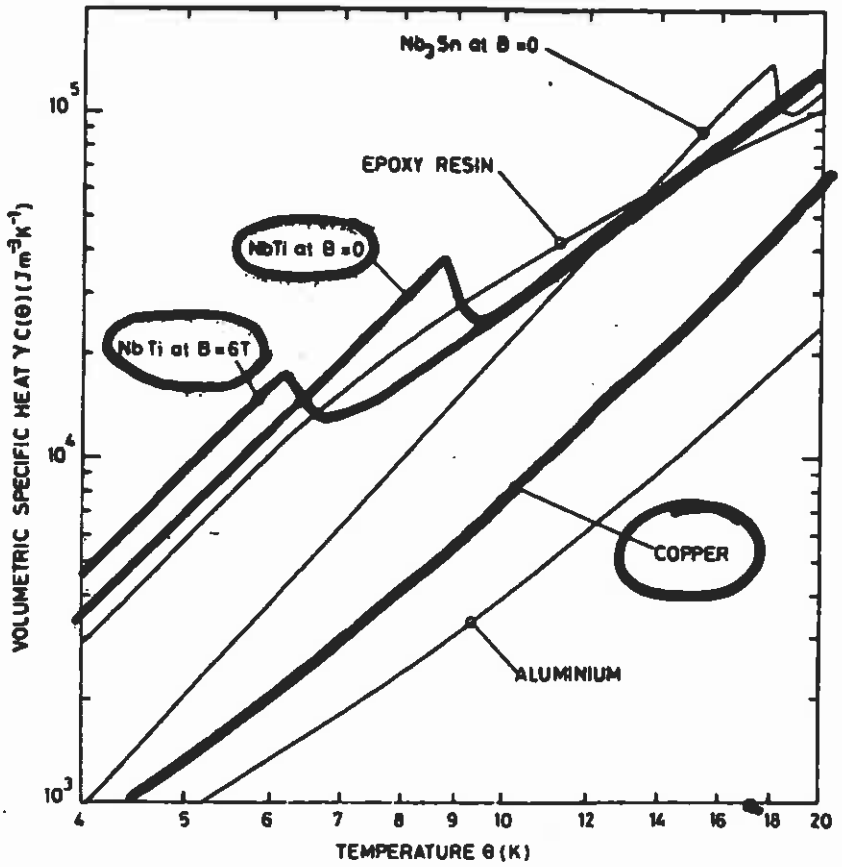

Fig. 5.3. Volumetric specific heat of some materials commonly used in magnets. Data for NbTi are average values based on measurements by J. Corsan, National Physical Laboratory (private communication) and R. Lagnier and E. Bonjour, CEN Grenoble (private communication). Data for Nb_3Sn is from Grigsby D. L. (US Department of Commerce NTIS Report AD-838469) and remaining data is from Johnson (1961).

* Wilson, 1983

Specific Heat and Enthalpy Comparison

	C_p (4.35K) J/m³K	C_p (10K) J/m³K	$\Delta H_{4.35K}^{10K}$ J/m³
Cu	970	7700	19 700
NbTi (0T)	4800	26200	118 000
NbTi (7T)	7800	26200	89 000
Helium (4atm)	540 000	135 000	(-) 260 000

DAPNIA/STCM 99-05 September 1999

ARGONNE LECTURES ON PARTICLE ACCELERATOR MAGNETS

VOLUME B

Arnaud Devred

(Prepared for the US Particle Accelerator School at Argonne National Laboratory, sponsored by the University of Chicago, June 14-25, 1999)

ARGONNE LECTURES ON PARTICLE ACCELERATOR MAGNETS

VOLUME B

Arnaud Devred

Service des Techniques de Cryogénie et de Magnétisme
Commissariat à l'Energie Atomique/Saclay
F–91191 GIF-SUR-YVETTE CEDEX
FRANCE

(Prepared for the US Particle Accelerator School
at Argonne National Laboratory,
sponsored by the University of Chicago,
June 14–25, 1999)

TABLE OF CONTENTS

VOLUME A

Lecture 1: Magnet Systems for Large Circular Accelerators 1–1

1.1 On the Need of High Energy Accelerators 1–3
1.2 Accelerator Types 1–9
1.3 Synchrotron-Type Accelerators 1–25
1.4 Layout of Large Circular Accelerators 1–37
1.5 Dipole and Quadrupole Magnets for Large Circular Accelerators 1–37
1.6 How to Produce Ideal Dipole and Quadrupole Magnetic Flux Densities? 1–55 1–71

Lecture 2: Superconductivity Applied to Particle Accelerator Magnets 2–1

2.1 Why Superconductivity? 2–3
2.2 Origin of Superconductivity and Critical Temperature 2–9
2.3 Magnetic States of Superconductors and Critical Fields 2–27
2.4 Transport Properties of Superconductors and Critical Current Density 2–51
2.5 Critical State Model 2–63
2.6 Review of Superconducting Particle Accelerators 2–85
2.7 Prominent Features of Superconducting Accelerator Magnets 2–107
2.8 Superconducting Accelerator Magnet R&D 2–119

Lecture 3: Conductor and Conductor Insulation for Particle Accelerator Magnets 3–1

3.1 Review of Superconducting Materials 3–3
3.1.1 NbTi Alloys 3–3
3.1.2 Nb3Sn Compounds 3–15
3.1.3 HTS 3–27
3.2 Superconducting Multifilamentary Composites 3-31
3.3 Transition of Multifilamentary Wires 3–47
3.4 Manufacturing of NbTi Wires 3–69

3.5 Manufacturing of Nb_3Sn Wires 3–91
3.6 Critical Surface Parametrizations 3–119
3.7 Rutherford-Type Cables 3–131
3.8 Interstrand Resistances in Rutherford-Type Cables 3–157
3.9 Critical Current Measurements on Rutherford-Type Cables 3–171
3.10 Cable Insulation 3–183
Appendix: Material Properties at Low Temperatures 3–203

VOLUME B

Lecture 4: Magnetic Design of Particle Accelerator Magnets 4–1

4.1 Complex Formalism for Two-Dimensional Fields 4–3
4.2 Multipole Field Expansion for Two-Dimensional Fields 4–15
4.3 Field Computations for Simple Current Distributions 4–33
4.4 Two-Dimensional Cosθ and Cos2θ Coil Designs 4–59
4.5 Iron Yoke Contribution 4–81
4.6 Operating Current Margin 4–87
4.7 Saddle-Shaped Coil End Designs 4–99
4.8 Other Designs 4–121
4.9 Sagitta of Arc Dipole Magnets 4–135
4.10 High Order Multipole Field Corrector Magnets 4–139

Lecture 5: Mechanical Design of Particle Accelerator Magnets 5–1

5.1 Components of the Lorentz Force in Cosθ and Cos2θ Magnetic Designs 5–3
5.2 Azimuthal Pre-Compression 5–15
5.3 Coil Mechanical Properties 5–31
5.4 Collar Designs 5–47
5.5 Radial Support 5–75
5.5.1 Designs with Self-Supported Collared-Coil Assemblies 5–75
5.5.2 Designs with Fully-Mated Yoke 5–79
5.5.3 Design with Yoke Midplane Gap 5–119
5.5.4 RHIC Magnets 5–143
5.5.5 Azimuthal Pre-Compression Versus Radial Support 5–149
5.6 End Support 5–161
5.7 Other Designs 5–185

Lecture 6: Asssembly of Particle Accelerator Magnets 6–1

6.1 Coil Winding 6–3
6.2 Coil Curing 6–17
6.3 Azimuthal Coil Size Measurements 6–31
6.4 Coil Assembly and Internal Splicing 6–45

6.5	Collaring	6–55
6.6	Collar Deflection Measurements	6–77
6.7	External Splicing	6–87
6.8	Yoke Stacking and Shell Welding	6–93
6.9	Yoke Midplane Gap Measurements	6–107
6.10	Cryostating	6–121
6.11	Instrumentation	6–135

VOLUME C

Lecture 7: Field Quality of Particle Accelerator Magnets 7–1

7.1 Field Quality Requirements 7–3
7.2 Field Quality Measurements 7–13
7.3 Geometric Errors 7–29
7.4 Iron Saturation 7–63
7.5 Superconductor Magnetization 7–91
7.6 Time Drift of Superconductor Magnetization at Injection 7–109
7.7 Interstrand Coupling Currents 7–149
7.8 Periodic Pattern 7–197

Lecture 8: Quench Performance of Particle Accelerator Magnets 8–1

8.1 Temperature and Enthalpy Margins 8–3
8.2 Magnet Cooling 8–17
8.3 What is a quench? 8–41
8.4 Magnet Training and Quench Plateau 8–47
8.5 Quench Origins 8–61
8.6 Phenomenological Model of Mechanical Training 8–73
8.7 Improving Quench Performance 8–77
8.8 Quench Performance as a Function of Ramp Rate 8–97
8.9 Specifications on Quench Performance 8–119

Lecture 9: Quench Protection of Particle Accelerator Magnets 9–1

9.1 Quench Development 9–3
9.1.1 Simple Theoretical Model 9–3
9.1.2 Measuring Quench Propagation Using Voltage Taps 9–15
9.1.3 Measuring Quench Propagation Using Quench Antenna 9–27
9.1.4 Review of Propagation Velocity Measurements 9–39
9.2 The Effects of a Quench 9–51
9.3 Hot Spot Temperature 9–59
9.4 Quench Detection 9–79
9.5 Quench Protection Heaters 9–87
9.6 Protection of a Single Magnet 9–101
9.7 Protection of a Magnet String 9–113

LECTURE 4: MAGNETIC DESIGN OF PARTICLE ACCELERATOR MAGNETS

4.1 Complex Formalism for Two-Dimensional Fields 4–3

4.2 Multipole Field Expansion for Two-Dimensional Fields 4–15

4.3 Field Computations for Simple Current Distributions 4–33

4.4 Two-Dimensional Cosθ and Cos2θ Coil Designs 4–59

4.5 Iron Yoke Contribution 4–81

4.6 Operating Current Margin 4–87

4.7 Saddle-Shaped Coil End Designs 4–99

4.8 Other Designs 4–121

4.9 Sagitta of Arc Dipole Magnets 4–135

4.10 High Order Multipole Field Corrector Magnets 4–139

LECTURE 4: MAGNETIC DESIGN OF PARTICLE ACCELERATOR MAGNETS

4.1 Complex Formalism for Two-Dimensional Fields

4.2 Multipole Field Expansion for Two-Dimensional Fields

4.3 Field Computations for Simple Current Distributions

4.4 Two-Dimensional Cosθ and Cos2θ Coil Designs

4.5 Iron Yoke Contribution

4.6 Operating Current Margin

4.7 Saddle-Shaped Coil End Designs

4.8 Other Designs

4.9 Sagitta of Arc Dipole Magnets

4.10 High Order Multipole Field Corrector Magnets

CONDUCTOR MODEL AND PROBLEM SYMMETRY

– Let $(O,\vec{x},\vec{y},\vec{z})$ designate a rectangular coordinate system and let us consider an ensemble of conductors parallel to the z-axis and uniform in z.

– Let Σ designate the conductor surface and let $V(\Sigma)$ designate the volume inside the conductors [note that Σ and $V(\Sigma)$ may be multiply connected].

– Furthermore, let us assume that the conductors carry a constant current density, parallel to the z-axis and uniform in z.

– Finally, let G designate a given point of space and let $\vec{J}_G$ designate the current density at G. We have:

$$\vec{J}_G = J_{G,z}(x,y)\,\vec{z} \qquad \text{for G, } G \in V(\Sigma)$$

and

$$\vec{J}_G = \vec{0} \qquad \text{for G, } G \notin V(\Sigma)$$

where $J_{G,z}$ is the z-component of $\vec{J}_G$.

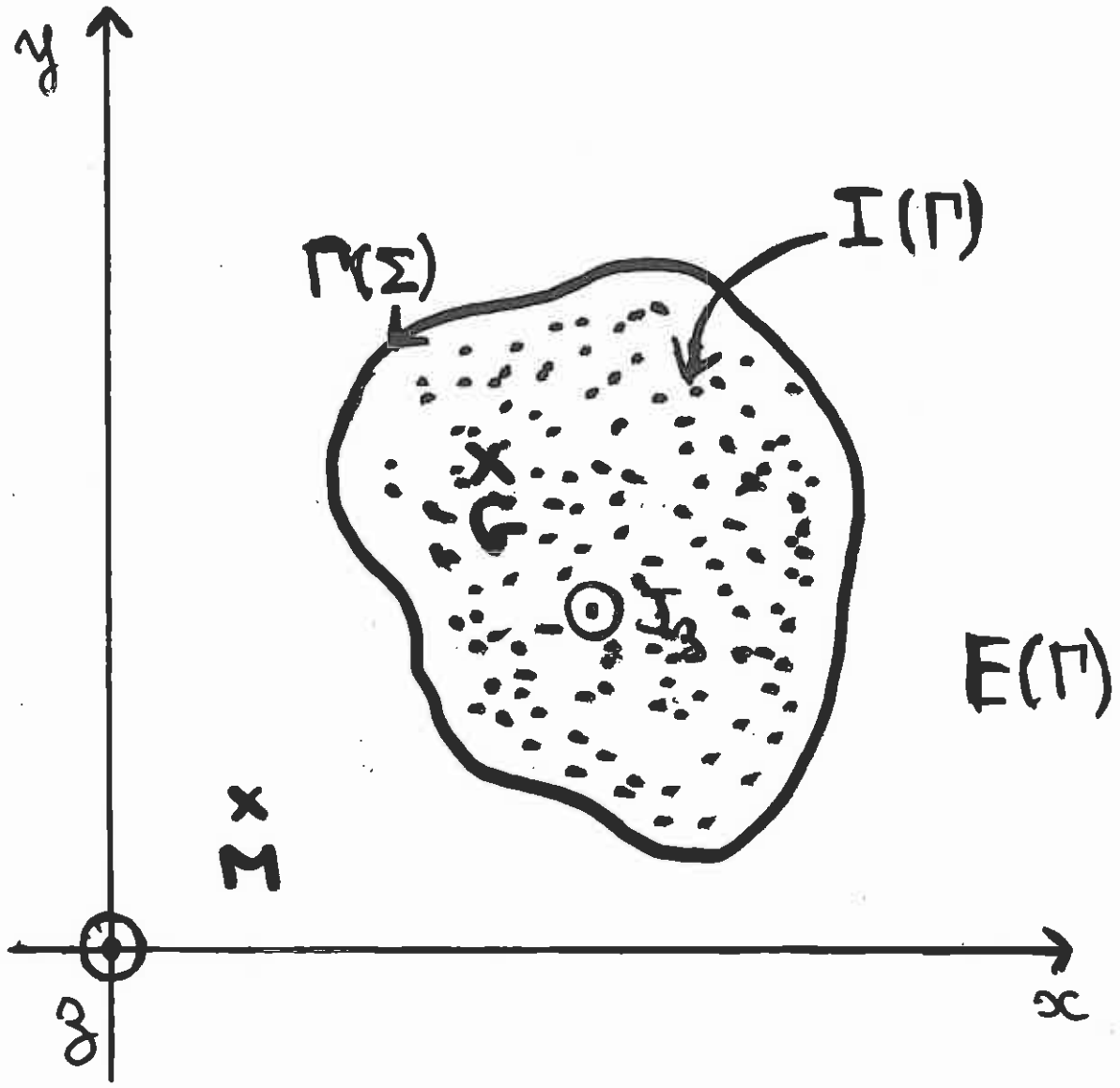
y
Γ(Σ)
I(Γ)
E(Γ)
M
z
x

CONDUCTOR MODEL AND PROBLEM SYMMETRY (CONT.)

– Given the problem symmetry, the magnetic flux density, $\vec{B}_M$, produced at a given point M of space by the currents carried by the conductors is expected to be uniform in z.

– Hence, we can write:

$$\vec{B}_M = B_{M,x}(x,y)\ \vec{x} + B_{M,y}(x,y)\ \vec{y} + B_{M,z}(x,y)\ \vec{z}$$

where $B_{M,x}$, $B_{M,y}$ and $B_{M,z}$ are the x-, y- and z-components of $\vec{B}_M$.

COMPONENTS OF MAGNETIC FLUX DENSITY

– According to Biot and Savart's law, $\vec{B}_M$ can be computed as:

$$\vec{B}_M = \iiint_{V(\Sigma)} dV_G \vec{J}_G \times \frac{\vec{GM}}{GM^3}$$

where G is a given point of $V(\Sigma)$, dV_G is an elementary volume in the vicinity of G, and GM is the absolute value of $\vec{GM}$.

– It follows that:

$$\vec{B}_M = \vec{z} \times \left(\iiint_{V(\Sigma)} dV_G J_{G,z} \frac{\vec{GM}}{GM^3} \right)$$

which shows that the magnetic flux density is perpendicular to the z-axis and that:

$$B_{M,z}(x,y) = 0 \qquad \text{for all } x \text{ and all } y$$

– In the following, we drop the indices M and G and we simply refer to the current density and the magnetic flux density at a given point of space by $\vec{J}$ and $\vec{B}$.

Also, we designate by Γ the intersection of Σ with the $(O,\vec{x},\vec{y})$ plane and we designate by $I(\Gamma)$ [respectively, $E(\Gamma)$] the interior (respectively, exterior) of Γ.

PROPERTIES DERIVED FROM MAXWELL-GAUSS' EQUATION

– According to Maxwell-Gauss' equation, the magnetic flux density, $\vec{B}$, everywhere satisfies:

$$\nabla.\vec{B} = 0$$

It follows that:

$$\frac{\partial B_x(x,y)}{\partial x} + \frac{\partial B_y(x,y)}{\partial y} = 0 \qquad \text{for all } x \text{ and all } y$$

PROPERTIES DERIVED FROM MAXWELL-AMPERE'S EQUATION

– Let us assume that the magnetic permeability of the entire space [including $V(\Sigma)$] is that of vacuum, $\mu_0 = 4\,\pi\,10^{-7}$ H/m.

– Then, the magnetic field, $\vec{H}$, is everywhere related to the magnetic flux density, $\vec{B}$, by:

$$\vec{H} = \frac{1}{\mu_0}\,\vec{B}$$

– Furthermore, according to Maxwell-Ampère's equation, $\vec{H}$ is everywhere related to the current density, $\vec{J}$, by:

$$\nabla \times \vec{H} = \vec{J}$$

which yields:

$$\nabla \times \vec{B} = \mu_0 \vec{J}$$

– We get:

$$\frac{\partial B_y(x,y)}{\partial x} - \frac{\partial B_x(x,y)}{\partial y} = \mu_0 J_z(x,y)$$

for (x,y), $(x,y) \in I(\Gamma)$

and

$$\frac{\partial B_y(x,y)}{\partial x} - \frac{\partial B_x(x,y)}{\partial y} = 0$$

for (x,y), $(x,y) \in E(\Gamma)$

COMPLEX MAGNETIC FLUX DENSITY OUTSIDE THE CONDUCTORS

– Let us consider the exterior of the conductors, $E(\Gamma)$, and let s designate the complex variable defined as:

$$s = x + i\,y$$

– Furthermore, let us introduce the complex magnetic flux density, B, defined as:

$$B(s) = B_y(x,y) + i\,B_x(x,y)$$

– The real and imaginary parts, Re(B) and Im(B), of B are simply:

$$Re(B) = B_y(x,y) \quad \text{and} \quad Im(B) = B_x(x,y)$$

PROPERTIES OF COMPLEX MAGNETIC FLUX DENSITY

– The complex function, B, is continuous and single-valued over the entire space.

– Let us show that it is differentiable on E(Γ). To do so, let us demonstrate that Re(B) and Im(B) satisfy Cauchy-Riemann's conditions.

– On one hand, we have:

$$\frac{\partial \mathrm{Re}(\mathbf{B})}{\partial x} - \frac{\partial \mathrm{Im}(\mathbf{B})}{\partial y} = \frac{\partial B_y(x,y)}{\partial x} - \frac{\partial B_x(x,y)}{\partial y}$$

which, by combination with Maxwell-Ampère's equation over the conductors' exterior, yields:

$$\frac{\partial \mathrm{Re}(\mathbf{B})}{\partial x} - \frac{\partial \mathrm{Im}(\mathbf{B})}{\partial y} = 0 \qquad \text{for } (x,y),\ (x,y) \in \mathrm{E}(\Gamma)$$

– On the other hand, we have:

$$\frac{\partial \mathrm{Re}(\mathbf{B})}{\partial y} + \frac{\partial \mathrm{Im}(\mathbf{B})}{\partial x} = \frac{\partial B_y(x,y)}{\partial y} + \frac{\partial B_x(x,y)}{\partial x}$$

which, by combination with Maxwell's Gauss equation yields:

$$\frac{\partial \mathrm{Re}(\mathbf{B})}{\partial y} + \frac{\partial \mathrm{Im}(\mathbf{B})}{\partial x} = 0$$

PROPERTIES OF COMPLEX MAGNETIC FLUX DENSITY (CONT.)

– It follows from the above equations that B is a single-valued, analytic function on E(Γ).

– Note that to derive Cauchy-Riemann's conditons from Maxwell's equations, the complex magnetic flux density must be defined as $(B_y + iB_x)$ [or $(B_x - iB_y)$] and not as $(B_x + iB_y)$.

LECTURE 4: MAGNETIC DESIGN OF PARTICLE ACCELERATOR MAGNETS

4.1 Complex Formalism for Two-Dimensional Fields

4.2 Multipole Field Expansion for Two-Dimensional Fields

4.3 Field Computations for Simple Current Distributions

4.4 Two-Dimensional Cosθ and Cos2θ Coil Designs

4.5 Iron Yoke Contribution

4.6 Operating Current Margin

4.7 Saddle-Shaped Coil End Designs

4.8 Other Designs

4.9 Sagitta of Arc Dipole Magnets

4.10 High Order Multipole Field Corrector Magnets

POWER SERIES EXPANSION

– Let us again consider an ensemble of conductors parallel to the z-axis and uniform in z, and let us assume that these conductors are located outside a cylinder whose generator are parallel to the z-axis and whose director is a circle, Γ_i, of center, O, and radius, R_i, located in the $(O,\vec{x},\vec{y})$ plane. This case is representative of a coil assembly around the aperture of an accelerator magnet.

– Within the cylinder, the current distribution produces a two-dimensional magnetic flux density which can be represented by the single-valued and analytic function B defined in the previous section.

– Furthermore, let $D(\Gamma_i)$ designate the disk of center, O, and of radius, R_i, based on Γ_i. The analytic function, B, can be expanded into a Taylor's series around the disk origin:

$$B(s) = \sum_{n=0}^{+\infty} B^{(n)}(0) \frac{s^n}{n!} \qquad \text{for } s,\ |s| < R_i$$

where $B^{(n)}(0)$ is the n-th derivative of B with respect to s.

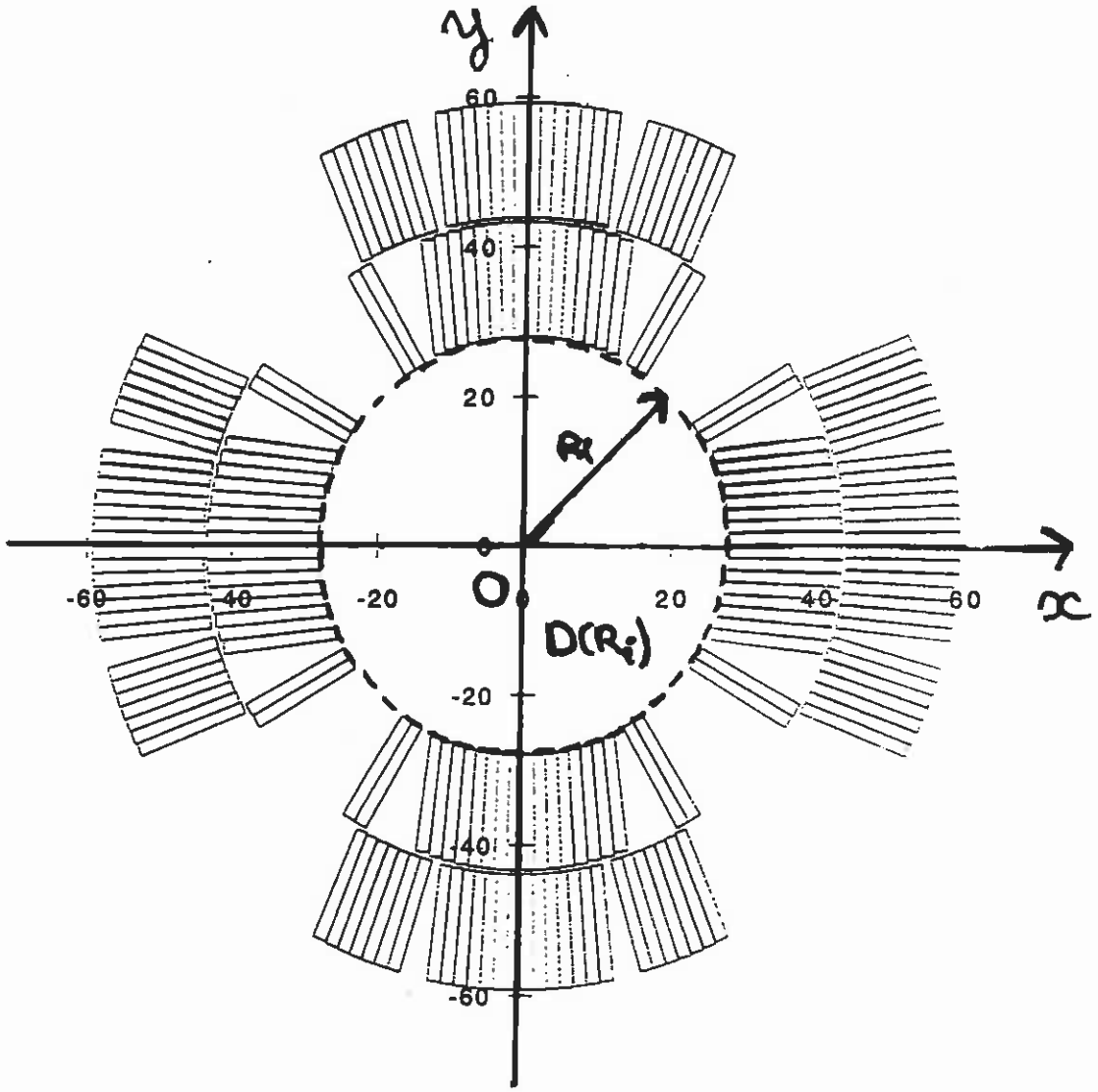
y
60
40
20
R
-60
-40
-20
O
20
40
60
x
D(Ri)
-20
-40
-60

CUSTOMARY NOTATIONS

– In the United States (US), it is customary to re-write the previous power series expansion under the form:

$$\mathrm{B(s)} = \sum_{n=0}^{+\infty} (B_n + \mathrm{i}\, A_n) \left(\frac{\mathrm{s}}{R_{\mathrm{ref}}}\right)^n \qquad \text{for s, } |\mathrm{s}| < R_i$$

where R_{ref} is a reference radius and A_n and B_n are constant coefficients related to $\mathrm{B}^{(n)}(0)$ by:

$$B_n + \mathrm{i}\, A_n = \frac{\mathrm{B}^{(n)}(0)}{n!}\, R_{\mathrm{ref}}^{\,n} \qquad \text{for } n,\ n \geq 0$$

– In the European Community (EC), most authors prefer to re-write the power series expansion under the form:

$$\mathrm{B(s)} = \sum_{n=1}^{+\infty} (B_n + \mathrm{i}\, A_n) \left(\frac{\mathrm{s}}{R_{\mathrm{ref}}}\right)^{n-1} \qquad \text{for s, } |\mathrm{s}| < R_i$$

Here, A_n and B_n are related to $\mathrm{B}^{(n-1)}(0)$ by:

$$B_n + \mathrm{i}\, A_n = \frac{\mathrm{B}^{(n-1)}(0)}{(n-1)!}\, R_{\mathrm{ref}}^{\,n-1} \qquad \text{for } n,\ n \geq 1$$

ON THE USE OF POWER SERIES EXPANSION

– The representation of the magnetic flux density by a power series expansion is that used in the accelerator physics community to compute beam orbits through magnet strings and to carry out particle tracking simulations.

– In the following, we shall (mostly) rely on EC customary notations.

DIPOLE FIELD COEFFICIENTS

– Let us first consider a magnet such that, in the series expansion of B, all the coefficients are nil, except B_1. Then we have:

$$\mathrm{B} = B_y + \mathrm{i}\, B_x = B_1$$

The magnetic flux density is thus uniform and vertical. This corresponds to a pure normal dipole magnetic flux density with a pole axis parallel to the y-axis.

– Let us now consider a magnet such that, in the series expansion of B, the only non-zero coefficient is A_1. Then we have:

$$\mathrm{B} = B_y + \mathrm{i}\, B_x = \mathrm{i}\, A_1$$

The magnetic flux density is thus uniform and horizontal. This corresponds to a so-called pure *skew* dipole magnetic flux density, with a pole axis rotated by an angle $(-\pi/2)$ with respect to the y-axis.

– Although A_1 and B_1 have the dimensions of magnetic flux densities, it is customary to refer to them as *skew* and *normal dipole field coefficients.*

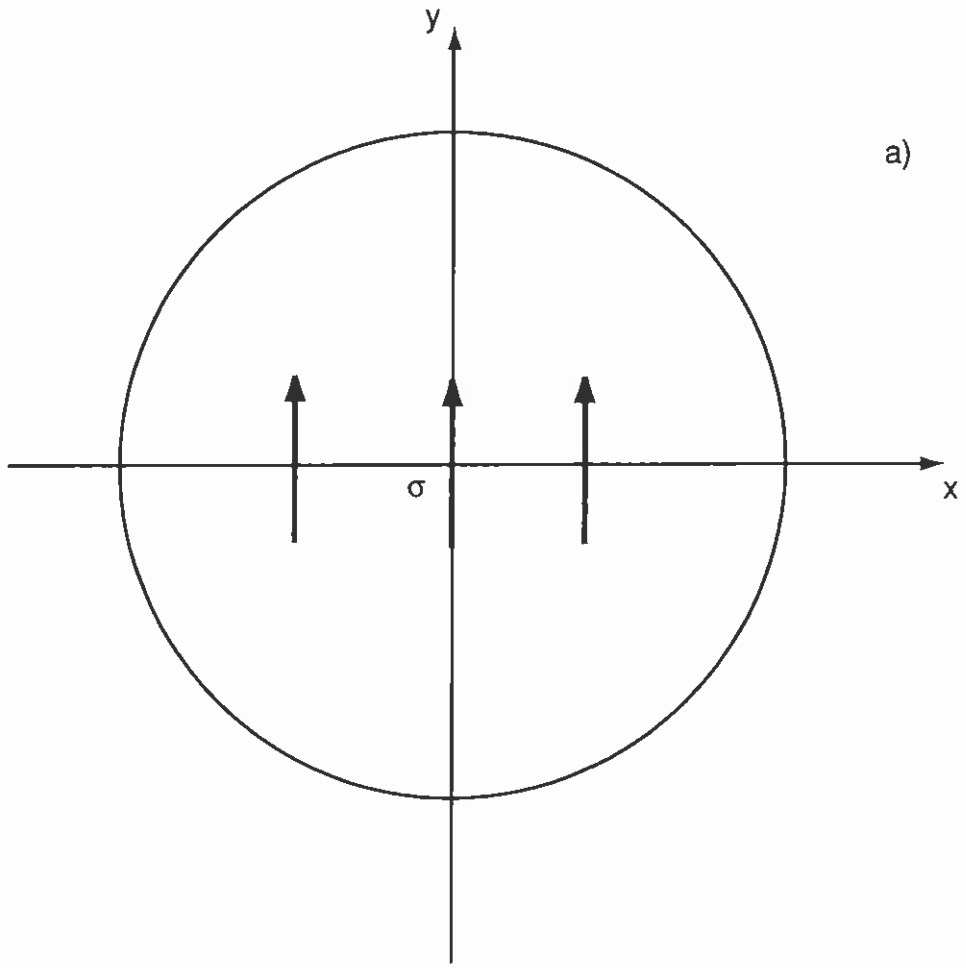
y
a)
σ
x

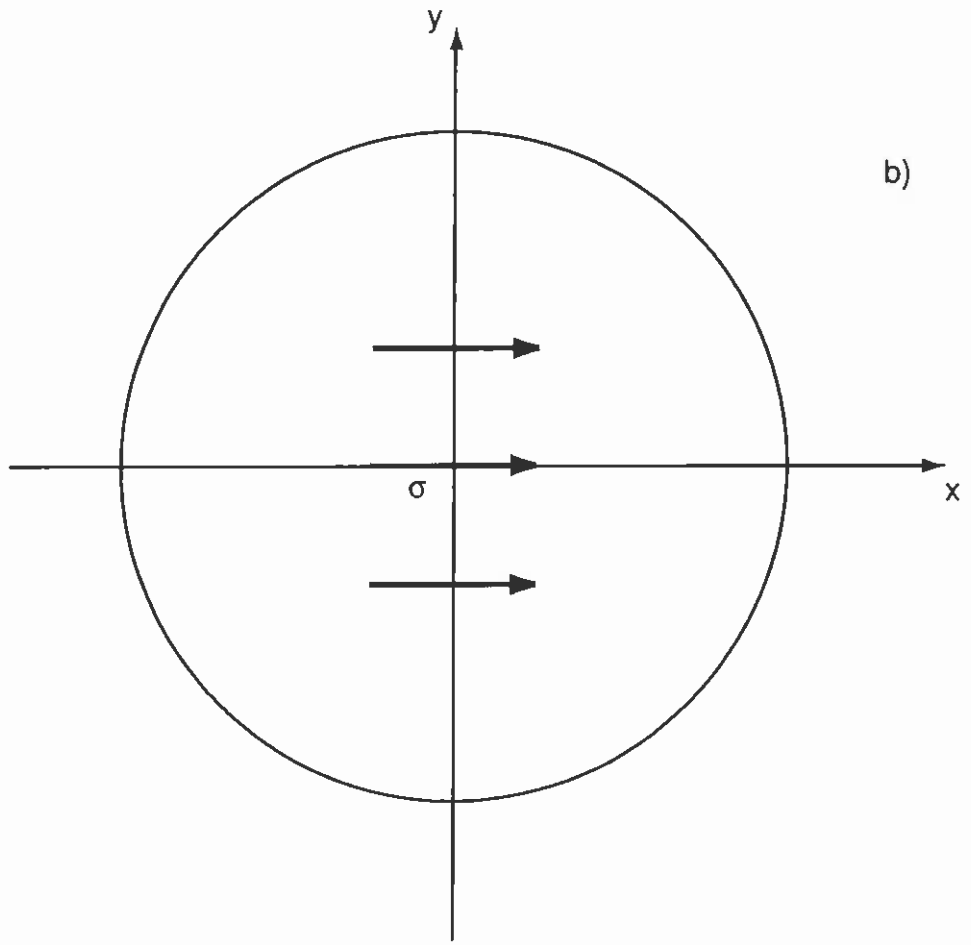
y
b)
σ
x

QUADRUPOLE FIELD COEFFICIENTS

– Let us now consider a magnet such that, in the series expansion of B, all the coefficients are nil, except B_2. Then we have:

$$\mathrm{B} = B_\mathrm{y} + \mathrm{i}\, B_\mathrm{x} = \frac{B_2}{R_\mathrm{ref}} (x + \mathrm{i}\, y)$$

The y-component of the magnetic flux density is thus proportional to x, while the x-component is proportional to y, and the coefficients of proportionality are equal.

This corresponds to a pure normal quadrupole magnetic flux density, with pole axes parallel to the first and second bisectors of the x–y plane.

The quadrupole field gradient, g, is defined as

$$g = \frac{B_2}{R_\mathrm{ref}}$$

The units of g are teslas per meter.

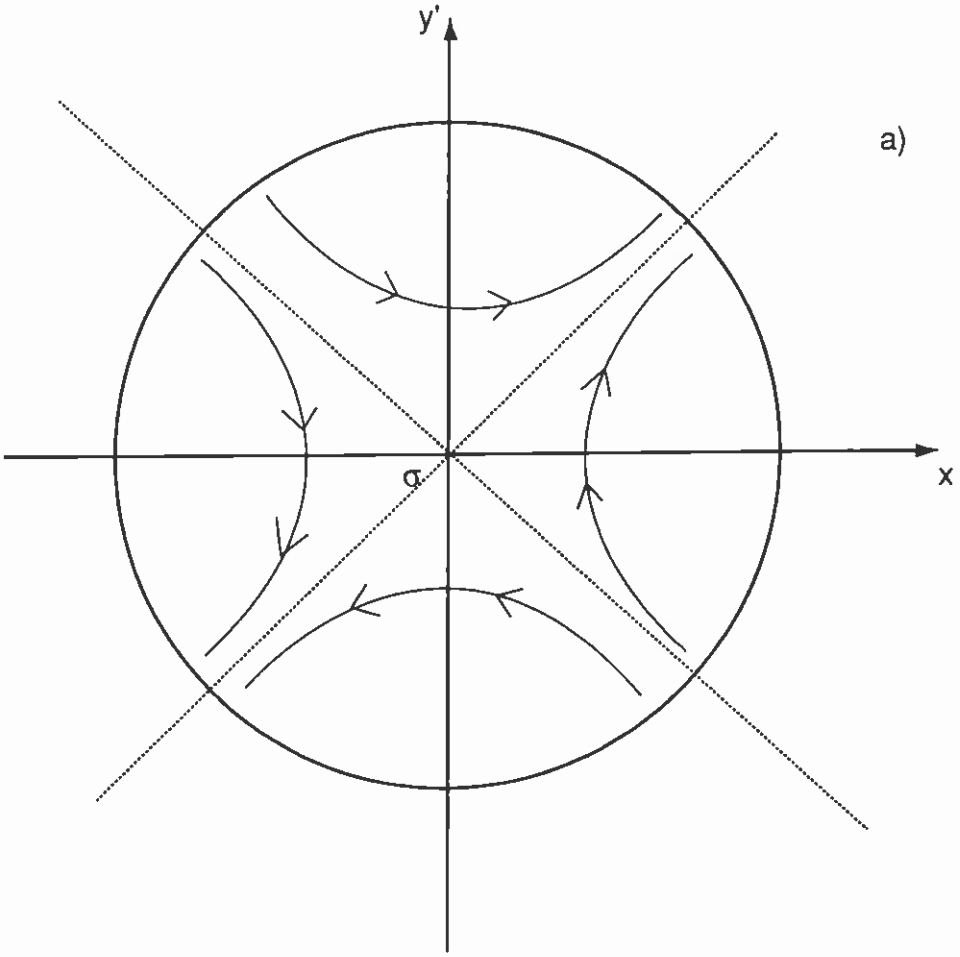
y'
a)
σ
x

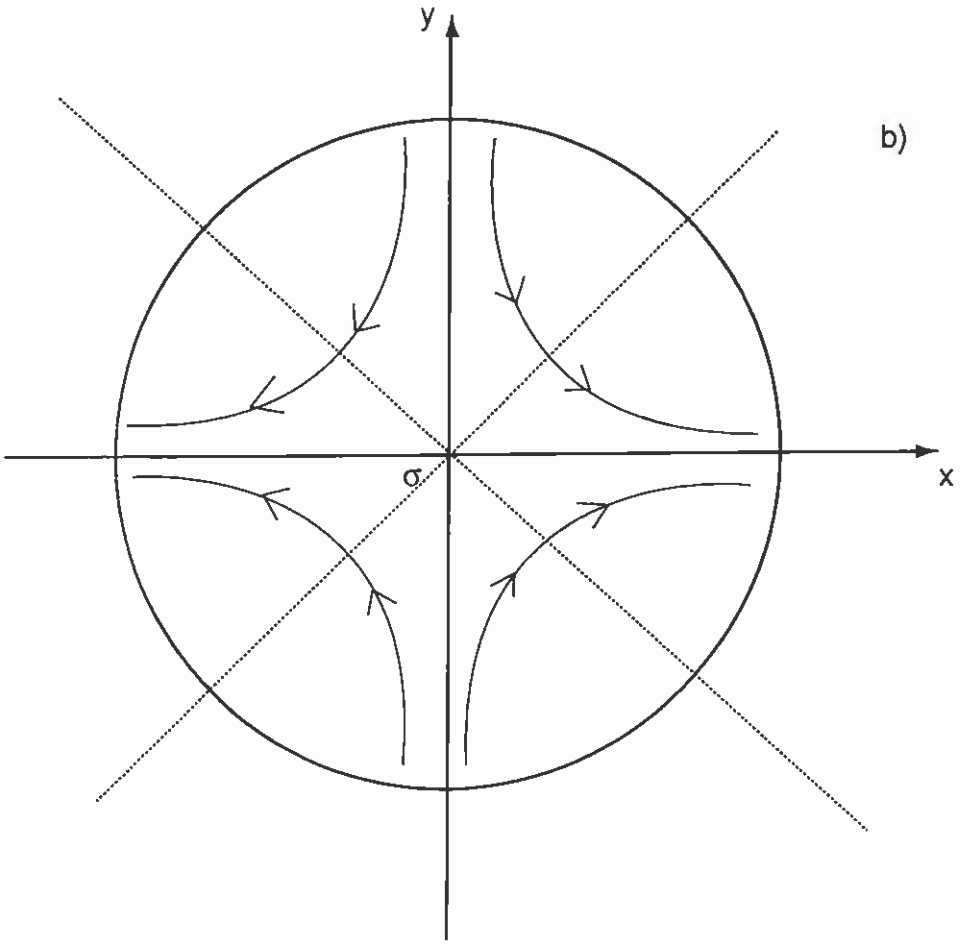
y
b)
σ
x

QUADRUPOLE FIELD COEFFICIENTS (CONT.)

– Let us now consider a magnet such that, in the series expansion of B, the only non-zero coefficient is A_2. Then we have:

$$\mathrm{B} = B_y + \mathrm{i}\, B_x = \frac{A_2}{R_{\mathrm{ref}}} (-y + \mathrm{i}\, x)$$

This corresponds to a so-called pure *skew* quadrupole magnetic flux density, with pole axes rotated by an angle $(-\pi/4)$ with respect to the first and second bisectors.

Here, the gradient, g, is given by:

$$g = \frac{A_2}{R_{\mathrm{ref}}}$$

– The coefficients A_2 and B_2 are called *skew* and *normal quadrupole field coefficients.*

2*N*-POLE FIELD COEFFICIENTS

– **Similary to the cases $n = 1$ and $n = 2$, it can be shown that the coefficients A_n and B_n correspond to pure $2n$-pole magnetic flux densities, and that the pole axes of the magnetic flux density associated with A_n are rotated by an angle $[-\pi/(2n)]$ with respect to the pole axes of the magnetic flux density associated with B_n.**

– **The coefficients A_n and B_n are called *skew* and *normal 2n-pole field coefficients.***

REFERENCE RADIUS

– The definitions of the multipole field coefficients show that, except for $n = 1$, they depend on the reference radius, and their values change when the reference radius is changed.

– Let A_n et B_n designate the multipole field coefficients defined for a reference radius, R_{ref}, and let A_n' et B_n' designate the multipole field coefficients defined for a different reference radius, R_{ref}'. We have:

$$B_n' + i\,A_n' = \left(\frac{R_{ref}'}{R_{ref}}\right)^{n-1} (B_n + i\,A_n)$$

CHOICE OF REFERENCE RADIUS

– The choice of reference radius has evolved in time.

– It was 1 inch (25.4 mm) for the magnets developed for the Tevatron, which had a 3-inch (76.2-mm) aperture, and it was 25 mm for the magnets developed for HERA, which had a 75-mm aperture. In those days, the rule of thumb was to take for R_{ref} one third of the magnet aperture.

– For the magnets developed for SSC and for the early LHC prototypes and models, the value of R_{ref} was taken to be 10 mm, while the magnet apertures were 40 to 56 mm.

– There are no compelling reasons to prefer one definition over the other, except the fact that, for a given magnetic design, the smaller the reference radius, the smaller the multipole field coefficients, and, therefore, the more politically correct they may appear...

– The LHC reference radius was recently (1998) increased to 17 mm.

COORDINATE SYSTEM TRANSLATION

– Let us consider a rectangular coordinate system, $(O', \vec{x}', \vec{y}')$, such that $\vec{x}$ and $\vec{x}'$ are one and the same, $\vec{y}$ and $\vec{y}'$ are one and the same, and:

$$\overrightarrow{OO'} = \Delta x\, \vec{x} + \Delta y\, \vec{y}$$

– Furthermore, let s' and B' designate the complex variable and the complex magnetic flux density associated with the new coordinate system. We have:

$$B = B' \quad \text{and} \quad s = s' + \Delta x + i\,\Delta y$$

– Starting from the power expansion of B as a function of s, we get:

$$B'(s) = \sum_{n=1}^{+\infty} (B_n + i\,A_n) \left(\frac{s' + \Delta x + i\,\Delta y}{R_{ref}} \right)^{n-1}$$

$$= \sum_{n=1}^{+\infty} (B_n + i\,A_n) \left[\sum_{k=0}^{n-1} \frac{(n-1)!}{k!(n-1-k)!} \left(\frac{s'}{R_{ref}} \right)^{k} \left(\frac{\Delta x + i\,\Delta y}{R_{ref}} \right)^{n-1-k} \right]$$

$$= \sum_{n=1}^{+\infty} \left[\sum_{k=n}^{+\infty} (B_k + i\,A_k) \frac{(k-1)!}{(n-1)!(k-n)!} \left(\frac{\Delta x + i\,\Delta y}{R_{ref}} \right)^{k-n} \right] \left(\frac{s'}{R_{ref}} \right)^{n-1}$$

where we recognize the multipole field expansion of B' around the new origin.

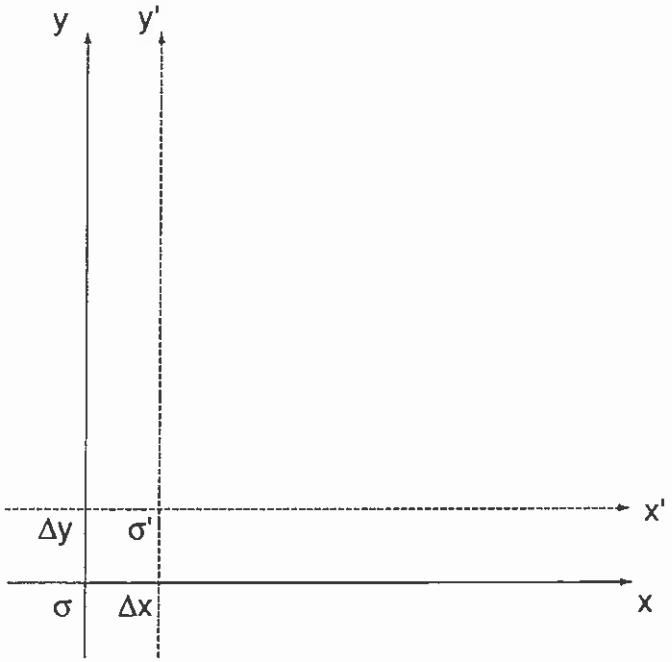
y
y'
x'
Δy
σ'
σ
Δx
x

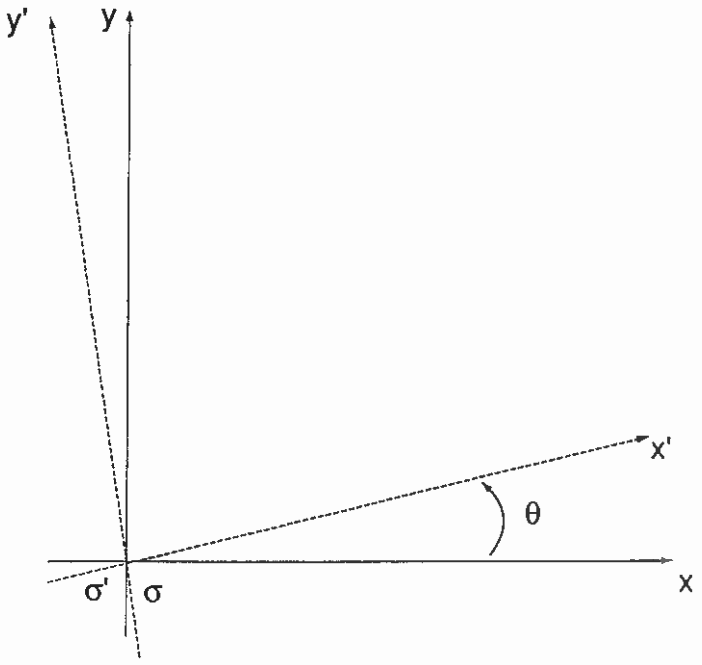
y'
y
x'
θ
σ'
σ
x

COORDINATE SYSTEM TRANSLATION (CONT.)

– Hence, the multipole field coefficients, A_n' and B_n', in the new coordinate system are related to the multipole field coefficients, A_n and B_n in the old coordinate system by:

$$B_n' + \mathrm{i}\, A_n' = \sum_{k=n}^{+\infty} (B_k + \mathrm{i}\, A_k) \frac{(k-1)!}{(n-1)!(k-n)!} \left(\frac{\Delta x + \mathrm{i}\, \Delta y}{R_{ref}} \right)^{k-n}$$

$$= (B_n + \mathrm{i}\, A_n) + n\ (B_{n+1} + \mathrm{i}\, A_{n+1}) \left(\frac{\Delta x + \mathrm{i}\, \Delta y}{R_{ref}} \right) + \ldots$$

– The above equation shows that the $2n$-pole field coefficients in the translated coordinate system are equal to the $2n$-pole field coefficients in the original coordinate system plus so-called *feed-down* terms from higher order multipole field coefficients.

COORDINATE SYSTEM ROTATION

– Let us now consider a rectangular coordinate system, $(O', \vec{x}', \vec{y}')$, such that O' and O are one and the same and the x'- and y'-axes are rotated by an angle θ with respect to the x- and y-axes.

– Let again s' and B' designate the complex variable and the complex magnetic flux density associated with the new coordinate system. We have:

$$B = B' e^{-i\theta} \qquad \text{and} \qquad s = s' e^{i\theta}$$

– Starting again from the power series expansion of B as a function of s, we now get:

$$B'(s) = \left[\sum_{n=1}^{+\infty} (B_n + i A_n) \left(\frac{s' e^{i\theta}}{R_{ref}} \right)^{n-1} \right] e^{i\theta}$$

$$= \sum_{n=1}^{+\infty} \left[(B_n + i A_n) e^{in\theta} \right] \left(\frac{s'}{R_{ref}} \right)^{n-1}$$

– The above equation shows that the multipole field coefficients in the new coordinate system, A_n' and B_n', are rotated by an angle $(n\theta)$ with respect to the multipole field coefficients, A_n and B_n in the old coordinate system:

$$B_n' + i A_n' = (B_n + i A_n) e^{in\theta}$$

LECTURE 4: MAGNETIC DESIGN OF PARTICLE ACCELERATOR MAGNETS

4.1 Complex Formalism for Two-Dimensional Fields

4.2 Multipole Field Expansion for Two-Dimensional Fields

4.3 Field Computations for Simple Current Distributions

4.4 Two-Dimensional Cosθ and Cos2θ Coil Designs

4.5 Iron Yoke Contribution

4.6 Operating Current Margin

4.7 Saddle-Shaped Coil End Designs

4.8 Other Designs

4.9 Sagitta of Arc Dipole Magnets

4.10 High Order Multipole Field Corrector Magnets

MAGNETIC FLUX DENSITY PRODUCED BY A SINGLE CURRENT LINE IN FREE SPACE

– Let $(O,\vec{x},\vec{y},\vec{z})$ designate a rectangular coordinate system and let $(O,\vec{u}_r,\vec{u}_\theta,\vec{z})$ designate a cyclindrical designate coordinate system deduced from $(O,\vec{x},\vec{y},\vec{z})$ by a rotation of angle, θ, around the z-axis.

– Furthermore, let us consider a current line of intensity, $(-I)$, parallel to the z-axis, and crossing the $(O,\vec{x},\vec{y})$ plane at O. (The choice of a negative current line intensity will be explained later.)

– Given the problem symmetries, the magnetic flux density, $\vec{B}$, produced by this current line is expected to be uniform in θ and z. Hence, we can write:

$$\vec{B} = B_r(r)\,\vec{u}_r + B_\theta(r)\,\vec{u}_\theta + B_z(r)\,\vec{z}$$

where B_r, B_θ, and B_z are the radial, azimuthal and z-components of $\vec{B}$.

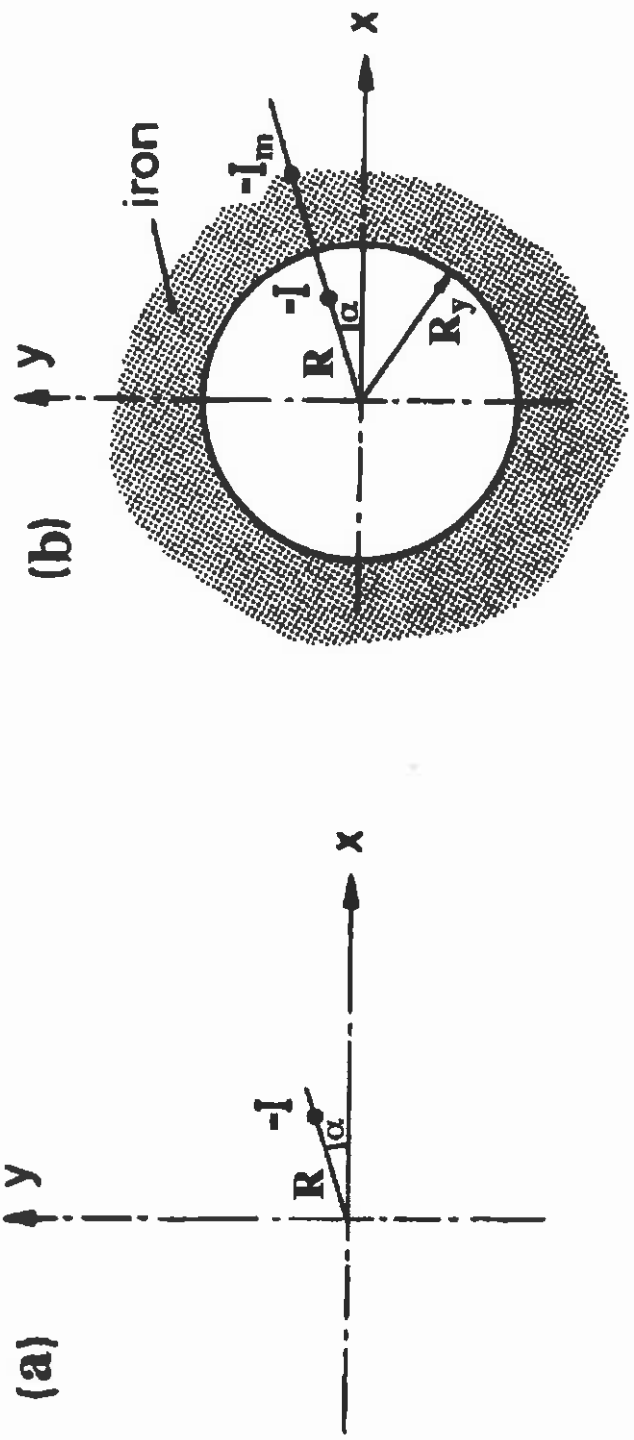
x
iron
$-I_m$
-I
α
R
R_7
y
(b)
x
-I
α
R
y
(a)

MAGNETIC FLUX DENSITY PRODUCED BY A SINGLE CURRENT LINE IN FREE SPACE (CONT.)

– By writing Biot and Savart's law, we get:

$$B_z(r) = 0 \qquad \text{for all } r$$

– By applying Gauss' theorem to the surface of a cylindrical element, whose generators are parallel to the z-axis, whose director is a circle of center, O, and radius, r, located in the $(O,\vec{x},\vec{y})$ plane, and which extends between two planes perpendicular to the z-axis, it can be shown that:

$$B_r(r) = 0 \qquad \text{for all r}$$

– Finally, by applying Ampère's theorem to a circle, Γ, of center, O, and radius, r, located in the $(O,\vec{x},\vec{y})$ plane, and by assuming that the magnetic permeablity of the entire space is μ_0, it can be derived that:

$$B_\theta(r) = \frac{-\mu_0 I}{2\pi r}\,\vec{u}_\theta$$

– Going back to the rectangular coordinate system, we get:

$$B_x = \frac{\mu_0 I}{2\pi r}\sin\Theta \quad \text{and} \quad B_y = \frac{-\mu_0 I}{2\pi r}\cos\Theta$$

COMPLEX MAGNETIC FLUX DENSITY PRODUCED BY A SINGLE CURRENT LINE IN FREE SPACE

– From the above equations, it follows that the complex magnetic flux density, B, produced by the current line at a point, $s = r\ e^{i\theta}$, different from 0 is given by:

$$B(s) = B_y(x,y) + iB_x(x,y)$$

$$= -\frac{\mu_0 I}{2\pi r}(\cos\Theta - i\sin\Theta)$$

$$= -\frac{\mu_0 I}{2\pi s}$$

– Furthermore, it is straightforward to derive that the complex magnetic flux density, B, produced by a current line, $(-I,R,\alpha)$, of intensity, $(-I)$, parallel to the z-axis, and crossing the $(O,\vec{x},\vec{y})$ plane at a point, a, $a = R\ e^{i\alpha}$, different from O is given by:

$$B(s) = -\frac{\mu_0 I}{2\pi}\frac{1}{s-a} \qquad \text{for } s,\ s \neq a$$

POWER SERIES EXPANSION FOR A SINGLE CURRENT LINE IN FREE SPACE

– The expression of the complex magnetic flux density produced by a single current line, $(-I,R,\alpha)$ in free space can be re-written:

$$B(s) = \frac{\mu_0 I}{2\pi}\,\frac{1}{a}\,\frac{1}{1-\left(\frac{s}{a}\right)}$$

– Furthermore, we have:

$$\frac{1}{1-\left(\frac{s}{a}\right)} = \sum_{n=0}^{+\infty}\left(\frac{s}{a}\right)^n \qquad \text{for s, } |s| < |a|$$

which yields:

$$B(s) = \sum_{n=1}^{+\infty}(B_n + i\,A_n)\left(\frac{s}{R_{ref}}\right)^{n-1} \qquad \text{for s, } |s| < |a|$$

where:

$$B_n + i\,A_n = \frac{\mu_0 I}{2\pi R_{ref}}\left(\frac{R_{ref}}{a}\right)^n$$

$$= \frac{\mu_0 I}{2\pi R_{ref}}\left(\frac{R_{ref}}{R}\right)^n \left[\cos(n\alpha) - i\,\sin(n\alpha)\right]$$

(Note that the current line intensity was chosen to be negative in order to get a positive factor in front of the second member of the above equation.)

SINGLE CURRENT LINE WITHIN A CYLINDRICAL IRON YOKE

– Let us now assume that the current line considered previously is located inside a cylindrical iron yoke of inner radius, R_y.

– The contribution of the iron yoke to the magnetic flux density can be shown to be the same as that of a mirror current line, of intensity, $(-I_m)$, and position, a_m, in the complex plane, where:

$$I_m = \frac{\mu-1}{\mu+1} I \qquad \text{and} \qquad a_m = \frac{R_y^2}{a^*}$$

Here μ designates the relative magnetic permeability of the iron yoke and a^* designates the complex conjugate of a.

– Note that the mirror image method is only applicable if the iron yoke is not saturated and as long as its permeability is uniform.

QUADRUPLET OF CURRENT LINES WITH DIPOLE SYMMETRY

– Let us now consider the quadruplet of current lines with a "dipole symmetry": $(-I,R,\alpha)$, $(+I,R,\pi-\alpha)$, $(+I,R,\pi+\alpha)$ and $(-I,R,-\alpha)$.

– The magnetic flux density produced by this quadruplet can be estimated by summing the contributions from each current line. We get:

$$B_y + iB_x = \sum_{k=0}^{+\infty} B_{2k+1} \left(\frac{s}{R_{ref}}\right)^{2k} \qquad \text{for s, } |s| < R$$

where

$$B_{2k+1} = \frac{2\mu_0 I}{\pi R_{ref}} \left(\frac{R_{ref}}{R}\right)^{2k+1} \cos[(2k+1)\alpha]$$

– The first term ($k = 0$) of the series corresponds to a pure normal dipole field parallel to the y-axis.

– The B_1, B_3, B_5..., B_{2k+1},... coefficients are called the *allowed* multipole field coefficients of this current distribution.

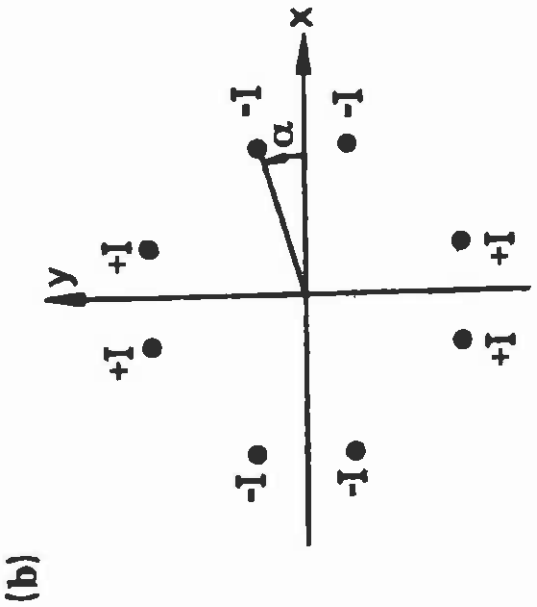

(b)

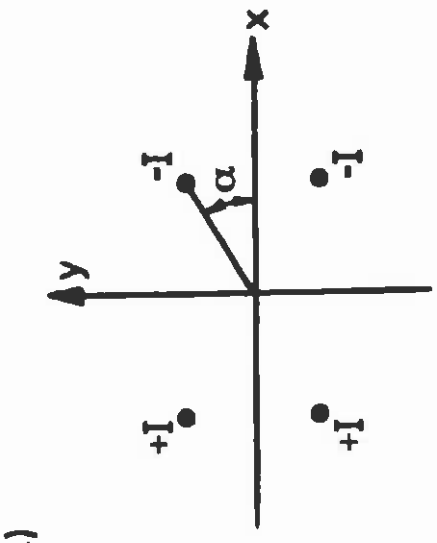

(a)

OCTUPLET OF CURRENT LINES WITH QUADRUPOLE SYMMETRY

– Similarly, the magnetic flux density produced by an octuplet of current lines with a "quadrupole symmetry" can be shown to be:

$$B_y + iB_x = \sum_{k=0}^{+\infty} B_{4k+2} \left(\frac{s}{R_{ref}}\right)^{4k+1} \qquad \text{for s, } |s| < R$$

where:

$$B_{4k+2} = \frac{4\mu_0 I}{\pi R_{ref}} \left(\frac{R_{ref}}{R}\right)^{4k+2} \cos[(4k+2)\theta]$$

– Here, the first term ($k = 0$) of the series corresponds to a pure normal quadrupole field whose axes are parallel to the first and second bisectors.

– The allowed multipole field coefficients of this current distribution are are the normal 2(4k+2)-pole field coefficients (B_2, B_6, B_{10}...).

COS$P\Theta$ CURRENT SHEETS

– Let us now consider a cylindrical current sheet of radius, R, carrying a linear current density of the form $[-j\cos(p\,\theta)]$ where j is a constant (in A/m).

– The magnetic flux density produced within the cylinder can be computed by dividing the sheet into elementary current lines of intensity $[-jR\cos(p\,\theta)\,\mathrm{d}\theta]$ and by integrating their contributions over (2π). We get:

$$B_y + iB_x = B_p \left(\frac{s}{R_{ref}}\right)^{p-1} \qquad \text{for } s,\ |s| < R$$

where:

$$B_p = \frac{\mu_0 j}{2} \left(\frac{R_{ref}}{R}\right)^{p-1}$$

– Hence, a $\cos(p\,\theta)$-type current sheet produces a pure normal $2p$-pole field.

SIN$P\Theta$ CURRENT SHEETS

– Similarly, a cylindrical current sheet of radius, R, carrying a linear current density $[+j\sin(p\theta)]$, produces a pure skew $2p$-pole field:

$$B_y + iB_x = i A_p \left(\frac{s}{R_{ref}}\right)^{p-1} \qquad \text{for } s,\ |s| < R$$

where:

$$A_p = \frac{\mu_0 j}{2} \left(\frac{R_{ref}}{R}\right)^{p-1}$$

CYLINDRICAL CURRENT SHELLS

– Let us now consider a cylindrical current shell of inner radius, R_i, outer radius, R_o, extending between the angles $(-\alpha_0)$ and $(+\alpha_0)$ in the half-space x, $x \geq 0$ and between the angles $(\pi-\alpha_0)$ and $(\pi+\alpha_0)$ in the half-space x, $x \leq 0$, and carrying an uniform current density $(-J)$ for x, $x > 0$, and $(+J)$ for x, $x < 0$.

– The magnetic flux density produced within the cylinder can be computed by dividing the shell into quadruplets of current lines having a "dipole symmetry" and carrying intensities $[\pm JR\mathrm{d}\theta\mathrm{d}R]$, and by integrating the quadruplet contributions over a shell quadrant. We get:

$$B_y + iB_x = \sum_{k=0}^{+\infty} B_{2k+1} \left(\frac{s}{R_{ref}}\right)^{2k} \qquad \text{for s, } |s| < R_i$$

where:

$$B_1 = \frac{2\mu_0 J}{\pi} (R_o - R_i) \sin\alpha_0$$

and:

$$B_{2k+1} = \frac{2\mu_0 J R_{ref}}{\pi(2k+1)(2k-1)} \left[\left(\frac{R_{ref}}{R_i}\right)^{2k-1} - \left(\frac{R_{ref}}{R_o}\right)^{2k-1}\right] \sin[(2k+1)\alpha_0]$$

for k, $k \geq 1$

– Note that B_3 (first allowed multipole field coefficient after B_1 in a current distribution with a dipole symmetry) is nil for $\theta_0 = \pi/3$.

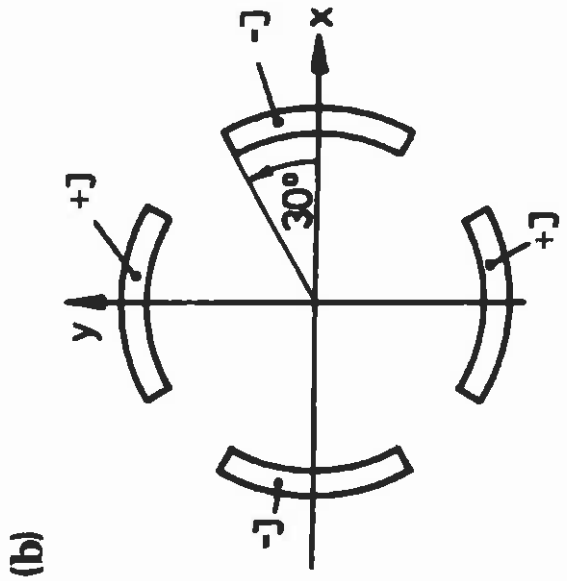

(b)

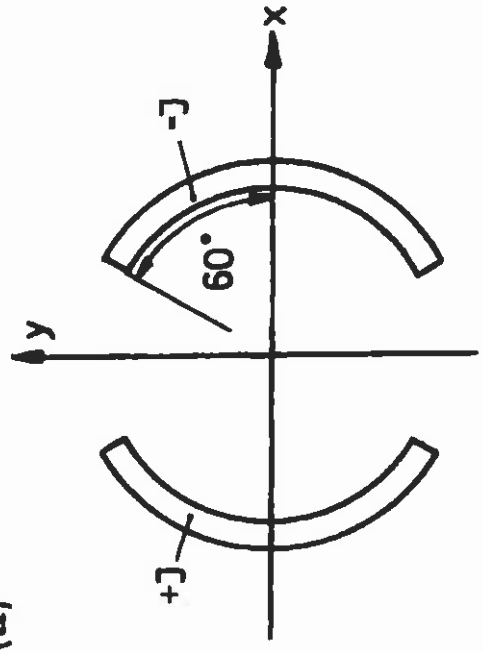

(a)

CYLINDRICAL CURRENT SHELLS WITH QUADRUPOLE SYMMETRY

– Similarly, the magnetic flux density produced by a cylindrical current shell with a "quadrupole symmetry" is given by:

$$B_y + iB_x = \sum_{k=0}^{+\infty} B_{4k+2} \left(\frac{s}{R_{ref}}\right)^{4k+1} \qquad \text{for } s,\ |s| < R_i$$

where:

$$B_2 = \frac{2\mu_0 J R_{ref}}{\pi} \ln\left(\frac{R_o}{R_i}\right) \sin 2\alpha_0$$

and:

$$B_{4k+2} = \frac{\mu_0 J R_{ref}}{\pi k(4k+2)} \left[\left(\frac{R_{ref}}{R_i}\right)^{4k} - \left(\frac{R_{ref}}{R_o}\right)^{4k}\right] \sin[(4k+2)\alpha_0]$$

$$\text{for } k,\ k \geq 1$$

– Note that B_6 (first allowed multipole field coefficient after B_2 in a current distribution with a quadrupole symmetry) is nil for $\alpha_0 = \pi/6$.

CYLINDRICAL CURRENT SHELLS WITHIN A CYLINDRICAL IRON YOKE

– Let us now assume that the current shell with a "dipole symmetry" considered previously is located inside a cylindrical iron yoke of inner radius, R_y.

– the contribution of the iron yoke to the magnetic flux density can be shown to be the same as that of a mirror current shell, of inner radius, R_{im}, and outer radius, R_{om}, where:

$$R_{im} = \frac{R_y^2}{R_o} \qquad \text{and} \qquad R_{om} = \frac{R_y^2}{R_i}$$

and carrying an uniform current density, J_m, such that:

$$J_m = \frac{\mu-1}{\mu+1} \frac{R_o^2 - R_i^2}{R_{om}^2 - R_{im}^2} J = \frac{\mu-1}{\mu+1} \frac{R_o^2 R_i^2}{R_y^4} J$$

Here μ designates the relative magnetic permeability of the iron yoke. [The above eauation expresses that the total intensity of the current circulating in the mirror shell is the same as that circulating in the original shell times the ratio $(\mu-1/\mu+1)$.]

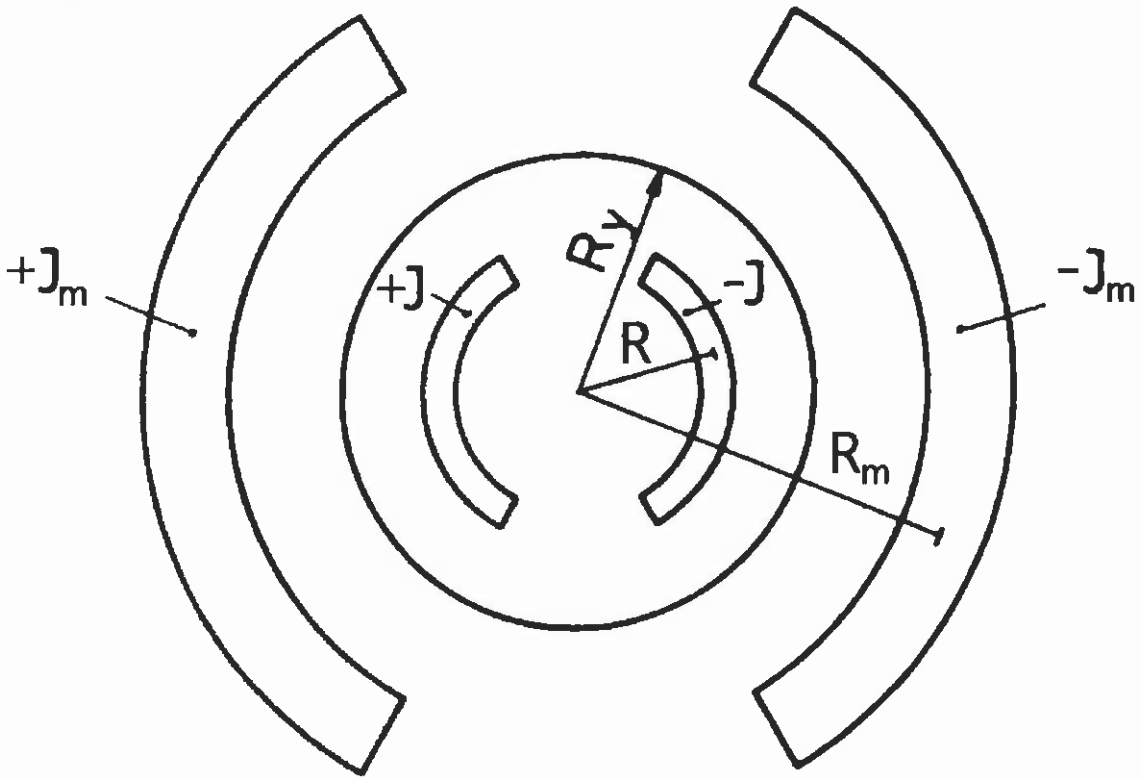
+Jm
+J
Ry
-J
R
Rm
-Jm

CYLINDRICAL CURRENT SHELLS WITHIN A CYLINDRICAL IRON YOKE (CONT.)

– Then, it is easy to show that the contribution of the iron yoke to the $2n$-pole field coefficient, B_n^{yoke}, is:

$$B_n^{yoke} = \frac{\mu-1}{\mu+1}\left(\frac{R_i R_o}{R_y^2}\right)^n B_n^{shell}$$

where B_n^{shell} is the $2n$-pole field coefficient produced by the current shell alone.

– Hence, the presence of the iron yoke results in an enhancement of the multipole field coefficients which can be estimated as:

$$1 + \frac{\mu-1}{\mu+1}\left(\frac{R_i R_o}{R_y^2}\right)^n$$

Example: for $R_i = 40$ mm, $R_o = 50$ mm and $R_y = 60$ mm (RHIC arc dipole magnet design), the computed enhancement (without saturation) is about 56% on B_1, 17% on B_3, and 5% on B_5. In practice, yoke saturation reduces the enhancement to about 35% on B_1.

– Note that the above equation remains the same for a cylindrical current shell with a "quadrupole symmetry".

CYLINDRICAL CURRENT SHELLS WITH ANGULAR WEDGES

– Let us finally consider a cylindrical current shell with a "dipole symmetry", but let us assume that it includes four angular wedges dividing each shell quadrant into two current blocks.

– It is straightforward to show that the magnetic flux density produced by this current distribution is again given by:

$$B_y + iB_x = \sum_{k=0}^{+\infty} B_{2k+1} \left(\frac{s}{R_{ref}}\right)^{2k} \qquad \text{for } s,\ |s| < R_i$$

where:

$$B_1 = \frac{2\mu_0 J}{\pi} (R_o - R_i) \left[\sin\alpha_0 - \sin\alpha_1 + \sin\alpha_2\right]$$

and:

$$B_{2k+1} = \frac{2\mu_0 J R_{ref}}{\pi(2k+1)(2k-1)} \left[\left(\frac{R_{ref}}{R_i}\right)^{2k-1} - \left(\frac{R_{ref}}{R_o}\right)^{2k-1}\right] \left\{\sin[(2k+1)\alpha_0] - \sin[(2k+1)\alpha_1] + \sin[(2k+1)\alpha_2]\right\}$$

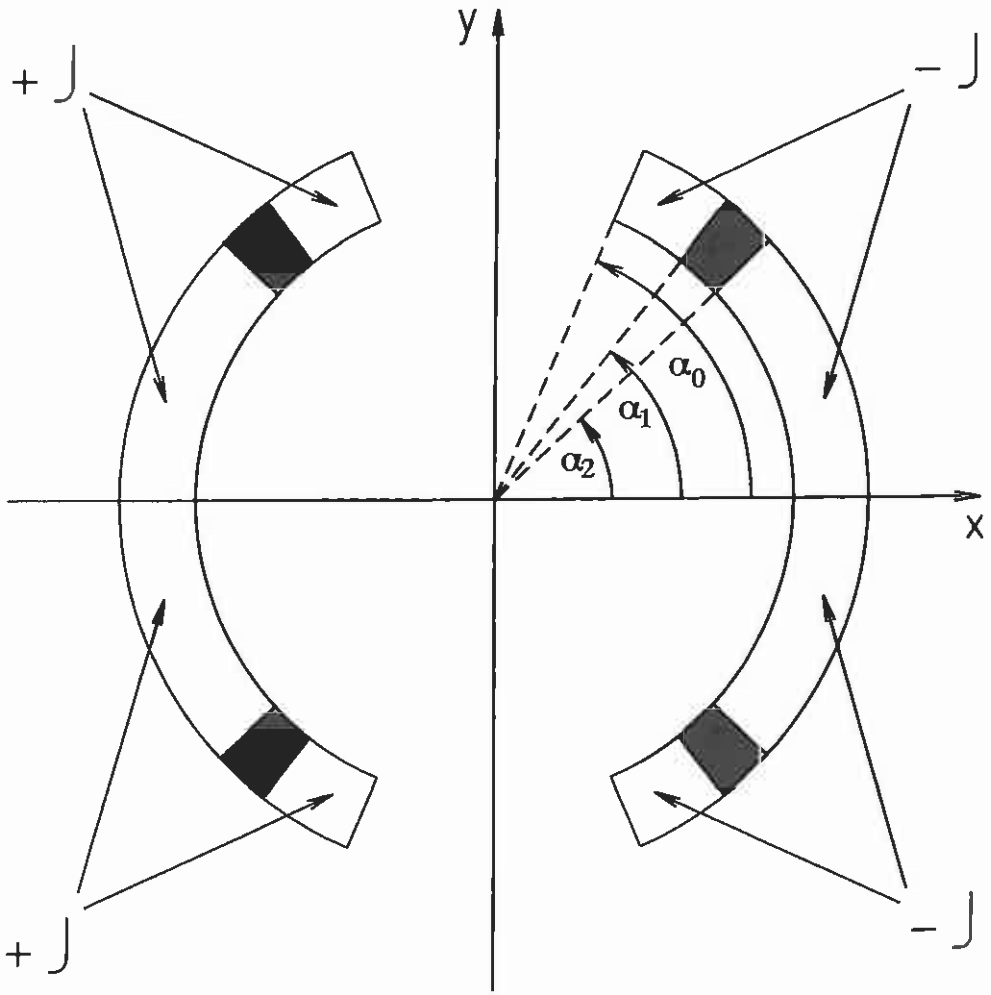
y
x
+ J
– J
+ J
– J
α_0
α_1
α_2

ON THE USE OF ANGULAR WEDGES

– We have seen that in the case of a cylindrical shell with a "dipole symmetry" and no angular wedge, the sextupole field coefficient, B_3, could be set to zero by choosing a pole angle, α_0, such that:

$$\sin(3\alpha_0) = 0.$$

This gave: $\alpha_0 = 60°$.

– The main interest of angular wedges is that they provide additional free parameters to set to zero other high order, allowed multipole field coefficients.

ON THE USE OF ANGULAR WEDGES (CONT.)

– For instance, in the case of a cylindrical shell with a dipole symmetry and one angular wedge per quadrant, the angles α_0, α_1 and α_2 can be chosen to have simultaneously:

$$B_3 = B_5 = B_7 = 0$$

– This yields the following system of three equations and three unknowns:

$$\sin(3\alpha_0) - \sin(3\alpha_1) + \sin(3\alpha_2) = 0$$
$$\sin(5\alpha_0) - \sin(5\alpha_1) + \sin(5\alpha_2) = 0$$

and

$$\sin(7\alpha_0) - \sin(7\alpha_1) + \sin(7\alpha_2) = 0$$

– The solutions of the above system are:

$\alpha_0 \approx 67.2753°$, $\alpha_1 \approx 52.1526°$ and $\alpha_2 \approx 43.1791°$

ON THE USE OF ANGULAR WEDGES (CONT.)

– Implementing a second wedge per quadrant (which divides each quadrant into three current blocks) provides two additional parameters which can be determined to obtain:

$$B_3 = B_5 = B_7 = B_9 = B_{11} = 0$$

And so on.

– In theory, N wedges allow to set to zero up to $(2N+1)$ allowed multipole field coefficients.

– Note that the angular wedges introduce a spacing in the current distribution which, on a circle of radius, R, where R, $R_i \leq R \leq R_o$, tends towards the ideal $\cos\theta$ current sheet distribution that was shown to produce a pure dipole field.

ON THE USE OF ANGULAR WEDGES (END)

– In a similar fashion, angular wedges can be implemented into cylindrical current shells having a quadrupole symmetry.

– In the case of one angular wedge per octant, dividing each octant into two current blocks, the angles α_0, α_1 and α_2 can be chosen to get simultaneously:

$$B_6 = B_{10} = B_{14} = 0$$

– This yields the following system of three equations and three unknowns:

$$\sin(6\alpha_0) - \sin(6\alpha_1) + \sin(6\alpha_2) = 0$$
$$\sin(10\alpha_0) - \sin(10\alpha_1) + \sin(10\alpha_2) = 0$$

and

$$\sin(14\alpha_0) - \sin(14\alpha_1) + \sin(14\alpha_2) = 0$$

– The solutions of the above system of equations are one half of the solutions of the system of equations for cylindrical current shells with a "dipole symmetry".

LECTURE 4: MAGNETIC DESIGN OF PARTICLE ACCELERATOR MAGNETS

4.1 Complex Formalism for Two-Dimensional Fields

4.2 Multipole Field Expansion for Two-Dimensional Fields

4.3 Field Computations for Simple Current Distributions

4.4 Two-Dimensional Cosθ and Cos2θ Coil Designs

4.5 Iron Yoke Contribution

4.6 Operating Current Margin

4.7 Saddle-Shaped Coil End Designs

4.8 Other Designs

4.9 Sagitta of Arc Dipole Magnets

4.10 High Order Multipole Field Corrector Magnets

SYMMETRY CONSIDERATIONS

– The field computations presented in the previous slides have shown that current distributions with "dipole symmetry" (*i.e.*, even with respect to the x-axis and odd with respect to the y-axis) were suitable for generating dipole fields, whereas current distributions with "quadrupole symmetry" (*i.e.*, even with respect to the x- and y-axes and odd with respect to the first and second bisectors) were suitable for generating quadrupole fields.

– Starting from these premises, the coil geometry can be optimized to obtain the required dipole or quadrupole field strength within the desired aperture.

– In addition, in most accelerator designs, it is required that the high order multipole fields be as small as possible. Hence, the coil geometry optimization is also carried out to minimize the contributions from non-dipole or non-quadrupole terms.

COMMONLY USED COIL DESIGNS

– The coil geometries the most commonly used for dipole and quadrupole magnets are approximations of the intersecting circles or ellipses discussed in lecture 1.

– The approximation is obtained by stacking into an arch the slightly keystoned cables described in lecture 3.

Approximating a pure normal dipole field

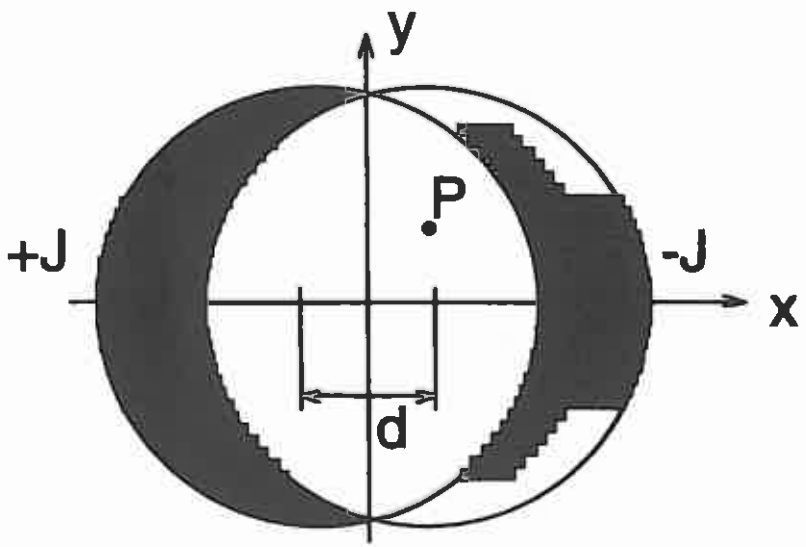

packed array of cables approximating the ideal current distribution

Approximating a pure quadrupole field

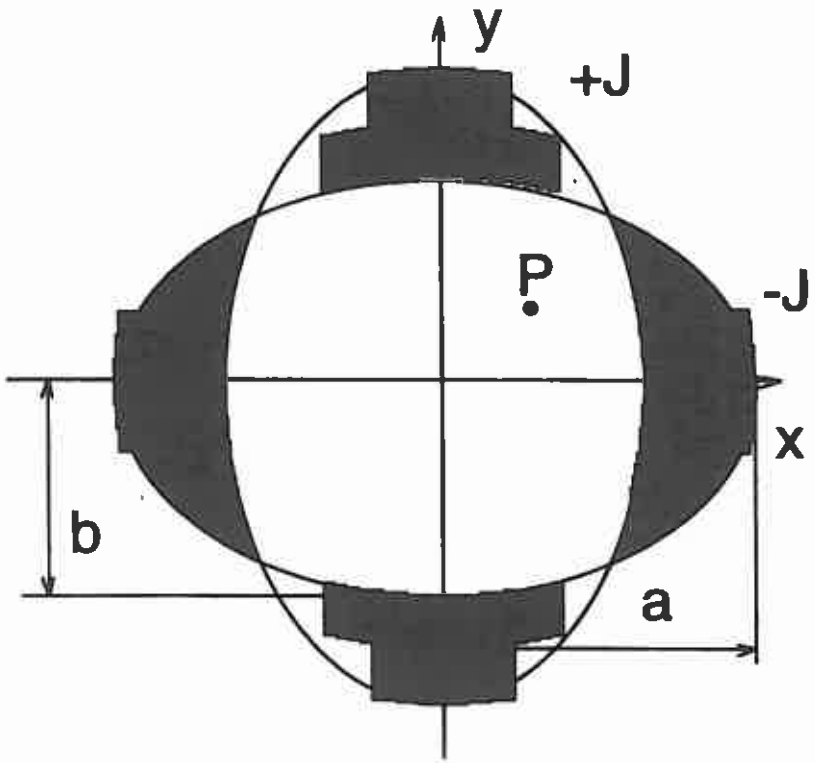

packed array of cables approximating the ideal current distribution

HOW TO ACHIEVE THE REQUIRED FIELD STRENGTH?

– We have seen that the dipole field component produced by a cylindrical current shell is of the form:

$$B_1 \approx \frac{2\mu_0 J}{\pi} (R_o - R_i) \sin\alpha_0$$

where J is the overall current density in the shell, $(R_o - R_i)$ is the shell radial width and α_0 is the pole angle.

– The above equation shows that B_1 is an increasing function of J and $(R_o - R_i)$. In practice, however, the value of J is limited by the critical current density of the superconductor and the cable radial width is limited by cabling wind-ability considerations.

– The cabling wind-ability problems are circumvented by using multiple layer coils whose field contributions add up. (Besides, multipole layer coils can provide better approximations of the intersecting-circles-or-ellipses current distributions).

– Increasing the high-field critical current density of the superconductor requires either to lower the operating temperature (*e.g.*, from 4.2 K to 1.9 K) ot to change of material (*e.g.*, from NbTi to Nb_3Sn).

EXAMPLES OF COIL DESIGNS

– The low-field magnets for RHIC rely on a single coil layer wound from NbTi cables operated around 4.5 K.

– The moderate-field Tevatron, HERA, UNK, and SSC magnets rely on two coil layers wound from NbTi cables operated around 4.5 K.

– The high-field LHC magnets rely on two coil layers wound from wide NbTi cables operated at 1.9 K.

– The high-field LBNL dipole magnet model D20 counts four layers wound from NbSn cables.

RHIC 8-cm-Aperture Dipole

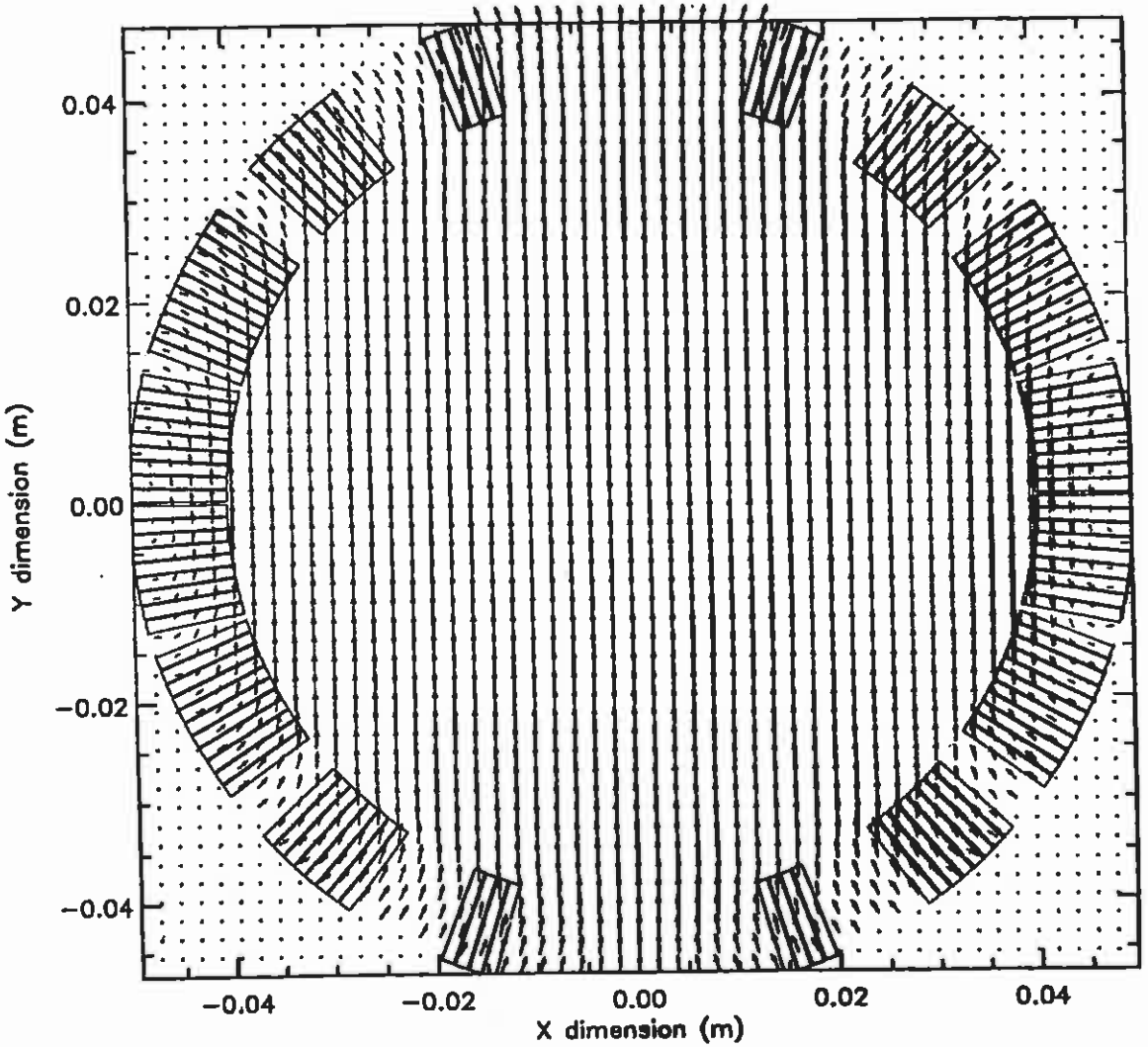

$I_0 \sim 5000\,A \quad B_1 \sim 3.5\,T \quad r_0 = 2.5\,cm$

SSC 5-cm-Aperture Dipole

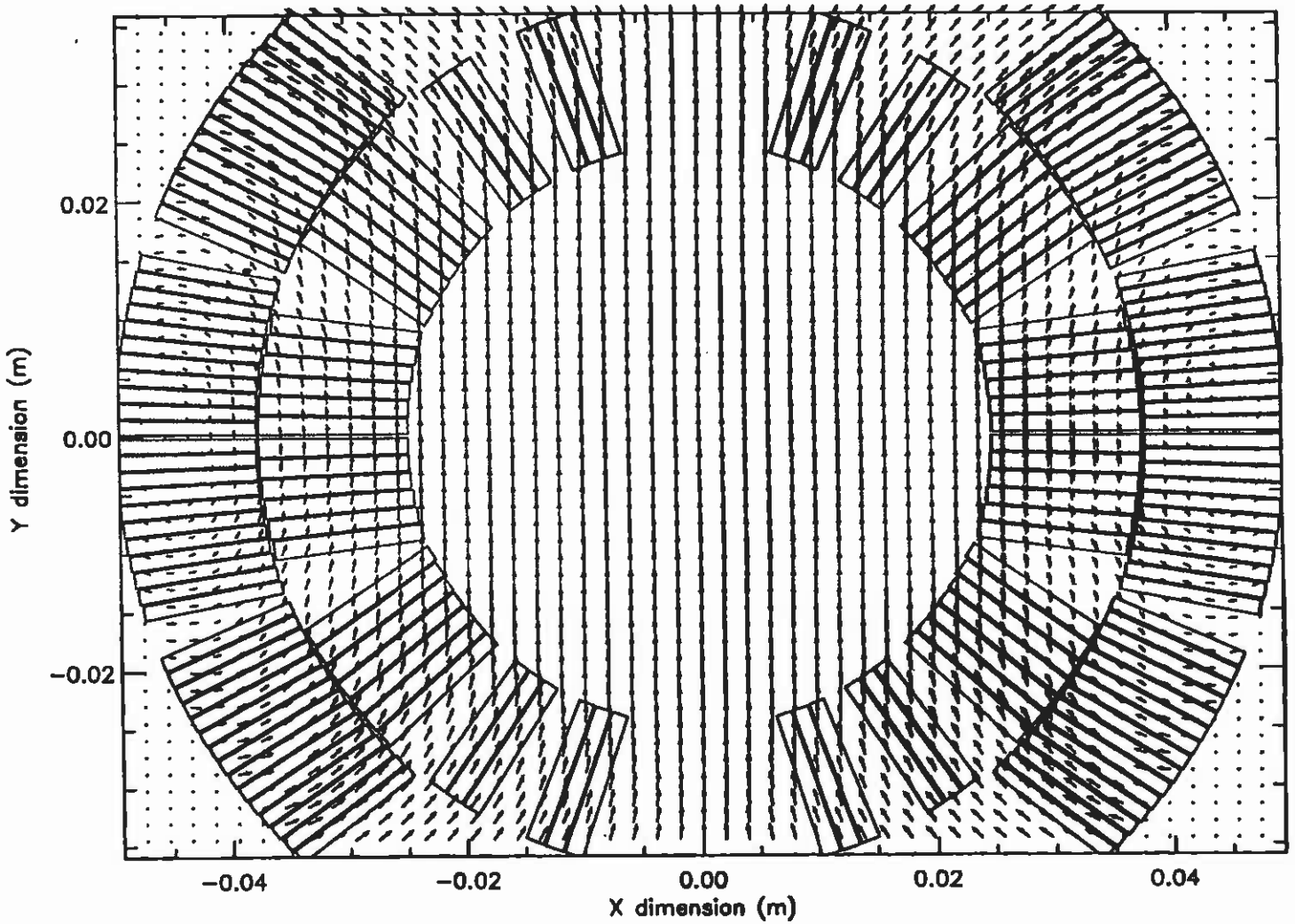

$I_0 \sim 6500\,A \quad B_1 \sim 6.6\,T \quad r_0 = 1\,cm$

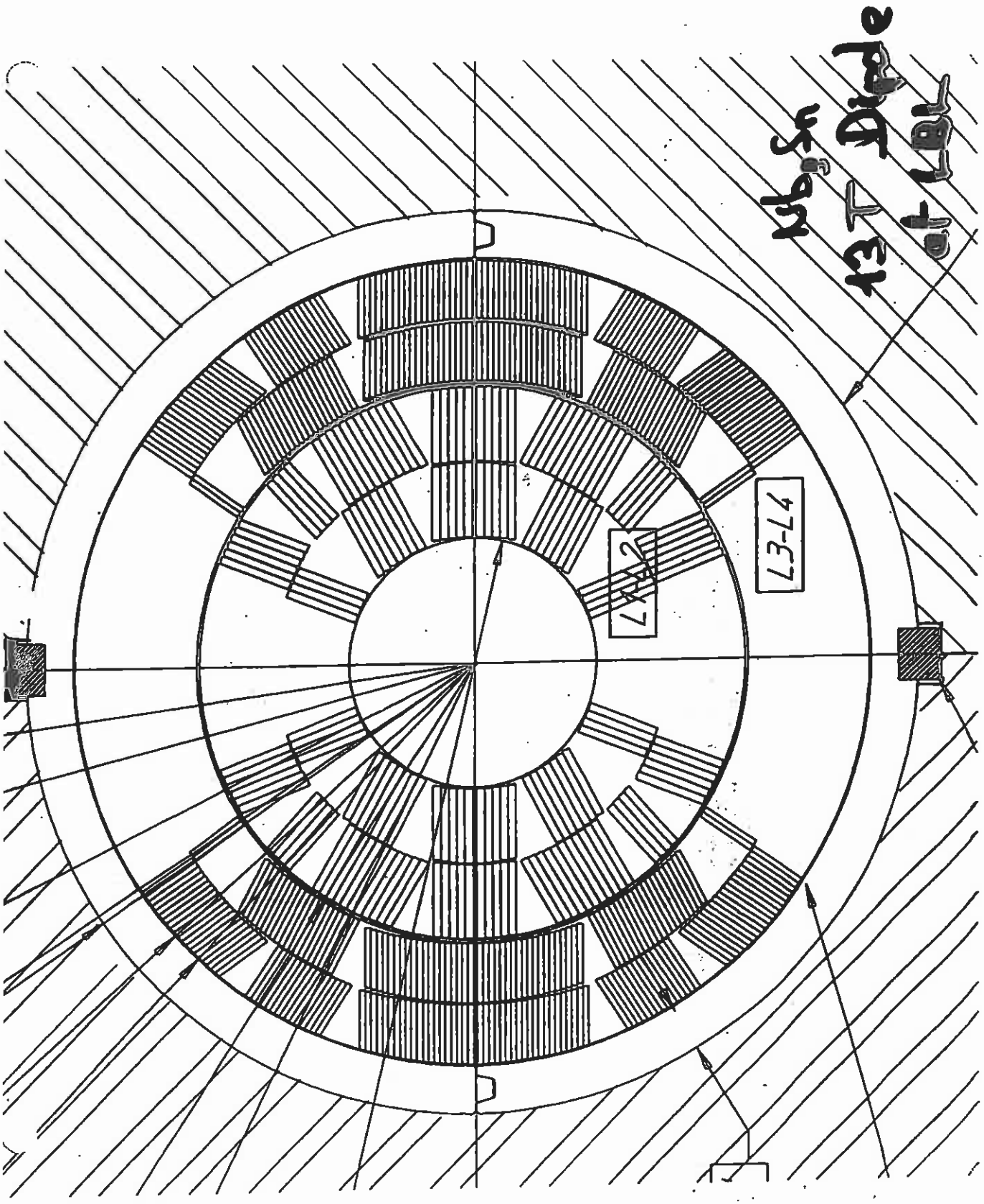

Courtesy D. Dell'Orco

HOW TO ELIMINATE HIGH ORDER MULTIPOLE FIELD COEFFICIENTS?

– The Tevatron coils do not include angular wedges, and the only geometric parameters available for cross-section optimization are the pole angles of the two layers. Hence, only a small number of high order multipole field coefficients can be tuned up.

– Starting with HERA, the magnet coils include several angular wedges which are used to eliminate all the high order multipole field coefficients which need to be eliminated.

Tevatron 3"-Aperture Dipole

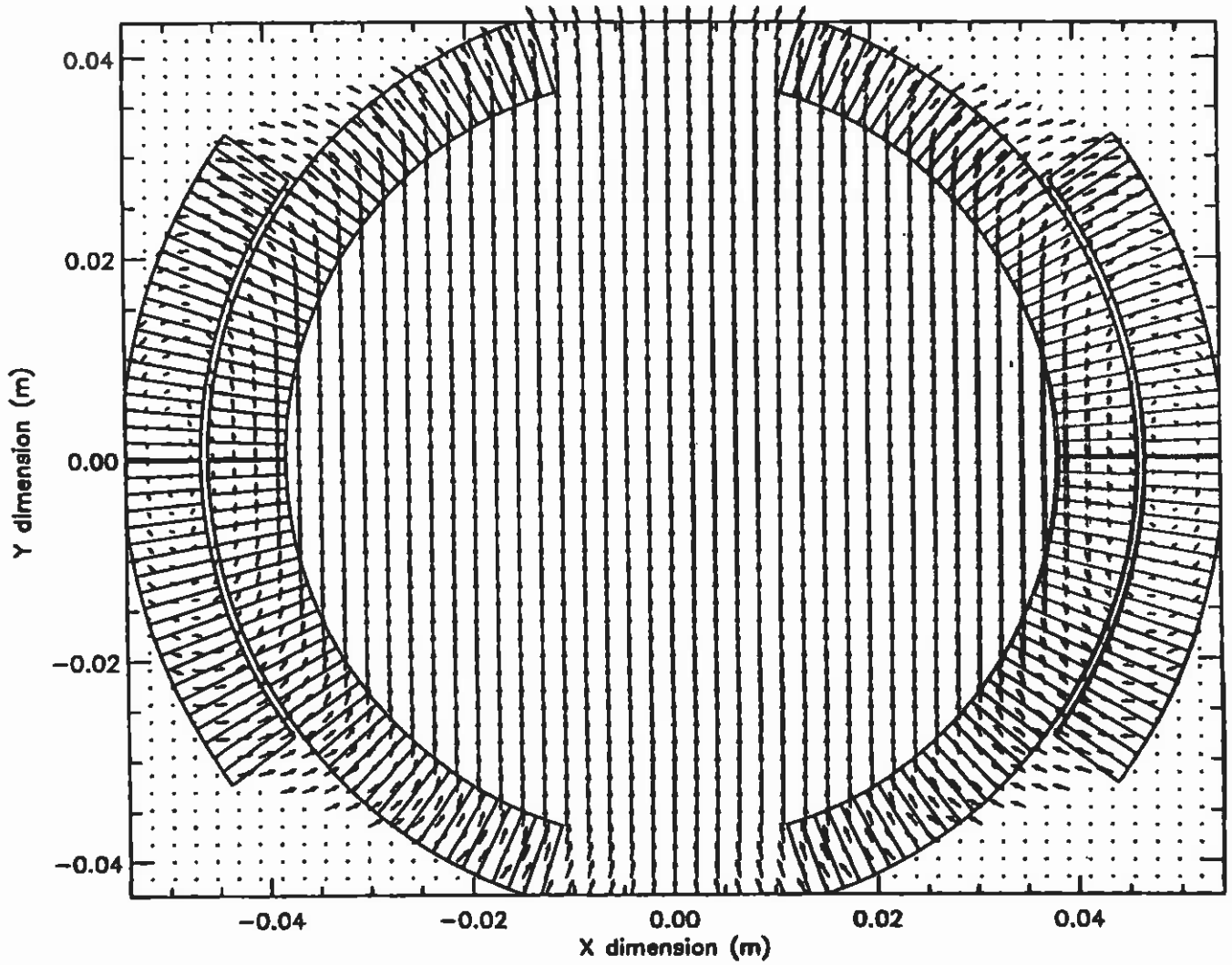

$I_0 \sim 4500\,A \quad B_0 \sim 4.5\,T \quad r_0 = 1"$

HERA 7.5-cm-Aperture Dipole

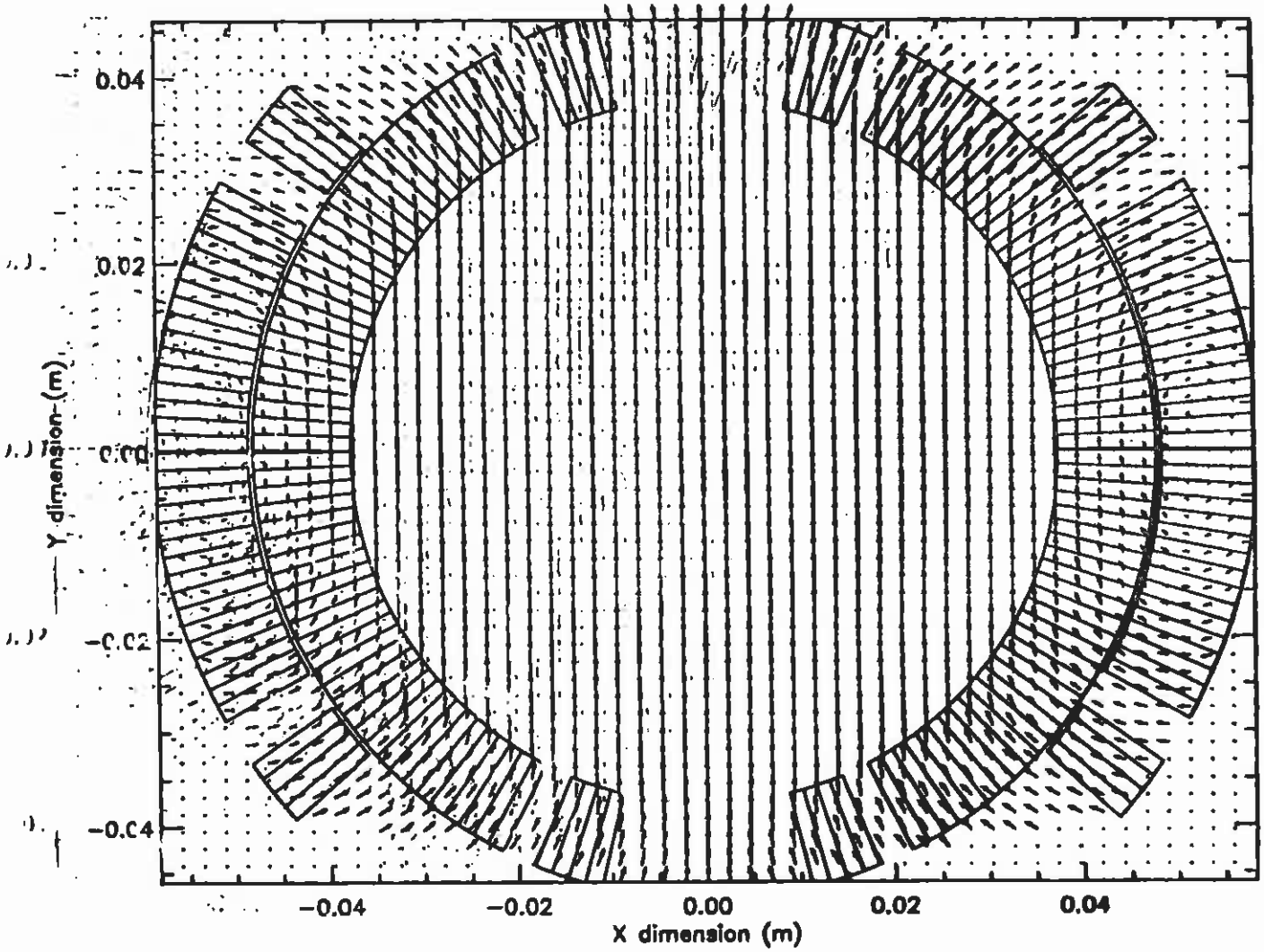

$I_0 \sim 5000$ A $B_0 \sim 4.7$ T $r_0 = 2.5$ cm

$COS\Theta$ AND $COS2\Theta$ COIL DESIGNS

– As explained in previous slides, the angular wedges are introduced in the magnets coils to eliminate high order multipole field coefficients and approach the ideal $\cos\theta$ and $\cos2\theta$ current distributions.

– By analogy, such coil geometries are often referred to as $cos\theta$ and $cos2\theta$ designs.

– The $cos\theta$ and $cos2\theta$ designs are very compact and make the most effective use of conductors by bringing them close to the useful aperture.

CABLE KEYSTONING REQUIREMENT

– In the case of Tevatron, HERA and UNK magnets, the cable keystone angle is large enough to allow the formation of an arch with the desired aperture.

Furthermore, each coil turn lies along a radius vector pointing toward the aperture's center.

– In the case of SSC and LHC magnets, the coil aperture is reduced to minimize the required volume of superconductor. This results in a keystone angle requirement deemed unacceptable from the point of view of cabling degradation.

Hence, in these magnets, the cables are not sufficiently keystoned to assume an arch shape and the wedges between conductor blocks must be made asymmetrical to compensate for this lack.

Also, the coil turns end up being non-radial, which is not favorable to support the effects of the Lorent forces.

Examples: Short LHC dipole magnet models MBSMS 5 blocks and 6 blocks. In the 6-block design, the conductors of the inner coil block next to the pole are more radial than the in the 5-block design. This may have contributed to the better quench performance of these models.

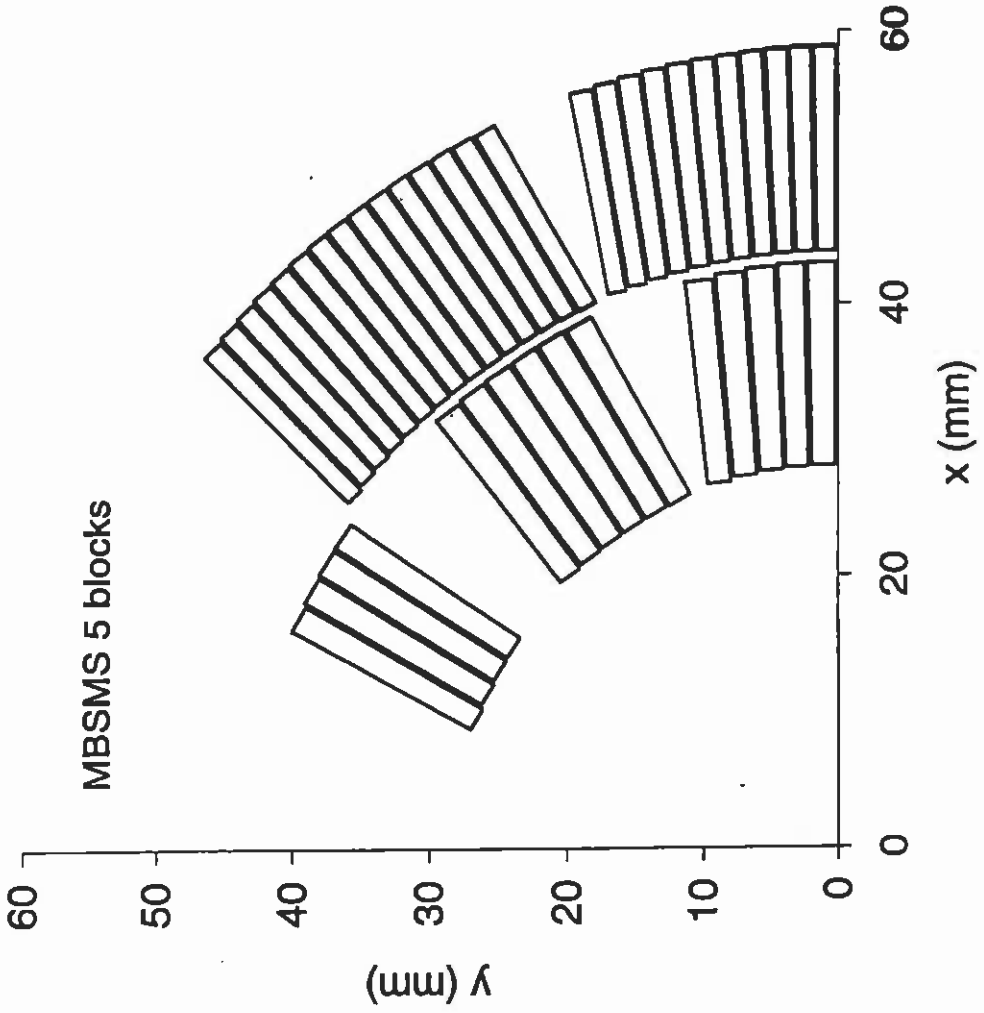

LHC 56-mm-Aperture, 5-block Dipole Magnet Design (Courtesy L. Bottura)

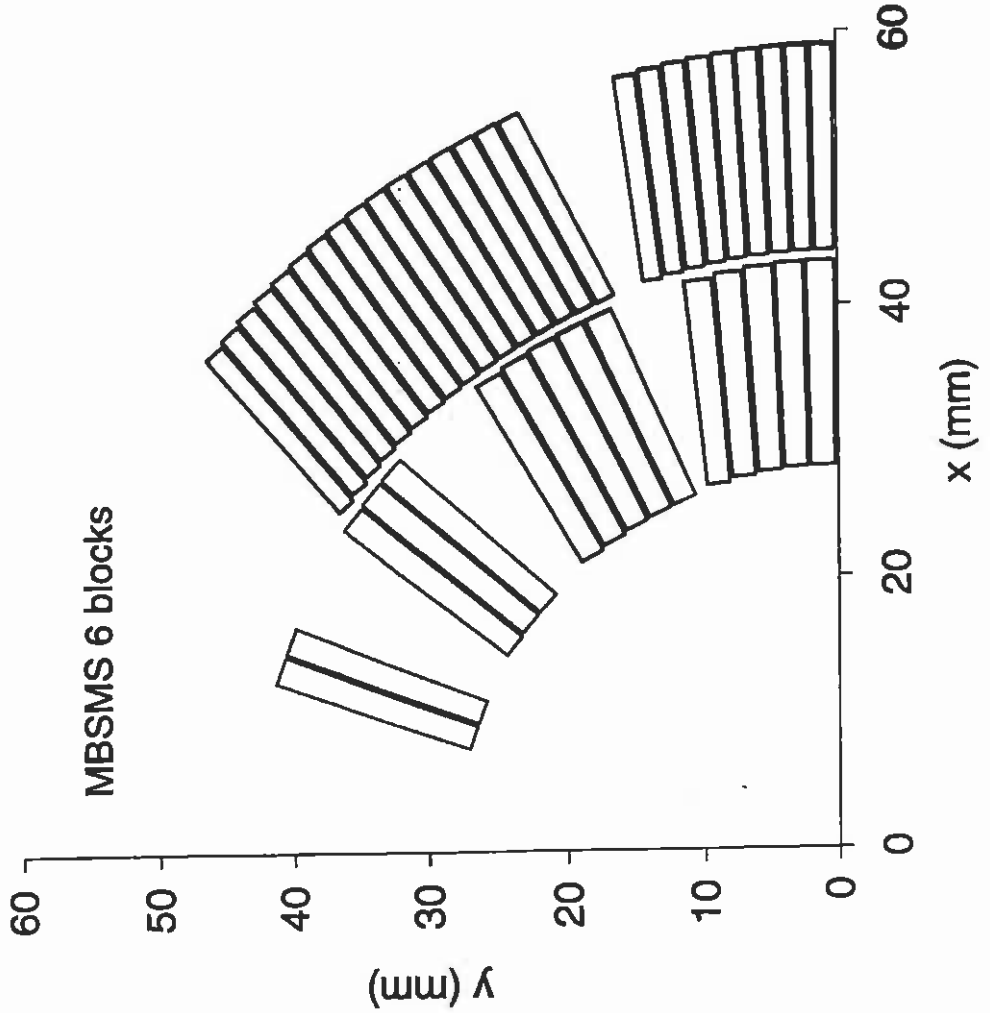

LHC 56-mm-Aperture, 6-Block Dipole Magnet Design
(Courtesy L. Bottura)

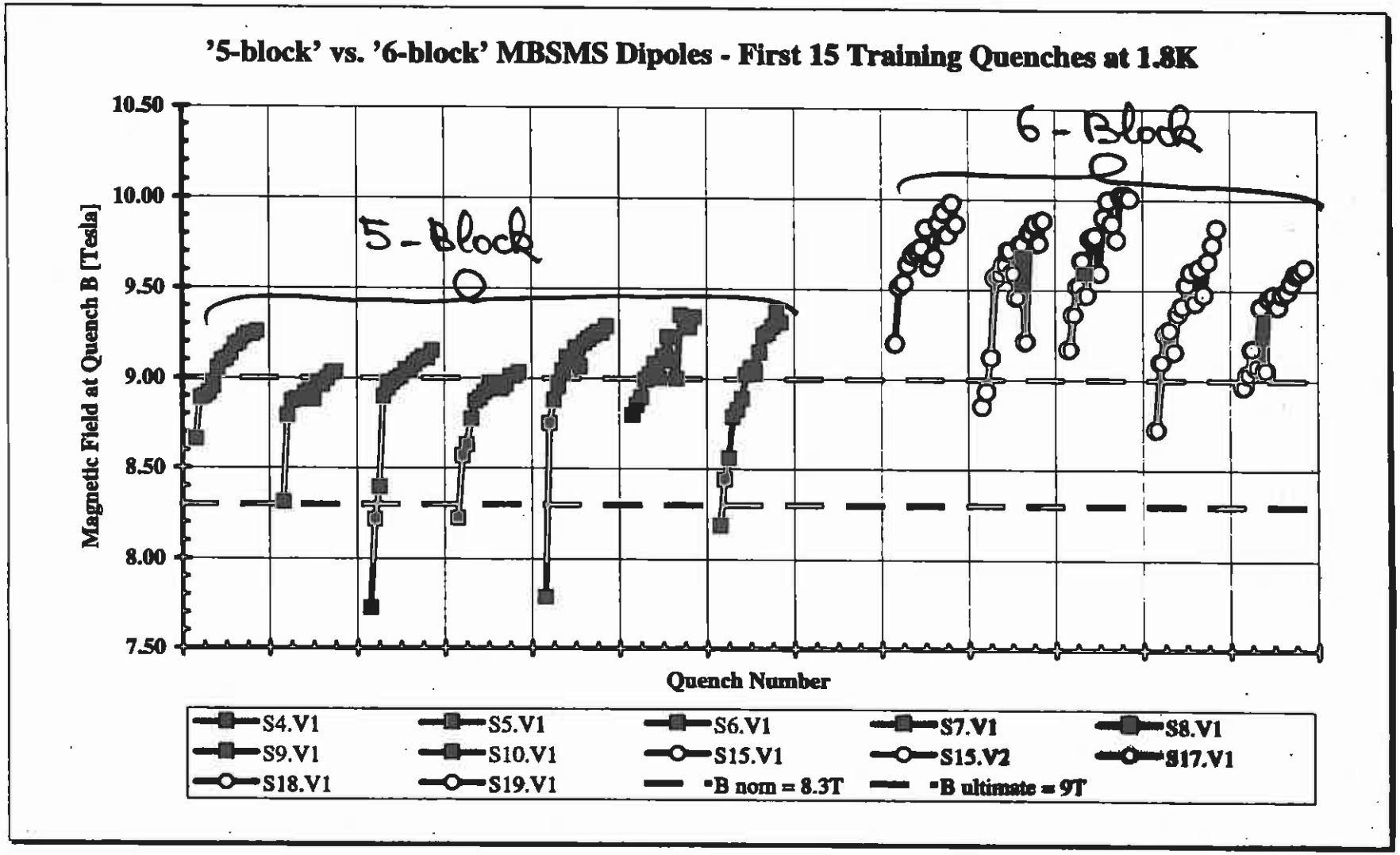

Courtesy A. Siemko

Quench_sum_1_ss'.xls - PAC'99_L ; Revised - 22/02/1999 ; Printed - 8/6/99

FIELD COMPUTATIONS

– The magnetic flux density produced by a magnet coil can be accurately computed by dividing each turn into two rows of elementary current lines parallel to the z-axis and approximately equal in number to the number of cable strands.

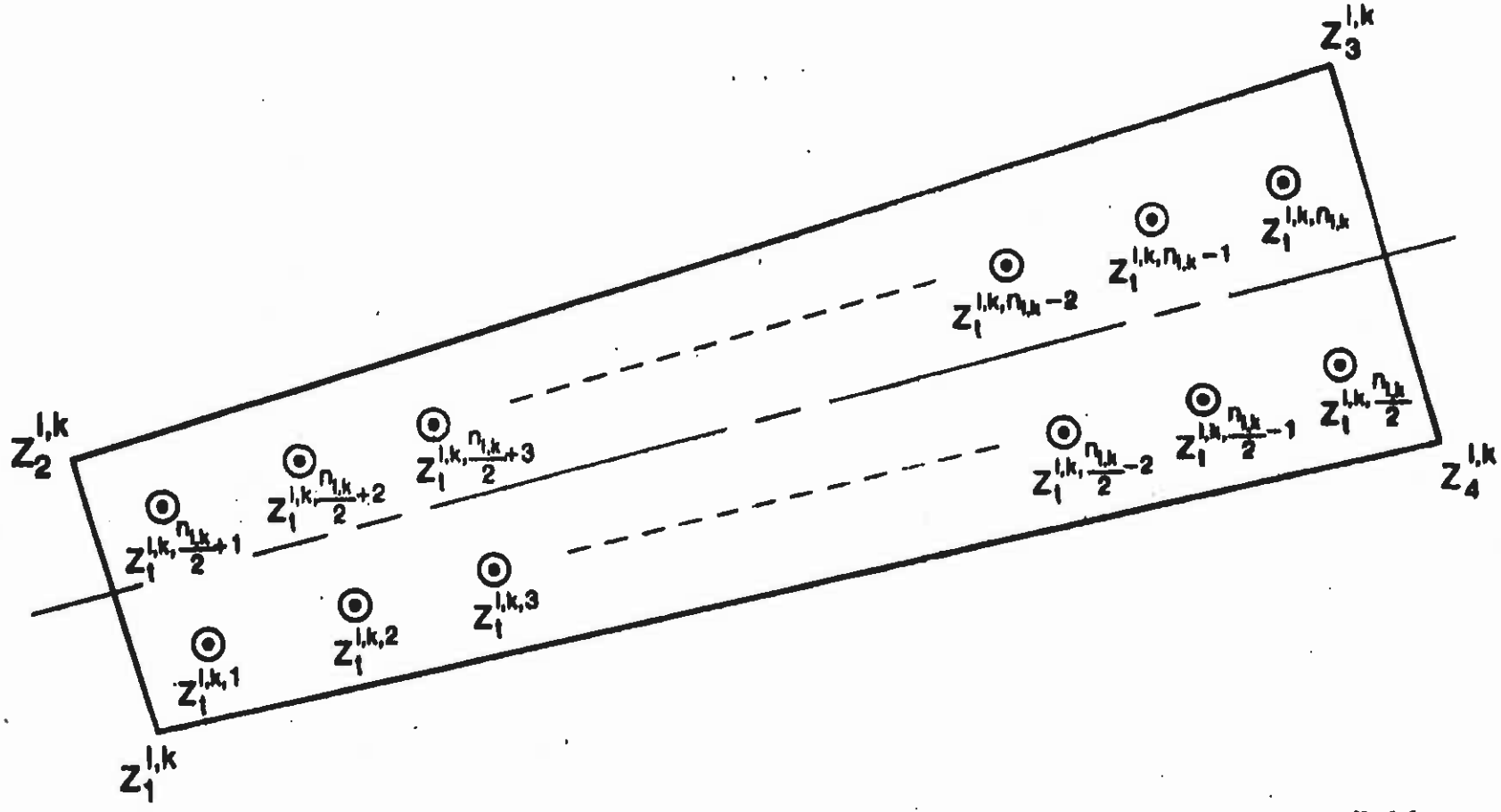

FIGURE 14: Current-line model for the calculation of the transport-current field produced by a given turn of a two-layer cosine-theta coil wound with Rutherford-type cables.

LECTURE 4: MAGNETIC DESIGN OF PARTICLE ACCELERATOR MAGNETS

4.1 Complex Formalism for Two-Dimensional Fields

4.2 Multipole Field Expansion for Two-Dimensional Fields

4.3 Field Computations for Simple Current Distributions

4.4 Two-Dimensional Cosθ and Cos2θ Coil Designs

4.5 Iron Yoke Contribution

4.6 Operating Current Margin

4.7 Saddle-Shaped Coil End Designs

4.8 Other Designs

4.9 Sagitta of Arc Dipole Magnets

4.10 High Order Multipole Field Corrector Magnets

IRON YOKE CONTRIBUTION

– The coils of particle accelerator magnets are usually surrounded by a cylindrical iron yoke, which provides a return path for the magnetic flux while enhancing the central field or field gradient.

– We have seen that the the smaller the yoke inner radius, the larger the field enhancement. However, there are two limitations on how close the iron can be brought to the coils:

- Room must be left for the support structure,

- Iron saturates for fields above 2 T, resulting in undesirable distortions (see lecture on field quality).

IRON YOKE CONTRIBUTION (CONT.)

– As already mentioned, the Tevatron magnets use a warm iron yoke (*i.e.*, placed outside the helium containment and vacuum vessel), but starting with HERA, the iron yoke is included within the magnet cold mass.

– For SSC dipole magnets, the field enhancement due to the yoke is of the order of 20%.

– In LHC magnets, two coil assemblies (powered with opposite polarity) are placed within a common iron yoke. This twin-aperture design results in left/right asymmetries in the yoke around each coil assembly taken individually. These asymmetries must be taken into account when calculating field quality.

LHC dipole

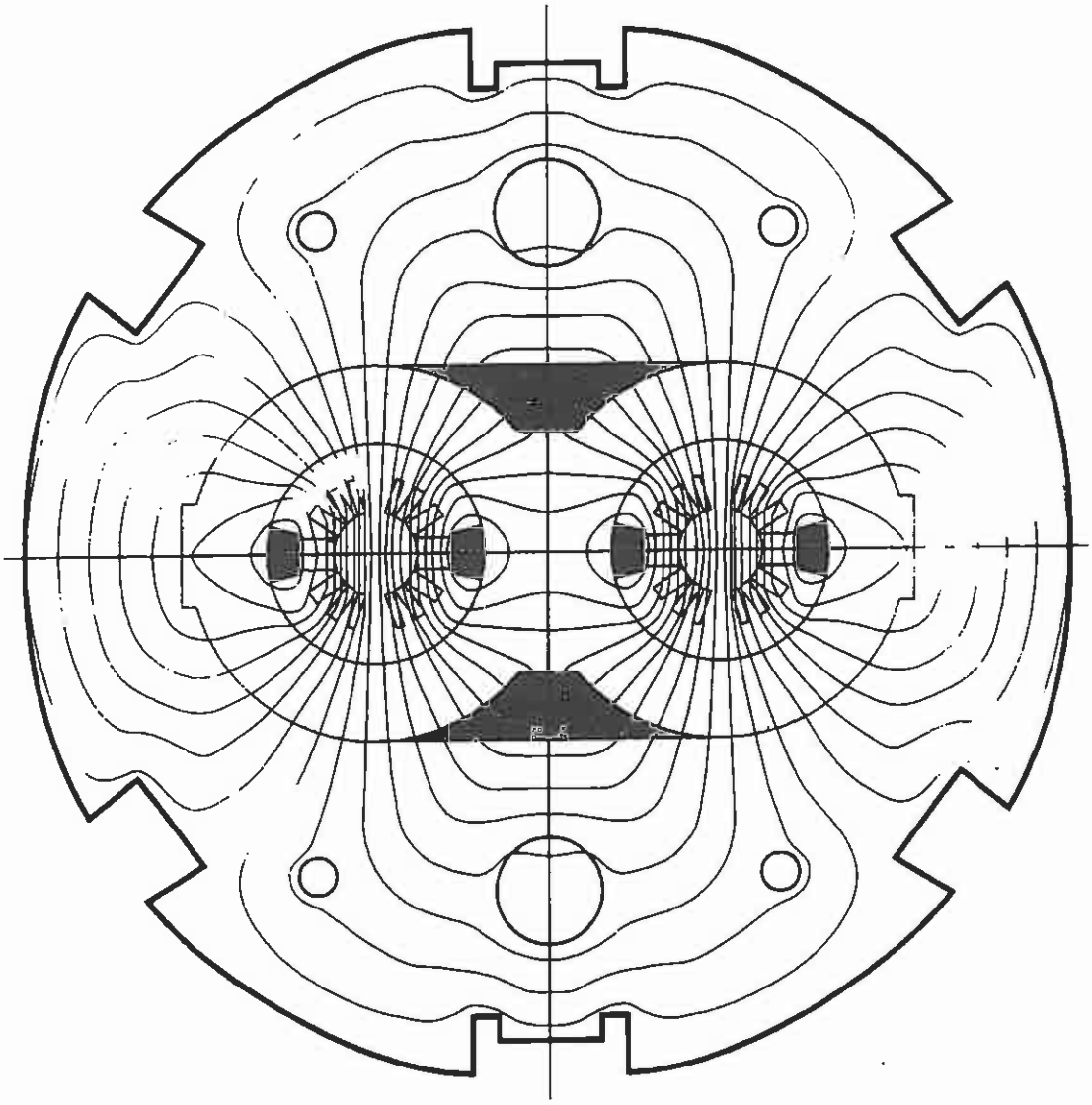

Computed magnetic flux map at B_0=10 Tesla

LECTURE 4: MAGNETIC DESIGN OF PARTICLE ACCELERATOR MAGNETS

4.1 Complex Formalism for Two-Dimensional Fields

4.2 Multipole Field Expansion for Two-Dimensional Fields

4.3 Field Computations for Simple Current Distributions

4.4 Two-Dimensional Cosθ and Cos2θ Coil Designs

4.5 Iron Yoke Contribution

4.6 Operating Current Margin

4.7 Saddle-Shaped Coil End Designs

4.8 Other Designs

4.9 Sagitta of Arc Dipole Magnets

4.10 High Order Multipole Field Corrector Magnets

FACTORS INFLUENCING OVERALL CURRENT DENSITY IN MAGNET COIL

– To achieve high fields and high field gradients, it is desirable to maximize the overall current density in the magnet coil. This can be done by three means:

- *Maximizing superconductor performance,*
- *Minimizing copper-to-superconductor ratio* in cable strands,
- *Minimizing turn-to-turn insulation* thickness.

– As explained in previous lectures, there are lower bounds on the values of copper-to-superconductor ratio and insulation thickness in order to limit conductor heating in case of a quench and to ensure proper electrical insulation.

PEAK FIELD IN MAGNET COIL

– Regarding superconductor performance, the upper limit is determined by the critical current density at the operating temperature and magnetic flux density.

– The magnetic flux density to which the conductor is exposed is non-uniform over the magnet coil, but the maximum current-carrying capability of the conductor is determined by the section where the magnetic flux density is the highest.

– In most cases, the so-called *peak field* is located in the pole turn of the innermost coil layer.

V6-1

21/01/99 16.52

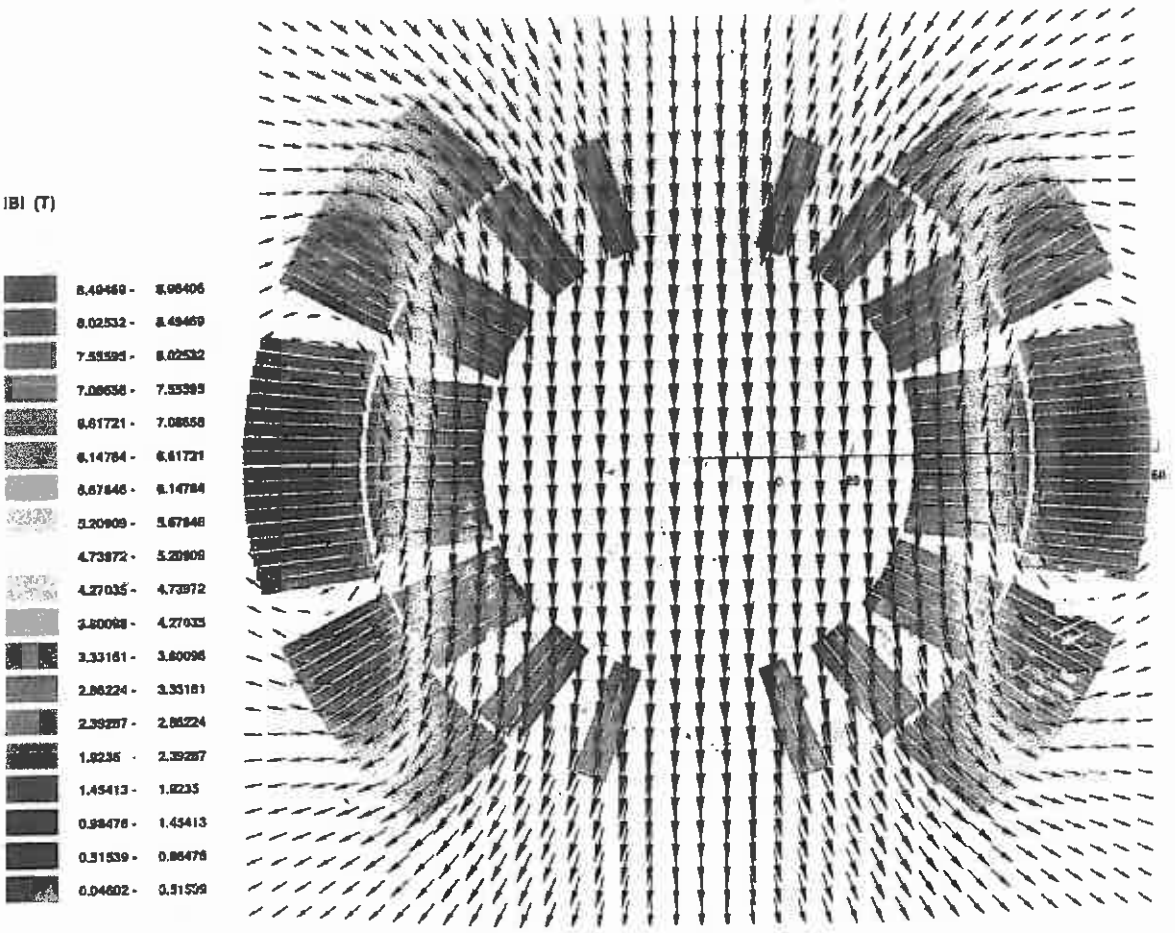

ROXIE 6.0

LHC

$I_0 = 11500$ A

$B_1 = 8.35$ T

MAXIMUM QUENCH CURRENT OF MAGNET

– Let $B_p = f(I)$ designate the peak magnetic flux density on the coil as a function of supplied current, I, and let $I_C = f(B,T_0)$ designate the supposedly known cable critical current as a function of applied magnetic flux density, B, at the operating temperature, T_0.

– The intersection between these two curves determines the maximum quench current of the magnet at T_0, $I_{qm}(T_0)$.

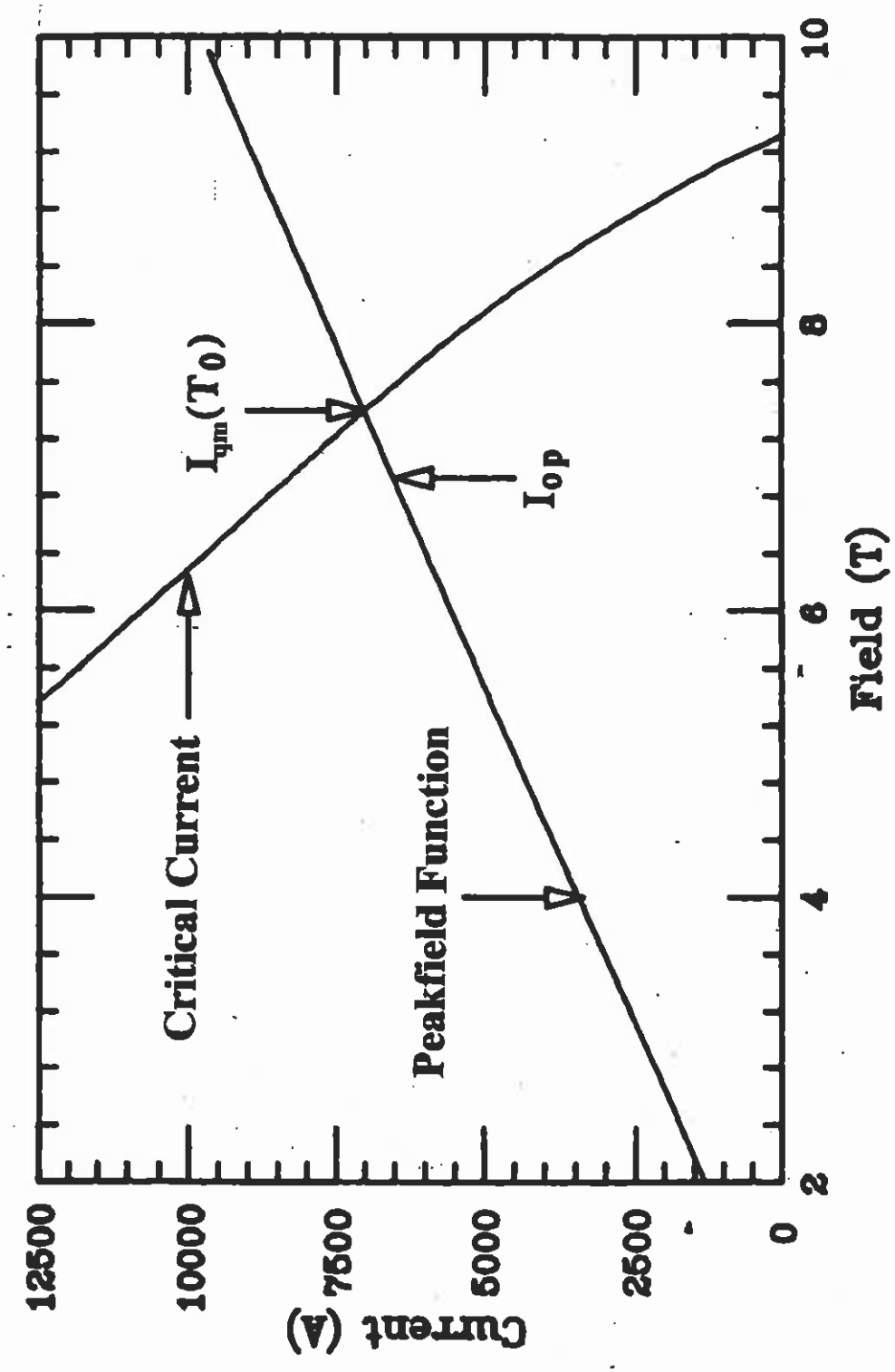
Critical Current
Peakfield Function
$I_{qm}(T_0)$
I_{op}
Current (A)
Field (T)
12500
10000
7500
5000
2500
0
2
4
6
8
10

OPERATING CURRENT MARGIN

– In practice, magnets must be operated below I_{qn} so as to ensure that the entire coil is in the superconducting state and as to limit the risks of quenching.

– Let I_{op} designate the operating current. Then, the operating current margin of the magnet, m_I, is defined as

$$m_I(T_0) = 1 - \frac{I_{op}}{I_{qn}(T_0)}$$

CURRENT MARGIN REQUIREMENTS

– The excellent quench performance of the HERA magnets suggests that the current margin can be set to as little as 10%, but it is safer to aim for 20%.

– In comparison to other superconducting magnets, such as solenoids for magnetic resonance imaging, a current margin of 10 to 20% is quite small.

– This implies that accelerator magnets are operated very close to the superconductor critical surface and are very sensitive to any kind of disturbances that may cause the magnet to cross the critical surface and lead to a quench.

416 HERA dipole magnets quench data

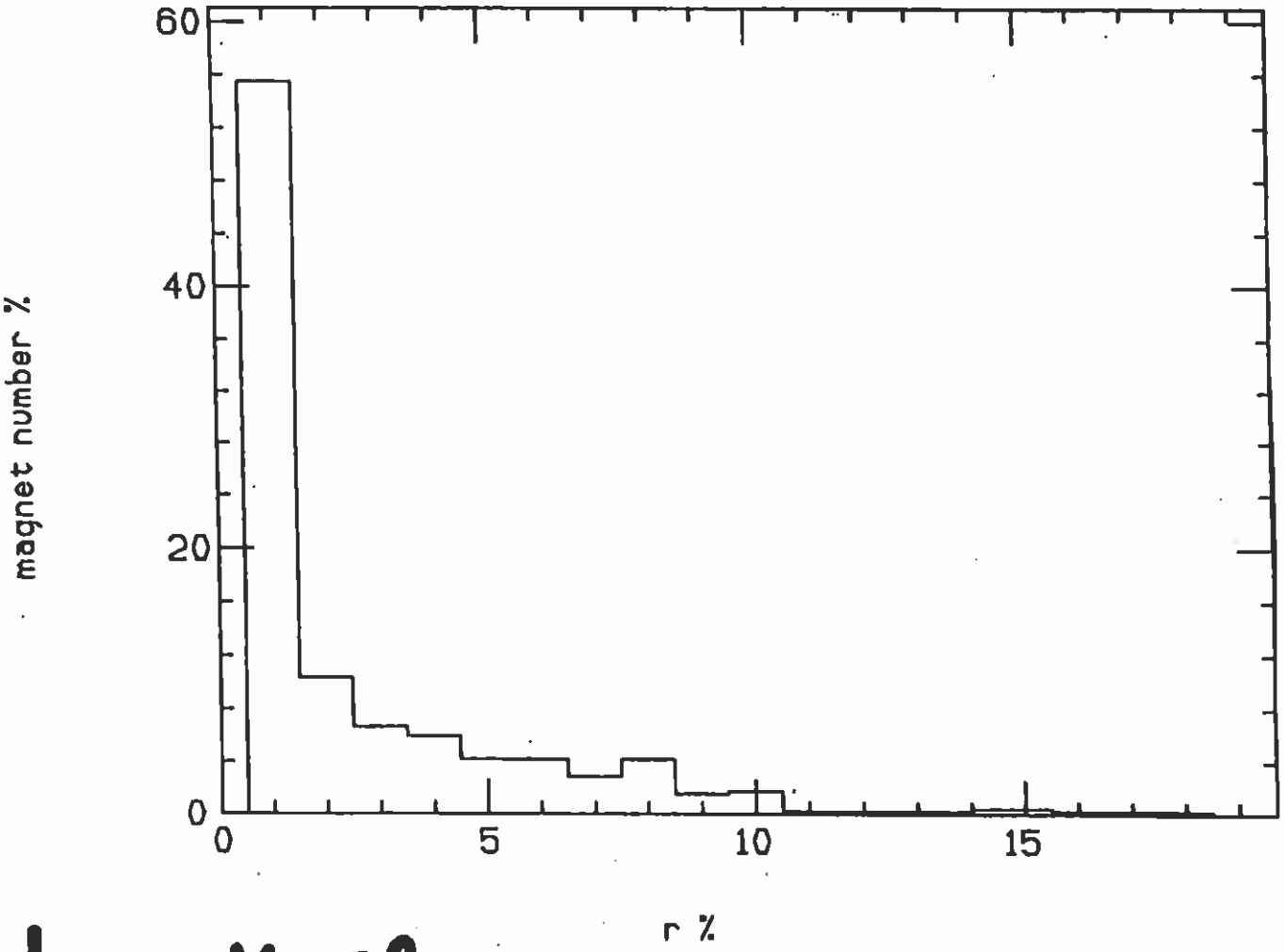

Courtesy Y. Zhao

220 HERA quadrupole magnets quench data*

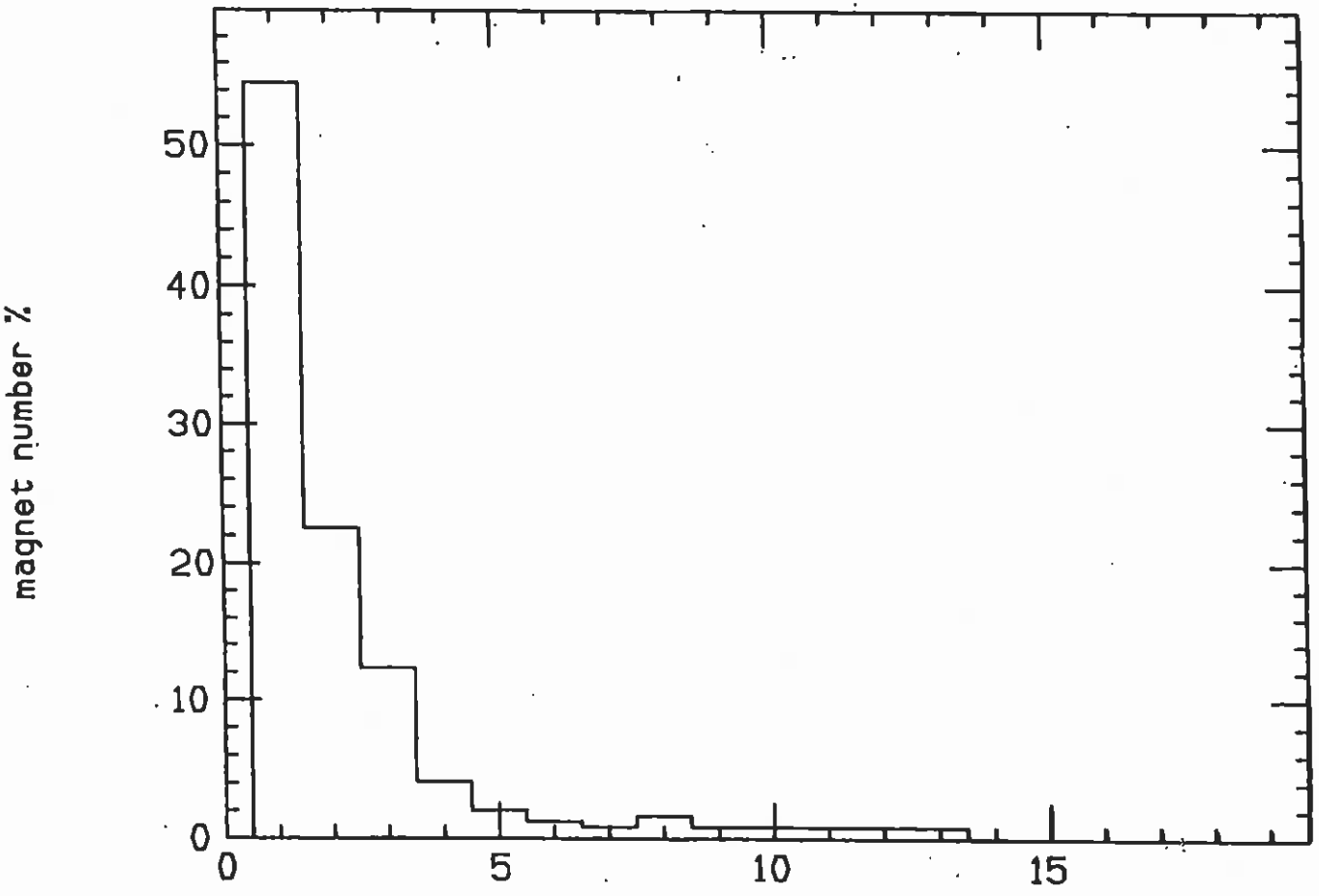

*Courtesy Y. Zhao

CONDUCTOR GRADING

– A particularity of two-layer, cosθ dipole magnet coil designs is that the peak magnetic flux density in the outermost layer is quite a bit lower than in the innermost layer.

– Hence, when using the same cable and current for both layers, the outer layer is operated with a much higher current margin than the inner layer, which can be considered as a waste of costly superconductor.

– The conductor used for the outer layers of SSC and LHC dipole magnet coils is smaller than the conductor used for the inner layers.

This results in a higher overall current density in the outer layer and reduces the difference in current margins. Such action is referred to as conductor *grading*.

– The main disadvantage of grading is that it requires splices between the cables of the two layers, which, of course, are connected electrically in series (and require only one power supply).

– It should be noted that for two-layer, cos2θ quadrupole magnet coil designs, the peak magnetic flux density is almost the same for the two layers and that there is no point in conductor grading.

LECTURE 4: MAGNETIC DESIGN OF PARTICLE ACCELERATOR MAGNETS

4.1 Complex Formalism for Two-Dimensional Fields

4.2 Multipole Field Expansion for Two-Dimensional Fields

4.3 Field Computations for Simple Current Distributions

4.4 Two-Dimensional Cosθ and Cos2θ Coil Designs

4.5 Iron Yoke Contribution

4.6 Operating Current Margin

4.7 Saddle-Shaped Coil End Designs

4.8 Other Designs

4.9 Sagitta of Arc Dipole Magnets

4.10 High Order Multipole Field Corrector Magnets

SADDLE-SHAPED COILS

– One of the main difficulties of $\cos\theta$ and $\cos 2\theta$ designs is the realization of coil ends: in the coil straight section, the conductors run parallel to the magnet axis, but, in the ends, the conductors must be bent sharply to make U-turns over the beam tube inserted within the magnet coil assembly.

– This confers to the coil a *saddle shape.*

MBSMSO RETURN END 13/03/95 17.54

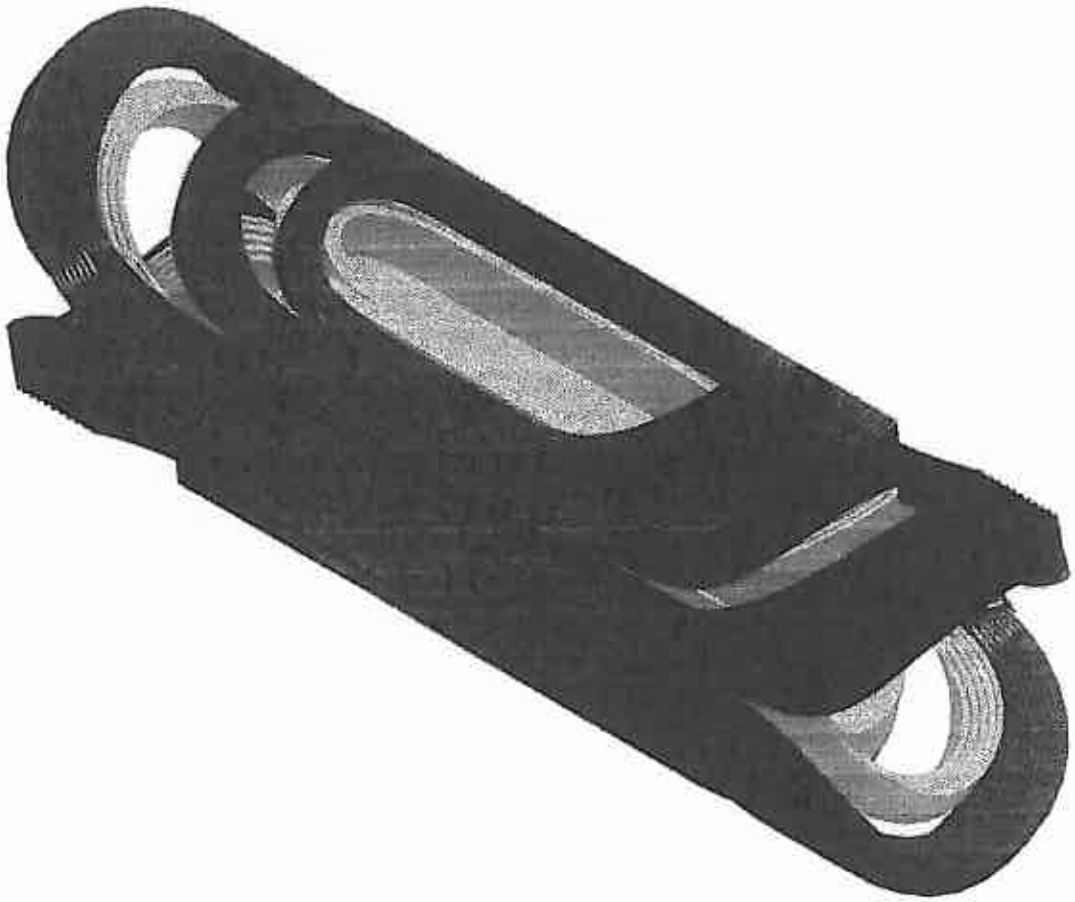

ROXIE3.4

Courtesy S. Russenschuck

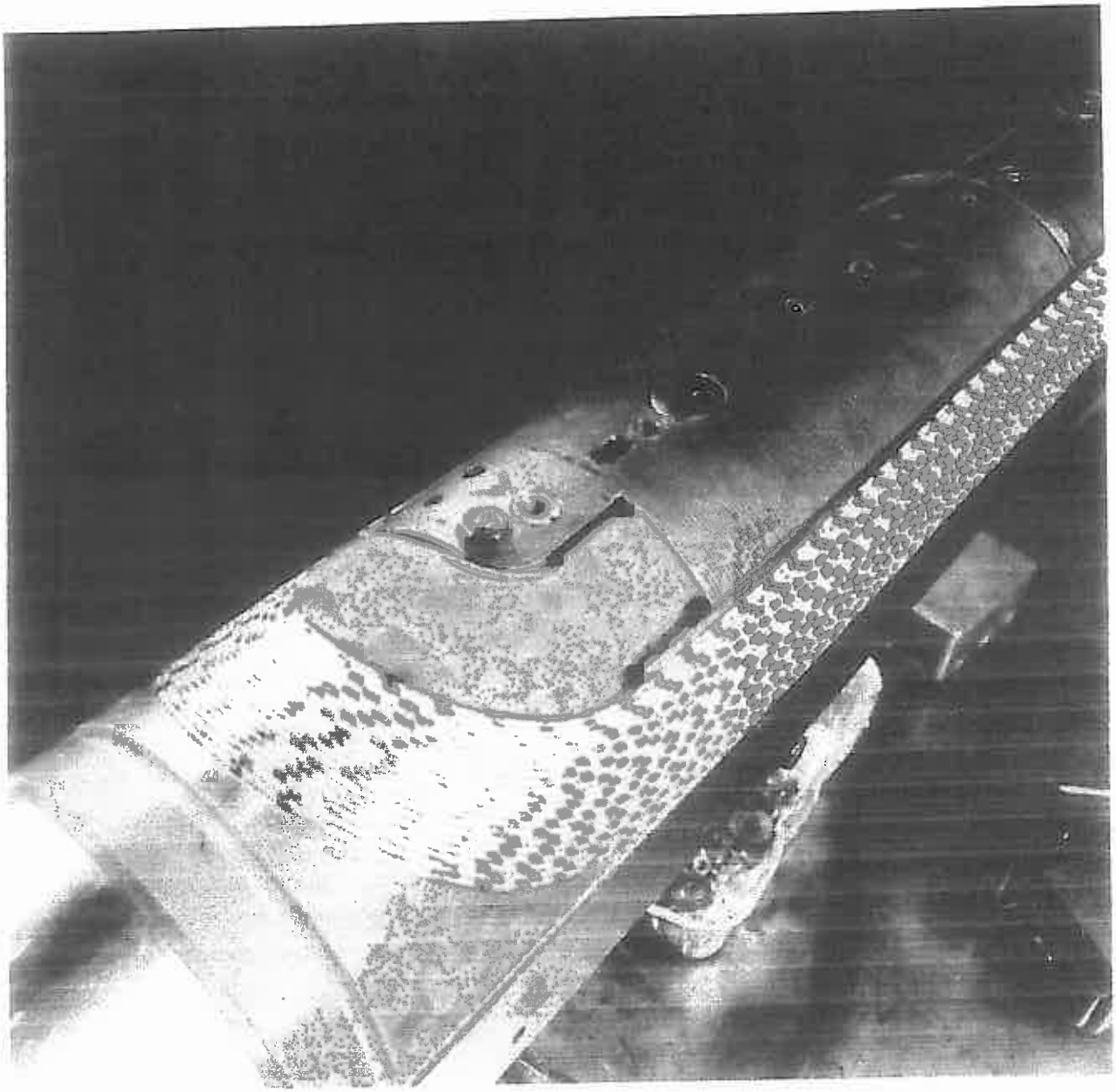

COIL END DESIGN

– If nothing is done, the peakfield is located in the turnaround of the coil pole turn and the coil ends can add significant contributions to some of the multipole field components.

– Starting with HERA, the coil ends include spacers which are used to lower the field over the ends and to tune up the multipole contents (in that respect, end spacers play a role similar to that of angular wedges in the 2-D cross-section).

Tevatron Ends*

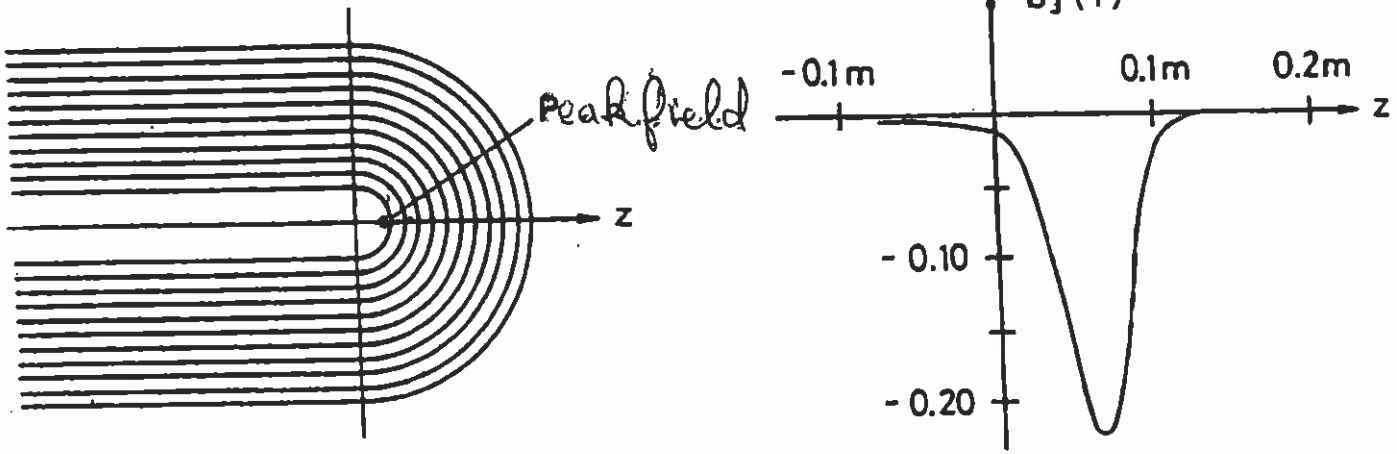

a) Unwrapped view of simple coil head configuration. The highest field in the coil is at the point P.

b) Sextupole field in the coil head for a central field of 4.5 T.

- Negative sextupole in ends is corrected by positive sextupole in straight sections
- Peak field on conductor is at the worst location

* Courtesy P. Schmüser

656 Tevatron Dipole Magnets

$I_0 = 4500$ A (4.5 T) $r_0 = 1''$

Normal Harmonic Coefficient	Upstream mean	Upstream rms	Center mean	Center rms	Downstream mean	Downstream rms	Average mean	Average rms	Upstream Downstream Difference rms
Sextupole	-7.86	2.81	13.39	2.70	-7.80	2.74	0.48	2.66	1.22
Octupole	-0.18	0.93	-0.10	0.85	-0.37	0.93	-0.20	0.81	0.83
Decapole	-2.06	1.42	+1.11	1.38	-1.57	1.40	-0.64	1.33	0.58
12-pole	-0.07	0.36	-0.07	0.39	-0.05	0.35	-0.06	0.32	0.33
14-pole	5.07	0.52	5.63	0.49	5.25	0.51	5.35	0.46	0.39
18-pole	-12.44	0.36	-12.57	0.37	-12.34	0.36	-12.46	0.30	0.35
22-pole	3.60	0.32	3.79	0.40	3.79	0.36	3.70	0.26	0.40
Skew Harmonic Coefficient									
Sextupole	-0.43	1.78	0.12	1.26	0.63	1.56	0.12	1.19	2.36
Octupole	-0.11	1.55	-0.08	1.43	-0.10	1.48	-0.10	1.42	0.80
Decapole	0.05	0.50	-0.08	0.52	-0.25	0.51	-0.10	0.45	0.47
12-pole	-0.11	0.59	-0.01	0.57	-0.10	0.61	-0.06	0.55	0.42
14-pole	-0.19	0.42	-0.05	0.40	-0.15	0.37	-0.12	0.29	0.49
18-pole	0.04	0.62	-0.03	0.59	-0.02	0.59	-0.08	0.36	0.85
22-pole	-0.04	0.38	0.08	0.39	0.17	0.37	0.07	0.23	0.53

Table 1. Values of mean and rms of distributions of harmonic coefficients. All values are in standard units as defined in the text.

(NB: $T_0 = 4.65$ K)

HERA Ends*

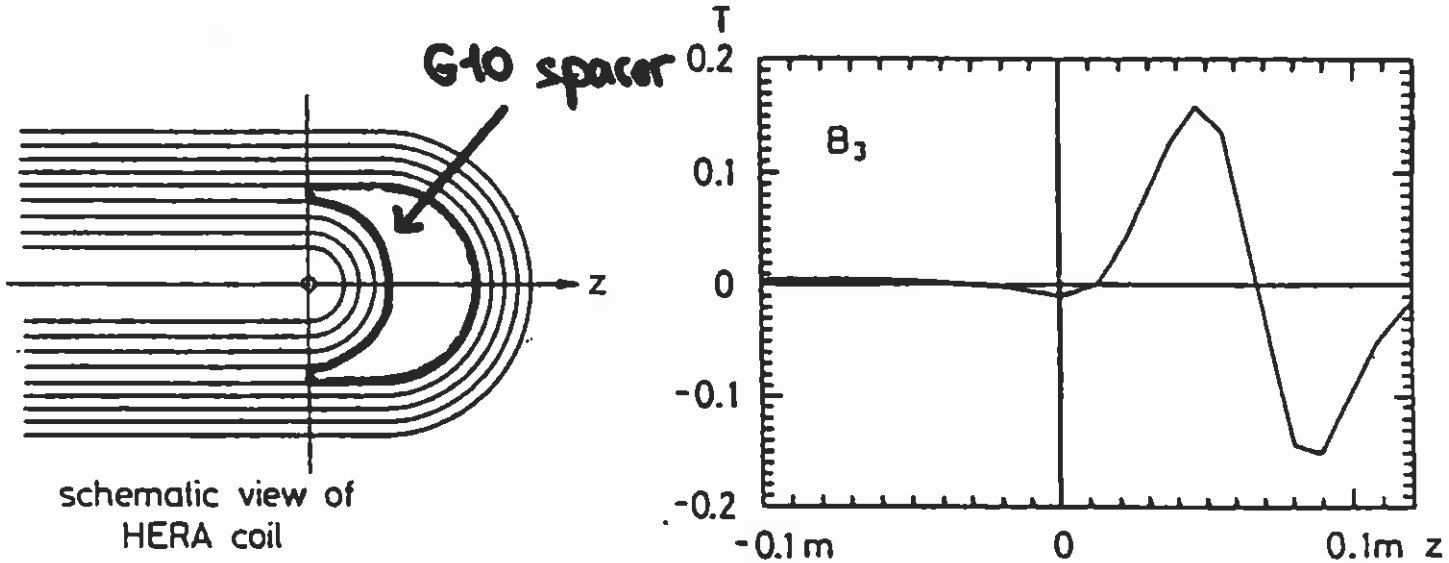

a) Schematic view of HERA coil head with spacers

b) Computed sextupole field of HERA dipole

- Average b_2 and b_4 are zero
- No field enhancement in ends

* Courtesy P. Schmüser

COIL END DESIGN (CONT.)

– Starting with SSC, the electromagnetic computations are coupled with 3-D mechanical computations so as to determine the conductor trajectories minimizing strain energy.

Nevertheless, the end spacer design often requires winding tests to determine correction factors.

– The end spacers used in SSC and LHC magnet coils are precisely machined and turn out to be very costly items.

– In comparison to saddle-shaped coils, the ends of racetrack-type coils are far simpler.

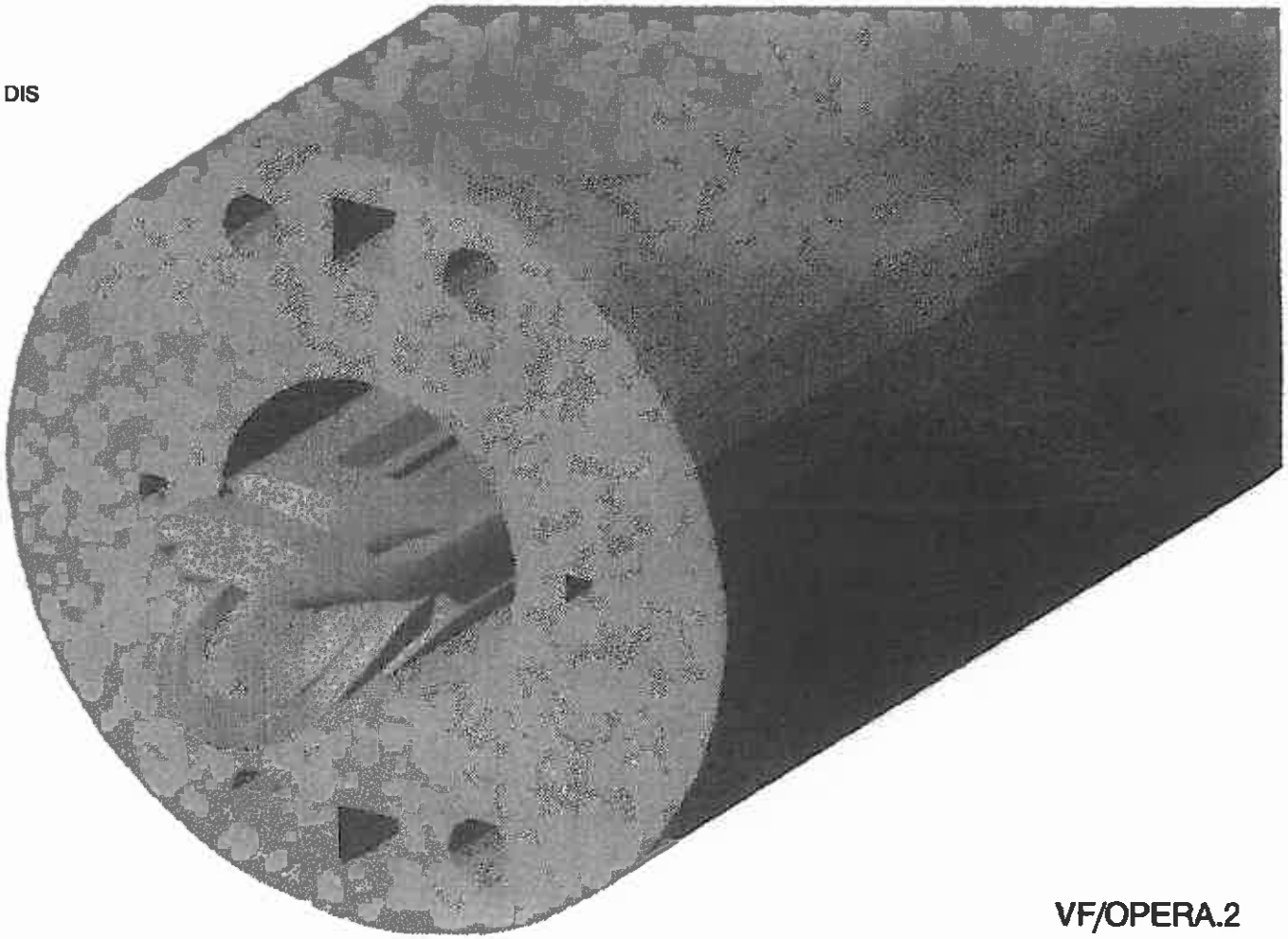

Courtesy D. Orrel

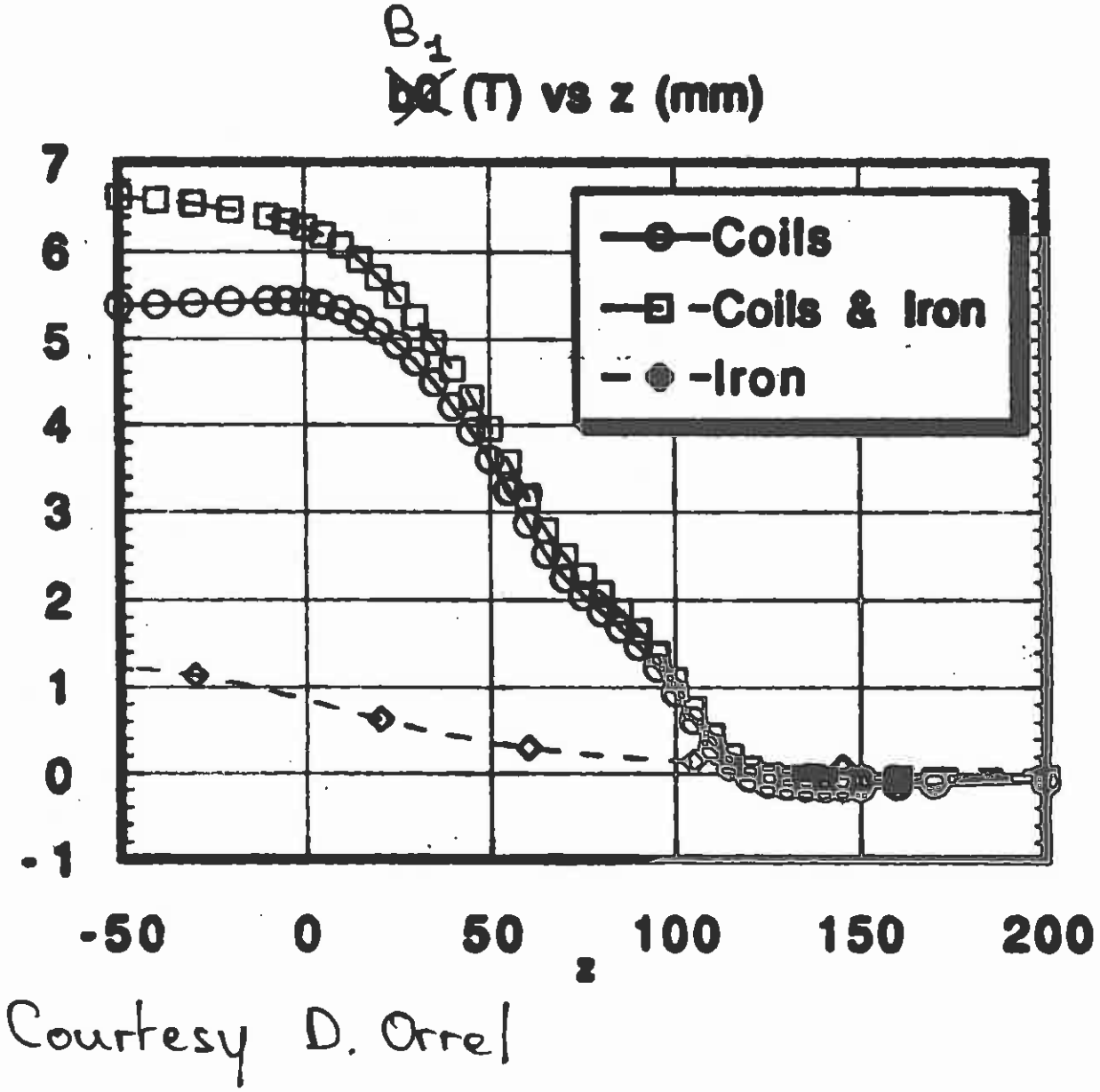

Courtesy D. Orrel

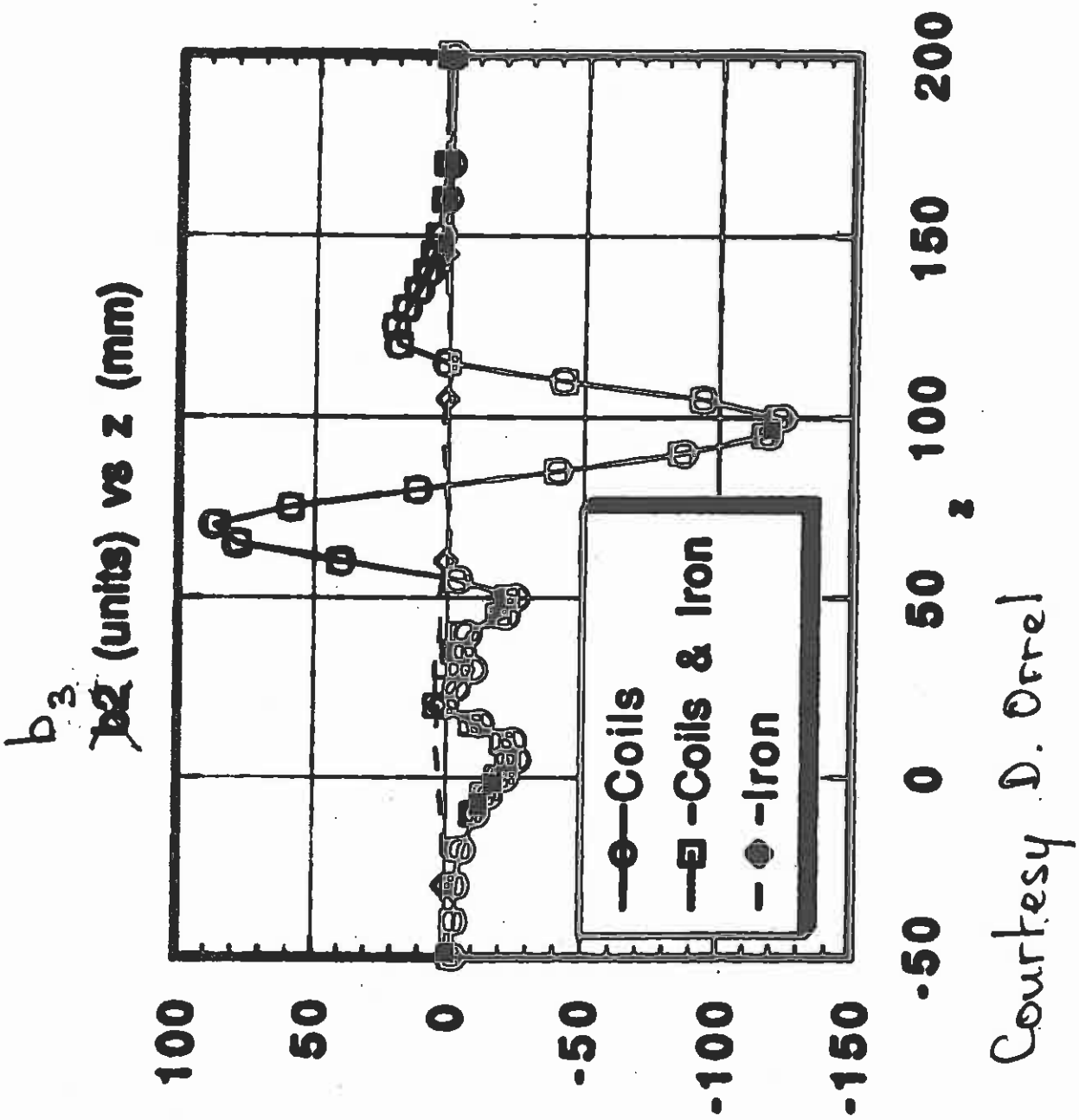
b3
b2 (units) vs z (mm)
100
50
0
-50
-100
-150
-50
0
50
100
150
200
z
Coils
Coils & Iron
Iron
Courtesy D. Orrel

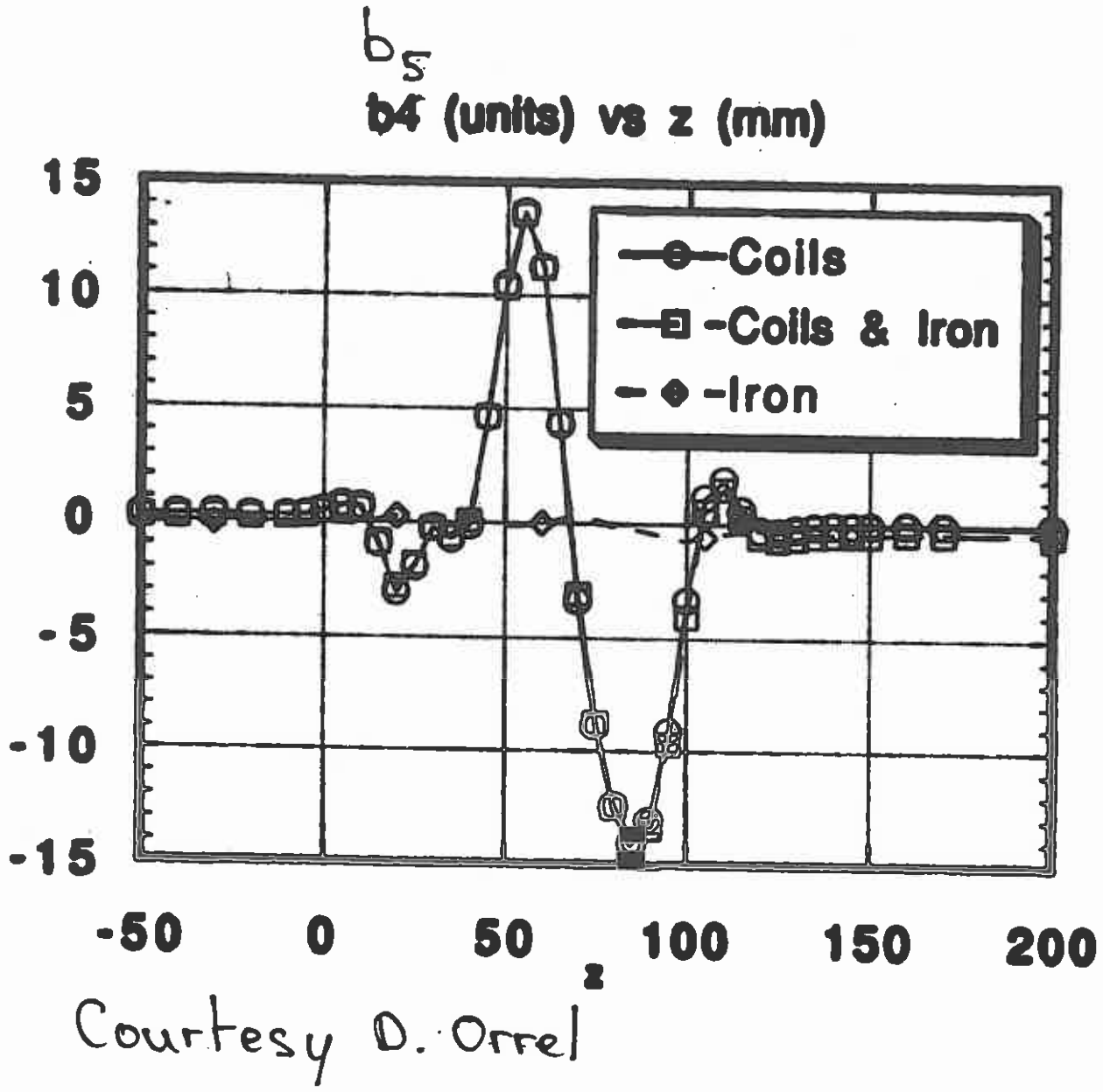
b_5
b4 (units) vs z (mm)
15
10
5
0
-5
-10
-15
-50
0
50
100
150
200
z
Coils
-Coils & Iron
-Iron
Courtesy D. Orrel

Courtesy D. Perini

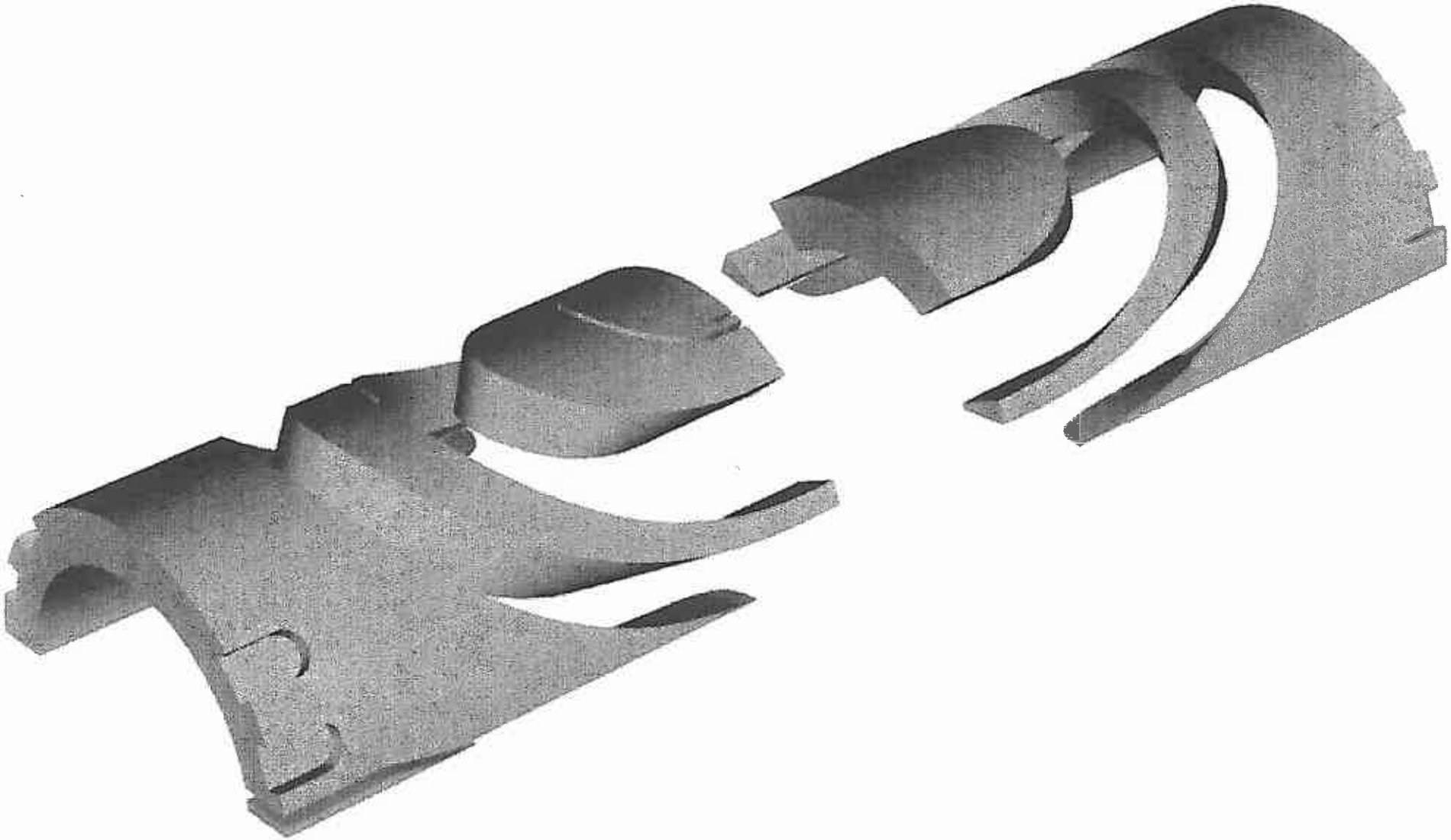

Courtesy D. Perini

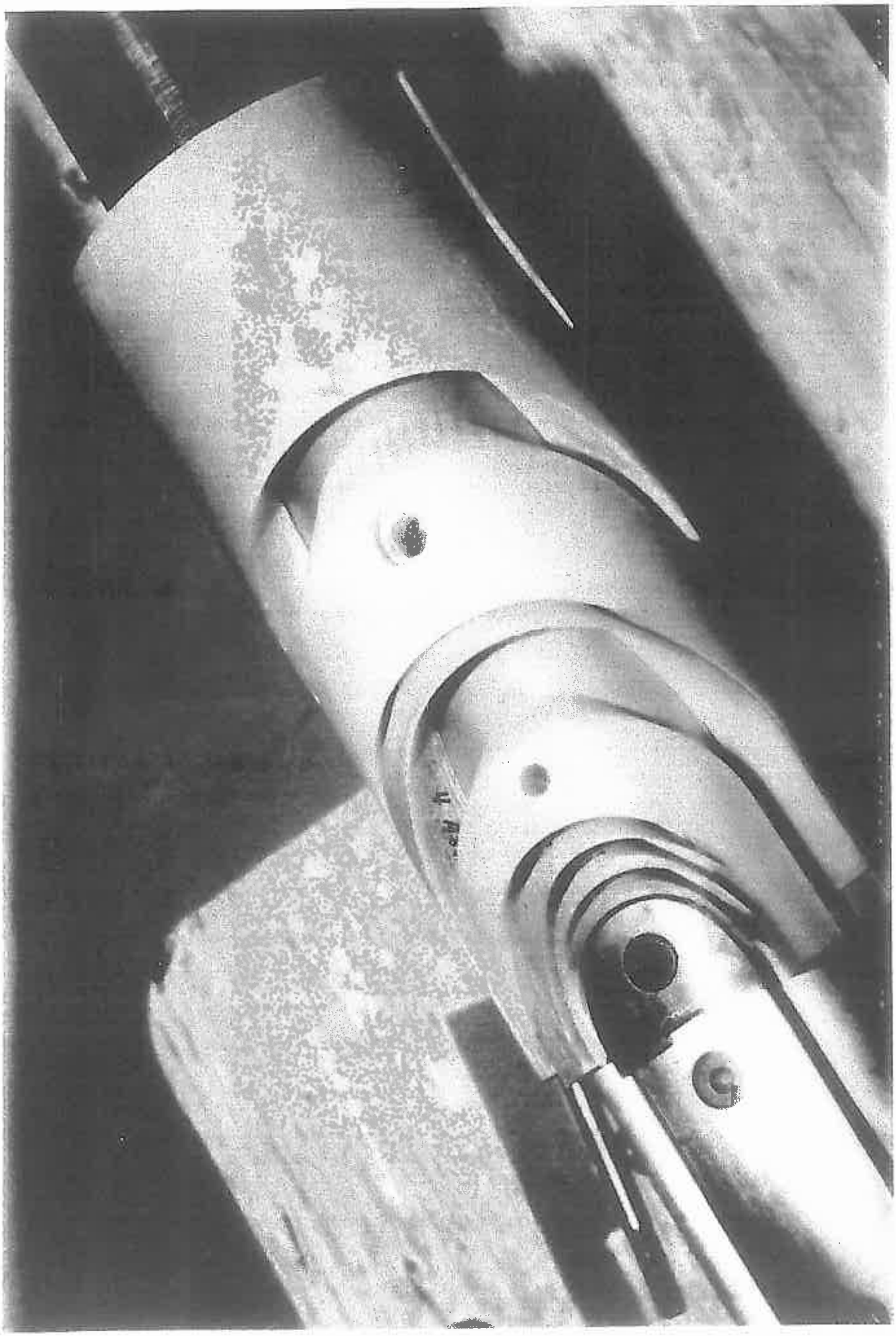

Courtesy D. Perini

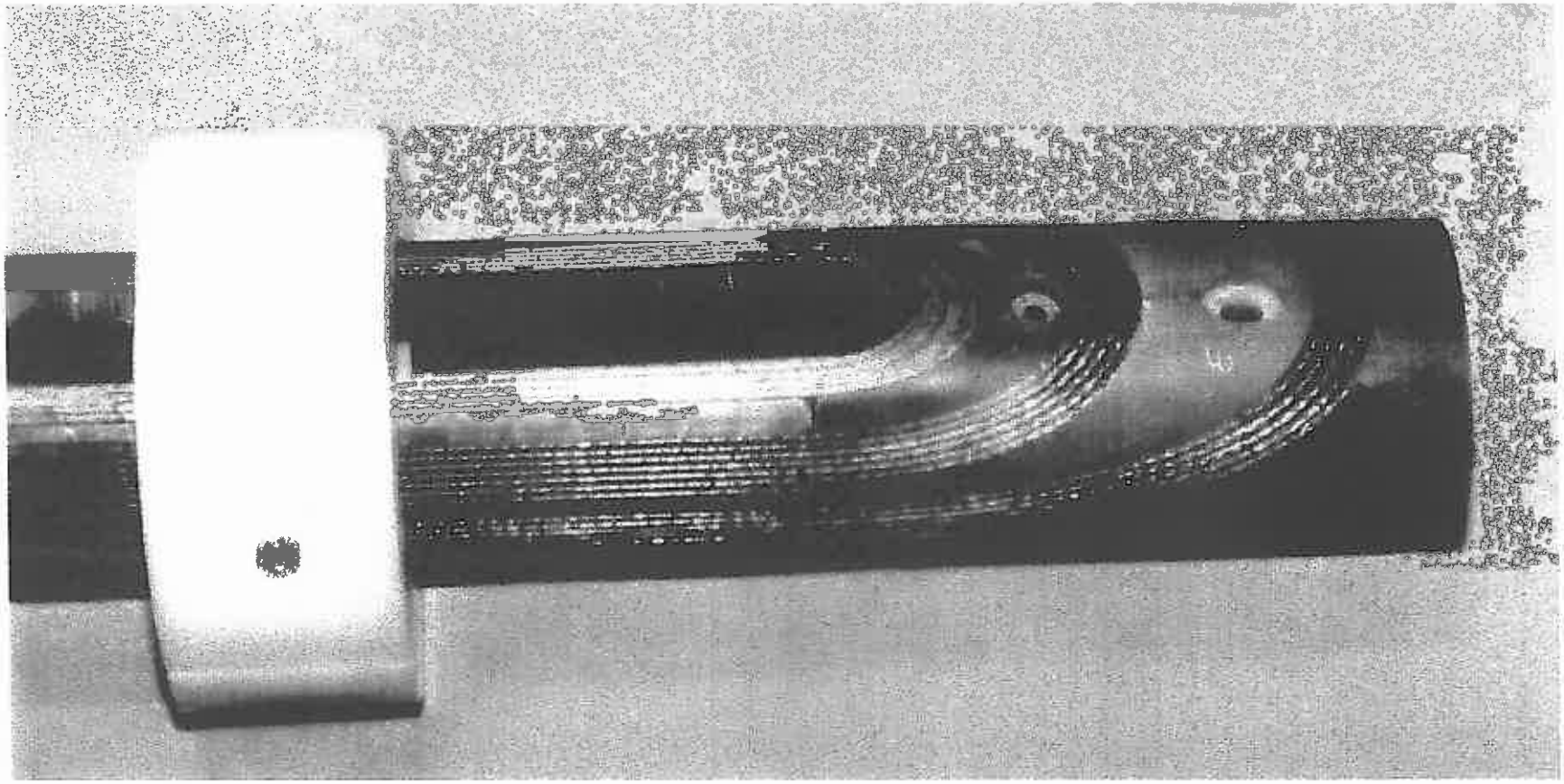

Courtesy D. Perini

MAGNETIC DESIGN OF INTERCONNECTS

– In magnet with tight field quality requirements, the trajectories of the conductors moving in and out of the coils must be optimized to avoid the production of unwanted multipole coefficients.

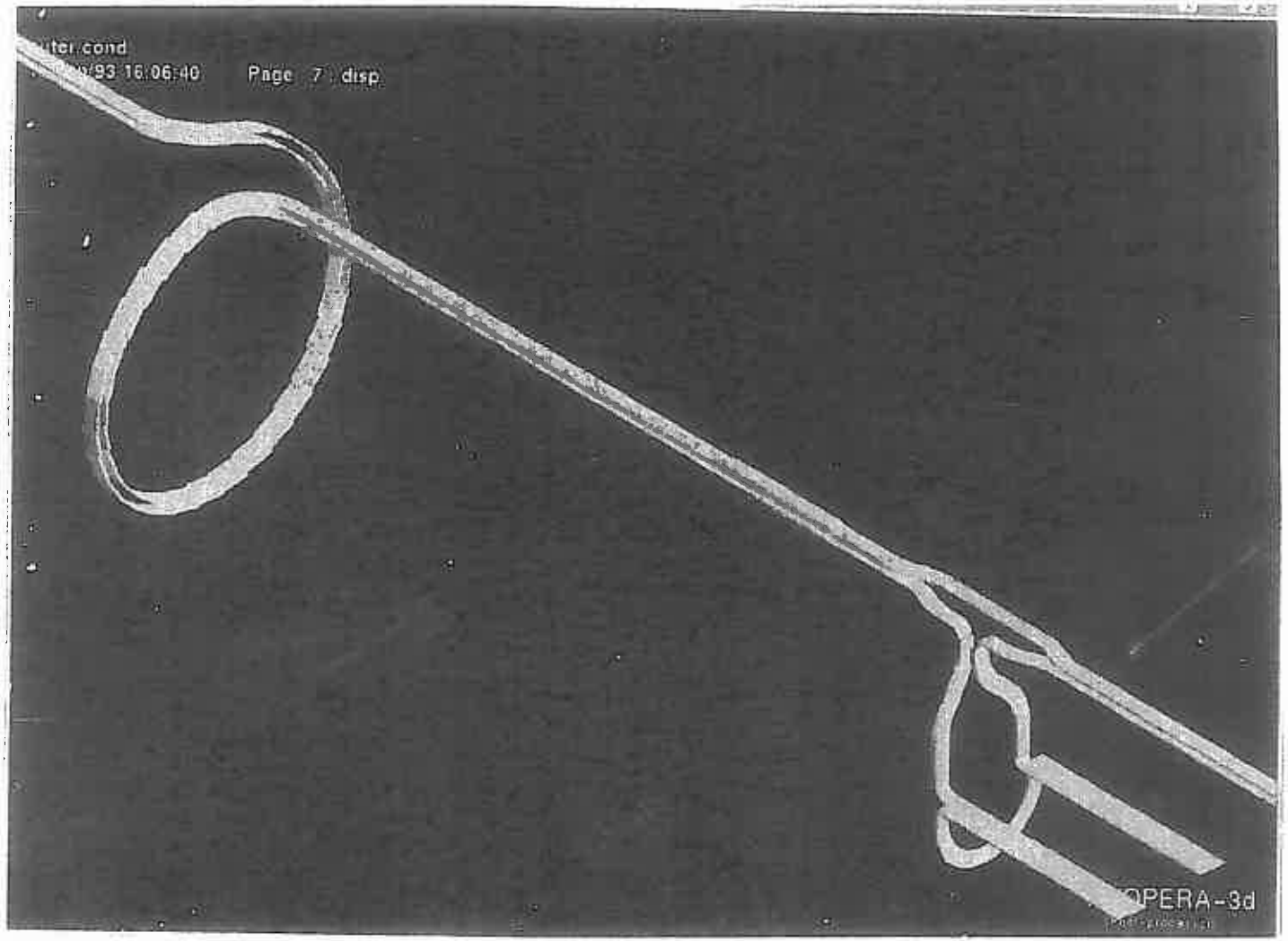

Courtesy D. Orrel

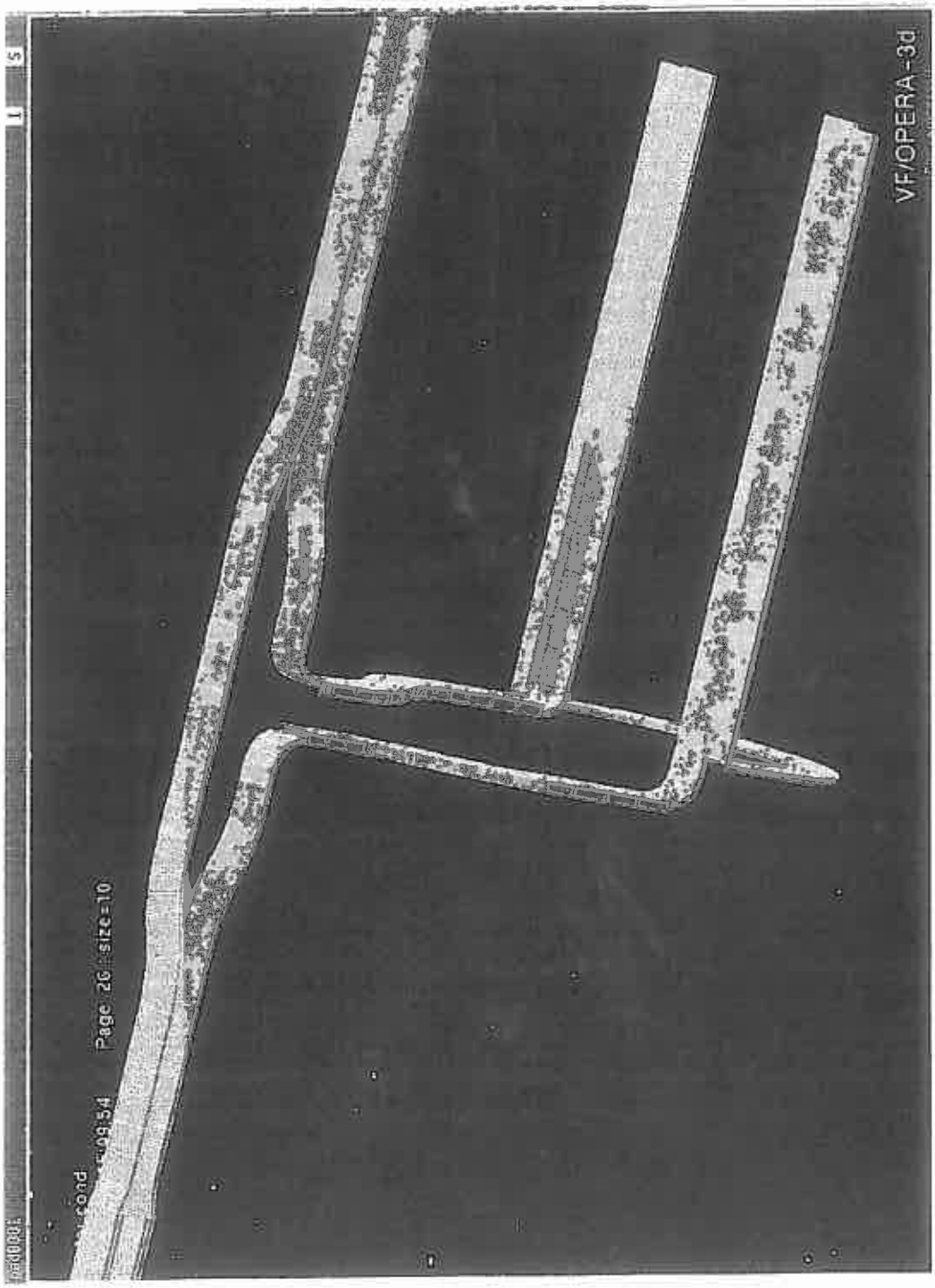

Courtesy D. Orrel

LECTURE 4: MAGNETIC DESIGN OF PARTICLE ACCELERATOR MAGNETS

4.1 Complex Formalism for Two-Dimensional Fields

4.2 Multipole Field Expansion for Two-Dimensional Fields

4.3 Field Computations for Simple Current Distributions

4.4 Two-Dimensional Cosθ and Cos2θ Coil Designs

4.5 Iron Yoke Contribution

4.6 Operating Current Margin

4.7 Saddle-Shaped Coil End Designs

4.8 Other Designs

4.9 Sagitta of Arc Dipole Magnets

4.10 High Order Multipole Field Corrector Magnets

LIMITATIONS OF COSΘ COIL DESIGN

– **The cosθ coil design has been very successful until now, with a record dipole field of 13.5 T reached by the LBNL short dipole magnet model D20 (using Nb_3Sn cables at 1.8 K). However, it has two main drawbacks:**

- *Coil ends are difficult to make,*

- *Due to the Lorentz force distribution, there is a stress accumulation in the azimuthal direction* which results in high transverse pressures on the midplane conductors of the coil assemblies.

– **For very high field magnets, requiring the use of A15 (or even possibly HTS) superconductors, which are strain sensitive, the high transverse pressures at the coil midplane may result in significant critical current degradation.**

Lorentz Force Distribution in a Dipole Coil

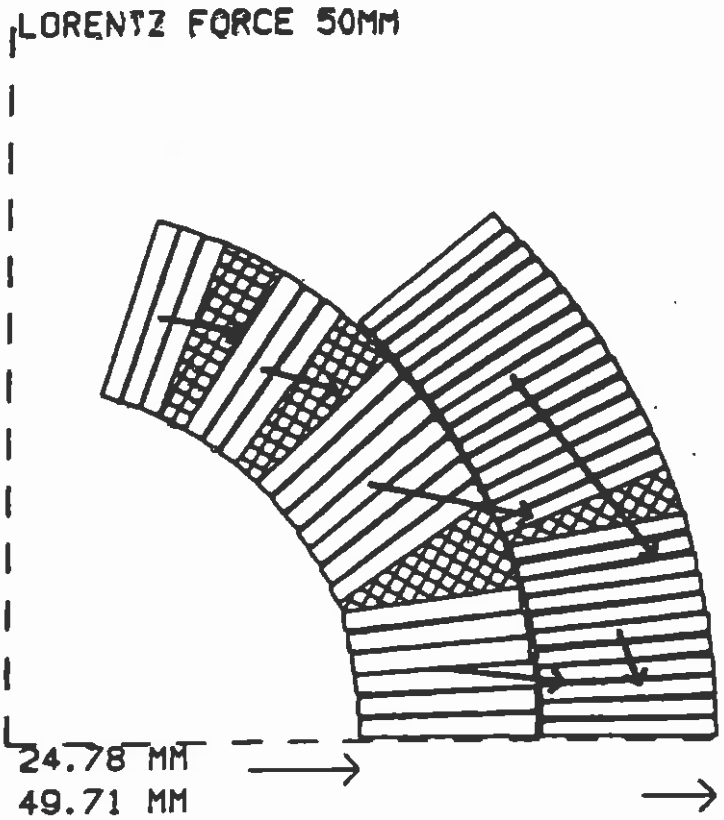

+ Axial Component Pulling on Coil Ends

OTHER MAGNET DESIGNS

– A number of alternative coil designs have been investigated which may allow a better management of the Lorentz stress within the magnet coil.

– All of these designs make a less effective use of superconductor.

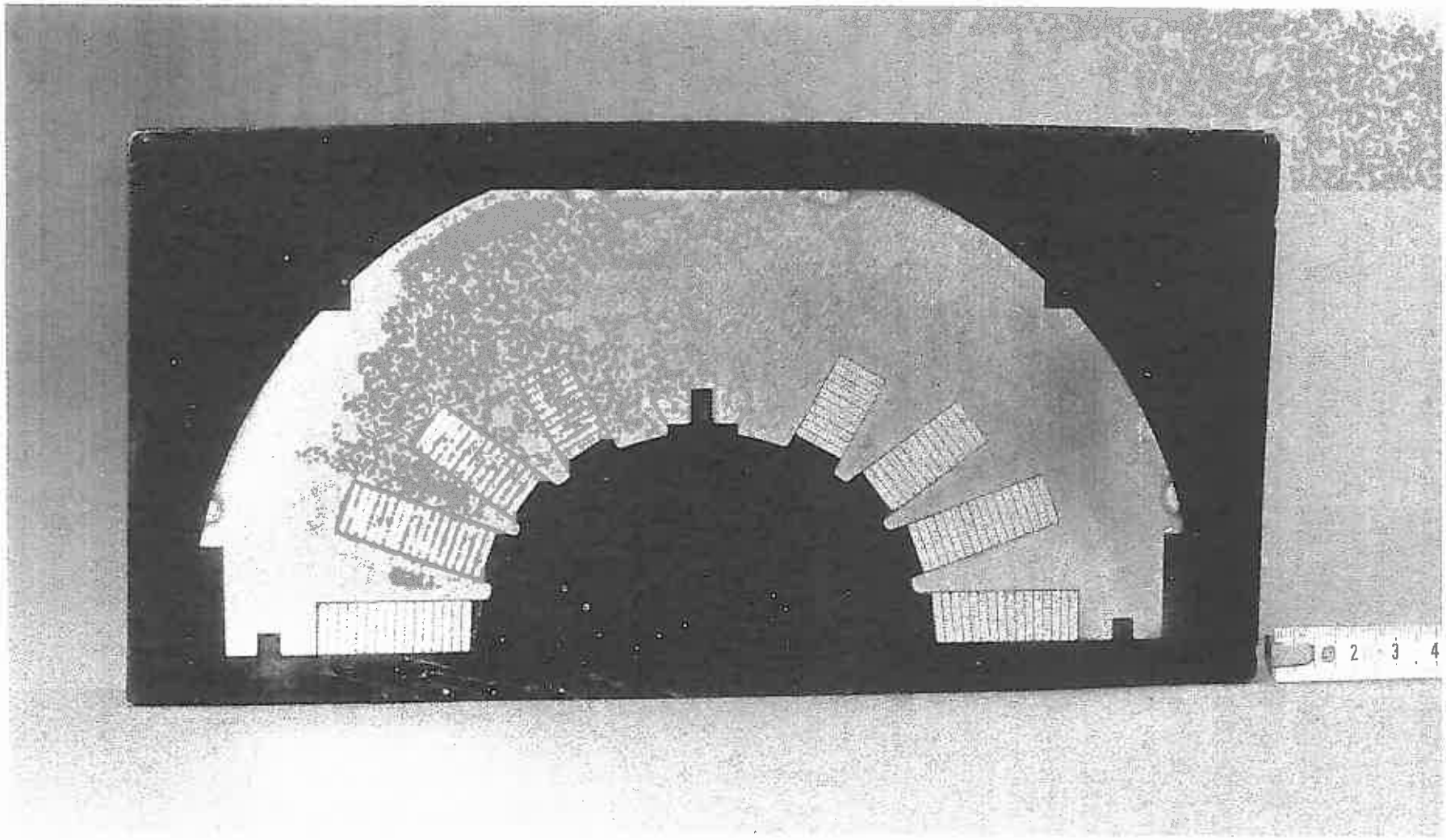

Courtesy J. Pérot

Courtesy J. Pérot

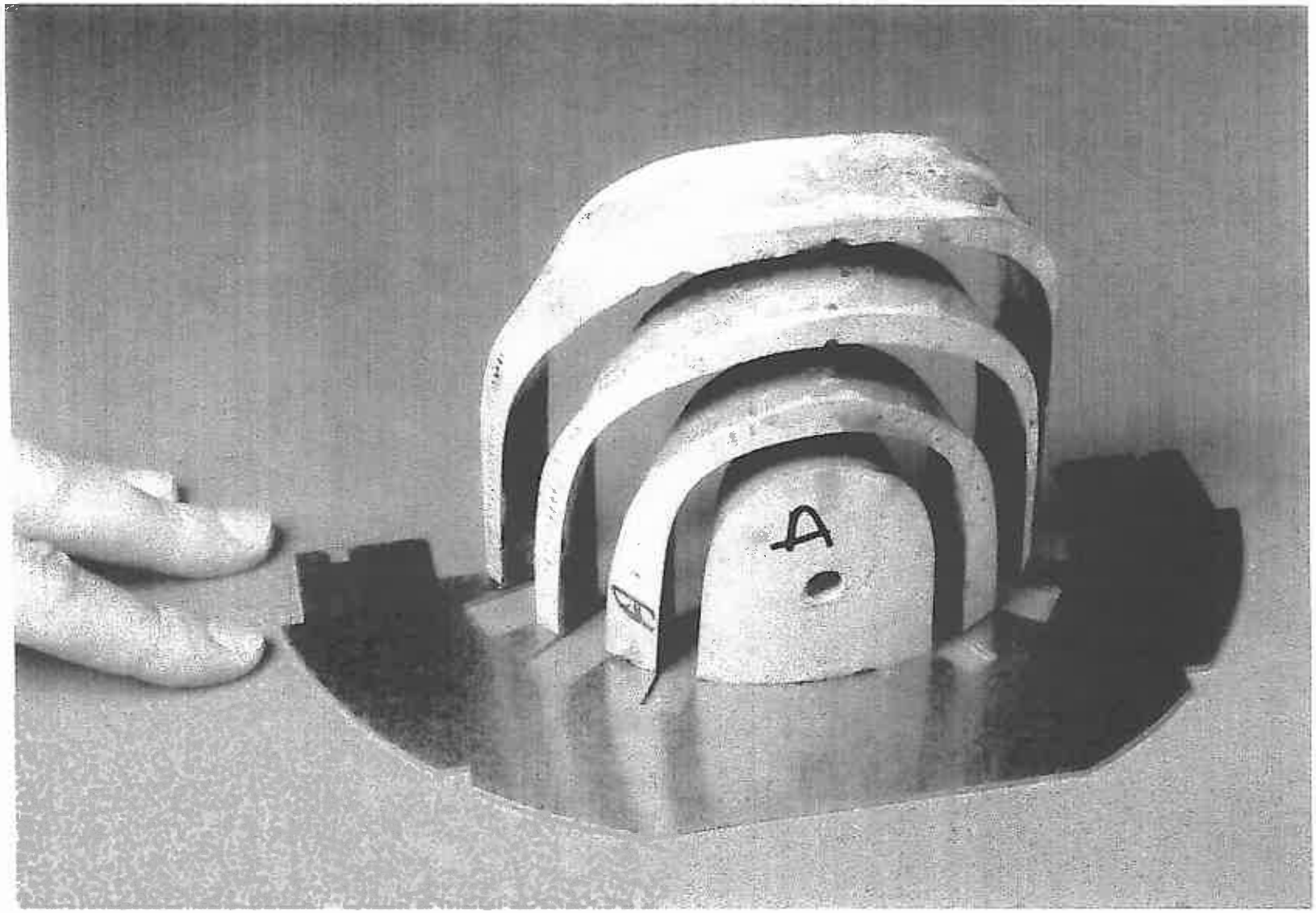

Courtesy J. Pérot

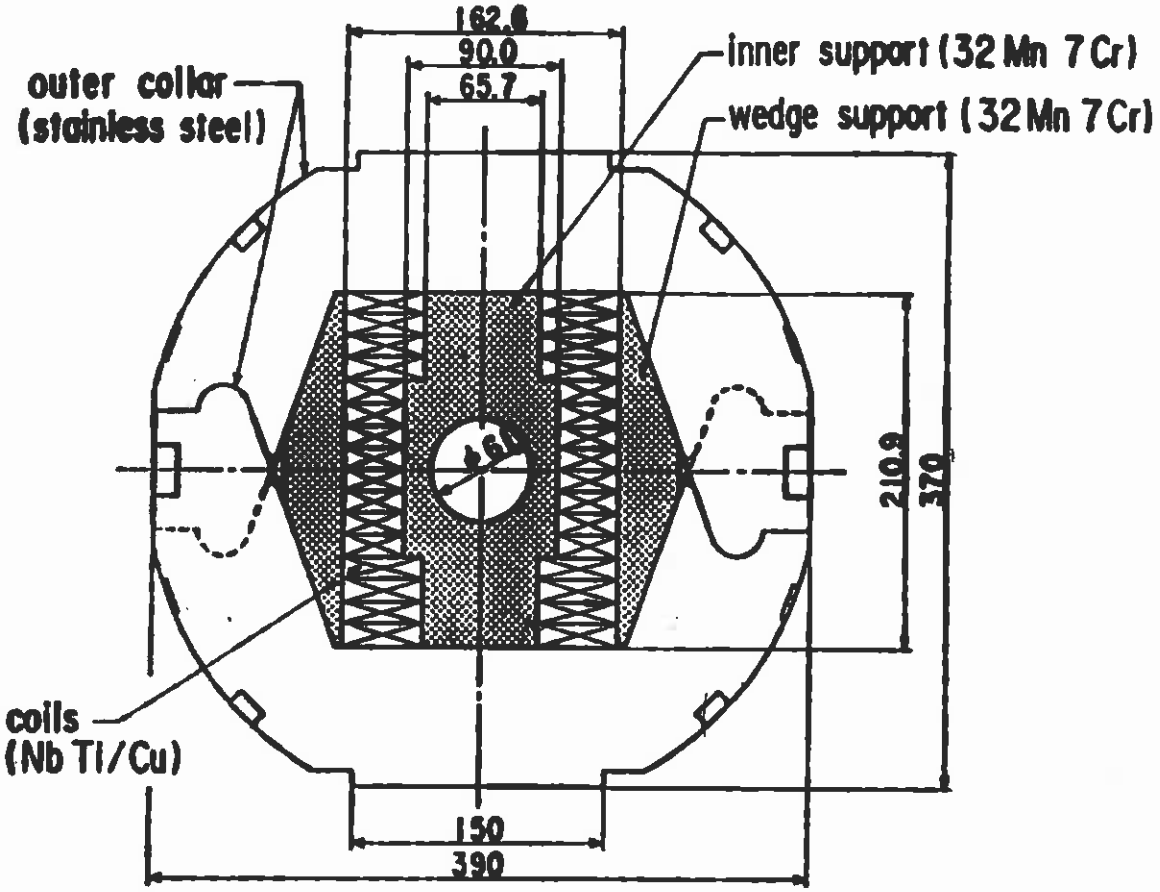

10 T マグネットのコイル及びカラー断面

Courtesy K. Tsuchiya

LBNL

HIGH FIELD (10T-15T) TWIN APERTURE SUPERCONDUCTING DIPOLE

COMMON COIL DESIGN

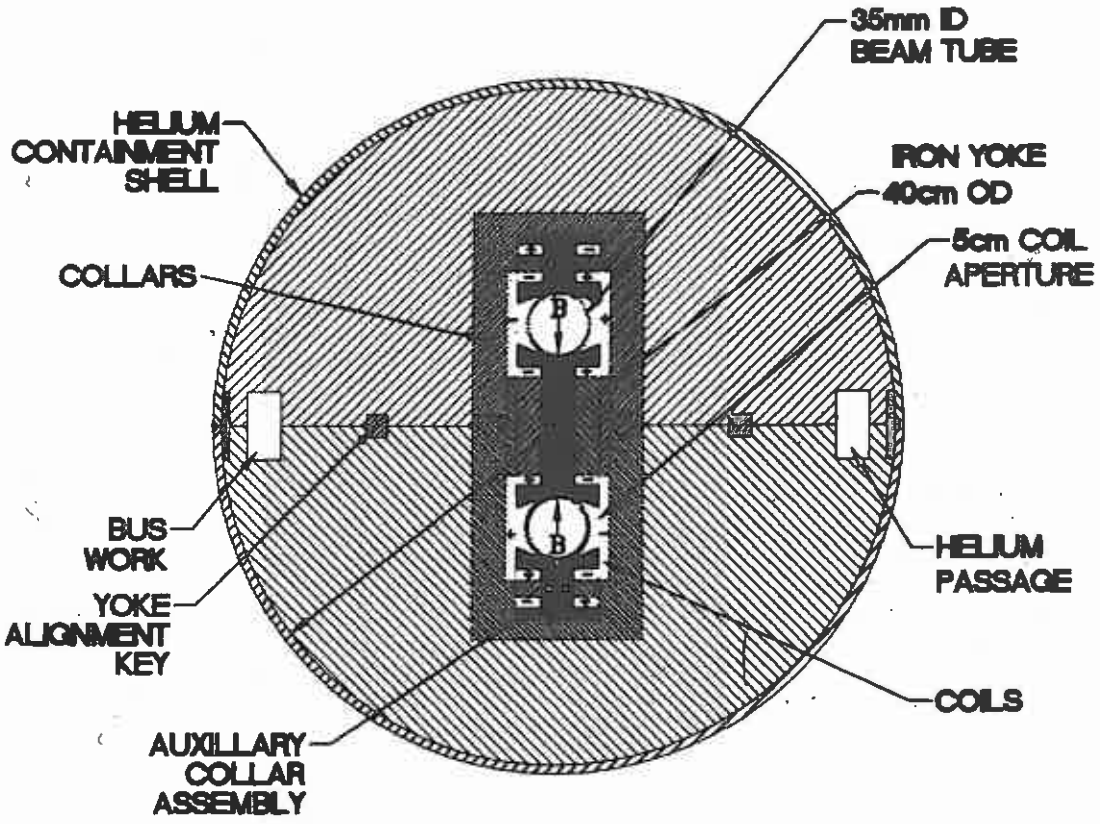

COLD MASS CROSS-SECTION

SCALE 1/4

Courtesy R. Gupta

LBNL

Field Lines at 15 T in a Common Coil Design Magnet

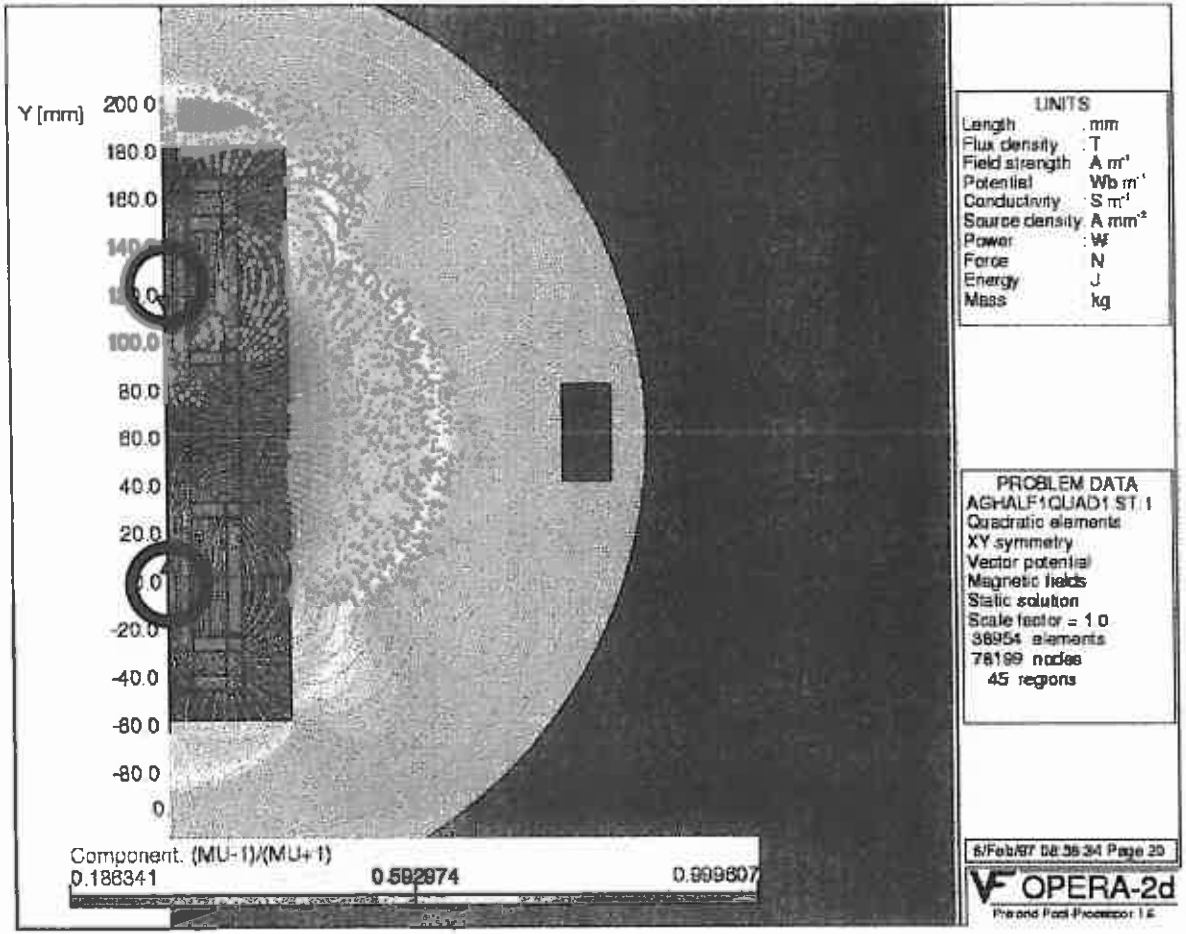

Courtesy R. Gupta

TAMU

16 Tesla Block-Coil Dual Dipole

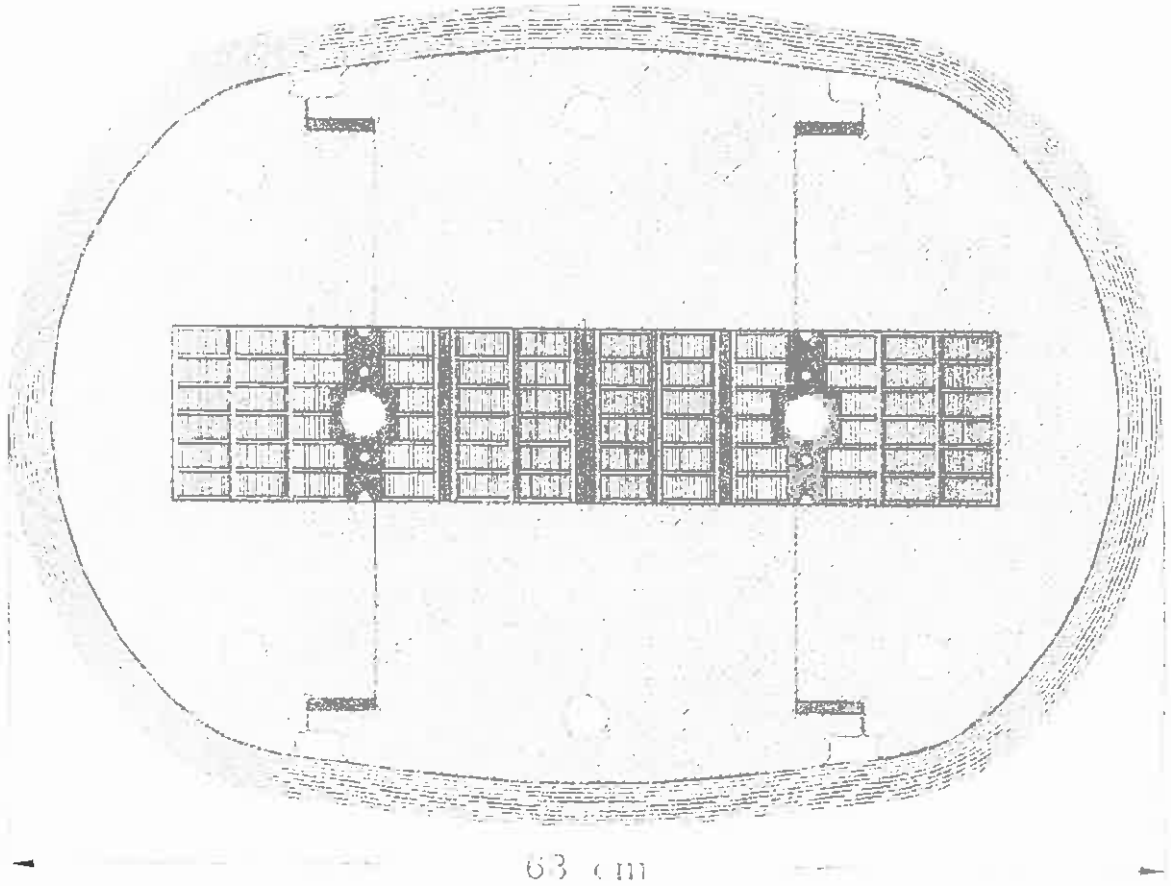

Courtesy P. McIntyre

TAMU 16-T Block-Coil Dual Dipole Magnet

Main parameters

•	Maximum field strength	16	T
•	Minimum field strength	0.5	T
•	Operating temperature	4.2	^{o}K
•	Operating current at max field	9,200	A
•	Inductance, both bores	81	mH/m
•	Stored energy, both bores	3.47	J/m
•	Mass of dual dipole	1,457	kg/m
•	Overall size of cold mass	64	cm
•	multipoles: b_1	-0.53	cm^{-1}
•	b_2	+0.36	cm^{-2}
•	b_3	-0.06	cm^{-3}
•	b_4	+1.05	cm^{-4}

Courtesy P. McIntyre

TAMU 16-T Block-Coil Dual Dipole Magnet

Separate Nb_3Sn, Cu in cable, Use NbTi cable in low-field segment

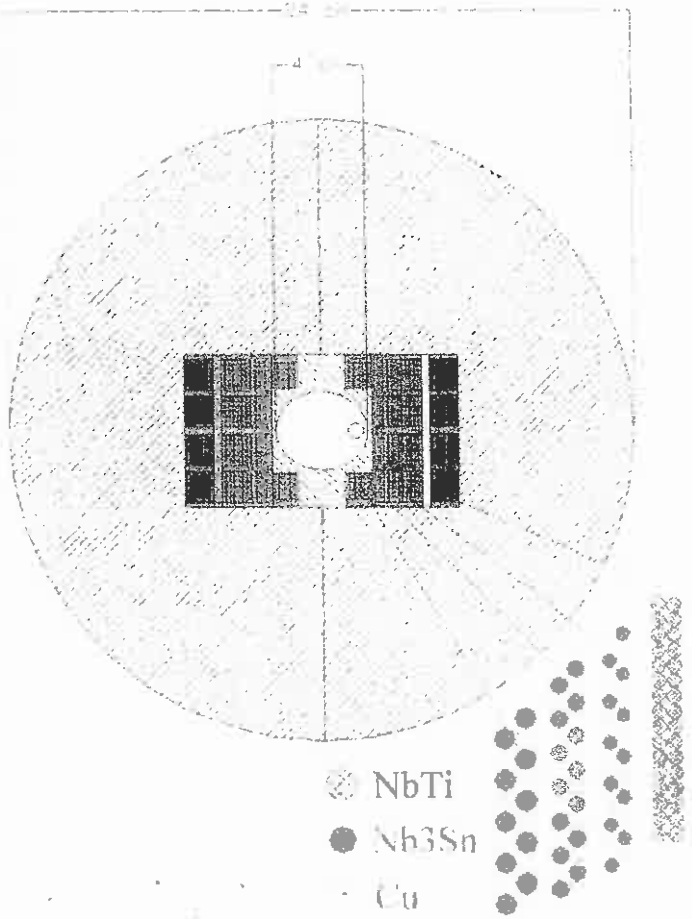

Courtesy P. McIntyre

LECTURE 4: MAGNETIC DESIGN OF PARTICLE ACCELERATOR MAGNETS

4.1 Complex Formalism for Two-Dimensional Fields

4.2 Multipole Field Expansion for Two-Dimensional Fields

4.3 Field Computations for Simple Current Distributions

4.4 Two-Dimensional Cosθ and Cos2θ Coil Designs

4.5 Iron Yoke Contribution

4.6 Operating Current Margin

4.7 Saddle-Shaped Coil End Designs

4.8 Other Designs

4.9 Sagitta of Arc Dipole Magnets

4.10 High Order Multipole Field Corrector Magnets

SAGITTA

– To limit the number of coil ends and of magnet interconnects around the accelerator ring, the arc dipole and quadrupole magnets are made as long as possible.

– As we have seen, the circulation of a charged beam in a dipole magnet, of magnetic length, l_d, results in an angular deflection, ϕ, given by:

$$\phi \approx \frac{0.3\, q_e\, B_1\, l_d}{\varepsilon_{GeV}}$$

where B_1 is the dipole field strength, q_e is the particle charge in units of electron charge, and ε_{GeV} is the particle energy in giga electron volts (GeV).

– Consequently, the long dipole magnets used in large accelerator rings must be bent slightly to accompany the particle trajectory. This bending, which is implemented in the $(\vec{x}, \vec{z})$ plane, is referred to as *sagitta*.

LECTURE 4: MAGNETIC DESIGN OF PARTICLE ACCELERATOR MAGNETS

4.1 Complex Formalism for Two-Dimensional Fields

4.2 Multipole Field Expansion for Two-Dimensional Fields

4.3 Field Computations for Simple Current Distributions

4.4 Two-Dimensional Cosθ and Cos2θ Coil Designs

4.5 Iron Yoke Contribution

4.6 Operating Current Margin

4.7 Saddle-Shaped Coil End Designs

4.8 Other Designs

4.9 Sagitta of Arc Dipole Magnets

4.10 High Order Multipole Field Corrector Magnets

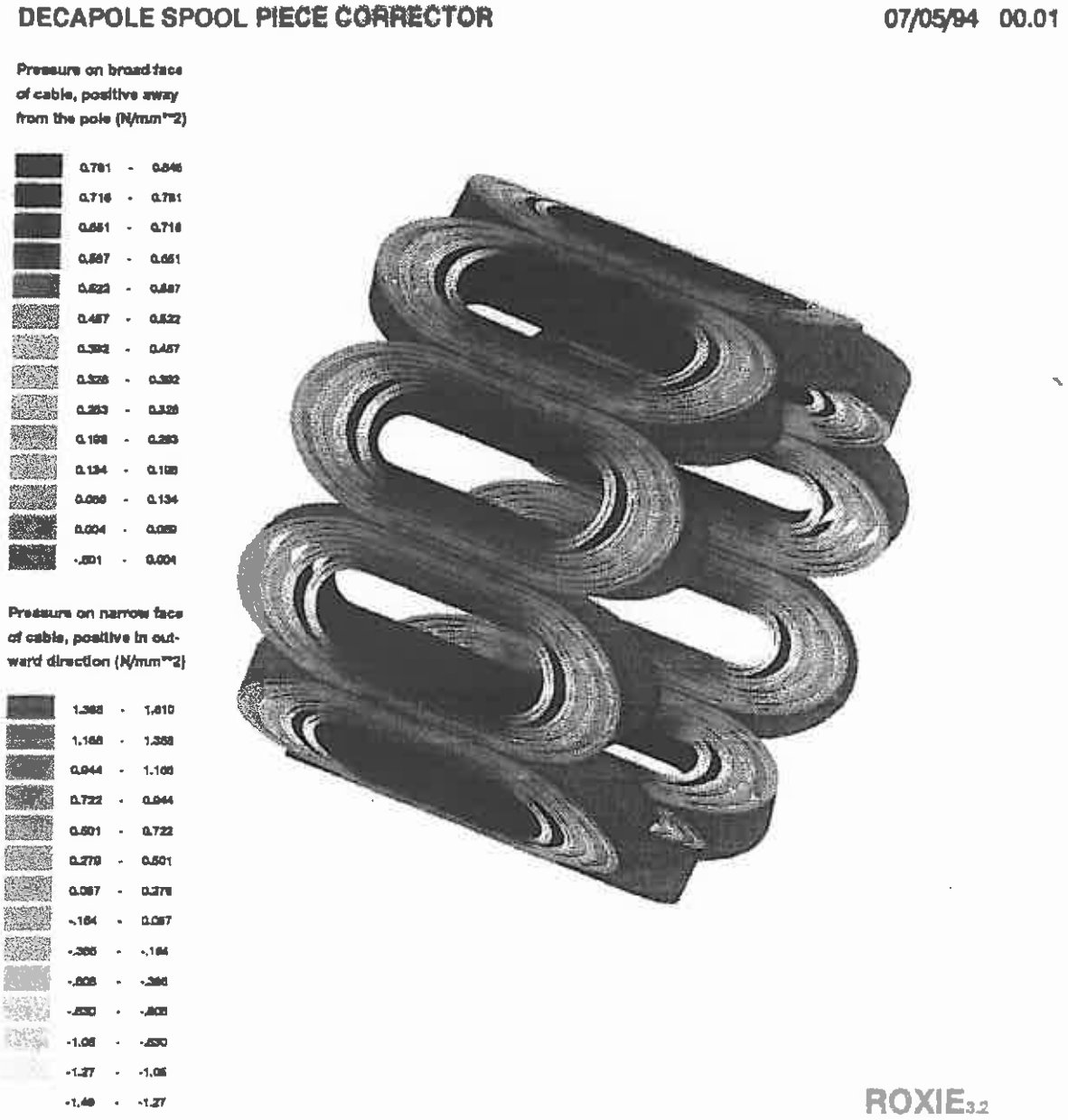

Courtesy S. Russenschuck

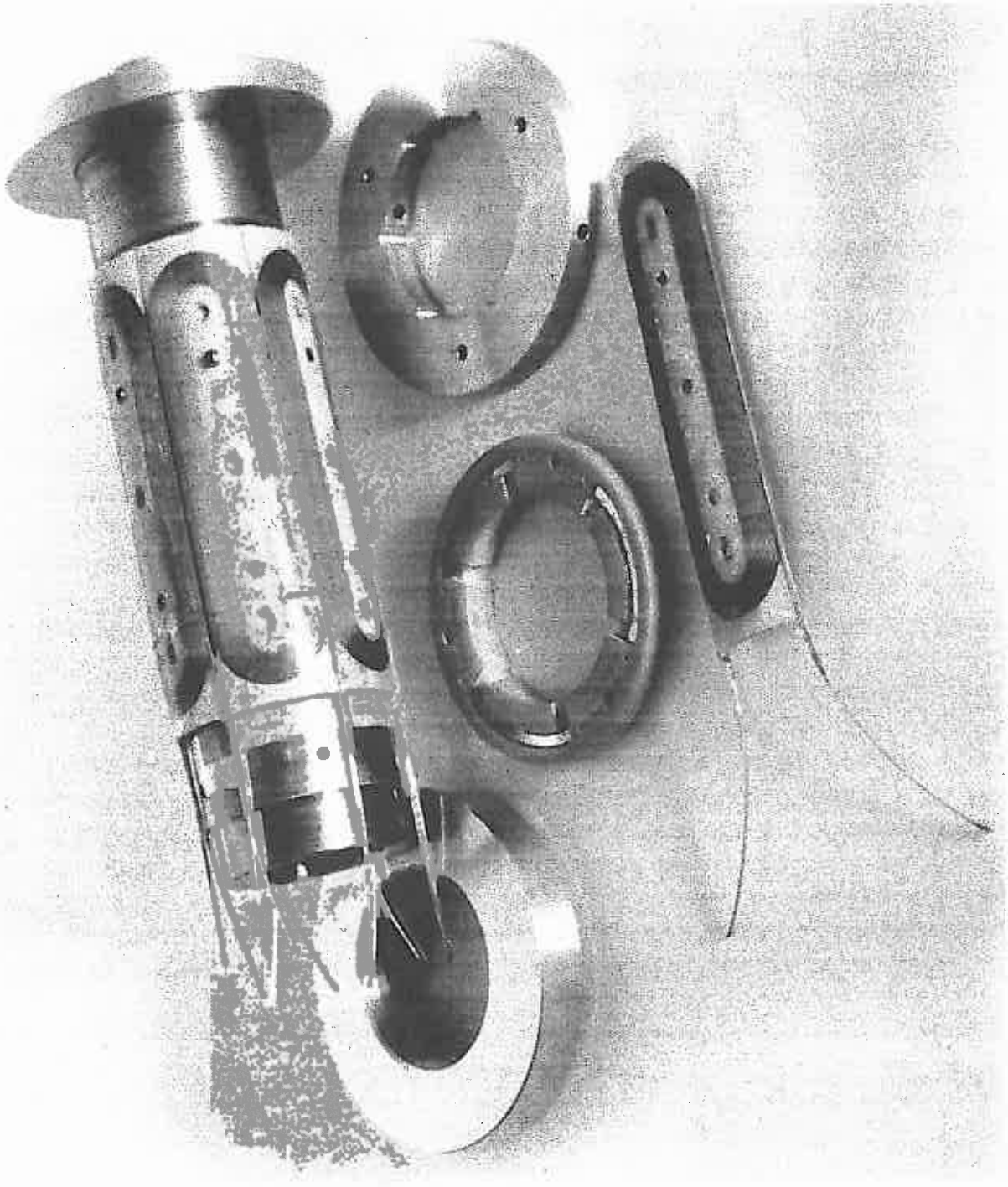

Courtesy A. Ijspeert

LECTURE 5: MECHANICAL DESIGN OF PARTICLE ACCELERATOR MAGNETS

5.1 Components of the Lorentz Force in Cosθ and Cos2θ Magnetic Designs 5–3

5.2 Azimuthal Pre-Compression 5–15

5.3 Coil Mechanical Properties 5–31

5.4 Collar Designs 5–47

5.5 Radial Support
- 5.5.1 Designs with Self-Supported Collared-Coil Assemblies 5–75
- 5.5.2 Designs with Fully-Mated Yoke 5–79
- 5.5.3 Design with Yoke Midplane Gap 5–119
- 5.5.4 RHIC Magnets 5–143
- 5.5.5 Azimuthal Pre-Compression Versus Radial Support 5–149

5.6 End Support 5–161

5.7 Other Designs 5–187

LECTURE 5: MECHANICAL DESIGN OF PARTICLE ACCELERATOR MAGNETS

5.1 Components of the Lorentz Force in Cosθ and Cos2θ Magnetic Designs

5.2 Azimuthal Pre-Compression

5.3 Coil Mechanical Properties

5.4 Collar Designs

5.5 Radial Support
- 5.5.1 Designs with Self-Supported Collared-Coil Assemblies
- 5.5.2 Designs with Fully-Mated Yoke
- 5.5.3 Design with Yoke Midplane Gap
- 5.5.4 RHIC Magnets
- 5.5.5 Azimuthal Pre-Compression Versus Radial Support

5.6 End Support

5.7 Other Designs

COMPONENTS OF THE LORENTZ FORCE

– The high currents and fields in an accelerator magnet coil produce a large Lorentz force on the conductors.

– In a dipole coil, the Lorentz force has three main components:

• ***an azimuthal component,*** which tends to squeeze the coil towards the coil assembly midplane [which, in the coordinate system defined previously, corresponds to the horizontal ($\vec{x}$, $\vec{z}$) plane],

• ***a radial component,*** which tends to bend the coil outwardly, with a maximum displacement at the coil assembly midplane (along the horizontal *x*-axis),

• ***an axial component,*** arising from the solenoidal field produced by the conductor turnaround at the coil ends and which tends to stretch the coil outwardly (along the *z*-axis).

Lorentz-Force Distribution in a Dipole Coil (Courtesy R. Gupta)

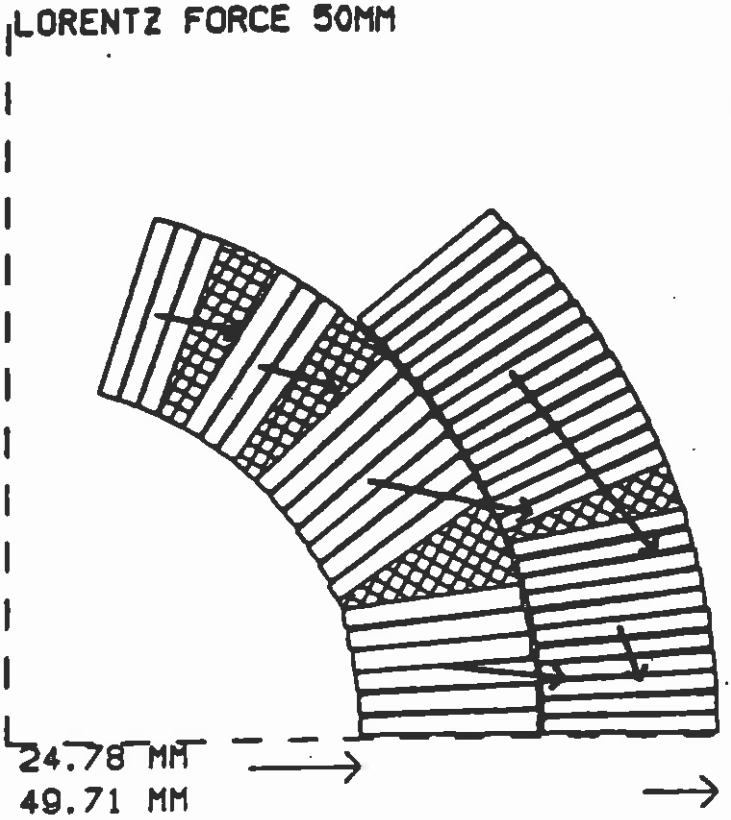

+ Axial Component Pulling on Coil Ends

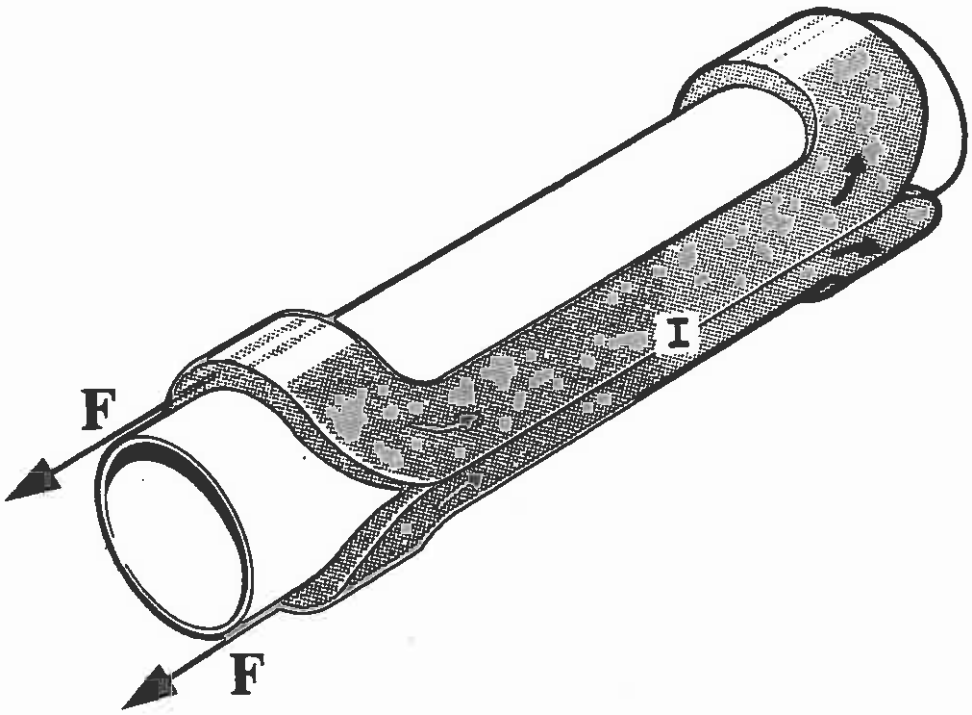
F
I
F

Lorentz-Force Distribution in a Quadrupole Coil

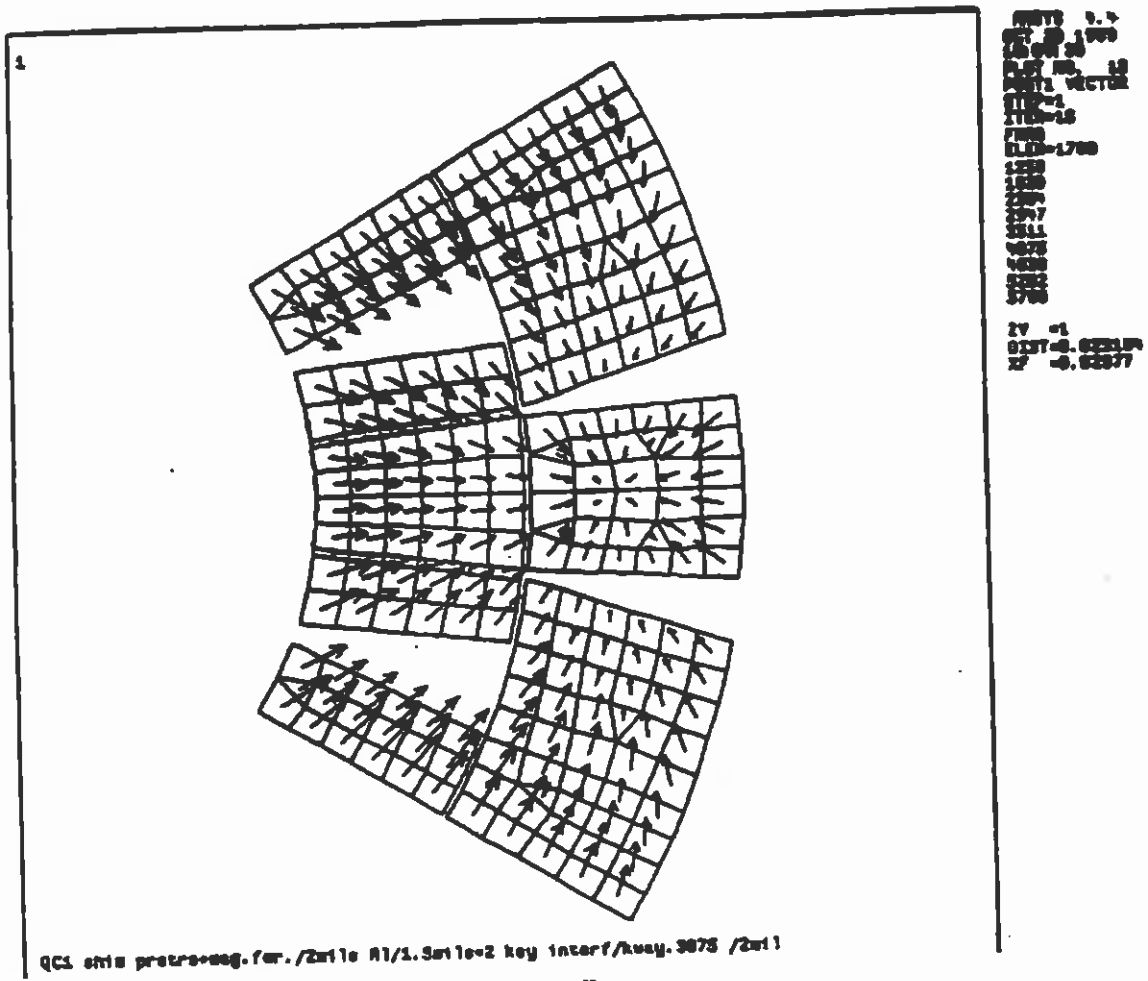

Fig. 7: Lorentz forces on the coils

STABILITY AGAINST MECHANICAL DISTURBANCES

– Because accelerator magnets are operated close to the critical current limit of their cables, their minimum quench energy, referred to as MQE, and defined as the minimum energy deposition needed to trigger a quench, is very small.

– As a matter of fact, the MQE of accelerator magnets is of the same order of magnitude as the electromagnetic work produced by minute wire motions in the coil.

– If the motions are purely elastic, no heat is dissipated and the coil remains superconducting, but if the motions are frictional, the associated heat dissipation may be sufficient to initiate a quench.

– This leaves two possibilities:

• Either to prevent wire or coil motion by providing a rigid support against the various components of the Lorentz force,

• Or to reduce to a minimum the friction coefficients between potentially moving parts of magnet assembly.

CONCEPTUAL DESIGN

– The mechanical design concepts used in present accelerator magnets are more or less the same and were developed at the time of the Tevatron.

– In the radial direction: the coils are confined within a rigid cavity defined by laminated collars which are locked around the coils by means of keys or tie rods.

– In the azimuthal direction: the collars are assembled so as to pre-compress the coils.

– In the axial direction: the coils either are free to expand or are restrained by means of stiff end-plates.

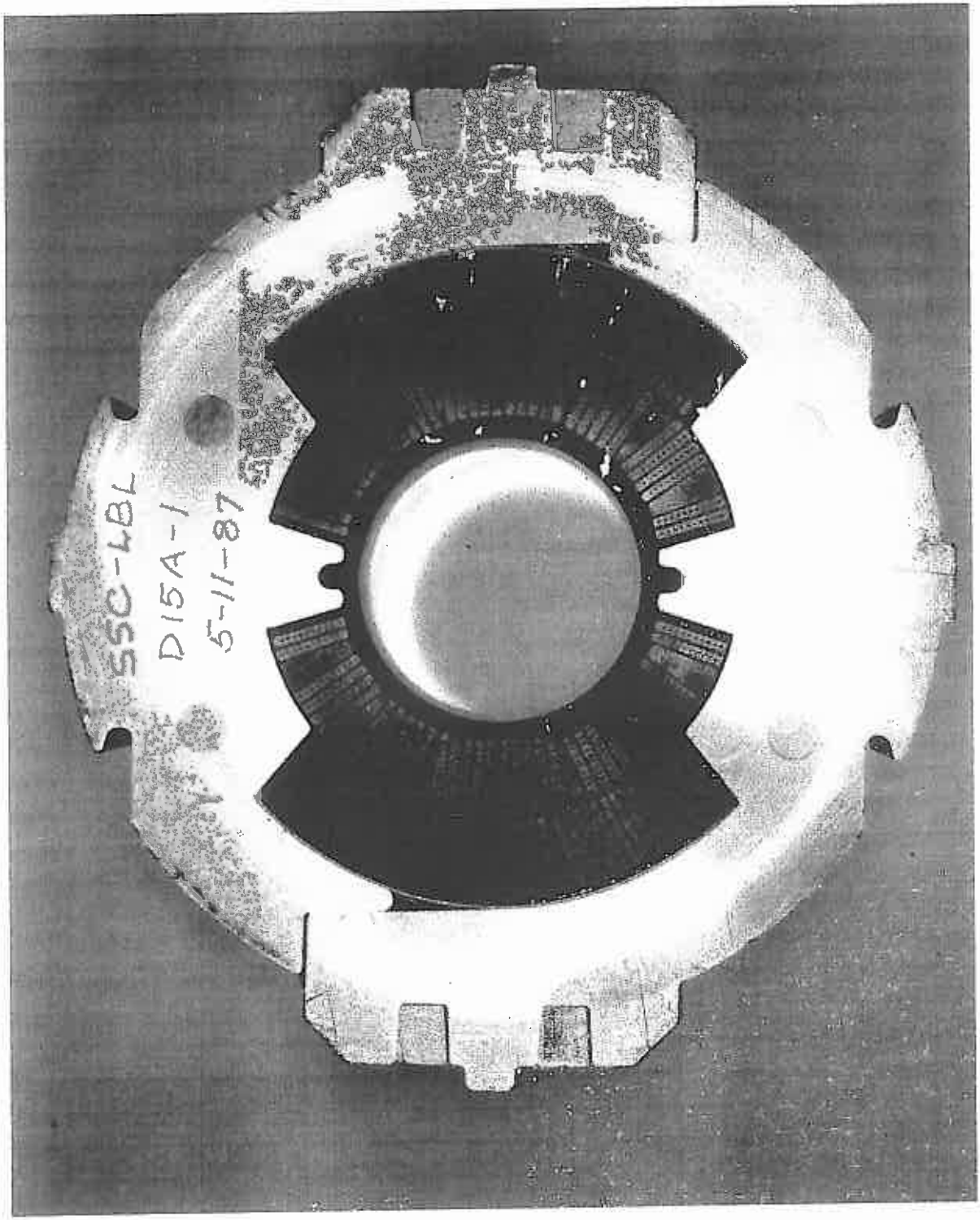
SSC-LBL
D15A-1
5-11-87

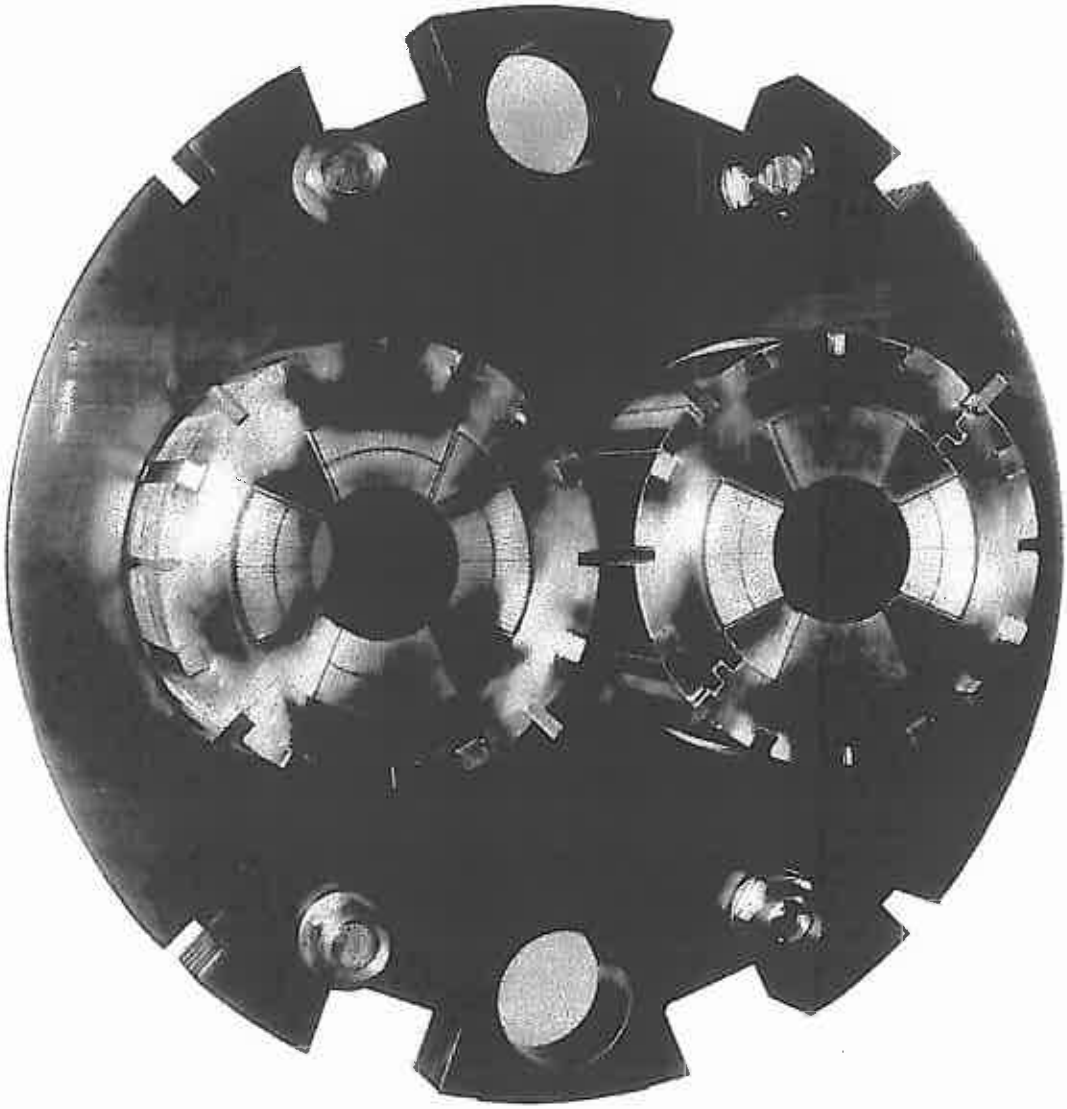

ON THE USE OF LAMINATED COLLARS

– The use of laminated collars, pioneered at the Tevatron, was a real breakthrough in achieving a rigid mechanical support while keeping tight tolerances over magnet assemblies which are a few meters in length and which must be mass-produced.

– The laminations are usually stamped by a fine blanking process allowing a dimensional accuracy of the order of one hundredth of a millimeter to be achieved.

LECTURE 5: MECHANICAL DESIGN OF PARTICLE ACCELERATOR MAGNETS

5.1 Components of the Lorentz Force in Cosθ and Cos2θ Magnetic Designs

5.2 Azimuthal Pre-Compression

5.3 Coil Mechanical Properties

5.4 Collar Designs

5.5 Radial Support
- 5.5.1 Designs with Self-Supported Collared-Coil Assemblies
- 5.5.2 Designs with Fully-Mated Yoke
- 5.5.3 Design with Yoke Midplane Gap
- 5.5.4 RHIC Magnets
- 5.5.5 Azimuthal Pre-Compression Versus Radial Support

5.6 End Support

5.7 Other Designs

AZIMUTHAL PRE-COMPRESSION

– As we have described, the azimuthal component of the Lorentz force tends to squeeze the coil towards the midplane.

– At high fields, it may happen that the coil pole turns move away from the collar poles, resulting in variations of coil pole angle, which distort the central field and create a risk of mechanical disturbances.

– To prevent conductor displacements, the coils are pre-compressed azimuthally.

– This azimuthal pre-compression is acchieved by squeezing the coils into cavities which are smaller than their sizes at rest. The cavities are defined by the inner boundaries of the collars which are assembled and locked around the coils.

– The pre-compression is applied at room temperature and must be sufficient to ensure that, after cooldown and energization, there is still contact between coil pole turns and collar poles.

PRE-COMPRESSION REQUIREMENTS

– To determine the proper level of room temperature azimuthal pre-compression, at least three effects must be taken into account:

• ***Stress relaxation and insulation creep*** following the collaring operation,

• ***Thermal shrinkage differentials*** between coil and collars during cooldown (if any),

• ***Stress redistribution*** due to the azimuthal component of the Lorentz force.

– In addition, the collaring procedure must be optimized to ensure that the peak pressure seen by the coils during the operation (which may be significantly higher than the residual pre-compression) does not overstress the insulation.

Strain-Gauge Instrumentation

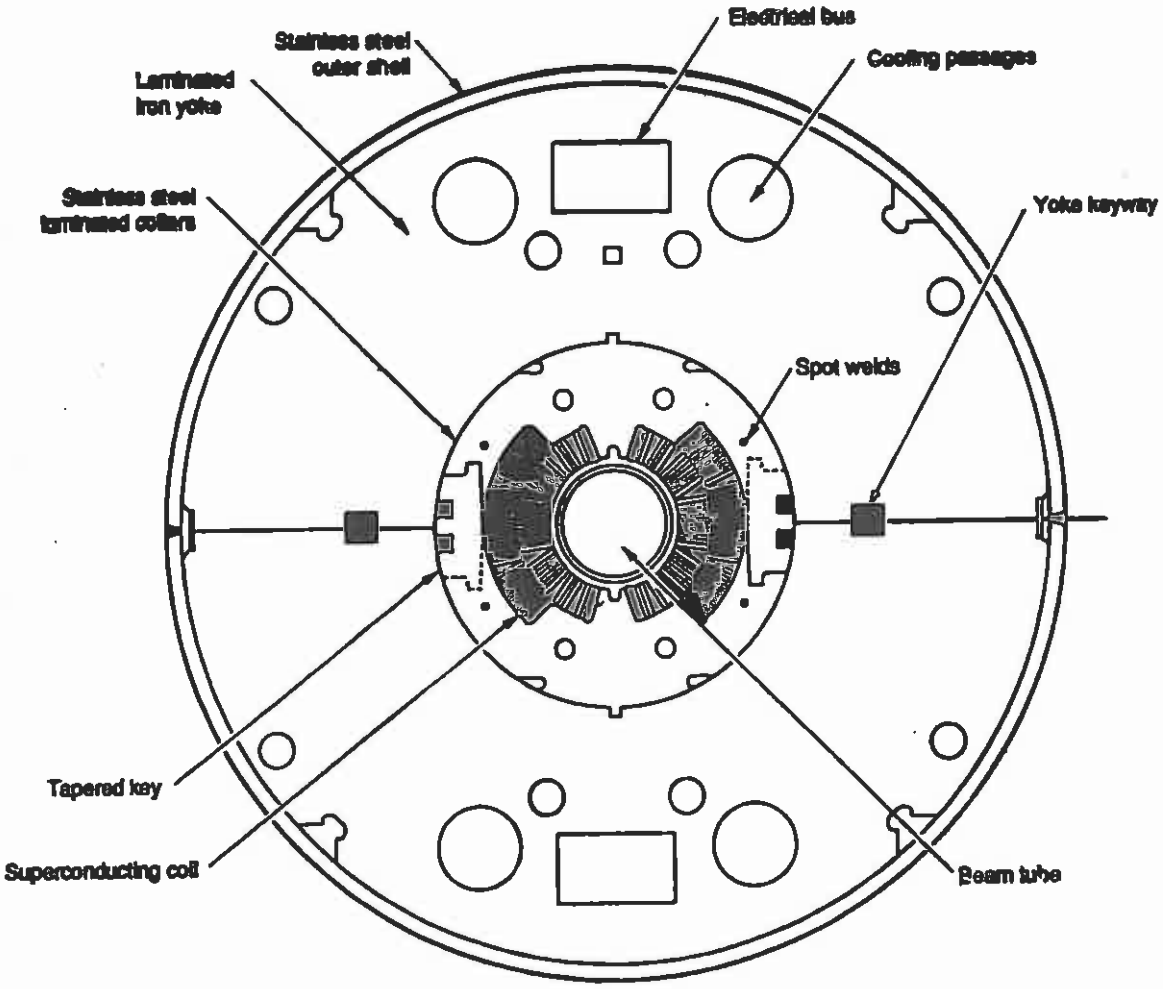

Beam-Type Strain-Gauge Trans.
(Pressure exerted by coil against collar pole)

COIL STRESS HISTORY OF 17-M LONG SSC COLLIDER DIPOLE PROTOTYPE DD0026 (courtesy J. R. Turner)

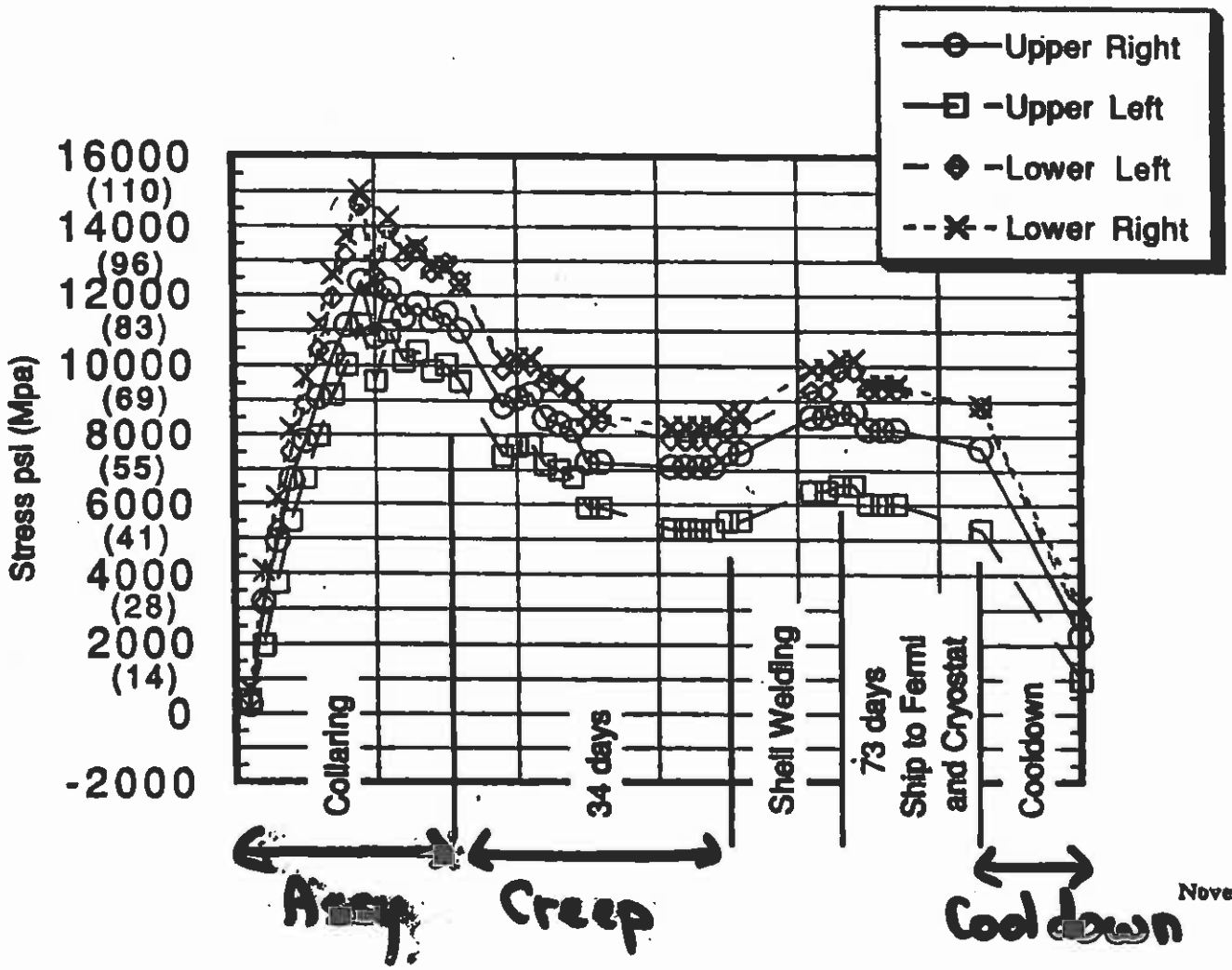

SSC/FNAL 5-cm-Aperture, 15-m-long Dipole Magnets

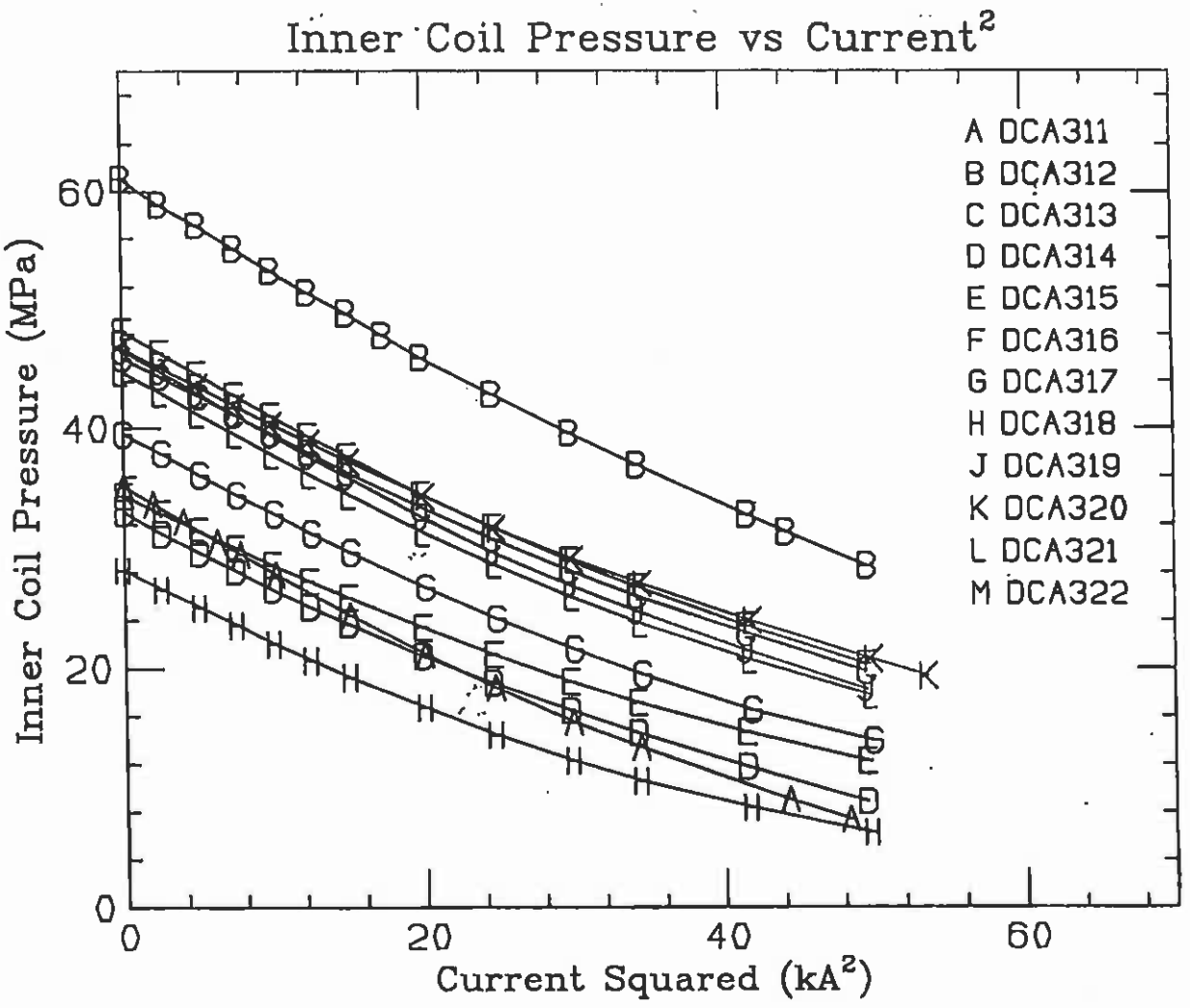

Stress Distribution Across the Inner Pole Face

Stress Distribution Across the Outer Pole Face

Stress Distribution Across the Coil Midplane

Satin

Cartes des pressions brutes
Extrait de l'échantillon n°2

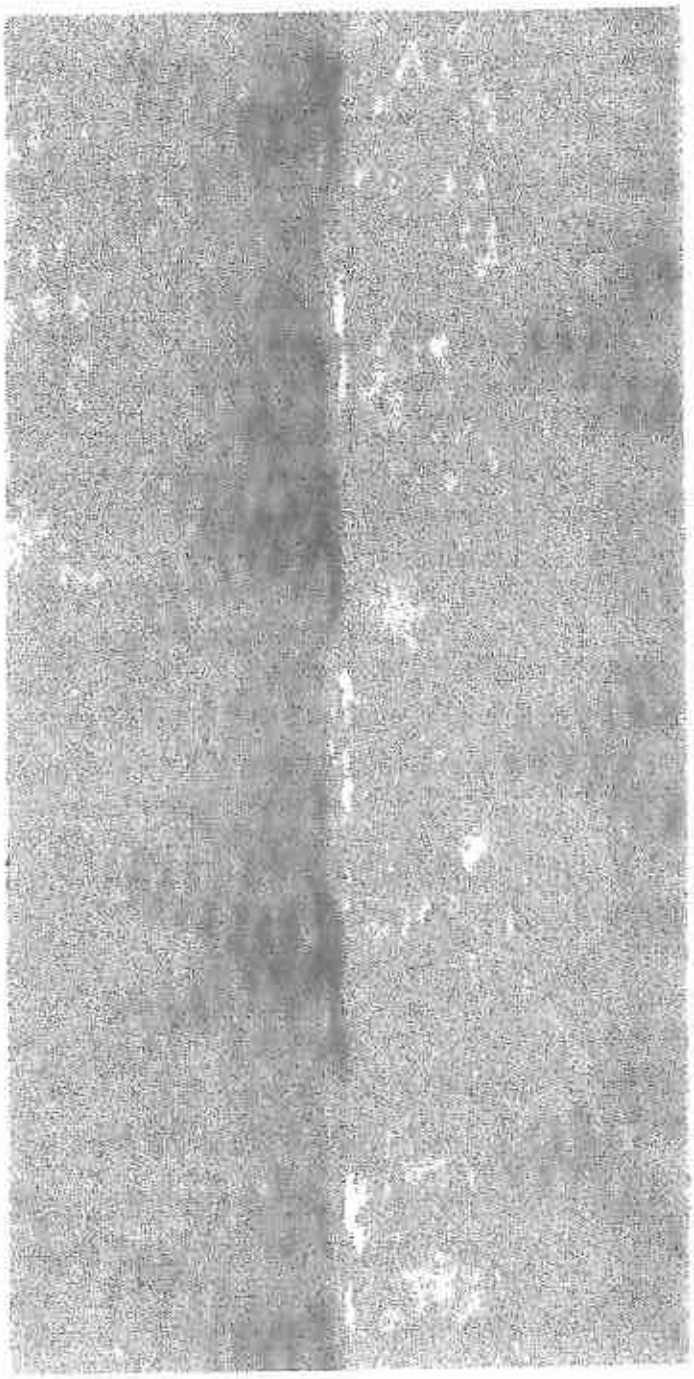

Bas

Echelle des pressions

0 3 6 9 ~~daN/mm²~~ 12c MPa

17 janvier 199

HOW TO LIMIT PRE-COMPRESSION REQUIREMENTS

– Insulation creep is unavoidable (especially given that the yield point of the most commonly used polyimide insulation is 69 MPa at 3% elongation and 296 K).

– Azimutal component of the Lorentz force is given by the electromagnetic design.

– The only parameter left is the pre-compression loss during cooldown.

KAPTON® Type V Film

PROPERTY	TYPICAL VALUES Film Gauge 50 µm (2 mil)	75 µm (3 mil)	125 µm (5 mil)	TEST METHOD
Tensile Strength MPa (psi) @ 296K (23°C). Machine Direction (MD) and Transverse Direction (TD).	165 (25,000)	186 (25,000)	186 (25,000)	ASTM D-882, Method A using an Instron Tensile Tester (specimen size: 25 x 127 mm (1" x 5", jaw separation: 50 mm (2"), jaw speed: 50 mm (2")/min.) Average of 5 specimens based on original measured thickness.
Elongation, % MD and TD	70	70	70	Same method as above
Shrinkage, % MD and TD Typical after 60 min. @ 473K (200°C).	.02	.02	.02	Average of 3 measurements in each direction before and after exposure to 473K (200°C) for 60 min. Film must be allowed to come to equilibrium with equivalent room conditions before and after exposure.

KAPTON® Type F Film

PROPERTY	TYPICAL VALUES Film Type* 120F616	150F619	250F629
Ultimate Tensile Strength (MD), MPa (psi)			
296K (23°C)	165 (24,000)	117 (17,000)	172 (25,000)
473K (200°C)	119 (16,000)	76 (11,000)	110 (16,000)
Yield Point at 3% (MD), MPa (psi)			
296K (23°C)	62 (9,000)	50 (7,300)	66 (10,000)
473K (200°C)	38 (5,500)	28 (4,000)	55 (8,000)
Stress at 5% Elongation (MD), MPa (psi)			
296K (23°C)	86 (12,500)	62 (9,000)	
473K (200°C)	52 (7,500)	38 (5,500)	
Ultimate Elongation (MD)			
296K (23°C)%	85	75	89
473K (200°C)%	95	85	
Tensile Modulus, MD GPa (psi)			
296K (23°C)	2.86 (415,000)	2.21 (320,000)	
473K (200°C)	1.48 (215,000)	1.19 (173,000)	
Impact Strength at 296K (23°C)			
g-m (Kg-cm/µm)	70 (7)	70 (7)	
g-m/µ (Kg-cm/mil)	2.3 (6.0)	1.8 (4.5)	
Tear Strength—Propagating (Elmendorf)			
g	20		
g/µm (g/mil)	0.39 (10)	0.53 (13.5)	0.47 (12)
Tear Strength—Initial (Graves)			
g	850		
g/µm (g/mil)	19 (750)	17 (435)	
Weight % Polyimide	80	57	73
Weight % FEP	20	43	27
Density Kg/m³x10⁻³	1.53	1.67	1.57

*Since a number of combinations of polyimide film and fluorocarbon coating add up to the same total gauge, it is necessary to distinguish among them. A three digit system is used in which the middle digit represents the nominal thickness of the base KAPTON film in mils. The first and third digits represent the nominal thickness of the coating of TEFLON FEP fluorocarbon resin in mils. The symbol 9 is used to represent 13 µm (½mil), and 6 to represent 2.5 µm (1/10 mil). Example: 120F616 is a 120-gauge structure consisting of a 25 µm (1-mil) base film with a 2.5 µm (1-10 mil) coating of TEFLON on each side. See page 22 for construction explanation.

5

PRE-COMPRESSION LOSS DURING COOLDOWN

– The pre-compression loss during cooldown, $\Delta\sigma$, can be estimated from:

$$\Delta\sigma \approx E_{coil}(\alpha_{coil} - \alpha_{collar})$$

where E_{coil} is the coil Young's modulus in the azimuthal direction, and α_{coil} and α_{collar} are the thermal expansion coefficients of the coil (in the azimuthal direction) and of the collars, integrated between room and operating temperatures.

Note that the above equation is derived with the assumptions that E_{coil} does not depend on temperature and that the collars are infinitely rigid.

INTEGRATED THERMAL EXPANSION COEFFICIENTS

– Typical values of integrated thermal expansion coefficients (between 4.2 K and room temperature) are (in mm/m):

Stack of insulated cables (polyimide/glass)	5.1[a)]
Stack of insulated cables (all-polyimide)	5.6[a)]
Copper (OFHC)	3.1
Aluminum	4.2
Stainless steel (304/316)	2.9
Low carbon steel	2.0

a) transverse direction; SSC inner cables.

CHOICE OF COLLAR MATERIAL

– To limit cooldown loss, it is preferable to use for the collars a material whose integrated thermal expansion coefficient matches more or less that of the coil.

For NbTi coils with polyimide/glass or all-polyimide insulation, this suggests aluminum alloy.

– However, and as will be described in the section on radial support, it is also desirable that the collars be as rigid as possible or have an integrated thermal expansion coefficient approaching that of the low carbon steel used for the yoke.

This favors austenitic stainless steel, which has a lower integrated thermal expansion coefficient and whose Young's modulus is 195 GPa at room temperature and 203 GPa at 4.2 K, compared to 72 GPa at room temperature and 80 GPa at 4.2 K for aluminum alloy.

– Note also that austenitic stainless steel presents a better resistance to stress cycling at low temperature, but has a higher density (7800 kg/m^3 compared to 2800 kg/m^3 for aluminum alloy) and is thus more expensive.

CHOICE OF COLLAR MATERIAL (CONT.)

– There is no ideal choice between stainless steel and aluminum alloy and magnets with both types of collar materials have been built:

• HERA dipole magnets and early LHC dipole magnet prototypes use aluminum alloy collars,

• Tevatron dipole magnets, most SSC dipole magnet prototypes and coming (1999) LHC dipole magnet prototypes rely on stainless steel collars.

– In any case, and whichever collar material is chosen, a thorough mechanical analysis of the structure under the various loading conditions is required.

LECTURE 5: MECHANICAL DESIGN OF PARTICLE ACCELERATOR MAGNETS

5.1 Components of the Lorentz Force in Cosθ and Cos2θ Magnetic Designs

5.2 Azimuthal Pre-Compression

5.3 Coil Mechanical Properties

5.4 Collar Designs

5.5 Radial Support
- 5.5.1 Designs with Self-Supported Collared-Coil Assemblies
- 5.5.2 Designs with Fully-Mated Yoke
- 5.5.3 Design with Yoke Midplane Gap
- 5.5.4 RHIC Magnets
- 5.5.5 Azimuthal Pre-Compression Versus Radial Support

5.6 End Support

5.7 Other Designs

COIL MECHANICAL PROPERTIES

– The coils of accelerator magnets consitute a highly composite medium and their stress-strain curves present large hystereses between loading and unloading branches.

– The first loading-unloading cycle on a virgin coil is usually different from subsequent ones, but, after 2 or 3 cycles, the stress-strain curve becomes more or less reproducible.

– The amplitude of the hysteresis depends on the maximum pressure reached during the loading cycle.

– The loading branch of the stabilized curve is usually more or less linear while the unloading branch can be approximated by a second order polynomial.

Example: for a LHC dipole magnet coil package, the loading spring rate is 3709 MN/m^2, the unloading spring rate is of the order of 7045 MN/m^2 at 80 MPa, it decreases to 5140 MN/m^2 at 65 MPa and 4435 MN/m^2 at 50 MPa.

– The amplitude of the hysteresis is smaller at liquid helium temperature than at room temperature and the loaded coils are 20 to 30% stiffer.

– The coil mechanical properties strongly depend on the choice of insulation system.

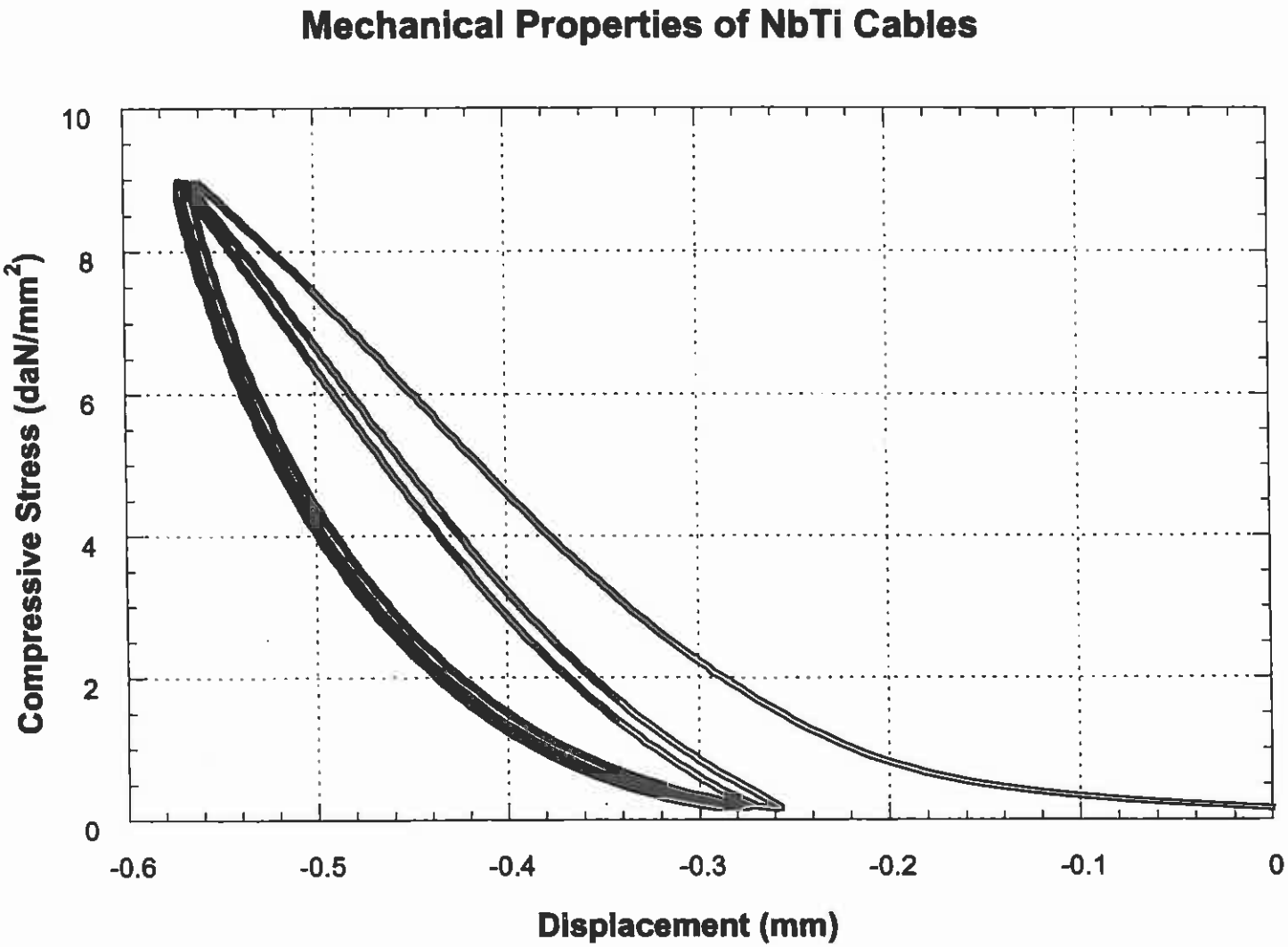

Courtesy C. Gourdin

INFLUENCE OF PEAK STRESS ON MECHANICAL HYSTERESIS

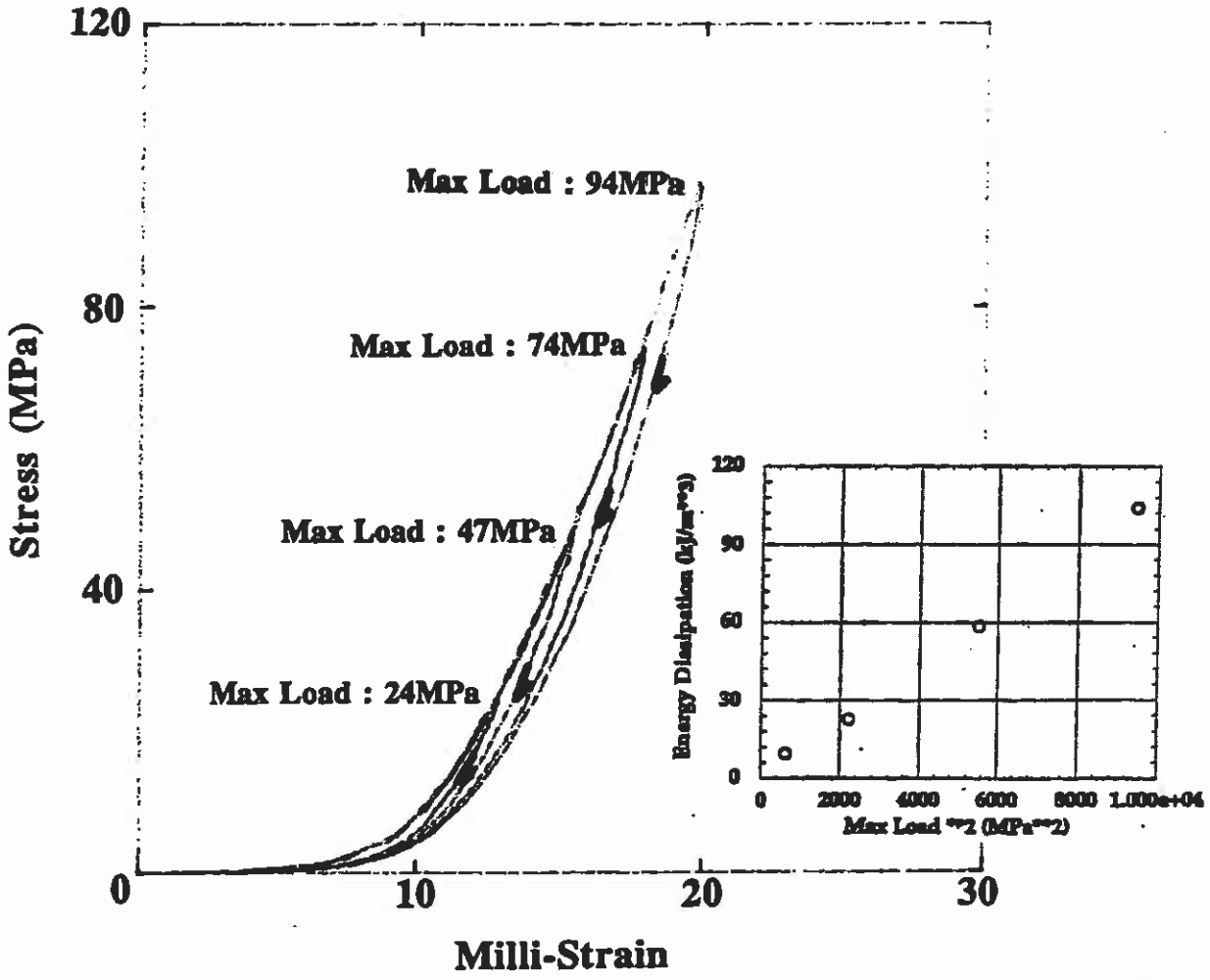

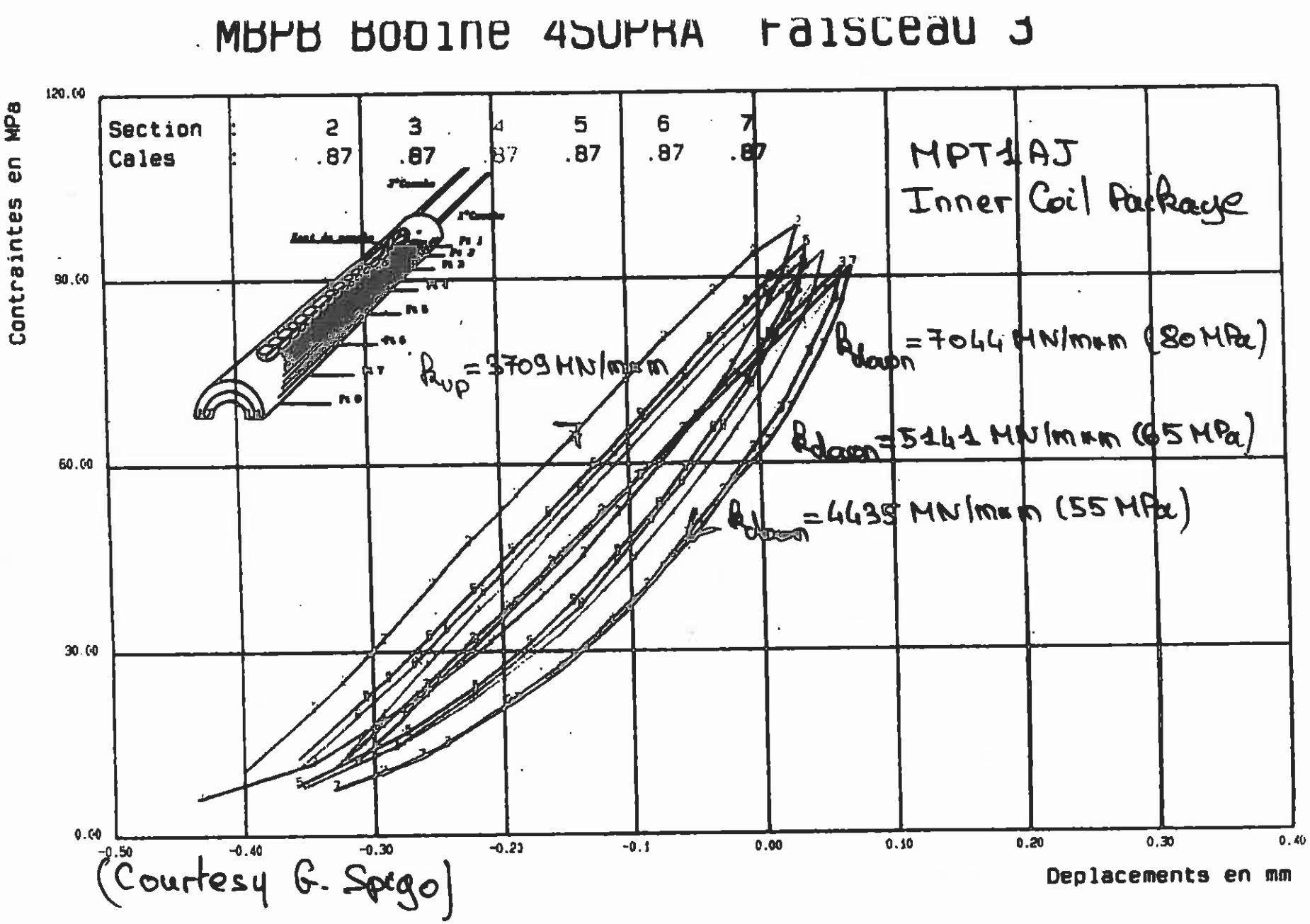
MBPB Bobine 45UPHA Faisceau 3
Section : 2 3 4 5 6 7
Cales : .87 .87 .87 .87 .87 .87
MPT1AJ
Inner Coil Package
Contraintes en MPa
Deplacements en mm
120.00
90.00
60.00
30.00
0.00
-0.50
-0.40
-0.30
-0.20
-0.1
0.00
0.10
0.20
0.30
0.40
R_{up} = 3709 MN/mm
R_{down} = 7044 MN/mm (80 MPa)
R_{down} = 5141 MN/mm (65 MPa)
R_{down} = 4439 MN/mm (55 MPa)
(Courtesy G. Spigo)

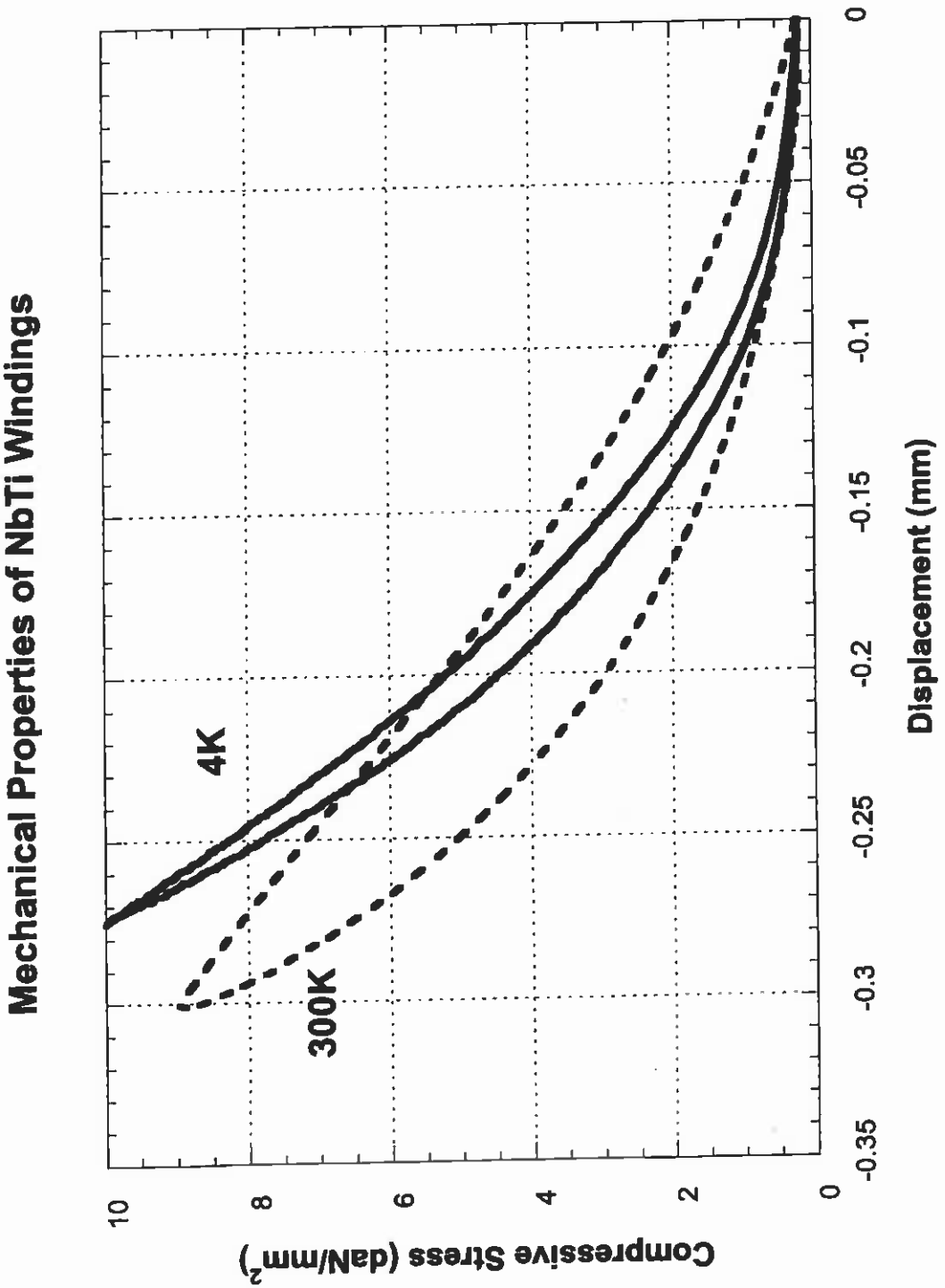

Courtesy C. Gourdin

Mechanical Properties of different Windings at Room Temperature

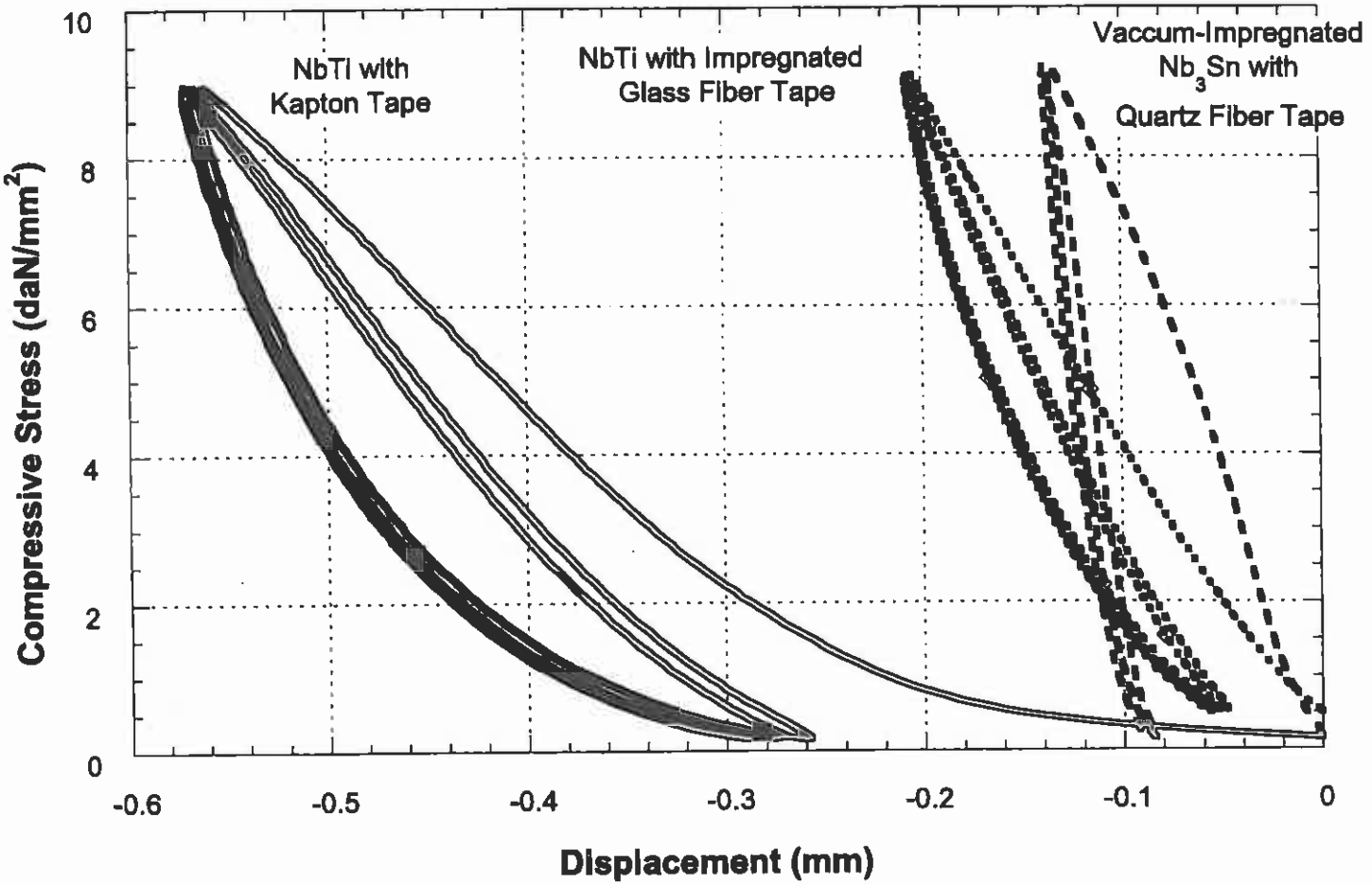

Courtesy C. Gourdin

ORIGIN OF MECHANICAL HYSTERESIS

– The mechanical hysteresis has at least four origins:

• *Plastic deformations in the high purity,* and thus, soft, *copper of cable strands,*

• *Friction between cable strands,*

• *Plastic deformations in cable insulation,*

• *Friction at the interface between insulation and cable strands.*

EXPERIMENTAL SETUP

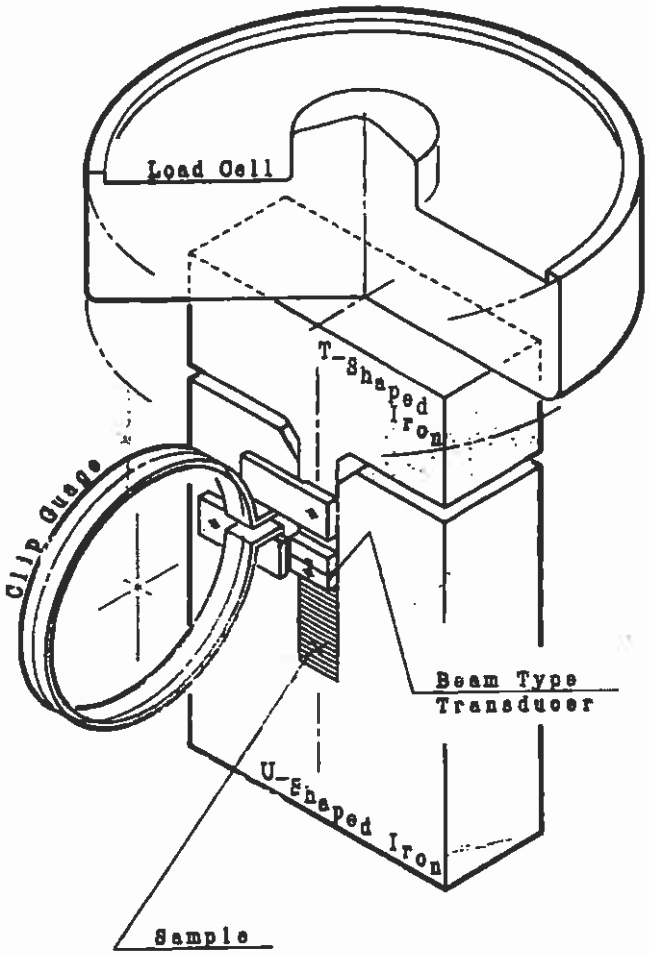

STRESS-STRAIN CURVE OF A COIL STACK

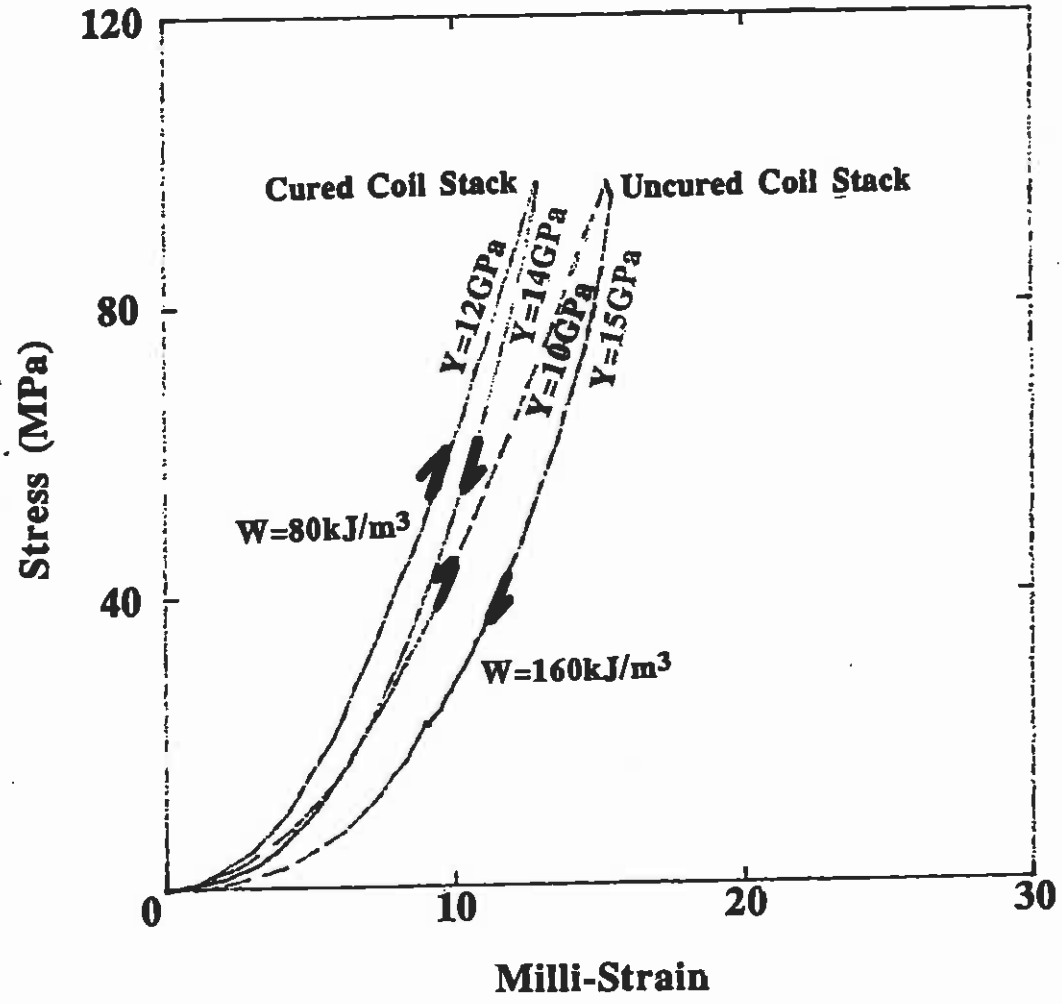

ORIGIN OF MECHANICAL HYSTERESIS IN COIL STACK part I

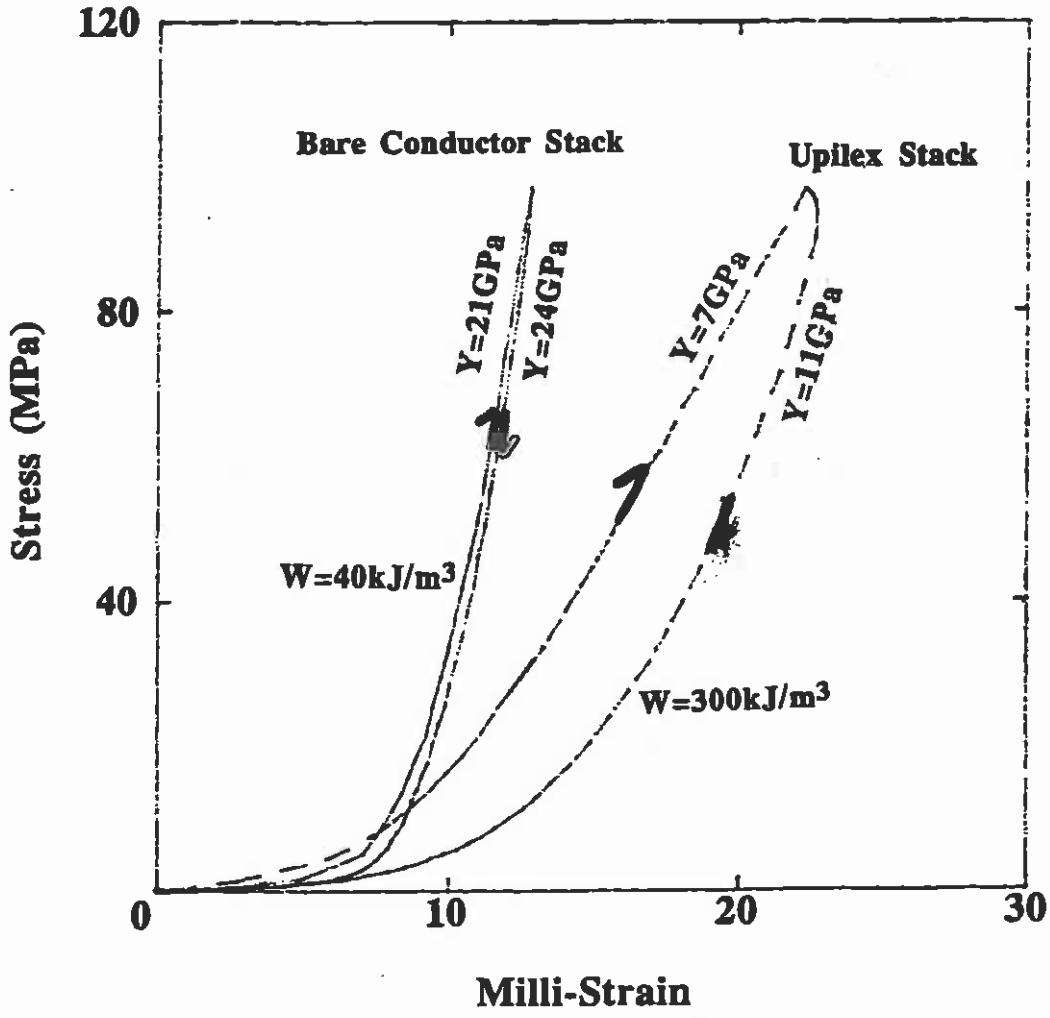

ORIGIN OF MECHANICAL HYSTERESIS IN COIL STACK part II

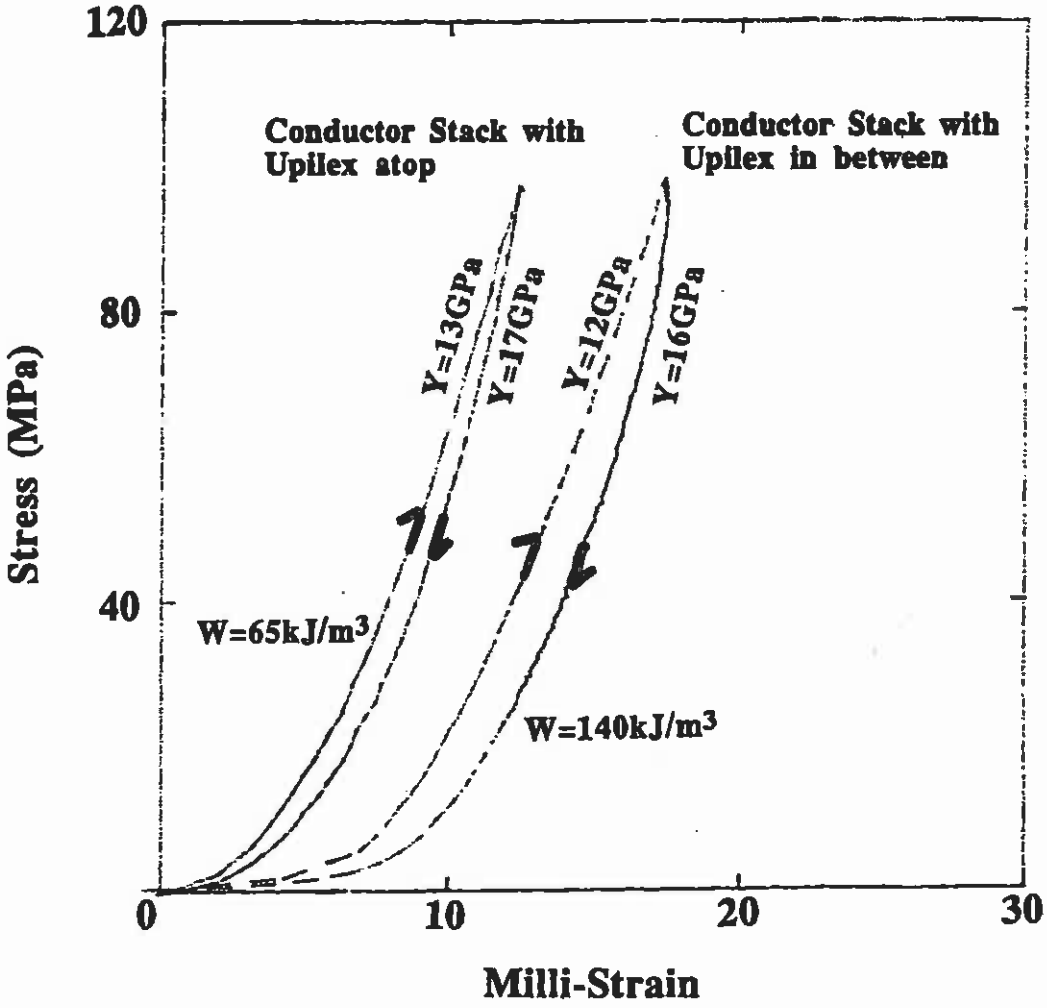

PRE-STRESS COMPUTATIONS

– Problem: What mechanical properties to use for the coils in the finite element computations (especially during cooldown)?

Simulation of Coil Stress History Measured by Clip Gauge During Magnet Assembly & Testing

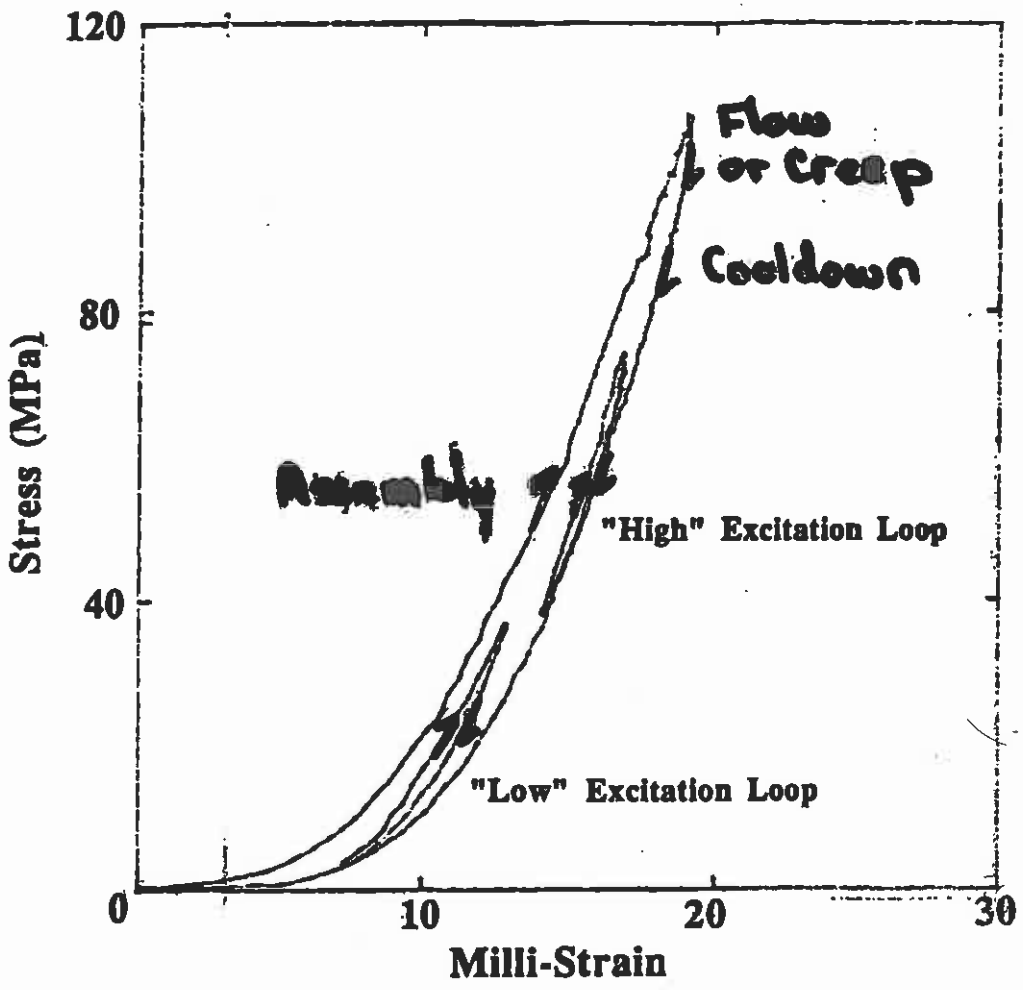

LECTURE 5: MECHANICAL DESIGN OF PARTICLE ACCELERATOR MAGNETS

5.1 Components of the Lorentz Force in Cosθ and Cos2θ Magnetic Designs

5.2 Azimuthal Pre-Compression

5.3 Coil Mechanical Properties

5.4 Collar Designs

5.5 Radial Support
- 5.5.1 Designs with Self-Supported Collared-Coil Assemblies
- 5.5.2 Designs with Fully-Mated Yoke
- 5.5.3 Design with Yoke Midplane Gap
- 5.5.4 RHIC Magnets
- 5.5.5 Azimuthal Pre-Compression Versus Radial Support

5.6 End Support

5.7 Other Designs

DIPOLE MAGNET COLLARING

– Dipole magnets rely on collar pairs, which are designed to be mated.

– To facilitate and speed up assembly, the collar pairs are usually stacked into packs, held together by rods.

– The packs are also assembled by pairs, one top and one bottom, so that, when placed together around the coil assembly, the collars of a given pair of packs fit into one another.

– Once the pairs of packs are put in place, they are locked arround the coil assembly either by means of full-length tie rods housed at the collars' midplane or by means of short length keys inserted at the collar sides.

– The use of full-length tie rods requires a full-length collaring press, while the insertion of short length keys can be done in section.

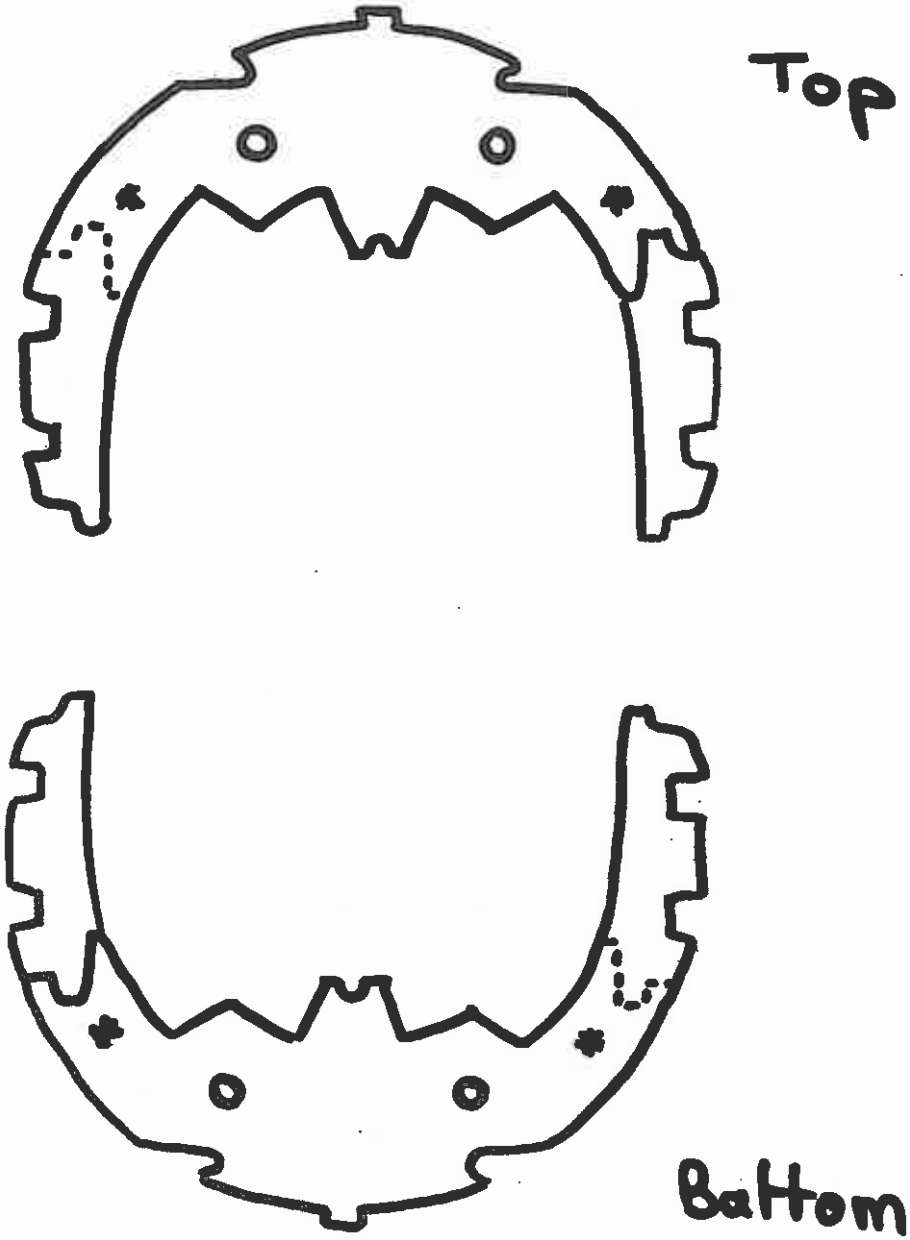
Top
Bottom

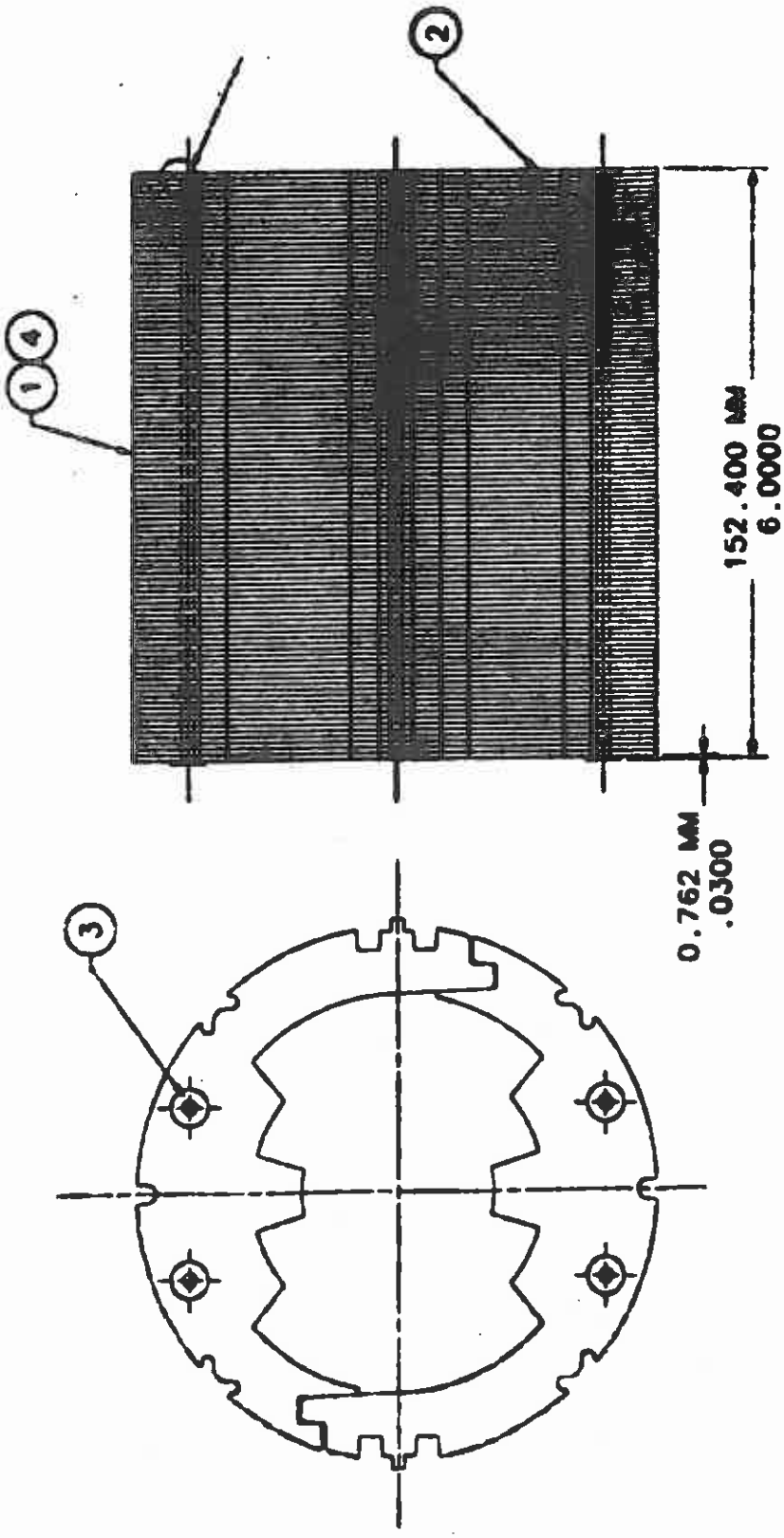
2
1
4
152.400 MM
6.0000
0.762 MM
.0300
3

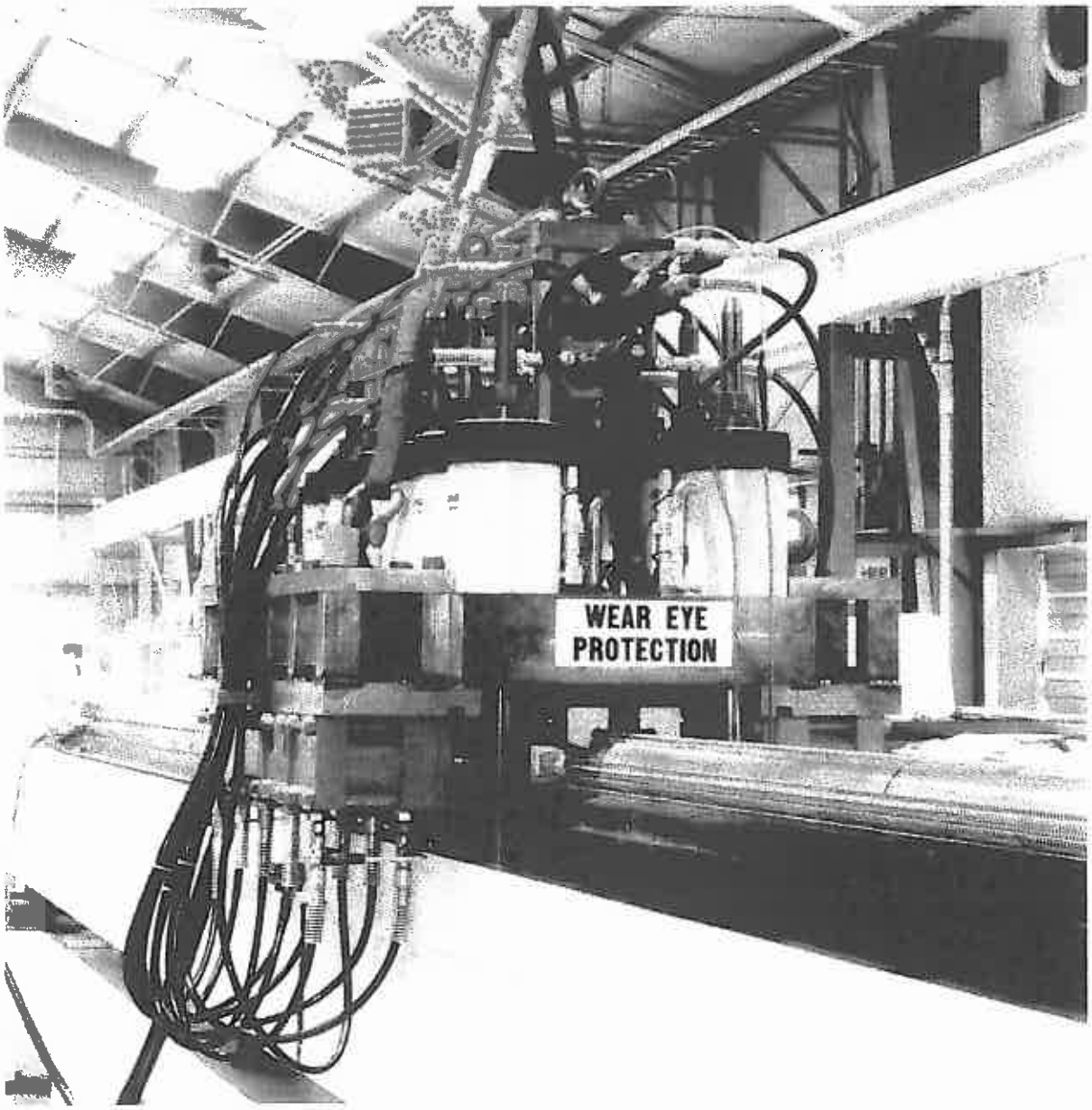
WEAR EYE
PROTECTION

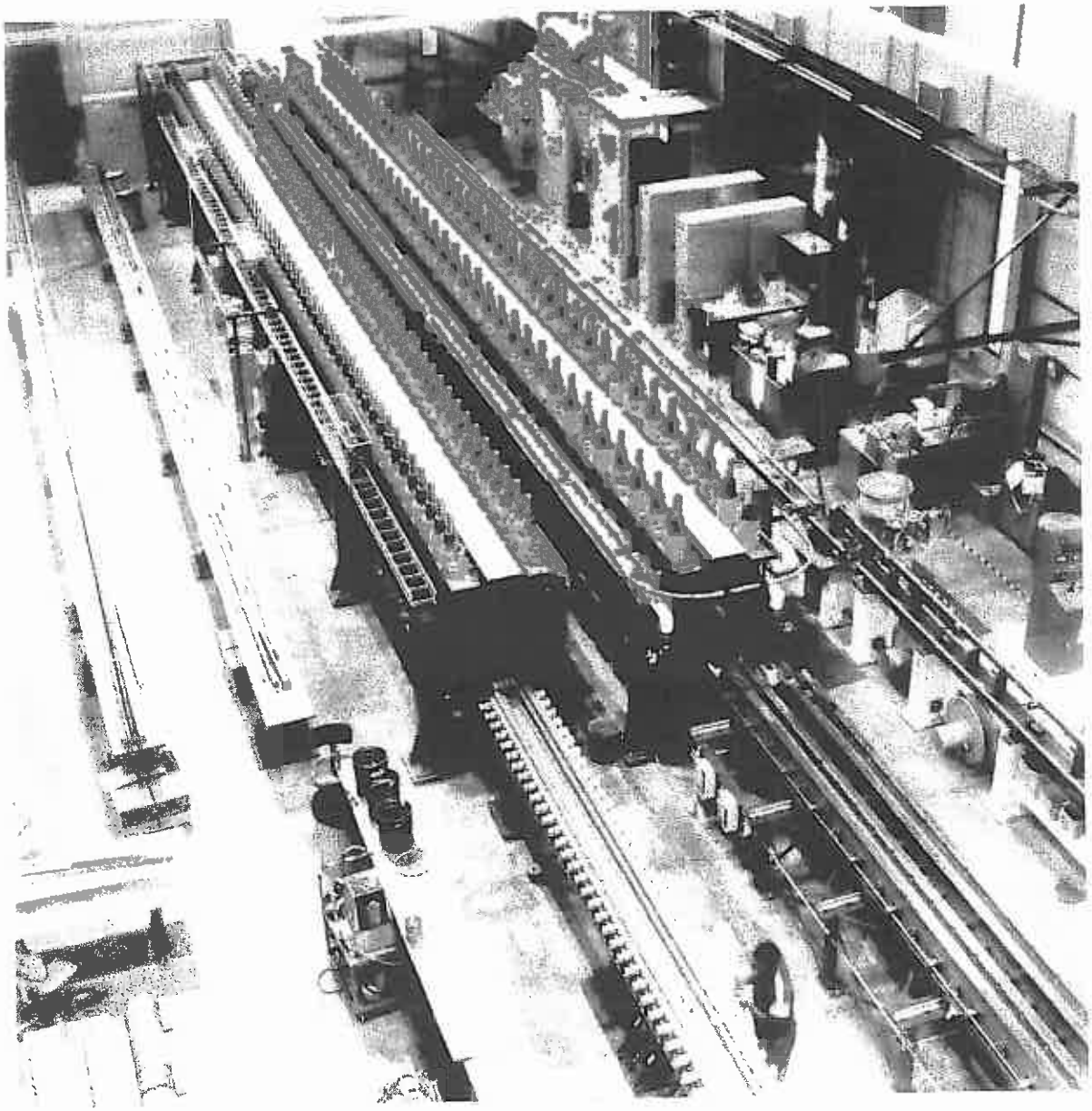

TWIN-APERTURE DIPOLE MAGNET COLLARING

– In the course of the twin-aperture dipole magnet R&D program for LHC, CERN has considered various collar designs:

- Common, aluminum collars held by full-length tie rods (in a 2-piece, vertically-split yoke),

- Separate aluminum collars held by full-length tie rods (in a 2-piece, vertically-split yoke),

- Separate, stainless steel collars held by short length keys (in a 3-piece vertically split yoke).

At present (1999), the preferred design relies on common, stainless steel collars held by full-length tie rods (in a 2-piece, vertically-split yoke).

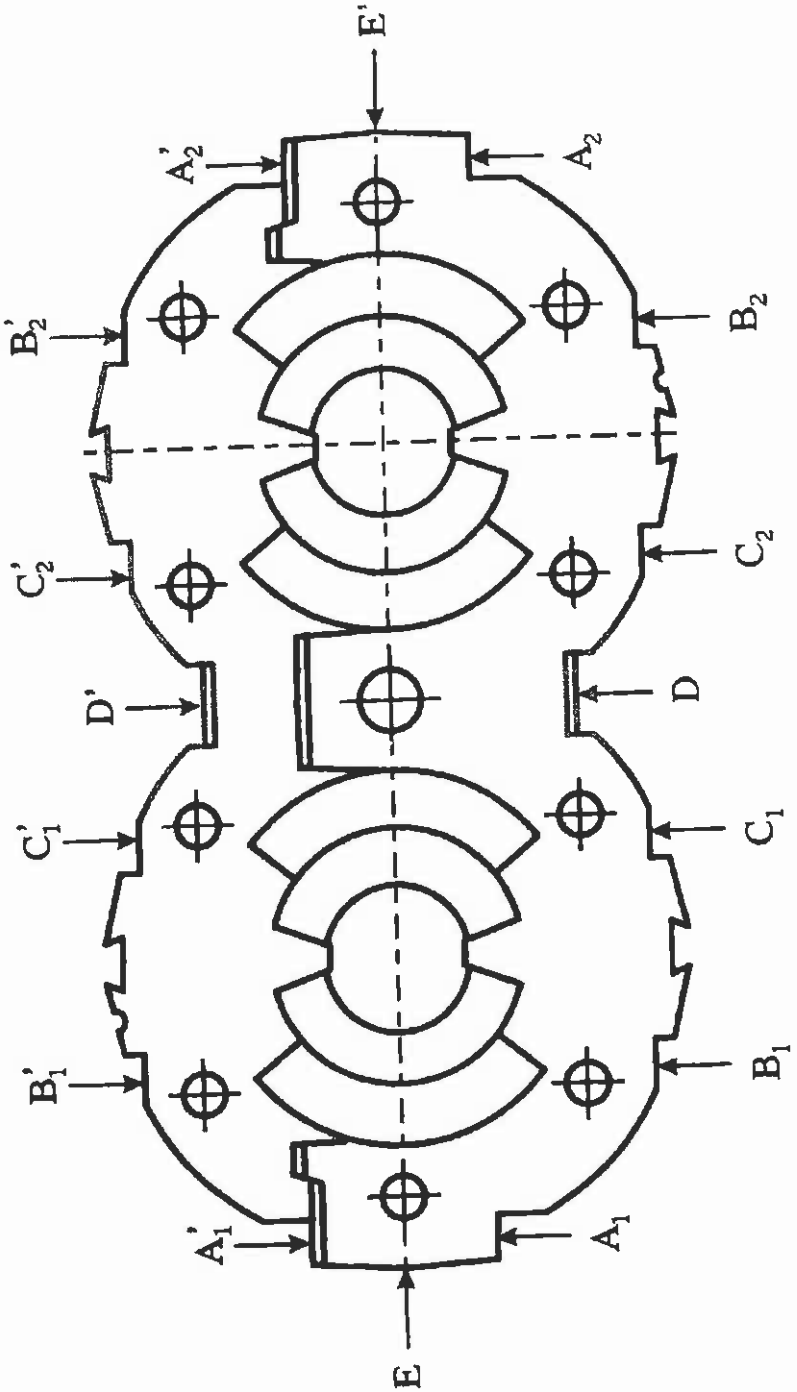
E'
A'2
A2
B'2
B2
C'2
C2
D'
D
C'1
C1
B'1
B1
A'1
A1
E

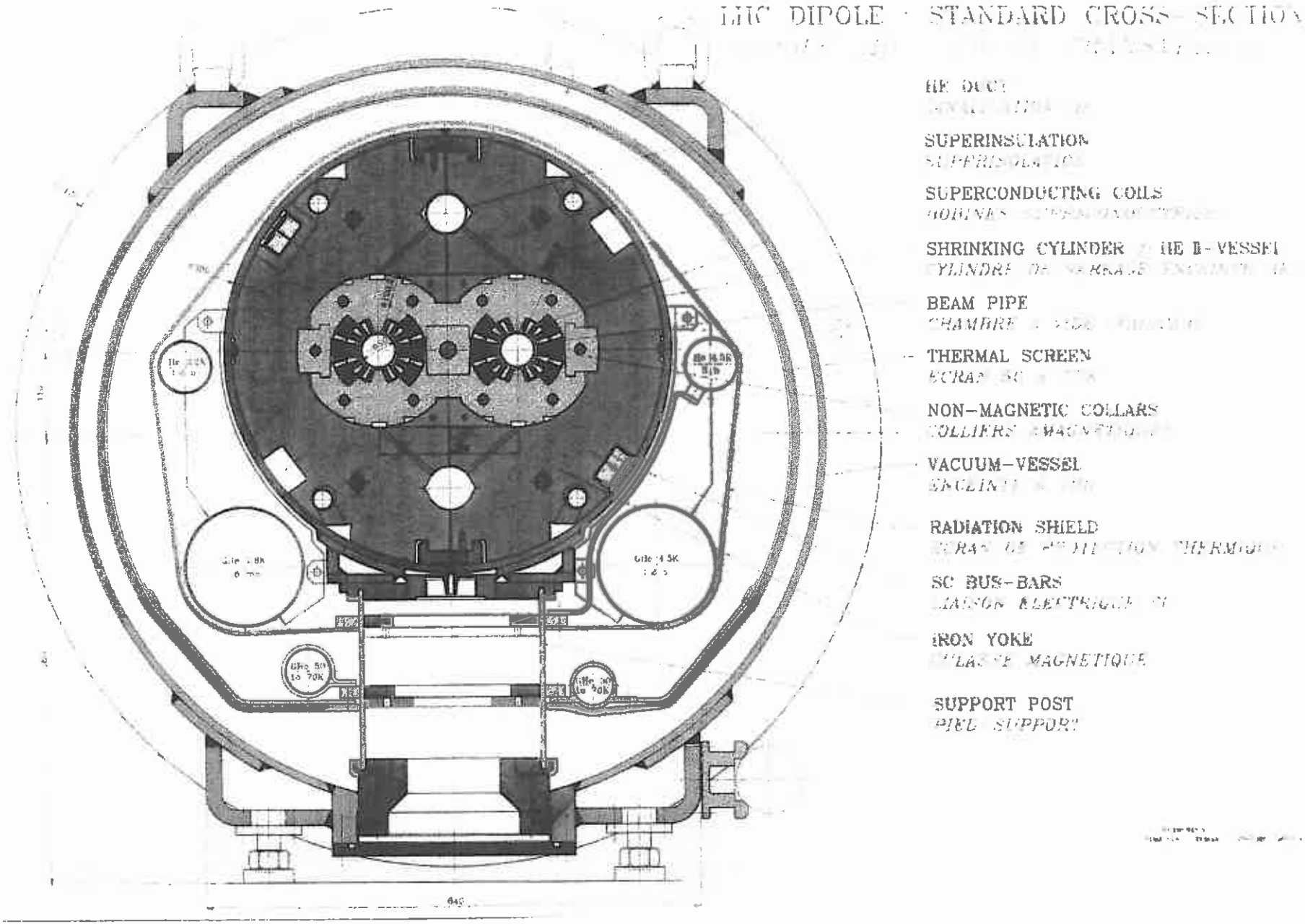
LHC DIPOLE STANDARD CROSS-SECTION
HE DUCT
SUPERINSULATION
SUPERCONDUCTING COILS
SHRINKING CYLINDER HE II-VESSEL
BEAM PIPE
THERMAL SCREEN
NON-MAGNETIC COLLARS
VACUUM-VESSEL
RADIATION SHIELD
SC BUS-BARS
IRON YOKE
SUPPORT POST
PIED SUPPORT

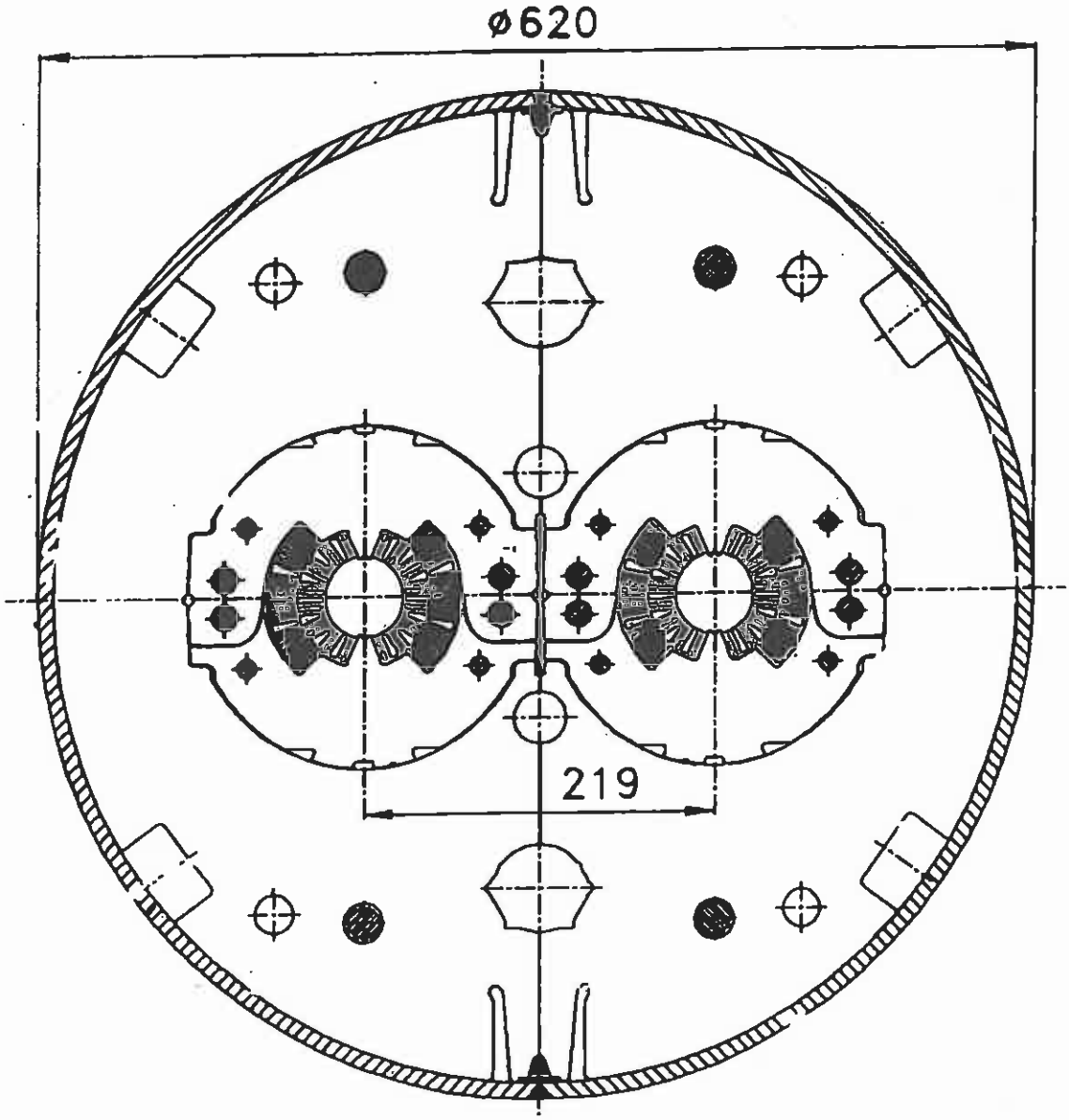
ø620
219

CERN Model

i.c.diameter 50mm

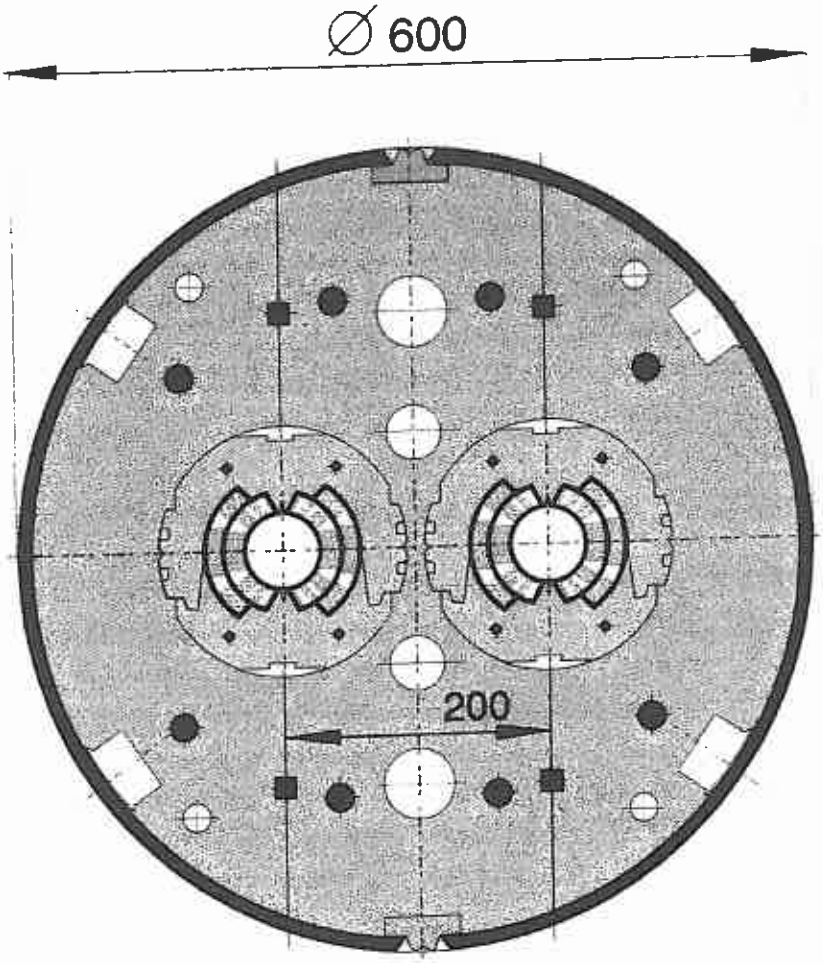

LHC cables (17 mm)

Inner cable 26 x 1.29 mm cu : sc 1.6

Outer cable 40 x 0.84 mm cu : sc 1.8

S . C . Filaments 5 μm

QUADRUPOLE MAGNET COLLARING

– Various collar designs have been used for quadrupole magnets:

• ***Alternated 2-piece, 180° collars,*** which requires a vertical collaring.

Examples: HERA and LHC arc quadrupole magnets developed at CEA/Saclay.

• ***4-piece, 90° collars,*** which requires a 4-way, horizontal collaring.

Example: SSC arc quadrupole magnet prototypes developed at LBNL.

• ***Dipole-like collars with inner spacers,*** which can use existing dipole tooling.

Example: UNK quadrupole magnet model and SSC interaction region quadrupole magnet prototype.

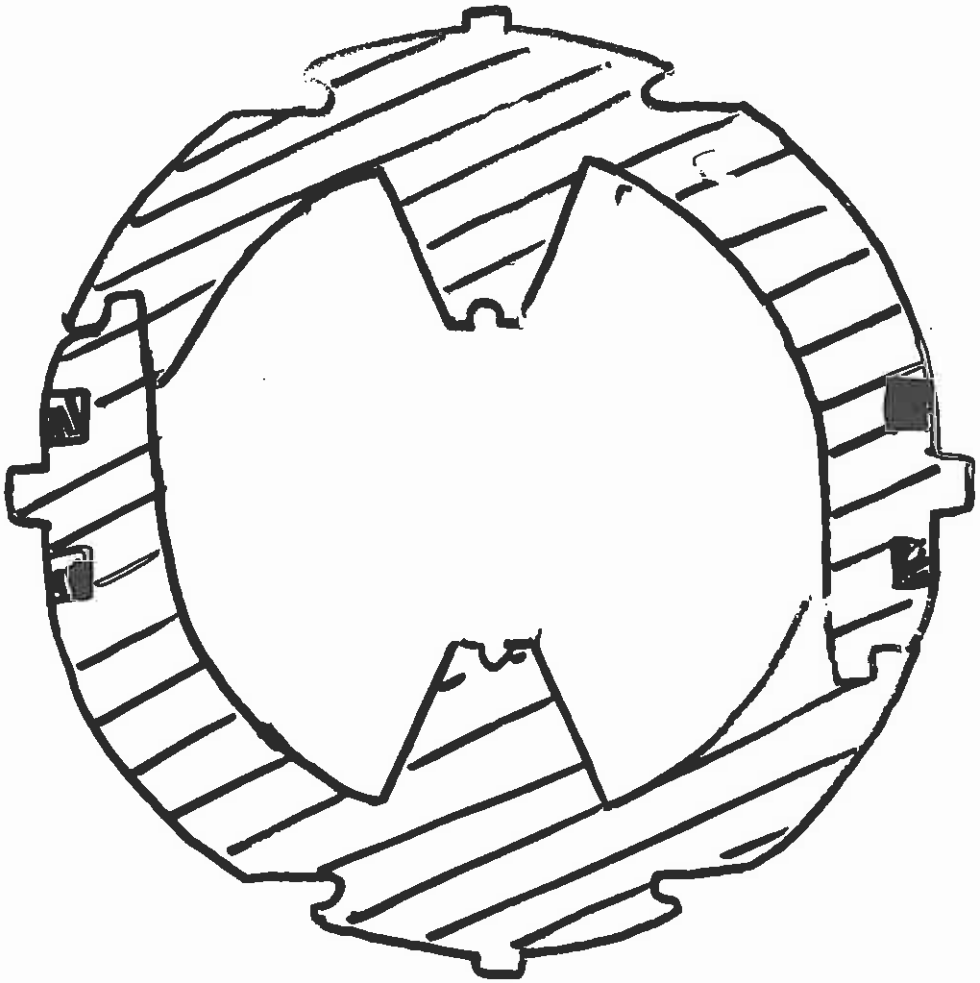

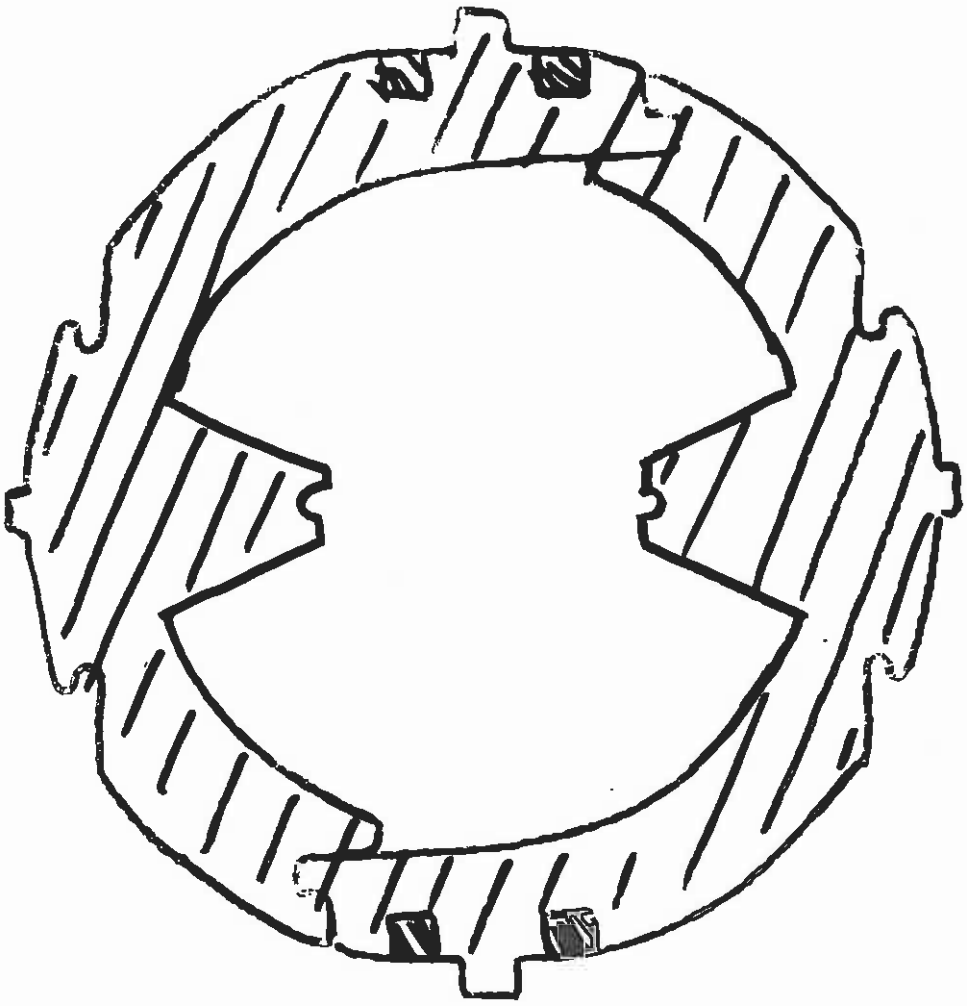

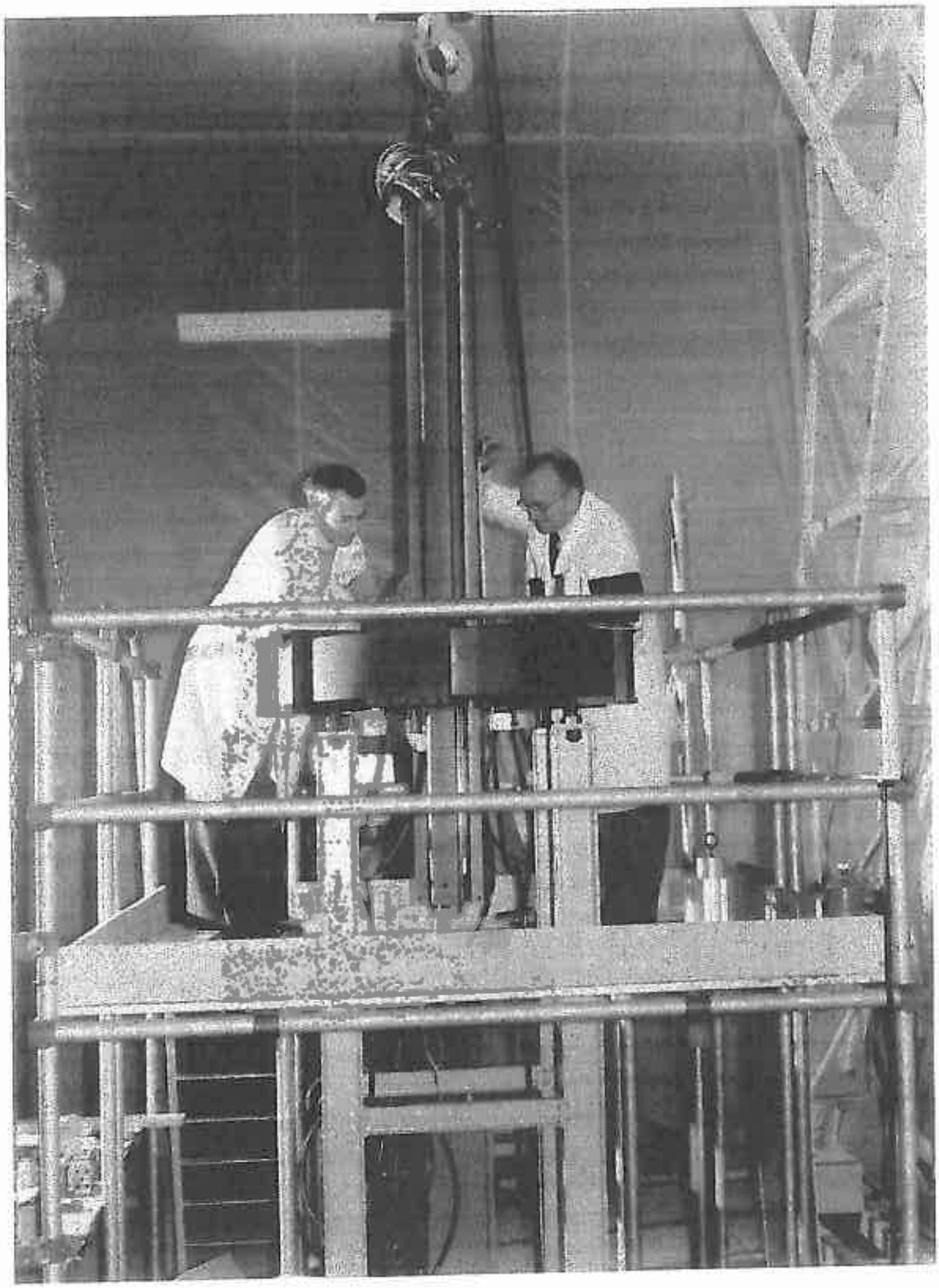

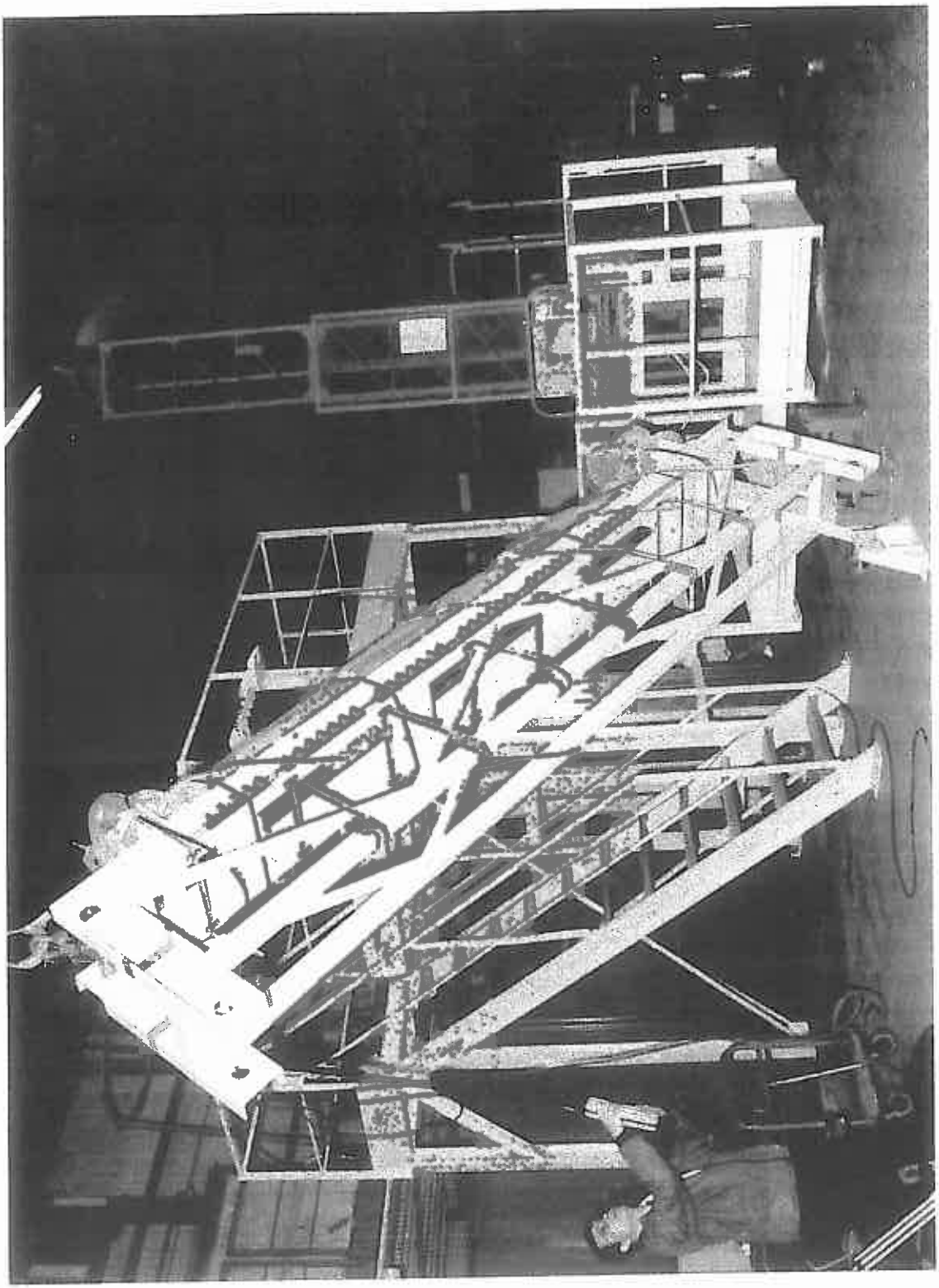

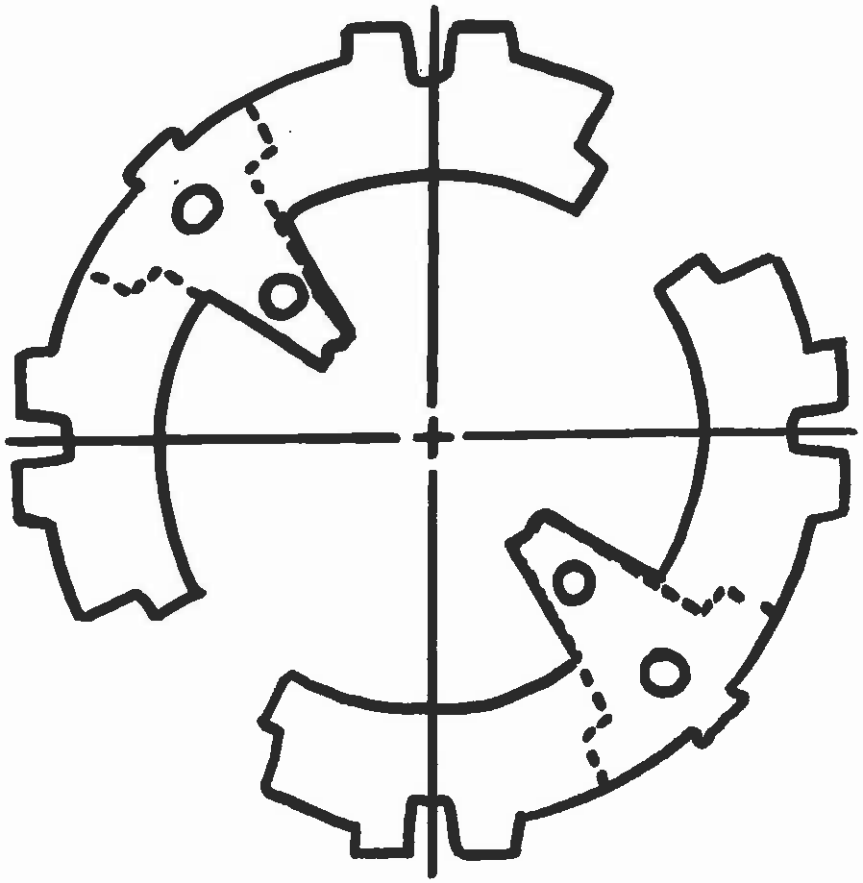

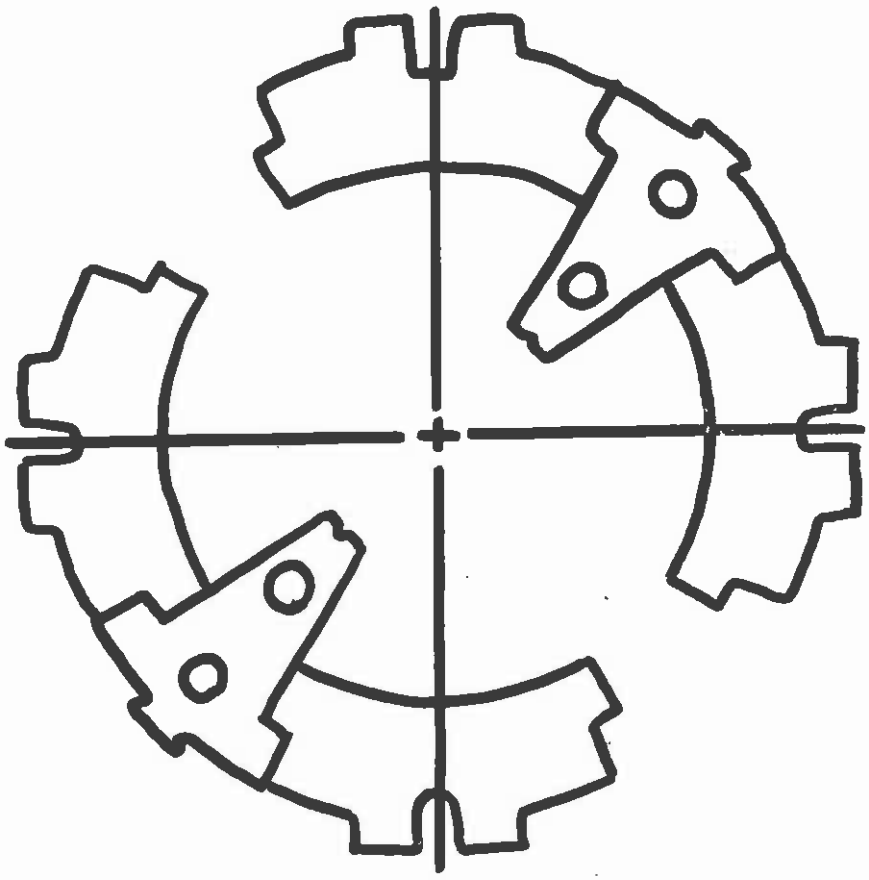

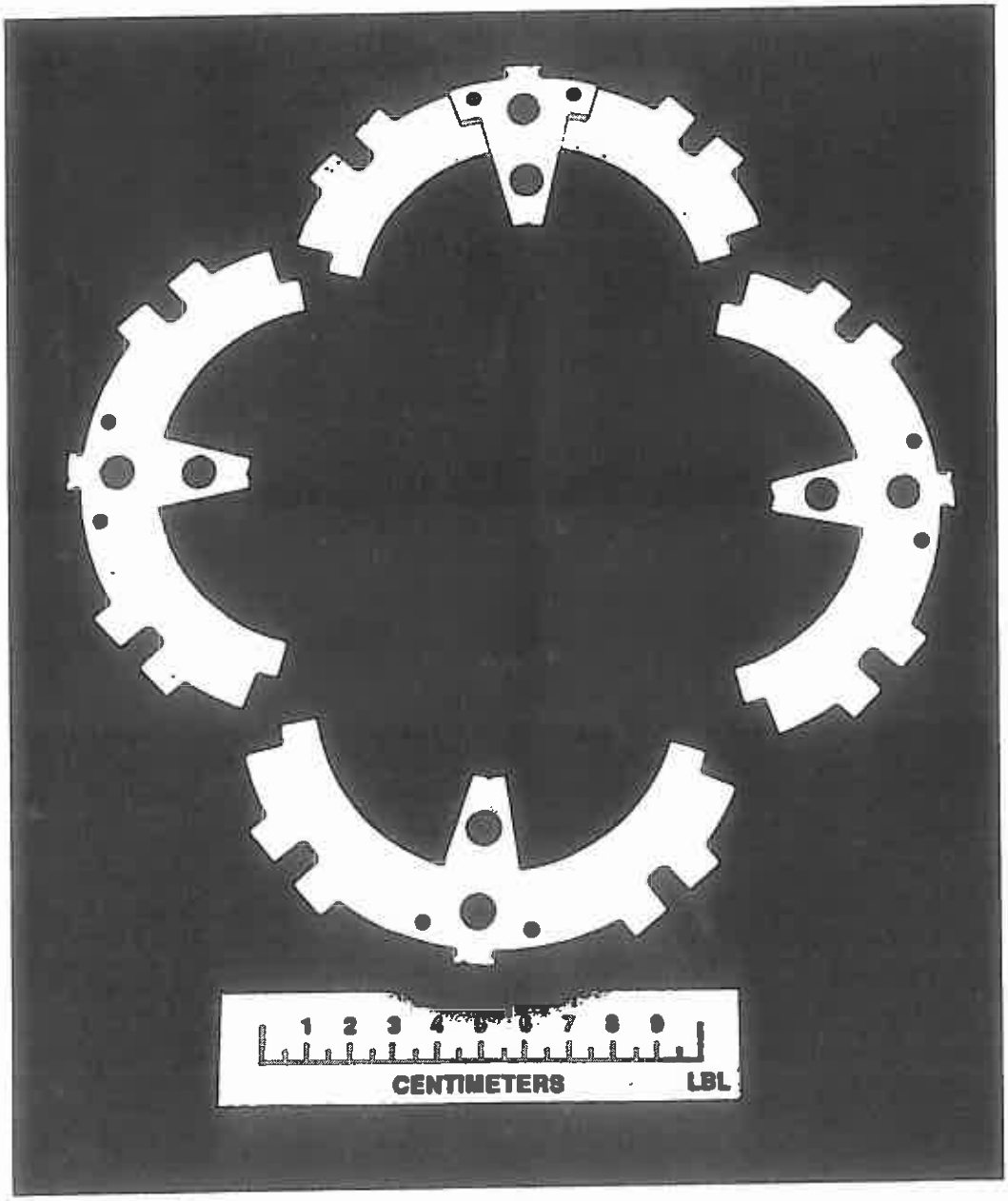
1 2 3 4 5 6 7 8 9
CENTIMETERS
LBL

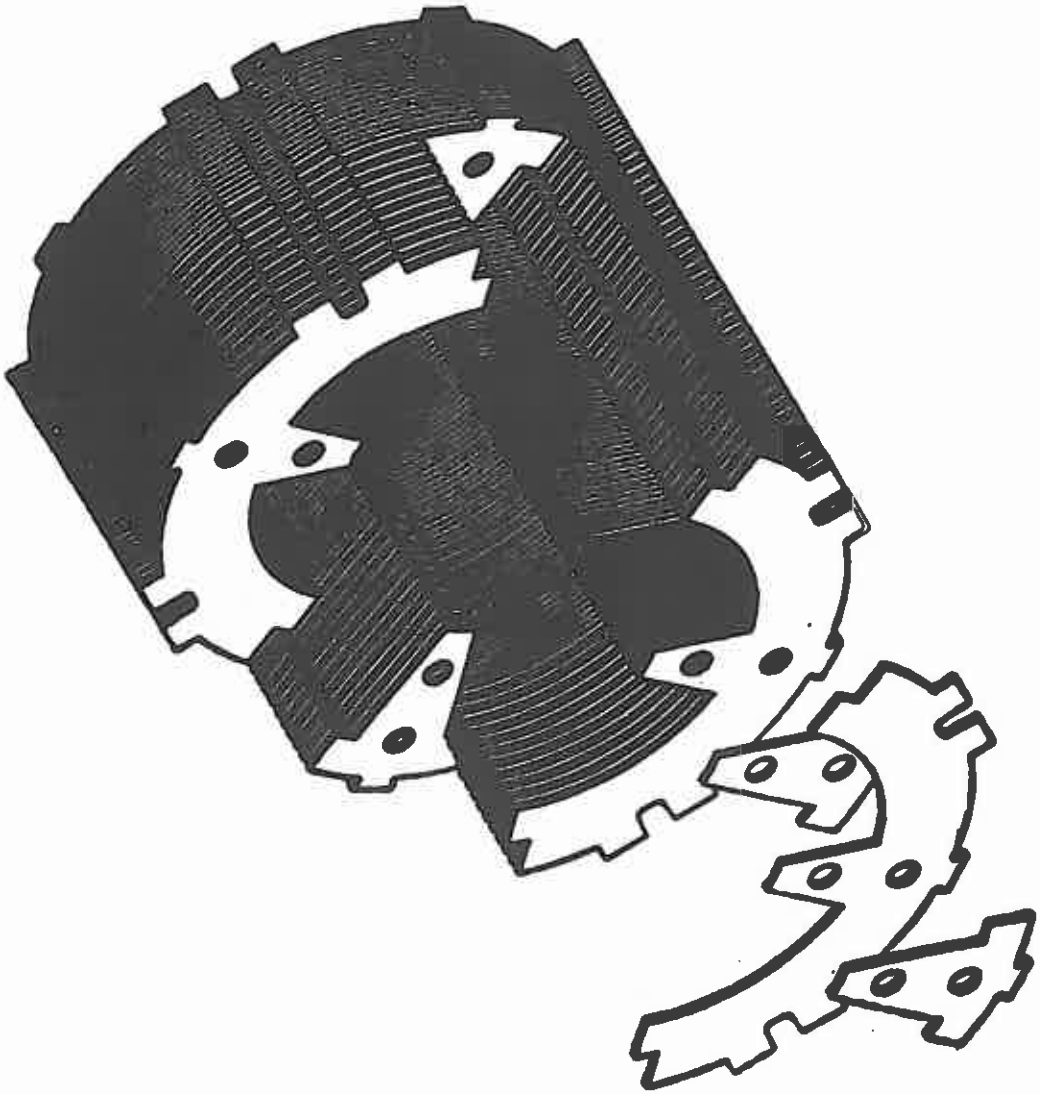

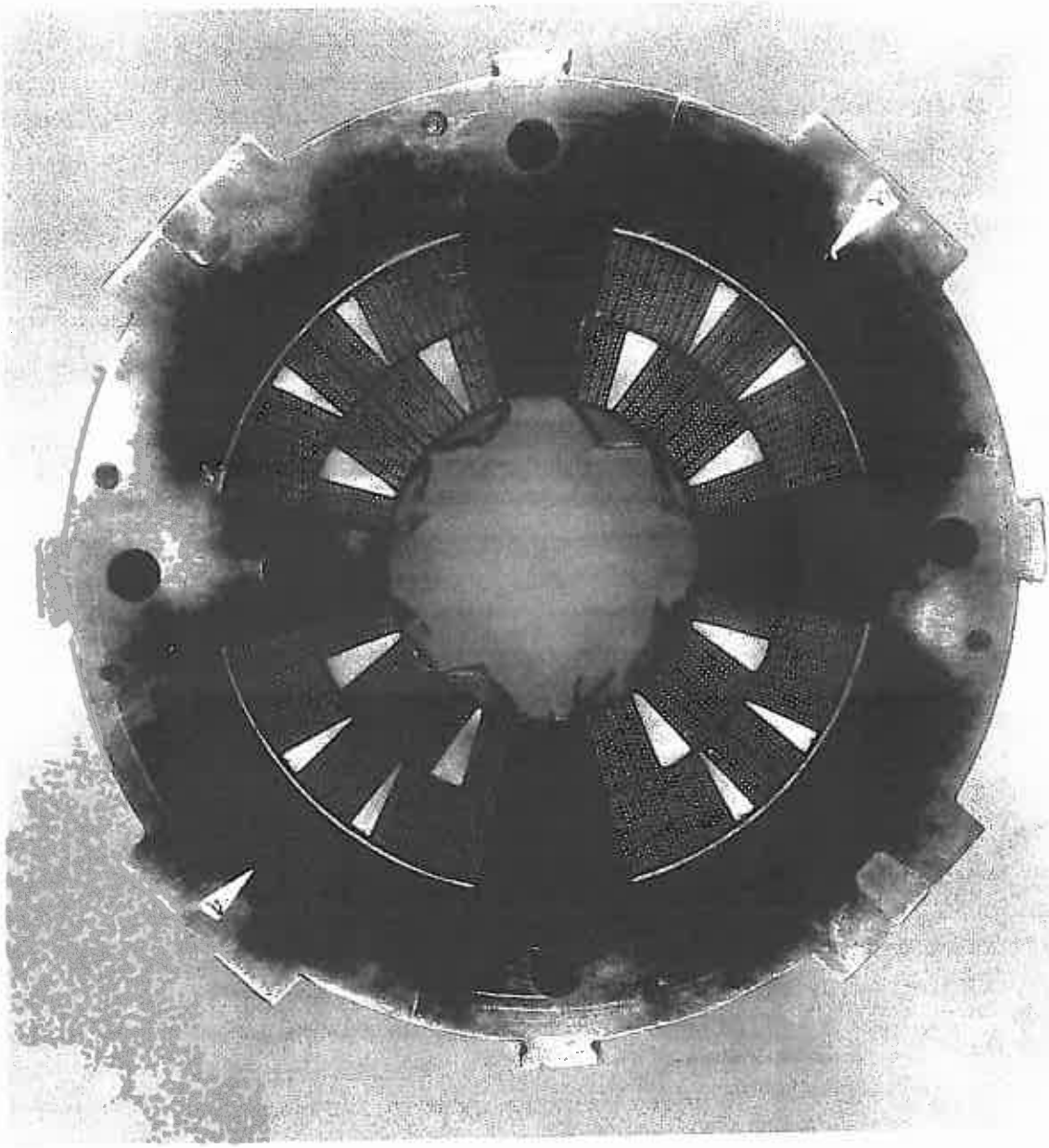

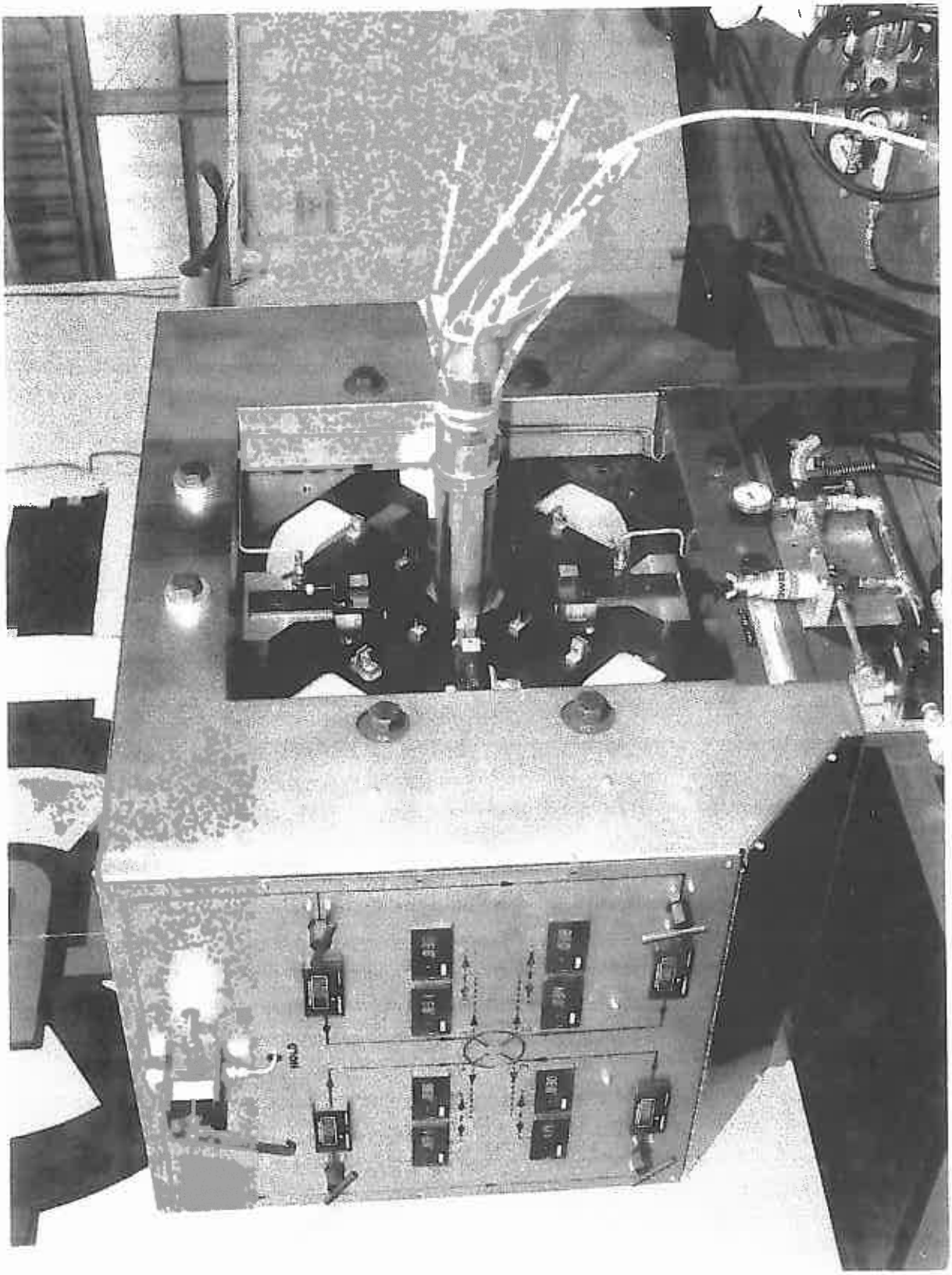

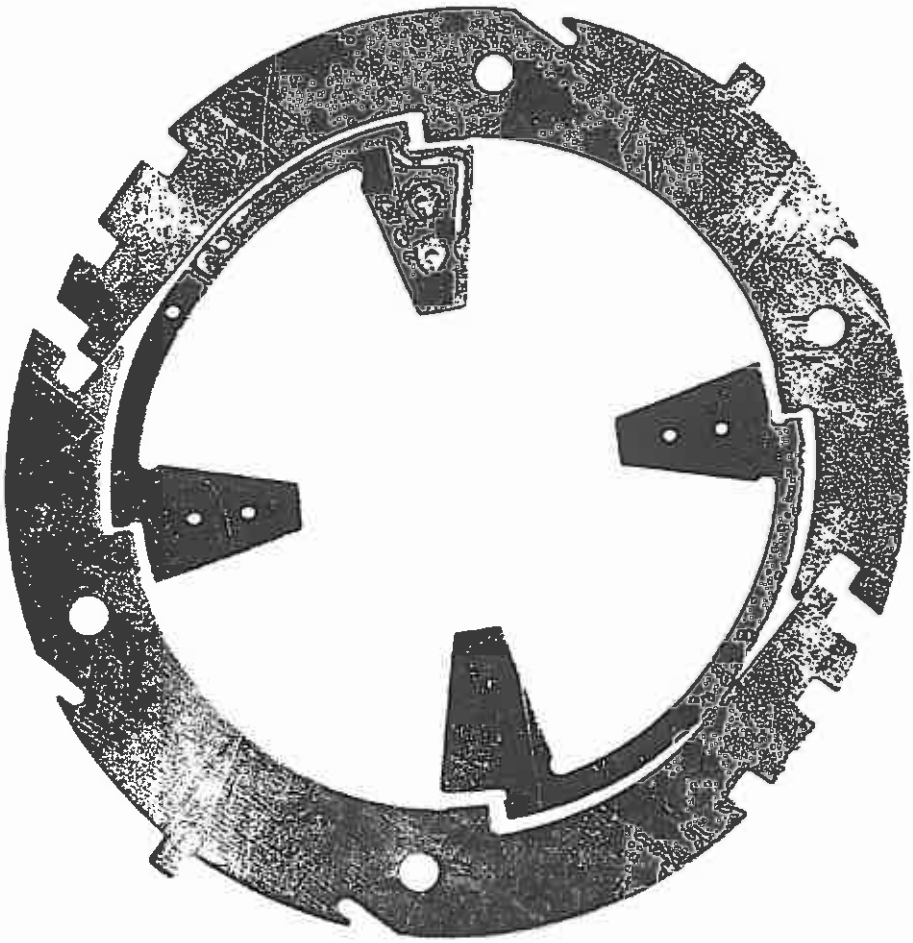

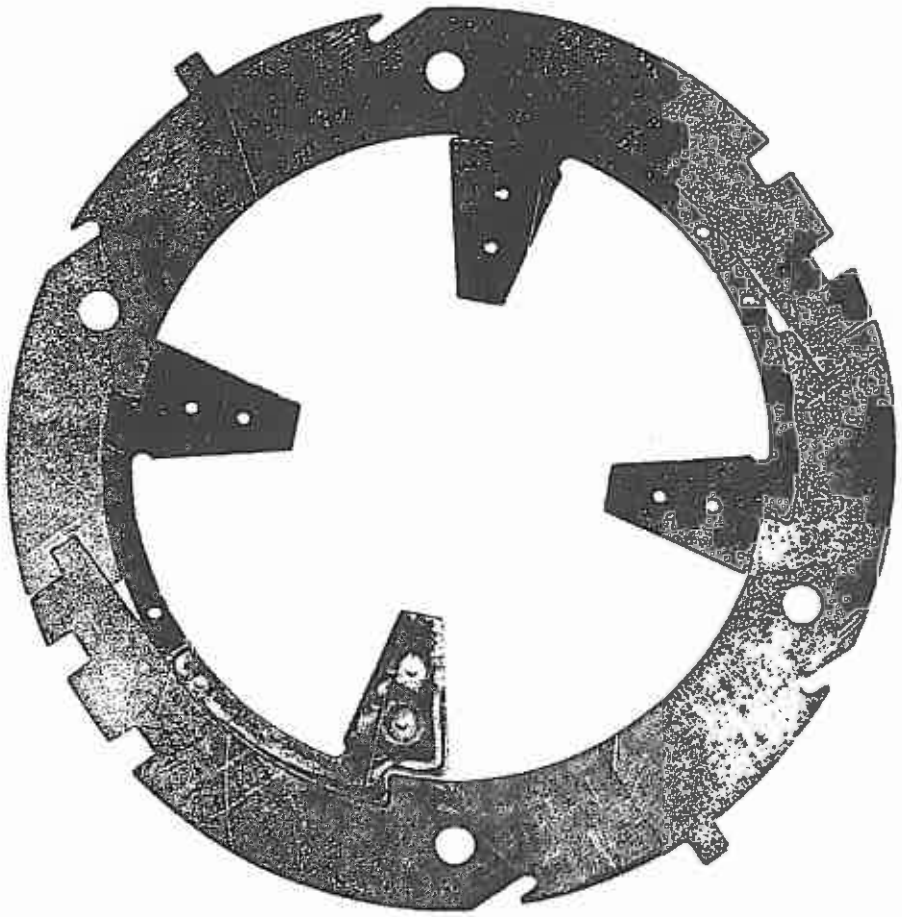

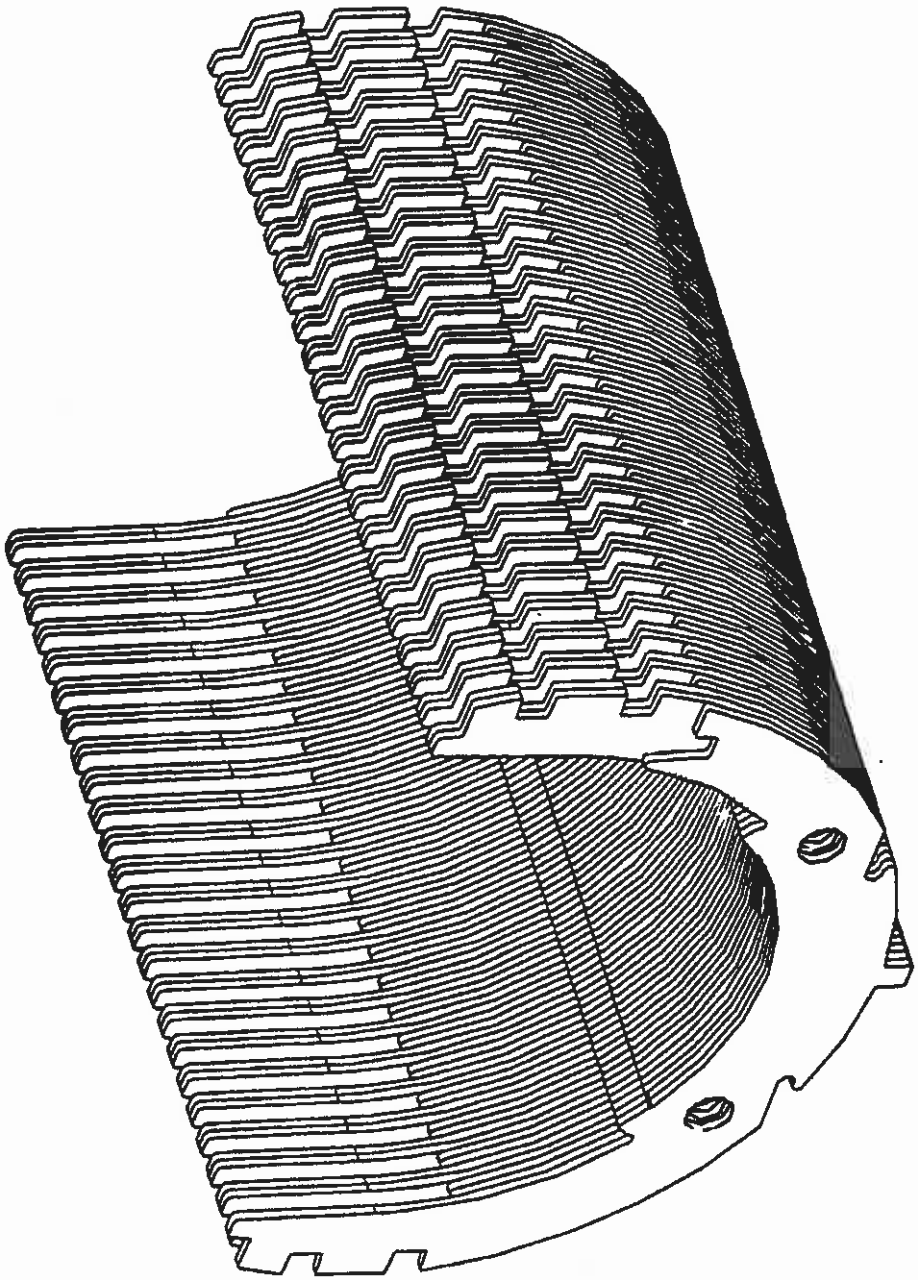

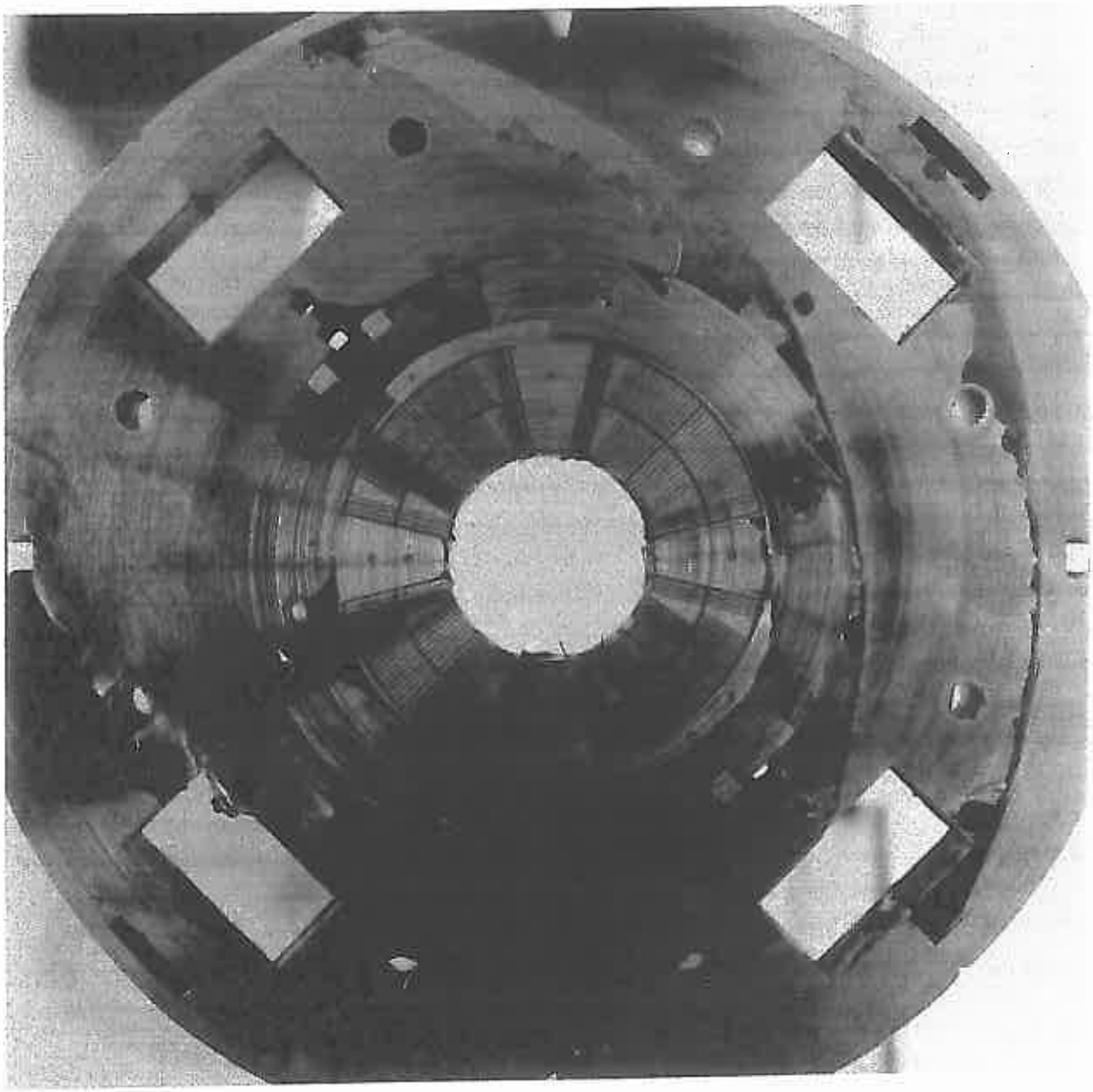

LECTURE 5: MECHANICAL DESIGN OF PARTICLE ACCELERATOR MAGNETS

5.1 Components of the Lorentz Force in Cosθ and Cos2θ Magnetic Designs

5.2 Azimuthal Pre-Compression

5.3 Coil Mechanical Properties

5.4 Collar Designs

5.5 Radial Support
5.5.1 Designs with Self-Supported Collared-Coil Assemblies
5.5.2 Designs with Fully-Mated Yoke
5.5.3 Design with Yoke Midplane Gap
5.5.4 RHIC Magnets
5.5.5 Azimuthal Pre-Compression Versus Radial Support

5.6 End Support

5.7 Other Designs

LIMITING RADIAL DEFLECTIONS

– As we have described, the radial component of the Lorentz force tends to bend the coil outwardly, with a maximum displacement at the coil assembly midplane.

– At high fields, this bending results in shear stresses between coil turns and in an ovalization of the coil assembly (along the horizontal x-axis for a dipole magnet), which generates field distortions.

– To prevent displacements or deformations, the radial deflections of the coil assembly must be limited to, typically, less than 0.05 mm.

SELF-SUPPORTED COLLARED-COIL ASSEMBLIES

– The main support against the radial component of the Lorentz force is provided by the collars.

– If the collars can be made wide and stiff enough to limit collared-coil assembly deflections within the desired range, there is no need to seek out yoke support and the mechanical structure remains fairly simple.

Examples: HERA and LHC arc quadrupole magnets.

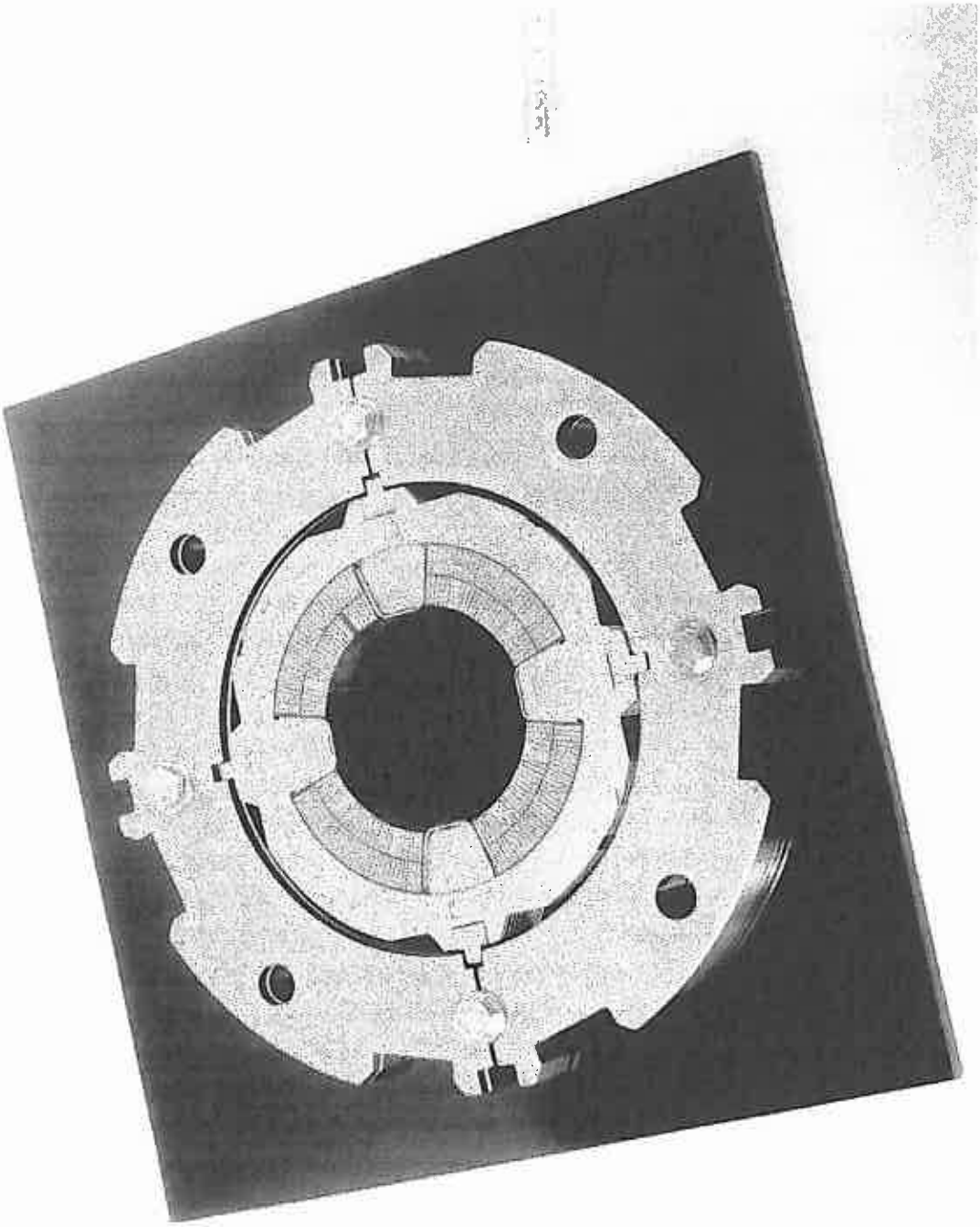

LECTURE 5: MECHANICAL DESIGN OF PARTICLE ACCELERATOR MAGNETS

5.1 Components of the Lorentz Force in Cosθ and Cos2θ Magnetic Designs

5.2 Azimuthal Pre-Compression

5.3 Coil Mechanical Properties

5.4 Collar Designs

5.5 Radial Support

5.5.1 Designs with Self-Supported Collared-Coil Assemblies

5.5.2 Designs with Fully-Mated Yoke

5.5.3 Design with Yoke Midplane Gap

5.5.4 RHIC Magnets

5.5.5 Azimuthal Pre-Compression Versus Radial Support

5.6 End Support

5.7 Other Designs

CLOSE-IRON STRUCTURES

– In the magnetic design of high field magnets, the field enhancement provided by the iron yoke is maximized by bringing it as close as possible to the coil.

– This reduces the space left for the collars, whose rigidity then becomes insufficient to hold the Lorentz force.

– In such structures, the yoke and helium containment shell must also be used as part of the coil support system.

Examples: Early 4-cm-aperture, 17-m-long SSC dipole magnet prototypes, such as DD0010, were designed with a gap between collars and yoke and had bad quench performance. The performance was greatly improved by implementing shims locking the collared-coil assembly within the yoke, as in DD0012.

40mm Dipole Cross Section
C358D Design

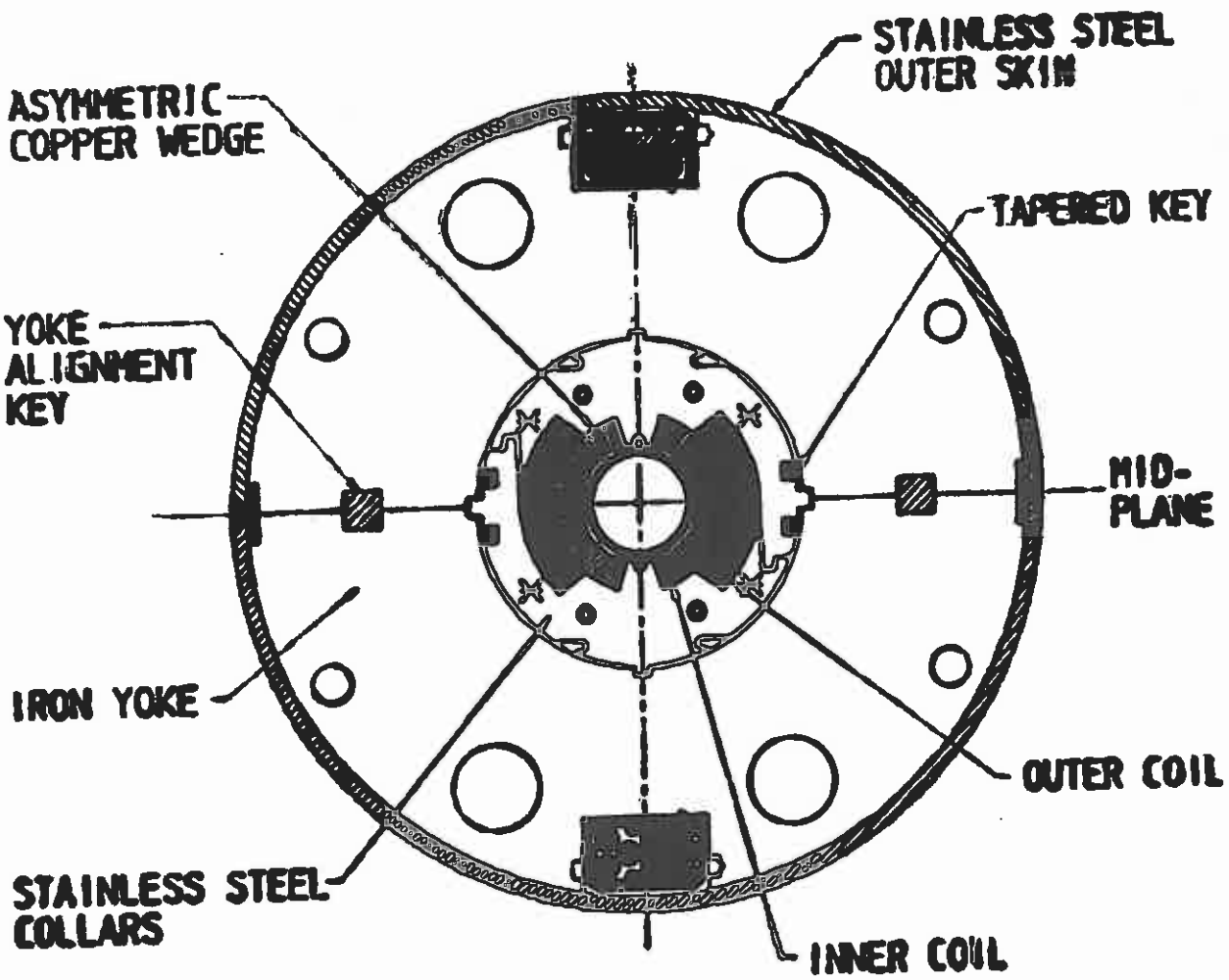

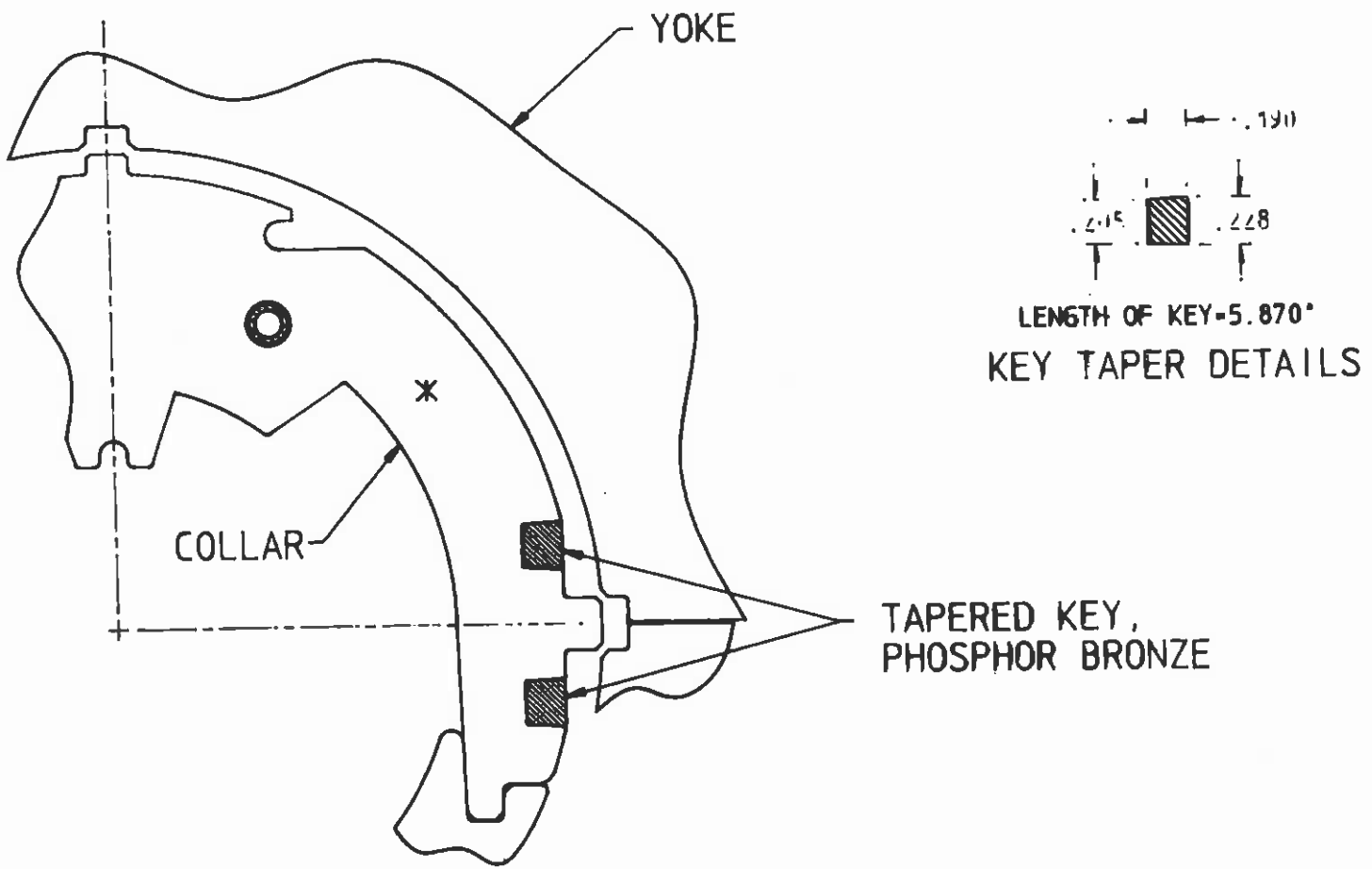

EXPLODED VIEW - COLLAR WITH TAPERED KEYS

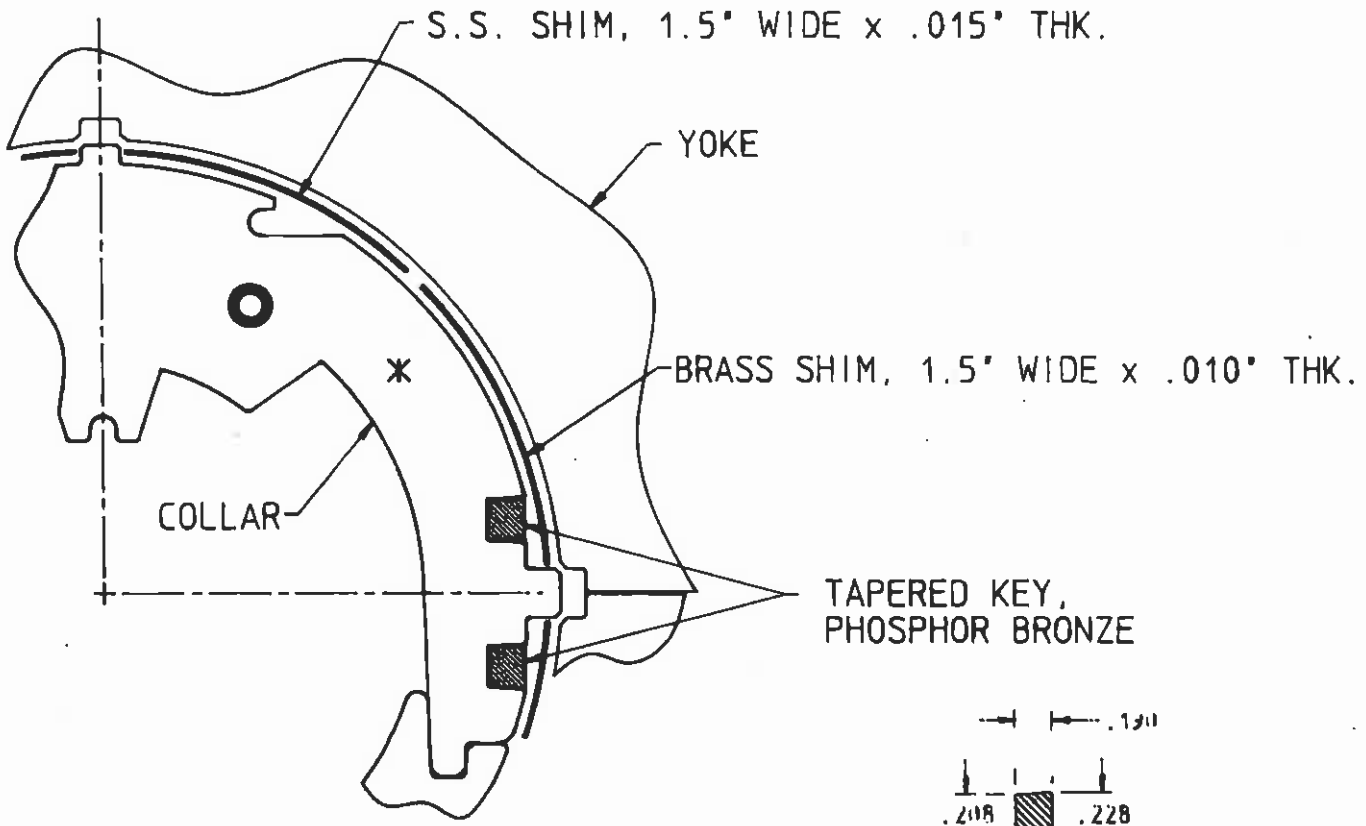

EXPLODED VIEW - COLLAR & YOKE SHIMS WITH TAPERED KEYS

INFLUENCE OF YOKE-COLLAR INTERFACE AND AXIAL SUPPORT ON QUENCH PERFORMANCE: TESTS RESULTS OF BNL 17-m LONG DIPOLES DD0010 & DD0012

a) Loose Yoke–Collar Assembly and Thin Split End Plates (DD0010)

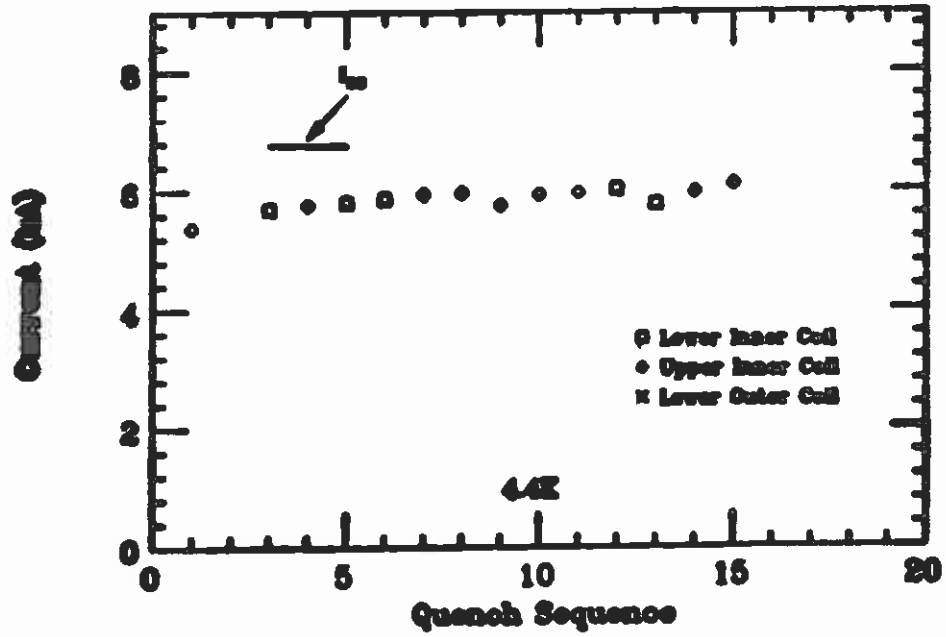

b) Tight Yoke–Collar Assembly and Thick Solid End Plates (DD0012)

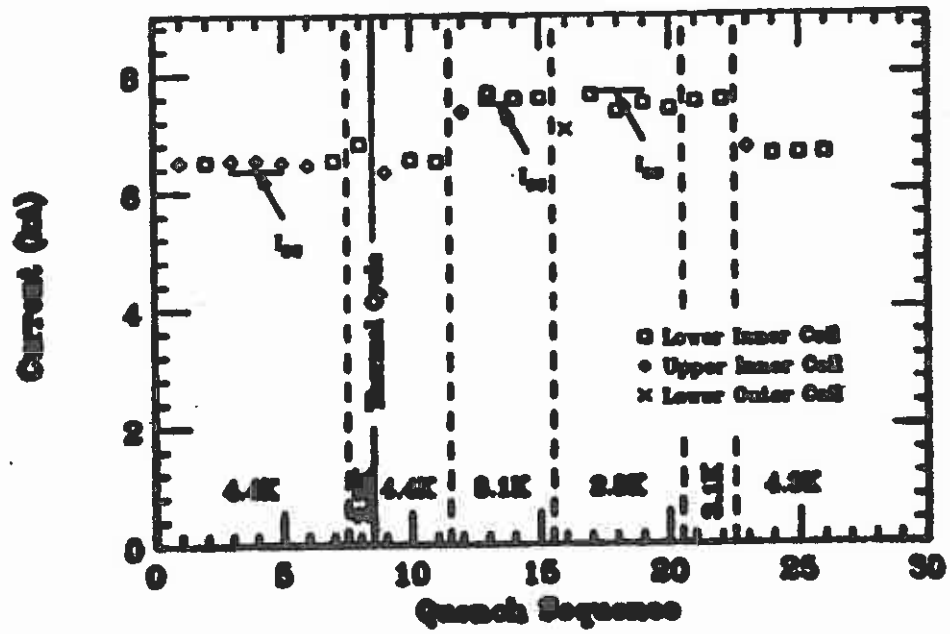

SEEKING YOKE SUPPORT

– The mechanical design of magnets where the yoke is needed to support the collared-coil assembly is complicated by the fact that the collar material (stainless steel or aluminum) shrinks more during cooldown than the low carbon steel used for the yoke.

– This thermal shrinkage differential must be compensated to ensure that, when the magnet is cold and energized, there is a proper contact between the collared-coil assembly and the yoke along the axis of maximum potential displacements.

– Such contact limits the deformations of the collared-coil assembly and allows a partial transfer (up to 50% in some LHC dipole magnet prototypes) of the radial component of the Lorentz force to the yoke and the shell.

THERMAL SHRINKAGE DIFFERENTIAL BETWEEN COLLARS AND YOKE

– The thermal shrinkage differential, Δr, between collar and yoke can be estimated as

$$\Delta r = R_{collar} (\alpha_{collar} - \alpha_{yoke})$$

where R_{collar} is the collar outer radius and α_{yoke} is the thermal expansion coefficient of the yoke, integrated between room and operating temperatures.

– To limit contact loss due to thermal shrinkage differential it is preferable to use for the collars a material whose integrated thermal expansion coefficient approaches that of low carbon steel. This suggests the use of austenitic stainless steel.

– However, and as described in the section on choice of collar material, it is also desirable to limit the cooldown loss of coil pre-compression, which favors the use of aluminum alloy.

Thermal Shrinkage (I)

50mm SSC MAGNET

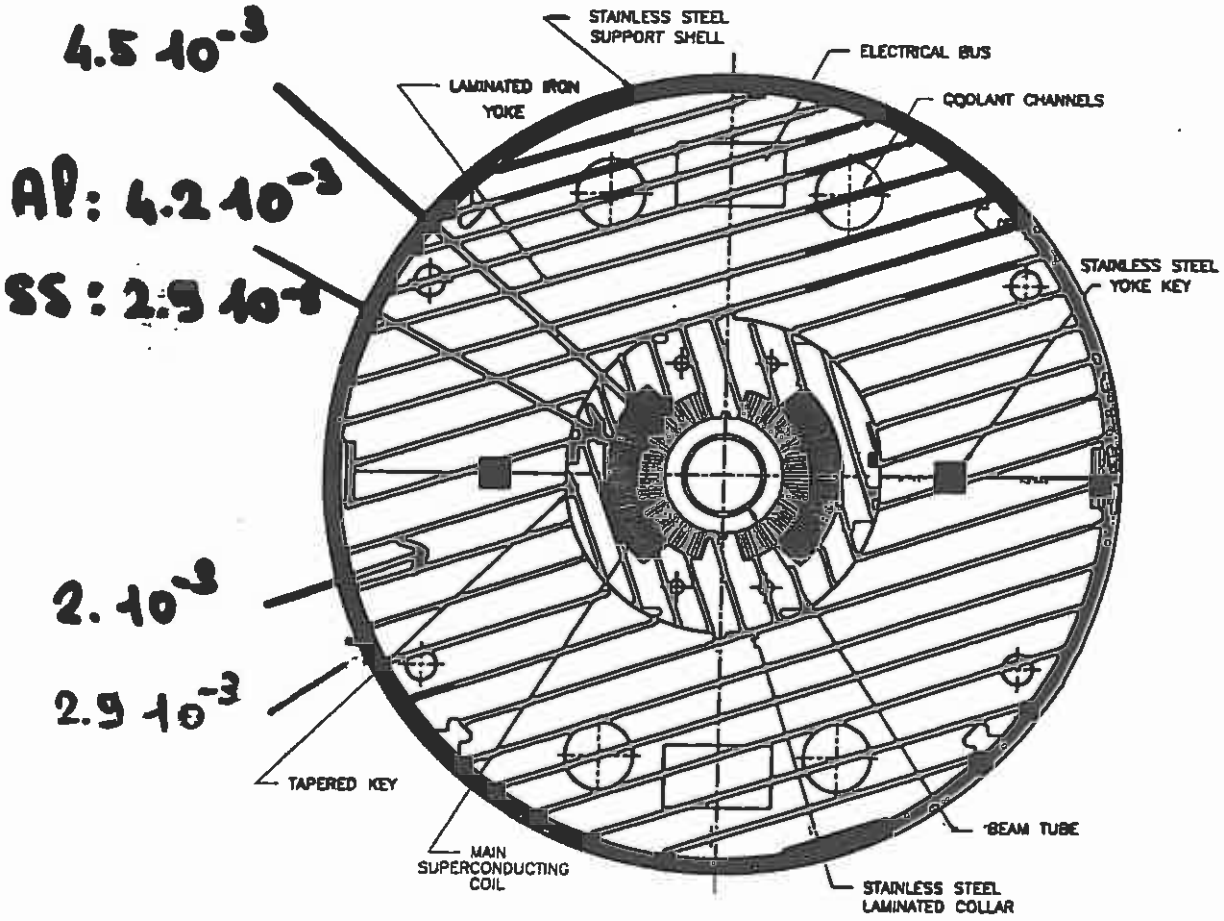

MECHANICAL DESIGN WITH FULLY-MATED YOKE ASSEMBLY

– To facilitate assembly, the yoke of dipole magnets is usually split into two halves which are mounted around the collared-coil assembly.

– The shell, which is also made up of two halves, is then placed around the yoke and welded.

– If the thermal shrinkage differential between collars and yoke is not too large (as in the case of stainless steel collars), it can be compensated for by introducing a shrinkage allowance into the geometry of either the collars or the yoke, and by welding the shell so as to exert a compressive load onto the two yoke halves which force them to mate at room temperature.

– During cooldown, the collared-coil assembly shrinks away from the two yoke halves which remain fully mated. This results in a decrease of the compressive load exerted by the yoke, but, as long as suitable contacts are maintained over selected areas, can still ensure a locking of the collared-coil assembly.

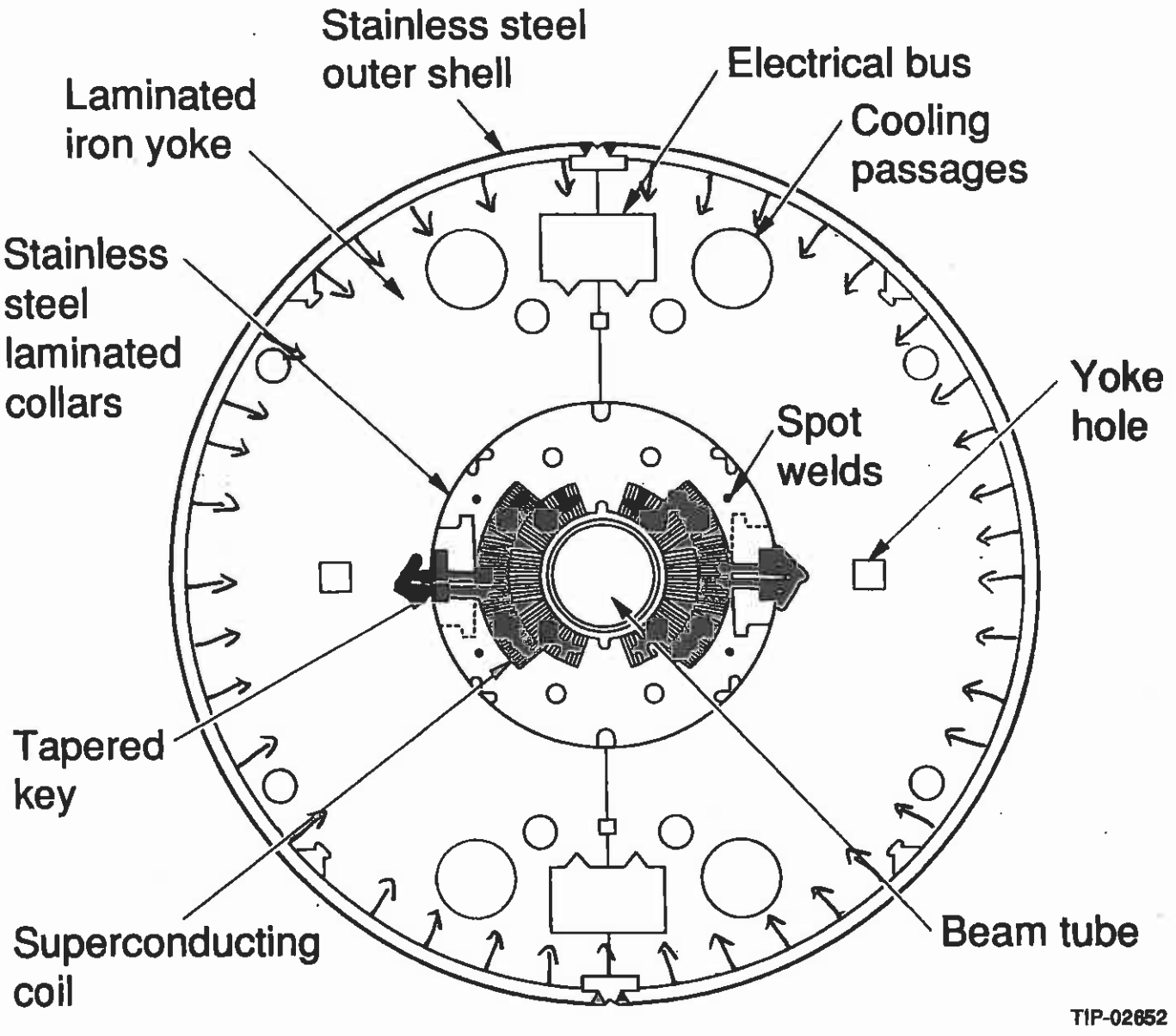
Stainless steel
outer shell
Electrical bus
Laminated
iron yoke
Cooling
passages
Stainless
steel
laminated
collars
Yoke
hole
Spot
welds
Tapered
key
Superconducting
coil
Beam tube
TIP-02652

YOKE SPLIT ORIENTATION

– In practice, the compressive load provided by the yoke is directed along a given axis. The choice of the axis drives the choice of yoke split orientation.

– Note, however, that the pre-compressed coils exert a large pressure against the collar poles. This internal pressure causes a large outward deflection of the collared-coil assembly along the vertical diameter and a slight inward deflection along the horizontal diameter. These deflections must be taken into account when working out yoke design.

Examples:

• The SSC dipole magnet prototypes built at FNAL use (keyed) stainless steel collars and a ***vertically-split yoke*** with a yoke/collar compressive load directed along the horizontal x-axis.

• The SSC dipole magnet prototypes built at BNL use (keyed) stainless steel collars and a ***horizontally-split yoke*** with a yoke/collar compressive load directed along the vertical y-axis.

Both types of magnets performed very well.

BNL

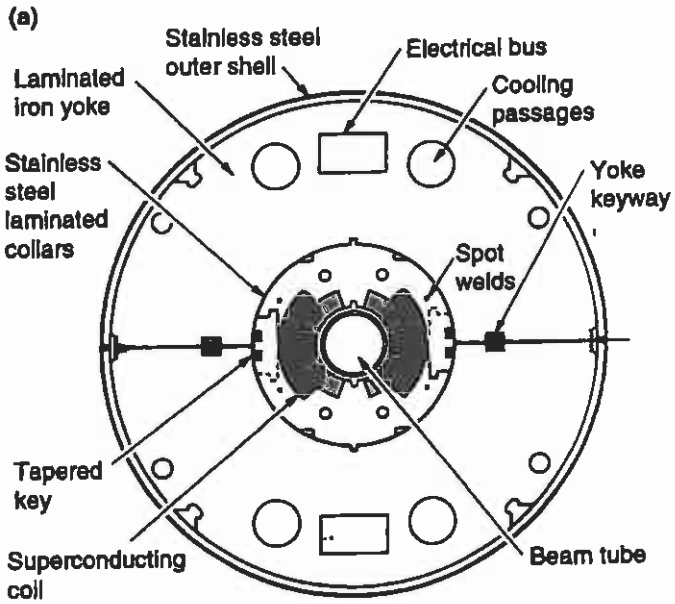
(a)
Stainless steel outer shell
Electrical bus
Laminated iron yoke
Cooling passages
Stainless steel laminated collars
Yoke keyway
Spot welds
Tapered key
Superconducting coil
Beam tube

FNAL

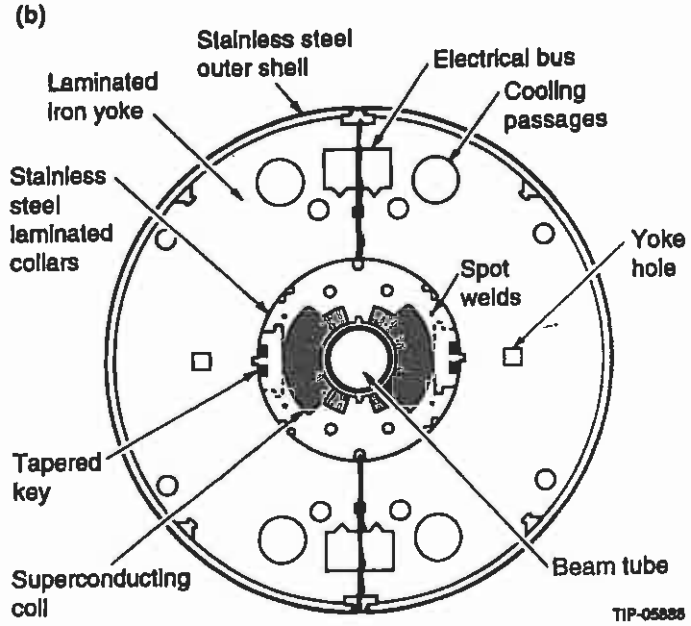
(b)
Stainless steel outer shell
Electrical bus
Laminated iron yoke
Cooling passages
Stainless steel laminated collars
Yoke hole
Spot welds
Tapered key
Superconducting coil
Beam tube
TIP-05888

SSC/FNAL VERTICALLY-SPLIT YOKE DESIGN

– Collars and yoke are designed so that the vertical outer diameter of the keyed collars (with no coils in them) is about 900 μm smaller than the yoke inner radius, while the horizontal diameter is about 300 μm larger.

– The clearance along the horizontal diameter is introduced to allow yoke assembly and compensate for the vertical deflections of the collared-coil assembly resulting from the forces exerted by the pre-compressed coils against the collar poles.

– The shrinkage allowance along the horizontal diameter is introduced to compensate for the thermal shrinkage differential between collars and yoke and ensure that there is always contact between the two where the effects of the radial component of the Lorentz force are the largest.

– The existence of a built-in shrinkage allowance between collars and yoke requires the use of press during the welding of the outer shell. The press is used to close the gap between the two yoke halves at room temperature and ensure that the yoke halves are mated with a force at least equal to the fraction of the horizontal component of the Lorentz force that is transmitted to the yoke during excitation.

Collar Deflections
(after collaring)

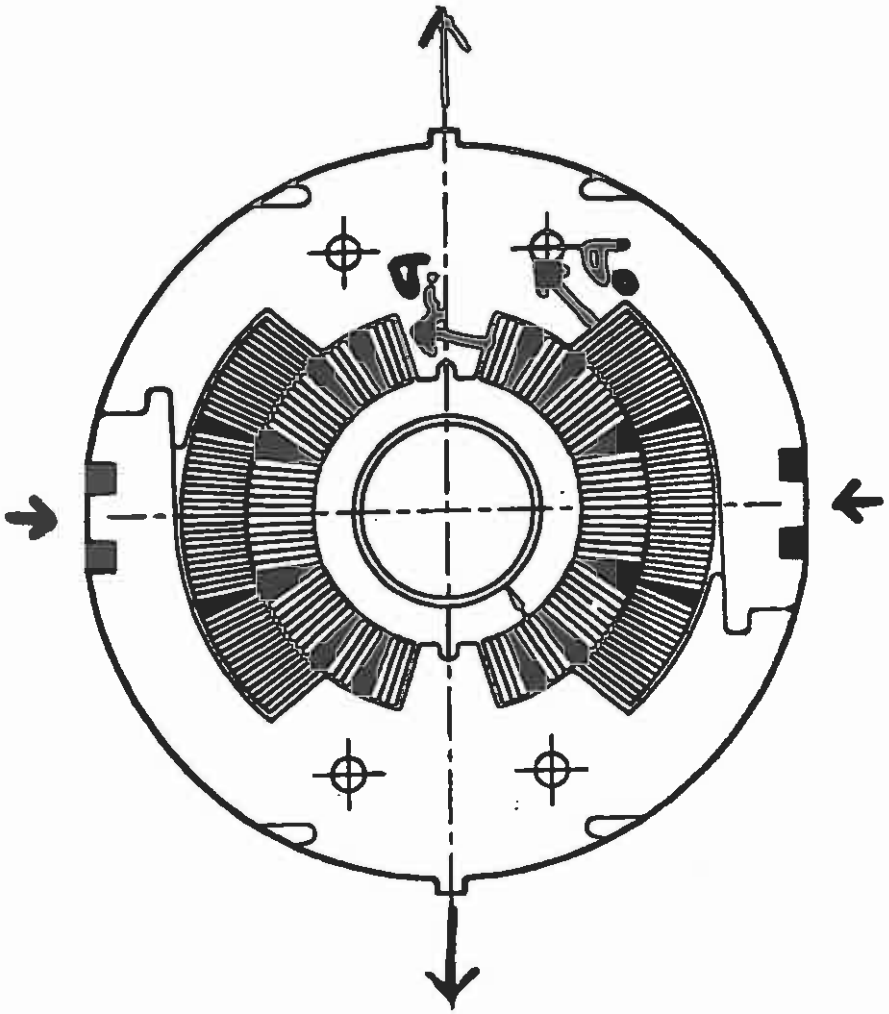

FNAL Vertically-Split Yoke Design

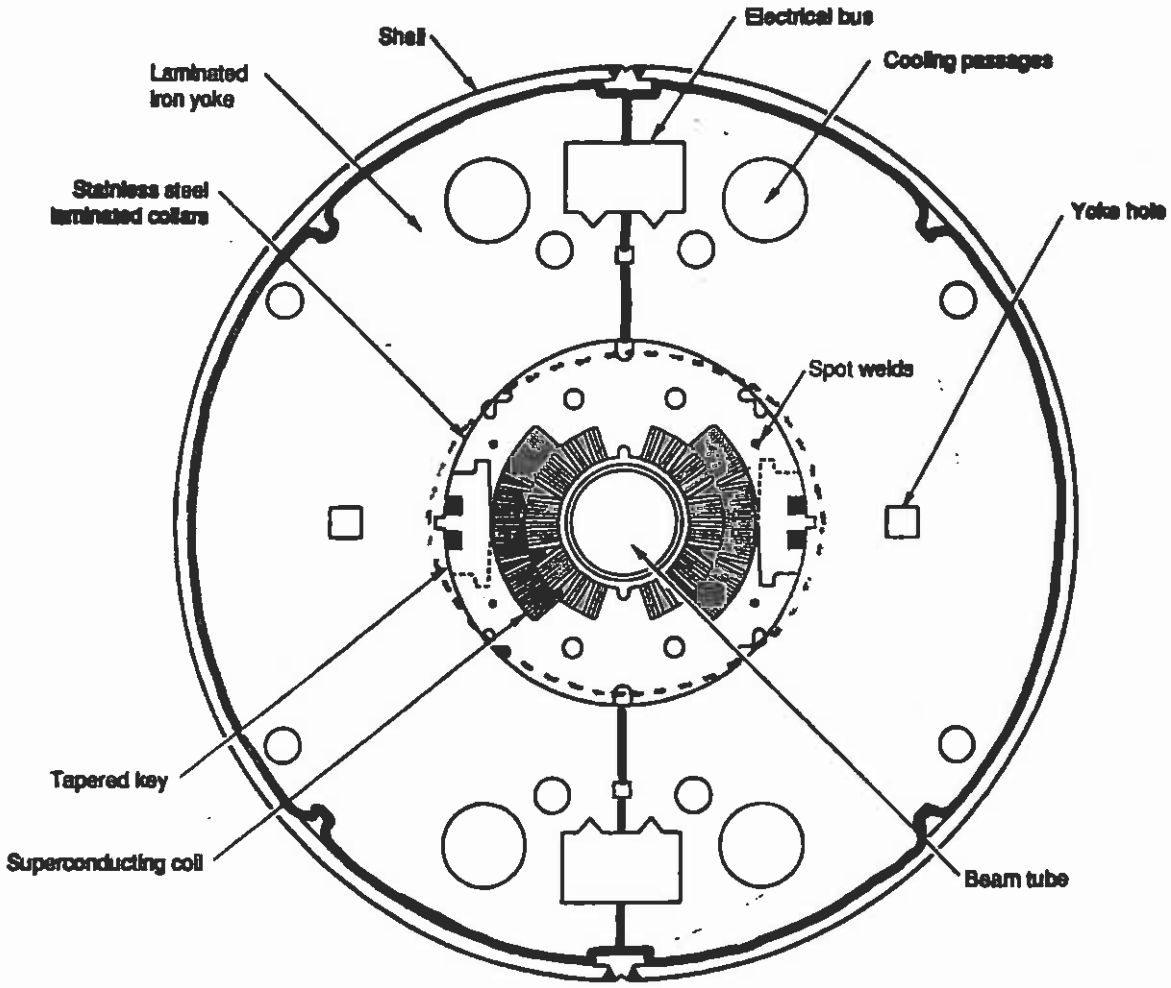

"Builtin"
Horizontal Interference
~300/350 μm on ϕ at Room Temp.

SSC/FNAL VERTICALLY-SPLIT YOKE DESIGN DURING EXCITATION

– During excitation, the yoke provides a quasi-infinitely stiff support against the radial component of the Lorentz force, and the collars do not bend.

– The unloading of the collar pole thus only results from the compression of the coil under the azimuthal component of the Lorentz force.

Lorentz Force Distribution in FNAL 2-D X-section

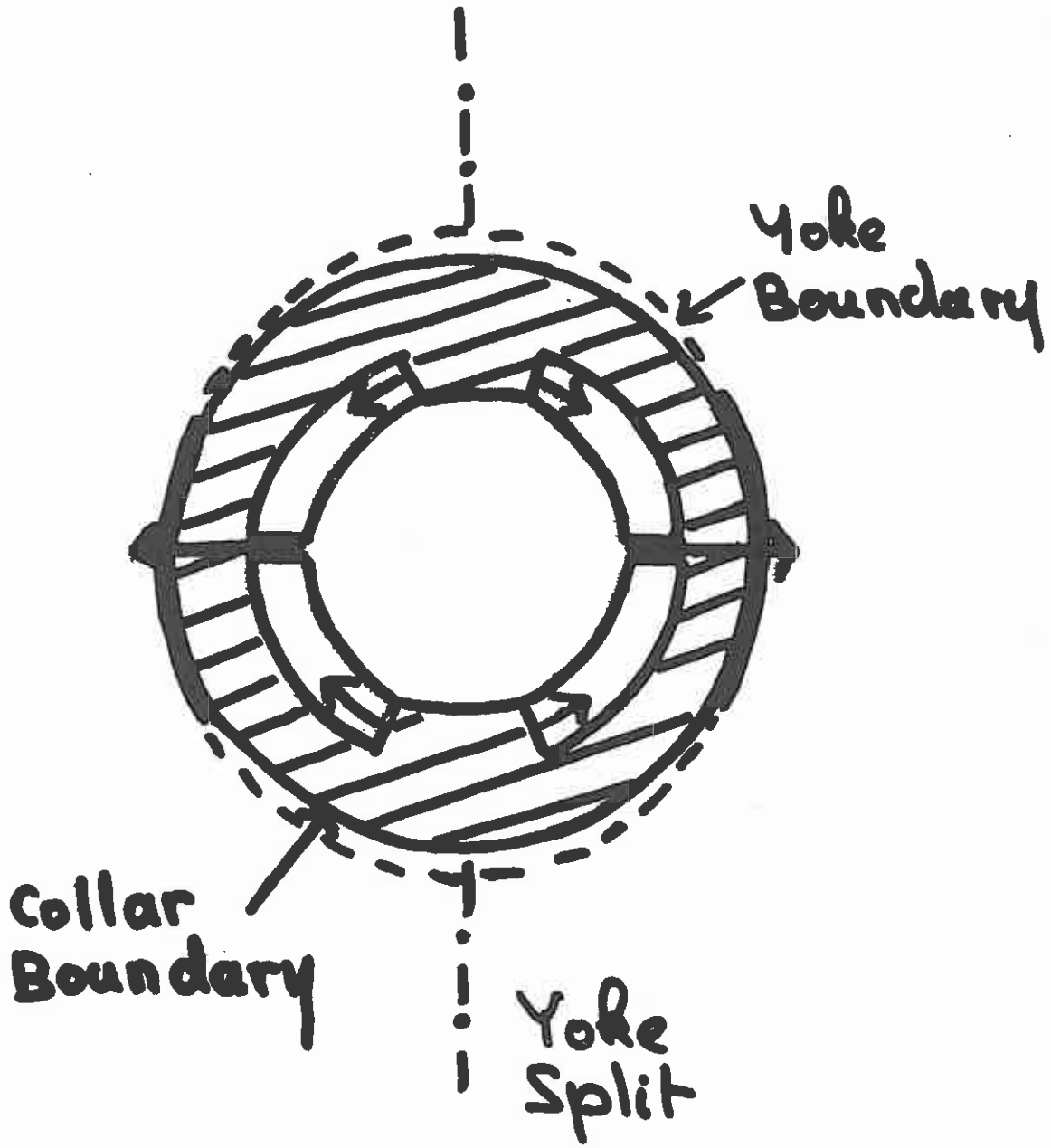

FNAL Magnets

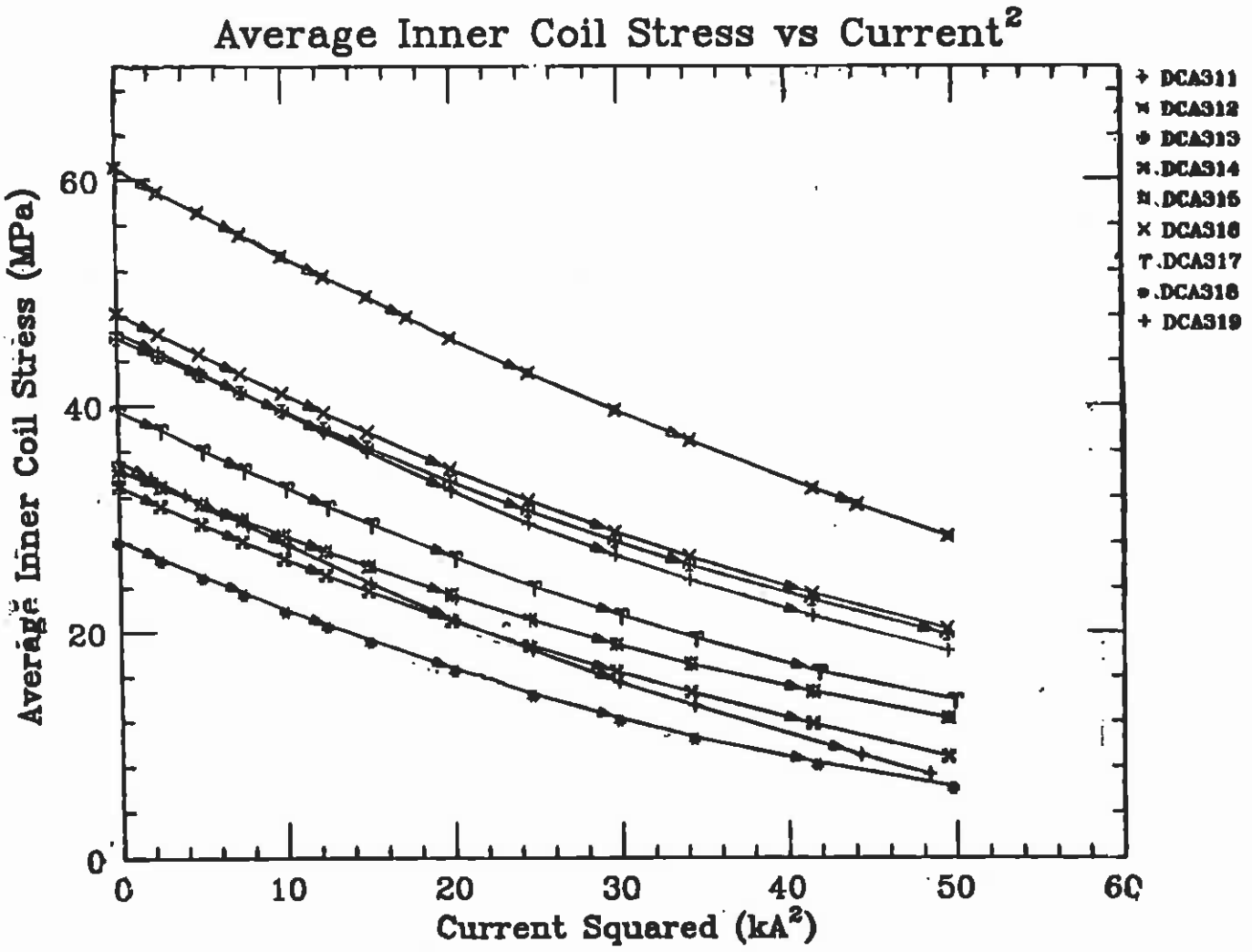

FNAL Magnets

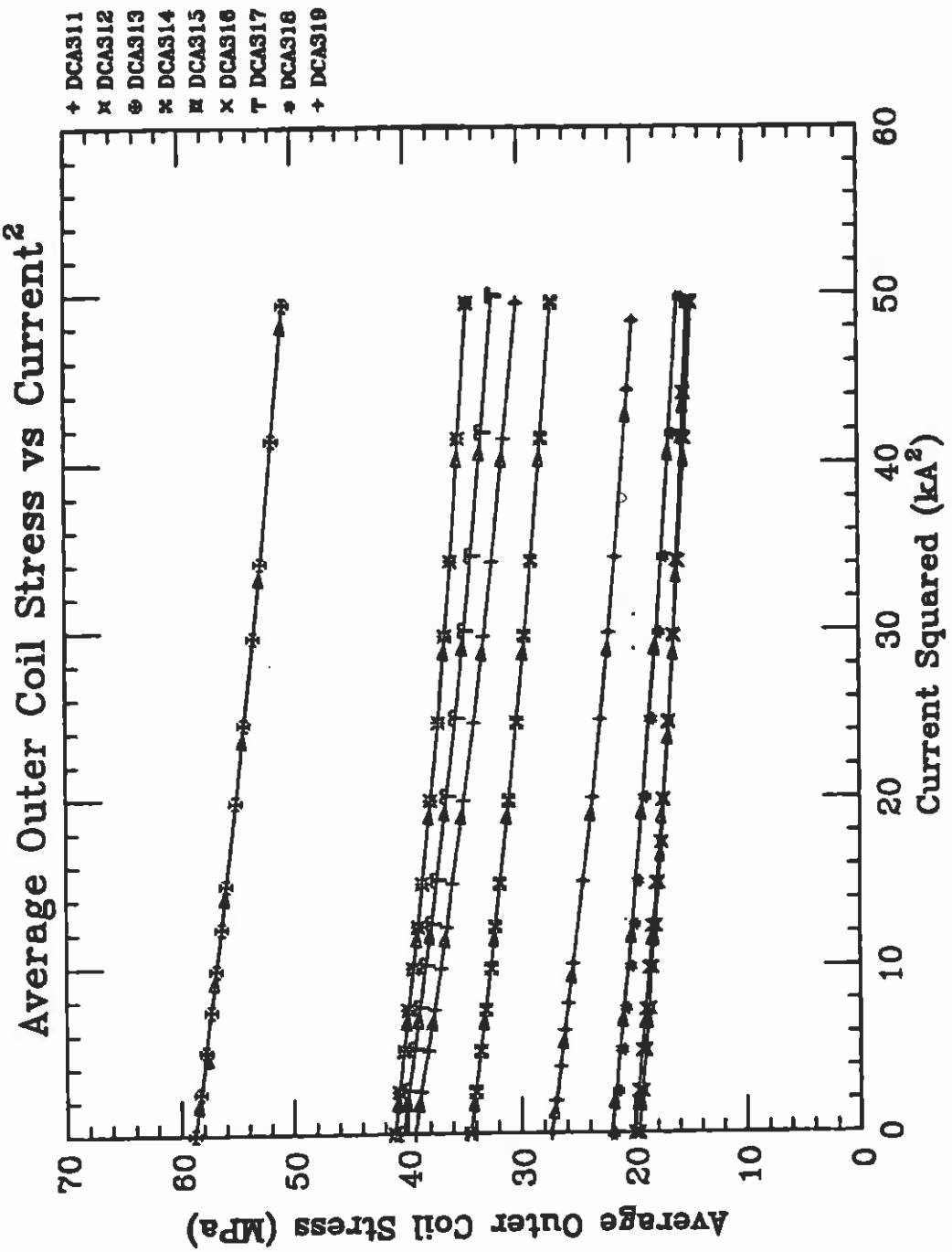

SSC/FNAL 5-cm-Apert., 15-m-long Dipole Magnets

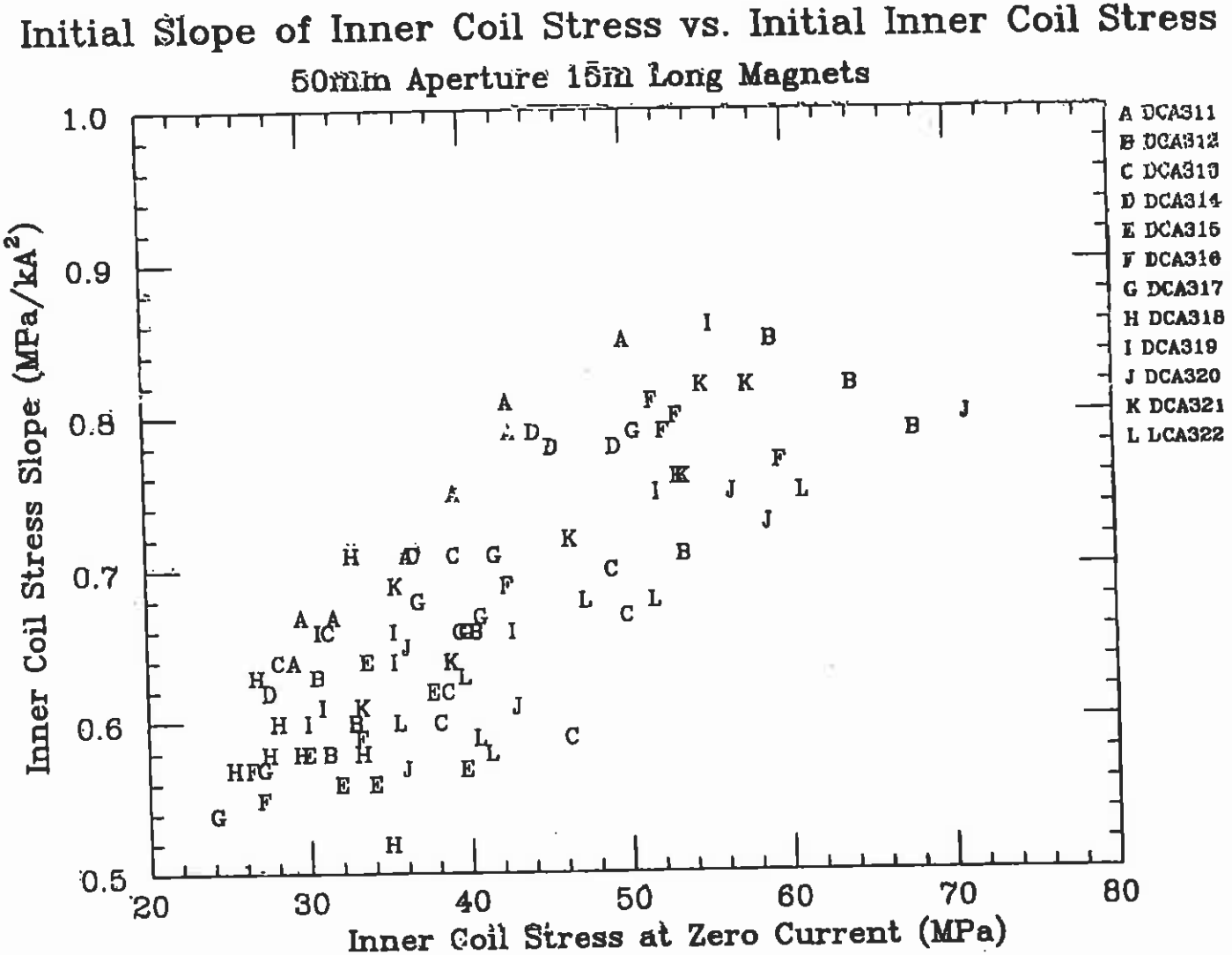

SSC / FNAL

Quench Performance of Full Length 50mm Aperture SSC Dipoles

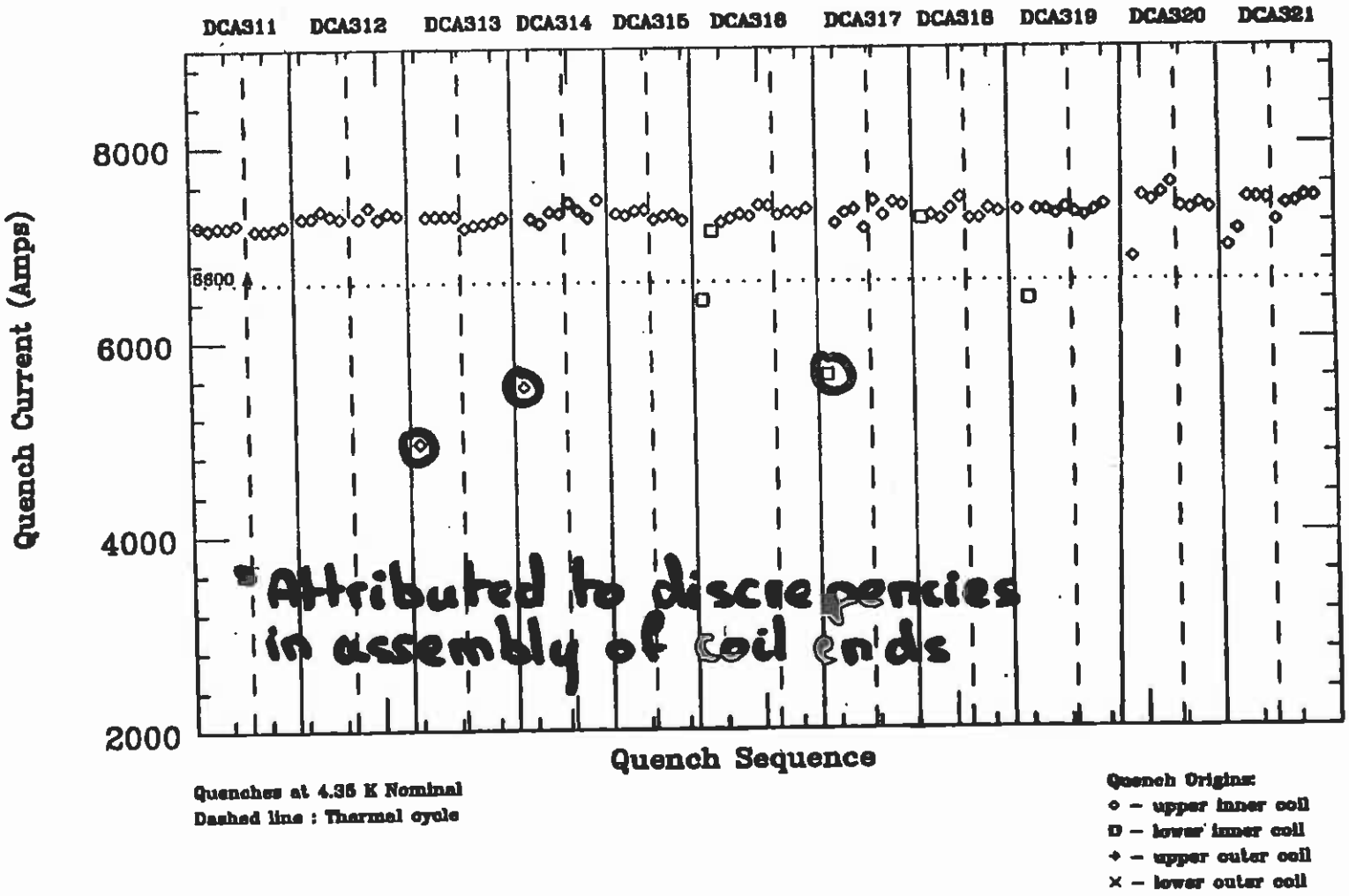

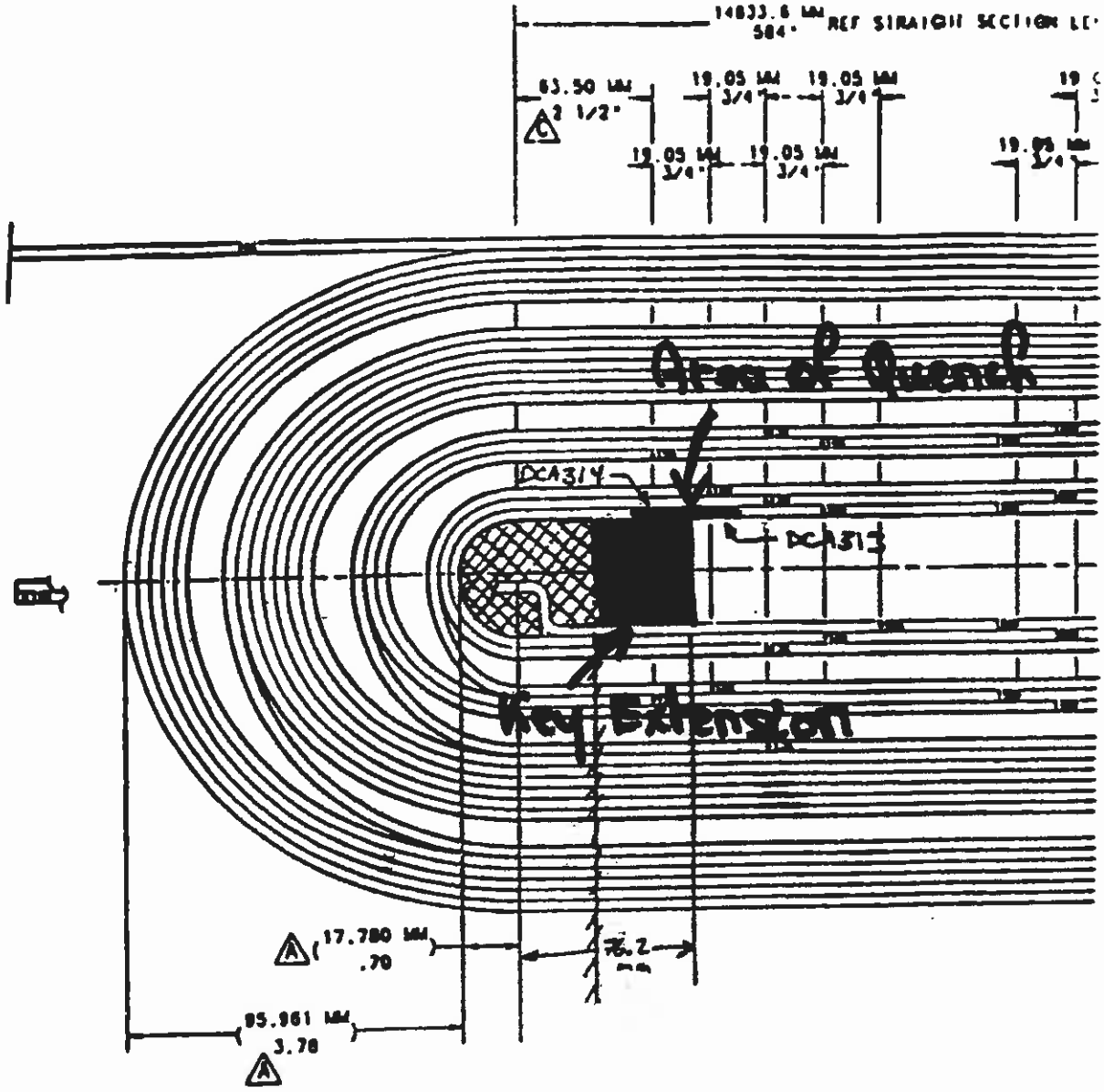

(Courtesy J. Strait)

SSC/BNL HORIZONTHALLY-SPLIT YOKE DESIGN

– Collars and yoke are designed so that the vertical outer diameter of the keyed collars (with no coils in them) is about 100 μm smaller than the yoke inner radius, while the horizontal diameters are the same.

– As we have explained, after collaring, the forces exterted by the compressed-coils against the collar poles result in a large outward deflection of the collared-coil assembly along the vertical diameter and a small inward deflection along the horizontal diameter.

– The slight inward deflection allows to assemble the horizontally-split yoke around the collared coil, but the large outward deflection along the vertical diameter can result in a gap between the two yoke halves.

– During welding, the shell is put into tension and compresses the two yoke halves, which, in turn, compresses the collared-coil assembly along the vertical diameter. This results in a progressive closure of the yoke midplane gap.

– At the end of shell welding, the yoke midplane gap is closed and there is a line-to-line fit between outer circumference of the collared-coil assembly and the inner circumference of the yoke.

BNL Horizontally-Split Yoke Design

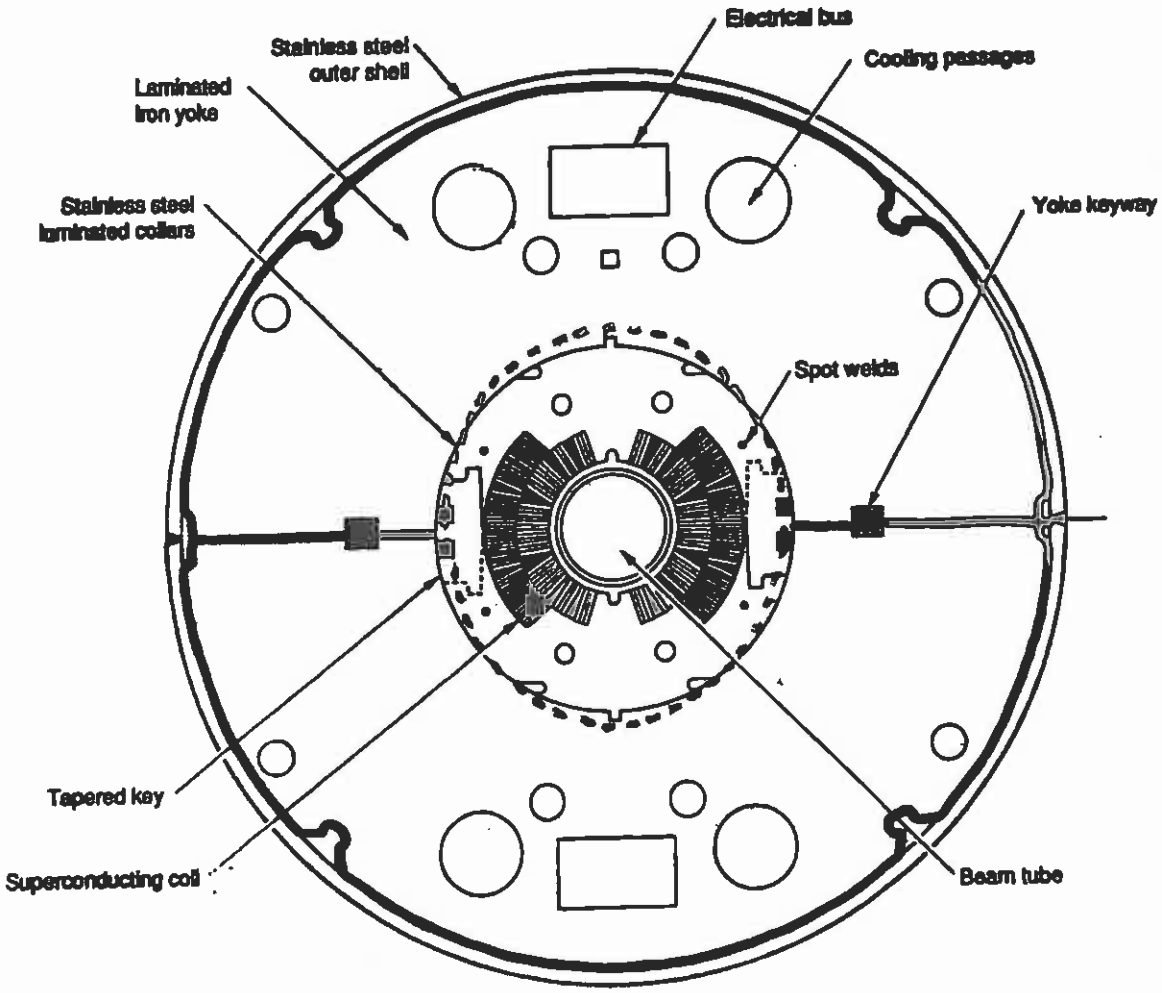

Vertical Interference
~ +10 μm on ϕ at Room Temp.
Resulting from Collaring Spring-Back

SSC/BNL HORIZONTHALLY-SPLIT YOKE DESIGN DURING COOLDOWN

– During cooldown, the coil shrinks more than the stainless steel collars, which, in turn, shrinks more than the low carbon steel yoke.

– The pressure exerted by the coil against the collar poles decreases, but remains large enough to keep deflecting the collars, thereby maintaining contact with the yoke along the vertical diameter.

– Along the horizontal diameter, however, the thermal shrinkage differentials result in a small gap between the collared-coil assembly and the yoke.

SSC/BNL HORIZONTHALLY-SPLIT YOKE DESIGN DURING EXCITATION

– During excitation, the azimuthal component of the Lorentz force causes a redistribution of the coil stress, resulting in a decrease of the pressure exerted by the coil against the collar poles.

– At the same time, the radial component of the Lorentz force causes a bending of the collars, with a maximum displacement along the horizontal diameter, at the location of the gap between the collared-coil assembly and the yoke.

– As the current increases, the bending moment increases, and the collars keep deflecting along the horizontal diameter, until they come into contact with the yoke.

– At high currents, the collared-coil assembly touches the yoke on a large perimeter on both sides of the horizontal plane, and the yoke provides an extremely stiff support against the radial component of the Lorentz force.

Lorentz Force Distribution in BNL 2-D X-section

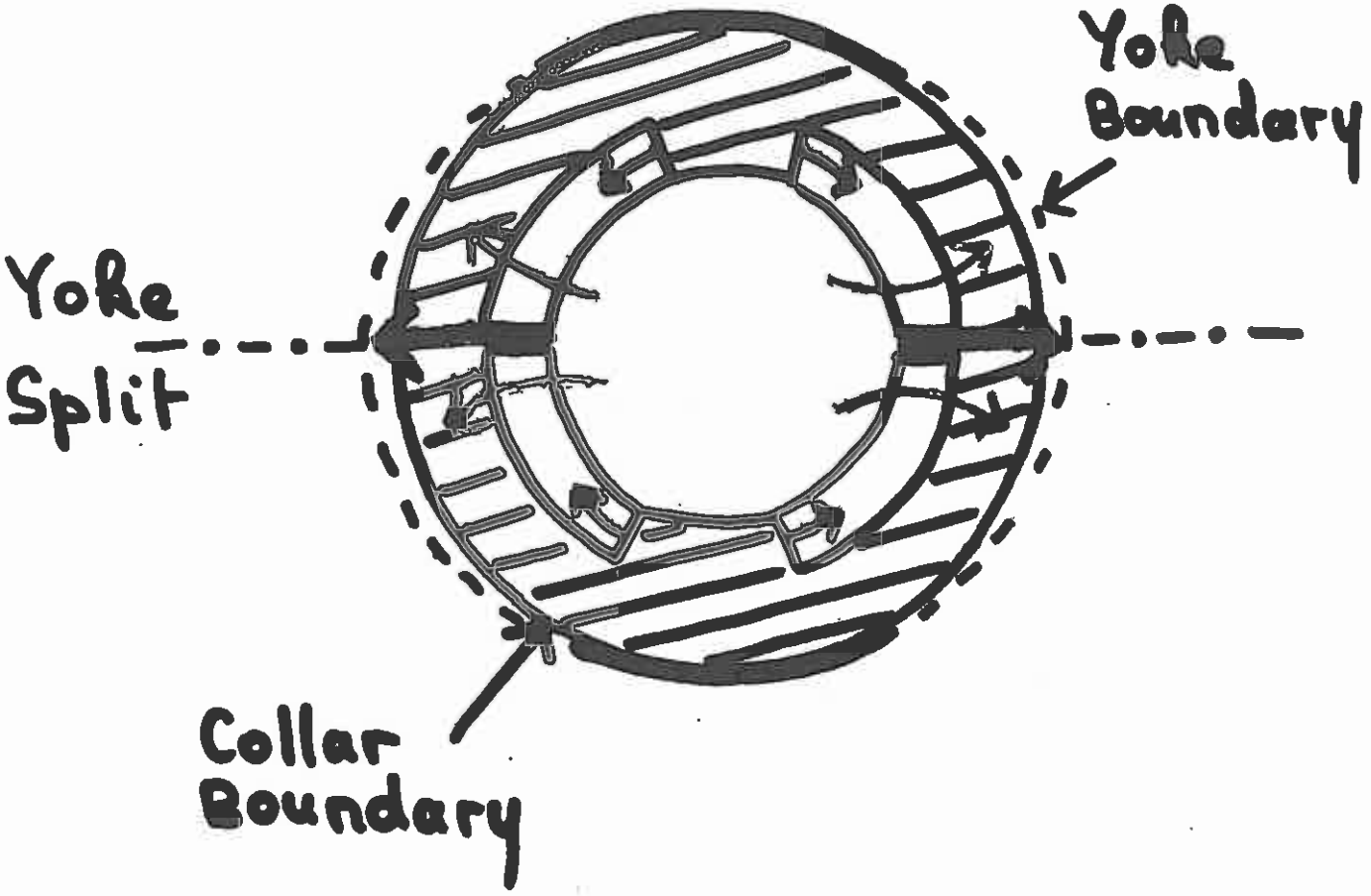

SSC/BNL HORIZONTHALLY-SPLIT YOKE DESIGN DURING EXCITATION (CONT.)

– As long as the collars are not in contact with yoke, the unloading of the coil from the collar pole results from two causes:

- The compression of the coil under the *azimuthal component of the Lorentz force,*

- The bending of the coil under *the radial component of the Lorentz force.*

– However, once the collars are in contact with the yoke, the unloading of the collar pole only results from the azimuthal component of the Lorentz force, and the BNL magnets should behave similarly to the FNAL magnets.

– After the fast initial unloading, we are thus expecting the pressure plots of the BNL magnets to exhibit a change in slope, and to become parallel to that of the FNAL magnets.

BNL Magnets

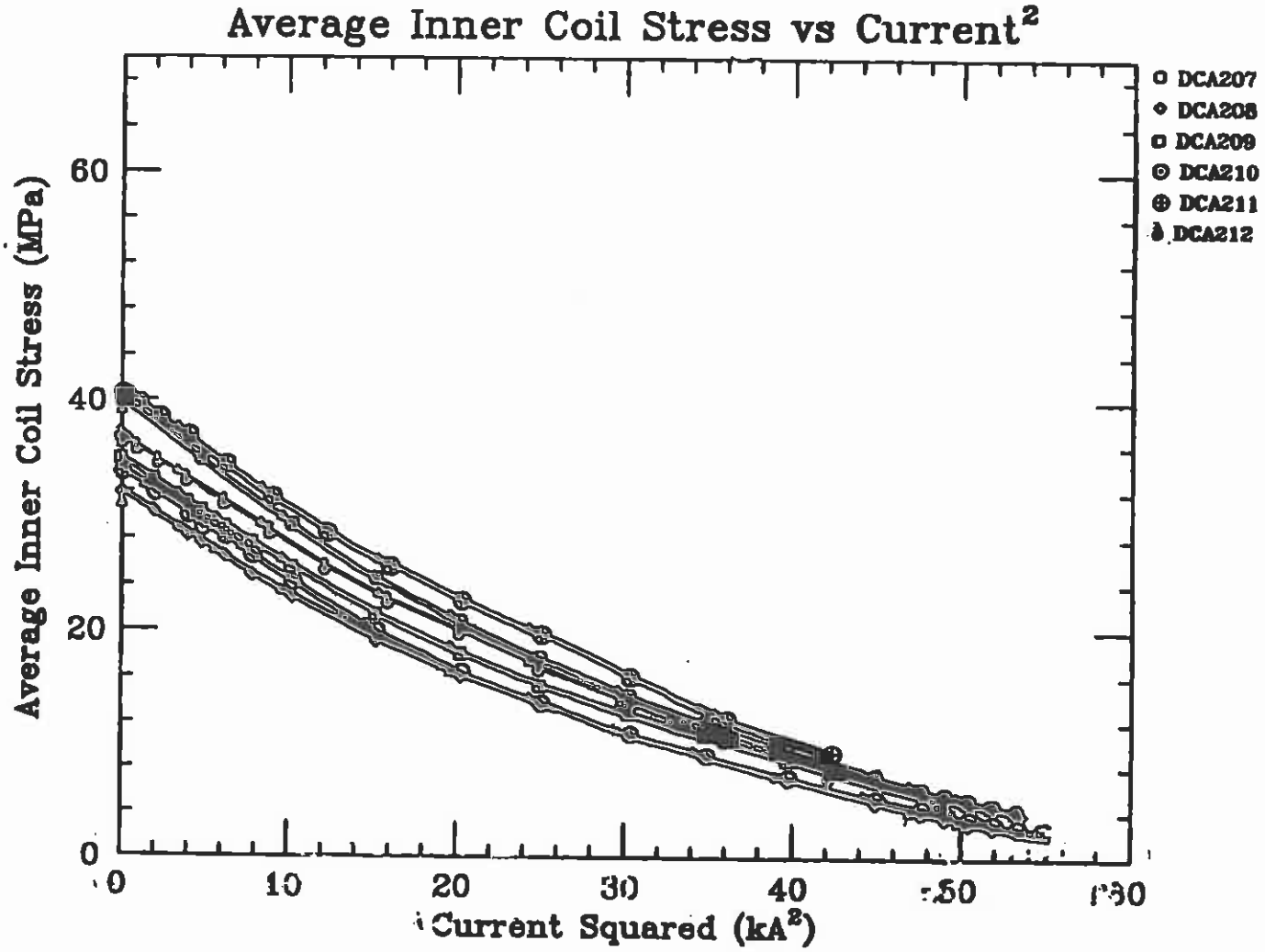
Average Inner Coil Stress vs Current²
Average Inner Coil Stress (MPa)
0
20
40
60
0
10
20
30
40
50
60
Current Squared (kA²)
DCA207
DCA208
DCA209
DCA210
DCA211
DCA212

BNL Magnets

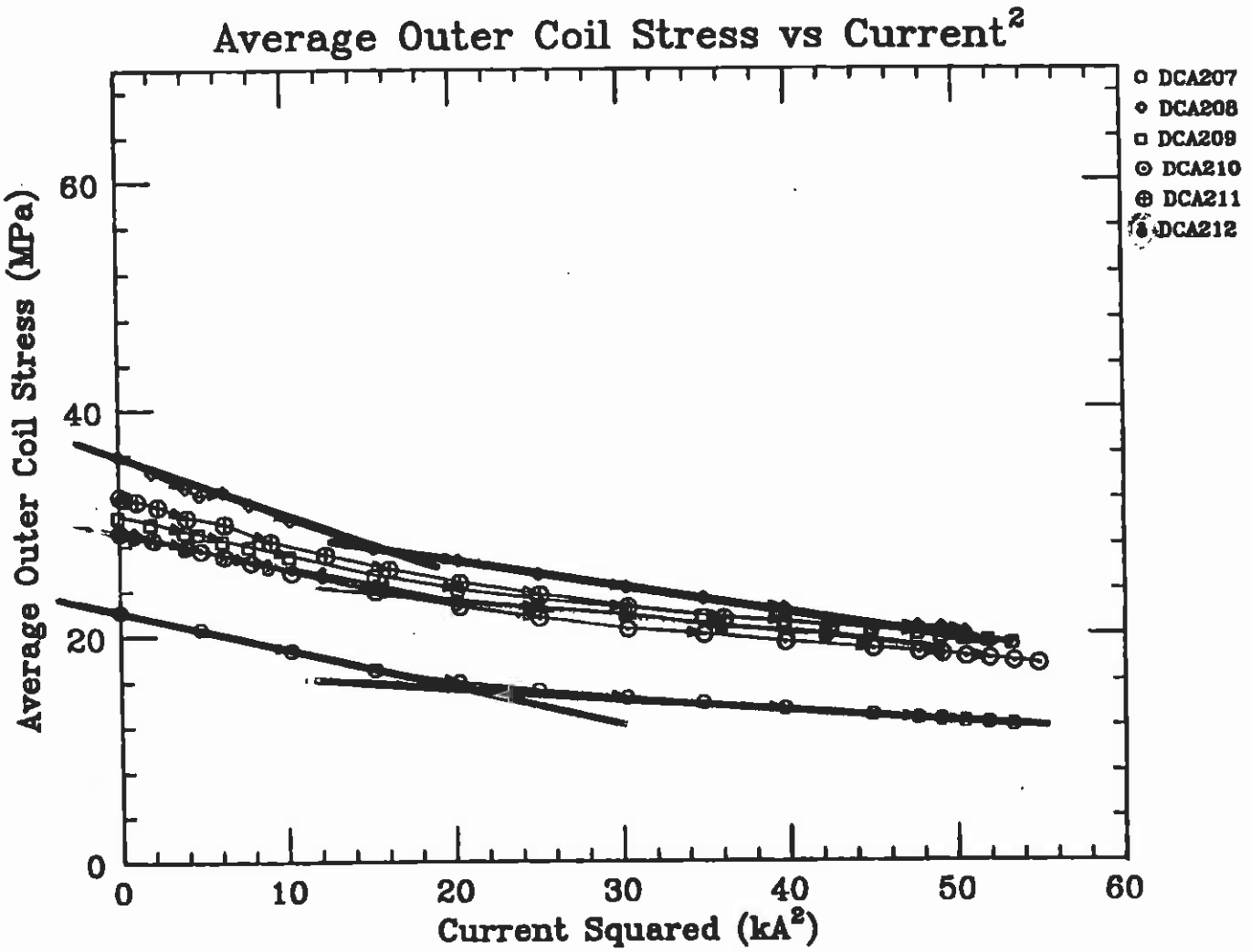
Average Outer Coil Stress vs Current²
Average Outer Coil Stress (MPa)
Current Squared (kA²)
0
20
40
60
0
10
20
30
40
50
60
DCA207
DCA208
DCA209
DCA210
DCA211
DCA212

SSC 5-cm-Apert., 15-m-long Dipole Magnets

Coil Pressure Unloading Rate vs. Coil Pressure at Zero Current

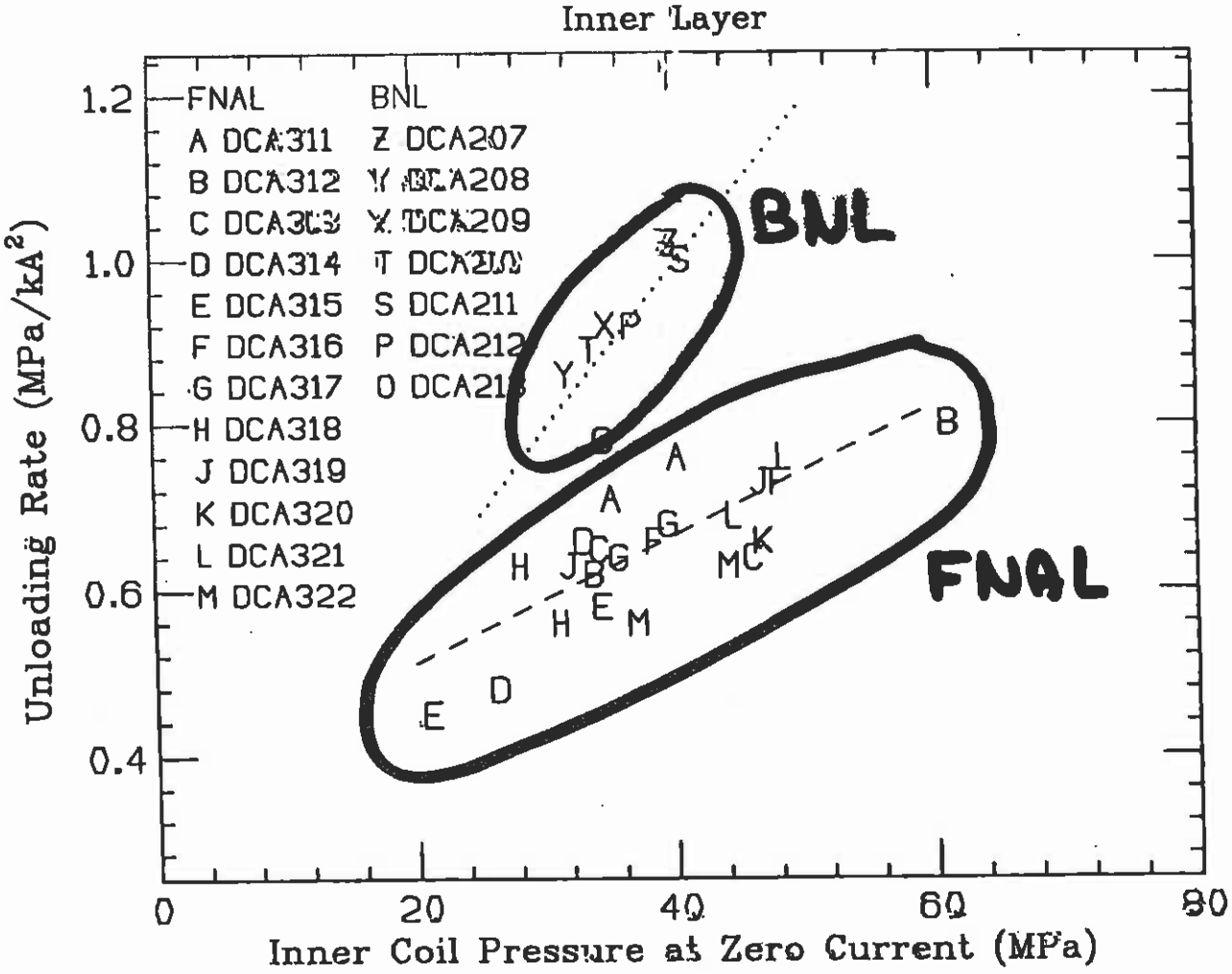

SSC 5-cm-Apert., 15-m-long Dipole Magnets

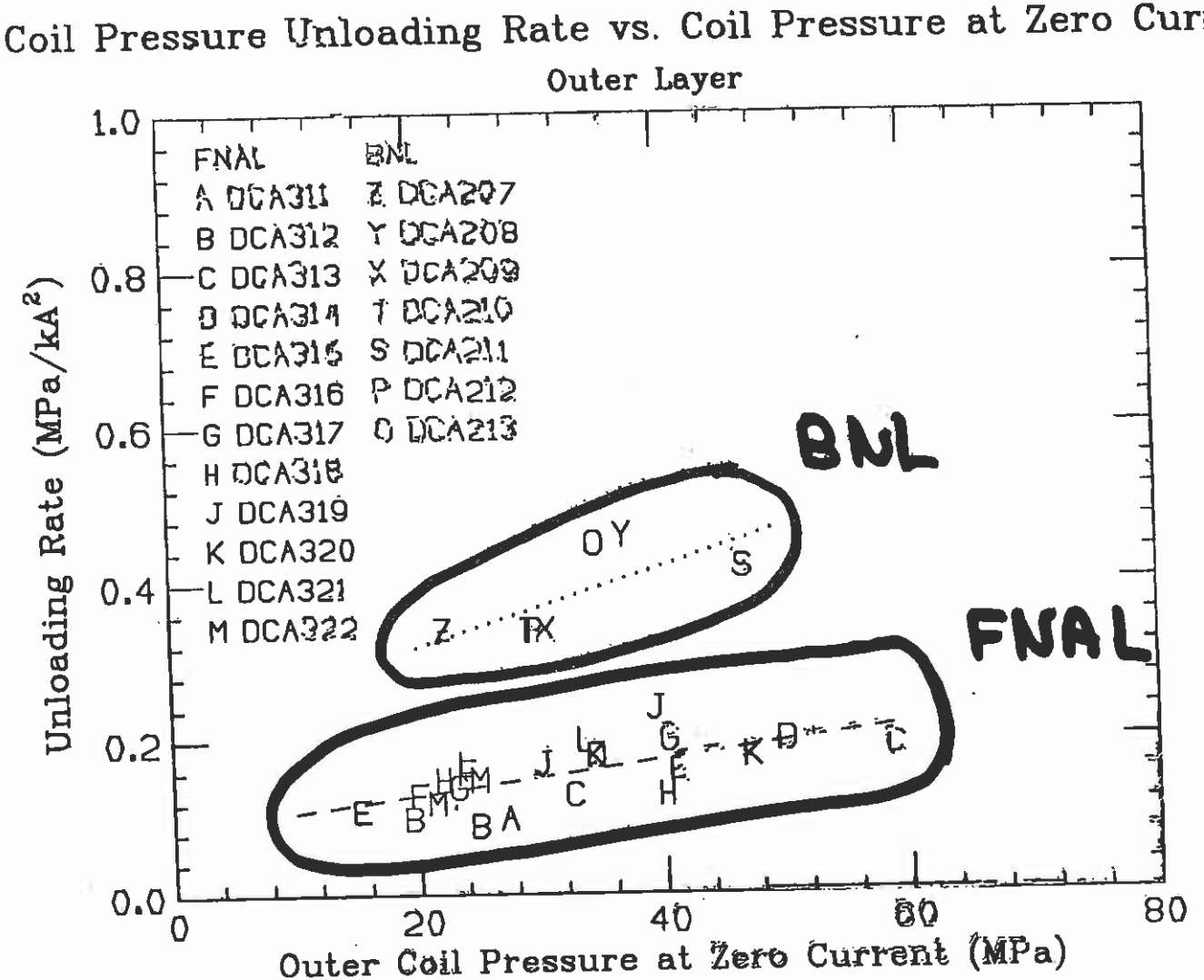

SSC/BNL

Quench Performance of Full Length 50mm Aperture SSC Dipoles

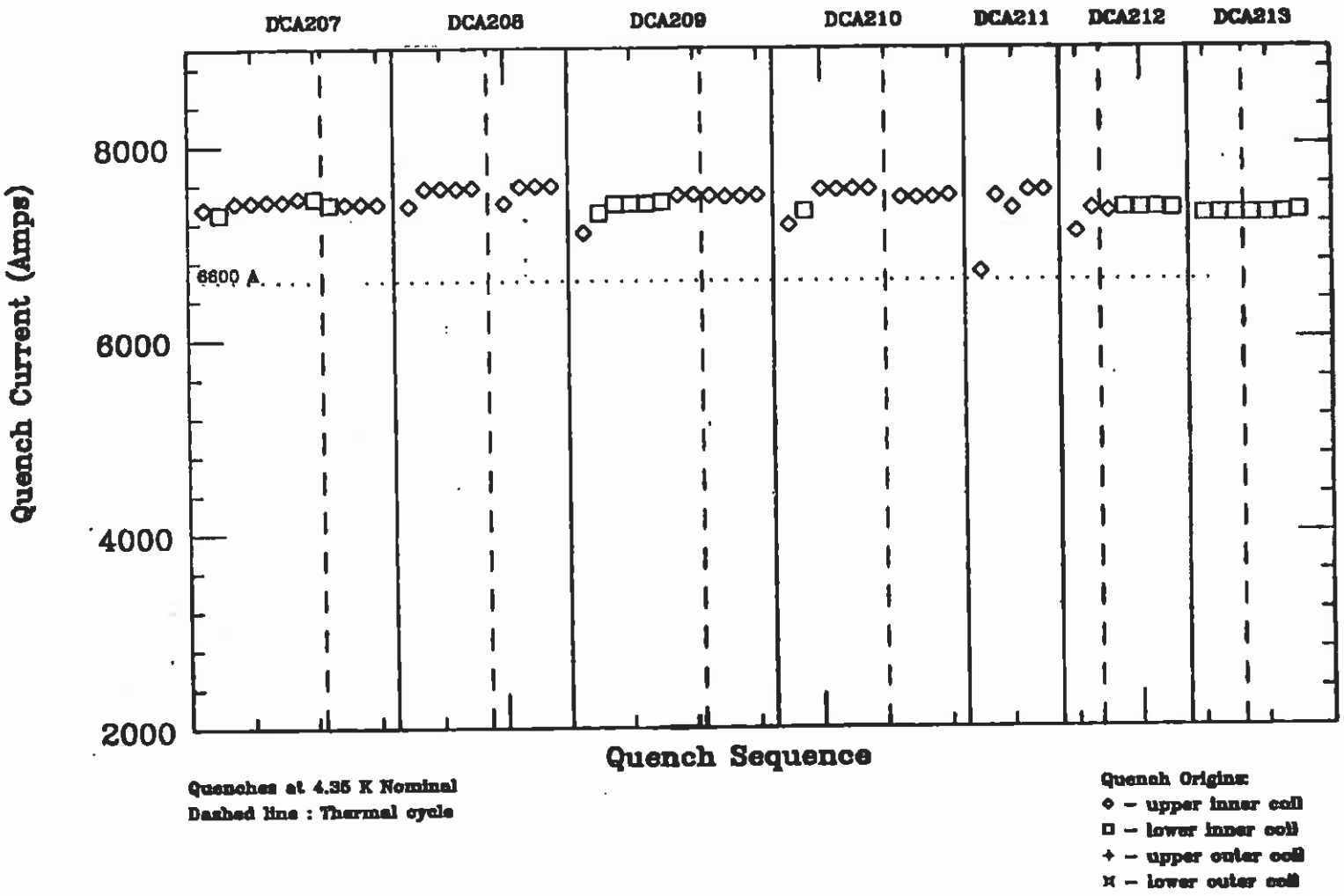

HORIZONTHALLY-SPLIT YOKE DESIGN WITH HIGH MANGANESE STAINLESS STEEL COLLARS

– The occurence, during cooldown, of a gap between collars and yoke along the horizontal diameter can be avoided by the use of high manganese stainless steel collars.

– Indeed, the integrated thermal expansion of high manganese steel (between room and liquid helium temperature) is of the order of $1.7\ 10^{-3}$, compared to $2.0\ 10^{-3}$ for low carbon steel.

4-cm-Apert., 17-m-long BNL Magnets *

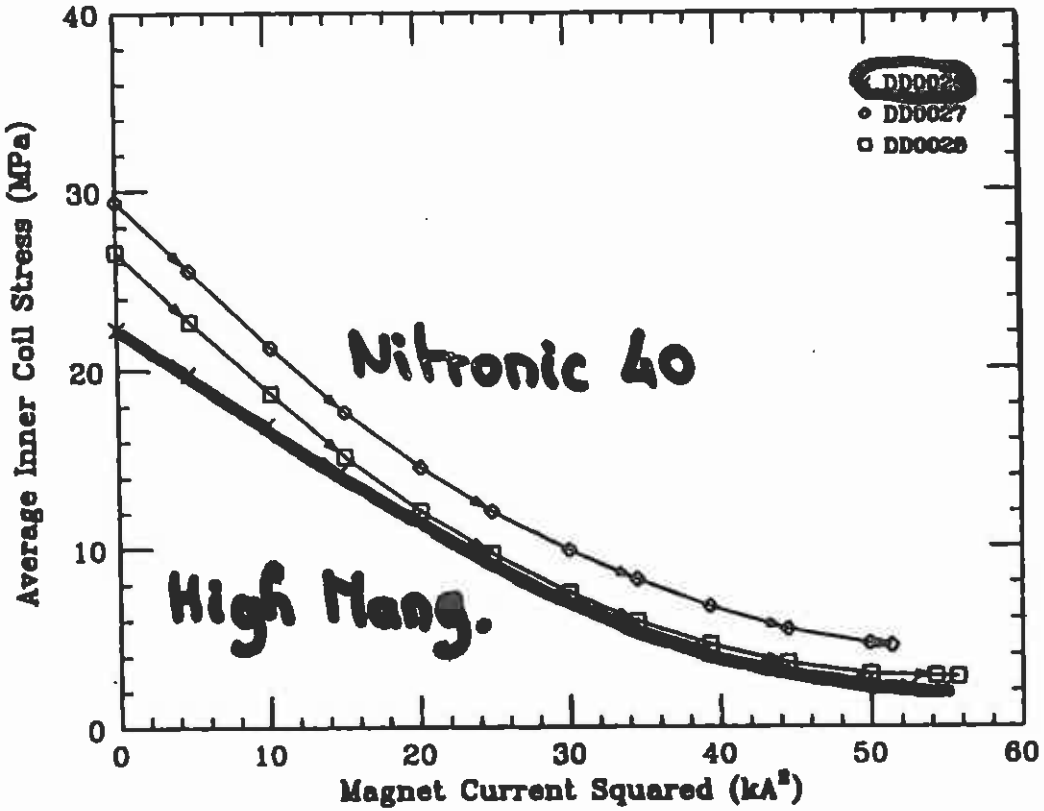

* SSCL-Preprint-6

4-cm-Apert., 17-m-Long BNL Magnets*

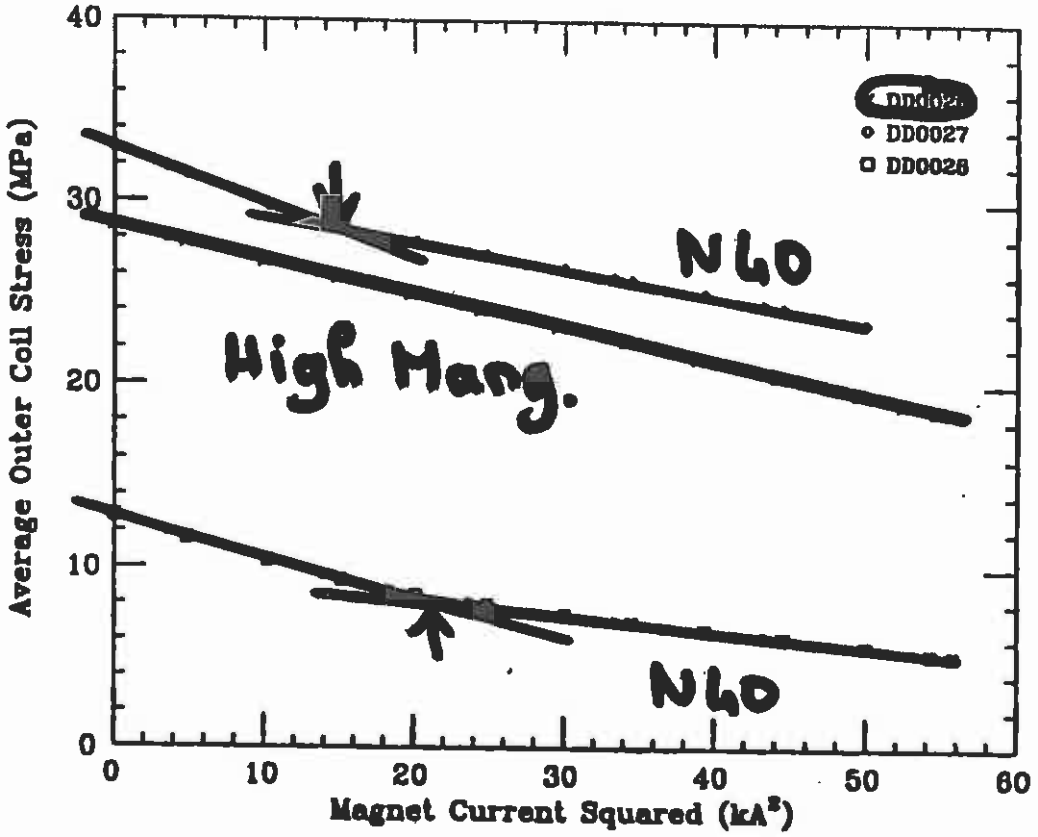

*SSCL-Preprint-6

BNL 4-cm-Aperture, 17-m-Long Dipole Magnets

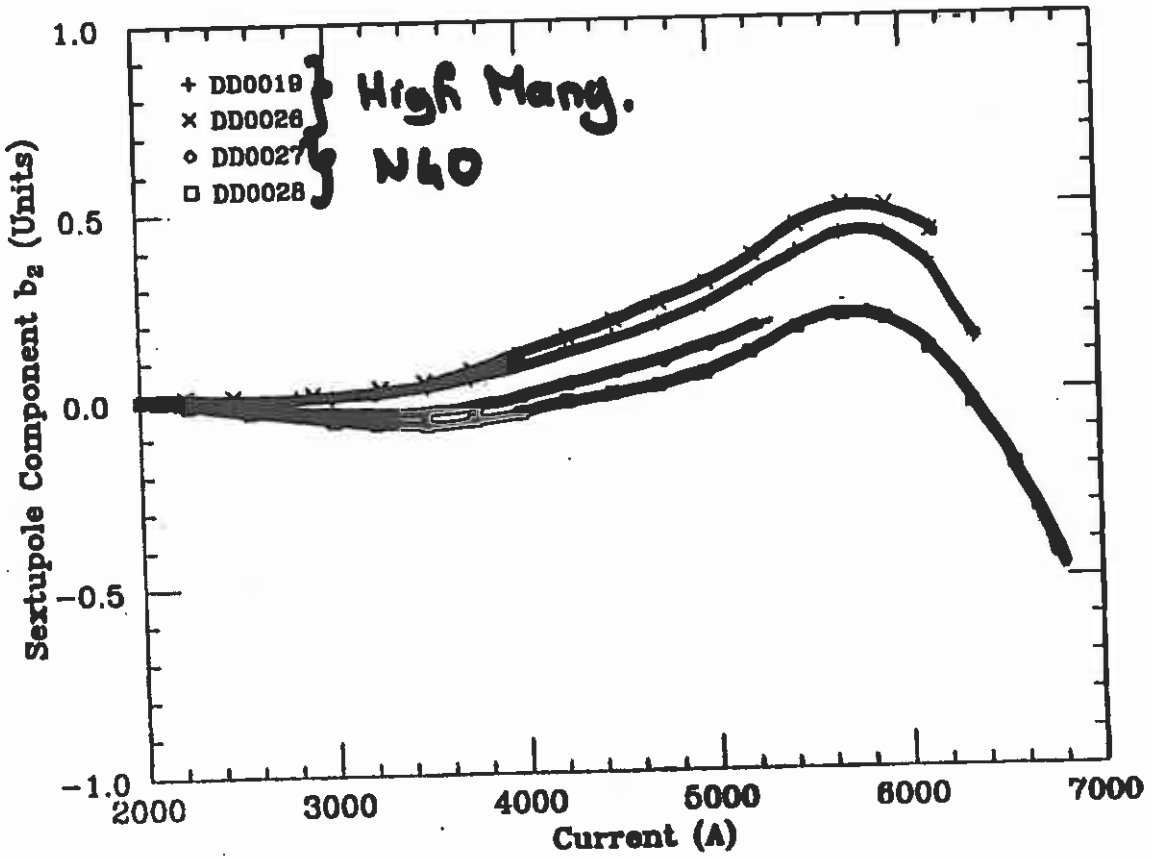

Figure 30. Examples of measurements of the sextupole component of the magnetic field during current cycles of some of the most recent BNL 4-cm-aperture, 17-m-long collider dipole magnet prototypes. The measurements are averaged over the up- and down-ramps of the current. The data are plotted using the same Y-scale, but the plots were translated along the vertical axis so that the 2000-A values would coincide.

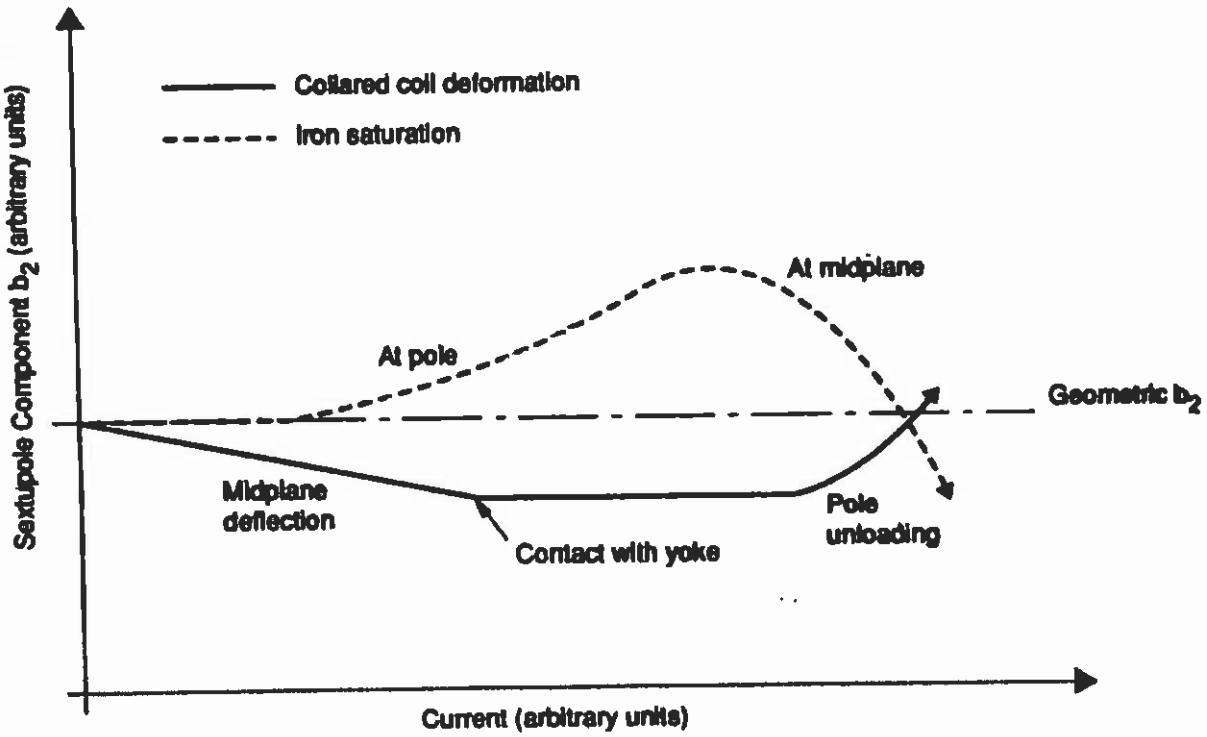

Figure 29. Expected changes in the sextupole component of the magnetic field during an excitation of a BNL 4-cm-aperture, 17-m-long collider dipole magnet prototype due to the deformations of the collared-coil assembly (continuous line) and the effects of iron yoke saturation (dashed line).

LECTURE 5: MECHANICAL DESIGN OF PARTICLE ACCELERATOR MAGNETS

5.1 Components of the Lorentz Force in Cosθ and Cos2θ Magnetic Designs

5.2 Azimuthal Pre-Compression

5.3 Coil Mechanical Properties

5.4 Collar Designs

5.5 Radial Support
- 5.5.1 Designs with Self-Supported Collared-Coil Assemblies
- 5.5.2 Designs with Fully-Mated Yoke
- **5.5.3 Design with Yoke Midplane Gap**
- 5.5.4 RHIC Magnets
- 5.5.5 Azimuthal Pre-Compression Versus Radial Support

5.6 End Support

5.7 Other Designs

MECHANICAL DESIGN WITH YOKE MIDPLANE GAP AT ROOM TEMPERATURE

– For large thermal shrinkage differentials (as in the case of aluminum collars), the shrinkage allowance and the yoke/collar compressive load required at room temperature for a full compensation would overstress the collared-coil assembly and a more sophisticated mechanical design must be used.

– The twin-aperture LHC dipole magnet prototypes with common, aluminum collars rely on a two-piece, vertically-split yoke with an open gap at room temperature and a welded outer shell made of a material (stainless steel or aluminum) that shrinks more during cooldown than the low carbon steel yoke.

LHC DIPOLE MAGNET DESIGN WITH YOKE MIDPLANE GAP AT ROOM TEMPERATURE

– The yoke of the LHC dipole magnet prototypes using common, aluminum collars is designed so that, when placed around the collared-coil assembly at room temperature with no pressure applied to it, there remains an opening between the two yoke halves of the order of the expected thermal shrinkage differential.

– The yoke midplane gap is then closed in two stages:

• ***During shell welding,*** as a result of the compressive load arising from weld shrinkage,

• ***During cooldown,*** as a result of the compressive load arising from thermal shrinkage differential between yoke and shell. This compressive load forces the two yoke halves to follow the shrinkage of the collared-coil assembly and to maintain a contact along the horizontal x-axis.

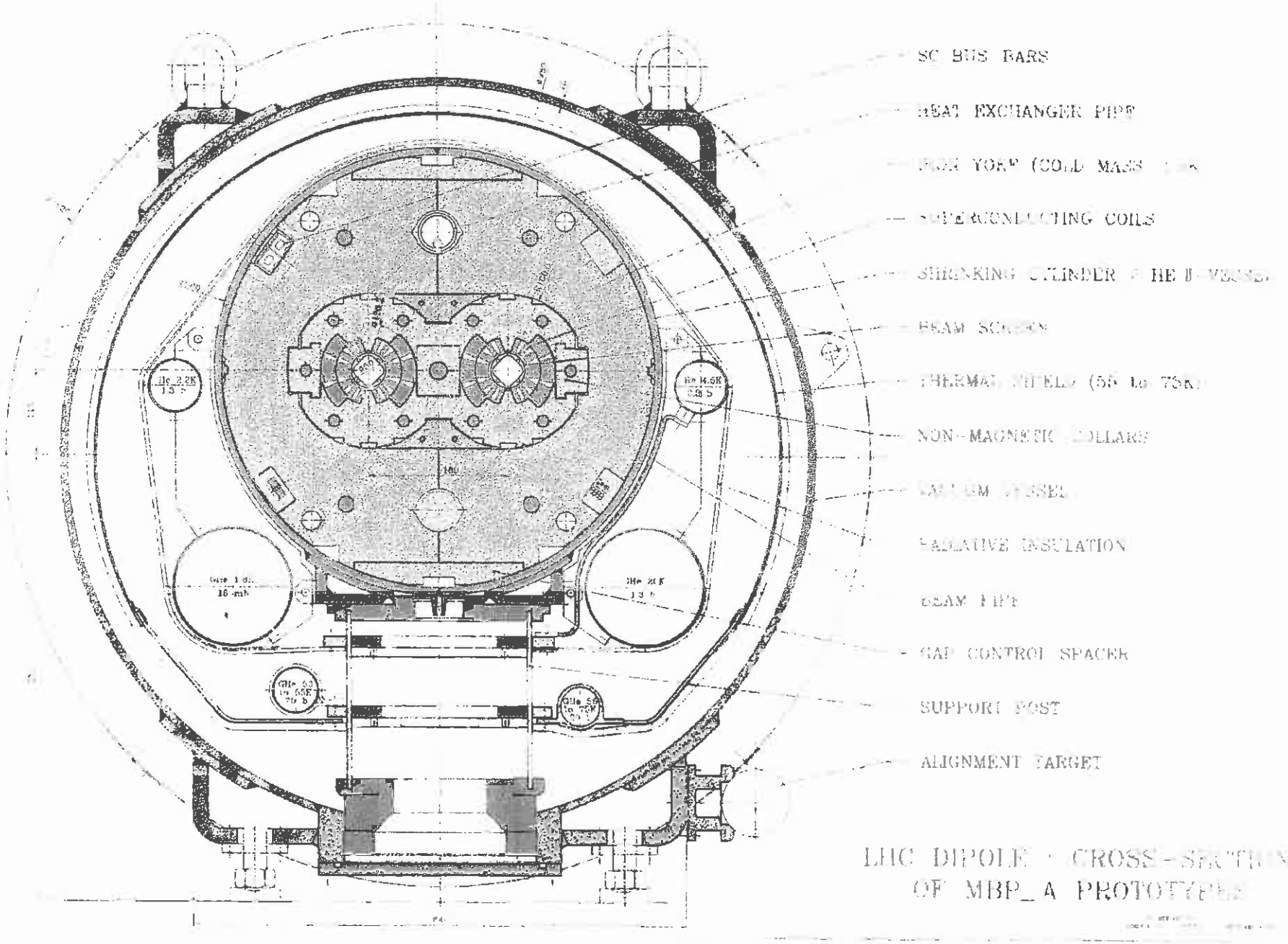

LHC DIPOLE : CROSS-SECTION
OF MBP_A PROTOTYPES

LHC YOKE MATING FORCE

– The yoke midplane gap must be fully closed at the end of cooldown and must remain closed during excitation to ensure that the structure is very rigid and to avoid any risk of oscillations.

– To fullfill this requirement, we not only need a good contact between the two yoke halves at the end of cooldown, but we also need the two yoke halves to be mated with a compressive force at least equal to the fraction of the x-component of the Lorentz force transmitted by the collared-coil assembly to the yoke.

Finite element computations show that this fraction is of the order of 50%.

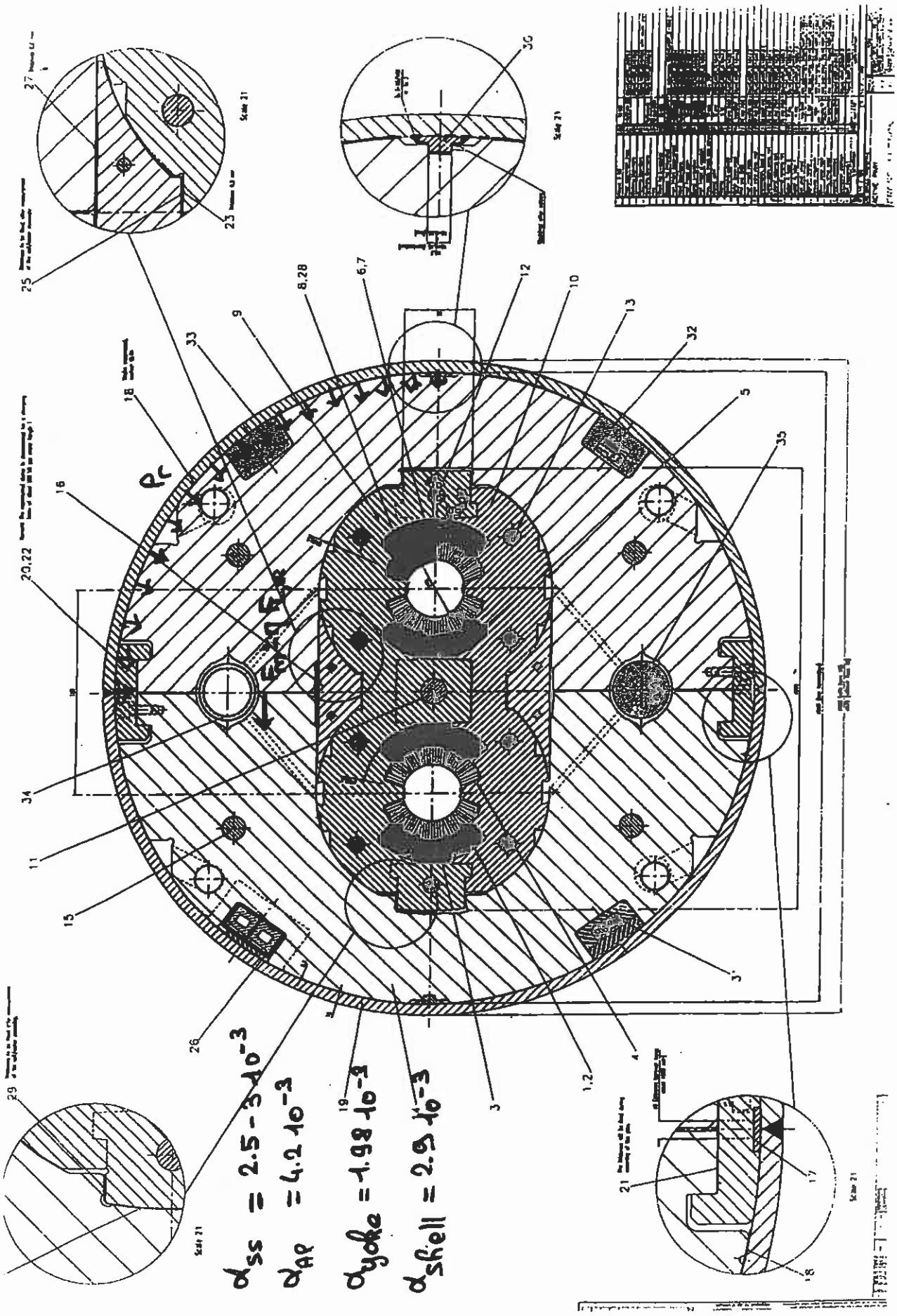
$d_{ss} = 2.5 - 3\,10^{-3}$
$d_{AP} = 4.2\,10^{-3}$
$d_{yoke} = 1.98\,10^{-3}$
$d_{shell} = 2.9\,10^{-3}$

LHC YOKE TAPER

– A particularity of the two-piece, vertically split yoke used in LHC dipole magnets is that it has a pronounced C-shape.

– When a compressive load is applied by the shell to these components, bending moments arise which tend to deflect the top and bottom arms of the C's inwardly.

– Hence, if nothing were done, one could end up, at the end of cooldown, in a situation where the yoke midplane gap is closed at the outer radius of the yoke, but remains open at the inner radius.

– The occurence of such situation is prevented by introducing a slight taper in the yoke midplane gap: the yoke is designed so that when placed around the collared-coil assembly at room temperature with no pressure applied to it, there remains a larger opening at the yoke outer radius than at the yoke inner radius.

– During shell welding and cooldown, the bending moments applied to the arms of the C's then bring the mating faces of the two yoke halves parallel and the yoke midplane gap closes down progressively.

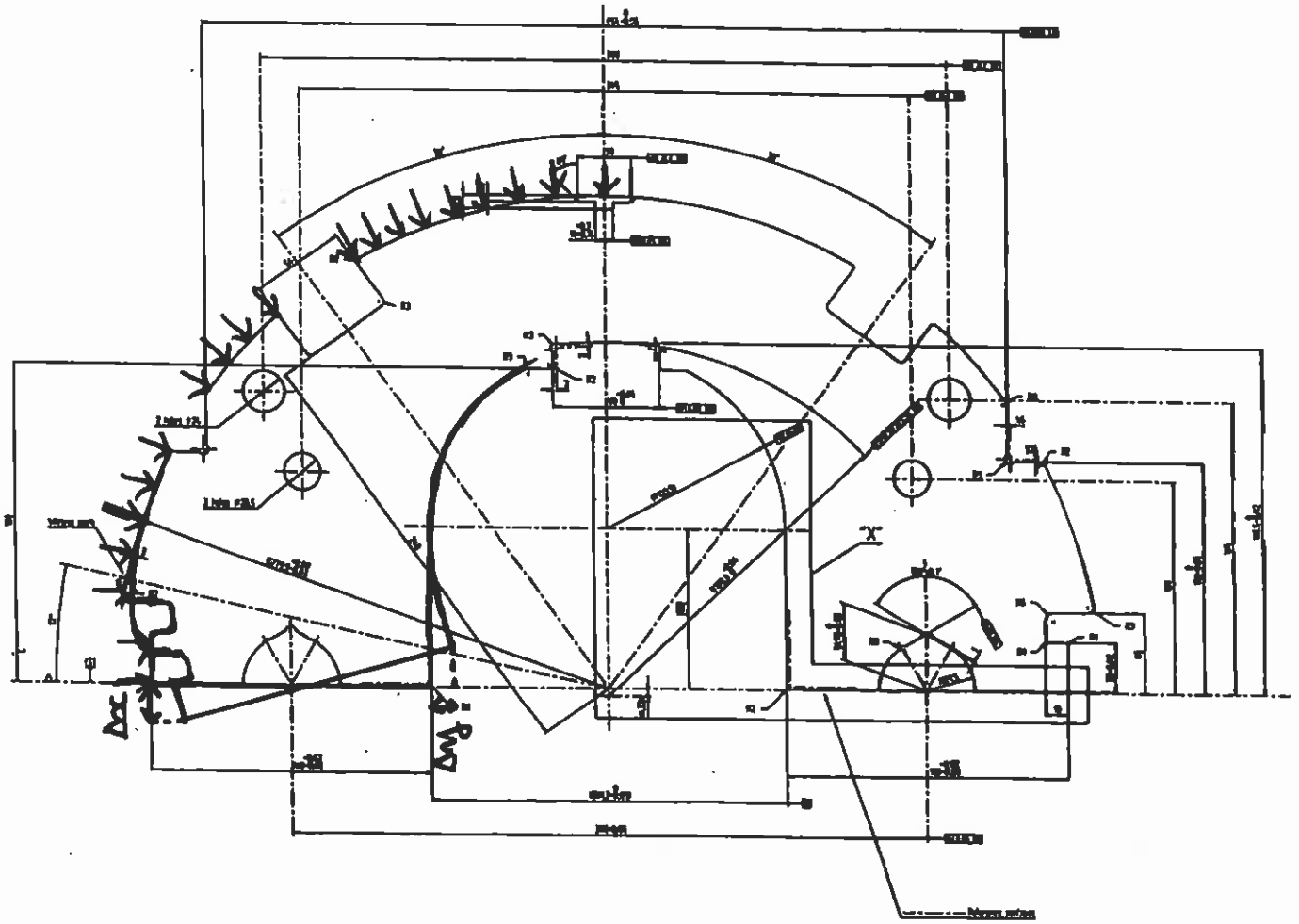

Figure 5(a) Drawing of the Yoke Laminations Used in the Body of the First 50-mm-Aperture, 10-m-Long LHC/Noell Dipole Magnet Prototype.

VERTICAL SUPPORT OF LHC COLLARED-COIL ASSEMBLY

– For the LHC dipole magnets using common collars, it is necessary to ensure a support along the vertical axis of the central part of the collared-coil assembly.

– This support is needed to prevent unwanted displacements and enhance the mechanical rigidity of the structure. It also relieves the concentration of stress in the vicinity of the tie rod located at the collared-coil assembly center.

– In the design discussed in this lecture, the support is provided by two magnetic inserts which rest against the central part of the collared-coil assembly and which are compressed by the inward bending of the C-shaped yoke.

– One problem with the application of such vertical forces is that part of them are transmitted to the coils and result in an increase of azimuthal pre-compression.

– There is therefore an upper limit on what is admissible and the magnet assembly must be carefully watched to avoid overstressing the collared-coil assembly.

ALUMINUM CONTROL GAP SPACERS

– As we have seen, the vertical forces supporting the central part of the collared-coil arise from the bending of the C-shaped yoke during shell welding, and these forces must be limited to avoid overstressing the coils.

– In some LHC prototypes, the closure of the yoke midplane gap is controlled by means of aluminum spacers located between the two yoke halves.

– The spacers are dimensioned to have a spring rate similar to that of the collared-coil assembly and they prevent the gap from closing at room temperature. During cooldown, however, they shrink more than the yoke and cease to be effective.

– The concept of aluminum control gap spacer was first thought of at SSC and was first tried on a short dipole magnet model (using NbTi cables) built at LBNL. The LBNL model reached 10.06 T at 1.8 K.

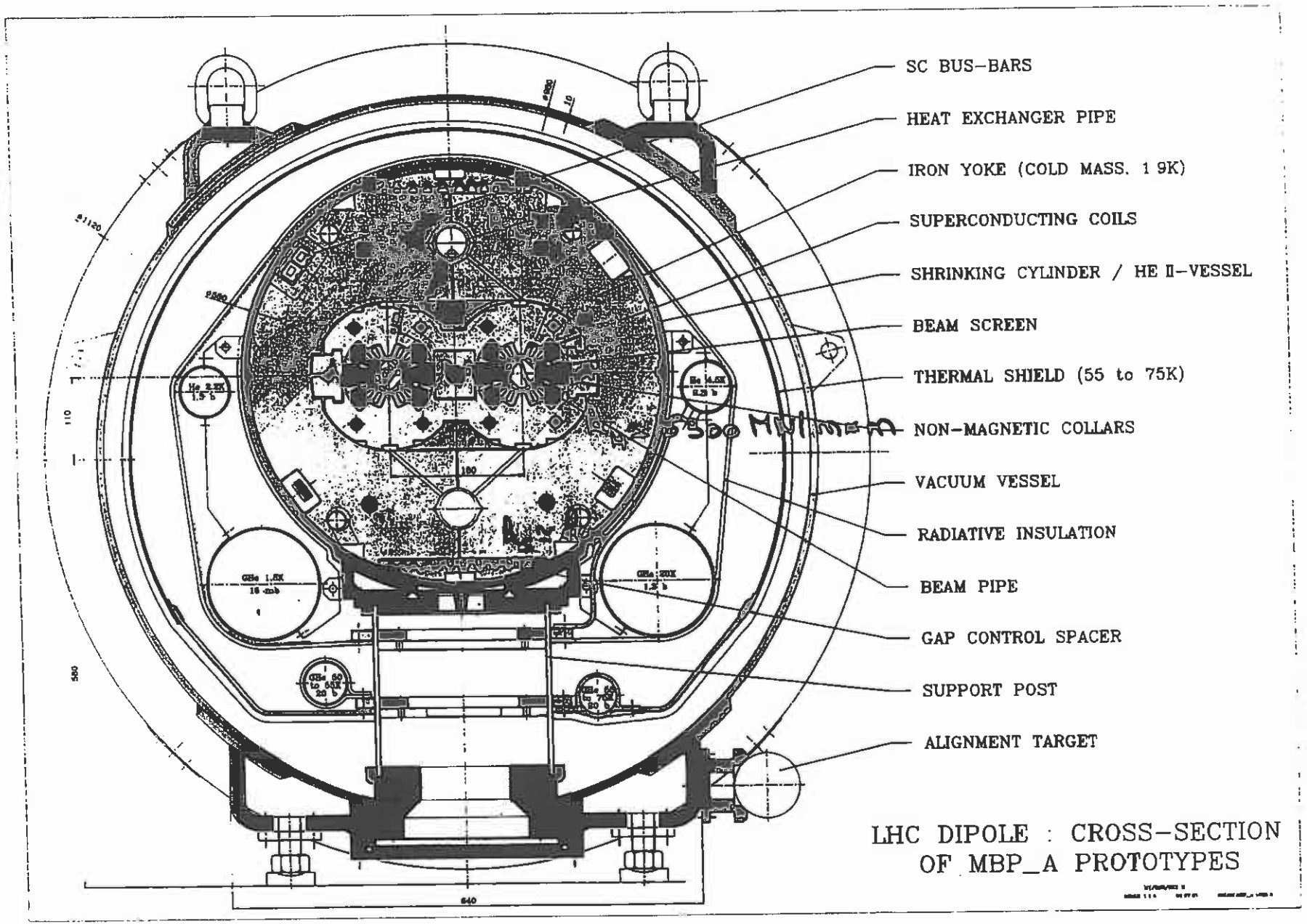
SC BUS-BARS
HEAT EXCHANGER PIPE
IRON YOKE (COLD MASS. 1 9K)
SUPERCONDUCTING COILS
SHRINKING CYLINDER / HE II-VESSEL
BEAM SCREEN
THERMAL SHIELD (55 to 75K)
NON-MAGNETIC COLLARS
VACUUM VESSEL
RADIATIVE INSULATION
BEAM PIPE
GAP CONTROL SPACER
SUPPORT POST
ALIGNMENT TARGET
LHC DIPOLE : CROSS-SECTION
OF MBP_A PROTOTYPES

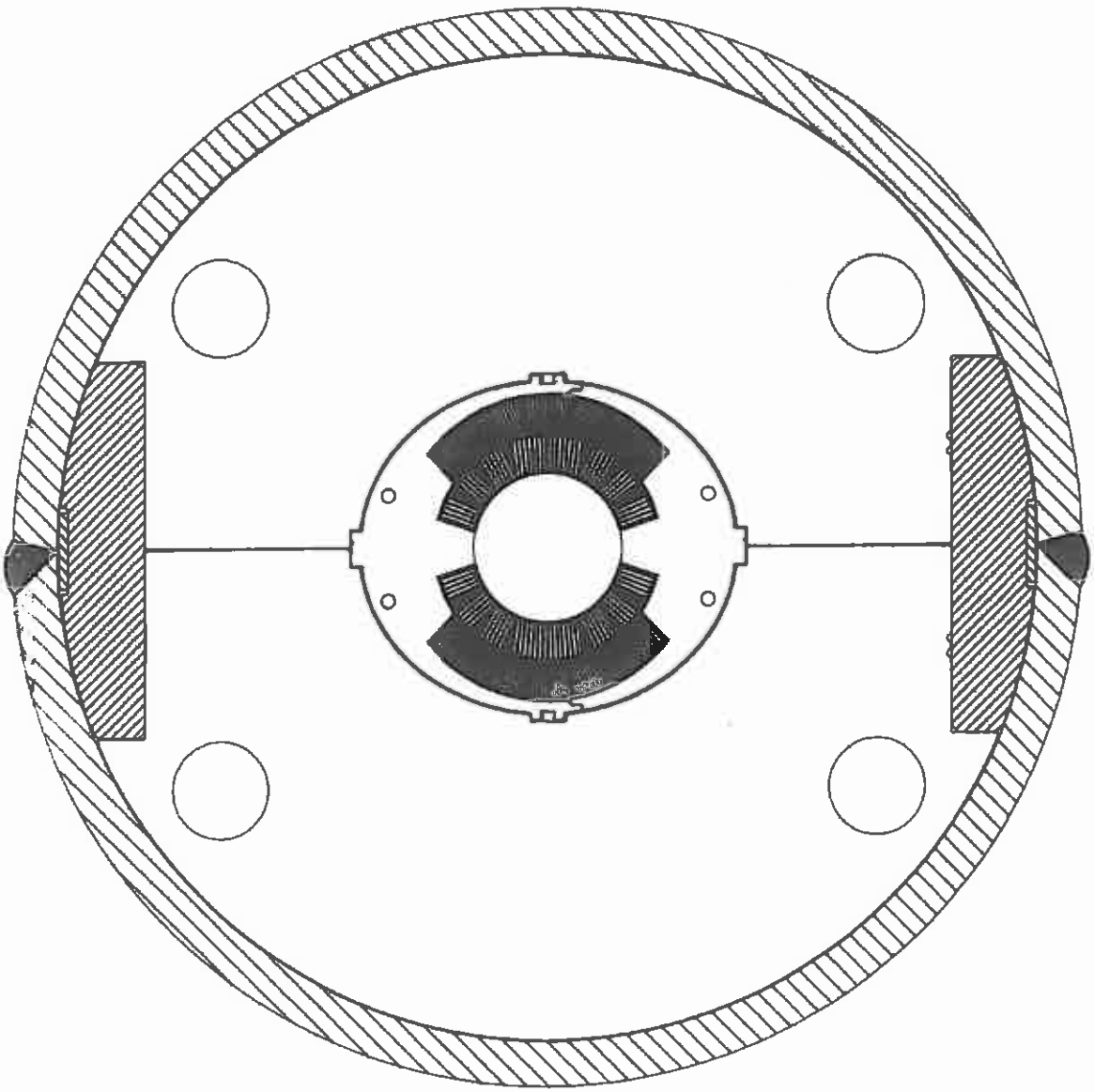

D-19 STRAIGHT SECTION

LBL D19 Dipole Magnet

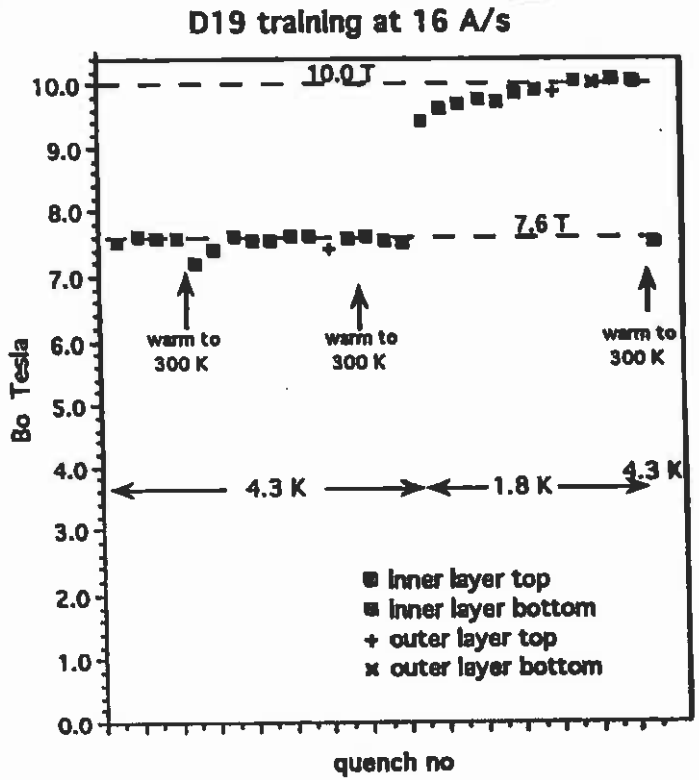

MANUFACTURING OF MAGNET DESIGN WITH YOKE MIDPLANE GAP AT ROOM TEMPERATURE

– In summary, a gap too close may result in coil overstressing at room temperature whereas a gap too open may result in contact loss during cooldown.

– A crucial issue is then the ability of performing the shell welding operation in a reproducible way during mass production, ensuring the achievment of the desired yoke midplane gap value at room temperature while keeping a tight tolerance on this value (of the order of 0.1 mm).

Examples: Gap closure data from 3 full-length LHC dipole magnet prototypes.

The first prototype, MTP1A3, includes aluminum control gap spacers, and the yoke midplane gap appears to close and open at the desired temperature during cooldown and warmup.

The second prototype, MTP1N1, does not include control gap spacer and the yoke midplane gap appears to close too early during cooldown (gap too closed at room temperature).

The third prototype, MTP1AJ, does not include control gap spacer and the yoke midplane gap appears to close too late during cooldown (gap too open at room temperature).

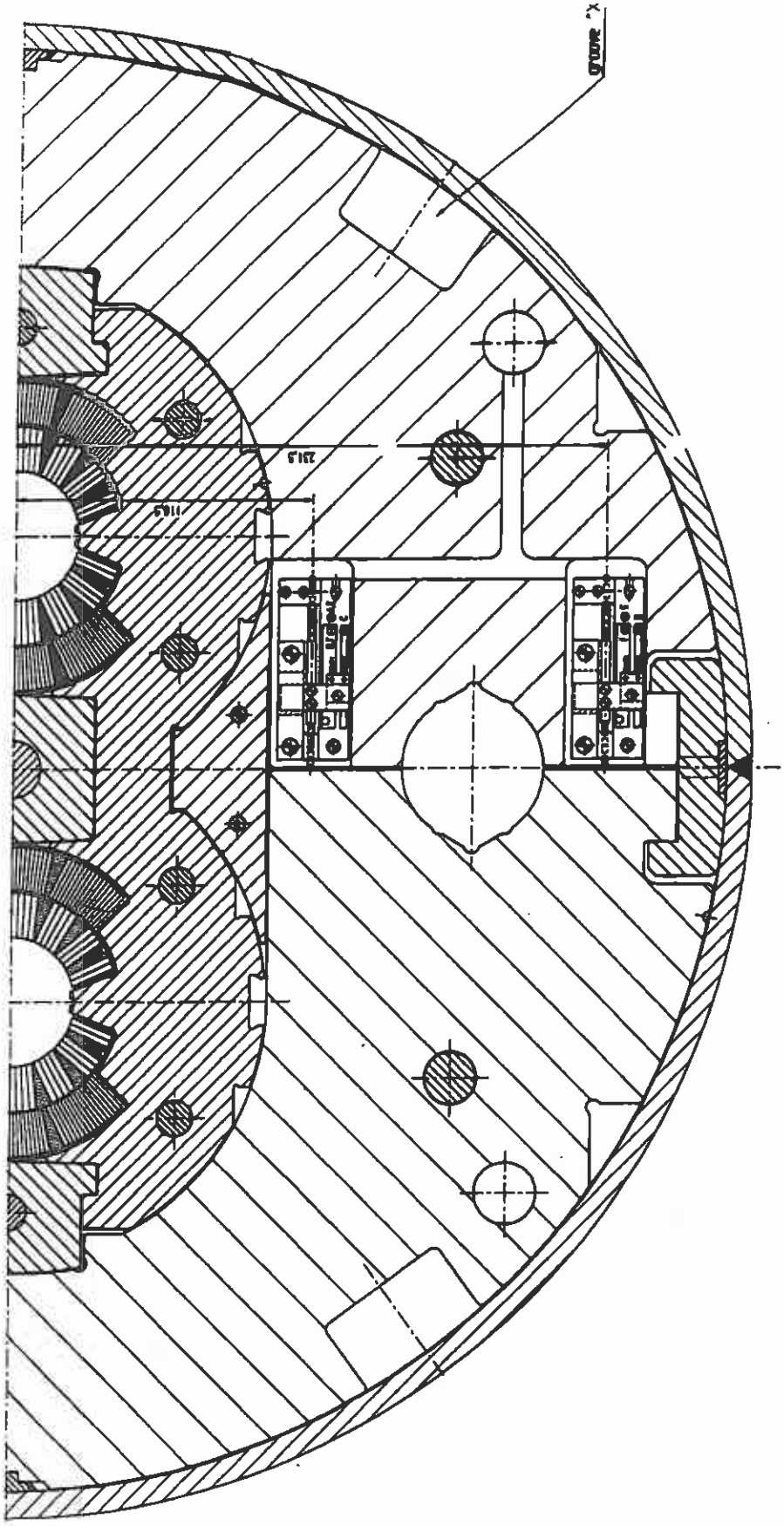
SECTION C-C

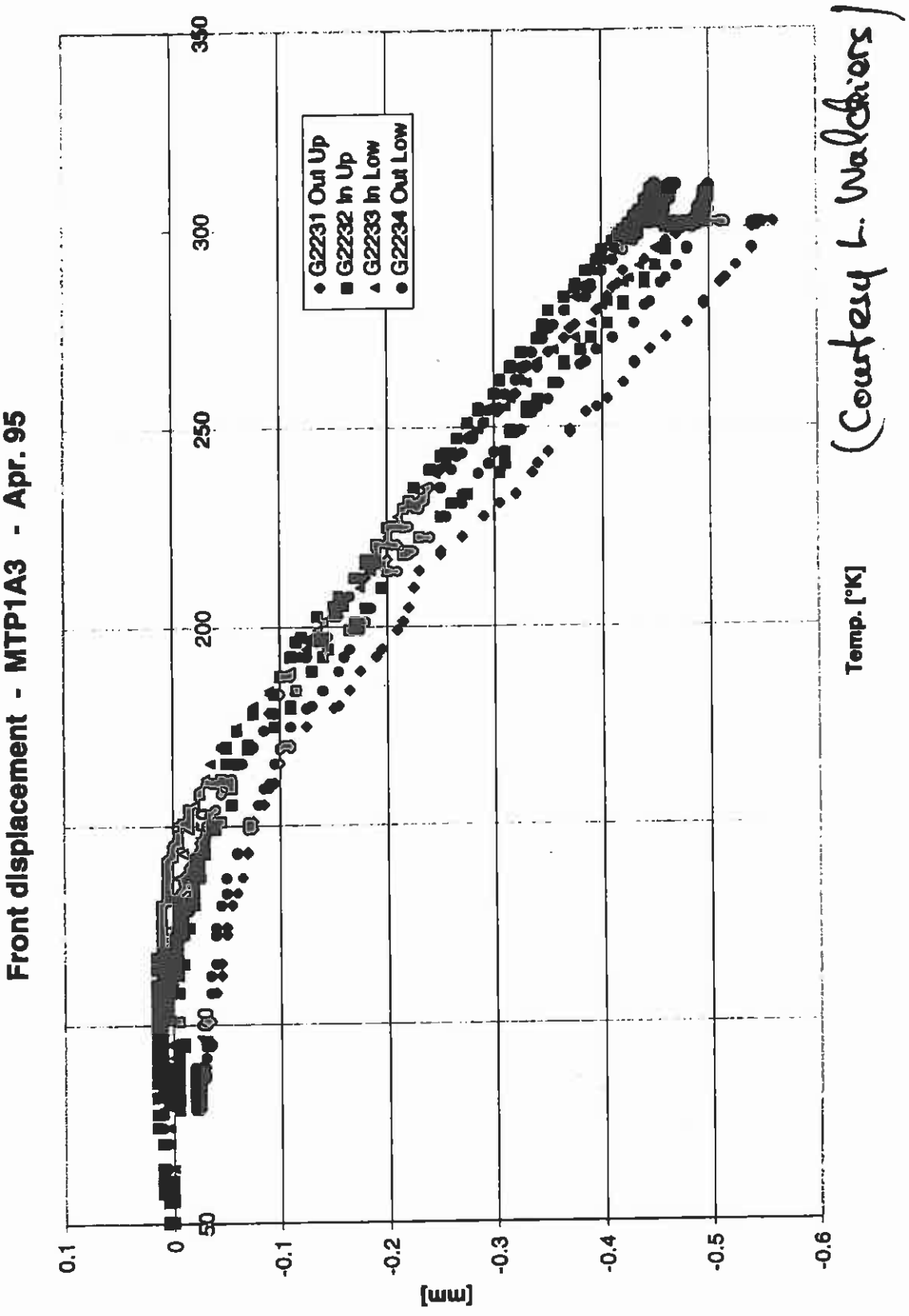
Front displacement - MTP1A3 - Apr. 95
G2231 Out Up
G2232 In Up
G2233 In Low
G2234 Out Low
Temp. [°K]
[mm]
0.1
0
-0.1
-0.2
-0.3
-0.4
-0.5
-0.6
50
200
250
300
350
(Courtesy L. Walckiers)

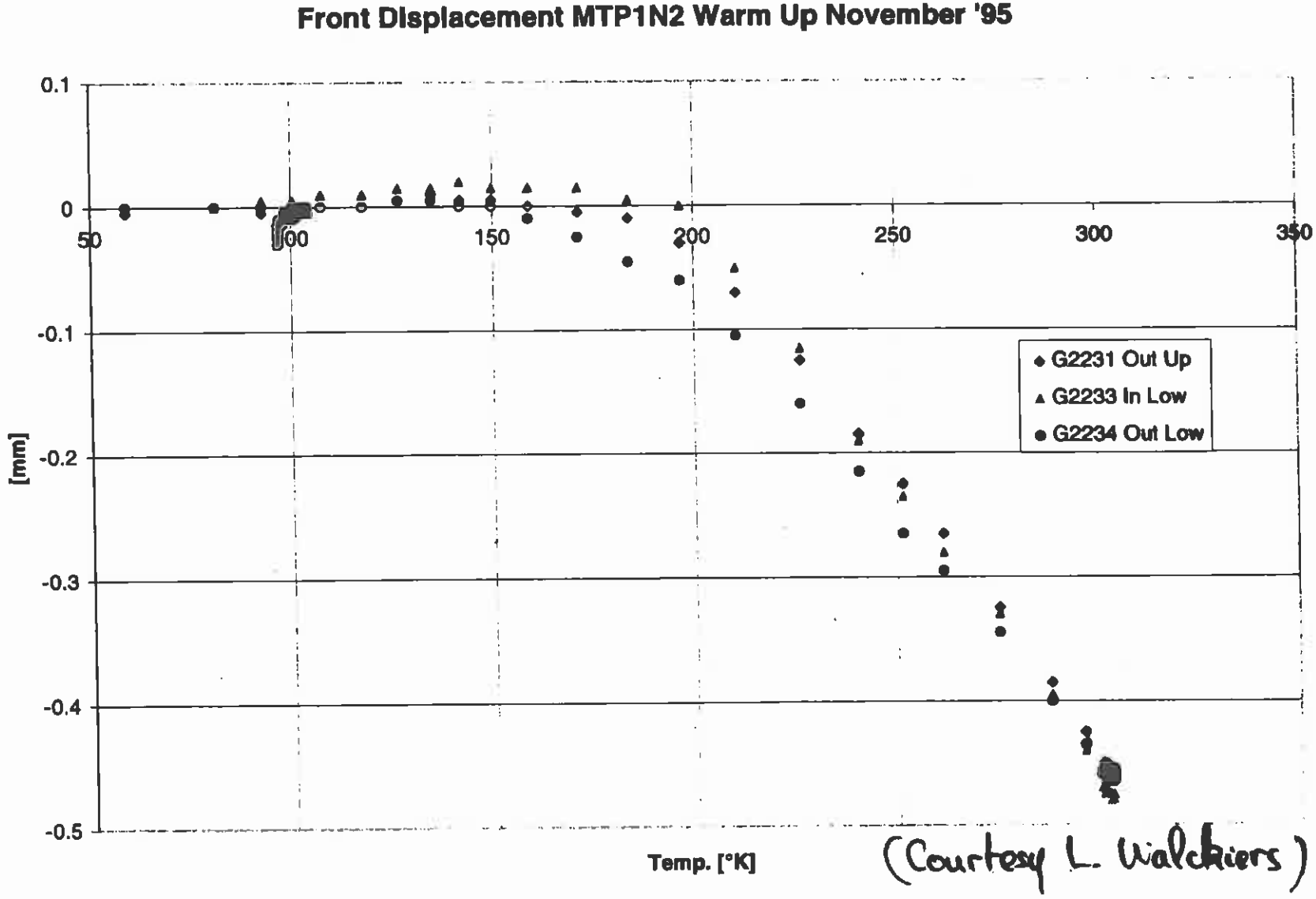
Front Displacement MTP1N2 Warm Up November '95
0.1
0
-0.1
-0.2
-0.3
-0.4
-0.5
[mm]
50
100
150
200
250
300
350
Temp. [°K]
G2231 Out Up
G2233 In Low
G2234 Out Low
(Courtesy L. Walckiers)

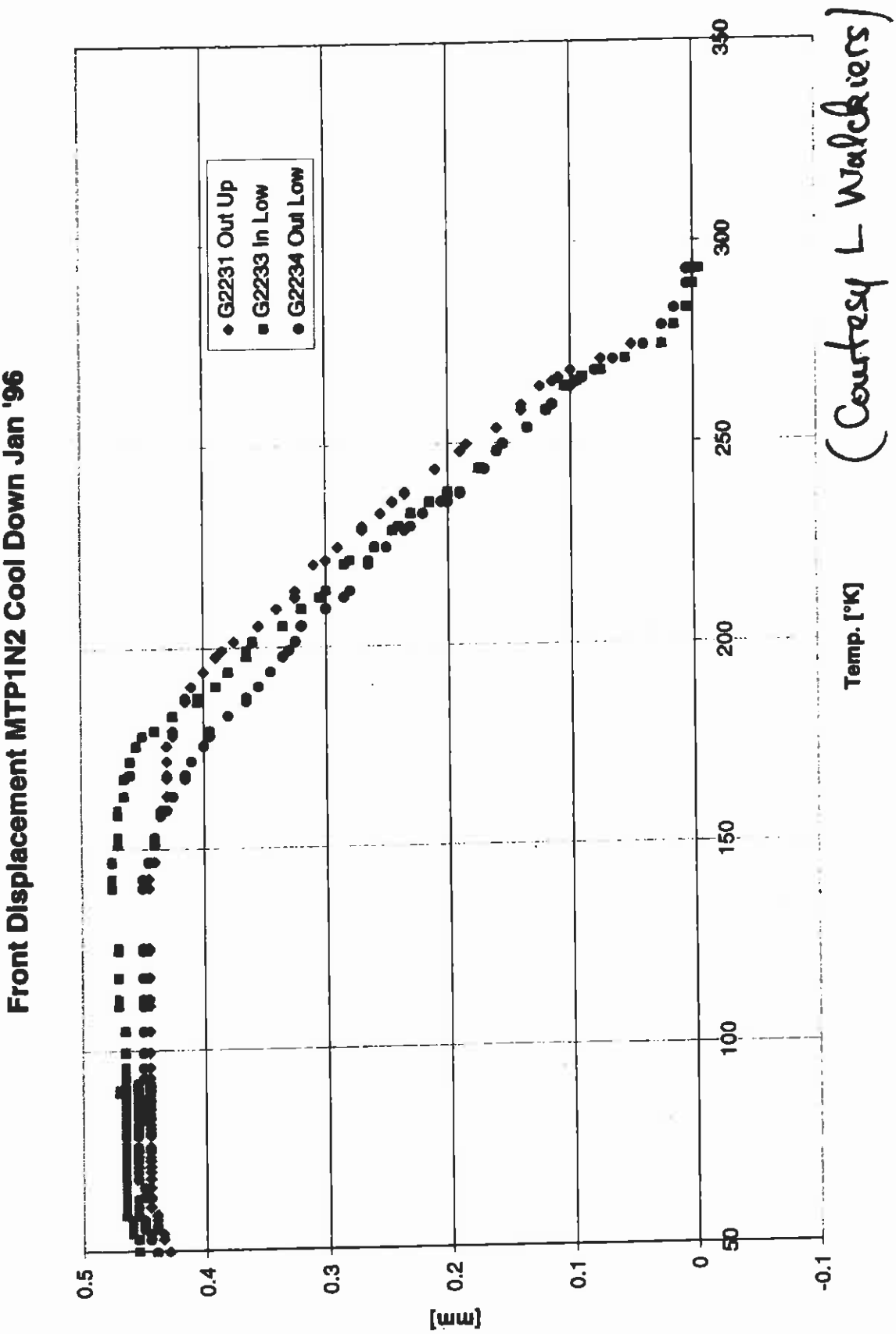
Front Displacement MTP1N2 Cool Down Jan '96
G2231 Out Up
G2233 In Low
G2234 Out Low
0.5
0.4
0.3
0.2
0.1
0
-0.1
[mm]
350
300
250
200
150
100
50
Temp. [°K]
(Courtesy L Walckiers)

G2232

Change in Displacement Gauge G2232 Section B-B Inner Yoke Gap (MTP1N1)

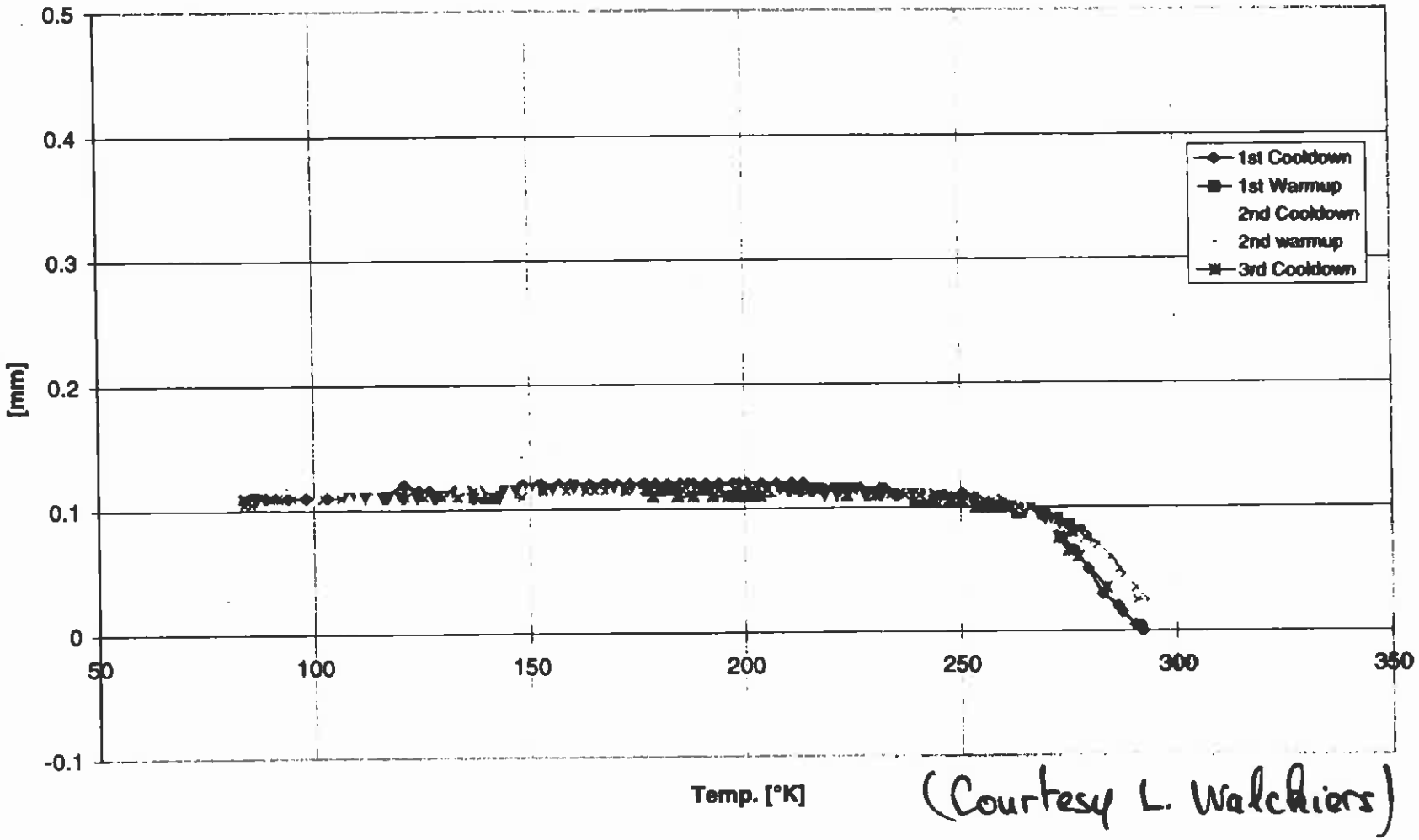

(Courtesy L. Walckiers)

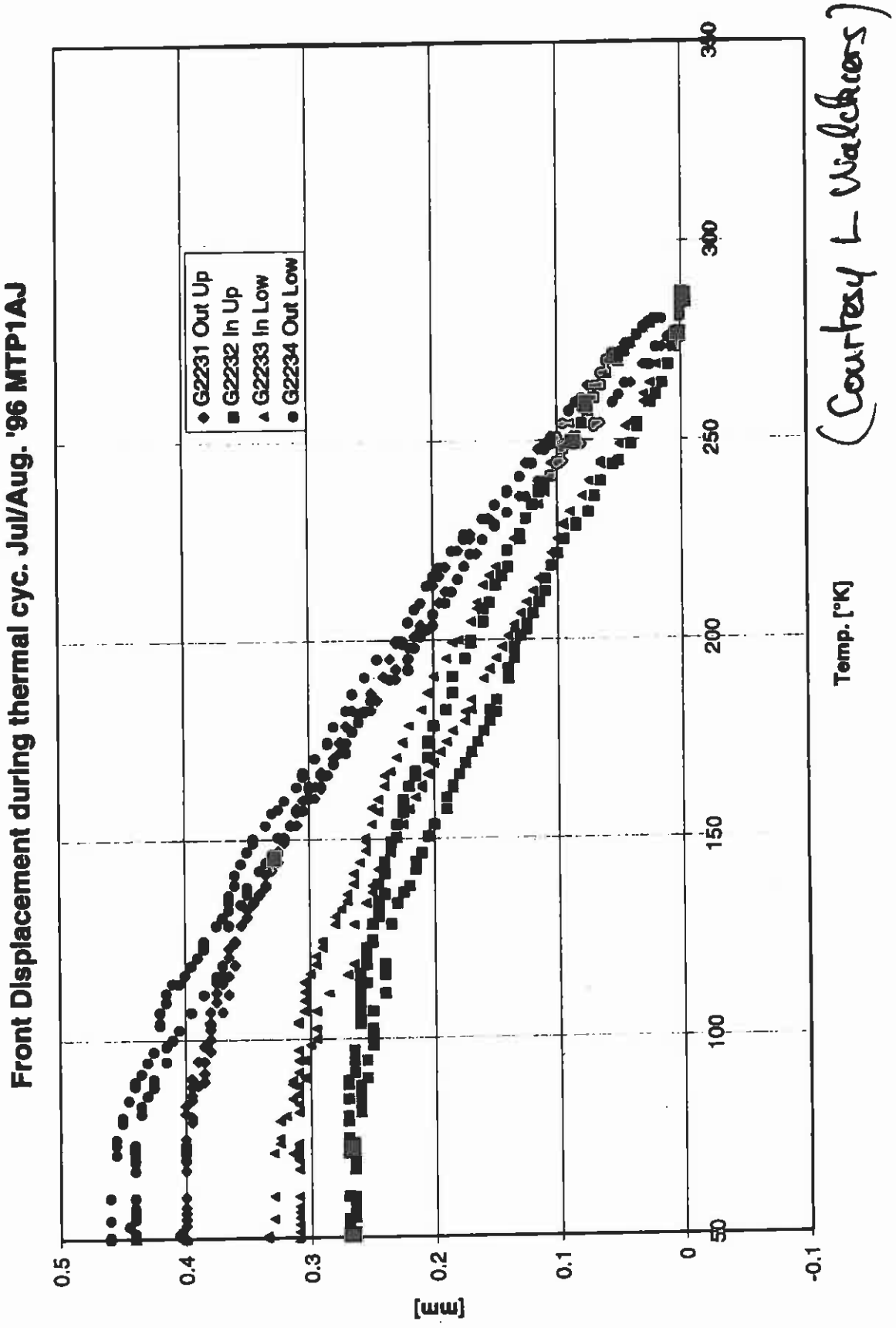
Front Displacement during thermal cyc. Jul/Aug. '96 MTP1AJ
G2231 Out Up
G2232 In Up
G2233 In Low
G2234 Out Low
[mm]
0.5
0.4
0.3
0.2
0.1
0
-0.1
Temp. [°K]
50
100
150
200
250
300
340
(Courtesy L Walchuck)

Training of LHC 10m-long Dipole Models

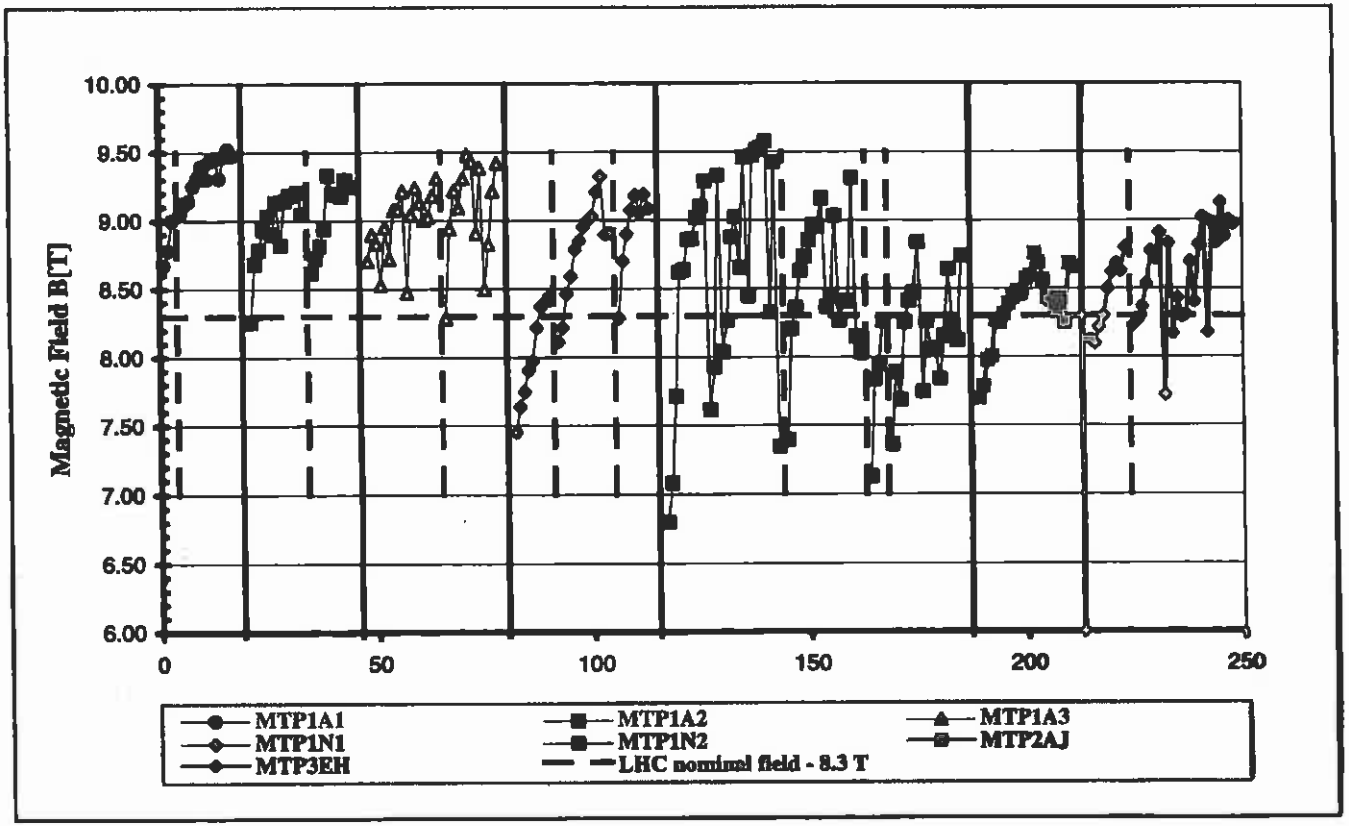

8/10/96 protos_tr_abs_exp Prot_sum Page 1

LHC DIPOLE MAGNET DESIGN

– At present (1999), CERN is developing a new dipole magnet design, relying on common, stainless steel collars and a two-piece, vertically split yoke, assembled with a closed midplane gap at room temperature.

– In this very robust design, 80% of the radial component of the Lorentz force is taken by the collars and only 20% is transmitted to the yoke and shell.

LHC DIPOLE : STANDARD CROSS-SECTION

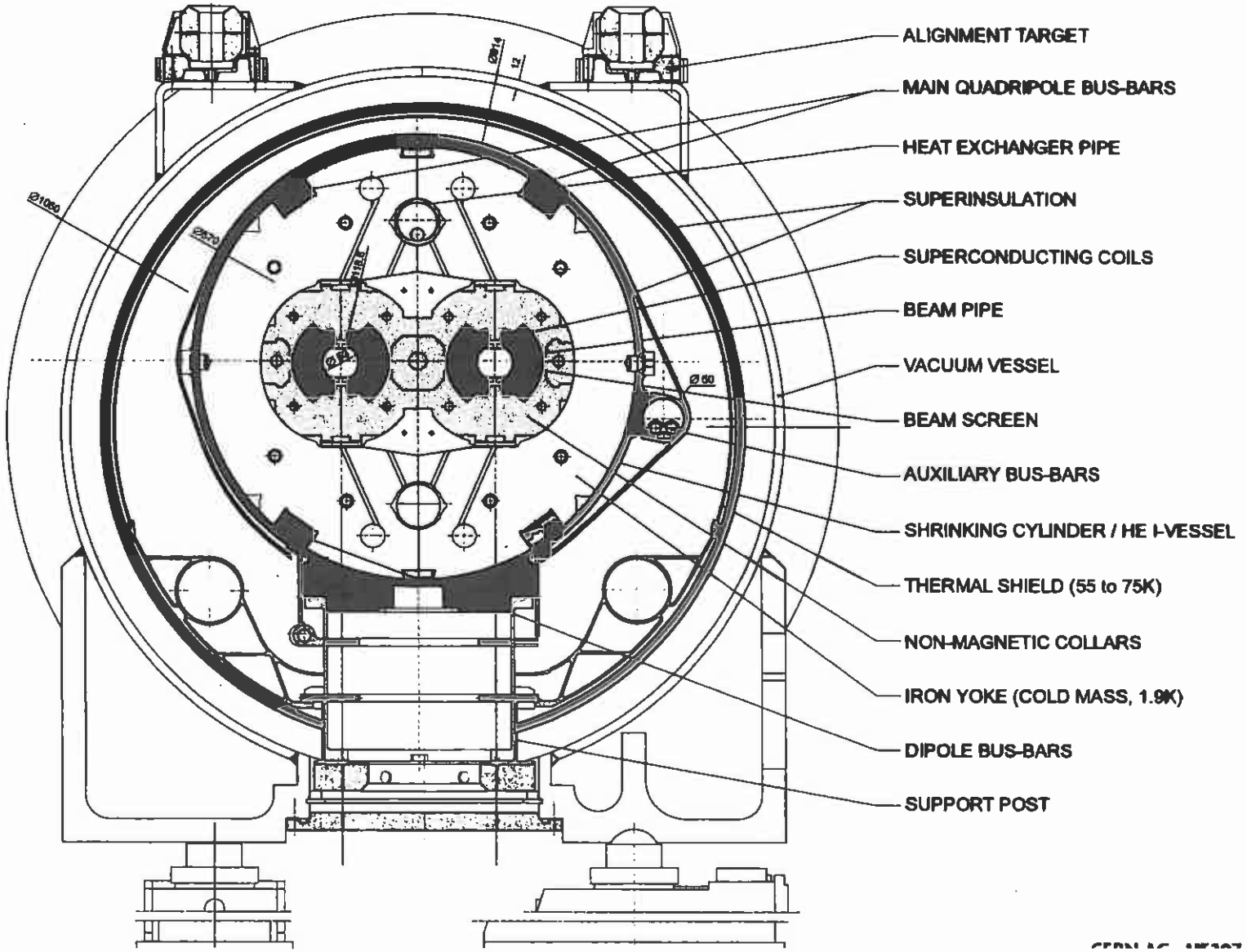

LECTURE 5: MECHANICAL DESIGN OF PARTICLE ACCELERATOR MAGNETS

5.1 Components of the Lorentz Force in Cosθ and Cos2θ Magnetic Designs

5.2 Azimuthal Pre-Compression

5.3 Coil Mechanical Properties

5.4 Collar Designs

5.5 Radial Support
- 5.5.1 Designs with Self-Supported Collared-Coil Assemblies
- 5.5.2 Designs with Fully-Mated Yoke
- 5.5.3 Design with Yoke Midplane Gap
- **5.5.4 RHIC Magnets**
- 5.5.5 Azimuthal Pre-Compression Versus Radial Support

5.6 End Support

5.7 Other Designs

RHIC MAGNETS

– In RHIC dipole and quadrupole magnets, collar and yoke designs are altogether simplified by replacing the collars by reinforced plastic spacers and by using directly the yoke to pre-compress the one-layer coils.

– This design has proven to be adequate for the low field and low field gradient needed for RHIC, but it remains to be seen if this structure could be scaled-up to higher fields.

RHIC ARC DIPOLE

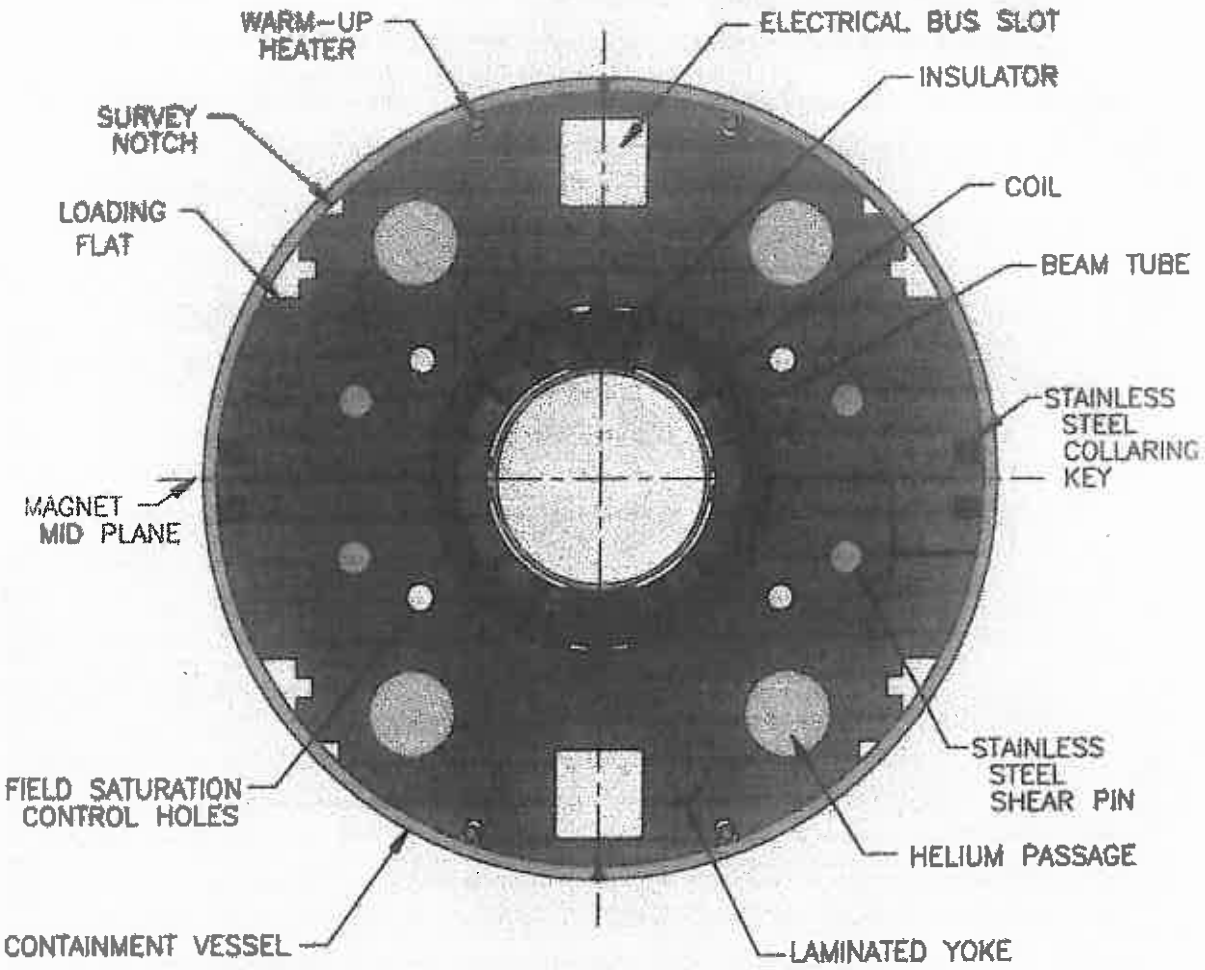

RHIC ARC QUADRUPOLE

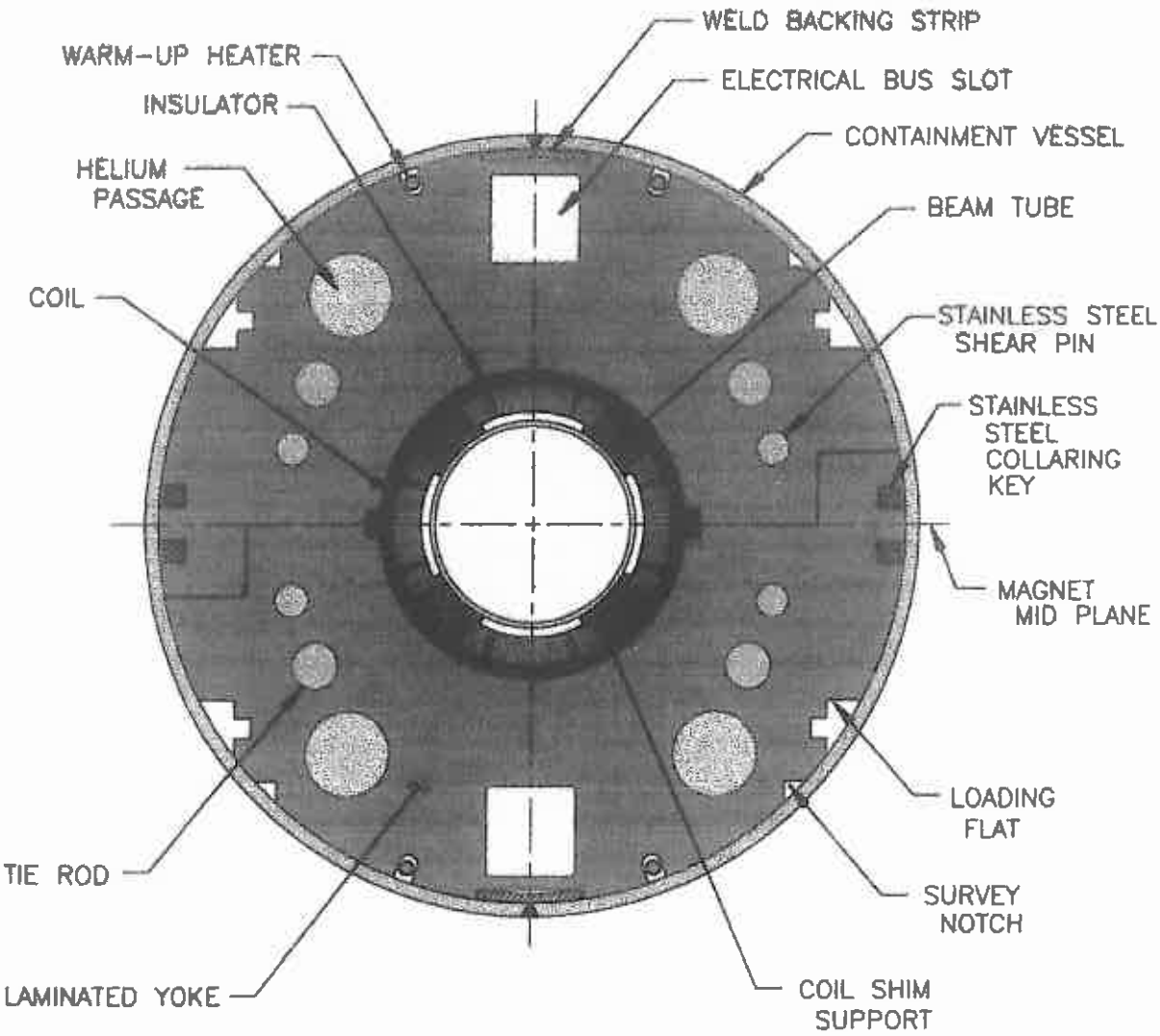

LECTURE 5: MECHANICAL DESIGN OF PARTICLE ACCELERATOR MAGNETS

5.1 Components of the Lorentz Force in Cosθ and Cos2θ Magnetic Designs

5.2 Azimuthal Pre-Compression

5.3 Coil Mechanical Properties

5.4 Collar Designs

5.5 Radial Support

5.5.1 Designs with Self-Supported Collared-Coil Assemblies

5.5.2 Designs with Fully-Mated Yoke

5.5.3 Design with Yoke Midplane Gap

5.5.4 RHIC Magnets

5.5.5 Azimuthal Pre-Compression Versus Radial Support

5.6 End Support

5.7 Other Designs

INFLUENCE OF COIL SUPPORT STRUCTURE RIGIDITY

– The short, single-aperture LHC dipole magnet models relying on aluminum collars exhibit a slow training for fields above 8.6–8.8 T.

Furthermore, the slope of the training curve is more or less the same for all the models.

– One short magnet model (MBSMS3 version 4 and higher) was rebuilt using stainless steel collars.

The training did not disappear, but the slope of the training curve of the rebuilt magnet is higher than the slope of the curves measured on aluminum–collar magnets.

As a result, the more rigid structure reaches in 15 quenches a magnetic flux density that is about 0.5 T higher than the maximum flux density reached on previous versions of this model.

– This provides a fairly good illustration on how the radial support can influence the magnet performance.

THE STRUCTURE

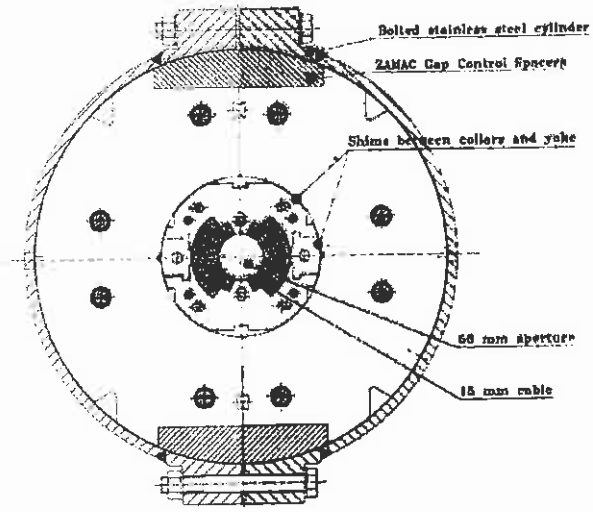

MBSMS : Cross-section

- *56 mm bore;*
- *15 mm cables;*
- *coils collared with 12 mm rods;*
- *possibility of using end cages;*
- *shims to adjust collars-yoke interference;*
- *half yokes assembled with four tie rods;*
- *Vertical yoke gap*
- *ZAMAC Gap Control Spacers;*
- *50 mm thick end plates;*
- *bolted stainless steel shrinking cylinder*
- *2 bullets gauges per side;*
- *easily demountable structure.*

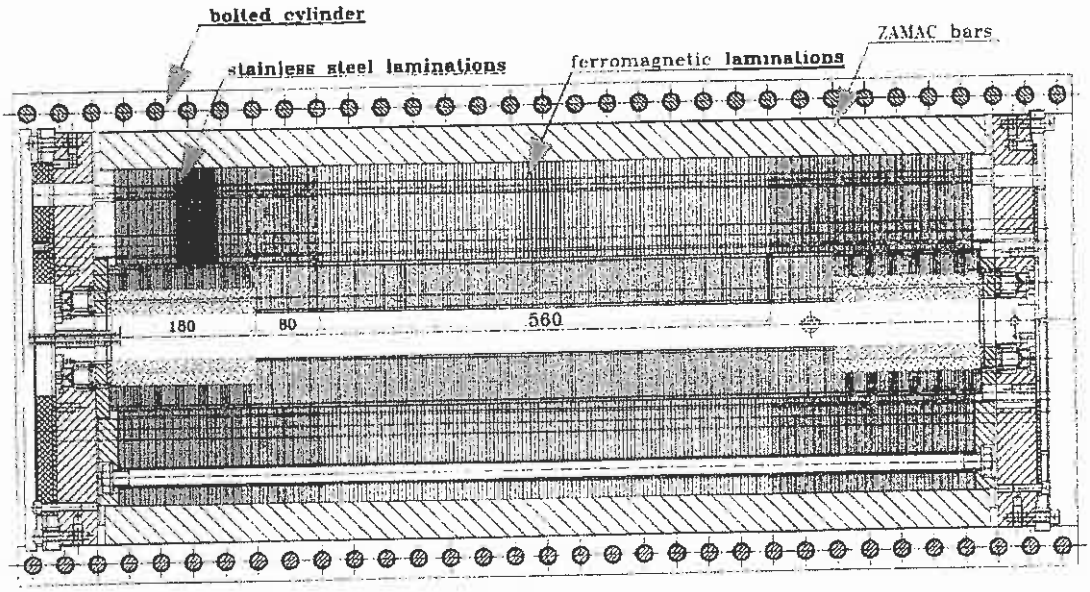

MBSMS : Longitudinal section

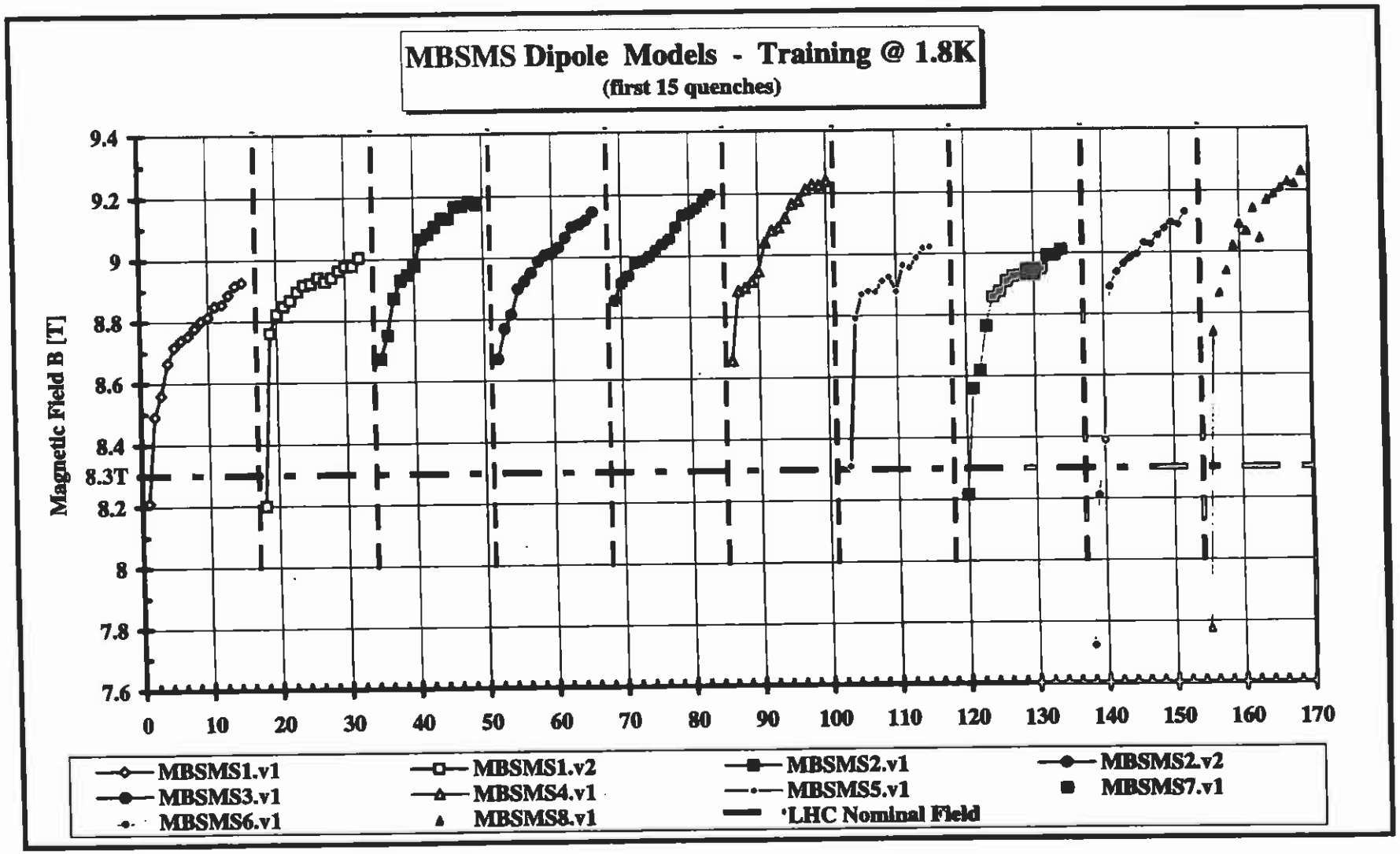

Mbsmssum MBSMS15 Printed 19/9/96

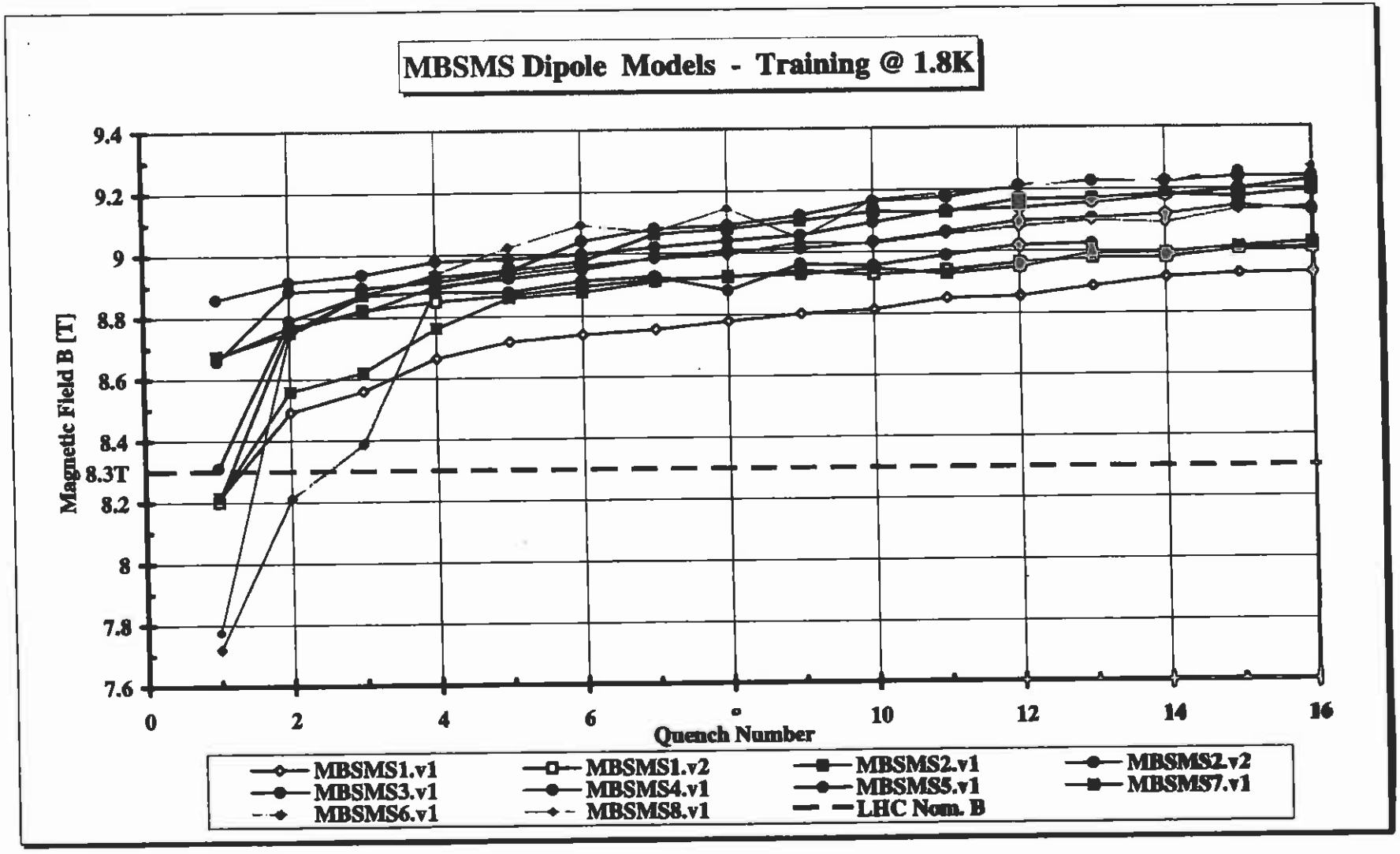

Mbsmssum MBSMS_Tr_over15 Printed 19/9/96 19:18

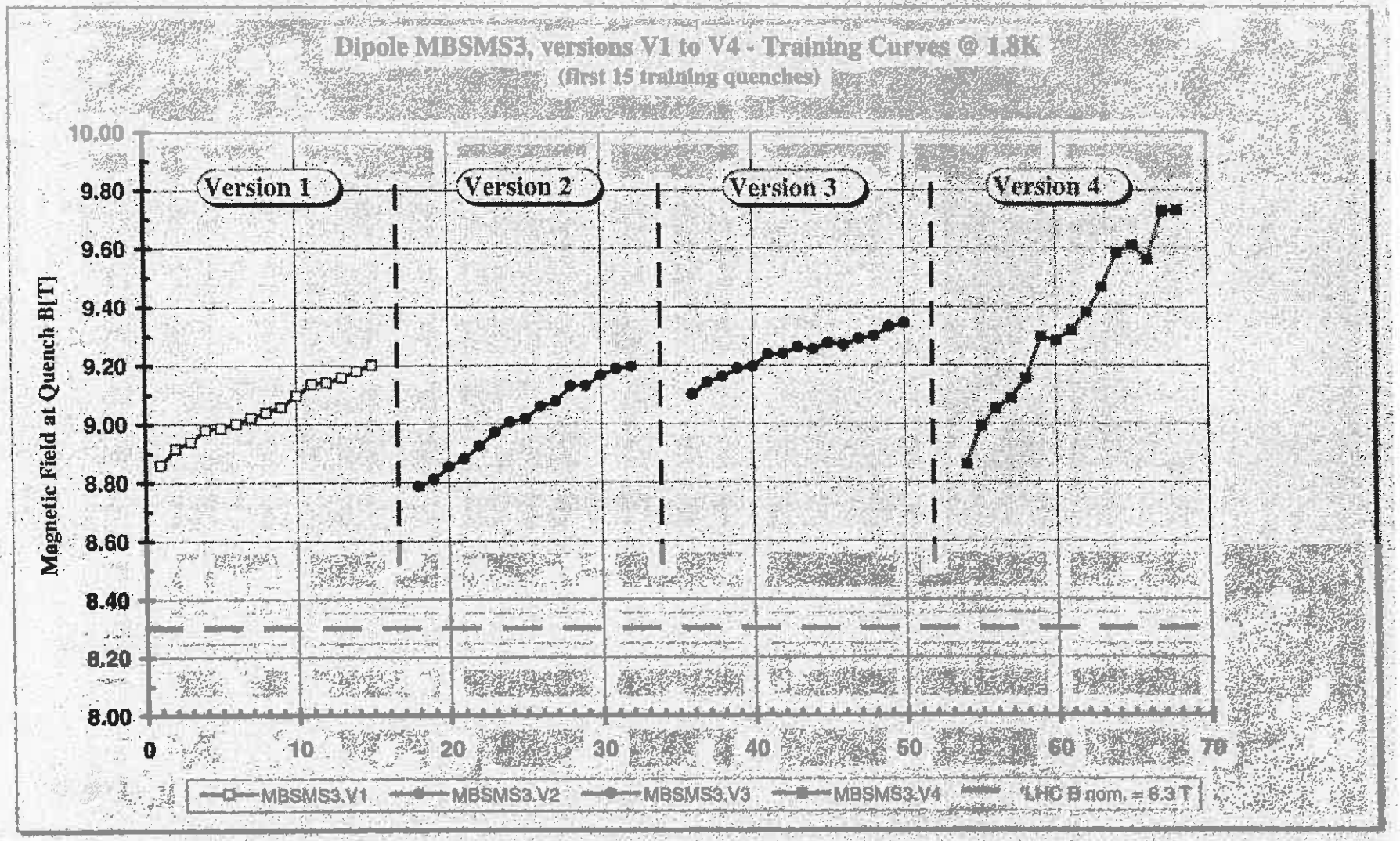
Dipole MBSMS3, versions V1 to V4 - Training Curves @ 1.8K
(first 15 training quenches)
Magnetic Field at Quench B[T]
10.00
9.80
9.60
9.40
9.20
9.00
8.80
8.60
8.40
8.20
8.00
Version 1
Version 2
Version 3
Version 4
0
10
20
30
40
50
60
70
MBSMS3.V1
MBSMS3.V2
MBSMS3.V3
MBSMS3.V4
LHC B nom. = 8.3 T
MBSMS3_sum MBSMS3 Training Printed 20/3/97

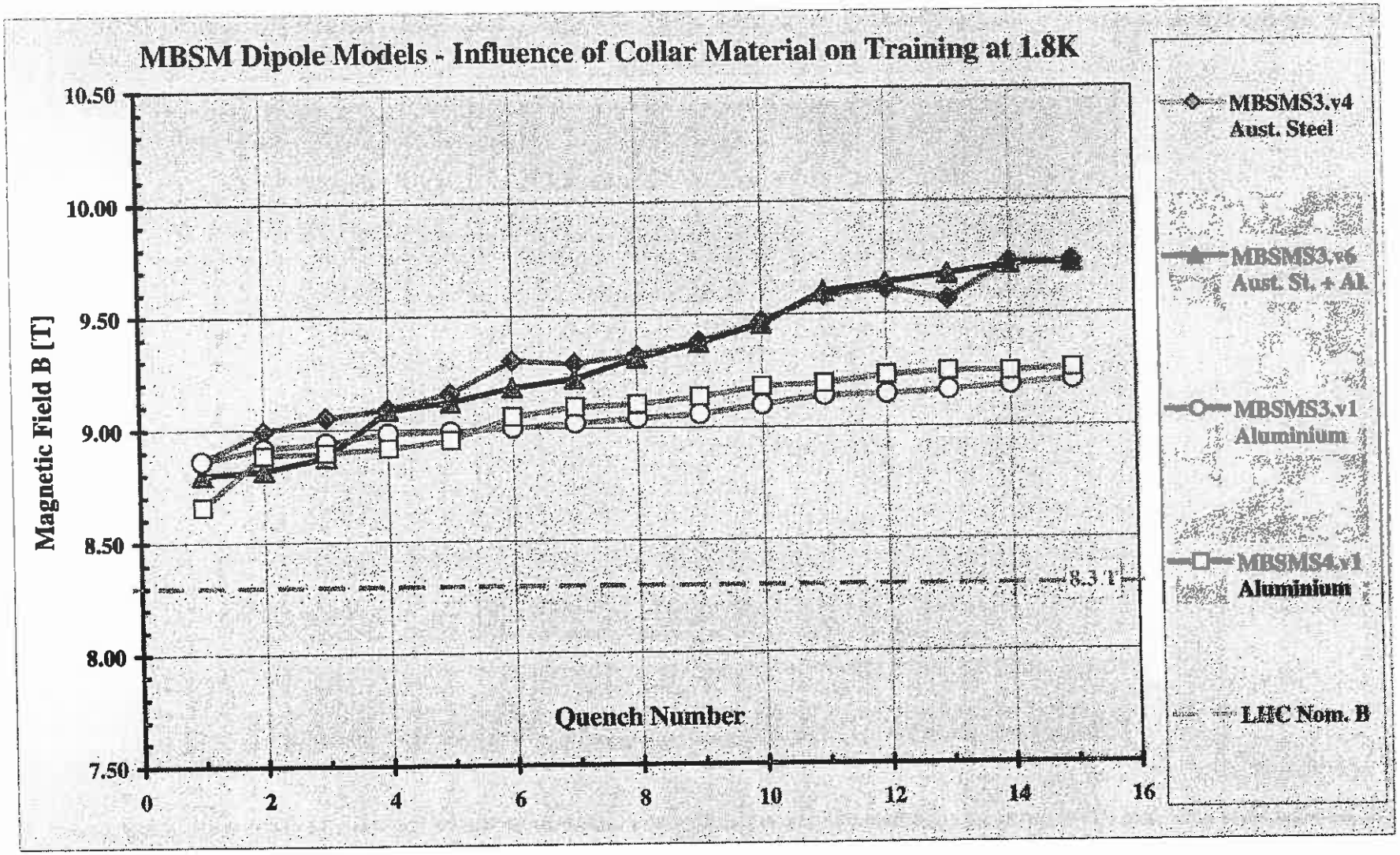

MAC'98_Quench_sum_1.xls S3,4_collar_material Printed 8/6/99 14:18

COIL PRE-COMPRESSION VERSUS RADIAL SUPPORT

– One very debated question regarding the mechanical design of acelerator magnets is: do we really need to pre-compress the coils azimuthally?

– Data from a short SSC dipole magnet model built at KEK (magnet SD501/01) suggest that if the radial support is not good enough, a high pre-compression can improve quench performance.

– However, data from a short SSC dipole magnet model built at BNL (magnet DSV016) show that if the collared-coil assembly is fully locked by the yoke, then pre-compression may not be that important for quench performance.

INFLUENCE OF COIL PRESTRESS ON QUENCH PERFORNANCE: TEST RESULTS OF KEK 1-m Long DIPOLE SD501/01
(Courtesy T. Shintomi, KEK)

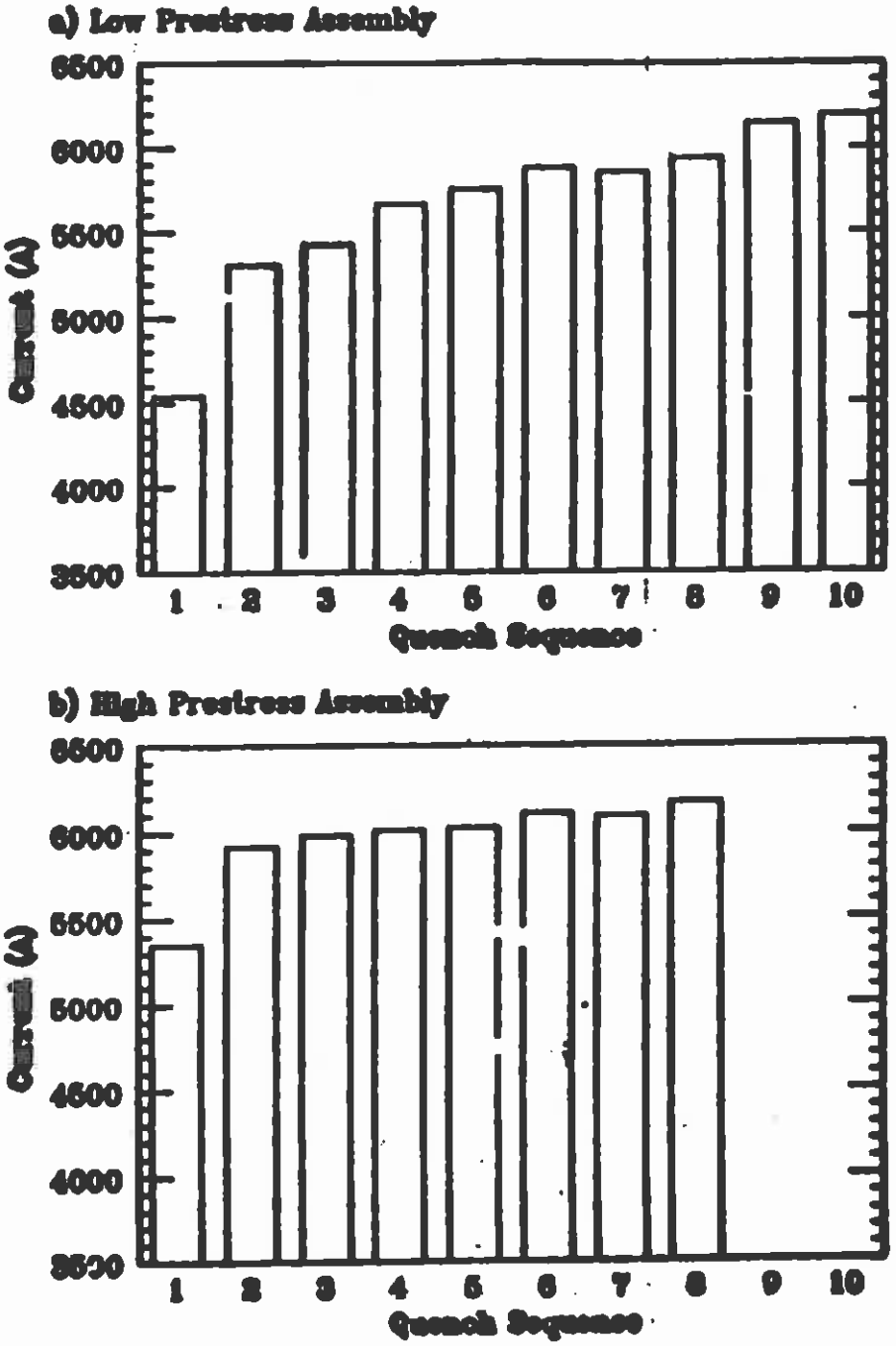

INFLUENCE OF COIL PRESTRESS ON QUENCH PERFORNANCE OF LINE-TO-LINE FIT DESIGN MAGNET: TEST RESULTS OF BNL 1.8-m LONG DIPOLE DSV016 (Courtesy P. Wanderer, BNL)

a) High Prestress Assembly

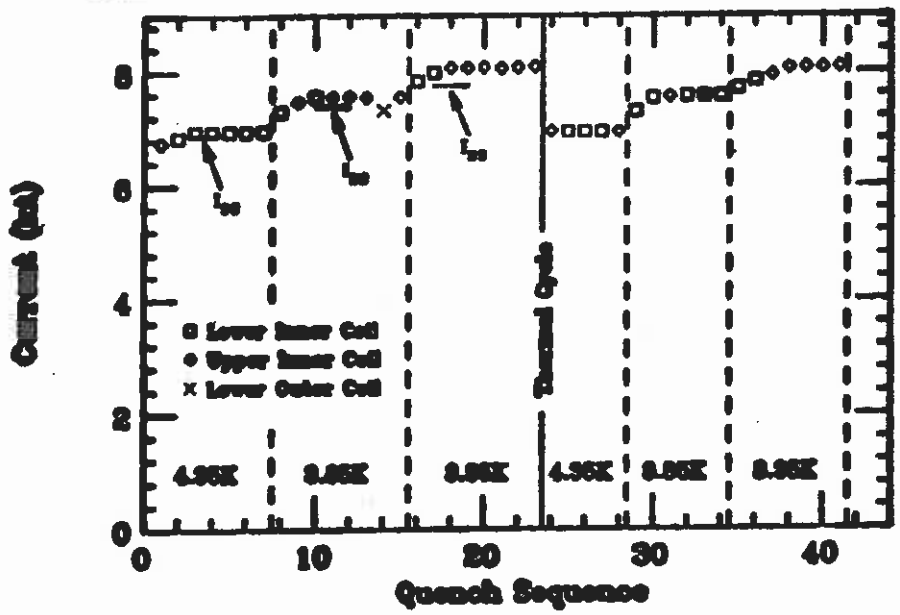

b) Low Prestress Assembly

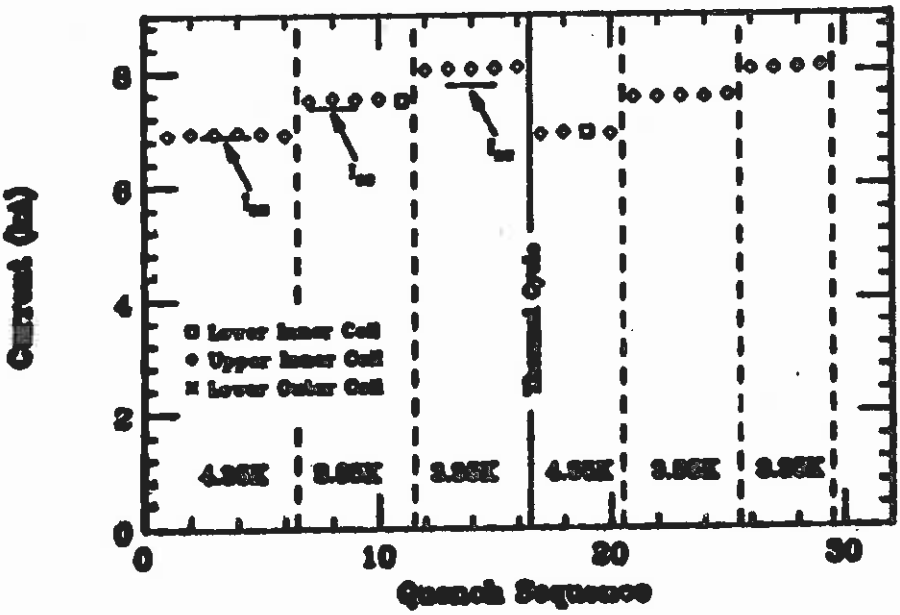

EVOLUTION OF PRESSURE EXERTED BY INNER COIL AGAINST COLLAR POLE DURING ENERGIZATION OF BNL 1.8-m LONG DIPOLE DSV016 (Courtesy J. Muratore, BNL)

a) High Prestress Assembly

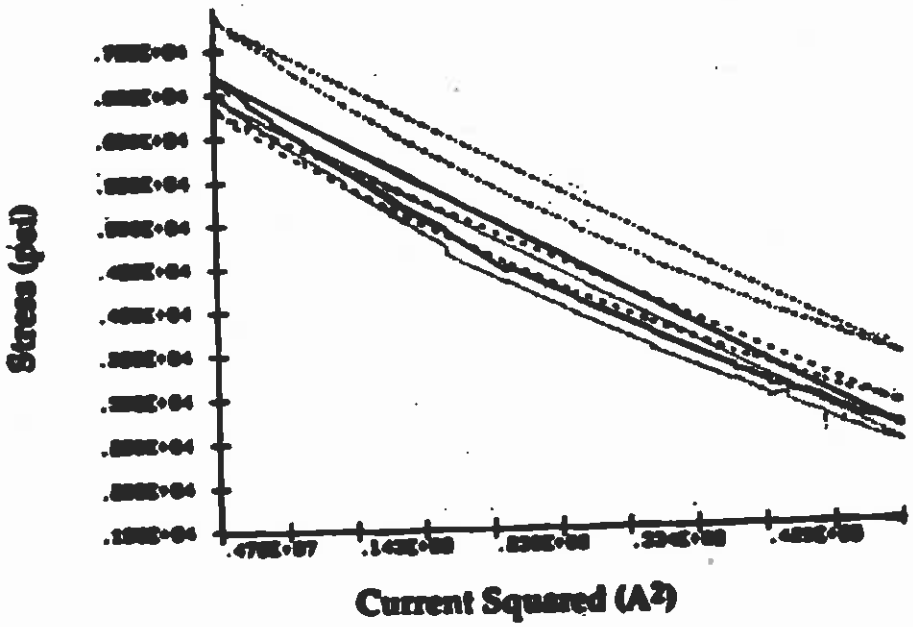

b) Low Prestress Assembly

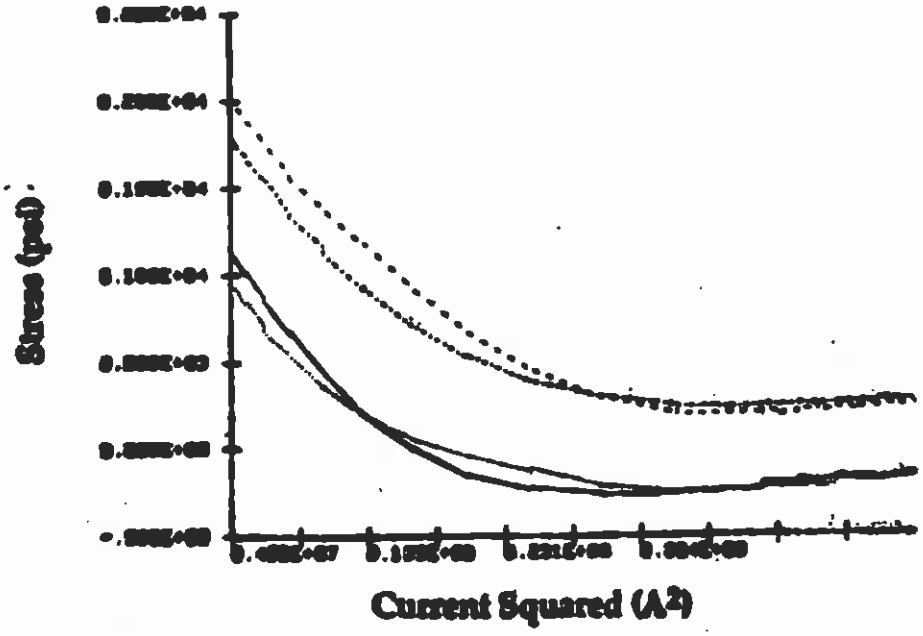

LECTURE 5: MECHANICAL DESIGN OF PARTICLE ACCELERATOR MAGNETS

5.1 Components of the Lorentz Force in Cosθ and Cos2θ Magnetic Designs

5.2 Azimuthal Pre-Compression

5.3 Coil Mechanical Properties

5.4 Collar Designs

5.5 Radial Support
- 5.5.1 Designs with Self-Supported Collared-Coil Assemblies
- 5.5.2 Designs with Fully-Mated Yoke
- 5.5.3 Design with Yoke Midplane Gap
- 5.5.4 RHIC Magnets
- 5.5.5 Azimuthal Pre-Compression Versus Radial Support

5.6 End Support

5.7 Other Designs

END SUPPORT

– As we have described, the axial component of the Lorentz force tends to stretch the coil outwardly along the z-axis.

– In magnets where the yoke is not needed to support the collared-coil assembly, a clearance can be left between the two. If the axial stresses resulting from the Lorentz force do not exceed the yield stress of the coil, it is possible to let the collared-coil expand freely within the iron yoke.

Examples: Quadrupole magnets designed at CEA/Saclay for HERA, SSC and LHC.

– However, in magnets where there is contact between collar and yoke, it is essential to prevent stick/slip motions of the laminated collars against the laminated yoke and to provide a stiff support against the axial component of the Lorentz force.

Examples: The ends of SSC and LHC dipole magnet coils are contained by thick stainless steel end plates welded to the shell.

Ratcheting of Laminated Collared-Coil Assembly within Laminated Yoke

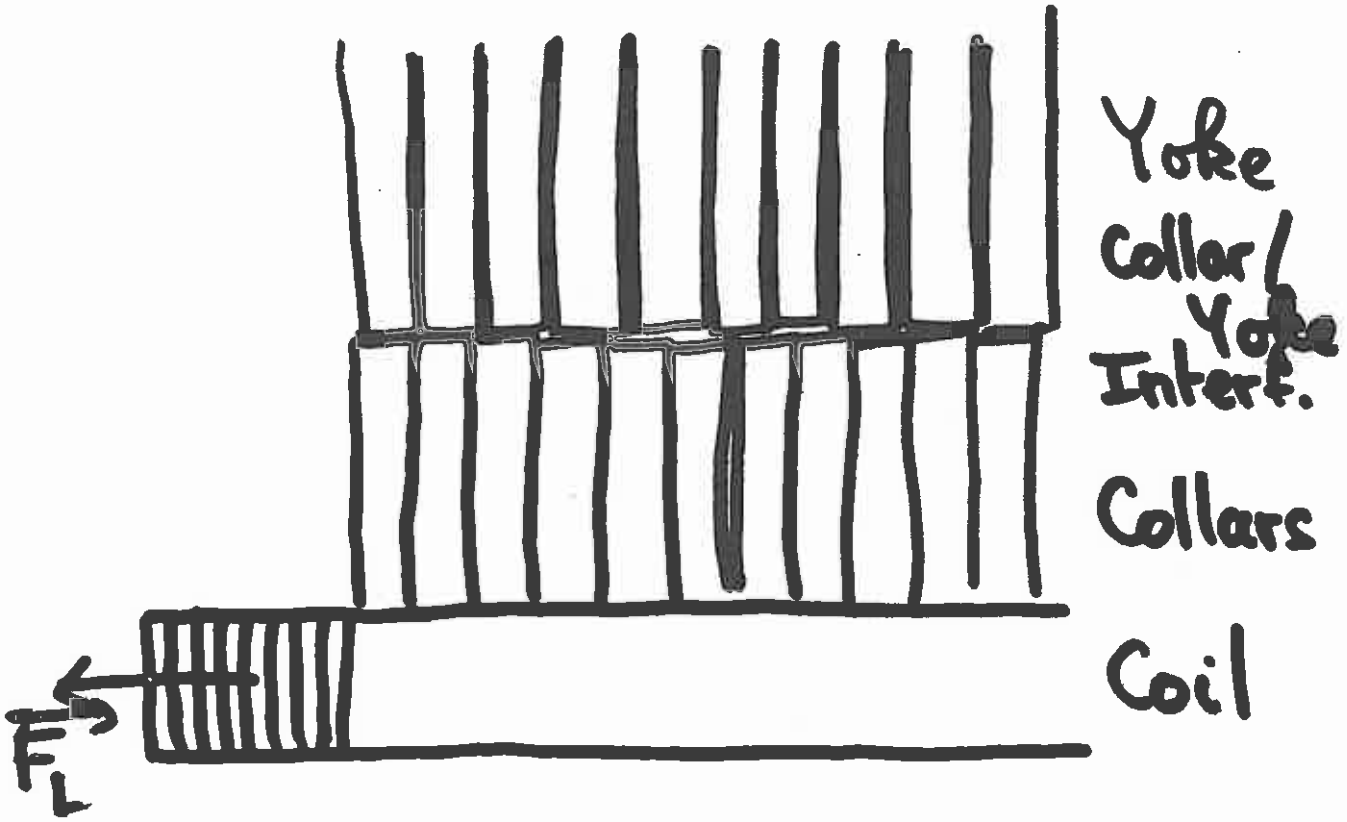

EVIDENCES OF RATCHETTING

– SSC dipole magnet prototype DD0010 had ill defined collar/yoke interface and thin (3/4" thick), split end plates.

The measured axial force exerted by the coils against the end plates appears to increase after each excitation cycle and ramp to quench.

– SSC dipole magnet prototype DD0012 had good clamping of the collared-coil assembly by the yoke and thick (1.5"), single-piece end plates.

The measured axial end force at zero current appears to remain roughly constant throughout cold test.

EVOLUTION OF THE FORCE EXERTED BY THE COIL AGAINST THE END PLATES DURING THE QUENCH TESTING OF BNL 17-m LONG DIPOLES DD0010 & DD0012 (Courtesy J. R. Turner, SSCL)

a) Loose Yoke-Collar Assembly and Thin Split End Plates (DD0010)

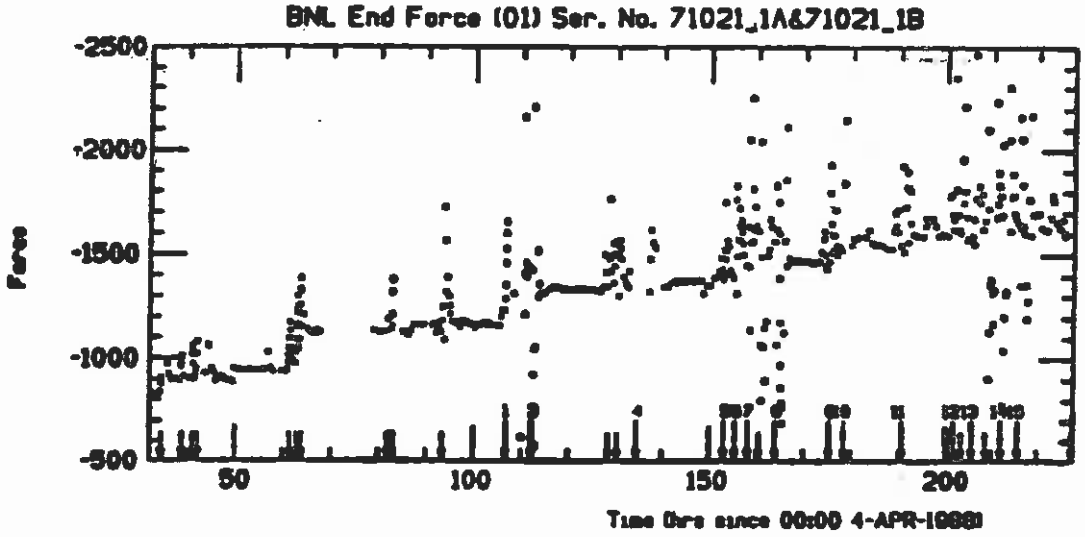

b) Tight Yoke-Collar Assembly and Thick Solid End Plates (DD0012)

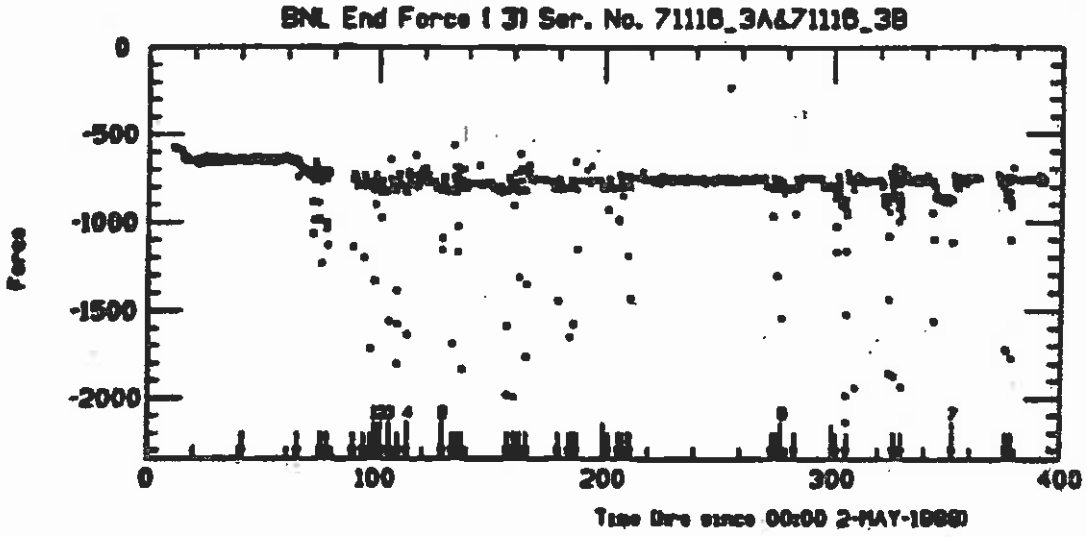

Early SSC/BNL 4-cm-Aperl., 17-m-long SSC Dipole Magnets*

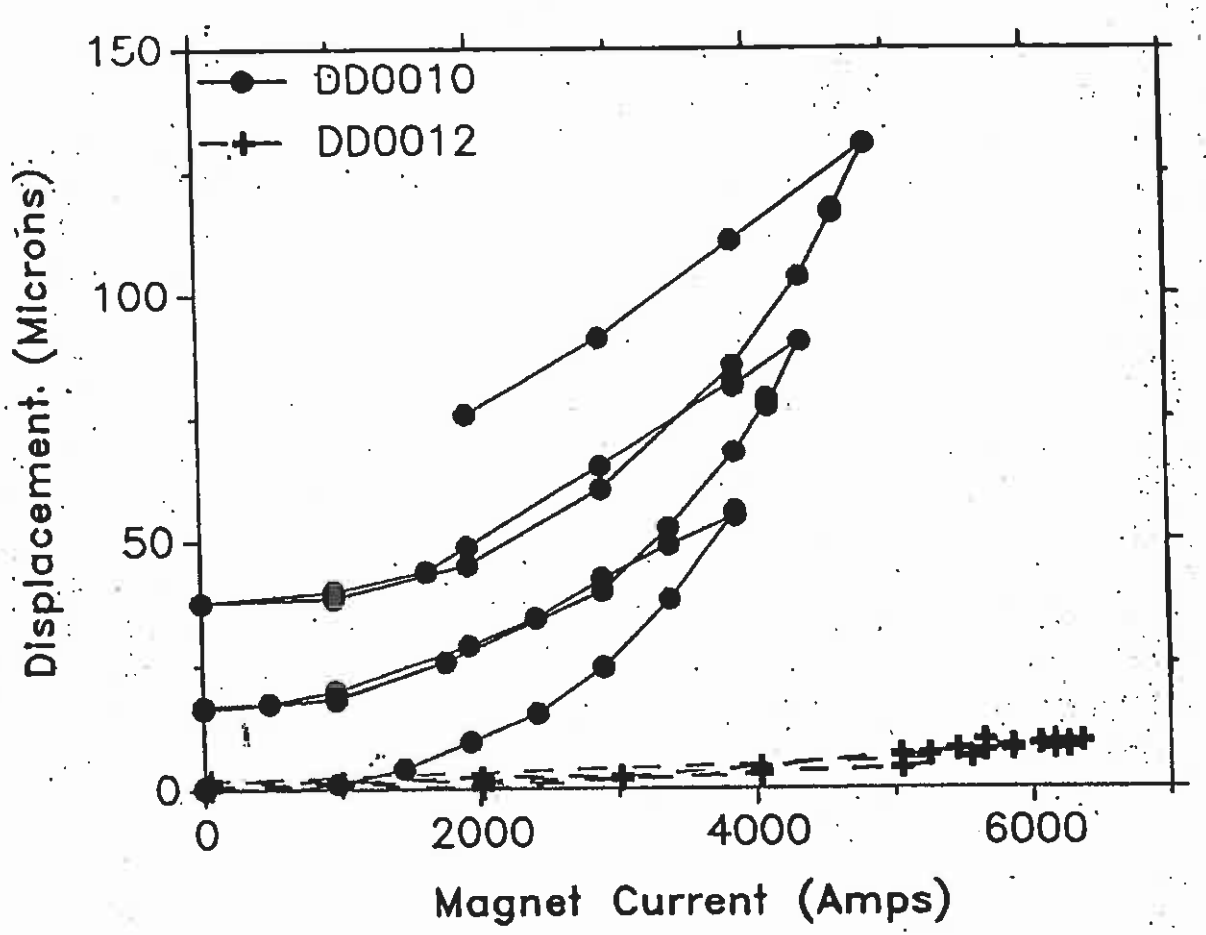

Figure 3. Deflection of the lead end plate as a function of current for three excitations of each magnet.

*Courtesy J. Strait

INFLUENCE OF YOKE-COLLAR INTERFACE AND AXIAL SUPPORT ON QUENCH PERFORMANCE: TESTS RESULTS OF BNL 17-m LONG DIPOLES DD0010 & DD0012

a) Loose Yoke–Collar Assembly and Thin Split End Plates (DD0010)

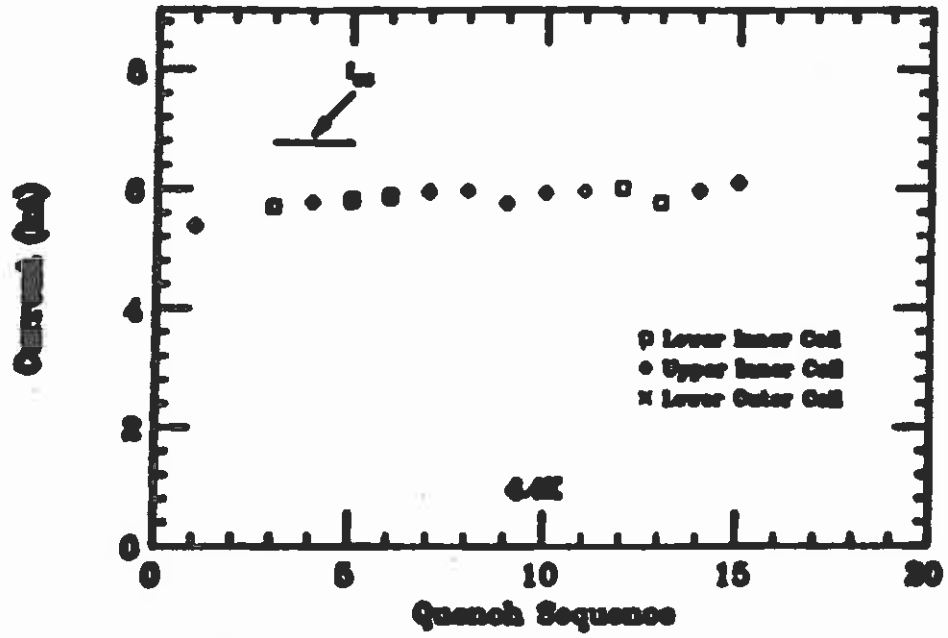

b) Tight Yoke–Collar Assembly and Thick Solid End Plates (DD0012)

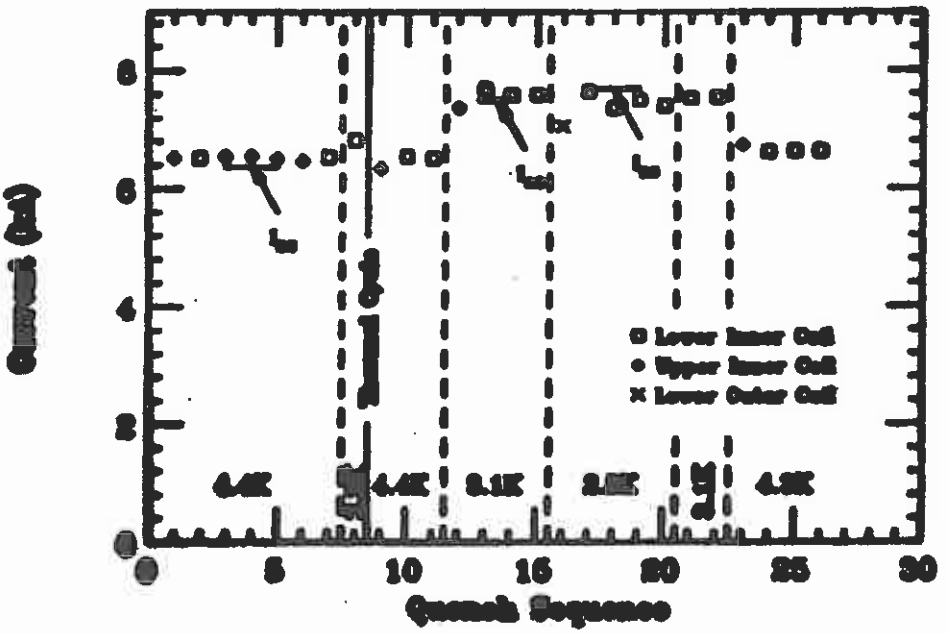

OTHER EVIDENCES OF THE NEED OF AXIAL SUPPORT

– 4-cm-aperture, 17-m-long SSC dipole magnet prototype DC0201 was first assembled with end constraints and exhibited very good quench perfomance.

– The constraint was then removed at one end and the magnet was retested. The quench performance appeared seriously degraded, with quenches originating in the outer coils.

BNL 4-cm-Apert., 17-m-Long Dipole Magnet

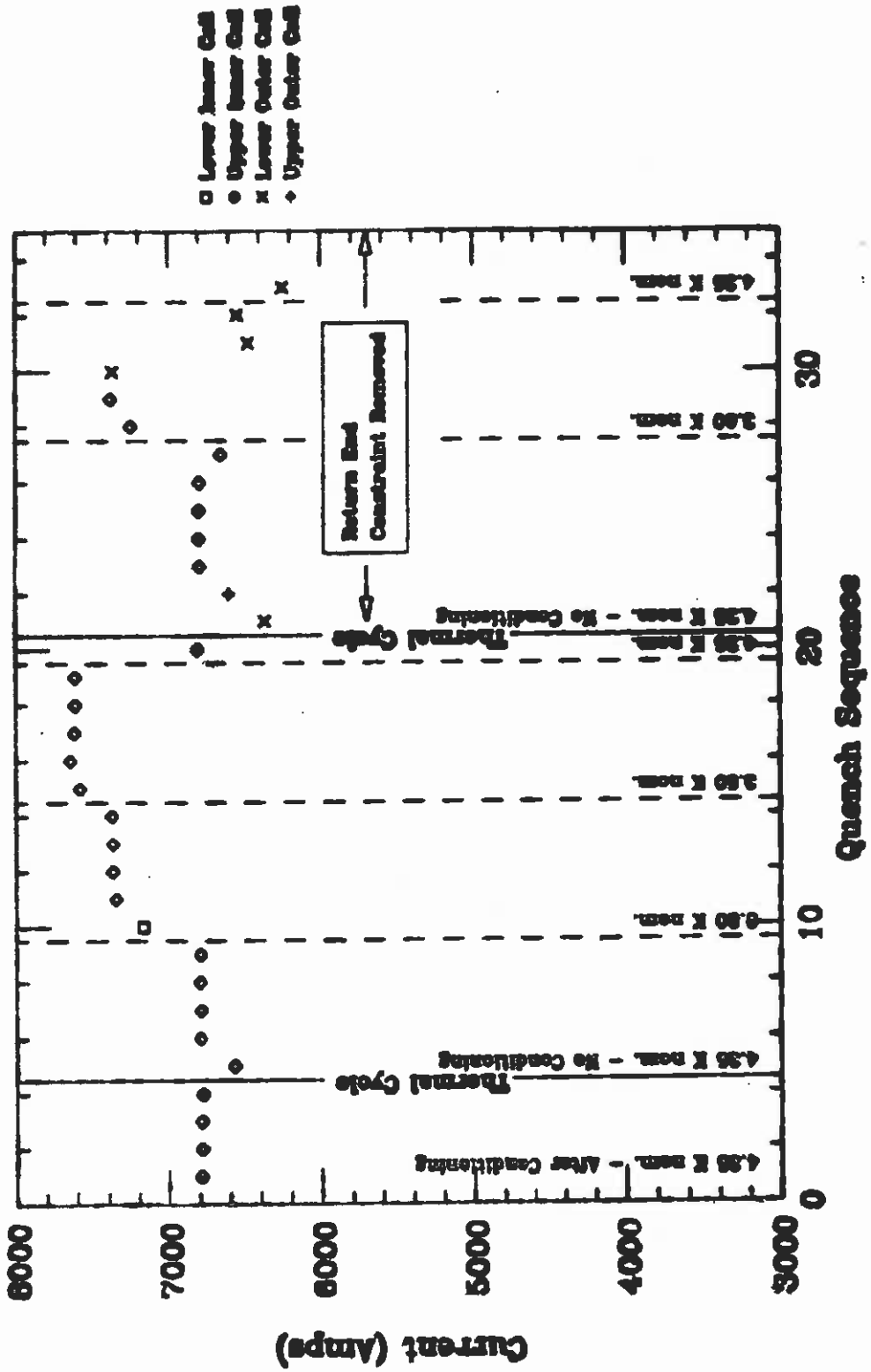

MODEL OF AXIAL MECHANICS

– The axial component of the Lorentz force pull on the coil ends and push against the coil end spacers.

– Furthermore, part of this force is shared by friction between the collared-coil assembly, the yoke and the outer shell.

– As a result, only a fraction of the computed electromagnetic force is actually transferred to the end plates. This fraction depends on:

- ***The rigidity of the coil ends,***

- ***The clamping of the collared-coil assembly by the yoke.***

Example: The clamping of the collared-coil assembly by the yoke is tighter in the 5-cm-aperture, 15-m-long SSC dipole magnet prototypes developed at FNAL than in the prototypes developed at BNL.

As a result, more of the axial component of the Lorentz force is redistributed to the yoke and the shell and the fraction tansmitted to the end plate is smaller.

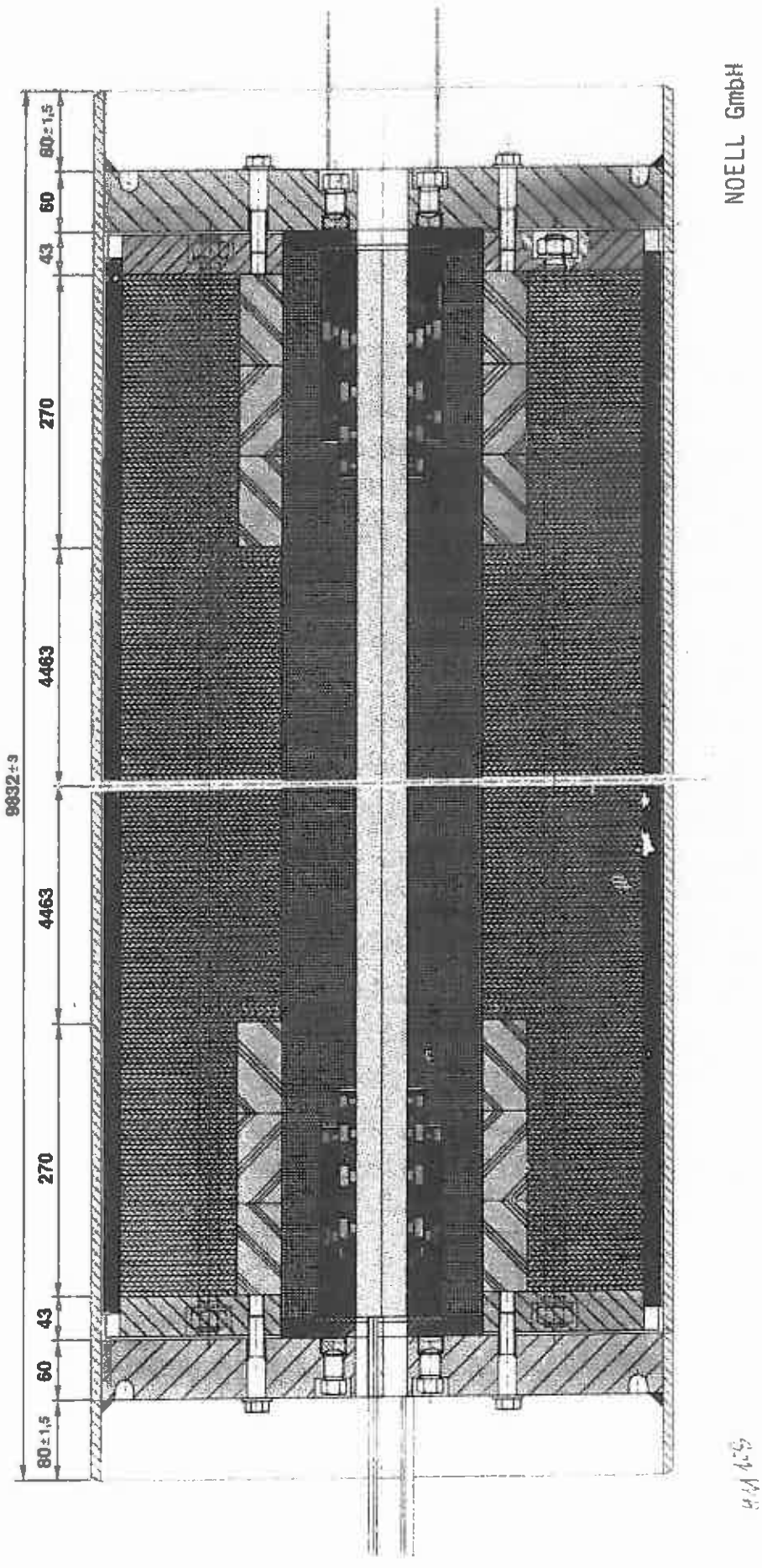
NOELL GmbH
9932±3
80±1,5
60
43
270
4463
4463
270
43
60
80±1,5

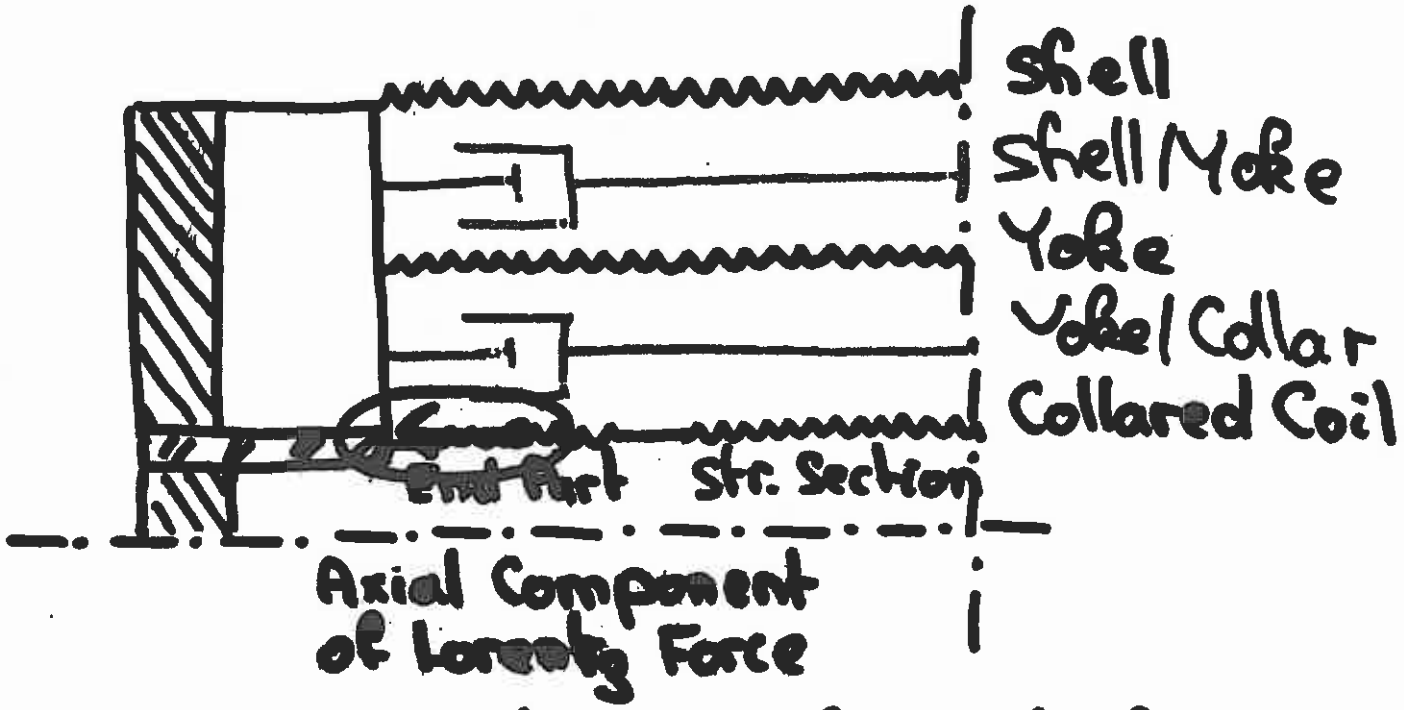

Effect of axial comp. of Lorentz force depends on

- End Part Stiffness
- Yoke/Collar Interference

FNAL Magnets

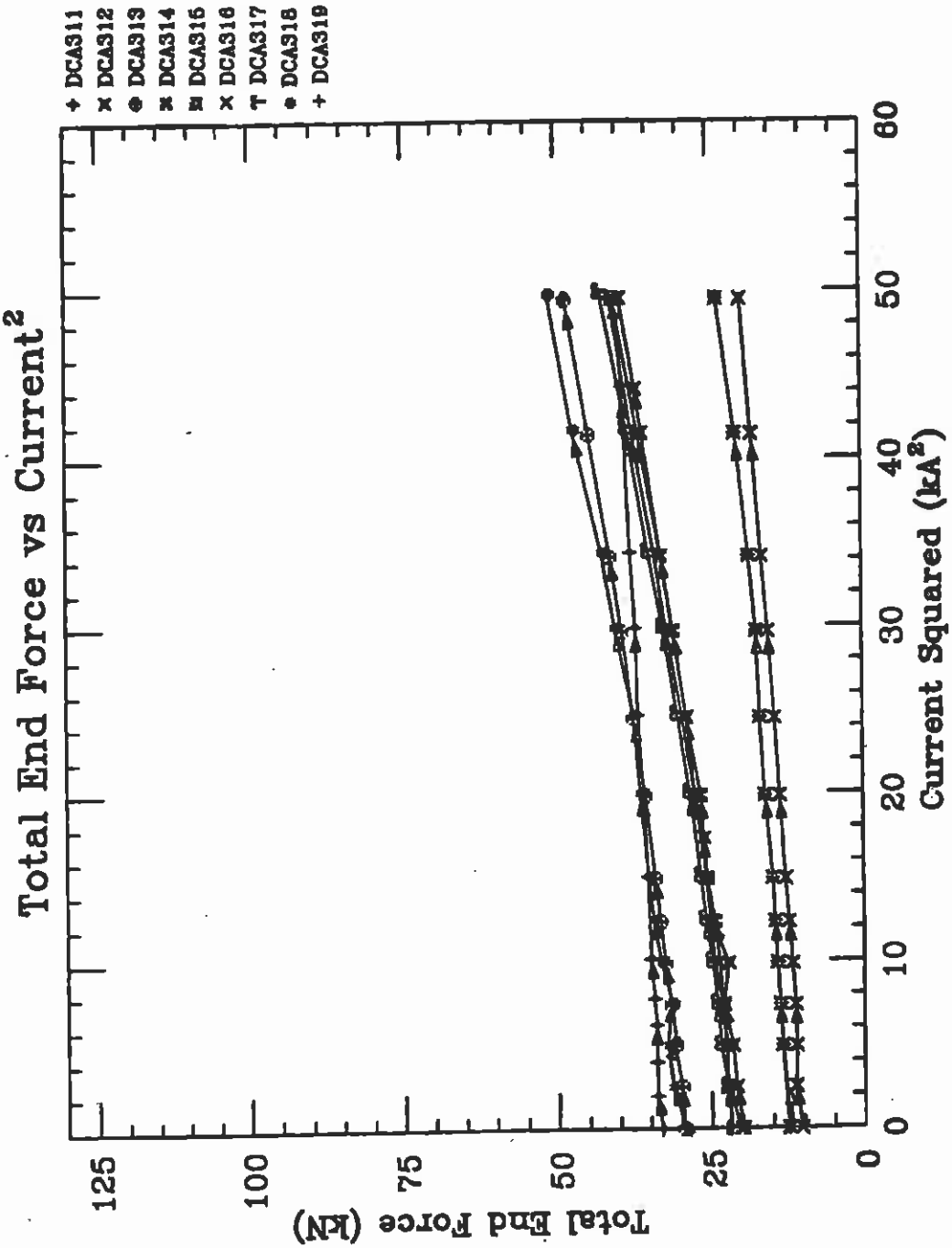

BNL Magnets

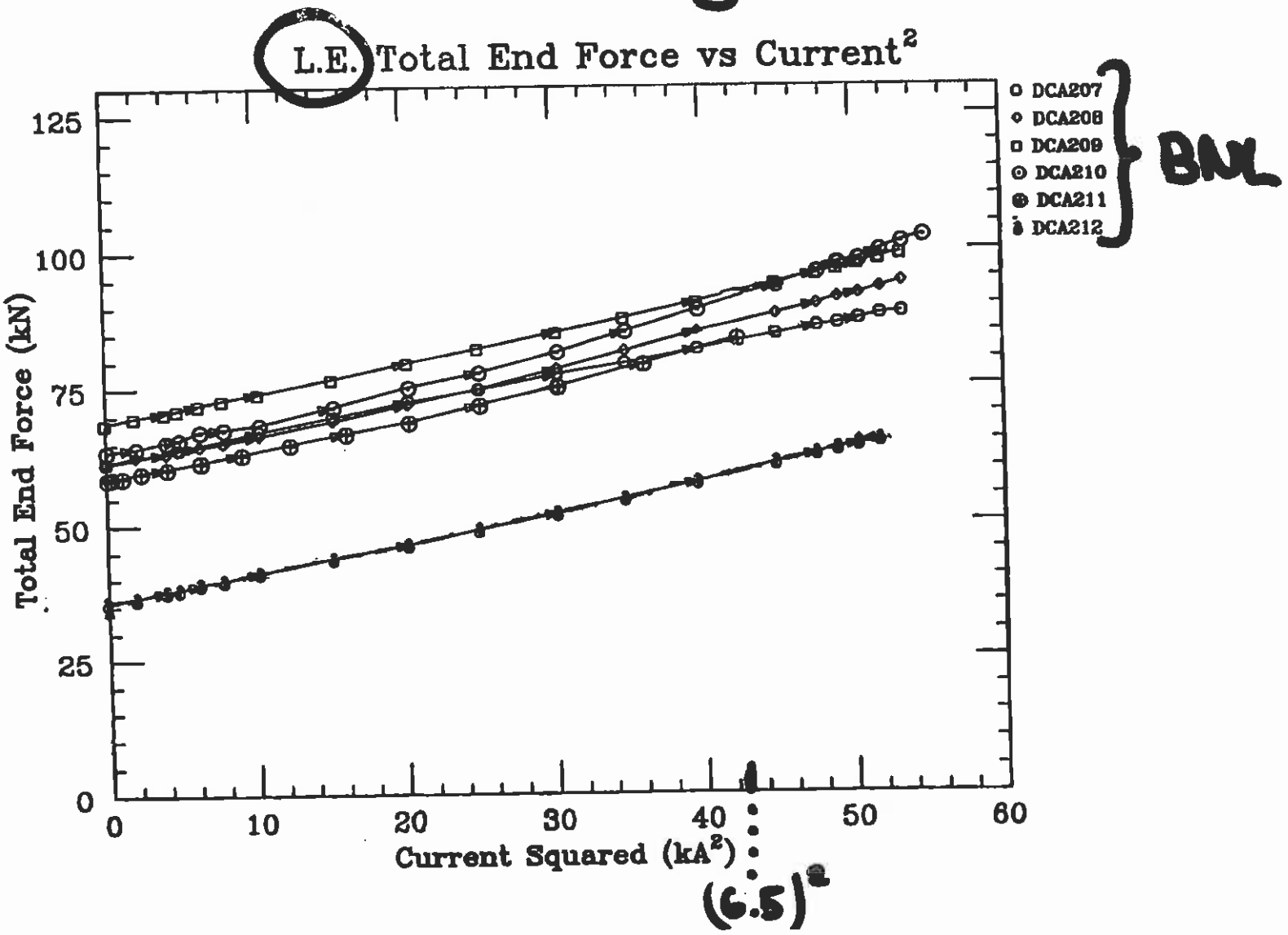
L.E. Total End Force vs Current²
Total End Force (kN)
Current Squared (kA²)
0
25
50
75
100
125
0
10
20
30
40
50
60
DCA207
DCA208
DCA209
DCA210
DCA211
DCA212
BNL
(6.5)²

Predicted Slope ≃ 2 kN/kA² *

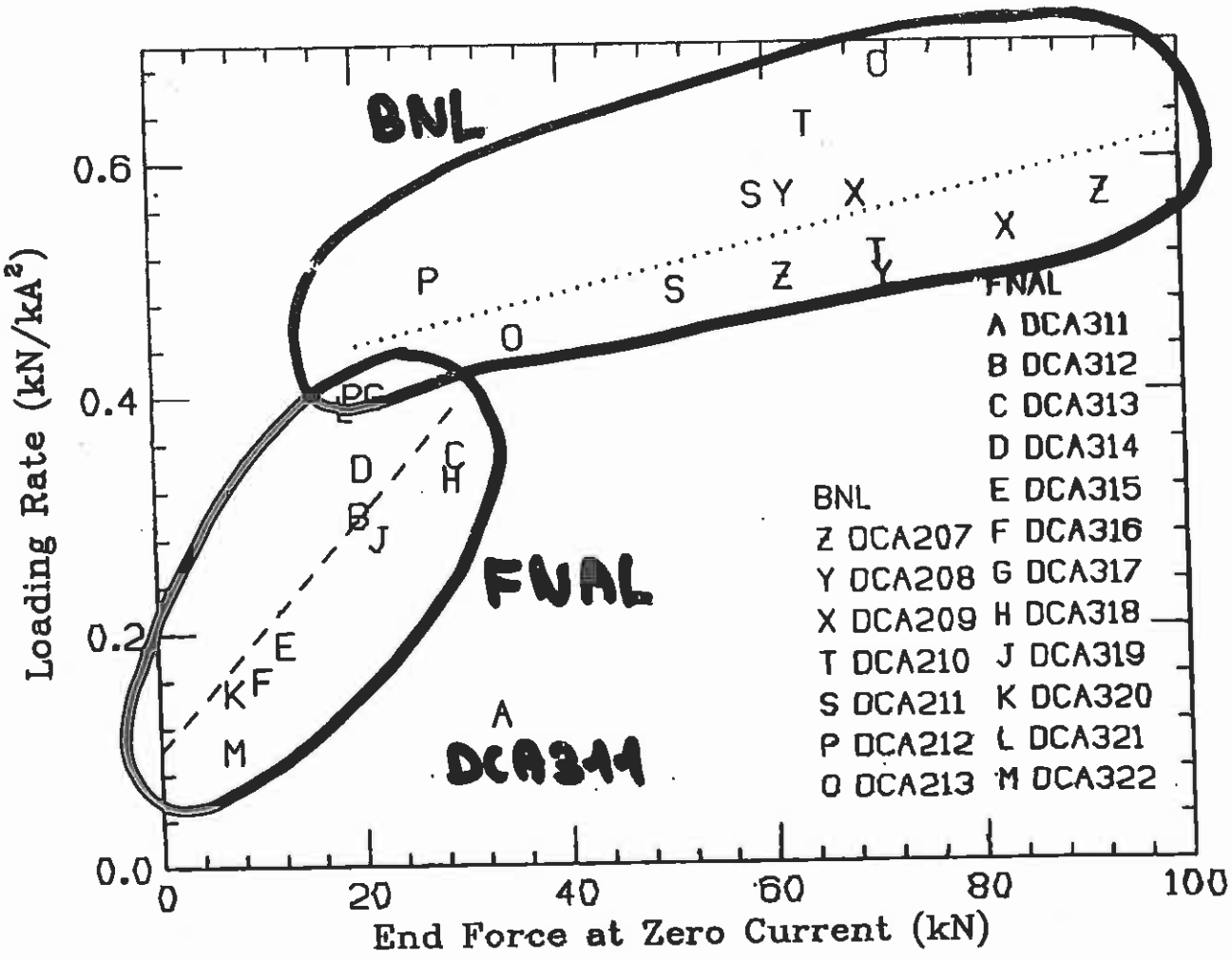

* Courtesy D. Orrel

SHARING OF THE AXIAL COMPONENT OF THE LORENTZ FORCE

– The sharing of the force between the collared-coil and the yoke takes place over a certain length.

– The tighter the yoke clamping, the shorter the transition length and the smaller the fraction of the Lorentz force transmitted to the end plates.

Example: axial strain measurements on the shells of SSC dipole magnet prototypes DD0010 and DD0012. The transition length is shorter for magnet DD0012 where the collared-coil assembly is more tightly clamped by the yoke than for magnet DD0010.

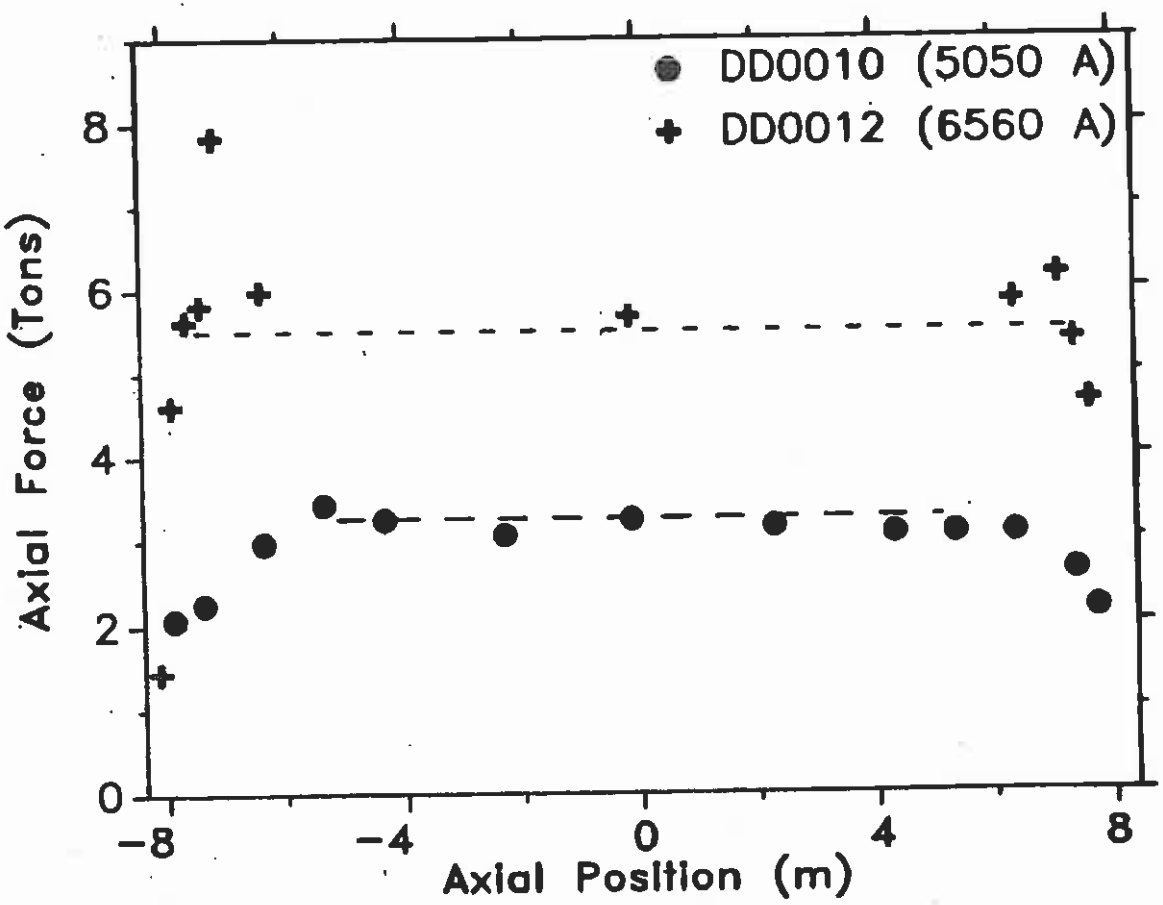

Figure 2. Axial Lorentz force transmitted to the cold mass skin as a function of position along the magnet. The left and right boundaries of the figure represent the ends of the magnet. The dashed lines show the expected force if the load is fully shared between the coil and the skin.

AXIAL PRE-LOADING

– As we have seen, in magnet designs where the radial support of the yoke is needed, it is preferable to prevent axial elongations of the collared-coil assembly. This is done by blocking the coils against stiff end plates which are welded to the outer shell.

– However, during cooldown, it can happen that the collared-coil assembly shrinks more than the shell-end-plate assembly, resulting in a gap between the coil ends and the end plates.

– To prevent the occurence of such a gap, the coil ends are usually *pre-loaded* at room temperature by means of set screws mounted on the end plates.

This axial pre-load also helps increasing the compaction and the rigidity of the coil ends.

– Note, however, that unlike the azimuthal pre-compression, which is of same direction as the azimuthal component of the Lorentz force, the axial pre-load is of opposite direction to the axial component of the Lorentz force, which is not favorable.

THERMAL SHRINKAGE (II)

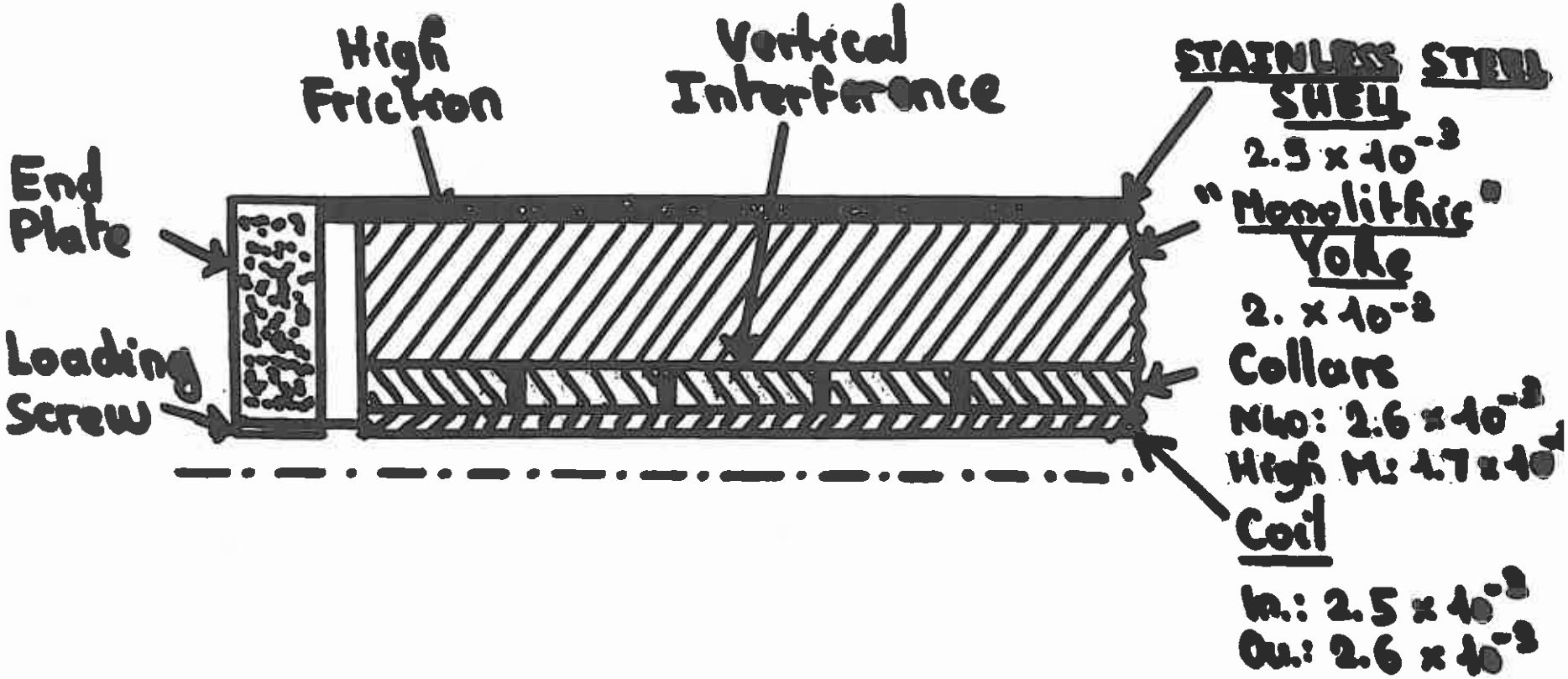

BNL End Design (5 cm Apert.)

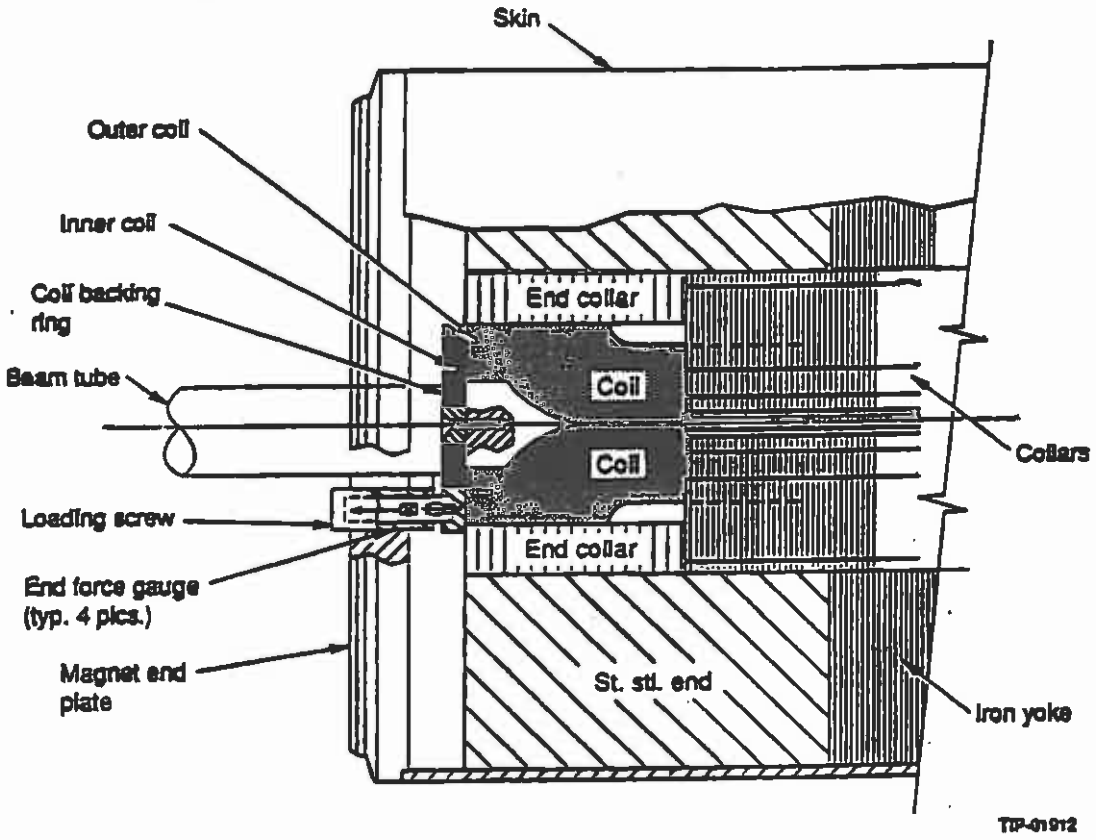

- Internal Splice
- Collars over Ends

AXIAL PRE-TENSIONING

– The coil ends of most SSC dipole magnet prototypes and of some LHC interaction region quadrupole magnet models developed at FNAL are clamped radially by aluminum collets.

– In one LHC interaction region quadrupole magnet model (HGQ05) the collets were bolted to the end plates, while set screws, also mounted on the end plates, applied an axial pre-load to the coil ends.

During cooldown, the collared-coil assembly is expected to shrink more in the axial direction than the shell-end-plate assembly.

Then, bolting the collets to to the end plates should result, at the end of cooldown, in a tensile axial force pulling on the coil straight section.

This tensile force, when combined with the axial pre-load applied by the set screws, should ensure that the coil ends are compacted and remain in compression.

Furthermore, this axial pre-tensionning is also of the same direction as the axial component of the Lorentz force, which is more favorable.

– Magnet model HGQ05 was rather successful in terms of quench performance, but the details of this complicated axial support still need to be worked out.

FNAL (Lead End) Design

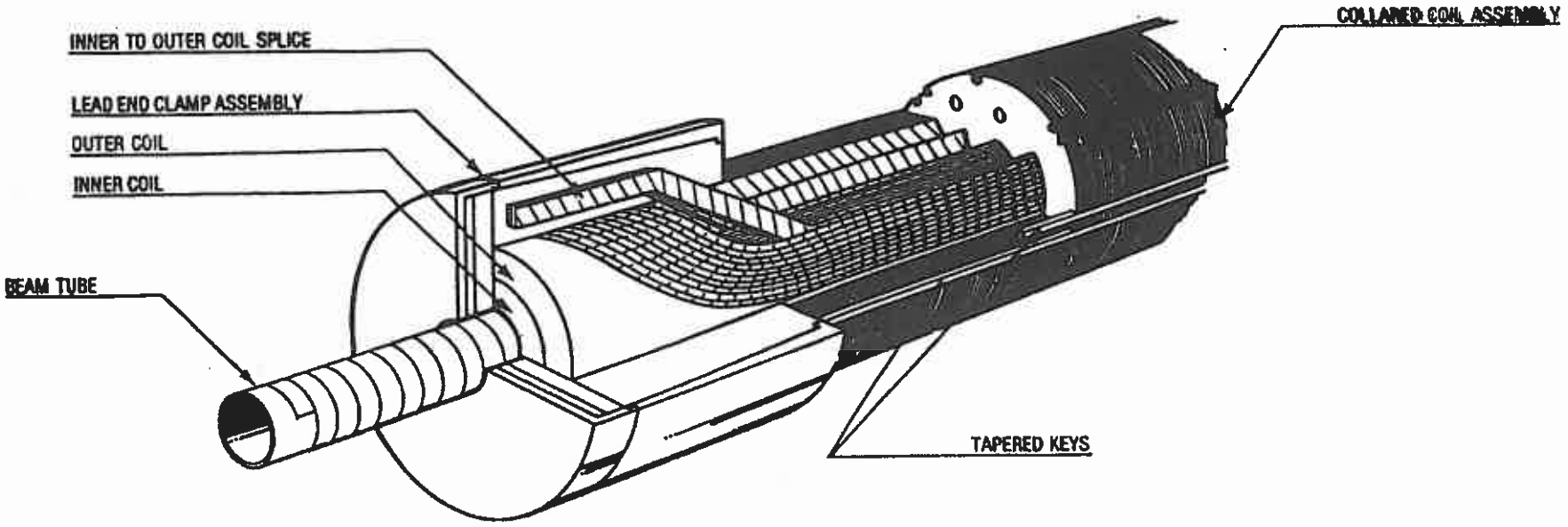

- External Splice
- Collet over Coil Ends

HGQ for LHC IR

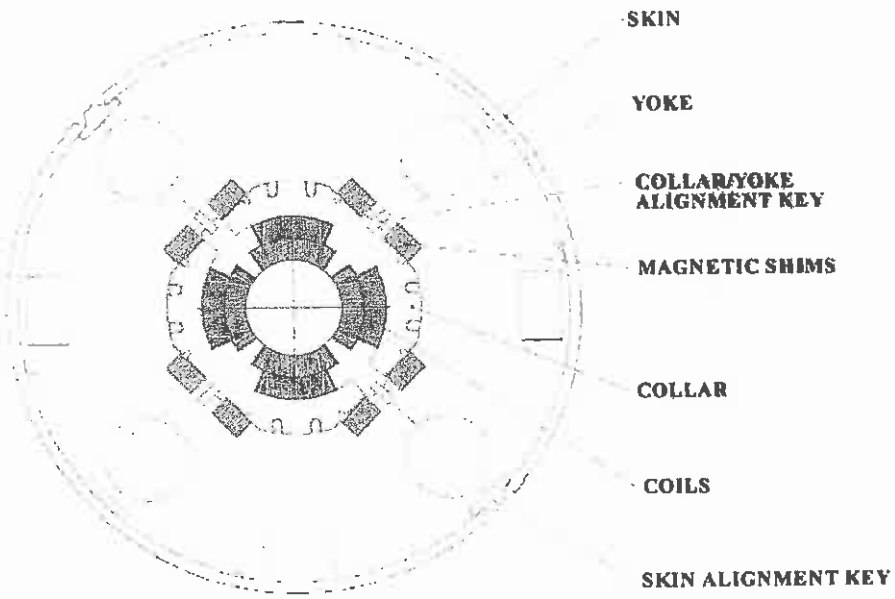

Magnet bore -	70 mm
Magnetic length -	6.3/5.5 m
Nominal field gradient -	200 T/m @ 1.9 K

HGQ for LHC IR

Strand Parameters*

Parameter	Inner cable	Outer cable
Strand diameter [mm]	0.808	0.648
Filament diameter [μm]	6	6
Cu:SC ratio	1.3:1	1.8:1
RRR	100	100
Twist pitch [mm]	10	13
Twist direction	left	right
Ic(5T,4.2K) [A]	600	320
Jc (5T,4.2K) [kA/mm^2]	2.75	2.75

* - SSC strands are used.

Cable Parameters

Parameter	Inner cable	Outer cable
Radial width [mm]	15.4	15.4
Minor edge [mm]	1.326	1.054
Major edge [mm]	1.587	1.238
Keystone angle [deg]	0.990	0.690
Mean thickness [mm]	1.456	1.146
Packing factor	0.91	0.91
Number of strands	38	46
Strand diameter [mm]	0.808	0.648

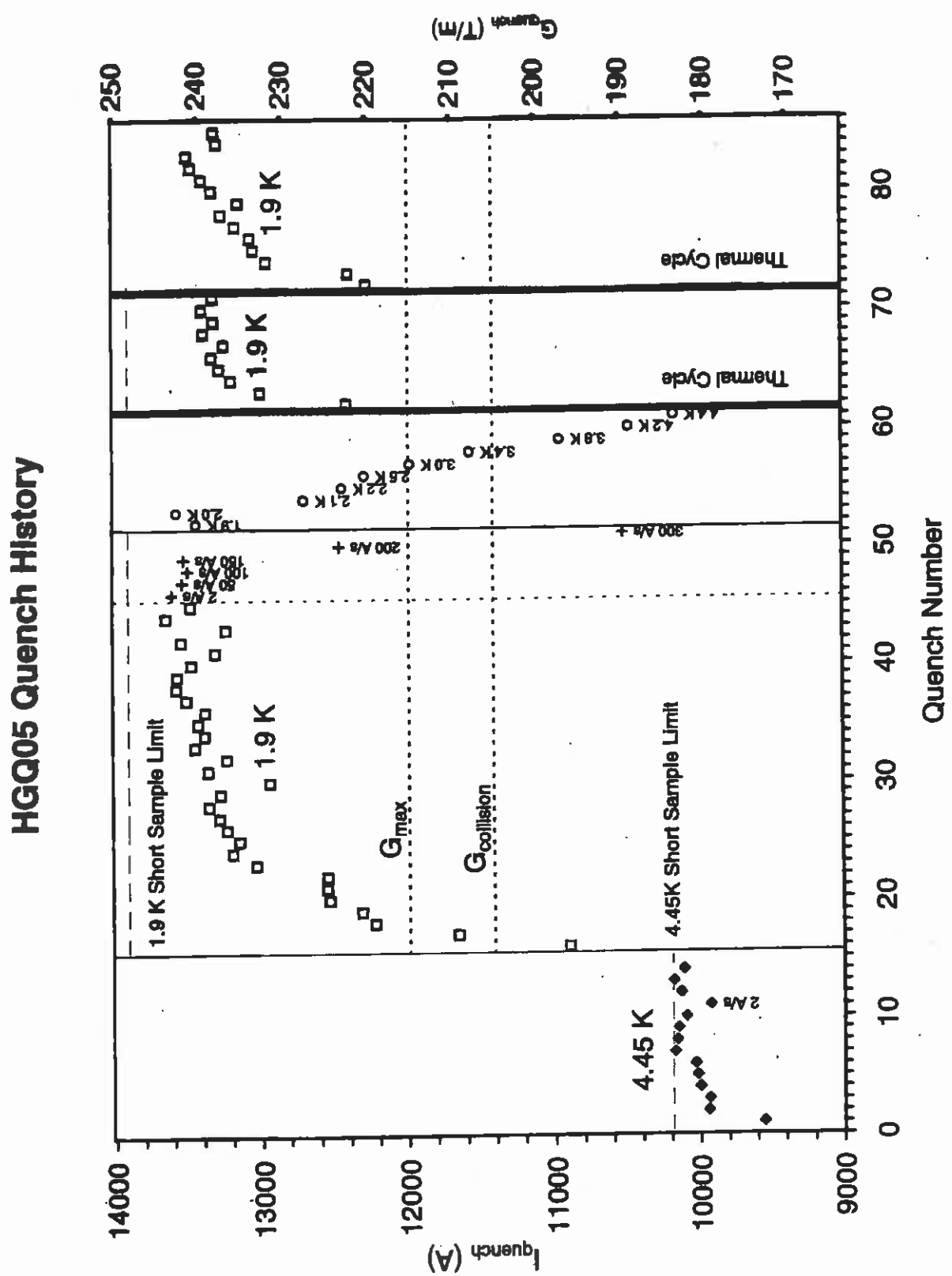
HGQ05 Quench History
I_quench (A)
G_quench (T/m)
Quench Number
1.9 K Short Sample Limit
4.45K Short Sample Limit
G_max
G_collision
1.9 K
4.45 K
Thermal Cycle
Thermal Cycle
2 A/s
200 A/s
300 A/s

LECTURE 5: MECHANICAL DESIGN OF PARTICLE ACCELERATOR MAGNETS

5.1 Components of the Lorentz Force in Cosθ and Cos2θ Magnetic Designs

5.2 Azimuthal Pre-Compression

5.3 Coil Mechanical Properties

5.4 Collar Designs

5.5 Radial Support
- 5.5.1 Designs with Self-Supported Collared-Coil Assemblies
- 5.5.2 Designs with Fully-Mated Yoke
- 5.5.3 Design with Yoke Midplane Gap
- 5.5.4 RHIC Magnets
- 5.5.5 Azimuthal Pre-Compression Versus Radial Support

5.6 End Support

5.7 Other Designs

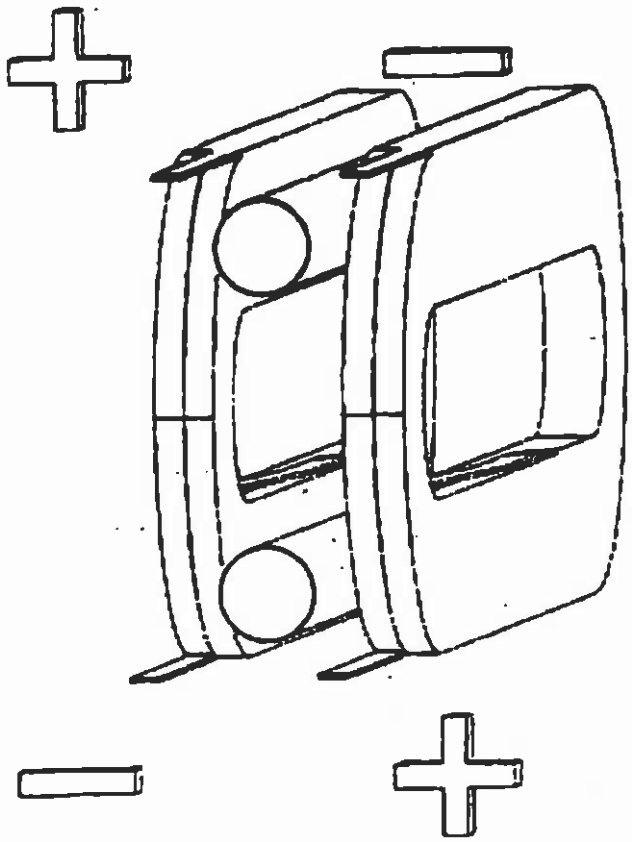

Figure. 1: Schematic of "Common-Coil" Magnet

LBNL Common-Coil
Dipole Magnet Design

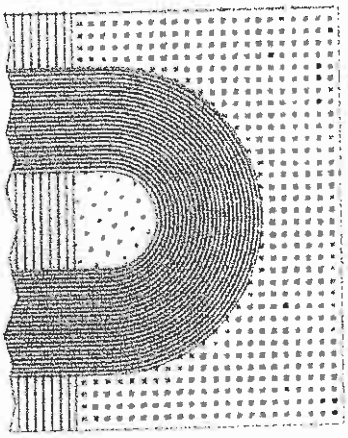

LBNL Common Coil
Dipole Magnet Design

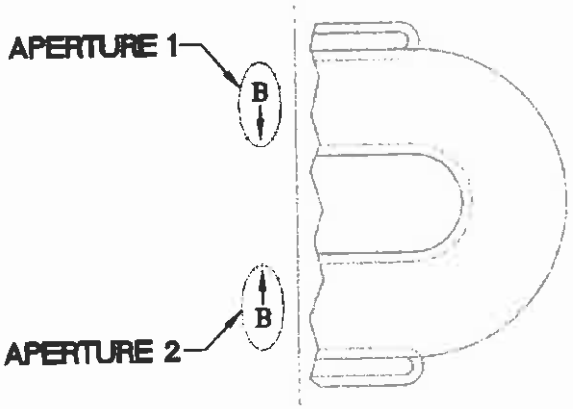

NON-LEAD
COIL END - SIDE VIEW
SCALE 1/4

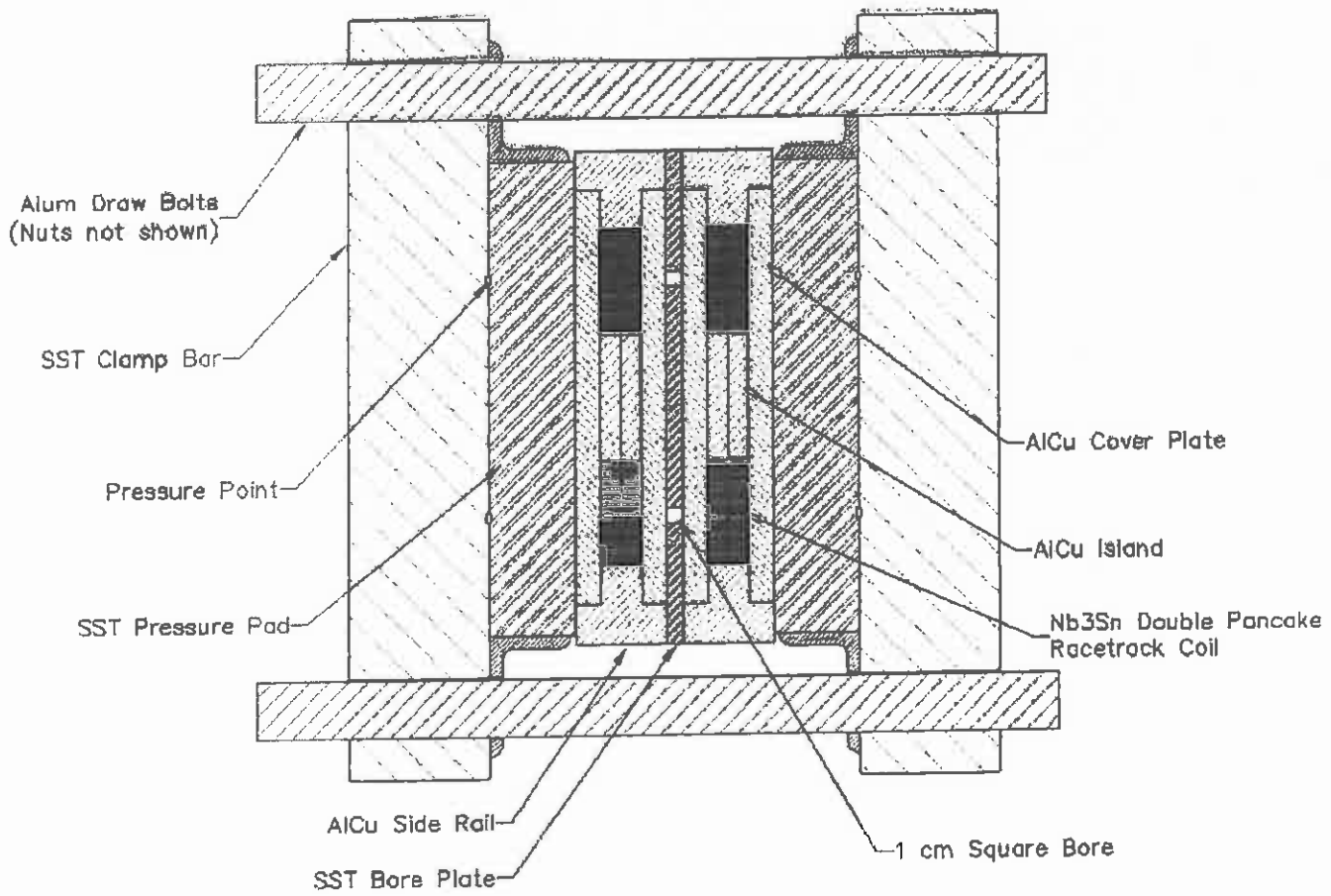

Courtesy S. Gourlay (LBNL)

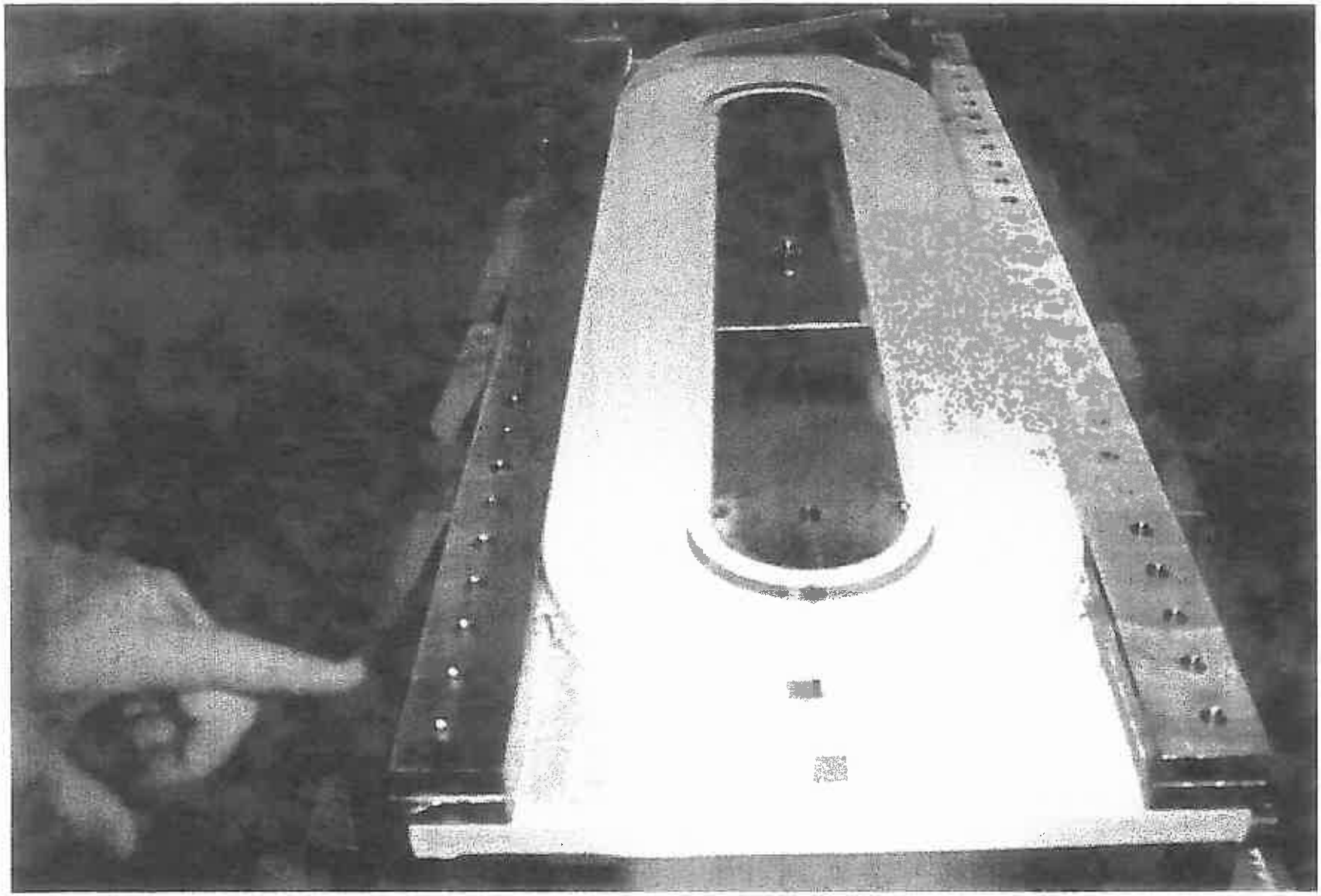

Courtesy S. Gourlay

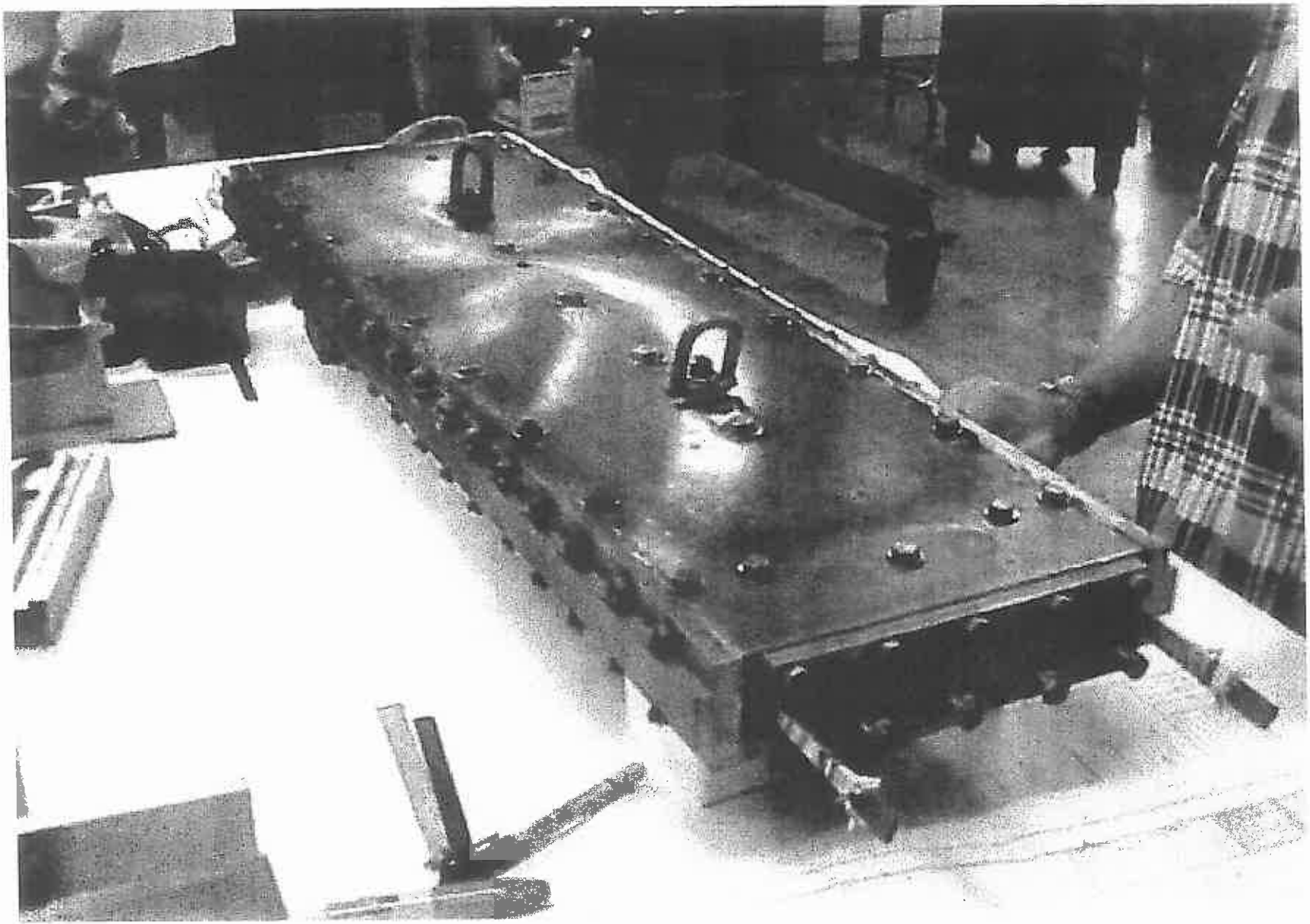

Courtesy S. Gourlay

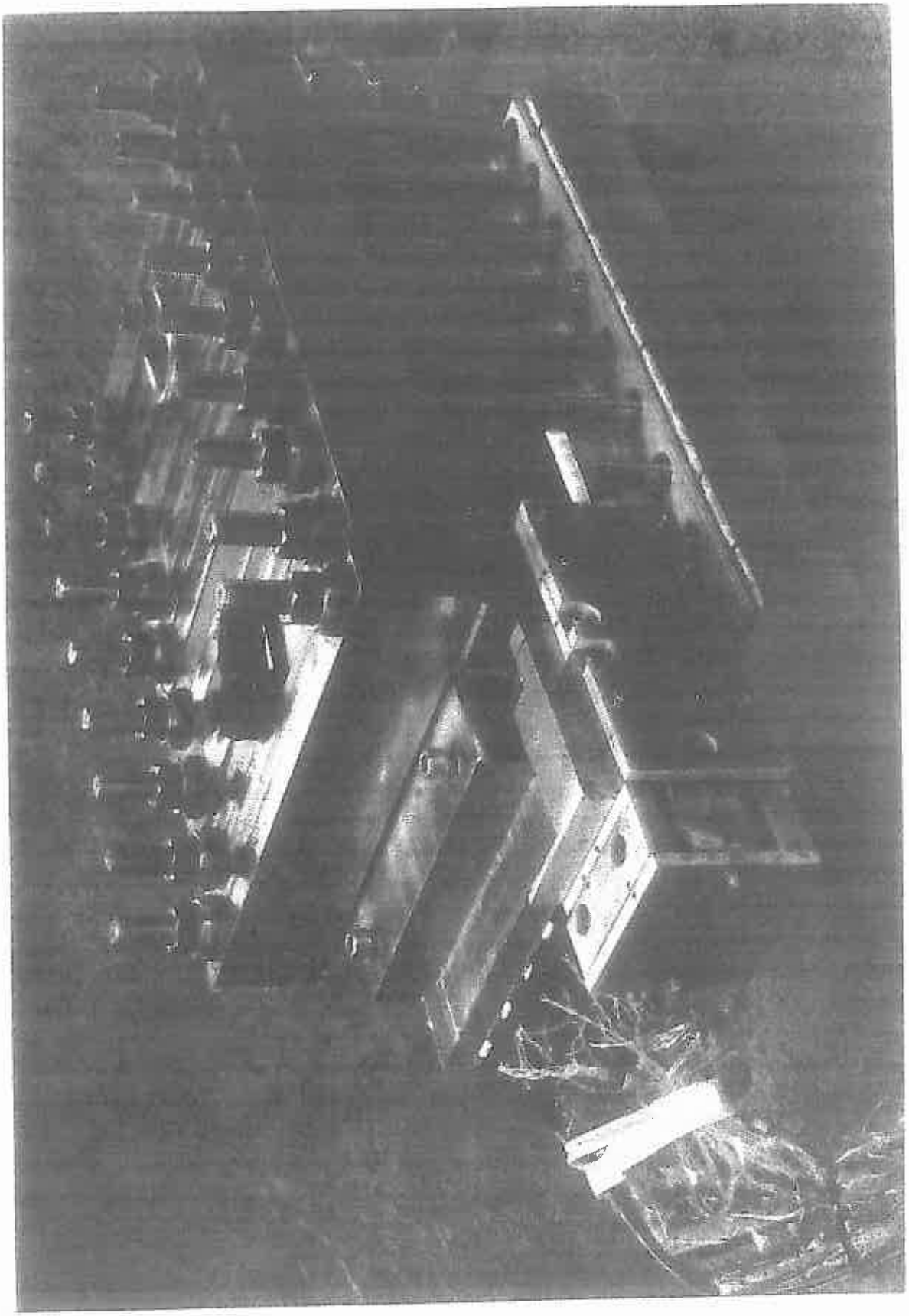

Courtesy S. Gourlay

LBNL Common-Coil Dipole Magnet Model

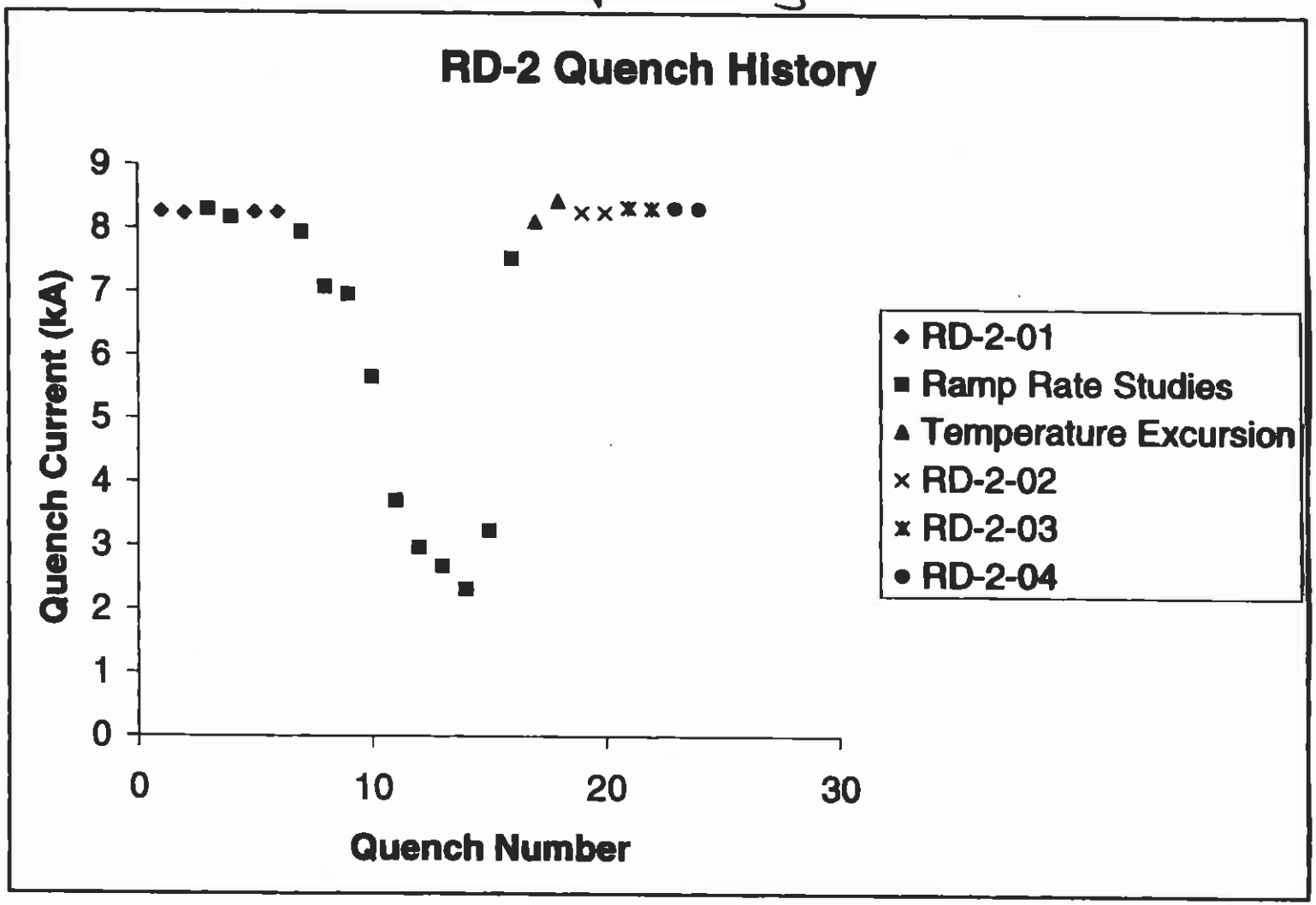

Courtesy S. Gourlay

LBNL Common-Coil Dipole Magnet Model

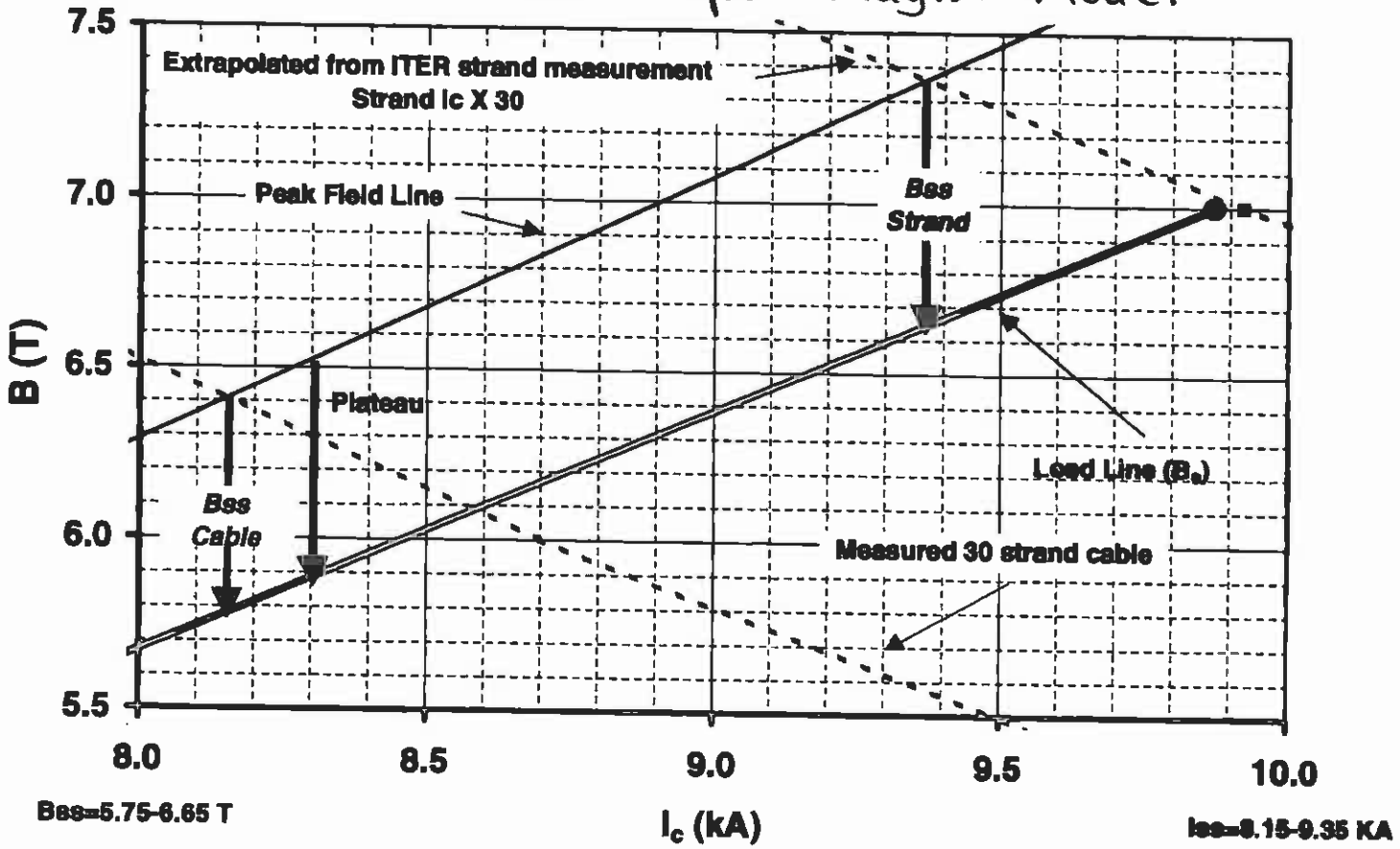

Courtesy S. Gourlay

TAMU Block-Coil Dual Dipole Magnet

16 Tesla Block-Coil Dual Dipole

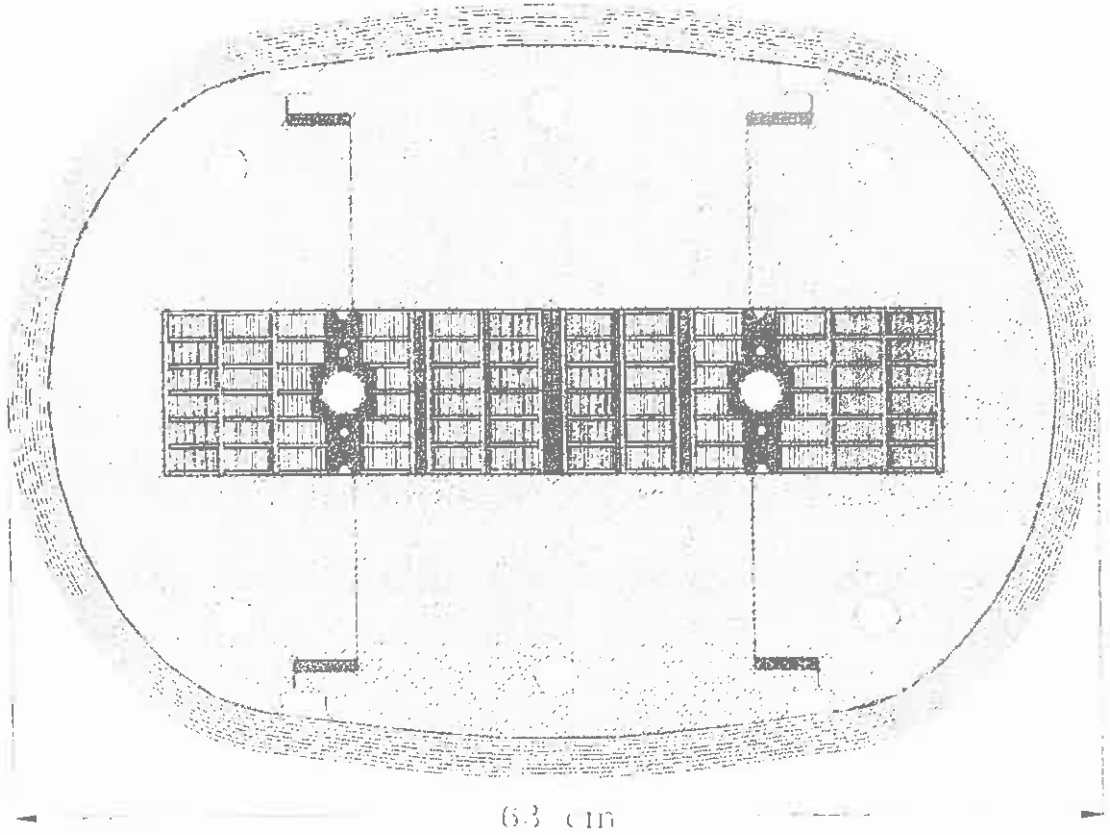

Courtesy P. McIntyre

Stress Management

Intercept the stress from the inner part of the coil, bypass it through stiff structure so that it cannot accumulate in the outer part of the coil.

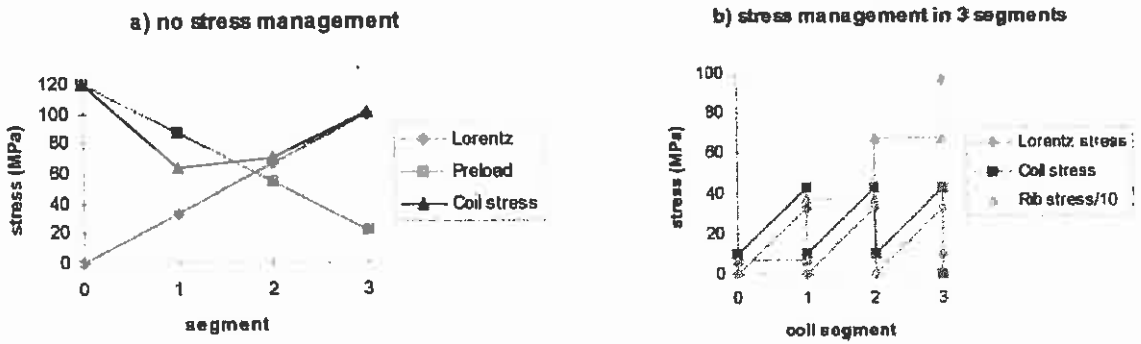

Courtesy P. McIntyre

The devil is in the details:

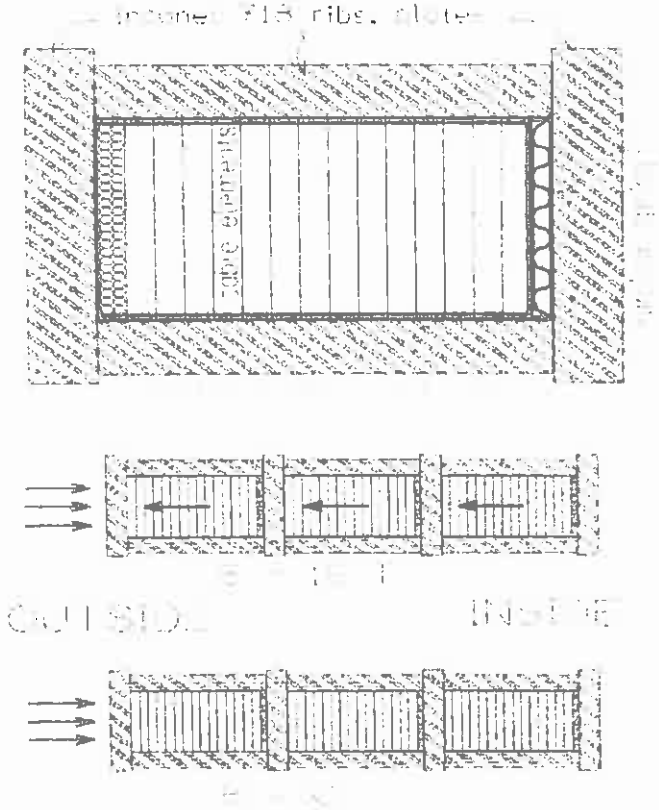

Courtesy P. McIntyre

Stress management requires four ingredients

	modulus		yield strength	
• The coil: cables, epoxy	40	GPa	100	MPa
• Support matrix: Inconel	210	GPa	1,300	MPa
• Laminar spring: Inconel	0.1	GPa	900	MPa
• Shear release: mica paper				

Plates

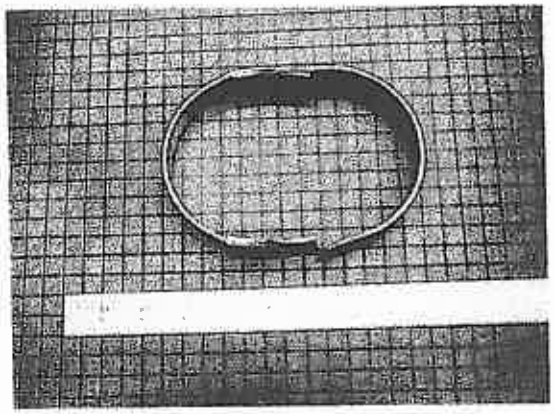

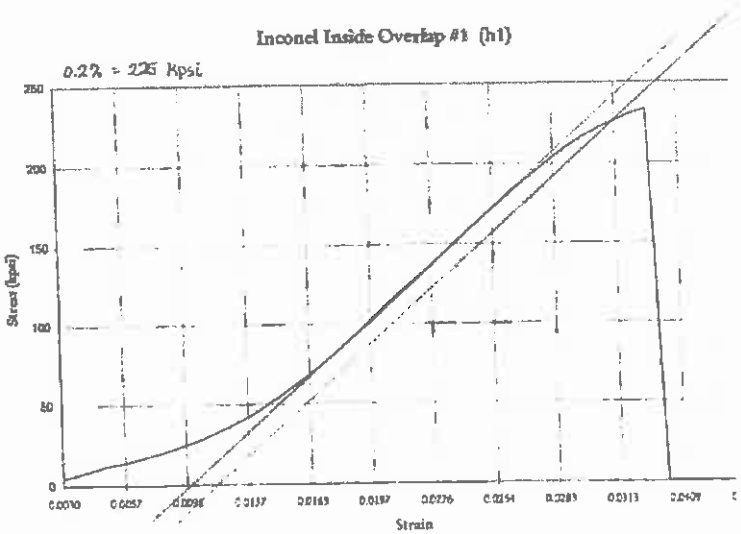

Courtesy P. McIntyre

Ribs

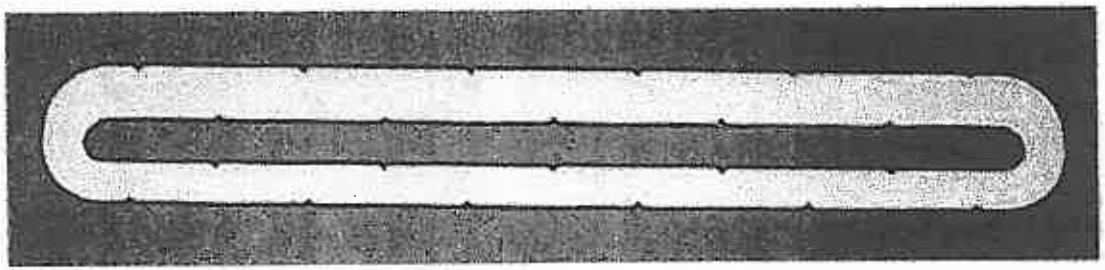

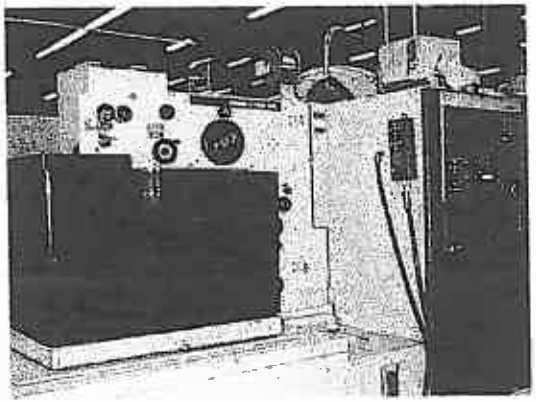

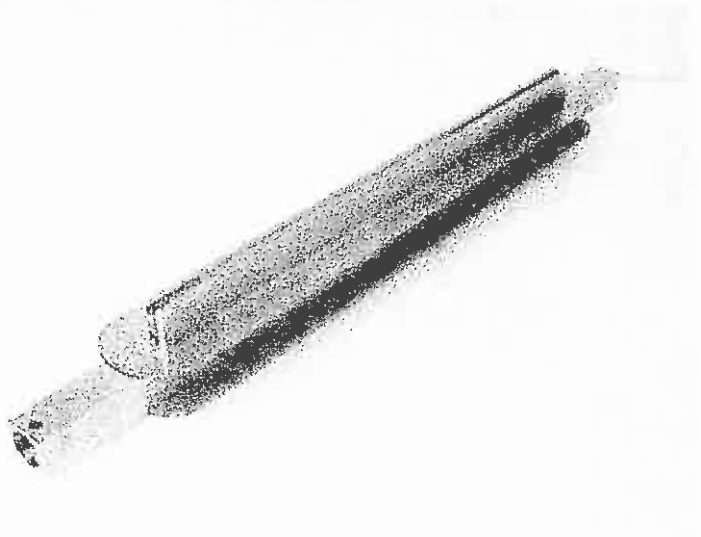

Courtesy P. McIntyre

Shear Release

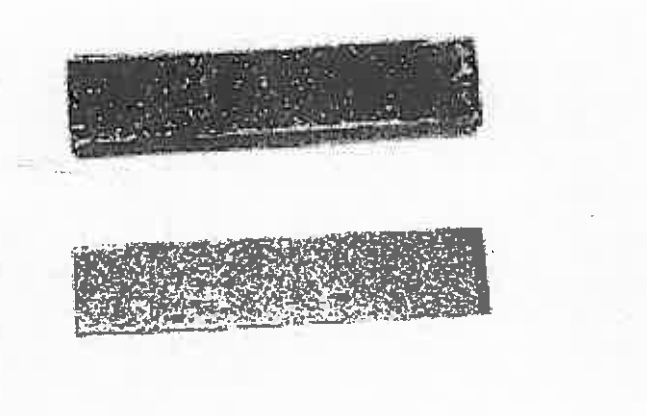

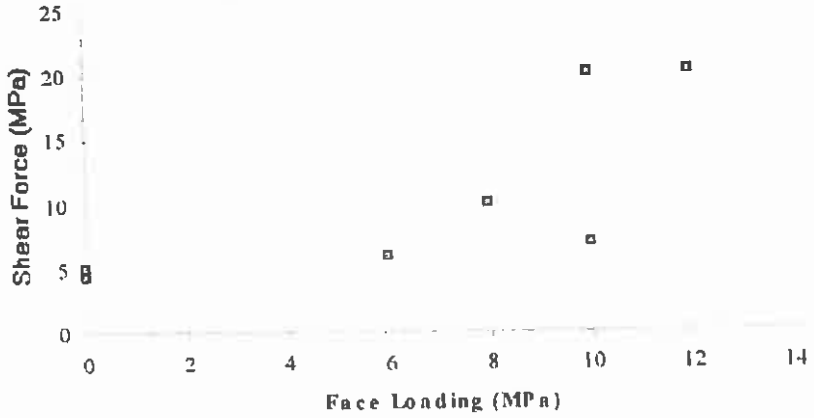

Courtesy P. McIntyre

Laminar Springs

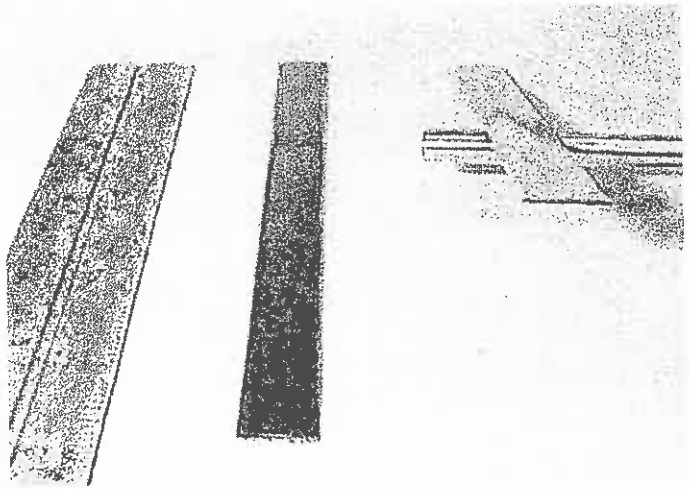

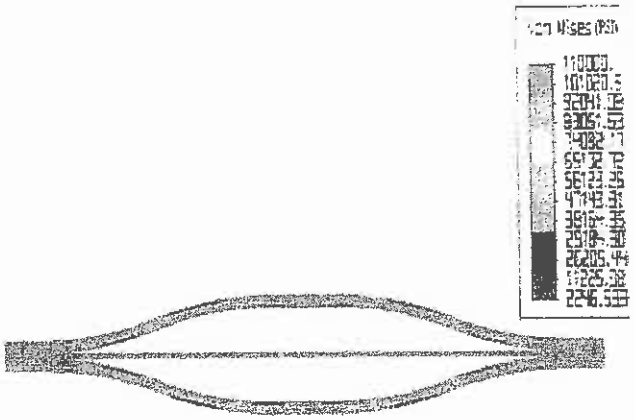

1 mm thick

10 MPa effective modulus

0.2 mm linear stroke

survives Nb_3Sn bake

Courtesy P. McIntyre

Horizontal, Vertical Stress Distribution at Coil/Rib Interfaces

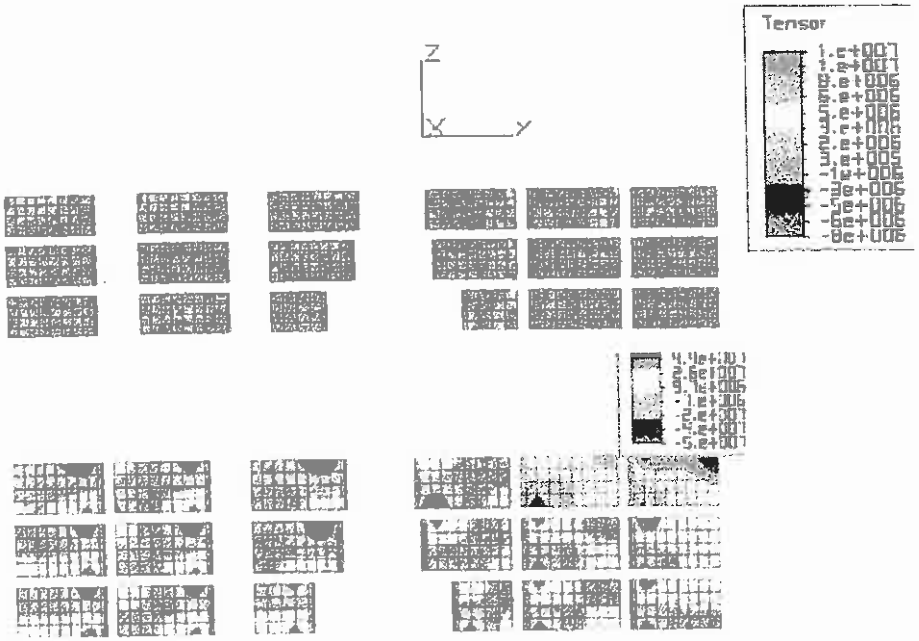

Courtesy P. McIntyre

LECTURE 6: ASSSEMBLY OF PARTICLE ACCELERATOR MAGNETS

6.1 Coil Winding 6–3

6.2 Coil Curing 6–17

6.3 Azimuthal Coil Size Measurements 6–31

6.4 Coil Assembly and Internal Splicing 6–45

6.5 Collaring 6–55

6.6 Collar Deflection Measurements 6–77

6.7 External Splicing 6–87

6.8 Yoke Stacking and Shell Welding 6–93

6.9 Yoke Midplane Gap Measurements 6–107

6.10 Cryostating 6–121

6.11 Instrumentation 6–135

LECTURE 6: ASSEMBLY OF PARTICLE ACCELERATOR MAGNETS

6.1 Coil Winding

6.2 Coil Curing

6.3 Azimuthal Coil Size Measurements

6.4 Coil Assembly and Internal Splicing

6.5 Collaring

6.6 Collar Deflection Measurements

6.7 External Splicing

6.8 Yoke Stacking and Shell Welding

6.9 Yoke Midplane Gap Measurements

6.10 Cryostating

6.11 Instrumentation

ANSALDO
ANSALDO
ANSALDO
ANSALDO

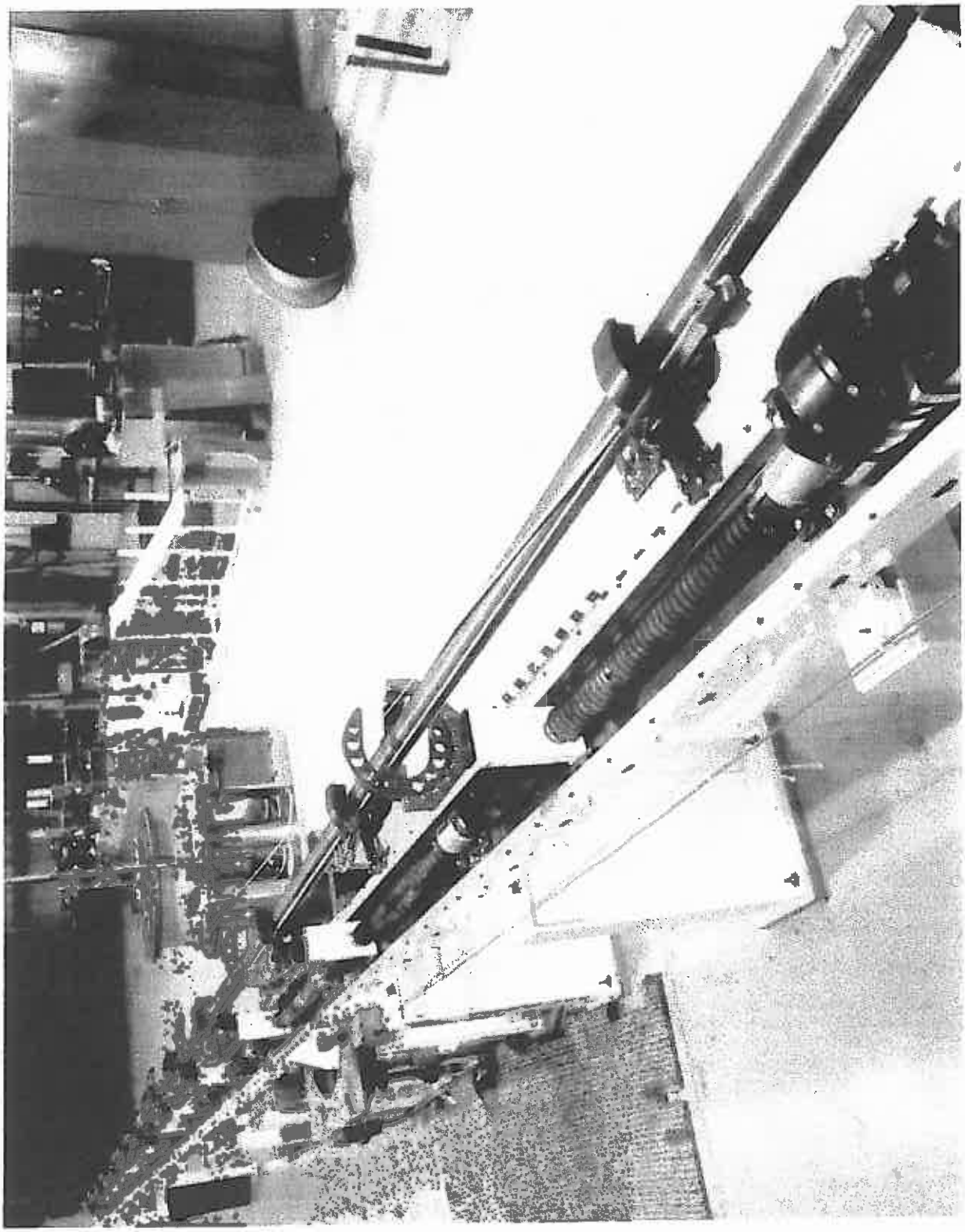

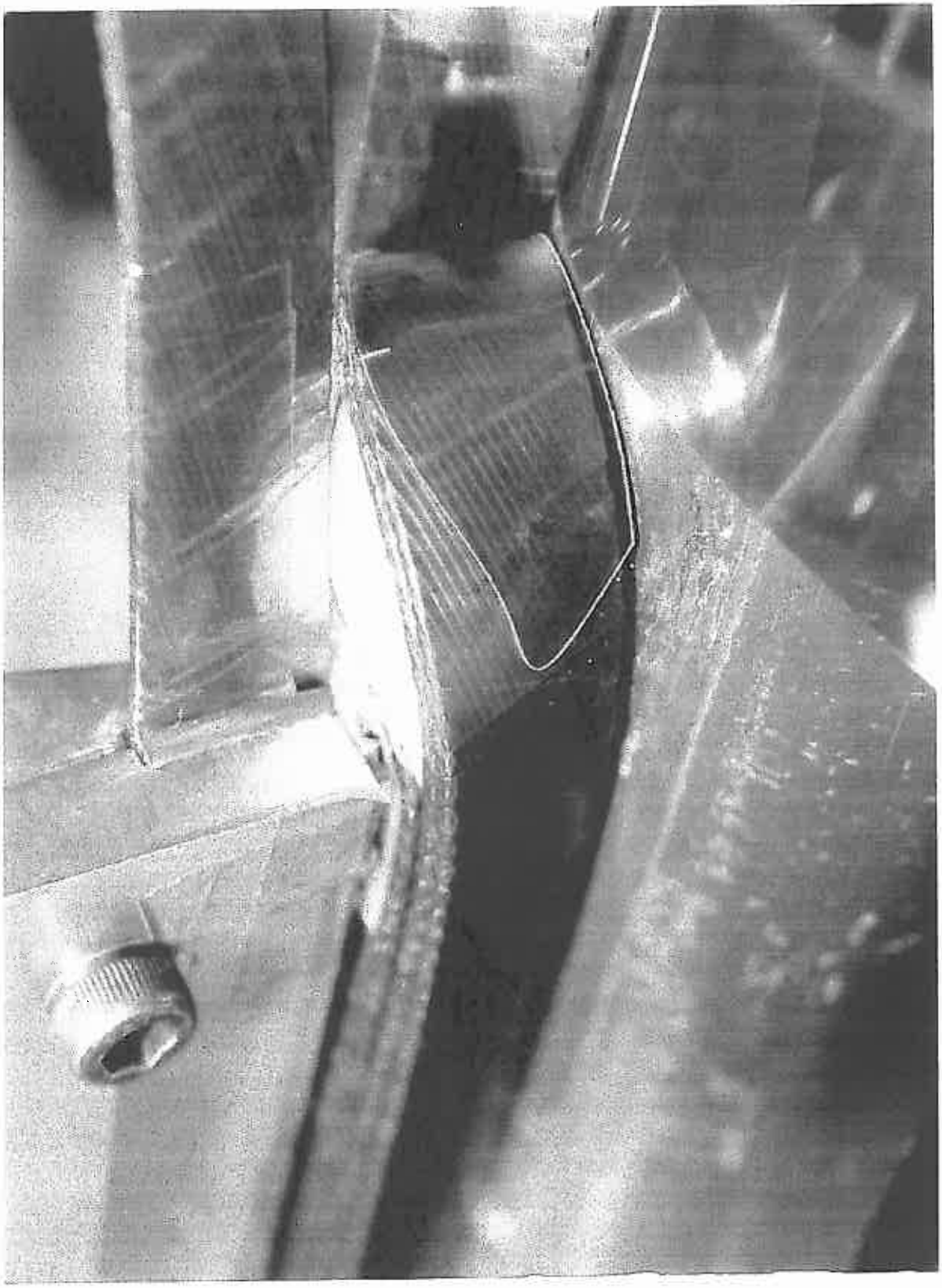

STRAND AND CABLE TWIST

– As we have seen in the lecture on conductors, strands and cables are both twisted.

– A twist direction similar to that of a right-handed screw is usually designated by the letter Z, while a twist direction similar to that of a left-handed screw is designated by the letter S.

– It is usually preferred to have opposite twist directions for strands and cables, to limit strand deformation during cabling and to avoid residual cable twist.

CABLE TWIST AND WINDING ORIENTATION

– Furthermore, the cable twist direction affects the cable behavior during winding of the coil ends.

– For instance, a S-twisted cable has a tendency to open up at the beginning and to close down at the end of a clockwise turn while a Z-twisted cable has the opposite tendency.

– Most coil manufacturers prefer to wind cables which open up at the beginning and close down at the end of turns, because at the turn beginning, the opening can be limited by using the winding tension to flatten the cable against the mandrel.

Example: For LHC dipole magnets, the inner coils are wound counter-clockwise, while the outer coils are wound clockwise. Hence, the preferred cable twist directions are: Z for inner coils and S for outer coils.

CABLE TWIST AND INTERNAL SPLICING ORIENTATION

– In the case of a two-layer coil assembly with an internal splice, another issue that may be taken into consideration while choosing cable twist direction is the respective orientation of the inner and outer cable strands directly in contact at the splice.

– Indeed, depending on twist direction, the strands can either be parallel or perpendicular.

– It is believed that it is preferable to have strands running perpendicularly because it forces a more uniform transfer of current from the strands of the inner cable to the strands of the outer cable. This may help reducing the risk of large current unbalance among cable strands.

CHOICE OF CABLE TWIST ORIENTATION

– In the case of the LHC dipole magnets the inner and outer cable lay directions were chosen so as to ensure that the outer cable, which has the largest aspect ratio, is wound in the favorable direction, and that, when spliced together, the strands of the two cables run perpendicularly.

– As a result, the inner cable is wound in the unfavorable direction, which is deemed acceptable given its lower aspect ratio.

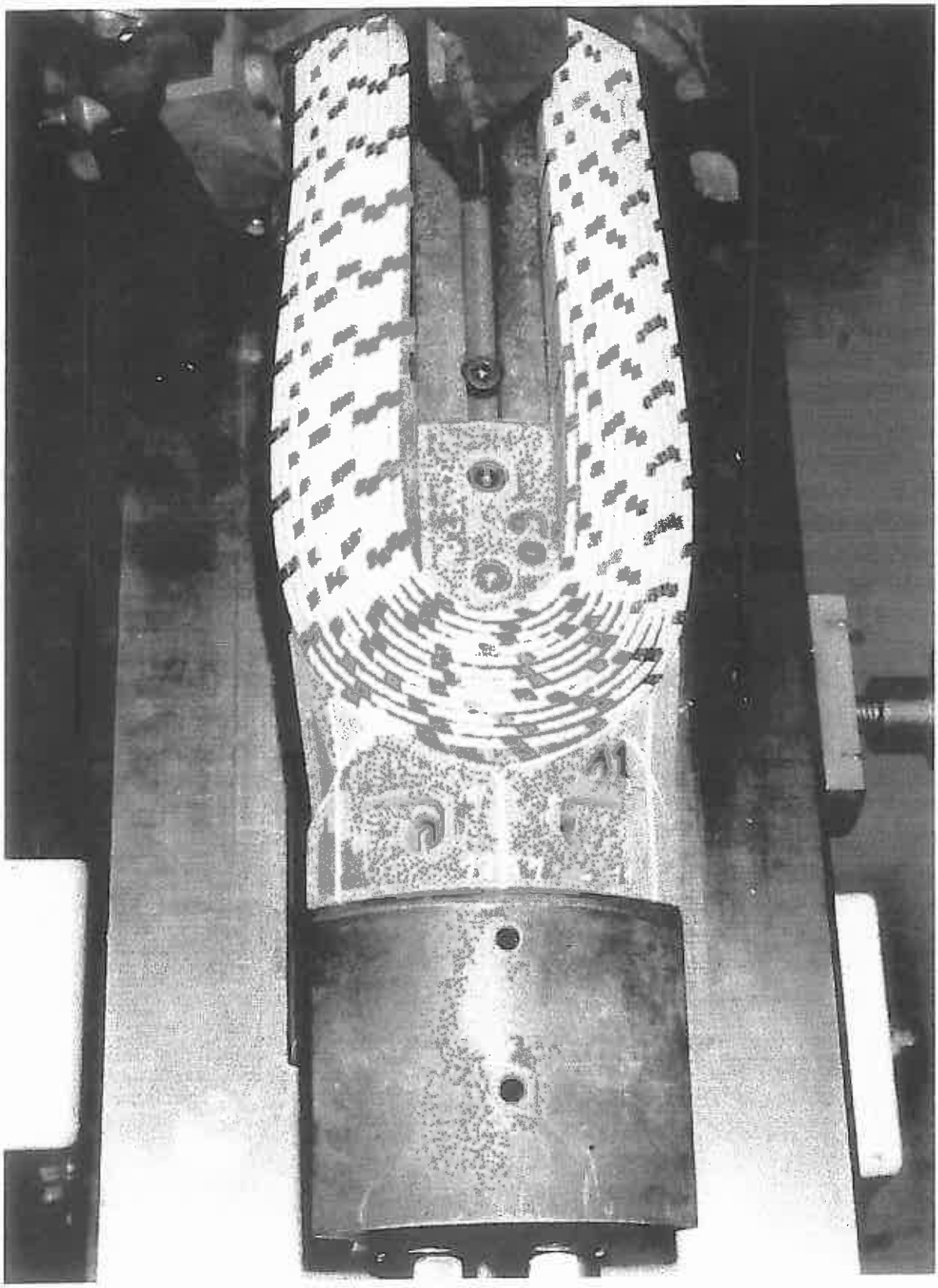

CAFE

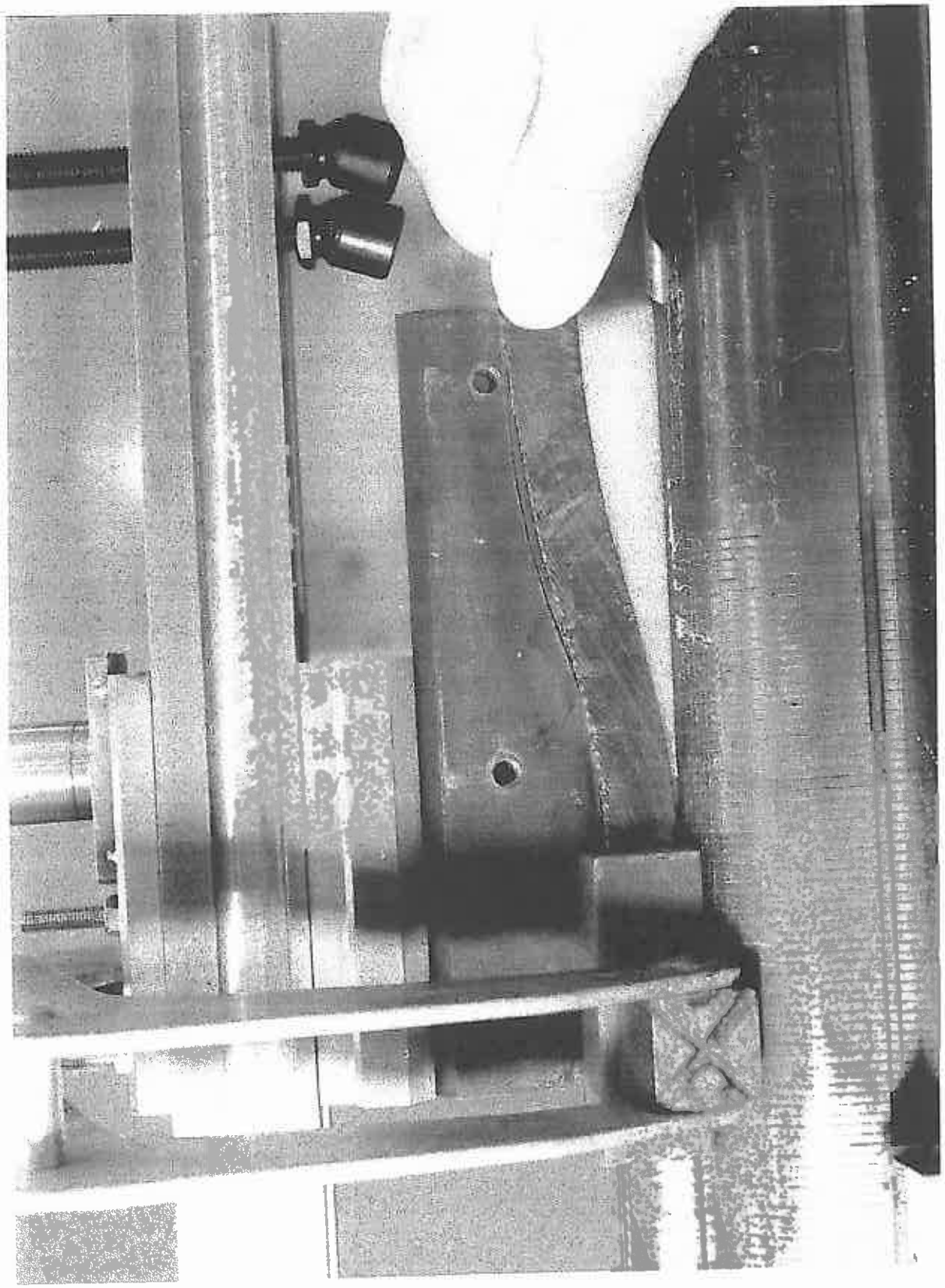

LECTURE 6: ASSEMBLY OF PARTICLE ACCELERATOR MAGNETS

6.1 Coil Winding

6.2 Coil Curing

6.3 Azimuthal Coil Size Measurements

6.4 Coil Assembly and Internal Splicing

6.5 Collaring

6.6 Collar Deflection Measurements

6.7 External Splicing

6.8 Yoke Stacking and Shell Welding

6.9 Yoke Midplane Gap Measurements

6.10 Cryostating

6.11 Instrumentation

OBJECTIVES OF CURING

– The objective of curing is three-fold:

• To polymerize the epoxy or the polyimide adhesive of the cable insulation in order to make the coil rigid and easier to assemble,

• To form the coil into the correct shape and the correct dimensions,

• To make the coil as uniform as possible along its length.

– Correctness of coil dimensions is important for field quality.

– Uniformity of coil is also required to achieve uniform pre-compression after collaring.

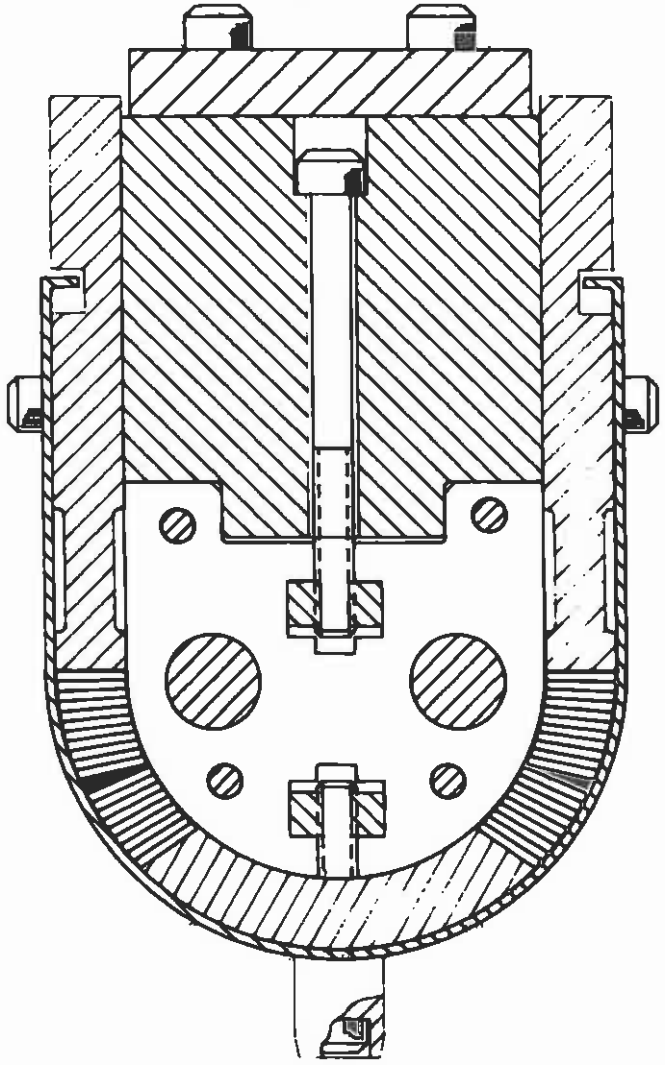

MANDREL, COIL, PUSHER BAR & RETAINER

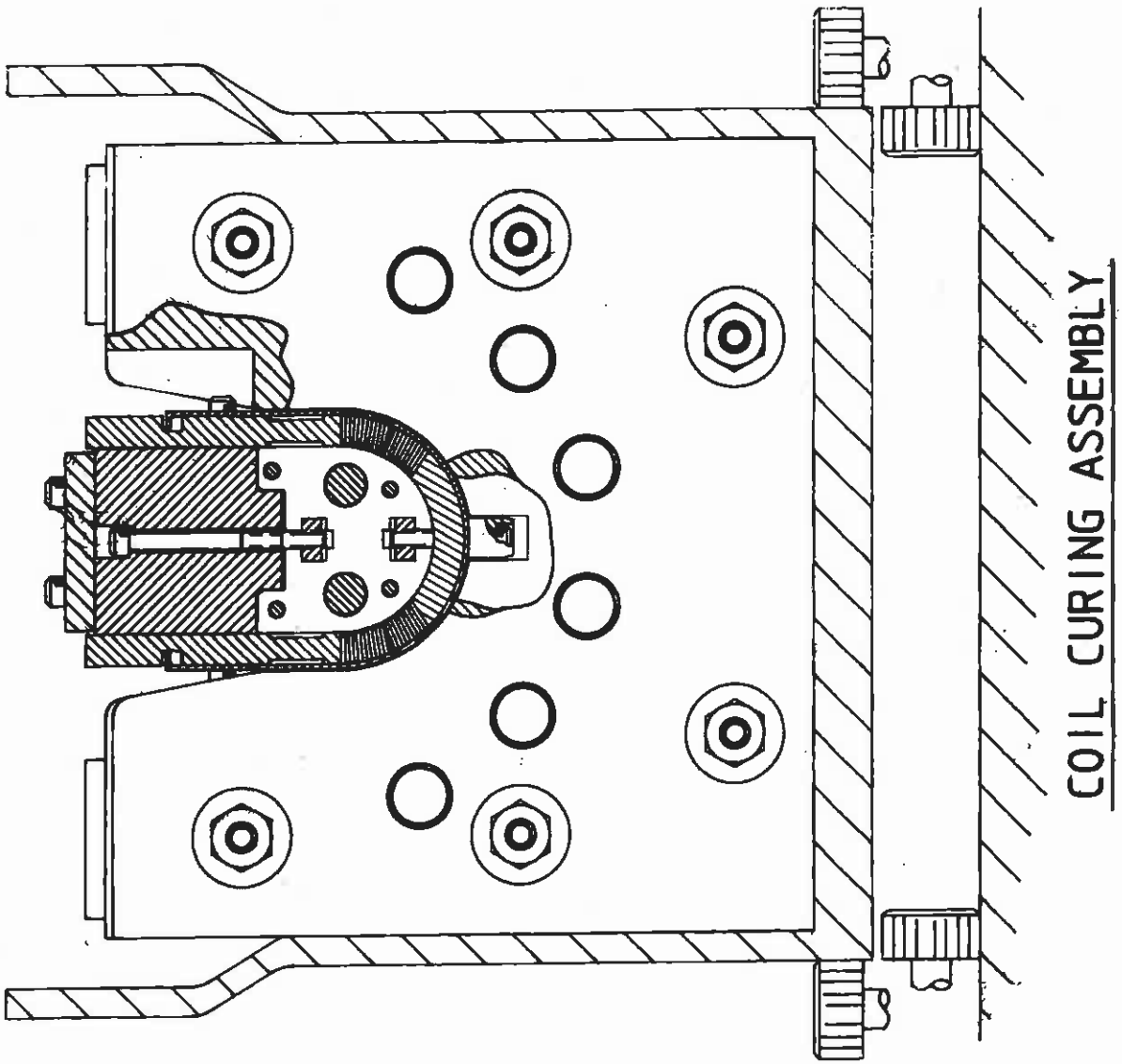
COIL CURING ASSEMBLY

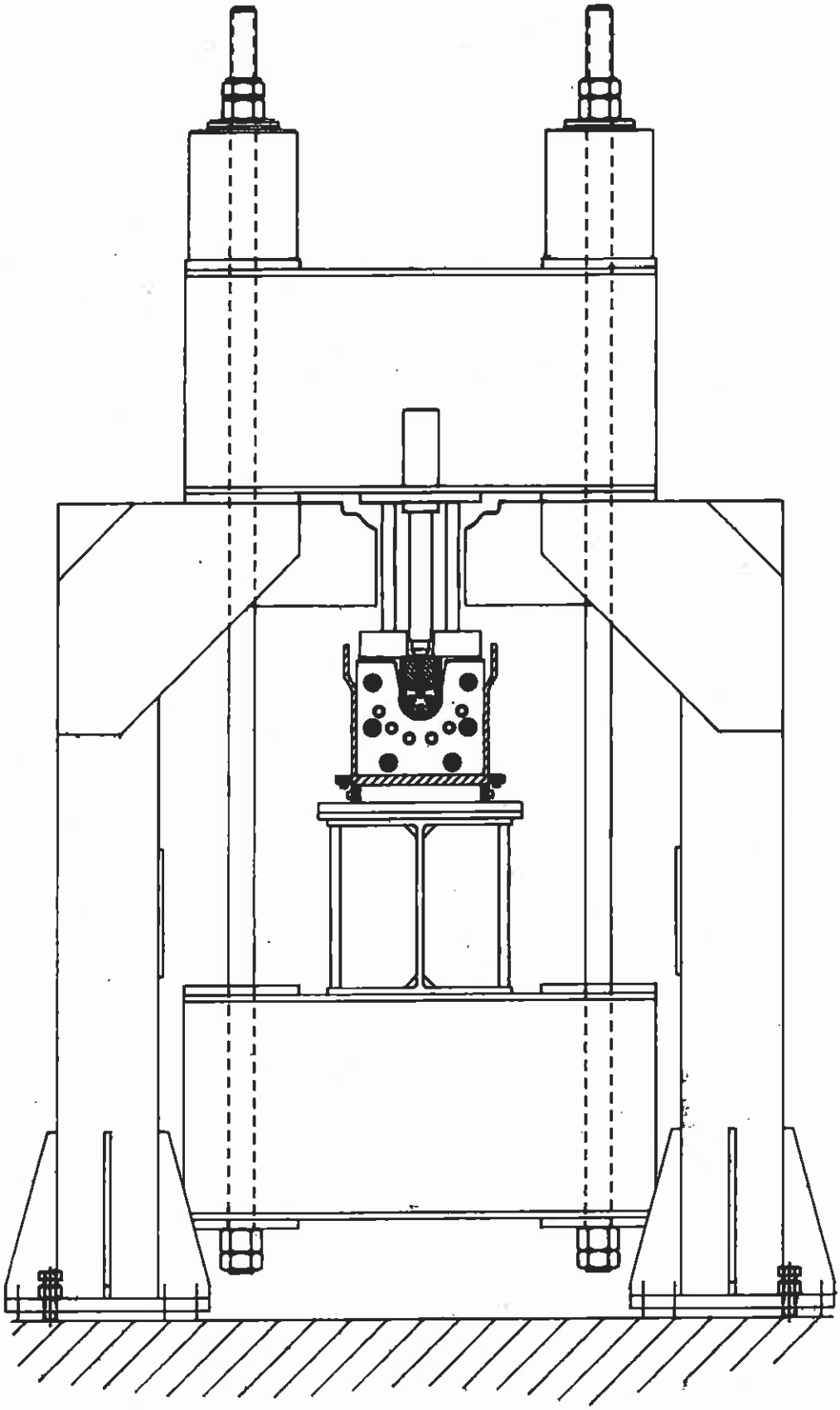

COIL CURING FIXTURE & PRESS

CURING PROCEDURE

– Coil curing is realized in a mold, ususally made of laminated steel blocks constructed to very accurate dimensions.

– The blocks are heated by a circulation of hot oil and are pressed upon by means of hydraulic cylinders.

– The curing temperature and curing pressure schedule depends on cable insulation and on coil manufacturers.

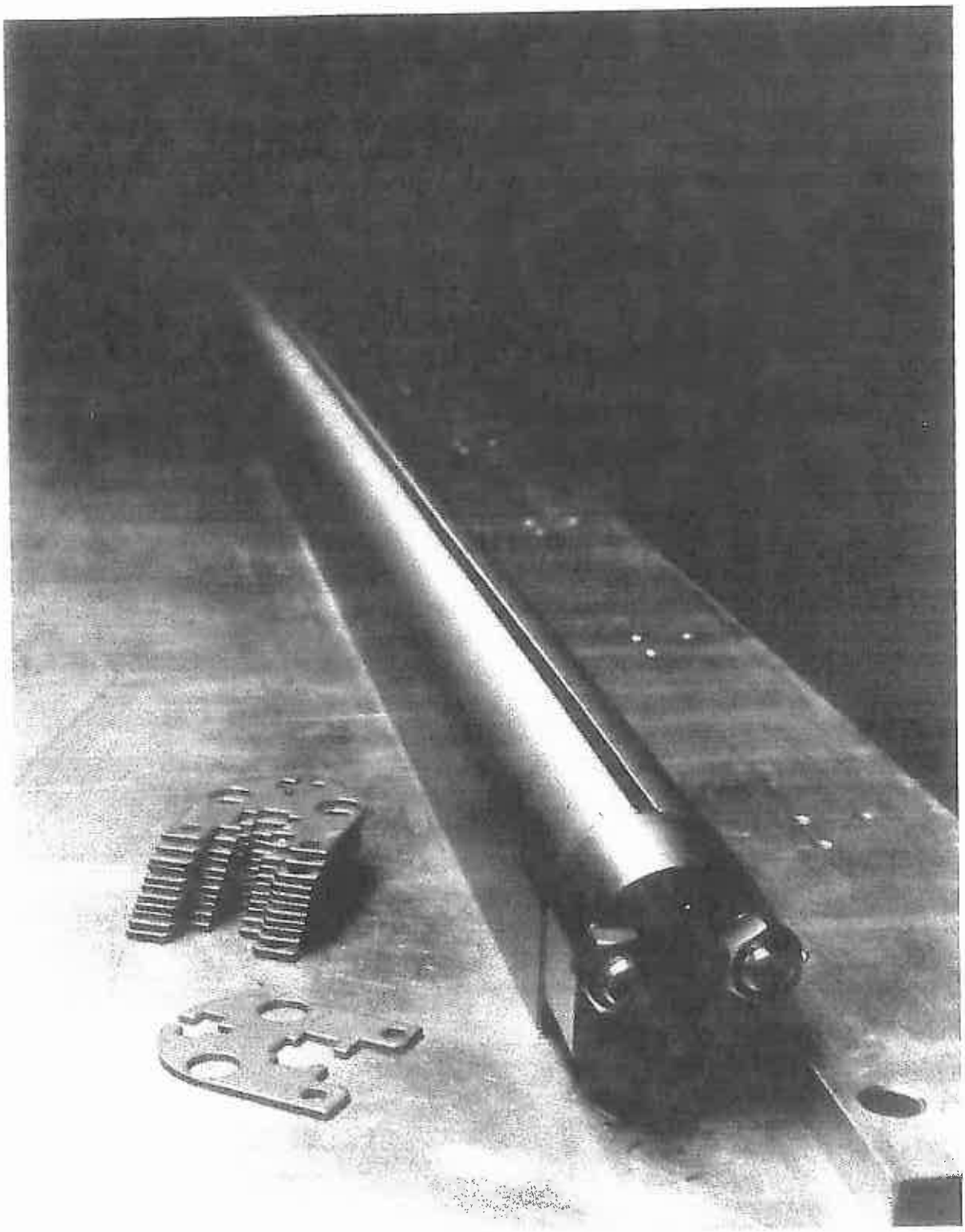

2200 kg

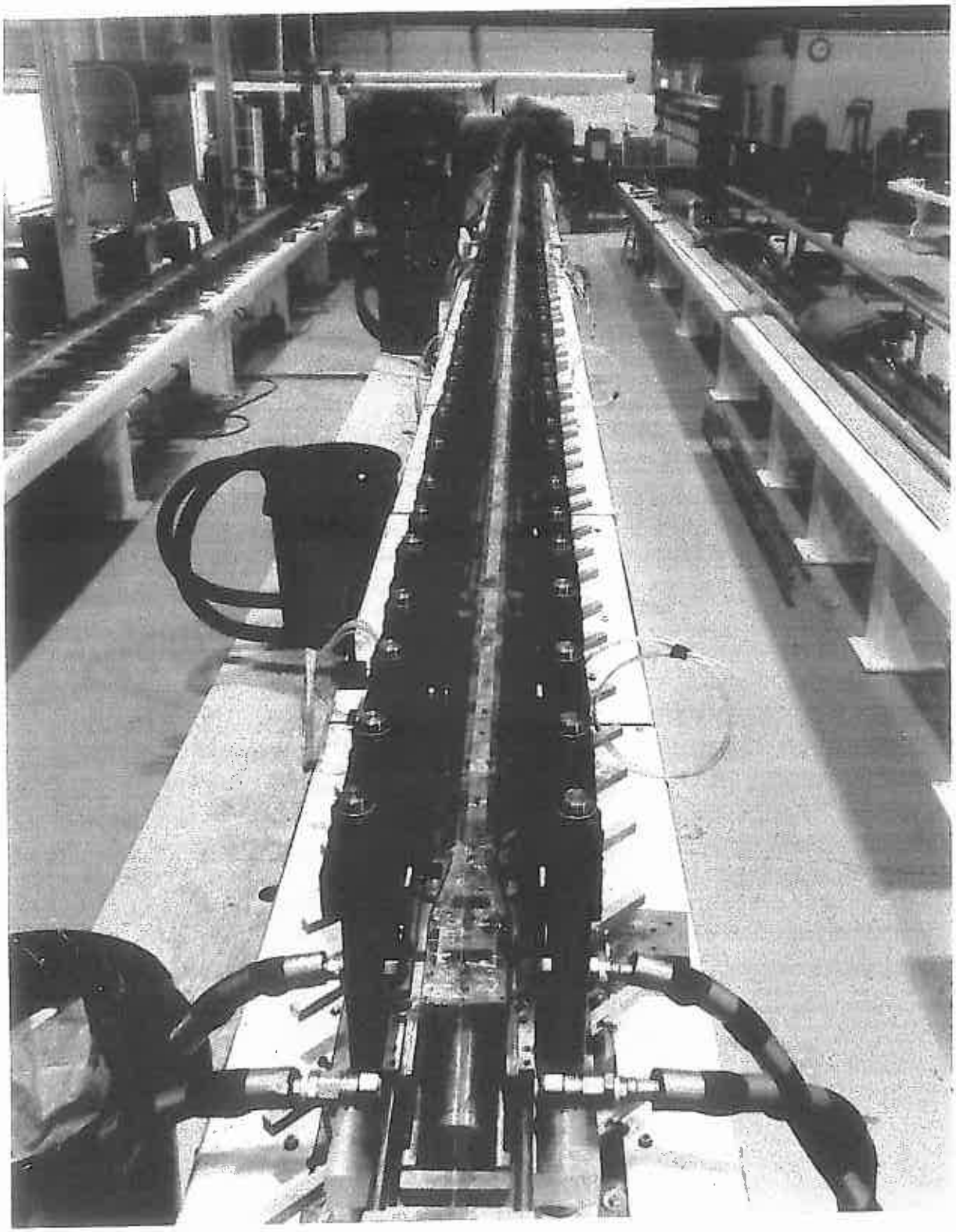

OPTIMIZATION OF CURING CAVITY DIMENSION

– One of the goal of curing is to form the coil so that it assumes the desired azimuthal size under the target pre-compression.

– The coil azimuthal size under a given pressure is determined by the conductor and insulation thicknesses and by the curing cavity dimension.

– The curing cavity dimensions can be tuned (within a certain range) so as to obtain the desired coil size.

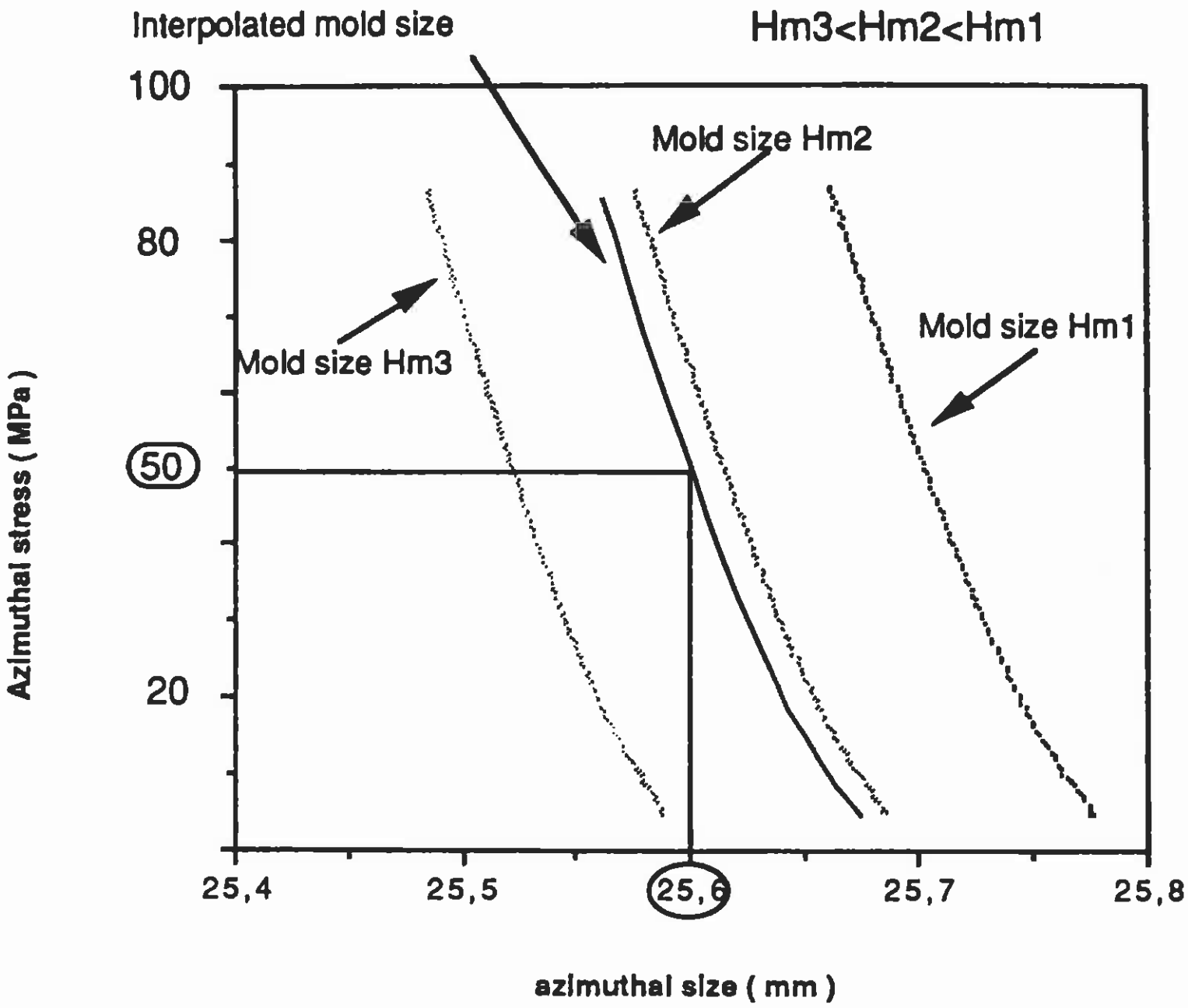
Interpolated mold size
Hm3<Hm2<Hm1
100
80
50
20
Mold size Hm2
Mold size Hm3
Mold size Hm1
Azimuthal stress (MPa)
25,4
25,5
25,6
25,7
25,8
azimuthal size (mm)

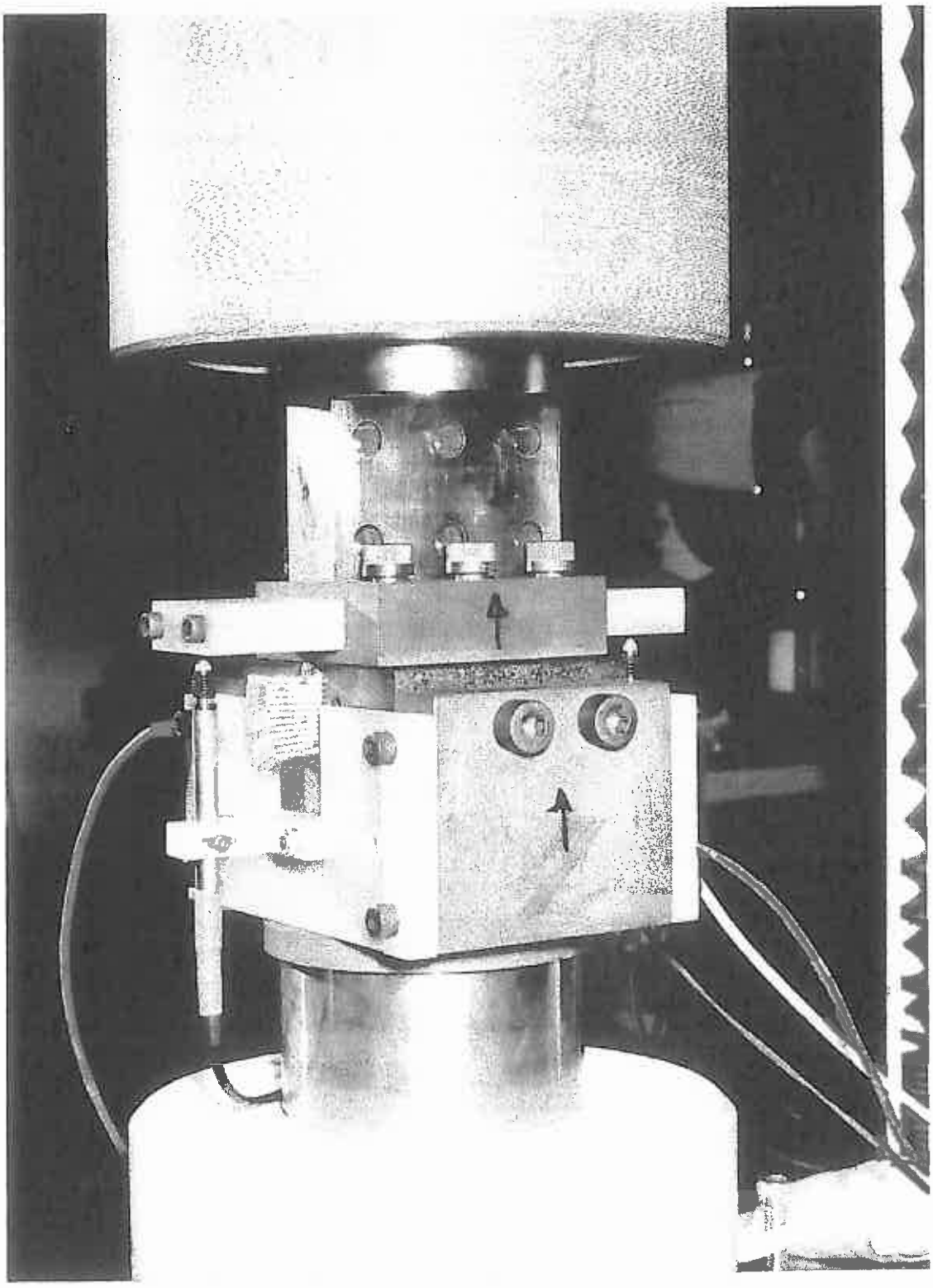

LECTURE 6: ASSSEMBLY OF PARTICLE ACCELERATOR MAGNETS

6.1 Coil Winding

6.2 Coil Curing

6.3 Azimuthal Coil Size Measurements

6.4 Coil Assembly and Internal Splicing

6.5 Collaring

6.6 Collar Deflection Measurements

6.7 External Splicing

6.8 Yoke Stacking and Shell Welding

6.9 Yoke Midplane Gap Measurements

6.10 Cryostating

6.11 Instrumentation

Coil Agimuthal Sige Measurements

σ_0 = Target Pre-compression

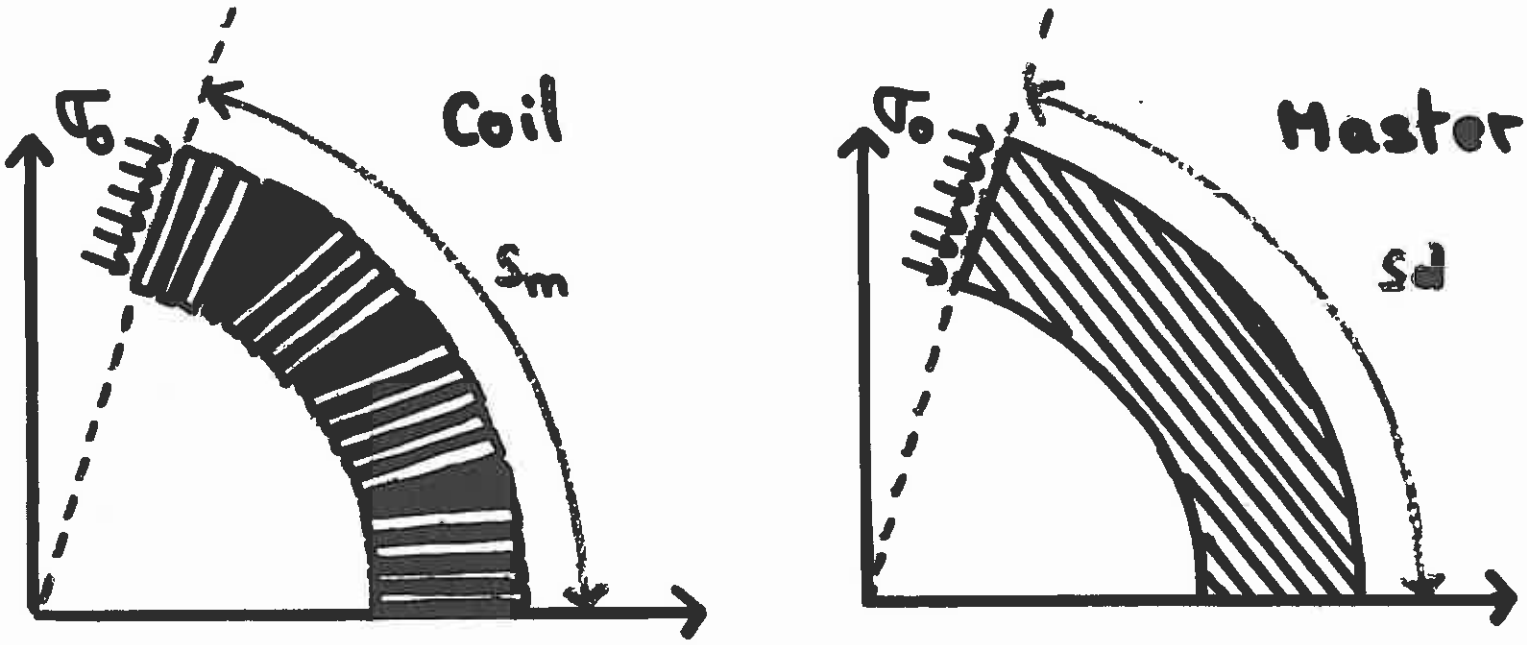

Coil Sige Deviation = $s_m - s_d$

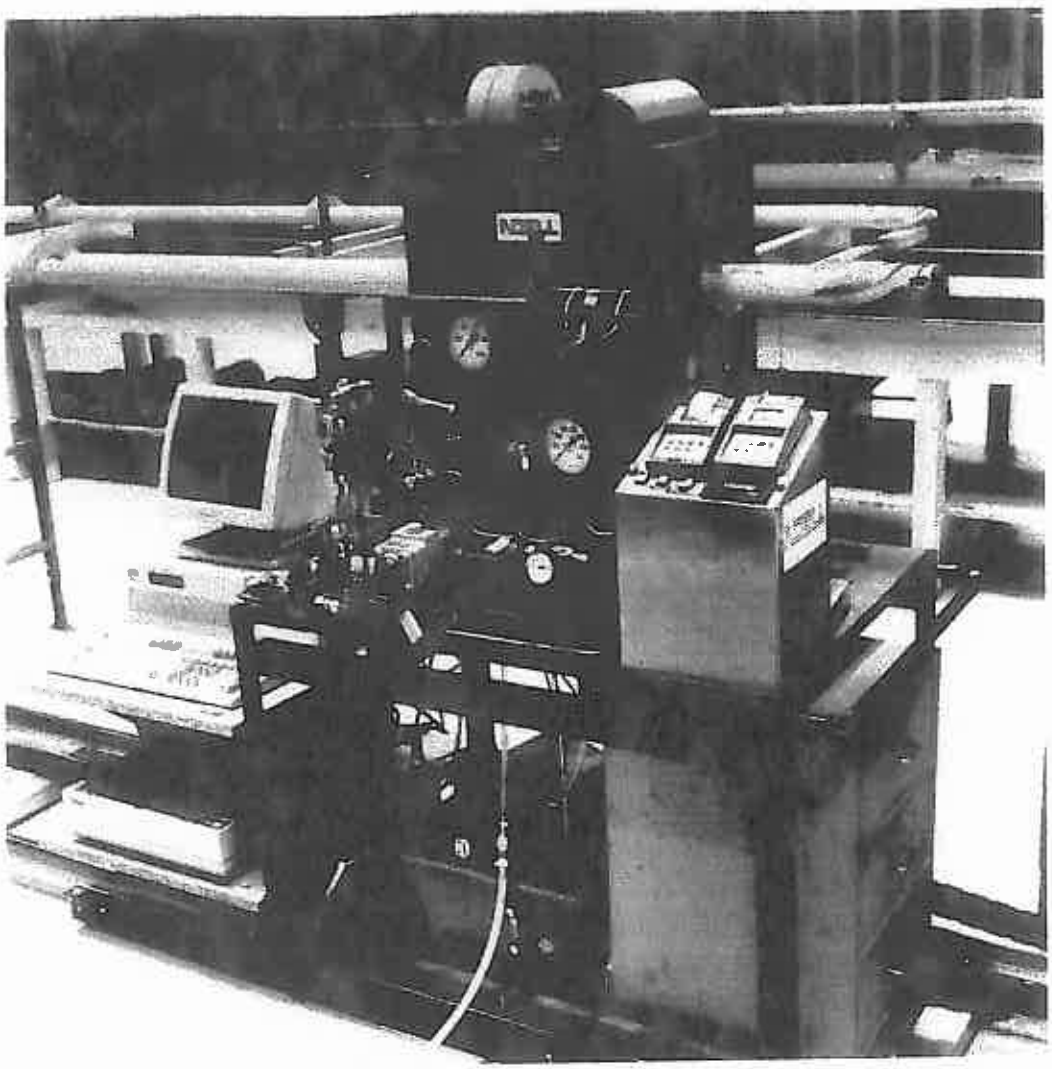

Young's modules measurement equipment for LHC dipoles with computer-controlled NC measuring and evaluation.

NOELL GMBH

NOELL

A member of Preussag

NU 097-E/09.93-Fo

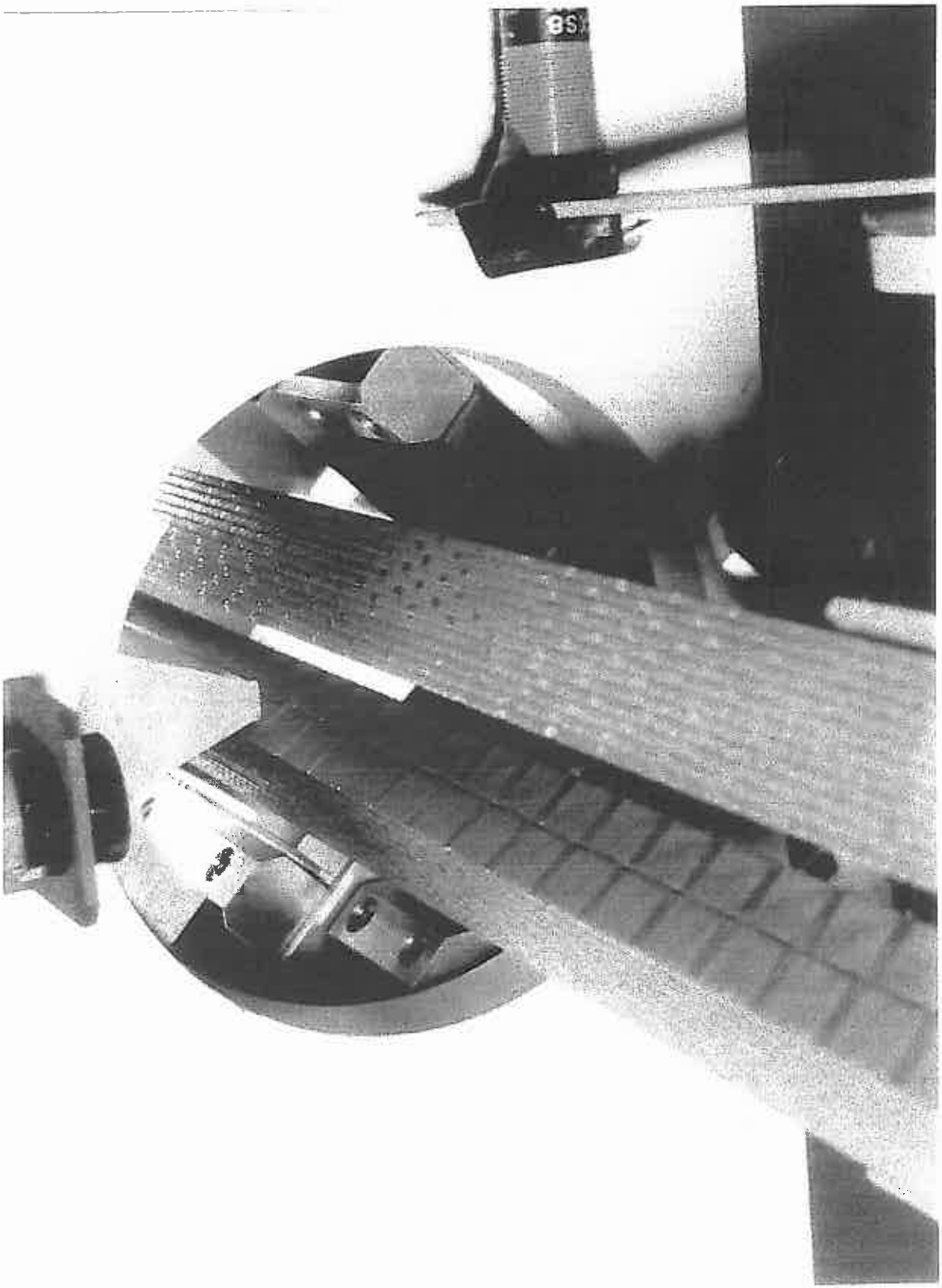

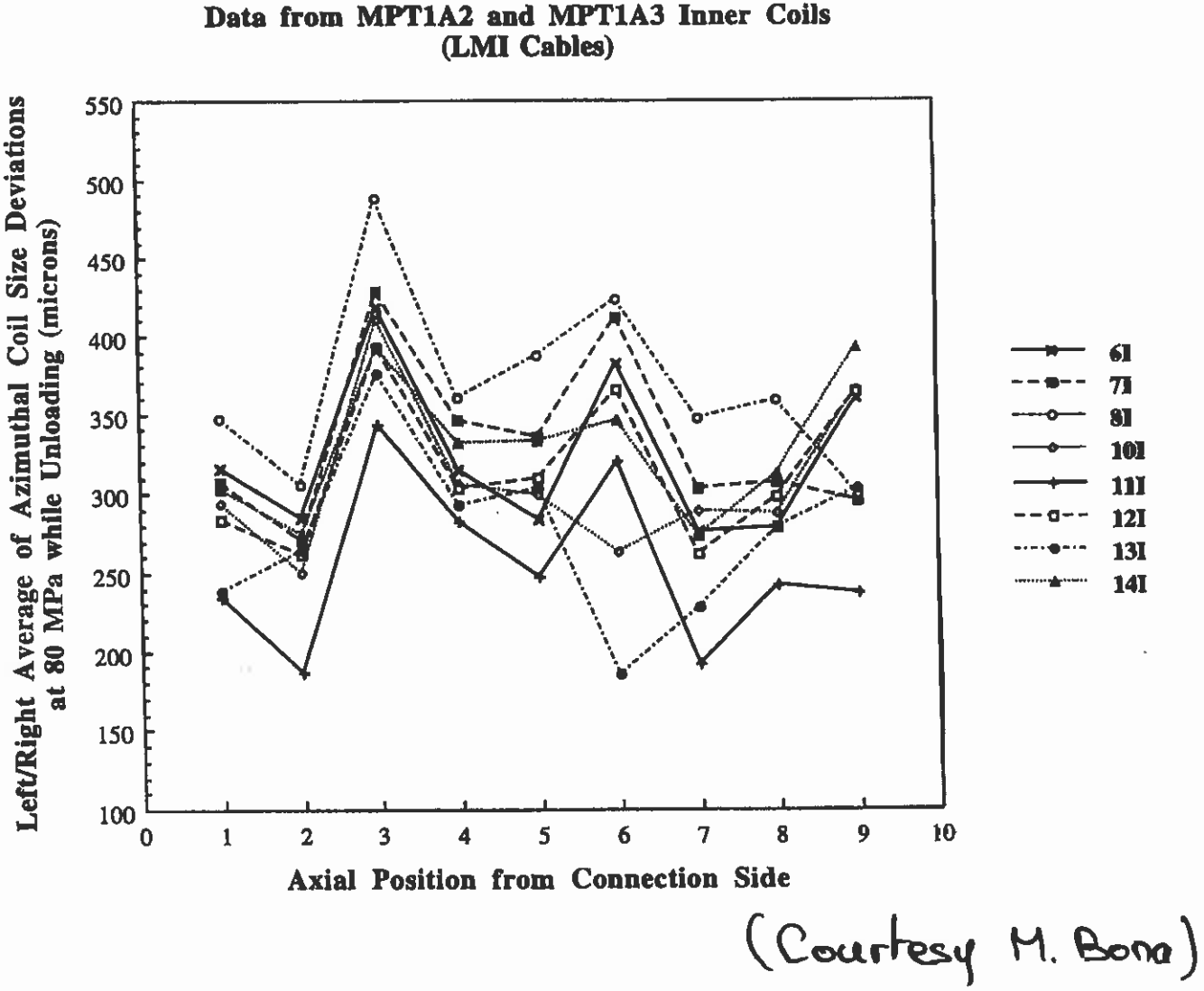

(Courtesy M. Bona)

Data from MTP1A2 and MTP1A3 Outer Coils

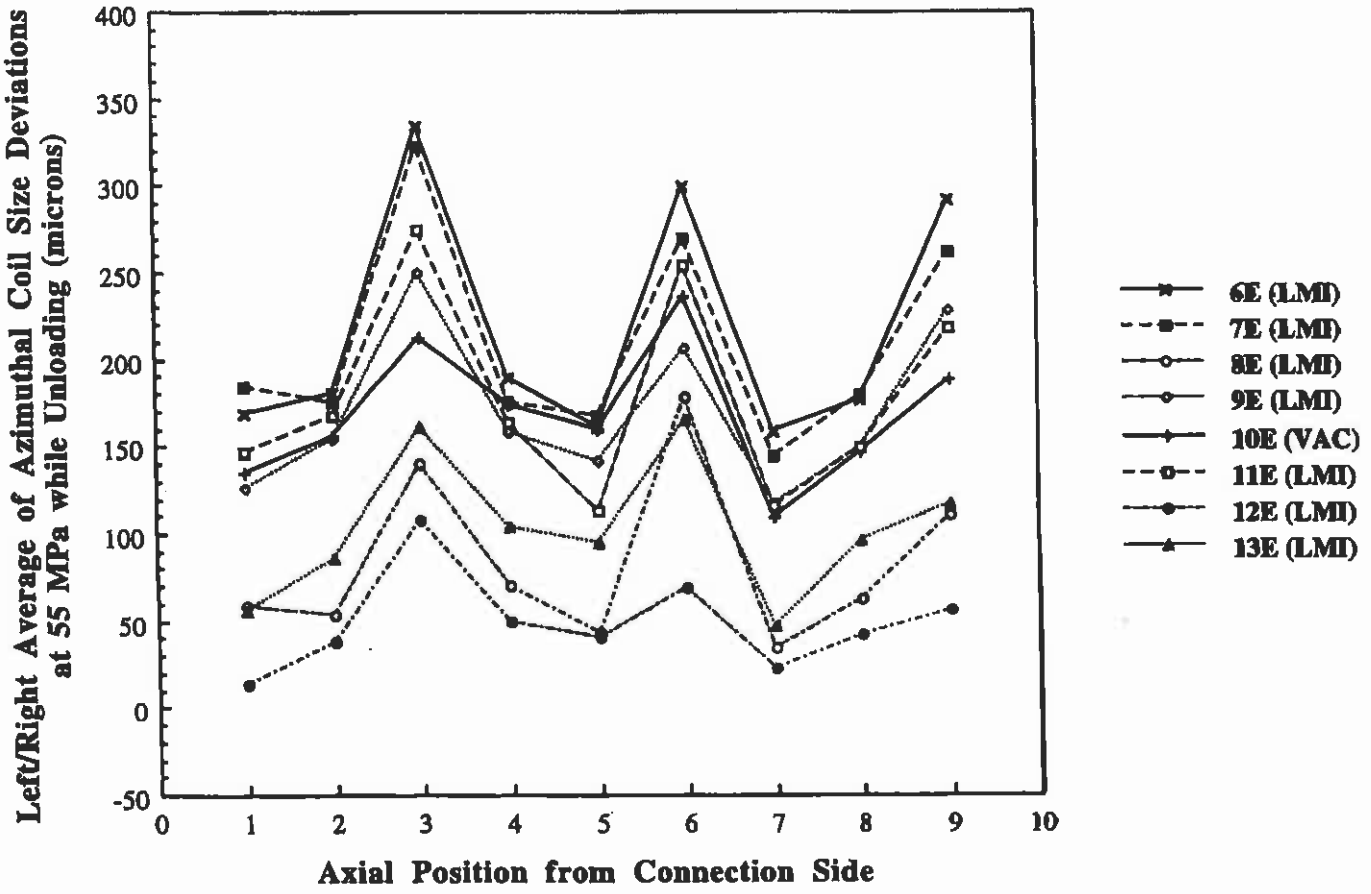

(Courtesy M. Bora)

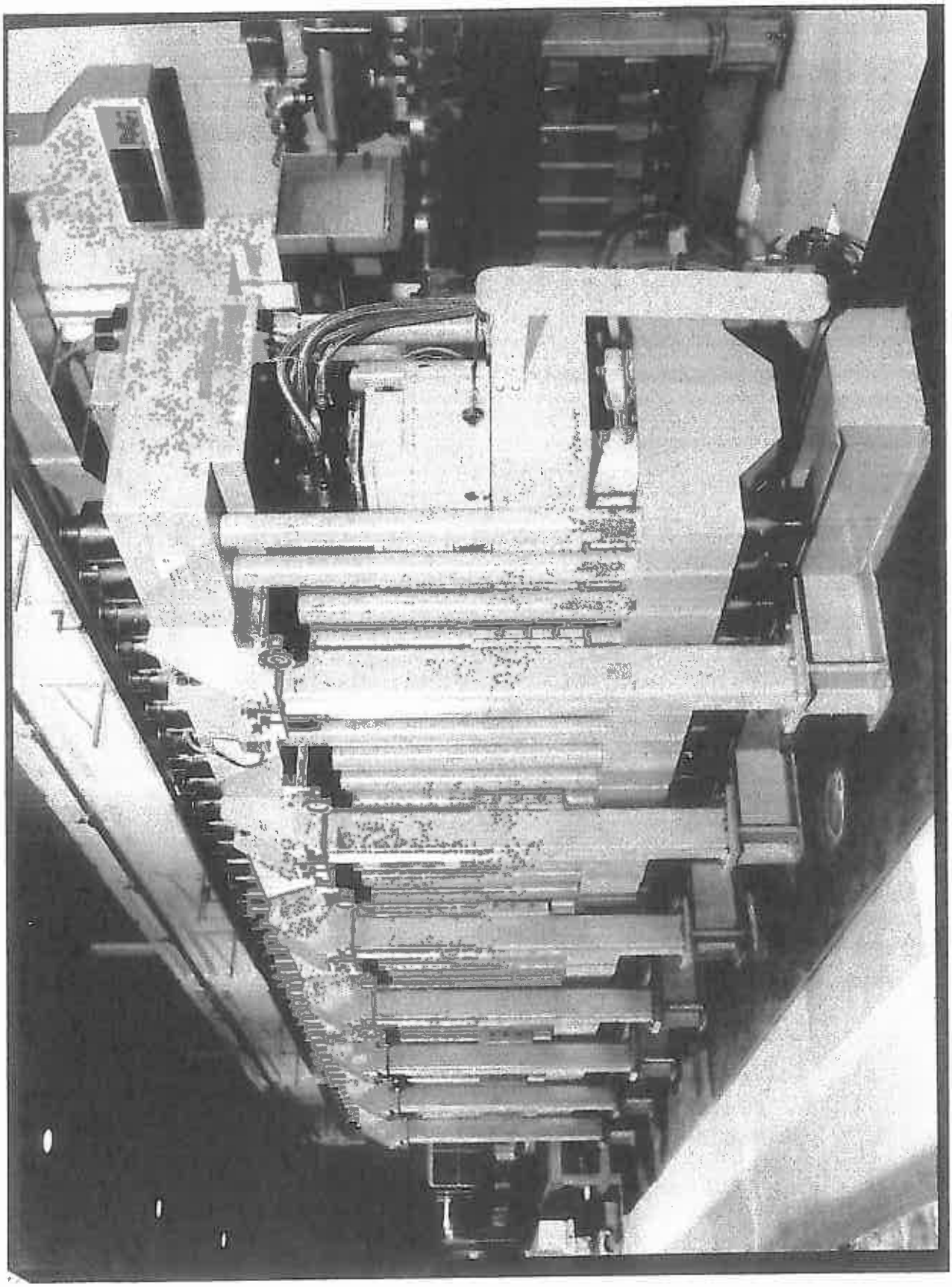

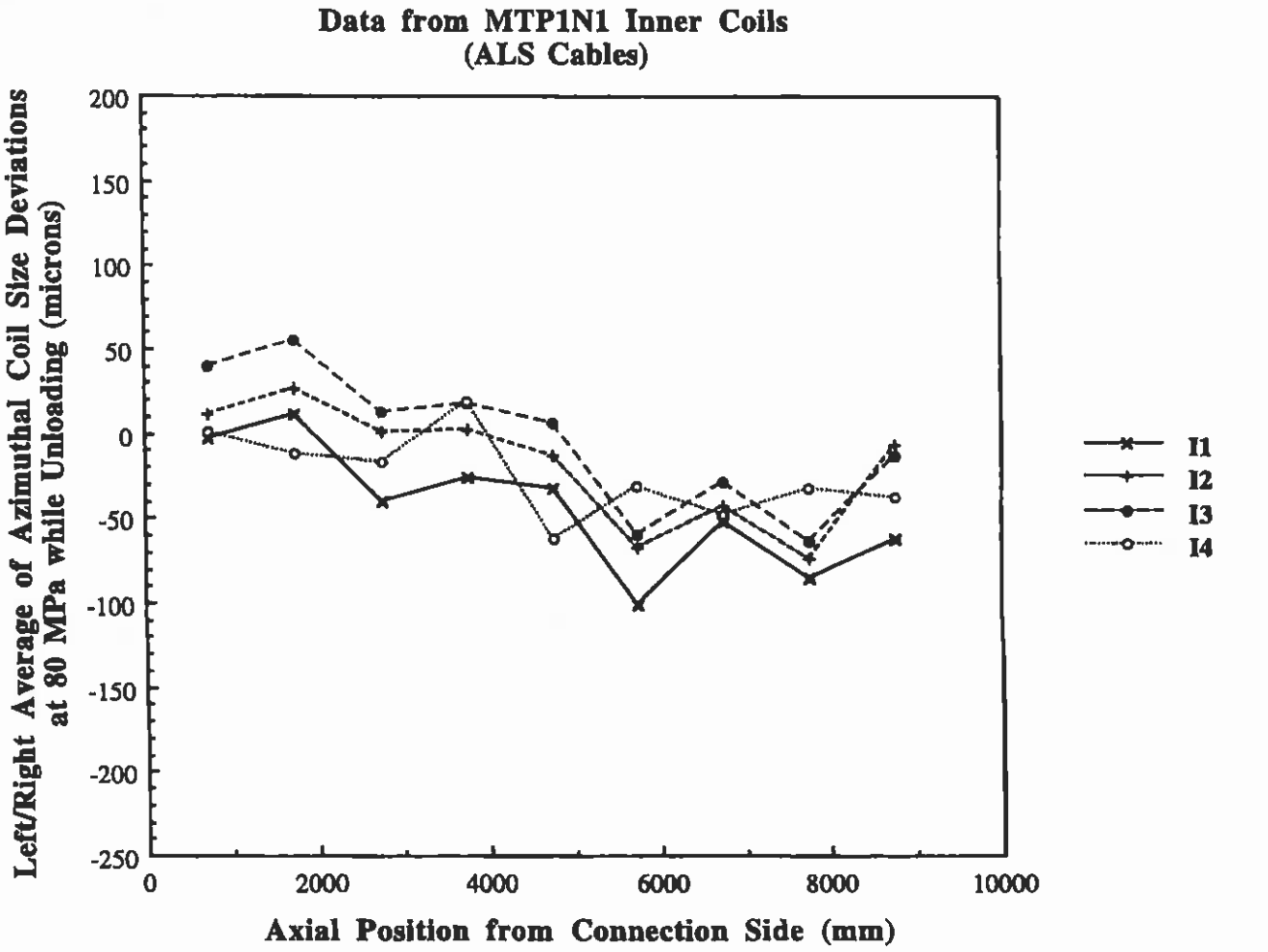

(Courtesy W. Thomi)

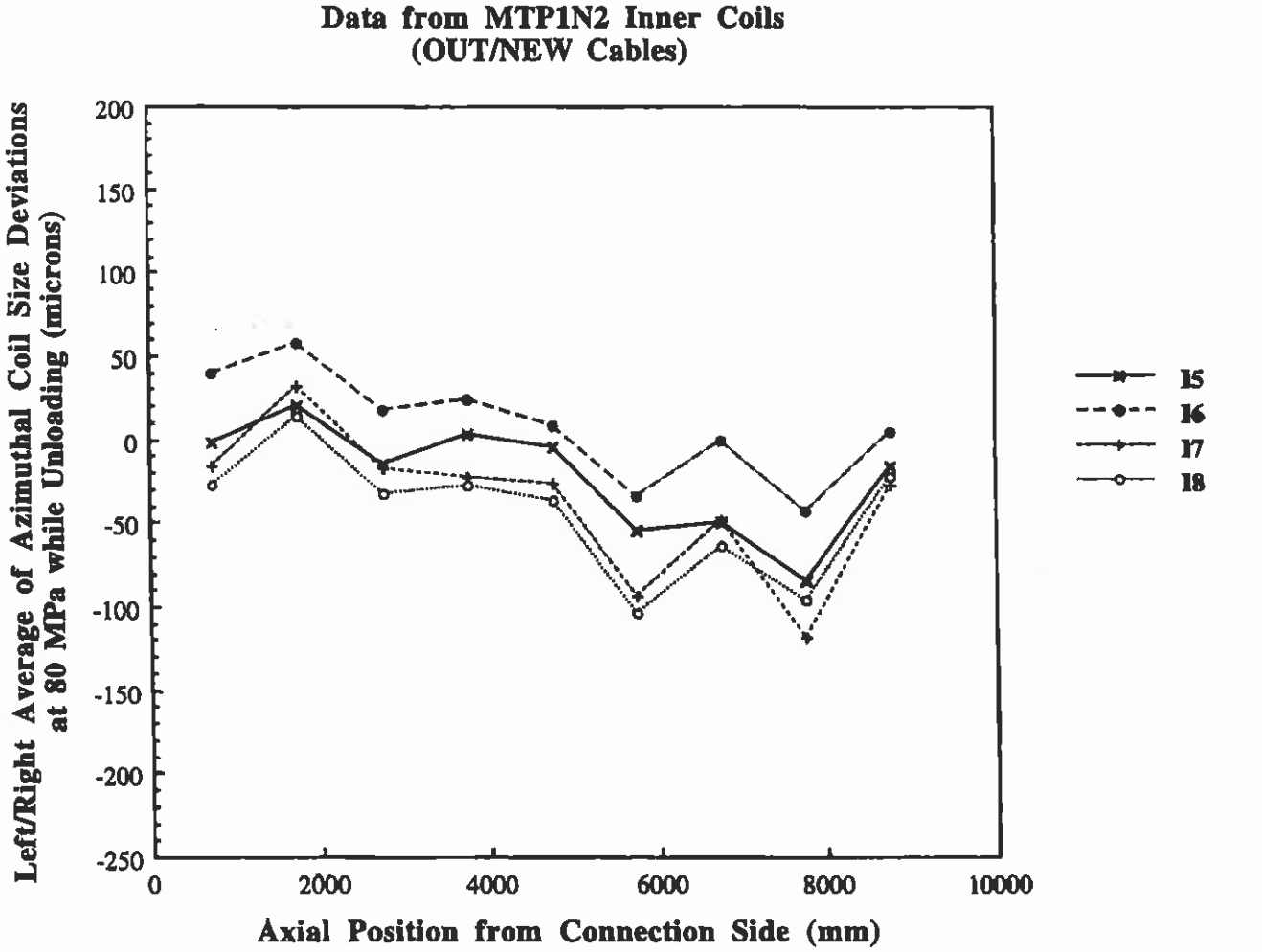

(Courtesy W. Thomi)

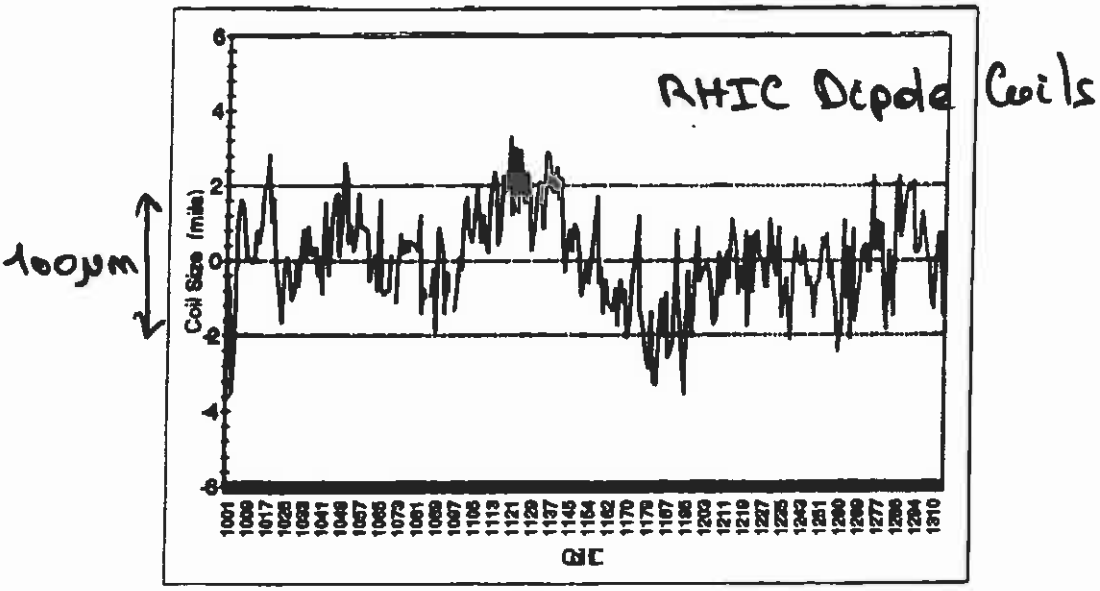

Fig. 4. RHIC 8 cm Dipole Mean Coil Azimuthal Size.

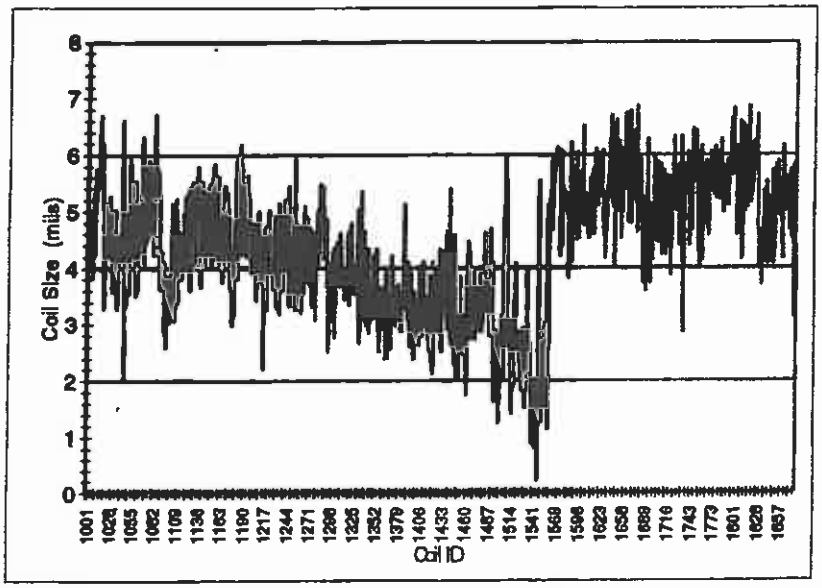

Fig. 5. RHIC 8 cm Quadrupole Mean Coil Azimuthal Size.

M. Anerella, et al. (1996)

LECTURE 6: ASSEMBLY OF PARTICLE ACCELERATOR MAGNETS

6.1 Coil Winding

6.2 Coil Curing

6.3 Azimuthal Coil Size Measurements

6.4 Coil Assembly and Internal Splicing

6.5 Collaring

6.6 Collar Deflection Measurements

6.7 External Splicing

6.8 Yoke Stacking and Shell Welding

6.9 Yoke Midplane Gap Measurements

6.10 Cryostating

6.11 Instrumentation

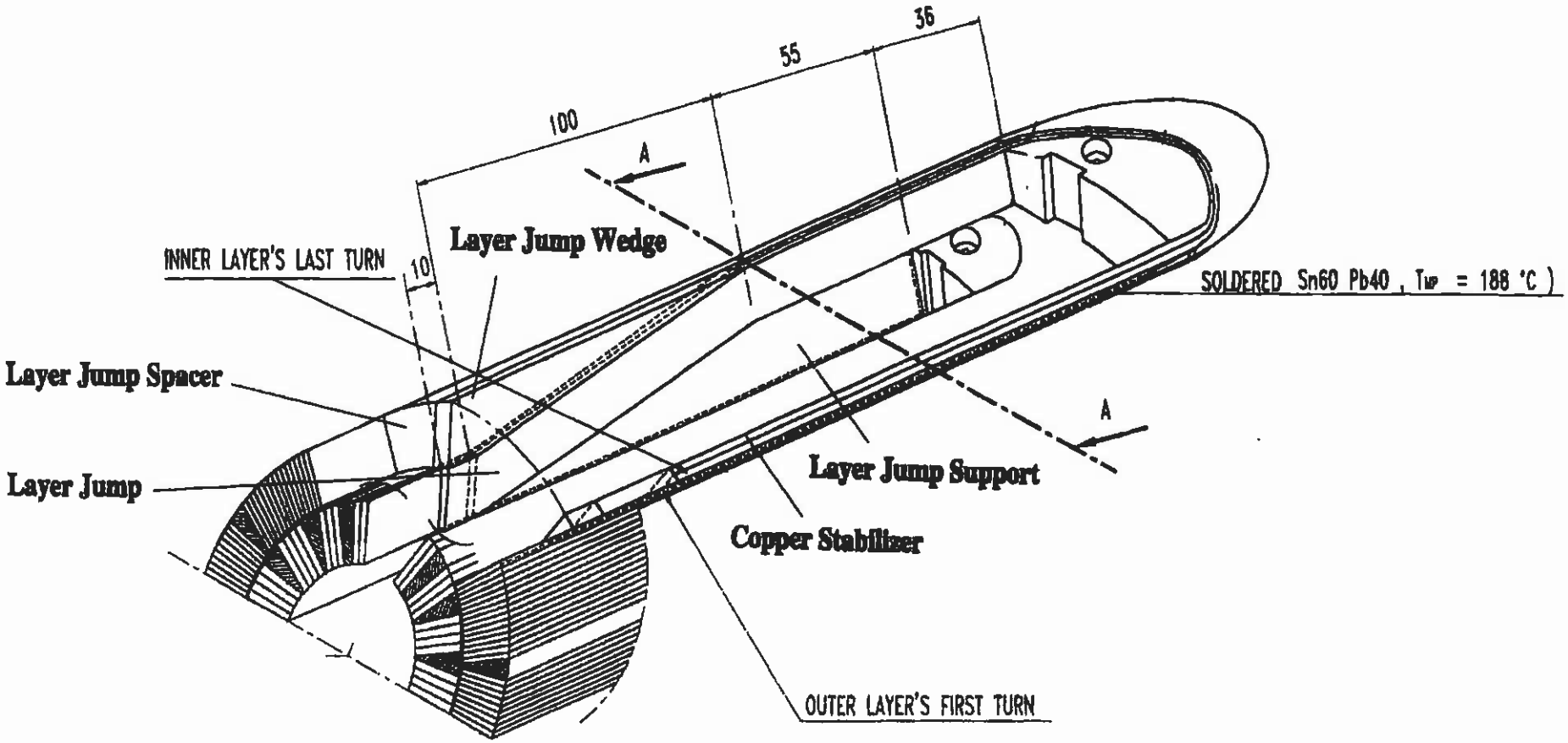
36
55
100
A
Layer Jump Wedge
INNER LAYER'S LAST TURN
10
SOLDERED Sn60 Pb40 , Tw = 188 °C)
Layer Jump Spacer
A
Layer Jump
Layer Jump Support
Copper Stabilizer
OUTER LAYER'S FIRST TURN

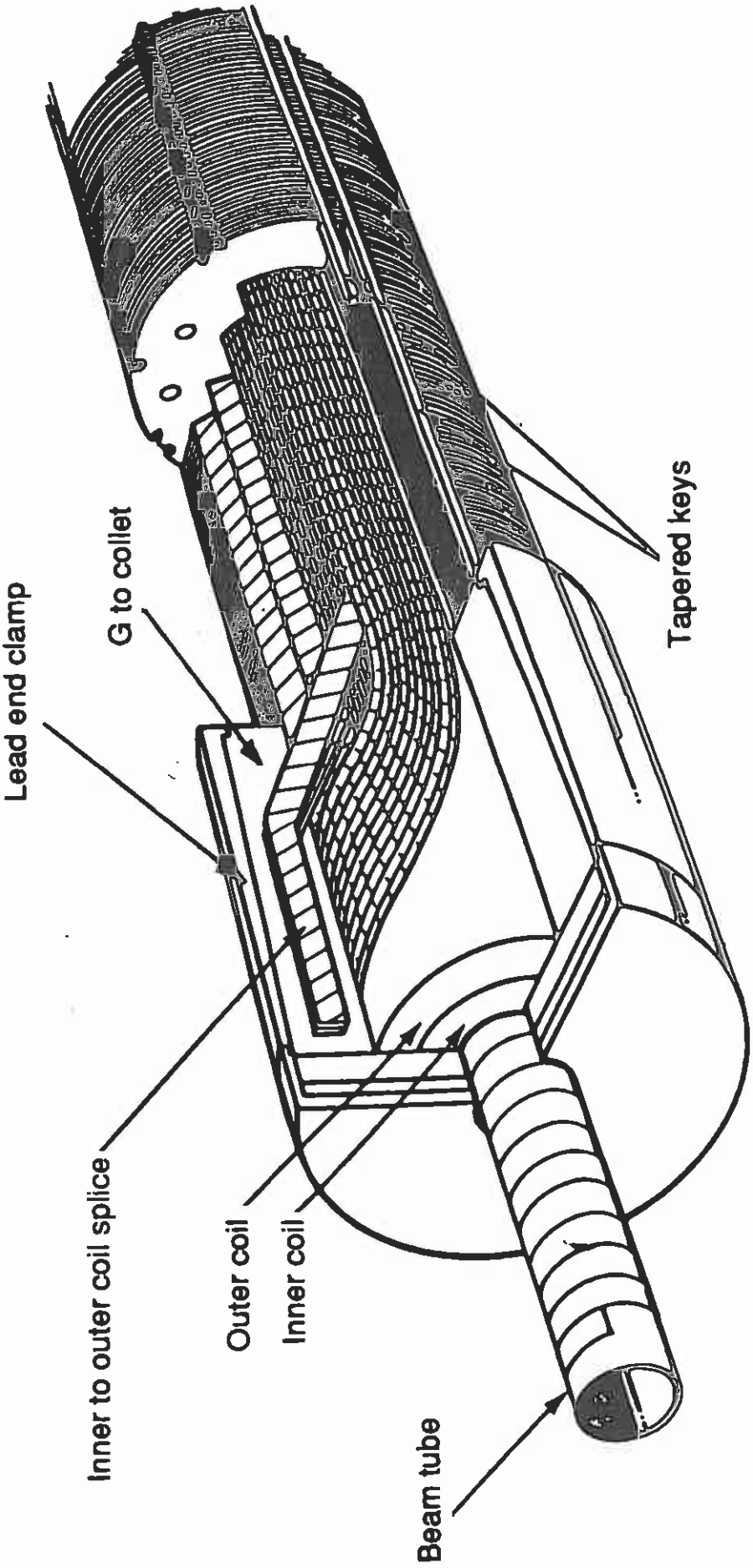
Lead end clamp
G to collet
Tapered keys
Inner to outer coil splice
Outer coil
Inner coil
Beam tube

HGQ for LHC IR

Internal splice

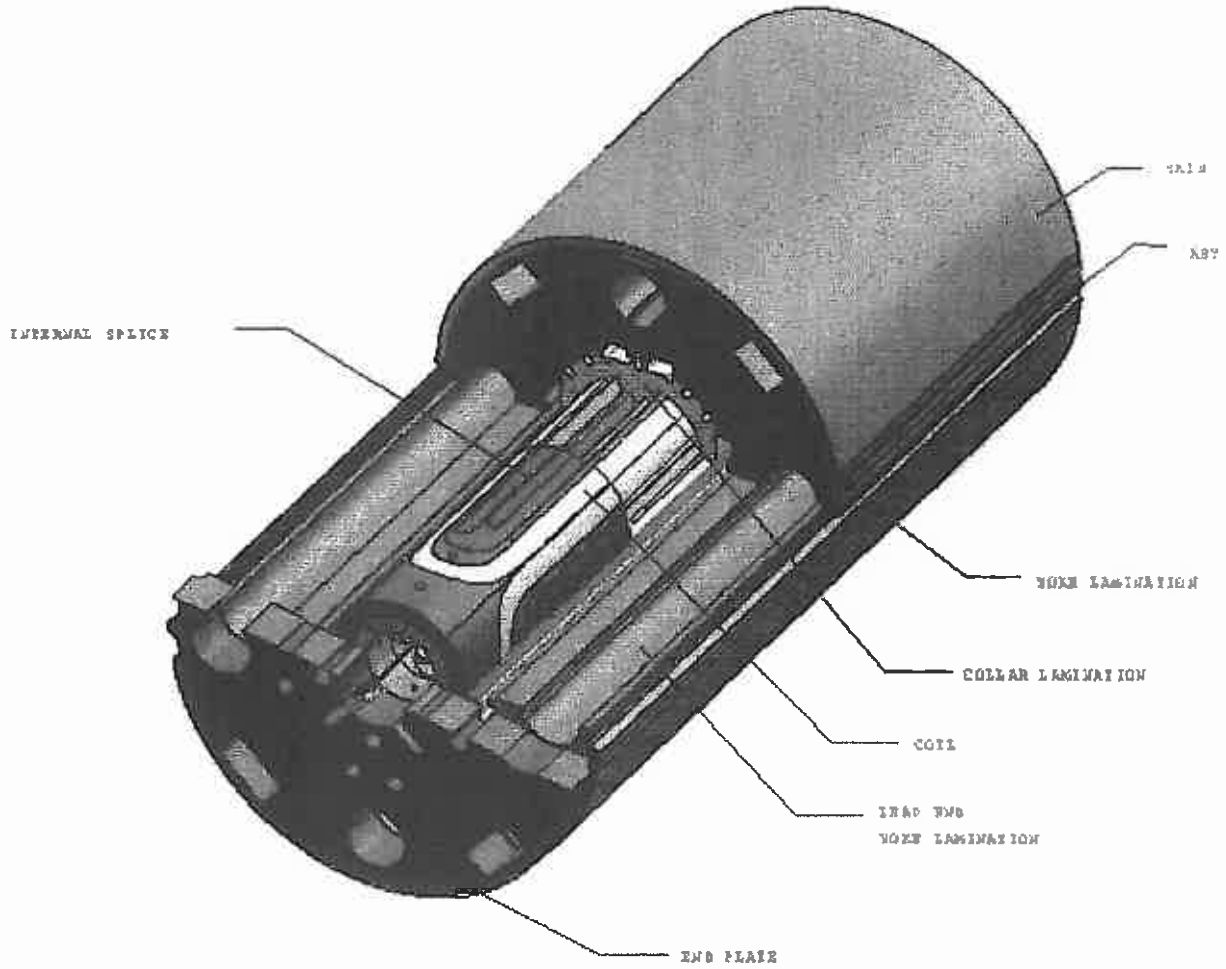

HGQ for LHC IR

External splice

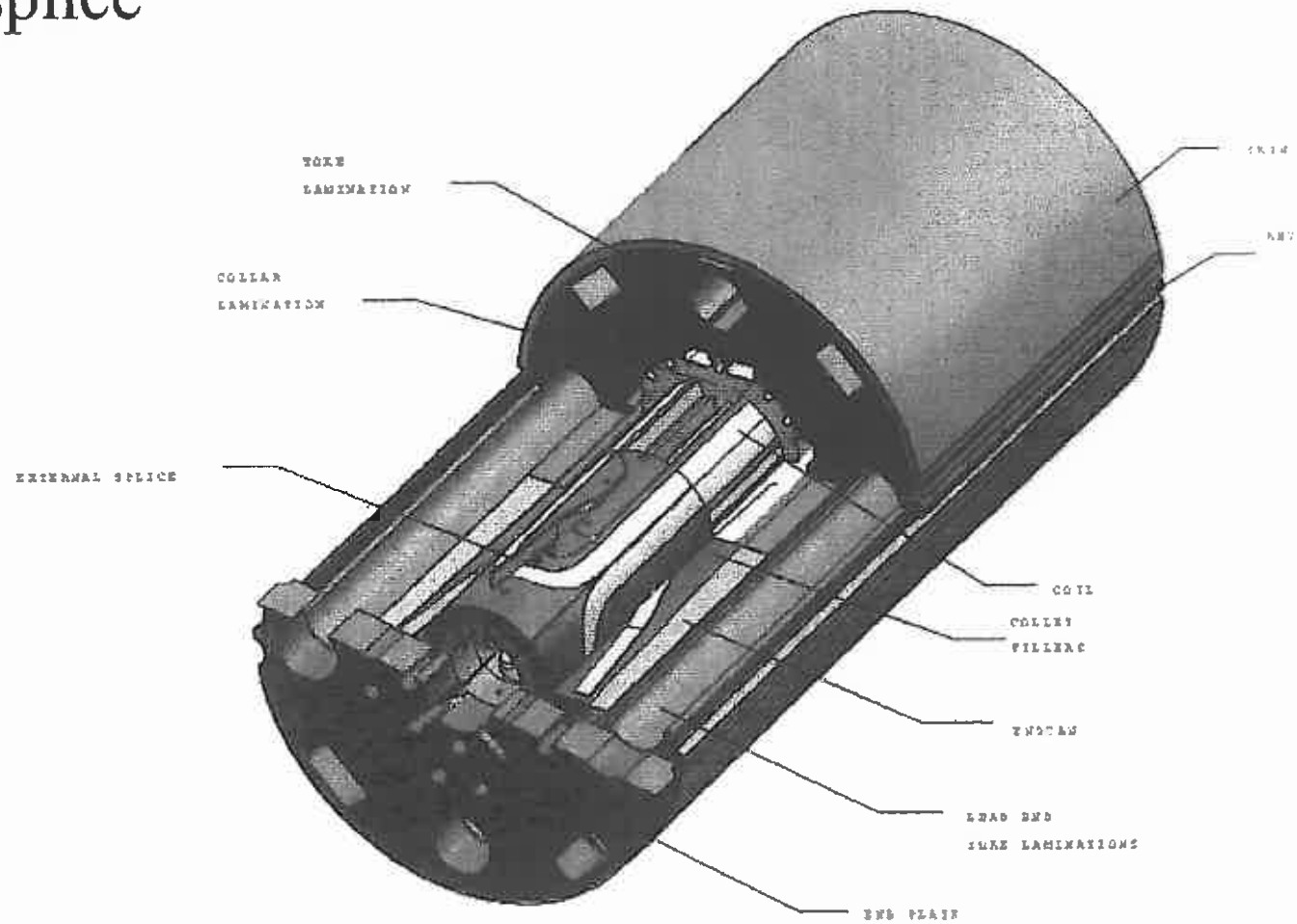

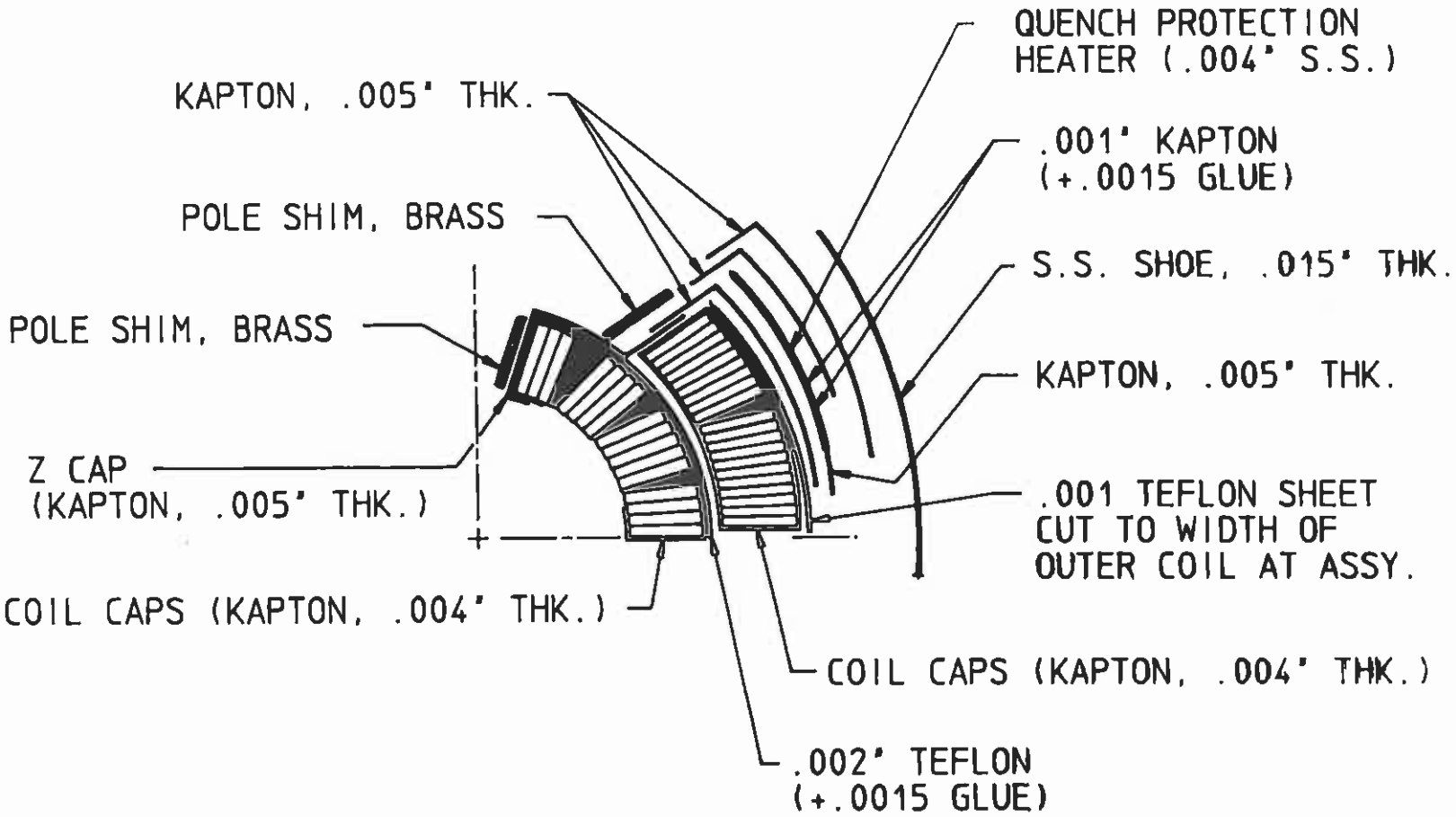

EXPLODED VIEW - COIL QUADRANT

(COLLAR REMOVED FOR CLARITY)

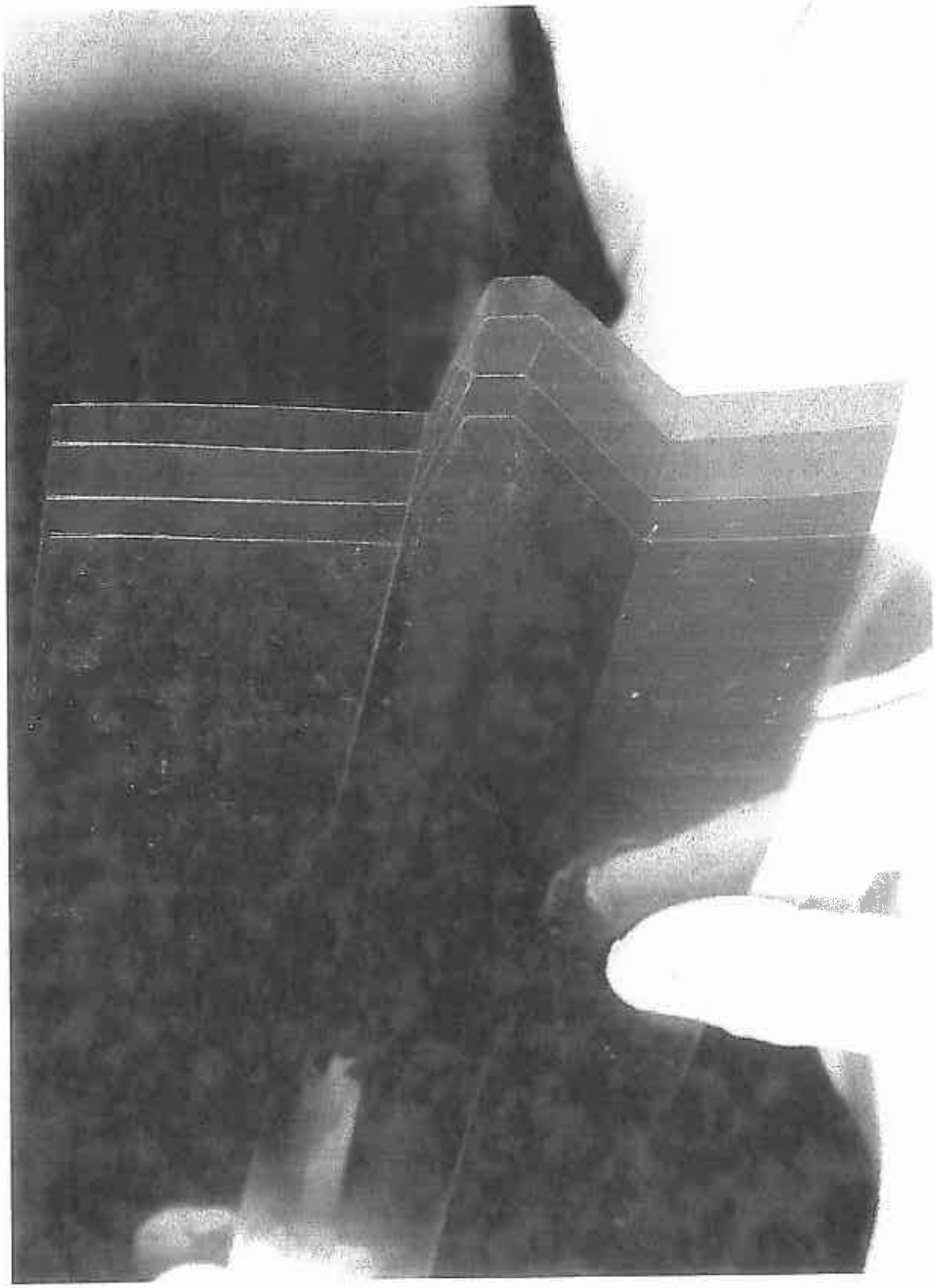

LECTURE 6: ASSEMBLY OF PARTICLE ACCELERATOR MAGNETS

6.1 Coil Winding

6.2 Coil Curing

6.3 Azimuthal Coil Size Measurements

6.4 Coil Assembly and Internal Splicing

6.5 Collaring

6.6 Collar Deflection Measurements

6.7 External Splicing

6.8 Yoke Stacking and Shell Welding

6.9 Yoke Midplane Gap Measurements

6.10 Cryostating

6.11 Instrumentation

COLLARING

– As we have seen, the collars are designed to restrain the coils radially and to pre-compress the coils azimuthally.

The azimuthal pre-compression is needed to avoid parting of the coils from the collar poles under the effects of the azimuthal components of the Lorentz forces.

– The desired level of pre-compression is achieved by squeezing the coils into cavities which are smaller than their sizes at rest.

The cavities are defined by the inner boundaries of the collars which are assembled and locked around the coils.

– The collar interlocking is ensured either by full-length tie rods located at, or right above and right below, the collared-coil assembly midplane, or by short length keys inserted on both sides of the collared-coil assembly.

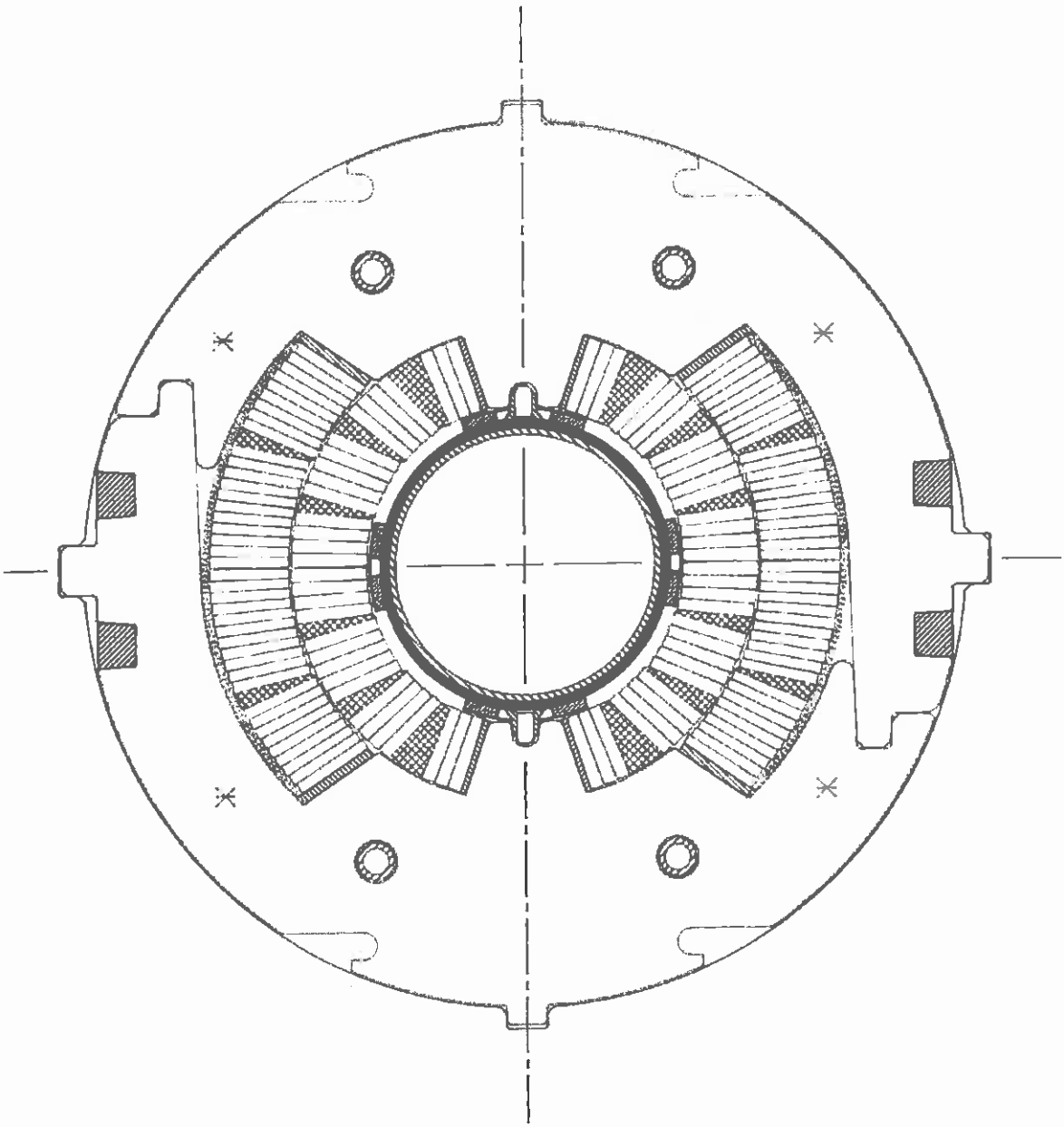

COLLARED COIL X-SECTION

4-cm Apert., C35BD

DIPOLE MAGNET COLLARING PROCEDURE

– The collaring operation starts by mounting the laminated collars, which may be grouped into packs, around the coil assembly.

– Then, the loosely-collared coil assembly is placed onto a press bed and vertical forces are applied on top and bottom of the collar laminations (which may incorporate dedicated cutouts).

– The vertical forces are transmitted to the coils which are loaded azimuthally. They are increased until proper clearances are obtained to insert the tie rods or the keys into their dedicated housing holes or keyways.

– Once the tie rods or the keys are inserted, the forces are released and the locked collars start reacting against the loaded coils. The structure is then left to relax and to find its own mechanical equilibrium.

– This equilibrium depends on the respective stiffness of the collars and the coils, and since the collars are not infinitely rigid, the achieved residual stresses in the coils may be significantly lower than the maximum loads applied by the press.

– Several techniques can be used to limit coil overpressure during collaring.

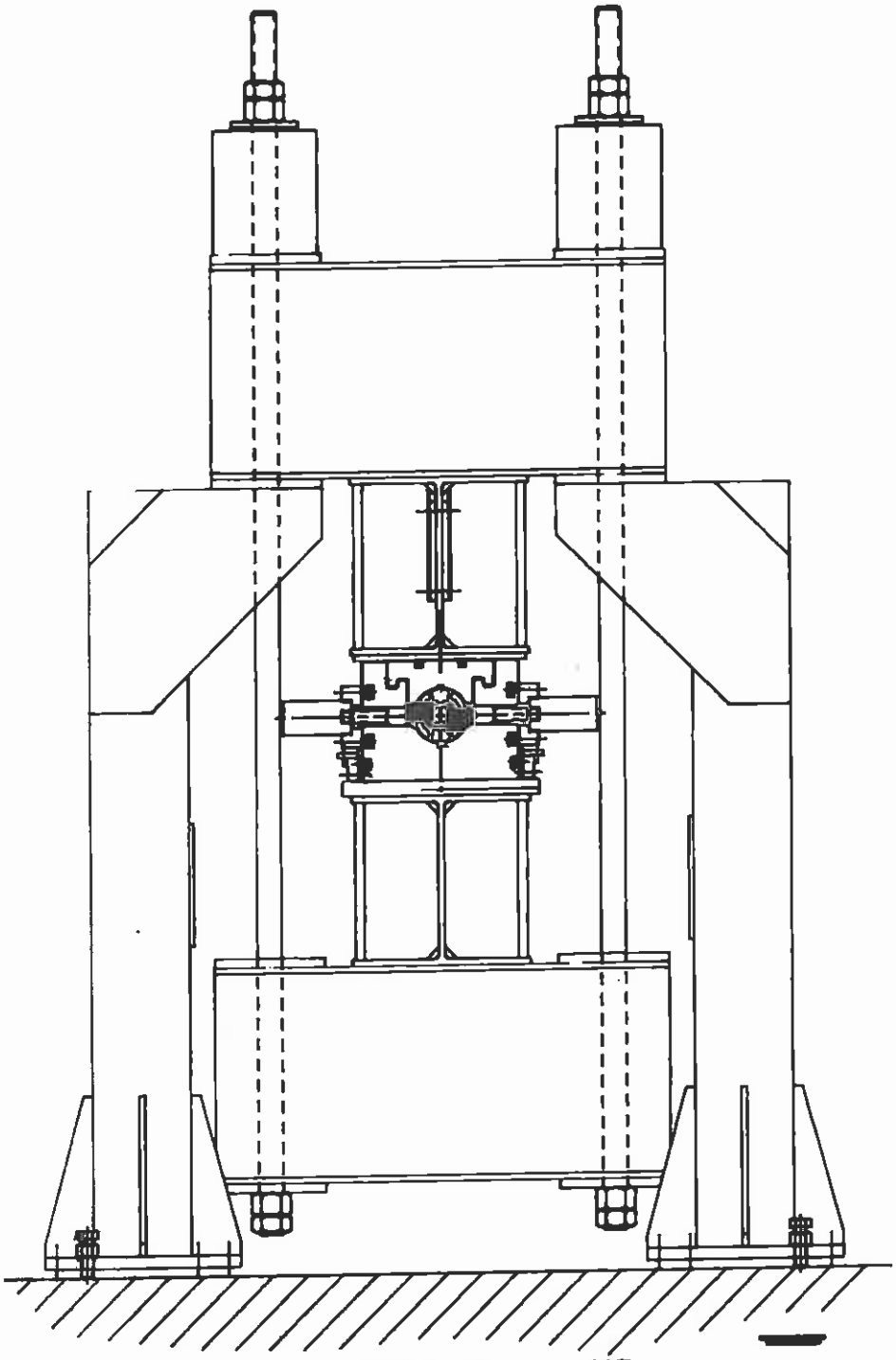

COIL COLLAR/KEYING
FIXTURE & PRESS

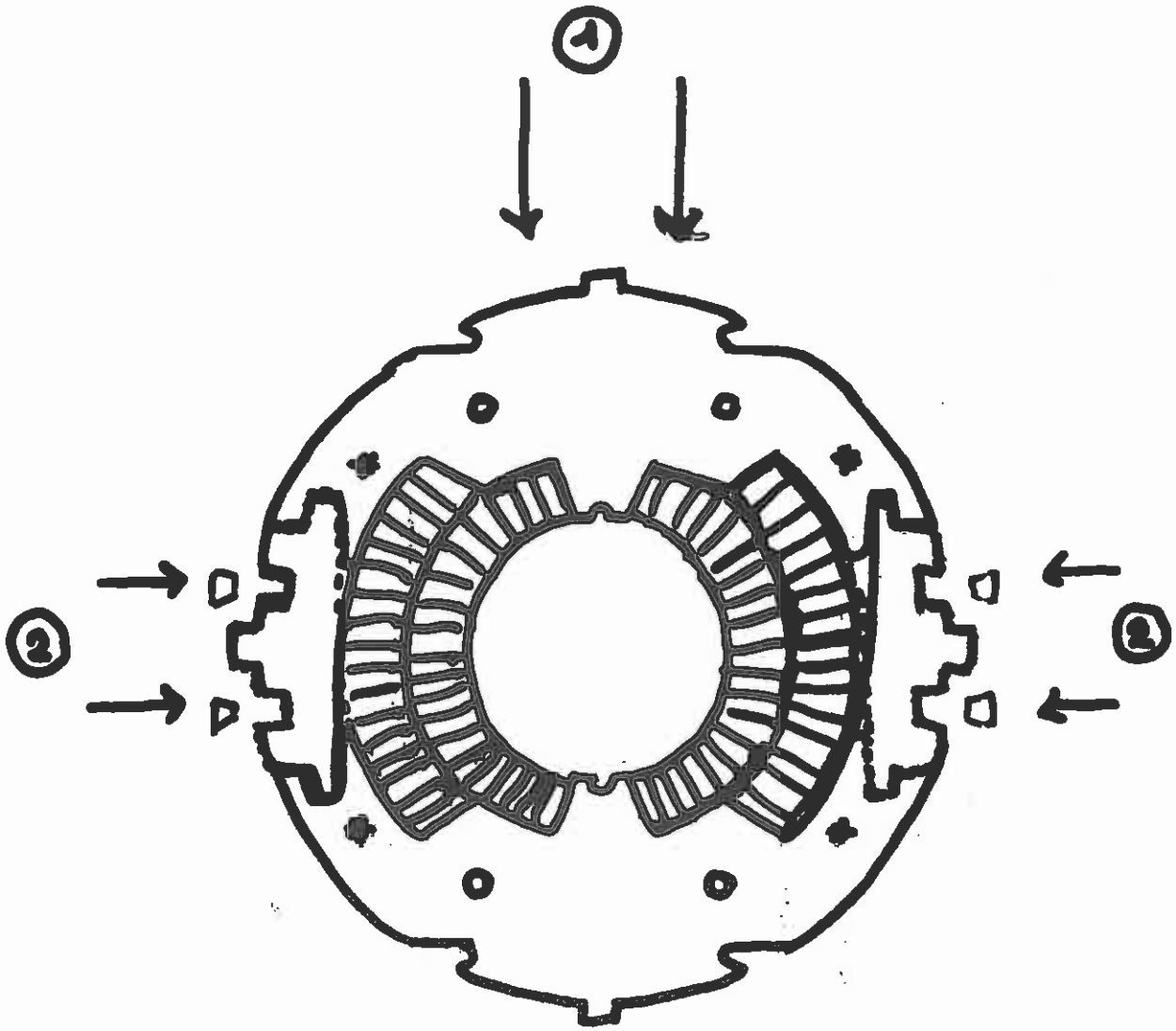

1. Vert. Pres. to open keyways at collar sides
2. Hor. Pres. to insert keys into keyways
3. Release of Vert. and Hor. Pres.

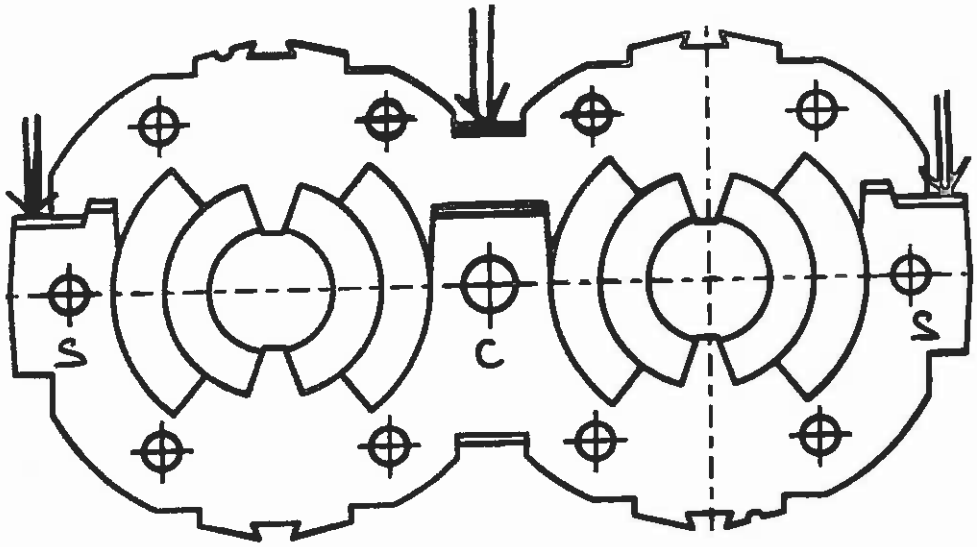

Rod sizes (mm)

	C	S
MTP1A1	21.90	13.95
MTP1A2	21.95	13.95
MTP1A3	22.00	13.95
MTP1N1	22.00	14.00
MTP1N2	22.00	14.00

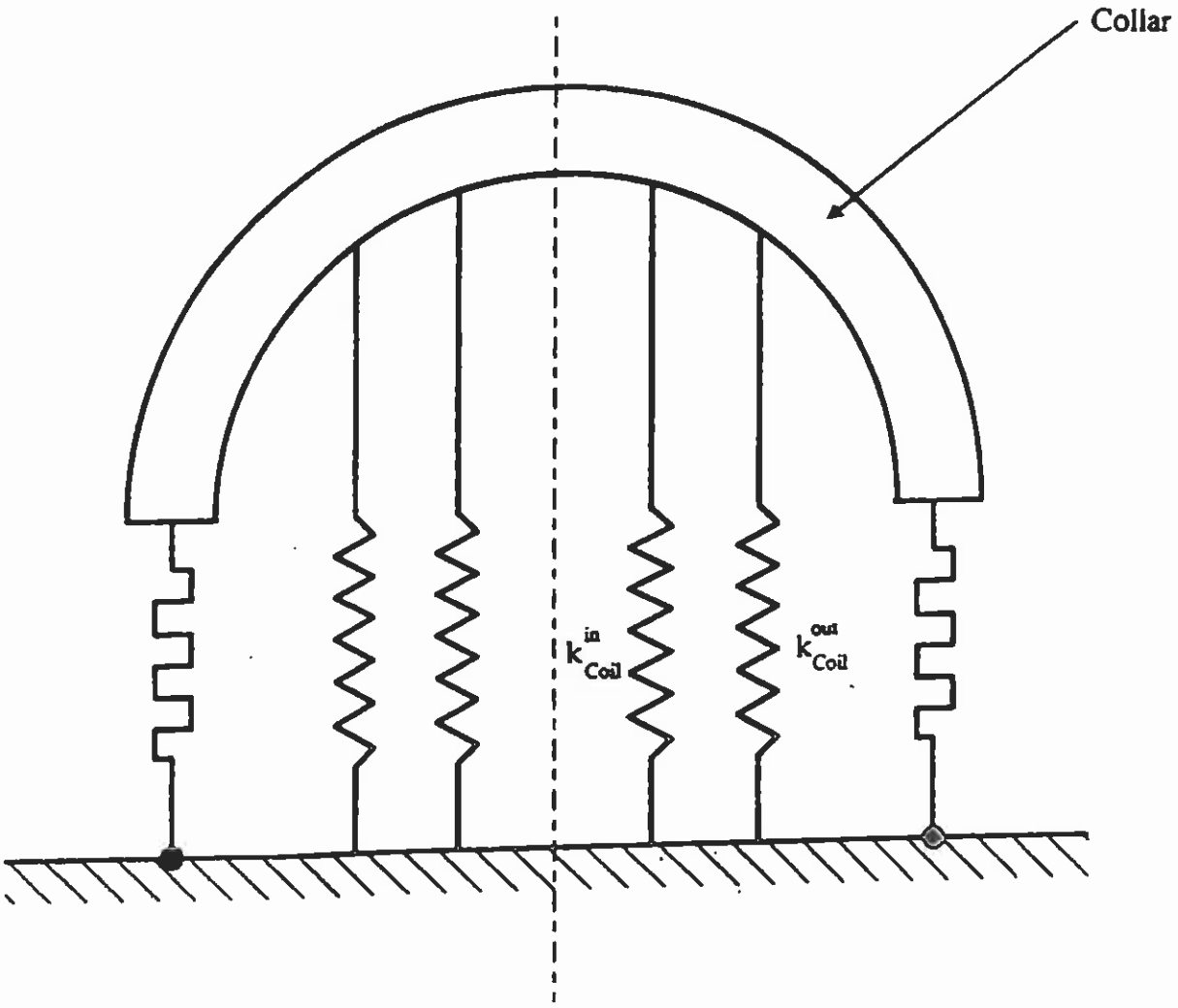
Collar
k_{Coil}^{in}
k_{Coil}^{out}

RESIDUAL AZIMUTHAL PRE-COMPRESSION

– According to the description presented in the previous slide, the loading conditions experienced by the coils during collaring can be divided into two phases:

• ***a loading phase,*** corresponding to the application of vertical forces by the press,

• ***an unloading phase,*** corresponding to the relaxation of the collared-coil assembly upon press release.

– The level of azimuthal pre-compression depends on the parameters of these two phases.

– The maximum load provided by the press during the collaring operation can be estimated from the minimum arc length to which the coils are compressed along the loading branches of their stress-strain curves.

– The amount of stress relaxation within the collared-coil assembly is determined by the effective spring rate of the collars along the vertical diameter and by the effective unloading spring rate of the coil assembly package.

– Hence, and as already discussed, accurate computations of collaring stresses require a detailed knowledge of the coil stress-strain curves.

Simulation of Coil Stress History Measured by Beam Strain Gauge During Magnet Assembly & Testing

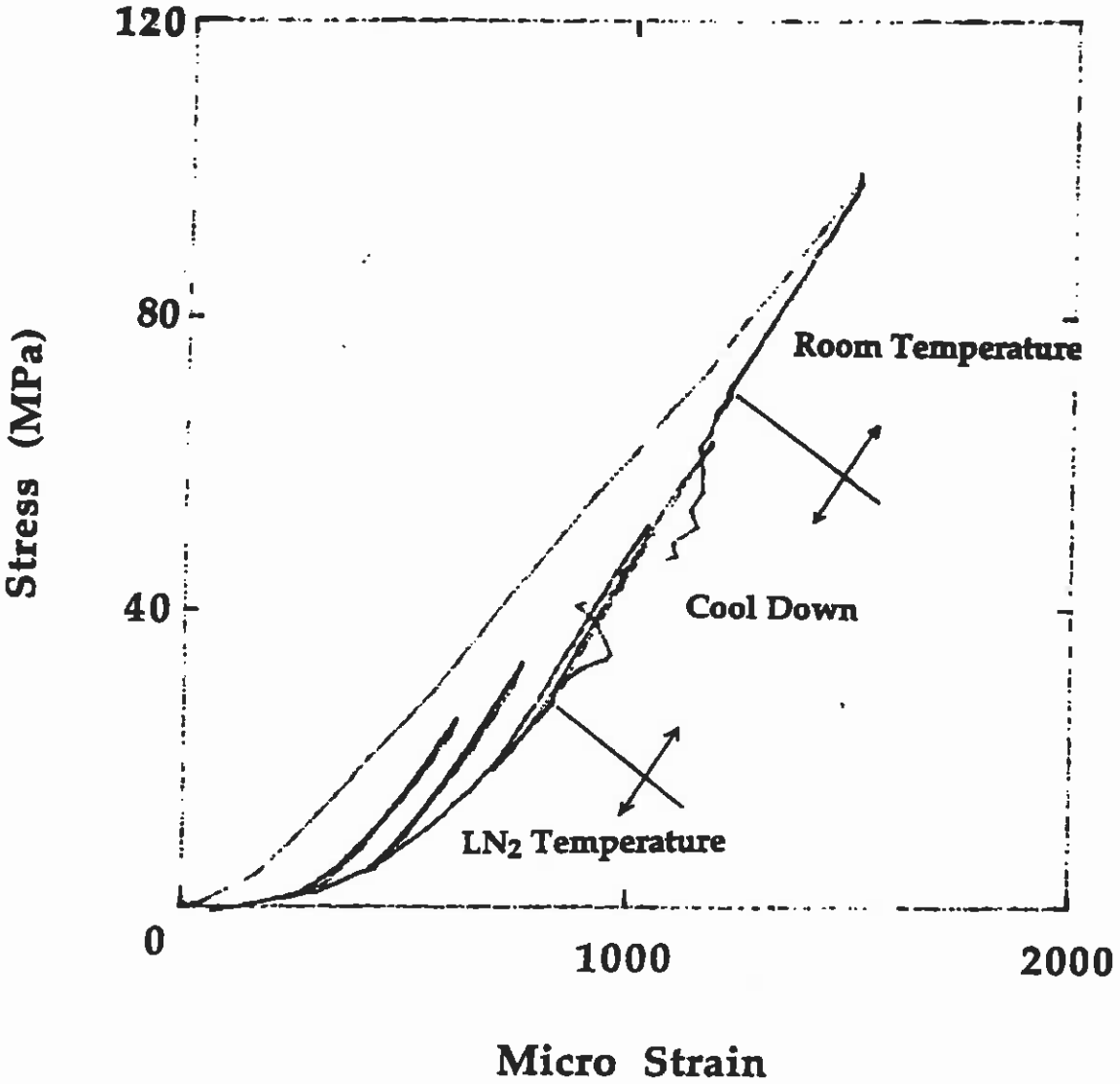

COLLARING SHIMS

– Discrepancies in the azimuthal sizes of the coil assemblies can be compensated by means of shims of adjustable thicknesses.

– There are two types of collaring shims:

- ***pole shims,*** mounted at the collar poles,

- ***midplane shims,*** placed at the coil assembly midplane.

– The shim thicknesses are determined on the basis of the measured azimuthal coil sizes so as to ensure a suitable level of pre-compression.

– Note, however, that the pole shims displace the coil pole faces and that the midplane shims displace the coil assembly midplane.
Such displacements result in undesirable field distortions.

– Hence, the use of collaring shims is only conceivable in the course of a magnet R&D program and should be avoided during magnet production.

Pre-compression Optimization

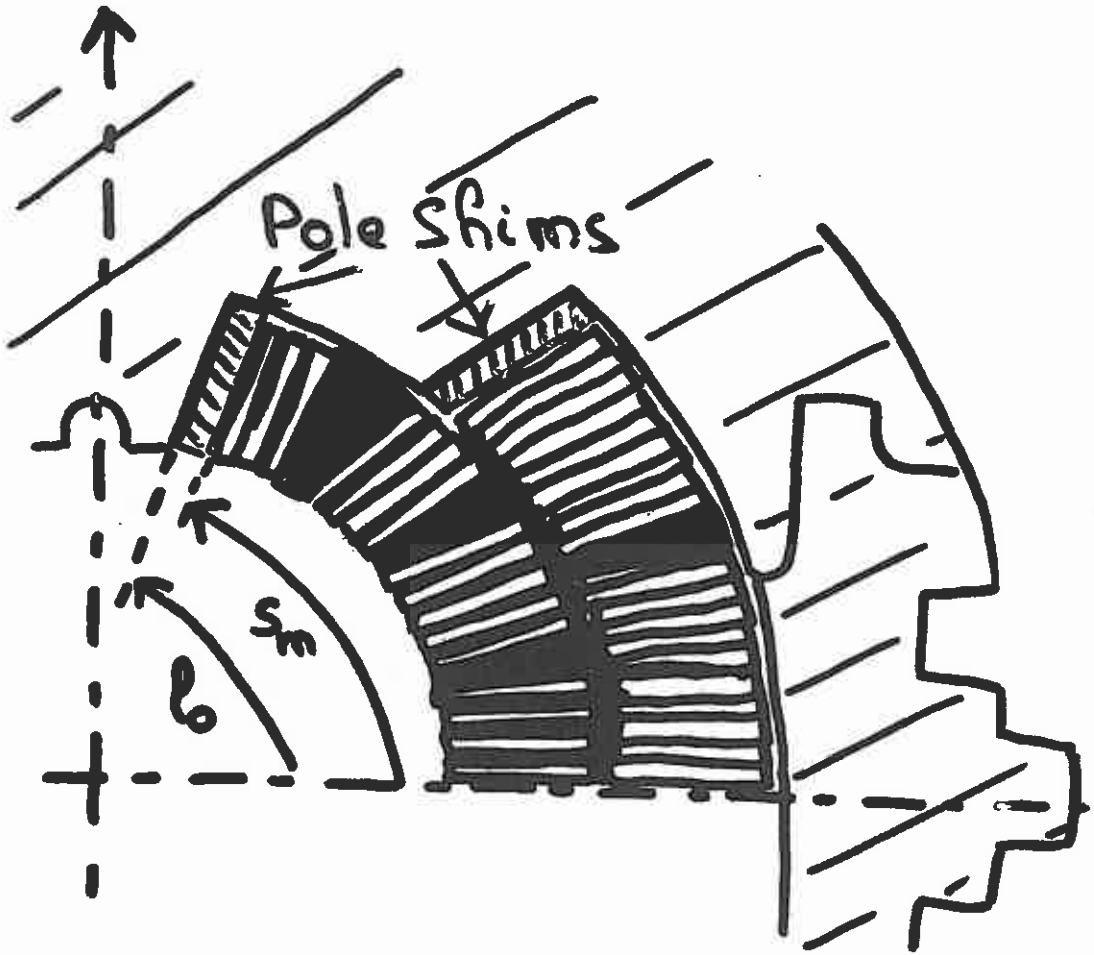

Pole shims
thicknesses

$t = l_o - s_m$ *

* several corrections needed

HOW TO LIMIT PEAK PRESSURE DURING COLLARING: SQUARE VERSUS TAPERED KEYS

– In the case of square keys, both halves of the collar need to be perfectly joined and the keyways need be fully open before insertion of the keys.

– In the case of tapered keys, part of the horizontal driving force can be used to fully open the keyways, and thus to complete the conjunction of the collar halves.

– Because the keyways need not be as open as for the square keys, less vertical pressure is required to start the key insertion, which in turn allows one to limit the peak stress seen by the coil during collaring.

SQUARE VERSUS TAPERED KEYS (CONT.)

– Another advantage of the tapered keys over the square keys is that the assembly procedure can be worked out to reduce the amount of relaxation upon release of the collaring pressure.

– This relaxation comes from the fact that, while they are under the collaring press, the collar arms are almost stress-free, while, after collaring completion, the collar arms of the keyed assembly are in tension.

Hence, at the time of the collaring pressure release, the collar arms spring back from zero into tension.

– This spring back is particularly dramatic for the square key collars which can end up overcompressed to fully open the keyways.

– In the case of tapered keys, they can be driven against the loading surfaces of the collar keyways, thereby pre-tensioning and elongating the collar arms (in the elastic range) as they end up in the keyed assembly.

– A last feature of the tapered-key insertion method is that, as the keys load the collar keyways and complete the collar halves conjunction, they increase the clamping force on the coil. The vertical collaring pressure can then be decreased accordingly to maintain a constant coil pressure during the operation.

Square Key vs. Tapered Key

- More Vertical Pres.
- More Spring-back
- No Key/Keyway deformations

- Limited Overpres.
- Limited/no Spring-back
- Key/Keyway deformations

(5-cm Apert., 15-m Long DCA 313 Stress History Plot)

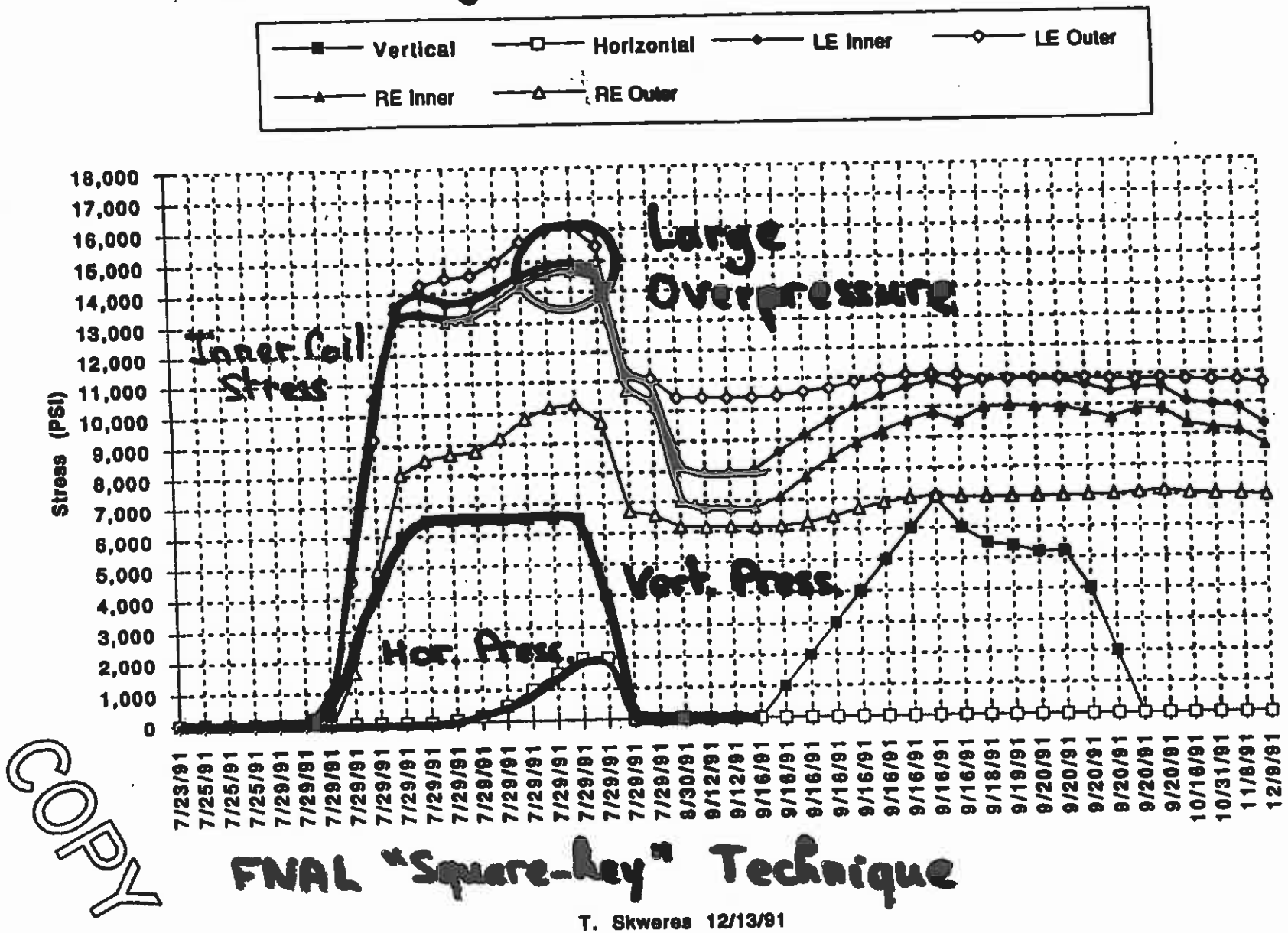

COPY

FNAL "Square-Key" Technique

T. Skwerer 12/13/91

BNL "Tapered-Key" Technique

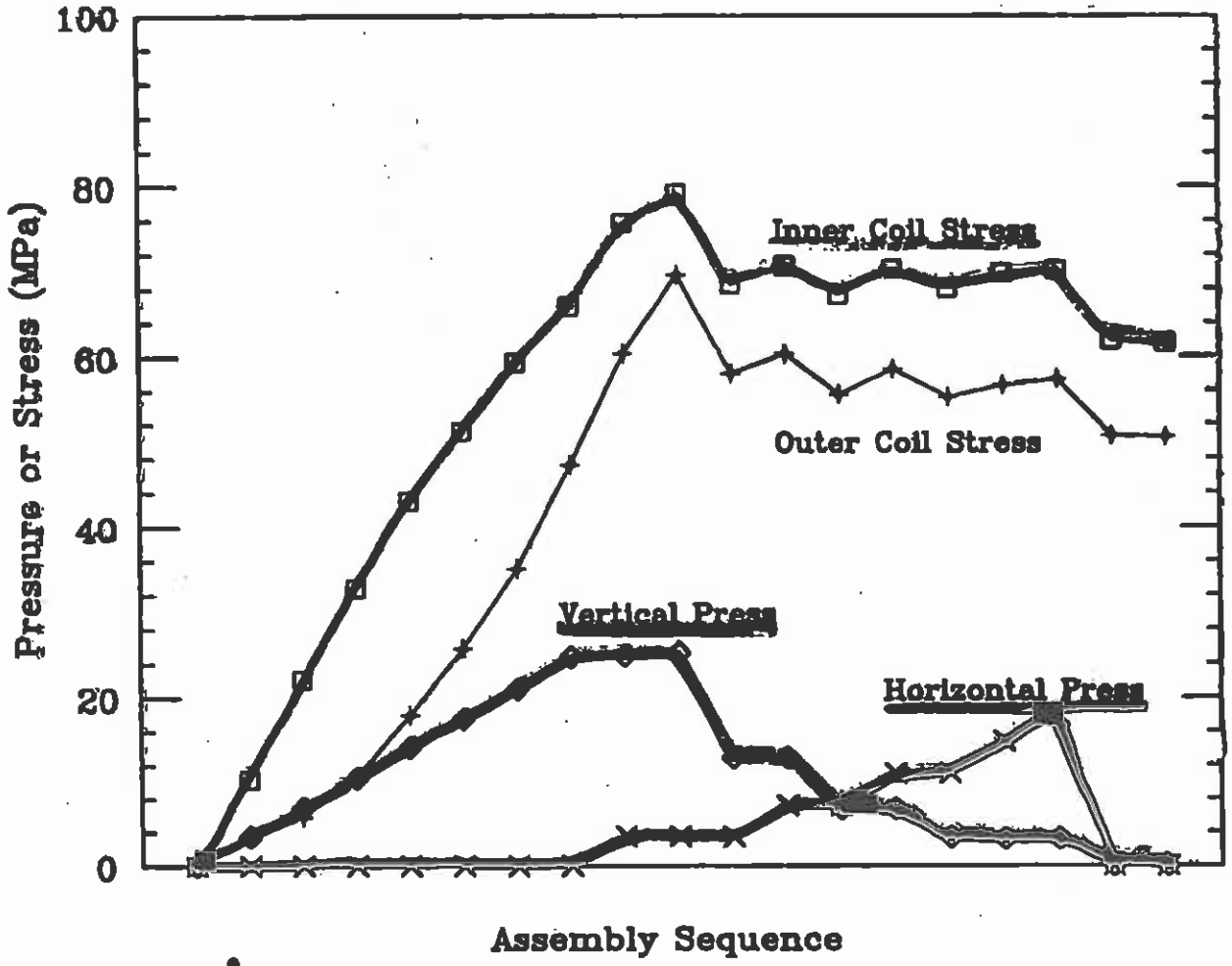

(4-cm-Apert., 17-m-Long DCO2&4)

HOW TO LIMIT PEAK PRESSURE DURING COLLARING: STEPWISE ROD INSERTION

– The simplest way of performing the collaring of a magnet relying on tie rods is to press vertically and uniformly on the collar packs, until a proper clearance is obtained to insert the tie rods into their housing holes.

This, however, similarly to the square-key technique, requires a large vertical force and results in large coil overpressure.

– To limit the force requirement and reduce coil overpressure, advantage can be taken from the fact that the collars can be bent or elastically elongated to perform the collaring in several steps.

– This stepwise collaring technique is the tie-rod equivalent of the tapered-key collaring technique.

STEPWISE ROD INSERTION PROCEDURE

– As an illustration, let us describe the collaring procedure followed for the LHC twin-aperture dipole magnet prototypes relying on common collars and full-length tie rods.

– First, reduced vertical forces are applied to the collars' central part and sides, and rods of smaller diameters than the design ones are inserted into the housing holes.

This first operation allows elimination of any residual staggering of the collar packs.

Once the small diameter rods are inserted, the reduced vertical forces are removed.

– Second, a large vertical force is applied to the collars' central part, which put the nearby collars' arms into tension, and the small diameter rod at the collars' center is replaced by the final one.

Once, the final rod is inserted, the large vertical force on the collars' central part is removed, but the rod keeps the nearby collars' arms in tension.

– Third, large vertical forces are applied to the collars' sides, which, this time, put the arms on the collars' sides into tension, and the two remaining small diameter rods are replaced by the final ones.

Once again, after insertion of the rods, the large vertical forces are removed, but the rods keep the arms on the collars' sides into tension.

STEPWISE ROD INSERTION PROCEDURE (CONT.)

– During a stepwise collaring, the repartition of forces is determined by shims of adjustable thickness which are placed on top of the collars' central part and sides.

– Relying on elastic elongations of the collar arms helps reducing the force needed to bring the housing holes of the top and bottom collars into correspondance.

– In addition, and as in the case of the squared-key collaring technique, the stepwise collaring procedure can be optimized to reduce the spring back of the collars' arms which accompany the removal of the press force.

LECTURE 6: ASSSEMBLY OF PARTICLE ACCELERATOR MAGNETS

6.1 Coil Winding

6.2 Coil Curing

6.3 Azimuthal Coil Size Measurements

6.4 Coil Assembly and Internal Splicing

6.5 Collaring

6.6 Collar Deflection Measurements

6.7 External Splicing

6.8 Yoke Stacking and Shell Welding

6.9 Yoke Midplane Gap Measurements

6.10 Cryostating

6.11 Instrumentation

Measurements of Collar Deflections

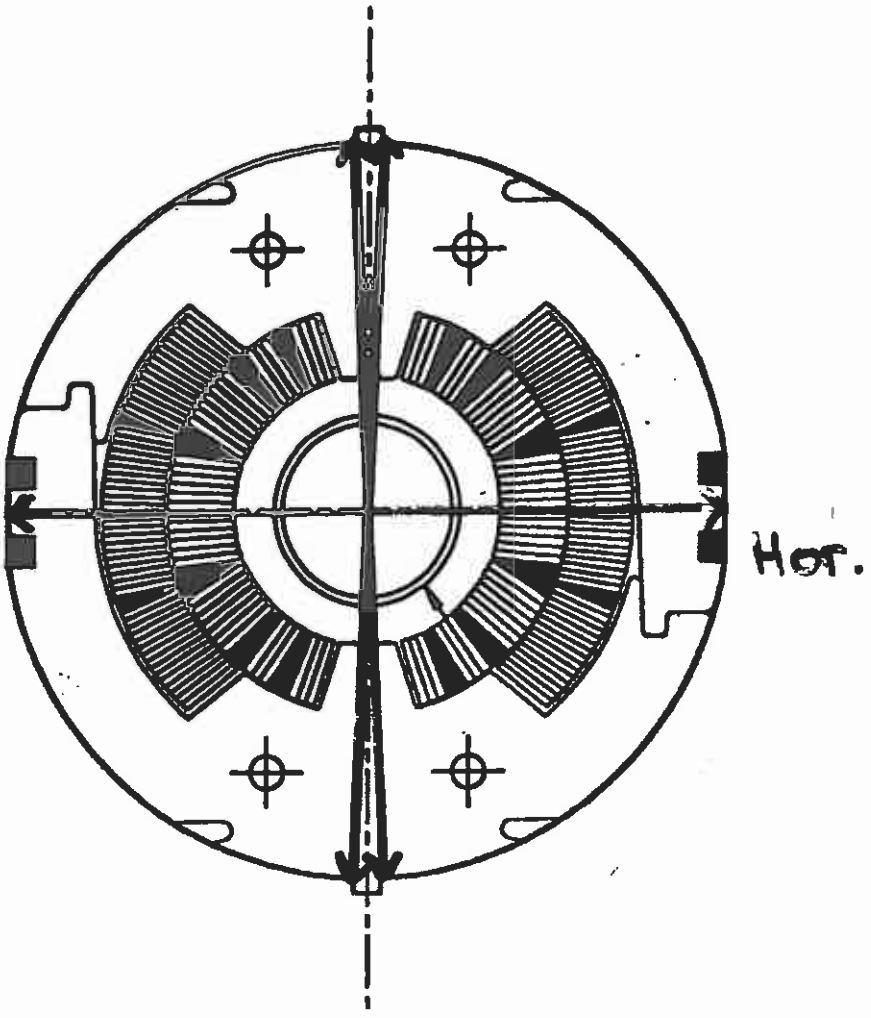

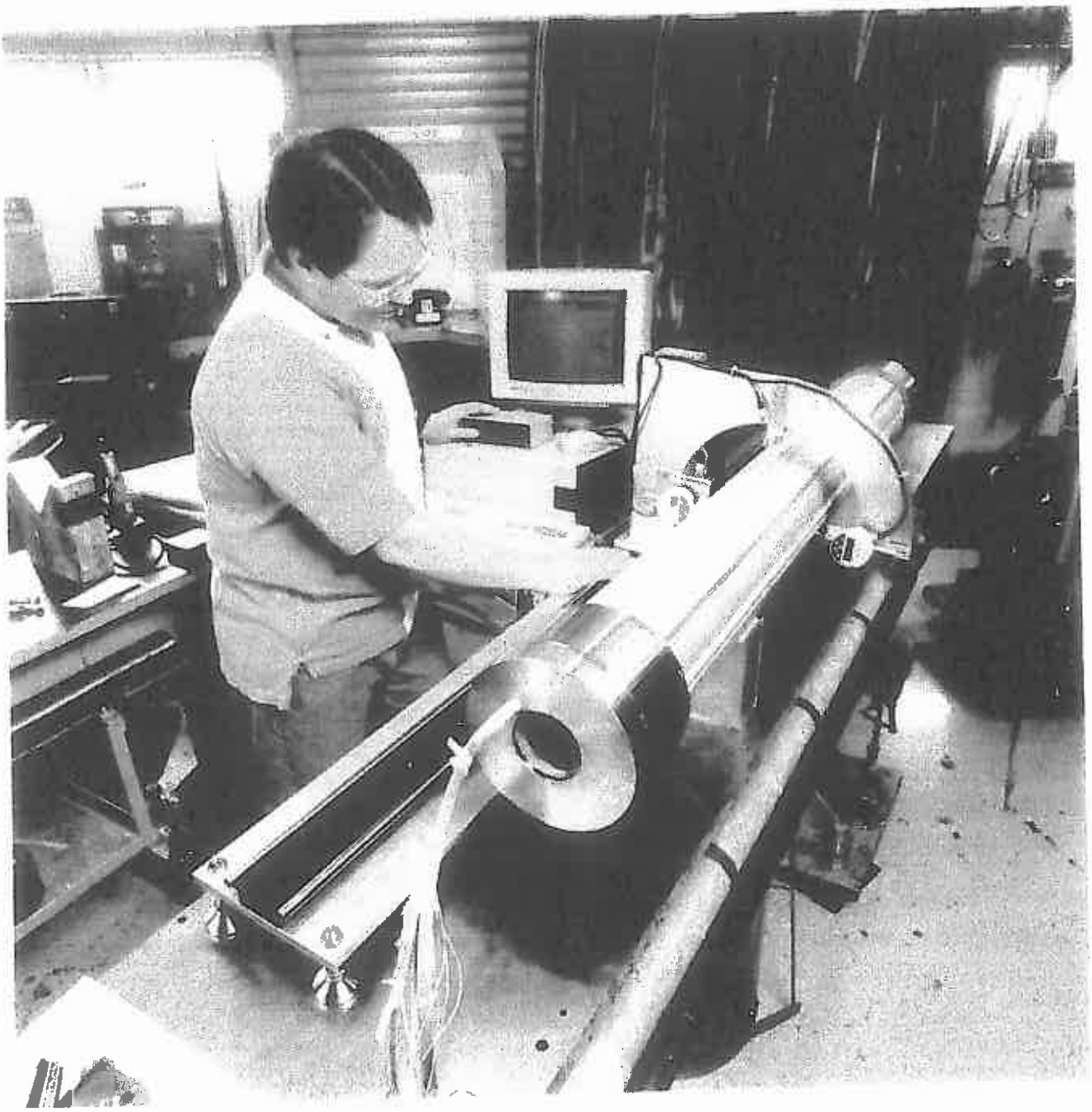

BNL 4-cm-Apert., 17-m-Long Dipole Magnet

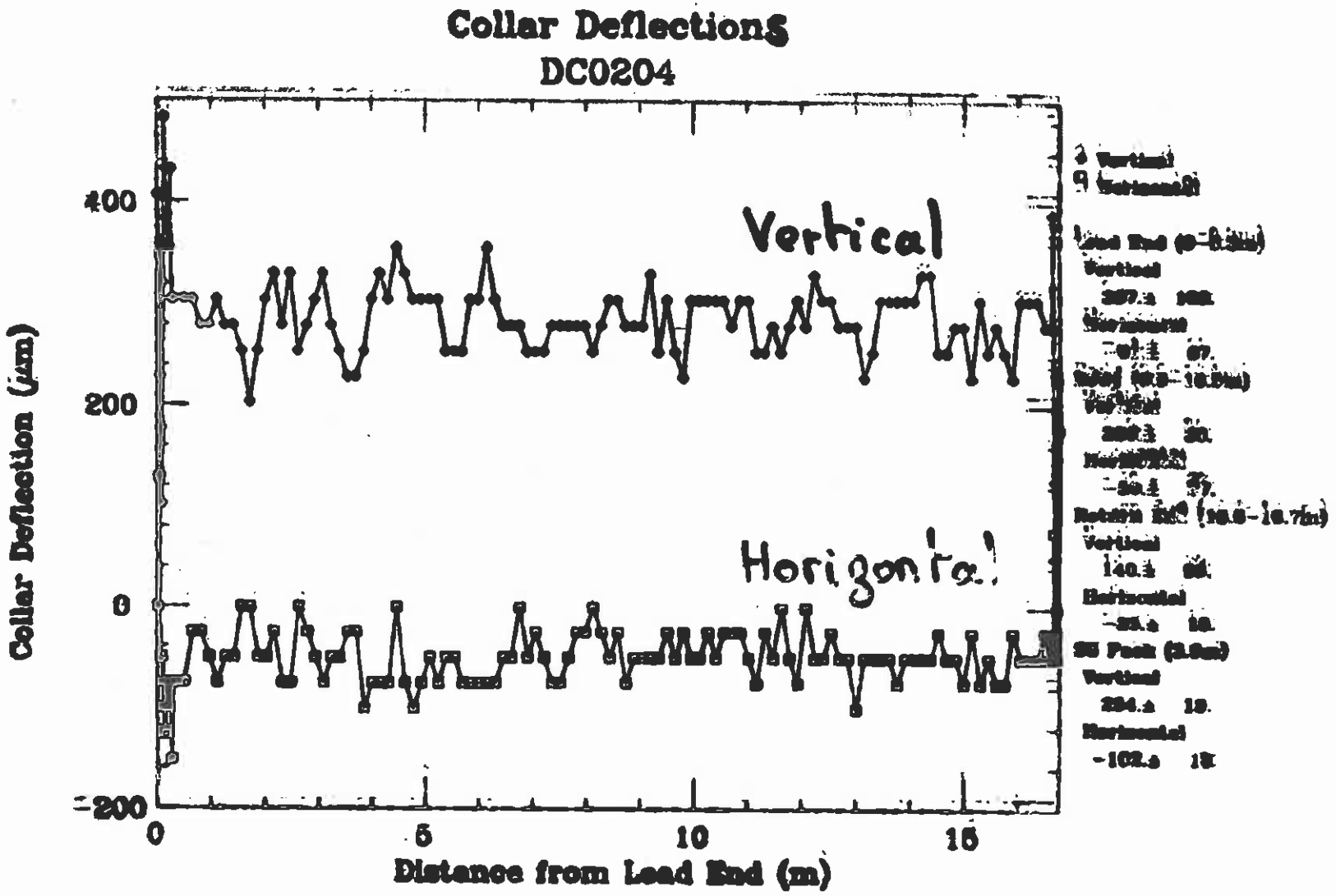

4-cm-Apert., 1.8-m-long BNL Magnets

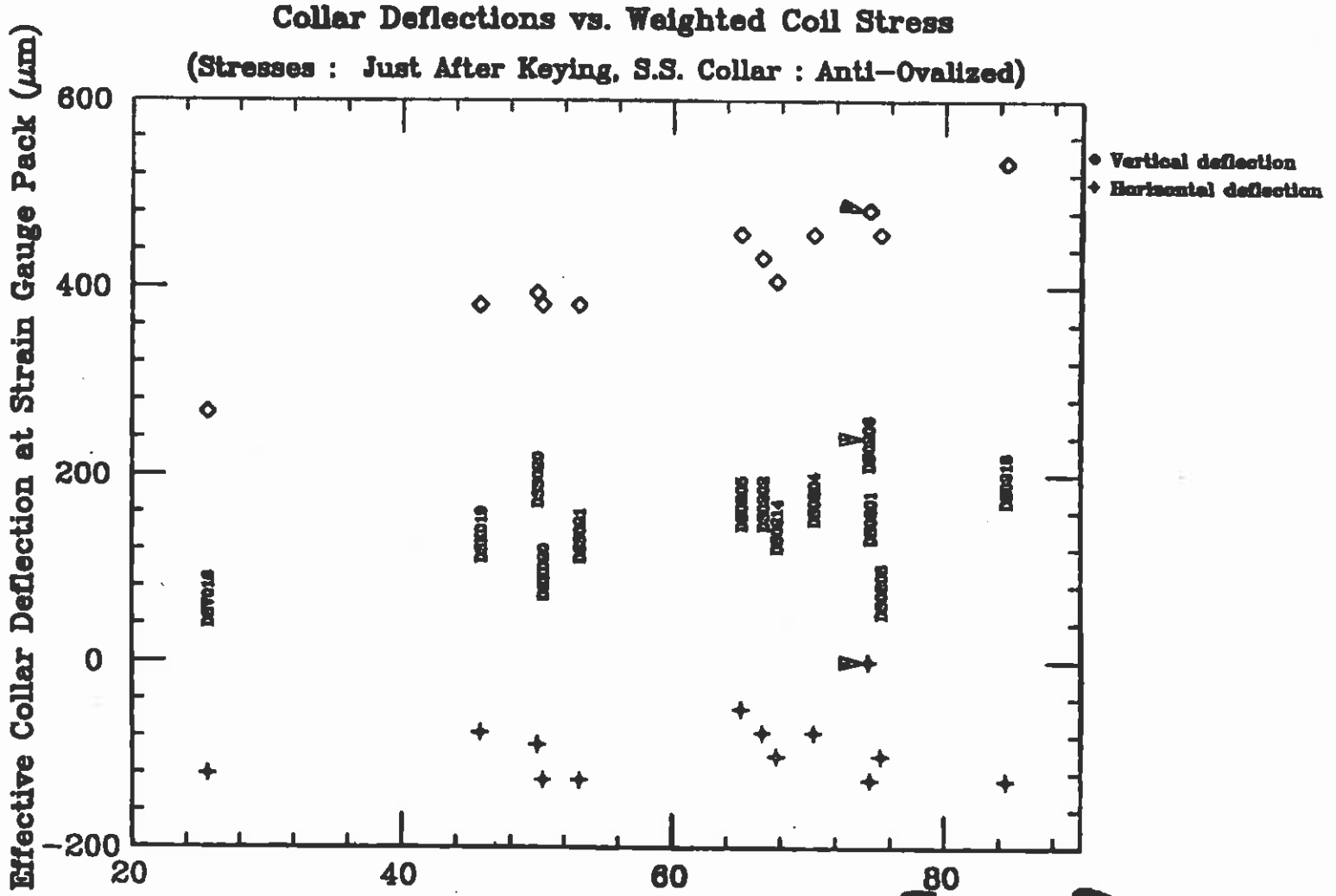

$$\frac{\sigma_i \omega_i + \sigma_o \omega_o}{\omega_i + \omega_o}$$

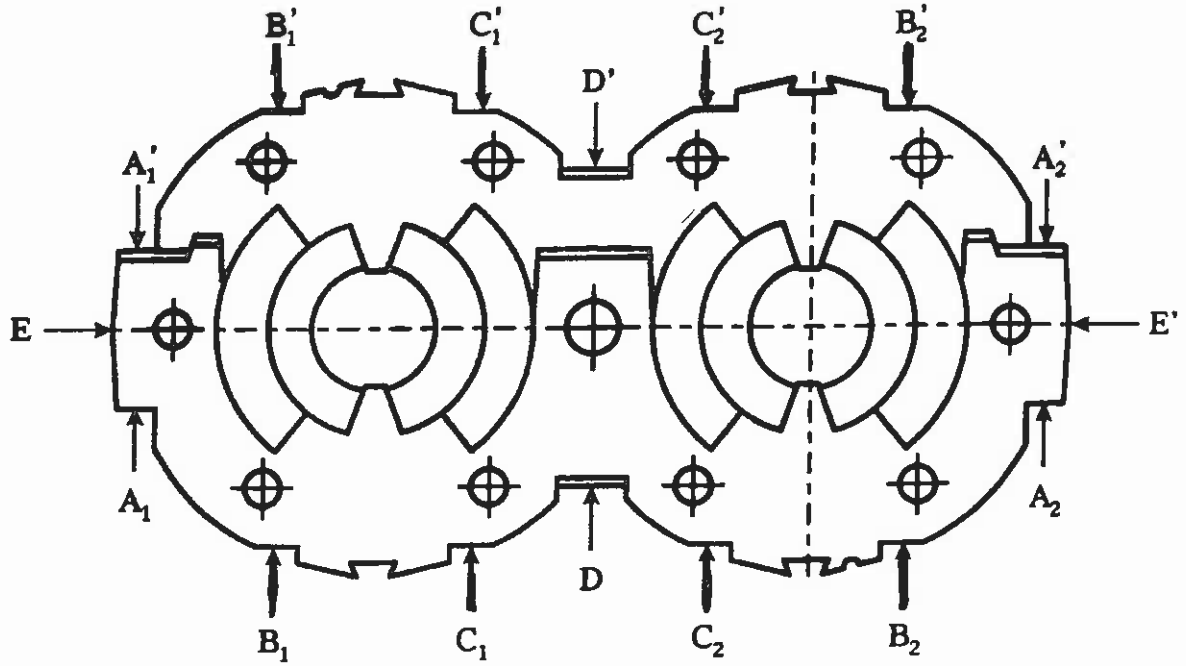
B'1
C'1
C'2
B'2
D'
A'1
A'2
E
E'
A1
A2
D
B1
C1
C2
B2

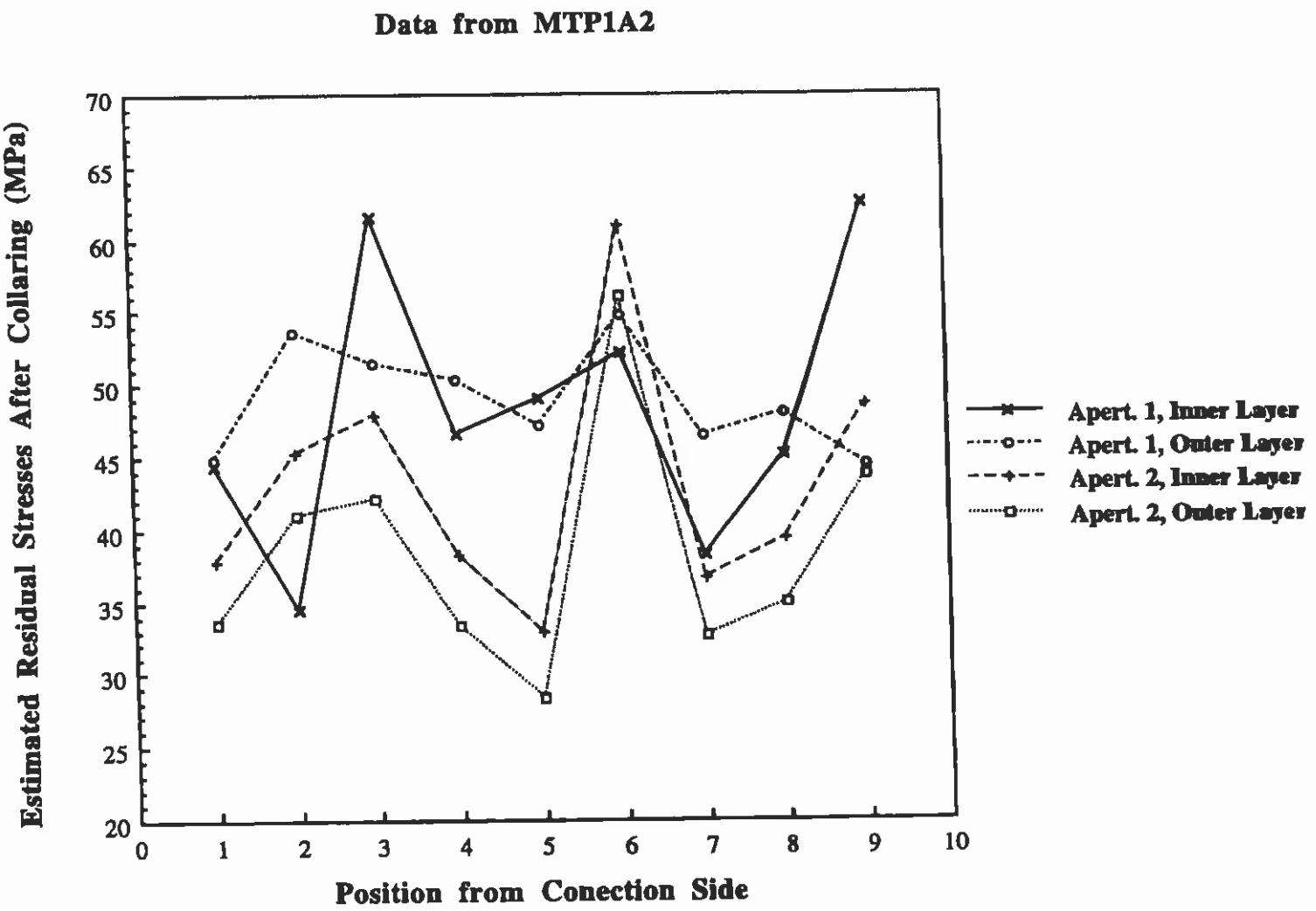
Data from MTP1A2
Estimated Residual Stresses After Collaring (MPa)
70
65
60
55
50
45
40
35
30
25
20
0
1
2
3
4
5
6
7
8
9
10
Position from Conection Side
Apert. 1, Inner Layer
Apert. 1, Outer Layer
Apert. 2, Inner Layer
Apert. 2, Outer Layer

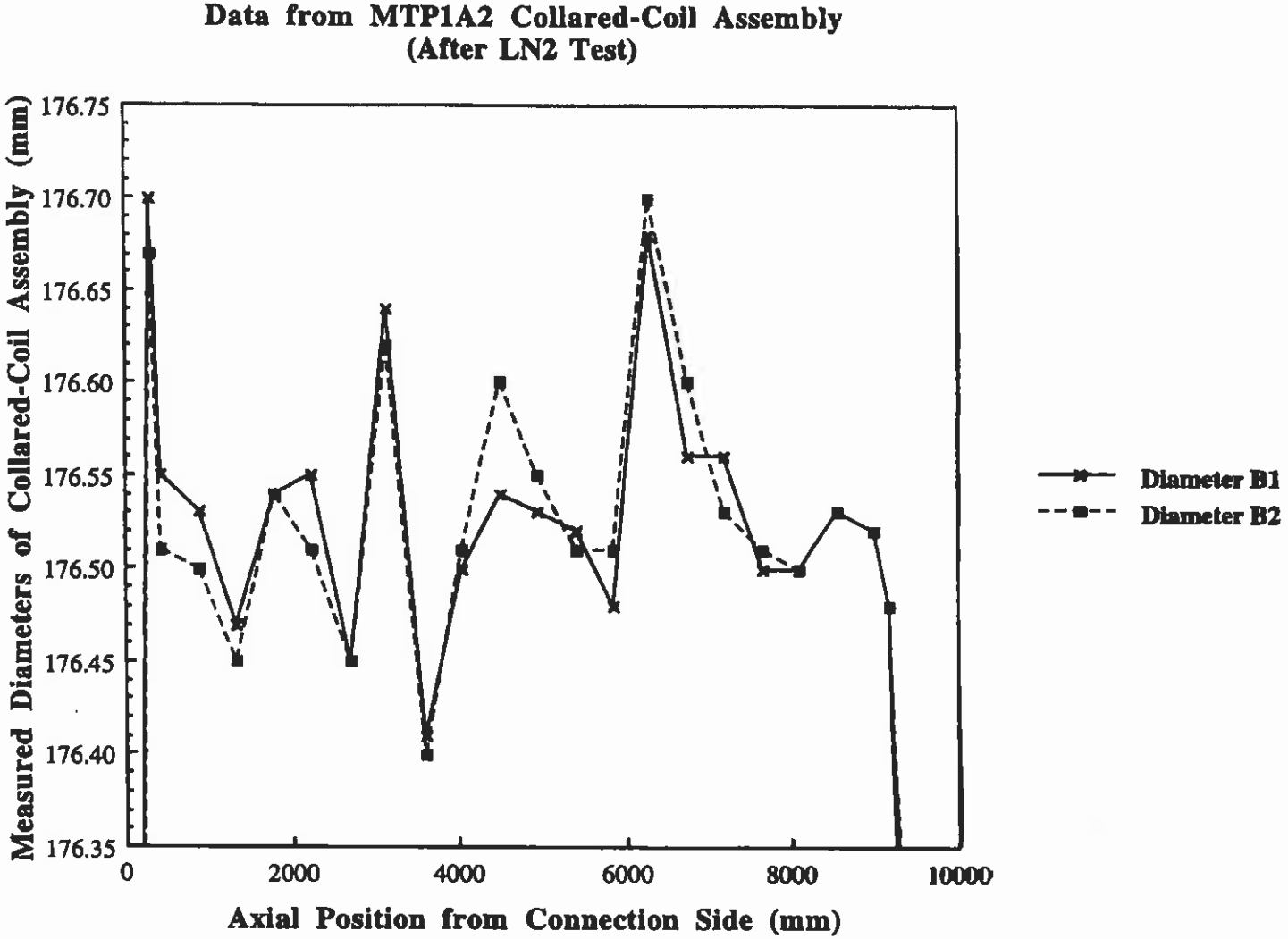

(Courtesy M. Bona)

LECTURE 6: ASSSEMBLY OF PARTICLE ACCELERATOR MAGNETS

6.1 Coil Winding

6.2 Coil Curing

6.3 Azimuthal Coil Size Measurements

6.4 Coil Assembly and Internal Splicing

6.5 Collaring

6.6 Collar Deflection Measurements

6.7 External Splicing

6.8 Yoke Stacking and Shell Welding

6.9 Yoke Midplane Gap Measurements

6.10 Cryostating

6.11 Instrumentation

LHC/Saclay 56-mm-twin-Aperture.

COLD MASS CROSS SECTION

quadrupole

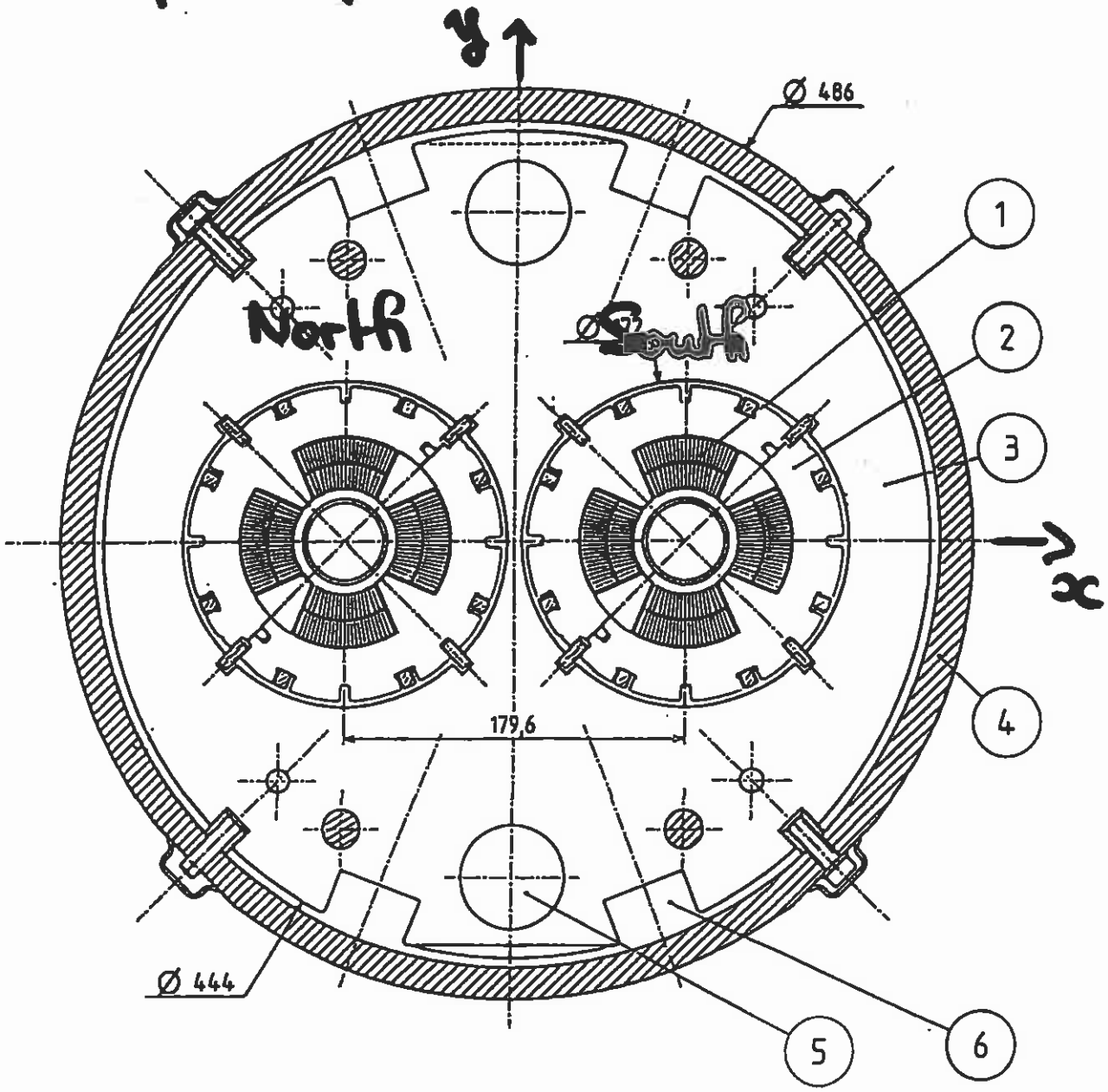

1 Coils
2 Stainless steel collars
3 Laminated iron core
4 Helium wessel (inertia tube)
5 Helium
6 Busbars grooves

Nom. Current 15060A
Nom. Gradient 252T/m
Apert. 56 mm
Magn. Length 3 m

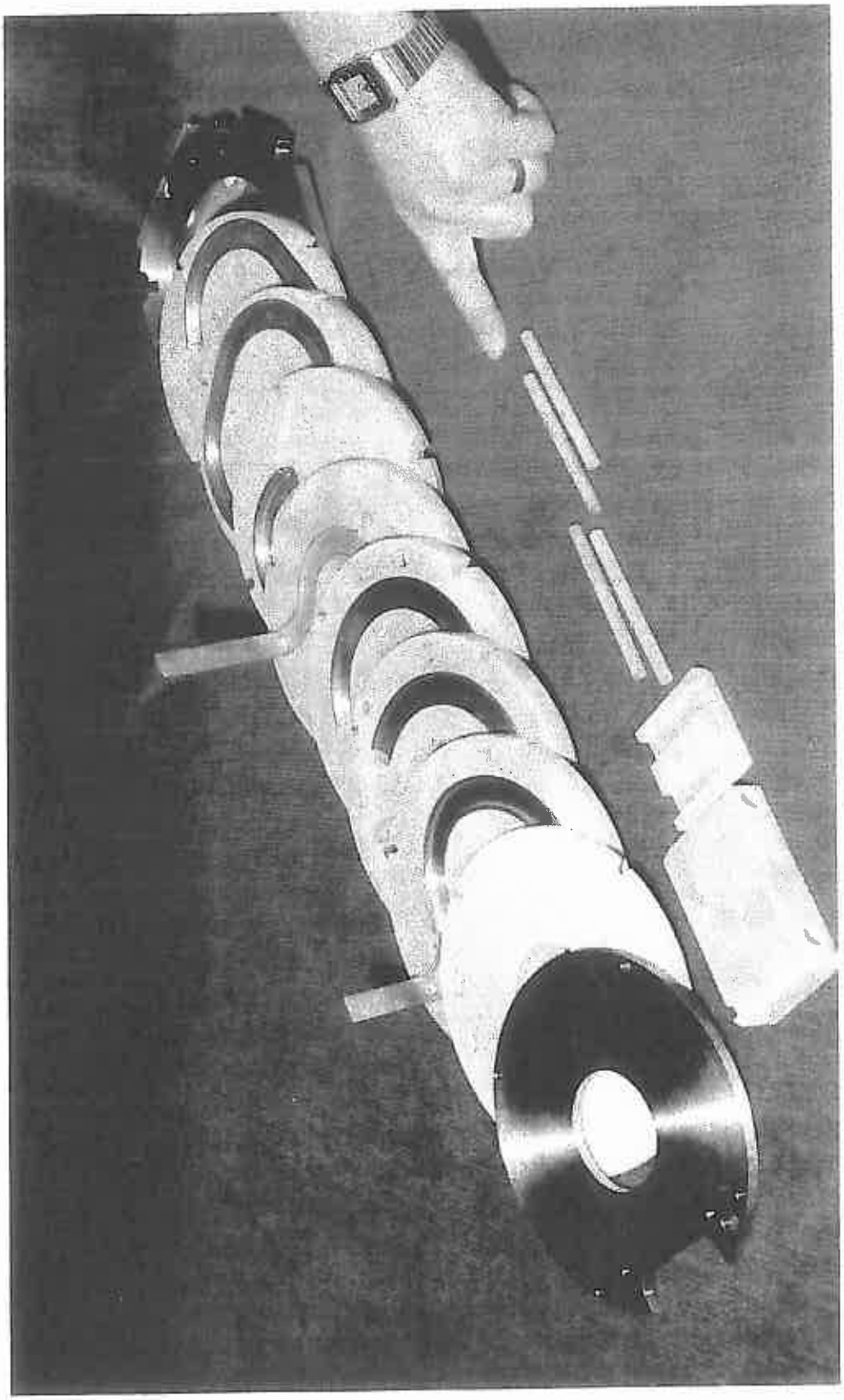

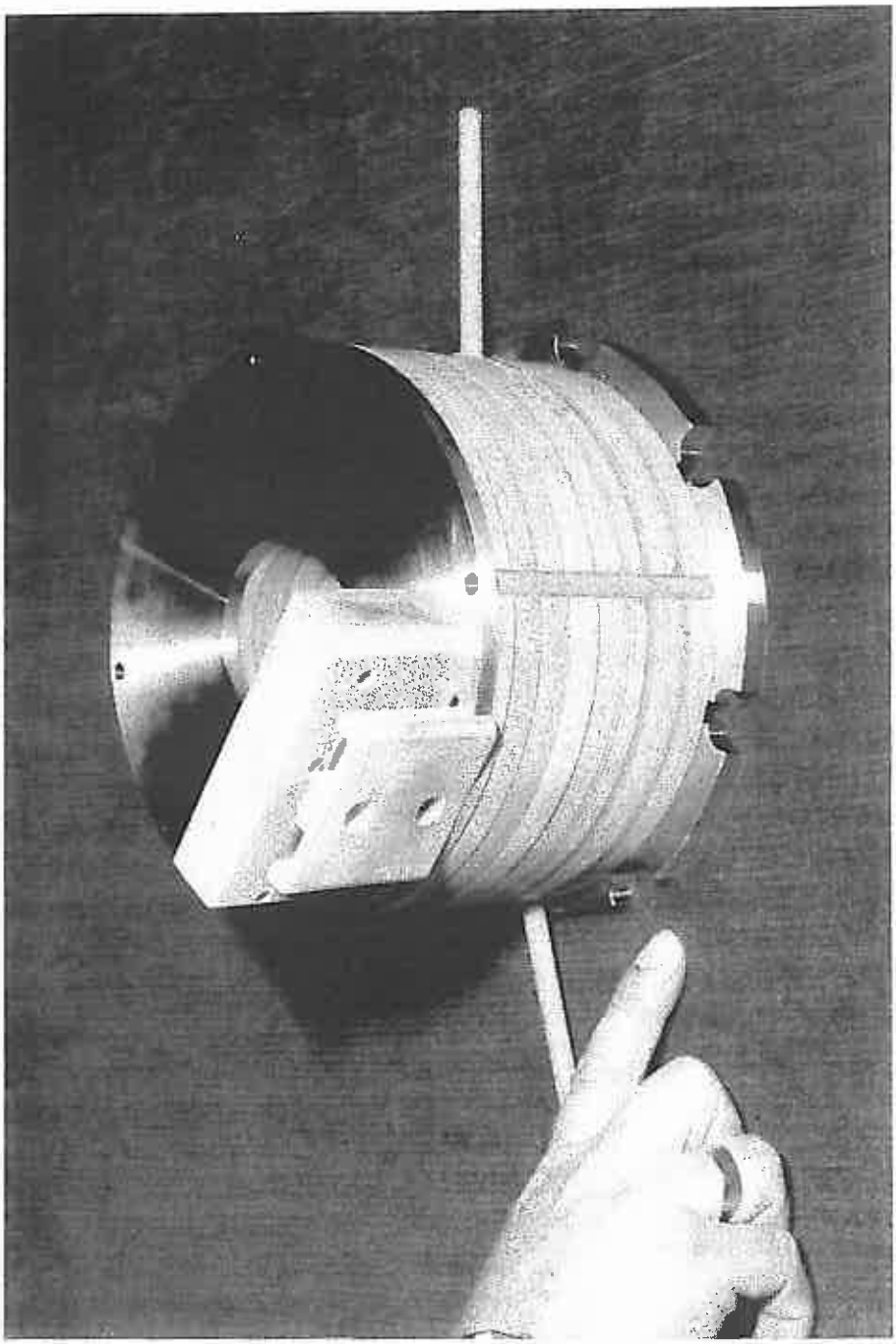

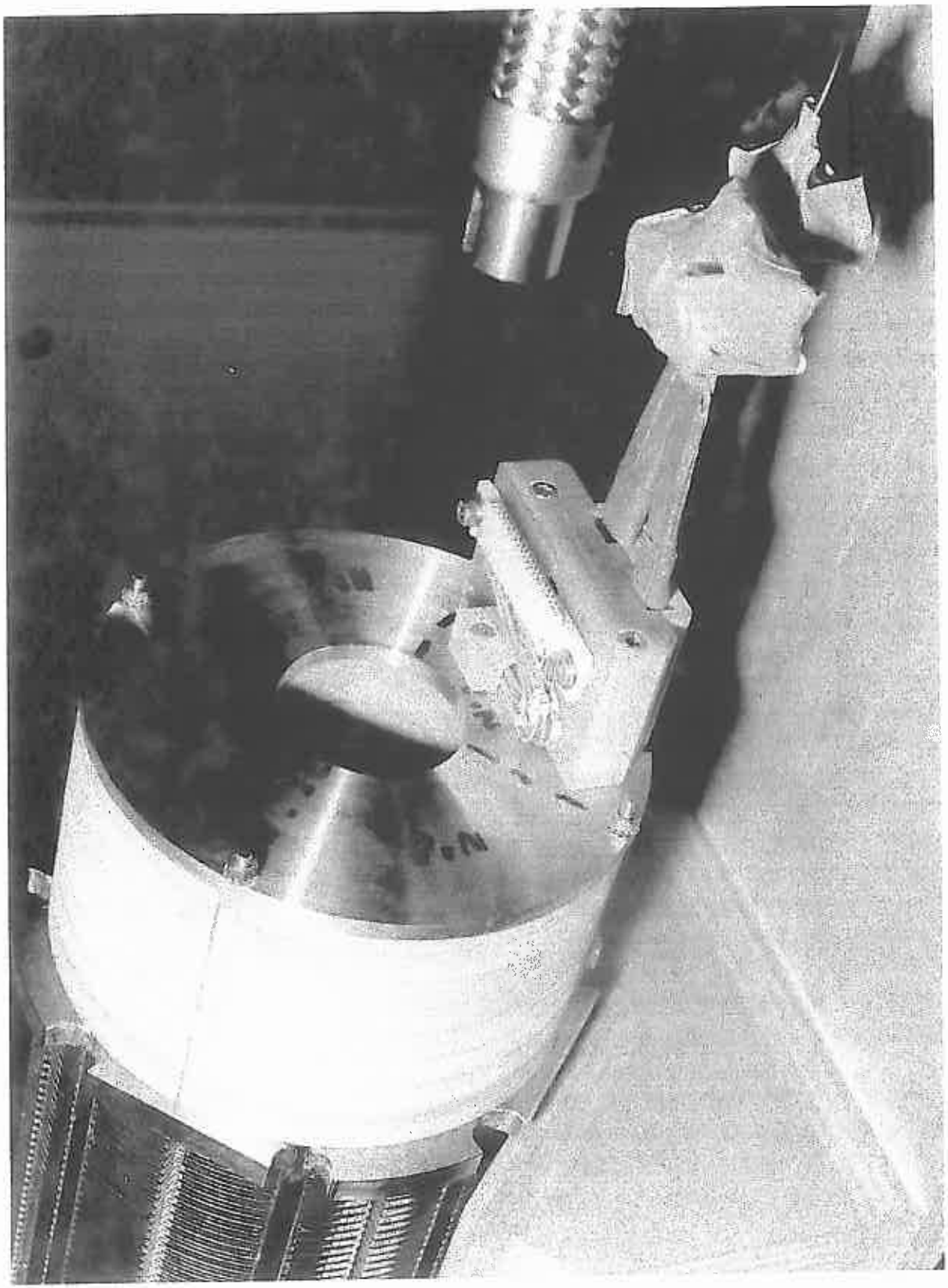

LECTURE 6: ASSSEMBLY OF PARTICLE ACCELERATOR MAGNETS

6.1 Coil Winding

6.2 Coil Curing

6.3 Azimuthal Coil Size Measurements

6.4 Coil Assembly and Internal Splicing

6.5 Collaring

6.6 Collar Deflection Measurements

6.7 External Splicing

6.8 Yoke Stacking and Shell Welding

6.9 Yoke Midplane Gap Measurements

6.10 Cryostating

6.11 Instrumentation

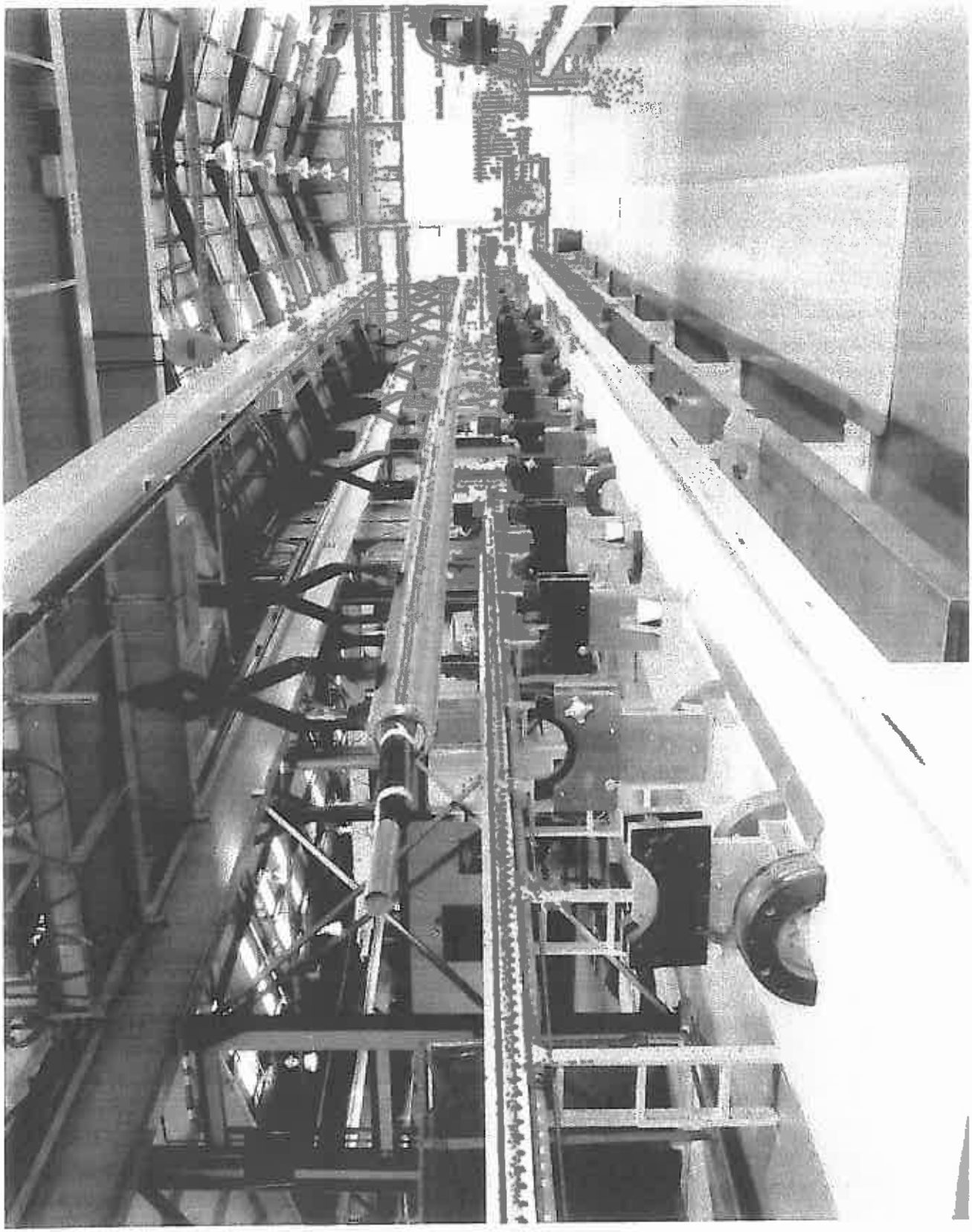

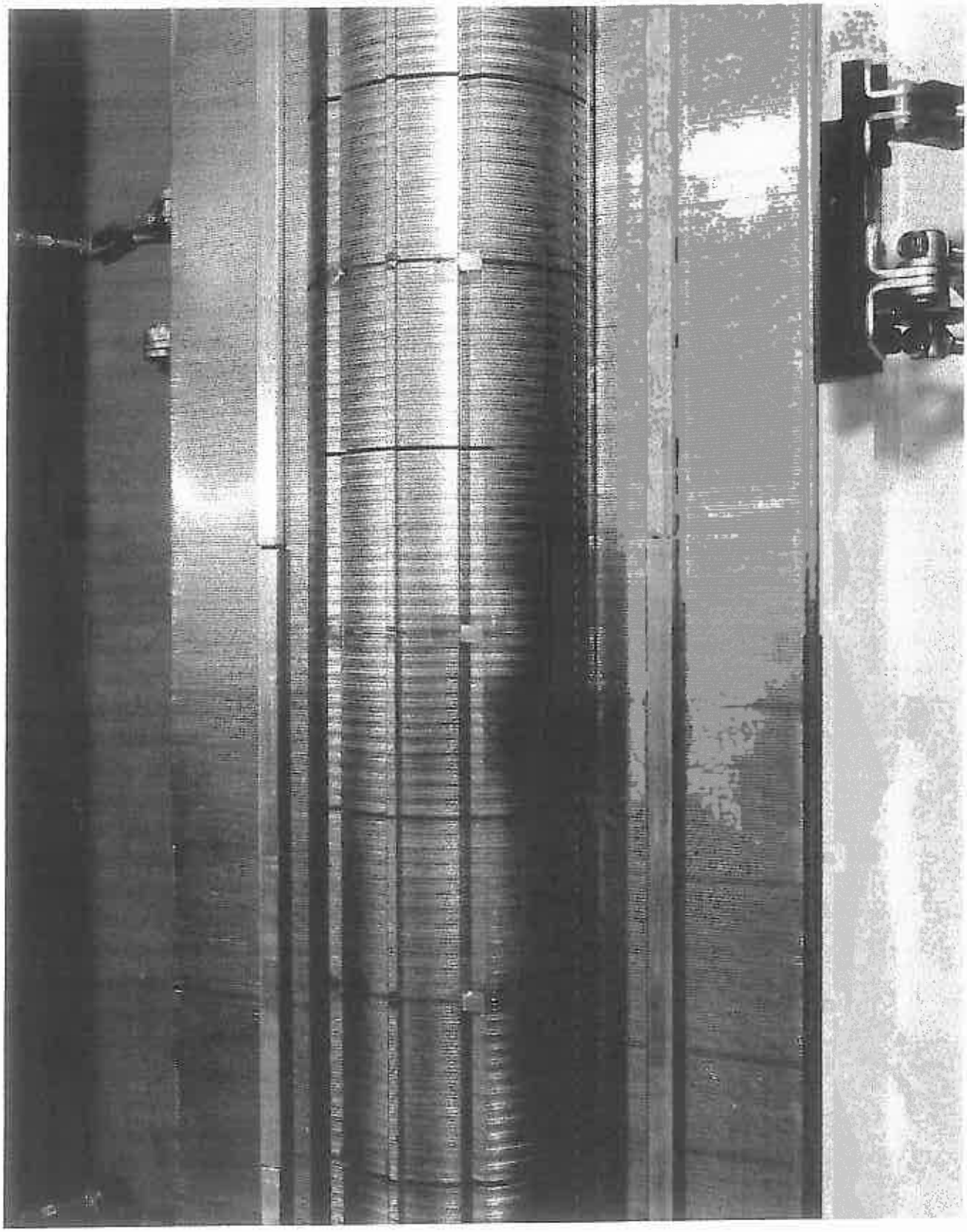

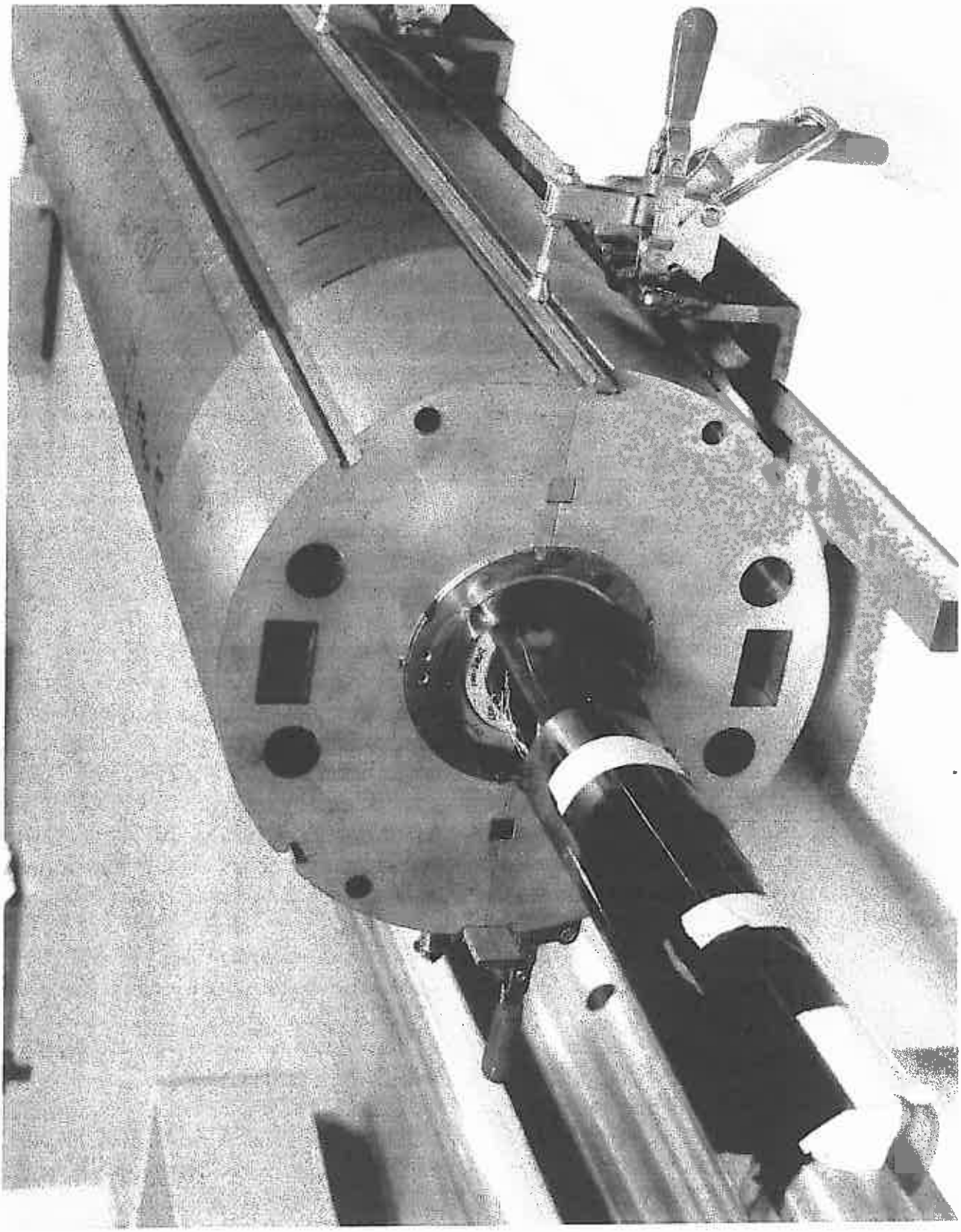

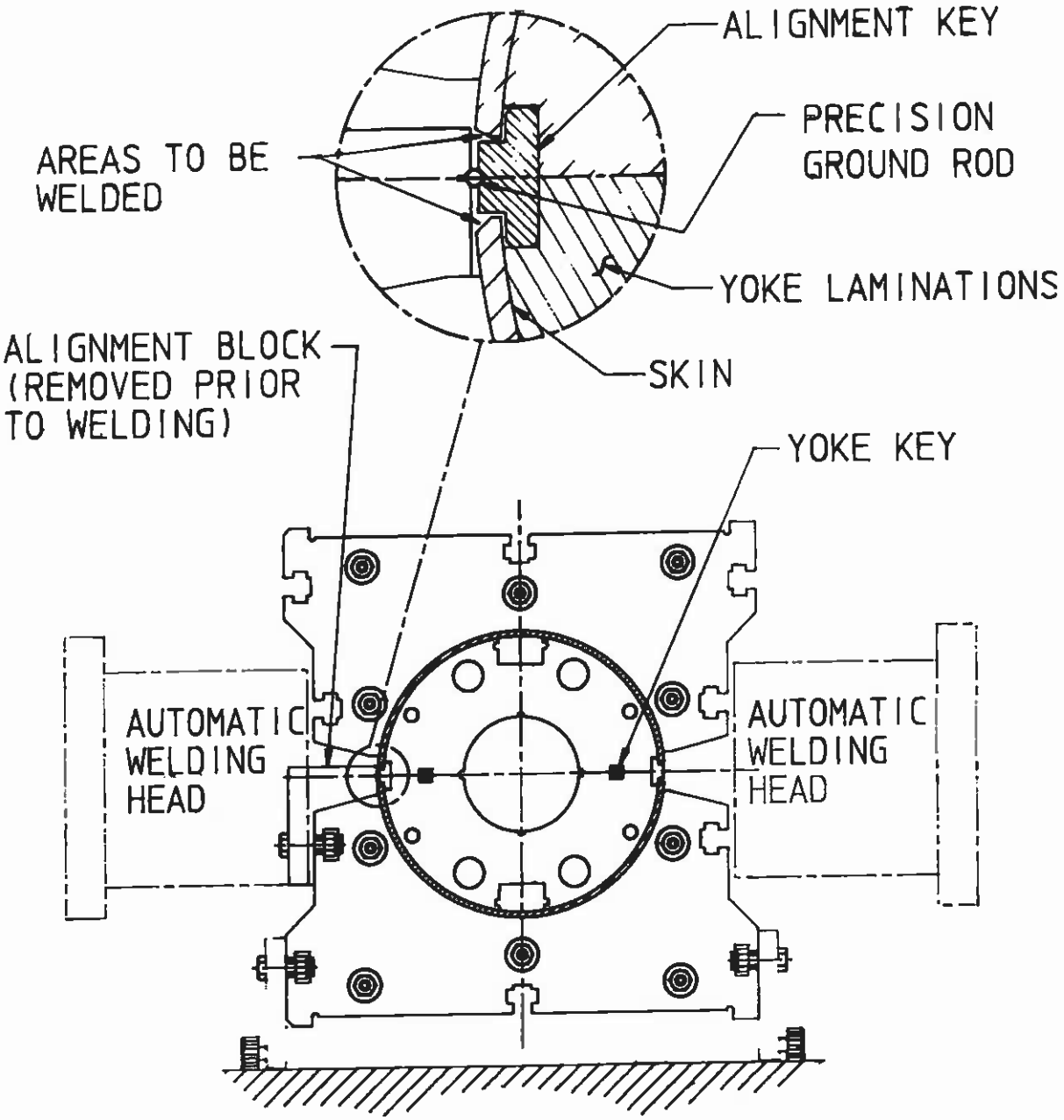

YOKE/SKIN ALIGNMENT FIXTURE

SSC/BNL 4-cm-Apert., 17-m-Long Dipole Magnet (Hor. Split Yoke)

DD0028 File 900928

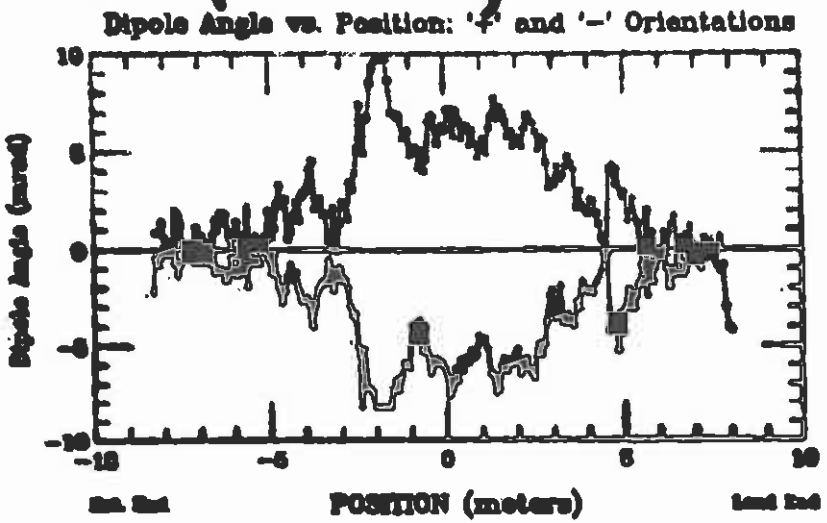

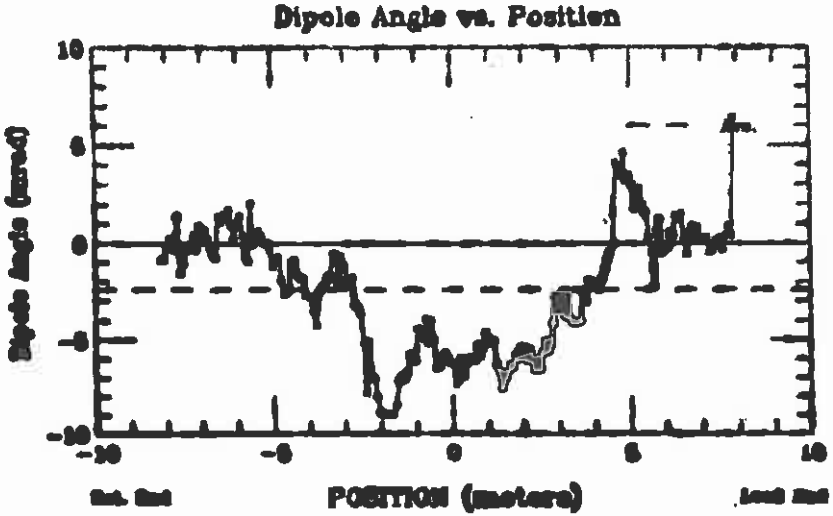

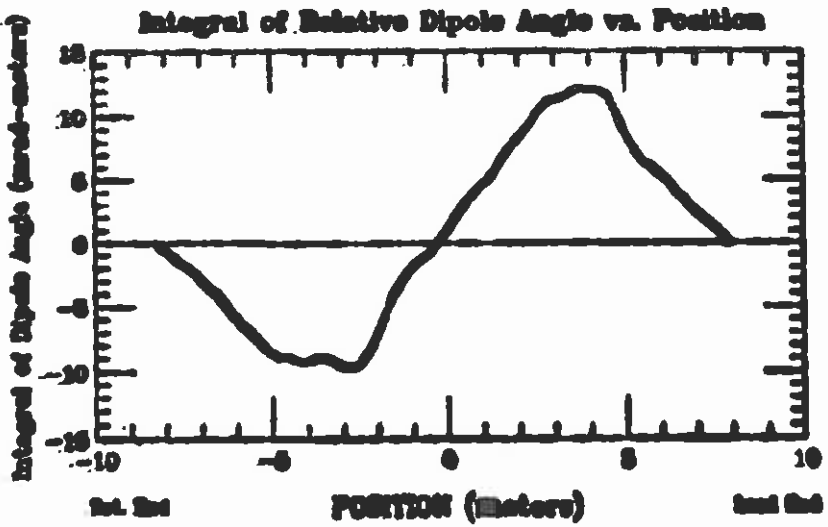

Angle Extrema = 6.74 mrad
(Relative to Average)

Angle S. Dev. = 3.22 mrad

Integral Extrema = 12.14 mrad-m

Measurement at MTF before TC#1

SSC/FNAL 4-cm-Apert., 17-m-Long Dipole Magnet (Hor. Split Yoke) DC0301 File 901004

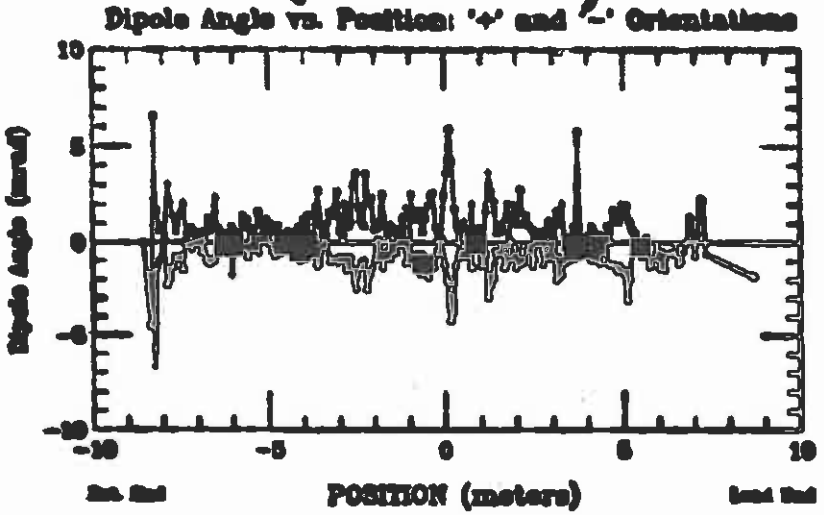

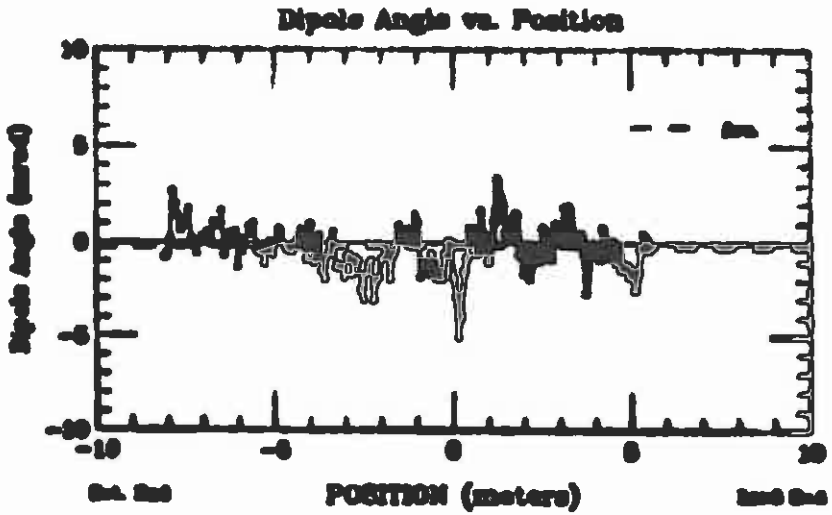

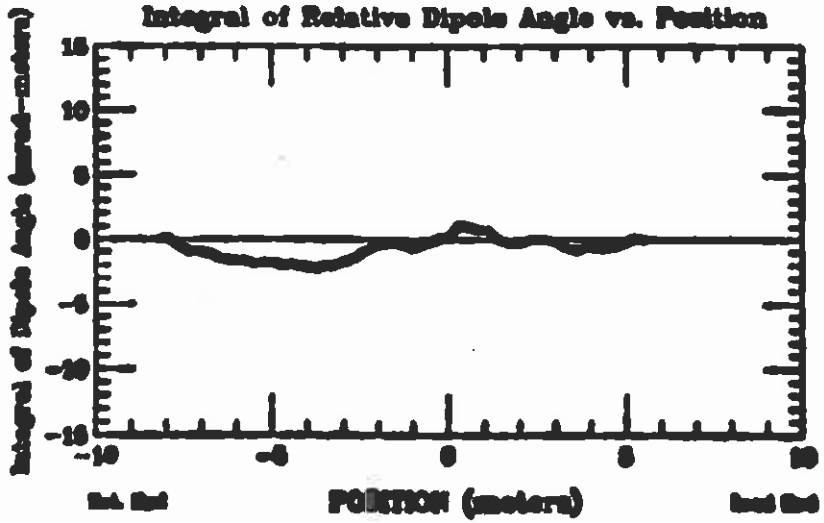

Angle Extrema = −4.81 mrad
(Relative to Average)

Angle S. Dev. = 1.21 mrad

Integral Extrema = −2.24 mrad-m

Measurement at ICB

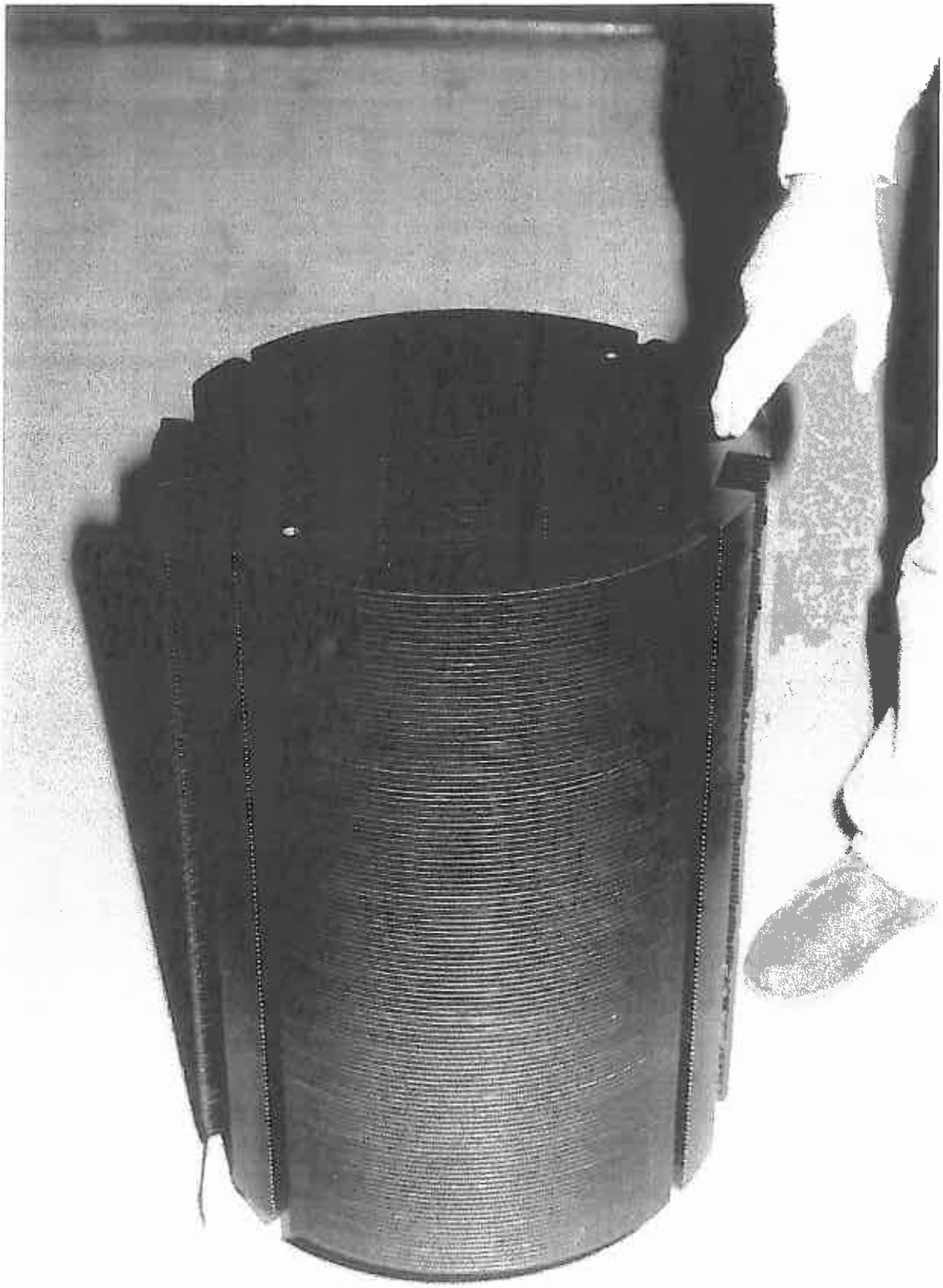

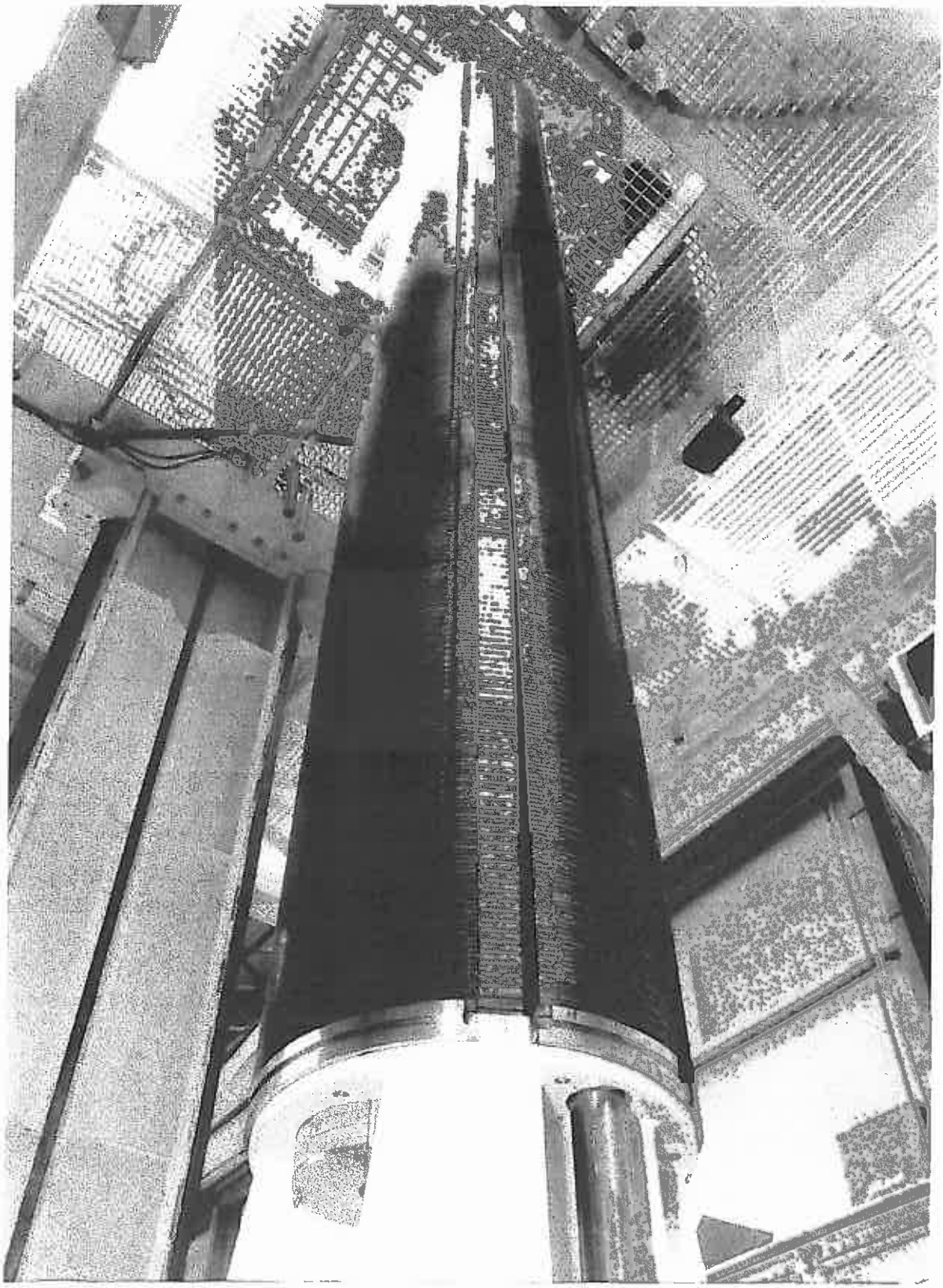

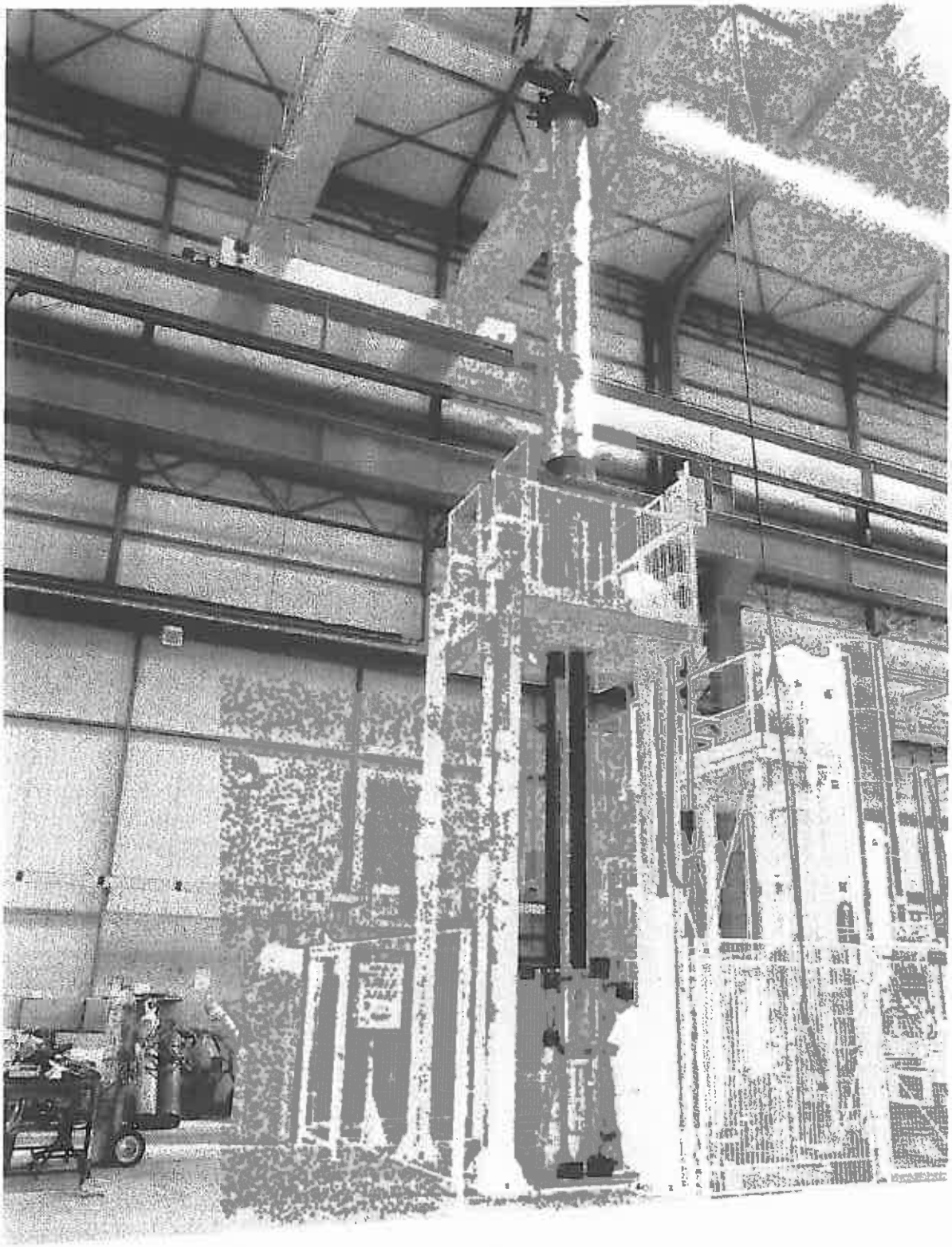

LECTURE 6: ASSSEMBLY OF PARTICLE ACCELERATOR MAGNETS

6.1 Coil Winding

6.2 Coil Curing

6.3 Azimuthal Coil Size Measurements

6.4 Coil Assembly and Internal Splicing

6.5 Collaring

6.6 Collar Deflection Measurements

6.7 External Splicing

6.8 Yoke Stacking and Shell Welding

6.9 Yoke Midplane Gap Measurements

6.10 Cryostating

6.11 Instrumentation

COUPE C-C

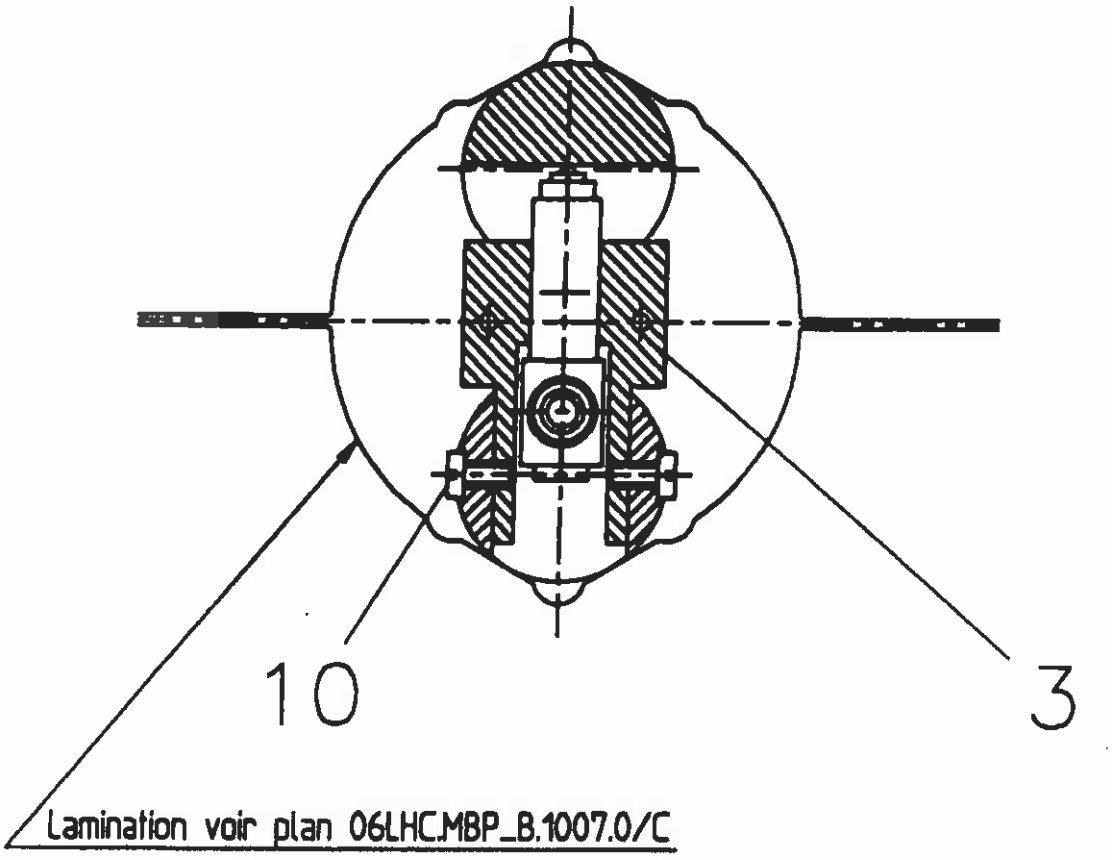

Development of superconducting dipole magnets

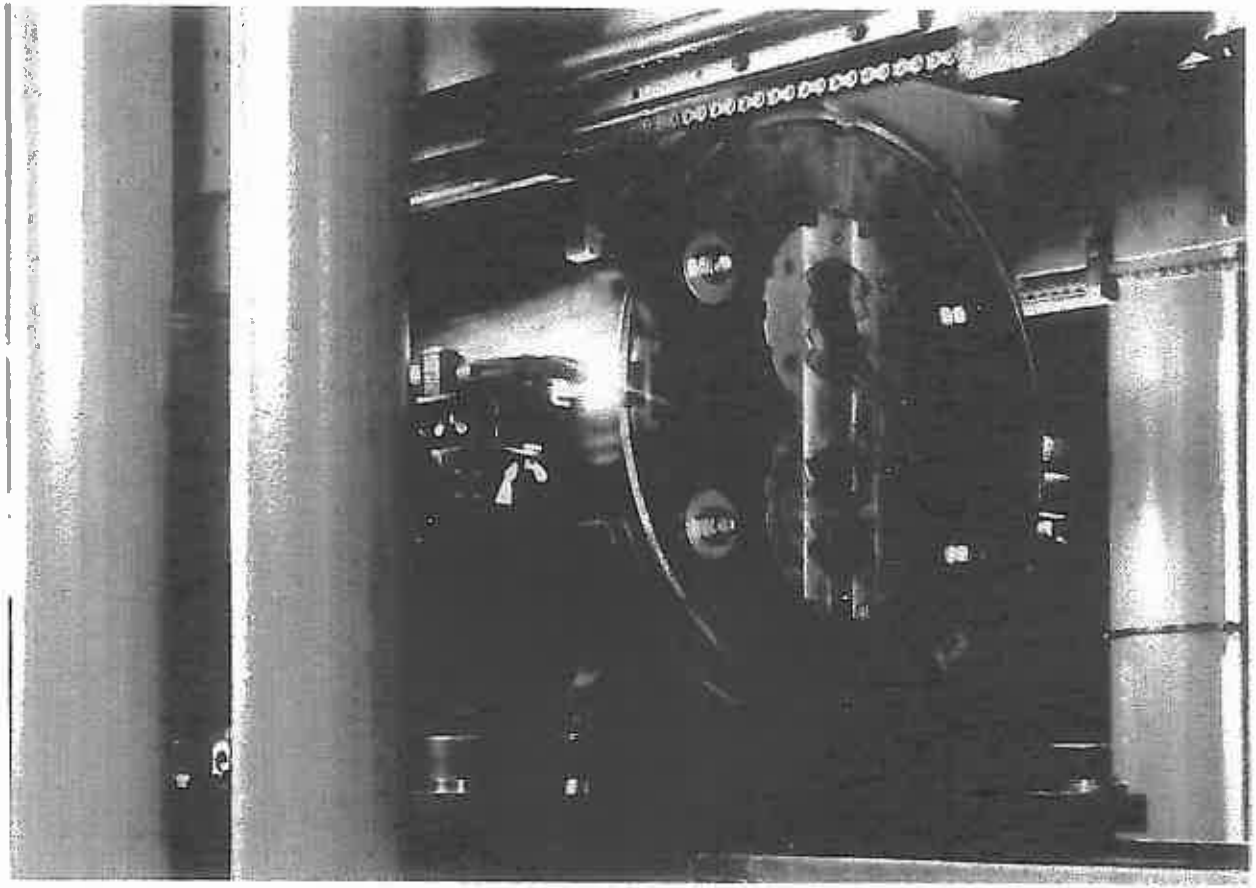

Welding test on full-size cross section for LHC dipole magnets

Noell-KRC Energie- und Umwelttechnik GmbH

PREUSSAG NOELL

NU 147-E/08.96 ffg

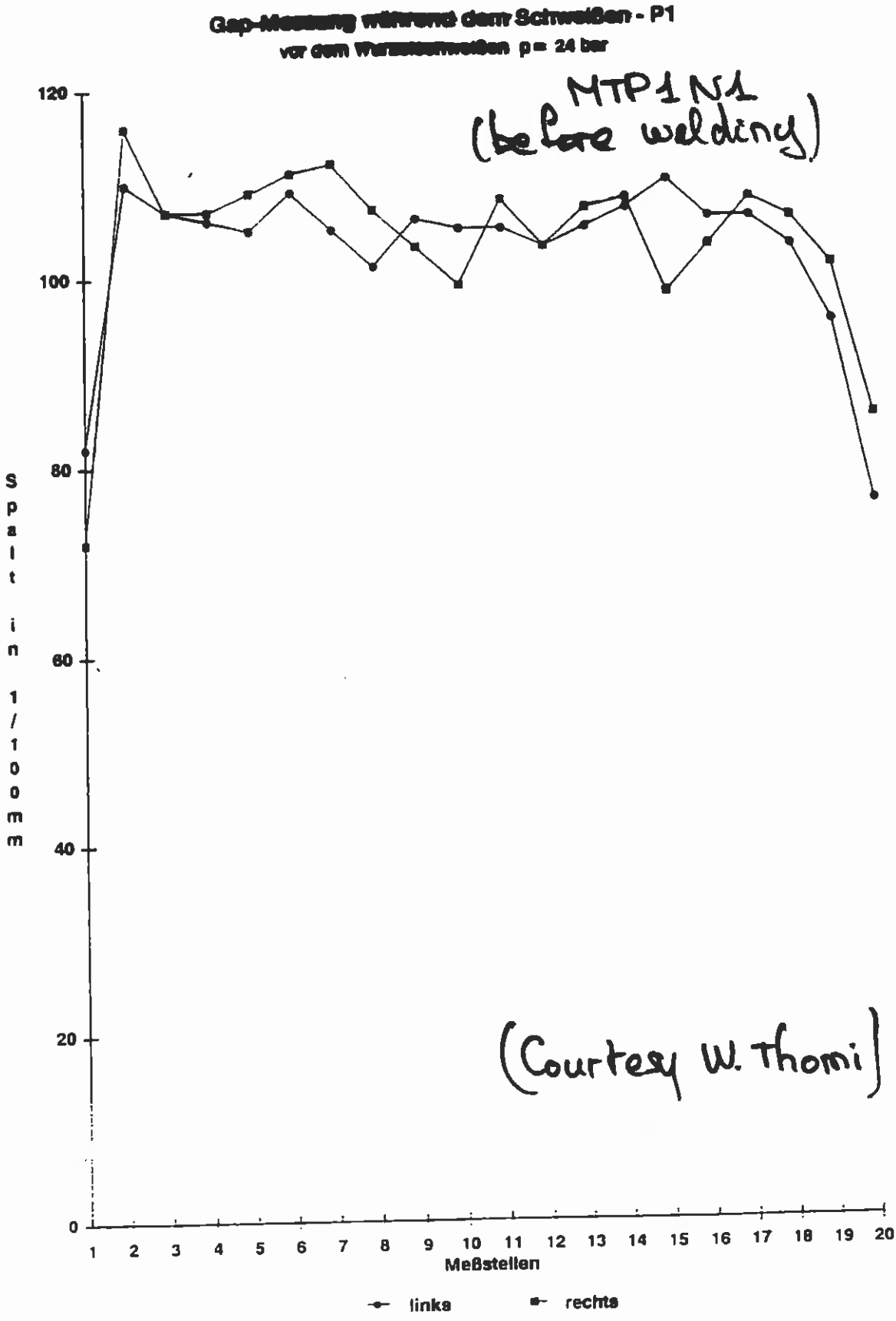
Gap-Messung während dem Schweißen - P1
vor dem Warmdrahtschweißen p= 24 bar
MTP1N1
(before welding)
120
100
80
60
40
20
0
Spalt in 1/100mm
1 2 3 4 5 6 7 8 9 10 11 12 13 14 15 16 17 18 19 20
Meßstellen
links
rechts
(Courtesy W. Thomi)

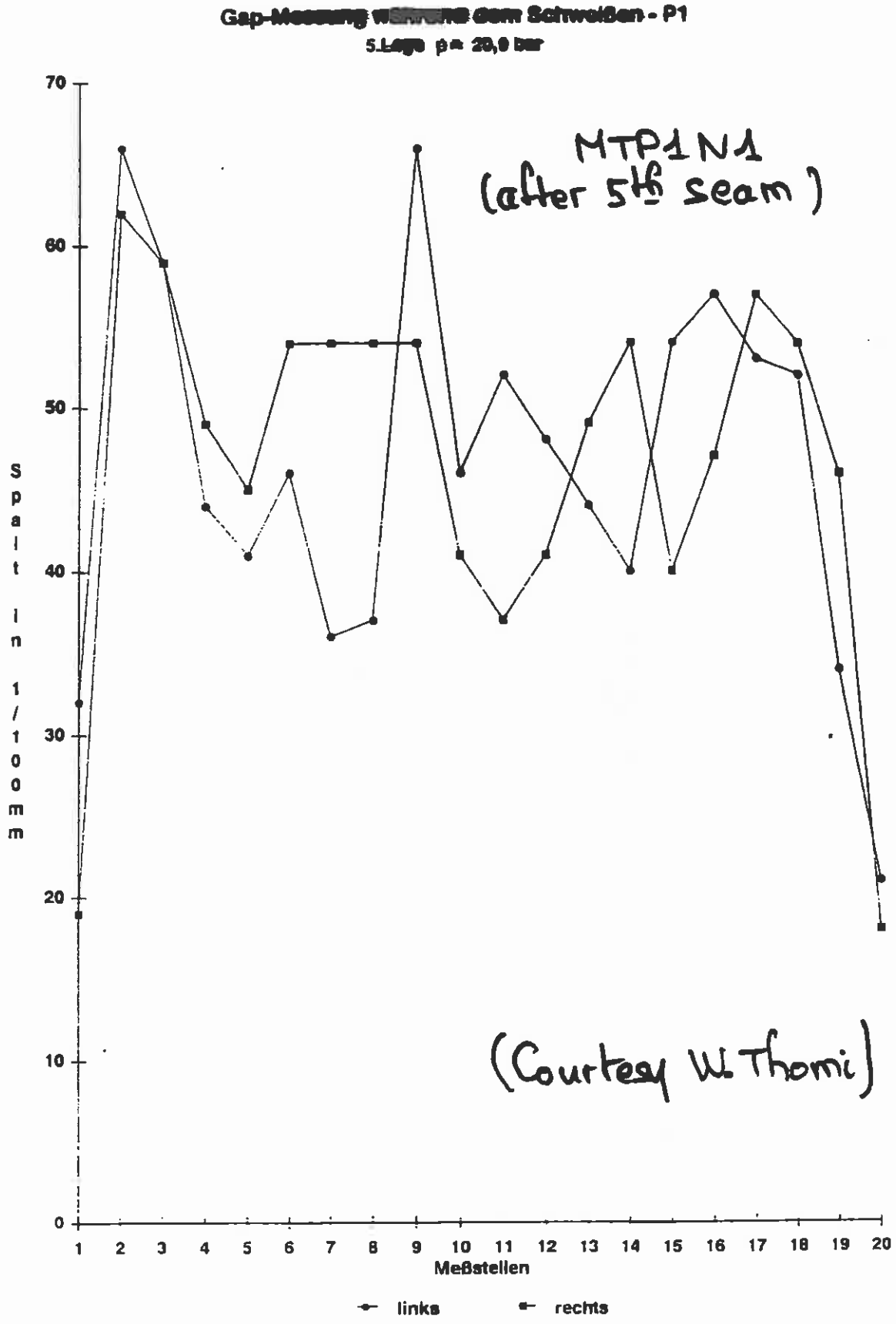
Gap-Messung [illegible] dem Schweißen - P1
5.Lage p= 20,0 bar
MTP1N1
(after 5th seam)
(Courtesy W. Thomi)
Spalt in 1/100 mm
70
60
50
40
30
20
10
0
1 2 3 4 5 6 7 8 9 10 11 12 13 14 15 16 17 18 19 20
Meßstellen
links
rechts

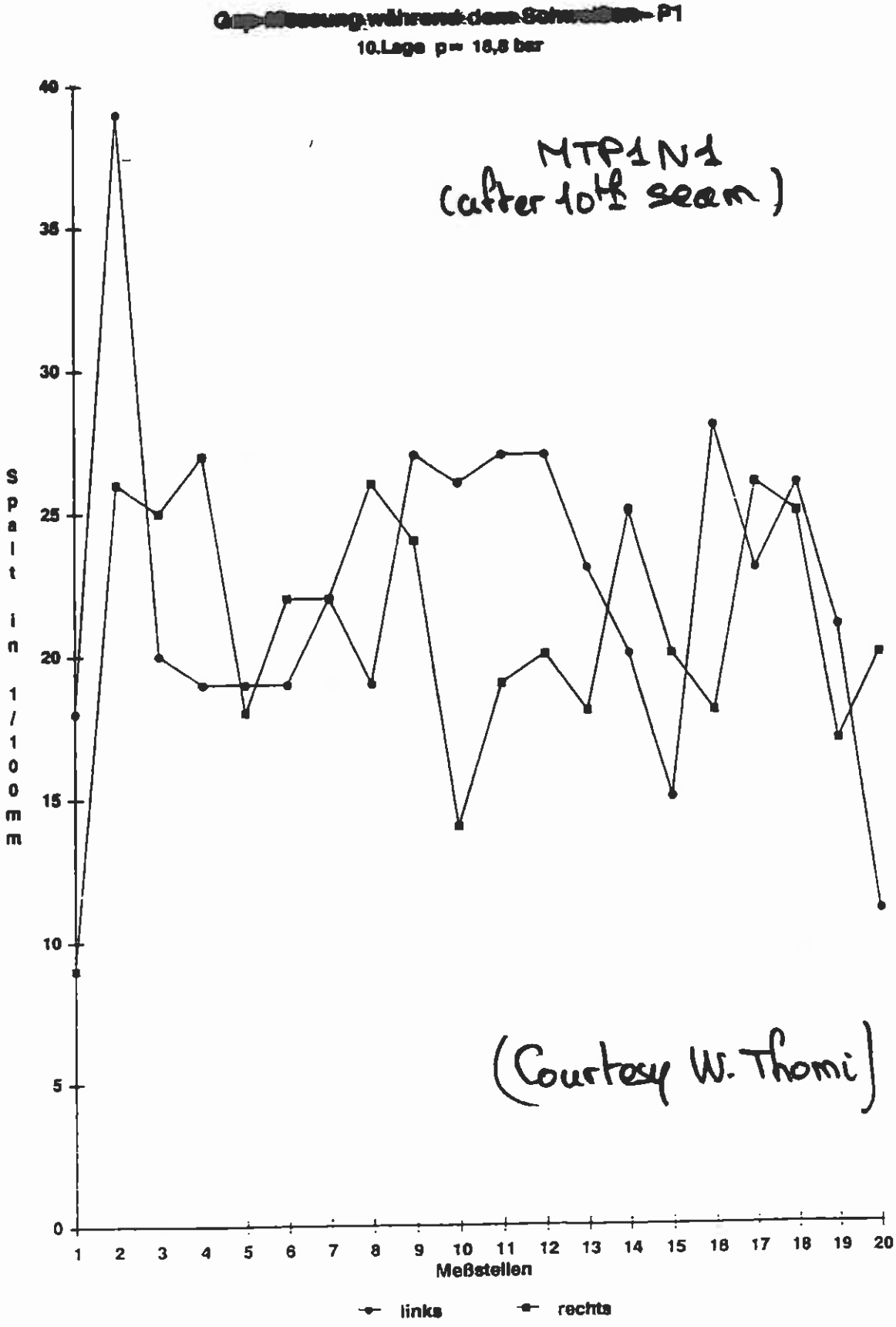
P1
10.Lage p= 16,8 bar
MTP1N1
(after 10th seam)
Spalt in 1/100mm
0
5
10
15
20
25
30
35
40
1 2 3 4 5 6 7 8 9 10 11 12 13 14 15 16 17 18 19 20
Meßstellen
links
rechts
(Courtesy W. Thomi)

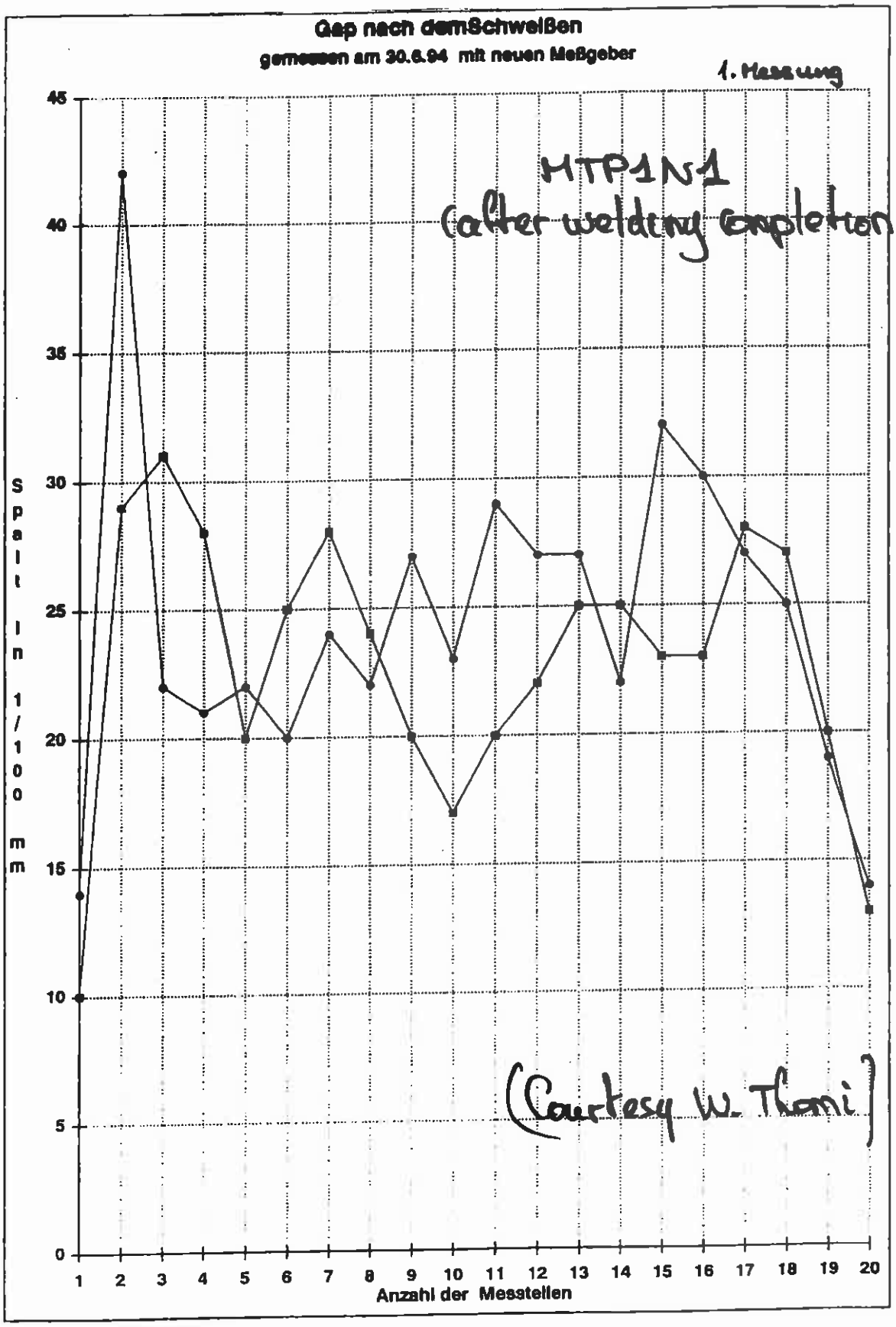
Gap nach demSchweißen
gemessen am 30.6.94 mit neuen Meßgeber
1. Messung
HTP1N1
(after welding completion)
Spalt in 1/100 mm
0
5
10
15
20
25
30
35
40
45
1 2 3 4 5 6 7 8 9 10 11 12 13 14 15 16 17 18 19 20
Anzahl der Messtellen
(Courtesy W. Thani)

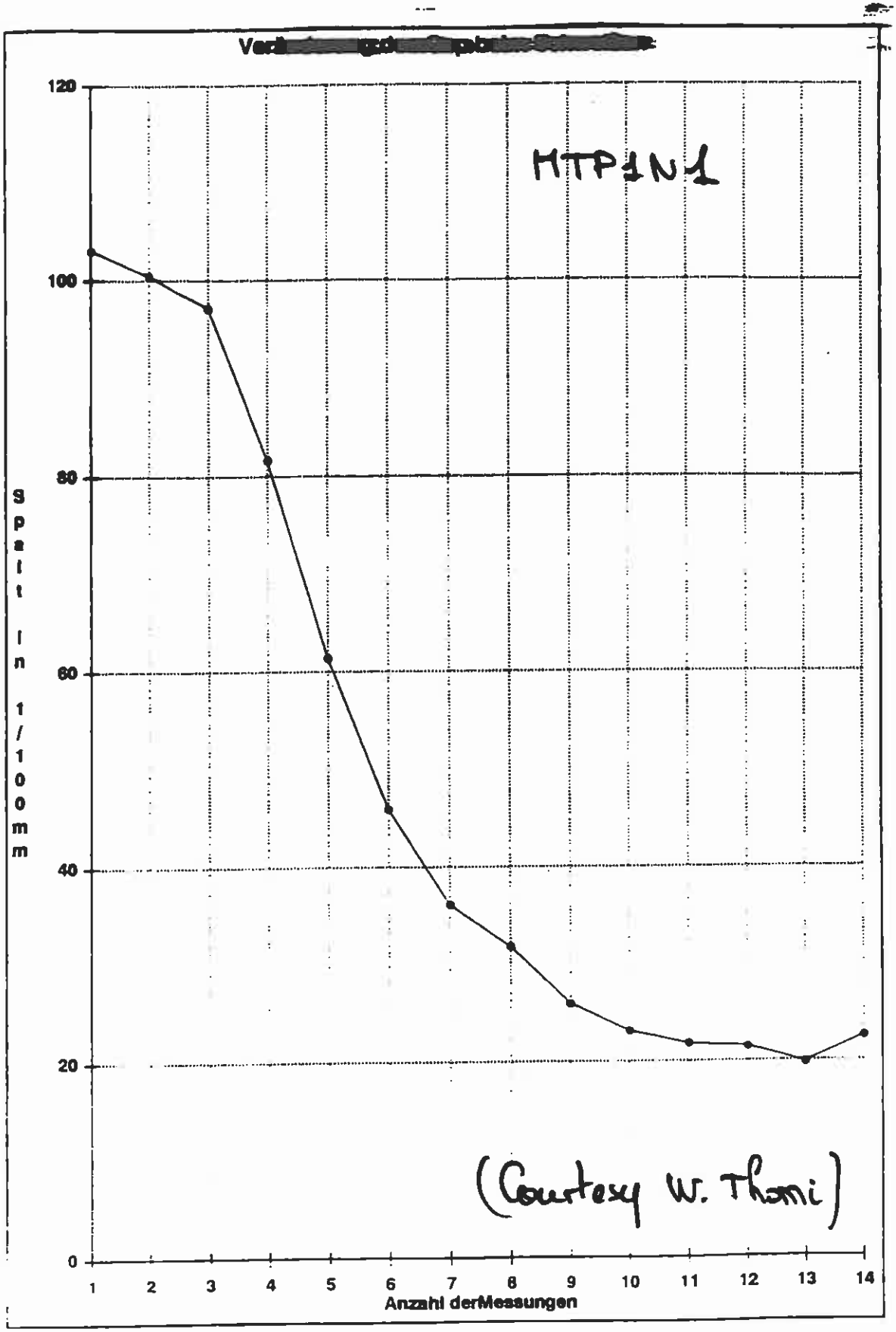
MTP1N1
120
100
80
60
40
20
0
Split in 1/100mm
1
2
3
4
5
6
7
8
9
10
11
12
13
14
Anzahl derMessungen
(Courtesy W. Thoni)

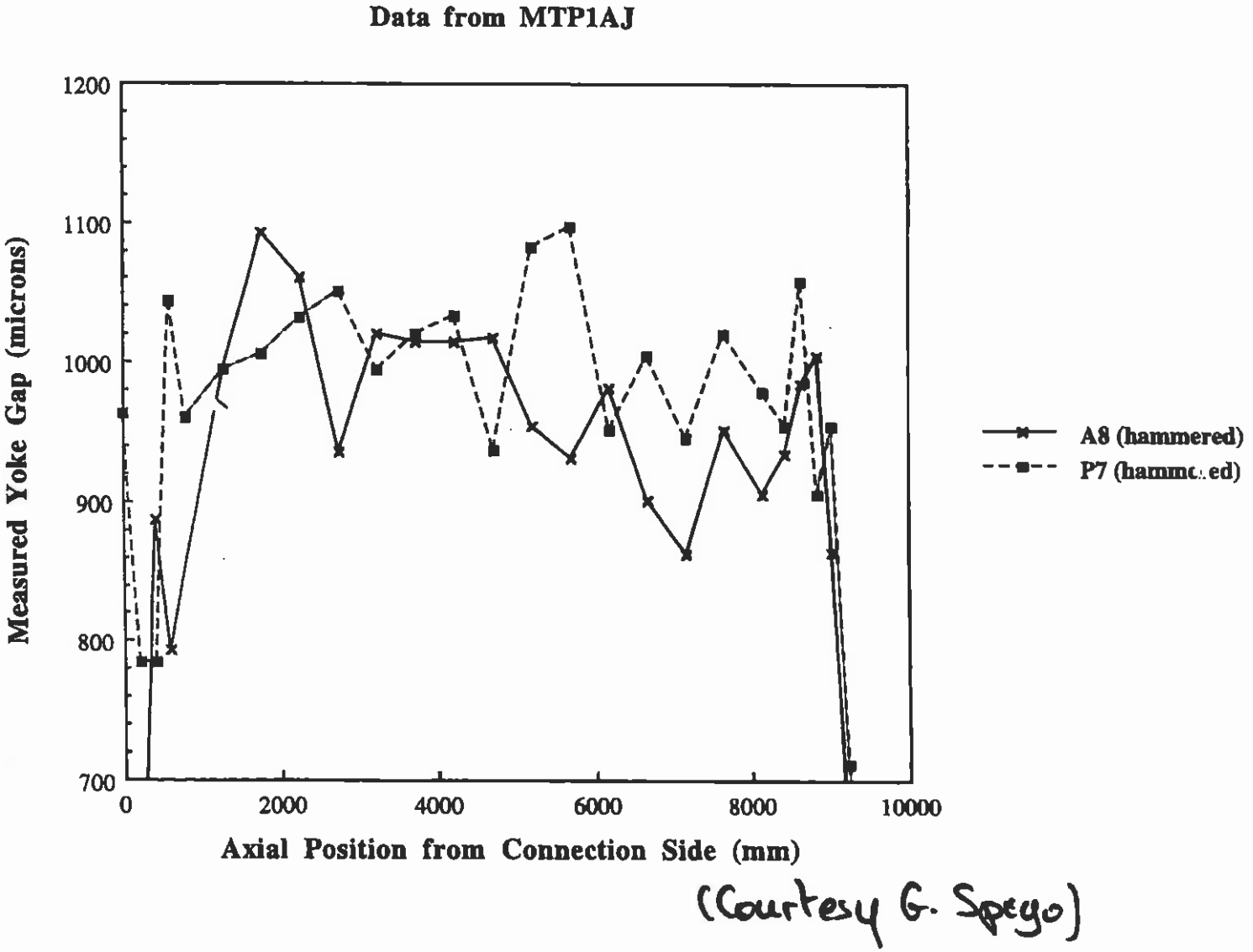

(Courtesy G. Spiego)

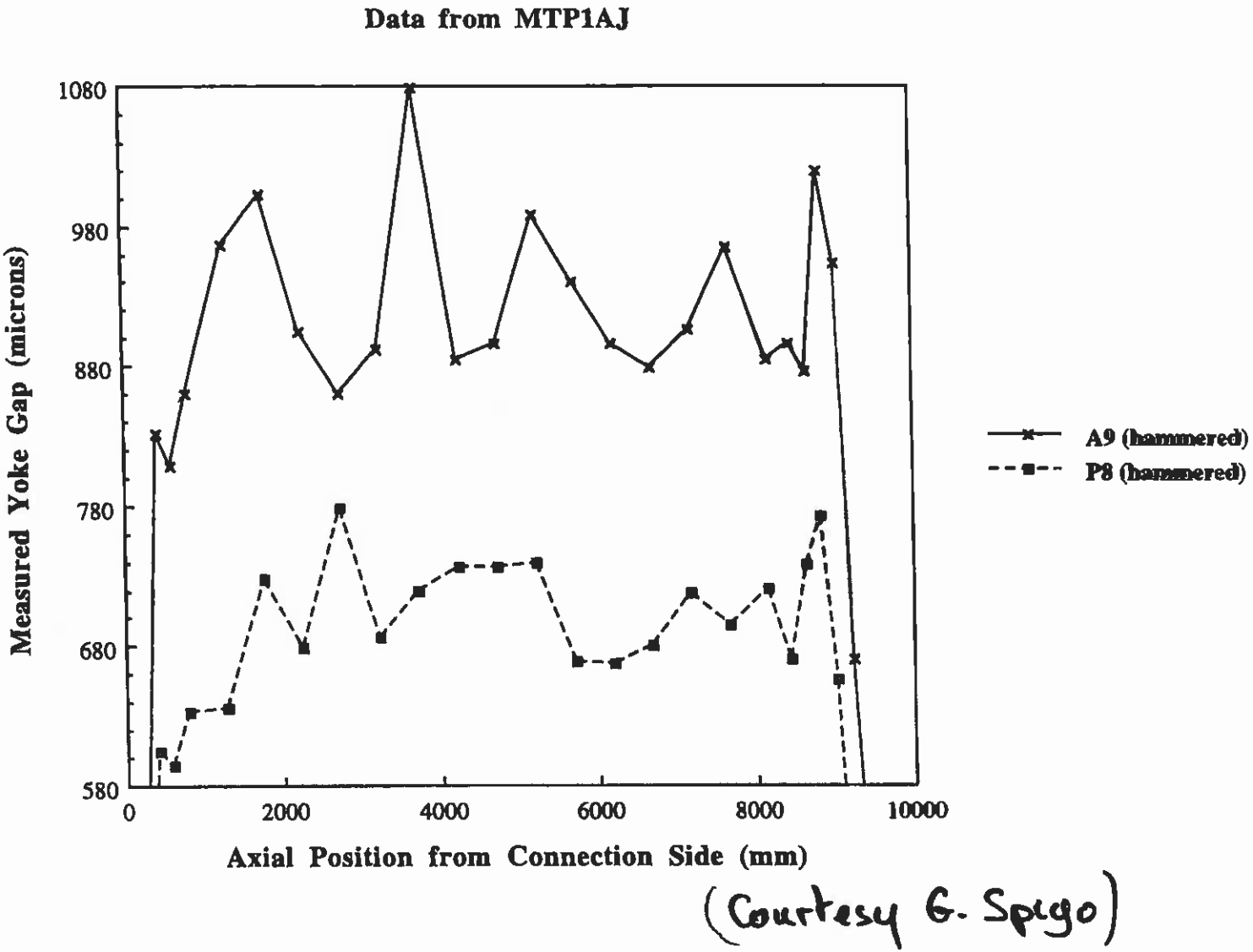

(Courtesy G. Spigo)

Data from MTP1AJ

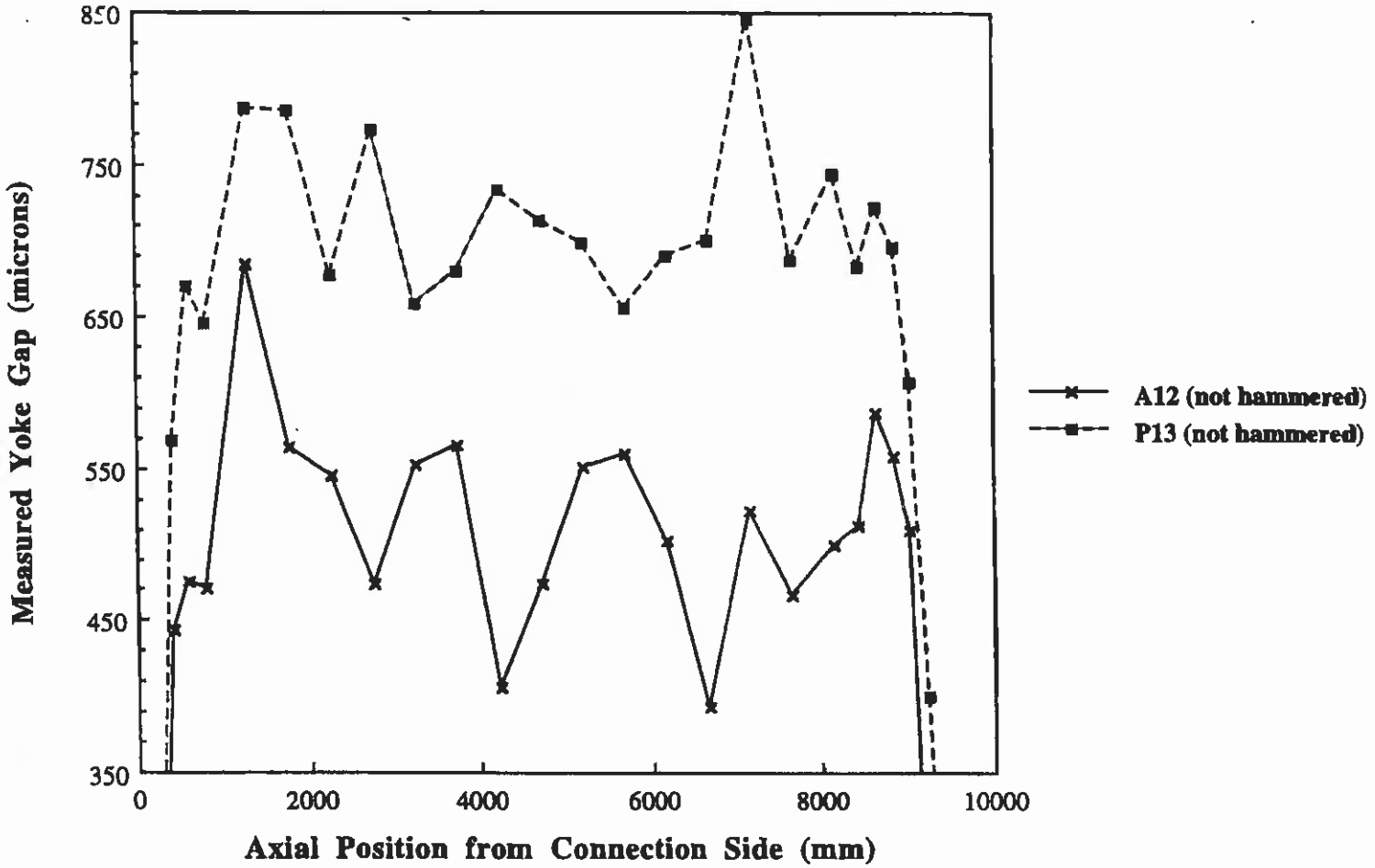

(Courtesy G. Spigo)

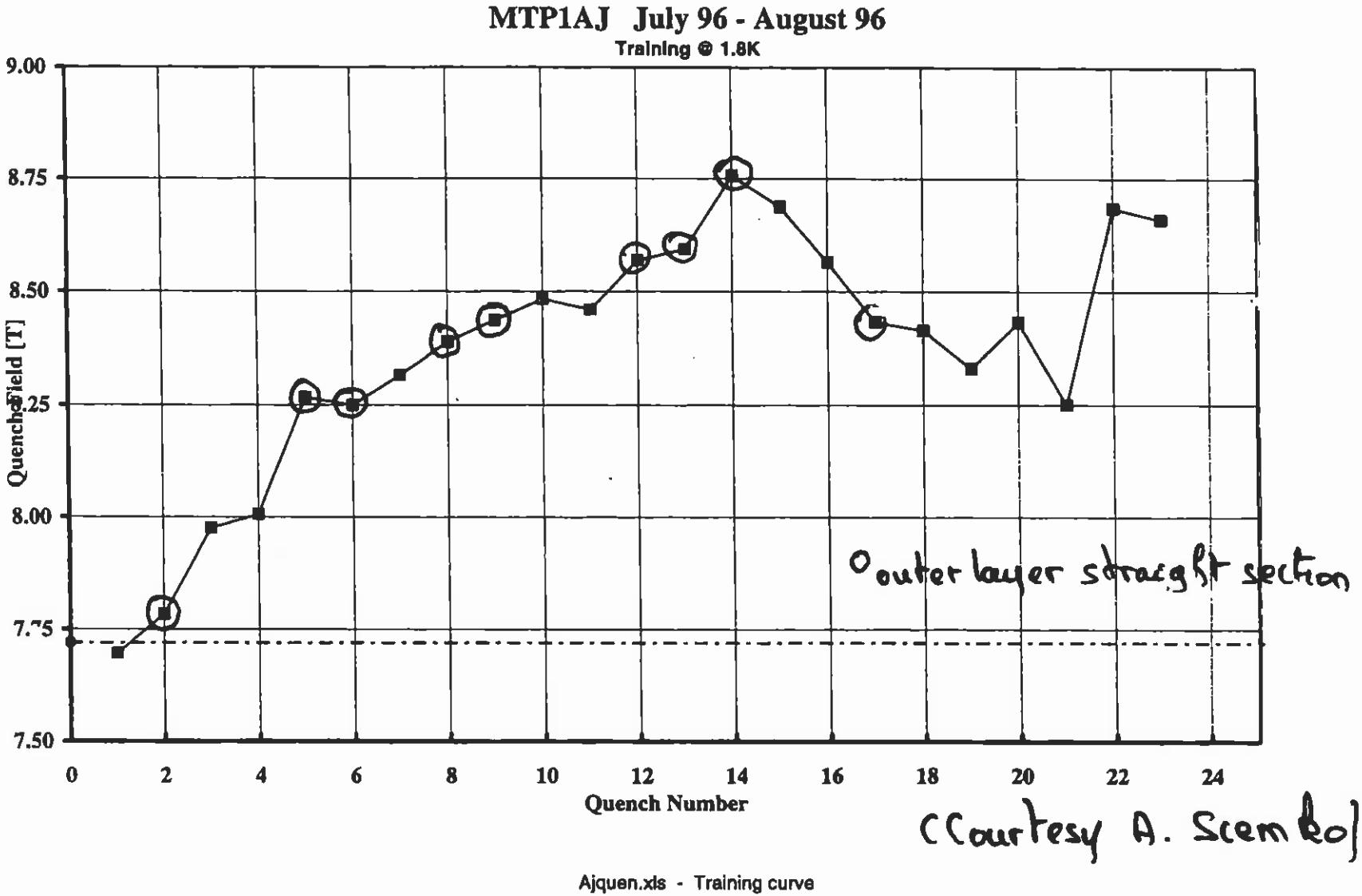
MTP1AJ July 96 - August 96
Training @ 1.8K
Quench Field [T]
9.00
8.75
8.50
8.25
8.00
7.75
7.50
0
2
4
6
8
10
12
14
16
18
20
22
24
Quench Number
Ajquen.xls - Training curve
O outer layer straight section
(Courtesy A. Siemko)

LECTURE 6: ASSSEMBLY OF PARTICLE ACCELERATOR MAGNETS

6.1 Coil Winding

6.2 Coil Curing

6.3 Azimuthal Coil Size Measurements

6.4 Coil Assembly and Internal Splicing

6.5 Collaring

6.6 Collar Deflection Measurements

6.7 External Splicing

6.8 Yoke Stacking and Shell Welding

6.9 Yoke Midplane Gap Measurements

6.10 Cryostating

6.11 Instrumentation

MAGNET CRYOSTAT

– To maintain magnet cold masses at low temperature it is necessary to limit heat losses.

– There are three main mechanisms of heat transfer:

- *Convection,*
- *Radiation,*
- *Conduction.*

– The convection losses are eliminated by mounting the cold masses into cryostats which are evacuated.

– The radiation losses, which scale in proportion with the effective emissivities of the surfaces facing each other and with the fourth power of their temperatures, are reduced by surrounding the cold masses with blankets of multilayer insulation and thermal shields at intermediate temperatures.

– The main sources of conduction losses are the support posts, the power leads and the cryogenic feedthroughs which are designed to offer large thermal resistances.

SSC Design B Dipole Magnet Cryostat

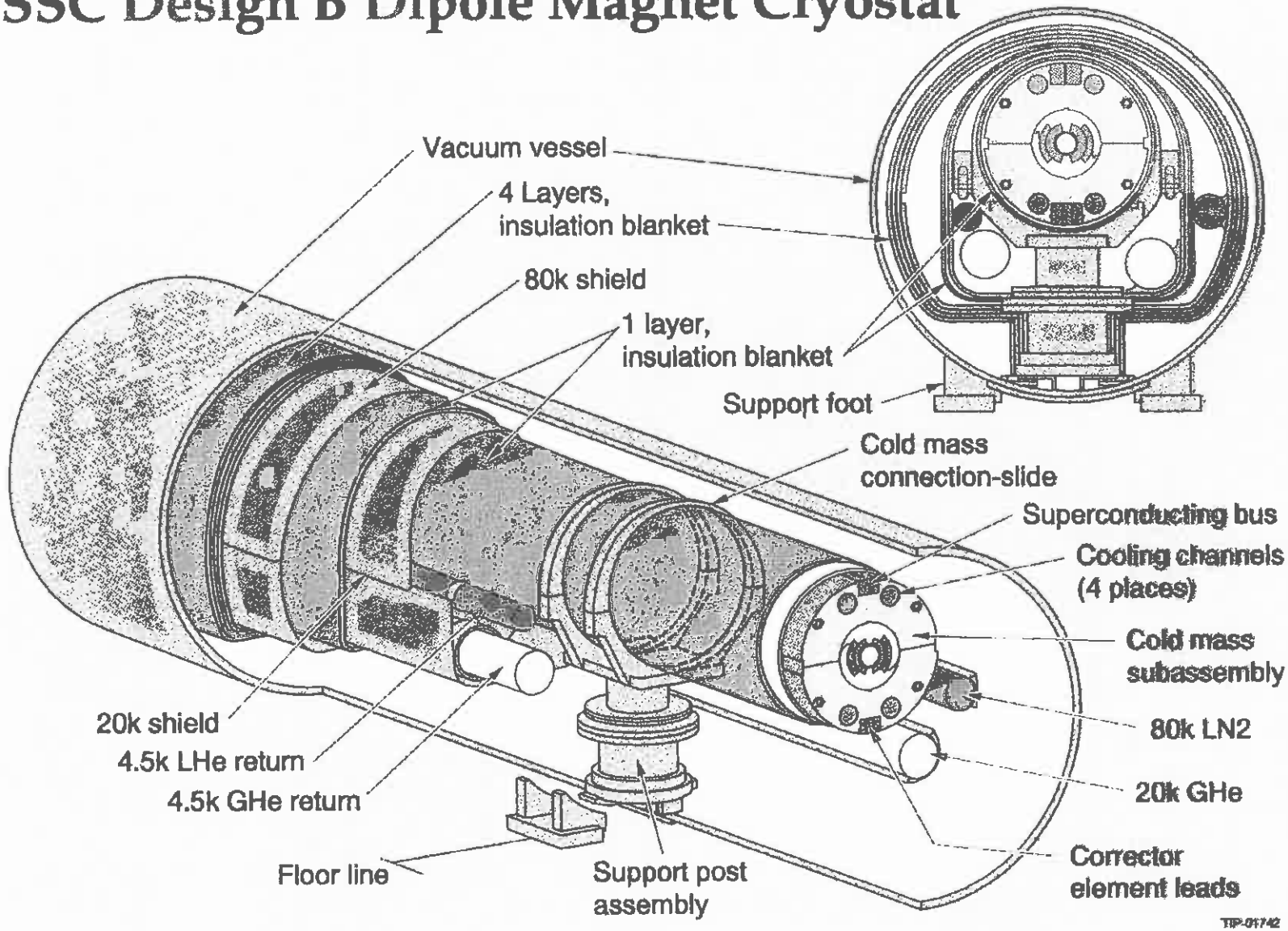

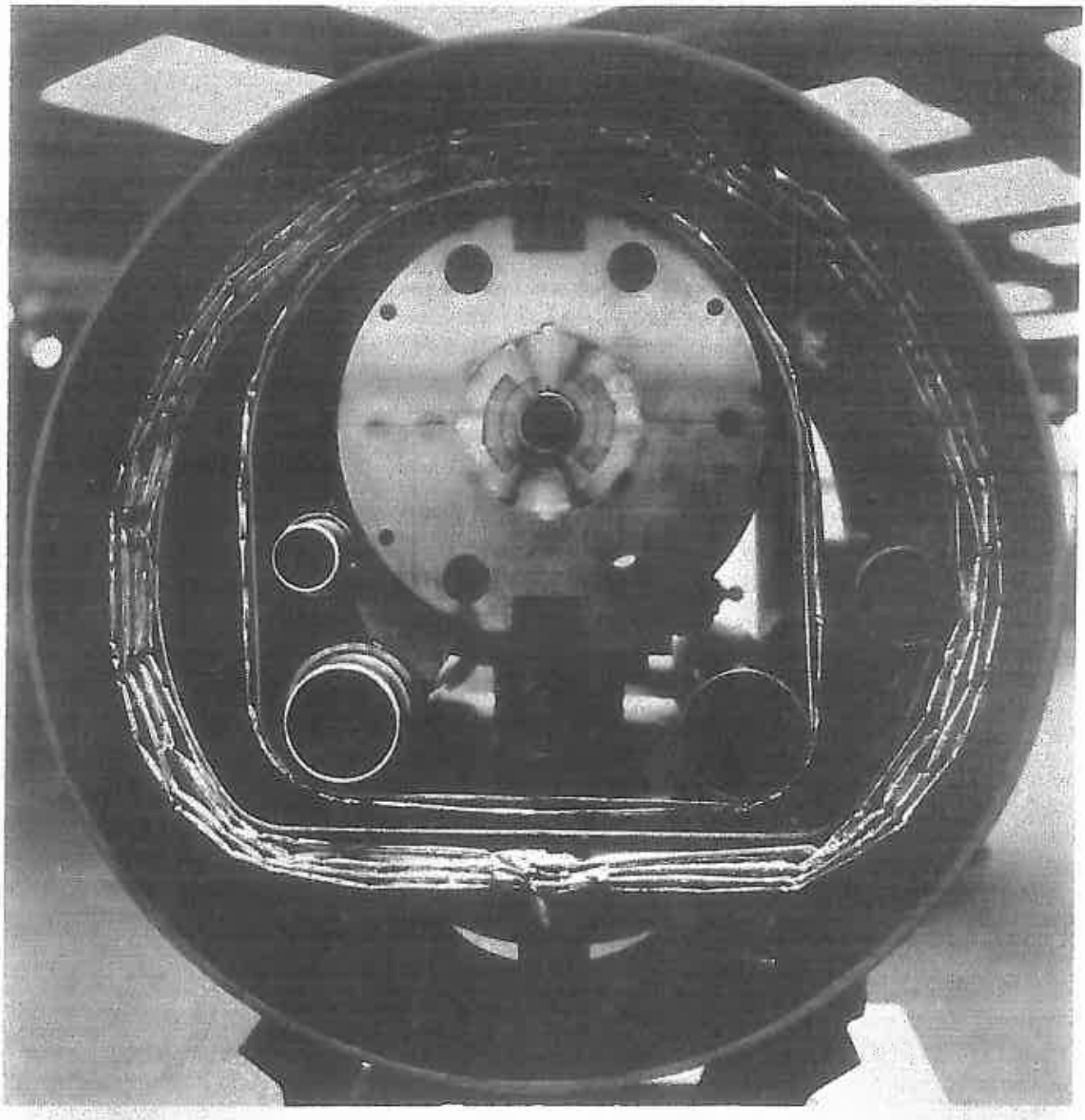

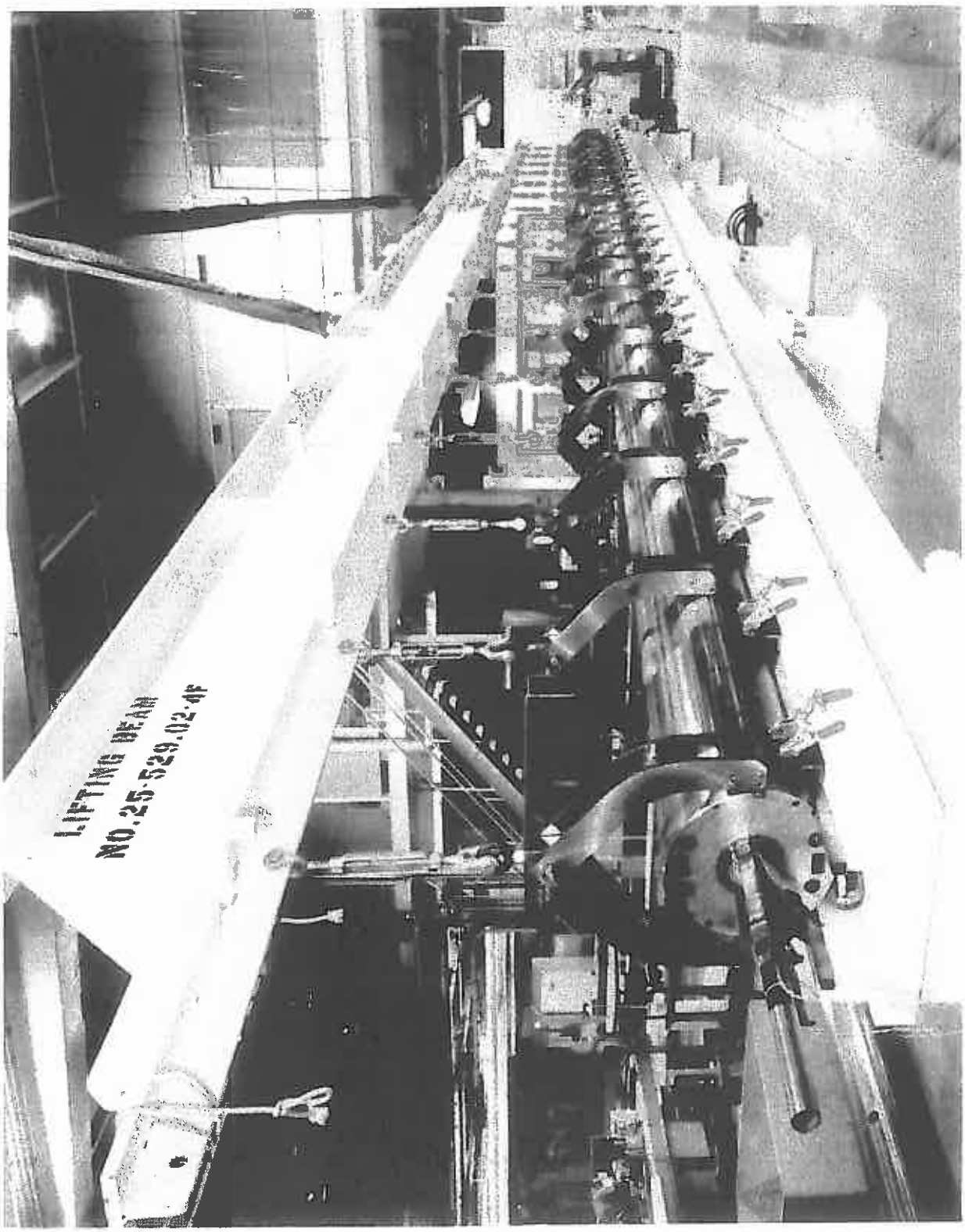
LIFTING BEAM
NO. 25-529.02-4F

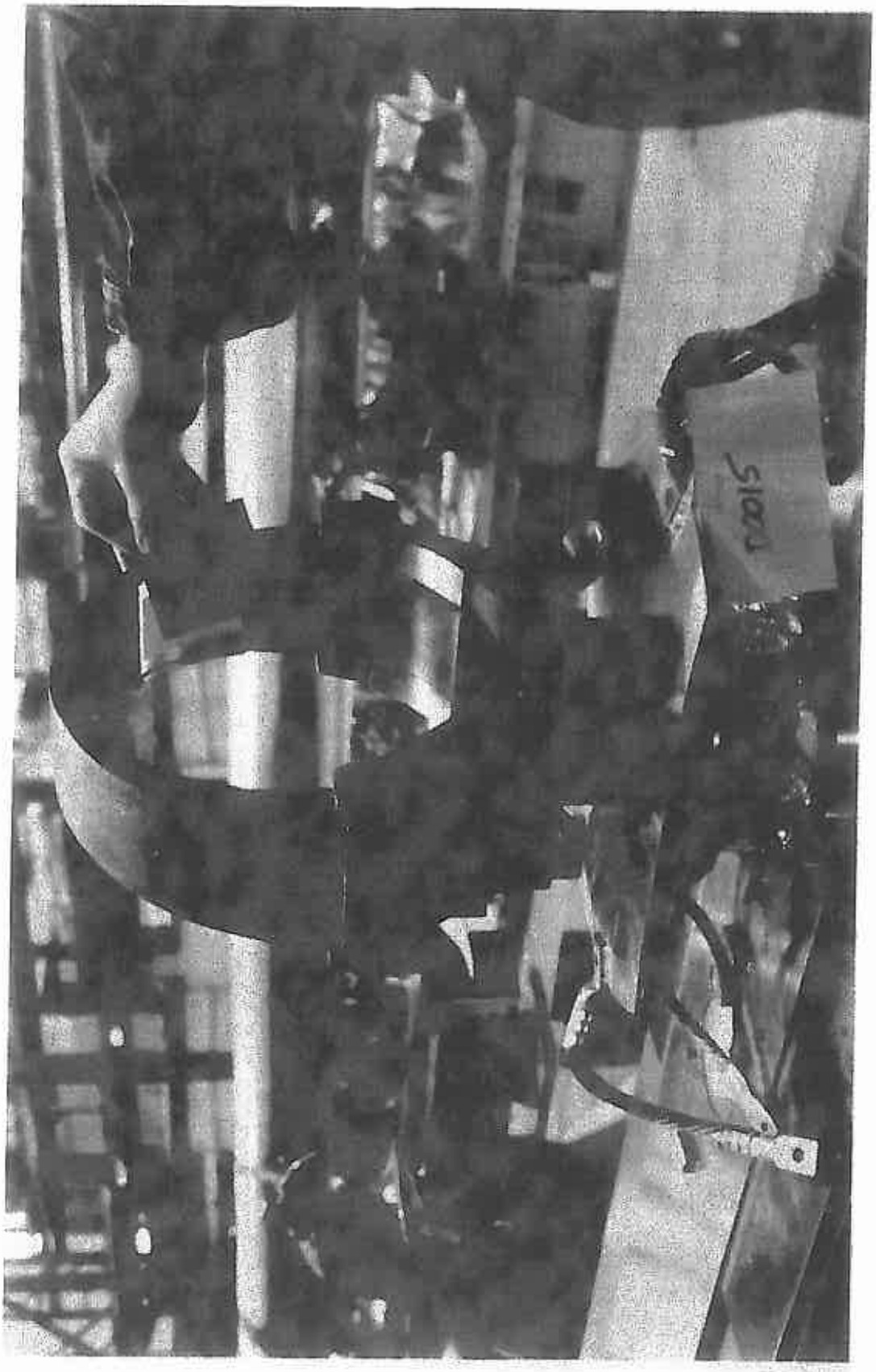

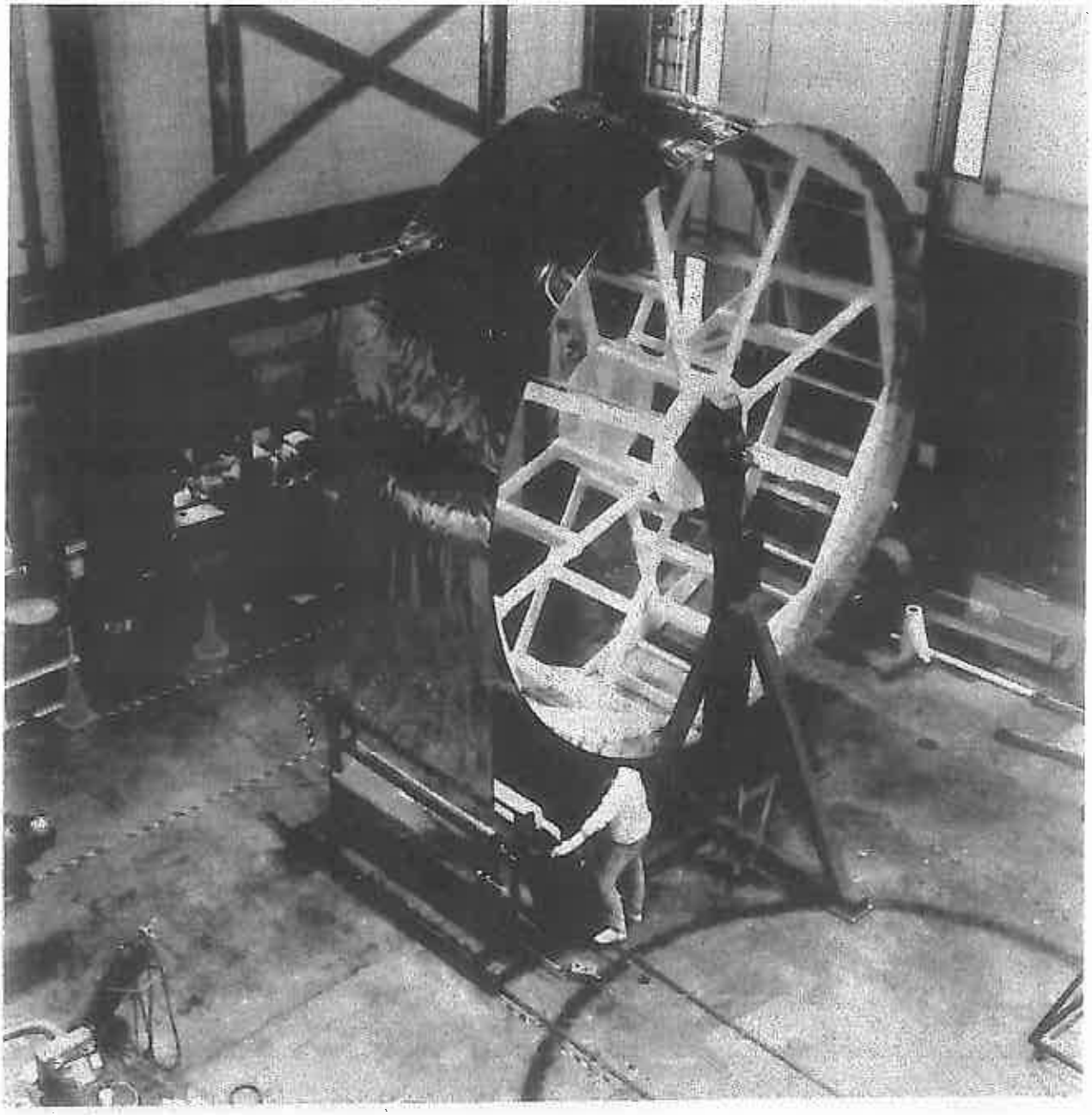

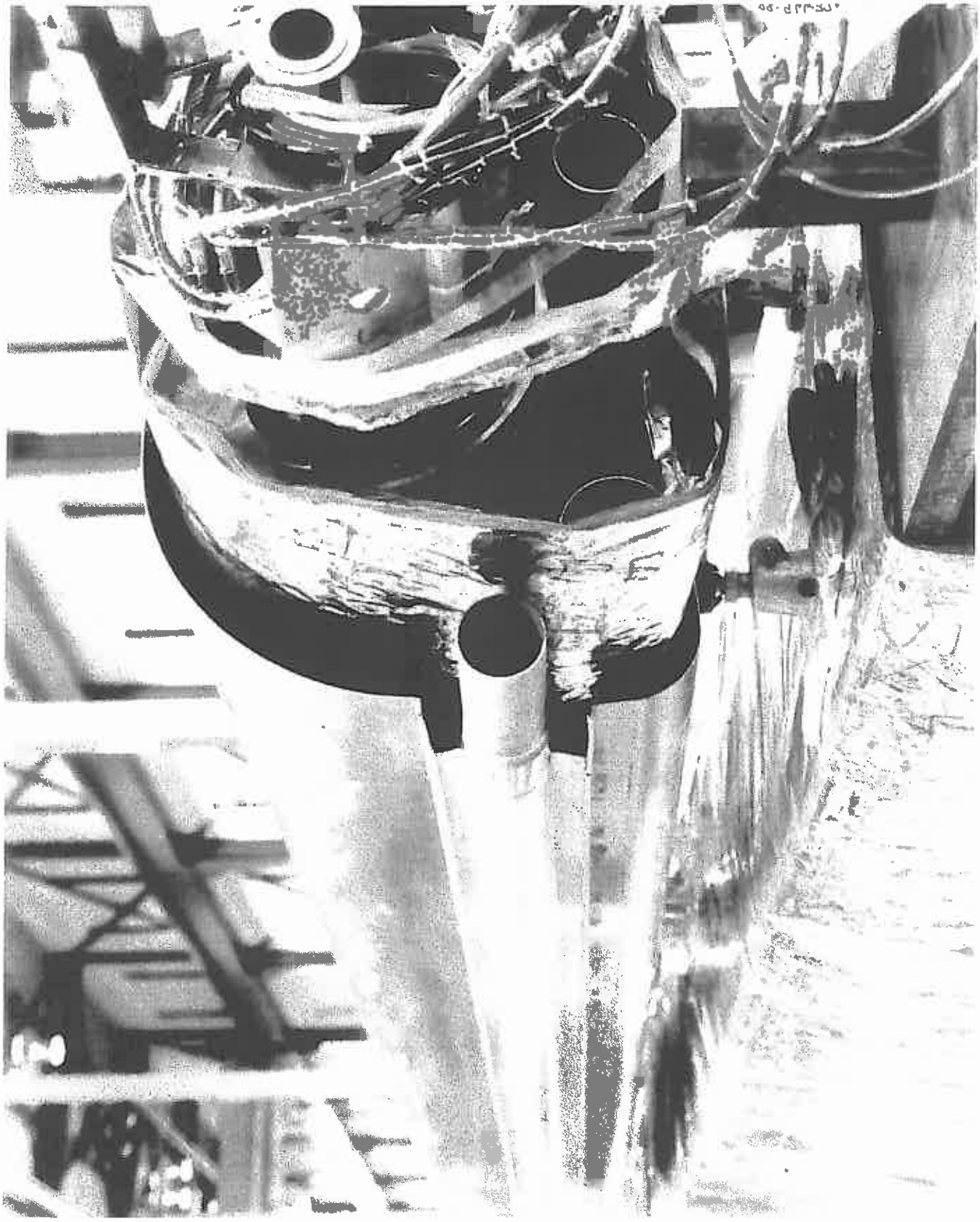

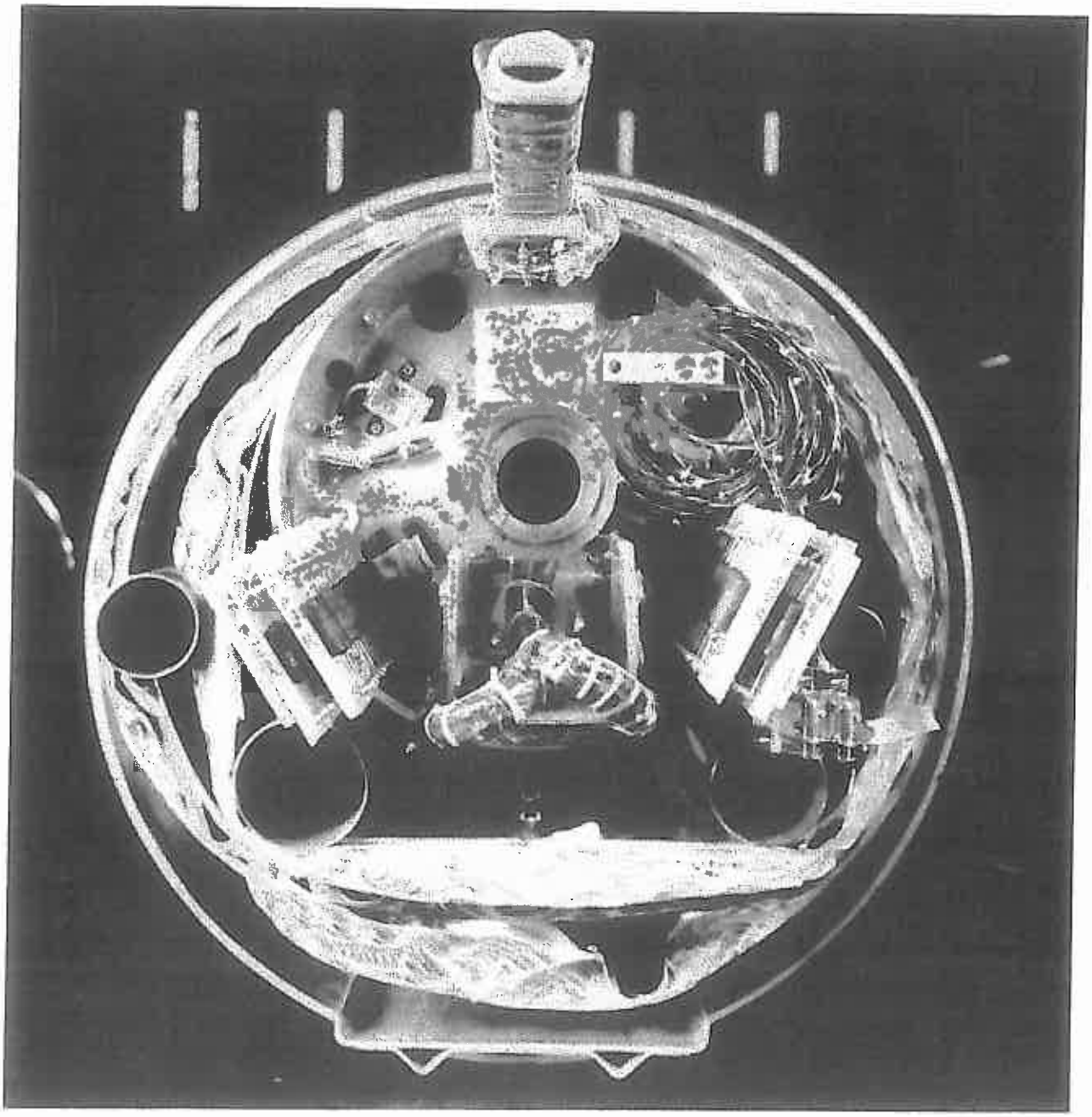

MAGNET CRYOSTAT (CONT.)

– Cryostat of quadrupole magnets is usually the repository of various utilities (such as corrector magnets, cryogenic modules, quench protection diodes, beam positon monitors...).

– For single magnet testing, the magnet cold mass is inserted into a built-in cryostat that is part of the test station.

LHC Short Straight Section

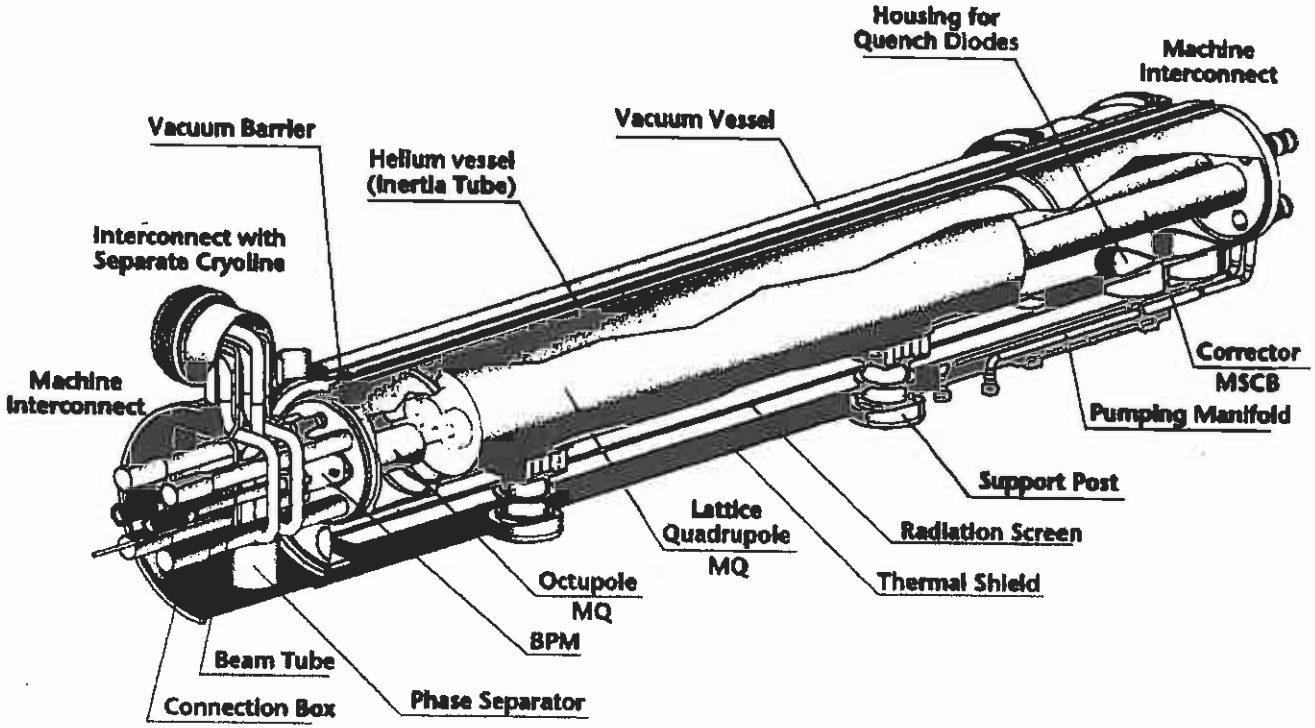

CERN AC _ EI2-10E

LECTURE 6: ASSEMBLY OF PARTICLE ACCELERATOR MAGNETS

6.1 Coil Winding

6.2 Coil Curing

6.3 Azimuthal Coil Size Measurements

6.4 Coil Assembly and Internal Splicing

6.5 Collaring

6.6 Collar Deflection Measurements

6.7 External Splicing

6.8 Yoke Stacking and Shell Welding

6.9 Yoke Midplane Gap Measurements

6.10 Cryostating

6.11 Instrumentation

SPECIFIC INSTRUMENTATION DEVELOPED FOR ACCELERATOR MAGNET COLDMASS

– Beam-type strain gauge transducers to measure pressure exerted by coils against collar poles.

– Capacitive gauge transducers to measure coil azimuthal stress.

– Bullet-type strain gauge transducer to measure force exerted by coils against end plates.

Beam-Type Strain-Gauge Transducers

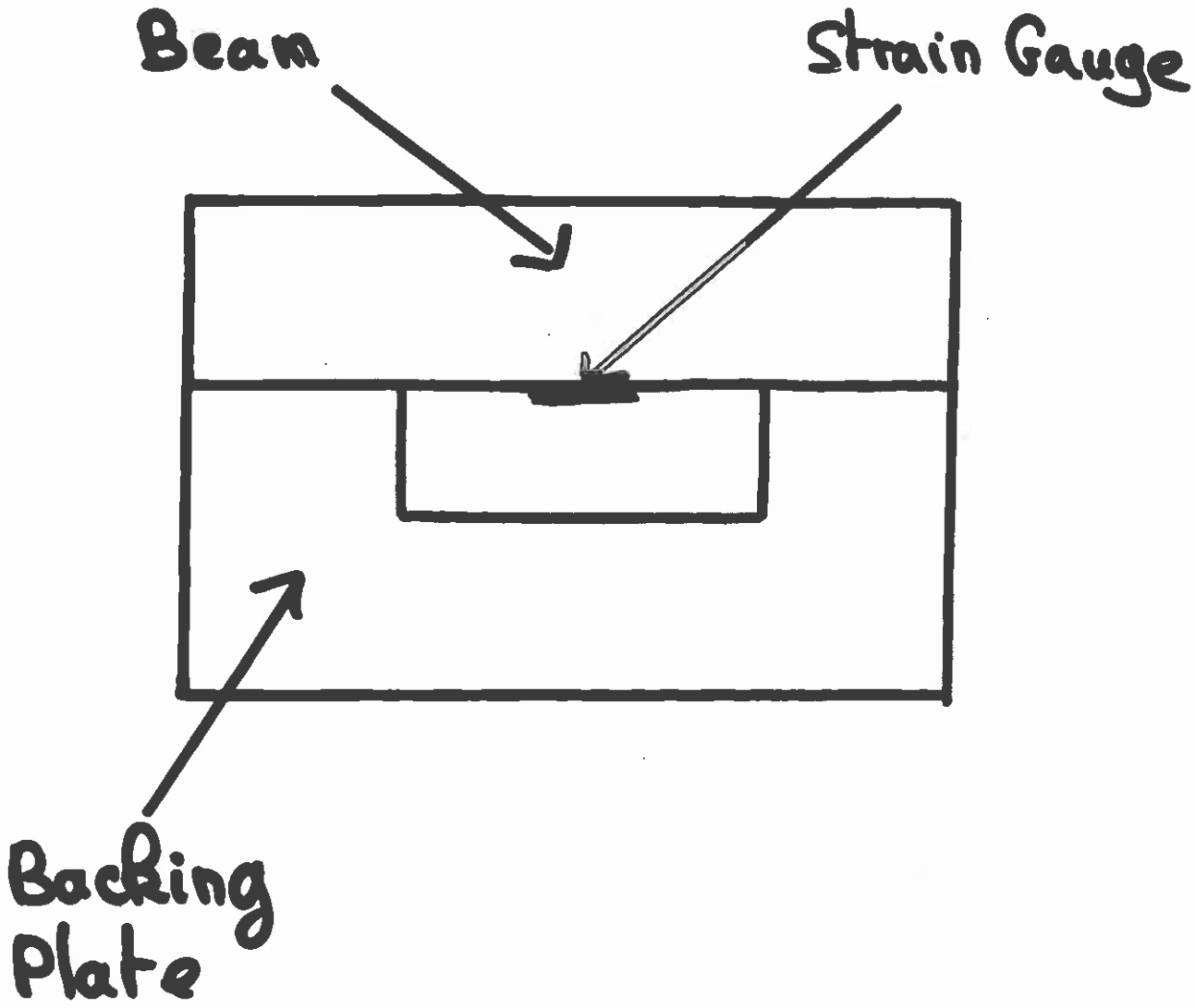

Beam-Type Strain-Gauge Transducers (Cont.)

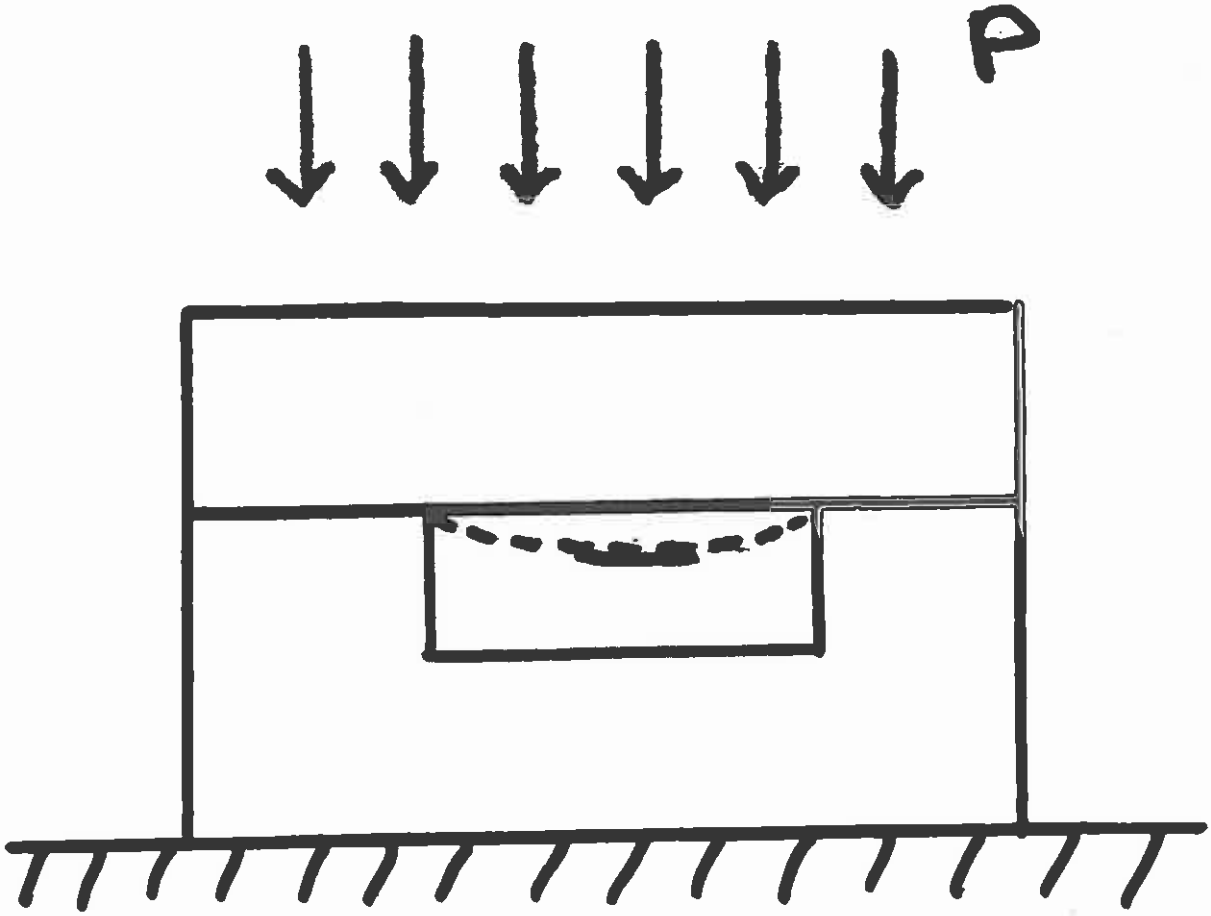

Sensitivity:

70 MPa ~ 25 μm
(10 kpsi) (1 mil)

Resistance vs. Temperature Measurement
Gauge #71001-1
(for Karma-Type Gauge)
Degrees Kelvin
350
349.5
349
348.5
348
(Courtesy C. Goodyear)

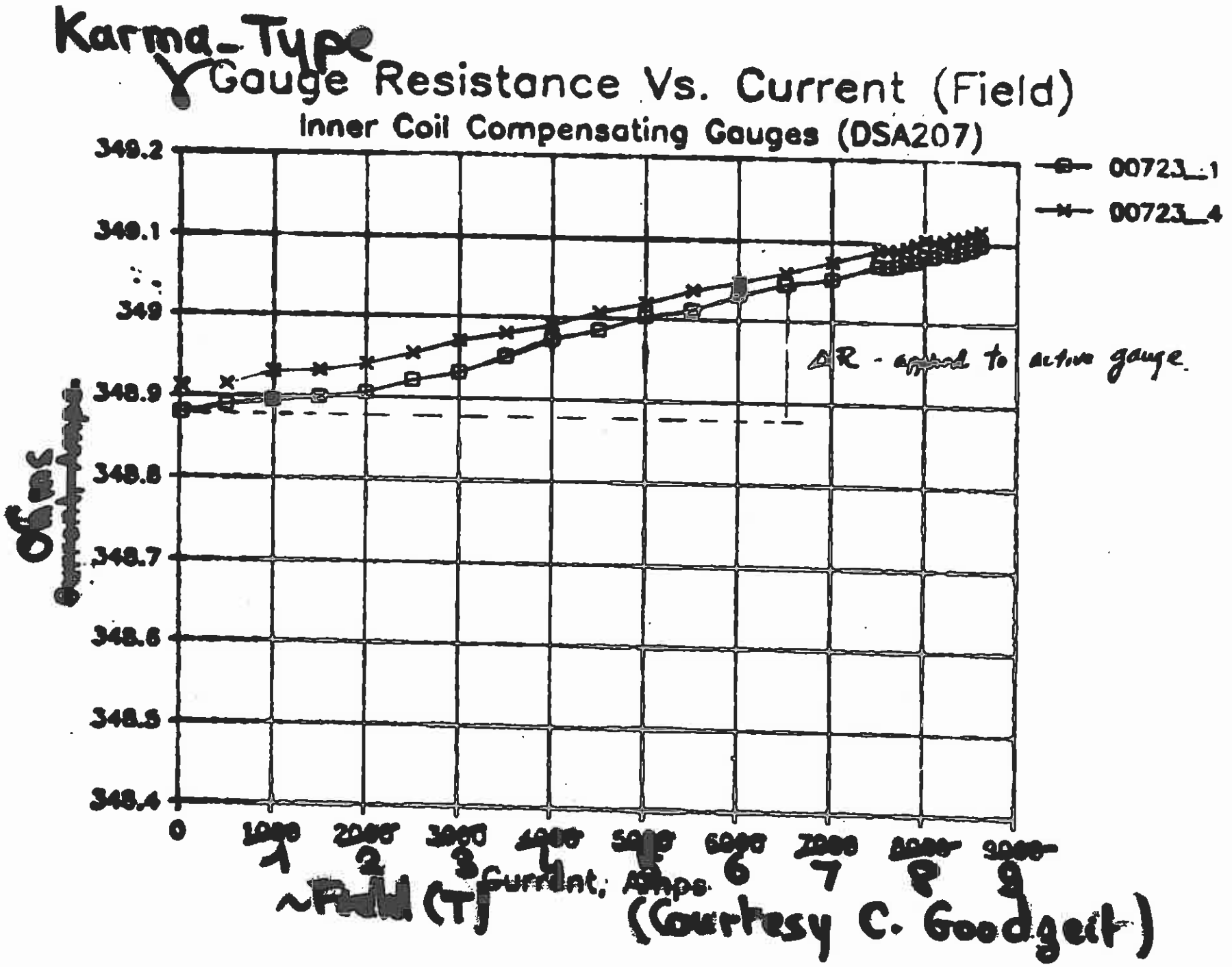
Karma-Type
Gauge Resistance Vs. Current (Field)
Inner Coil Compensating Gauges (DSA207)
00723_1
00723_4
ΔR - applied to active gauge.
348.2
348.1
349
348.9
348.8
348.7
348.6
348.5
348.4
0
1
2
3
6
7
8
9
Current, Amps
(Courtesy C. Goodgeit)

Temperature and Field Compensation

- "Active" Gauge

$$R_a(T,B,\sigma) = R_0 + \Delta R(T) + \Delta R(B) + \Delta R(\sigma)$$

- "Compensating" Gauge

$$R_c(T,B,\sigma=0) = R_0 + \Delta R(T) + \Delta R(B)$$

Difference between R_a and R_c eliminates T and B effects

BEAM-TYPE STRAIN GAUGE TRANSDUCER
(Courtesy C. L. Goodzeit, SSCL)

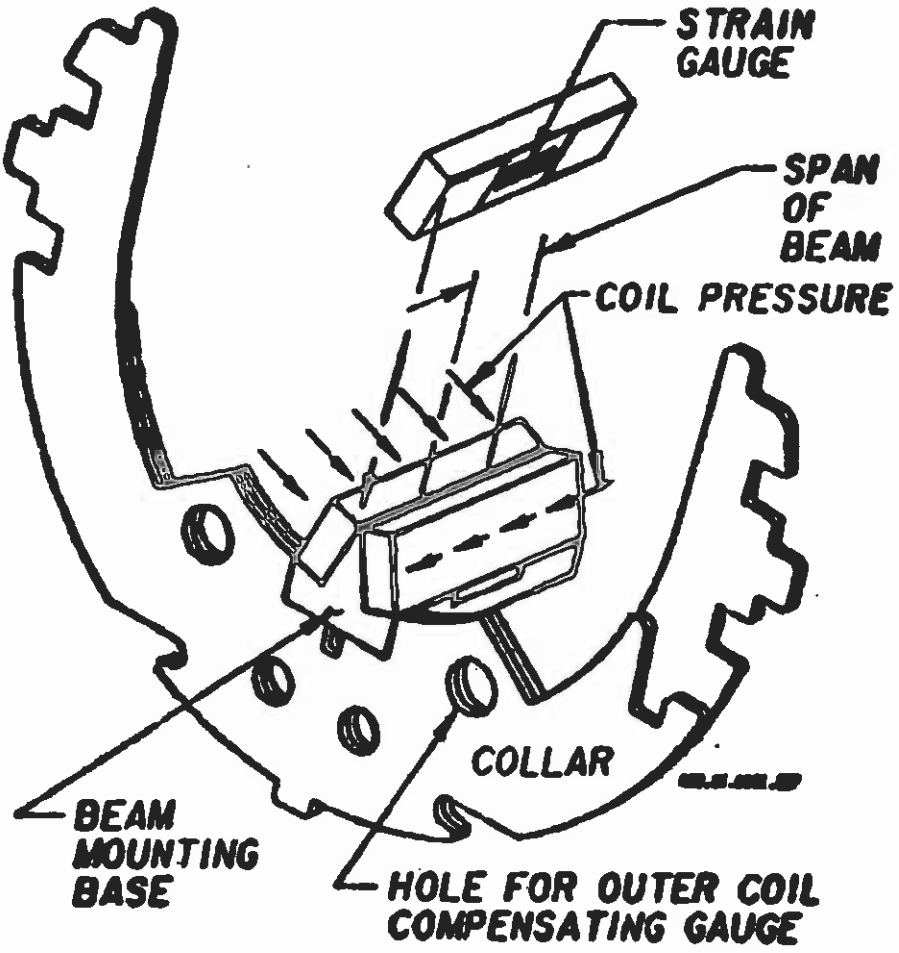

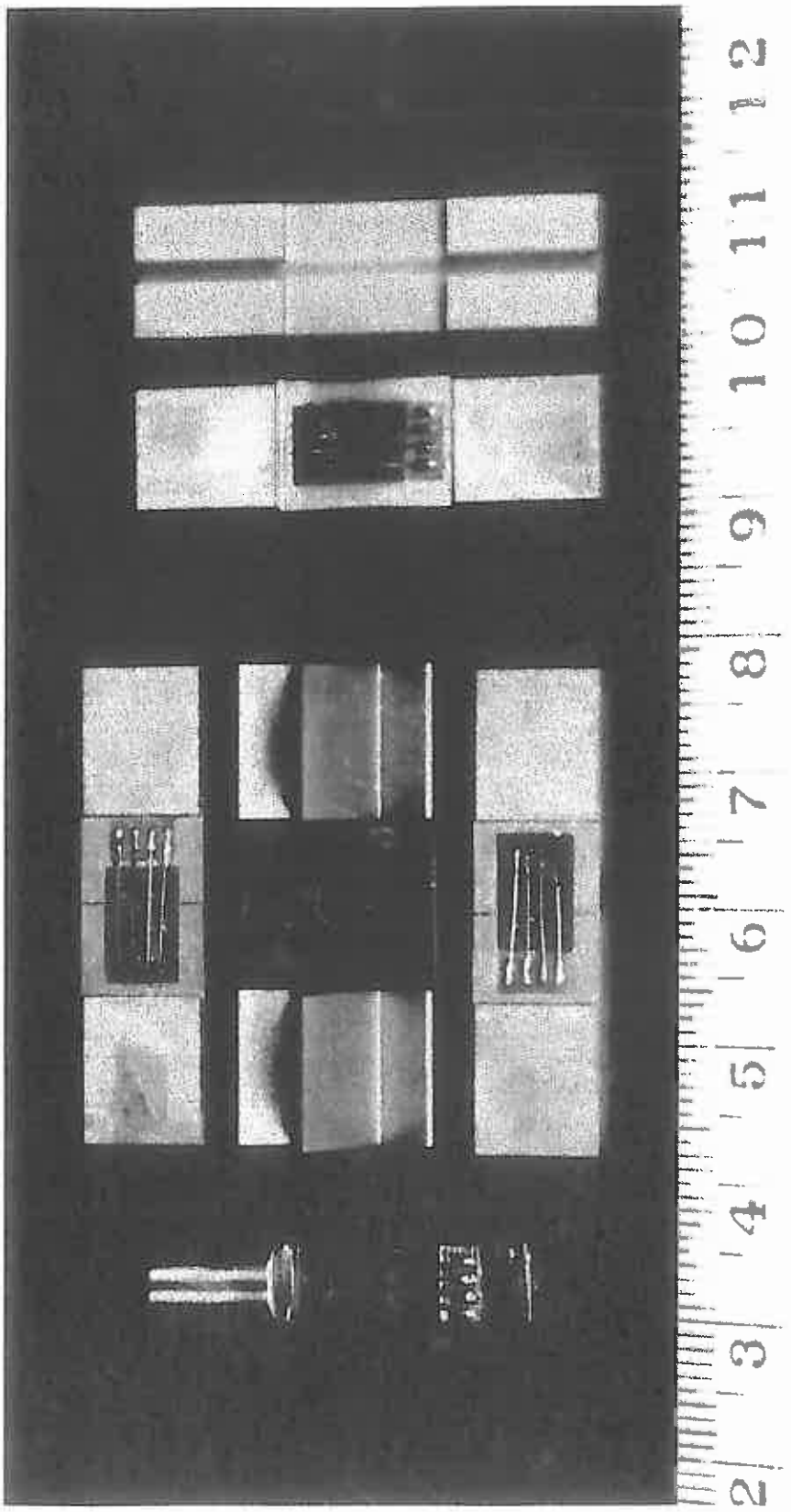
2
3
4
5
6
7
8
9
10
11
12

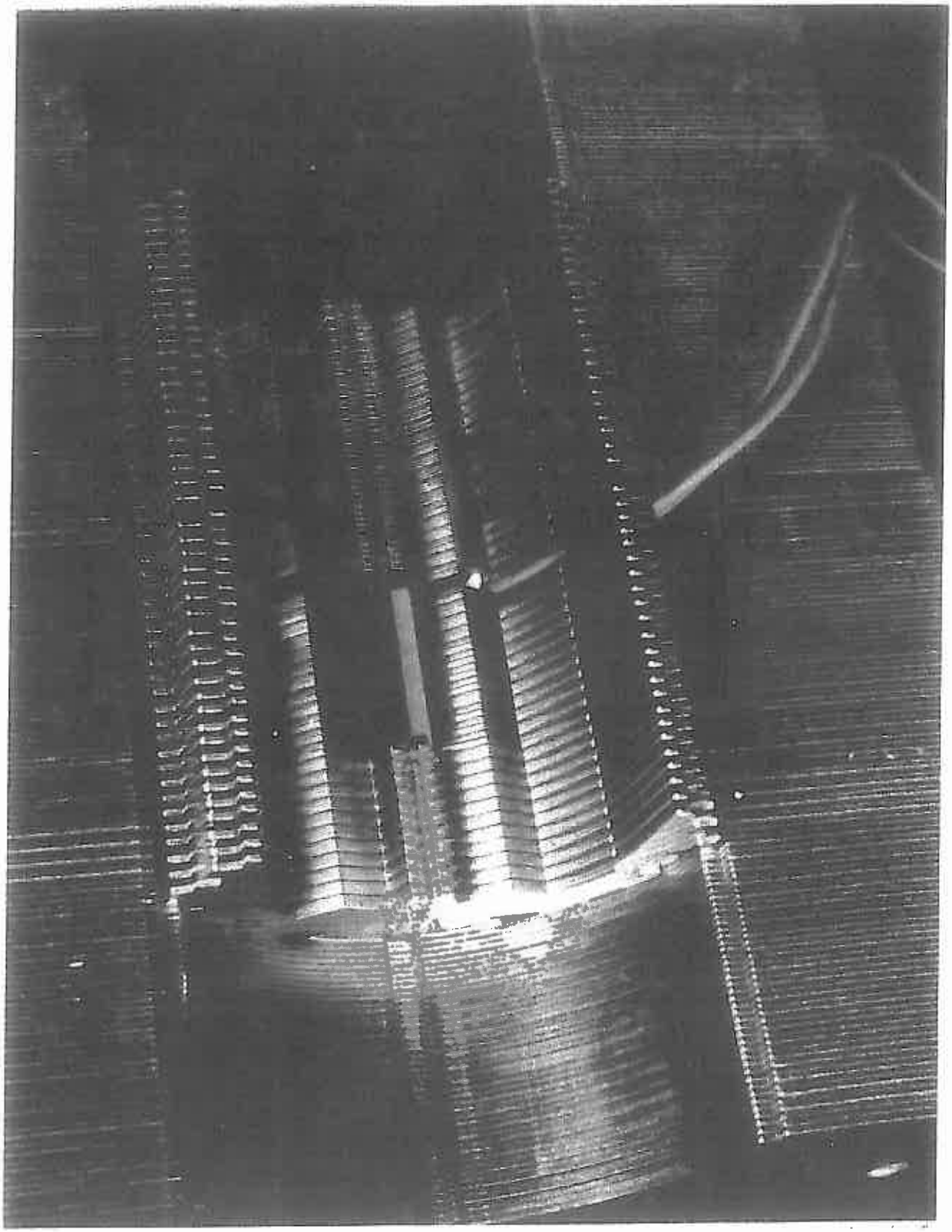

Transducer Alignment

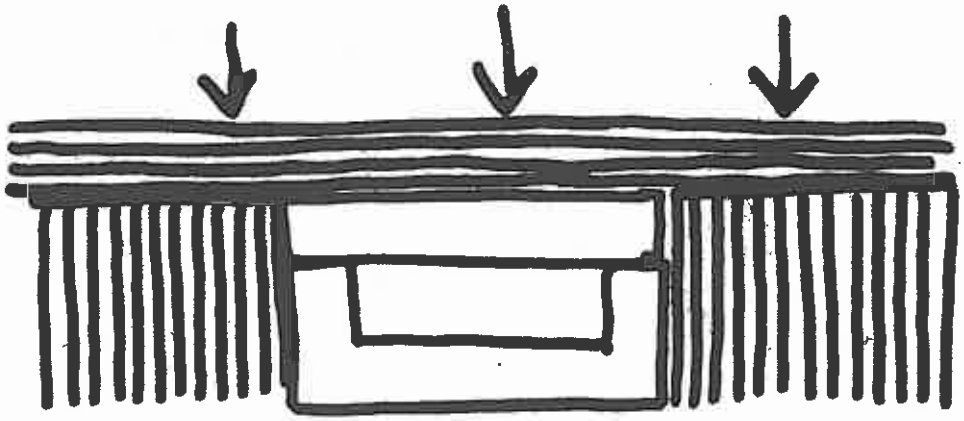

Effects of a Parallel Misalignment

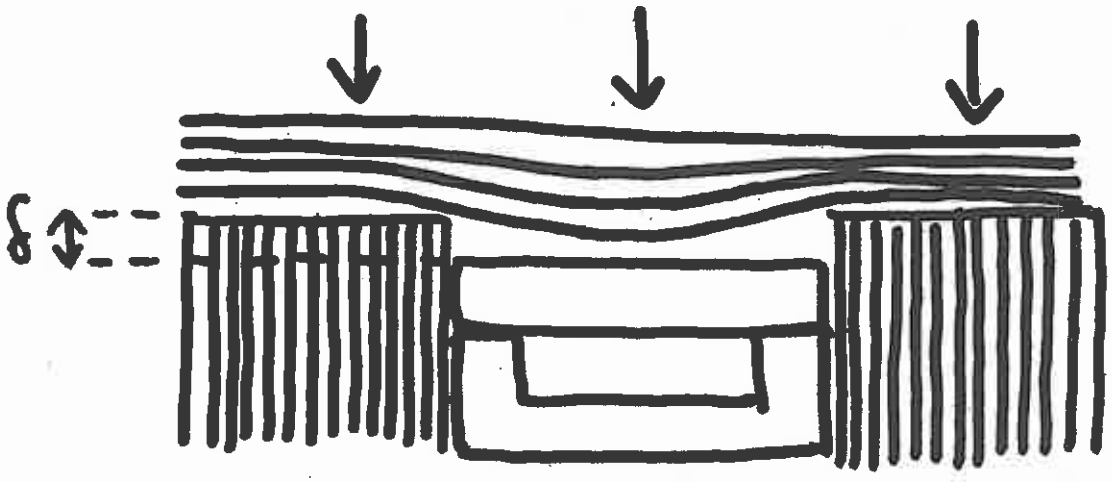

$\delta \sim 25\,\mu m \iff \Delta\sigma \sim 14\,MPa^{*}$

*Measured by Z. Wolf, T. Ogitsu, et al.

Capacitive Force Sensors

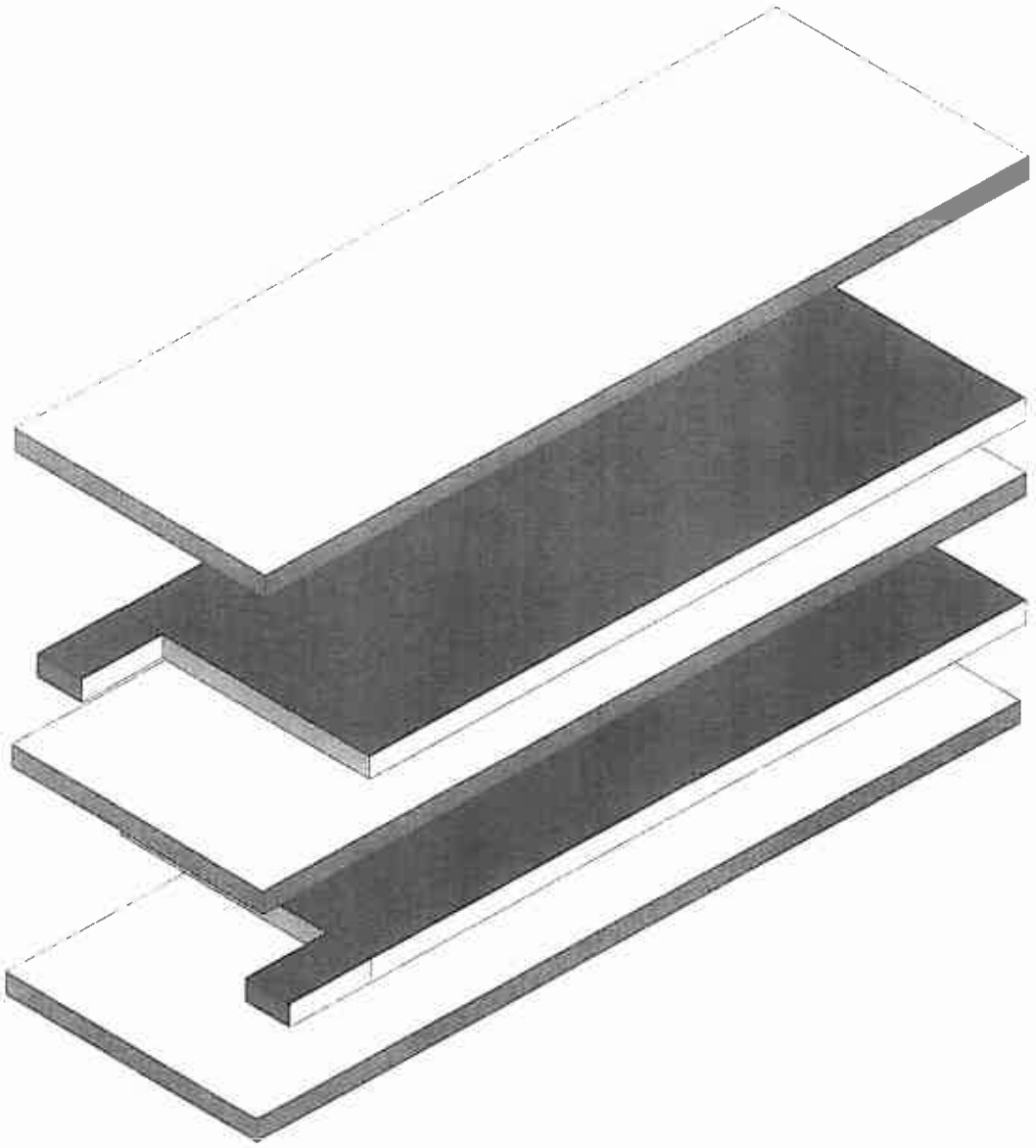

Insulation

Copper

Dielectric material

Copper

Insulation

$$C = \frac{\varepsilon S}{[\delta(1-\sigma/E)]}$$

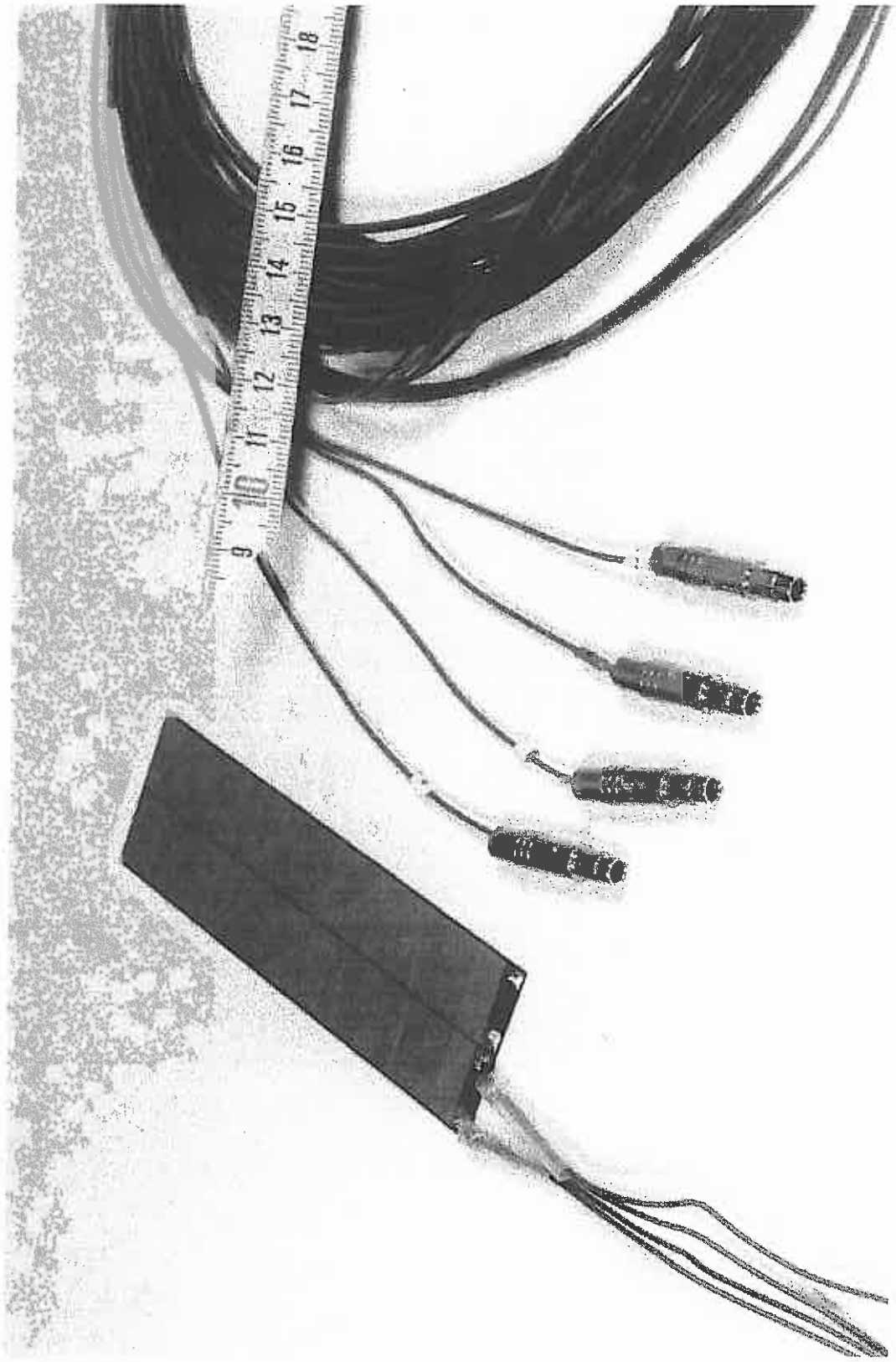
9
10
11
12
13
14
15
16
17
18

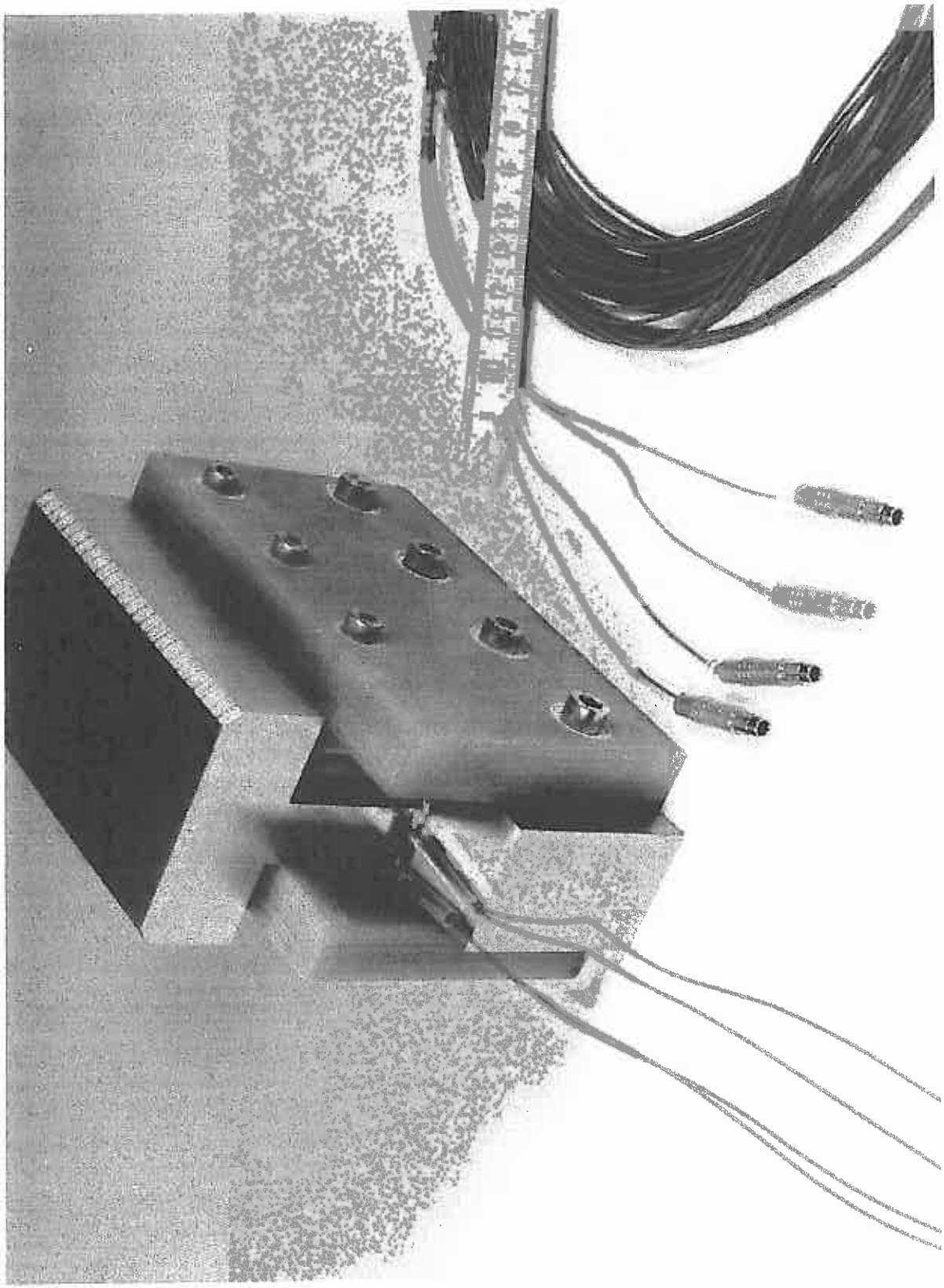

Capacitives Strain Gauges - Calibration curves -

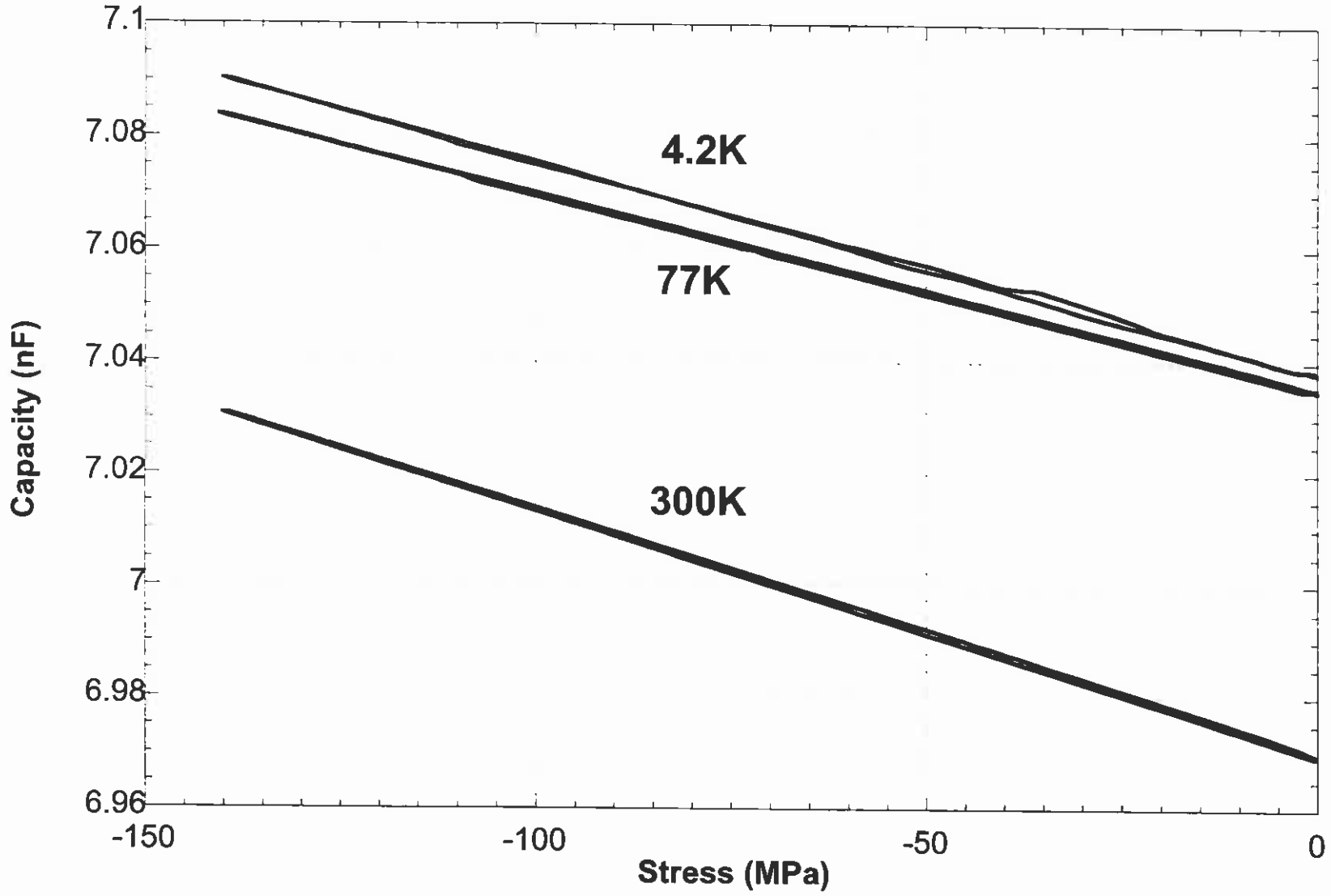

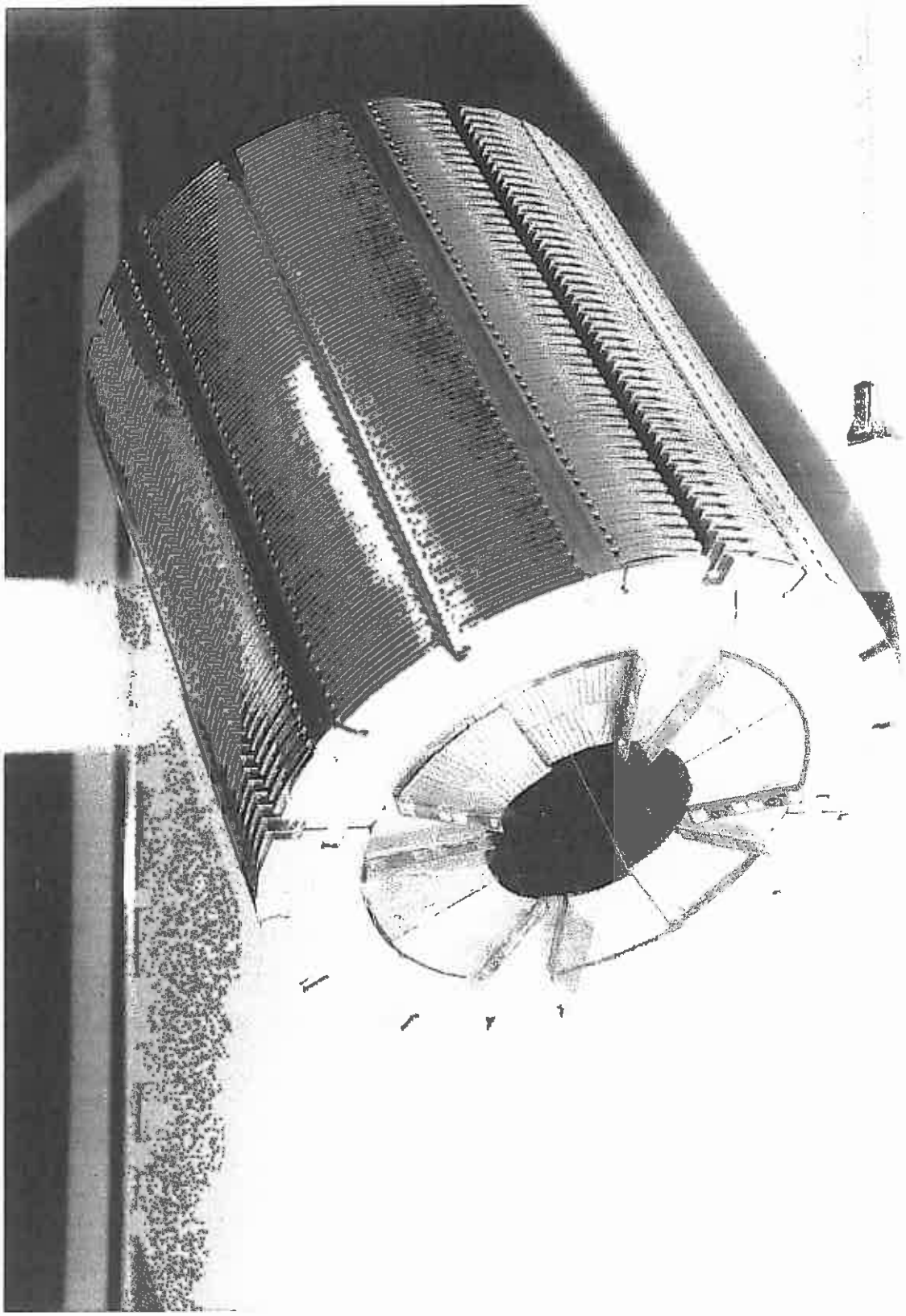

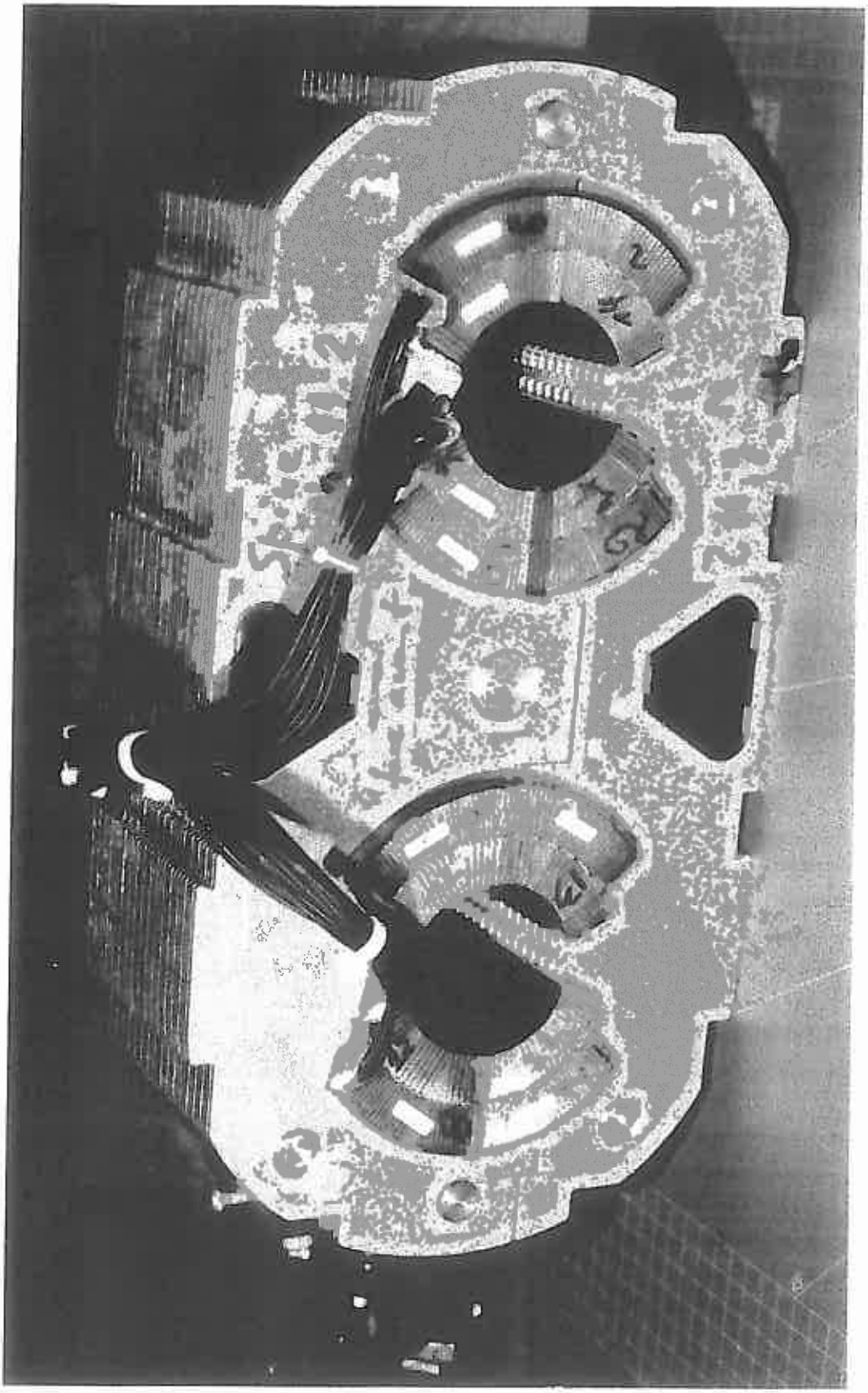

Strain-Gauge Instrumentation (Cont.)

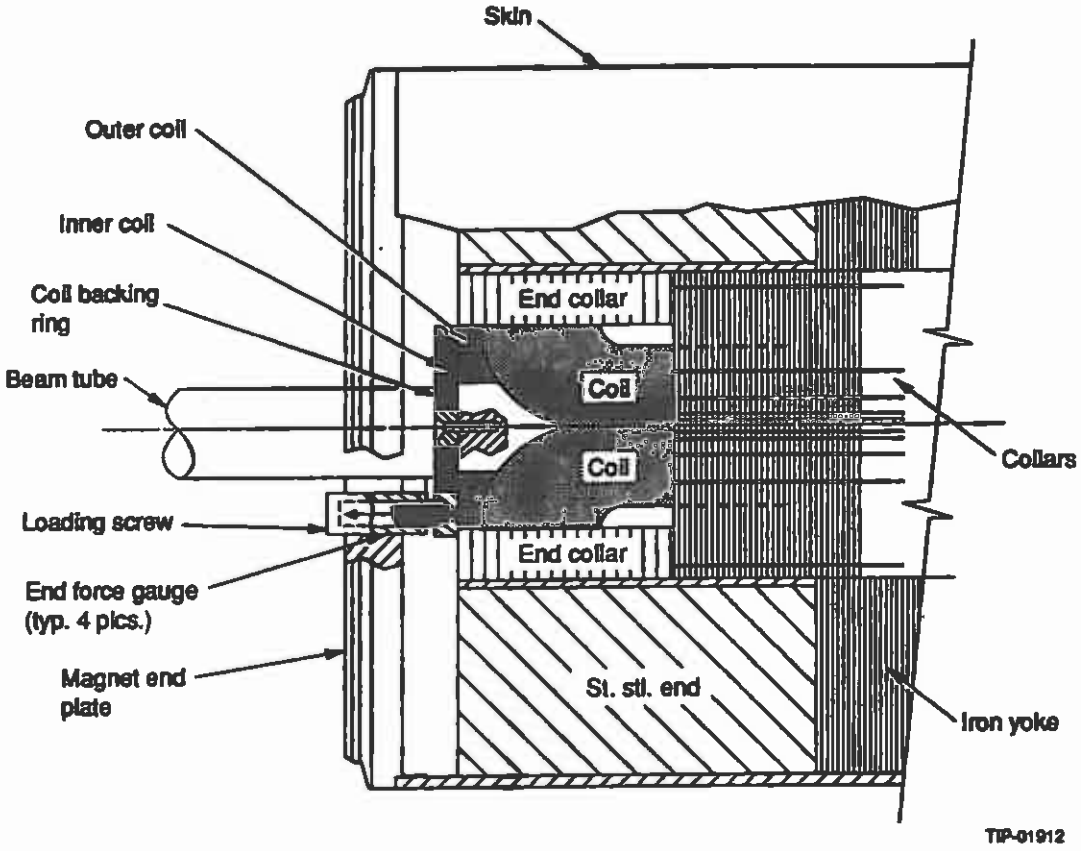

Bullet-Type Strain-Gauge Trans. (Force exerted by coil against end-plate)

Bullet-Type Strain-Gauge Transducers (Cont.)

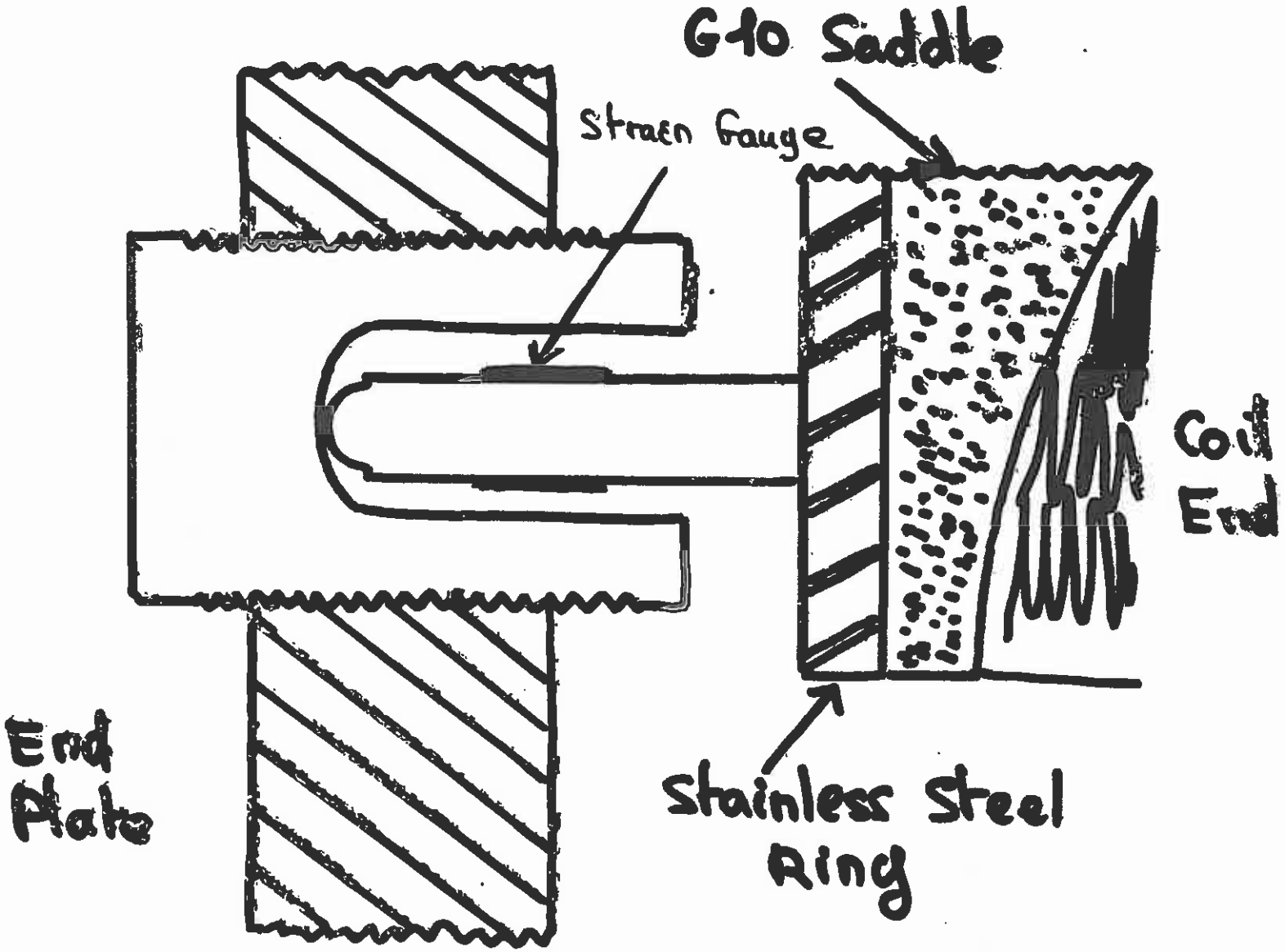

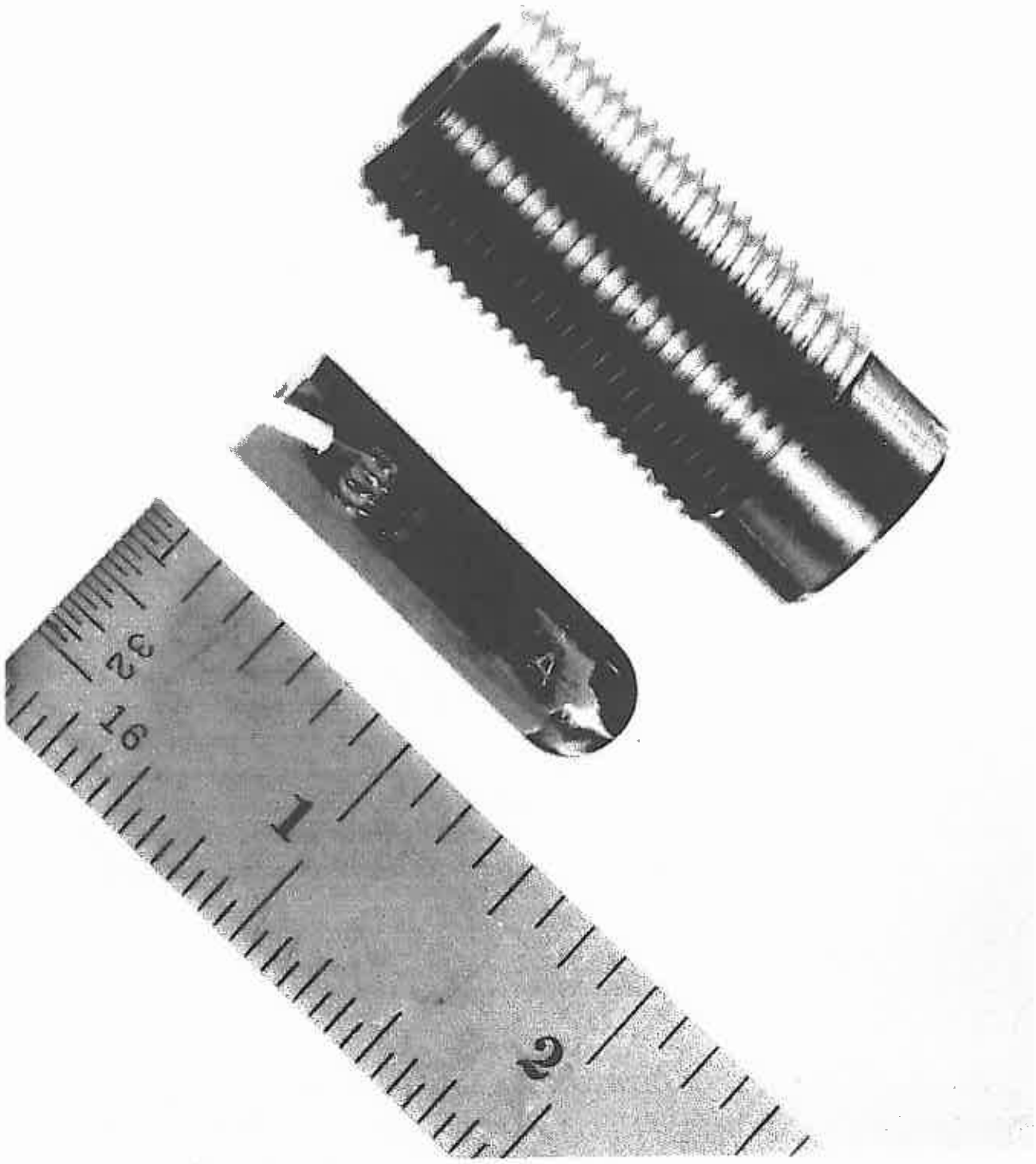
32
16
1
2

EXAMPLES OF QUENCH BEHAVIOR

– Some magnets do not require training and always reach their short sample limit on the first quench after cooldown.

Example: 5-cm-aperture, 15-m-long SSC dipole magnet prototype DCA315.

– Some magnets require training after the first cooldown, but do not require re-training upon subsequent cooldowns.

Example: 5-cm-aperture, 15-m-long SSC dipole magnet prototype DCA313.

– Some magnets require training and re-training after each cooldown.

Example: 4-cm-aperture, 17-m-long SSC dipole magnet prototype DD0017.

– Some magnets do not require training after the first cooldown but do require training on the second cooldown.

Example: 4-cm-aperture, 17-m-long SSC dipole magnet prototype DD0027.

– Some magnets keep quenching erratically and cannot be trained to a stable plateau.

Example: 4-cm-aperture, 17-m-long SSC dipole magnet prototype DD0010.

– Some magnets appear reach a stable plateau but this plateau is well bellow the expected short sample limit.

Example: 4-cm-aperture, 17-m-long SSC dipole magnet prototype DD0016.

SSC/FNAL 5-on-Apert., 15-m-long Dipole

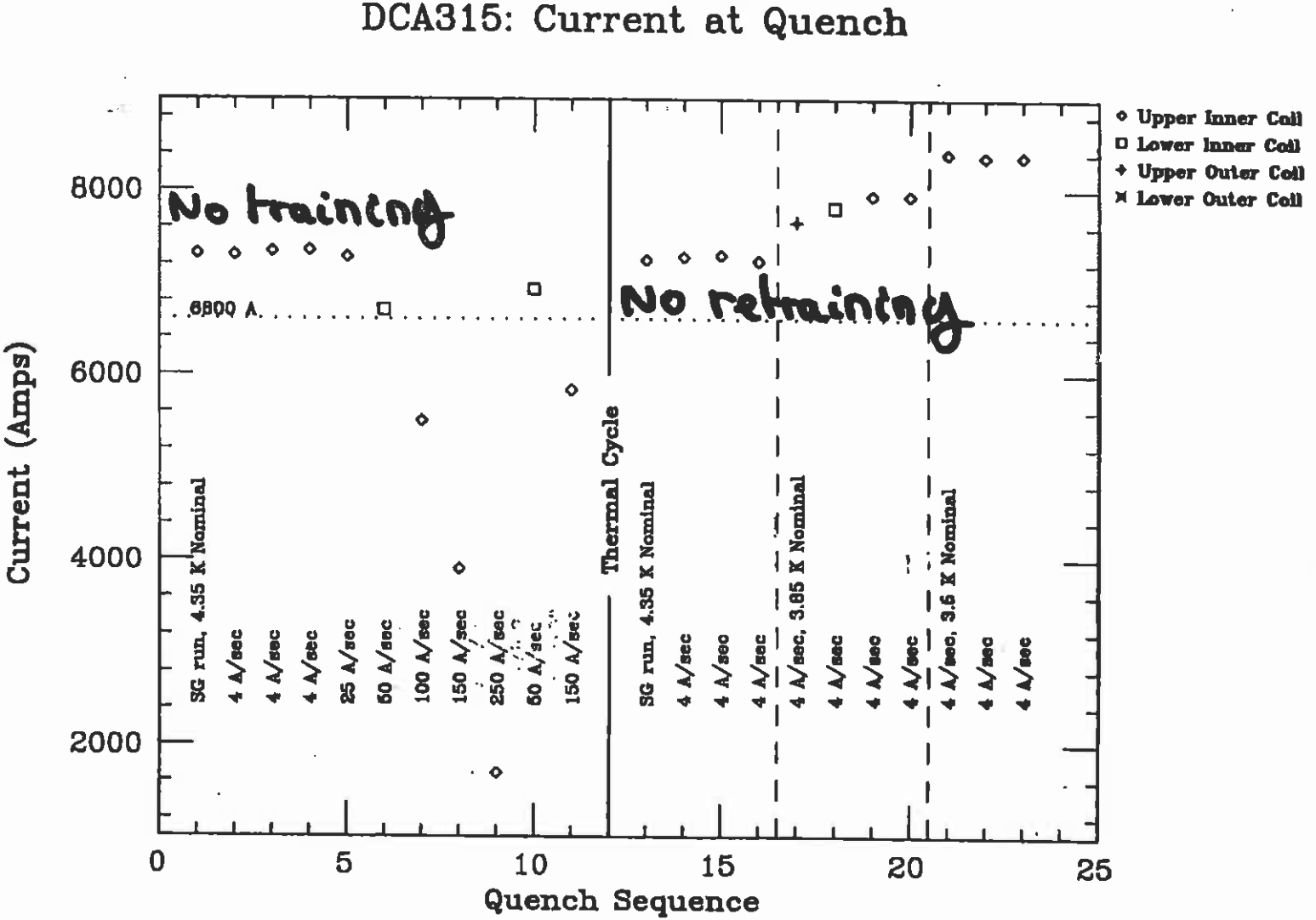

SSC/FNAL 5-cm-Apert., 15-m-long Dipole

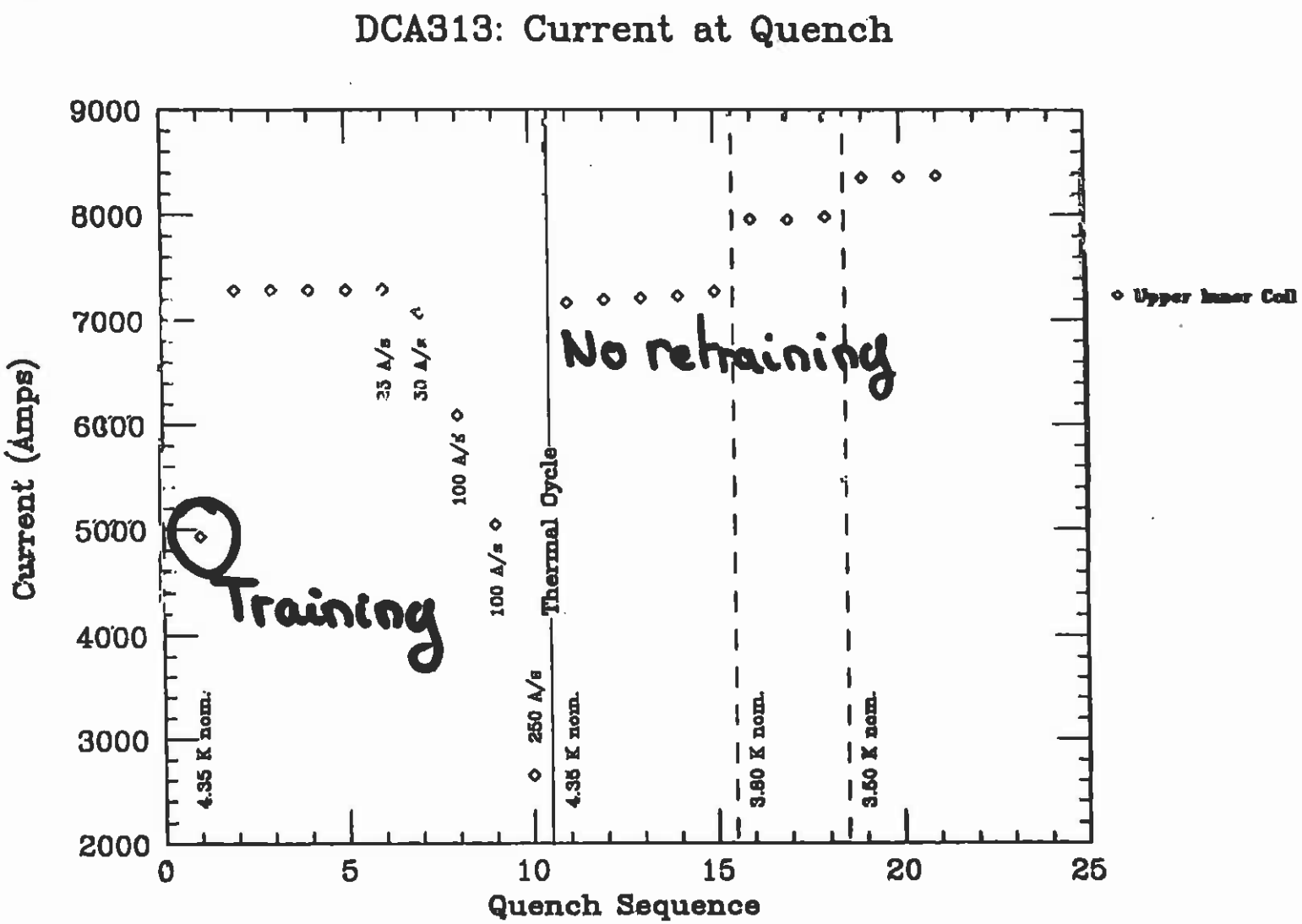

SSC/BNL 4-on-1 per l., 17-m-long Dipole

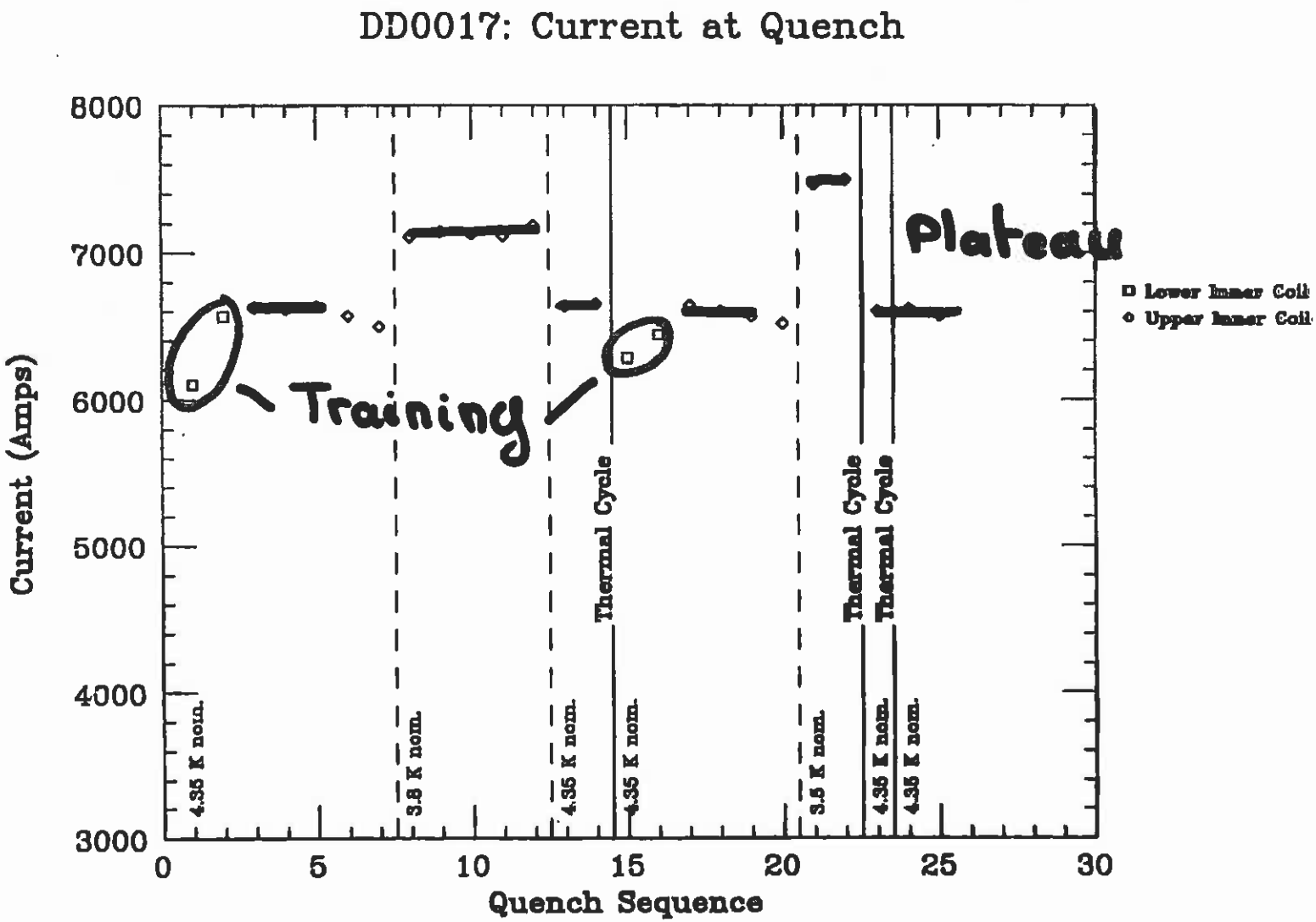

SSC/BNL 4-in-Apert., 17-m-Long Dipole

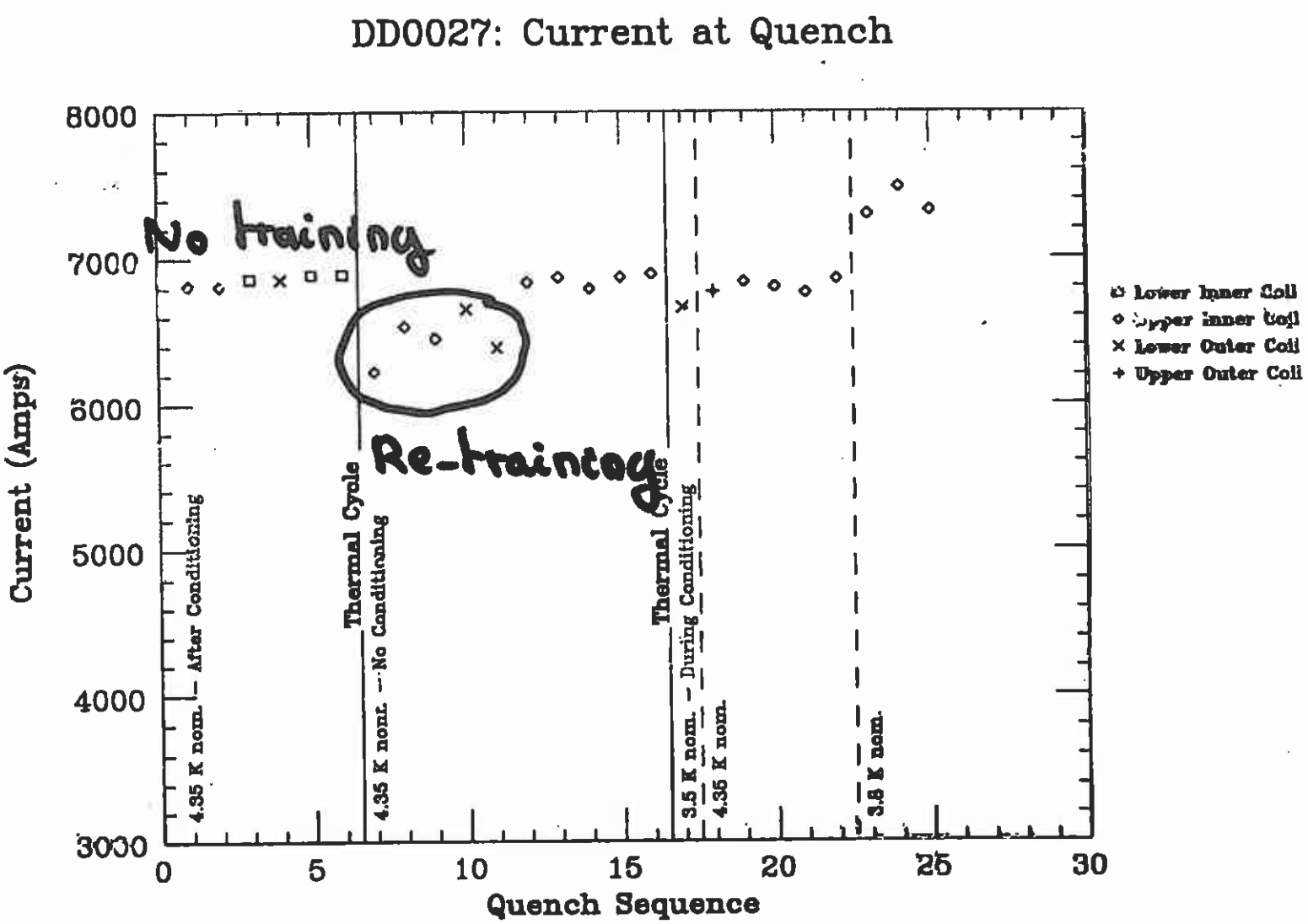

SSC/BNL 4-cm-Apert., 17-m-Long Dipole

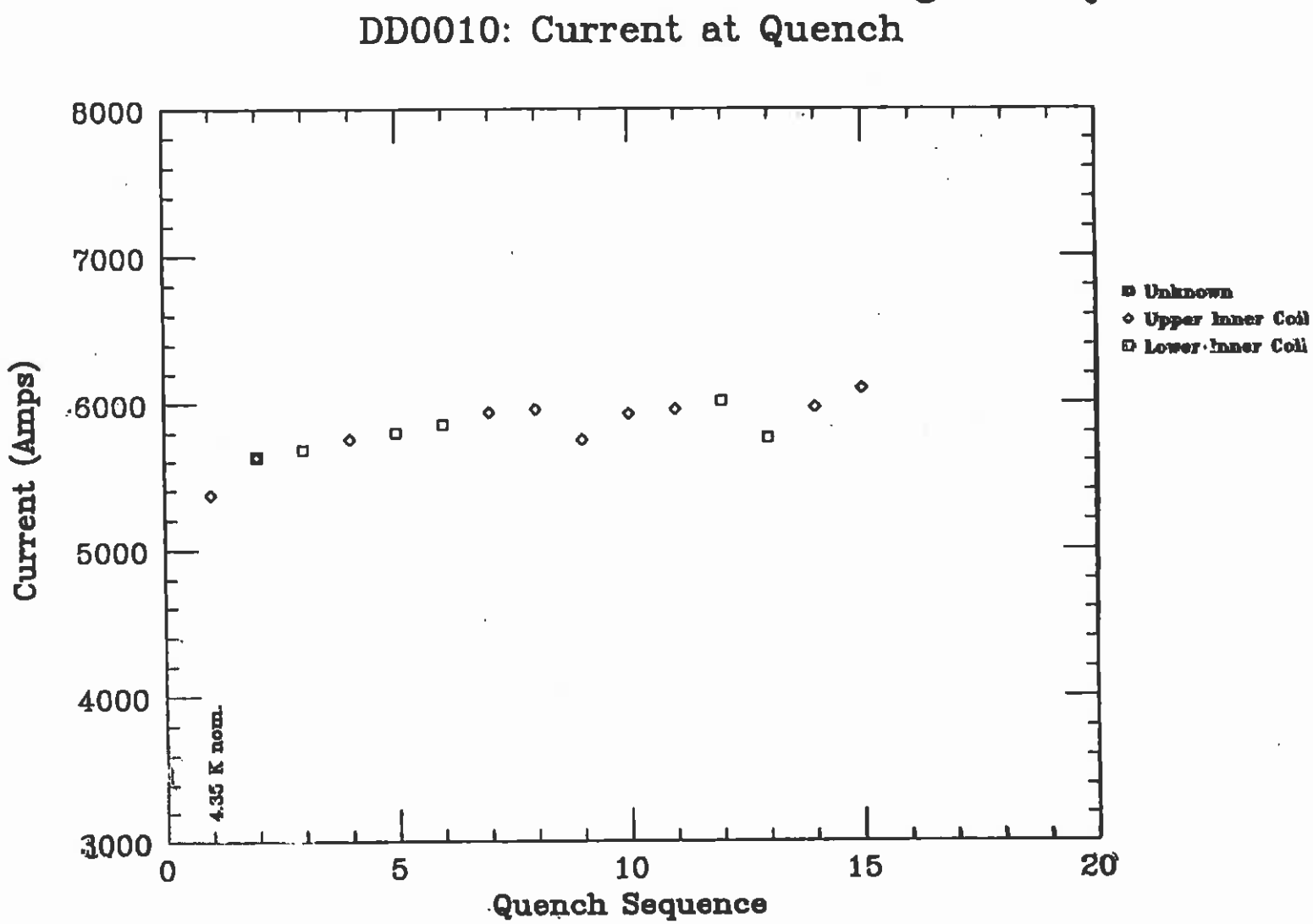

SSC/BNL 4-cm-Apert., 17-m-Long Dipole

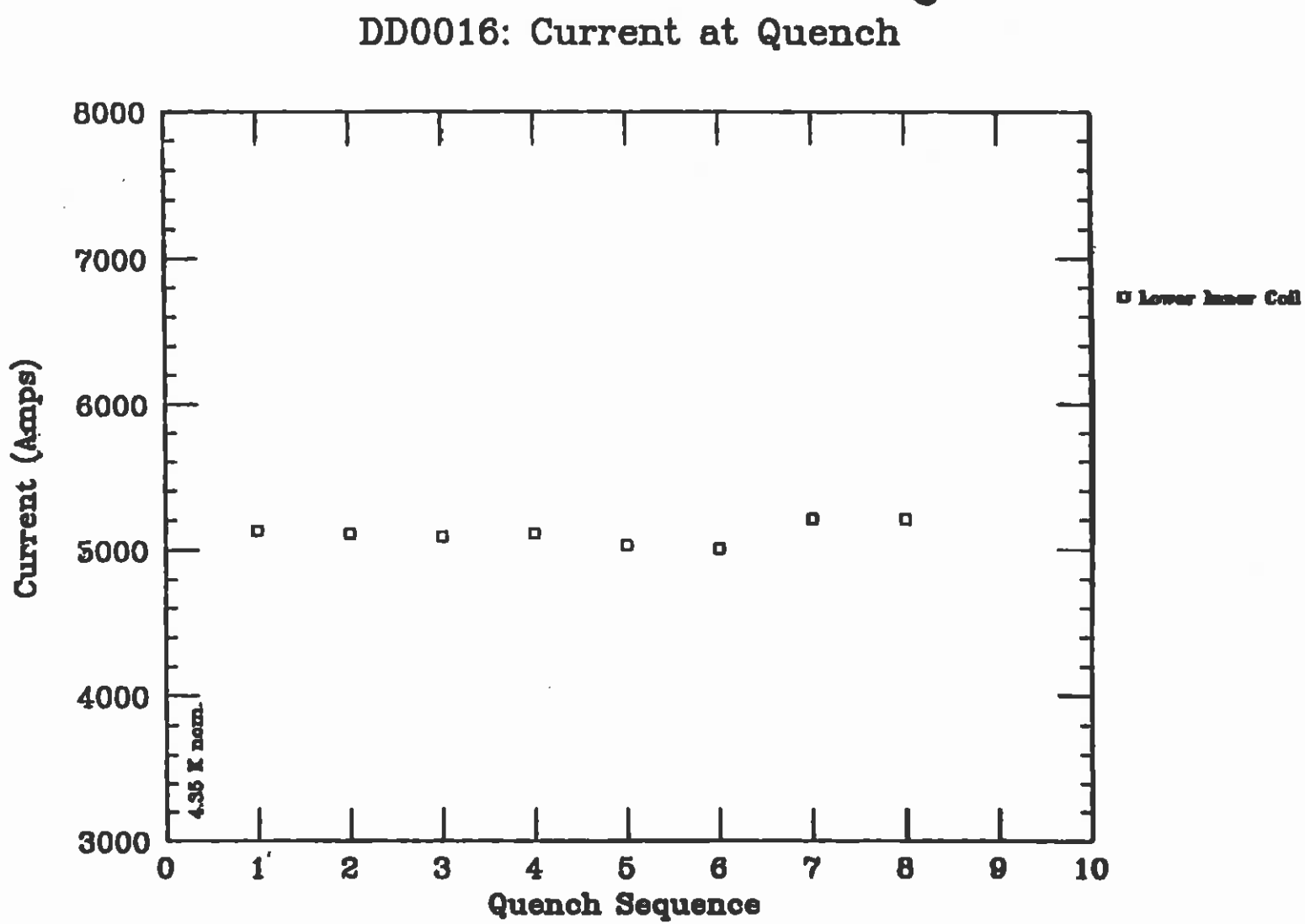

ACCURACY OF SHORT SAMPLE CURRENT LIMIT ESTIMATIONS

– One question that arises is how reliable are the short sample current limit estimations.

– As we have seen, these estimations are usually based on critical current measurements on a well cooled short sample which may or may not be representative of the full length of cable in the magnet coil environment.

– Furthermore, and as explained in the section on transition of multifilamentary wires, the critical current is defined by relying on empirical criterions which may be suited for some applications but may turn out to be inadequate for some other.

– One way of answering this question is to compare short sample current limit estimations with actual plateau quench currents achieved in real magnets.

Data from a series of 5-cm-aperture, 15-m-long SSC dipole magnet prototypes tested at 4.35 K, 3.8 K and 3.5 K show that short sample estimations are fairly reliable.

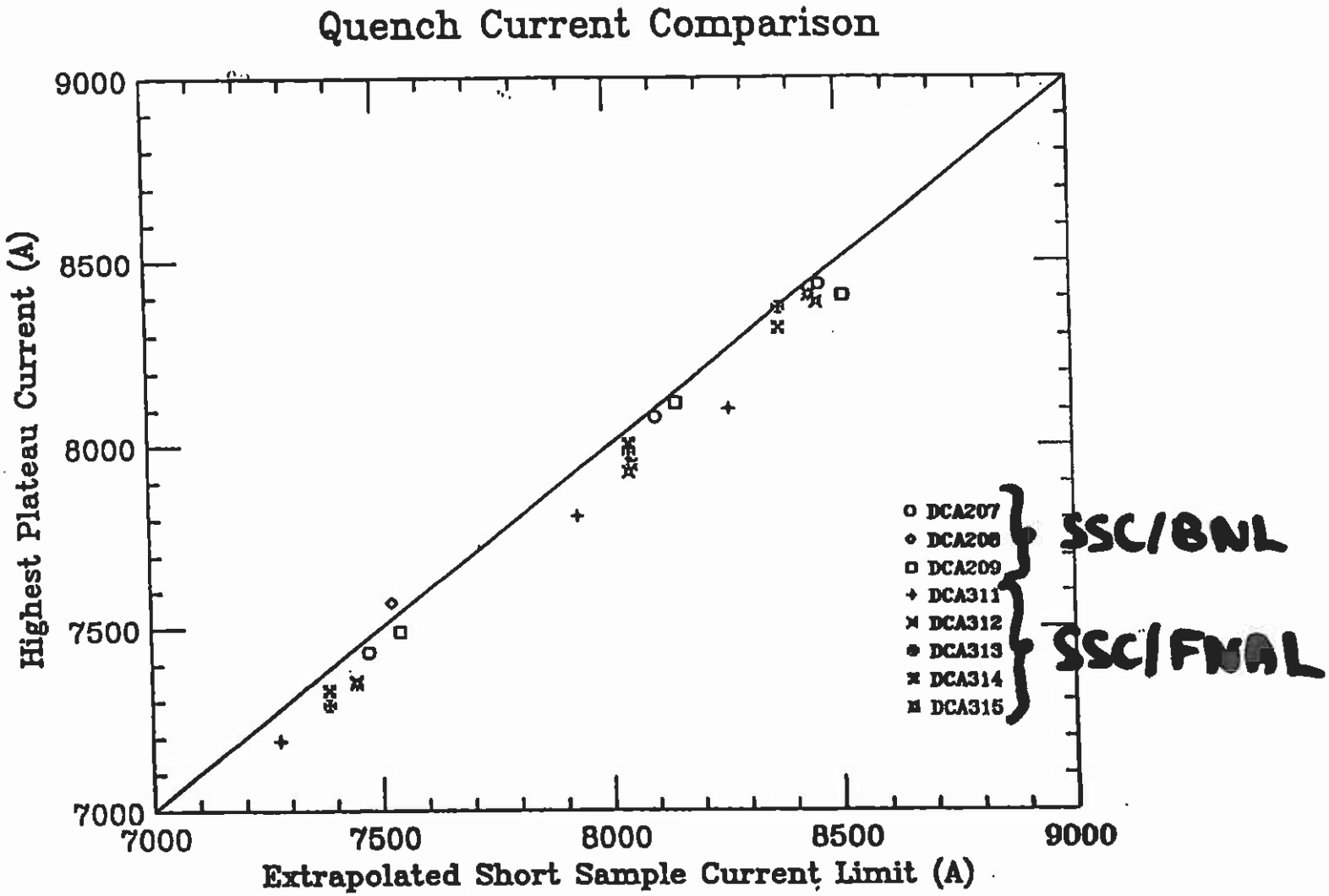
Quench Current Comparison
Highest Plateau Current (A)
Extrapolated Short Sample Current Limit (A)
9000
8500
8000
7500
7000
7000
7500
8000
8500
9000
DCA207
DCA208
DCA209
DCA311
DCA312
DCA313
DCA314
DCA315
SSC/BNL
SSC/FNAL

LECTURE 8: QUENCH PERFORMANCE OF PARTICLE ACCELERATOR MAGNETS

8.1 Temperature and Enthalpy Margins

8.2 Magnet Cooling

8.3 What is a quench?

8.4 Magnet Training and Quench Plateau

8.5 Quench Origins

8.6 Phenomenological Model of Mechanical Training

8.7 Improving Quench Performance

8.8 Quench Performance as a Function of Ramp Rate

8.9 Specifications on Quench Performance

QUENCH ORIGINS

– As we have seen, quenches originate because of a crossing of the superconductor critical surface somewhere in the magnet coil.

– This crossing occurs either along the "peak magnetic flux density versus transport current density" line or along the temperature axis.

CROSSING THE CRITICAL SURFACE ALONG THE "PEAK FIELD VERSUS TRANSPORT CURRENT DENSITY" LINE

– The maximum quench current at a given temperature is estimated using a parametrization of the superconductor critical surface and assuming an average value of J_C at 4.2 K and 5 T over the magnet coil.

The average J_C is usually determined from measurements on a cable short sample.

– Nevertheless, it can happen that the crossing of the critical surface along the peak field line occur at an overall cable current that is below the expected I_{qm} or I_{ss}.

Such quenches have at least two origins:

• *A local cable degradation,* which results in a local decrease of the critical current and of the critical current density,

• *A large current imbalance* among the cable strands, which results in a strand carrying much more current than average and hitting the critical surface ahead of the others.

CROSSING THE CRITICAL SURFACE ALONG THE "PEAK FIELD VERSUS TRANSPORT CURRENT DENSITY" LINE (CONT.)

– Quenches due to a local cable degradation are of the same nature as quenches occurring at the short-sample limit and they can all be identified as *conductor-limited* quenches.

– Quenches due to large current imbalance are more likely to occur at high ramp rates and are discussed in the section on quench performance versus ramp rate.

CROSSING THE CRITICAL SURFACE CONSECUTIVELY TO A TEMPERATURE RISE

– The temperature rises which initiate quenches result from energy depositions on the magnet coil.

– These energy depositions have at least three origins:

• *Mechanical disturbances,* such as stress relief or frictional motion under the Lorentz force,

• *Synchrotron radiation or beam losses,*

• *Power dissipation from interstrand coupling currents.*

– Quenches of the first origin are referred to as *mechanically-induced* quenches and reveal flaws in the mechanical design or in the assembly procedures which must be analyzed and corrected.

– The effects of synchrotron radiation or beam losses can be reduced by implementing an intercepting screen within the beam tube.

– Coupling losses are only of concern for fast current cycles.

DISCRIMINATING BETWEEN CONDUCTOR-LIMITED AND MECHANICALLY-INDUCED QUENCHES

– Conductor-limited quenches correspond to a crossing of the critical surface along the peak magnetic flux density line.

When changing the operating temperature from T_0 to $(T_0 + \Delta T_0)$, the quench current should follow the superconductor critical surface and vary from $I_q(T_0)$ to $I_q(T_0+\Delta T_0)$.

Hence, the currents of conductor-limited quenches are expected to exhibit a strong correlation with temperature.

– Conversely, the energy depositions resulting from mechanical disturbances should mainly depend on the Lorentz force level and should be relatively insensitive to small temperature variations.

Hence the currents of mechanically-induced quenches are not expected to be strongly related to magnet temperature.

– Thus a practical method for discriminating between conductor-limited quenches and mechanically-induced quenches is to vary the operating temperature of the magnet slightly — for example, to increase it and then decrease it by 50 mK — and to see if the quench current follows the change or not.

EXAMPLES OF DISCRIMINATION

– 4-cm-aperture, 17-m-long SSC dipole magnet prototype DD0017 exhibited a few training quenches before reaching a plateau corresponding to its expected short sample limit.

The training quenches appear mechanically induced while the plateau quenches are conductor limited.

– 4-cm-aperture, 17-m-long SSC dipole magnet prototype DD0010 quenched erratically without reaching a stable plateau.

All quenches appear mechanically induced.

– 4-cm-aperture, 17-m-long SSC dipole magnet prototype DD0016 reached a plateau well bellow its expected short sample limit.

The quenches appear conductor-limited.

(Upon disassembly of this magnet it was found that the area where the quenches originated corresponded to a cable lead which should have been cut prior to winding and where all the strands had a coldweld.)

SSC/BNL 4-cm-Aperl., 17-m-long Dipole

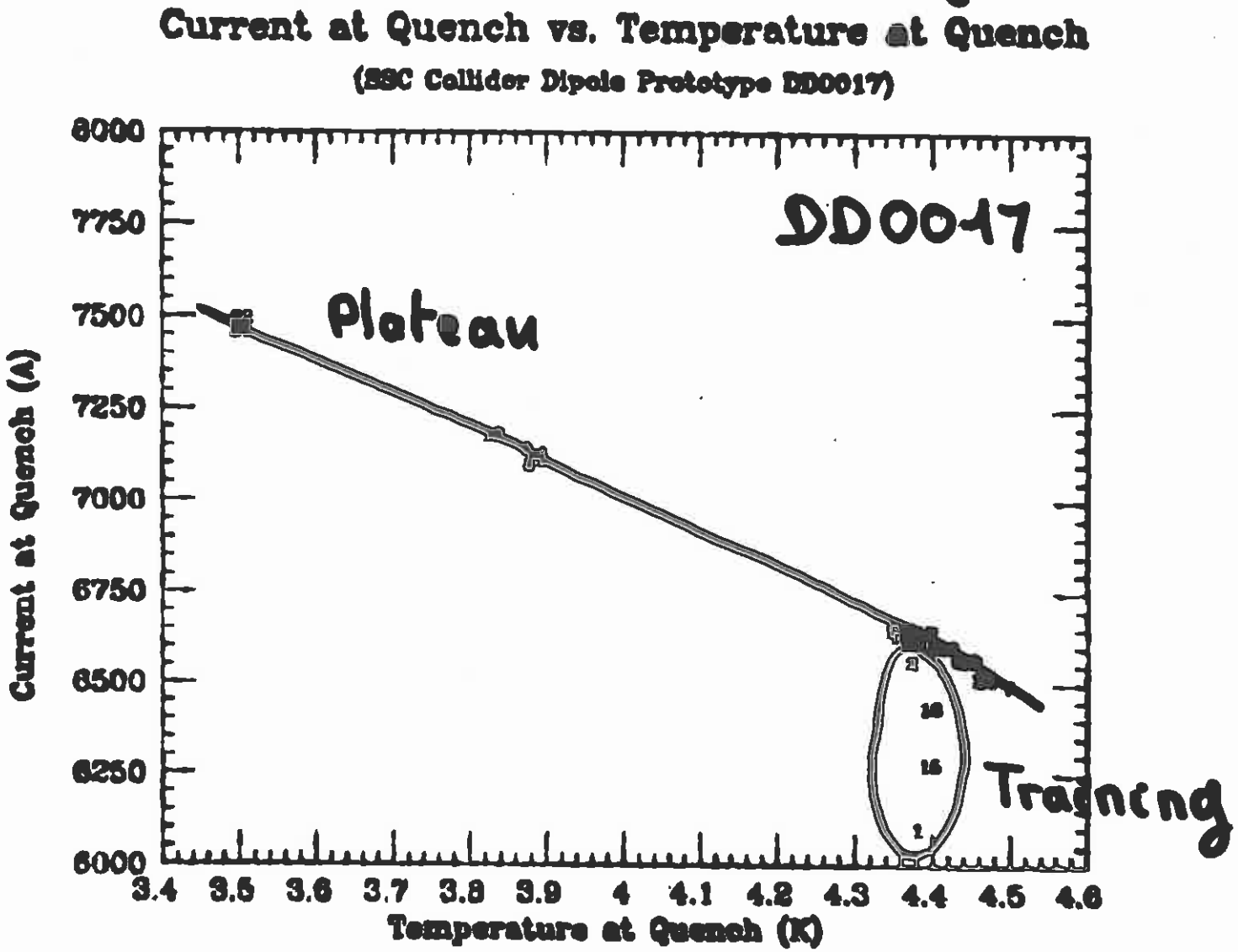

SSC/BNL 4-cm-Apert., 17-m-long Dipole

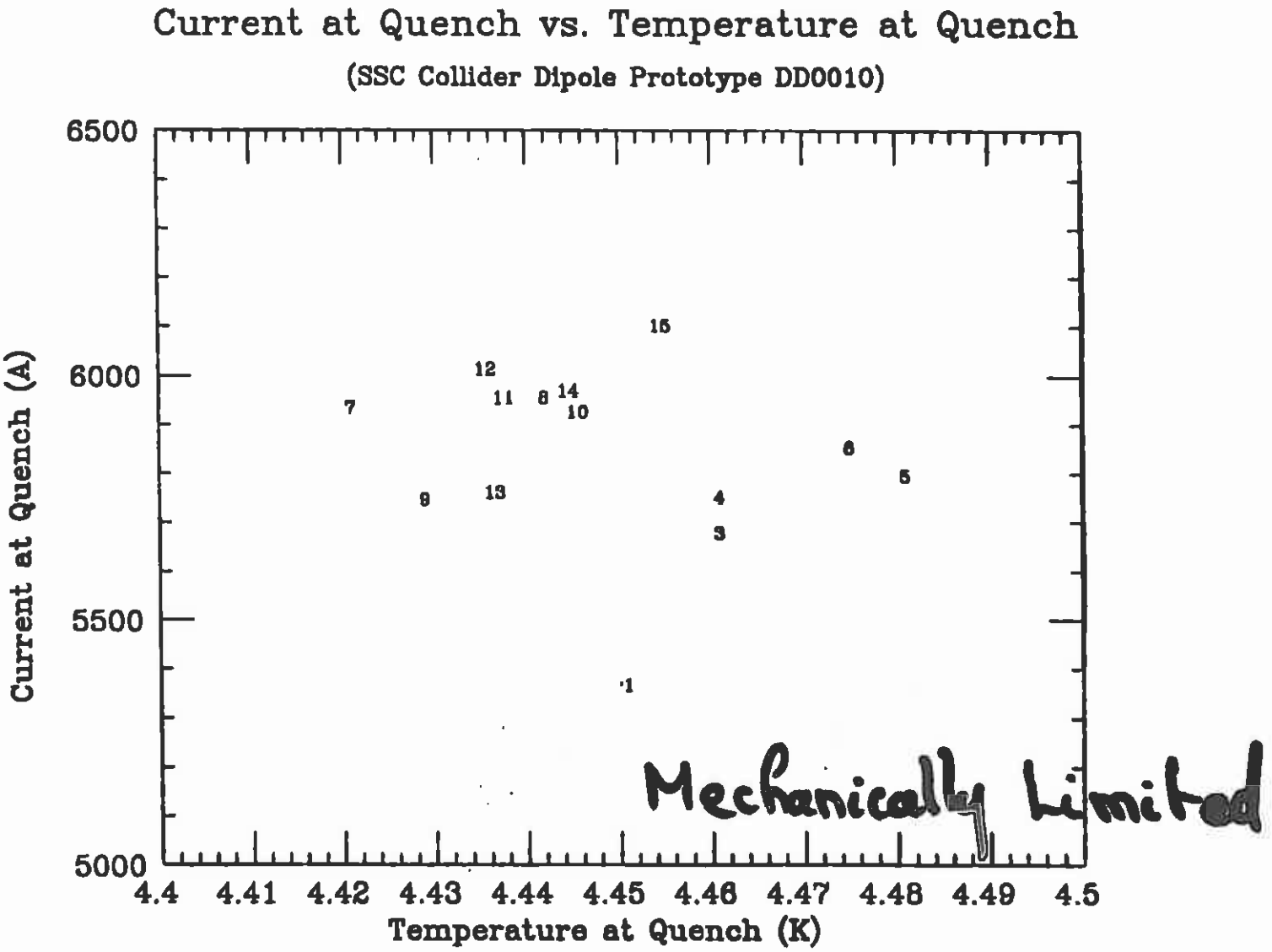

SSC/BNL 4-in-Apert., 17-m-Long Dipole

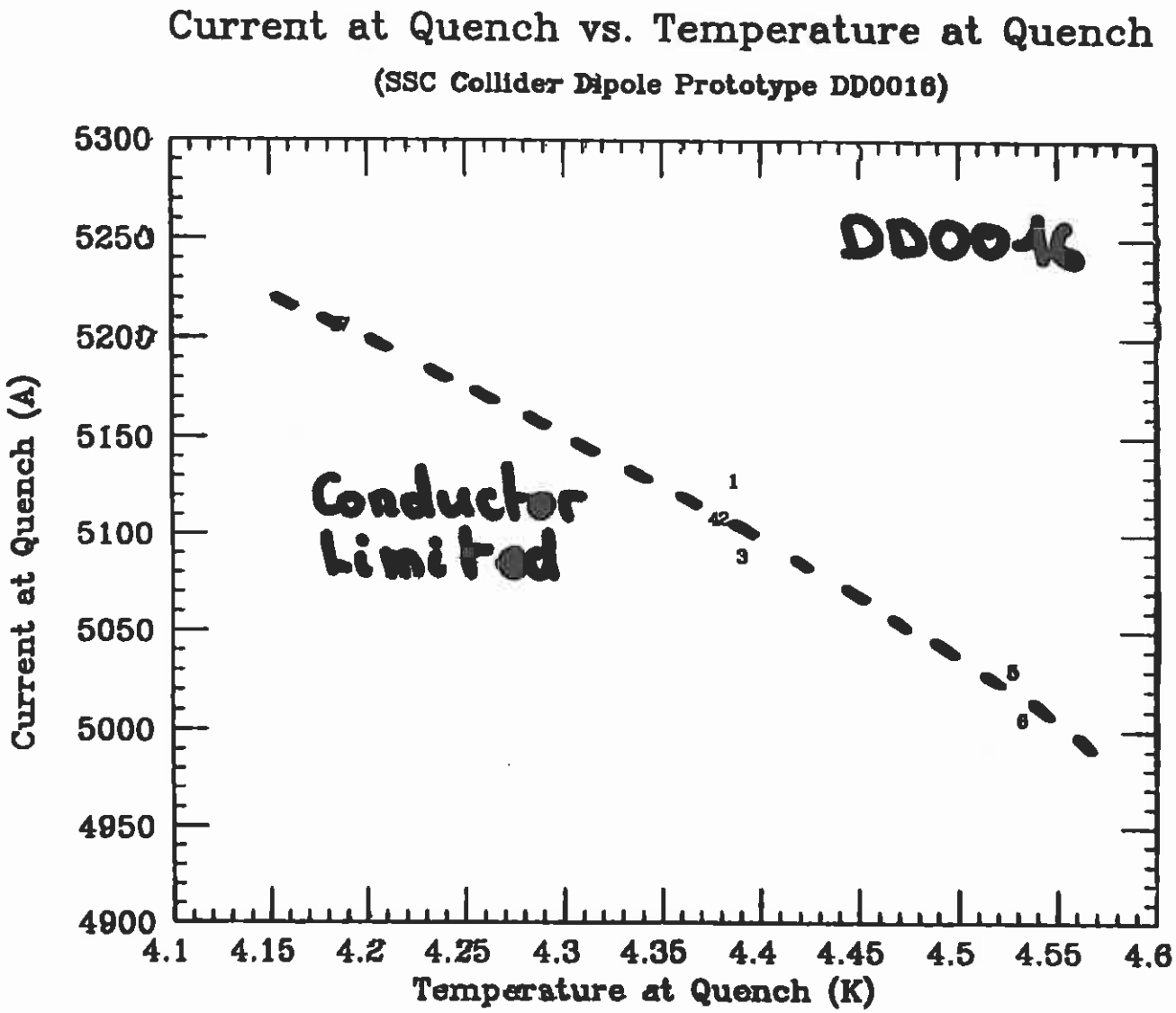

LECTURE 8: QUENCH PERFORMANCE OF PARTICLE ACCELERATOR MAGNETS

8.1 Temperature and Enthalpy Margins

8.2 Magnet Cooling

8.3 What is a quench?

8.4 Magnet Training and Quench Plateau

8.5 Quench Origins

8.6 Phenomenological Model of Mechanical Training

8.7 Improving Quench Performance

8.8 Quench Performance as a Function of Ramp Rate

8.9 Specifications on Quench Performance

PHENOMENOLOGICAL EXPLANATION OF MECHANICAL TRAINING

– Among the various quench origins considered above, only the mechanical disturbances are likely to be affected by successive ramps to quench and lead to the kind of improvement in magnet performance referred to as training.

A phenomenological explanation of magnet training is as follows.

– When energizing a magnet, strong Lorentz forces are applied to the conductor strands which are transmitted to the coil support system through the insulation.

– In a geometry as complex as that of a dipole or a quadrupole coil assembly, there are many interfaces where the Lorentz forces have tangential components which are counteracted by friction.

– As the current is ramped up and the Lorentz forces increase, it can happen that, somewhere in the coil, a static-friction coefficient is exceeded.

Sliding then occurs, which results in heat dissipation and a local temperature rise.

If the local temperature rise is large enough, a quench is initiated.

PHENOMENOLOGICAL EXPLANATION OF MECHANICAL TRAINING (CONT.)

– In the case of a quench caused by a so-called *stick-slip motion* in the magnet assembly, the motion responsible for the quench and/or the thermal stresses developed in the magnet coil during the quench can improve the mechanical stability of the troubled interface.

As a result, upon subsequent energizations, the Lorentz forces are better supported in the previously troubled area and the same current level can be achieved without exceeding the local static-friction coefficient.

– Then, the current can be further ramped up until, somewhere else in the coil, another static-friction coefficient is exceeded, which, in turn, provokes a frictional motion large enough to initiate a quench — and so on.

– Quench after quench, the current can be ramped up to higher levels until it is reaches the maximum quench current.

– Of course, if the mechanical flaws at the origins of the disturbances are too large, the magnet cannot be trained and keeps quenching erratically.

LECTURE 8: QUENCH PERFORMANCE OF PARTICLE ACCELERATOR MAGNETS

8.1 Temperature and Enthalpy Margins

8.2 Magnet Cooling

8.3 What is a quench?

8.4 Magnet Training and Quench Plateau

8.5 Quench Origins

8.6 Phenomenological Model of Mechanical Training

8.7 Improving Quench Performance

8.8 Quench Performance as a Function of Ramp Rate

8.9 Specifications on Quench Performance

IMPROVING QUENCH PERFORMANCE

– As we have seen, low current quenches are usually due to local heat depositions resulting from mechanical disturbances.

– The main efforts to improve quench performance should therefore be aimed at reducing the spectrum of mechanical disturbances.

– Some efforts can also be devoted at understanding and, if possible, improving the magnet stability against thermal disturbances.

REDUCING SPECTRUM OF MECHANICAL DISTURBANCES

– An accelerator magnet is made up of a large number of small details which, given the reduced operating margin, can all influence the magnet behavior.

– Each of these details must be worked out and integrated into a coherent mechanical design and an optimized assembly process, relying on robust and easy-to-implement concepts and technologies.

– The fabrication must be carried out under a tight assurance quality plan and all discrepancies must be analysed and recorded.

– The design concepts and assembly processes must be validated before starting series production.

This validation can be done on a pre-series of fully instrumented magnet models and prototypes, subjected to extended test cycles.

MAGNET STABILITY

– The initiation of a quench can be divided into two phases:

• First, a local heat deposition raises the temperature of a small volume of conductor above the current sharing temperature,

• Second, the heat dissipated by the Joule effect in the small volume of conductor launches the propagation of a normal zone.

Quench Origin, part I: Frictional Heating of Conductor

$$\int_{T_o}^{T_{crit}} C\,dT = Q - \int \frac{P_{He}}{A}\,dt$$

Conductor Heating — Disturbance — Helium Cooling

Quench Origin, part II
Developing a Quench

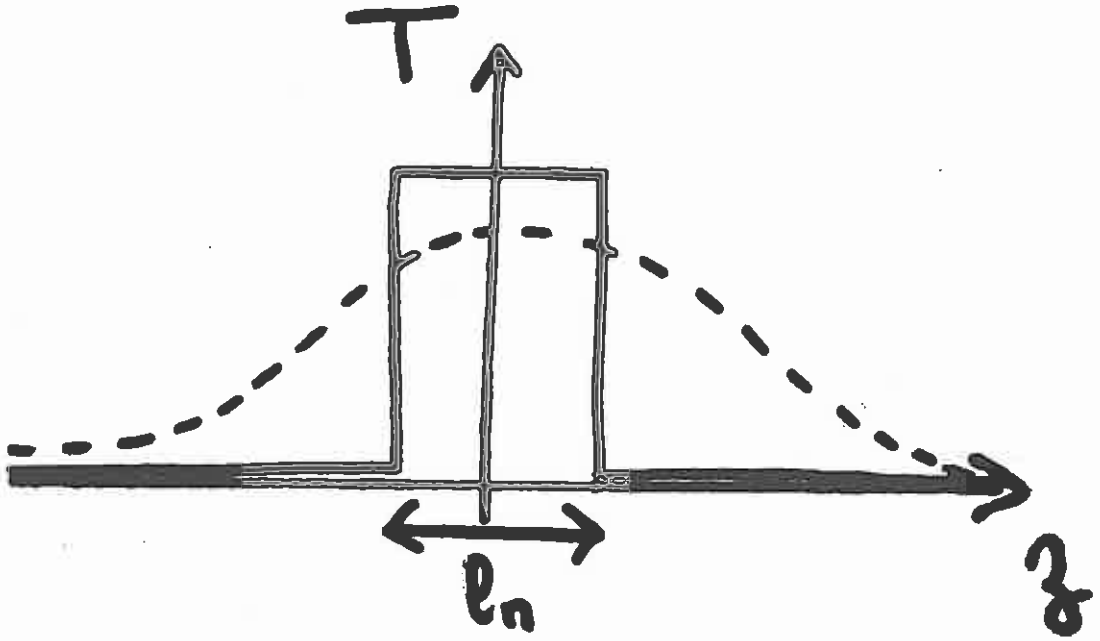

$$C\frac{\partial T}{\partial t} = \underbrace{\rho_J}_{\text{Joule Heating}} + \underbrace{k\frac{\partial^2 T}{\partial z^2}}_{\text{Heat Conduction}} - \underbrace{P_{He}}_{\text{Helium Cooling}}$$

$l_n >$ minimum (MPZ)

Quench Origin, ~~Part~~ I:
~~Frictional~~ Heating of Conductor
Improving Quench Performance

$$\int_{T_o}^{T_{crit}} C\,dT = Q - \int \frac{P_{He}}{A}\,dt$$

Larger Enthalpy Margin — Better Cooling

- Lower Operating Tuire ($T_o \downarrow$)
- Lower J_{NbTi} ($T_{crit} \uparrow$)
  - ↳ Lower copper to superconductor ratio

Quench Origin, Part II

~~Developing a Quench~~ Improving Quench Performance

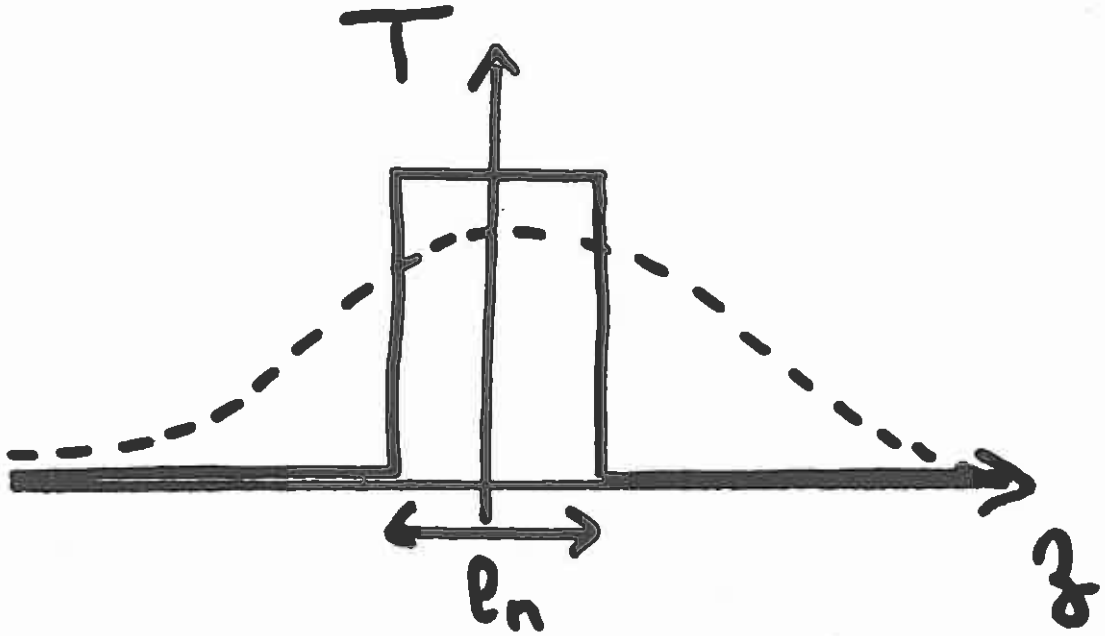

$$C\frac{\partial T}{\partial t} = \underbrace{P_J} + k\frac{\partial^2 T}{\partial z^2} - \underbrace{P_{He}}$$

Lower Joule heating — Better cooling

$\Rightarrow$ Lower J_{cu}

↳ Higher copper to superconductor ratio

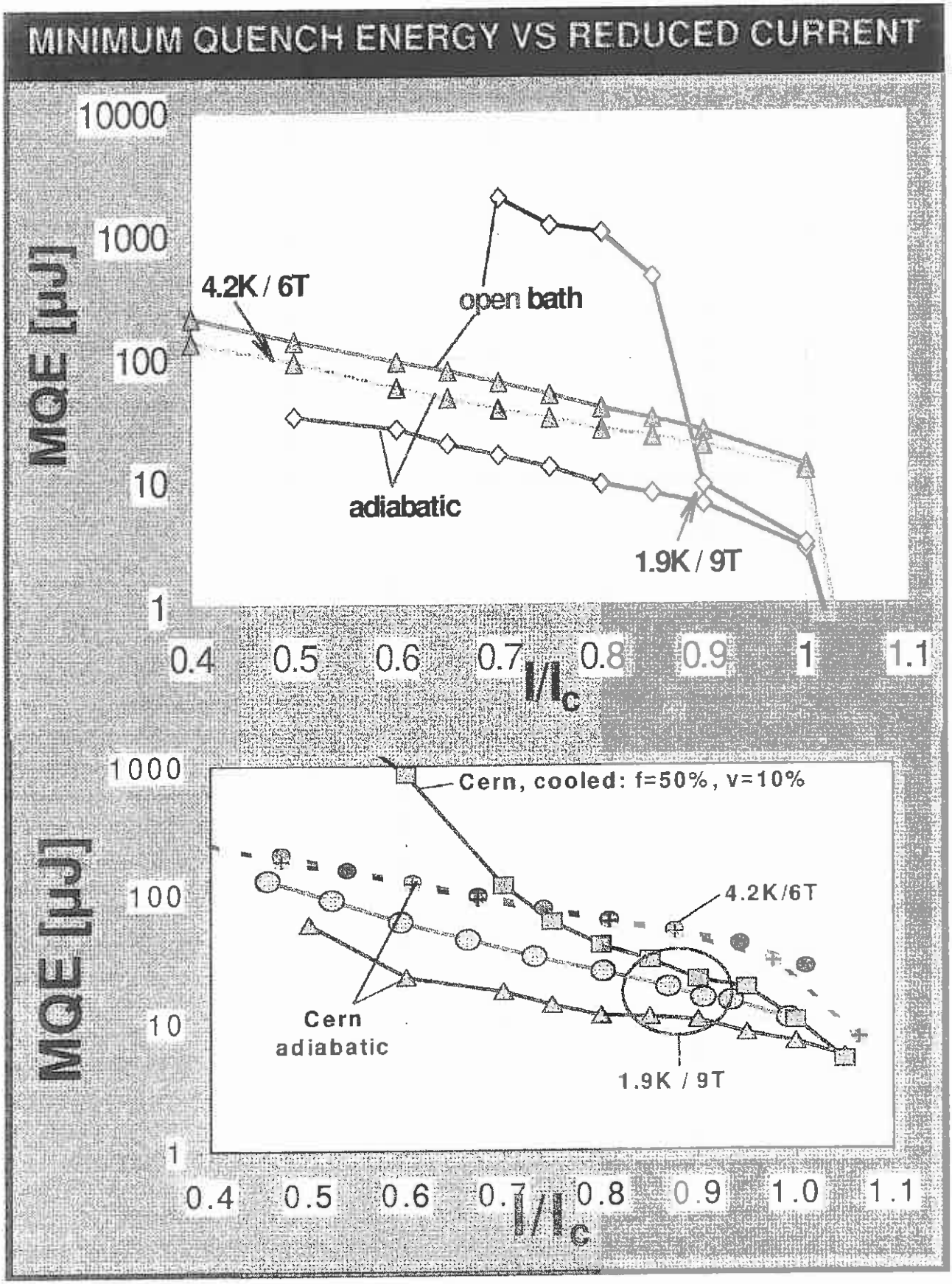

Courtesy P. Bauer

Courtesy P. Bauer

Courtesy P. Bauer

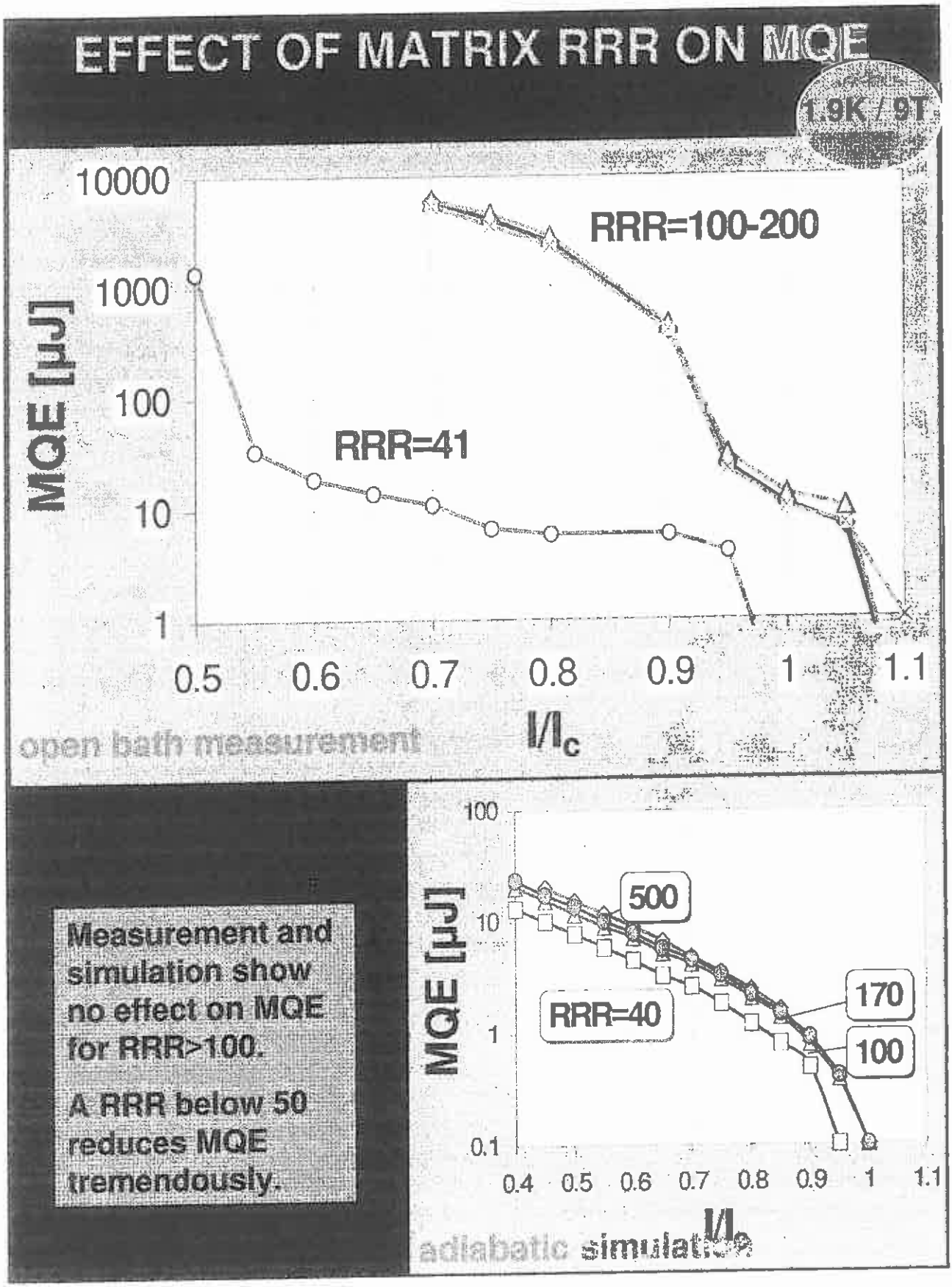

Courtesy P. Bauer

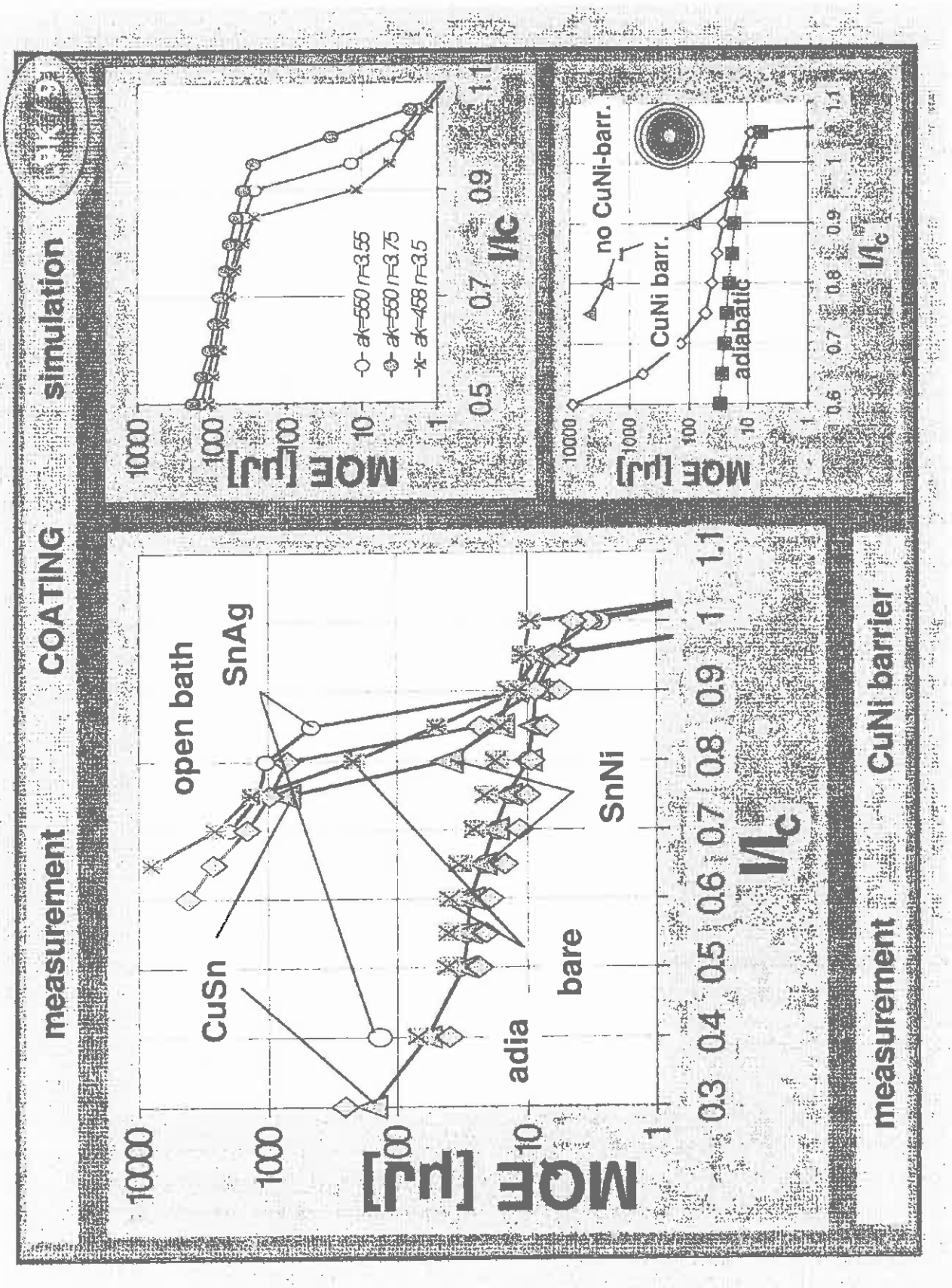

Courtesy P. Bauer

Fig 41 Global comparison of different cable types

Runs 3-1 and 7-1 Ext field = 7 T perpendicular Run 5-1 7.2T perpendicular
Run 8-3 Ext filed = 7 T par

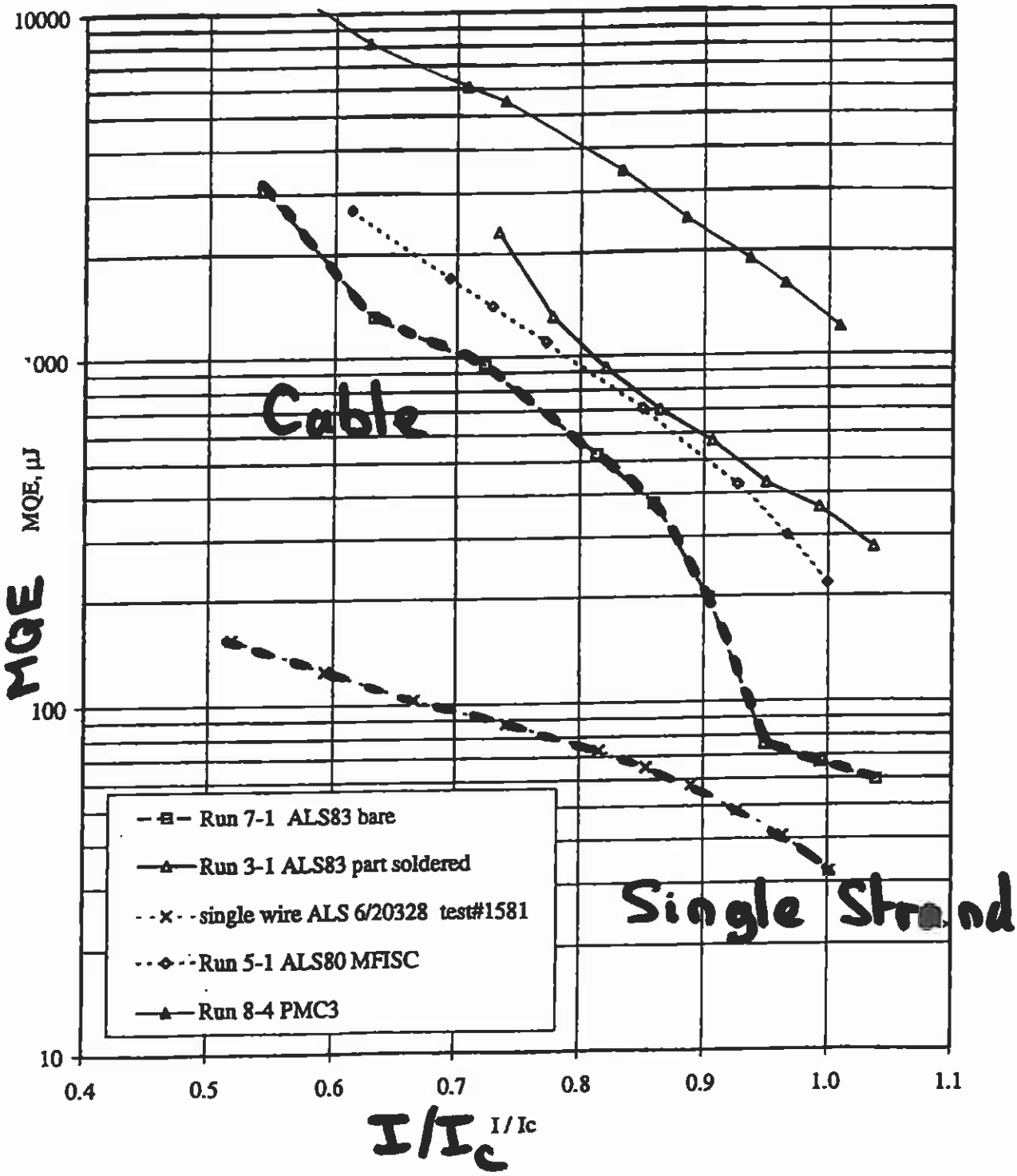

(Courtesy M.N. Wilson)

MAGNET CONDITIONING

– Let us consider a magnet designed to be operated at a temperature, T_0, where its short sample current limit is $I_{ss}(T_0)$, and which exhibits a few training quenches close to $I_{ss}(T_0)$.

– These training quenches are likely to be due to small mechanical disturbances, which produce large enough heat depositions to overcome the reduced enthalpy margin of the conductor.

– One can imagine, however, that, if the mechanical disturbances are small enough, a slight increase in enthalpy margin could be sufficient to absorb the deposited energy and avoid the occurence of a quench.

Such increase in temperature margin can be obtained by cooling down the magnet to a temperature $(T_0 - \Delta T_0)$.

– The idea then comes into mind, to, before operating the magnet at T_0, cool it down to $(T_0 - \Delta T_0)$ and cycle it a few times up to $I_{ss}(T_0)$.

These cycles up to a force level similar to the one achieved when operating the magnet to its limit at T_0 should help settling things down and eliminate the mechanical disturbances causing the last few training quenches.

– Such operating mode is caused *conditioning*.

EXAMPLES OF MAGNET CONDITIONING

– 4-cm-aperture, 15-m-long SSC dipole magnet prototype DD0028 was subjected to an extended test cycle which included several warm-ups to room temperature.

After half of the cool-downs, the magnet was first conditioned at 3.5 K before being quench-tested at 4.5 K, while after the other half, it was directly quench-tested at 4.5 K.

It turns out that, for each testing cycle starting with a conditioning, the magnet went right away to its short sample current limit, while for most of the testing cyles where the magnet was not conditioned, it exhibited a small number of training quenches.

Hence, for this prototype the conditioning did help eliminating the small mechanical disturbances at the origins of the few training quenches.

– Of course, if the mechanical disturbances are too large, the small increase in enthalpy margin gained by lowering the magnet temperature will not be of any use, as illustrated by the poorly behaving 5-cm-aperture, 1-m-long SSC dipole magnet model DSA333.

– Conditioning is only of interest for magnets operated at 4 to 5 K and can be made more efficient by going to superfluid helium.

SSC/BNL 4-cm-Apert., 17-m-long Dipole Magnet

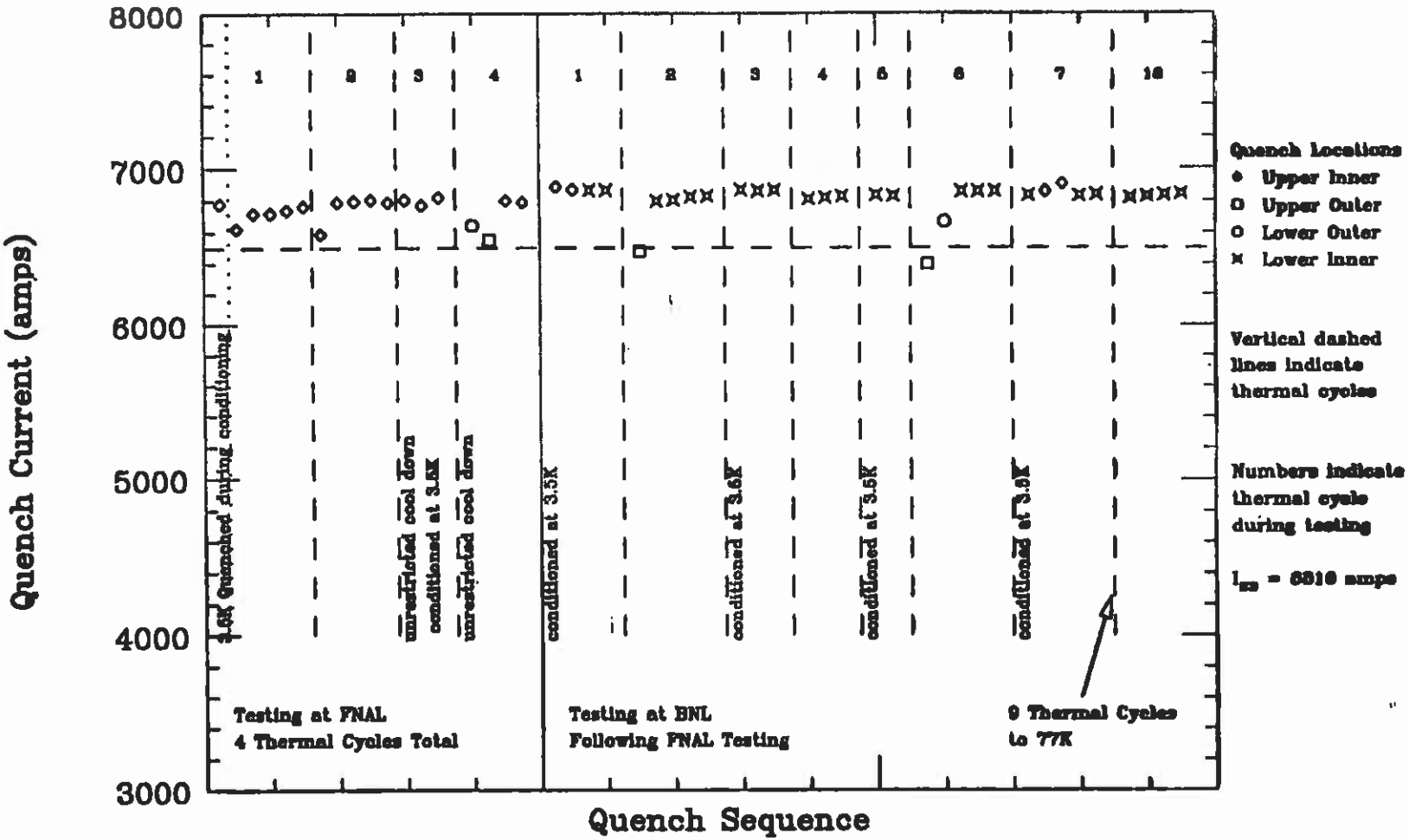

SSC/FNAL 5-cm-Apert., 1-m-long Dipole

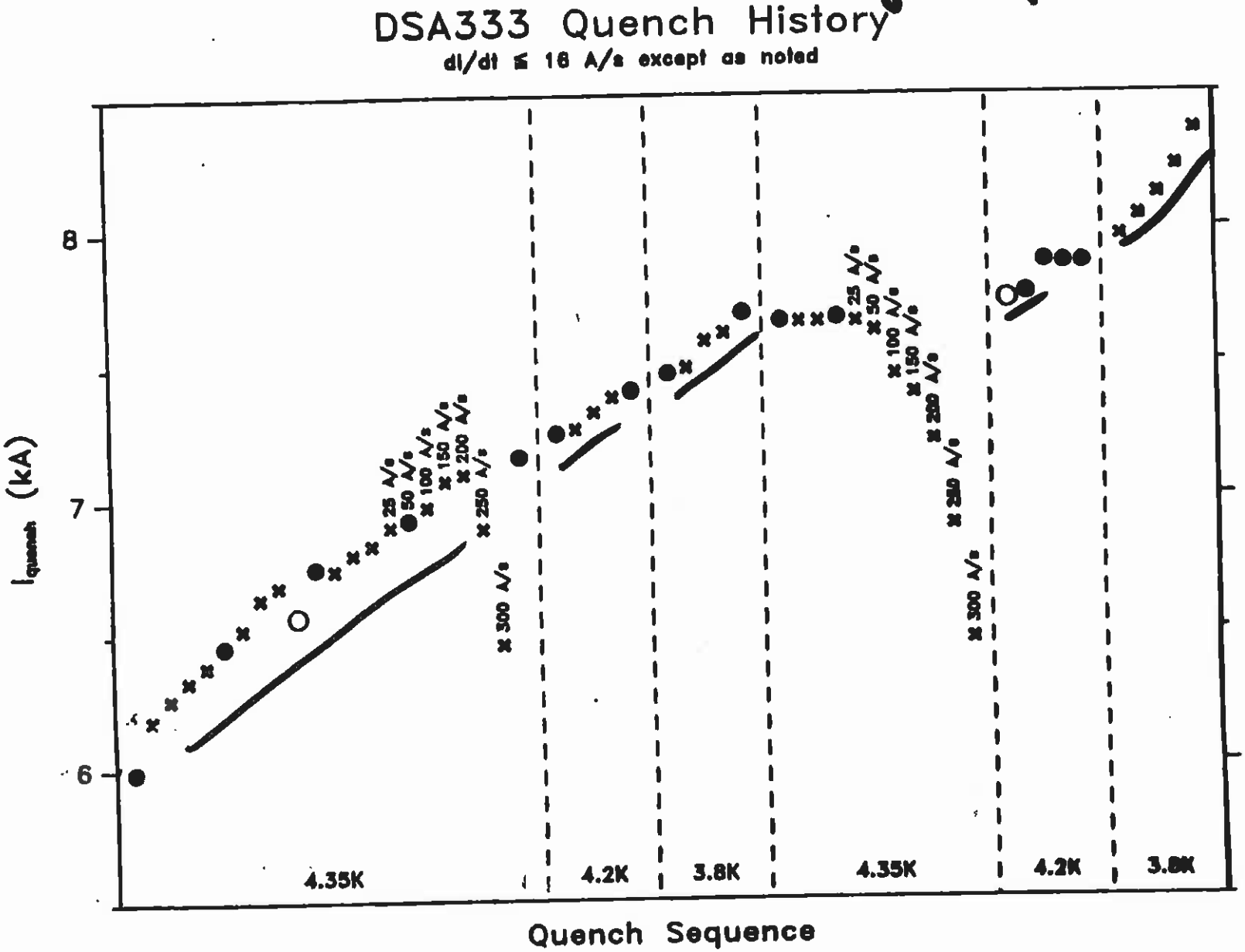

LECTURE 8: QUENCH PERFORMANCE OF PARTICLE ACCELERATOR MAGNETS

8.1 Temperature and Enthalpy Margins

8.2 Magnet Cooling

8.3 What is a quench?

8.4 Magnet Training and Quench Plateau

8.5 Quench Origins

8.6 Phenomenological Model of Mechanical Training

8.7 Improving Quench Performance

8.8 Quench Performance as a Function of Ramp Rate

8.9 Specifications on Quench Performance

QUENCH PERFORMANCE AS A FUNCTION OF RAMP RATE

– Let us consider an accelerator magnet which has been trained to a stable plateau. When subsequently performing ramps to quench at increasing ramp rates, at least two mechanisms are in competition to degrade the quench performance:

• *The generation of interstrand coupling currents,* which are superimposed to the transport current and dissipate power when crossing the interstrand resistances

• *The possible modification of the transport-current distribution among cable strands* which can result in the apparition of large current imbalances.

– The interstrand coupling currents, which have been described in a specific section, are expected to increase as a function of ramp rate, leading to a monotonic decrease of the quench current.

– Determining how the distribution of transport current among the cable strands is influenced by the ramp rate requires additional background informations.

TRANSPORT CURRENT DISTRIBUTION AS A FUNCTION OF RAMP RATE

– As we have seen, the Rutherford-type conductor used in superconducting particle accelerator magnets consists of a few tens of strands, twisted together, and shaped into a flat, two-layer, slightly keystoned cable.

Each cable strand is characterized by a voltage-current curve and a self-inductance.

Each strand pair is characterized by a mutual inductance.

Also, all the strands are coupled through the interstrand resistances and the splice resistances at the coil ends.

– During energization, the current distributes itself among the cable strands according to this intricate network of resistances and inductances.

At low ramp rate, the current distribution is mainly determined by the resistive elements of the circuit.

However, as the ramp rate is increased, the inductive elements start to play a role, and end up being the dominant elements at large ramp rate.

TRANSPORT CURRENT DISTRIBUTION AS A FUNCTION OF RAMP RATE (CONT.)

– If the strands are identical and interchangeable, they all carry the same current, and changing the ramp rate is not expected to have any influence.

– However, if for one reason or another, the strands are not identical or are not interchangeable, the static and dynamic current distributions can be different.

Then, as the ramp rate is increased, the current distribution changes from one to the other, resulting in a quench current evolving between two asymptotic values:

- *One for ramp rates tending towards zero,*

- *One for large ramp rates.*

– This implies that, unlike in the case of interstrand coupling currents, the quench current degradation arising from transport current imbalances is expected to flatten out at large ramp rates.

TYPE A AND TYPE B BEHAVIORS

– The ramp rate behavior of the 5-cm-aperture, 15-m-long SSC dipole magnet prototypes can be classified into two main categories (which correspond to the manufacturer and the production batch of the inner cable strands).

– For the magnets of the first category, referred to as *type A*, the quench current remains roughly constant for ramp rates up to 25 A/s, above which it starts to decrease linearly as a function of ramp rate.

The worst case is magnet DCA312, which, at 200 A/s, quenches at 2180 A, corresponding to about 30% of its initial quench current.

– For the magnets of the second category, referred to as *type B*, the quench current starts by dropping significantly at low ramp rates, while the degradation is much milder at large ramp rates.

The worst case is magnet DCA319, for which the quench current decreases from 7334 A at 1 A/s to 6156 A/s at 25 A/s, but is still of the order of 5000 A at 250 A/s.

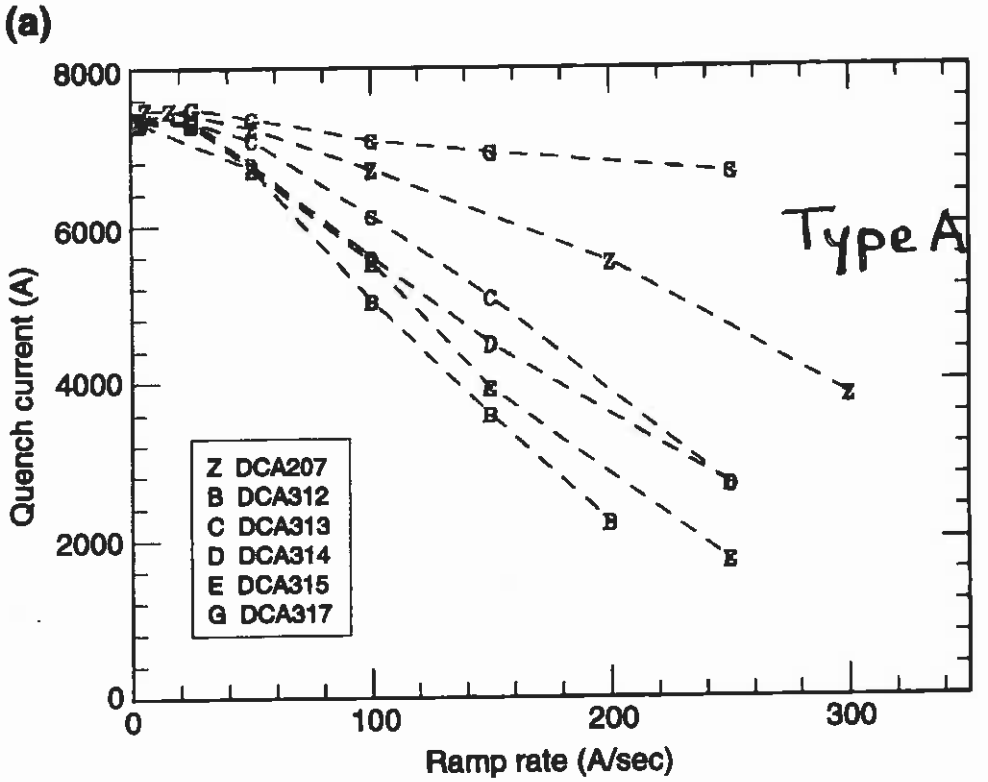
(a)
Quench current (A)
Ramp rate (A/sec)
Type A
Z DCA207
B DCA312
C DCA313
D DCA314
E DCA315
G DCA317

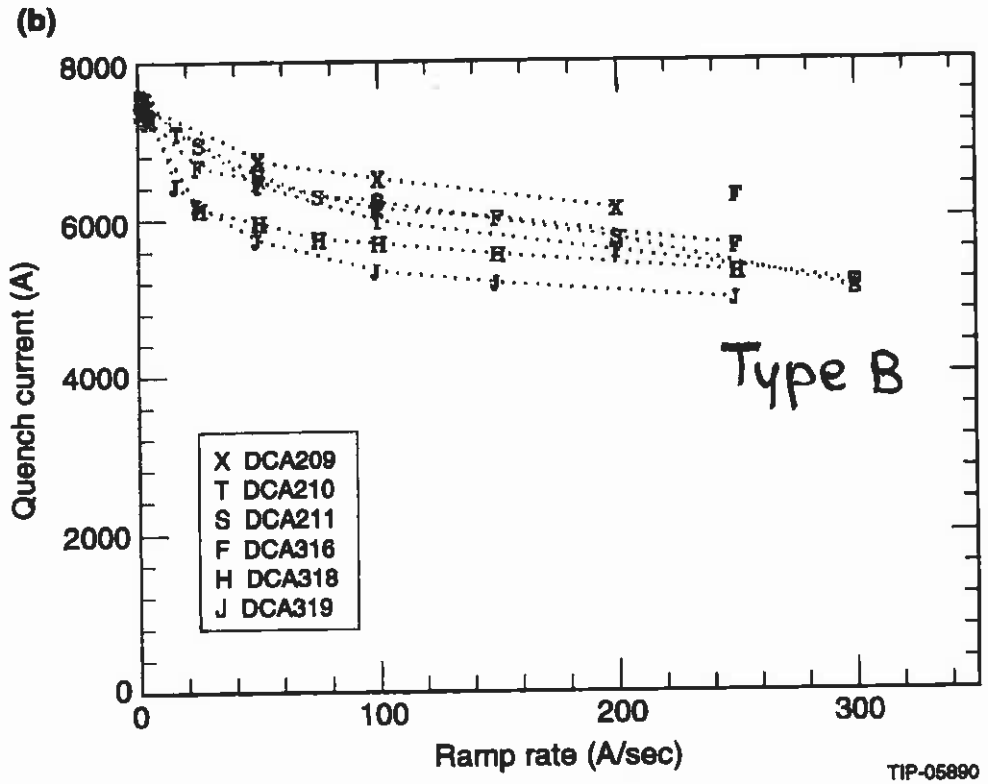
(b)
Quench current (A)
Ramp rate (A/sec)
Type B
X DCA209
T DCA210
S DCA211
F DCA316
H DCA318
J DCA319
TIP-05890

RAMP RATE SENSITIVITY OF MULTIPOLE COEFFICIENTS

– The multipole coefficients of the type-A magnets show a strong sensitivity to the ramp rate, while those of the type-B magnets seem little affected.

Examples: Magnetic measurement data from type-A magnet DCA312 and from type-B magnet DCA318.

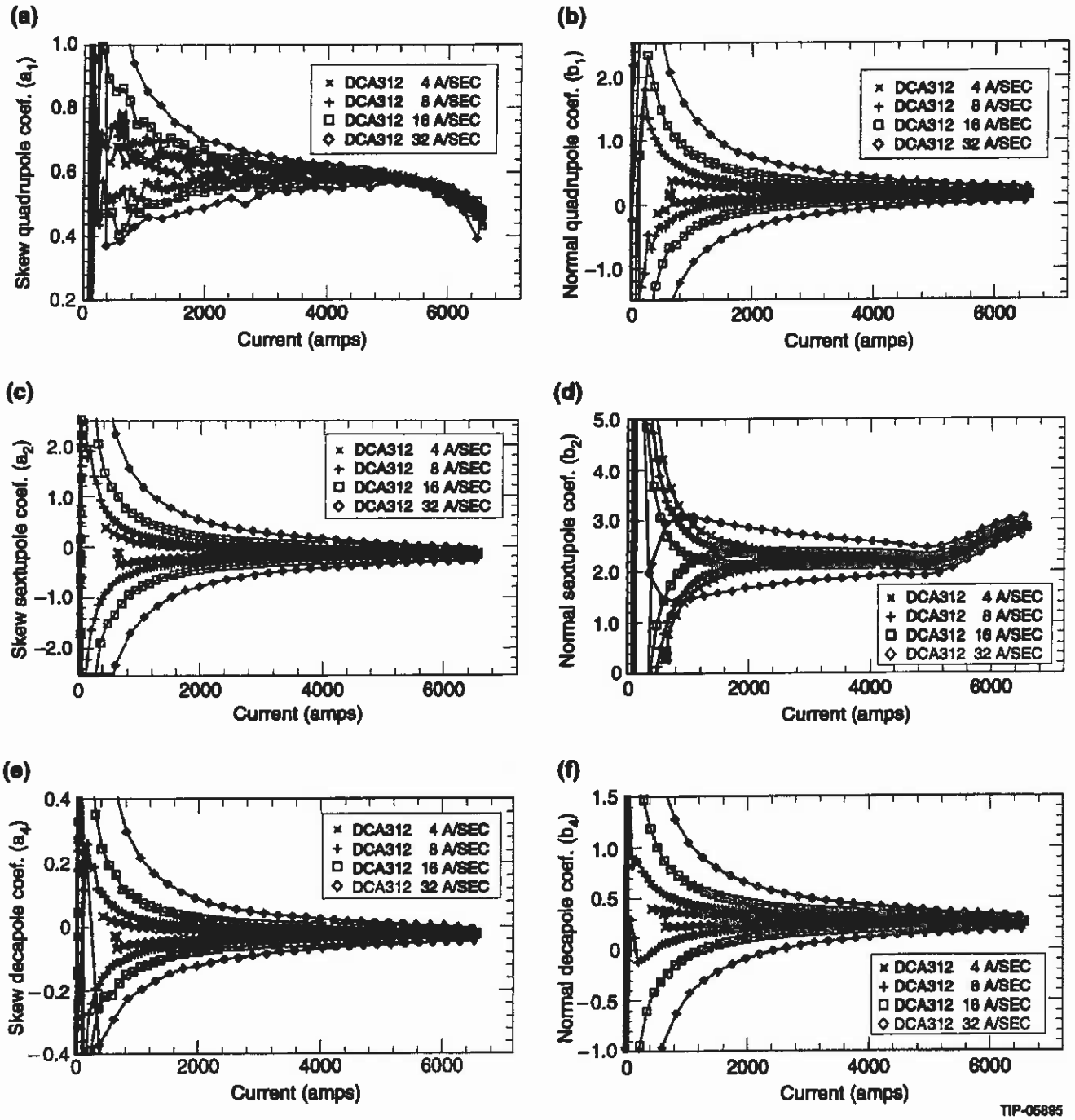
(a)
Skew quadrupole coef. (a_1)
1.0
0.8
0.6
0.4
0.2
0
2000
4000
6000
Current (amps)
× DCA312 4 A/SEC
+ DCA312 8 A/SEC
□ DCA312 16 A/SEC
◇ DCA312 32 A/SEC
(b)
Normal quadrupole coef. (b_1)
2.0
1.0
0
−1.0
0
2000
4000
6000
Current (amps)
× DCA312 4 A/SEC
+ DCA312 8 A/SEC
□ DCA312 16 A/SEC
◇ DCA312 32 A/SEC
(c)
Skew sextupole coef. (a_2)
2.0
1.0
0
−1.0
−2.0
0
2000
4000
6000
Current (amps)
× DCA312 4 A/SEC
+ DCA312 8 A/SEC
□ DCA312 16 A/SEC
◇ DCA312 32 A/SEC
(d)
Normal sextupole coef. (b_2)
5.0
4.0
3.0
2.0
1.0
0
0
2000
4000
6000
Current (amps)
× DCA312 4 A/SEC
+ DCA312 8 A/SEC
□ DCA312 16 A/SEC
◇ DCA312 32 A/SEC
(e)
Skew decapole coef. (a_4)
0.4
0.2
0
−0.2
−0.4
0
2000
4000
6000
Current (amps)
× DCA312 4 A/SEC
+ DCA312 8 A/SEC
□ DCA312 16 A/SEC
◇ DCA312 32 A/SEC
(f)
Normal decapole coef. (b_4)
1.5
1.0
0.5
0
−0.5
−1.0
0
2000
4000
6000
Current (amps)
× DCA312 4 A/SEC
+ DCA312 8 A/SEC
□ DCA312 16 A/SEC
◇ DCA312 32 A/SEC
TIP-05895

Type A

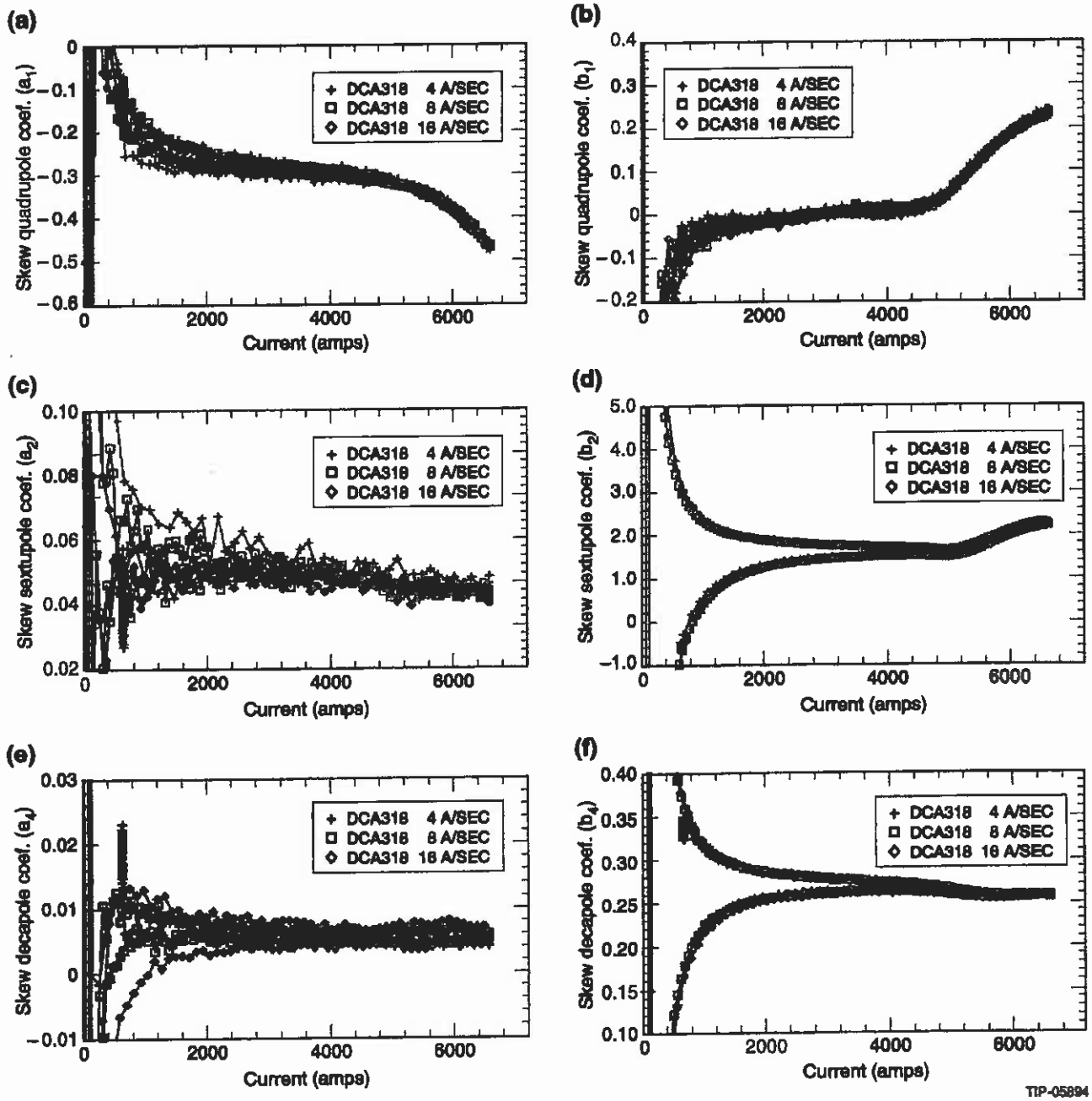
(a)
Skew quadrupole coef. (a_1)
0
−0.1
−0.2
−0.3
−0.4
−0.5
−0.6
0
2000
4000
6000
Current (amps)
+ DCA318 4 A/SEC
□ DCA318 8 A/SEC
◇ DCA318 16 A/SEC
(b)
Skew quadrupole coef. (b_1)
0.4
0.3
0.2
0.1
0
−0.1
−0.2
0
2000
4000
6000
Current (amps)
+ DCA318 4 A/SEC
□ DCA318 8 A/SEC
◇ DCA318 16 A/SEC
(c)
Skew sextupole coef. (a_2)
0.10
0.08
0.06
0.04
0.02
0
2000
4000
6000
Current (amps)
+ DCA318 4 A/SEC
□ DCA318 8 A/SEC
◇ DCA318 16 A/SEC
(d)
Skew sextupole coef. (b_2)
5.0
4.0
3.0
2.0
1.0
0
−1.0
0
2000
4000
6000
Current (amps)
+ DCA318 4 A/SEC
□ DCA318 8 A/SEC
◇ DCA318 16 A/SEC
(e)
Skew decapole coef. (a_4)
0.03
0.02
0.01
0
−0.01
0
2000
4000
6000
Current (amps)
+ DCA318 4 A/SEC
□ DCA318 8 A/SEC
◇ DCA318 16 A/SEC
(f)
Skew decapole coef. (b_4)
0.40
0.35
0.30
0.25
0.20
0.15
0.10
0
2000
4000
6000
Current (amps)
+ DCA318 4 A/SEC
□ DCA318 8 A/SEC
◇ DCA318 16 A/SEC
TIP-05894

Type B

ENERGY LOSS MEASUREMENTS

– Superconducting magnets do not ordinarily dissipate energy when supplied with a constant current.

– However, a number of dissipative mechanisms are known to occur when the current is cycled. Among them are:

• losses due the *persistent magnetization currents* generated in the superconductor,

• losses due to the *magnetization of the iron yoke,*

• losses due to *intrastrand and interstrand coupling currents.*

– For a given current cycle, the energy dissipated by the persistent magnetization currents and by the iron yoke magnetization is expected to be constant, independent of the ramp rate.

– The power dissipated by the coupling currents is proportional to the square of the ramp rate.

Hence, for a given current cycle, the energy dissipated by the coupling currents is expected to increase linearly as a function of ramp rate.

– Measuring energy loss as a function of ramp rate thus provides a mean to assess the relative importance of coupling currents.

AC Loss DATA ACQUISTION

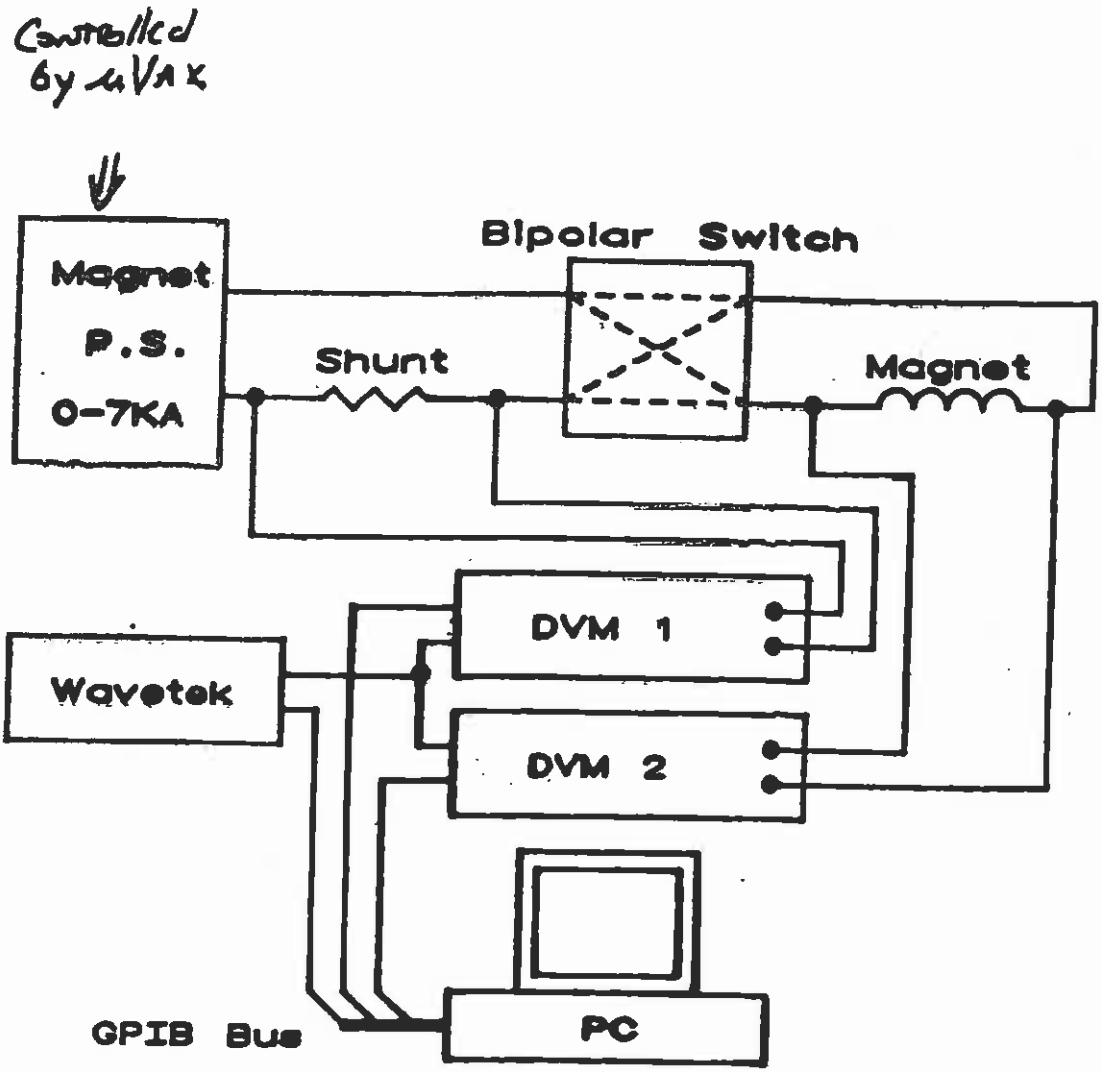

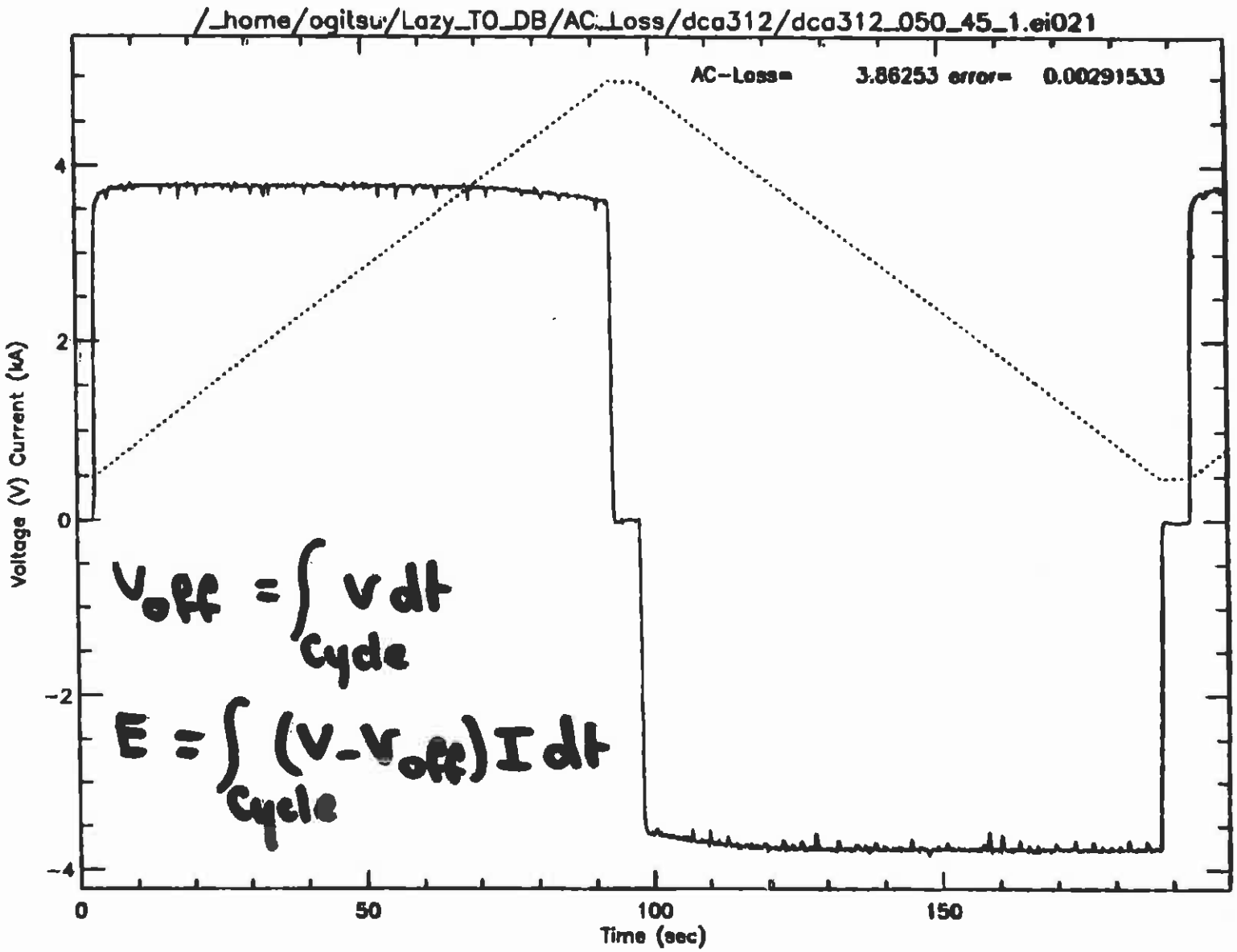
/_home/ogitsu/Lazy_TO_DB/AC_Loss/dca312/dca312_050_45_1.ei021
AC-Loss= 3.86253 error= 0.00291533
Voltage (V) Current (kA)
Time (sec)
4
2
0
-2
-4
0
50
100
150
$V_{off} = \int_{cycle} V\,dt$
$E = \int_{cycle} (V - V_{off}) I\,dt$

ENERGY LOSS MEASUREMENTS (CONT.)

– The energy losses per cycle measured as a function of ramp rate on the type-A magnets appear to increase linearly as a function of ramp rate, and, for most magnets, the slopes of the curves are rather large.

– In comparison, the energy losses per cycle measured on the type-B magnets are smaller and do not increase as rapidly as a function of ramp rate.

– The slopes of the "energy loss per cycle versus ramp rate" curves can be used to estimate an effective cable crossover resistance (assumed to be uniform througout the coils).

For most type-A magnets the estiamted effective crossover resistance is less than 10 μΩ, while for the type-B magnets it is above 80 μΩ.

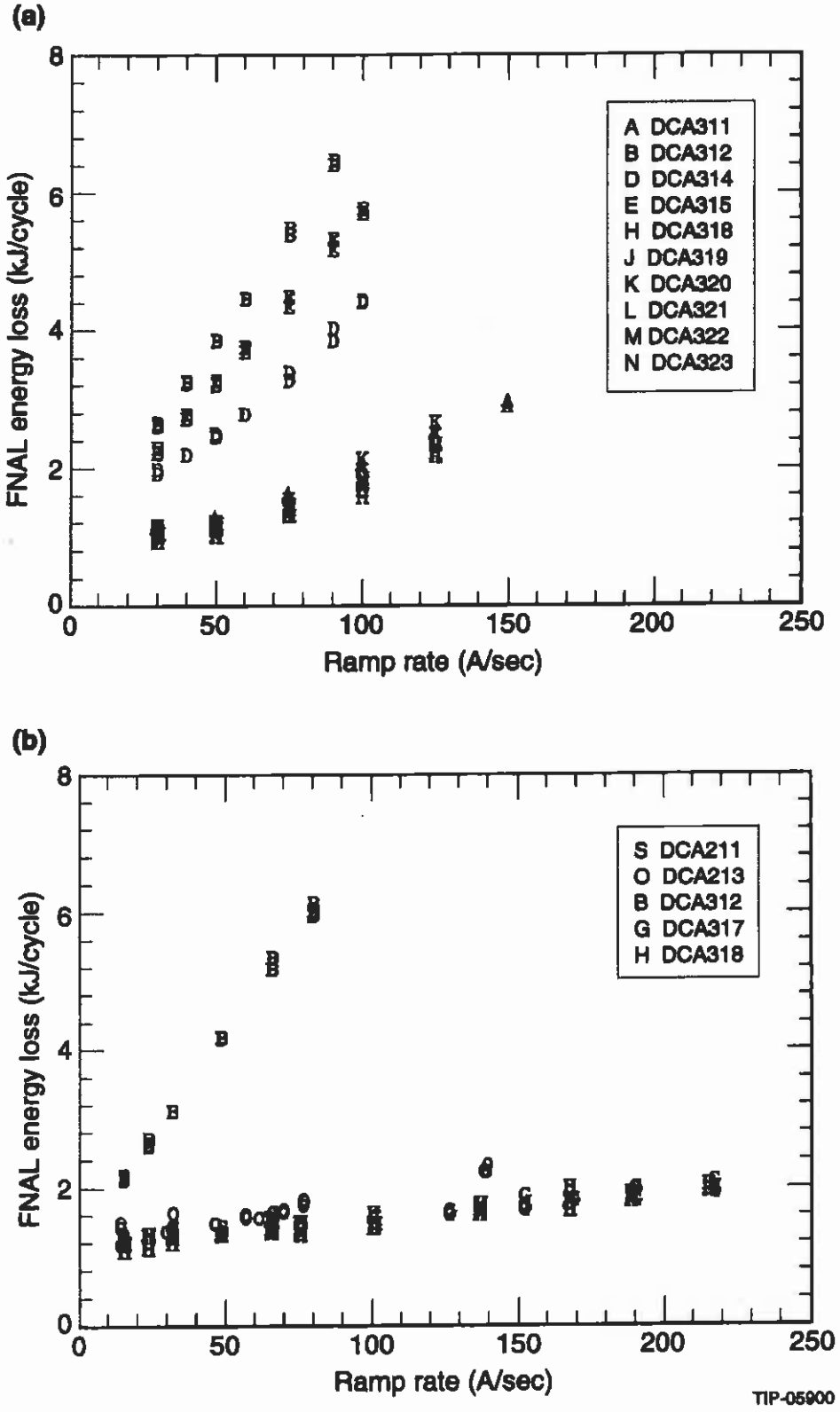
(a)
FNAL energy loss (kJ/cycle)
Ramp rate (A/sec)
A DCA311
B DCA312
D DCA314
E DCA315
H DCA318
J DCA319
K DCA320
L DCA321
M DCA322
N DCA323
(b)
FNAL energy loss (kJ/cycle)
Ramp rate (A/sec)
S DCA211
O DCA213
B DCA312
G DCA317
H DCA318
TIP-05900

FUNNY RAMPS

– Data from a type-B SSC dipole magnet prototype (magnet DCA318) show that the high ramp rate quench current depends on the magnet excitation history since the last quench.

14-JUNE-93
21:41:32

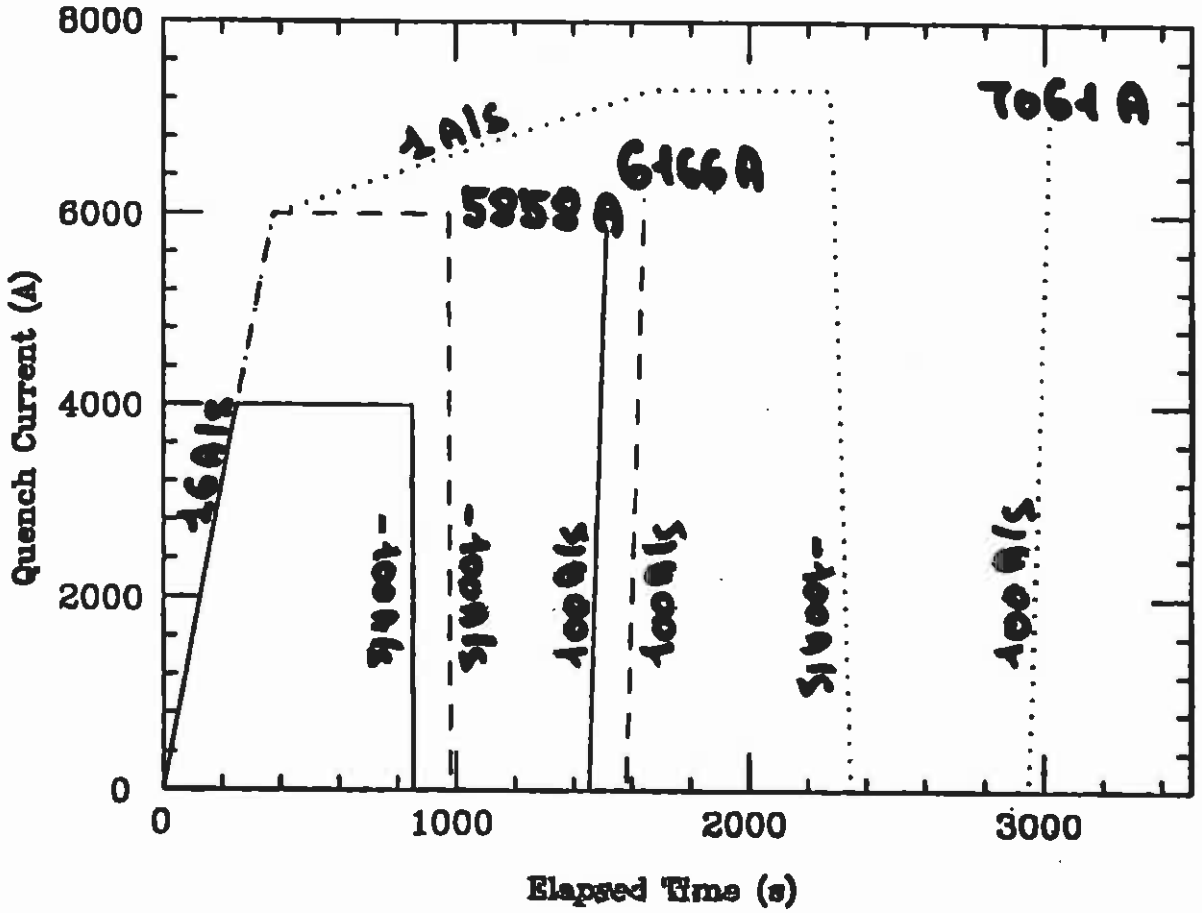

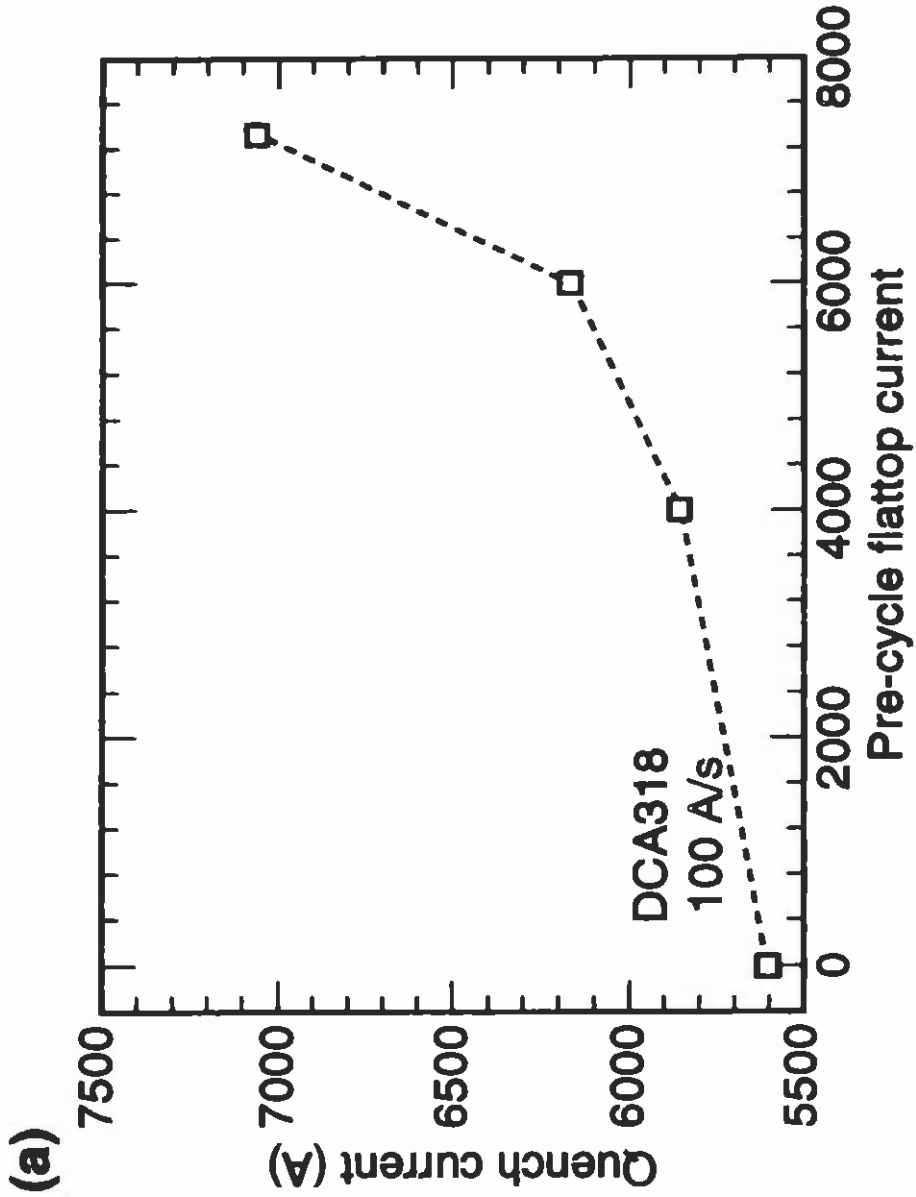
(a)
Quench current (A)
7500
7000
6500
6000
5500
0
2000
4000
6000
8000
Pre-cycle flattop current
DCA318
100 A/s

ORIGINS OF TYPE-A AND TYPE-B BEHAVIORS

– The type-A behavior is believed to be dominated by interstrand coupling currents arising from low and non-uniform interstrand resistances in the Rutherford-type cables.

– The type-B behavior is believed to be dominated by imbalances in the transport-current distribution.

The exact origin of these imbalances has not been identified

Quench localization vs. Ramp Rate*

- At low ramp-rates, quenches are expected to occur at the pole turn, where the field is the highest
- At large ramp-rates, quenches are expected to shift towards the midplane, where the cable eddy-current losses are the largest

* for a dipole magnet

SSC 5-cm. Aperture Dipole*

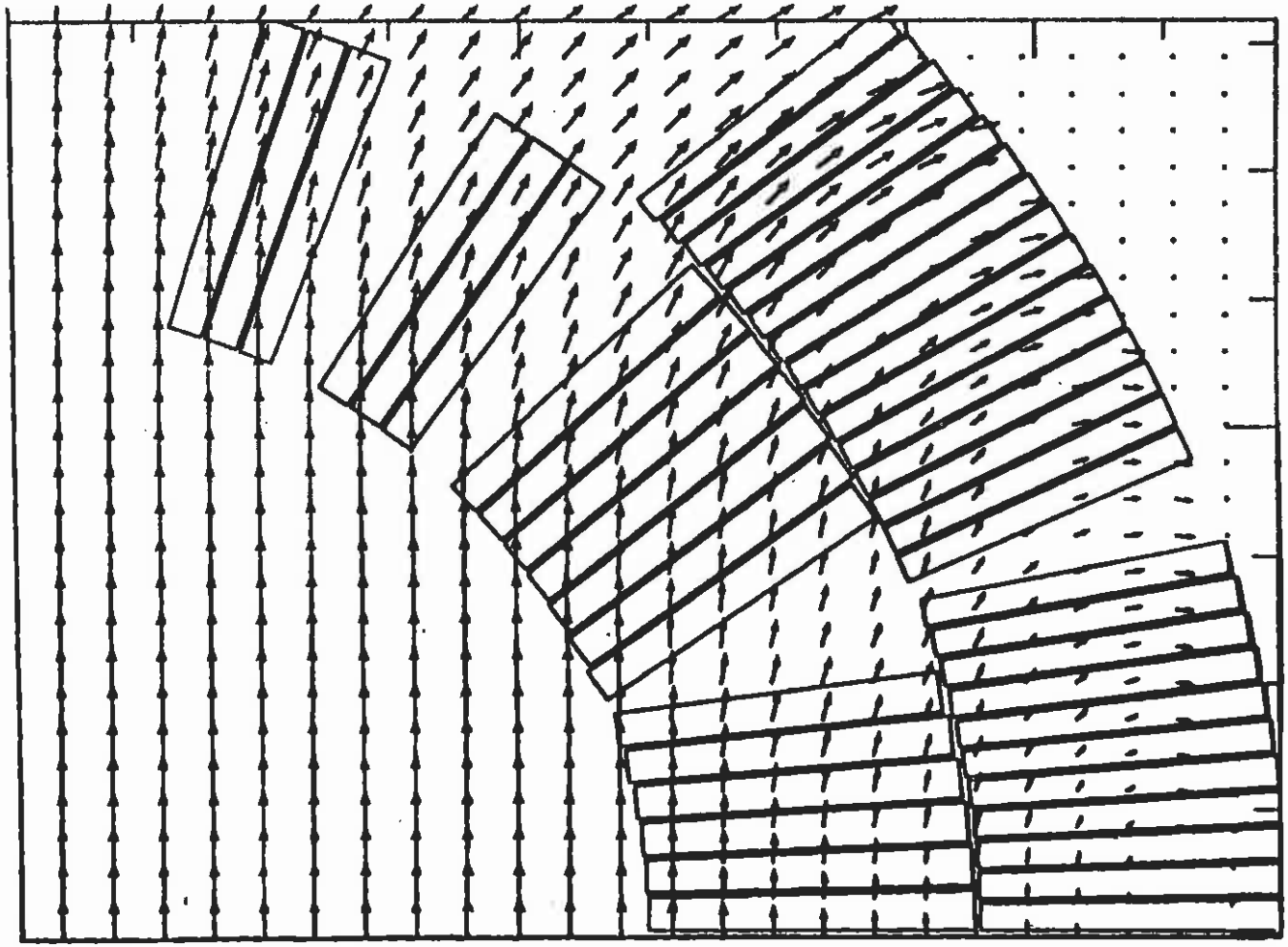

*Courtesy T. Ogitsu

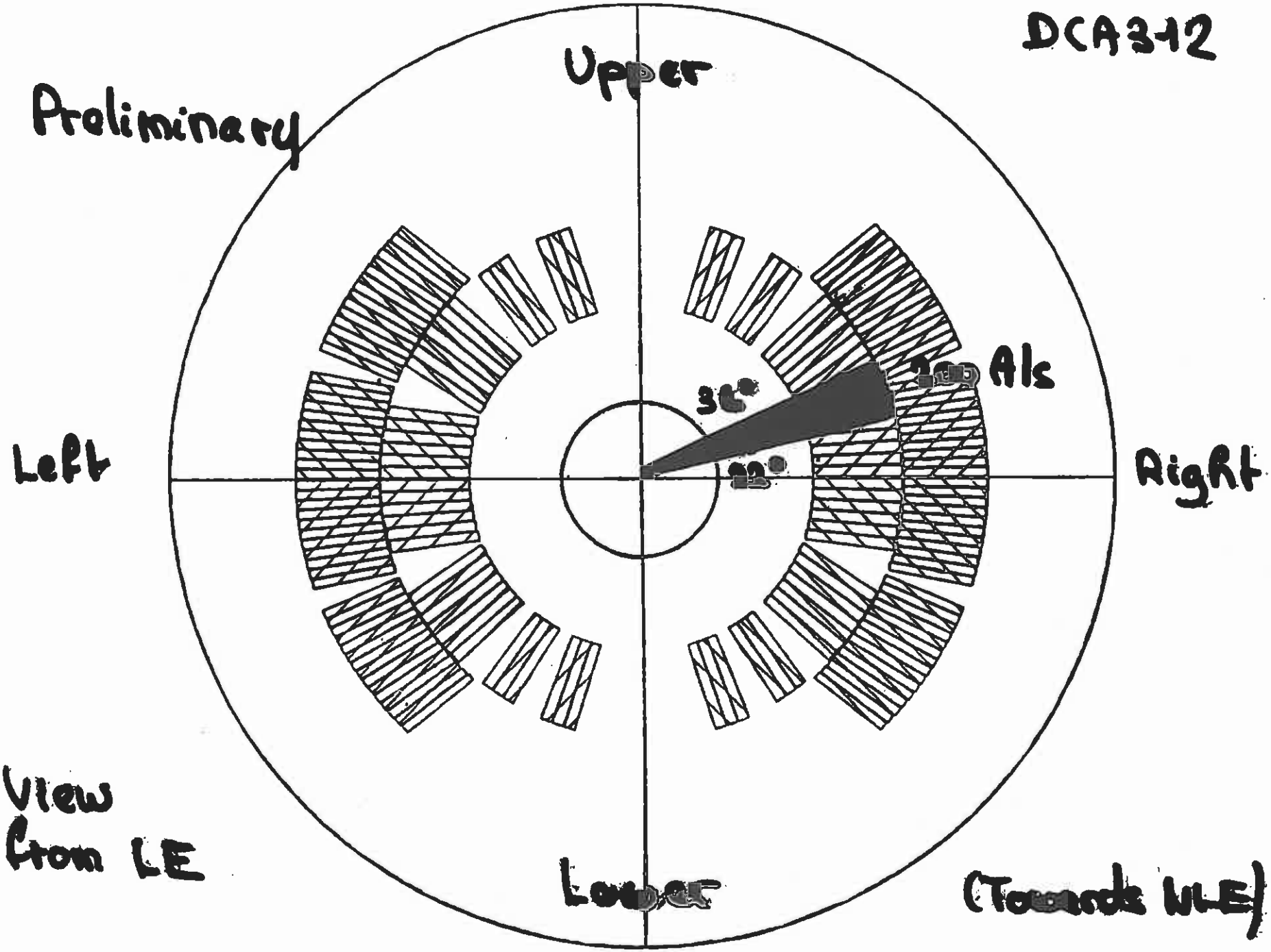
DCA312
Preliminary
Upper
Left
Right
Lower
View from LE
(Towards WLE)

LECTURE 8: QUENCH PERFORMANCE OF PARTICLE ACCELERATOR MAGNETS

8.1 Temperature and Enthalpy Margins

8.2 Magnet Cooling

8.3 What is a quench?

8.4 Magnet Training and Quench Plateau

8.5 Quench Origins

8.6 Phenomenological Model of Mechanical Training

8.7 Improving Quench Performance

8.8 Quench Performance as a Function of Ramp Rate

8.9 Specifications on Quench Performance

SPECIFICATIONS ON QUENCH PERFORMANCE

– The possibility of training superconducting magnets is rather encouraging for it leaves the hope that, even if the first quenches are below the expected maximum quench current, the performance may improve and the magnet may finally reach the design current.

– Nevertheless, it is not reasonable to build an accelerator with several hundred or several thousand magnets that need to be trained each time they are put into operation (or at least, each time they are warmed up to room temperature).

– If the magnet prototypes exhibit some training, the origin of this training has to be understood, and the design of the magnet has to be modified so as to eliminate, or at least to limit, the training quenches to levels which are well above the operating current of the accelerator.

– In any case, it is indispensable to carry out systematic tests before installing the magnets into the tunnel to ensure that their quench performance is adequate and does not degrade upon extended current and thermal cycling.

LECTURE 9: QUENCH PROTECTION OF PARTICLE ACCELERATOR MAGNETS

9.1 Quench Development
- 9.1.1 Simple Theoretical Model 9–3
- 9.1.2 Measuring Quench Propagation Using Voltage Taps 9–15
- 9.1.3 Measuring Quench Propagation Using Quench Antenna 9–27
- 9.1.4 Review of Propagation Velocity Measurements 9–39

9.2 The Effects of a Quench 9–51

9.3 Hot Spot Temperature 9–59

9.4 Quench Detection 9-79

9.5 Quench Protection Heaters 9–87

9.6 Protection of a Single Magnet 9–101

9.7 Protection of a Magnet String 9–113

LECTURE 9: QUENCH PROTECTION OF PARTICLE ACCELERATOR MAGNETS

9.1 Quench Development

9.1.1 Simple Theoretical Model

9.1.2 Measuring Quench Propagation Using Voltage Taps

9.1.3 Measuring Quench Propagation Using Quench Antenna

9.1.4 Review of Propagation Velocity Measurements

9.2 The Effects of a Quench

9.3 Hot Spot Temperature

9.4 Quench Detection

9.5 Quench Protection Heaters

9.6 Protection of a Single Magnet

9.7 Protection of a Magnet String

Voltage Taps Analysis

Progagation of the Normal Zone

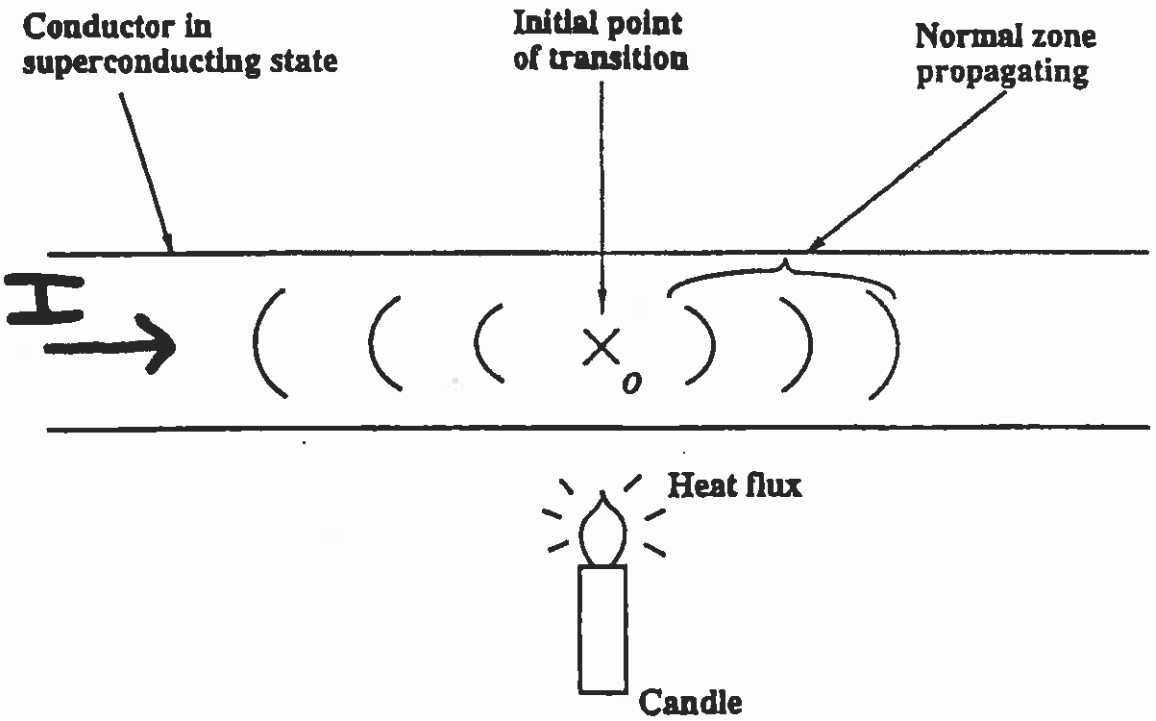

Simple Model of Quench Development (Cont.)

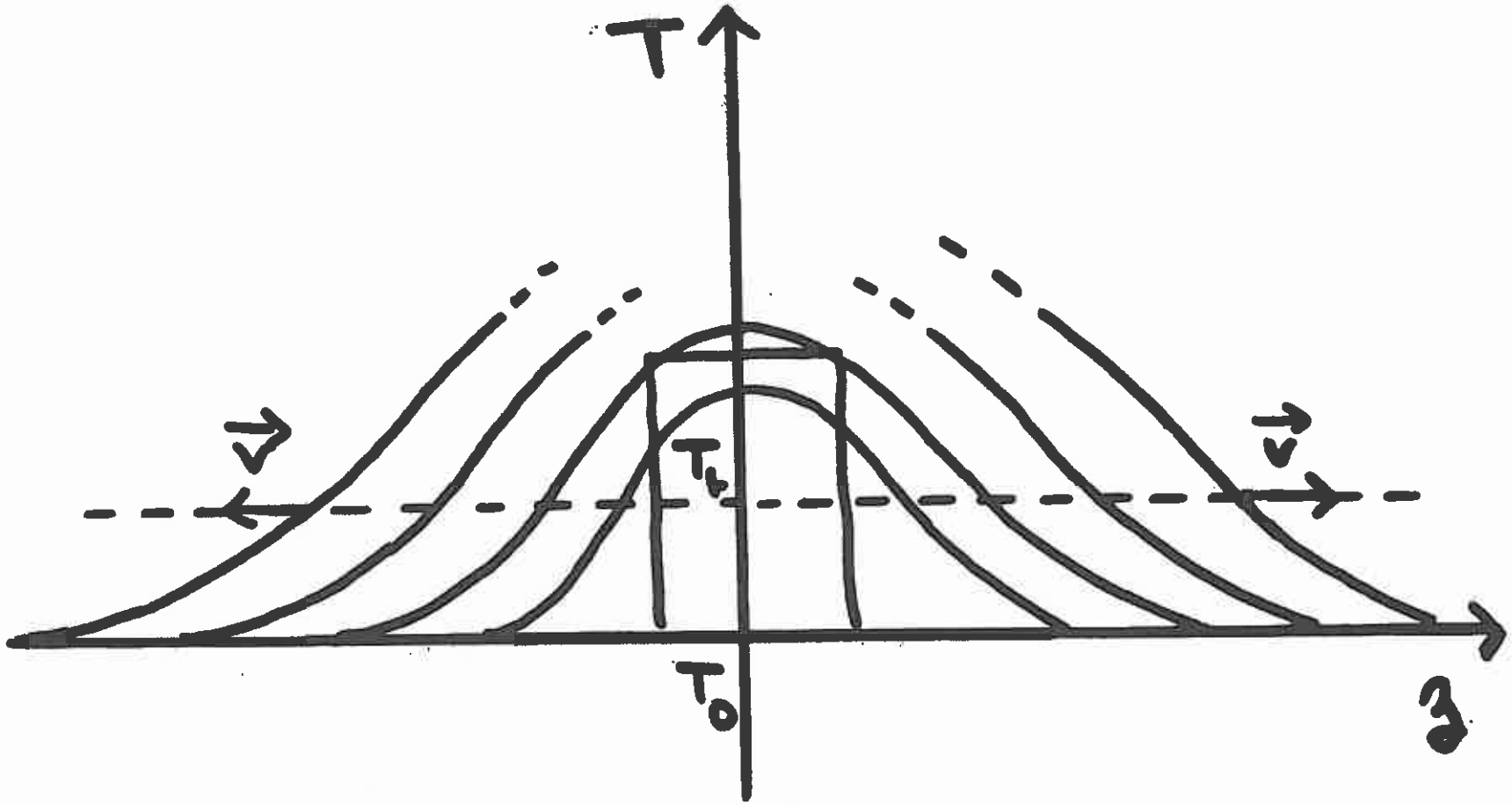

Simple Model of Quench Development

- In the normal zone

$$C\frac{\partial T(z,t)}{\partial t} = K\frac{\partial^2 T(z,t)}{\partial z^2} + P_J$$

for $T > T_f$

- In the superconducting zone

$$C\frac{\partial T(z,t)}{\partial t} = K\frac{\partial^2 T(z,t)}{\partial z^2}$$

for $T < T_f$

Propagating Wave Solution

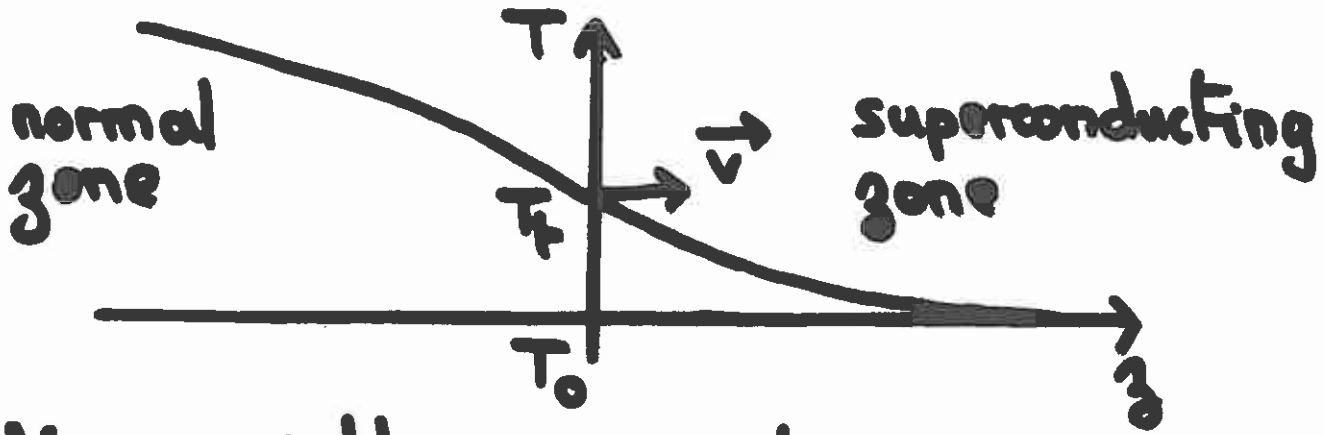

New variables: $u = vt - z$

$$\frac{\partial}{\partial t} = \frac{1}{v}\frac{\partial}{\partial u} \qquad \frac{\partial}{\partial z} = -\frac{\partial}{\partial u}$$

- In the normal zone

$$\frac{d^2T}{du^2} - \frac{v}{D_n}\frac{dT}{du} + \frac{P_J}{R} \qquad \text{for } u \geq 0$$

- In the superconducting zone

$$\frac{d^2T}{du^2} - \frac{v}{D_n}\frac{dT}{du} = 0 \qquad \text{for } u < 0$$

where: $D_n = R/C$ (m^2/s)

Thermal Diffusivity

Boundary Conditions

- At infinity in s.g.

$$\lim_{u \to -\infty} T(u) = T_0$$

- At boundary between s.g. and n.g.

$$\left.\begin{aligned} \lim_{\substack{u \to 0 \\ < }} T(u) &= T_f \\ \lim_{\substack{u \to 0 \\ > }} T(u) &= T_f \end{aligned}\right\} \text{ Temperature continuity}$$

$$\left.\begin{aligned} \lim_{\substack{u \to 0 \\ < }} \frac{dT}{du} &= \lim_{\substack{u \to 0 \\ > }} \frac{dT}{du} \end{aligned}\right\} \text{ Flux continuity}$$

- At infinity in n.g.

$$\lim_{u \to +\infty} \frac{T(u)}{T_a(u)} \leq 1$$

where $T_a(u)$ is solution of : $C \frac{\partial T_a}{\partial u} = P_J$

$$T_a(u) = T_f + \frac{P_J}{VC} u \quad \text{for } u \geq 0$$

Analytical Expressions

- Normal zone

$$T(u) = T_f + \frac{P_J}{vC}\,u \qquad \forall u,\ u \geq 0$$

- Superconducting zone

$$T(u) = T_0 + (T_f - T_0)\exp\left(\frac{v}{D_{th}}\,u\right) \qquad \forall u,\ u \leq 0$$

- Propagation velocity

$$v = \sqrt{\frac{D_{th}\,P_J}{\Delta H}}$$

where

$$\Delta H = \int_{T_0}^{T_f} dT\, C(T)$$) Enthalpy of s.g.

Simple Model of Quench Development (Cont.)

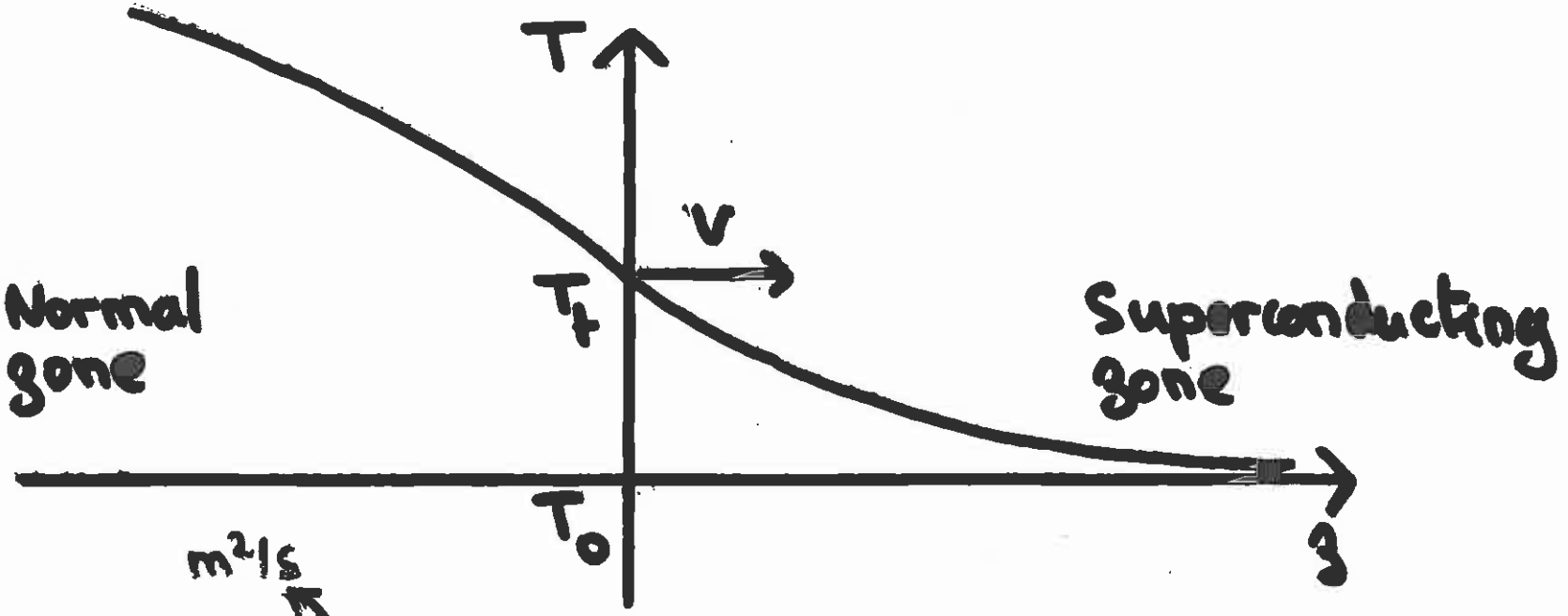

$$\underbrace{\frac{D_H}{v} P_J}_{\text{Fraction of Joule Heating Transmitted to s.z.}} = \underbrace{v \, \Delta H}_{\text{Rate of Heating of s.z.}}{}^{*}$$

D_H: m^2/s

v: m/s

* Several corrections needed...

Influences on the Propagation Velocity

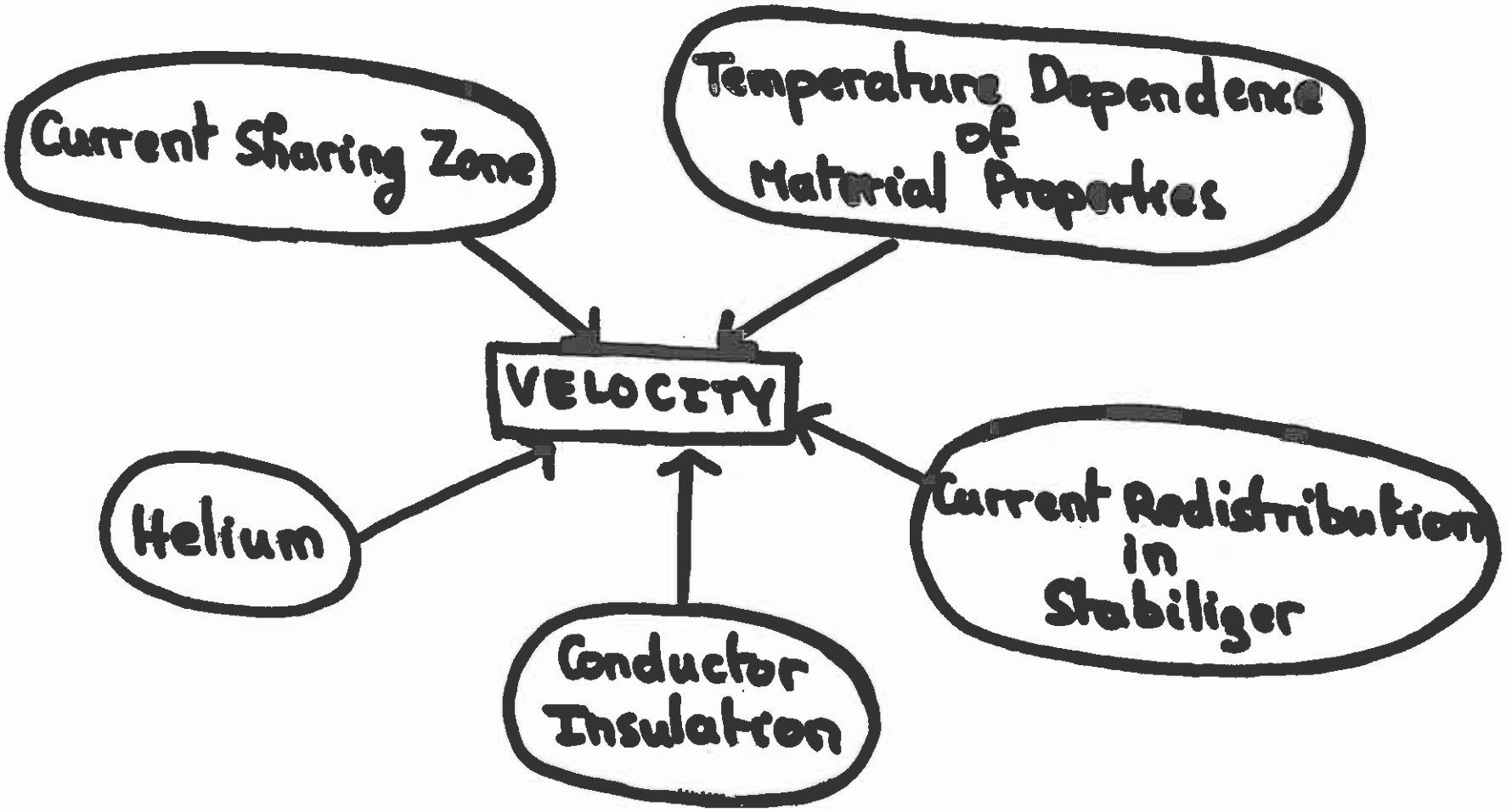

Influence of Current sharing

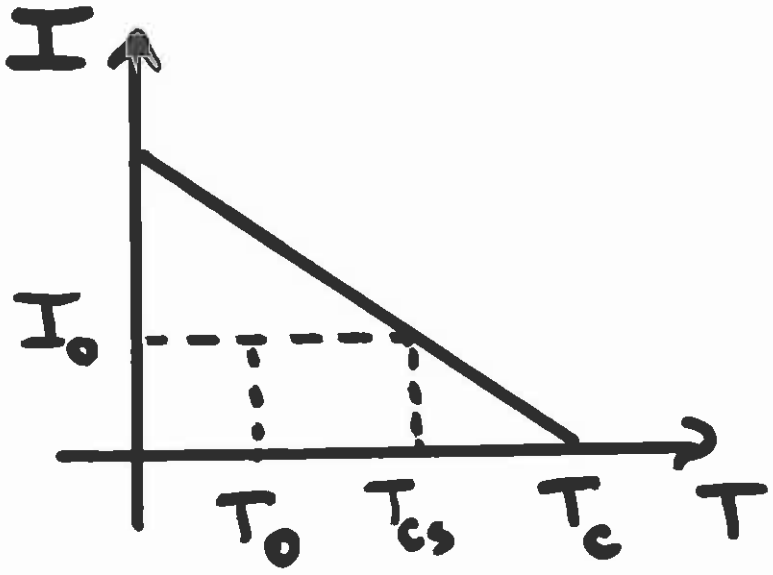

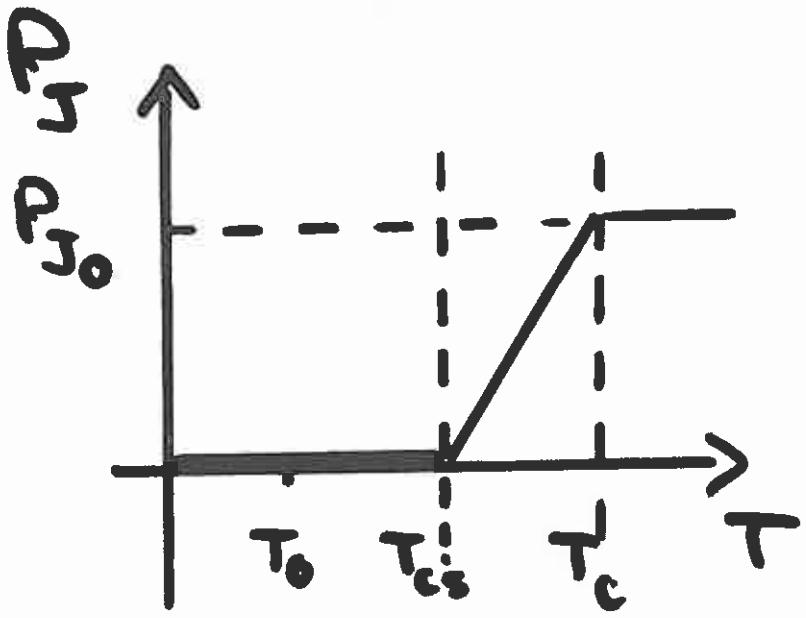

SSC Strand

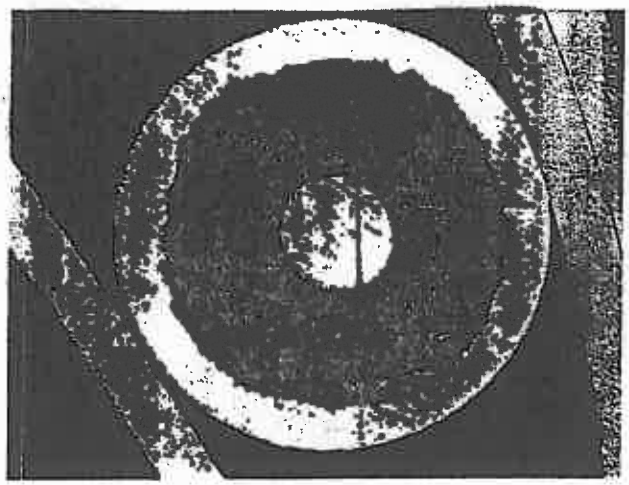

1G-C 100X

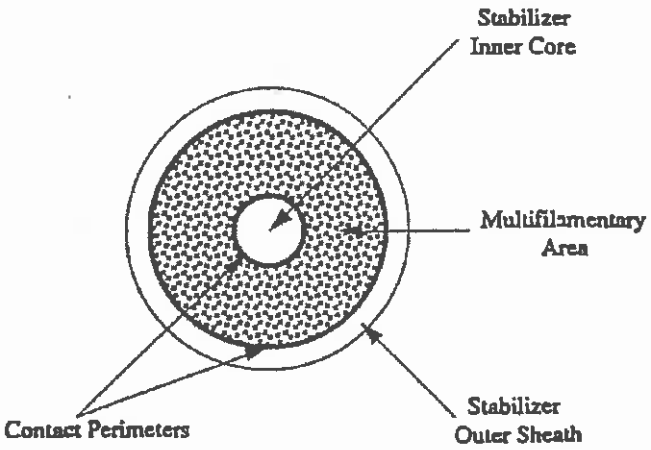

Figure 1: The conductor cross-section.

LECTURE 9: QUENCH PROTECTION OF PARTICLE ACCELERATOR MAGNETS

9.1 Quench Development
9.1.1 Simple Theoretical Model
9.1.2 Measuring Quench Propagation Using Voltage Taps
9.1.3 Measuring Quench Propagation Using Quench Antenna
9.1.4 Review of Propagation Velocity Measurements

9.2 The Effects of a Quench

9.3 Hot Spot Temperature

9.4 Quench Detection

9.5 Quench Protection Heaters

9.6 Protection of a Single Magnet

9.7 Protection of a Magnet String

Voltage Taps Analysis

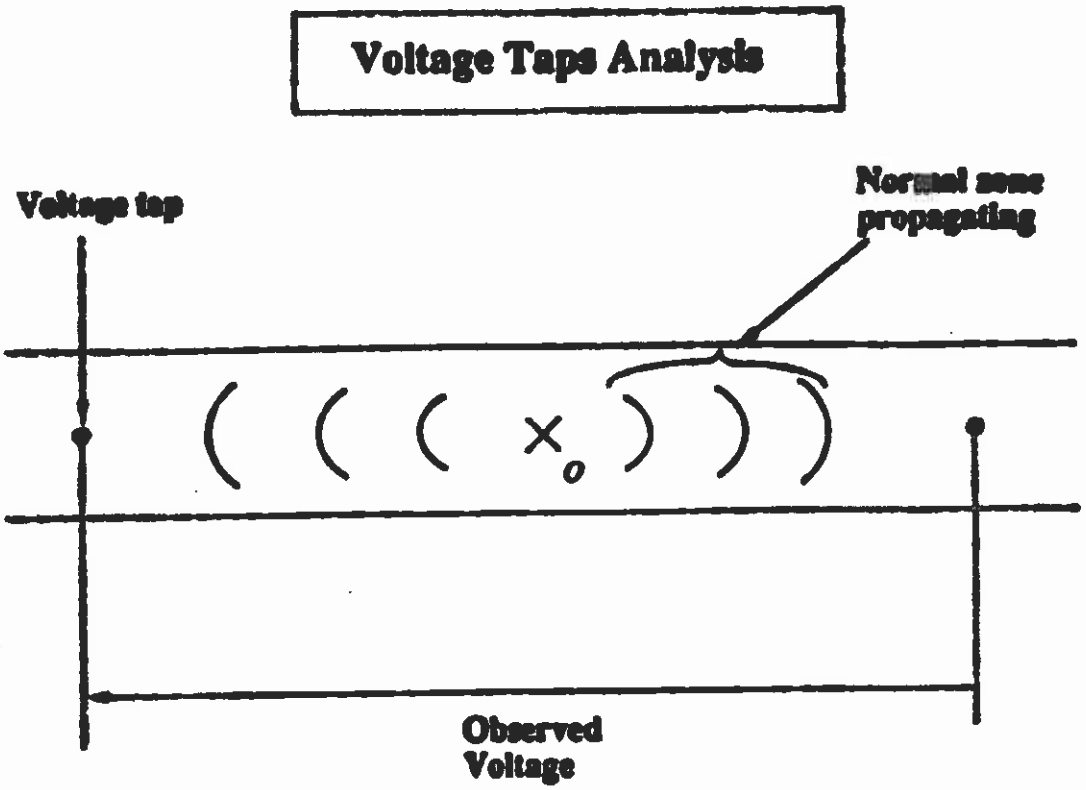

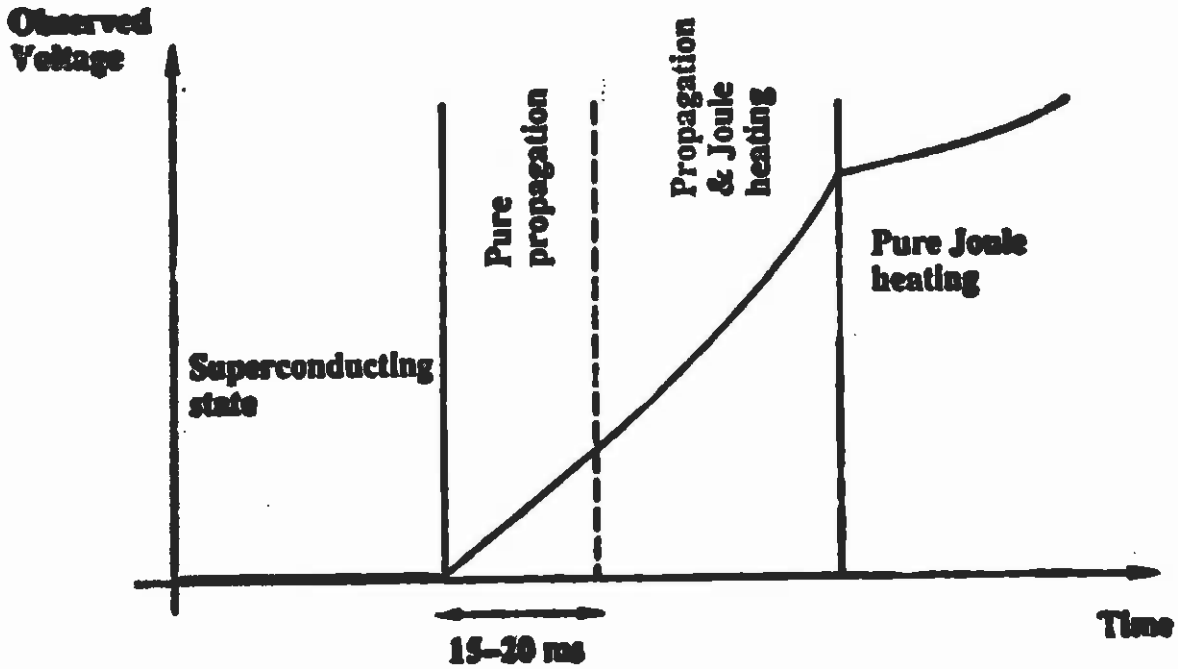

DD0010-12 VOTAGE TAP SCHEMATIC

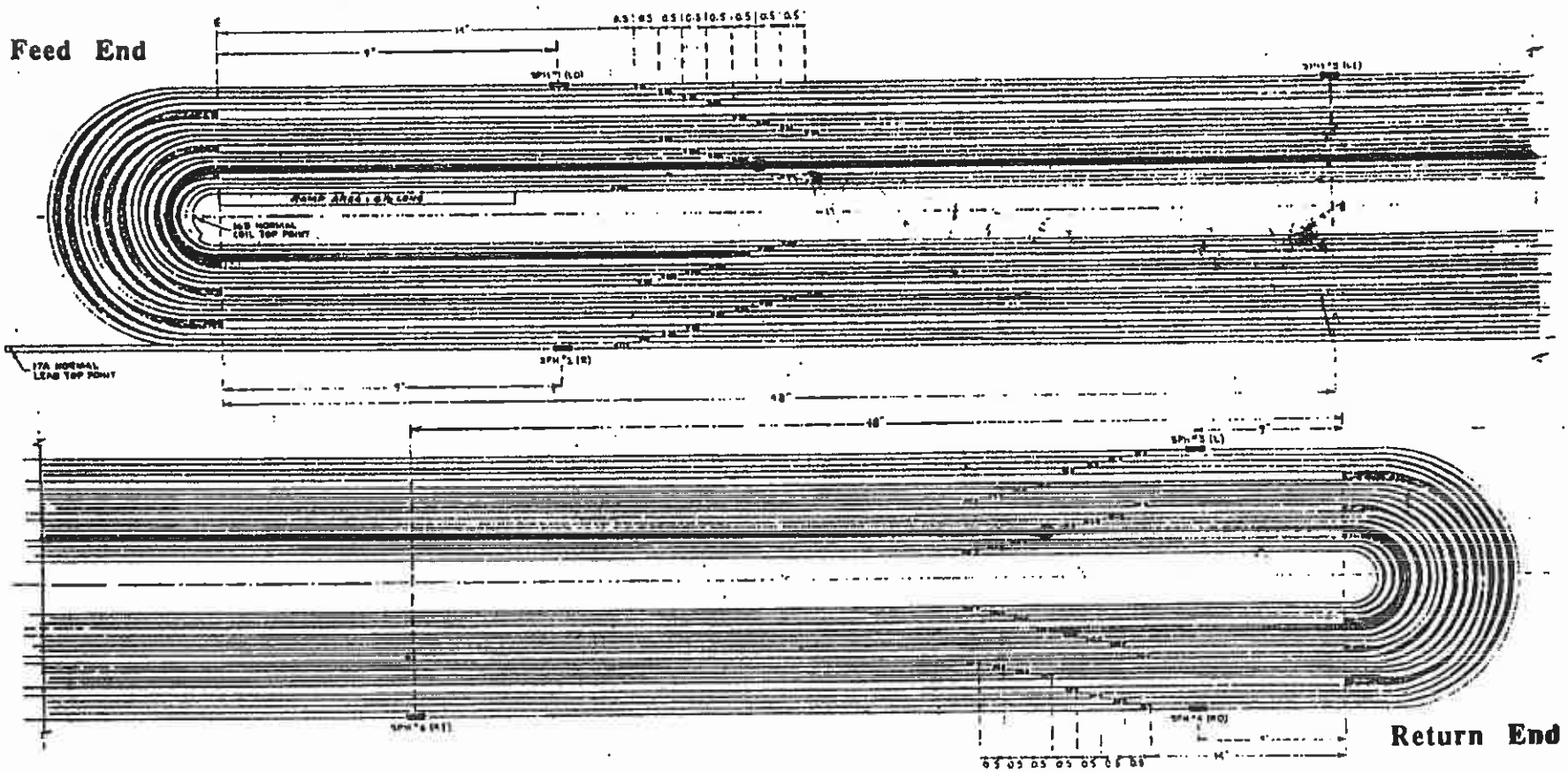

QUENCH LOCALIZATION TECHNIQUE

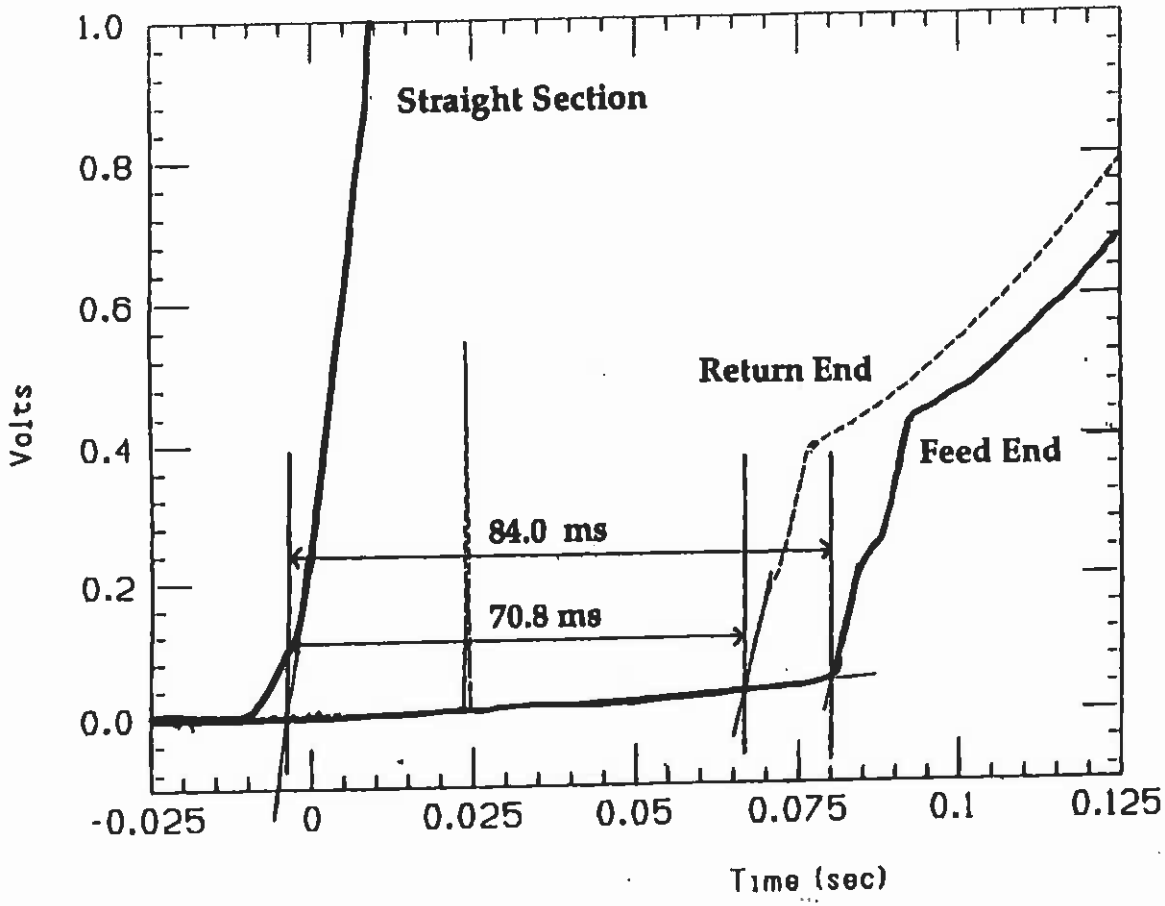

Turn 13

Section length:	**15.73 m**
Time of flight:	**154.8 ms**
Velocity:	**101.6 m/s**
Quench origin: (from return–end tap)	**7.2 m**

000010 Data File No. : 20 8-APR-88 16:10:26 Quench No. : 3 Current = 5680.2

Quench Localigation

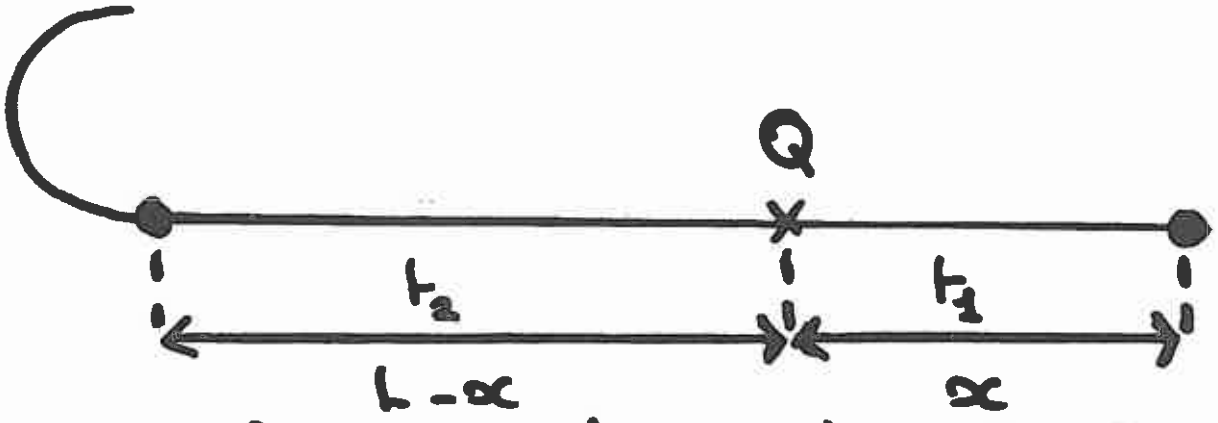

(where L is distance between taps)

$$\begin{cases} x = v.t_1 \\ L-x = v.t_2 \end{cases} \Rightarrow \begin{cases} v = L/(t_1+t_2) \\ x = v.t_1 \end{cases}$$

Calculating the Velocity from the Initial Voltage Slope

We have

$$U(t) = \frac{\rho[B(t)]\, l_n(t)}{A} I(t)$$

where A is the conductor x-sectional area, and l_n is the normal zone length.

If I is almost constant:

$$I(t) \sim I_0 \text{ and } B(t) \sim B_0$$

and it comes

$$\frac{du}{dt} = \frac{\rho(B_0) I_0}{A} \frac{dl_n}{dt}$$

where

$$\frac{dl_n}{dt} = N v$$

N: Number of transition fronts (1 or 2)

Hence

$$v = \frac{A}{N \rho(B_0) I_0} \left(\frac{du}{dt}\right)_{t \sim 0}$$

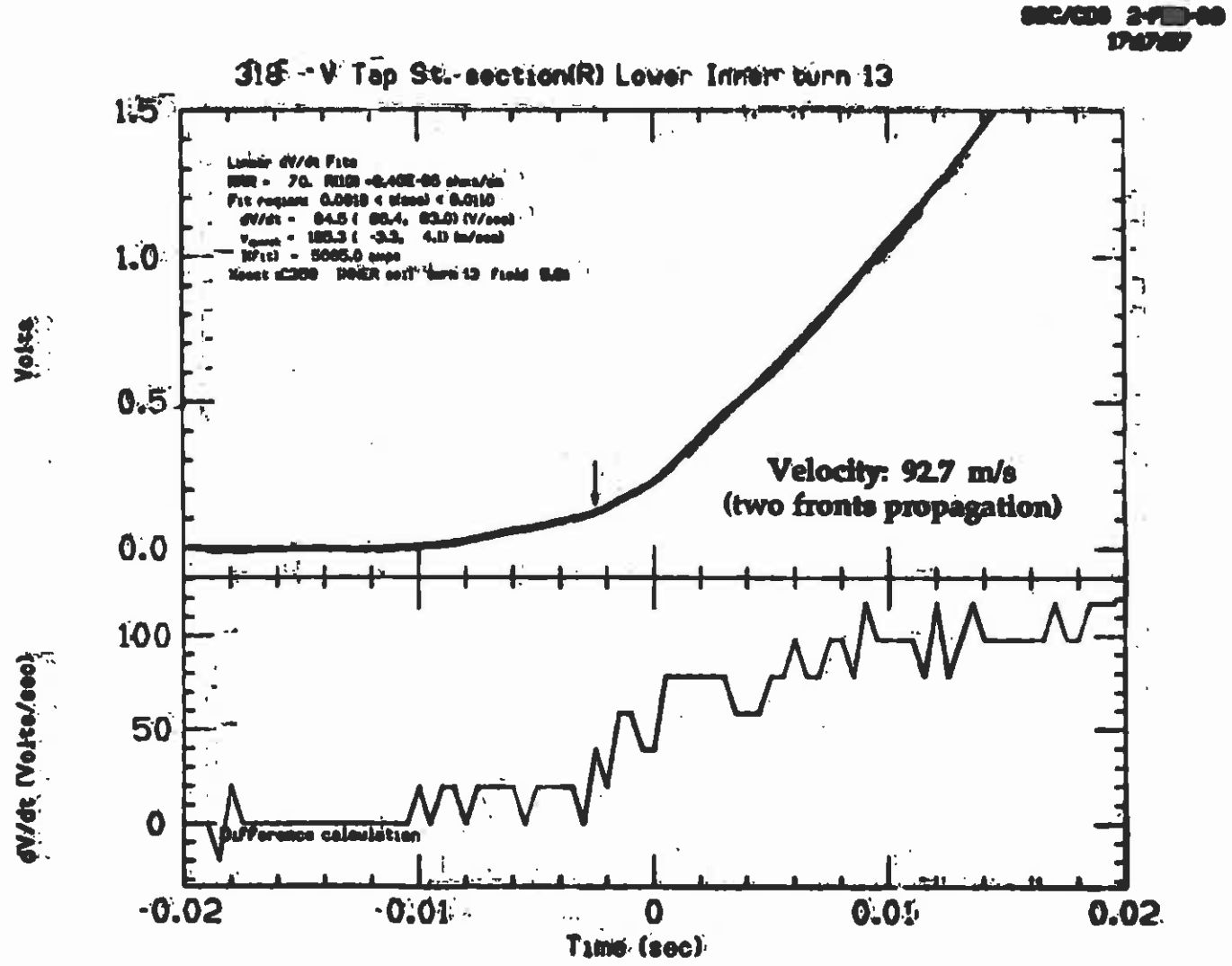
318 - V Tap St.-section(R) Lower Inner turn 13
Velocity: 92.7 m/s
(two fronts propagation)
Volts
dV/dt (Volts/sec)
Time (sec)
1.5
1.0
0.5
0.0
100
50
0
-0.02
-0.01
0
0.01
0.02
Difference calculation

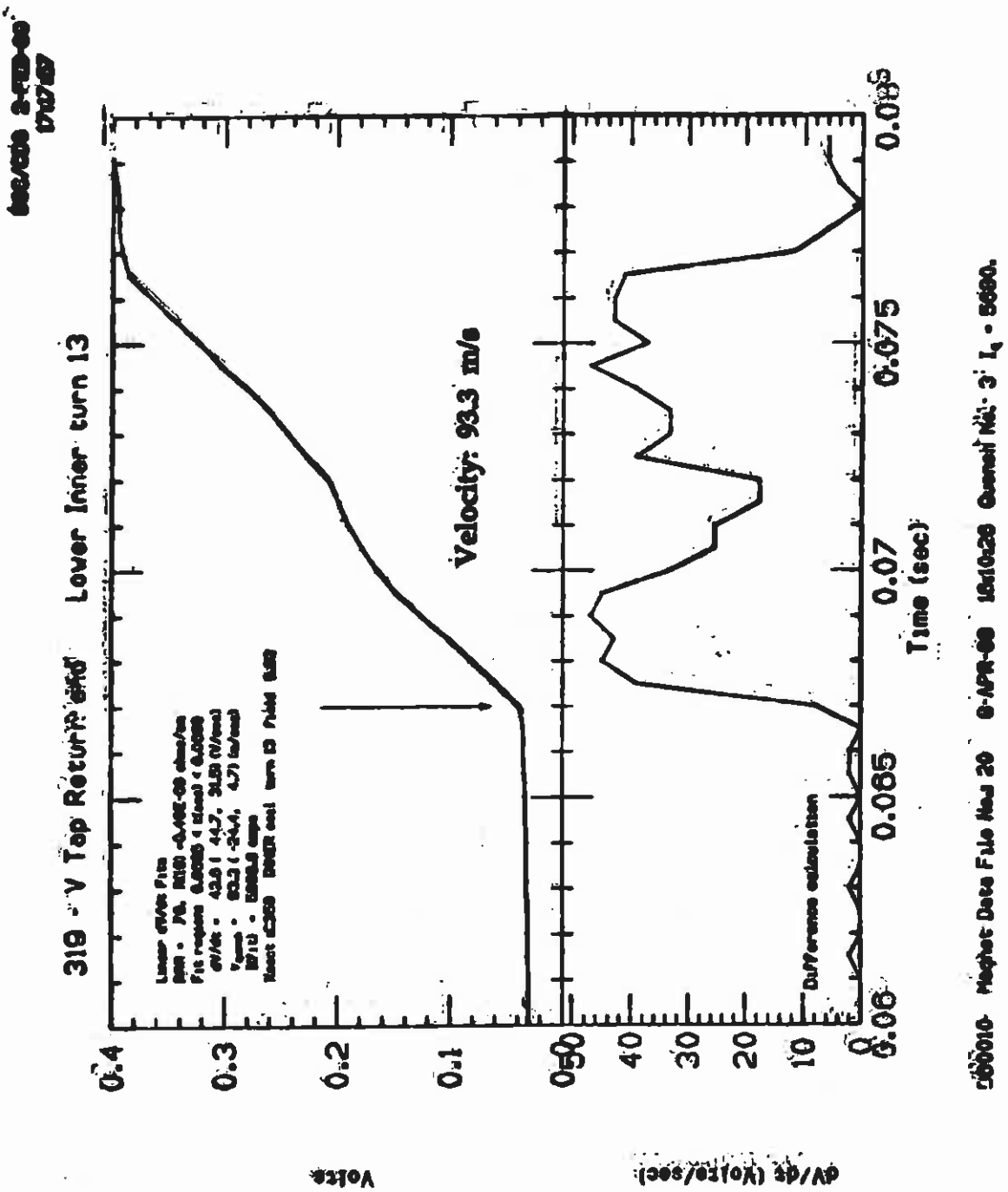
319 - V Tap Return and Lower Inner turn 13
Velocity: 93.3 m/s
Difference calculation
Time (sec)
Volts
dV/dt (Volts/sec)
0.06
0.065
0.07
0.075
0.08
0.4
0.3
0.2
0.1
0
50
40
30
20
10
0

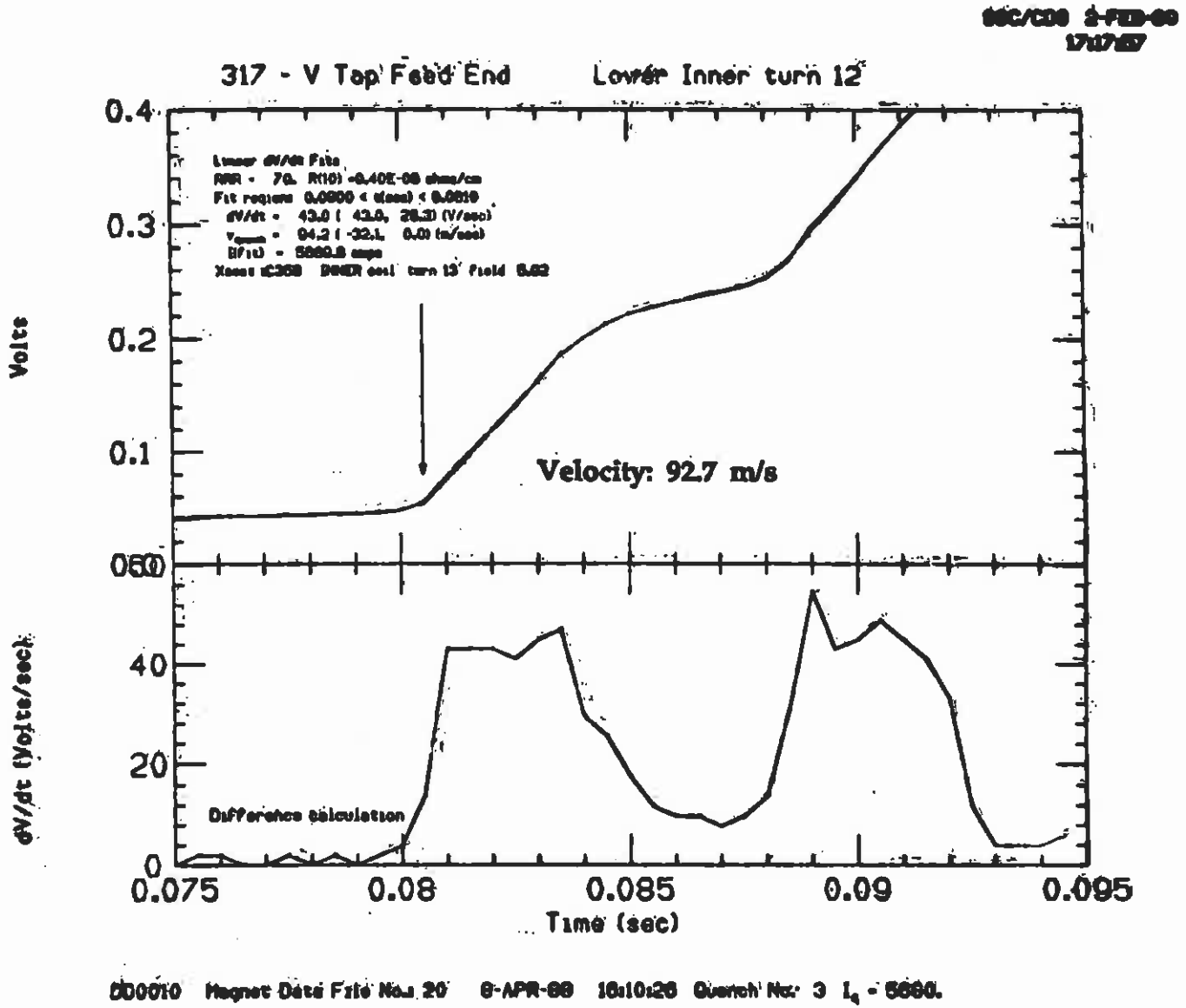
317 - V Top Feed End
Lower Inner turn 12
Volts
0.4
0.3
0.2
0.1
0
Velocity: 92.7 m/s
dV/dt (Volts/sec)
40
20
0
Difference calculation
0.075
0.08
0.085
0.09
0.095
Time (sec)

DD0017&18 RAMP SPLICE VOLTAGE TAPS

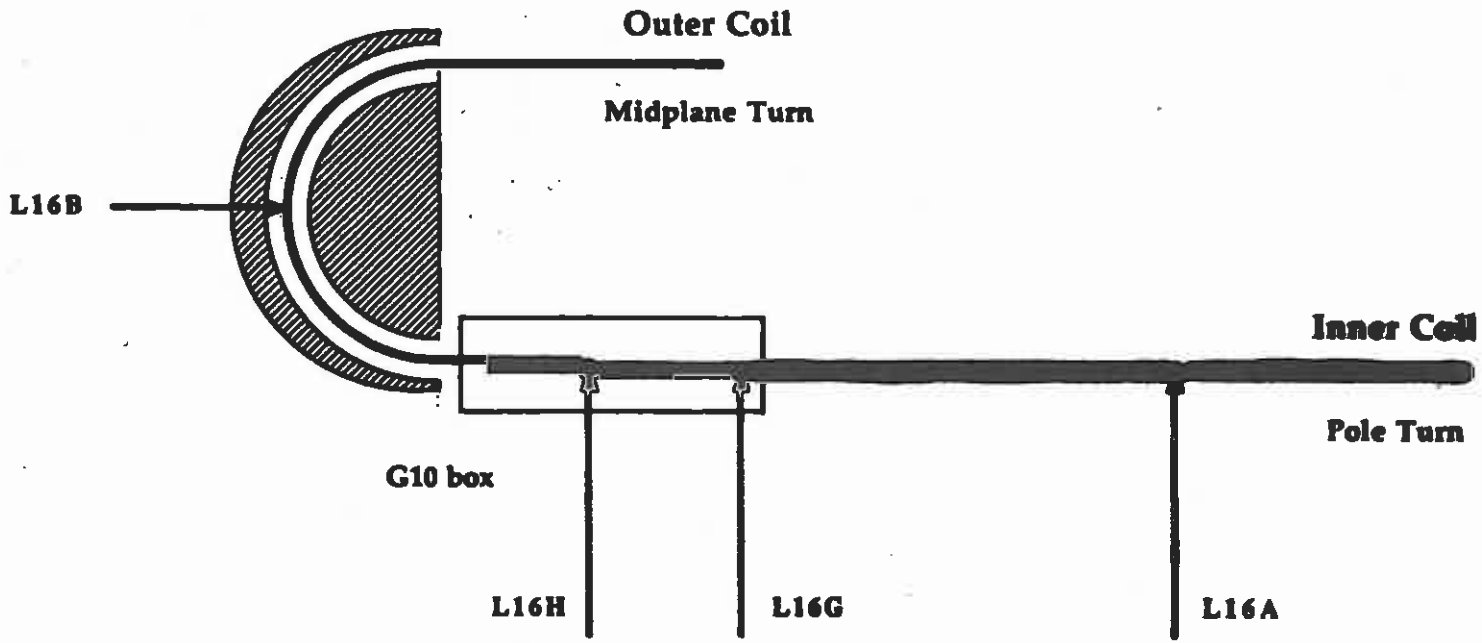

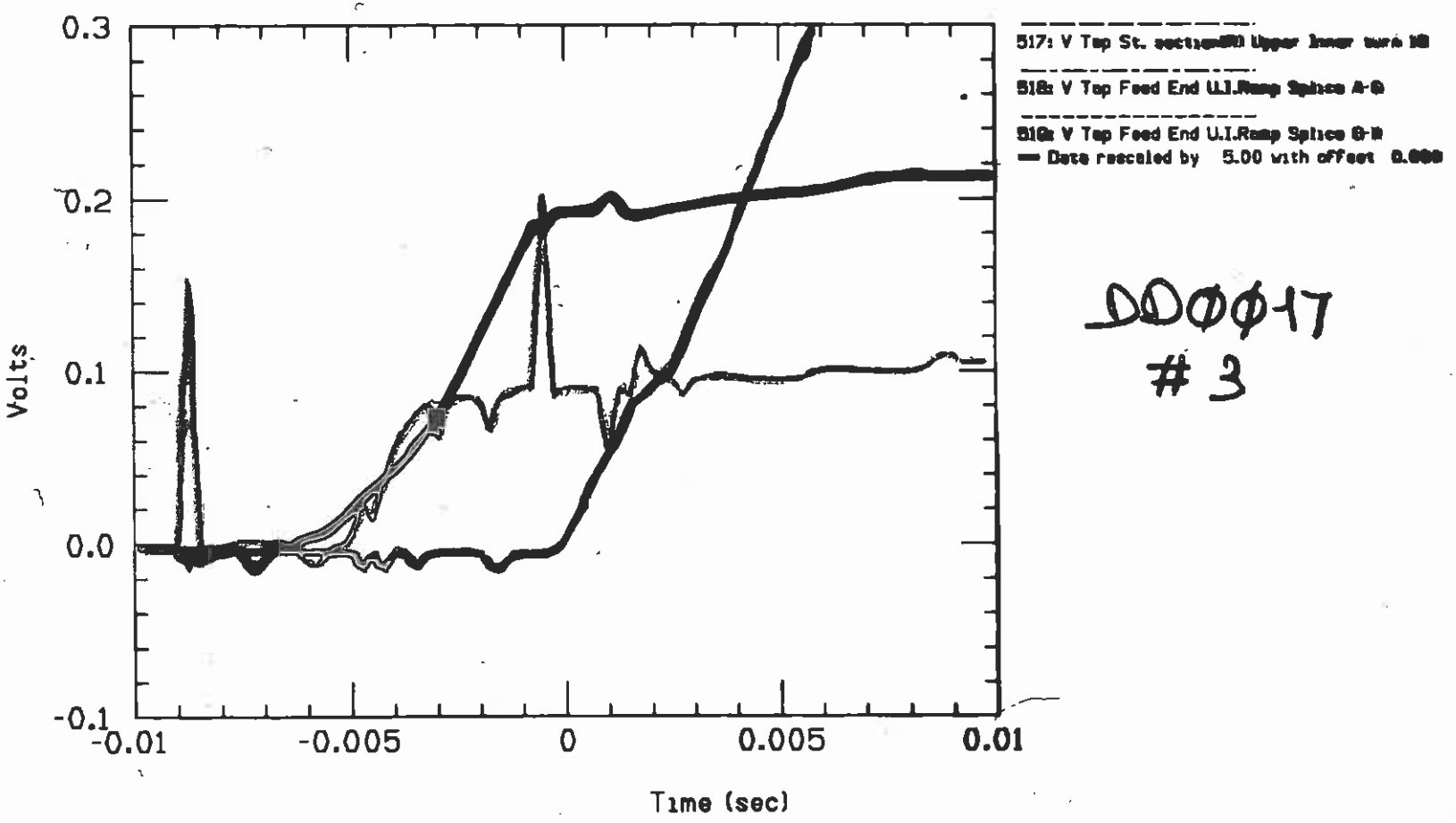

DD0017
#3

DD0017 Data File No. : 9 9-MAR-89 12:31:09 Quench No. : 3 Current = 6626.9

LECTURE 9: QUENCH PROTECTION OF PARTICLE ACCELERATOR MAGNETS

9.1 Quench Development
9.1.1 Simple Theoretical Model
9.1.2 Measuring Quench Propagation Using Voltage Taps
9.1.3 Measuring Quench Propagation Using Quench Antenna
9.1.4 Review of Propagation Velocity Measurements

9.2 The Effects of a Quench

9.3 Hot Spot Temperature

9.4 Quench Detection

9.5 Quench Protection Heaters

9.6 Protection of a Single Magnet

9.7 Protection of a Magnet String

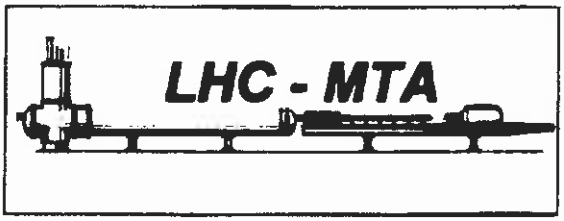

Quench Antenna

Quench Location in Magnet 2D Cross-section by "Inverse Problem Method"

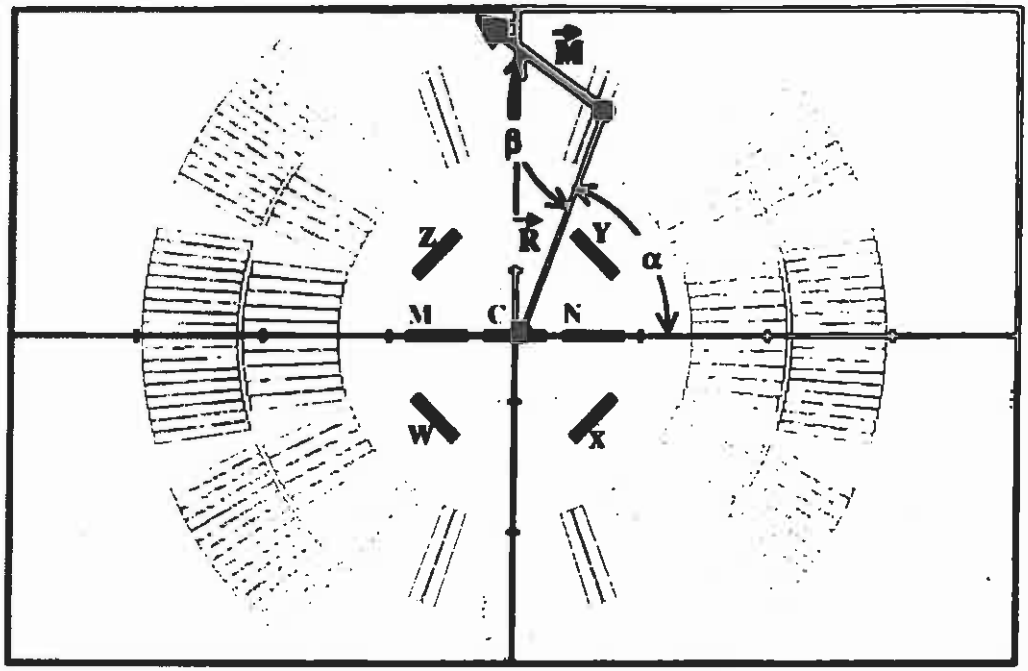

Unknown:	**Measured Signals:**
Magn. Moment Strength – **M**,	**Z –X,**
Radial position – **R**,	**W –Y,**
Azimuthal Position – **α**,	**M – C,**
Magn. Moment Direction – **β**.	**M – N.**

LHC-MTA/A.S.

Measurement Setup for Magnet DCA318

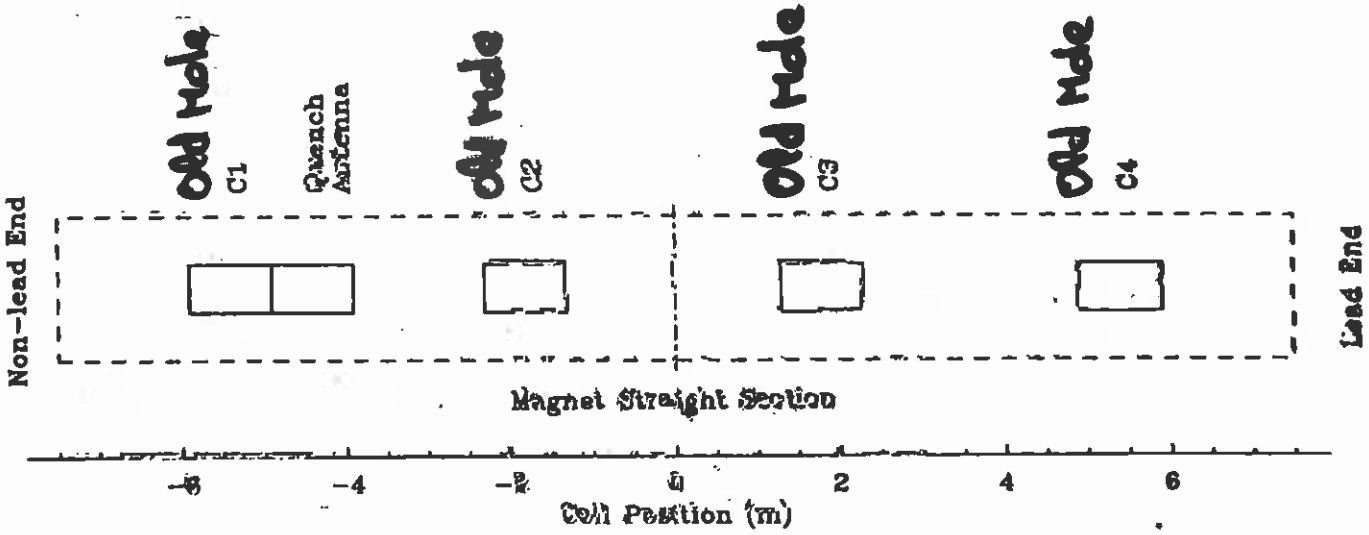

Example of Quench Antenna and old Hole Coils Signals for Magnet DCA318

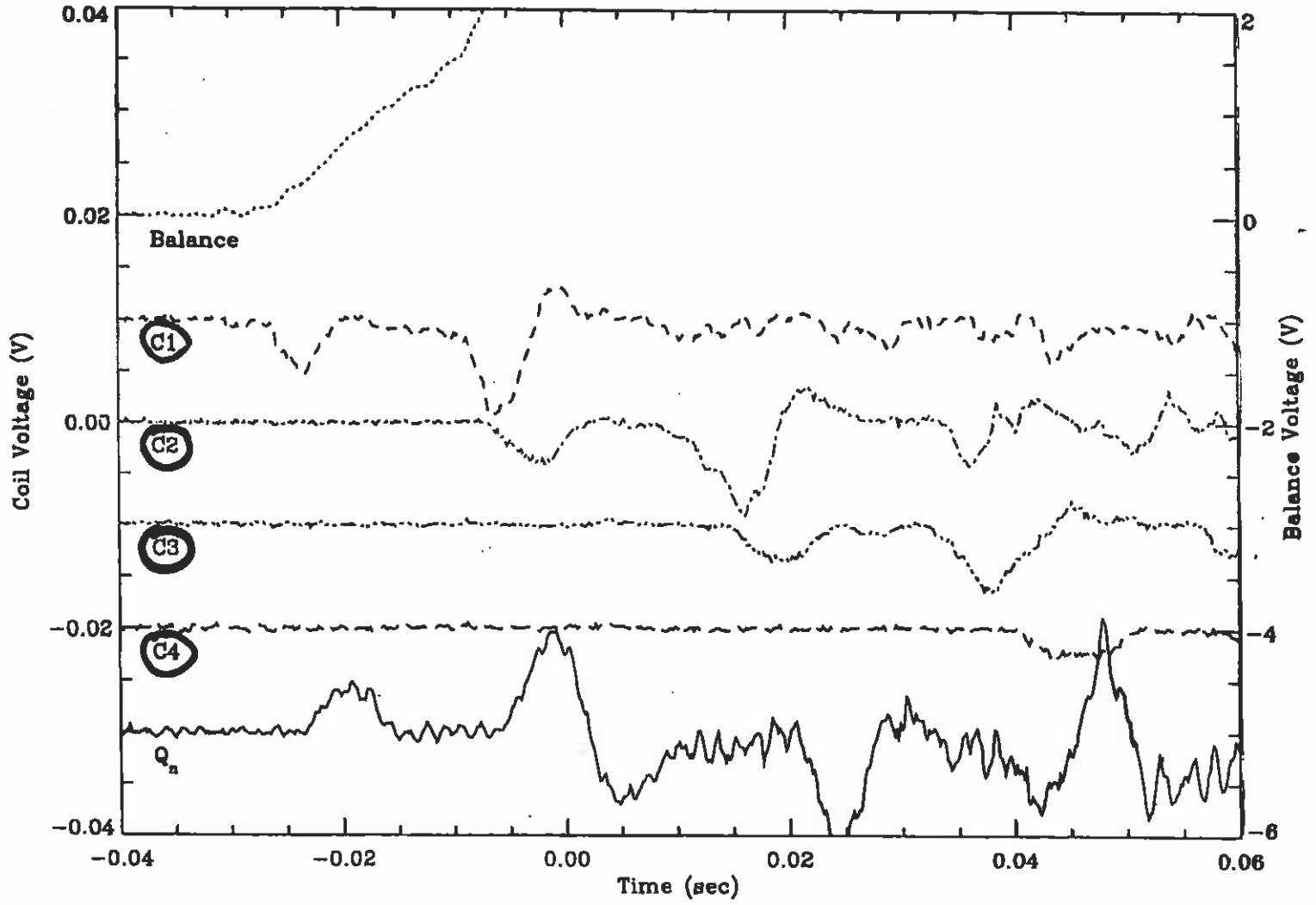

$I_q = 6150$ A at 100 A/s (3.5 K)

Example of Quench Antenna Signals for Magnet DCA318

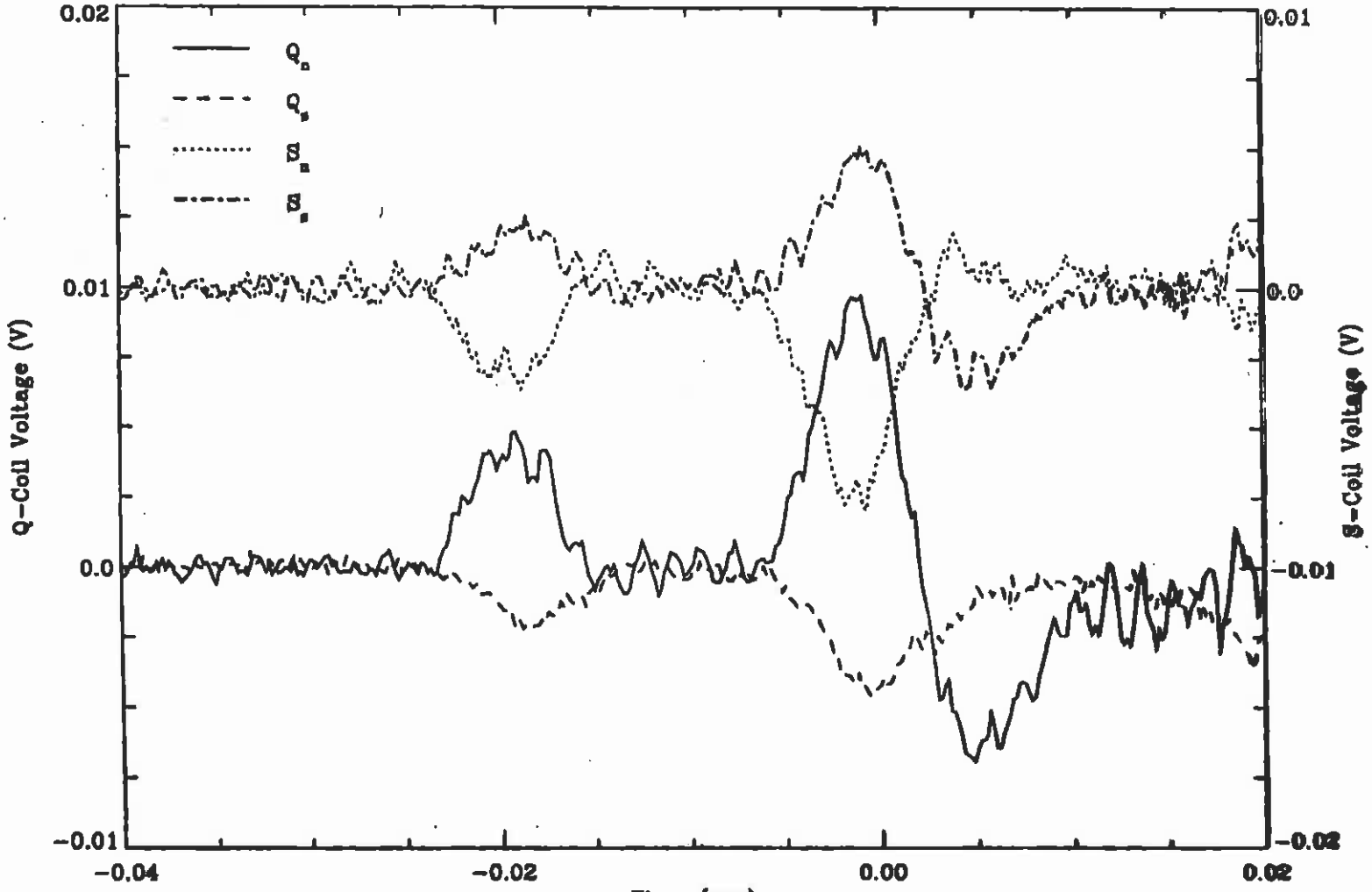

$I_q = 6150$ A at 100 A/s (3.5 K)

Example of Quench Start Localization Using Quench Antenna on Magnet DCA 3-18

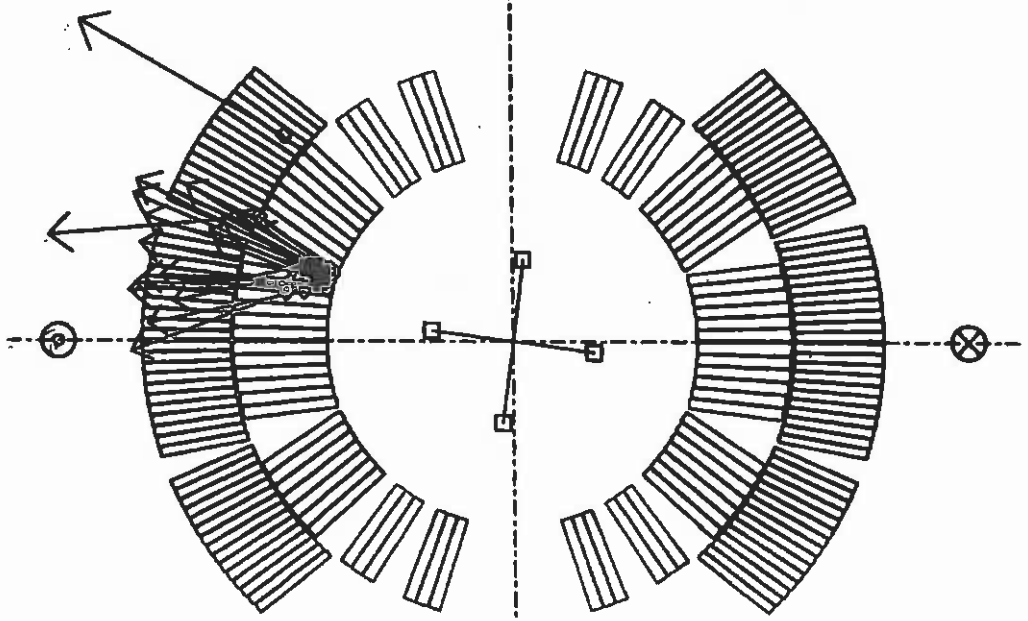

$I_q = 6150$ A at 100 A/s (3.5 K)

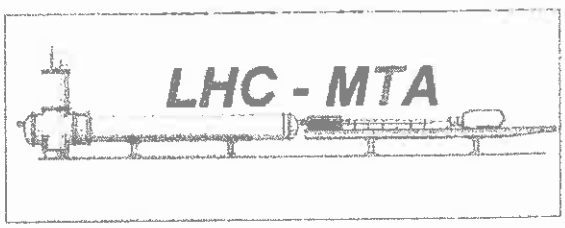

Dipole MBSMS12.V1
Quench File L0731172.402

Axial Propagation Recorded by Quench Antenna

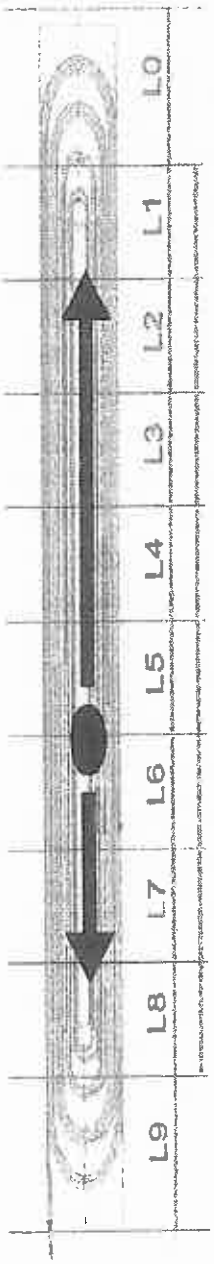

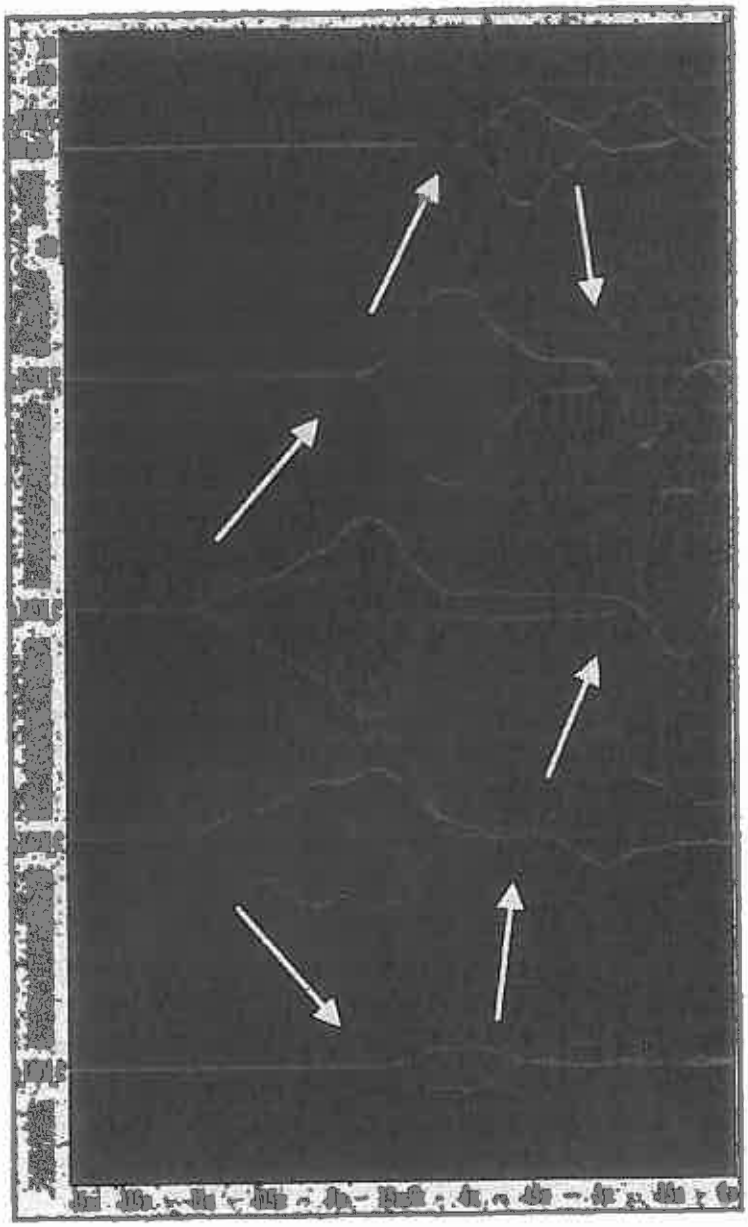

Courtesy A. Siemko

DCA317 Setup
Lead End
C4
NQ2
C2
Quench Antenna
Non-lead End
Magnet Straight Section
Coil Position (m)
6
4
2
0
-2
-4
-6

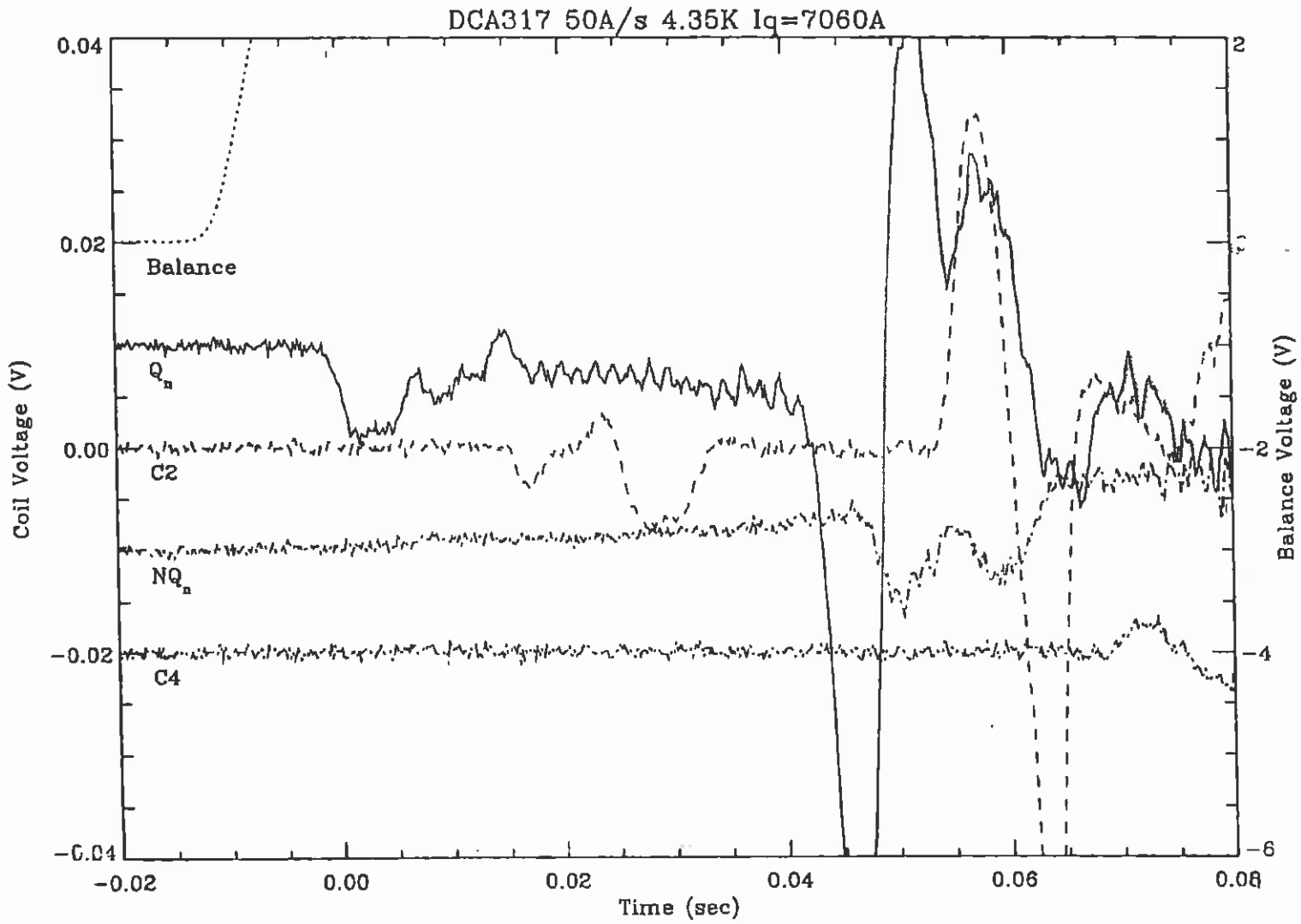
DCA317 50A/s 4.35K Iq=7060A
Balance
Q_n
C2
NQ_n
C4
Coil Voltage (V)
Balance Voltage (V)
Time (sec)
0.04
0.02
0.00
−0.02
−0.04
2
−2
−4
−6
−0.02
0.00
0.02
0.04
0.06
0.08

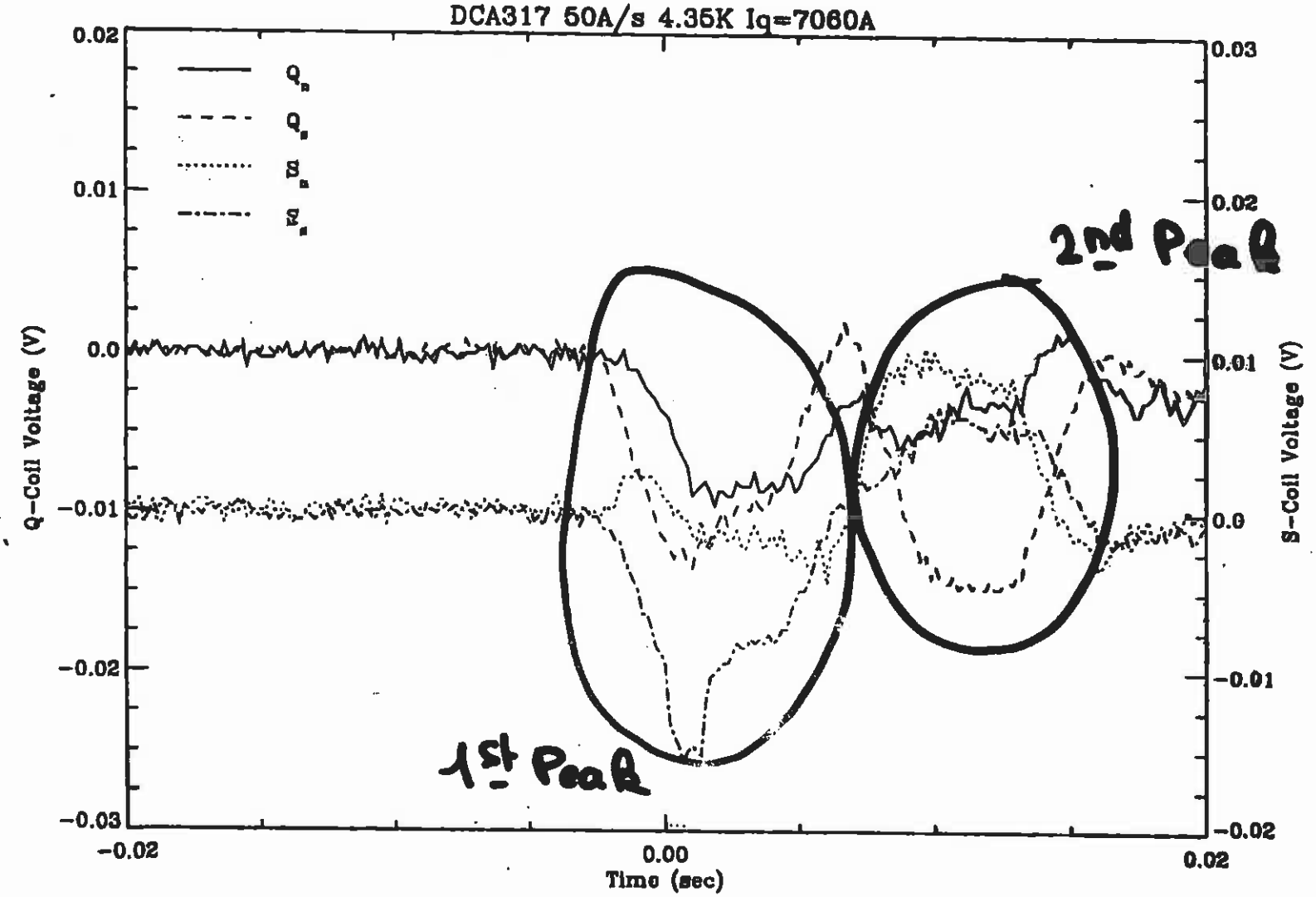
DCA317 50A/s 4.35K Ig=7060A
Q_n
Q_s
S_n
S_s
2nd Peak
1st Peak
Q-Coil Voltage (V)
S-Coil Voltage (V)
Time (sec)
0.02
0.01
0.0
-0.01
-0.02
-0.03
0.03
-0.02
0.00
0.02

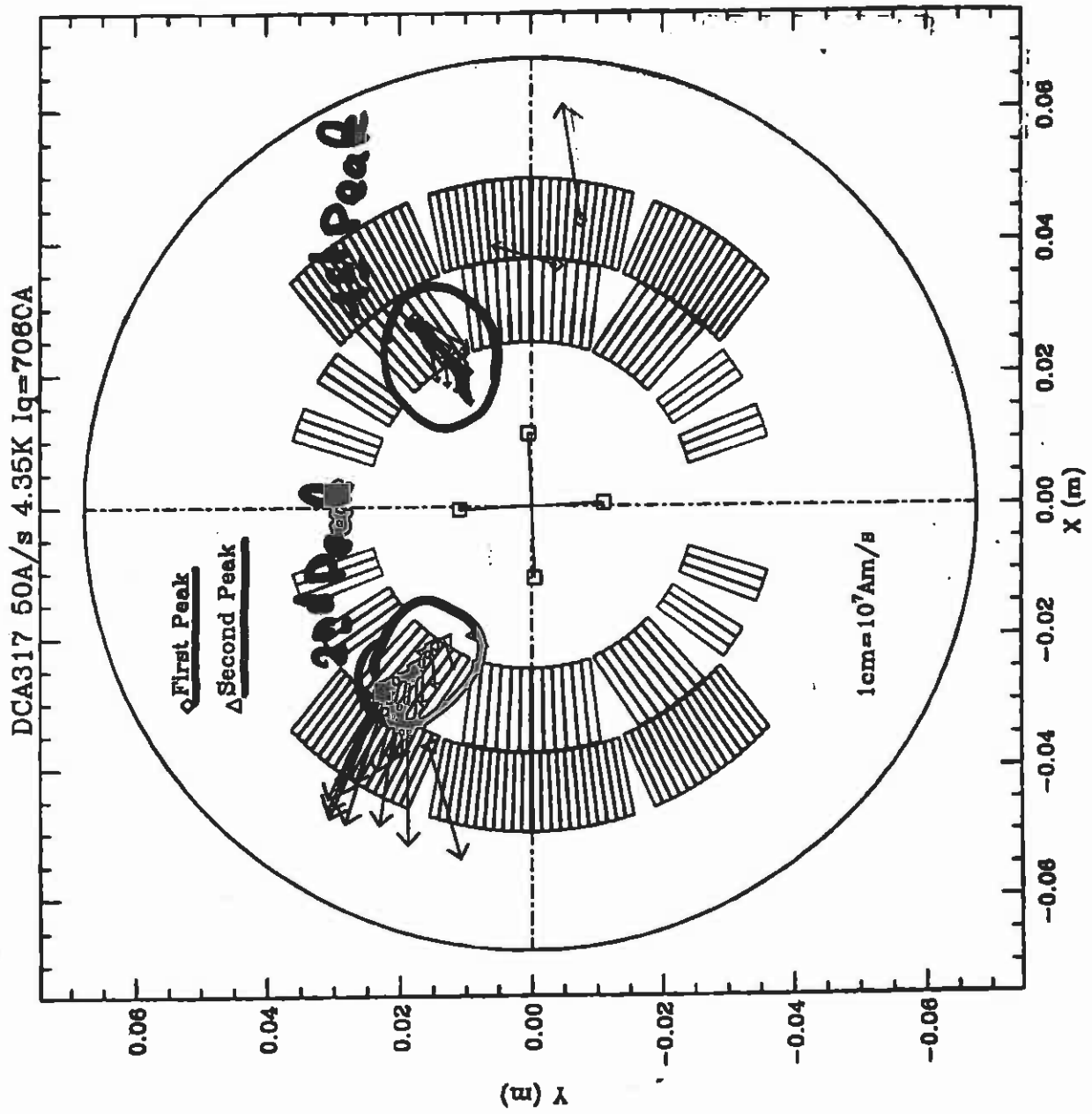
DCA317 50A/s 4.35K Iq=706CA
First Peak
Second Peak
1cm=10⁷Am/s
X (m)
Y (m)
0.06
0.04
0.02
0.00
-0.02
-0.04
-0.06

LECTURE 9: QUENCH PROTECTION OF PARTICLE ACCELERATOR MAGNETS

9.1 Quench Development
9.1.1 Simple Theoretical Model
9.1.2 Measuring Quench Propagation Using Voltage Taps
9.1.3 Measuring Quench Propagation Using Quench Antenna
9.1.4 Review of Propagation Velocity Measurements

9.2 The Effects of a Quench

9.3 Hot Spot Temperature

9.4 Quench Detection

9.5 Quench Protection Heaters

9.6 Protection of a Single Magnet

9.7 Protection of a Magnet String

SSC/FNAL 5-cm-Apert., 15-m-long Dipole

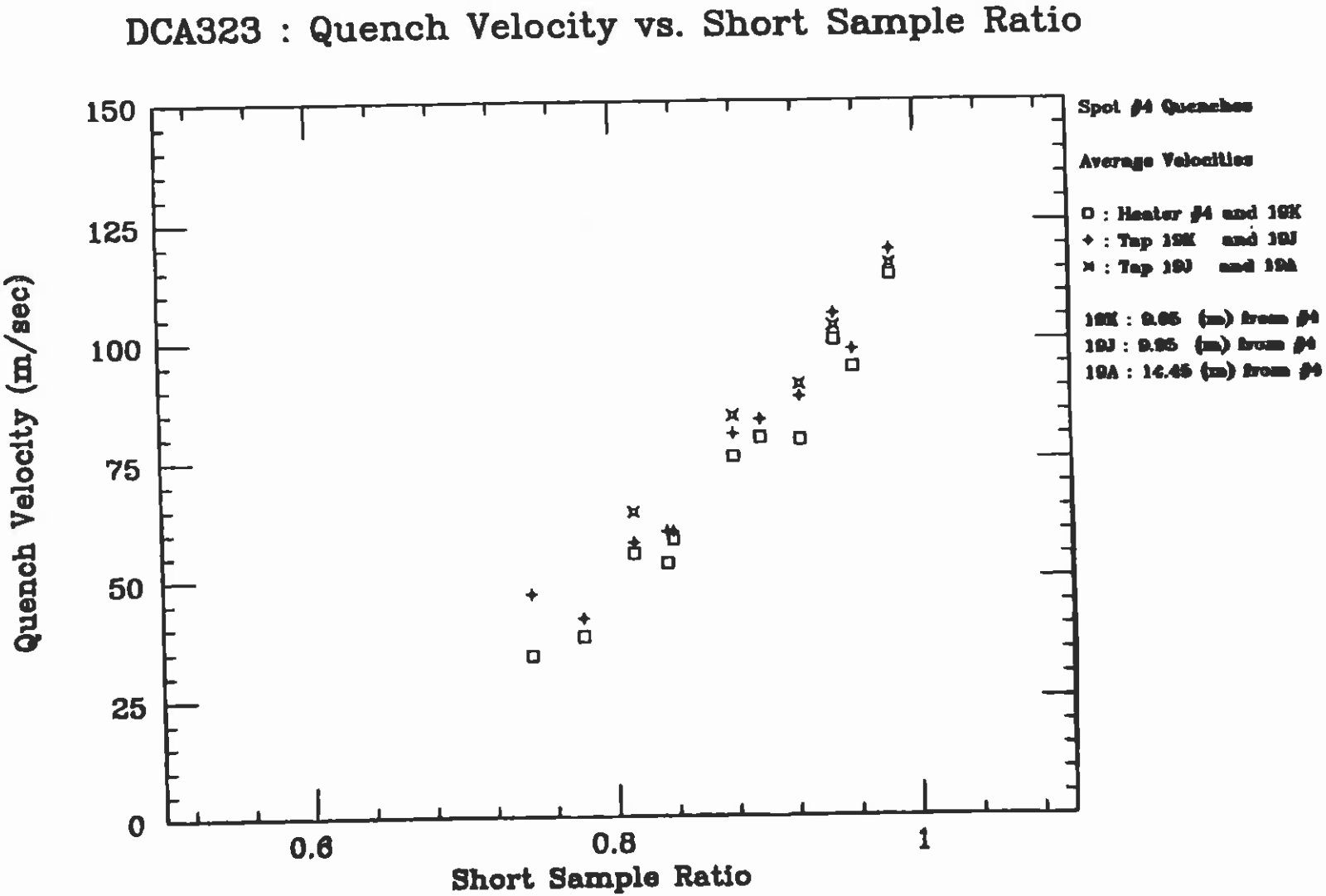

LONGITUDINAL VELOCITY VERSUS FRACTION OF SHORT SAMPLE

(SSC/BNL 4-cm-Apert., 17-m-Long Dipoles)

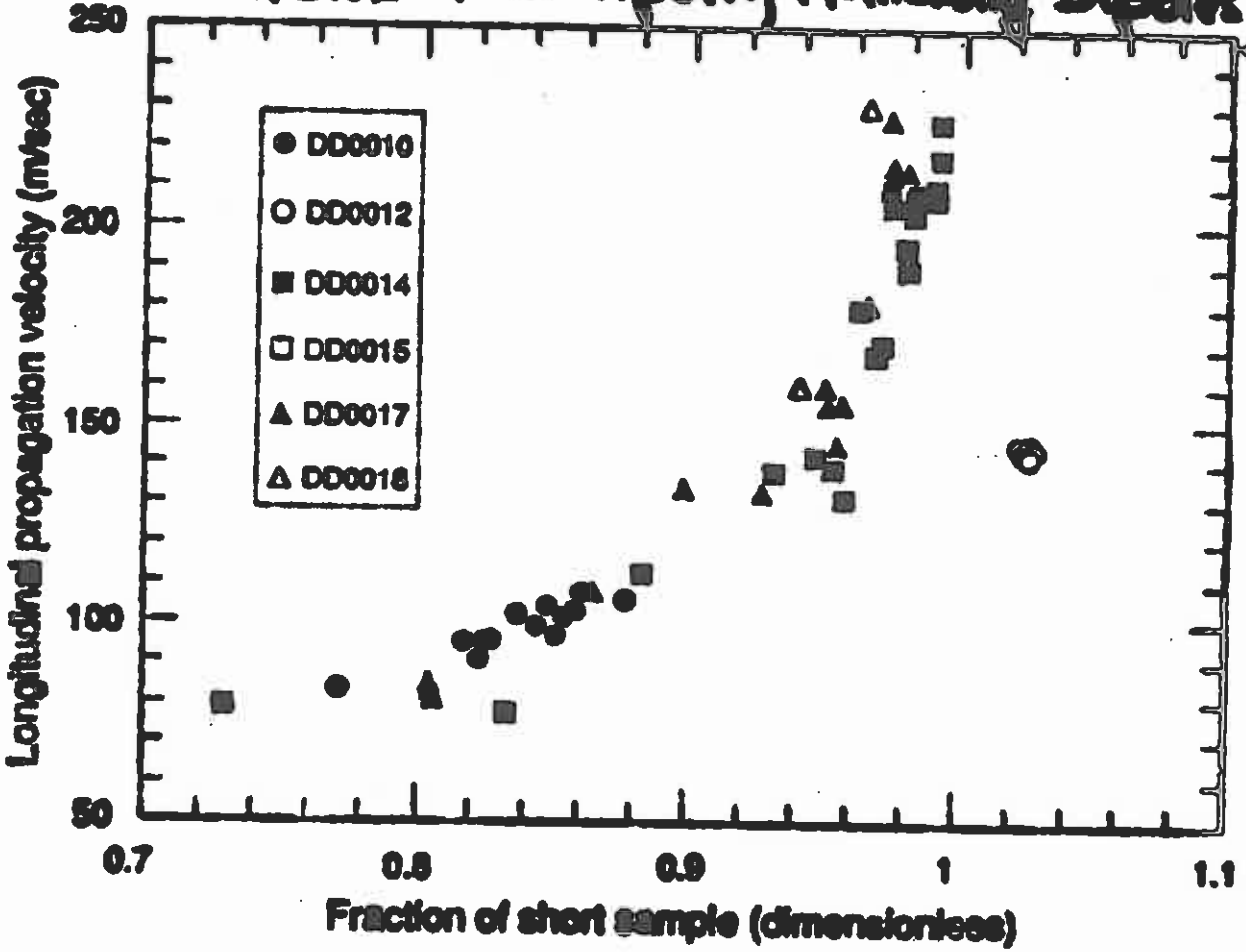

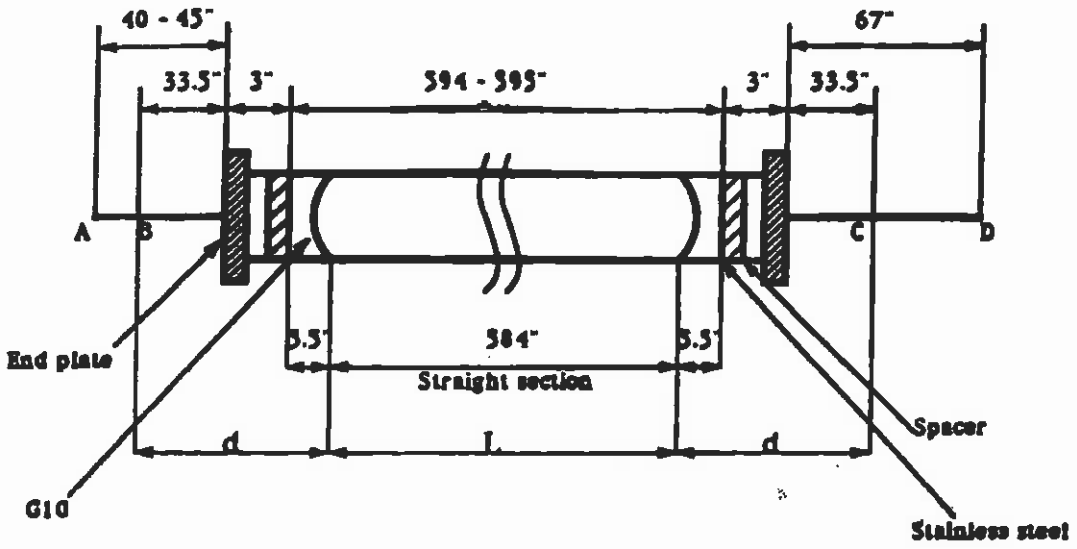

Lead end **Non-lead end**

A,D : Locations of 25 Bar Siemens Transducer (Siemens 5F10)
B, C : Locations of 10 Bar Siemens Transducer (Siemens 5F25)
Distance between B and C : 668"

Fig. 7 Locations of CPT sensors

Location of Pressure Transducers at FNAL/MTF (5-00-Apert. Dipole)

SSC/BNL 4-cm-Apert., 17-m-long Dipole Magnet

Figure 2 V-Tap and CPT Signals during Quench

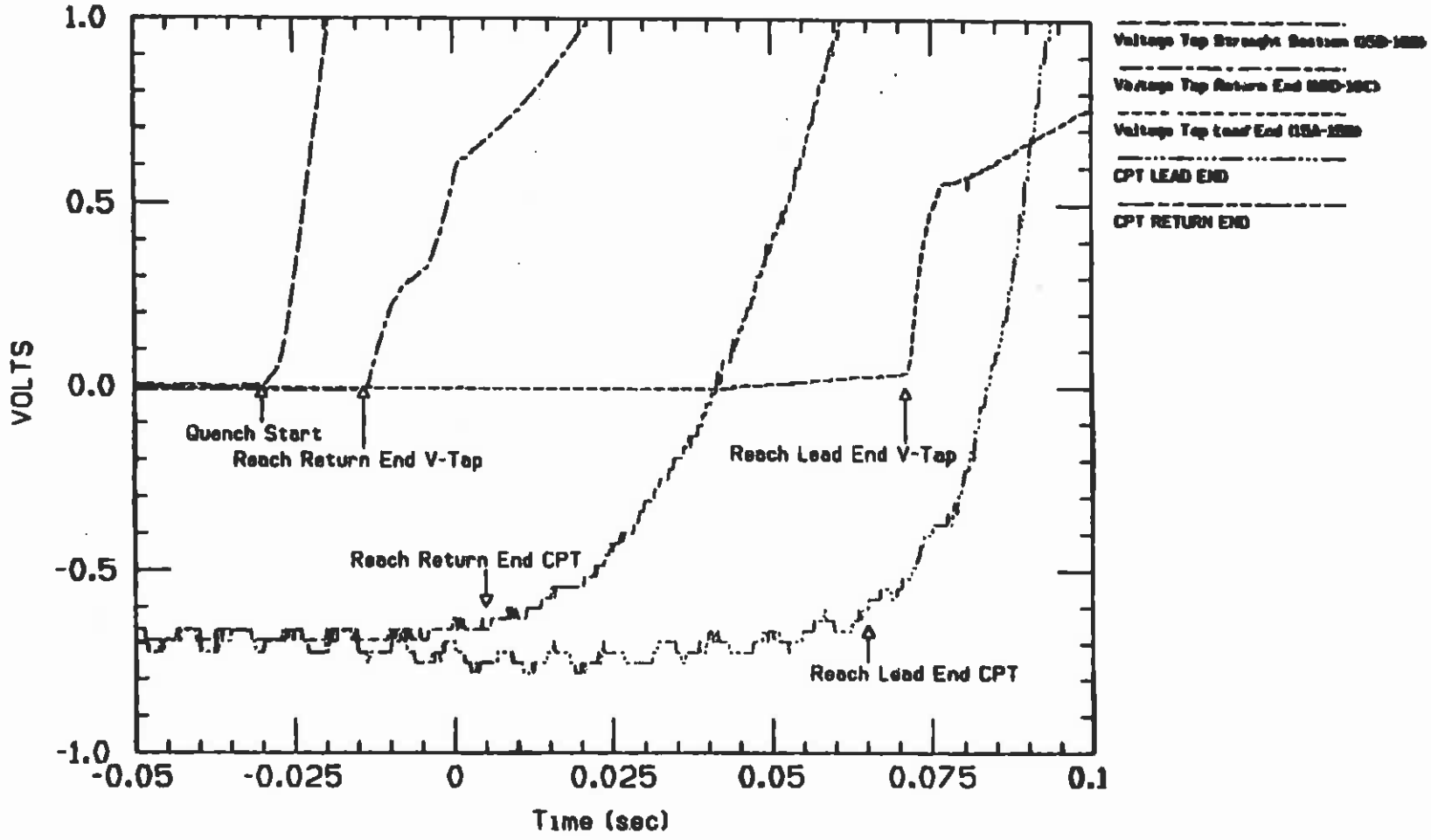

DC0204 Data File No. : 46 19-NOV-90 21:48:54 Quench No. : 0 Current = 6935.0

SSC/BNL 4-cm-Apert., 17-m-long Dipoles

Fig.1 Time to Reach CPT vs Quench Localization

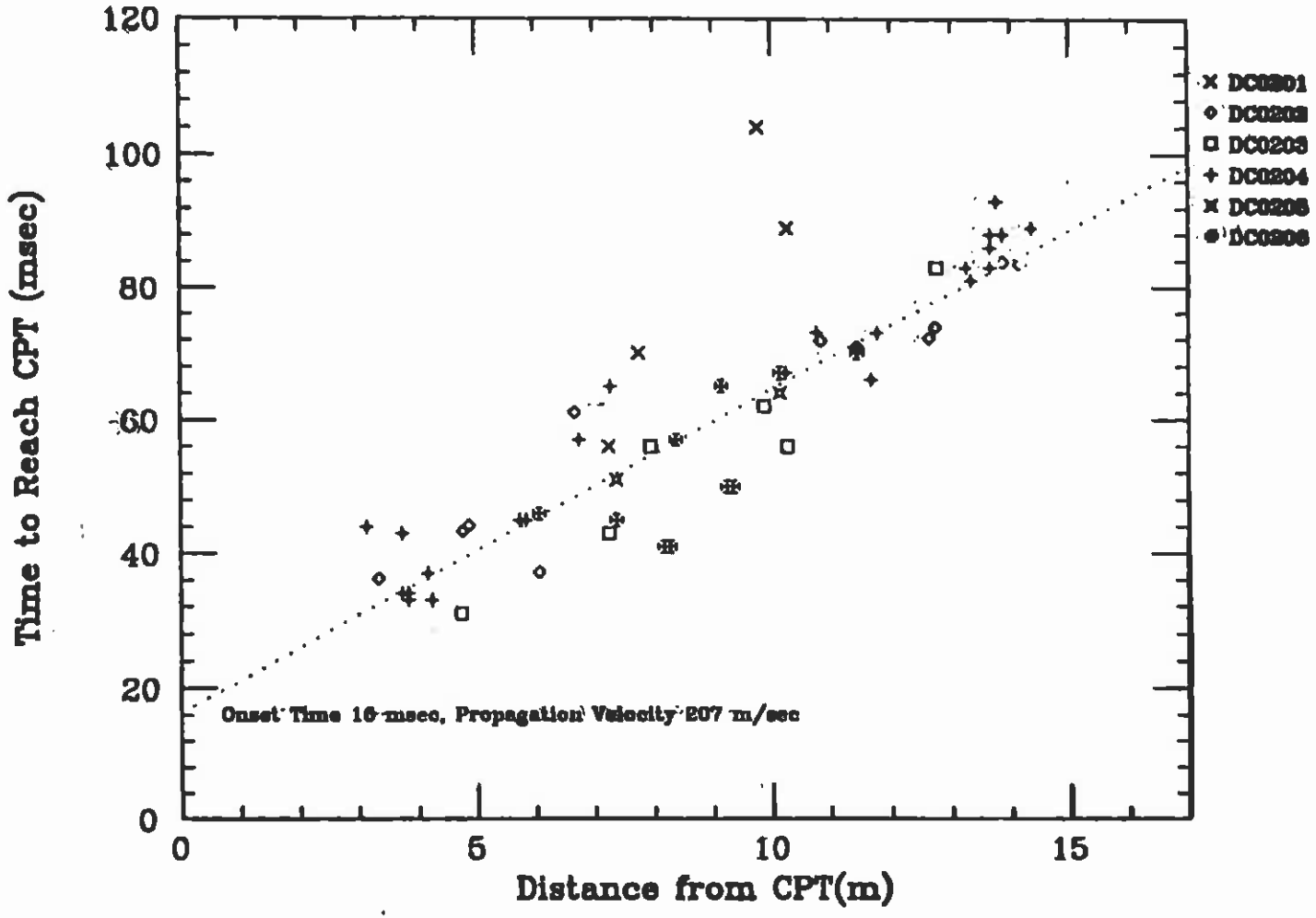

Case of a limited volume of Helium

Computer simulations predict a Thermal Hydraulic Quench back*

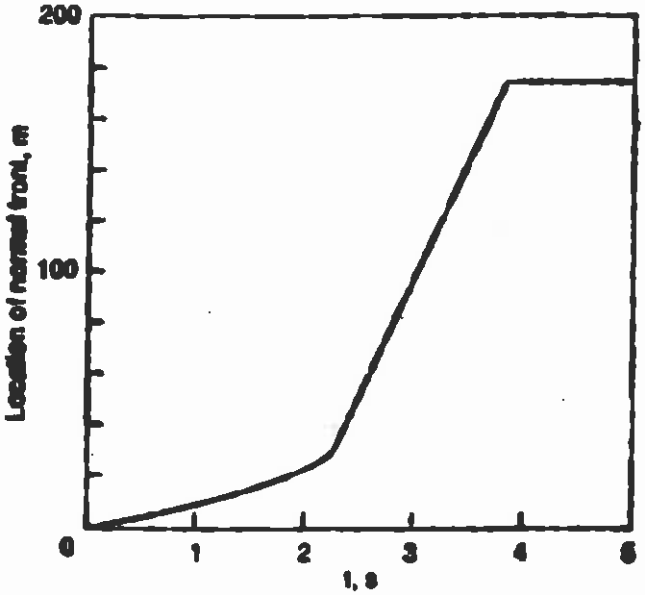

Figure 12. Simulation of Experimental Data of Walters et al. Normal Front Propagation in 4.2 K Helium

⇒ Maybe the case for SSC dipoles, but needs more study.

*C.A Luongo, et al, 1989.

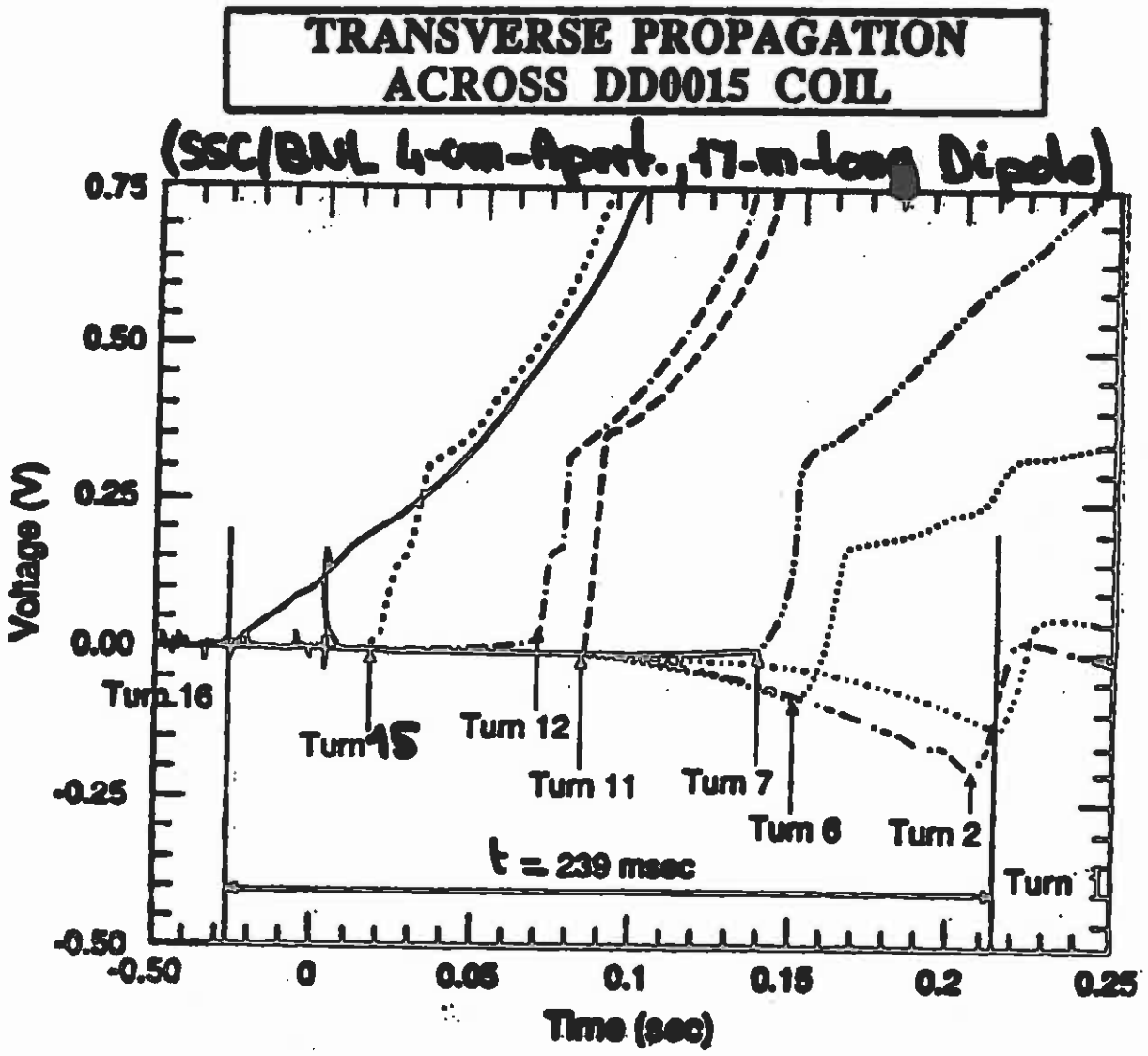

$$\omega = \frac{\eta}{\tau}$$

$I = 5625$ A
$T_0 = 4.39$ K

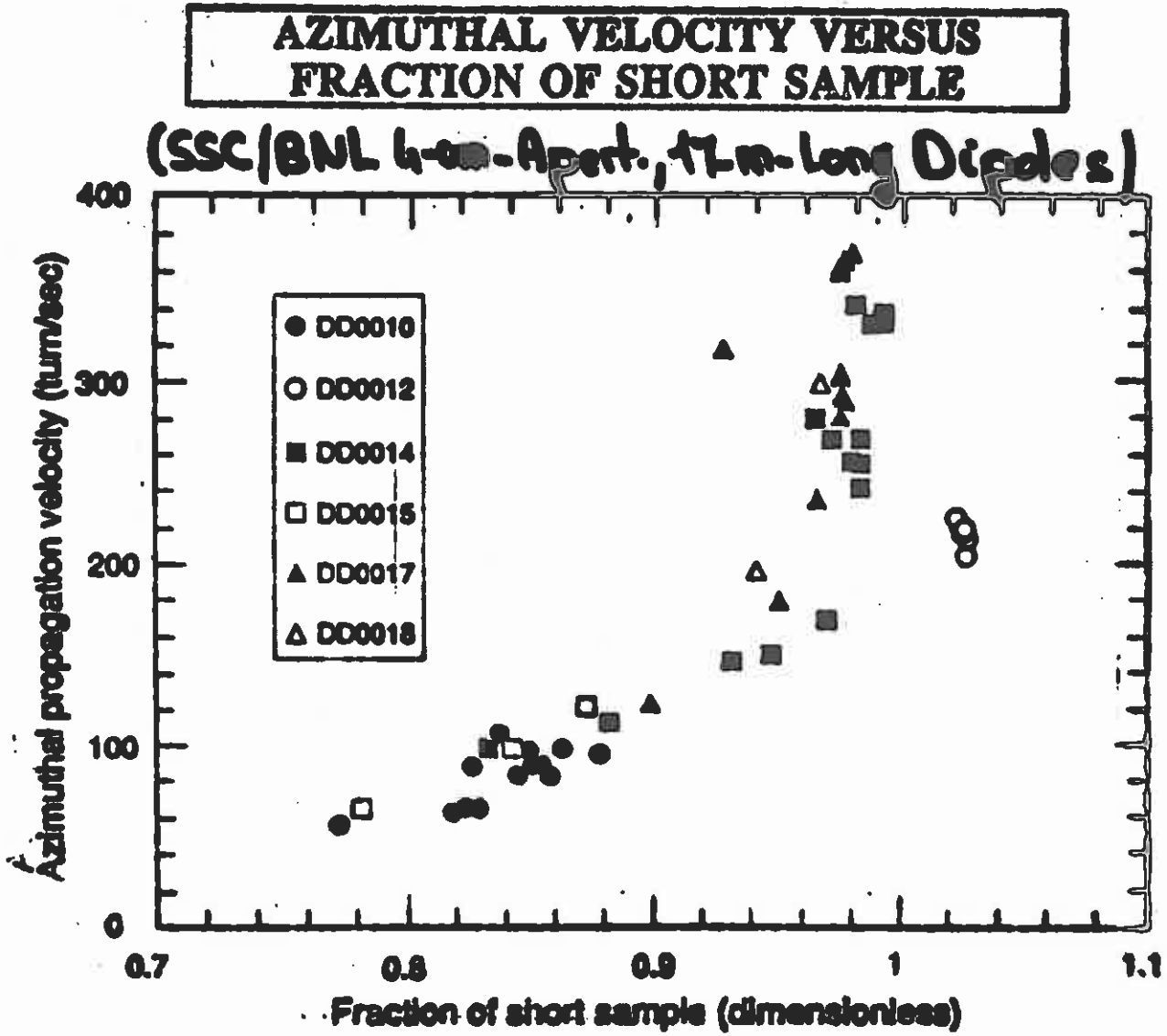
AZIMUTHAL VELOCITY VERSUS
FRACTION OF SHORT SAMPLE
(SSC/BNL 4-cm-Apert., 17-m-Long Dipoles)
Azimuthal propagation velocity (turn/sec)
Fraction of short sample (dimensionless)
DD0010
DD0012
DD0014
DD0015
DD0017
DD0018
0
100
200
300
400
0.7
0.8
0.9
1
1.1

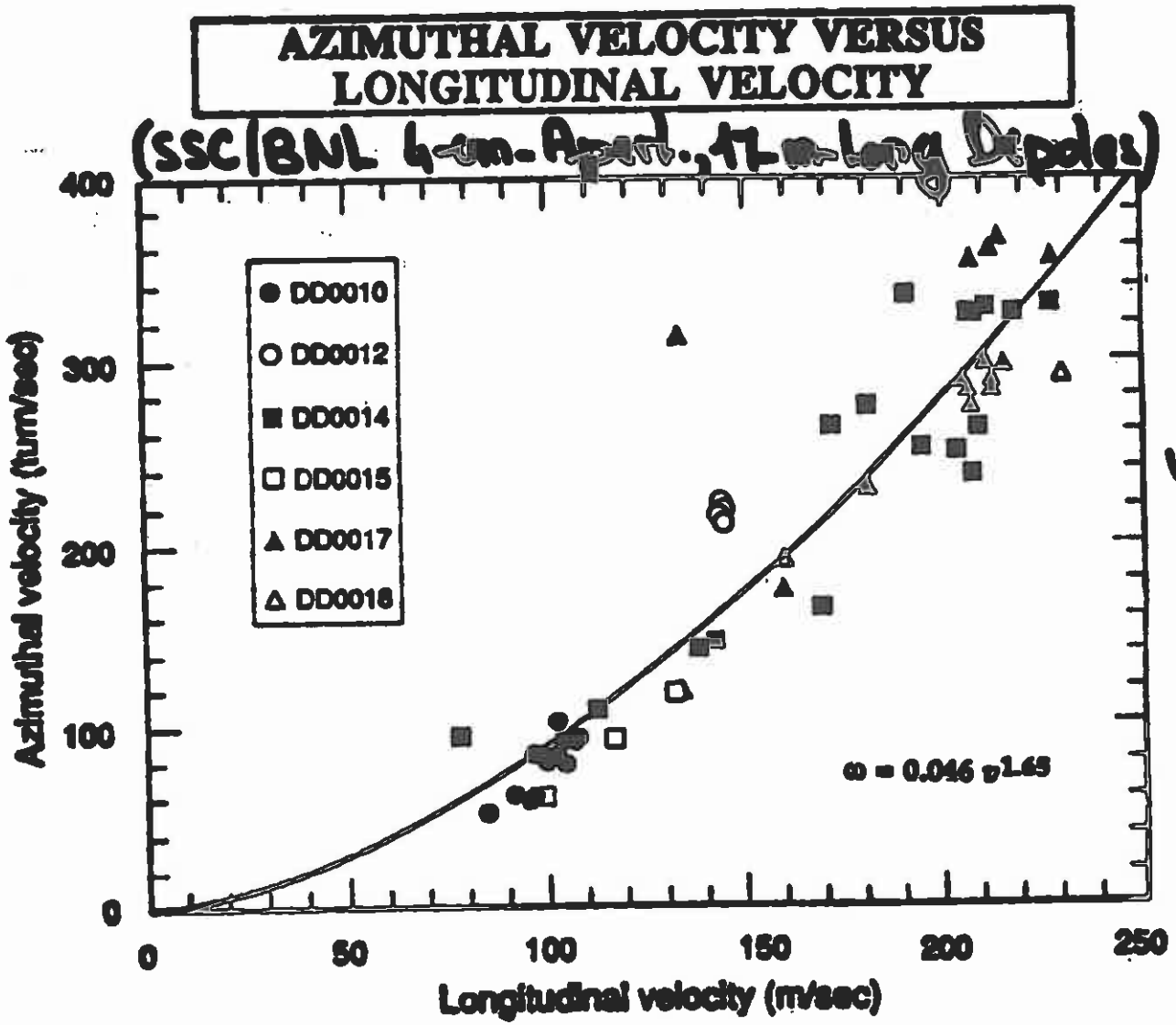

$\omega = 0.046$
$\times v^{1.65}$

LECTURE 9: QUENCH PROTECTION OF PARTICLE ACCELERATOR MAGNETS

9.1 Quench Development
- 9.1.1 Simple Theoretical Model
- 9.1.2 Measuring Quench Propagation Using Voltage Taps
- 9.1.3 Measuring Quench Propagation Using Quench Antenna
- 9.1.4 Review of Propagation Velocity Measurements

9.2 The Effects of a Quench

9.3 Hot Spot Temperature

9.4 Quench Detection

9.5 Quench Protection Heaters

9.6 Protection of a Single Magnet

9.7 Protection of a Magnet String

THE EFFECTS OF A QUENCH

– Although most R&D programs have been successful in developing magnet designs that can be mass-produced and meet accelerator requirements, quenches do occur in accelerator operations.

These quenches must be handled in order to avoid any damage of the quenching magnet, to ensure the safety of the installation and to minimize down time.

– As we have seen in the section on what is a quench, once a small volume of conductor has switched to the normal resistive state, it dissipates power by the Joule effect.

A fraction of this dissipated power is transferred to the surroundings of the initial volume of transition (either along the conductor, or, transversely, to the conductor insulation or the helium), but the main part is consumed locally in overheating the conductor.

In a very short time (a few tenths of a second in the case of a dipole or quadrupole magnet) the conductor temperature, initially that of the helium, reaches room temperature, and, if the magnet is not discharged, keeps on increasing.

MAXIMUM TEMPERATURE REQUIREMENTS

– The temperature rise consecutive to a quench must be limited for at least three reasons:

• *To restrict the thermal stresses* induced in the quenching coil,

• *To prevent degradation of superconductor properties,*

• *To avoid insulation damage.*

MAXIMUM TEMPERATURE REQUIREMENTS (CONT.)

– For most materials, thermal expansion starts to be significant for temperatures above 100 K.

– The critical current density of NbTi is affected by exposure to temperatures above 250 °C.

The degradation amplitude depends on the temperature level and on the duration of the exposure: at 250 °C, it takes of the order of 1 hour to get a significant degradation, while it may take less than a minute at 400–450 °C.

This degradation results from a growth of the β-phase grains in the NbTi alloy microstructure, which affects the distribution of α-Ti precipitates and alters pinning. (The α-Ti precipitates get dissolved for temperatures above 600 °C).

– Finally, the polyimide materials used to insulate NbTi cables lose most of their mechanical properties for temperatures above 500 °C.

– It follows that an upper limit for conductor heating consecutively to a quench is 400 °C.

Most magnets are designed not to exceed 300 to 400 K, and whenever possible, the limit should be set to 100 K.

PROTECTING A QUENCHING MAGNET

– The source of conductor heating in a quenching magnet is power dissipation by the Joule effect.

– Power keeps being dissipated as long as there is current in the magnet coil.

– To eliminate the heat source and limit the temperature rise, it is thus necessary to ramp the current down.

ON THE NEED OF QUENCH HEATERS

– To discharge a quenching magnet, all its stored magnetic energy must be converted into resistive power.

– If the quench propagates very slowly, and the zone where the conductor has switched to the normal state remains confined to a small volume, there is a risk that a large fraction of the stored energy be dissipated in this volume.

In the case of a string of magnets connected electrically in series, it may even happen that the energy of the whole string be dissipated in the quenching magnet.

– Hence, to prevent burnout, it is desirable to maximize the volume in which the energy is dissipated by ensuring that the normal resistive zone spreads rapidly throughout the quenching coil.

– This can be done by means of heaters, implemented near the magnet coils and fired as soon as a quench is detected.

These heaters are referred to as *quench protection heaters.*

PROTECTION OF RHIC DIPOLE MAGNETS

– In comparison to other superconducting magnets, most accelerator magnets do require an active quench protection system because of the rapidity of the temperature rise resulting from the high current density and the low fraction of stabilizing copper in the cable strands.

– One notable exception are the RHIC dipole magnets, whose one-layer coil assemblies are wound from a cable with a high copper-to-superconductor ratio (2.25 to 1), and which do not rely on quench protection heaters.

LECTURE 9: QUENCH PROTECTION OF PARTICLE ACCELERATOR MAGNETS

9.1 Quench Development
- 9.1.1 Simple Theoretical Model
- 9.1.2 Measuring Quench Propagation Using Voltage Taps
- 9.1.3 Measuring Quench Propagation Using Quench Antenna
- 9.1.4 Review of Propagation Velocity Measurements

9.2 The Effects of a Quench

9.3 Hot Spot Temperature

9.4 Quench Detection

9.5 Quench Protection Heaters

9.6 Protection of a Single Magnet

9.7 Protection of a Magnet String

HOT SPOT TEMPERATURE

– The volume of conductor that heats up the most significantly during a quench is the spot where the quench first originated.

It is called the *hot spot.*

– An upper limit of the hot spot temperature, T_{max}, can be determined by assuming that, near the hot spot, all the power dissipated by the Joule effect is used to heat up the conductor.

– Then, near the hot sport, the heat balance equation reduces to

$$C(T)\,\frac{\mathrm{d}T}{\mathrm{d}t} = \rho(T)\left[\frac{I(t)}{S}\right]^2$$

where C is the overall specific heat per unit volume of conductor, ρ is the overall conductor resistivity in the normal state, S is the conductor cross-sectional area and $I(t)$ is the current at time t.

MIIT INTEGRAL

– The previous equation can be rewritten:

$$S^2 \frac{C(T)}{\rho(T)}\, \mathrm{d}T = I(t)^2 \mathrm{d}t$$

where the left member only depends on temperature and on cable properties, and the right member only depends on time and on current decay characteristics.

– By integration over the duration of a quench, we get:

$$\frac{S^2}{10^6} \int_{T_0}^{T_{max}} \mathrm{d}T\, \frac{C(T)}{\rho(T)} = MIIT$$

where t_0 is the time of quench start, T_0 is the coil temperature at t_0, and $MIIT$ is the Mega I times I versus time Integral defined as:

$$MIIT = \frac{1}{10^6} \int_{t_0}^{+\infty} \mathrm{d}t\ I(t)^2$$

ESTIMATING HOT SPOT TEMPERATURE FROM NUMBER OF MIITS

– The value of the MIIT integral, referred to as *number of MIITs* can be computed using current data recorded during a quench.

– The number of MIITs can then be compared to tabulated values of the integral:

$$\frac{S^2}{10^6}\int_{T_0}^{T_{max}} dT\ \frac{C(T)}{\rho(T)}$$

and converted into an estimated T_{max}.

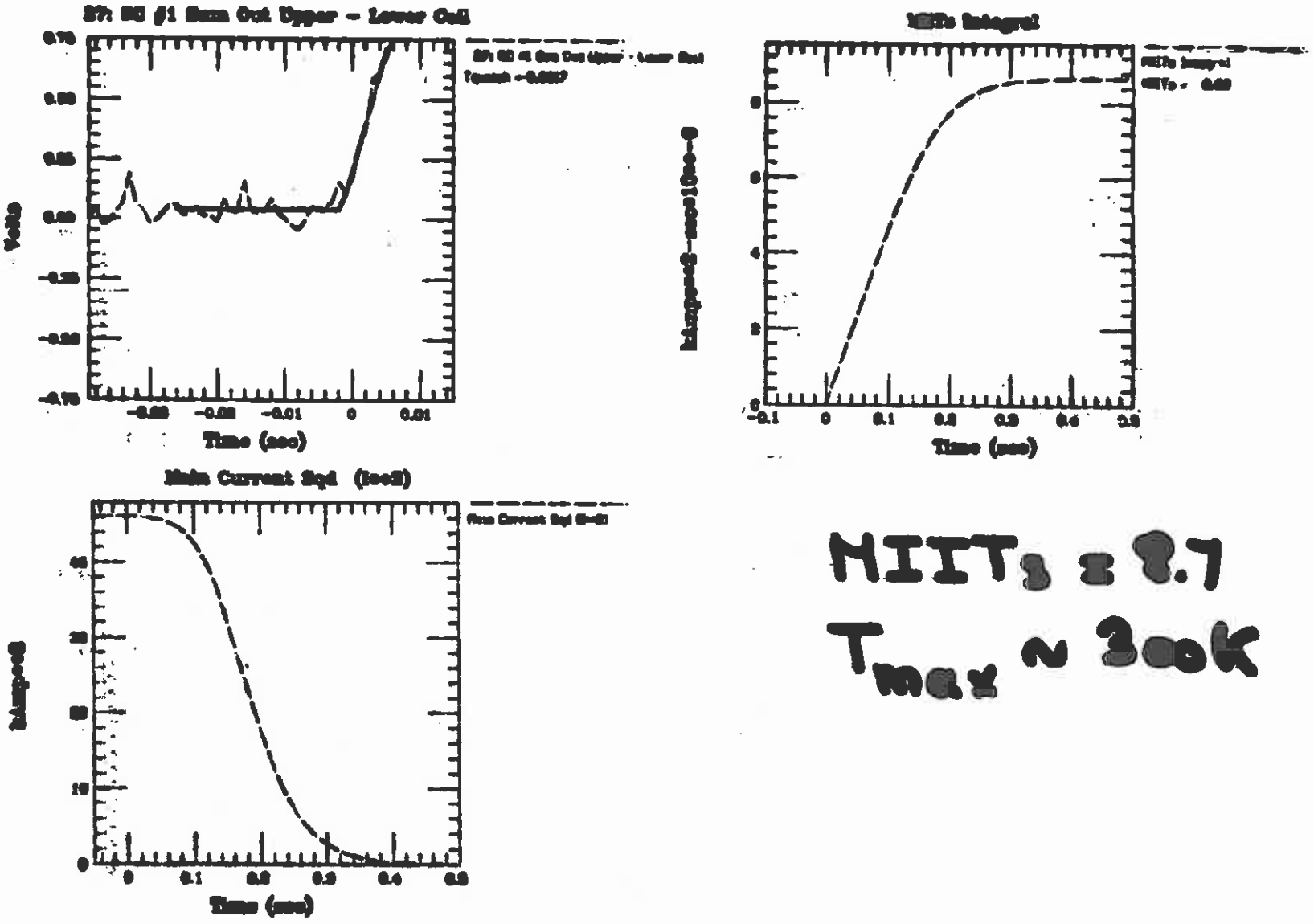
Time (sec)
Time (sec)
Time (sec)
MIIT$_3$ ≈ 8.7
T_{max} ~ 300K
4-cm-Apert. SSC Dipole DD0028 - I_q = 6781 A - Inner Coil

4-cm-Apert. SSC Dipole

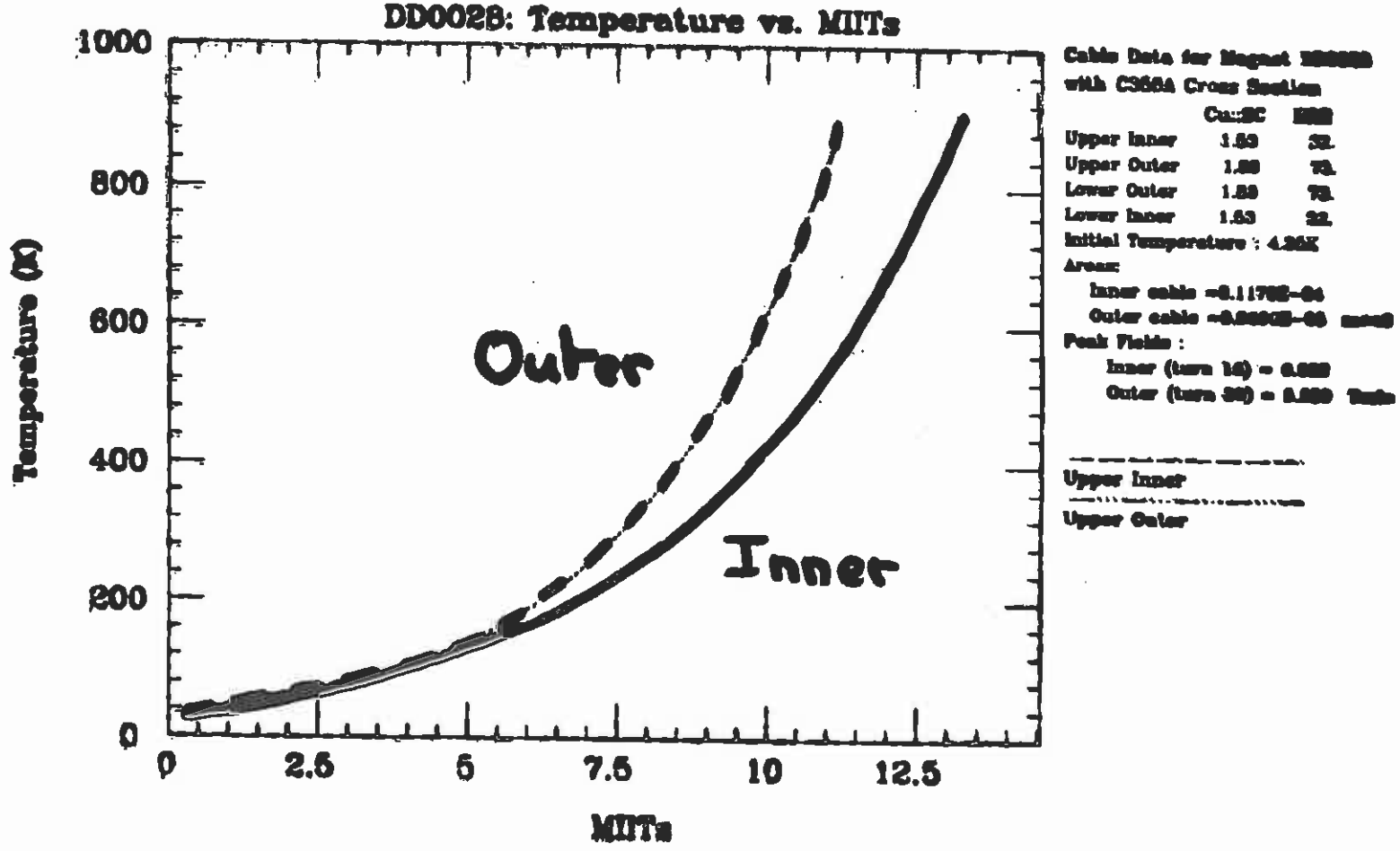

COMPARISON BETWEEN COMPUTED T_{MAX} AND MEASURED HOT SPOT TEMPERATURE

– **The maximum temperatures computed from the numbers of MIITs have been shown to be in fairly good agreement with actual measurements of hot spot temperatures on quenching magnets.**

How to Measure the Hot-Spot Temperature?

From the apparent resistance of a short length of conductor around the hot spot

$$\rho_{Cu}(RRR, T, B) \simeq \frac{r_{cus}}{1 + r_{cus}} \frac{S}{L} \frac{U}{I}$$

where

- L and S are the length and X-sectional area of conductor
- r_{cus} : copper-to-superconductor ratio
- RRR: copper residual resistivity ratio

$\Rightarrow$ Spot heater closely surrounded by 2 voltage taps

Fracture and Deformation Div., NBS, Boulder, CO
9-13-67 E.J.S., R.P.R

CRYOGENIC PROPERTIES OF COPPER AND COPPER ALLOYS

MATERIAL	C10100 – C10700 COPPER (ANNEALED, COLD-WORKED)	PROPERTY	ELECTRICAL RESISTIVITY vs. TEMPERATURE, RRR

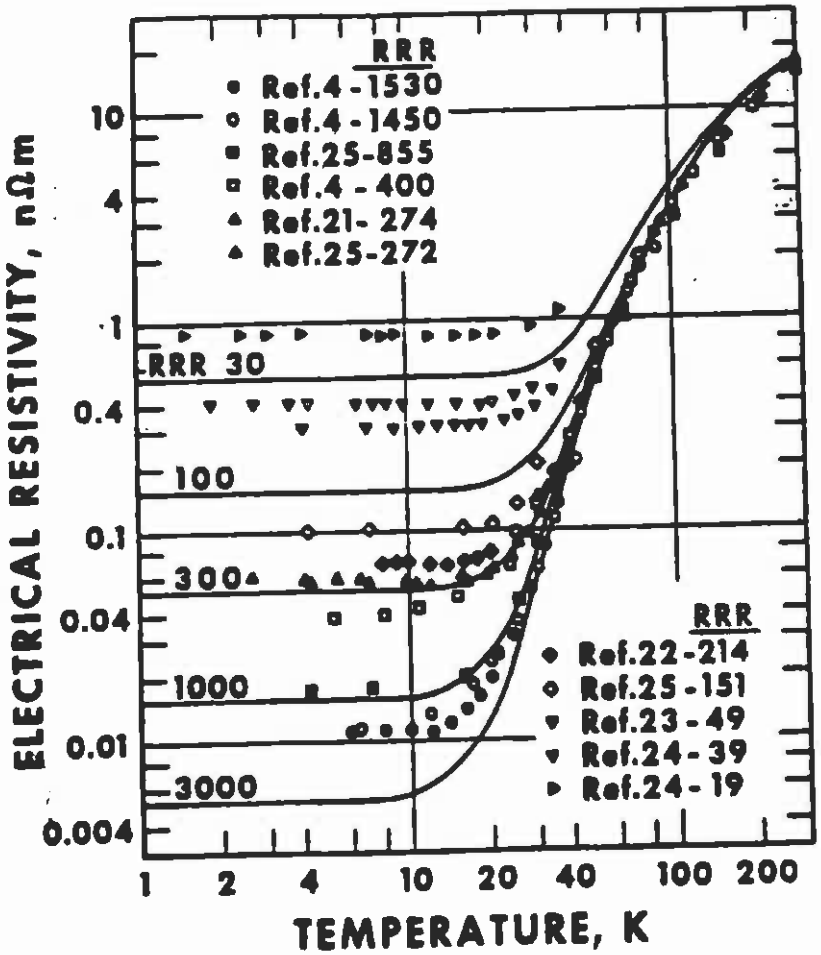

Figure 1. The data shown were used in the analysis described in Reference 27 to compute the constants for Equation (1). The curves represent Equation (1) for the series of RRR values indicated.

DD0017 VOLTAGE TAP SCHEMATIC

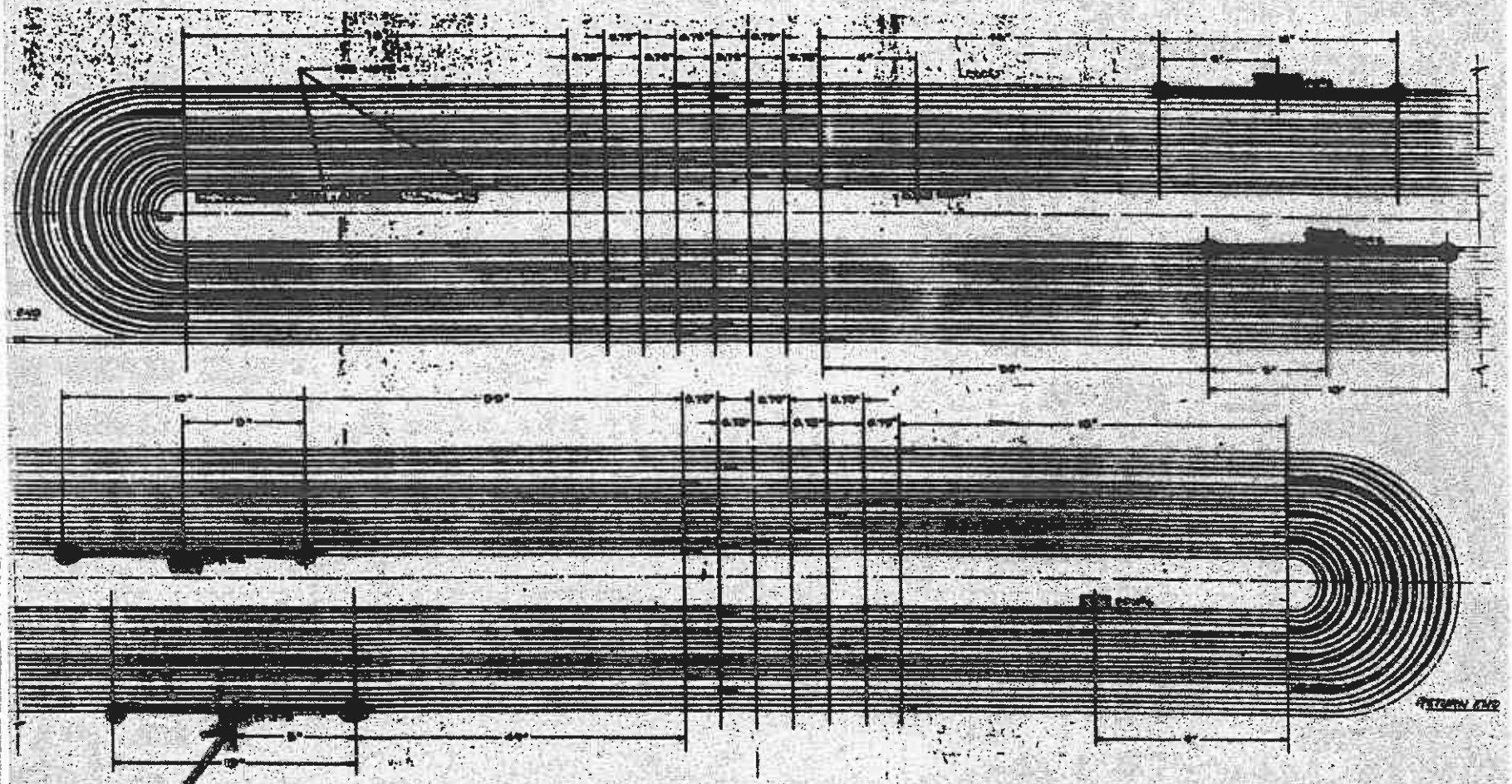

TYPICAL CURRENT DECAY

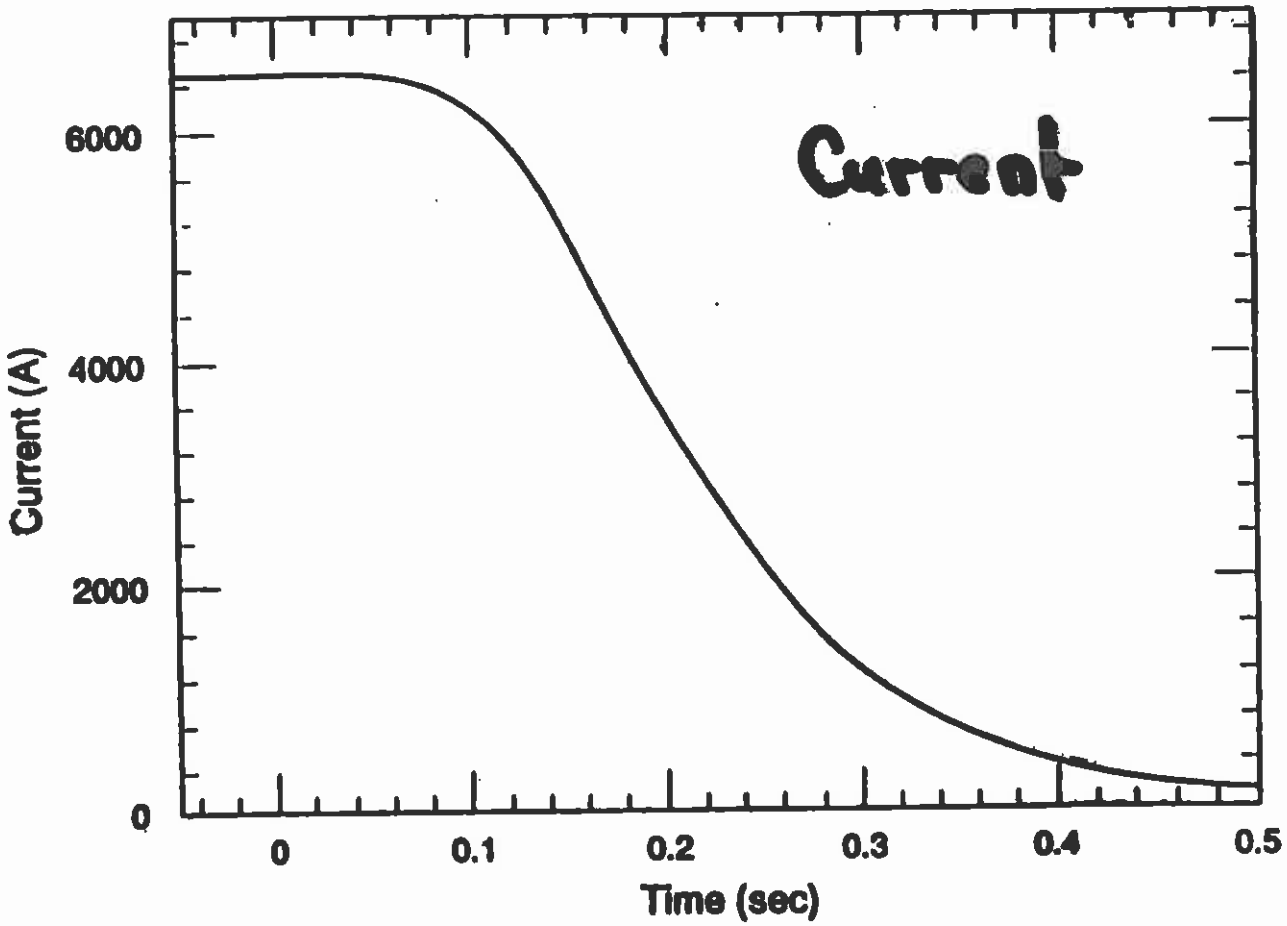

TYPICAL VOLTAGE EVOLUTION ACROSS SPOT-HEATER TAPS

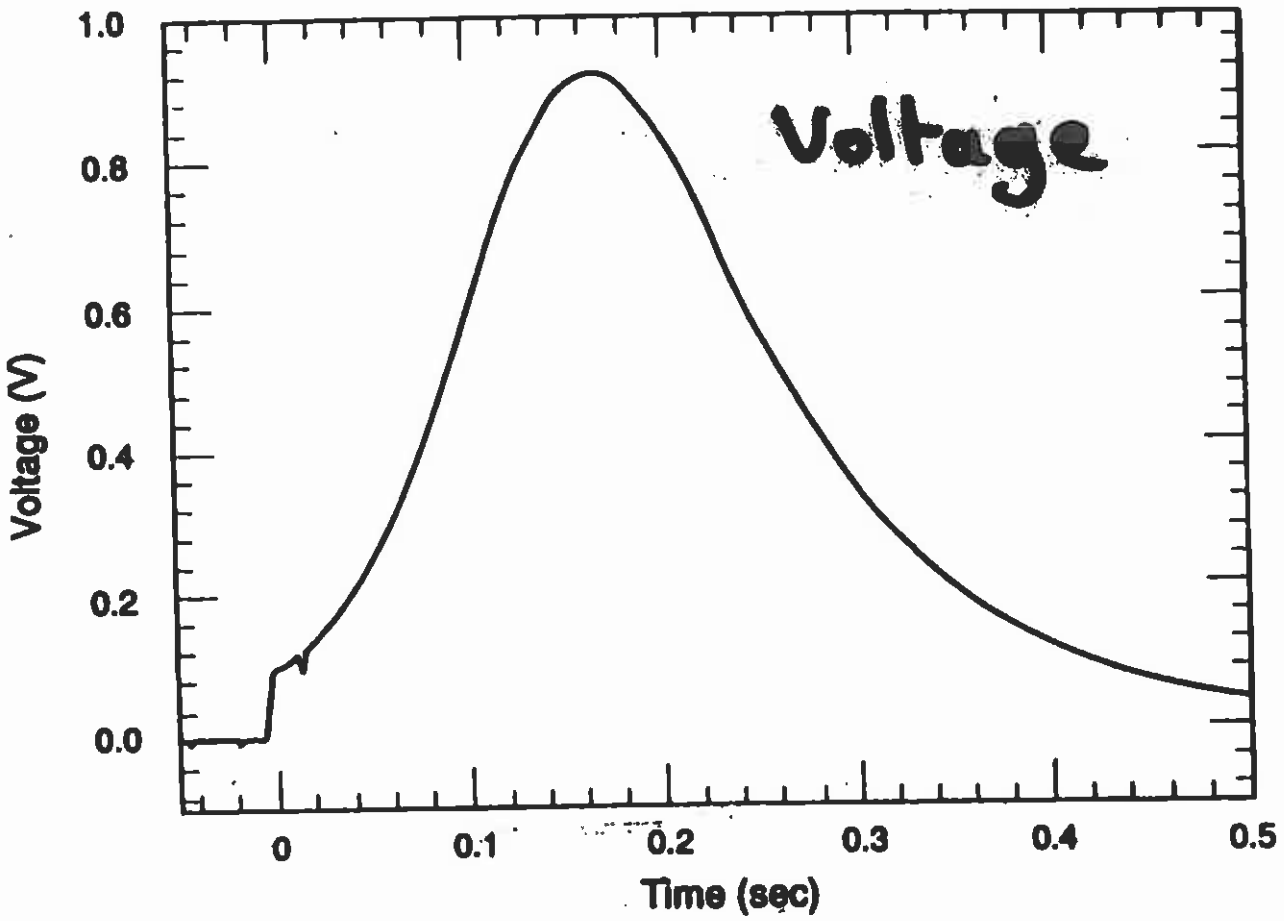

TYPICAL TEMPERATURE RISE (INNER-LAYER QUENCH)

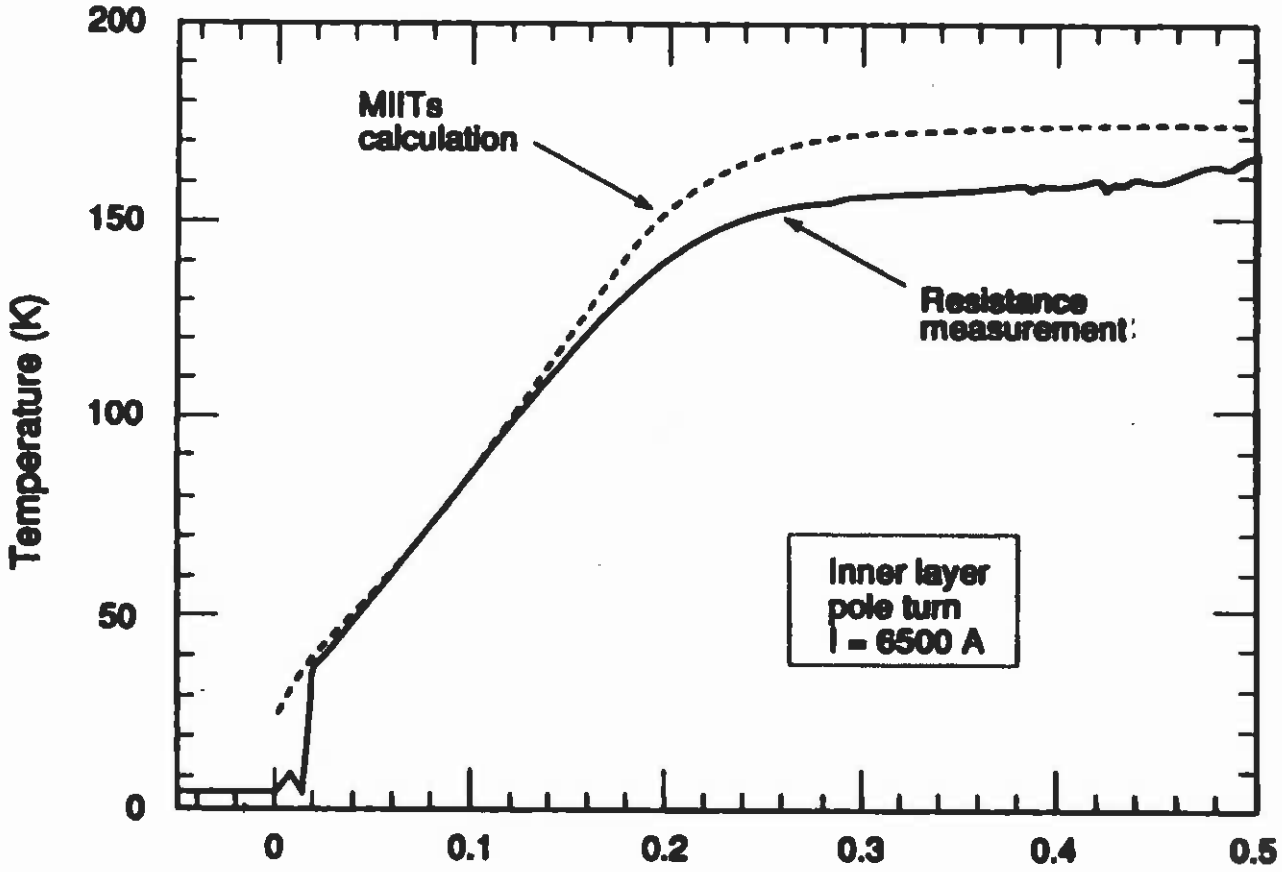

4-cm-Apert. SSC Dipole

TEMPERATURE VERSUS MIITs CORRELATIONS

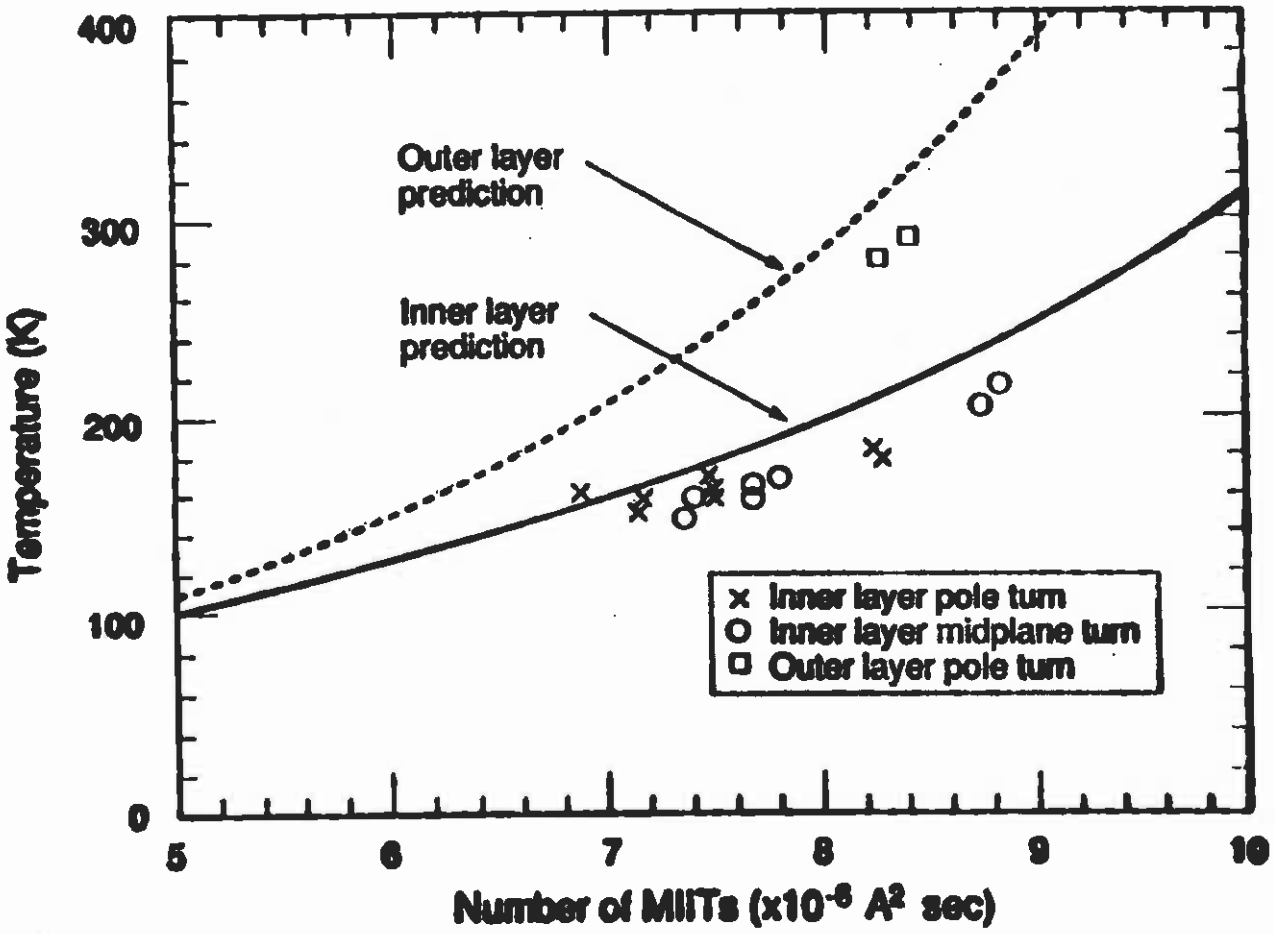

TEMPERATURE DISTRIBUTION CONSECUTIVELY TO A QUENCH

– The same analyses can be performed to determine the average temperatures reached consecutively to a quench in various coil sections instrumented with voltage taps.

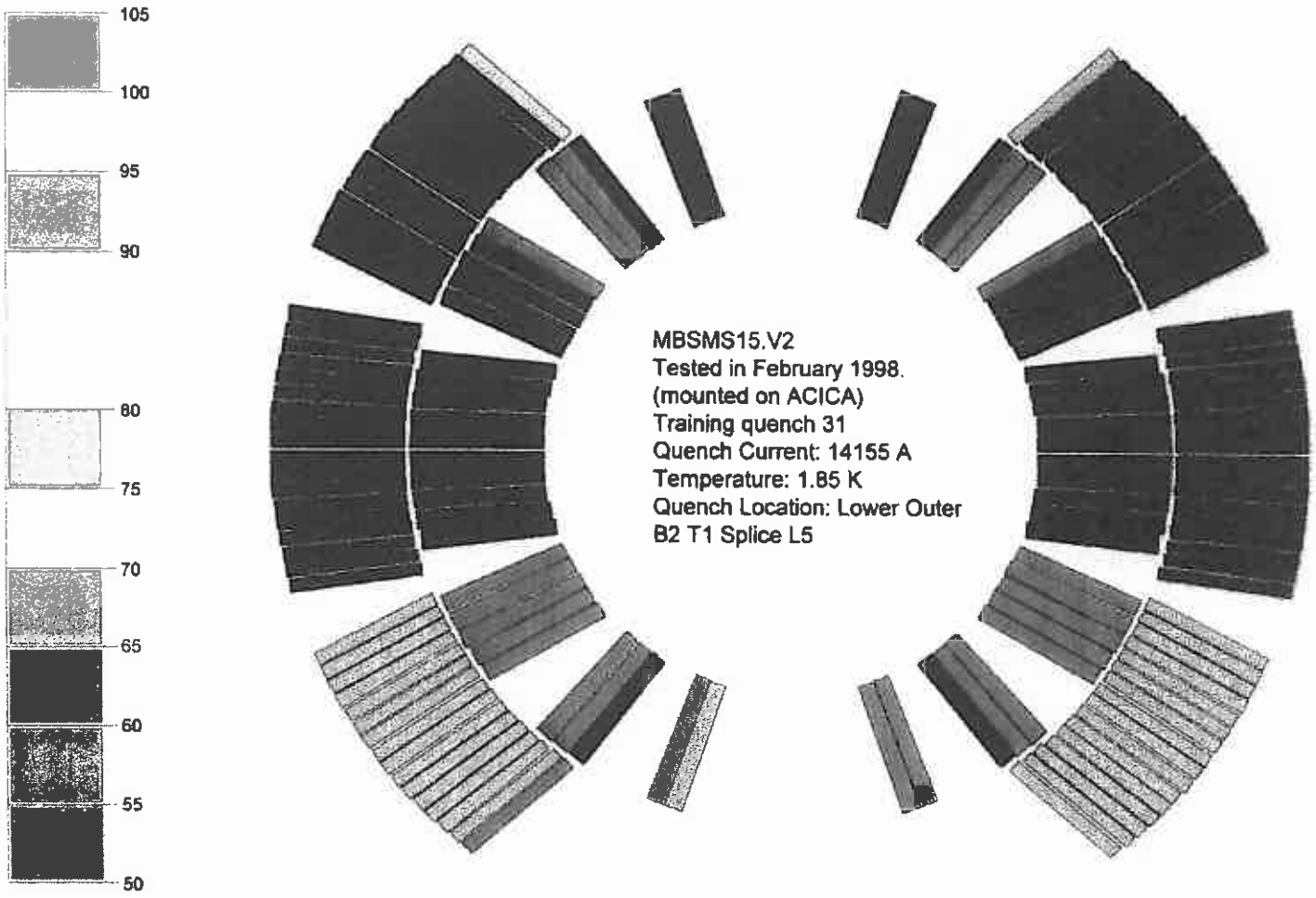

Courtesy A. Siemko

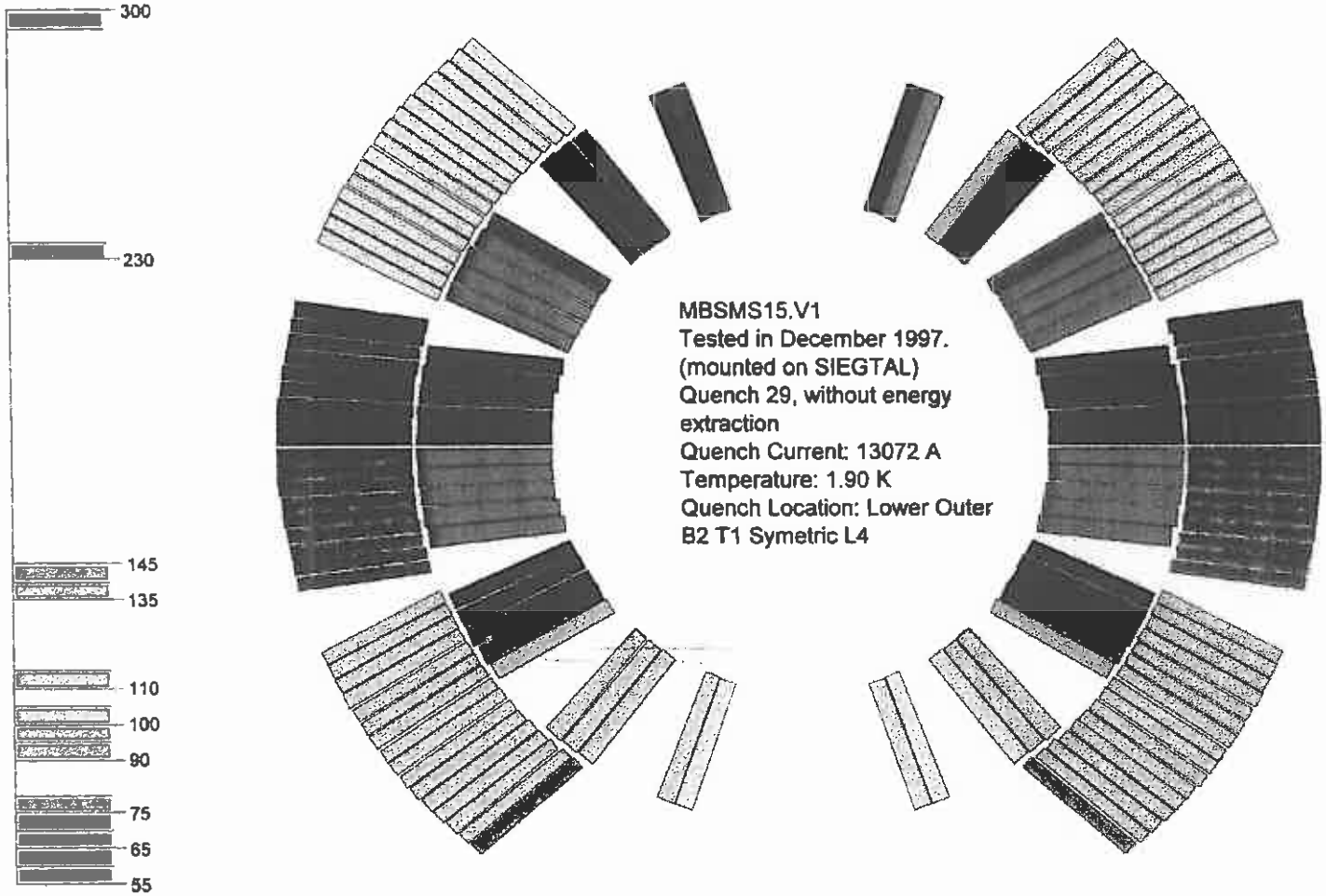

Courtesy A. Siemko

LIMITING HOT SPOT TEMPERATURE

– The hot spot temperature can be limited by acting on either member of the equation:

$$\frac{S^2}{10^6}\int_{T_0}^{T_{max}} dT\,\frac{C(T)}{\rho(T)} = MIIT$$

– Regarding the left member, the only conceivable action is to reduce the overall conductor resistivity by increasing the copper-to-superconductor ratio.

However, and as explained in the conductor section, the copper-to-superconductor ratio must also be optimized to ensure a high overall critical current.

– Regarding the right member, the number of MIITs can be minimized by:

• *Detecting the quench* as soon as possible,

• *Turning off the power supply* (case of a single magnet) or *forcing the current to bypass the quenching magnet* (case of a magnet string),

• *Firing quench protection heaters,*

• *Discharging* the quenching magnet or the magnet string.

LECTURE 9: QUENCH PROTECTION OF PARTICLE ACCELERATOR MAGNETS

9.1 Quench Development
- 9.1.1 Simple Theoretical Model
- 9.1.2 Measuring Quench Propagation Using Voltage Taps
- 9.1.3 Measuring Quench Propagation Using Quench Antenna
- 9.1.4 Review of Propagation Velocity Measurements

9.2 The Effects of a Quench

9.3 Hot Spot Temperature

9.4 Quench Detection

9.5 Quench Protection Heaters

9.6 Protection of a Single Magnet

9.7 Protection of a Magnet String

QUENCH DETECTION

– The magnets are connected to quench detection systems which monitor the occurrence of a resistive voltage in the coil windings or the coils leads.

– The resistive voltage has to be discriminated from inductive voltages arising from magnet ramping.

– The inductive components are cancelled out by considering voltage differences across two identical coil assemblies or two identical parts of a given coil assembly (*e.g.*, the upper and lower half coils in a dipole magnet).

– When the resistive voltage exceeds a preset threshold over a time exceeding a preset duration, the detection system generates a trigger which signals the occurrence of a quench.

– The quench detection threshold should not be too large to limit the delay between the quench start and its detection and should not be too small to avoid untimely triggering on noise.

Principle of Quench Detection e.g., Dipole Magnet

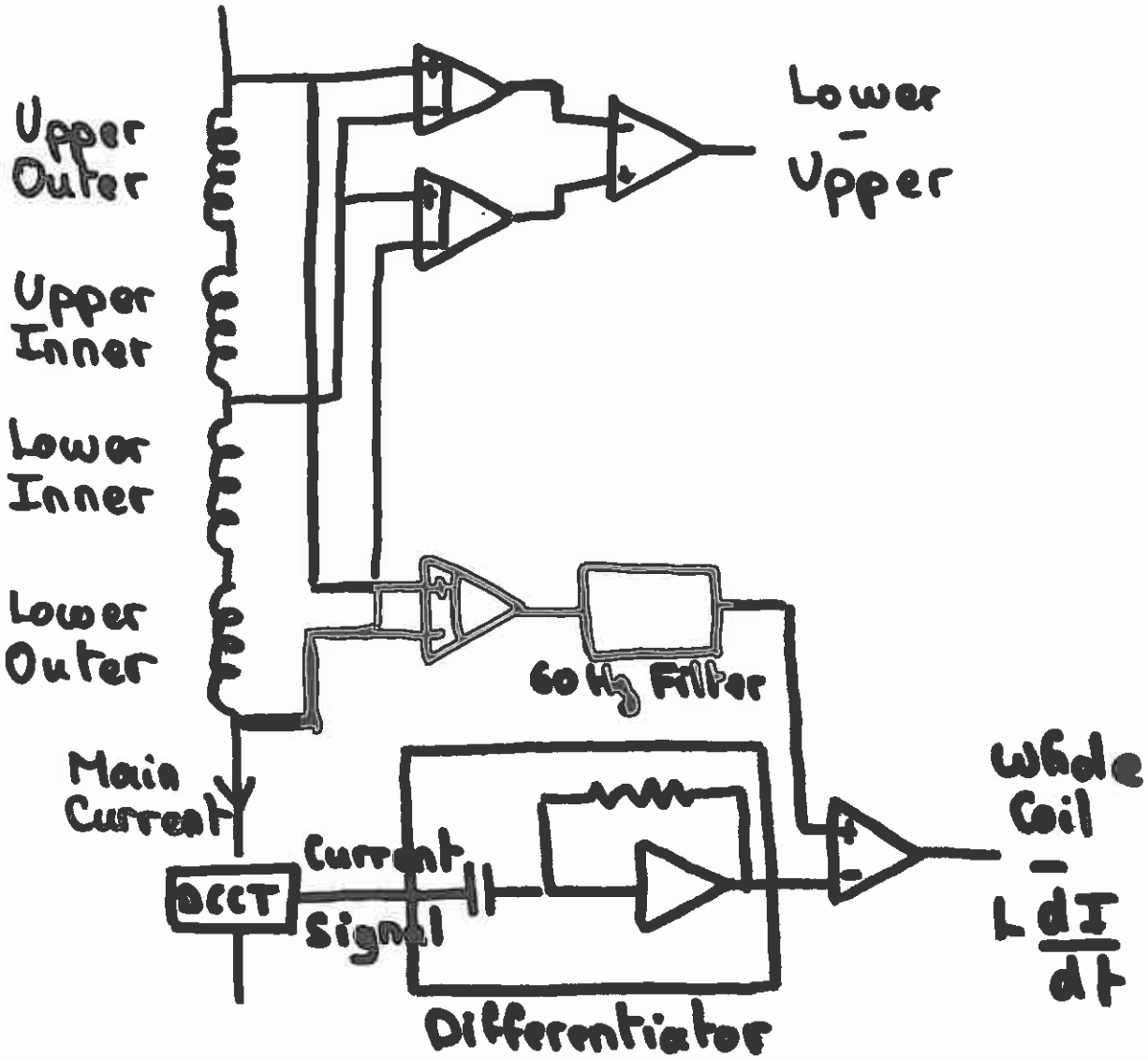

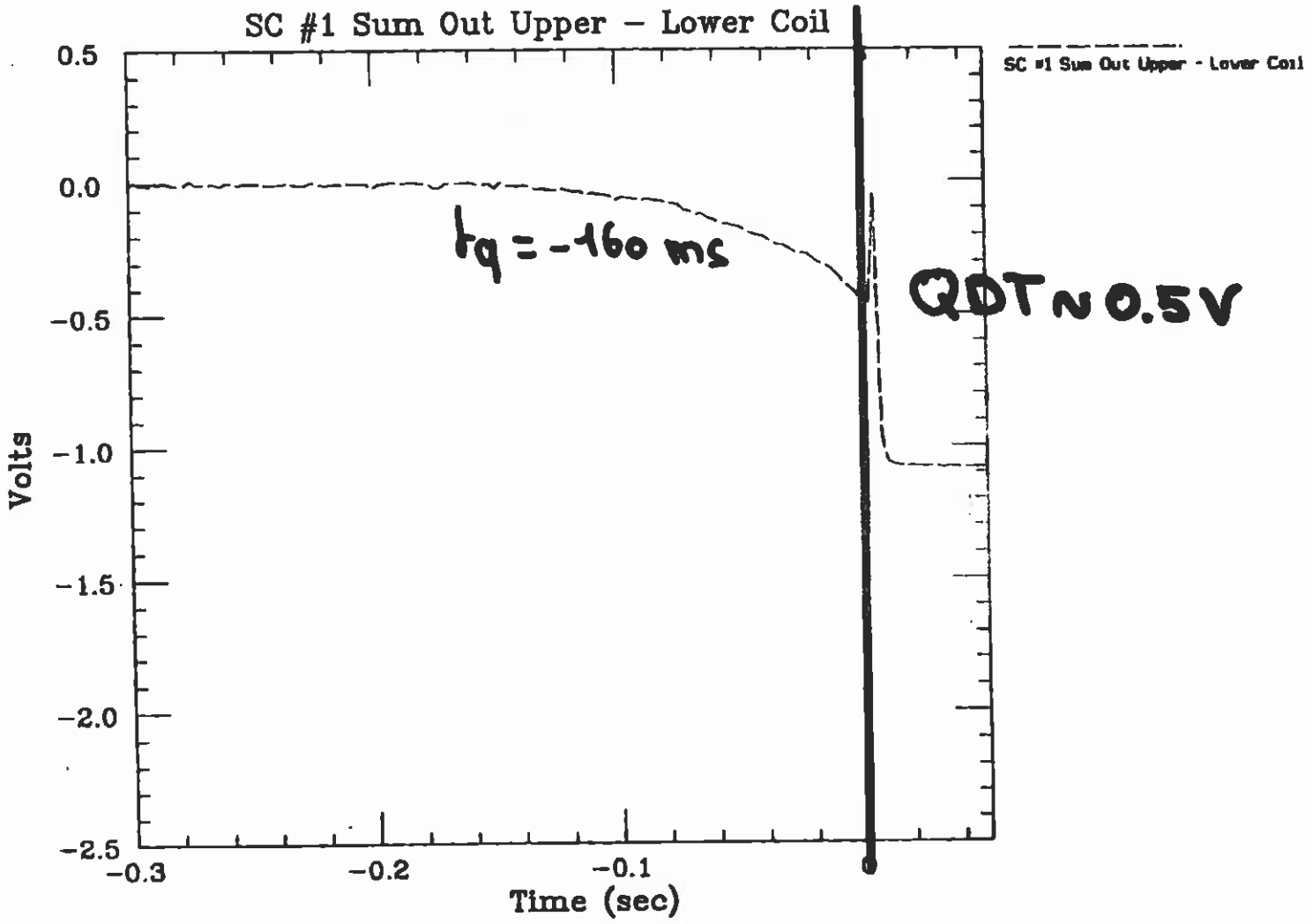

Magnet: DCA323 File: DCA323.08134 7-DEC-92 21:49:58 Iq: 4977.0 (amps) Tq = -.1375 MIITs = 15.27 Ramp rate = 25. (a/sec) QDC # 1 Quench # 0

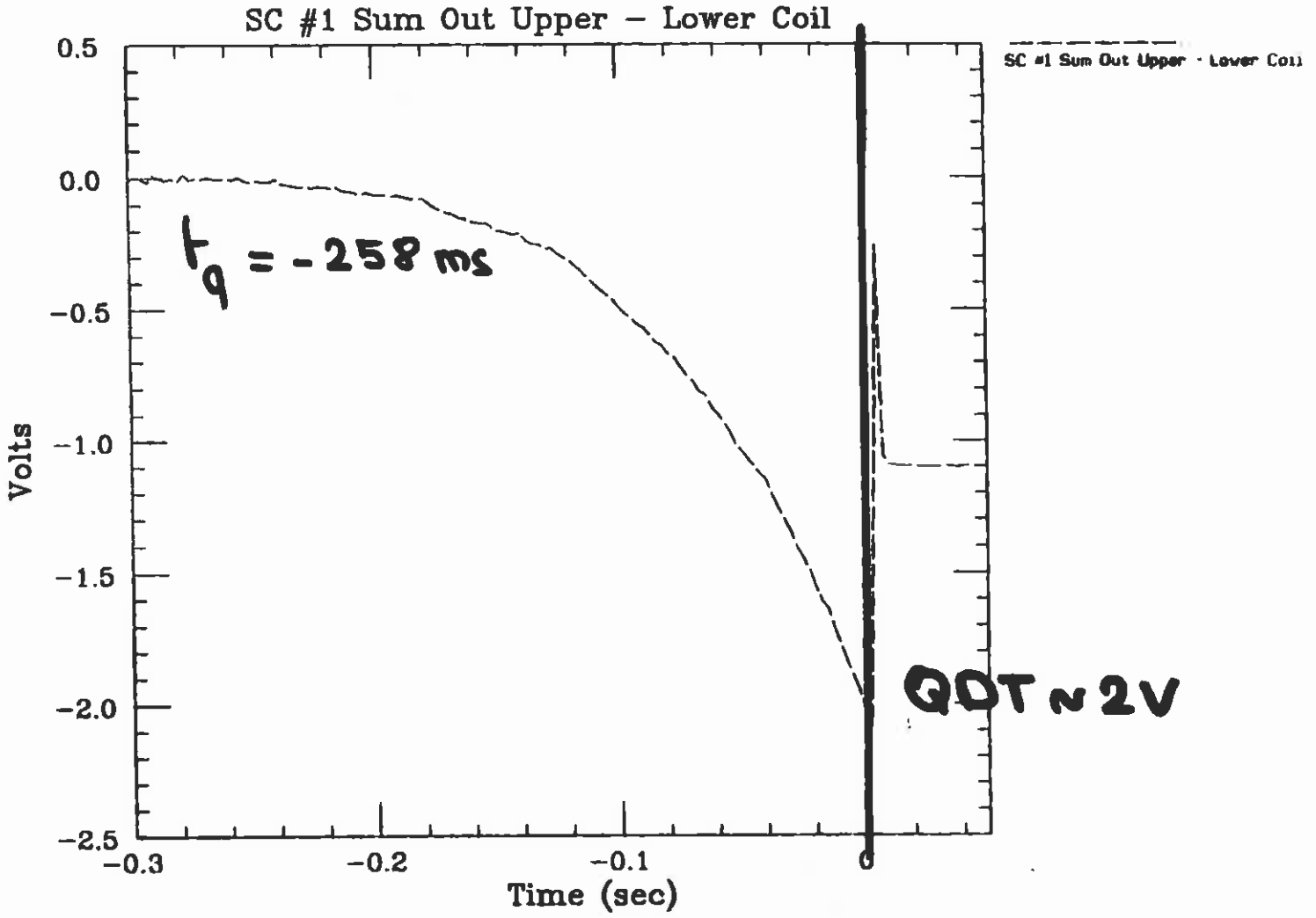

Magnet: DCA323 File: DCA323.08157 15-DEC-92 13:61:56 Iq: 4977.0 (amps) Tq = -.2400 MIITs = 16.07 Ramp rate = 50. (a/sec) QDC # 1 Quench # 0

Outer Coils of 5-cm Aperl. Dipoles (5000 A)

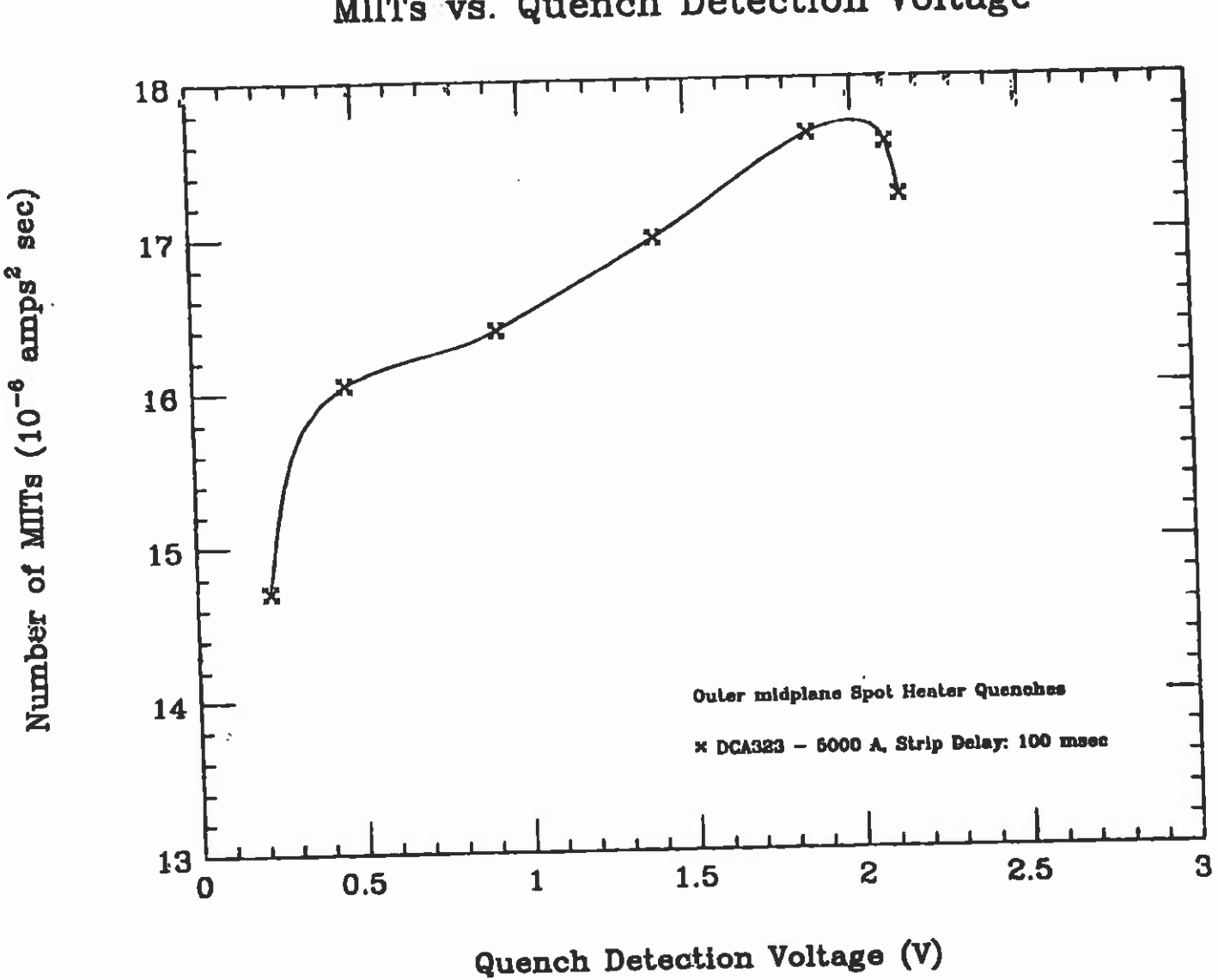

LECTURE 9: QUENCH PROTECTION OF PARTICLE ACCELERATOR MAGNETS

9.1 Quench Development
- 9.1.1 Simple Theoretical Model
- 9.1.2 Measuring Quench Propagation Using Voltage Taps
- 9.1.3 Measuring Quench Propagation Using Quench Antenna
- 9.1.4 Review of Propagation Velocity Measurements

9.2 The Effects of a Quench

9.3 Hot Spot Temperature

9.4 Quench Detection

9.5 Quench Protection Heaters

9.6 Protection of a Single Magnet

9.7 Protection of a Magnet String

QUENCH PROTECTION HEATERS

– As we have described, to speed up and uniformize quench development, most accelerator magnets rely on quench protection heaters which are fired as soon as a quench is detected.

– The heaters are usually made of stainless steel strips, which are copper clad at regular intervals along their lengths and which are placed on the outer surface of the coil assemblies.

Courtesy F. Rodrigueg-Mateos

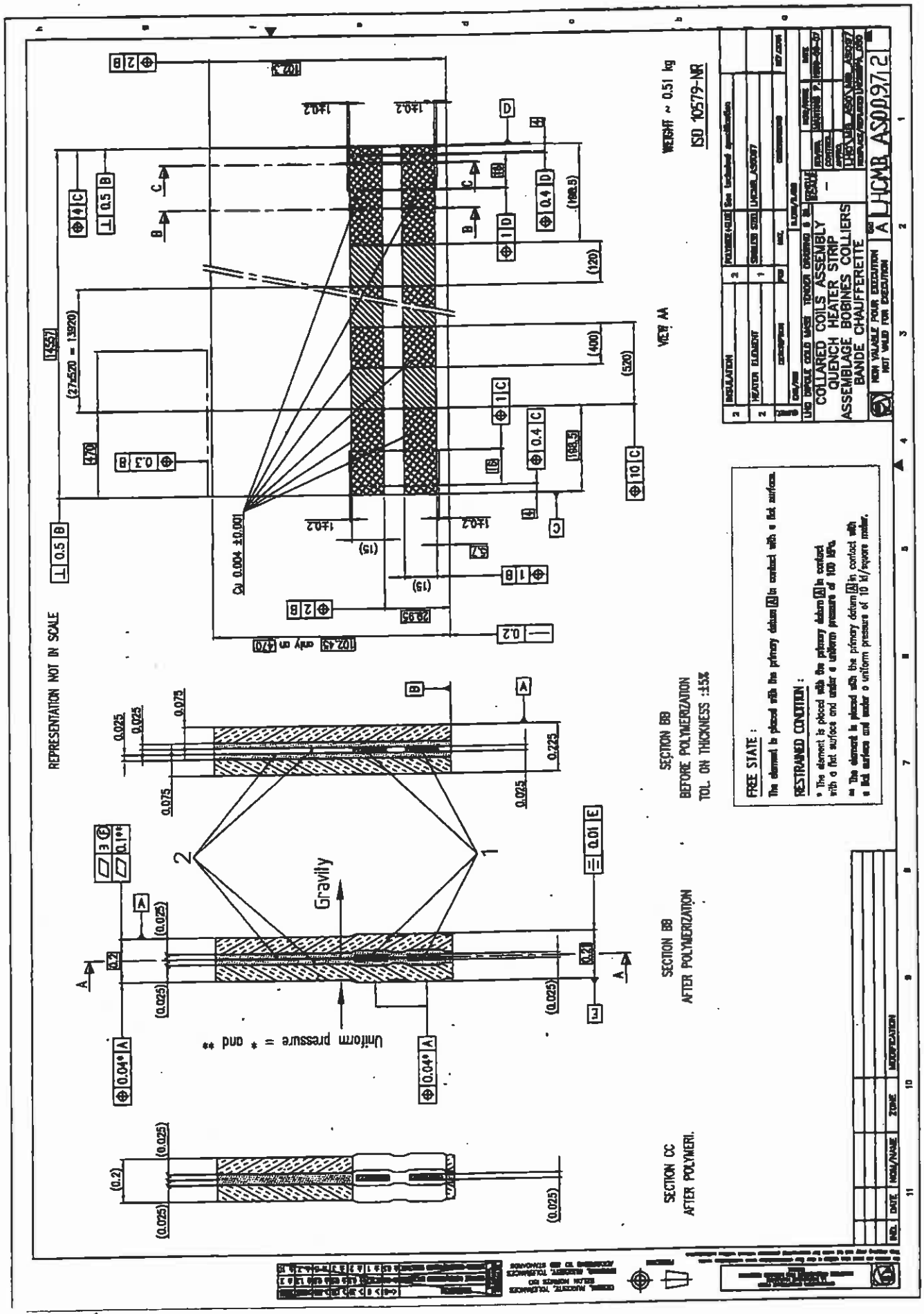

Courtesy F. Rodrigueg-Mateos

RC-980809-02

MOUNTING OF THE QUENCH PROTECTION HEATERS

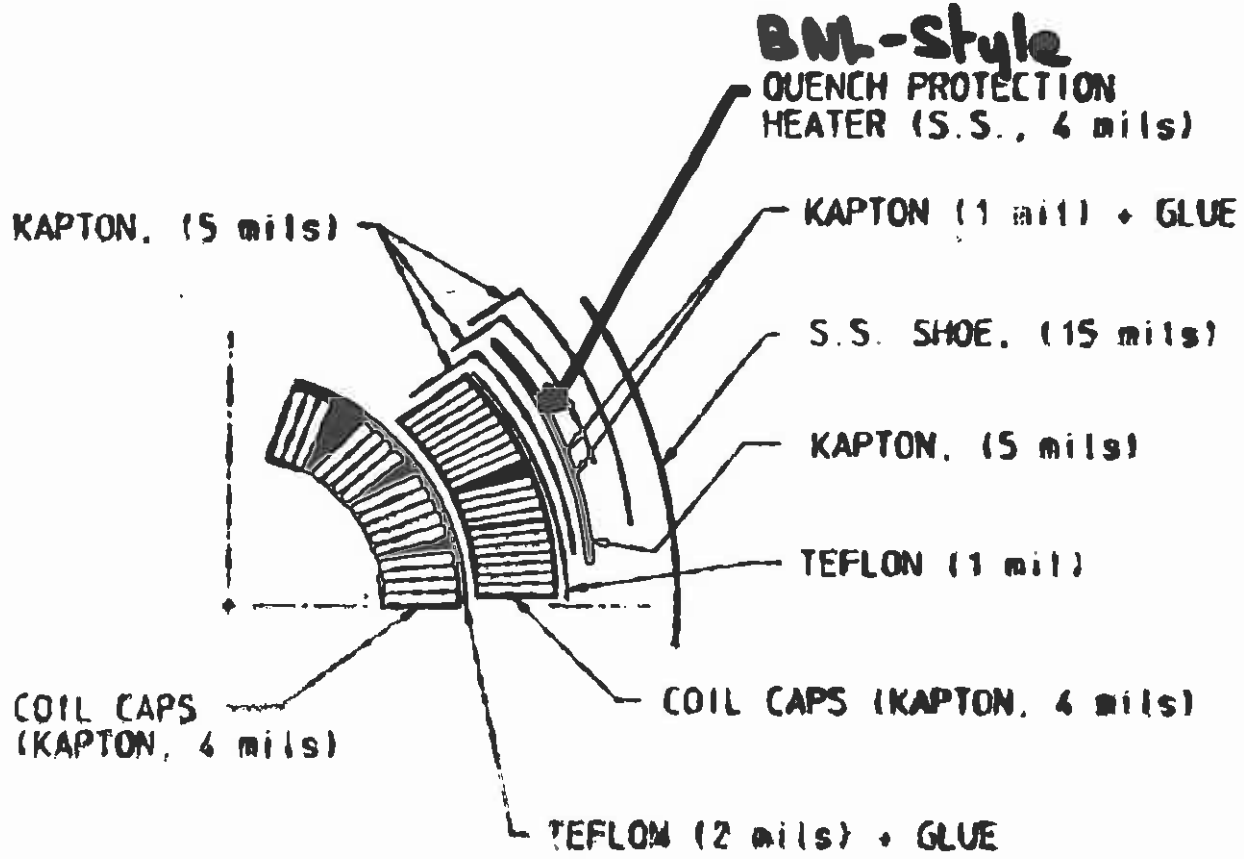

QUENCH PROTECTION HEATER EFFICIENCY

– Of course, the effect of the heaters is not instantaneous. This delay is due:

• To the fact that the heater firing unit relies on a capacitor bank and that it takes some time for the energy to be released,

• To the fact that the heaters have to be electrically insulated from the coil and that this electrical insulation introduces a thermal barrier,

• To the fact that, in order to switch to the normal resistive state, the superconductor must be heated up from its initial temperature to the current sharing temperature at the given field and current.

– The heaters and their implementations in the magnet assembly are optimized to reduce this delay.

BNL-Style Heaters

SSC/CDG 2-DEC-88
16:11:05

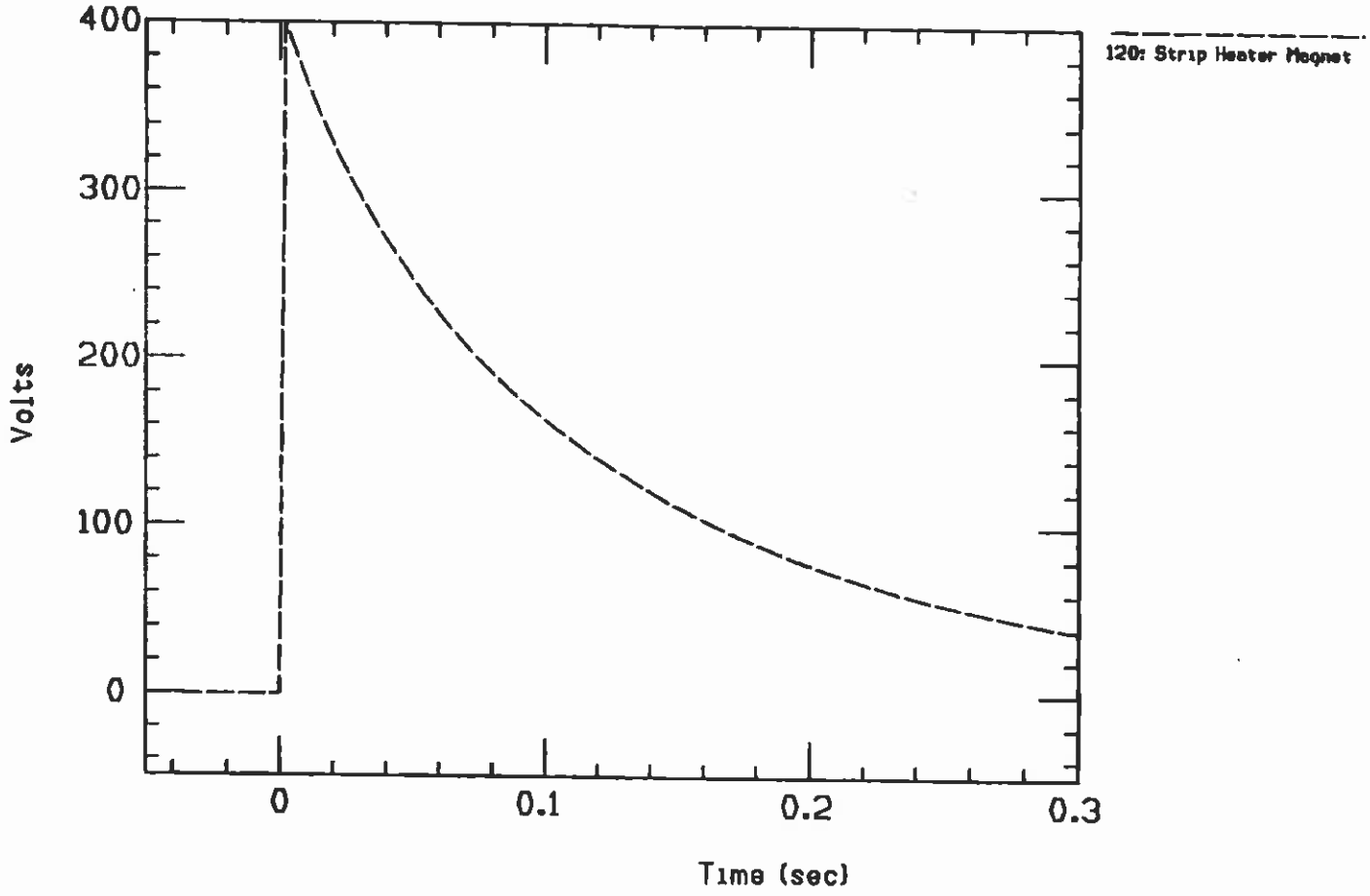

DD0010 Data File No. : 18 7-APR-88 21:21:56 Quench No. : 0 Current = 3020.8

BNL-Style Heaters

SSC/CDG 2-DEC-88
16:11:05

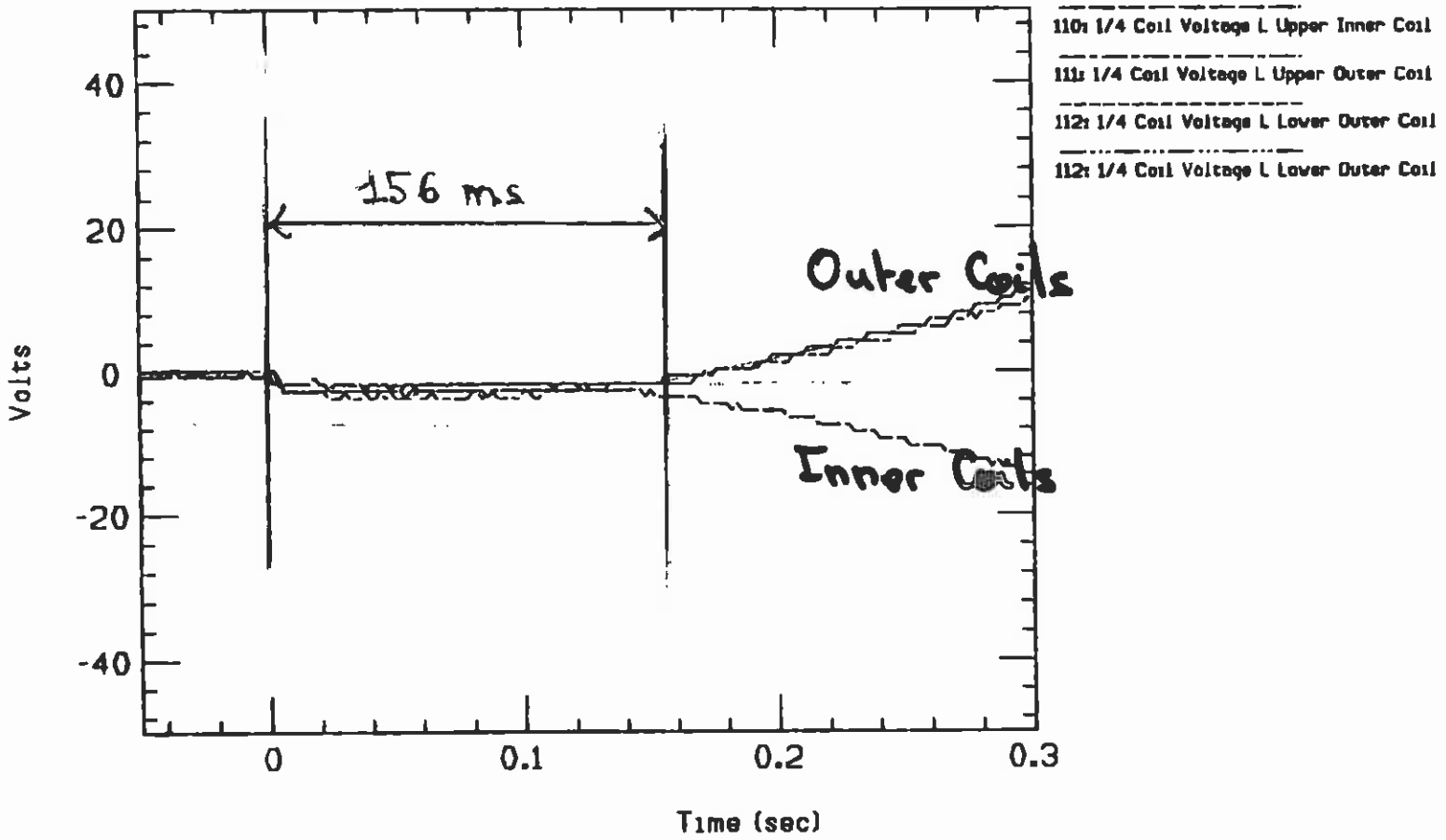

DD0010 Data File No. : 18 7-APR-88 21:21:56 Quench No. : 0 Current = 3020.8

3000 A

DELAY BETWEEN THE FIRING OF THE HEATERS AND THE QUENCHING OF THE OUTER COILS

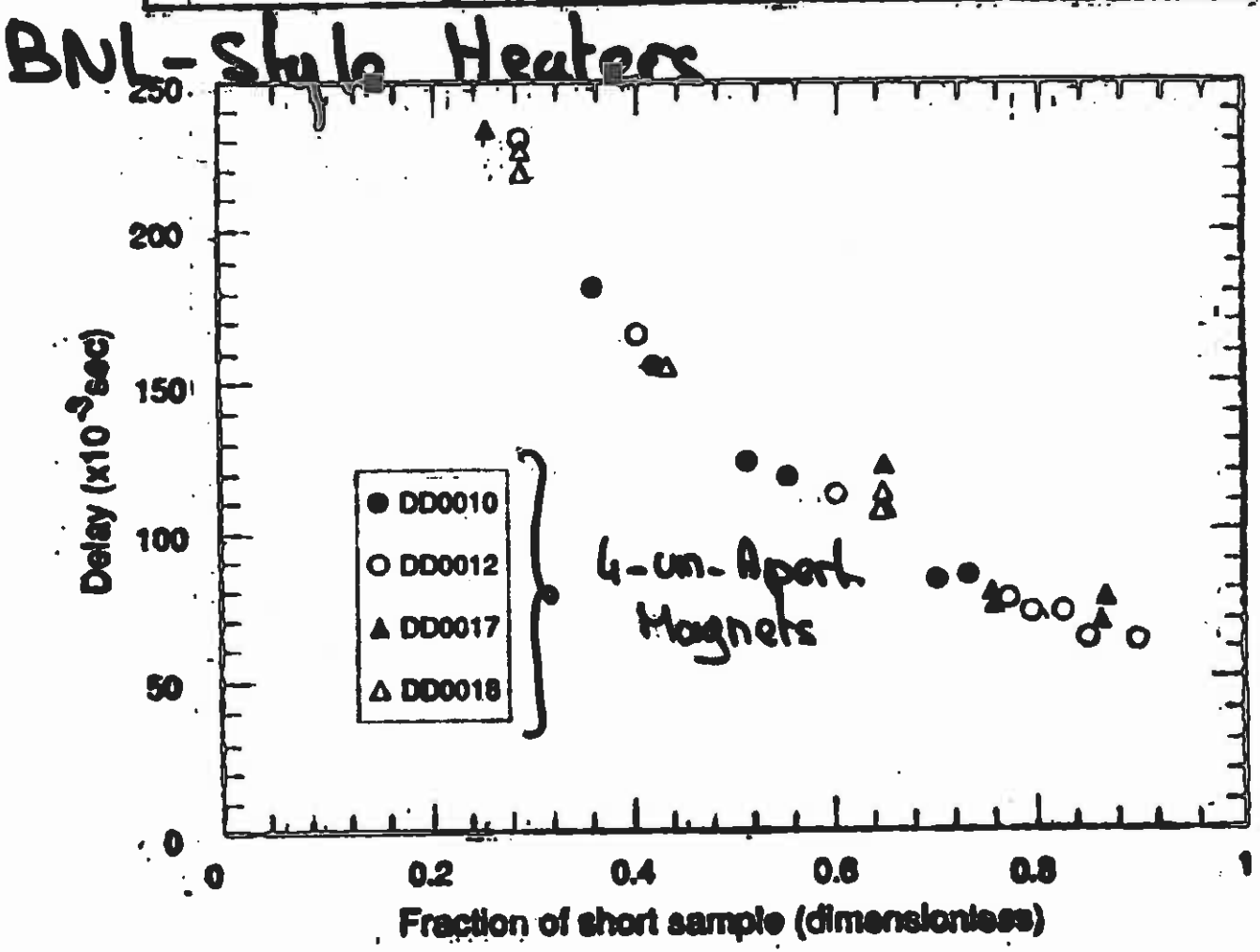

BNL-Style Heaters

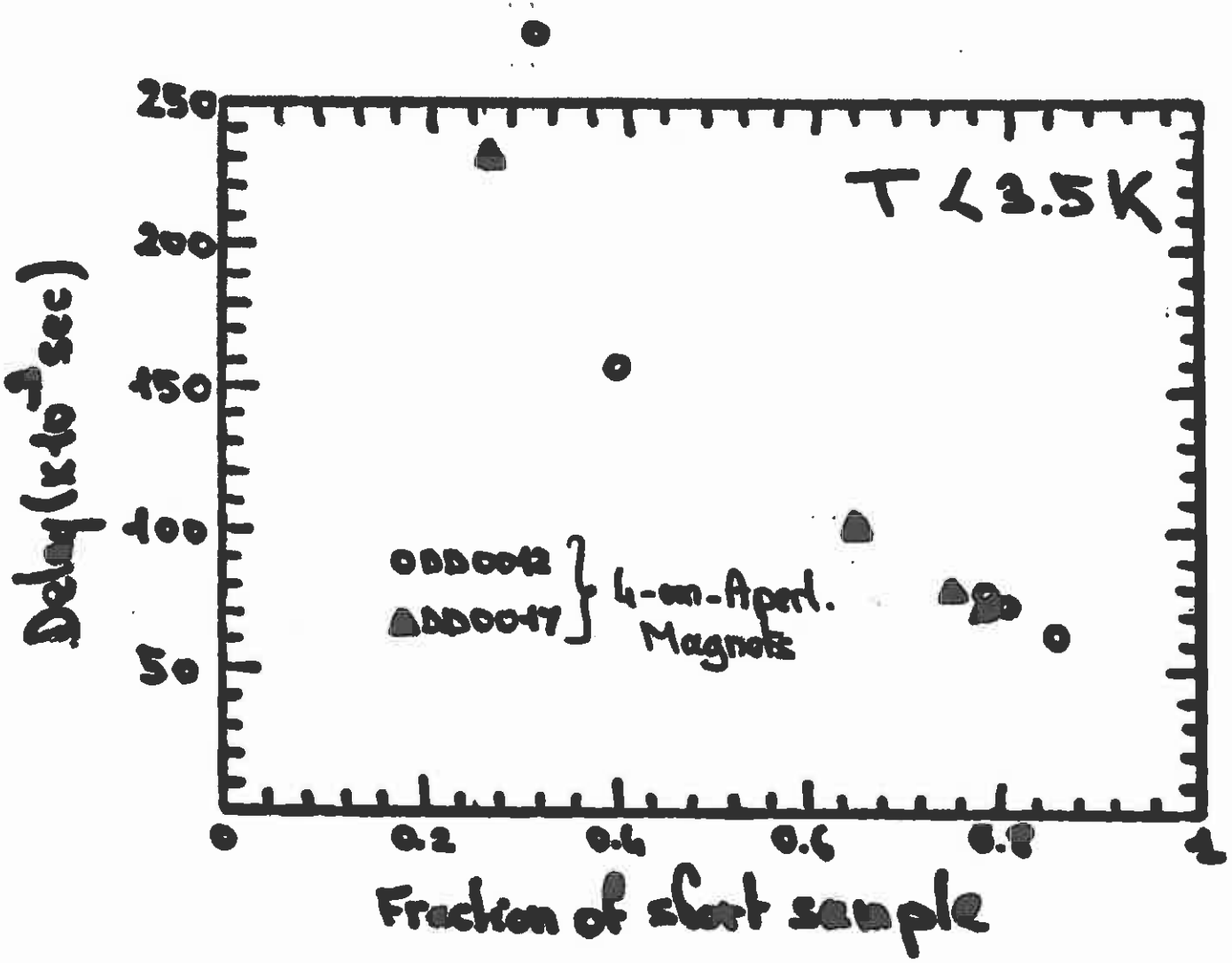

HEATER LOCALIZATION

– Data from a short LHC dipole magnet magnet (MBSMS17) suggest that heaters positionned on the inner surface of the outer coils are more efficient than heaters positionned on the outer surface.

– This is due to the fact that the magnetic flux density on the inner side of the outer coils is higher than on the outer side, resulting in lower current sharing temperatures and lower enthalpy margins.

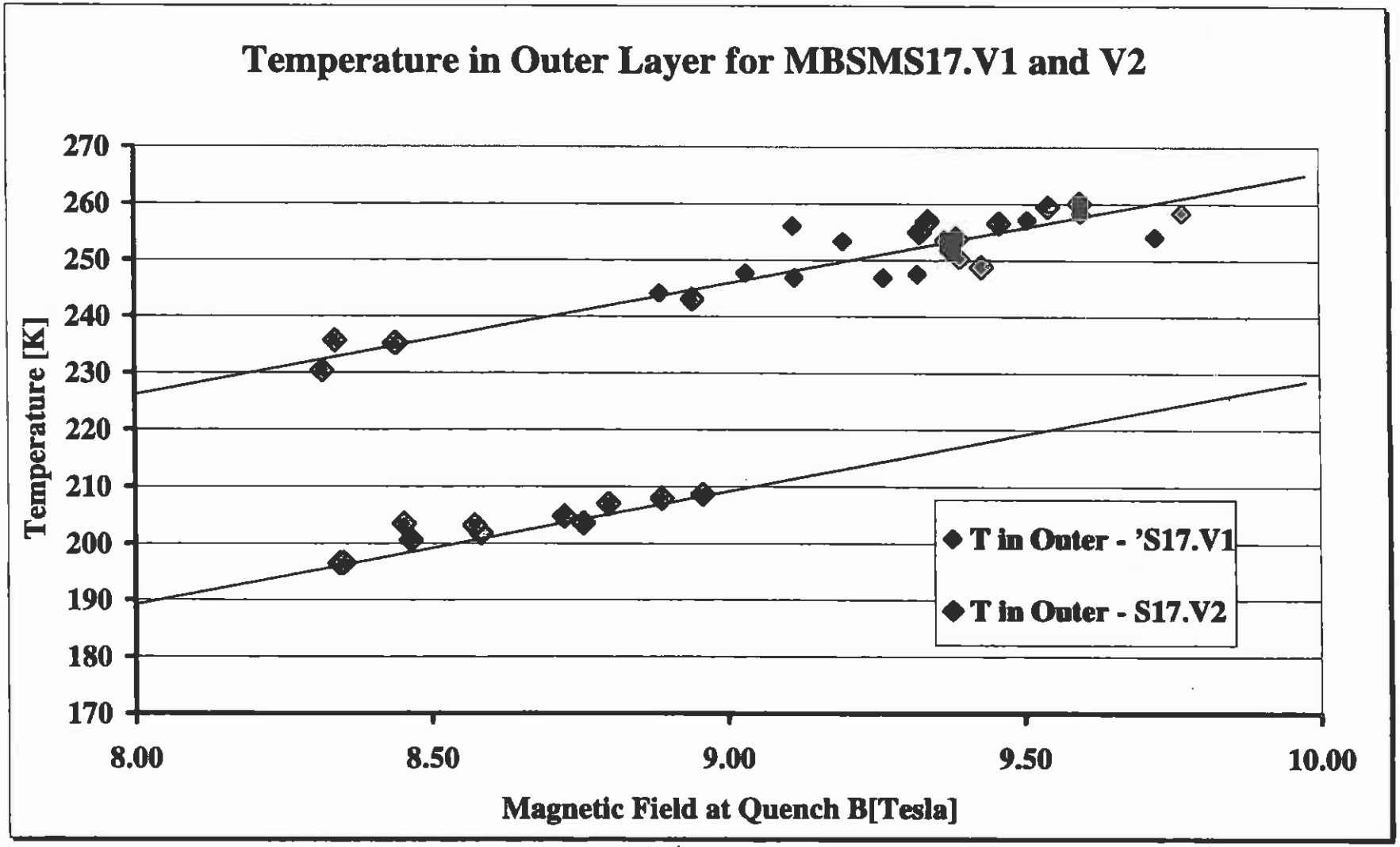

Courtesy A. Siemko

Quench_sum_1_as'.xls T In outer (4) 8/6/99

LECTURE 9: QUENCH PROTECTION OF PARTICLE ACCELERATOR MAGNETS

9.1 Quench Development
- 9.1.1 Simple Theoretical Model
- 9.1.2 Measuring Quench Propagation Using Voltage Taps
- 9.1.3 Measuring Quench Propagation Using Quench Antenna
- 9.1.4 Review of Propagation Velocity Measurements

9.2 The Effects of a Quench

9.3 Hot Spot Temperature

9.4 Quench Detection

9.5 Quench Protection Heaters

9.6 Protection of a Single Magnet

9.7 Protection of a Magnet String

EQUATIONS OF CURRENT DECAY IN A SINGLE MAGNET TEST

– Let us first consider the case of a single magnet and let us assume that, once a quench is detected, the power supply is turned off and the magnet is switched to an external dump resistor, R_{ext}.

– The current decay is determined by:

$$L_m \frac{dI}{dt} + [R_q(t)+R_{ext}]\ I = 0$$

where L_m is the magnet inductance and $R_q(t)$ is the developing resistance in the quenching coils.

– Furthermore, the total voltage across the magnet, V_m, is given by:

$$V_m = R_{ext}\ I(t)$$

ACCELERATING CURRENT DECAY IN A SINGLE MAGNET TEST

– To limit the number of MIITs, it is desirable to have a fast current decay.

– The previous equations show that fast decay rates are obtained either by means of a large R_{ext} or by ensuring that $R_q(t)$ increases rapidly.

– For some magnets, an external resistor can be used to extract a significant fraction of the stored magnetic energy.

– However, it is also required to keep V_m to a reasonable level (typically: less than 1 kV) to avoid insulation breakdown.

Given the order of magnitude of I (up to 15 kA), this imposes a small R_{ext} (typically: a few hundredth of ohms) which, during a quench, is soon overcome by $R_q(t)$.

– Hence, for accelerator magnets, the current decay is largely dominated by the resistance development in the quenching coils and the decay rate can be increased only by speeding up $R_q(t)$.

In practice, this is done by firing quench protection heaters.

Discharge on an External Resistor (Single Magnet Test)

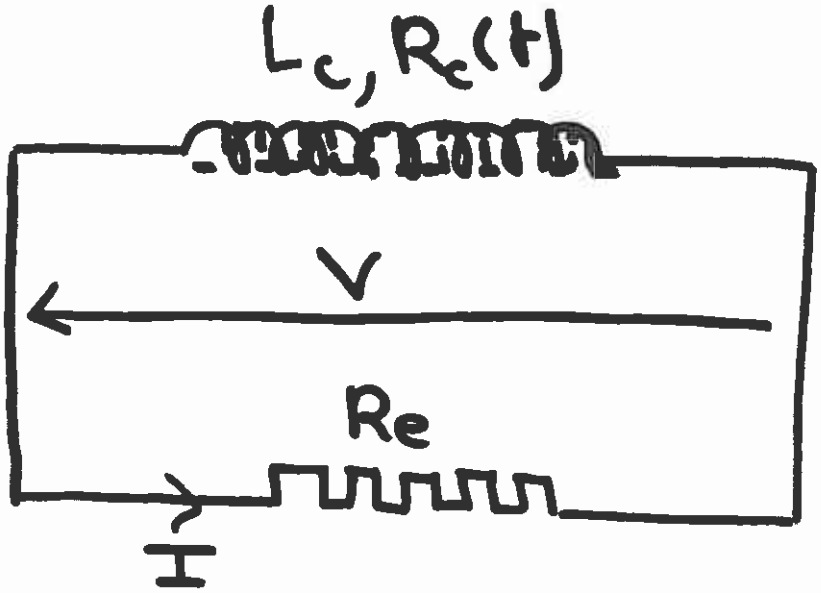

$I_0 \simeq 6500\,A$
$V < 1000\,V$
$\Rightarrow R_e < 150\,m\Omega$

Not very useful!

MAXIMUM VOLTAGE TO GROUND IN A SINGLE MAGNET TEST

– The developing resistance in the quenching coil separates the coil impedance into several parts:

• *un-quenched parts* across which the voltage is mainly inductive

• *quenched parts* across which the voltage is mainly resistive.

– The resistive and inductive voltages compensate each other partially so that their sum equals V_m.

– The voltage distribution with respect to ground depends on the respective sizes and locations of these various parts.

MAXIMUM VOLTAGE TO GROUND IN A SINGLE MAGNET TEST (CONT.)

As an illustration, let us consider the case of a single magnet where V_m is assumed to be nil and R_q is assumed to be concentrated near two thirds of the magnet length.

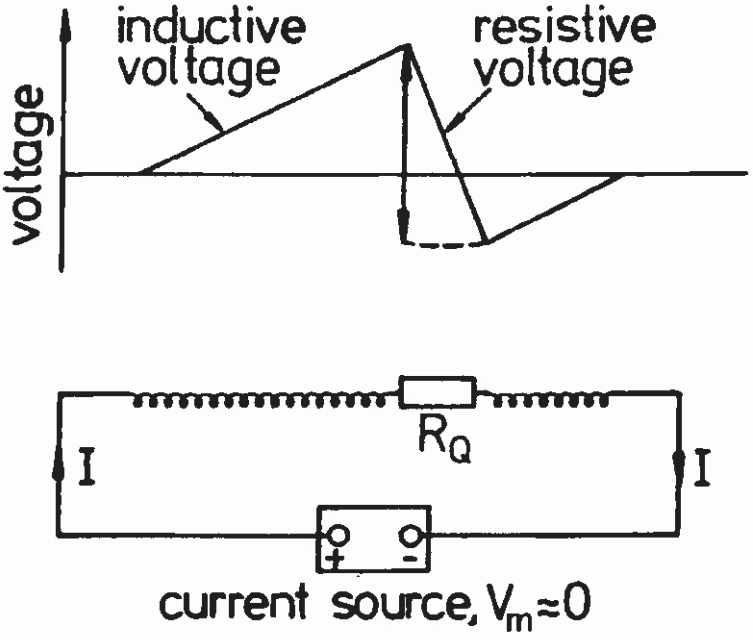

– It is easy to see that, the more uniform the quench development, the lower the maximum voltage to ground.

The quench development can be uniformized by using quench protection heaters covering large coil sections.

TYPICAL MIITS VERSUS CURRENT CURVE ON A SINGLE MAGNET

– For a given magnet, operated under given conditions (including, quench detection threshold, quench heaters power and delay, and so on), the "MIITs versus Current" curve usually goes through a maximum at an intermediate current.

– The curve shape can be explained by two competing effects:

• *The increase in peak current,* resulting in a direct increase of the MIIT integral,

• *The increase in propagation velocity,* resulting in a faster quench development and a shorter time constant.

– At high currents, the faster quench development overcomes the increase in peak current and the number of MIITs decrease.

– It follows that all magnet tests regarding quench protection should be carried out at the current corresponding to the maximum of MIITs (and not at the operating current).

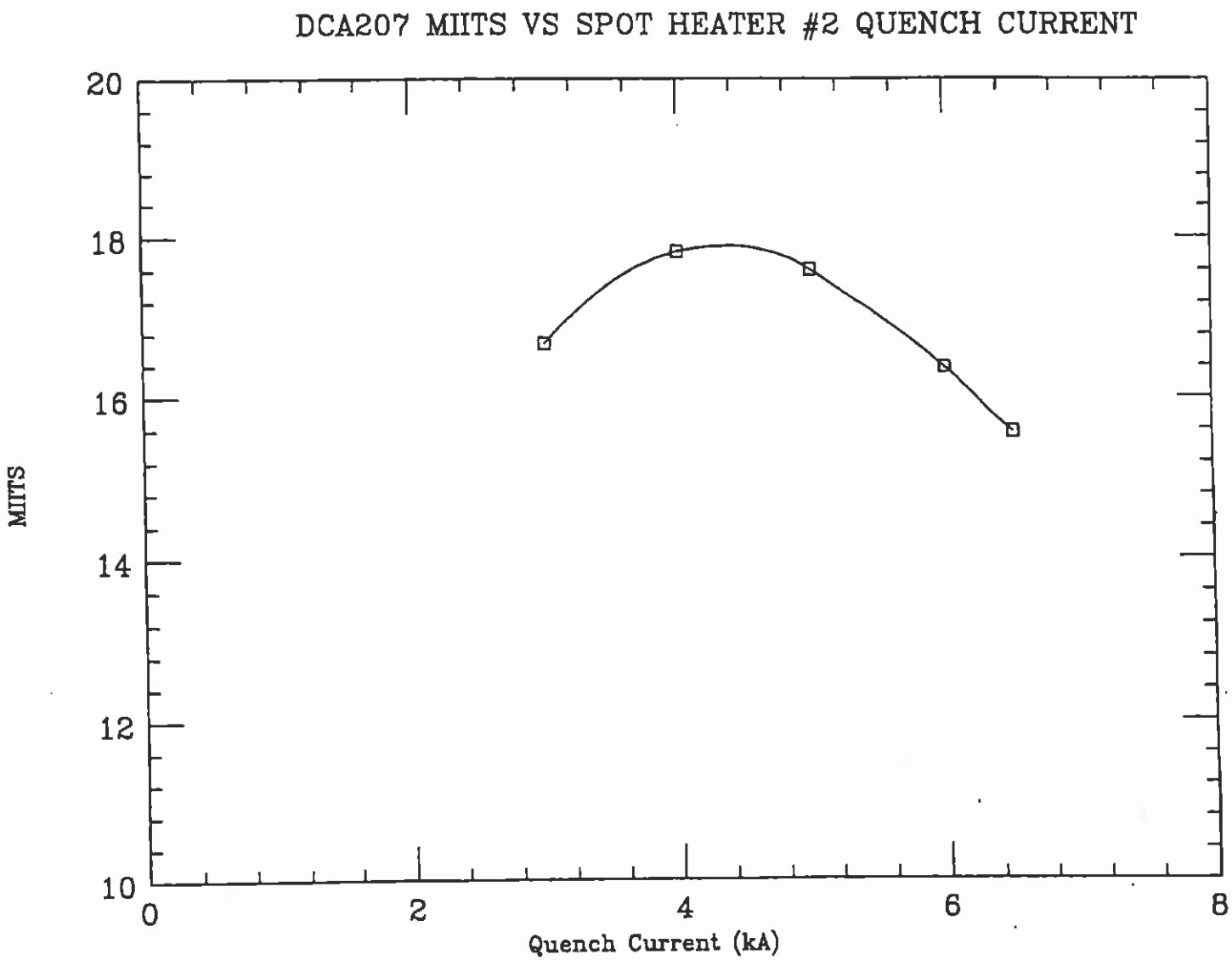

Note: Spot heater #2 is on the lower inner coil midplane turn, near the return end.
Strip heater time delay is 80ms.
Test temperature is 4.35K (nom).

ON THE NEED OF QUENCH PROTECTION HEATERS

– Data from 5-cm-aperture, 15-m-long SSC dipole magnet prototypes show that the hot spot temperature reached for quenches at 6000 A with no delay on the firing of quench protection heaters is less than 300 K while that reached with a quasi-infinite delay can exceed 500 K.

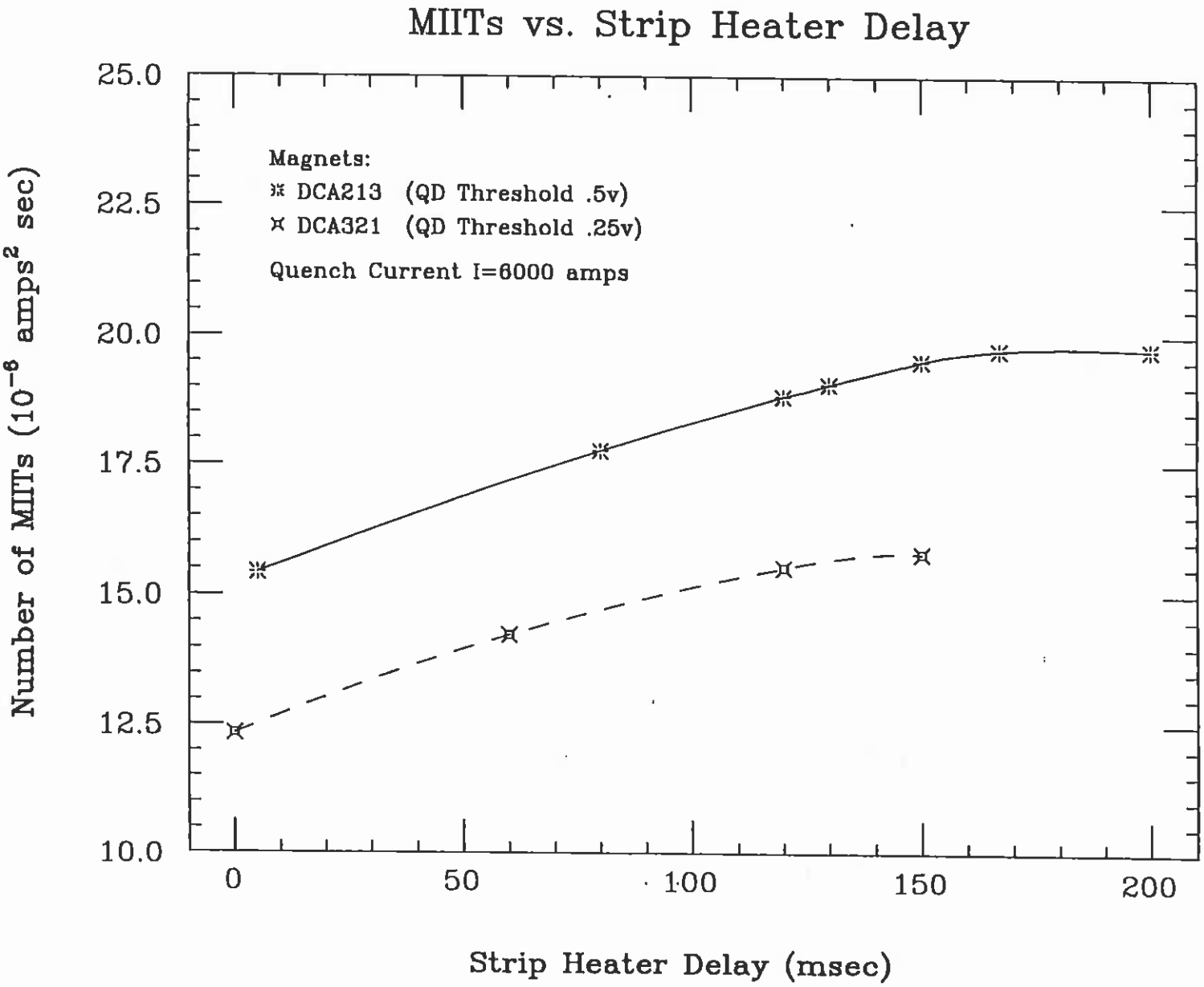
MIITs vs. Strip Heater Delay
Magnets:
DCA213 (QD Threshold .5v)
DCA321 (QD Threshold .25v)
Quench Current I=6000 amps
Number of MIITs (10^{-6} amps^2 sec)
25.0
22.5
20.0
17.5
15.0
12.5
10.0
0
50
100
150
200
Strip Heater Delay (msec)

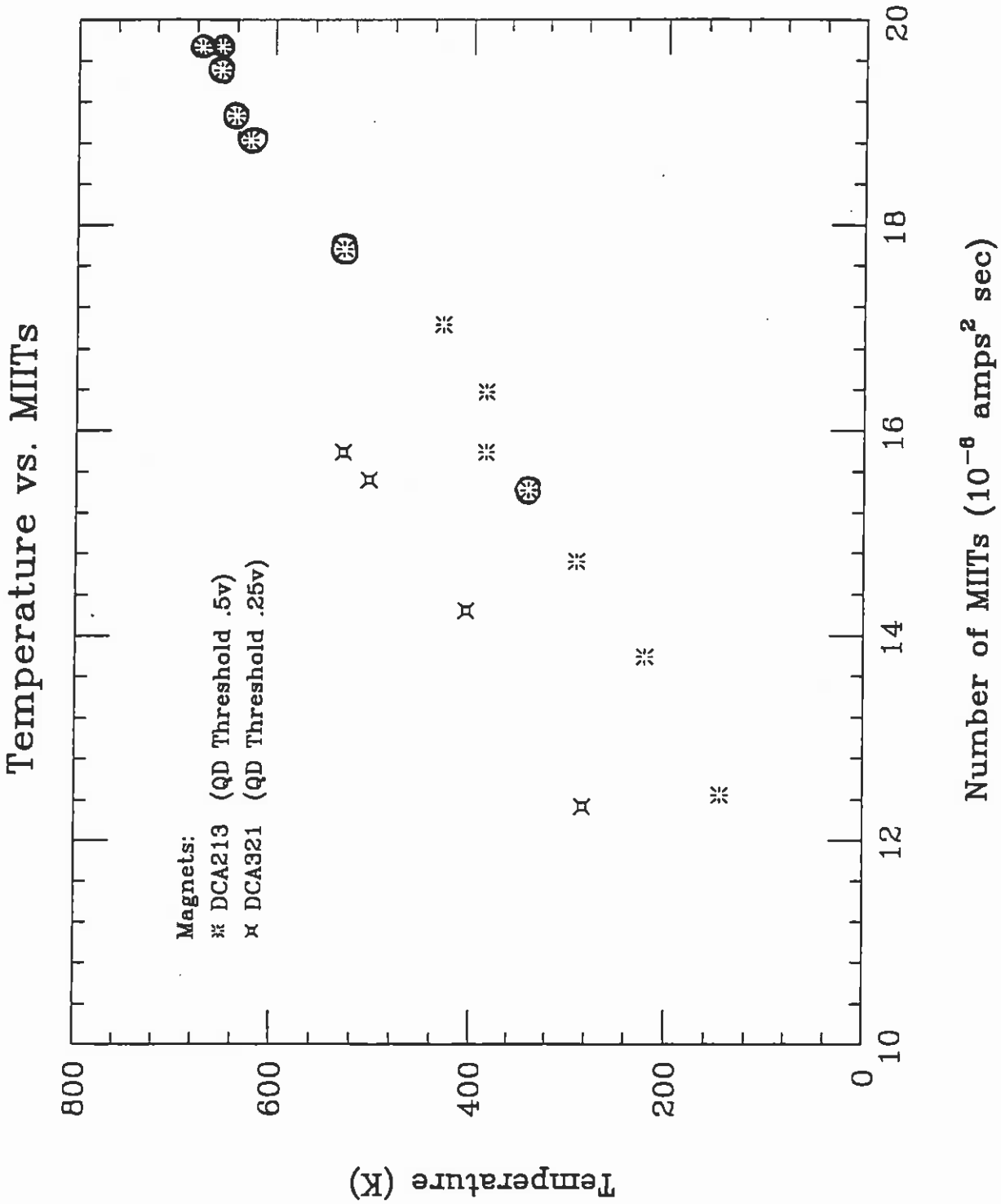
Temperature vs. MIITs
Magnets:
DCA213 (QD Threshold .5v)
DCA321 (QD Threshold .25v)
Temperature (K)
Number of MIITs (10^{-6} amps^2 sec)
800
600
400
200
0
10
12
14
16
18
20

LECTURE 9: QUENCH PROTECTION OF PARTICLE ACCELERATOR MAGNETS

9.1 Quench Development
- 9.1.1 Simple Theoretical Model
- 9.1.2 Measuring Quench Propagation Using Voltage Taps
- 9.1.3 Measuring Quench Propagation Using Quench Antenna
- 9.1.4 Review of Propagation Velocity Measurements

9.2 The Effects of a Quench

9.3 Hot Spot Temperature

9.4 Quench Detection

9.5 Quench Protection Heaters

9.6 Protection of a Single Magnet

9.7 Protection of a Magnet String

PROTECTION OF A MAGNET STRING

– In an accelerator, the magnet ring is divided into several sectors made up of series-connected magnets.

– The sectors are powered independently and are electrically independent.

– Once a quench is detected in a magnet, the power supply of the sector to which the magnet belongs is turned off and the sector is discharged over a dump resistor.

DISCHARGE OF A MAGNET STRING

– Unlike in the case of a single magnet, the current decay rate in the sector must be limited for at least two reasons:

• ***To prevent the induction of large coupling currents in the magnet coils*** (which may quench the remaining magnets in the sector, resulting in general warming and significant helium venting),

• ***To avoid the occurrence of unacceptable voltages to ground*** (because of the large overall inductance of the sector).

– A too slow decay rate, however, creates the risk that a significant fraction of the total energy stored in the sector be dissipated in the quenching magnet, resulting in destructive overheating.

Example: For LHC, the total inductance of one sector of twin-aperture dipole magnets is 15.7 H and the dump resistors are 2x75 mΩ. It follows that the time constant of the current discharge is 105 s, yielding a decay rate of the order of 125 A/s.

QUENCH PROTECTION DIODES

– These contradictory considerations can be reconciled by forcing the current to bypass the quenching magnet and by ramping the current down at the desired rate in the remaining unquenched magnets.

– The bypass elements consist of diodes (or thyristors) connected in parallel to individual or small groups of magnets.

As long as the magnets are superconducting, the current flows through the magnets.

Once a magnet has quenched and starts to develop a resistive voltage, the main current is bypassed through the diode connected in parallel and the quenching magnet is discharged over the diode circuit.

The current decay is determined by an equation similar to that of a single magnet, except that R_{ext} has to be replaced by the resistance associated with the bypass element, R_b.

Courtesy D. Hagedorn

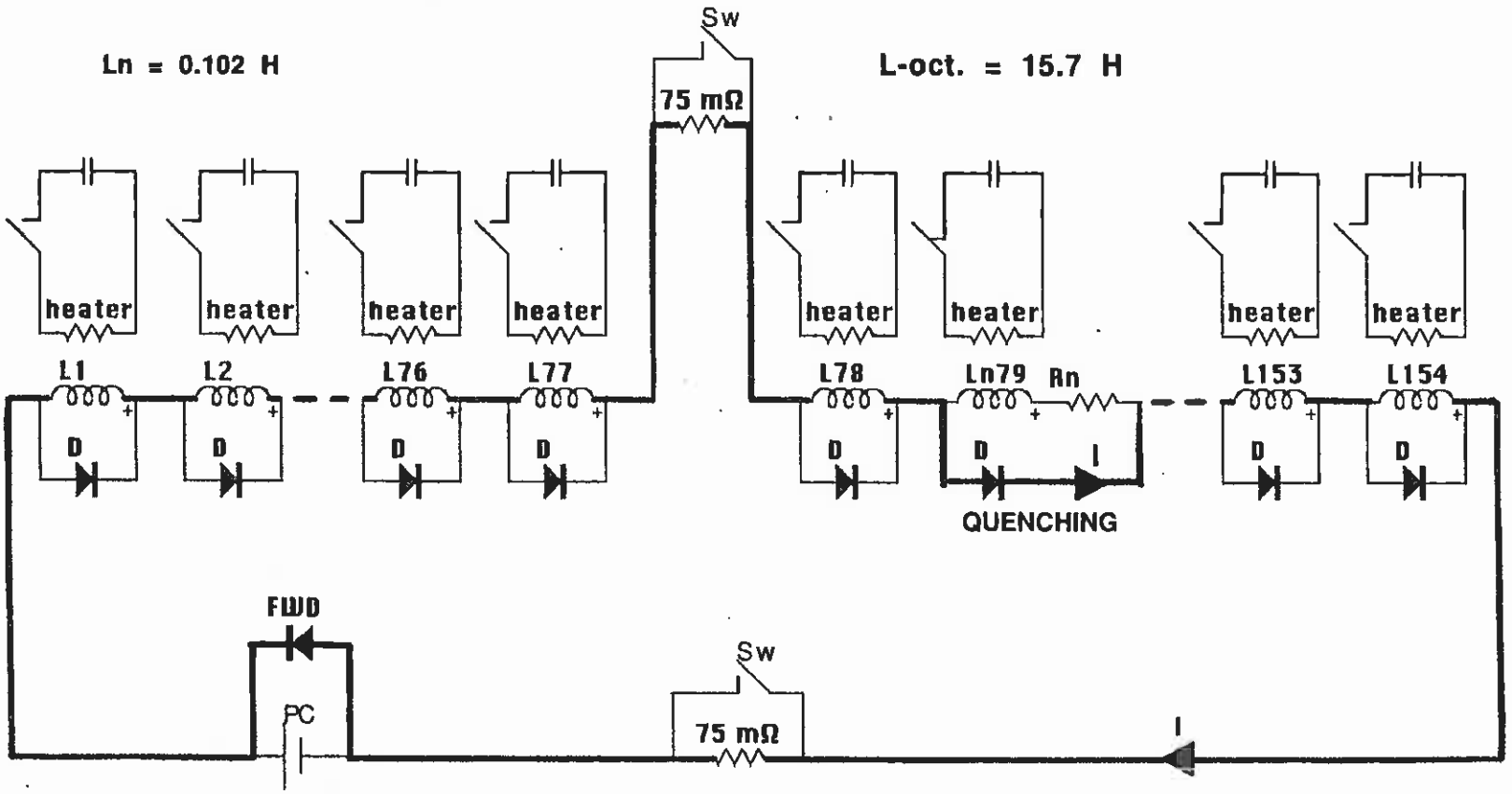

- self protected magnet with heaters
- only stored energy of the quenching magnet itself will be dissipated
- safe de-excitation of still superconducting magnets

Simplified Powering and Protection Scheme for one LHC-sector (1/8 of LHC)
with by-pass diodes

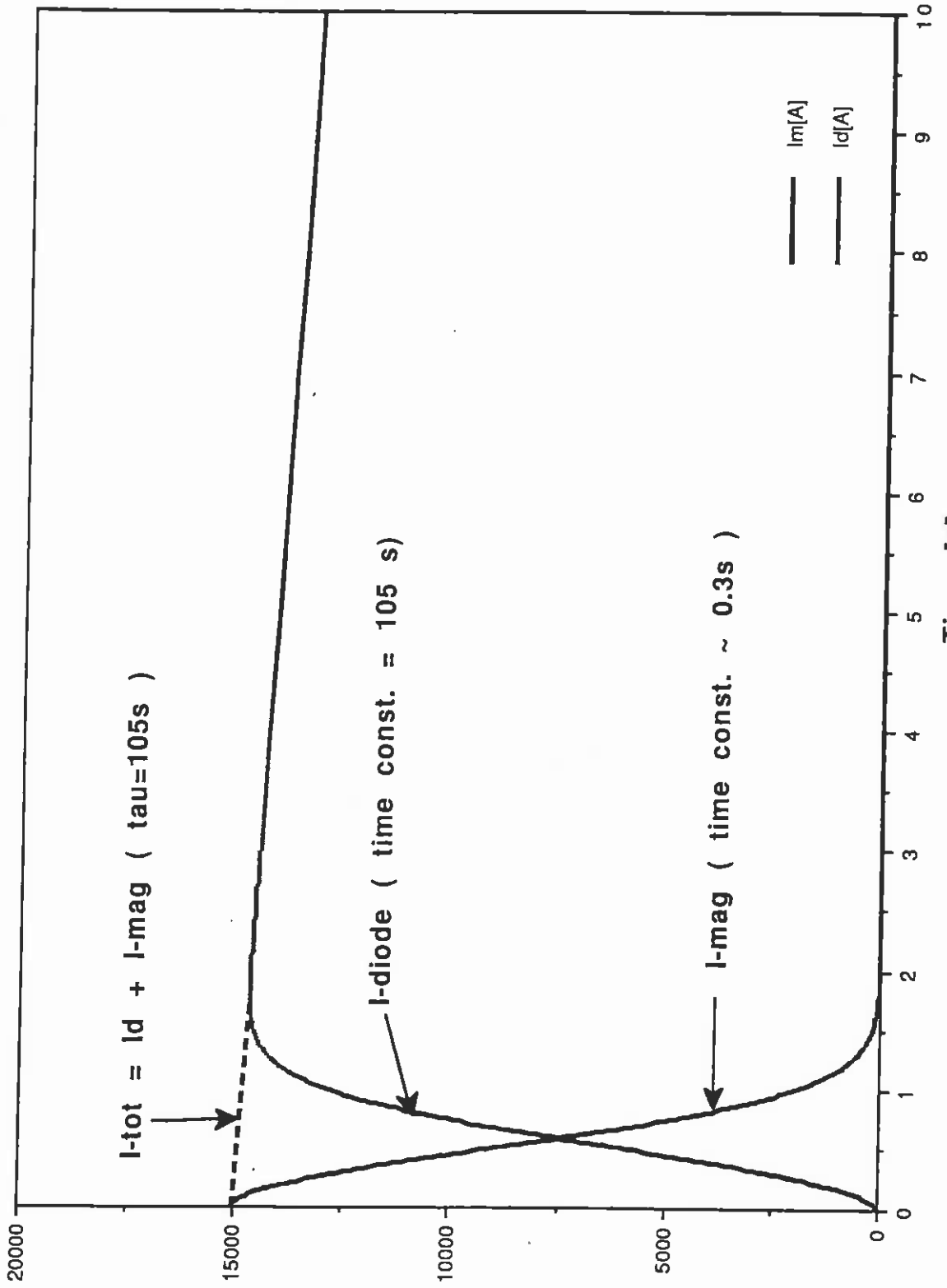

Courtesy D. Hagedorn

Magnet-current I-mag and diode-current I-diode versus time during quench and octant discharge.

DIODE REQUIREMENTS

– HERA, RHIC and LHC rely on silicon diodes which are mounted inside the helium cryostats and operate at cryogenic temperatures.

– The main requirements for these cold diodes are :

• ***A large enough forward voltage,*** V_f, to permit magnet charging at the desired ramp rate during the acceleration phase of the ring,

Example: The total inductance of a twin-aperture LHC dipole magnet is 0.1 H, and the LHC ramping rate is 11 A/s. Hence, V_f *must be larger than 1.1 V.*

• ***A forward voltage and a dynamic resistance as small as possible*** to limit power dissipation in the diodes,

Example: For the LHC arc dipole magnets, the peak current is 13 kA and the discharge time constant of a sector is 105 s. Hence, the power dissipated in the diodes is of the order of (1.365xV_f *MJ).*

• ***A large backward voltage,*** V_b, to permit a reasonably fast discharging of the still superconducting magnets of a given sector when a quench has occurred.

Example: For LHC, the decay rate is of the order of 125 A/s. Hence, V_b *must be larger than 13 V.*

• **Good radiation hardness.**

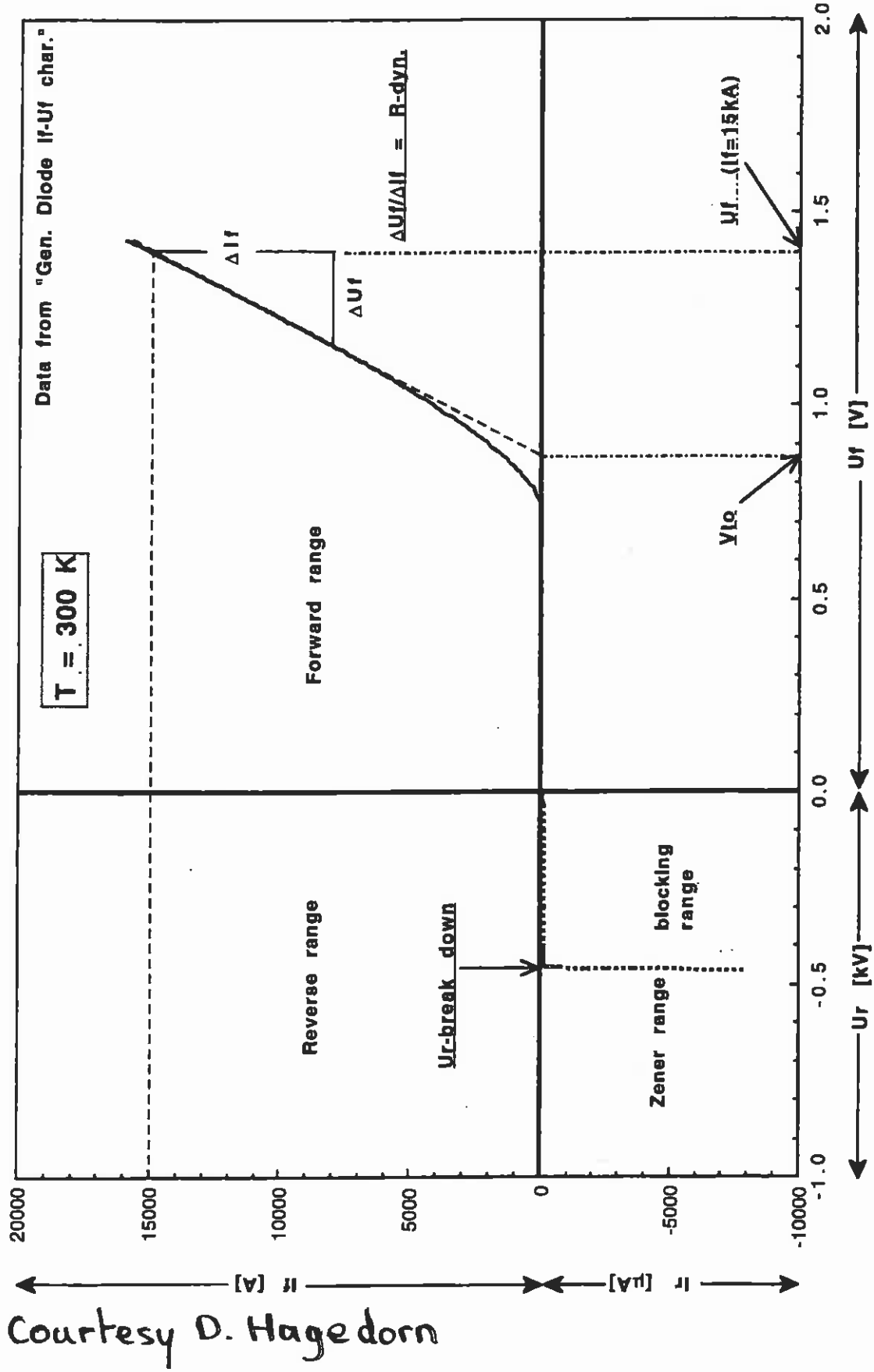

General definitions for the electrical characteristics of a power diode

Courtesy D. Hagedorn

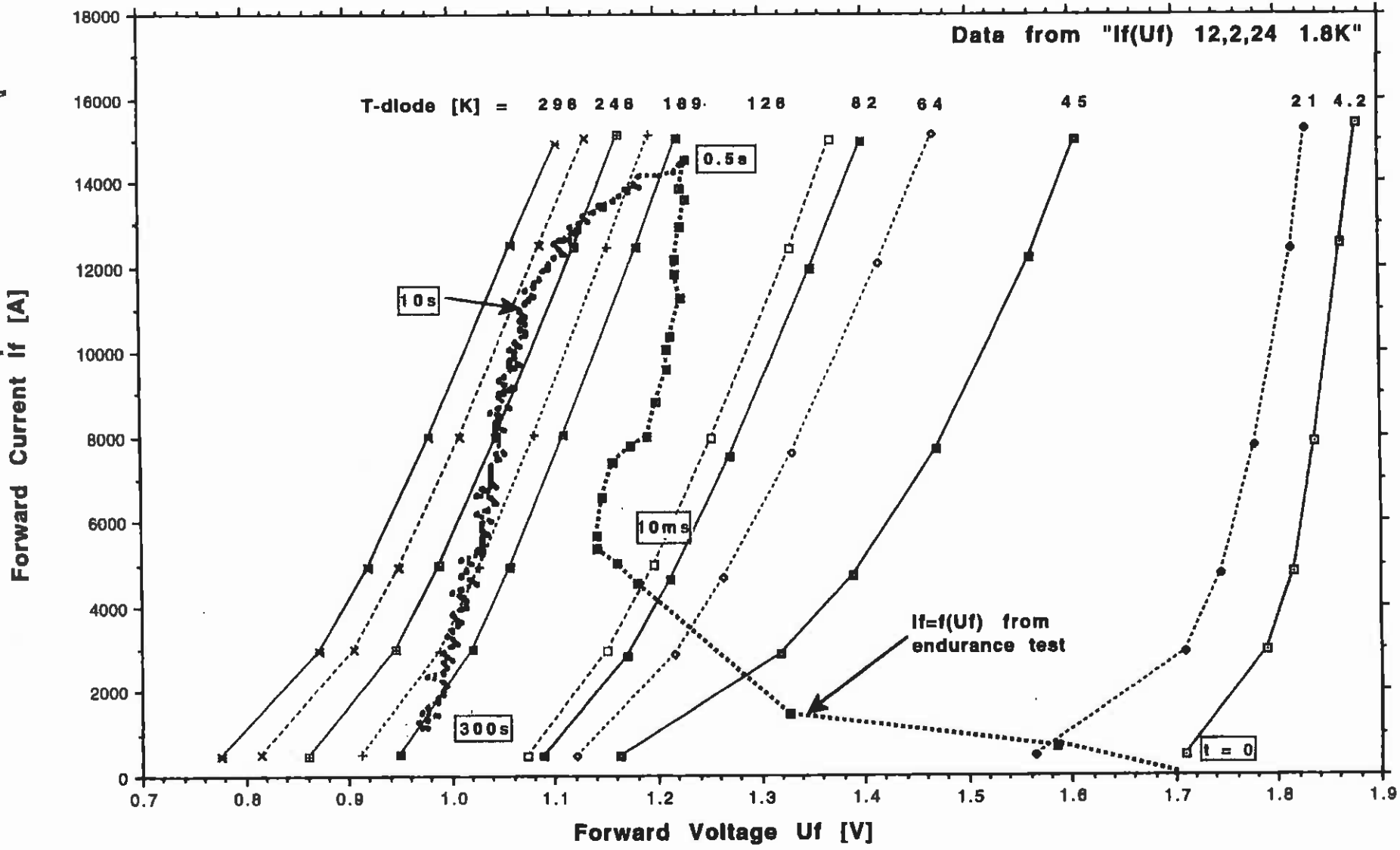

Measured current-voltage characteristic If(Uf) of an Epitaxial Diode at different temperatures and during an endurance test

CASE OF FAST CYCLING MACHINES

– In the case of the Tevatron, which has a short current ramp time resulting in large inductive voltages across the bypass elements, the diodes are replaced by thyristors operating as fast switches.

The thyristors are located outside the magnet cryostats and require additional power leads and cryogenic feedthroughs.

STRING TEST

– As for the cryogenic system, the protection system of a magnet ring must be carefully designed and thoroughly tested before starting up the machine.
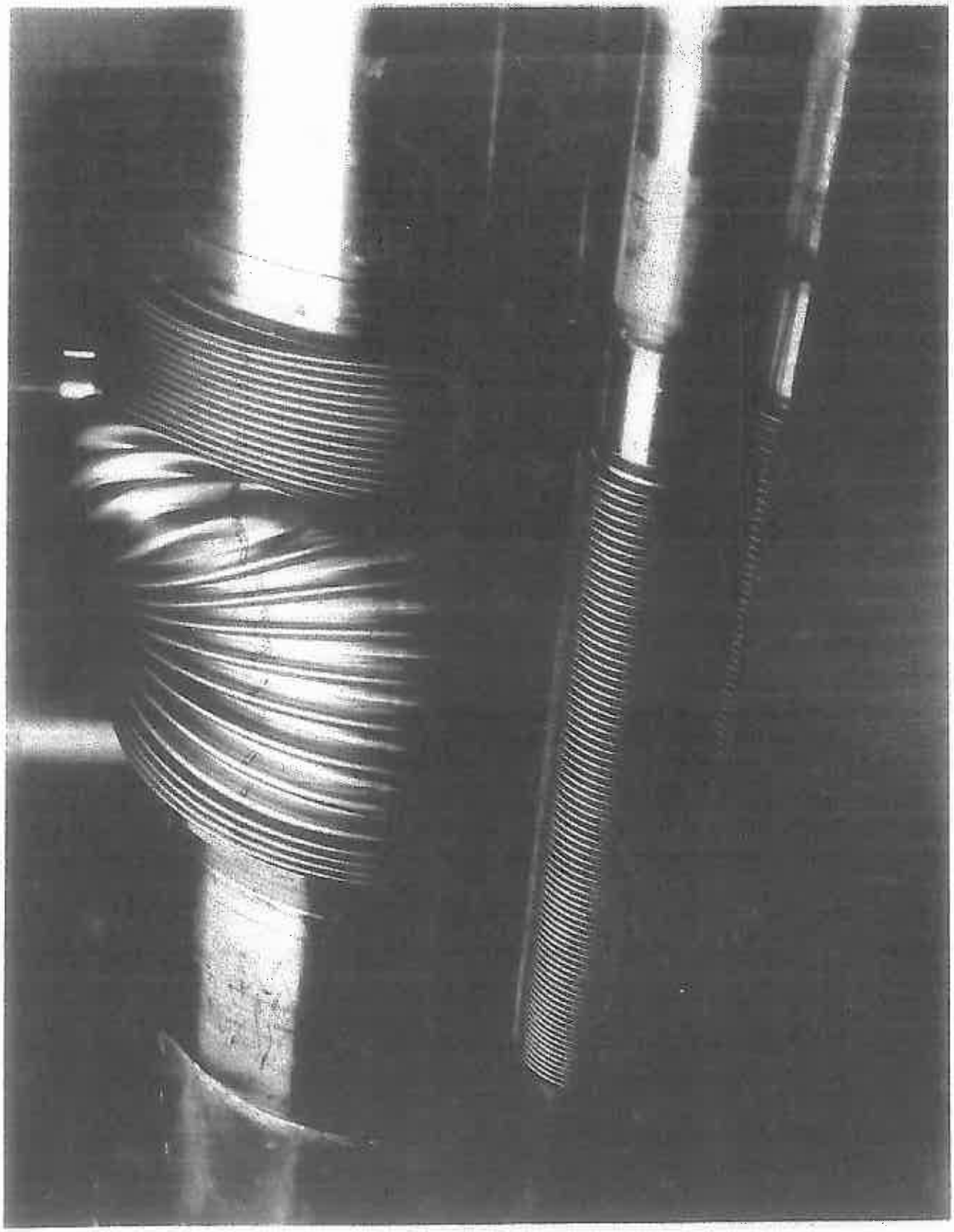
The system tests are usually carried out on a cell or a half-cell representative of the magnet lattice and all failure modes are investigated